UNIVERSITE DE NICE-SOPHIA ANTIPOLIS – UFR Sciences

Ecole Doctorale Sciences Fondamentales et Appliquées

THESE

Pour obtenir le titre de

Docteur en Sciences

de l'Université de Nice-Sophia Antipolis

Spécialité : Sciences de la Terre et de l'Univers – Géophysique

Présentée et soutenue par

Clément PERRIN

Relations entre propriétés des failles et propriétés des forts séismes

Relations between fault and earthquake properties

Thèse dirigée par Isabelle MANIGHETTI et Bertrand DELOUIS

Préparée au laboratoire Géoazur, Sophia Antipolis

Soutenue publiquement le 11 juillet 2014 devant le jury composé de :

Michel BOUCHON	Directeur de Recherche (CNRS, ISTerre)	Rapporteur
Bertrand DELOUIS	Professeur (UNS, Géoazur)	Co-Directeur de thèse
Anne DESCHAMPS	Directeur de Recherche (CNRS, Géoazur)	Examinateur
Yves GAUDEMER	Professeur (UPD, IPGP)	Examinateur
Isabelle MANIGHETTI	Physicien des Observatoires (OCA, Géoazur)	Directeur de thèse
Christopher SCHOLZ	Professeur (Columbia Univ., LDEO)	Rapporteur
Paul TAPPONNIER	Professeur (NTU, Earth Obs. of Singapore)	Examinateur

Abstract

My objective was to examine the relations between the properties of the long-term geological faults, and the properties of the large earthquakes produced by these faults. For 26 large (Mw ≥ 6.4) historical continental earthquakes of various locations and slip modes, I have analyzed satellite imagery to map the entire traces of the long-term faults along with the associated fault networks. This provided me information on the fault slip mode, sense of long-term lateral propagation, lateral segmentation, nature of the zones between the fault segments. For 21 of these earthquakes, I have jointly analyzed the seismological information available in the literature (Mw, M0, rupture length, width, coseismic slip distribution, moment release function, duration, etc) and mapped the rupture traces to identify which long-term fault segments broke. This coupled fault and earthquake information forms the core data of my work. I have complemented these data with information on various static earthquake parameters available in the literature for 50 more large historical earthquakes (continental and subduction), with earthquake surface slip-length data available on ~230 continental earthquakes, and with tectonic information available for ~50 of the broken long-term faults. The combined analysis of the faults and earthquakes data shows that: i) Long-term faults have a number of generic properties, i.e., properties independent on fault size, slip mode, location, among which, a similar arrangement of the fault networks, a similar lateral segmentation of the fault traces, a similar form of cumulative slip distribution; ii) Faults evolve in space and time as they accumulate more slip and grow in length, and this evolution can be described as the fault structural maturity. I provide scaling relations between fault parameters to qualify the degree of structural maturity of the faults; iii) Large earthquakes also share common, generic properties, among which a similar coseismic slip-length and slip-width slip profile, a similar decrease in rupture width along the rupture length, a similar number of broken segments, a similar stress drop on the broken segments, a similar relative distance between hypocenter and zone of maximum slip; iv) Some of the long-term fault properties govern some of the large earthquake properties. The structural maturity of the faults is the tectonic property most impacting the behavior of large earthquakes. It plays a role in the location of the earthquake initiation; it defines the fault section where the maximum coseismic slip develops, and governs the maximum amplitude of that slip, as the direction of the coseismic slip decrease; it dictates the number of major fault segments that are broken, and hence it controls the rupture length and its overall stress drop; it plays a role on the rupture propagation efficiency and speed. The structural maturity likely acts in reducing both the static friction and the geometric complexity of the fault plane. My results therefore suggest that the earthquake source models should be modified to integrate the structural maturity of the broken faults along with related properties such as lateral fault segmentation, 3D fault architecture and heterogeneous state of the crustal medium around faults. Large earthquakes should also be considered as 3D multi-segment ruptures, therefore having a variable stress drop over the broken area, a variable focal mechanism along the rupture length, a variable rupture speed, A 3D strain and stress distribution. To understand the behavior and the physics of earthquakes, it seems inescapable to analyze jointly the tectonic properties of the broken faults and the seismological properties of the earthquakes.

Résumé

Mon objectif était d'examiner les relations entre les propriétés des failles géologiques long-termes et les propriétés des forts séismes que produisent ces failles. Pour 26 forts (Mw≥6.4) séismes historiques survenus en des lieux différents et ayant des modes de glissement variables, j'ai cartographié, sur la base de l'analyse d'images satellitaires, la totalité du système de faille sur lequel s'est produit l'événement. Cette analyse morpho-tectonique m'a apporté des informations sur le mode de glissement, la direction de propagation long-terme et la segmentation latérale des failles analysées. Pour 21 de ces séismes, j'ai conjointement analysé les données sismologiques disponibles dans la littérature (Mw, M0, longueur et largeur rompues, distributions de glissement co-sismique, durée de la rupture, fonction source, etc) et cartographié les traces de rupture en surface afin d'identifier quels segments de la faille long terme ont rompu. Cette information couplée faille-séisme pour 21 événements historiques forme les données de base de mon travail. J'ai complété ces données avec des informations sur divers paramètres statiques des séismes disponibles dans la littérature pour 45 forts séismes historiques supplémentaires (intra continentaux et de subduction), avec des données de déplacement-longueur disponibles pour ~230 séismes continentaux, et avec des informations tectoniques sur une cinquantaine des failles long-termes rompues par les séismes analysés. L'analyse combinée des failles et des séismes montre que : i) les failles long-termes ont un certain nombre de propriétés génériques, c'est-à-dire des propriétés indépendantes de leur taille, de leur mode de glissement, de leur localisation, parmi lesquelles : une organisation similaire des réseaux de failles, une segmentation latérale similaire des tracés de failles, une forme similaire de distribution du glissement cumulé le long des failles ; ii) les failles évoluent dans l'espace et dans le temps et cette évolution peut être décrite par le concept de « maturité structurale ». J'ai établi des lois d'échelle entre certains paramètres des failles long-termes (tels que longueur, âge, déplacement maximum cumulé, vitesse de glissement) et ces lois permettent de qualifier le degré de maturité structurale des failles; iii) les forts séismes partagent également des propriétés communes, indépendantes de leur magnitude, de leur mode de glissement, de leur contexte, tels que : une forme similaire de distribution du glissement cosismique le long des ruptures, en surface comme en profondeur ; un nombre semblable de segments rompus ; une chute de contrainte similaire sur chaque segment majeur rompu ; une distance relative similaire entre hypocentre et zone de glissement maximum ; iv) Certaines propriétés des failles long-termes gouvernent clairement certaines propriétés des forts séismes. La maturité structurale des failles est la propriété tectonique qui impacte le plus le comportement des forts séismes. Il est probable qu'elle diminue la friction statique et la complexité géométrique du plan de faille. De fait, elle contrôle en partie la localisation de la zone d'initiation du séisme ; elle définit la section de faille sur laquelle se produit le glissement co-sismique maximum ; elle contrôle l'amplitude maximum du glissement cosismique, ainsi que la direction de décroissance de ce glissement; elle dicte le nombre de segments majeurs qui peuvent être rompus par l'événement, et par conséquent, elle contrôle la longueur totale et la chute de contrainte globale de la rupture; elle contrôle la « capacité » de la rupture à se propager et gouverne ainsi sa vitesse de propagation. Mes résultats suggèrent donc que les modèles de source des séismes devraient être modifiés pour intégrer la maturité structurale des failles rompues ainsi que les propriétés connexes comme la segmentation latérale des failles, leur architecture 3D et l'hétérogénéité du volume crustal autour des failles (propriétés inélastiques). Les forts séismes devraient aussi être considérés comme des ruptures 3D multi-segments, ayant donc des chutes de contraintes variables sur la surface rompue, un mécanisme au foyer et une vitesse de rupture également variables le long de la rupture, et une distribution 3D des contraintes et des déformations cosismiques. Pour comprendre le comportement et la physique des forts séismes, il semble donc indispensable d'analyser conjointement les propriétés des failles rompues et les propriétés des séismes produits.

Remerciements

Au terme de ces quatre années, je souhaiterais remercier tous ceux qui m'ont accompagné et soutenu de près ou de loin dans cette aventure (ou « galère » diront certains) qu'est la thèse. Collègues, familles, amis et plus, ces lignes sont pour vous !

Je tiens tout d'abord à remercier ma directrice de thèse, Isabelle Manighetti, qui a proposé ce beau sujet de thèse, et qui m'a transmis sa passion pour « les failles et leurs copines ». Merci à toi, Isabelle, pour toutes ces discussions captivantes sur les failles, pour les prises de têtes sur certains séismes et les nombreux graphs, pour ta disponibilité et ton énergie débordante, de m'avoir permis de voir des failles de tailles XXL, sachant mon goût pour le terrain, du Mexique jusqu'en Nouvelle Zélande, pour les coups de stress aux moments opportuns, pour ton soutien sans failles (et sans mauvais jeu de mots) durant les étapes difficiles de la thèse, et il y en a eu !

Je tiens également à remercier mon co-directeur Bertrand Delouis, pour sa gentillesse et sa patience à m'expliquer les rouages des modèles d'inversions de la source. Merci également pour les quelques notes de musiques échangées en salle de conférence en compagnie de Sébastien Migeon et Maurin Vidal.

Je remercie Yves Gaudemer de m'avoir si bien accueilli à l'IPGP au début de ma thèse et d'avoir accepté de faire partie de mon Jury de thèse. Merci pour sa disponibilité et pour m'avoir initié « aux joies » de la programmation sous Matlab.

J'en profite pour remercier l'ensemble de mon Jury de thèse de me faire l'honneur de leur présence. Merci donc à Michel Bouchon, Anne Deschamps, Yves Gaudemer, Christopher Scholz et Paul Tapponnier.

Je remercie aussi l'ensemble du laboratoire Géoazur pour m'avoir accueilli chaleureusement à mon arrivée à Nice durant ses quatre belles années sous le soleil azuréen.

La thèse, c'est dur. Mais quand même, on n'est pas seuls dans cette galère, et je suis ravi d'avoir pu compter sur mes collègues et amis qui m'ont soutenu et supporté pendant toutes ces années.

Merci à mes co-bureaux d'hier et d'aujourd'hui, avec qui ces années ont été un réel plaisir à partager. Un grand merci à Elodie Delor, pour son aide précieuse et sa bonne humeur déterminantes en fin de thèse; à Alain Dujardin, pour les petits pains nourrissants du midi et nos « Tu te casses sur Mars »; à Clara Castellanos, pour nos nombreuses « discucións » sur le ciné, le vin… ; à Tran Dinh Trong pour son sourire à toute heure de la journée et nos discussions sur la musique ; à Flore Barat, pour les recherches inutiles du midi et les concours fumeux ; à Aurélien Bigot, le roi d'Er Mapper !; à Elodie Boucher, ma first co-bureau.

Merci à mes co-voitureurs d'avoir fait que les trajets Nice-Sophia soient des plus agréables (surtout au milieu des bouchons !). Merci donc à Quentin Bletery (le maître de « Tohoku »), Marc Hässig (compagnon de galère depuis le début !), mais aussi Olivier Cavalié, Thomas Maurin, Louis de Barros, Bruno Wilhelm… et tous ceux qui ont pu profiter de la super 5 jaune !

Je remercie également tous les thésards et amis de Géoazur que j'ai pu rencontrer au cours de ma thèse : à commencer par Benoit Derode, pour ses conversations (ou monologues ?) anthologiques et son aide précieuse en début de thèse. Merci à Swann, Victorien, Nestor, Clément V., Alice, Marianne M., Yevgeniya, Imane, Stephen, Edouard, Jeremy, Eduardo, Ingke (nickéooooo !!!), Adrien, Vincent, Sadrak, Maëlle, Chloé, Virginie, Marianne C., Erell, Côme, Maud, Yaser, Juan Carlos, Battulga, Dong….je suis sûr d'en oublier et je m'en excuse par avance !

La thèse a été aussi l'occasion de faire de l'enseignement, et je tiens à remercier l'ensemble du département TEE. Merci entre autres à Chrystelle Verati, Gérard Giannerini, Christophe Renac, Yann Rolland, Riad Hassani et tous les autres membres de l'équipe enseignante. Un merci tout particulier à ma « collègue » et amie Julie Schneider, je me souviendrai longtemps de mes débuts en tant que moniteur à tes côtés ! « -Bonjour je cherche Julie Schneider, qui enseigne la pétrologie magmatique » «-Ouais, c'est moi ». Merci pour tous ces bons moments passés sur Nice. J'en profite pour remercier Bruno Scalabrino et Agathe Deleau pour leur soutien tip-top en fin de thèse, et la petite bière qui remonte le moral ! Merci à Lucie Orsoni et Eric Ory pour la bière, le fromage et les barbeucs sur les hauteurs de Nice !

Un énorme merci à toute ma famille et tous mes amis des quatre coins de la France, du Cantal jusqu'à Paris, en passant par Montpellier, la Haute Savoie, Besançon et Lyon... Et oui Nice c'est beau mais c'est loin. Nous n'avons pas eu l'occasion de se voir souvent mais promis je vais rectifier ça ! Il me tarde de partager à nouveau pleins de bons moments avec vous tous !

Ai-je oublié quelqu'un ? Plutôt quelqu'Une…et non la moindre: celle qui m'a permis de tenir quatre longues années mais surtout celle qui a tenu le coup admirablement durant quatre longues années ! Celle qui a poussé le vice jusqu'à faire quelques courtes nuits au labo en ma compagnie pour finaliser cet imposant manuscrit ! Merci à toi, Elise, d'exiger de moi le meilleur et de m'avoir fait autant avancer. J'espère être à la hauteur pour te rendre la pareille !

Sommaire

CHAPTER I. INTRODUCTION I–1

1. The general question to be addressed in this work I–2

2. The general "ingredients" of the present vision of earthquakes I–8

CHAPTER II. CONSTRUCTION OF A FAULTS & HISTORICAL EARTHQUAKES DATABASE II–19

1. Principles to construct the Faults & Earthquakes databases II–20

2. Fault-Earthquakes extended ID II–40

2.1. Baja California 2010 II–40
2.2. Bogd 1957 II–57
2.3. Borah Peak 1983 II–66
2.4. Borrego Mountain 1968 II–83
2.5. Denali 2002 II–96
2.6. Dixie Valley & Fairview Peak 1954 II–117
2.7. Fort Tejon 1857 II–135
2.8. Fuyun 1931 II–155
2.9. Hebgen Lake 1959 II–167
2.10. Hector Mine 1999 II–177
2.11. Imperial Valley 1940 & 1979 II–197
2.12. Kunlun 2001 II–214
2.13. Landers 1992 II–227
2.14. Manyi 1997 II–248
2.15. Pleasant Valley 1915 II–261
2.16. San Francisco 1906 II–271
2.17. Sichuan 2008 II–284
2.18. Superstition Hills 1987 II–302
2.19. Yushu 2010 II–317
2.20. Historical earthquakes on the North Anatolian Fault: 1939 Erzincan, 1943 Tosya, 1944 Bolu Gerede, 1999 Izmit and 1999 Duzce earthquakes II–334

3. Other Faults and Earthquake data II–341

4. Short, preliminary synthesis II–342

CHAPTER III. ASYMETRY OF COSEISMIC SLIP PROFILES : A GENERIC PROPERTY TIGHTLY CONTROLLED BY THE EARTHQUAKE PROCESS III–355

1. Overall shape of earthquake slip profiles and degree of asymmetry III–357

2. Relation between asymmetry of earthquake slip profiles and rupture length and width III–364

3. Relation between asymmetry of earthquake slip profiles and earthquake stress drop III–365

4. Relation between asymmetry of earthquake slip profiles and number of broken fault segments III–369

5. Relation between asymmetry of earthquake slip profiles and rupture width III–378

6. Relation between asymmetry of earthquake slip profiles and structural maturity of the broken fault III–390

7. Relation between asymmetry of earthquake slip profiles and direction of long-term lateral propagation of the ruptured faults III–393

8. Relation between asymmetry of earthquake slip profiles and hypocenter position III–401

9. Relation between asymmetry of earthquake slip profiles and off-fault strain diffusion III–405

CHAPTER IV. WHICH SCALING RELATIONS TO DESCRIBE THE EARTHQUAKE « SIZES » ? IV–411

1. Earthquake slip-length scaling IV–412

2. Examining scaling relations between basic earthquake parameters IV–426

3. Examining a few scaling relations expected from the theoretical elastic framework IV–437

4. Estimating the earthquake stress drop IV–448

CHAPTER V. MODELING THE ASYMETRIC EARTHQUAKE SLIP PROFILES V–457

Introduction V–459

1. Model set-up V–463

2. Model results V–468

3. Discussion V–475

4. Conclusions V–481

Acknowledgements V–483

References V–483

CHAPTER VI. INITIATION AND ARREST OF EARTHQUAKE RUPTURES DESCRIBED BY EMPIRICAL RELATIONS VI–493

1. Questions posed VI–494

2. Approach to perform the measurements VI–495

3. Measurements **VI–496**
3.1. 2010 Baja California earthquake VI–496
3.2. 1957 Bogd earthquake VI–496
3.3. 1968 Borrego Mountains earthquake VI–497
3.4. 1983 Borah Peak earthquake VI–497
3.5. 2001 Denali earthquake VI–498
3.6. 1954 Dixie Valley earthquake VI–499
3.7. 1954 Fairview Peak earthquake VI–499
3.8. 1857 Fort Tejon earthquake VI–500
3.9. 1931 Fuyun earthquake VI–500
3.10. 1959 Hebgen Lake earthquake VI–501
3.11. 1999 Hector Mine earthquake VI–501
3.12. 1940 Imperial Valley earthquake VI–502
3.13. 1979 Imperial Valley earthquake VI–502
3.14. 2001 Kunlun earthquake VI–503
3.15. 1992 Landers earthquake VI–503
3.16. 1997 Manyi earthquake VI–504
3.17. 1915 Pleasant Valley earthquake VI–504
3.18. 1906 San Francisco earthquake VI–505
3.19. 2008 Sichuan earthquake VI–505
3.20. 1987 Superstition Hills earthquake VI–506
3.21. 2010 Yushu earthquake VI–506

4. Empirical relations and discussion **VI–507**
4.1. Rupture arrest: not anywhere on the broken fault VI–507
4.2. Propagation/arrest: which W and γ absolute values, and for which reasons? VI–510
4.3. The relative importance of W on the broken fault VI–522
4.4. Rupture initiation VI–529
4.5 Synthesis of major results VI–533

CHAPTER VII. SYNTHESIS OF MAJOR RESULTS, DISCUSSION AND PERSPECTIVES **VII–535**

1. Synthesis of major results **VII–536**

2. Discussion of a few implications **VII–540**

3. Perspectives **VII–550**

CONCLUSIONS **VII–553**

REFERENCES **VII–557**

CHAPTER I. INTRODUCTION

1. The general question to be addressed in this work

Moderate to large earthquakes (Mw ≥ 5.5-6) of tectonic origin represent a risk for our societies and environments since they have the capacity of damaging human infrastructures and of killing people. Figures 1 to 5 synthesize the major problems posed by large earthquakes (referred to as EQs in the following; note that I will use "large" for EQs with Mw ≥ ~6): 1) many large EQs occur every day in the world (Fig.1); 2) EQs may be expensive (Fig.2); 3) EQs may be deadly (Fig.3); 4) thus, large EQs could cause a recession (Fig.4); 5) EQs are a challenging scientific problem (Fig.5).

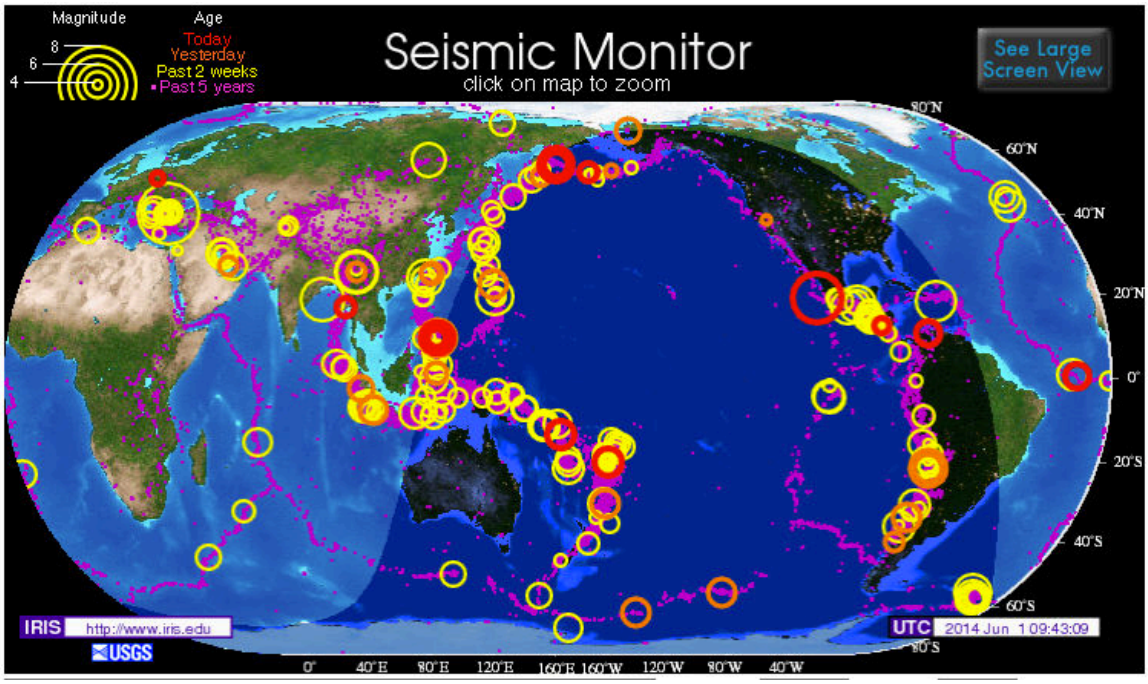


Fig. 1: World seismicity on 1st June 2014 (from http://www.iris.edu/seismon/)

Indeed, despite of the bulk of studies which have been conducted on EQs over the last century and especially in the last few decades, and despite the fact that many founding results have been found (among founding papers: Eshelby, 1957; Knopoff, 1958; Richter, 1958; Haskell, 1964; Aki, 1967; Scholz, 1968, 1982, 1989, 2002; McKenzie, 1969; Brune, 1970; Kanamori & Anderson, 1975; Kanamori, 1977; Madariaga, 1976; Bouchon and Aki, 1977; Sibson, 1977; Hanks and Kanamori, 1979; Rice, 1980; Aki and Richards, 1980; Das, 1981, 2003; Kanamori and Brodsky, 2004; Kagan, 2013) we still do not completely understand the physics of EQs. As a matter of fact, we still cannot anticipate exactly the place, the time nor the size of the forthcoming events (e.g., Kagan, 2007).



Fig. 2: Tsunami damage - Tohoku Japan earthquake of March 2011. 9000 deaths $300 billion of economic losses (Source : Insider Quarterly)

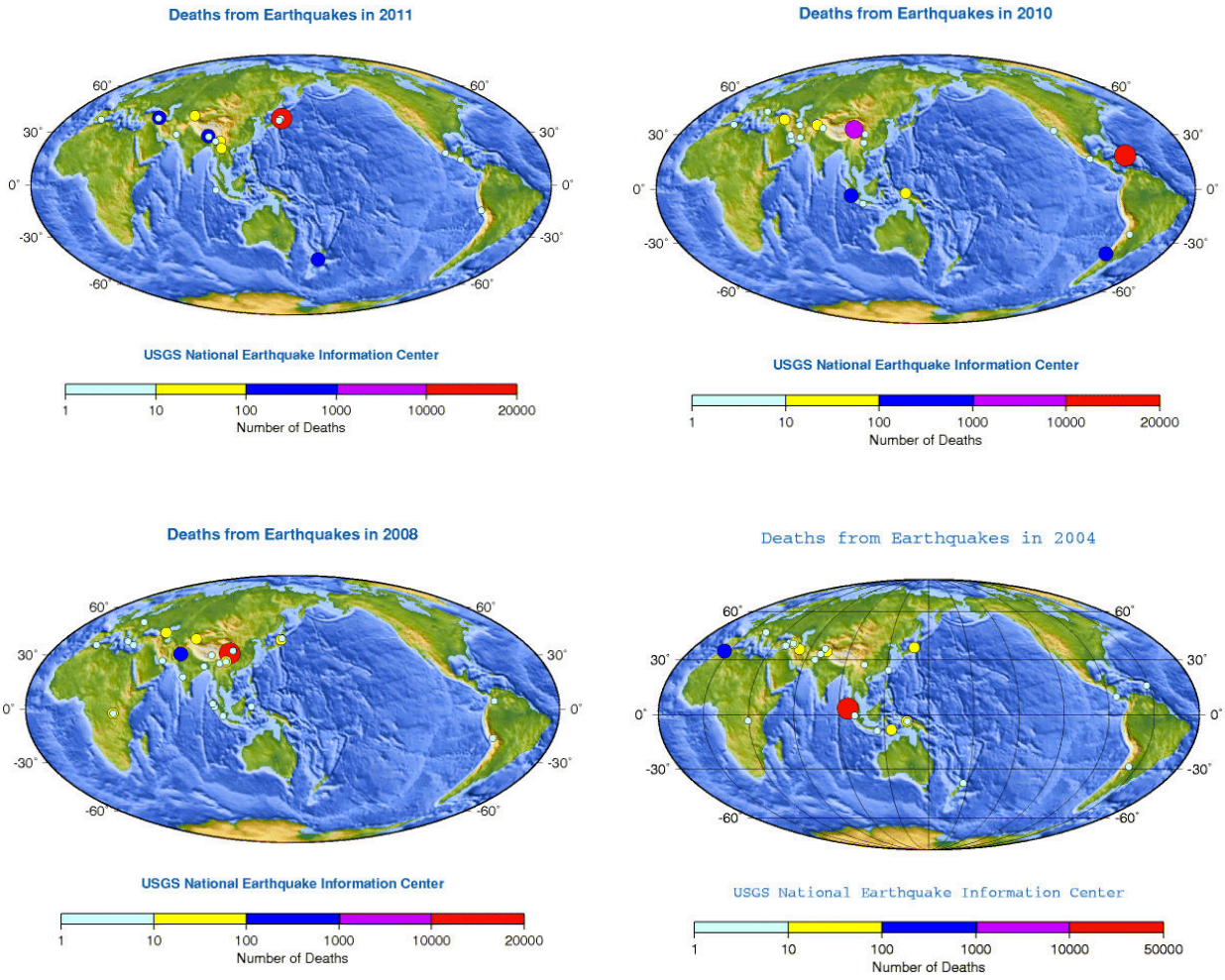


Fig.3: World map of deaths in earhquakes in 2011, 2010, 2008 and 2004, most due to the Tohoku Japan, Haïti, Sichuan and Sumatra EQs, repectively (USGS).

It results that every large EQ that occurs worldwide is a partial or complete surprise, having consequently dramatic effects. For instance, in the last few years, the 03/11/2011 Tohoku

Japan earthquake (Mw 9.1) has reminded us that we are still unable to properly anticipate the magnitude of the largest events. The 09/28/2004 Parkfield moderate EQ (Mw 6.0) has shown that the EQ occurrence models that have been developed (characteristic, and slip- and time-predictable models; e.g., Shimazaki and Nakata, 1980; Schwartz and Coppersmith, 1984) are not appropriate since they could not be used to correctly anticipate the time and size of the Parkfield EQ (e.g., Langbein et al., 2006; Murray and Langbein, 2006). The sequence of EQs in the Christchurch area, New Zealand (09/03/2010 Mw 7.1; 02/22/2011 Mw 6.3; 06/13/2011 Mw 6.0; 12/23/2011 Mw 5.8), has shown us that our present knowledge of the EQ sources – namely the seismogenic faults, is incomplete since the faults which broke in the Christchurch sequence had not been identified before the EQs.

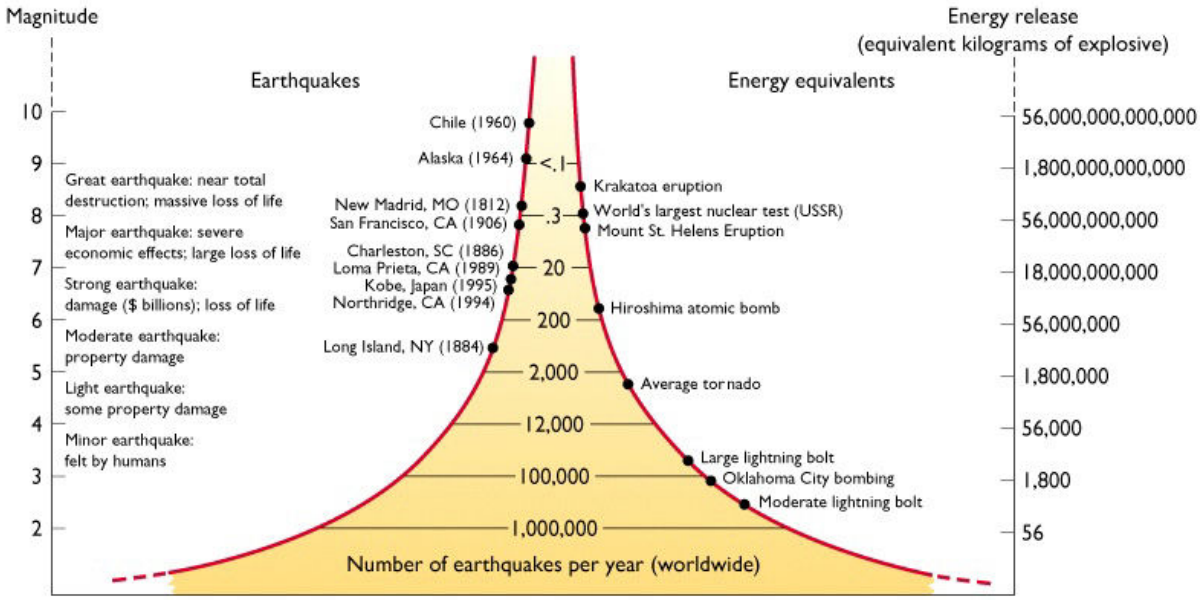


Fig.4 : Size of earthquakes and energy equivalents. Billion dollar losses are reported for large earthquakes (Mw>6). This diagram was produced in cooperation with the USGS and the University of Memphis.

The fact that every large EQ is a surprise, at least partial, poses the following question: does the surprise come from the fact that every EQ is singular and hence basically different from any other one, or does the surprise come from the fact that our understanding of EQs is still incomplete? In the former case where all EQs are different from one another, no anticipation will ever be possible, whereas, in the later case, there still exists a chance that our understanding of EQs gets improved up to a possible capacity to properly anticipate the forthcoming events.

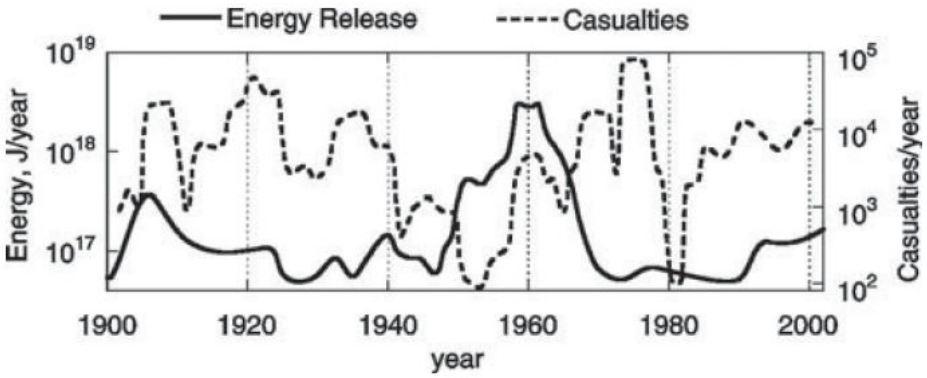


Fig.5: Energy release and casualties (number of deaths) per year during the 20th century (from Kanamori and Brodsky 2004). Casualties from EQs are not necessarily correlated to magnitude or overall level of seismicity. They are more closely related to the engineering infrastructures and preparedness of a region.

One way to answer the above questions is to examine a dense population of different EQs – different in size, slip mode, date, location, etc., and check whether or not these various EQs share any common properties. If it is found that every EQ has its own specific properties, no anticipation will ever be possible. But if it is found that at least some EQs share some common properties, then it might be thought that a common physics governs these common properties. Hope might thus be restored that such a common physics might be eventually understood and used as a solid basis to anticipate some of the properties of the forthcoming large EQs.

Hundreds of large EQs have occurred worldwide over the last decades. Most of them have been well recorded, with an increasing amount and variety of high-resolution data (seismological, geodetic, satellite, field observations). These data generally allow to recover most of the major properties of the events, especially their static properties: magnitude, location, hypocenter position, rupture length and width, coseismic slips at depth and surface, seismic moment, rupture duration, rupture speed, etc.

A first part of my PhD work has consisted to analyze a dense population of historical large EQs to examine whether these EQS would share common properties, that is would show source properties independent on the EQ magnitude, slip mode, location, tectonic context, etc. Such properties that might be found independent on the scale are called **"generic properties"** (e.g., Manighetti et al., 2001, 2005, 2007, 2009) and can be described by so-called **"scaling laws"**. I have extracted those properties from the dense information available

in the literature. The source properties, which I have most examined, are the rupture size (length, width, slip amplitude and distribution, magnitude, seismic moment), location, slip mode. **My approach is fundamentally empirical**.

Whatever their location, magnitude, context etc, all tectonic EQs occur on long-term geological faults, that is faults which have been existing and slipping for long prior to the EQ, over periods of time varying from a few thousands of years to tens of millions years. This is why these faults are called **"long-term faults"**: this is to say that, contrary to an EQ rupture which occurs in a few seconds to minutes, the fault that holds and generates the rupture has got a previous slip history that might have lasted thousands of years to millions of years. It is indeed extremely rare that an EQ would produce a new fault; this might only happen for very small faults and hence very small EQs. Rather, most EQS and all large EQs occur on pre-existing long-term faults, and thus are a process most concerned with friction than with rock fracturing (e.g., Scholz, 2002; Kanamori and Brodsky, 2004). The long-term faults that produce EQs are all different, for they have their own history of slip, with a proper age of initiation, a proper slip rate, a proper lateral propagation rate (i.e., rate at which the fault lengthens laterally over time, e.g., Manighetti et al., 1997, 1998, 2001a-b; Hubert-Ferrari et al., 2003), and, consequently, a proper size (especially length and amount of accumulated slip, called "cumulative slip").

A second part of my PhD work has consisted to analyze the long-term faults responsible for the historical large EQs I had examined earlier, with two objectives in mind:

1) Determine whether or not the long-term faults have common, generic properties;

2) Examine whether these properties have some impacts on the properties of the large EQs these faults produce.

I have analyzed the fault properties both from the dense information available in the literature, and from a precise fault mapping which I have performed using satellite images and topographic data. The fault properties which I have most examined are the fault overall architecture in map view (including associated secondary fault networks), the fault size (length, width, cumulative slip), the fault lateral segmentation, the slip mode, the slip rate, the age of initiation, the sense of lateral fault lengthening over the long-term. **My approach is here again fundamentally empirical**.

I suggest that my work is fairly original on three major points:

1) So far, most large EQs have been studied in case-by-case approaches, that is every EQ is analyzed in great details, yet independent on the others. Many papers then exist that analyze a given EQ in detail, but very few perform this analysis in the framework of the knowledge of the other historical events. Exceptions exist however which analyze dense populations of EQs (e.g., Kagan, 1994, 2004, 2013; Sommerville et al., 1999; Mai and Beroza, 2000; Manighetti et al., 2005, 2007; Wesnousky, 2008; Hecker et al., 2010 ; Schmedes et al., 2010). But most of these studies, either consider instrumental earthquake data taken as a whole with no particular attention to the EQ sources (such as studies analyzing the space-time distribution of instrumental EQs of all magnitudes, e.g., Kagan, 1994, 2004), approach the source information globally in a statistic manner that does not integrate any other complementary observation (such as a fault information; e.g., Sommerville et al., 1999; Mai and Beroza, 2000), or focus their attention on one source parameter only (ex: slip-length ratio, e.g., Shaw and Sholz, 2001; Manighetti et al., 2007; Shaw, 2013 and references therein).

2) So far, most EQs have been analyzed with few or no combined study of the long-term faults broken by the EQs. Many papers actually appear as treating the EQ as if it was an independent phenomenon, disconnected from the long-term fault which produced it. It is thus fairly rare to find studies that analyze both the EQ and the broken fault in the same details. And when the fault is analyzed, it is generally examined only in its ruptured section, whereas the long-term fault actually involved in the EQ is much longer that this broken section.

3) I am basically a geologist, not a seismologist. While this sometimes provided me some difficulties in understanding the seismological implications of my observations, the good part of it is that, on the one hand I could have a different, “simplifying” vision of the EQs, and on the other hand, thanks to my expertise of long-term faults, I had the capacity of looking at the two features –faults and EQs, together.

For reasons of time, I have mainly focused my analysis on intracontinental EQs which can be observed more directly and more “entirely”. However, I have also considered subduction EQ for many of the aspects that I will discuss in the following.

2. The general "ingredients" of the present vision of earthquakes

The objective of this section is not to provide a seismology class, but more simply to emphasize the principal pieces of knowledge that relate to the EQ (and some of the fault) properties that I will analyze in the rest of the work.

First, **the empirical observation of EQs show that they obey to a number of scaling laws** (e.g., Scholz et al., 1986, 2002; Kanamori and Brodsky, 2004) (Fig.6). Let's first recall that the most robust parameter to quantify the EQ size is the seismic moment M0 (in Nm). The seismic moment is a direct, well-constrained measure of the amount of radiated energy, and hence it does not depend on the response of a seismograph. It is computed from the source spectra of body and surface waves. As such, it is the most reliably determined EQ source parameter (e.g., Kanamori and Anderson, 1975; Kagan, 2007). When this M0 parameter is faced to a number of other source parameters, empirical scaling laws are found as illustrated in Fig.6: M0 appears to increase as a function of the rupture length (Scholz et al., 1986), but also as a function of the broken surface (Kanamori and Brodsky, 2004), of the mean displacement produced (Wells and Coppersmith, 1994), and of the EQ duration (Kanamori and Brodsky, 2004). On the other hand, the mean coseismic slip also appears to increase fairly regularly with the rupture length (Fig.7; Wells and Coppersmith, 1994). The EQ stress drop, which can be estimated either from M0, from the EQ slip to length ratio, or from energetic considerations (See details in Noda et al., 2013) appears to be roughly constant among all EQs worldwide, in the range 0.1-10 MPa, regardless of their magnitude, slip mode, context, etc (e.g., Ide and Beroza, 2001; Fig.8; references on the figure). Only the smallest EQs might have a different stress drop (e.g., Abercrombie, 1995; Prejean and Ellsworth, 2001), but this suggestion is under debate. Very large EQs have also been suggested to have a different, larger stress drop than the other EQs (See discussion in Shaw, 2009). When now looking at the EQ space-time distribution, it is observed that EQs increase in number as a power-law as their size decreases. This dependence is described as the Gutenberg-Richter (GR) relation (Fig.9, Ishimoto and Iida, 1939, Gutenberg and Richter, 1944, Kagan, 1994; Kanamori and Brodsky, 2004). An amazing output of this empirical scaling relation is that about one EQ with $M \geq 8$ occurs every year in the world (Fig.9). When the EQs considered are the aftershocks of a mainshock, it is also observed that the aftershock rate decays as a power law with time (Fig.10, Omori, 1894, Utsu, 2002; Kagan 1994). The existence of these empirical

scaling laws suggest that the EQ occurrence and behavior are not random, but rather obey specific, well-defined and likely physically-based laws. Furthermore, as pointed out by Kanamori and Brodsky (2004), "**the robustness and ubiquity of [these] laws tells us that at least parts of the earthquake process are insensitive to the microscopic physics that controls the failure, the friction, and the whole rupture**".

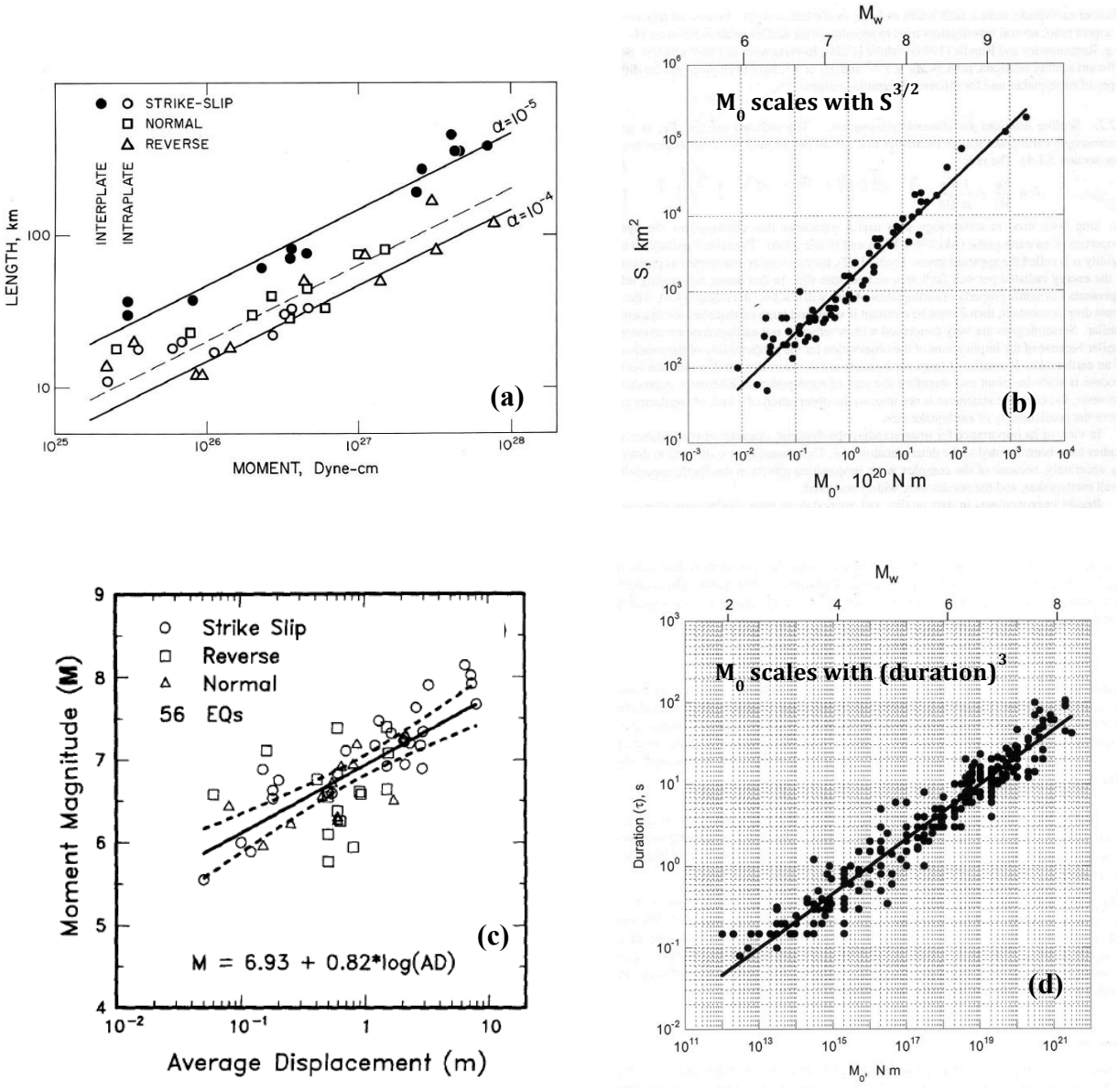


Fig.6: (a) Fault length versus seismic moment for interplate and intraplate earthquakes (10^{26} dyne.cm=10^{19} Nm) (Scholz et al., 1986) ; (b) M0 versus rupture area S for shallow earthquakes (Kanamori and Brodsky 2004 and references therein) ; (c) Mw versus average coseismic displacement (Wells and Coppersmith 1994) ; (d) M0 versus source duration for shallow EQs (depth <60 km) between 1991-2001 (Kanamori and Brodsky 2004).

This finding on EQs is somehow puzzling since both faults and EQs are complex features and phenomena. As I will describe it in more details later, faults are non-planar features, they likely have planes with variable rugosity and variable friction (e.g., Power et al., 1987; Kagan, 1994), they are segmented laterally at various scales (e.g., Segall and Pollard, 1980; Walsh et

al., 1999; Manighetti et al., 2009), they might be or not be associated with gouges (e.g., Marone, 1998), and they all are associated with many adjacent faults of different sizes and arrangements (e.g., Aviles et al., 1987; Scholz et al., 1993 ; Chester et al.,2003). Altogether these make faults 3D complex features. Similarly, EQs have variable slip and hence stress distributions (e.g., Kagan, 1994; Mai and Beroza, 2002; Liu-Zeng et al., 2005), they depend on microscopic friction, and their wave propagation much depends on the complexity of the medium around. Altogether these also make EQs 3D complex features. Therefore it is amazing that such combined complexities collapse and vanish to make EQs obeying a few universal-scaling laws.

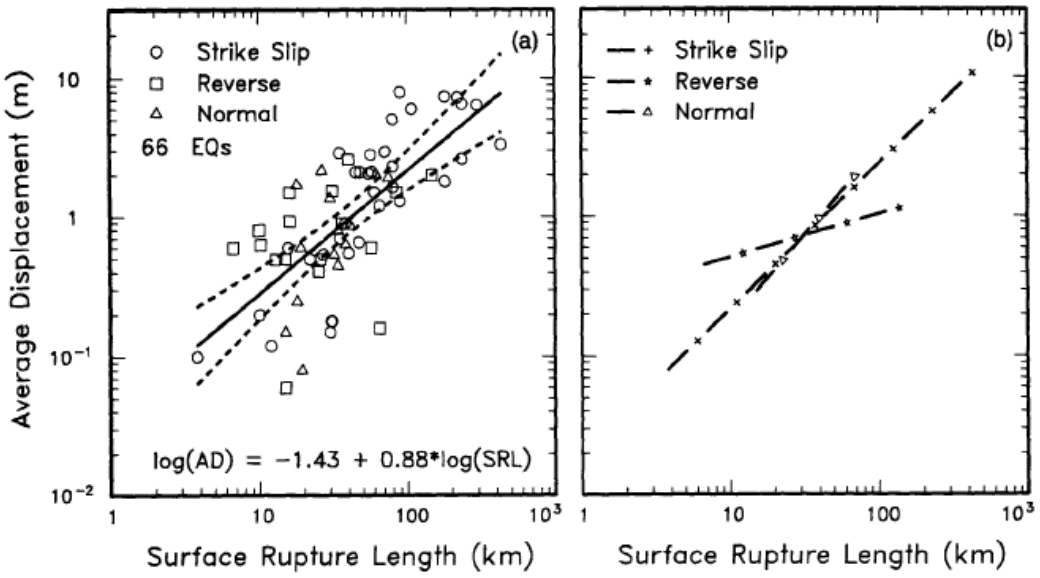


Fig.7: Surface rupture length versus average coseismic displacement at surface. Regressions shown for all-slip-type relationships. Short dashed line indicates 95% confidence interval. (b) Regressions for strike-slip, reverse, and normal ruptures (from Wells and Coppersmith 1994).

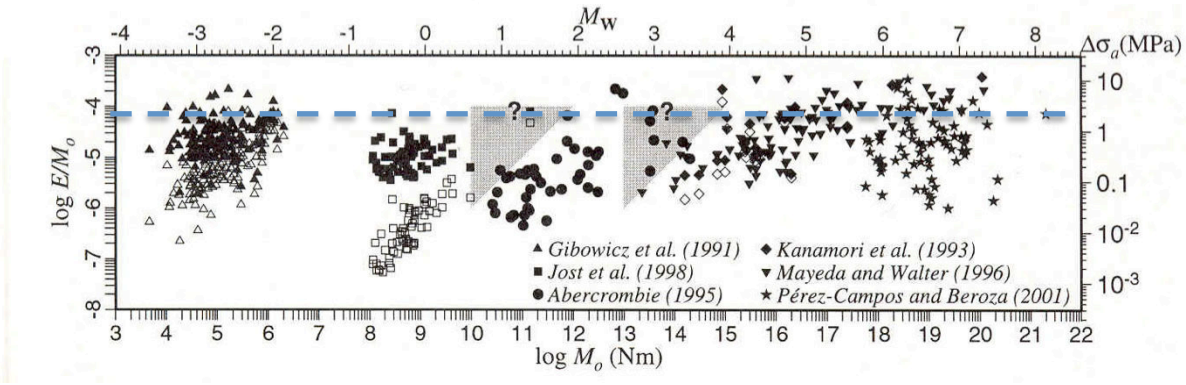


Fig.8 : Relation between earthquake stress drop and seismic moment (M0). References are on the figure.

This paradox actually shows that **we still do not understand how the microphysics that govern EQs transforms into macrophysics, obviously much more simple**. This is an important problem in seismology because many of the "ingredients" that are used in the available physical models to tentatively reproduce the EQs are derived from microphysics experiments. This is especially true for the physical description of the frictional sliding, that all relies on small-scale laboratory experiments. From these experiments, it has been suggested that EQ friction depends both on the state of the sliding interface and of the slip rate. Rate and state friction laws have thus been developed (See Marone 1998 for a review) and two of them (Dieterich, 1979a-b, Ruina, 1983), although different, are used in most available EQ models. However, although these two laws describe laboratory results equally well, they yield qualitatively different behavior in simulations of seismic phenomena, and we don't know yet which one is best (e.g., Marone 1998).

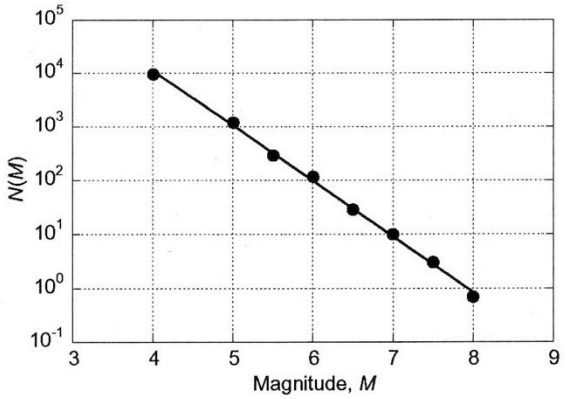


Fig.9: Magnitude–frequency relationship for earthquakes in the world for the period 1904 to 1980. N(M) is the number of earthquakes per year with the magnitude ≥ M. The solid line shows a slope of −1 on the semilog plot which corresponds to a b-value of 1. (from Kanamori and Brodsky 2004)

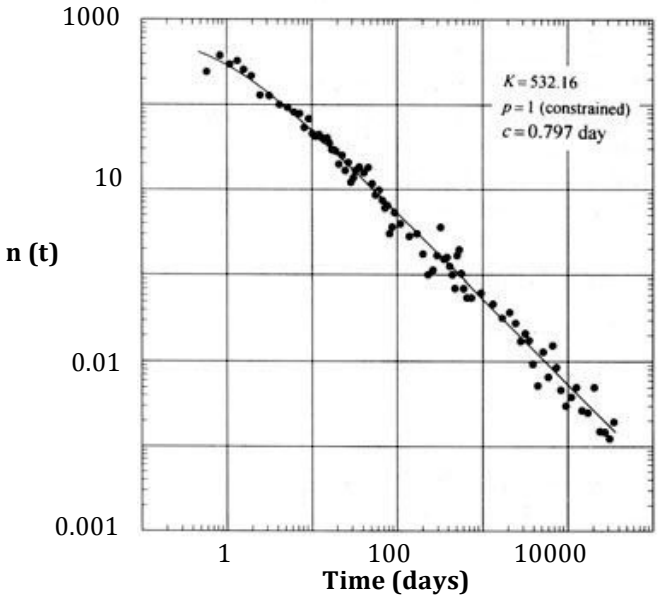


Fig.10: Omori's law describing the aftershocks decay after the 1891 Nobi earthquake (M 8) (Utsu, 2002).

On the basis of the overall EQ observation, a conceptual theoretical framework has been developed. The elastic wave-field generated by the sudden slip of EQs, along with most scaling laws found at the macro-scale, for EQs but also for long-term faults (such as cumulative slip increase with fault length; Fig. 11; e.g., Walsh and Watterson, 1988; Cowie and Scholz, 1992; Dawers et al., 1993; Schlische et al., 1996; Scholz, 2002), altogether suggest that EQs can be described in the framework of the crack or dislocation theory (e.g., Kanamori and Anderson, 1975; Anderson, 2005; Kagan, 2009). As a first approximation, EQs are seen as a large planar dislocation in a rock material that would be homogeneously elastic. As pointed out in Aki and Richards (2002), **the theory of elasticity actually lays the foundation for nearly every aspect of our understanding of seismic wave propagation and EQ source mechanics**.

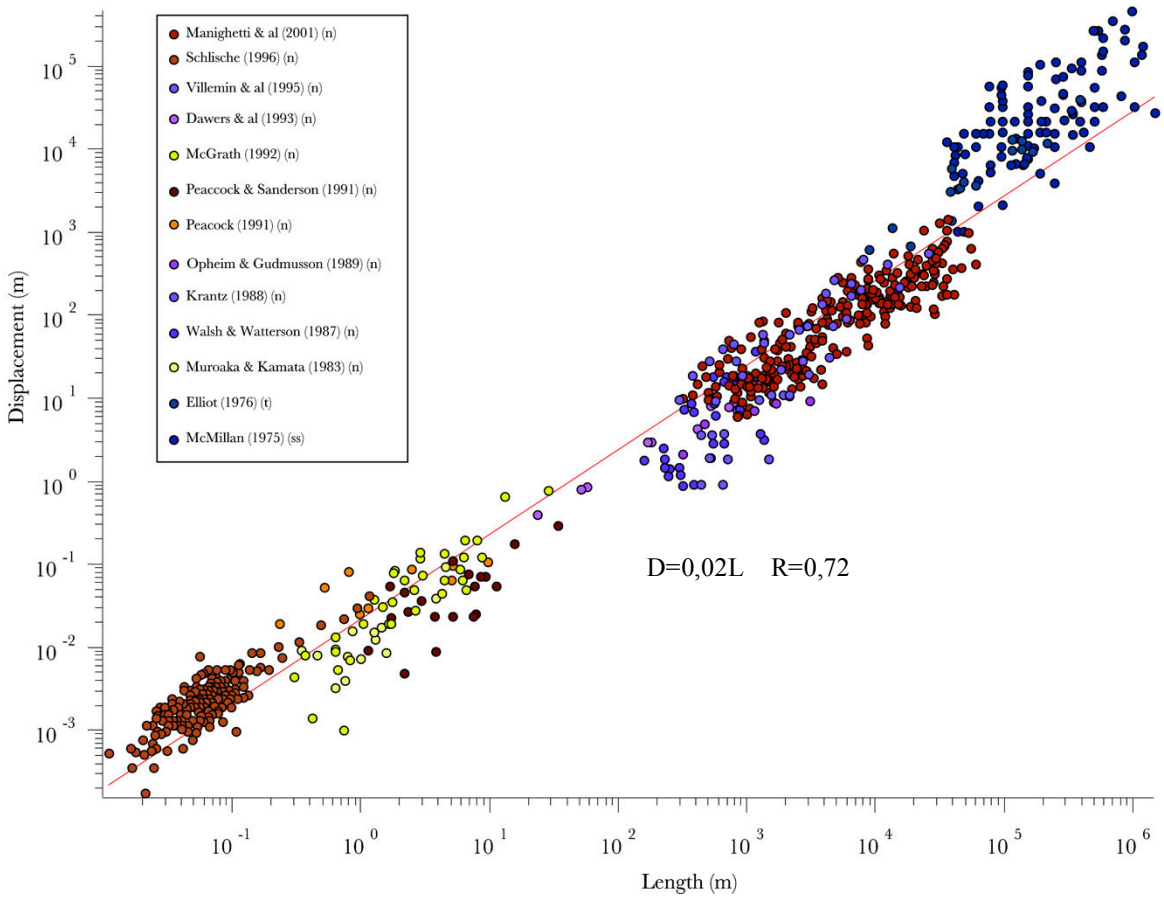


Fig.11: Compilation of worldwide cumulative fault displacement versus fault length (modified from Schlische et al., 1996)

A first outcome of this conceptual framework is that the rupture models which are developed are generally simplified compared to the natural faults and EQs (See discussion in Kagan, 1994 and in Harris and Day, 1997): in most models, the broken fault is a

smooth, planar surface (or, at best, a narrow zone of planar, collinear segments) embedded in a uniform elastic medium. On the rupture plane, the shear stress is governed by a frictional sliding law chosen among the few relations derived from laboratory experiments (generally slip-weakening friction law). An initial equilibrium stress state is assumed, because we ignore the natural stress distribution on fault planes. In general, new faults (or deformation) cannot be created in the model as the rupture evolves. The models that presently represent the source of the EQs thus include several weak aspects that might have strong implications on the model results.

A second outcome of the conceptual framework is that it allows deriving a number of physical relations between various EQ source parameters (See founding papers cited before). Among these relations, the best known is $M0 = \mu.Dmean.S$, where μ is the rigidity of the medium (assumed to be 3.10^{10} $N.m^{-2}$), Dmean is the mean coseismic slip (in m), and S is the broken area (in m^2). Up to now, the source data derived for the historical EQs have been said to satisfy this theoretical equation (e.g., Kanamori and Brodsky, 2004). Because M0 is fairly well determined, this suggests that μ, Dmean and S are also well determined. This is actually somehow surprising because i) we only have an indirect "vision" of the broken zone at depth (hence indirect vision of both Dmean and S), ii) knowing the mean value of a function requests knowing the complete function –and this is only from recent times that complete coseismic slip functions are measured, and iii) as it evolves with time, a fault, and likely also an EQ rupture, damages the medium around its plane (See Chapter VI and references therein), so that it is difficult to believe that the medium rigidity can be constant in space and time. I will come back to these points in the following.

Independent of the remarks above, a number of observations suggest that the theoretical framework may not be fully appropriate to describe the EQ rupture:

- The theoretical framework considers an EQ as a well-defined, single entity. Yet many EQs have been observed to break different faults, some within a time interval so short that the different ruptures could not be discriminated in the records (ex: Denali 2001 EQ), some with slightly longer intervals (ex: 1954 Fairview Peak-Dixie Valley EQs which occurred at 4 mn interval), some with even longer intervals (See EQ sequences in Italy and in Christchurch where successive EQs followed with several days to months-intervals). This poses the question of the definition of an EQ, and how these various situations can be handled in the theoretical framework (See also discussion in Kagan 2004).

- Most EQs are observed to break several distinct fault segments along a same fault (Fig.12). This again poses the question of the definition of an EQ, and how these multiple-segment ruptures can be handled in the theoretical framework (See also discussion in Kagan 2004).
- Recent seismological, geodetic and structural observations show that the medium around the long-term faults but also along the EQ ruptures, do not behave everywhere and/or at every moment, in an elastic fashion, but instead sustains significant inelastic deformations (See Chapter VI and references therein). How can such an inelastic behavior of the medium be handled in the theoretical framework?
- Some large EQs seem to have a rare behavior, apparently different from that of the majority of EQs. As an example, a few EQs were found to have a super shear rupture speed (e.g., Archuleta, 1984; Bouchon et al., 2001, 2002; Bouchon and Vallée, 2003; Robinson et al., 2010; Yue et al., 2013), much faster than that found for the majority of EQs worldwide. Super shear propagation is difficult to explain in the theoretical framework unless specific conditions exist on the fault.
- EQ ruptures with a similar length have been observed to have different seismic moments, to produce different amplitudes of coseismic slip, and to generate different amplitudes of ground motions. Such a variability is difficult to explain in the theoretical framework (e.g., Wells and Coppersmith, 1994).
- Small EQs (Mw<1-2) seem to obey different behaviors than large EQs (e.g., Abercrombie, 1995). Although this suggestion is still under debate, if it is exact, we have to understand why there is a scale break in the theoretical framework.

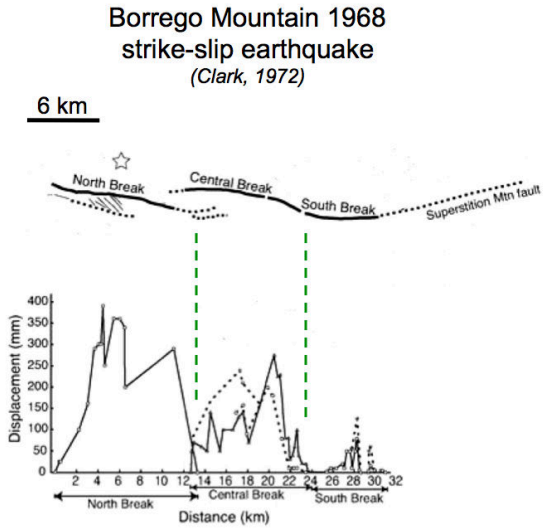


Fig.12: The coseismic slip profile of the 1968 Borrego Mountain shows coseismic slip deficit at the major intersegments of the broken fault (modified from Clark, 1972).

On the other hand, similar observations can be done on long-term faults: their actual architecture and behavior are not appropriately represented in the theoretical framework. In

particular, faults are non-planar features (e.g., Segall and Pollard, 1980; Walsh et al., 1999, 2002) and in particular faults are laterally segmented at various scales (e.g., Manighetti et al., 2009 and references therein); the slip interface has a certain thickness (e.g., Sibson, 2003); although they are not well-known, the properties of the slip zone are likely to vary with the fault history (so-called structural maturity of the faults, e.g., Manighetti 2007) and also possibly with the local geological context (ex: clayish rocks versus granitic rocks); faults are 3D objects in particular connected with many other smaller faults and fractures (Fig.13; e.g., Aviles et al., 1987; Salyards et al 1992 ; Scholz et al., 1993 ; Oskin et al. 2007; Savage and Brodsky, 2011); faults lengthen and grow in slip over their history so that the fault structure as its relations with the crust vary over time (e.g., Walsh and Watterson, 1988; Cowie and Scholz, 1992a-b; Schlagenhauf et al., 2008; ex: more or less sustaining gravity forces depending on how much vertical slip has been accumulated); the crustal medium is terribly heterogeneous and clearly not elastic everywhere and on every time scale (See references in Chapter V); the static stress distribution on faults is very heterogeneous (e.g., Liu-Zeng et al., 2005), etc.



Fig. 13 : Landsat and topographic map view of the San Andreas Fault system (white lines) made of the major San Andreas strike-slip fault and of an associated dense network of smaller strike-slip and reverse faults (from http://earthobservatory.nasa.gov/IOTD/view.php?id=3067)

Therefore it seems that the conceptual framework that is presently used to model EQs and to quantify the parameters that are subsequently used in EQ hazard assessment, might deserve to be modified to integrate the greater complexities of the faults and EQs. My PhD work is not dedicated to perform these modifications, well beyond my expertise. Rather, it is dedicated to try to better describe some of the fault and EQ properties that might be either more complex or more simple –in any case, different, from the description that is commonly done. It is also devoted to examine how these fault and EQ properties might be related to each other, and to

provide suggestions on how these possible relations might modify our understanding on the EQ behavior. As I said earlier, my work is basically empirical. Yet my objective is to make the possibly new empirical relations that I may find useful keys which seismologists and rupture modelers might subsequently use to modify certain aspects of the theoretical framework.

I am going to present my work as follows:

- **In Chapter II, I will present the fault and EQ data that I will then use in the following chapters**. I will thus describe which data I have collected and how. In particular, for 21 historical EQs (Baja California 2010, Bogd 1957, Borah Peak 1983, Borrego Mountain 1968, Denali 2002, Dixie Valley 1954, Fairview Peak 1954, Fort Tejon 1857, Fuyun 1931, Hebgen Lake 1959, Hector Mine 1999, Imperial Valley 1940 and 1979, Kunlun 2001, Landers 1992, Manyi 1997, Pleasant Valley 1915, San Francisco 1906, Sichuan 2008, Superstition Hills 1987, Yushu 2010), I have acquired satellite and topographic data that I have used to map and examine the broken faults and ruptures in great details. I have also acquired satellite and topographic data on the 1939 Erzincan, 1943 Tosya, 1944 Bolu Gerede, 1999 Izmit and 1999 Duzce EQs, and hence I have also analyzed these 5 EQs, yet in less details because I was lacking time. Altogether this part provides the most robust data which I have acquired and analyzed, and this explains that the corresponding section is fairly dense.
- **In Chapter III, I will examine the coseismic slip-length functions and show, on the one hand, that they have a generic shape, and on the other hand, that this generic shape results from different aspects of the EQ physics, which themselves are linked to specific properties of the broken faults.**
- **In Chapter IV, I will examine empirical relations between different EQ source parameters, and show that some of the properties of the broken faults much control these scaling.**
- **In Chapter V, I provide a paper, which has been published in G^3, on the modeling of the generic coseismic slip-length profiles.** The modeling work has been done in collaboration with F. Cappa. It shows again that some of the properties of the broken faults, namely here the off-fault long-term damage, markedly control the coseismic slip distributions.
- **In Chapter VI, I will use the fault and EQ maps that I have produced in Chapter II to examine the effects of the lateral fault segmentation on the EQ rupture development.**

Scaling laws will be proposed that describe the ability of an EQ rupture to initiate, propagate and arrest along the faults, especially across inter-segment zones.

- **Finally, in Chapter VII, I will synthesize the main results of my work, and provide a few lines of discussion and perspective on the question posed in the Introduction: can the new observations provide some keys to better understand the EQ physics?**

CHAPTER II. CONSTRUCTION OF A FAULTS & HISTORICAL EARTHQUAKES DATABASE

1. Principles to construct the Faults & Earthquakes databases

My objective being, on the one hand, to define the generic properties of both the long-term geological faults and of the large EQs, and on the other hand, to examine the relationships between fault properties and earthquake properties, the first step of my PhD work has been to examine a dense population of large historical EQ, along with the dense population of long-term faults that were broken by those EQs. I describe further below the kind of information I have been seeking on these EQs and faults.

Independent of their nature, I needed this information to be as accurate as possible. This revealed to be quite challenging. It was indeed fairly rare to find EQ cases where both the EQ and the ruptured fault have been together accurately studied. In the majority of cases described in the literature, the earthquake is well documented, especially when it has occurred recently. But the long-term fault on which the EQ occurred is not or hardly described, being at most documented in the EQ rupture zone; yet the faults involved in the EQs are generally much longer than the only rupture zone. In the cases of several decades old EQs, the literature might provide the opposite information: more detailed on the long-term fault involved in the EQ, but poorer on the EQ description (for recording instruments were lacking). Therefore, I had to deal with this heterogeneous information in two ways:

- For the large EQs that are best documented in the literature, I have acquired satellite and topographic data covering the entire long-term faults involved in those EQs. I have analyzed these satellite images, along with the information available in the literature, to produce tectonic maps of the broken long-term faults, from which I could derive the information I needed. For those well-documented faults and EQs couples, I have constructed extended "Identity sheets" (later referred to as ID), in which I describe the properties of both the broken long-term fault and of the large EQ produced. These extended IDs are presented in section III-2 below. They concern the 2010 Baja California, 1957 Bogd, 1983 Borah Peak, 1968 Borrego Mountain, 2002 Denali, 1954 Dixie Valley and Fairview Peak, 1857 Fort Tejon, 1931 Fuyun, 1959 Hebgen Lake, 1999 Hector mine, 1940 and 1979 Imperial Valley, 2001 Kunlun, 1992 Landers, 1997 Manyi, 1915 Pleasant Valley, 1906 San Francisco, 2008 Sichuan, 1987 Superstition Hills and 2010 Yushu EQs, all are intracontinental. I have also acquired satellite and topographic data on the 1939 Erzincan, 1943 Tosya, 1944 Bolu Gerede, 1999 Izmit and 1999 Duzce EQs, and hence I have also analyzed these 5 EQs, yet in

less details because I was lacking time. Of course, the IDs, which I have constructed are not exhaustive: some large EQs are missing (e.g. 1999 Chichi EQ), mainly for reasons of time.

- For the large EQs that are either less well documented in the literature, or that have occurred in environments where satellite imagery cannot be used to analyze the broken long-term faults (ex: subduction EQs), I have only compiled the data available in the literature and gathered them into a number of Tables which I present in section III-3 below. Again, the Tables that I have constructed are not exhaustive: some large EQs are missing, especially subduction EQs, mainly because I had not enough time to analyze them.

Constructing these two types of databases has been time-consuming because the literature on EQs is extremely dense, because I had to examine this information critically, and because identifying and mapping the surface traces of the long-term faults on satellite imagery is a fairly long work.

The critical examination of the information available in the literature about EQs is necessary because large EQs have been generally treated so far in case by case studies. That means that huge amounts of papers are produced for every large EQ that occurs, whereas very few synthetic articles are provided that would describe the combination of the observations and results on each EQ; papers then appear almost as independent from each other. It results that basic EQ parameters such as the surface rupture length or the maximum coseismic slip might sometimes vary from one paper to the other, depending on the author, on the method used for the measurement, on the time of the measurement, etc. Similarly, multiple source inversion models are produced for every recent EQ, which generally differ in a way or more from one another, mainly depending on the data and methods used to perform the model (Fig.14). This situation has forced me to face every observation or result provided in one paper to the other observations and results provided in the other papers and also derived from my own fault maps, so that, eventually, I could have a clearer vision of the robustness of the observations and results. I describe this critical discrimination of the data in the IDs and Tables presented below.

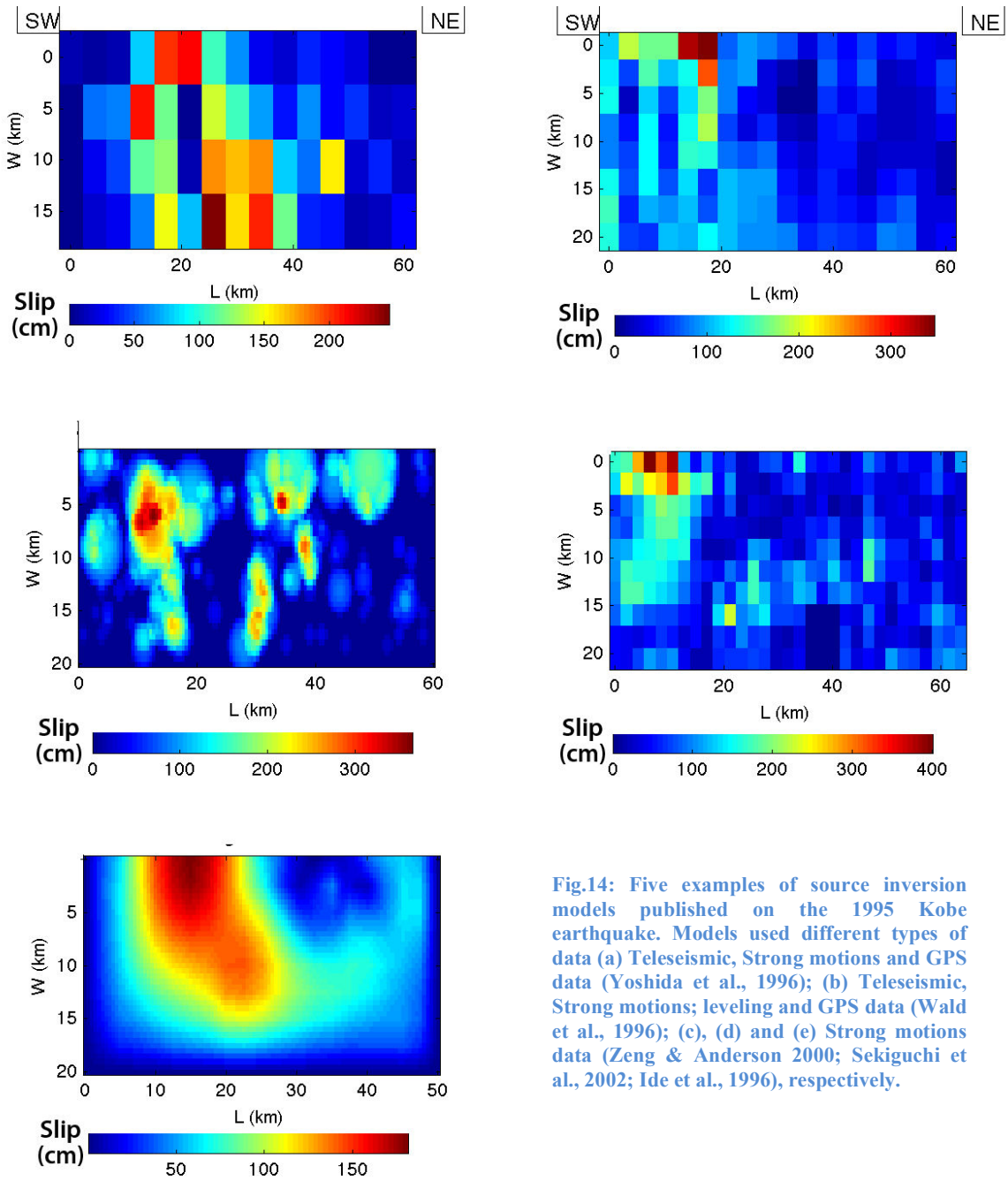


Fig.14: Five examples of source inversion models published on the 1995 Kobe earthquake. Models used different types of data (a) Teleseismic, Strong motions and GPS data (Yoshida et al., 1996); (b) Teleseismic, Strong motions; leveling and GPS data (Wald et al., 1996); (c), (d) and (e) Strong motions data (Zeng & Anderson 2000; Sekiguchi et al., 2002; Ide et al., 1996), respectively.

Mainly, the questions, which have guided my analysis are the following: What is the geometry/architecture of the long-term fault (and of the system it forms at a larger-scale with associated secondary faults) which broke, at least partly, in the EQ under study? What is the overall "tectonic history" of that fault (age of initiation, history of growth and lateral propagation, slip rate, structural maturity)? Which part of the fault broke in the EQ under study? (or which faults broke during the EQ?) Where did the EQ nucleate on the fault, where did it stop, which specific elements of the fault (i.e., segments) did it break, and what are the characteristics of these elements (such as length, etc)? Were there any specific fault elements,

which arrested the EQ propagation, and what are their characteristics? How did coseismic slip and EQ moment distribute on the fault elements? How did coseismic slip evolve from depth to surface? Etc…

To address these questions, I have mainly focused on the following data and observations:

- Satellite (Landsat, Spot, Aster GDEM, Google Earth, Lidar where available) and topographic data (SRTM, Aster, Spot) to map the long-term broken faults, the surrounding fault networks, and the rupture zones;
- Measurements and observations acquired at the ground surface (from literature): rupture and long-term trace, coseismic slip profile or sparce measurements, deformation fields inferred from Insar or optical satellite images, long-term fault offsets;
- Source inversion models (available from literature and from the http://equake-rc.info/SRCMOD/ Martin Mai website): rupture plane, coseismic slip distribution at depth, hypocenter location, broken fault area;
- EQ Source Functions (from literature and SCARDEC database [Vallée et al., 2011]): EQ moment release as a function of time;
- Other seismological observations (from literature and Global CMT catalog): seismic moment, magnitude, aftershocks, rupture duration, etc.

More precisely, on the long-term faults, the properties that I have considered in priority and hence that are discussed in the following databases are:

Fault structural maturity

Geologists and seismologists have observed that long-lived faults seem to produce lower stress drop EQs than young faults (e.g., Kanamori and Anderson, 1975; Scholz et al., 1986; Cao and Aki, 1986; Anderson et al., 1996; Stirling et al., 1996; Hecker et al., 2010; Fig.15). Progressively, the aging of faults has been referred to as the "structural maturity". Grossly, the structural maturity qualitatively describes how evolved is a fault in terms of repeated fault slips.

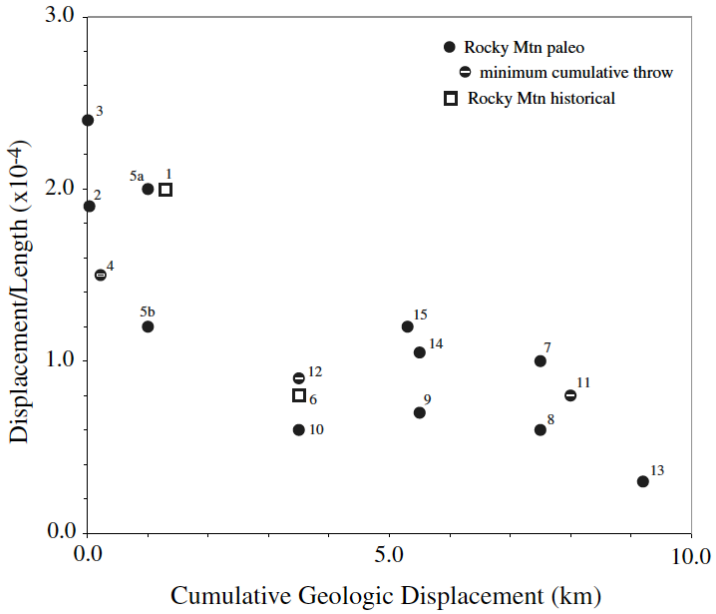


Fig.15: The EQ stress drop (approached through the Dmax/L ratio) decreases with the cumulative slip on the fault (from Hecker et al., 2010).

The concept of structural maturity was further defined by Manighetti et al. (2007), who tried to provide quantitative parameters to define it (See their Table 1). These authors suggested that several related fault parameters reflect the structural maturity of a fault, among which, the total fault length L (because faults lengthen over time as they grow and accumulate more slip), the maximum cumulative slip D_{Total} (because faults grow over time by accumulating more slip), the age of fault initiation I-Age (because a long-lived fault has generally slipped more than a fault formed recently), the mean slip rate MR (this parameter is less clear but it is expected that faults slipping faster –and hence breaking more frequently into EQS, mature more rapidly (i.e., smoothing of their fault plane) than faults that would rarely slip. According to their attempt of definition, a fault would be:

- Mature if: L > 1000 km and/or I-Age > 10 Ma and/or MR of a few cm/yr, and/or D_{Total} > 100 km;
- Of Intermediate maturity if: 300 < L < 1000 km and/or 5 < I-Age < 10 Ma and/or MR ~1 cm/yr, and/or D_{Total} ~ a few 10 km;
- Immature if: L < 300 km and/or I-Age < a few Ma and/or MR < 1 cm/yr, and/or D_{Total} < 10 km.

Of course, these quantitative values additionally depend on the fault slip mode (ex: dip-slip faults have rarely L > ~100 km and Dmax > a few km).

In the following, I will consider these three classes, but will also expand them on the basis of additional data.

Lateral major segmentation of faults

Geologist have also long described that long-term faults are segmented laterally at various scales (e.g., Tchalenko and Berberian, 1975; Segall and Pollard, 1980; Sibson, 1986; Barka and Kadinsky-Cade, 1988; Aydin and Schultz, 1990; Scholz 1991; Peacock and Sanderson 1991; Ferrill et al., 1999; Davis et al., 2005; Manighetti et al., 2007, 2009; Fig.16). That is, every fault of any slip mode and any size is divided along its length into smaller scale fault pieces, called 'fault segments'. These fault segments are fairly collinear and at least partly connected to each other so that altogether they form a single fault.

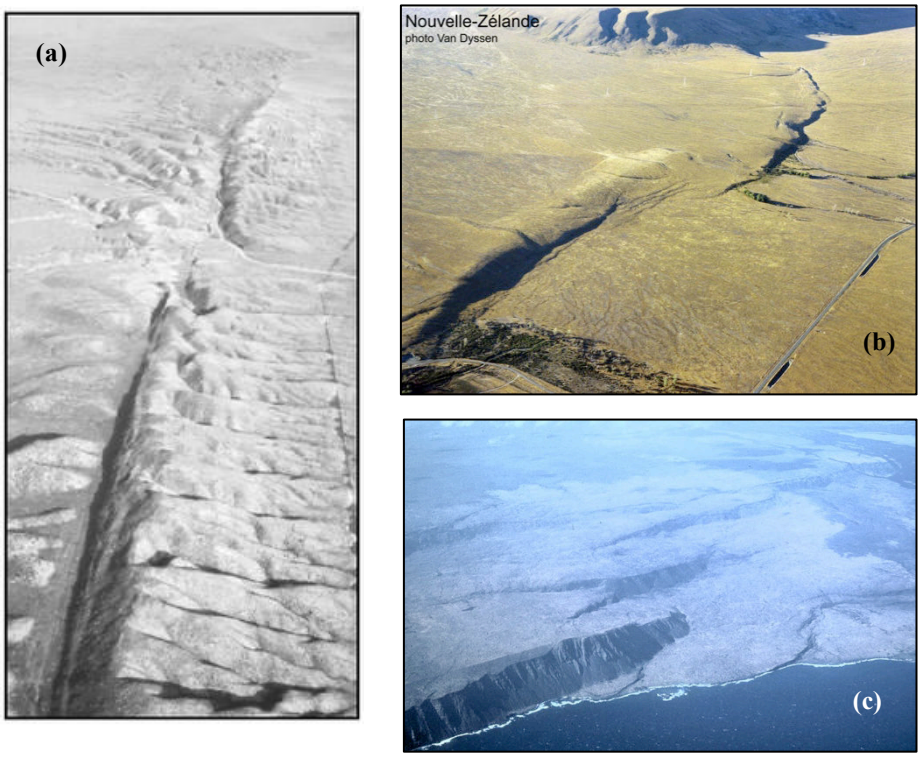


Fig.16: Aerial photos showing lateral fault segmentation (a) San Andreas strike slip fault ; (b) Reverse fault in New Zealand ; (c) Normal fault system in Hawaï.

There is not a total consensus on how the fault segments form over the whole fault history, but it is admitted that they are initially smaller faults that eventually connect to each other to form a longer fault. The zone through which two segments connect is generally called "inter-segment zone". Because it is a zone where the single fault is not yet fully developed, it is a zone of cumulative slip deficit (Fig.17). Therefore, in a fault cumulative slip profile, the inter-segments zones appear as slip troughs separating pronounced slip bumps that coincide with

the fault segments (Fig.17). Fault segments and inter-segments (at least the largest) are thus clearly recognizable within cumulative slip profiles (e.g., Manighetti et al., 2009).

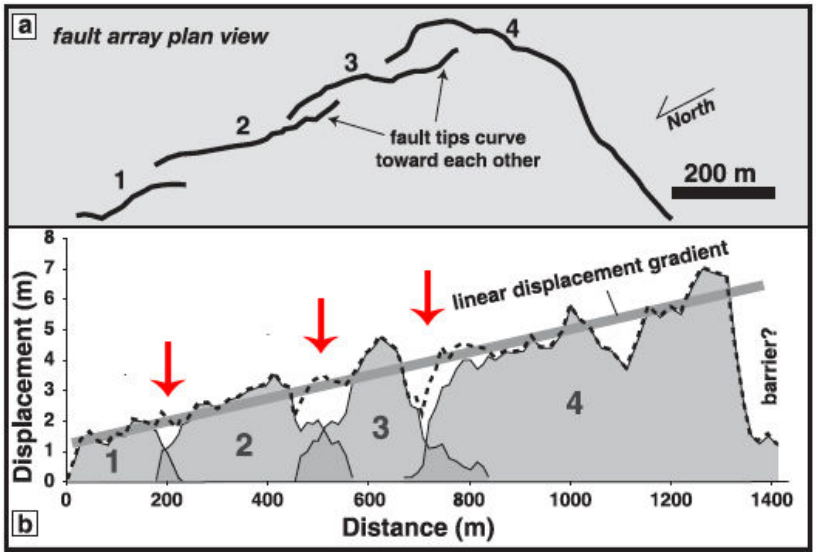
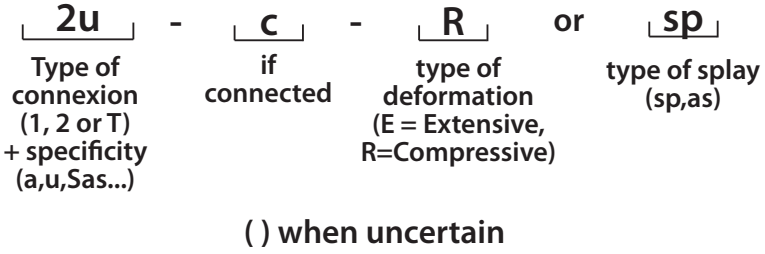


Fig.17 : (a) Gladstone fault trace map reveals four left-stepping en échelon segments. (b) Displacement–length profiles along each segment (1, 2, 3 and 4). Red arrows show cumulative slip deficit at each intersegment zone. Dashed line : summed displacement. (modified from Davis et al., 2005).

They also are clearly recognizable in the surface long-term fault trace (See figures 16 and 17). The segments, at least the longest and hence the best expressed ones, have generally a fairly continuous and linear trace (when observed at the scale of the entire fault), and this trace clearly stops or is deflected where it arrives in the inter-segment zone (Fig.16). The trace of the next segment is then generally separated from the previous trace in the fault perpendicular direction, so that a step exists between the two segments. This step is called “step-over”. In figure 18 (a, b), I have synthesized all the geometries of inter-segments that I have observed along the long-term faults I have analyzed. I present them here because they will help understanding some of my following analysis.

In figure 18 (a, b), I discriminate two types of inter-segments: a type 1, made of “simple connections”, and a type 2, made of step-overs. Simple connections are where two segments are not separated laterally, but rather simply connected “directly”, either through a bend in the fault trace (angular or rounded bend, types 1a and 1r, respectively), or through a change in dip either side of the connection zone (type 1d), or through a short horsetail termination at one of the segment tips (type 1 ht). Horsetail terminations are common features at fault tips, and more commonly at strike-slip fault tips; they are networks of oblique faults generally with a dip-slip component formed as a result of the large deflected stresses existing at the fault ends (e.g., Sylvester 1888; Du and Aydin, 1995; Anders and Schlische, 1994; Kim et al., 2004; Cooke, 1997; Savage and Brodsky, 2011; Fig.19). As such, they can be extensional or compressional.

Inter-segments of type 2 are step-overs. Step-overs can have different sizes and geometries (Fig.18b). In particular, the two segment traces can show no overlap along the fault strike (type 2), show a clear overlap (type 2o) or can underlap (type 2u). The step-overs can be releasing if they are submitted to an extensional stress regime, or restraining if they are submitted to a compressional stress regime. In some cases, the two segment traces are not directly connected through the step-over. In these cases, the step-overs are the sites of multiple oblique faults, most are dip-slip, that extend in between the two segments (types 2-c, 2o-c, 2u-c). In other cases, the two segment traces are directly and well connected to each other, so that the step-over looks like an ancient feature that is now cross-cut by the fault. In these cases, the fault trace double bends between the two segments (type 1b); that is, the oblique fault trace in between the two segments has the same slip mode than the two segments. In all the cases above, the strike of the two segments might differ slightly (type 1-2), whereas secondary faults might develop around or from the inter-segment zone (different geometries described as types 1+ and 2+, 1a or 1r-SP, 1a or 1r-AS; See details in figure caption, and further below). To describe these different types of inter-segments, I will use the labelling:



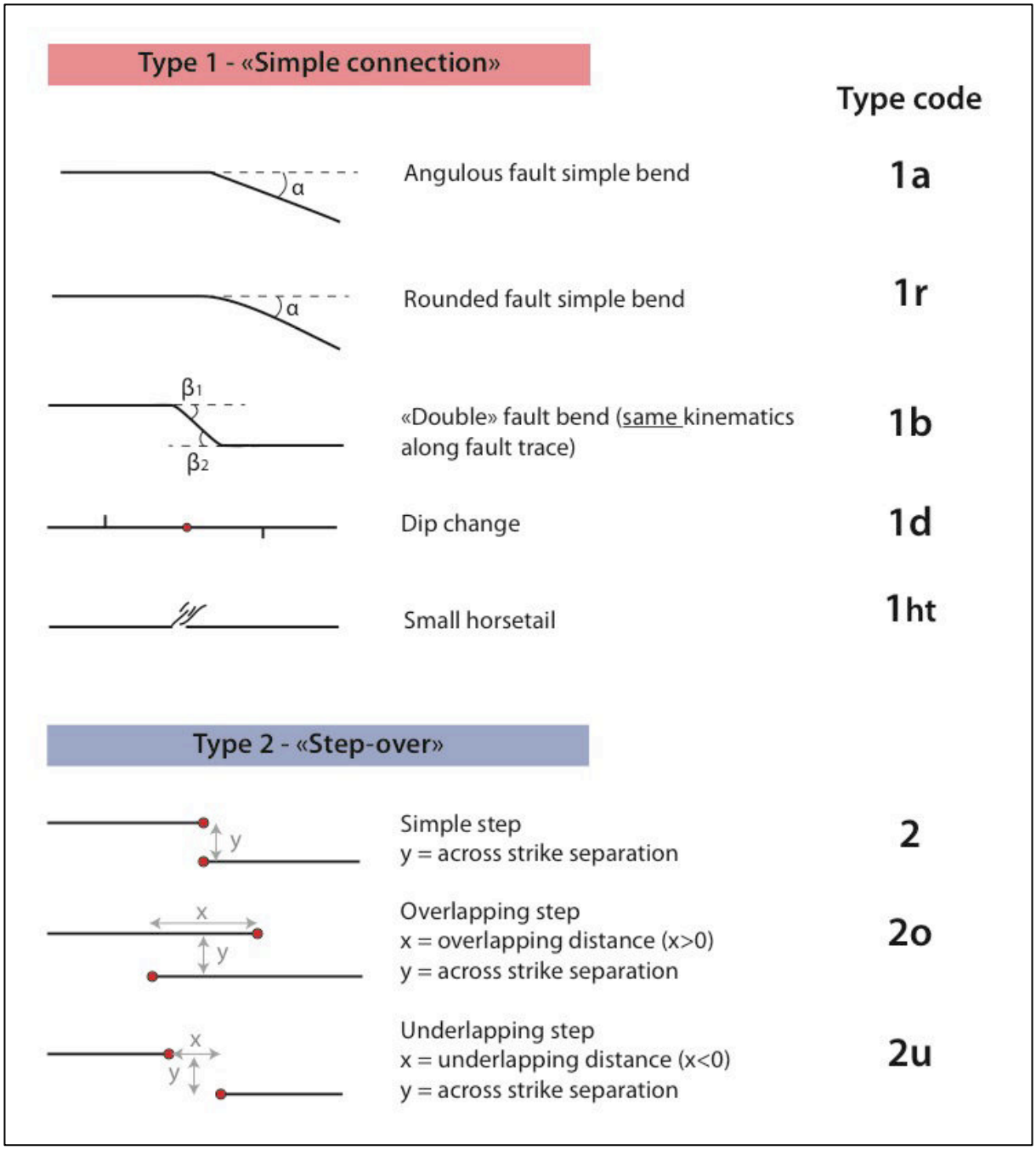


Fig.18: (a) Description of the main geometries of intersegment zones that I observed and corresponding codes used in my fault maps (See IDs section).

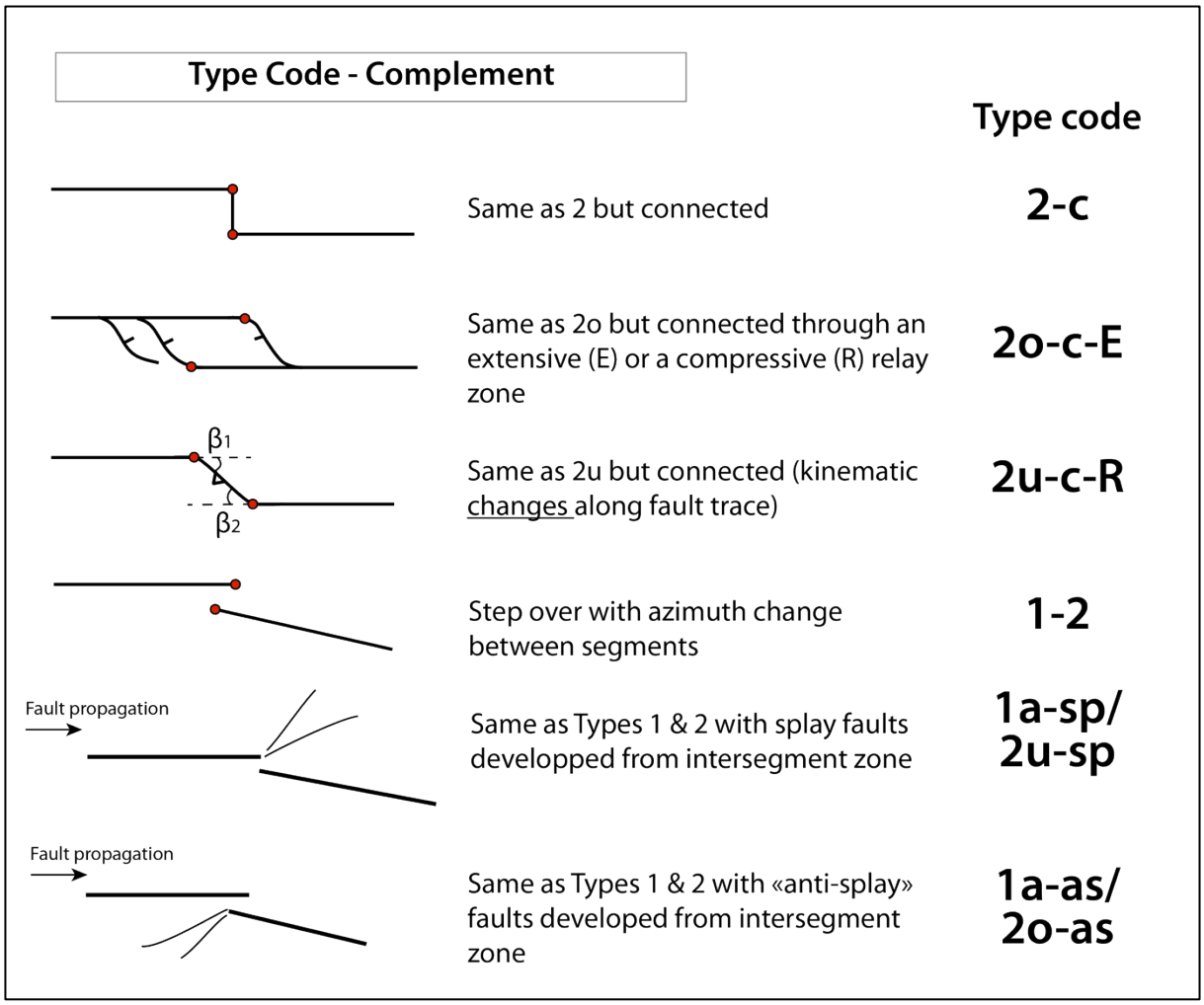


Fig.18: (b) Description of the specific structures that can be associated with the intersegment zones described in 18 (a). I call "splay or sp" the secondary faults that form angles < 90° to the master fault trace, and "anti-splay or as" the secondary faults that form angles > 90° to the master fault trace.

I have used the segments and inter-segments properties described above to identify the major segments, which form the long-term faults that I have analyzed. In all the figures showing these segments in the following, the principal criteria to identify the longest segments within a fault were their fairly linear trace being furthermore collinear with the rest of the fault, interrupted by one or other of the inter-segment types described above. I have considered the mean strike of the segments and measured their length along this mean strike (uncertainties will be indicated on the figures). I have also measured the angle changes between the mean strikes of the successive segments. Finally, I have measured the types and sizes of the inter-segments, as described further below. All these informations are reported into dedicated Tables.

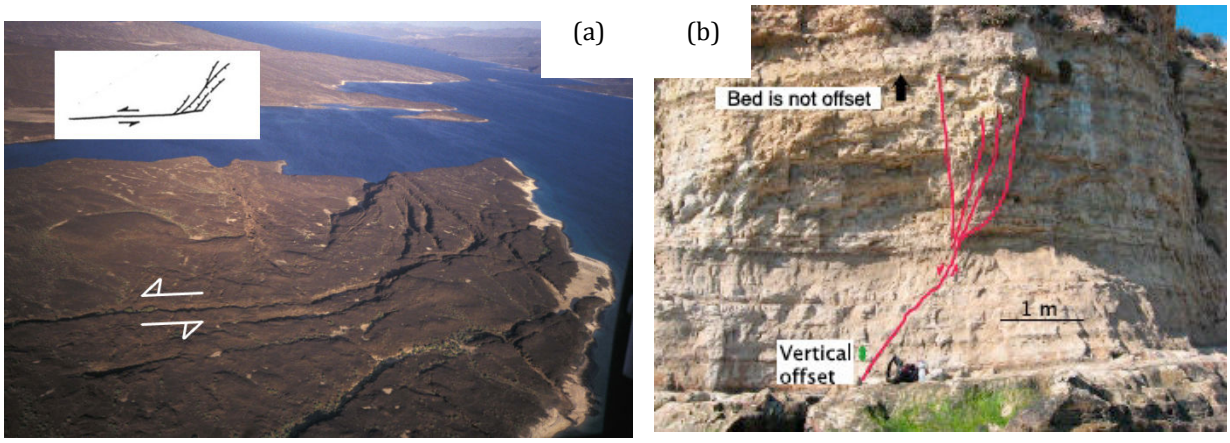


Fig.19: (a) Air photo of horsetail faults developed at the right tip of a strike-slip fault (Djibouti, picture from Manighetti I.)) and simplified sketch of an horsetail fault termination (Manighetti 1993), (b) Low Tide Fault at Four Mile Beach, California. The fault (red) ends near the top of the cliff, where it splays in a horsetail fashion (Savage and Brodsky 2011).

Note that the moderate resolution of the satellite and topographic data that I used allowed me to analyze only the two largest scales of fault lateral segmentation, that is the longest segments within faults and, in some cases only, the longest secondary segments within major segments (See Fig.20, where the notion of major and secondary segments is given). These two largest-scales are those of greatest interest for EQs, since only the largest inter-segments observed at surface can be thought to extend further at depth. Therefore, only the largest scales of fault segmentation can play a role on the EQ rupture, as it is actually observed: EQ slip decreases at the major fault inter-segments (See Fig.12 in Introduction), whereas some inter-segments have been shown to play a significant role in arresting some rupture propagations (e.g., Knuepfer, 1989; Zhang et al., 1999; Lettis et al., 2002; Wesnousky, 2006; Black and Jackson, 2008).

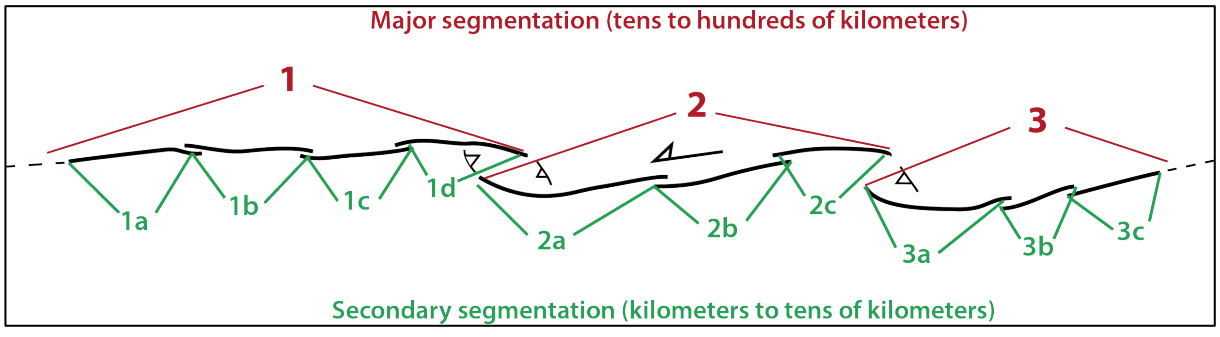


Fig.20: Simplified view of a segmented fault (black line) and of the two largest scales of lateral segmentation that I considered.

In the literature, it is generally admitted that faults are segmented laterally at various scales. However, only the largest scales of fault segmentation have been quantitatively analyzed.

From the analysis of about 1000 long-term normal faults of different lengths and ages, Manighetti et al. (2009) showed that all these faults are segmented similarly, in 4 ± 1 major segments, independent of the fault size, age or slip rate (Fig.21). Major segments are defined here as the longest segments within the faults, having a length of similar order than the fault itself. More recently, Manighetti et al. (2013) showed that the lateral segmentation of the faults is self-similar even at a lower scale, with every major segment being itself divided into 3-4 secondary segments. The self-similar lateral segmentation of the faults at the two largest-scales implies that the length of the longest fault pieces is not constant. This might not apply at the smaller scales; as a matter of fact, Klinger (2010) suggested that most faults are containing ~20 km long small segments.

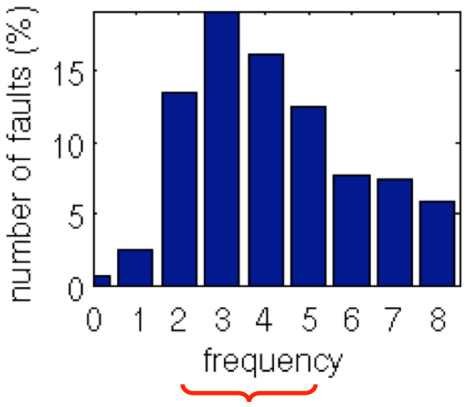


Fig.21: Distribution of spatial frequencies at which the frequency components have a maximum amplitude, for the total fault population. The graph shows that most faults are segmented in 2 to 5 major segments (from Manighetti et al., 2009).

Major inter-segments along faults

In the continuity of the work above, I have also noted the type of every major or secondary inter-segment along the faults which I analyzed, and measured their sizes and characteristics. I did this work because it has been suggested that inter-segments zones, especially step-overs, play a significant role in arresting the EQ rupture propagation (e.g., Knuepfer, 1989; Zhang et al., 1999; Lettis et al., 2002; Wesnousky, 2006; Black and Jackson, 2008). Therefore, I will use my new observations to examine this question.

Fault terminations:

I have also paid attention to the fault terminations. Those are important for many reasons but in particular, as I explain it below, because the architecture of the secondary fault networks developed at major fault tips often provides information on the direction of lateral propagation of the faults over the long-term.

I have identified different geometries of fault terminations, synthesized in Fig.24. All fault terminations involve the existence of "secondary" faults at the end of the "master fault" under consideration. Two principal types of relations are distinguished:

- In most cases, the "secondary faults" are genetically linked with the master fault. The most common case is the development of a network of secondary splay faults at the tip of the master fault (e.g., Sylvester 1988; Anders and Schlische, 1994; Du and Aydin, 1995 ; Cooke, 1997; Ando et al., 2009 ; Scholz et al., 2010; Savage and Brodsky, 2011). The splay network can be symmetric or asymmetric with respect to the master fault (types TSs and TSas). It is formed of oblique faults forming sort of a fishtail termination to the master fault (See prior definition in Manighetti, 1993; Fig.22). As we discuss it further below, this splaying geometry indicates the direction of long-term lateral propagation of the master fault (e.g., Du and Aydin, 1995). In other common cases, the master fault terminates in a horsetail fashion (See Fig.19 before; type T_{HT}). The horsetail also implies the development of oblique secondary faults at the tip of the master fault, but those are generally less oblique than the splay faults, and they have a clear dip-slip component of motion (either normal or reverse), contrary to most splay faults. They form as a result of the large deviatoric stresses at the master fault tips (e.g., Sylvester 1888; Du and Aydin, 1995; Anders and Schlische, 1994; Kim et al., 2004; Cooke, 1997; Savage and Brodsky, 2011; Scholz et al., 2010). In less common cases, the master fault ends at its tips by a sub-perpendicular secondary fault (type Tperp), which is strongly connected to the master fault and hence seems genetically related to it although it is not clear how this can be possible. Finally, in a few cases, the master fault under study is itself a splay fault of an even larger-scale fault (type T_{MF}). The two faults are oblique, and genetically related.
- In other cases, the "secondary faults" are not genetically linked with the master fault. This is especially the case where the master fault abuts against another existing fault (type Tob). That other fault might be of larger-scale than the fault under study. It is generally oblique to the fault under concern. In other cases, the master fault shows no or few secondary fault at its tips, but another, synthetic fault extends in the vicinity (type Tneighb). The large distance between the two faults suggests they are not (yet?) genetically related.



Fig.22: Principal fault terminations recognized in Manighetti, 1993. All, and especially the two to the right, are indicative of the sense of lateral propagation of the long-term master fault, indicated with the red arrow.

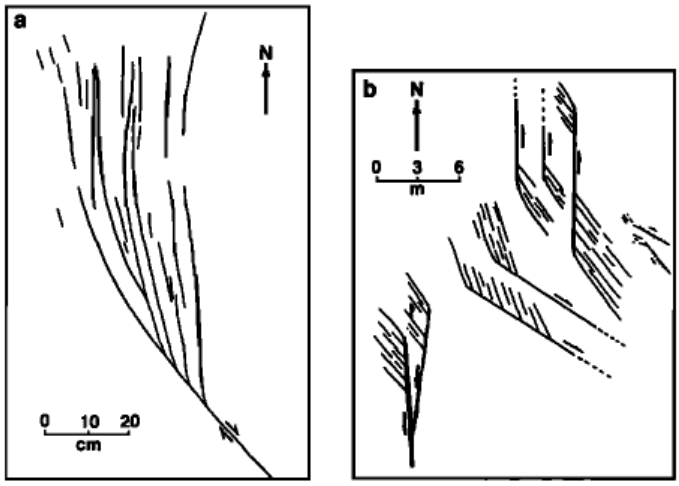


Fig.23: Splay fault terminations (from Cooke, 1997).

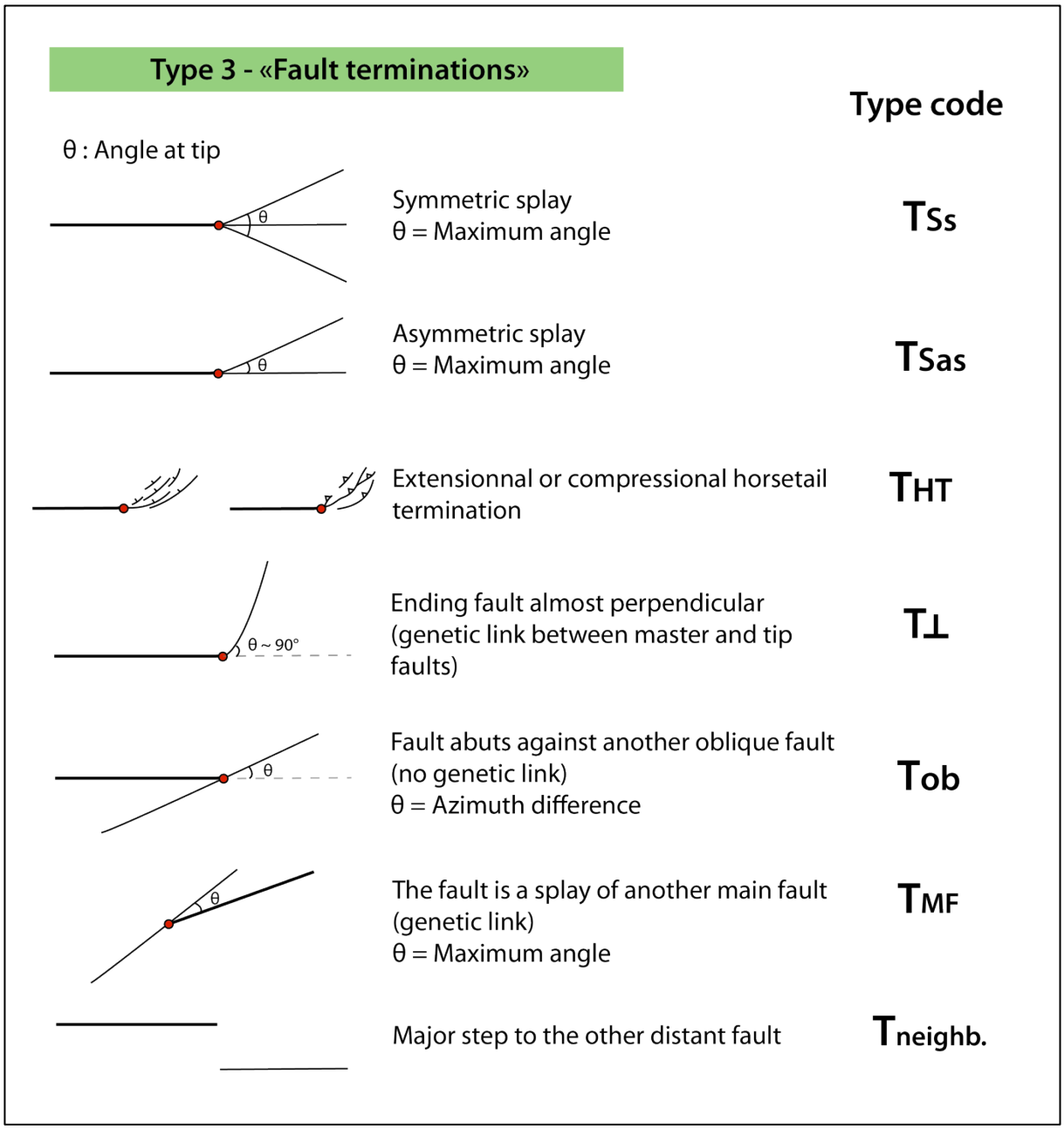


Fig.24: Description of the fault terminations that I observed and corresponding codes used in my fault maps (See IDs section). In thicker trace is the mater fault considered.

Direction of lateral propagation over the long-term

It is important to know the sense of lateral lengthening and thus propagation of a geological fault because it provides information on which parts of the fault were first formed over its whole history.

The best way to determine the sense of long-term fault propagation would be to date the fault initiation or at least the oldest fault offsets all along the fault strike. This can rarely be done however (for appropriate data are lacking), and therefore this information exists only for a

few faults worldwide (ex: North Anatolian Fault, e.g., Armijo et al., 1999; Hubbert-Ferrari et al., 2002).

Fortunately, several other pieces of evidence have been reported to indicate the sense of long-term fault propagation:

1) The along-strike decrease in cumulative slip indicates the sense of propagation, with the cumulative slip tapering in the direction of fault lengthening (e.g., Manighetti et al., 2001, 2009; Fig.25);

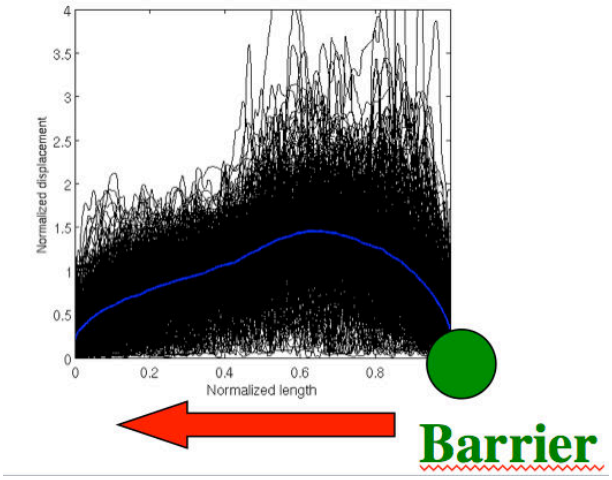


Fig.25: cumulative slip profiles (normalized to fault length and mean slip) on about 700 normal faults of different sizes and ages. The blue curve shows the average slip function. It tapers in the direction of lateral long-term fault propagation, as indicated with the red arrow (from Manighetti et al., 2001, 2009).

2) The generic, specific triangular shape of the along-strike decrease in cumulative fault slip (Fig.17) suggests that part of the fault slip is distributed in the medium around the fault, in the form of cumulative damage (e.g., Manighetti et al., 2004; Scholz and Lowler, 2004; see also Chapter VI and the references therein). The cumulative damage produces a triangular zone of secondary faulting whose apex in centered near the fault initiation and which widens in the direction of fault lengthening (Fig.26 below). Therefore, the enlargement of the secondary fault networks on either side (or on one side only) of a long-term fault indicates its direction of long-term propagation (back arrow in Fig.26 left) (e.g., McGrath and Davison, 1995; Manighetti et al., 2004; Aydin and Berryman, 2010).

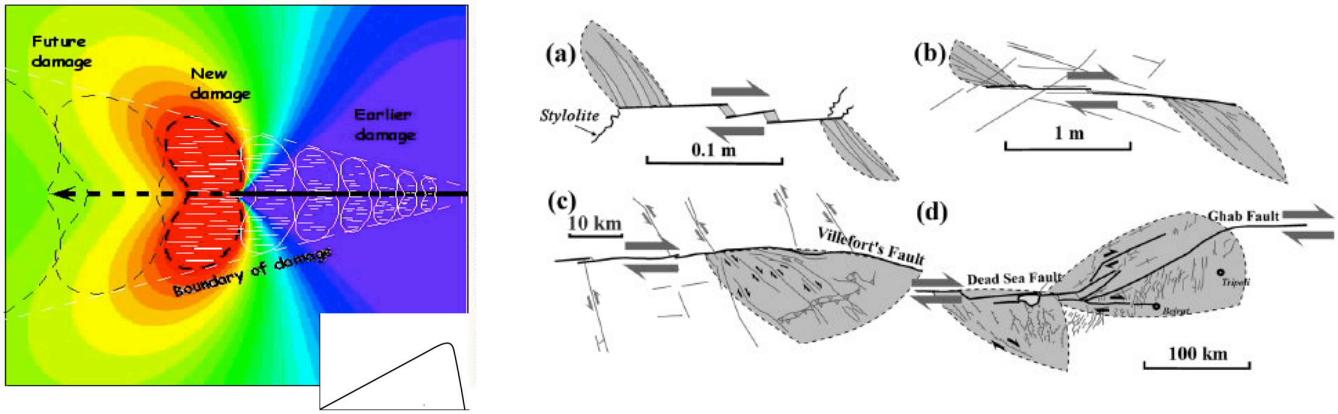


Fig.26: Triangular (in map view) long-term damage zones developed around propagating faults (from Manighetti et al., 2004 to the left, and from Kim et al., 2004 to the right).

3) Among the secondary faults that likely result from the long-term damage associated with the growth of a master fault, there is one type of faults which is commonly described in the literature: the splay faults (e.g., de Joussineau et al., 2007; Scholz et al., 2010). Splay faults are oblique secondary faults commonly developed at a master fault tip. They have been mainly described at the tips of strike-slip and of reverse (especially subduction) faults. Their fishtail architecture either side (or on one side only) of the master fault (See Fig.22 and 23) indicates the direction of fault lengthening and hence propagation over the long-term (e.g., McGrath and Davison, 1995; Du and Aydin, 1995; de Joussineau et al., 2007).

4) Finally, as a fault accumulates more slip and grows in length, its segments that were originally hardly connected to each other connect more and more, so that, eventually, the most ancient sections of a fault are made of strongly connected segments (e.g., Rahe et al. 1998; Marilyiani et al., 2013, and references therein). These strongly connected segments form a fairly linear trace (as most prior step-overs have been smoothed out or cross-cut by a more continuous fault trace), along which two initially disconnected segments might now appear as one single fault piece (Fig.27). Therefore, the architecture of the major segments along the faults varies depending on whether these segments are on the most ancient parts of the faults, or on the youngest, lengthening sections of the faults. In the former case, the segments might appear longer and with more linear traces than in the later case.

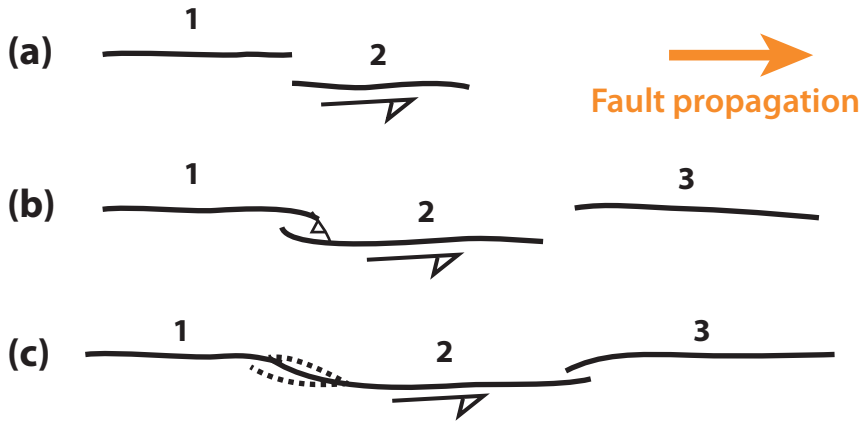


Fig.27: Simplified view of the growth of a segmented fault (black line) (a) segments 1 and 2 are hardly connected in the early stage of the fault evolution. (b) segments 1 and 2 growth and start to connect to each other. The new segment 3 forms and is hardly connected to segment 2. (c) Segments 1 and 2 are strongly connected; the trace of the fault is now continuous in between the two segments (double bended); segments 2 and 3 start to connect to each other.

In the following, I will use all these morpho-tectonic evidence, especially the architecture of the secondary fault networks associated with the master faults and the architecture of the segments along the faults, to derive information on the direction of long-term lateral fault propagation. This information will help me to define the most long-lived sections of the long-term faults, i.e. the most mature sections of the faults.

Critically assessing the robustness of the EQ data

As said earlier, before analyzing the data available in the literature, **I had to examine them critically, so that to determine the most robust values for each fault and EQ parameter under concern**. I provide below short discussions on the robustness of the EQ data which I analyzed in greater detail. Discussions on the fault data are provided in the IDs of section III-2.

Basically, the EQ data acquired at the surface generally include observation made both on the field and on satellite imagery, and altogether providing information on the EQ rupture trace, rupture length and displacements, recognition of the different components of slip. The points of discrepancy that I most commonly noted among the different studies, and hence which requested that I made choices among most robust and less robust data, were:

- The rupture length, especially for old earthquakes for which studies of the surface rupture are few and not necessary performed shortly after the earthquake: uncertainties thus arise on the identification of the fault traces actually and only due to the earthquake (e.g. 1915 Pleasant Valley earthquake section)

- The maximum coseismic displacement. Some surface measurements were made on non-tectonic features such as landslides (e.g. 1959 Hebgen Lake, 2008 Sichuan earthquakes). For old earthquakes whose rupture traces are unclear or badly preserved, the measurement of the maximum coseismic slip is uncertain, and furthermore generally includes a significant part of post-seismic slip. The measured slip might also result from more than one EQ (e.g. 1857 Fort Tejon earthquake). Some field measurements also revealed to be very different at the same place depending on the authors (differences of meters to several meters, e.g., 2001 Kunlun, 2008 Sichuan, Yushu 2010 EQs section).
- In a few cases, there is a lack of precise field data (e.g. 1997 Manyi earthquake). Radar imagery is thus used. Where the images are of good resolution (covering the entire rupture length, good weather conditions, no topography, no dense vegetation), the coseismic displacements are well recovered. However, Radar-based coseismic slips generally include a significant part of pre and post-seismic deformation. They also generally need assumptions on the fault dip and do not recover as well the different slip components. Altogether this provides uncertainties on the recovered slip amounts.

In the general case, the synthesis of multiple sources of information helped me to identify and discard the outlier measurements.

The data describing the EQs at depth generally include far-field observations –mainly teleseismic seismological records and GPS measurements, and near-field observations – mainly near-fault, regional or local seismological, strong-motion and geodetic records. These or parts of these data are then combined, using different modeling procedures, and sometimes including surface observations, to produce a source model. The source models produced for a same EQ generally differ however on a few or on many aspects:

- The imposed fault geometry (length and width, segmentation, azimuth, dip). Old inversion models (before 90s) generally used one single fault plane. More recent models introduce more complex fault geometries including different segments, azimuth changes, variations of the geometry at depth, etc. However, it is not always clear that these complexities reflect the fault reality, or are introduced because they allow a better fit between the model results and the observations.
- The size of the "sub faults" used in the models (grid resolution): This size is generally linked to the magnitude of the EQ (generally a larger size for larger magnitude). However, for a same EQ, different sizes of sub faults are used in the different models (e.g 1992 Landers EQ). If "sub-faults" are too large, this leads to a smoothing of the slip distribution. The

information on slip gradients is then missing, and so is also the information about segmentation/slip heterogeneity.

- Amount/quality of data used in the models: the robustness of the inversion model solutions greatly depends on the spatial distribution and density of the geodetic/seismological networks situated around the rupture.
- Type of data used in the models: different datasets used separately do not result in the same slip distribution (e.g. Wald et al., 1996; 1994 Northridge EQ). Seismological far field data better constrain the slip distribution at depth and the temporal evolution (directivity, propagation) of the rupture. By contrast, the amount of slip is less well constrained and is often underestimated (mainly due to the simplification of the fault parameters used in the calculations). On the other hand, local and fairly dense geodetic data (GPS, InSAR) better constrain the length of the rupture, the slip amount at surface and the localization of the major slip patches at depth, but they do not constrain very well the spatial distribution of the slip at depth. Pre- and post-seismic deformation can also be contained in the INSAR and optical geodetic data, what might be a source of error in the inversion model.

Therefore, I had to attempt discriminating the most robust source models. I made this discrimination based on the following points:

- Realistic dimension and segmentation of the broken fault;
- Integration of the surface data;
- Large amount of complementary data to be used in the model. In particular, dense and well distributed, near-field seismological and/or geodetic data greatly improve the quality of the models. Recent models are supposed to be best constrained because they benefit from denser and more rich data;
- Joint-inversion of complementary data reduces the sources of errors.

Short discussions explaining the choice or rejection of some of the EQ data are provided in Appendices section.

The data which I retain as most robust are also synthesized in the IDs below, and in the Tables provided in section III-3

2. Fault-Earthquakes extended ID

2.1. Baja California 2010

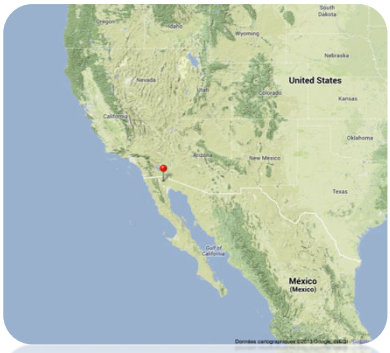
04/Apr/2010, Mexico

Mw 7.2

Epicenter : 32.30°N-115.30°W

Right-lateral strike-slip

(with normal component)



Broken long-term fault

The 2010 Baja California earthquake, also called 'El Mayor Cucapah earthquake', broke a part of the Elsinore fault, a southern branch of the San Andreas Fault. **Note that the San Andreas Fault is described in the sections "Fort Tejon 1857" (Southern San Andreas) and "San Francisco 1906" (Northern San Andreas). The relations of the San Andreas Fault with the Elsinore and the San Jacinto faults are discussed in section "Fort Tejon 1857".** The Elsinore Fault is the longest splay of the Southern San Andreas Fault.

General characteristics of the Elsinore Fault from literature (Fig.28):

- The Elsinore Fault strikes N130° –parallel to the most recent major segment 5 of the Southern San Andreas Fault (See section Fort Tejon) and to the San Jacinto Fault (Fig.28a). Although the Elsinore Fault is now interacting with and somehow offset by the Sierra Madre/San Gabriel faults in the north, it likely originated from the Southern San Andreas Fault. Therefore, the Elsinore Fault has propagated southward over geological time, and its total length is at least ~600 km long from Tejon Pass to the Gulf of California (It might be greater since part of the fault is in the Gulf of California; See Fig.29).
- The Elsinore Fault is taken to have initiated 1-2.5 Ma ago (e.g. Doser et al., 2012; Hull and Nicholson 1992). However, our mapping described below and in the section "Fort Tejon" suggests that the Elsinore Fault developed as a splay fault of the Southern San Andreas (as

also shown by Scholz 1977, 2010; Crowel 1979), when the later was mainly made of its northernmost segments (n°1-2, See section "Fort Tejon"). Since the Southern San Andreas Fault initiated ~12 Ma ago (Powell and Weldon 1992 and references therein; Sims 1993), we suspect that the northern part of the Elsinore Fault formed several Ma ago, possibly ~10 Ma ago. Currently, the Elsinore Fault is interacting in its southern part with the Gulf of California faults (Fig.29). Since the Gulf opened ~5 Ma ago (e.g. Spence and Normark 1979; Lonsdale 1989), we infer that the southern part of the Elsinore Fault is younger than 5 Ma. Together these confirm that the Elsinore Fault has been propagating southward over the long-term, likely over the last 5-10 Ma.

- Maximum cumulative lateral slip of 10-15 km estimated locally from matching offset crystalline rocks (Weber, 1977; Morton and Miller, 1987)
- The current lateral slip rate is suggested to be very low (Fialko, 2006). Meade and Hager (2005) (GPS) and Lundgren et al. (2009) (InSAR) estimate a maximum lateral slip rate of 2 ± 3 and 3 ± 1 mm/yr.
- Holocene lateral slip rate ~ 5 mm/yr (See Petersen and Wesnousky 1994; Magistrale and Rockwell 1996).

→ The 2010 Baja California EQ broke a part of the Elsinore Fault, which is a major splay of the Southern San Andreas Fault. The Elsinore Fault has an intermediate maturity (L ~600 km, I-Age 5-10 Ma, D_{total} ~15 km, and MR ~ 5 mm/yr), yet closer from mature than from immature (class "Interm → mature" in Table 5).

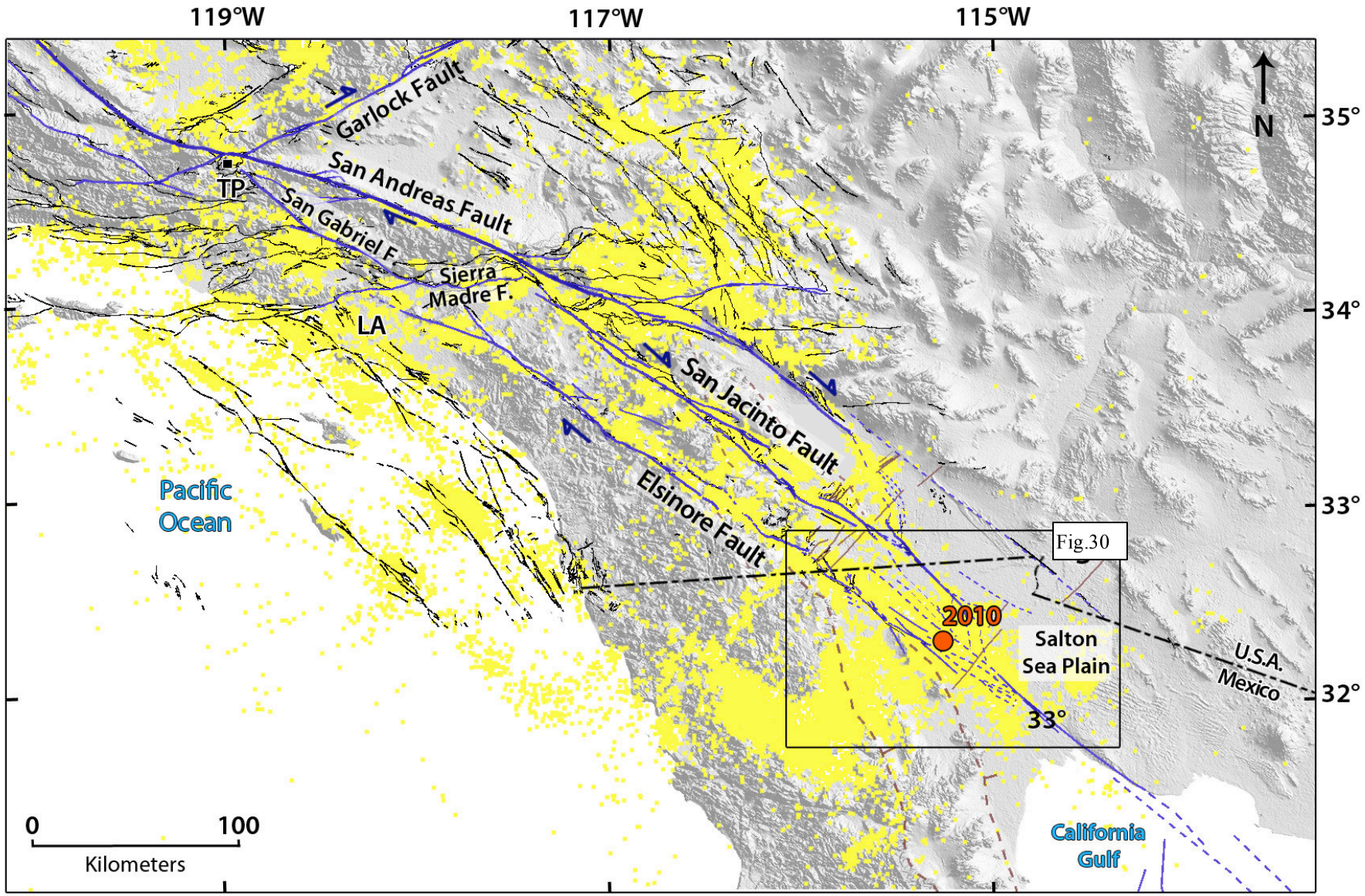


Fig.28: (a) General map of long-term faults in Southern California. In blue are the major active faults that we mapped. In black are the other Quaternary faults mapped by the U.S. Geological Survey and California Geological Survey, 2006. In dotted brown are ancient faults related to the Gulf of California (see also fig.29). In solid brown are preexisting lineaments likely related to the Gulf of California (see text). The orange circle shows the 2010 Baja California epicenter. The yellow dots are the instrumental earthquakes (Mw>2) recorded between 1981 and 2011 (Hauksson et al., 2012). LA : Los Angeles ; TP : Tejon Pass).

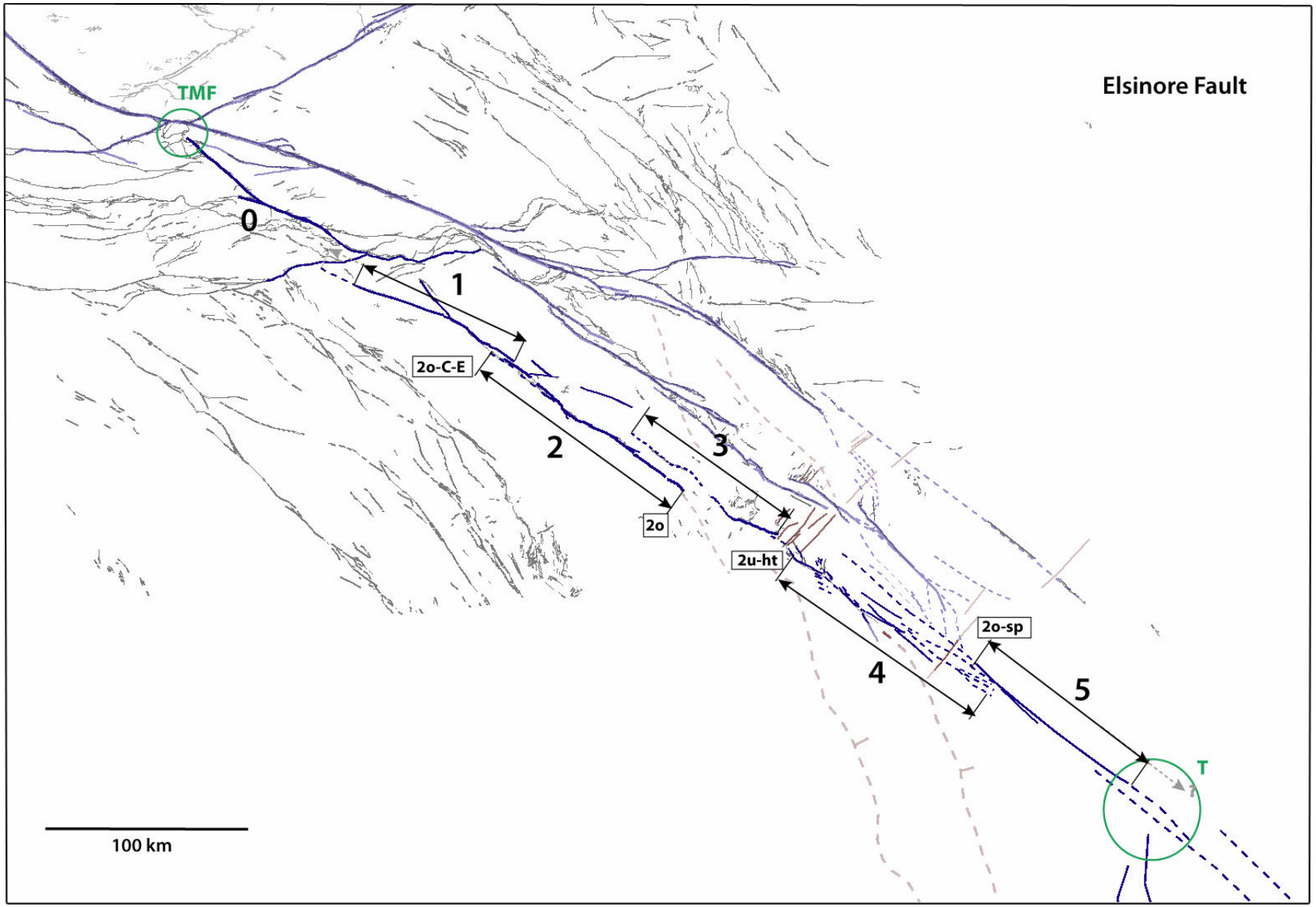


Fig.28: (b) Same active fault map as in 28 (b), but with focus on the major segments of the Elsinore fault. The segments are numbered from NW to SE and indicated by black arrows parallel to their mean strike. The grey prolongation of the arrows indicates the uncertainties on the segment lengths. Segment "0" is the likely very first segment of the Elsinore fault, before it was cross-cut by the Sierra Madre fault. The nature of the inter-segment zones is indicated in letters within boxes explained in Table 6. The nature of the fault tips is indicated in green (Table 6)

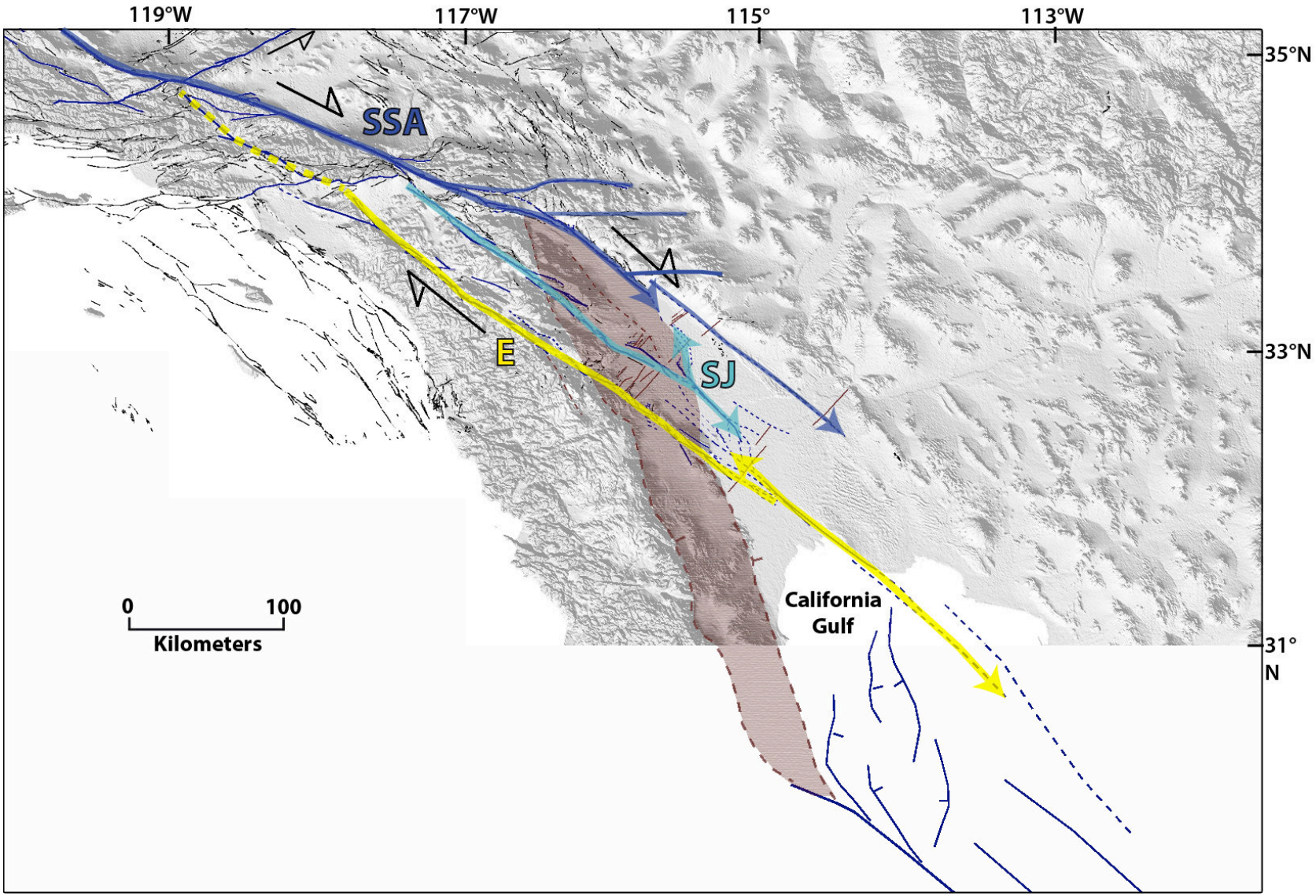


Fig. 29: General map showing the interaction zone between the southern San Andreas fault system and the Gulf of California (brown area). SSA : Southern San Andreas fault (Dark blue); SJ: San Jacinto fault (pale blue); E : Elsinore fault (yellow). In dotted brown lines are ancient faults related to the Gulf of California. Faults situated off shore in the Gulf of California are modified from Dorsey (2010). Arrows indicate direction of propagation.

Architecture and lateral major segmentation, from our and USGS mappings (Fig.28 & 30):

- Mapping done from Google Earth, Landsat and ASTER GDEM data combined with USGS detailed mapping (U.S. Geological Survey and California Geological Survey, 2006)
- The Elsinore Fault is ~35 km west of the sub-parallel San Jacinto Fault.
- To the NW, the main strand of the Elsinore Fault connects with the Sierra Madre/San Gabriel Fault. The fault trace continues further NW however, up to the San Andreas Fault to which it connects.
- To the SE, the Elsinore Fault terminates by splaying into multiple branches, which curve and die out in the Gulf of California. There, ~NS normal faults have developed which connect the Elsinore Fault, through a large pull-apart basin, with parallel transform faults further south in the Gulf (e.g. Lonsdale 1989, Fig.29).
- In its southern part, the Elsinore Fault intersects and interacts with pre-existing NNW faults that were likely formed when the Gulf of California opened (Fig.29). Clearly, the Elsinore Fault offsets the NNW Gulf faults, and hence is younger in this area. In the Salton Sea plain, numerous NE-trending small lineaments are observed, that we suspect to be ancient small faults developed at the northern tip of the major, normal NNW Gulf faults (in brown in Fig.29).
- The Elsinore Fault is divided into 6 major, fairly collinear segments (See Fig.28b where they are numbered), 5 of them form the main strand of the Elsinore Fault, south of its present connection with the Sierra Madre/San Gabriel Fault. The lengths and types of the segments and inter-segments are described in details in Table 6.
- The 5 major segments of the main strand have a length of similar order, in the range 80-120 km (length measured along the linear trace of each segment; Fig.28b).
- The fault trace is fairly linear along the 2 northernmost major segments (segts 1-2), and more sinuous and discontinuous along the central segments 3 and 4. The trace of the southernmost segment 5 is more difficult to define as part of it is inside or on the edge of the Gulf of California.
- Segments 1 and 2 are fairly well connected at the surface through a narrow pull-apart-type relay zone, hence of type $2_{O\text{-}C\text{-}E}$. Segment 3 is sub-parallel to segments 1 and 2, but its trace is more discontinuous. It is not directly connected at the surface to segment 2, the two segments being instead separated by a large relay zone of type 2_O. To the south, segment 3 terminates within a zone of multiple NE-trending, likely pre-existing fractures and faults. Segment 4 is sub-parallel to the other major segments, but has a discontinuous trace (See

below). It is separated from segment 3 by a zone of dense perpendicular fracturing. Furthermore, to the north, segment 4 terminates through small horsetail faulting. By contrast, to the south, segment 4 terminates by splaying into multiple secondary branches, which contribute to connect segment 4 to segment 5. The southernmost segment 5 extends up to the Gulf of California where it likely splays into multiple branches. To the north, segment 5 ends by splaying into multiple branches. Small faults at high angle to the segment 5' trace have also developed to achieve the pull-apart-type connection between the Elsinore and the San Jacinto faults.

- The linear trace of segments 1 and 2 as well as their clearer connection at surface, are in keeping with those segments having formed earlier along the Elsinore Fault than the segments 3-5.

→ South of its connection with the Sierra Madre/San Gabriel Fault, the Elsinore Fault is divided into 5 long-term, major collinear segments. The Elsinore Fault has propagated southwards over time; its northernmost section (at least coinciding with major segments 1 & 2) is thus likely the oldest and most mature.

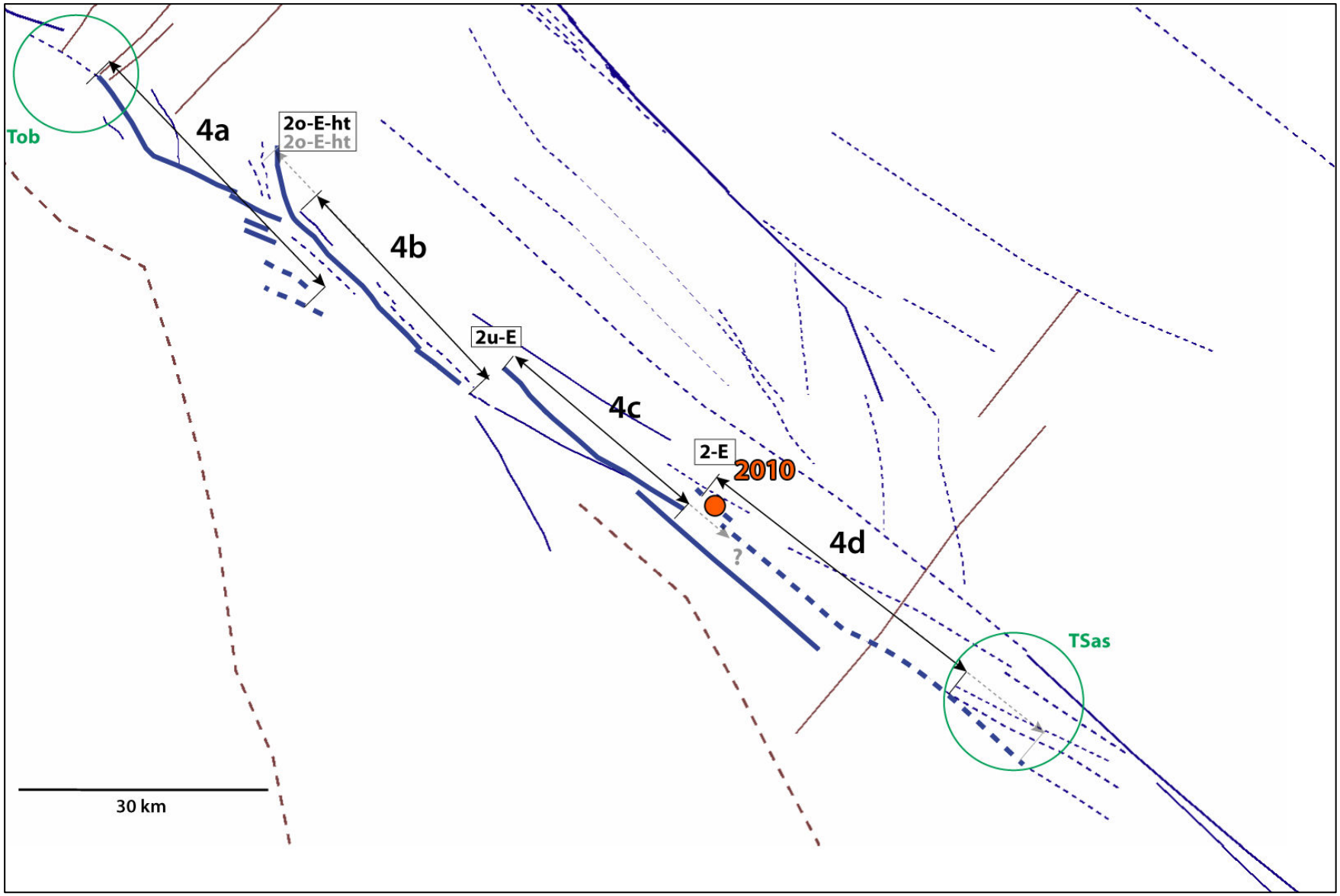


Fig. 30:(a) Map of the secondary segments that form the major segment 4 of the Elsinore fault. Same caption as in fig.28. The 4 secondary segments are en echelon disposed along the mean strike of the fault. Each is itself divided into en echelon smaller faults. The orange circle indicates the EQ epicenter.

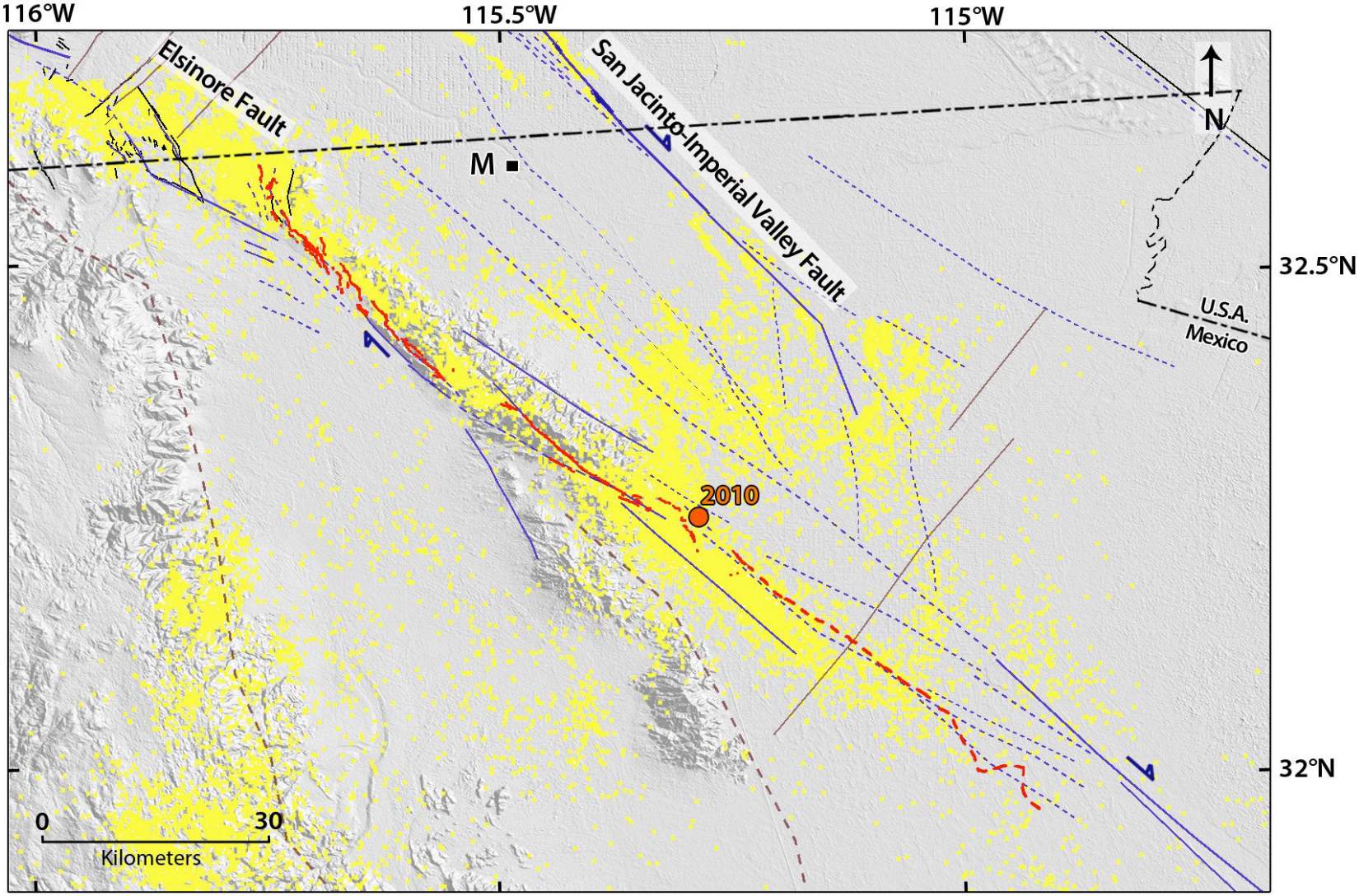


Fig.30: (b) Zoom on the broken section of the Elsinore fault, from Fig.28a (same caption). The surface rupture is indicated by the red line; the southeast part of the rupture is deduced from satellite image pixel correlation (red dotted line, Wei et al., 2011). The rest of the rupture mapping was done using airborne Lidar data (Oskin et al., 2012). M : Mexicali.

2010 Coseismic rupture

Surface trace and location on long-term Elsinore Fault :

- A large part of the 2010 surface rupture is visible on Google Earth (which include Lidar data available on http://www.opentopography.org/index.php). Yet the ruptures are distributed, making their mapping more difficult. The northern half part of the surface rupture trace of the 2010 earthquake has been precisely mapped and the displacements measured on the field (Fletcher 2010; Teran et al., 2011) and from LiDAR imagery (Oskin et al., 2012; Gold et al., 2013). The southern half of the rupture was more difficult to map on the field due to its location in an anthropized region. Displacements along the entire rupture length were estimated from InSAR and SPOT image analysis (Wei et al., 2011).
- Total surface rupture of ~120 km long.
- The EQ broke most of the major segment 4 of the Elsinore Fault.
- Major segment 4 is made of 4 secondary segments (4a, 4b, 4c, 4d, Fig.30a), disposed in a left-stepping echelon along the mean NW strike of major segment 4. The trace of segment 4a is subtle as it passes through a sedimentary plain. The 4 en echelon segments have a similar length of ~30 km. Although their overall trace is fairly linear, in more details each secondary segment appears itself divided into en echelon smaller faults.
- The 2010 EQ broke the 3 southernmost secondary segments 4b-c-d (Fig.30b). Their en echelon general arrangement and their en echelon segmentation at a smaller scale together explain why the surface trace of the 2010 rupture was so distributed and hence difficult to map.
- Because they are en echelon arranged, the secondary segments 4a to 4d are not directly connected to each other at the ground surface (except segments 4b and 4c in between which a small fault extends). Rather, they are separated by large steps and hence relay zones of type 2.
- The EQ nucleated near the inter-segment 4c-4d. Then the EQ propagated bilaterally towards the north and south. In the north, the rupture terminated in the distributed horsetail fault zone developed at the northern tip of segment 4b. In the south, the rupture ended within the splay fault zone developed at the southern tip of segment 4d.
- Since the Elsinore Fault has been propagating southward over geological time, the northern segment 4b is likely more mature than the southern segments 4c and 4d.

→ The 2010 Baja California EQ broke most of the southern major segment 4 of the Elsinore Fault. The EQ thus occurred on a fairly immature part of the Elsinore Fault. Within the major segment, the EQ broke three secondary segments of similar length, disposed en echelon along the mean fault trace.

Coseismic displacements measured at surface:

- *From Field measurements*: maximum lateral and normal slip of 3.1 and 2 m, respectively (net oblique slip of ~4 m; Fletcher 2010; Teran et al., 2011) measured on segment 4b.
- Because the rupture occurred in a sedimentary plain, and was furthermore distributed on multiple en echelon faults, it is likely that a fraction of the coseismic slip could not be measured; the values above might thus be underestimated.
- *From sub-pixel correlation in InSAR and SPOT images*: 3.5 m of lateral slip (See Fig.31b; Wei et al., 2011) measured on segment 4c.
- The complete slip profile is only inferred from InSAR/SPOT sub-pixel correlation (Wei et al., 2011), and therefore the vertical component of the slip is not resolved. However it is suggested that the maximum slip occurred in the northern part of the rupture.

→ Maximum oblique slip of 3.5-4 m at surface, which occurred on the northernmost segment 4b, i.e., on the most mature part of the broken fault section.

Source inversion models and slip distribution at depth (Fig.31b):

- We present one source inversion model that has been published on the 2010 Baja California earthquake (grid available Table 2).
- Wei et al. (2011): SPOT images, GPS, InSAR and teleseismic data. The model considers four fault planes: 1 for segment 4d; 1 for segments 4b+4c; 1 for the northern tip of segment 4b that we mapped as horsetail structures; 1 oblique fault plane for a NS normal blind fault centered on the epicenter (to take into account initial small normal component; see 'Other source parameters section'). L*W of the model = 135*18 km
- The model used a lot of different and complementary dataset. However we note some uncertainties: the model is better constrained in the northern part of the rupture where data are available and more accurate (SPOT images and GPS stations in U.S.). Although the surface offsets (Fig.31a) are used in the model, the displacements modeled near the surface (Fig.31d) are lower than those observed at surface.

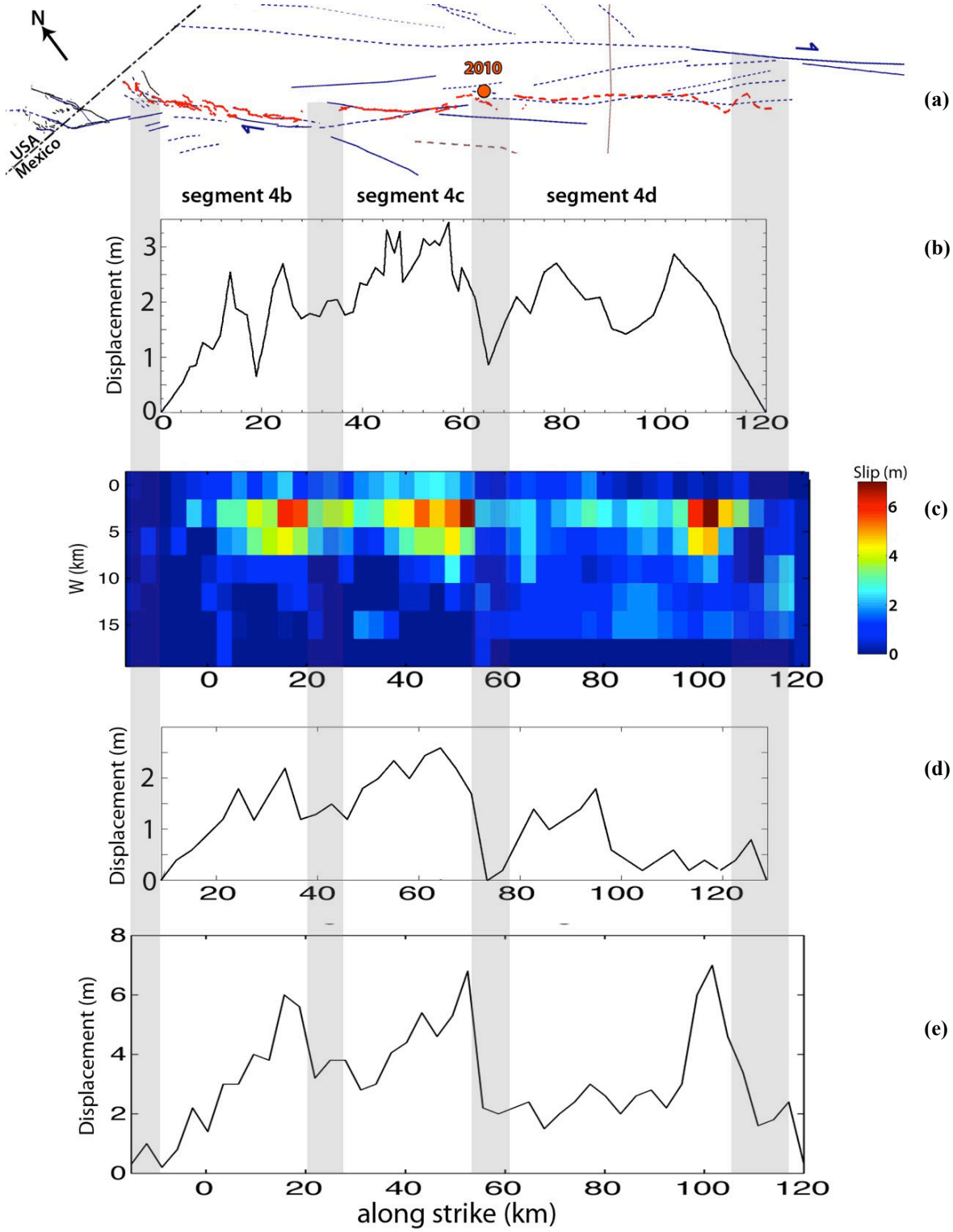


Fig.31: (a) Surface rupture trace, from Fig.30: b) lateral slip-length profile measured at surface from satellite image pixel correlation (Wei et al., 2011) ; (c) Inversion model from Wei et al., 2011 ; (d) profile of maximum slip inferred at surface from the source model in (c) ; (e) profile of maximum slip inferred at depth from the source model in (c). Grey areas represent the intersegment zones.

- The model shows three patches of large slip (6 m) concentrated at ≅5km depth (Fig.31c and 31e). The highest slip patch situated in the southern part of the rupture (where InSAR signal is noisy and the model resolution is lower) might be overestimated. Therefore we consider that the maximum slip occurred in the northern half part of the rupture
- Most of the slip occurred between 0 and 10-15 km depth, over a length of ~120 km

→ The source model suggests: L 120 km, W 10 km, Dmax at depth 6.3 m, 3 segments supposedly broken.

Other source parameters:

SCARDEC
Mainshock: 2010/04/04 at 22h40m43s GMT
Lat = 32.297° Lon = -115.278° (NEIC)
Mw 7.2; M0 = 8.17e19 Nm ;
0 <Z < 25 km ; Duration: 33s (Fig.32)
Strike, dip, rake:(133°,80°,172°)/ (224°,82°,11°)

Global CMT
Mainshock: 2010/04/04 at 22h41min09s GMT;
Lat = 32.31° Lon= -115.39°
Mw 7.2; M0 = 7.62e19 Nm;
Z = 12,8 km; Half-duration: 9.6s
Strike, dip, slip: (223°,84°,-2°)/ (313°,88°,174°)

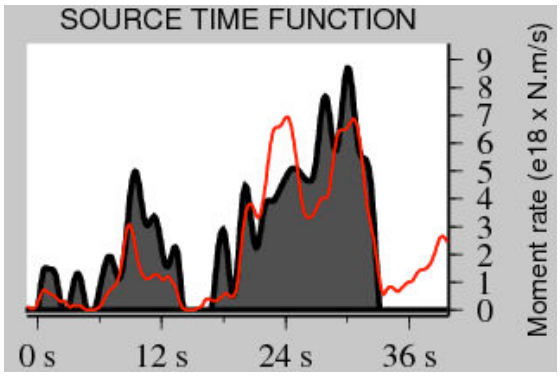


Fig.32: Source Time Function calculated with the SCARDEC method (Vallée et al., 2011). In grey : best STF ; in red : mean STF.

- The duration values differ between the two methods. However the rupture duration calculated from the model of Wei et al. (2011) (~ 30 s for the rupture along the main fault) is in fair agreement with the SCARDEC duration.
- Moment magnitude and seismic moment are in good agreement.
- Three peaks are distinguished in the mean Source Time Function (Fig.32, in red), suggesting the rupture of three distinct sections along the fault. The EQ energy increased progressively over time: the rupture primarily started with a small peak of energy release that lasted 6-8 s (between ~6 and 14 s). Then two large peaks of moment were released over the next 20 s

(between ~18 and 33 s). Since the rupture propagation was bilateral, it is difficult to interpret which segment broke first. One interpretation is that the two last and largest moment peaks coincide with the rupture of segments 4b and 4c where larger slip was measured. In that case, the first peak might correspond to the rupture of segment 4d. Hauksson et al. (2010) shown that the rupture actually began by a Mw 6 normal faulting event that occurred on an oblique fault in the center of the rupture (likely, a small en echelon fault either in the inter-segment zone 4c-4d where the EQ nucleated, or along segment 4c or 4d), then was followed 15s later by the main event.

Other information:

Past EQ activity:

- The 1892 (Mw 7.2) Laguna Salada earthquake is taken to have broken the range bounding section of segment 4b, which is ≅2 km to the west of the 2010 rupture traces (e.g. Mueller and Rockwell 1995; Hough and Elliot 2004).

2010 EQ:

- The aftershock zone extends over 120 km long, in agreement with the surface rupture length. The largest aftershock (Mw 5.7) occurred at the northern end of the rupture (Hauksson et al., 2010)

Parameters retained to describe the 2010 Baja California EQ (Tables 2-4):

Mw 7.2; M0 ~ 7.6-8.2 e19 Nm; L 120 km ; W 10-15 km; Dmax surface ~ 4 m ; Dmax depth ~ 6.3 m.

Number of segments broken on the Elsinore Fault: 1 major segment, partly; representing the rupture of 3 secondary segments.

The surface slip-length data of the Baja California earthquake fall between the third and fourth functions (orange and green curves; Fig.33) whereas the depth slip–length data fall on the third function (in green; Fig.34). Together these are in keeping with the EQ having ruptured three distinct segments on the long term Elsinore Fault. (See more discussion in chapters IV and VII, since secondary segments are concerned here).

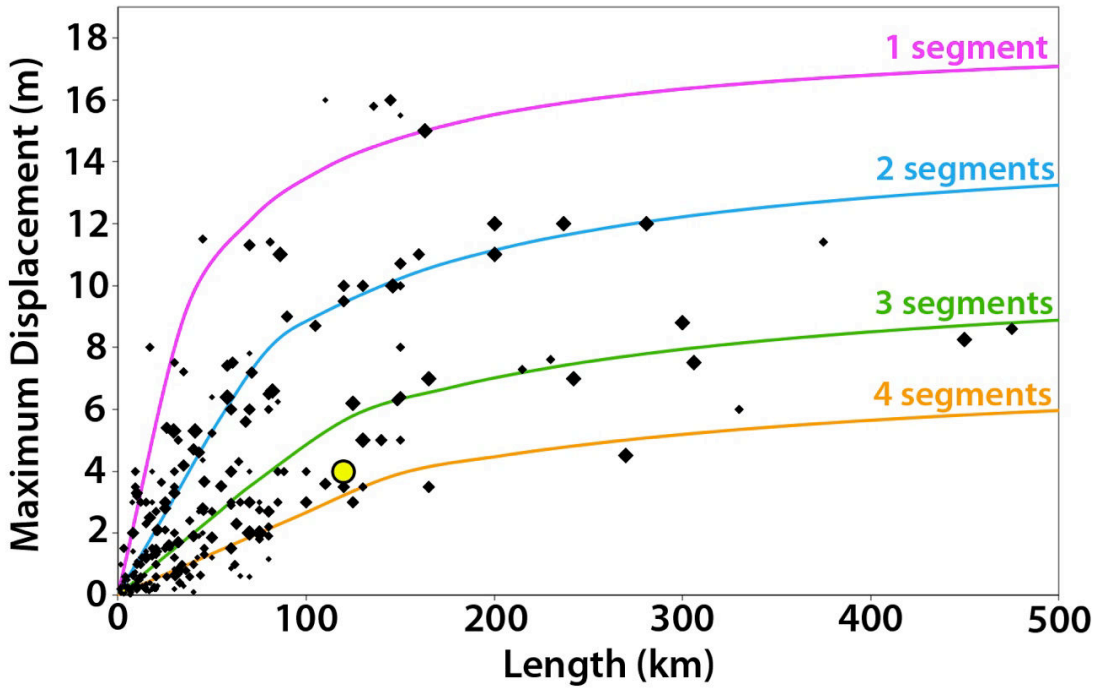


Fig.33: Earthquake displacement-length data measured at surface for 260 historical large continental earthquakes (Mw≥6). The 4 curves indicate the number of major long-term fault segments to have been broken by the earthquakes (modified from Manighetti et al., 2007 and Chapter IV). The yellow dot shows the 2010 Baja California earthquake surface slip-length data.

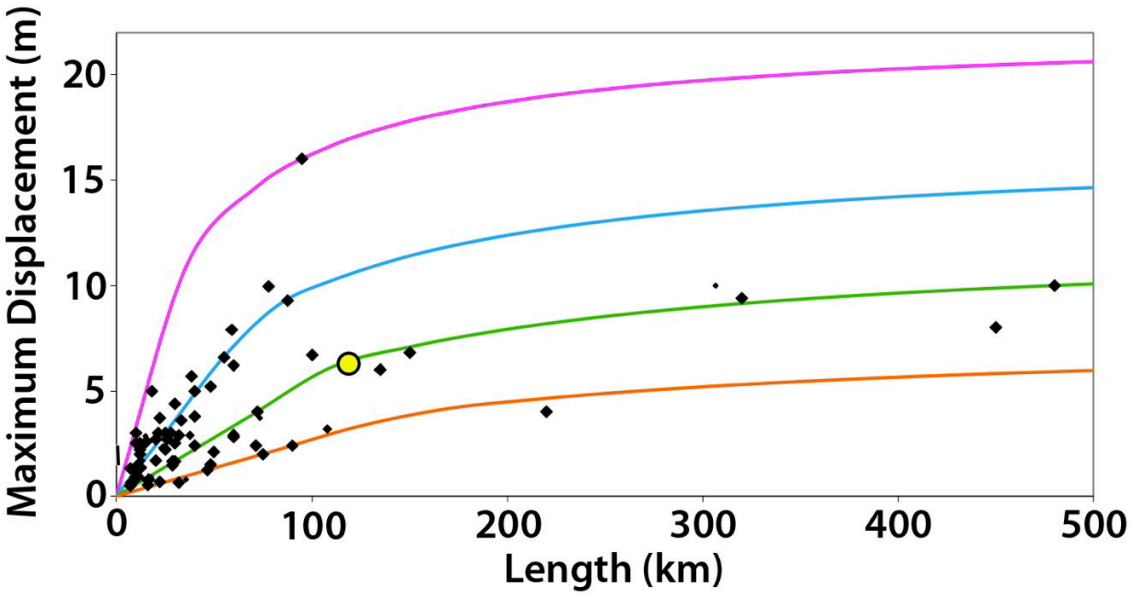


Fig.34: Earthquake displacement-length data inferred at depth for 90 historical large continental earthquakes (Mw≥6). The 4 curves indicate the number of major long-term fault segments to have been broken by the earthquakes (modified from Manighetti et al., 2007 and Chapter IV). The yellow dot shows the 2010 Baja California earthquake depth slip-length data.

References

Crowell, J. C. (1979). The San Andreas Fault system through time. *Journal of the Geological Society*, **136**(3), 293-302.

Dorsey, R. J. (2010). Sedimentation and crustal recycling along an active oblique-rift margin: Salton Trough and northern Gulf of California. *Geology*, **38**(5), 443-446.

Dorsey, R. J., G. J. Axen, T. C. Peryam, & M. E. Kairouz (2012), Initiation of the Southern Elsinore Fault at ~1.2 Ma: Evidence from the Fish Creek–Vallecito Basin, southern California, *Tectonics*, **31**, TC2006, doi:10.1029/2011TC003009.

Fialko, Y. (2006), Interseismic strain accumulation and the earthquake potential on the southern San Andreas Fault system, *Nature*, **441**, 968–971, doi:10.1038/nature04797.

Fletcher, J.M., Rockwell, T.K., Hudnut, K., Teran, O., Masana, E., Faneros, G., & Galetzka, J.E. (2010). Kinematic and Dynamic Analysis of the Mayor-Cucapah Earthquake: A Case for 3-D Strain Accommodation in a Single Earthquake Cycle. In *AGU Fall Meeting Abstracts* (Vol. 1, p. 07).

Gold, P.O., Oskin, M.E., Elliott, A.J., Hinojosa-Corona, A., Taylor, M.H., Kreylos, O., Cowgill, E. 2013. Coseismic slip variation assessed from terrestrial lidar scans of the El Mayor–Cucapah surface rupture. *Earth and Planetary Science Letters*, **366**, 151–162.

Hauksson, E., Stock, J., Hutton, K., Yang, W., Vidal-Villegas, J. A., & Kanamori, H. (2010). The 2010 M w 7.2 El Mayor-Cucapah Earthquake Sequence, Baja California, Mexico and Southernmost California, USA: Active Seismotectonics along the Mexican Pacific Margin. *Pure and applied geophysics*, **168**(8-9), 1255-1277.

Hauksson, E., W. Yang, & P.M. Shearer (2012). Waveform Relocated Earthquake Catalog for Southern California (1981 to June 2011); *Bull. Seismol. Soc. Am*., **102**, doi:10.1785/0120120010.

Hough, S. E., & Elliot, A. (2004). Revisiting the 23 February 1892 Laguna Salada Earthquake. *Bulletin of the Seismological Society of America*, **94**(4), 1571-1578.

Hull, A. G., & C. Nicholson (1992), Seismotectonics of the northern Elsinore fault zone, southern California, *Bull. Seismol. Soc. Am.,* **82**, 800–818.

Lonsdale, P. (1989). Geology and tectonic history of the Gulf of California. *The Geology of North America*, 499-521.

Lundgren, P., E. A. Hetland, Z. Liu, & E. J. Fielding (2009), Southern San Andreas-San Jacinto Fault system slip rates estimated from earthquake cycle models constrained by GPS and interferometric synthetic aperture radar observations, *J. Geophys. Res.,* **114**, B02403, doi:10.1029/2008JB005996.

Magistrale, H., & T. K. Rockwell (1996), The central and southern Elsinore fault zone*, Bull. Seismol. Soc. Am.,* **86**, 1793–1803.

Manighetti, I., M. Campillo, S. Bouley, and F. Cotton (2007), Earthquake scaling, fault segmentation, and structural maturity*, Earth Planet. Sci. Lett*., **253**, 429-438, doi:10.1016/j.epsl.2006.11.004

Meade, B. J., and B. H. Hager (2005), Block models of crustal motion in southern California constrained by GPS measurements*, J. Geophys. Res*., **110**, B03403, doi:10.1029/2004JB003209.

Morton, D. M., & F. C. Miller (1987), K/Ar apparent ages of plutonic rocks from the northern part of the Peninsular Ranges batholith, southern California, *Geol. Soc. Am. Abstr. Programs*, **19**, 435.

Mueller, K. J., & T. K. Rockwell (1995). Late Quaternary activity of the Laguna Salada Fault in northern Baja California, Mexico, *Geol. Soc. Am. Bull*. **107**, 8–18.

Oskin, M.E., Arrowsmith, J.R., Corona, A.H., Elliott, A.J., Fletcher, J.M., Fielding, E.J., Gold, P.O., Garcia, J.J.G., Hudnut, K.W., Liu-Zeng, J., Teran, O.J. 2012. Near-Field Deformation from the El Mayor–Cucapah Earthquake Revealed by Differential LIDAR. *Science*, **335**, 702–705.

Petersen, M. D., & Wesnousky, S. G. (1994). Fault slip rates and earthquake histories for active faults in southern California. *Bulletin of the Seismological Society of America*, **84**(5), 1608-1649.

Scholz, C. H. (1977). Transform fault systems of California and New Zealand: similarities in their tectonic and seismic styles. *Journal of the Geological Society*, ***133***(3), 215-228.

Scholz, C. H., Ando, R., & Shaw, B. E. (2010). The mechanics of first order splay faulting: The strike-slip case. *Journal of Structural Geology*, **32**(1), 118-126.

Spencer, J. E., & Normark, W. R. (1979). Tosco-Abreojos fault zone: A Neogene transform plate boundary within the Pacific margin of southern Baja California, Mexico. *Geology*, **7**(11), 554-557.

Teran, O. J., Fletcher, J. M., Rockwell, T. K., Hudnut, K., Oskin, M. E., Akciz, S. O., ... & Spelz, R. M. (2011). Structural Controls on the Surface Rupture Associated with the Mw7.2 El Mayor-Cucapah Earthquake of 4 April 2010: A Comparative Analysis of Scarp Array Kinematics, Orientation, Lithology and Width. In *AGU Fall Meeting Abstracts* (Vol. 1, p. 2348).

Vallée, M., J. Charléty, A.M.G. Ferreira, B. Delouis, & J. Vergoz, SCARDEC : a new technique for the rapid determination of seismic moment magnitude, focal mechanism and source time functions for large earthquakes using body wave deconvolution, *Geophys. J. Int.*, **184**, 338-358.

Weber, F. H. (1977), Seismic hazards related to geologic factors, Elsinore and Chino fault zones, northwestern Riverside county, California, *Calif. Div. Mines Geol. Open File Rep*., **77**-4, 96 pp.

Wei, S.J., Fielding, E., Leprince, S., Sladen, A., Avouac, J.P., Helmberger, D., Hauksson, E., Chu, R.S., Simons, M., Hudnut, K., Herring, T., Briggs, R. 2011. Superficial simplicity of the 2010 El Mayor–Cucapah earthquake of Baja California in Mexico. *Nat. Geosci*. **4**, 615–618.

2.2. Bogd 1957

04/Dec/1957, Mongolia

Mw 8.1

Epicenter : 45.31°N-99.21°E

Left-lateral strike-slip

(with reverse component)



Broken long-term fault

The EQ broke a part of the Bogd Fault in the Gobi Altaï Range, Mongolia.

General characteristics from literature:

- Fairly linear, left-lateral strike-slip fault oriented N100°E, about 430 km long (Fig.35, which shows the fault map I have done).
- The Bogd Fault would have formed as a result of the northward propagation of the Indo-Eurasia Cenozoic transpressive deformation (Molnar and Tapponnier 1975; Tapponnier and Molnar 1977, 1979), 8 to 2 Ma ago (e.g. Vassalo et al., 2007a).
- Total cumulative lateral slip is not known.
- Long-term slip rate over the Quaternary: 1 mm/yr and 0,1-0,2 mm/yr of lateral and vertical slip rate, respectively (Ritz et al., 1995, 2006; Vassalo et al., 2005, 2007b; Rizza et al., 2011) based on morphotectonic studies (offsets of fluvial terraces and alluvial fans) at different sites along the fault.
- Current lateral slip rate: ~1,2 mm/yr (Calais et al., 2003) based on two GPS stations either side of the fault.

→ The Bogd Fault has an intermediate maturity (L 430 km hence 300<L<1000 km, I-Age 2-8 Ma hence 5<I-Age<10, MR ~1 mm/yr hence < 10 mm/yr), yet likely closer from mature than from immature (very long length; class "Interm → mature" in Table 5).

Architecture and lateral major segmentation, from our mapping (Fig.35):

- Mapping done from Google Earth, Landsat and ASTER GDEM data combined with literature information.
- Long-term fault trace well expressed in surface morphology and topography (Fig.35).
- The Bogd Fault is surrounded with a dense network of sub-parallel left-lateral strike-slip and oblique reverse faults. The strike-slip faults are the major tectonic features of the region. The strike-slip fault network associated with the Bodg Fault becomes wider towards the east. Since some of the off-fault strike-slip faults might be splays of the Bodg master fault, we infer that the Bodg Fault has been propagating eastward over geological time.
- To the west, the Bogd Fault abuts and ends against a NW-trending Fault (T_{ob}-type termination, Fig.24) that bounds the Golbi Altay Range to the north. To the east, the Bogd Fault terminates by abutting a network of sub-perpendicular, secondary reverse faults (T⊥-type termination, Fig.24) (See discussion below).
- The Bogd Fault is divided into 5 major, fairly collinear segments (See Fig. 35b where they are numbered).
- Those 5 major segments have a length of 60-100 km (minimum length measured along the linear trace of each segment; Fig.35b and Table 6).
- The fault trace is linear along segments 1 and 2, and more sinuous and discontinuous along the three easternmost segments. The five segments are sub-parallel and all connected by compressive relay zones with across-fault separation distances in the range 1-20 km (Table 6). The large intersegment zone between major segments 1 and 2 is now crosscut by the main fault trace, what shows that the two segments are now well connected to each other. The major segment 3 is well connected to the segment 2 but the orientation of the 2 segments differs slightly (azimuth change of ~8°). Major segment 4 has a trace more sinuous and discontinuous than that of segments 1 to 3, while its connection with major segment 3 occurs in a large step-over with distributed faulting; furthermore, an oblique, NE-trending reverse fault intersects the segments 3-4 relay zone. Segments 3 and 4 are thus less strongly connected that are the other segments further west. Segment 4 ends to the east by curving towards major segment 5 located further south. Segments 4 and 5 are indeed separated by a large compressive step-over (across-strike distance of ~20 km), of type $2_{O\text{-}R}$. The two easternmost segments are thus hardly connected presently at the ground surface. The trace of segment 5 is fairly discontinuous. It curves to the west in a compressive horsetail fashion, in a process to connect with segment 4. Together these observations are in keeping with the Bogd Fault having propagated eastward over geological time.

→ The Bogd Fault is divided into 5 long-term major collinear segments, the three westernmost are well connected to each other and are likely the most mature along the fault, which has propagated eastward overall over geological time.

1957 Coseismic rupture

Surface trace and location on long-term Bogd Fault:

- The 1957 surface rupture is clear on Google Earth, Landsat 7 and Aster GDEM v2 images. The surface trace of the earthquake has been precisely mapped, and the displacements measured (See below), both on the field and from satellite imagery (e.g. Kurushin et al., 1997; Choi et al., 2012).
- Surface rupture of 250-260 km long.
- The EQ broke three major segments of the Bogd Fault: segments 2, 3 and 4 (Fig.36). Some of the secondary reverse faults in the intersegment zones were also broken, in particularly at the western termination of major segment 2, and in compressive zones adjacent to major segment 3 (in southern compartment; also called "forebergs"; e.g. Bayasgalan et al., 1999).
- It is suggested that the rupture initiated in the west (Fig.35, Chen and Molnar, 1977) and this initiation actually locates at the western end of major segment 2. The rupture thus propagated mainly unilaterally towards the east.
- The rupture stopped on either side in one of the two largest relay zones between major segments: to the west, it stopped in the intersegment area between major segment 1 and 2; to the east, it stopped before crossing the very large step-over between major segments 4 and 5.

→ The 1957 Bogd EQ broke 3 major segments of the Bogd Fault. The rupture initiated at the western end of major segment 2, which is one of the most mature along the fault.

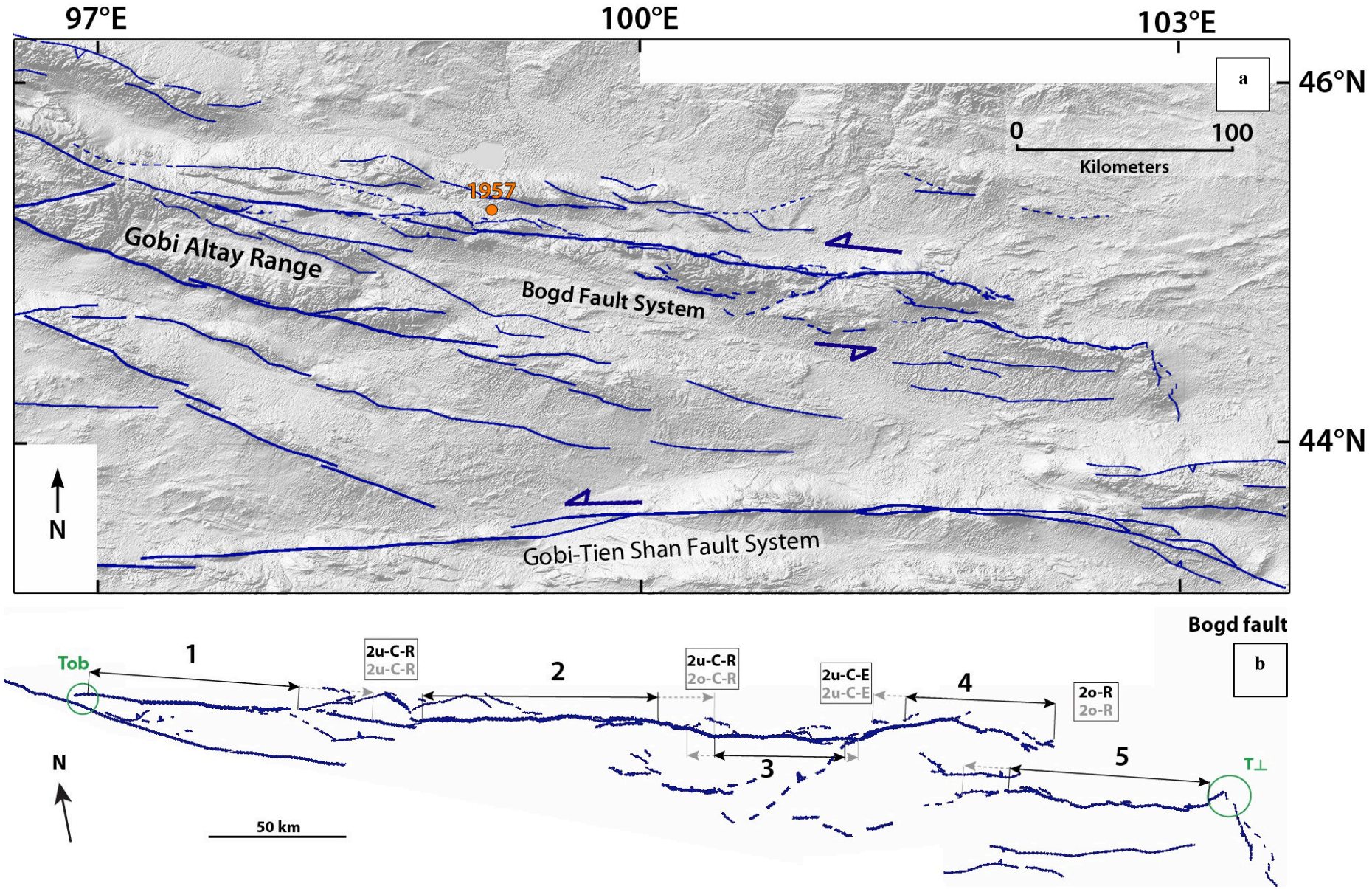


Fig.35: (a) General map of the main long term faults in Gobi Altaï (blue done from satellite image analysis). The orange circle shows the 1957 Bogd epicenter. (b) Focus on the major segments of the Bogd long term fault. The segments are numbered from W to E and indicated by black arrows parallel to their mean strike. The grey prolongation of the arrows indicates the uncertainties on the segment lengths.. The nature of the inter-segment zones is indicated in letters within boxes explained in Table 6. The nature of the fault tips is indicated in green (Table 6)

Coseismic displacements measured at surface:

- *From Field measurements*: The complete slip profile has been densely measured. The maximum lateral and vertical slip are ~7 m and 3-5m, respectively (Kurushin et al., 1997; Choi et al., 2012; Fig.36), measured on segment 2 and 3. The maximum lateral slip is on major segment 2.
- *From GPS measurements*: No GPS measurements were available at the time of the Bogd earthquake.
- The lateral slip represents the actual dominant displacement on the fault, whereas the vertical slip is only local, mainly occurring on small reverse faults developed at some of the inter-segments and on secondary reverse faults developed off- the master Bogd Fault (as south of major segment 3). There is thus a partitioning between lateral motion on the Bodg Fault and dip-slip motion on off-fault, slightly oblique, secondary structures. Therefore, the slip profile that characterizes the Bogd EQ rupture is the one that describes the lateral slip distribution.
- Although it shows a few gaps in the measurements, the profile of lateral slip has a fairly asymmetric triangular shape, with maximum slip at the western tip of the rupture, and slip tapering towards the east from that maximum slip.
- The inter-segments 2-3 and 3-4 are each marked by a pronounced slip deficit. The overall slip profile thus shows three major slip bumps that well coincide with the rupture of major segments 2, 3 and 4.

→ Maximum lateral slip of ~7 m well measured at surface, on segment 2 (western tip), that is on the most mature part of the broken fault section; fairly asymmetric triangular slip profile, tapering towards the east. Three main slip patches attesting of rupture of three major fault sections.

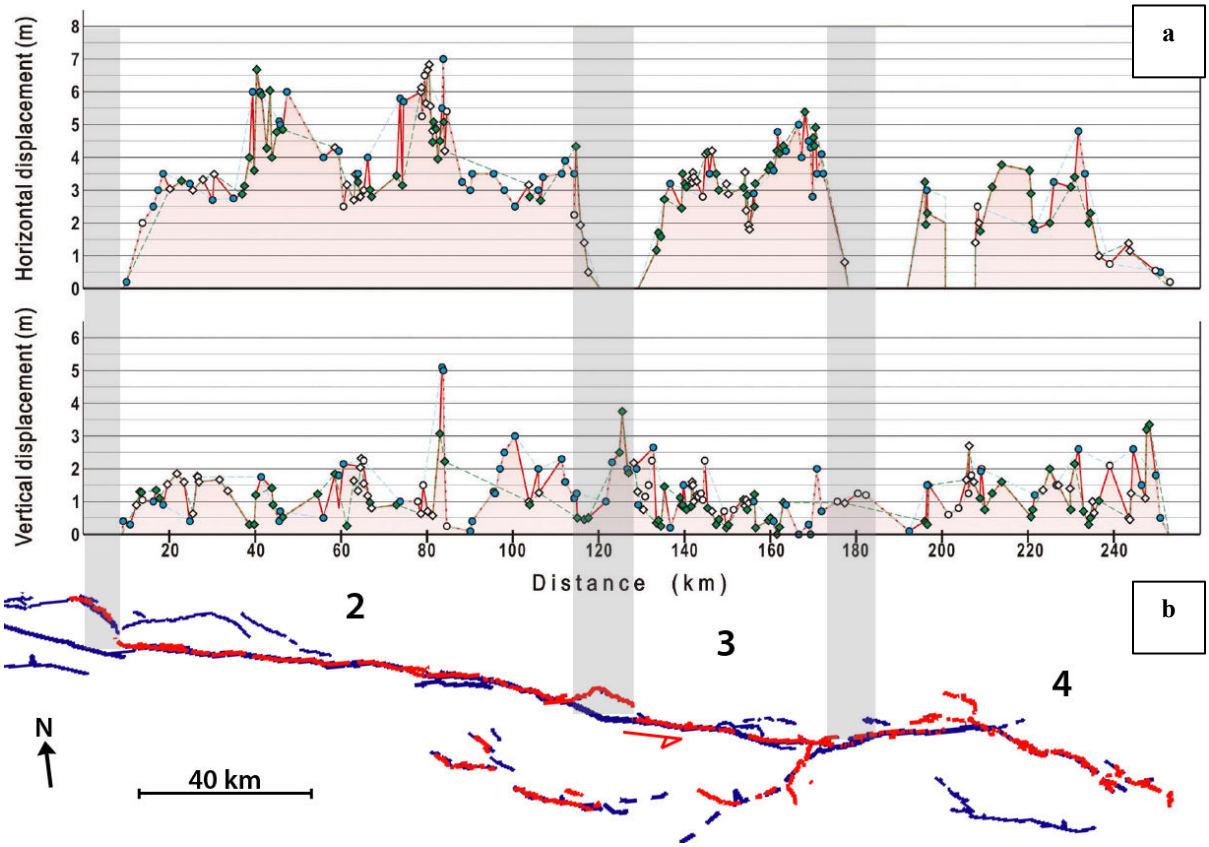


Fig.36: (a) Compilation of horizontal and vertical surface offsets measured after the 1957 Bogd earthquake (from Choi et al, 2012); (b) Surface rupture of the 1957 Bogd earthquake. Major segments are numbered and intersegment zones are shown by light grey areas.

Source parameters:

Calculated from long-period Rayleigh and Love wave spectral densities (Chen and Molnar 1977).

Lat = 45.31° Lon= 99.21°

M0 = 1,3e21 Nm; Z = 25 km (imposed, not inferred)

Strike, dip, slip: (-74°,42°,42°)

Other information:

Past EQ activity:

- The 1957 EQ belongs to a series of large events that broke in cluster the Mongolian fault system in a very short period of time (Fig.37), between 1905 and 1957: Tsetserleg 1905 (Mw 7.9), Bolnay 1905 (Mw 8.4), Fuyun 1931 (Mw 8.0) et Bogd 1957 (Mw 8.1). This clustering is described as stress triggering processes between faults during postseismic relaxation (Chery et al., 2001; Pollitz et al., 2003; Vergnolle et al., 2003).
- Rizza et al (2011) estimate recurrence times of 2500-5200 years for large earthquakes on the Bogd fault system. Offset measurements of Quaternary alluvial features suggest that the slip distribution was fairly similar along the fault on each previous large earthquake. Based on

those results, the authors assume that the Bogd fault system produces characteristic large earthquakes.

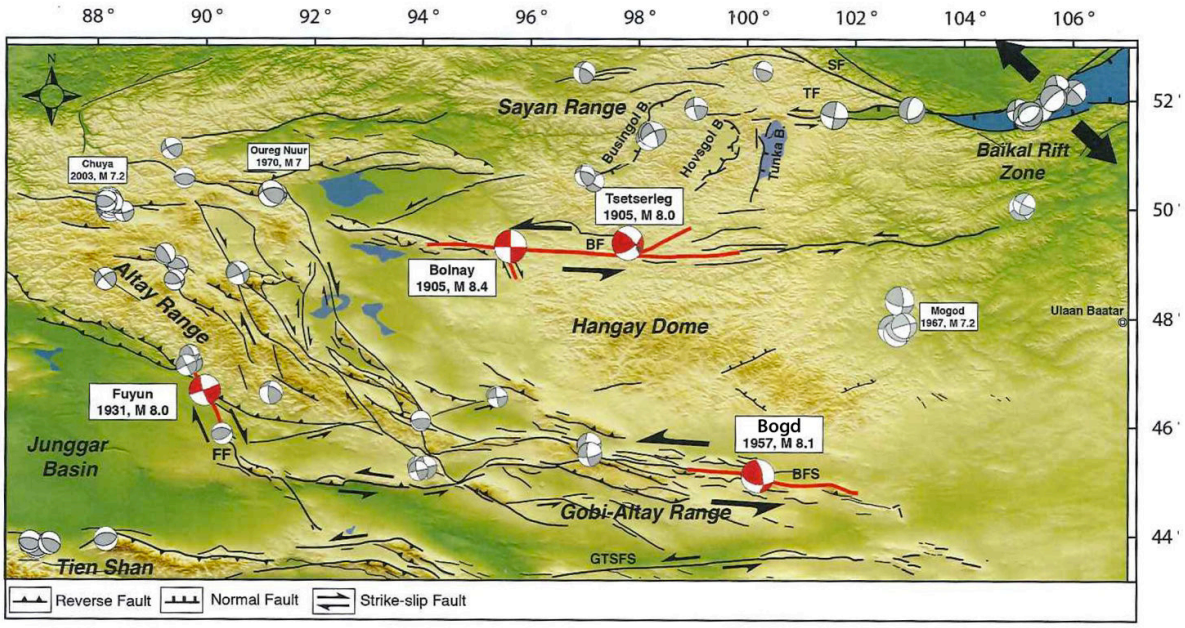


Fig.37: Topographic map showing active fault systems and major earthquakes in western Mongolia and neighboring regions (from Etchebes, 2011). Focal mechanisms, 6<M<8 in grey, M>B in red (Bayasgalan et al. 2005). Red lines are the surface ruptures associated with the large ones. GTSFS : Gobi-Tian Shan fault system; BFS : Bogd fault system; FF : Fuyun Fault ; BF : Bolnay Fault; TF : Tunka Fault; SF : Sayan Fault; B. : Basin.

Parameters retained to describe the1957 Bogd EQ (Tables 1 & 3):

Mw ~8.1; M0 ~ 1,3e21 Nm; L 250-260 km ; Dmax surface ~ 7 m ;

Number of major segments broken on the Bogd Fault: 3 major segments out of 5.

The surface slip-length data of the Bogd earthquake fall on the third function (green curve; Fig.38) in keeping with the EQ having ruptured three distinct major segments on the long term Bogd Fault.

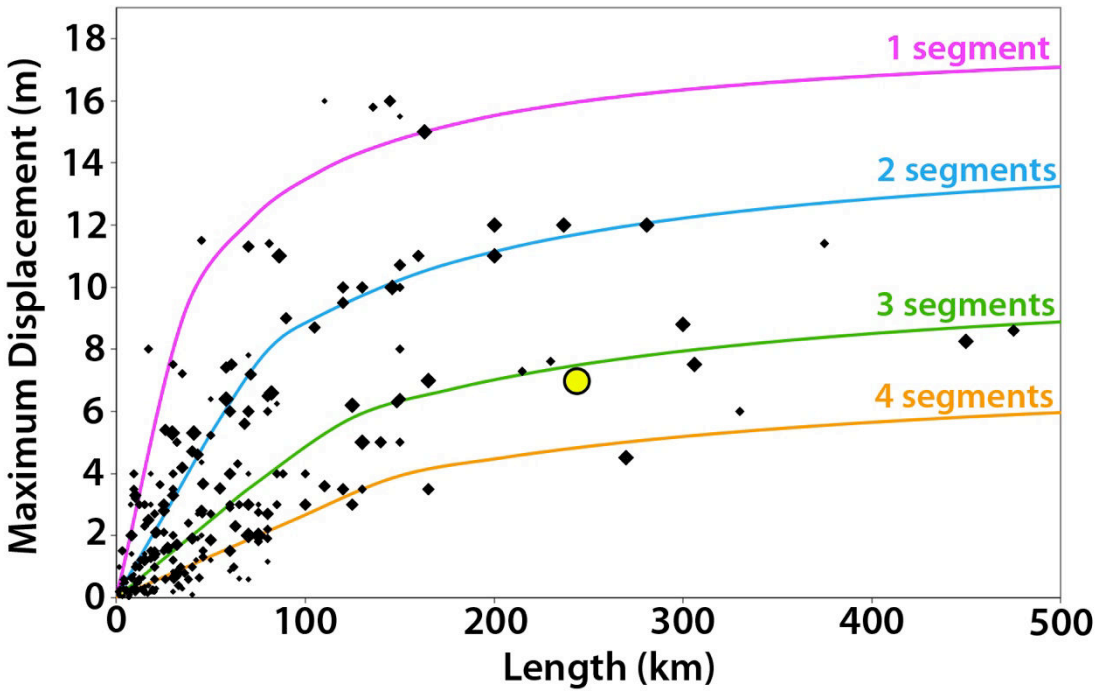


Fig.38: Earthquake displacement-length data measured at surface for 260 historical large continental earthquakes (Mw≥6). The 4 curves indicate the number of major long-term fault segments to have been broken by the earthquakes (modified from Manighetti et al., 2007 and Chapter IV). Yellow dot show the 1957 Bogd earthquake surface slip-length data.

References

Bayasgalan, A., J. Jackson, J.-F. Ritz, & S. Carretier (1999). 'Forebergs,' flower structures, and the development of large intra-continental strikeslip faults: The Gurvan Bogd fault system in Mongolia, *J. Struct. Geol.*, **21**, 1285–1302, doi:10.1016/S0191-8141(99)00064-4.

Bayasgalan, A., Jackson, J. & McKenzie, D. (2005), Lithosphere rheology and active tectonics in Mongolia: relations between earthquake source parameters, gravity and GPS measurements. *Geophysical Journal International*, **163**: 1151–1179. doi: 10.1111/j.1365-246X.2005.02764.x

Calais, E., M. Vergnolle, V. Sankov, A. Lukhnev, A. Miroshnitchenko, S. Amarjargal, & J. Déverchère (2003). GPS measurements of crustal deformation in the Baikal-Mongolia area (1994 – 2002): Implications for current kinematics of Asia, J. Geophys. Res., 108 (B10), 2501, doi:10.1029/2002JB002373.

Chen, W. P., & P. Molnar (1977). Seismic moments of major earthquakes and the average rate of slip in Central Asia, *J. Geophys. Res*., **82**, (20), 2945-2969.

Chéry, J., S. Carretier, & J. F. Ritz (2001). Postseismic stress transfer explains time clustering of large earthquakes in Mongolia, Earth Planet. Sci. Lett., 94, 277–286.

Choi, J.-H., K. Jin, D. Enkhbayar, B. Davvasambuu, A. Bayasgalan, & Y.-S. Kim (2012). Rupture propagation inferred from damage patterns, slip distribution, and segmentation of the 1957 MW 8.1 Gobi-Altay earthquake rupture along the Bogd Fault, Mongolia, *J. Geophys. Res.,* **117**, B12401, doi:10.1029/2011JB008676.

Kurushin, R. A., A. Bayasgalan, M. Olziybat, B. Enhtuvshin, P. Molnar, C. Bayarsayhan, K. W. Hudnut, & J. Lin (1997). The surface rupture of the 1957 Gobi-Altay, Mongolia, earthquake*, Spec. Pap. Geol. Soc. Am*., **320**, 143 pp.

Molnar, P. & Tapponnier, P. (1975). Cenozoic Tectonics of Asia : Effects of a Continental Collision. *Science,* **189**, 419–426.

Pollitz, F., M. Vergnolle, & E. Calais (2003). Fault interaction and stress triggering of twentieth century earthquakes in Mongolia, *J. Geophys. Res.,* **108**(B10), 2503, doi:10.1029/2002JB002375.

Ritz, J.-F., E. T. Brown, D. L. Bourles, H. Philip, A. Schlupp, G.M. Raisbeck, F. Yiou, & B. Enkhtuvshin (1995). Slip rates along active faults estimated with cosmic-ray-exposure dates: Application to the Bogd Fault, Gobi-Altai, Mongolia*, Geology*, **23**, 1019–1022, doi:10.1130/0091-7613(1995)023<1019:SRAAFE>2.3.CO;2.

Ritz, J.-F., R. Vassallo, R. Braucher, E. T. Brown, S. Carretier, & D. L. Bourles (2006). Using in situ produced 10 Be to quantify active tectonics in the Gurvan Bogd mountain range (Gobi-Altay, Mongolia), *Spec. Pap. Geol. Soc. Am*., **415**, 87–110.

Rizza, M., J.-F. Ritz, R. Braucher, R. Vassallo, C. Prentice, S. Mahan, S. McGill, A. Chauvet, S. Marco, M. Todbileg, S. Demberel & D. Bourlès (2011). Slip rate and slip magnitudes of past earthquakes along the Bogd left-lateral strike-slip fault (Mongolia). *Geophys. J. Int*., **186**, 897–927, doi:10.1111/j.1365-246X.2011.05075.x.

Vassallo, R., J.-F. Ritz, R. Braucher, & S. Carretier (2005). Dating faulted alluvial fans with cosmogenic 10Be in the Gurvan Bogd mountain range (Gobi-Altay, Mongolia): Climatic and tectonic implications, *Terra Nova*, **17**, 278–285, doi:10.1111/j.1365-3121.2005.00612.x.

Vassallo, R., Jolivet, M., Ritz, J. F., Braucher, R., Larroque, C., Sue, C., Todbileg, M. & Javkhlanbold, D. (2007a). Uplift age and rates of the Gurvan Bogd System (Gobi-Altay) by apatite fission track analysis, *Earth planet. Sci. Lett*., **259**, 333–346.

Vassallo, R., et al. (2007b), Transpressional tectonics and stream terraces of the Gobi-Altay, Mongolia, *Tectonics*, **26**, TC5013, doi:10.1029/2006TC002081.

Vergnolle, M., F. Pollitz, & E. Calais (2003). Constraints on the viscosity of the continental crust and mantle from GPS measurements and postseismic deformation models in western Mongolia. *J. Geophys. Res*., **108**(B10), 2502, doi:10.1029/2002JB002374.

Tapponnier, P. & P. Molnar (1977). Active faulting and tectonics in China. *J. Geophys. Res.* **82**, 2905–2930.

Tapponnier, P. & P. Molnar (1979). Active faulting and Cenozoic tectonics of the Tien Shan, Mongolia and Baikal regions, *J. Geophys. Res*., **84**, 3425–3459.

2.3. Borah Peak 1983

8/10/1983, Idaho, USA

Mw 6.9

Epicenter (USGS) : 44,05°N-113,89°W

Normal fault



Broken long-term fault

The EQ broke a part of the so-called "Lost River Fault", in the north of the Basin and Range.

General characteristics from literature:

- The NW-trending, ~120 km-long so-called "Lost River Fault" extends, as several sub-parallel neighboring faults, due north and perpendicular to the NE-trending Snake River Plain (Fig.39). The fault traces thus interrupt to the south where they intersect the Snake River Plain. The Snake River Plain marks the NE path followed by the Yellowstone Hotspot which propagated northeastwards (with respect to stable America) over ~650 km from southwest Idaho to northeast Wyoming in the last ~16 Ma (Fig.39; e.g. Scott et al., 1985 and references therein). Although the Snake River Plain is ~100 km wide, the deep hotspot magmatic activity has obviously affected a larger area of ~300 km-wide, roughly centered at the Plain axis. The lateral extension of the deep magmatic domain coincides with several NE-trending lineaments, which clearly imprint the topography (in purple, Fig.39). Such lineaments have been previously interpreted as right lateral shear zones (based on GPS horizontal velocities north of the Snake River Plain; Payne et al., 2008) and normal faults (based on geological mapping in the eastern part of the Snake River Plain; e.g. Rodgers et al., 2002). Two of those lineaments –a major one in the north, intersect the Lost River and neighboring NW-trending faults. All faults east of the Beaverhead Fault interrupt against the northern principal lineament, i.e., do not continue further northward. To the west, the Lost River and Lemhi faults look broken by the two lineaments into different sections that have

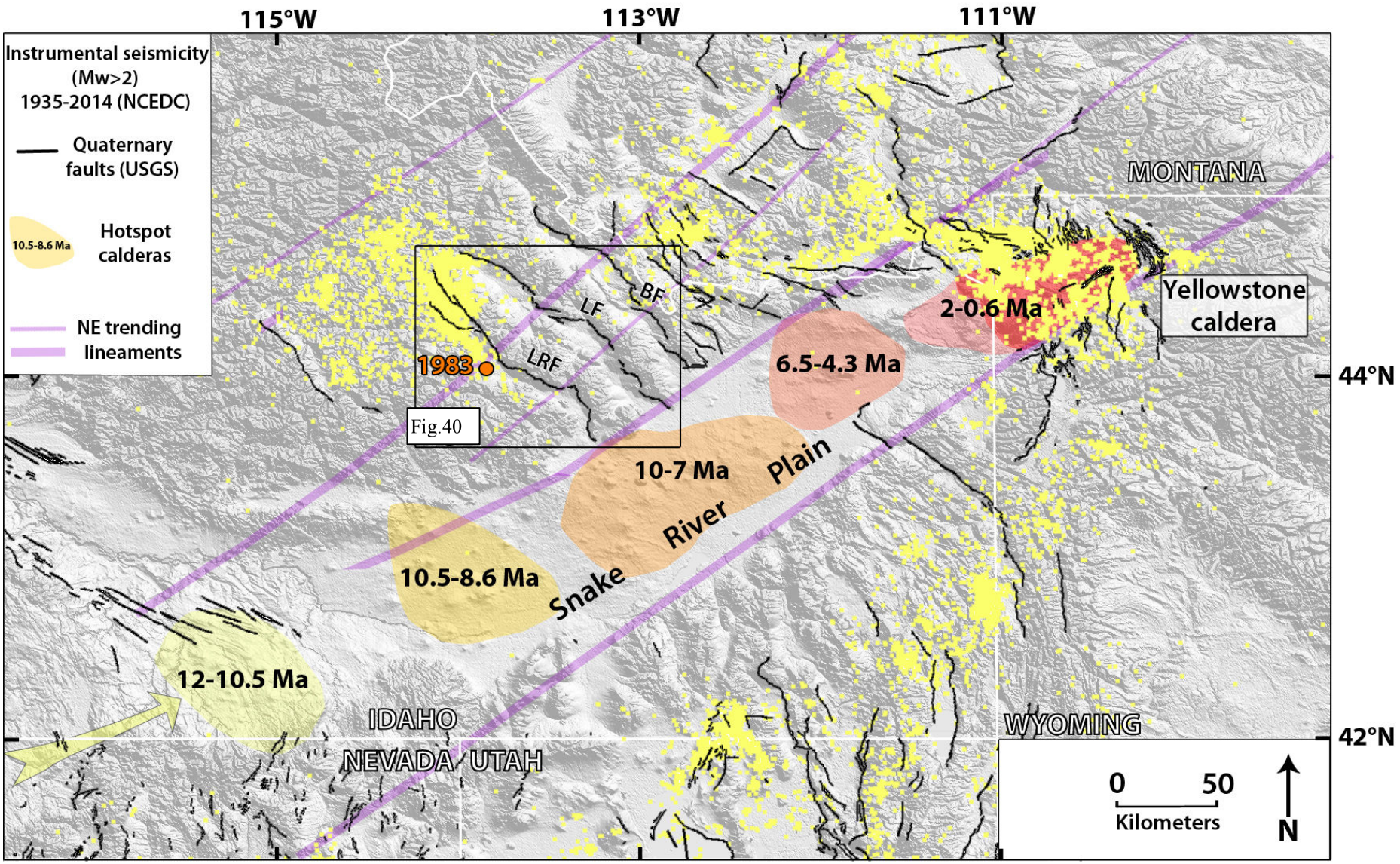


Fig.39: Track of the Yellowstone hotspot (modified from Smith and Siegel, 2000). Purple lines are related to the hotspot activity (See text for details). Black quaternary faults are from the U.S. Geological Survey and California Geological Survey, 2006. LRF : Lost River Fault ; LM : Lehmi fault ; BF : Beaverhead Fault. Yellow dots: instrumental earthquake epicenters of Mw>2 from the ANSS catalog from the Northern California Earthquake Data Center. The orange circle shows the 1983 Borah Peak epicenter .

different strikes. The so-called Lost River Fault is so divided into three sections (Fig.40), a southern section (named Arco Fault) trending ~NS and stopping to the north where it intersects the southern lineament; a central section (named Mackay Fault) trending NW, disconnected from the southern section and interrupting to the north where it intersects the northern lineament; and a northern section (named Thousand Springs Fault) trending NNW, hardly connected to the central section (See below), and vanishing ~50 km north of the northern lineament. This overall architecture suggests that the so-called Lost River Fault is not a unique, individual fault as commonly supposed, but rather a system of three distinct faults separated by deeply rooted structural and/or rheological, sub-perpendicular NE "boundaries" formed as a result of the Hotspot activity and propagation. The NE boundaries might be sub-planar conduits along which the magma migrated over time and space.

- It is possible that the three Arco, Mackay and Thousand Springs faults were originally a unique fault that was subsequently dissected by the hotspot-related NE "boundaries". It is also possible that the three faults formed subsequently to the Hotspot passage, from and in between the magmatic boundaries. This might be most likely as it is generally admitted that the Mountain range Faults in Idaho, north of the Snake River Plain, initiated 2-7 Ma ago (based on structural correlation between faults, sedimentary deposits and dated volcanic rocks; e.g. Scott et al., 1985; Christiansen 1986 and references therein).
- The 1983 Borah Peak EQ broke the northernmost Thousand Springs normal fault.
- The Thousand Springs fault is ~45 km long, and dips westward.
- Its total cumulative vertical slip is at least ~ 2,7 km, estimated from elevation differences between the highest point of Idaho ranges (Borah Peak) and the lowest point in the Thousand Spring Valley (1,9 km), plus the thickness of the sedimentary basin (0,6-0,9 km, see Fig.41) (e.g. Crosthwaite 1970; Crone and Machette 1984; Scott et al., 1985).
- Current slip rate: 0.5 to 1 mm/yr of horizontal extension (GPS; Payne et al., 2008) measured at a few locations along the Thousand Springs Fault.
- Geological slip rate: < 0.3 mm/yr of vertical displacement (over the Holocene; Scott et al., 1985 and references therein), yet not robustly constrained (estimated from offsets of alluvial surfaces estimated to be ~15 ka and reconstruction of geomorphic surfaces across the Thousand Springs Fault).
- Scott et al. (1985) and Payne et al. (2008) show that both the geological and the current slip rates of the Lost River Fault system seem to decrease southward.

→ The 1983 Borah Peak EQ occurred on the Thousand Springs normal fault, which is the northernmost fault of the Lost River system. The Thousand Springs Fault has likely an intermediate maturity (L ~45 km, I-Age 2-7 Ma, D_{total} ~3 km, and MR < 1 mm/yr), yet closer from immature than from mature (class "Interm → immature" in Table 5).

Architecture and lateral major segmentation, from our mapping (Fig.40 & 41):

- Mapping done from Google Earth, Landsat and Aster GDEM v.2 data combined with literature information.
- Long-term fault trace well expressed in surface morphology and topography.
- The Thousand Springs Fault has a fairly linear trace. To the NW, the fault terminates by splaying in a dense network of secondary oblique faults. Splays also formed along the fault, where they depart from the major inter-segment zones (See below). To the SE, the fault ends by curving by ~17° and then stopping at the intersection with the sub-perpendicular Mackay Fault (Fig. 41).
- The overall geometry of the fault zone suggests that the Thousand Springs Fault has been propagating northwestward over geological time.
- The Thousand Springs Fault is divided into 2, fairly collinear major segments (See Fig.41b where they are numbered), of similar length, 20-25 km (maximum length measured along strike).
- Major segment 1 in the south has a very linear trace, except in its ~9 km long southern termination where it curves by ~17°. A few secondary splay faults have developed from the bend in the segment 1 trace. The northern segment 2 has a more sinuous trace. It terminates in the north by splaying in multiple oblique branches. Segments 1 and 2 are fairly well connected by a narrow step-over (W < 0.5 km; Table 6). Between segments 1 and 2, an oblique relief has also developed in the western compartment – the "Willow creek hills", whose origin is unclear but seems related to a NNE-trending fault. From the step-over between the two segments, a small splay fault has developed in the western compartment. We interpret the NW-trending Lone Pine fault as a large splay of the Thousand Springs Fault, which likely developed originally at the northern tip of major segment 1.
- Our identification of fault segments differs from those reported in most previous studies (Scott et al., 1985; Crone and Haller, 1991). This is because we focus here on the major segments, while most previous studies described smaller scales of fault segmentation. Also, we consider the Thousand Springs Fault as an individual fault, not as a segment of the so-

called “Lost River Fault”. Note that Crone and Haller (1991) divided the “Thousand Spring section” into two segments, in agreement with our mapping.

→ The Thousand Springs Fault is divided into 2 long-term major collinear segments. It has propagated towards the NW over time, so that the southernmost major segment 1 is the most mature of the fault.

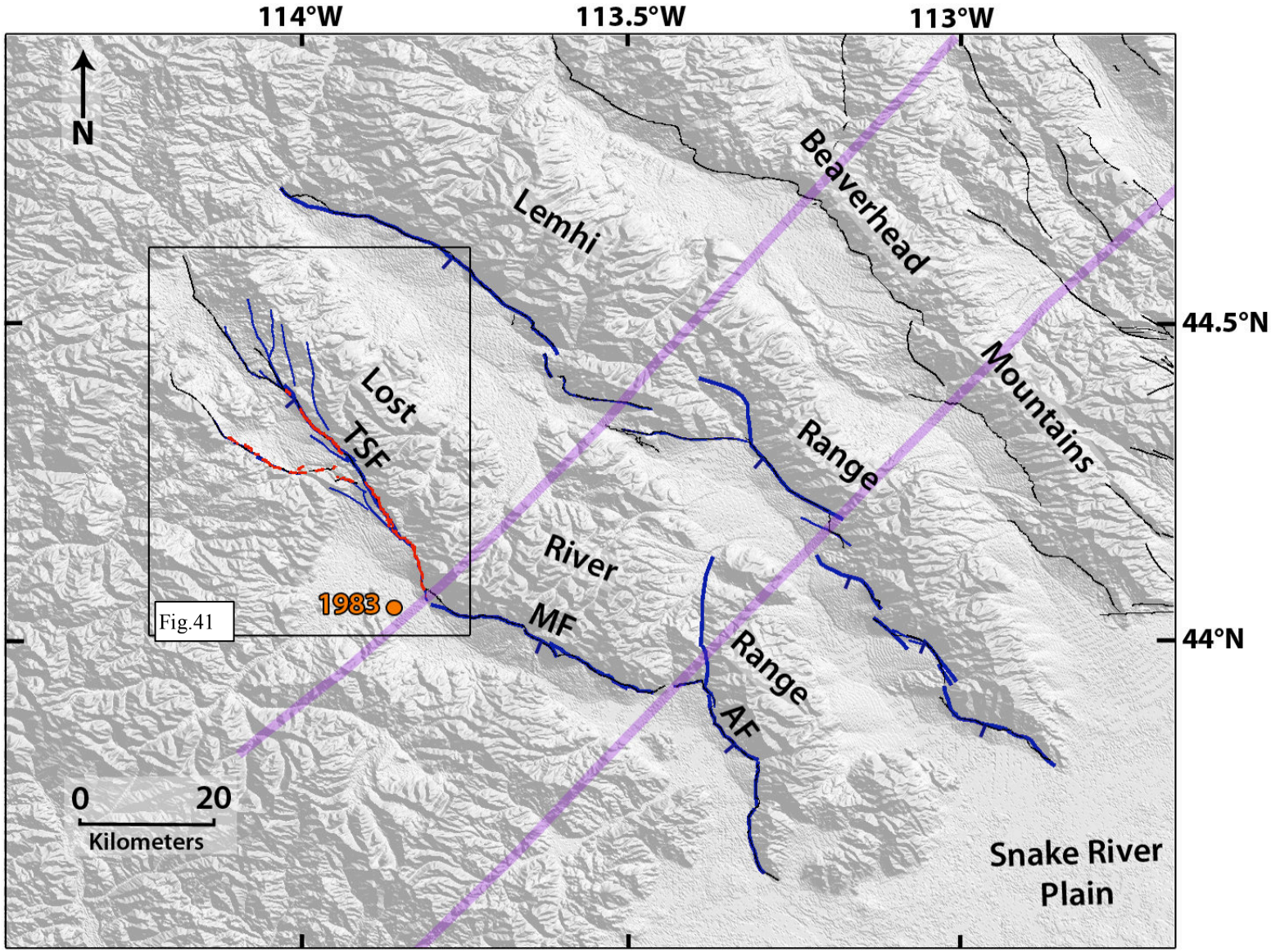


Fig. 40: General map of the main long term faults in North Basin and Range. In blue are the major active faults that we mapped. In black are the other Quaternary faults mapped by the U.S. Geological Survey and California Geological Survey, 2006. The surface rupture is indicated by the red line (from Crone & Machette 1984; Crone et al., 1987). The orange circle shows the 1983 Borah Peak epicenter. Purple lines show the NE lineaments described above in the text. TSF : Thousand Springs Fault ; MF : Mackay Fault ; AF : Arco Fault..

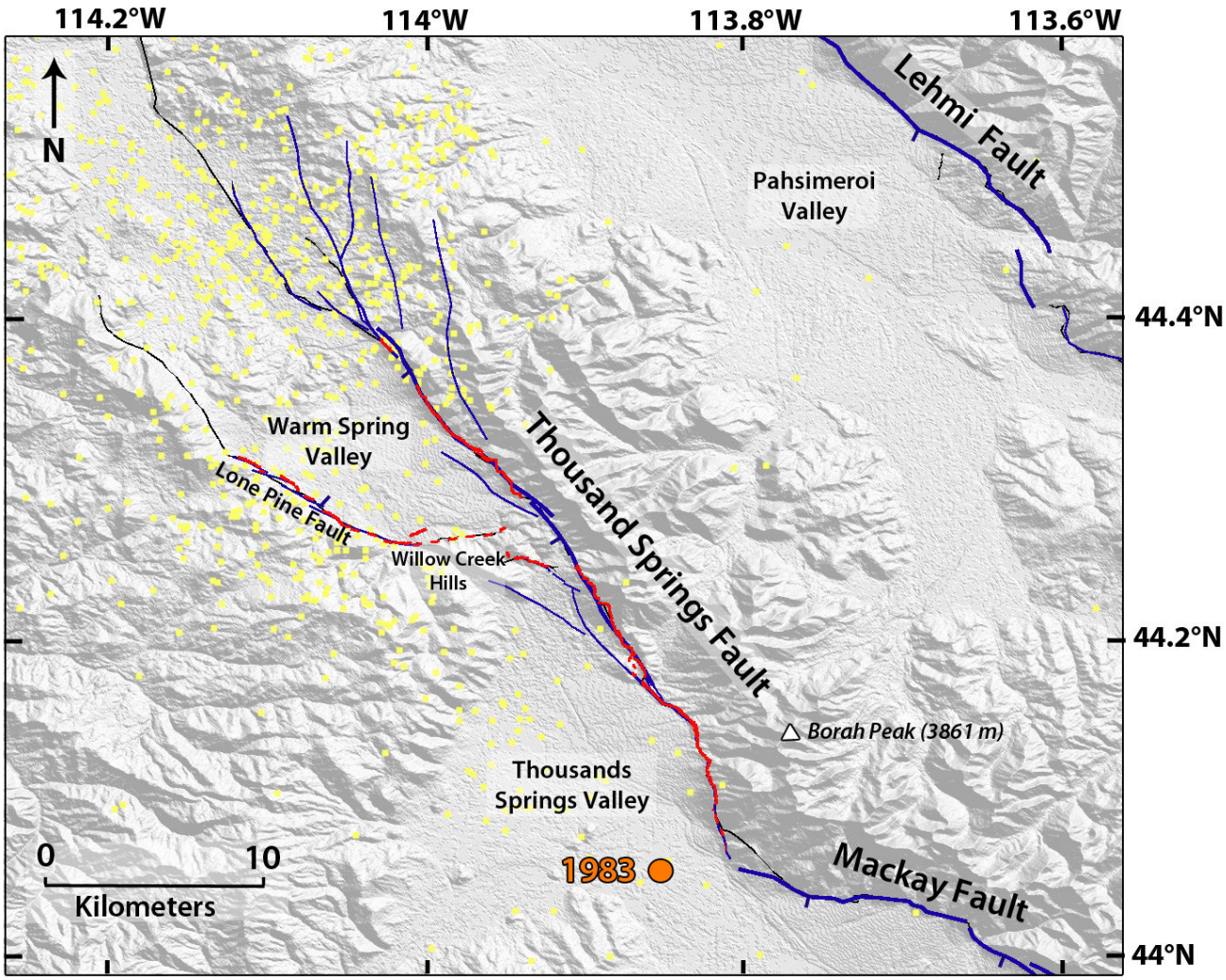


Fig.41:(a) Zoom on the broken section of the Thousand Springs Fault, from Fig.40 (same caption) Small yellow dots: earthquake locations (Mw>2) recorded between 1935 and 2014 (ANSS catalog from the Northern California Earthquake Data Center).

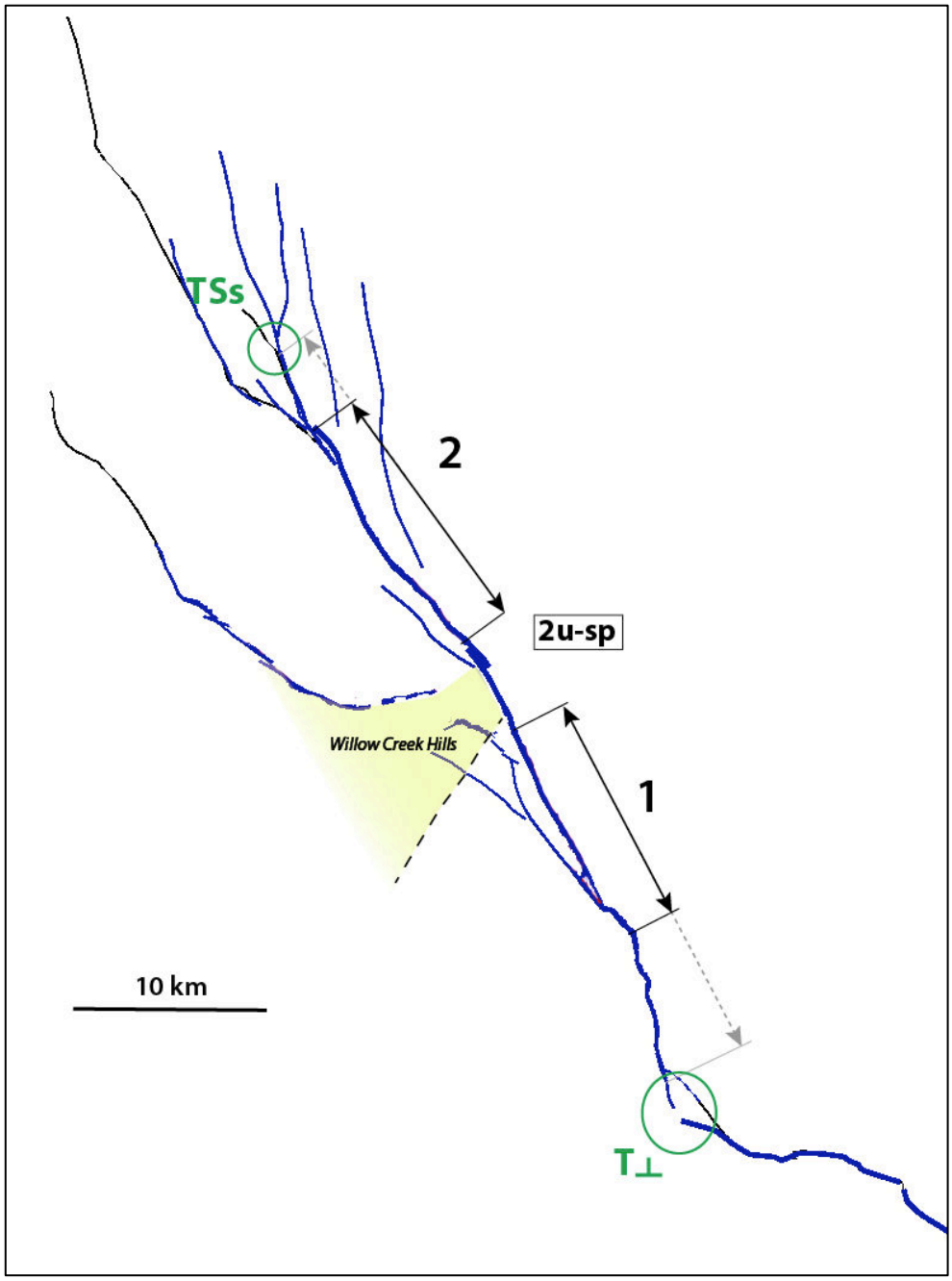


Fig.41:(b) Focus on the major segments of the Thousand Springs Fault. The segments are numbered from SE to NW and indicated by black arrows parallel to their mean strike. The grey prolongation of the arrows indicates the uncertainties on the segment lengths. The nature of the inter-segment zones is indicated in letters within boxes explained in Table 6. The nature of the fault tips is indicated in green (Table 6).

1983 Coseismic rupture

Surface trace and location on long-term Thousand Springs Fault:

- The 1983 surface rupture is still fairly clear on Google Earth images. The surface trace of the earthquake was precisely mapped on the field, and the displacements measured (See below) (Crone and Machette 1984; Crone et al., 1987).
- Surface rupture of 34-40 km long (Crone and Machette 1984; Crone et al., 1987).
- The EQ broke the Thousand Springs Fault entirely (except, apparently, the splays in the north), and hence broke its 2 major segments. It also broke partly the major Lone Pine splay developed in the western compartment.
- A gap in the surface rupture trace has been noted nearby the intersegment zone between major segments 1 and 2 (Fig.40 and 41). This gap is where a rupture trace is seen on the Lone Pine splay off- the main fault. This gap made some authors (e.g. Zhang et al., 1999; Crone and Haller, 1991) to suggest that the rupture stopped in the gap area; the surface ruptures further north would have been subsequently triggered by the severe shaking and the directivity of the rupture. We do not caution this hypothesis and more simply conclude that the EQ broke the two major segments of the fault; the gap in observed slip at the surface might be due to the distribution of the slip in the complex inter-segment zone area. The aftershocks recorded a few hours after the main shock (e.g. Richins et al., 1987) confirm that the entire fault broke over ~ 36 km (Fig.3). The wide distribution of the aftershocks in the north furthermore suggests that most of the northern splay faults also broke during or immediately after the EQ.
- The earthquake initiated at a depth of about 16 km (Doser and Smith 1985), nearby the sub-perpendicular intersection between the Thousand Springs and the Mackay faults (Susong et al., 1990). The rupture thus propagated unilaterally to the north that is from the most mature to the most recent section of the Thousand Springs Fault.
- The aftershocks distribution suggests that the broken Thousand Springs Fault dips by 40-50° at depth (Boatwright 1985; Richins et al., 1987).

→ The 1983 Borah Peak EQ broke the two major segments of the Thousand Springs Fault. The EQ initiated nearby the intersection of the fault with another, strongly oblique fault, and propagated northward unilaterally along the Thousand Springs Fault, from its most mature to its most immature section.

Coseismic displacements measured at surface:

- *From Field measurements*: Maximum vertical slip of 2,7 m (Crone and Machette 1984; Crone et al., 1987), measured on southern half of the southern major segment 1 (Fig.42). Authors mentioned that a small component of left lateral slip, representing ~ 17% of the dip-slip component, was observed locally.
- The complete slip profile was measured. Its overall shape is fairly triangular and asymmetric, with maximum slip deported at the southern tip of the rupture, and slip decreasing fairly regularly from its maximum value to zero at the northern rupture tip.
- In the inter-segment zone between major segments 1 and 2, part of the coseismic slip observed at surface occurred on a small parallel fault trace (yellow dots in Fig.42). In the northern part of the rupture, the slip measured is the sum of the slip on the main fault and on its Lone Pine splay.

From Geodetic measurements: ground deformations were studied using GPS profiles of vertical elevation, normal and parallel to the fault, which were acquired from 1933 to 1985 (so data include 50 yrs of interseismic strain): an elevation change of about 1,5 m was measured where maximum coseismic displacements were observed (Stein and Barrientos 1985; Ward and Barrientos 1986; Barrientos et al., 1987).

→ **Maximum slip of 2,7 m well measured at surface, located on the most mature southern section of the broken fault.**

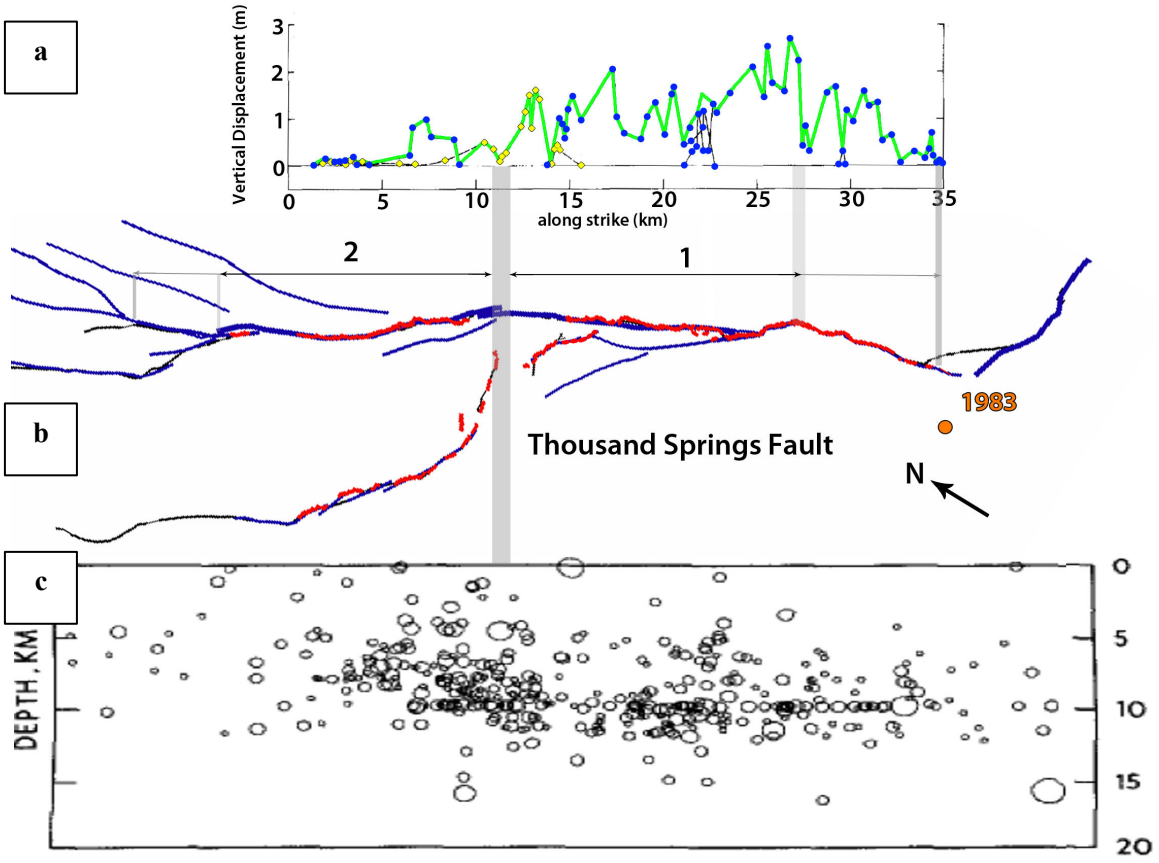


Fig.42: (a) Co-seismic slip profile measured at surface after the 1983 Borah Peak earthquake (Crone and Machette 1984 ; Crone et al., 1987). Blue dots and yellow diamonds : displacements measured along the Lost River fault and the secondary oblique Lone Pine Fault, respectively. Green curve shows the total vertical slip along the fault; (b) 1983 surface rupture and long term faults are indicated in red and blue, respectively. Segments are numbered. Grey areas indicate the limits of major segments (c) Aftershocks distribution along strike of the 1983 Borah Peak earthquake (modified after Richins et al., 1987).

Other source parameters:

Global CMT

Mainshock: 1983/10/28 at 14h06min23s GMT; Lat = 44.35° Lon= -113.98°

Mw 6.9; M0 = 3.12e19 Nm; Z = 13.7 km; Half-duration: 10s

Strike, dip, slip: (304°, 29°, -103°)/(138°, 62°, -83°)

Doser and Smith 1985:

Strike, dip, slip: (138° to 163°, 45° to 53°, -57° to -72°)

M0 = 2.1e19 Nm; Z = 16 km; Duration: 11s.

Source parameters are similar between the different studies. Only the duration is different and we are not able to determine which duration is best estimated.

Source inversion models and slip distribution at depth (Fig.43):

We compare two source inversion models that have been published on the 1983 Borah Peak earthquake; the grid data are available for one of them (Table 2).

The models differ principally from the data they used:

- Ward and Barrientos (1986): Geodetic data (leveling) and surface offsets. The model considers the broken fault as a single plane (50*26 km)
- Mendoza and Hartell (1988): Short and long period P-waves. The model considers the broken fault as a single plane (54*26,6 km).
- The two models are not fully constrained: the model from Mendoza and Hartzell (1988) is based only on teleseismic data and produces a maximum displacement at depth (20-25 km) which is lower than the maximum slip measured at the surface. The geodetic data used in the model from Ward and Barrientos (1986) contain a large period of interseismic (50 yr before the earthquake) and postseismic deformation. However, we consider that the model from Ward and Barrientos (1986) is the most robust because it uses surface offset data and near field geodetic data.
- Despite of their limitations, the two models provide a fairly similar slip distribution, with basically a dominant slip zone fairly coinciding with the rupture of major segment 1, and a shallower zone of lower slip fairly coinciding with the rupture of major segment 2 (Fig.43). Maximum slip at depth is however located further south on segment 1 than it is at surface. The slip profiles have an overall triangular and asymmetric shape, which is similar to the surface slip-length distribution.
- Both models suggest that the slip might extend down to 20-25 km depth along the fault dip.

→ **Maximum slip occurred on the southernmost and most mature section of the fault.**

→ **The source models suggest L 35-40 km, W 20-25 km, Dmax at depth 4.1 m.**

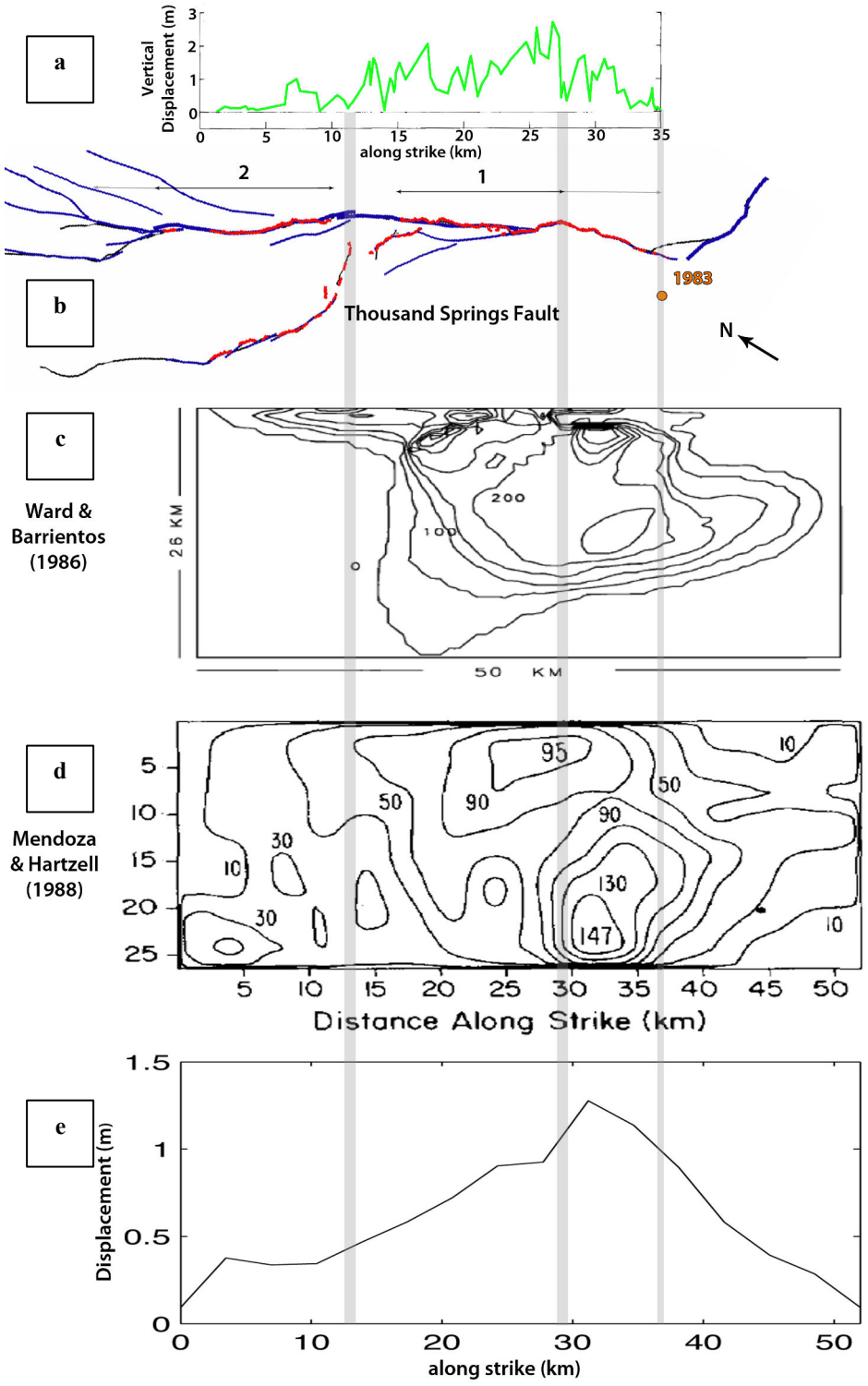


Fig.43: (a) Co-seismic slip profile measured at surface after the 1983 Borah Peak earthquake (Crone and Machette 1984 ; Crone et al., 1987); (b) 1983 surface rupture and long term faults are indicated in red and blue, respectively. Major segments are numbered. Grey zones show the limits of major segments; (c) Inversion model from Ward and Barrientos (1986) using Geodetic and surface offsets data. ; (d) Inversion model from Mendoza and Hartzell (1988) using Long and Short period P-waves data ; (e) Maximum slip profile derived from the model of Mendoza et Hartzell (1984).

Other information:

1983 EQ:

- There was no significant seismic activity in the Lost River system area before the 1983 EQ. No foreshock with Mw > 1 was recorded within a 20 km radius of the epicenter (e.g. King et al., 1987).
- Aftershocks range from 5 to 15 km in depth and extend over a length of about 37 km, in agreement with the surface rupture length (Fig.42; Boatwright 1985; Richins et al., 1987). We note that major segment 1 where most slip occurred is almost free of aftershocks except at the bottom edge of the broken zone, whereas major segment 2 where little slip occurred is site of numerous aftershocks. However, figure 41 shows that a large part of those northern aftershocks were distributed in a broad zone either side of the ruptured main fault, suggesting the post-seismic slip of most of the northern splay faults.
- Fault plane solutions indicate predominantly normal faulting with a small component of strike slip.

Past EQs:

- Paleoseismology studies (trenches) performed at several locations on the Lost River Fault system show evidence for only one prehistoric surface-faulting event, dated between 6-8 ka (Hanks and Schwartz 1987) and 12-15 ka (e.g. Scott et al., 1985).

Parameters retained to describe the 1983 Borah Peak event (Tables 1-4):

Mw 6.9; M0 ~ 2.6e19 Nm; L ~ 34 km; Dmax surface ~2.7 m; Dmax at depth = 4.1 m; Duration ~ 11-20 s; *Hypocenter*: Z ≈ 15 km (average).

Number of major segments broken on the Thousand Springs Fault: 2 major segments.

Both the Borah Peak surface and depth slip-length data fall fairly well on the second function (blue curve; Fig.44 and 45). This is in keeping with the EQ having broken 2 major segments of the fault on which it occurred.

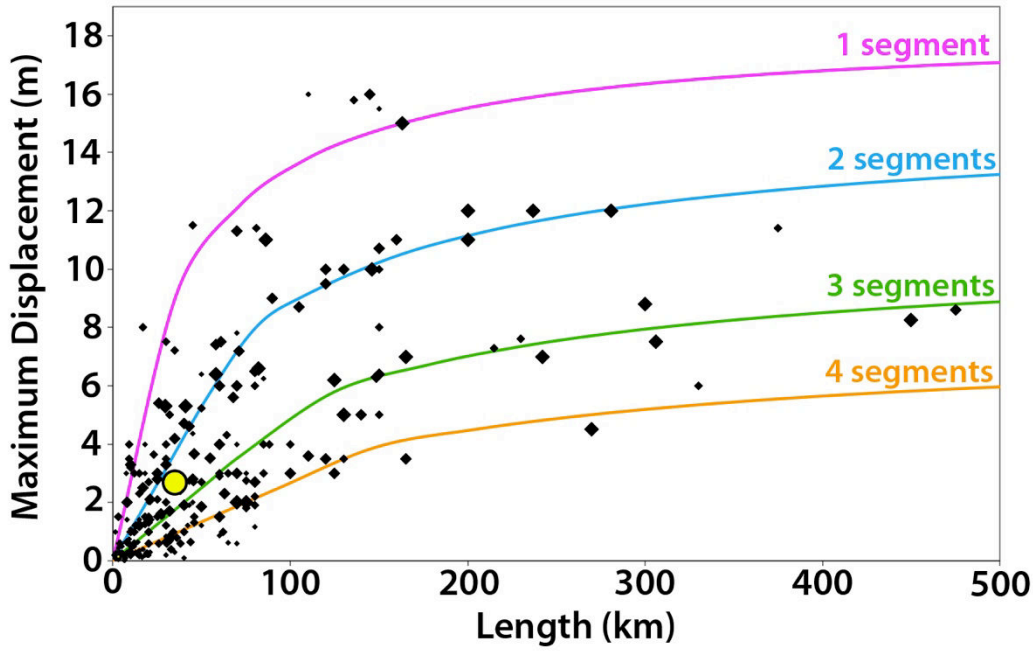


Fig.44: Earthquake displacement-length data measured at surface for 260 historical large continental earthquakes (Mw≥6). The 4 curves indicate the number of major long-term fault segments to have been broken by the earthquakes (modified from Manighetti et al., 2007, and Chapter IV). Yellow dot show the 1983 Borah Peak earthquake surface slip-length data.

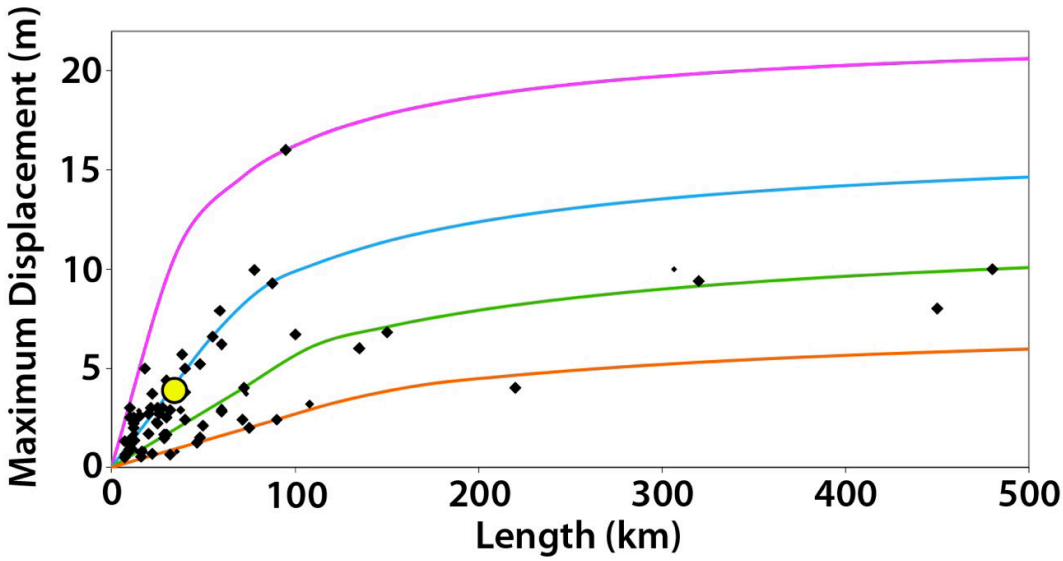


Fig.45: Earthquake displacement-length data deduced from inversion model at depth for 90 historical large continental earthquakes (Mw≥6). The 4 curves indicate the number of major long-term fault segments to have been broken by the earthquakes (modified from Manighetti et al., 2007 and Chapter IV). Yellow dot show the Borah Peak earthquake depth slip-length data.

References

Barrientos, S. E., Stein, R. S. & Ward, S. N. (1987) Comparison of the 1959 Hebgen Lake, Montana and the 1983 Borah Peak, Idaho, earthquakes from geodetic observations. *Bull. Seism. Soc. Am.*, **77**, 784-808

Boatwright, J. (1985). Characteristics of the aftershock sequence of the Borah Peak, Idaho, earthquake determined from digital recordings of the events. *Bull. Seism. Soc. Am.*, **75**, 1265-1284

Christiansen, R. L. (1986) The Quaternary and Pliocene Yellowstone Plateau Volcanic Field of Wyoming, Idaho,and Montana. *U.S. Geol. Surv. Professional Paper* **729**-G, 145 pp.

Crone, A. J. & Machette, M. N. (1984). Surface faulting accompanying the Borah Peak earthquake, central Idaho. *Geology,* **12,** 664-667

Crone, A. J., Haller, K. M., 1991. Segmentation of Basin and Range normal faults: examples from east-central Idaho and southwestern Montana. *J. Struct. Geol*. **13**, 151–164.

Crone, A. J., Machette, M. N., Bonilla, M. G., Lienkaemper, J. J., Pierce, K. L., Scott, W. E. & Bucknam, R. C. (1987). Surface faulting accompanying the Borah Peak earthquake and segmentation of the Lost River Fault, central Idaho. *Bull. Seismol. Soc. Am*. **77**, 730–770.

Crosthwaite, E. G., C. A. Thomas, & K. L. Dyer (1970). Water resources in the Big Lost River basin, south-central Idaho, U.S. Geol. Surv., Open-File Rept. 70-93, 109 p.

Doser, D. I. & Smith, R. B. (1985). Source parameters of the 28 October 1983 Borah Peak, Idaho, earthquake from body wave analysis. *Bull. Seism. Soc. Am.*, **75**, 1041-1051

Hanks, T. C. & Schwartz, D. P. (1987) Morphologic dating of the pre-1983 fault scarp on the Lost River Fault at Doublespring Pass Road, Custer County, Idaho. *Bull. Seism. Soc. Am.*, **77**, 837-846.

King, J. J., Doyle, T. E. & Jackson, S. M. (1987) Seismicity of the eastern Snake River Plain region, Idaho, prior to the Borah Peak, Idaho, earthquake : October 1972- October 1983. *Bull. Seism. Soc. Am*., **77**, 809-818.

Manighetti, I., M. Campillo, S. Bouley, and F. Cotton (2007), Earthquake scaling, fault segmentation, and structural maturity, *Earth Planet. Sci. Lett*., **253**, 429-438, doi:10.1016/j.epsl.2006.11.004

Mendoza, C., & S. H. Hartzell (1988). Inversion for slip distribution using teleseismic P waveforms; North Palm Springs, Borah Peak, and Michoacan earthquakes. *Bull. Seis. Soc. Am*. **78** (3),1092-1111.

Payne, S. J., McCaffrey, R., & King, R. W. (2008). Strain rates and contemporary deformation in the Snake River Plain and surrounding Basin and Range from GPS and seismicity. *Geology*, **36**(8), 647-650.

Richins, W. D., Pechmann, J. C., Smith, R. B., Langer, C. J., Goter, S. K., Zollweg, J. E. & King, J. J. (1987). The 1983 Borah Peak, Idaho, earthquake and its aftershocks. *Bull. Seism. Soc. Am*., **77**, 694-723.

Rodgers, D.W., Ore, H.T., Bobo, R.T., McQuarrie, N., & Zentner, N. (2002) Extension and subsidence of the eastern Snake River Plain, Idaho, in Bonnichsen, B., White, C.M., and McCurry, M., eds., Tectonic and Magmatic Evolution of the Snake River Plain Volcanic Province: *Idaho Geological Survey Bulletin* **30**, 121–155.

Scott, W.E., Pierce, K. L. & Hait, M. H. Jr. (1985) Quaternary tectonic setting of the 1983 Borah Peak earthquake, Central Idaho, *Bull. Seism. Soc. Am*., **75**, 1053-1066.

Smith, R. B., & Siegel, L. J. (2000). Windows into the earth: The geologic story of Yellowstone and Grand Teton national parks. *Oxford University Press*. ISBN-13:9780195105971, 256 pp.

Susong, D. D., Janecke, S. U. & Bruhn, R. L. (1990). Structure of a fault segment boundary in the Lost River fault zone, Idaho, and possible effect on the 1983 Borah Peak earthquake rupture. *Bull. Seism. Soc. Am*., **80**, 57-68.

Stein, R. S. and S. Barrientos (1985). Planar high-angle faulting in the Basin and Range : geodetic analysis of the 1983 Borah Peak, Idaho, earthquake, *J. Geophys. Res.* **90**, 11355-11366.

Ward, S. N. & S.E. Barrientos (1986). An inversion for slip distribution and fault shape from geodetic observations of the 1983, Borah Peak, Idaho, earthquake*, J. Geophys. Res.* **91**, 4909-4919

Zhang, P., Mao, F. & Slemmons, D. B. (1999). Rupture terminations and size of segment boundaries from historical earthquake ruptures in the Basin and Range Province. *Tectonophysics,* **308**, 37–52.

Waveform data, metadata, or data products for this study were accessed through the Northern California Earthquake Data Center (NCEDC).

2.4. Borrego Mountain 1968

09/Apr/1968, Californie, USA

Mw 6.5

Epicenter : 33.15°N-116.13°W

Right-lateral strike-slip



Broken long-term fault

The EQ broke a part of the San Jacinto fault, a southern branch of the San Andreas Fault. **Note that the San Andreas Fault is described in the sections "Fort Tejon 1857" (Southern San Andreas) and "San Francisco 1906" (Northern San Andreas). The relations of the San Andreas Fault with the San Jacinto and the Elsinore Faults are discussed in section "Fort Tejon 1857".** The San Jacinto Fault is one of the major splays of the Southern San Andreas Fault.

General characteristics of the San Jacinto Fault from literature (Fig.46) :

- The San Jacinto Fault strikes N140°E– parallel to the most recent major segment 5 of the Southern San Andreas Fault (See section Fort Tejon), is ~300 km long and is right lateral.
- It is taken to have initiated in the Late Tertiary, possibly 12 to 6 Ma,. in keeping with the San Jacinto Fault being a major splay of the Southern San Andreas faults, which formed ~12 Ma ago (Powell and Weldon 1992 and references therein; Sims 1993). However since the southern part of the San Jacinto Fault is interacting with the "young" Gulf of California (which opened ~5 Ma ago, e.g. Larson 1968), we infer that the southern section of the San Jacinto Fault is younger than ~5 Ma. Ages between 1.1 and 2.4 Ma have actually been proposed, based on stratigraphic and structural evidences in the Pleistocene Borrego formation (e.g. Lutz et al., 2006; Kirby et al., 2007). The San Jacinto Fault has thus propagated southward over time.

- Maximum cumulative lateral slip of at least 24 km based on offset measurements of intrusive igneous rocks in the central part of the fault (Sharp 1967).
- Current lateral slip rate of 20 to 25 mm/yr, based on InSAR data covering the Southern San Andreas, the San Jacinto and the Elsinore faults (Fialko 2006; Lundgren et al., 2009 ; Lindsey and Fialko 2013).
- Long-term lateral slip rate ~ 15 mm/yr in the northern part of the fault, and ~4 mm/yr in its southern part (Hudnut and Sieh 1989; Rockwell et al., 1990; Gurrola and Rockwell 1996; Kendrick et al., 2002; Blisniuk et al., 2010; Janecke et al., 2010; http://www.data.scec.org/Module/links/sratemap.html).

→ The 1958 Borrego Mountain EQ broke a part of the San Jacinto Fault, which is a major splay of the Southern San Andreas Fault. The San Jacinto Fault has an intermediate maturity (L ~300 km, I-Age 12-2 Ma depending on fault section, D_{total} ~25 km, and MR ~ 4-25 mm/yr depending on fault section), yet closer from mature than from immature (class "Interm → mature" in Table 5).

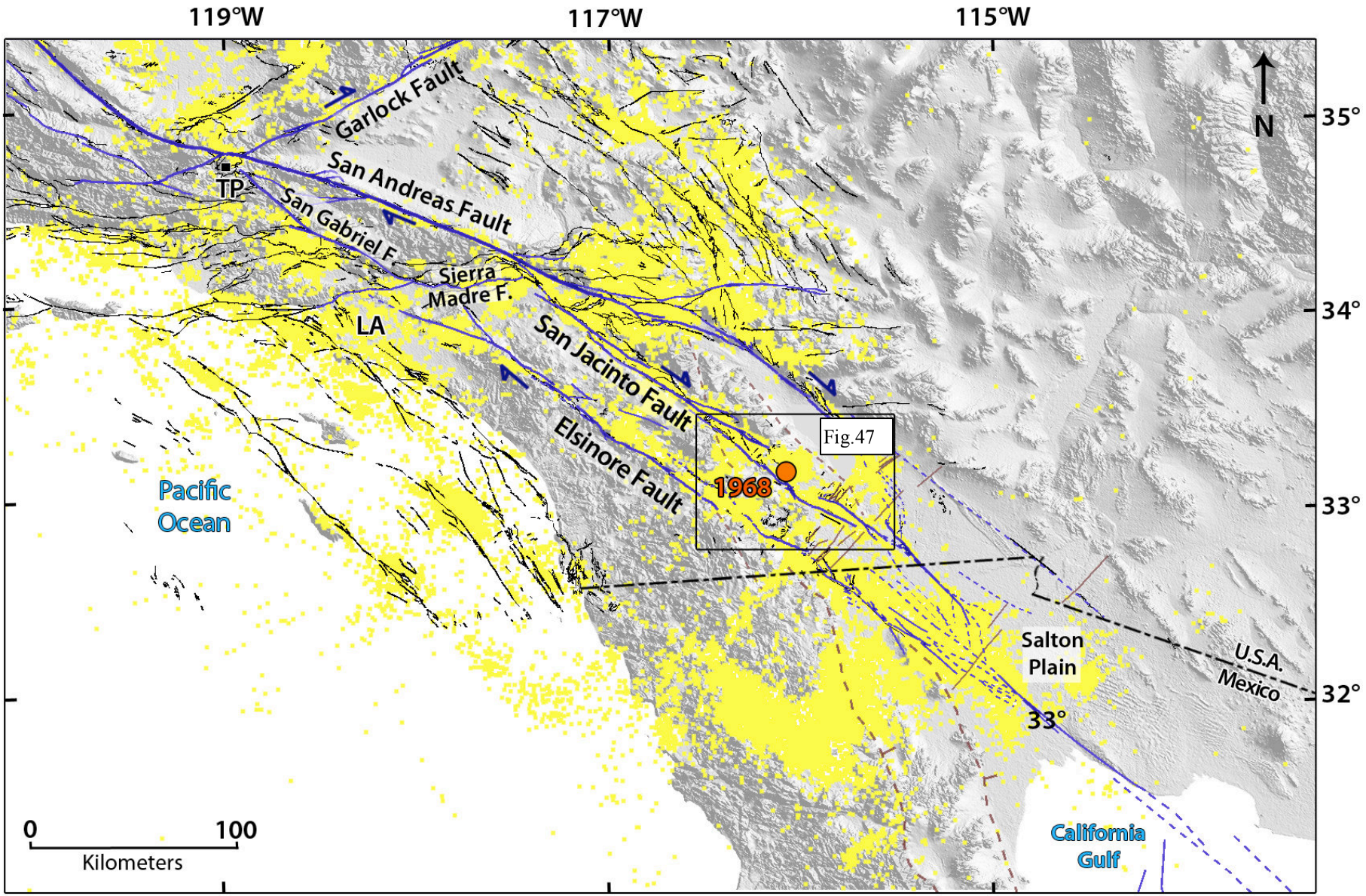


Fig.46: (a) General map of long term faults in Southern California. In blue are the major active faults that we mapped. In black are the other Quaternary faults mapped by the U.S. Geological Survey and California Geological Survey, 2006. In dotted brown are ancient faults related to the Gulf of California. In solid brown are preexisting lineaments likely related to the Gulf of California (see text). The orange circle shows the 1968 Borrego Mountain epicenter. The yellow dots are the instrumental earthquakes (Mw>2) recorded between 1981 and 2011 (Hauksson et al., 2012). LA : Los Angeles ; TP : Tejon Pass.

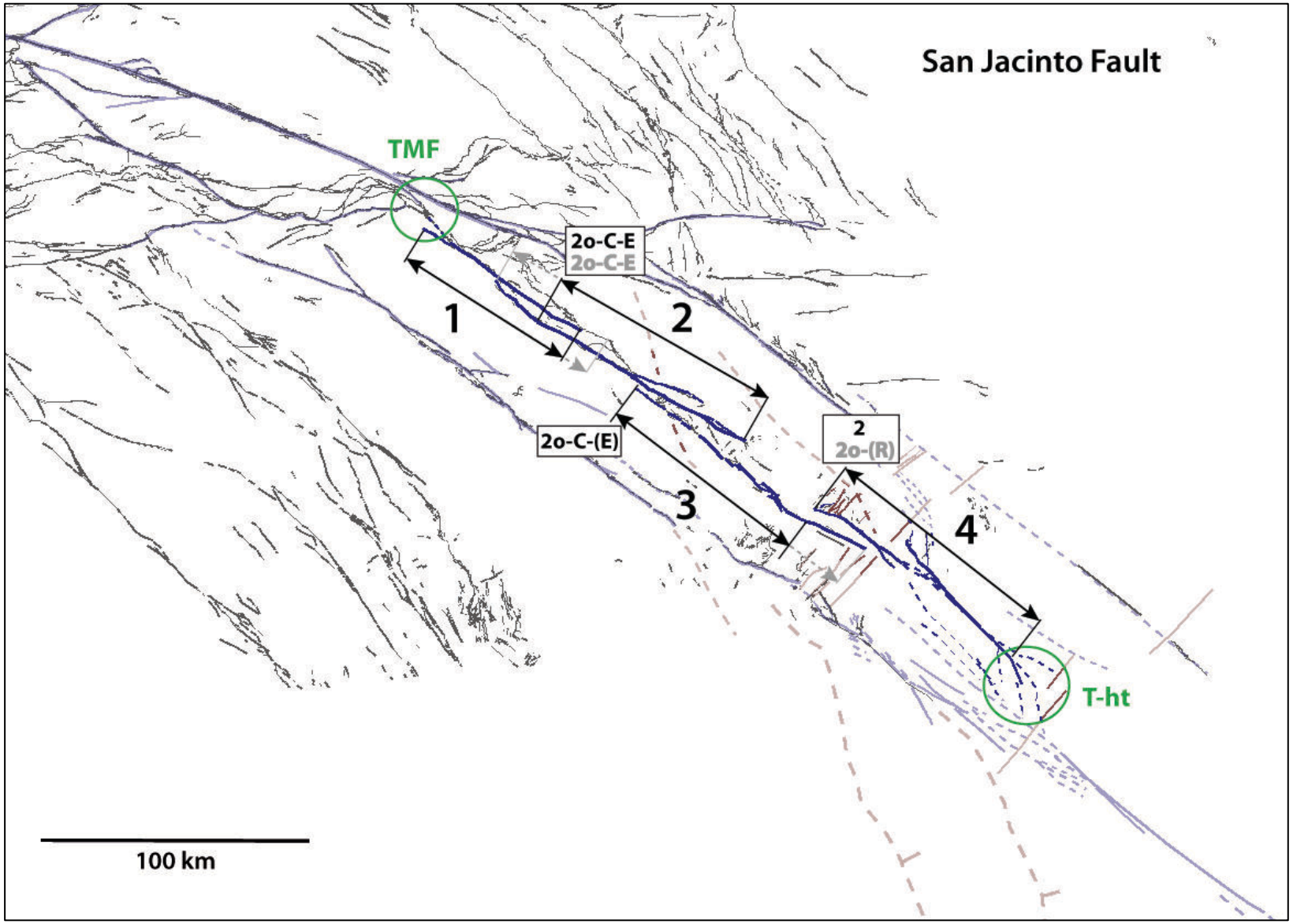


Fig.46: (b) Same active fault map as in 1a, but with focus on the major segments of the San Jacinto fault. The segments are numbered from NW to SE and indicated by black arrows parallel to their mean strike. The grey prolongation of the arrows indicates the uncertainties on the segment lengths. The nature of the inter-segment zones is indicated in letters within boxes explained in Table 6. The nature of the fault tips is indicated in green (Table 6).

Architecture and lateral major segmentation, from our and USGS mappings (Fig.46 & 47) :

- Mapping done from Google Earth, Landsat and ASTER GDEM data combined with USGS detailed mapping (U.S. Geological Survey and California Geological Survey, 2006).
- The San Jacinto Fault is ~45 km west of the southern trace of the San Andreas Fault, and ~35 km east of the sub-parallel Elsinore Fault.
- To the north, the San Jacinto Fault connects with the Southern San Andreas Fault, at the junction between its major segments 3 and 4 (See section Fort Tejon, and Fig.46).
- To the south, the San Jacinto Fault terminates in multiple small branches, most of them curve to connect the San Jacinto Fault with the Elsinore Fault, through a connection zone of pull-apart type.
- The San Jacinto Fault is thus ~310 km long.
- In its southern part, the San Jacinto Fault intersects and interacts with pre-existing NNW faults that were likely formed when the Gulf of California opened further south (in brown in Fig.46). Clearly, the San Jacinto Fault offsets the NNW Gulf faults, and hence is younger in this area. In the Salton Sea plain, numerous NE-trending small lineaments are observed, that we suspect to be ancient small faults developed at the northern tip of the major, normal NNW Gulf faults (in brown in Fig.46). As we show below, some of those lineaments have been reactivated during recent EQs on the San Jacinto Fault.
- The San Jacinto Fault is divided into 4 major, fairly collinear segments (See Fig.46b where they are numbered). The lengths and types of the segments and inter-segments are described in details in Table 6.
- The 4 major segments have a length of similar order, in the range 65-100 km (length measured along the linear trace of each segment; Fig.46b).
- The fault trace is fairly linear along the 2 northernmost major segments (segts 1-2), and more sinuous and discontinuous along the southernmost segments 3 and 4.
- Segments 1 and 2 are sub-parallel, and are connected through a large pull-apart-type relay zone, hence of type $2_{O\text{-}C\text{-}E}$. Small oblique faults have developed from both segments, and their splaying geometry is in keeping with segments 1 and 2 having propagated southwards over time. Segment 3 is sub-parallel to segments 1 and 2, and is more or less connected to segment 2 through a large relay zone of type $2_{O\text{-}C\text{-}(E)}$. The trace of segment 3 is more discontinuous and hence less linear than that of the northernmost segments. Segment 4 has a subtle trace because of the ongoing sedimentation in the Salton plain. The overall trace is parallel to that of the other segments. It is fairly linear yet discontinuous in its central part

(See further below). The two parts of segment 4 are extremely linear. Major segments 3 and 4 are not truly connected at the ground surface, but are rather separated by a large step-over of type 2_O. To the north, segment 4 terminates by connecting with multiple sub-perpendicular small faults and lineaments (in brown, Fig.46b). Similar lineaments are found at different places within the Salton Plain and are likely pre-existing structures. To the south, segment 4 terminates in a horsetail fashion, with the horsetail faults connecting the San Jacinto Fault with the southern Elsinore Fault. North of the center of major segment 4, en echelon subtle NW cracks and small faults are observed. Those en echelon cracks and faults are likely the surface expression of a NNW-trending fault zone (called the Brawley zone) that connects or is in the process of connecting the San Andreas and the San Jacinto faults. That connection fault zone is the site of a dense seismicity (Fig.46a).

- The linear trace of segments 1 and 2 as well as their clearer connection at surface, are in keeping with those segments having formed earlier along the San Jacinto Fault than the segments 3 and 4.

→ The San Jacinto Fault is divided into 4 long-term, major collinear segments. The San Jacinto Fault seems to have propagated southwards over time; its northernmost section (at least coinciding with major segments 1 & 2) is thus likely the oldest and most mature.

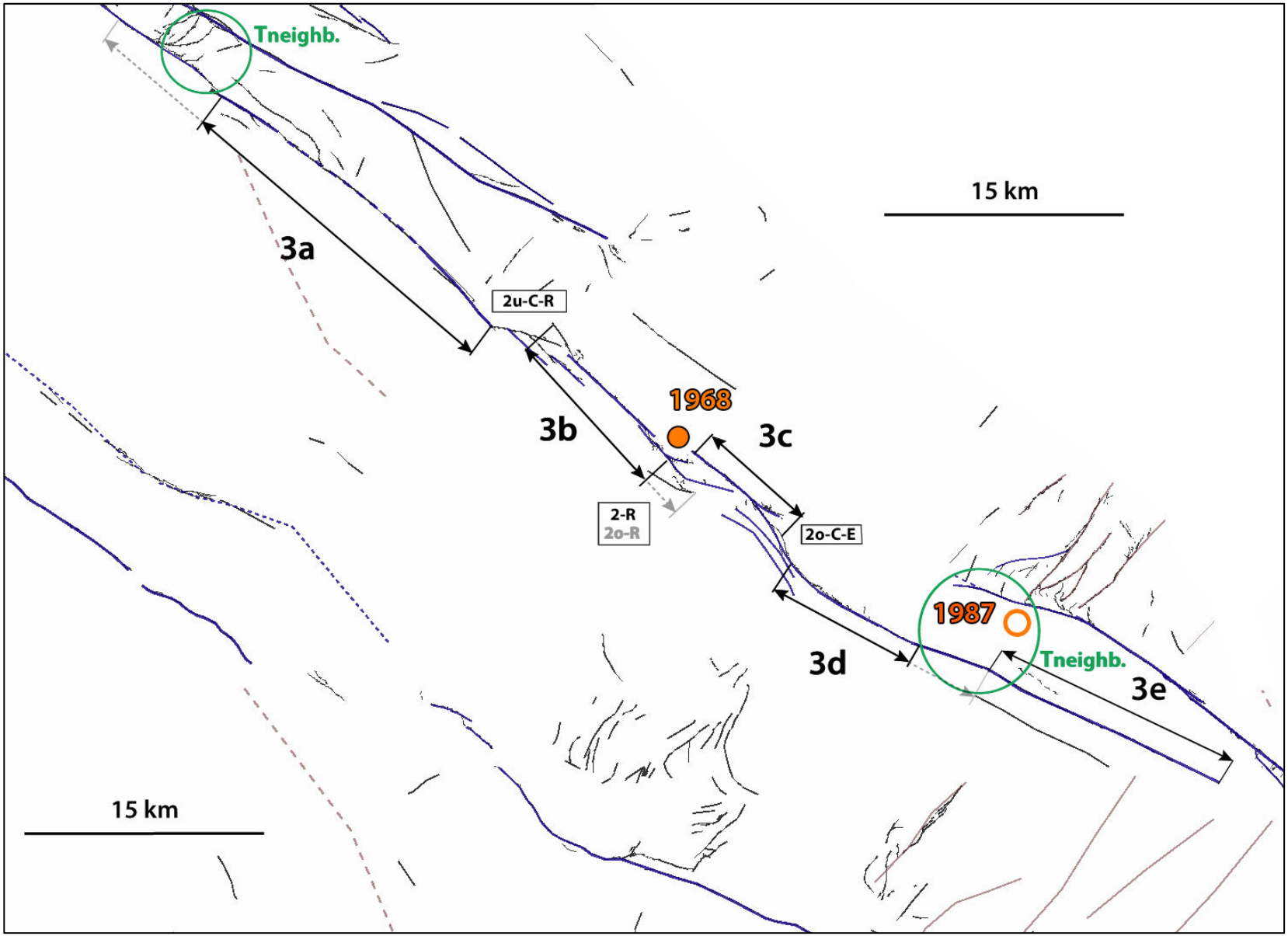


Fig.47: (a) Map of the secondary segments that form the major segment 3 of the San Jacinto fault. Same caption as in fig.46b. The solid orange circle indicates the 1968 Borrego epicenter. The 1987 Superstition Hills (Mw 6.6) epicenter is also indicated by the empty orange circle.

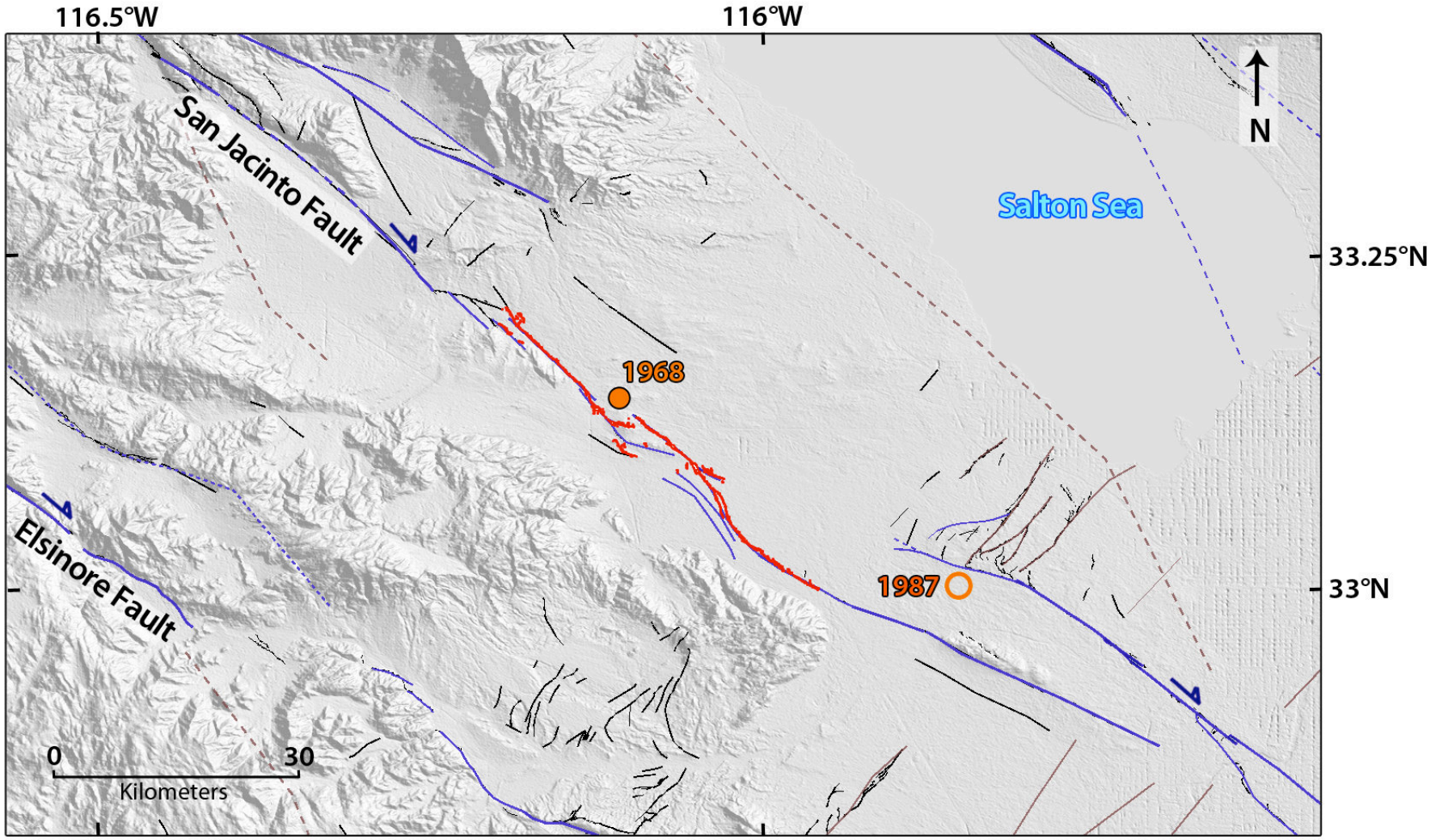


Fig.47: (b) Zoom on the broken section of the San Jacinto fault, from Fig.46a (same caption). The surface rupture is indicated with the red line (Clark 1972).

1968 Coseismic rupture

Surface trace and location on long-term San Jacinto Fault:

- The 1968 surface rupture is clear on Google Earth, Landsat 7 and Aster GDEM v2 images. The surface trace of the earthquake has been precisely mapped, and the displacements measured (See below) on the field (e.g. Clark 1972).
- Surface rupture of ~33 km long (Fig.47b).
- The EQ broke a part of one major segment of the San Jacinto Fault, major segment 3.
- According to its geometry, major segment 3 is divided into 5 collinear secondary segments (Fig.47a): from north to south, 3a-b-c-d-e. The secondary segment 3a is fairly linear and 30-35 km long. Further SE, the fault trace is more discontinuous: the secondary segments 3b, 3c, 3d and 3e are shorter, 10-18 km (Fig.47a), and generally separated by large step-overs of type 2 (1.5-2 km). Segment 3a is thus twice longer than the other secondary segments. The 1968 EQ broke the secondary segments 3b, 3c and 3d of the major segment 3.
- The earthquake initiated at a depth of ~11 km at the intersegment zone between the secondary segments 3b and 3c (Allen and Nordquist 1972).
- To the northwest, the rupture terminated in a ~3 km wide restraining step-over between secondary segments 3a and 3b, where multiple en echelon small faults have developed. To the southeast, the rupture stopped where the segment 3 starts overlapping the sub-parallel major segment 4, located at a perpendicular distance of ~6 km.

→ The 1968 Borrego Mountain EQ occurred on one major segment of the San Jacinto Fault (major segment 3), which it broke partially. The rupture indeed broke 3 over the 5 secondary segments that form the major segment 3. The rupture is taken to have initiated in the intersegment zone between secondary segments 3b and 3c.

Coseismic displacements measured at surface:

- *From Field measurements*: maximum lateral slip of 0.4 m (Clark 1972) measured on the secondary segment 3b (Fig.48).
- The complete slip profile was measured. Its overall shape is fairly triangular and asymmetric, with maximum slip deported at the northern tip of the rupture, and slip decreasing fairly regularly from its maximum value to zero at the southern rupture tip.
- The slip profile is shaped in three clear bumps separated by slip troughs, in keeping with the breakage of 3 distinct segments along the fault.

- *From GPS measurements*: No GPS measurements were available at the time of the Borrego Mountain earthquake.

→ Maximum lateral slip of ~0.4 m measured at surface, on secondary segment 3b, that is on the most mature part of the broken fault section; fairly asymmetric triangular slip profile.

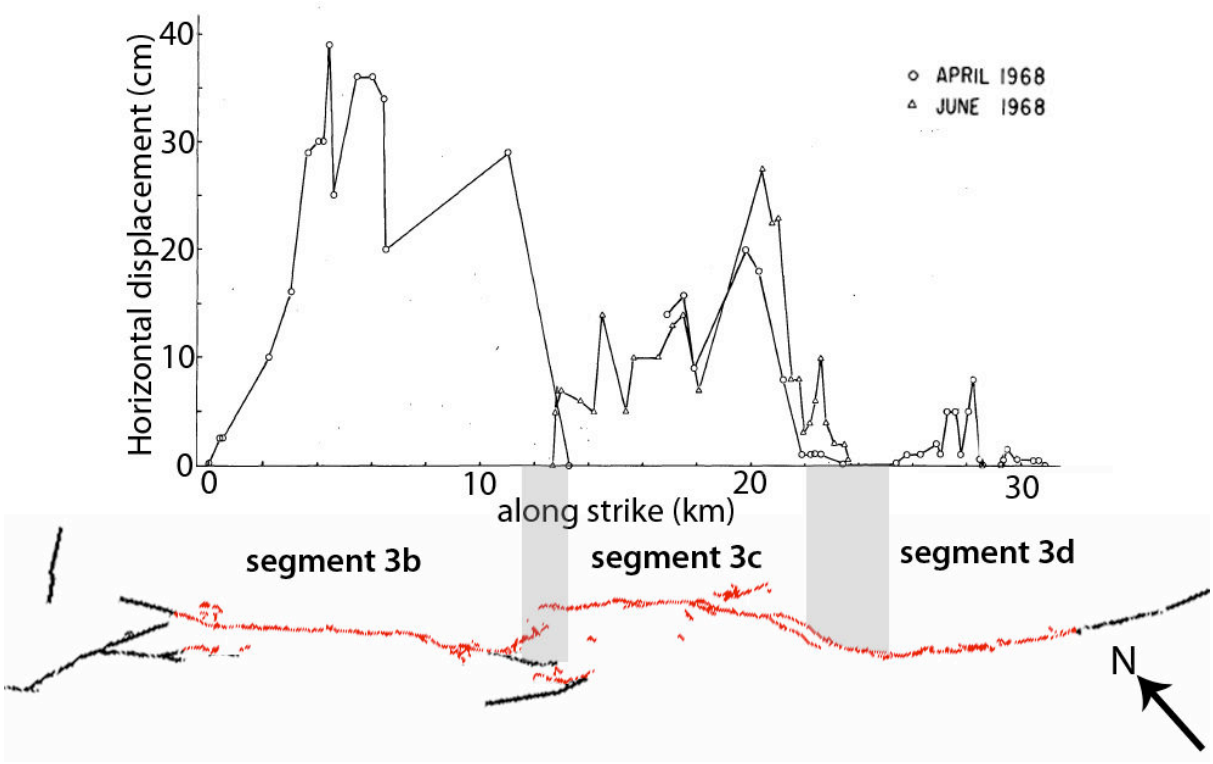


Fig.48: Top: Surface lateral slip measured right after the 1968 Borrego Mountain earthquake (Clark 1972) ; Bottom: Surface rupture trace of the 1968 EQ (Clark 1972). Secondary segments are numbered and intersegment zones are shown with light grey bars.

Source parameters:

Allen and Nordquist 1972 (Pasadena Network)

Mainshock: 1968/04/09 at 02h28min59s GMT ;

Lat = 33.18° Lon = -116.12° (NEIC)

Z = 11.1 km ; Strike,dip: N48°W,83°NE

M0=6.3e18 N.m calculated from teleseismic body waves (Wyss and Hanks 1972).

Other information:

Past EQ activity:

- Similar moderate earthquakes occurred on the San Jacinto Fault during the last decades: the 1940 and 1979 Imperial Valley earthquakes (Mw 7.0 & 6.5, respectively) and the 1987 Superstition Hills earthquake (Mw 6.6) broke parts of the major segment 4.

1968 EQ:

- Aftershocks are localized in the range 0-12 km depth and are mainly concentrated along segments 3c and 3d; where surface slip was lower (Hamilton 1972).

Parameters retained to describe the 1968 Borrego Mountain EQ (Tables 1 & 3):

Mw 6.5; M0 ≈ 6.3e18 Nm; L 33 km; Dmax surface = 0.4 m; W 12 km.
Number of segments broken on the San Jacinto Fault: 1 major segment, partly; representing the rupture of 3 secondary segments.

The surface slip-length data of the Borrego Mountain earthquake fall on the fourth function (orange curve; Fig.49). This is not in full agreement with our mapping, which reveals the rupture of three distinct segments, and not four, on the long term San Jacinto Fault. The broken segments are of secondary scale, not major segments. The discrepancy between the slip-length data and the number of broken segments might suggest that the measured surface slip is underestimated, which is likely for such a small amount of slip.

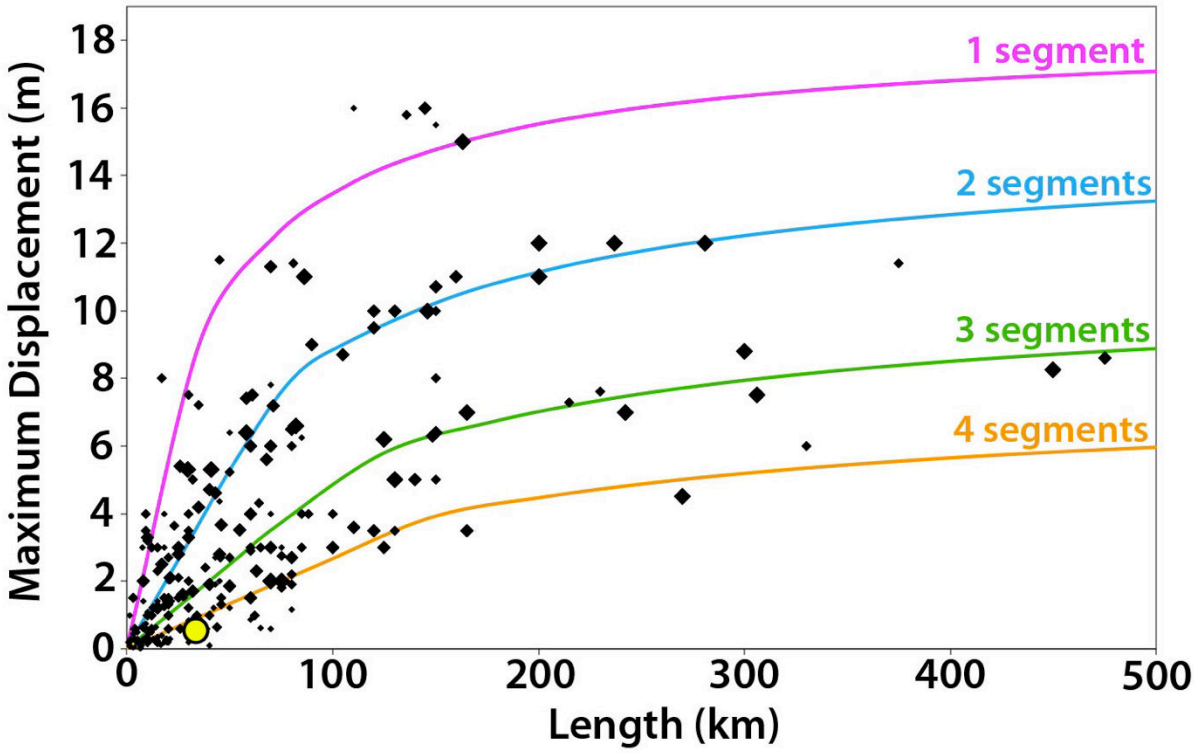


Fig.49: Earthquake displacement-length data measured at surface for 260 historical large continental earthquakes (Mw≥6). The 4 curves indicate the number of major long-term fault segments to have been broken by the earthquakes (modified from Manighetti et al., 2007 and Chapter IV). The yellow dot shows the 1968 Borrego Mountain earthquake surface slip-length data.

References

Allen, C. R., & Nordquist, J. M. (1972). Foreshock, main shock, and larger aftershocks of the Borrego Mountain earthquake. *US Geol. Surv. Profess. Paper,* **787**, 16-23.

Blisniuk, K., T. Rockwell, L. A. Owen, M. Oskin, C. Lippincott, M. W. Caffee, & J. Dortch. 2010. Late Quaternary slip rate gradient defined using high-resolution topography and 10 Be dating of offset landforms on the southern San Jacinto Fault zone, California. *J. Geophys. Res.,* **115**, B08401, doi:10.1029/2009JB006346.

Clark, M.M. (1972). Surface rupture along the Coyote Creek fault, in the Borrego Mountain Earthquake of April 9, 1968, *U.S. Geol. Sur. Prof. Paper* **787**, 55-86.

Fialko, Y. 2006. Interseismic strain accumulation and the earthquake potential on the southern San Andreas fault system, *Nature*, **441**, 968–971, doi:10.1038/nature04797

Gurrola, L. D., & T. K. Rockwell. 1996. Timing and slip for prehistoric earthquakes on the Superstition Mountain fault, Imperial Valley, southern California, *J. Geophys. Res.,* **101**, 5977–5985, doi:10.1029/95JB03061.

Hamilton, R. M. (1972). Aftershocks of the Borrego Mountain earthquake from April 12 to June 12, 1968. *US Geol. Surv. Profess. Paper,* **787**, 31-54.

Hudnut, K. W., & K. Sieh. 1989. Behavior of the Superstition Hills fault during the past 330 years, *Bull. Seismol. Soc. Am*., **79**, 304–329.

Janecke, S.U., Dorsey, R.J., Forand, D., Steely, A.N., Kirby, S.M., Lutz, A.T., Housen, B.A., Belgarde, B., Langenheim, V.E., & Rittenour, T.M. (2010), High Geologic Slip Rates since Early Pleistocene Initiation of the San Jacinto and San Felipe Fault Zones in the San Andreas Fault System: Southern California, USA: *Geological Society of America Special Paper* **475**, 48 p., doi: 10.1130/2010.2475.Â isbn 9780813724751

Kendrick, K. J., D. M. Morton, S. G. Wells, & R. W. Simpson. 2002. Spatial and temporal deformation along the northern San Jacinto fault, southern California: Implications for slip rates, *Bull. Seismol. Soc. Am*., **92**, 2782–2802, doi:10.1785-/0120000615.

Kirby, S. M., Janecke, S. U., Dorsey, R. J., Housen, B. A., Langenheim, V. E., McDougall, K. A., & Steely, A. N. (2007). Pleistocene Brawley and Ocotillo formations: Evidence for initial strike□slip deformation along the San Felipe and San Jacinto fault zones, southern California. *The Journal of geology*, **115**(1), 43-62.

Larson, R. L. (1972). Bathymetry, magnetic anomalies, and plate tectonic history of the mouth of the Gulf of California. *Geological Society of America Bulletin*, **83**(11), 3345-3360.

Lindsey, E. O., & Y. Fialko 2013. Geodetic slip rates in the southern San Andreas Fault system: Effects of elastic heterogeneity and fault geometry, *J. Geophys. Res. Solid Earth*, **118**, 689–697, doi:10.1029/2012JB009358.

Lundgren, P., E. A. Hetland, Z. Liu, and E. J. Fielding. 2009. Southern San Andreas-San Jacinto fault system slip rates estimated from earthquake cycle models constrained by GPS and interferometric synthetic aperture radar observations, *J. Geophys. Res*., **114**, B02403, doi:10.1029/2008JB005996

Lutz, A. T., R. J. Dorsey, B. A. Housen, & S. U. Janecke. 2006. Stratigraphic record of Pleistocene faulting and basin evolution in the Borrego Badlands, San Jacinto fault, southern California, *Geol. Soc. Am. Bull*., **118**, 1377–1397, doi:10.1130/B25946.1

Manighetti, I., M. Campillo, S. Bouley, and F. Cotton (2007), Earthquake scaling, fault segmentation, and structural maturity*, Earth Planet. Sci. Lett*., **253**, 429-438, doi:10.1016/j.epsl.2006.11.004

Rockwell, T. K., C. Loughman, & P. Merifield. 1990. Late Quaternary rate of slip along the San Jacinto fault zone near Anza, southern California, *J. Geophys. Res*., **95**, 8593–8605, doi:10.1029/JB095iB06p08593.

Sharp, R. V. 1967. San Jacinto Fault zone in the Peninsular Ranges of southern California*, Geol. Soc. Am. Bul*l., **78**, 705–730, doi:10.1130/ 0016-7606(1967)78[705:SJFZIT]2.0.CO;2.

Wyss, M., and T. C. Hanks (1972) The source parameters of the Borrego Mountain, California earthquake*, U.S. Geol. Survey Prof. Paper*, **787**, 24-30,.

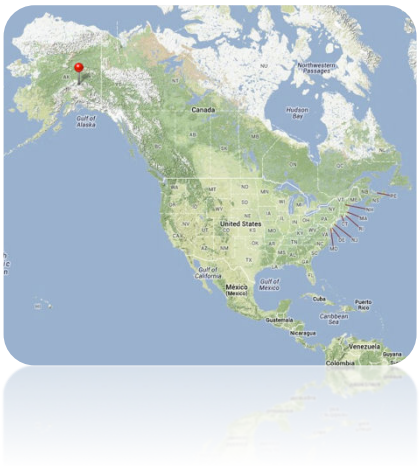
2.5. Denali 2002

03/nov/2002, Alaska, USA

Mw 7.9

Epicenter (USGS) : 63.52°N-147.53°W

Right-lateral strike-slip



Broken long-term fault

The EQ broke a part of the Denali fault system, Alaska. It broke three distinct faults in the system: Susitna, Denali and Totschunda (Fig.50); Denali is the major one, in the system, and in the rupture.

Denali Fault

General characteristics from literature:

- Arcuate right-lateral strike-slip fault, about 2000 km long.
- Would have initiated 55-70 Ma ago (Late Cretaceous-early Eocene), based on dating of granitic plutons offset by the fault (e.g. Nokleberg et al., 1985 and references therein; Plafker and Berg 1994).
- Maximum cumulative lateral slip of 300-400 km, estimated from multiple offset measurements on terrane boundaries, and on magmatic, metamorphic and sedimentary rocks (See synthesis in Lowey, 1998), on many sections of the Denali Fault.
- Current lateral slip rate: 6-10 mm/yr (InSAR, Biggs et al., 2007; GPS, Fletcher 2002) measured at many sites along the Denali Fault (between 152°W and 140°W, Fig.50).
- Long-term lateral slip rate: 12-13 mm/yr (over the Quaternary; Matmon et al., 2006; Mériaux et al., 2009) measured at several sites of the central sections of the Denali Fault (150°W-142°W). The slip rate seems lower, ~7 mm/yr, in western half of the fault (Fig.50; Matmon et al., 2006; Mériaux et al., 2009).

→ The Denali Fault is a mature fault (L 2000 km hence > 1000 km, I-Age 55-70 Ma hence > 10 Ma, MR 12-13 mm/yr hence > 1 cm/yr, D_{Total} ~400 km hence > 100 km).

Architecture and major lateral segmentation, from our mapping (Fig.50):

- Mapping done from Google Earth, Landsat and Aster GDEM v.2 data combined with literature information (e.g. Plafker and Berg 1994).
- Long-term fault trace well expressed in surface morphology and topography.
- The Denali Fault is surrounded by a number of sub-parallel, large strike-slip faults; the most important are 150-200 km away (Castle Mountain Fault and Border Ranges Fault in the south; Kaltag Fault and Tintina Fault in the north).
- The Denali Fault terminates at both tips by large-scale splays, made of a dense network of splaying secondary faults, oblique to the master fault, and being both right-lateral and reverse (Fig.50; e.g. Farewell, Goodnews Kanektok faults in the west; Aishihik Lake, Wellesley Lake faults in the east). Both fault terminations are thus of type T_S (Fig.50b) with the splay network being rather symmetric in the east, and rather asymmetric in the west. As it splays to the west, the fault trace curves counterclockwise before ending. To the east, the main fault of the splay abuts and ends against a ~N-S trending large fault (Chatham Strait Fault), so that the very easternmost termination of the Denali Fault is of T_{ob} type (Fig.50b). The fault tip splays suggest that the Denali Fault has been propagating bilaterally towards both the west and the east over geological time. The Chatham Strait Fault might however arrest the current eastward lateral propagation of the Denali Fault.
- Oblique, secondary faults have also developed along the Denali Fault, which they connect to. The longest secondary faults trend NE-SW in the western half of the Denali Fault where they extend south of the fault trace, while, in the eastern half of the Denali Fault, they strike NW-SE south of the fault trace and NE-SW north of it. The longest of these secondary oblique faults have developed from most of the connection zones between the Denali major segments (See below). The variable orientation of the oblique faults suggests they might be splay faults that developed at different times at the propagating tips of the major segments; this would be in keeping with the Denali Fault having propagated bilaterally from its center over geological time, i.e., towards the west in its western half and towards the east in its eastern half (Fig.50c). The fault center is the site of the most pronounced bend in the overall fault trace, at about the junction between major segments 3 and 4 (See below).
- The fault is divided into 6 and possibly 7 major segments (See Fig.50b where they are numbered). The principal characteristics of those segments (length, strike, etc) and the types

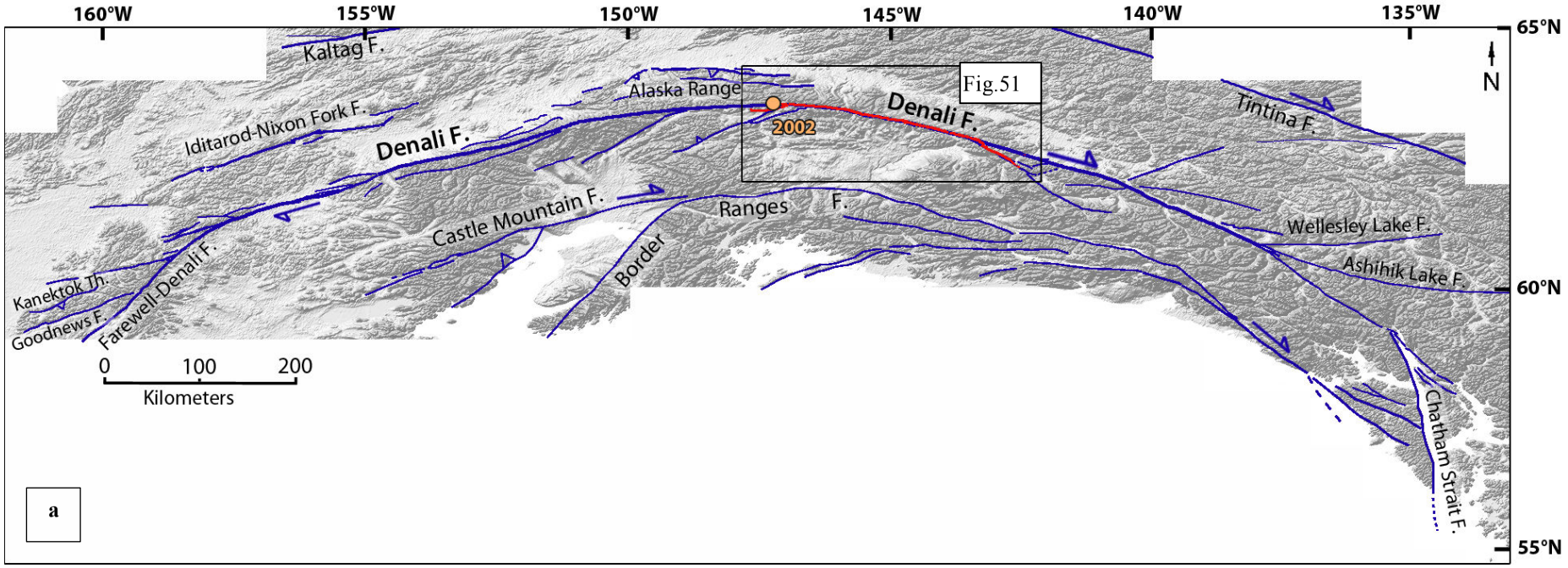


Fig.50: (a) General map (Geodetic coordinate system) of the major long term faults that we papped in Alaska (blue). In red is the surface rupture of the 2002 Denali earthquake. The orange circle shows the 2002 Denali epicenter.

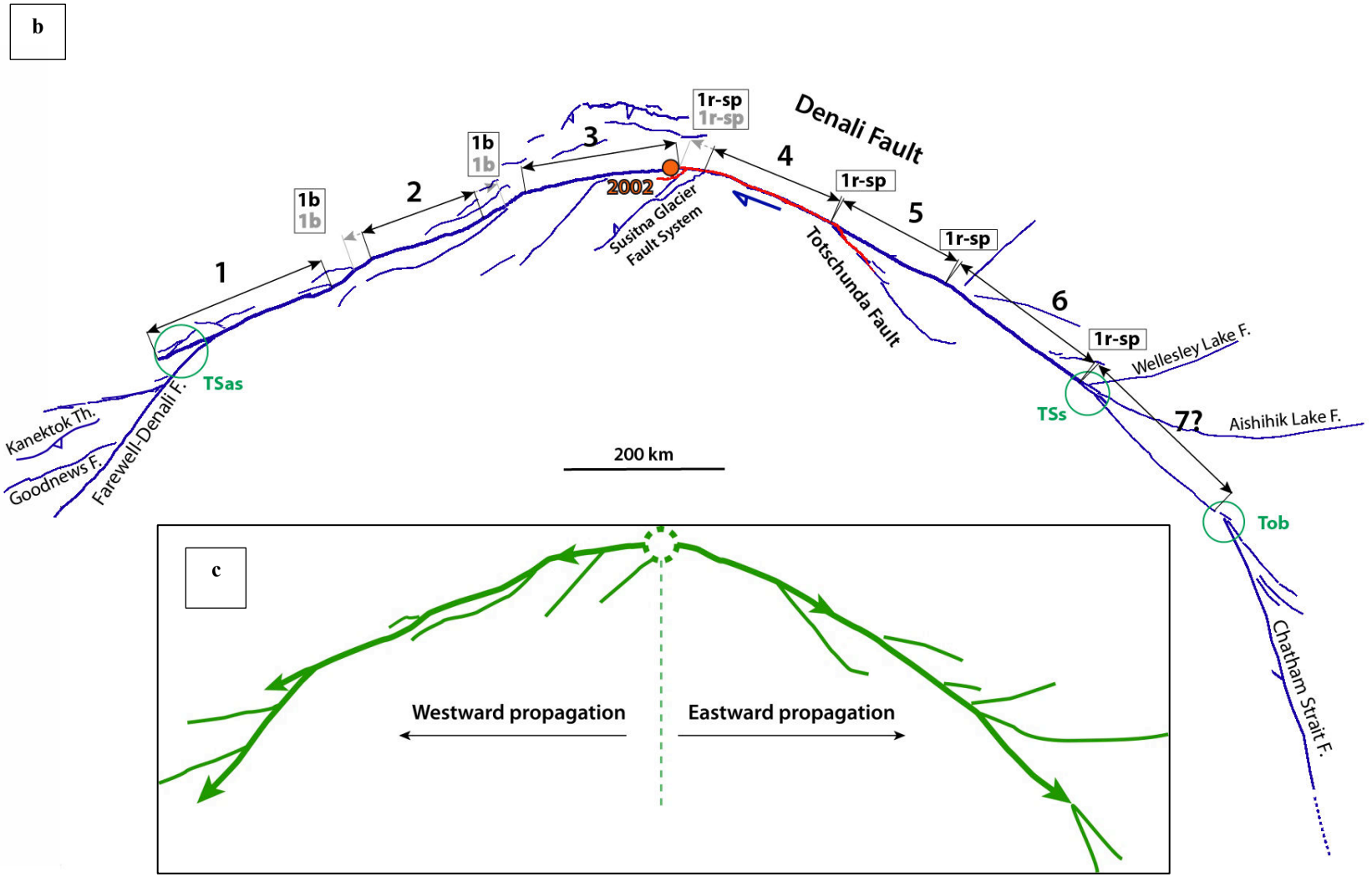


Fig.50: (b) Same active fault map as in 50a, but with focus on the major segments of the Denali fault (UTM projection). The segments are numbered from W to E and indicated by black arrows parallel to their mean strike. The grey prolongation of the arrows indicates the uncertainties on the segment lengths. The nature of the inter-segment zones is indicated in letters within boxes explained in Table 6. The nature of the fault tips is indicated in green (Table 6). (c) Simplified map showing the bilateral propagation of the Denali fault over geological time. Dashed circle is supposed to be the original point where the fault started to propagate.

of connection between them are described in Table 6 and Fig.50b. Note that segment 7 belongs to the eastern tip splay, and hence is not strictly comparable to the other segments.

- The 7 major segments have a similar length in the range 150-240 km and of ~200 km on average.
- The fault trace is linear along each major segment (Fig.50b). The mean strike of the fault rotates clockwise when one goes from one major segment to the next in the east direction, with strike changes ranging between ~2 and 30°. The most central major segments (3-4-5) are connected with "simple connections" (Fig.18) that is they are connected through single bends in the fault trace without any across-strike separation. The other segments are separated with step overs that are fully connected that is that now appear as double bends in the fault trace. The across-strike width of the connected step-overs ranges from ~7 to 20 km (Table 6). At inter-segments 2-3, 3-4, 4-5, 5-6, and 6-7, one or several fairly large, oblique, secondary, likely splay faults have developed. The Susitna and Totschunda faults are some of those oblique secondary faults splaying from the connection zone between segments 3 and 4, and between segments 4 and 5, respectively.
- Segment 4 is the only major segment of the fault to be free of any secondary faulting nearby its trace.

→ The Denali Fault is divided into 6 (possibly 7) well-connected, long-term, major segments, each of ~200 km length. The Denali Fault has propagated bilaterally from its center over geological time. Central major segments 3 and 4 are thus the most mature segments of the fault. The fault lateral propagation might be currently arrested in the east, but might be going on in the west.

Susitna Fault (Fig.50 & 51):

- Small, reverse fault not described in the literature before the 2002 earthquake because it had not been recognized.
- About 48 km long (Crone et al., 2004), the fault bounds to the south a small topographic relief. It extends at the level of a significant rounded bend in the Denali Fault trace (Fig.50b), which marks the connection zone between major segments 3 and 4, and to which the Susitna Fault is connected.
- The moderate resolution of the available images did not allow us to analyze the segmentation of the Susitna Fault.

Totschunda Fault (Fig.50, 51 & 52):

- Right lateral strike slip fault with a minor vertical component.
- Cumulative lateral and vertical displacements estimated of 9-10 km and 1.5 km, respectively (Richter and Matson, 1971). The fault is possibly as young as 0.65 Ma and no older than 2 Ma.
- Holocene right-lateral slip rate ~ 6 mm/yr (Matmon et al., 2006).
- The Totschunda Fault connects with the Denali Fault through a series of sub-parallel, NW-trending small fault branches (Schwartz et al., 2012).
- The Totschunda Fault seems to include 3-4 major collinear segments (Fig. 52). The 2002 EQ broke the northernmost of those major segments (major segment 1, Fig.52), on its entire length. Haeussler et al. (2004) reported that the rupture also broke, at least partly, the next major segment 2.

→ The 2002 rupture mainly broke one major segment of the Totschunda Fault (northernmost major segment 1), but possibly also part of the next major segment 2.

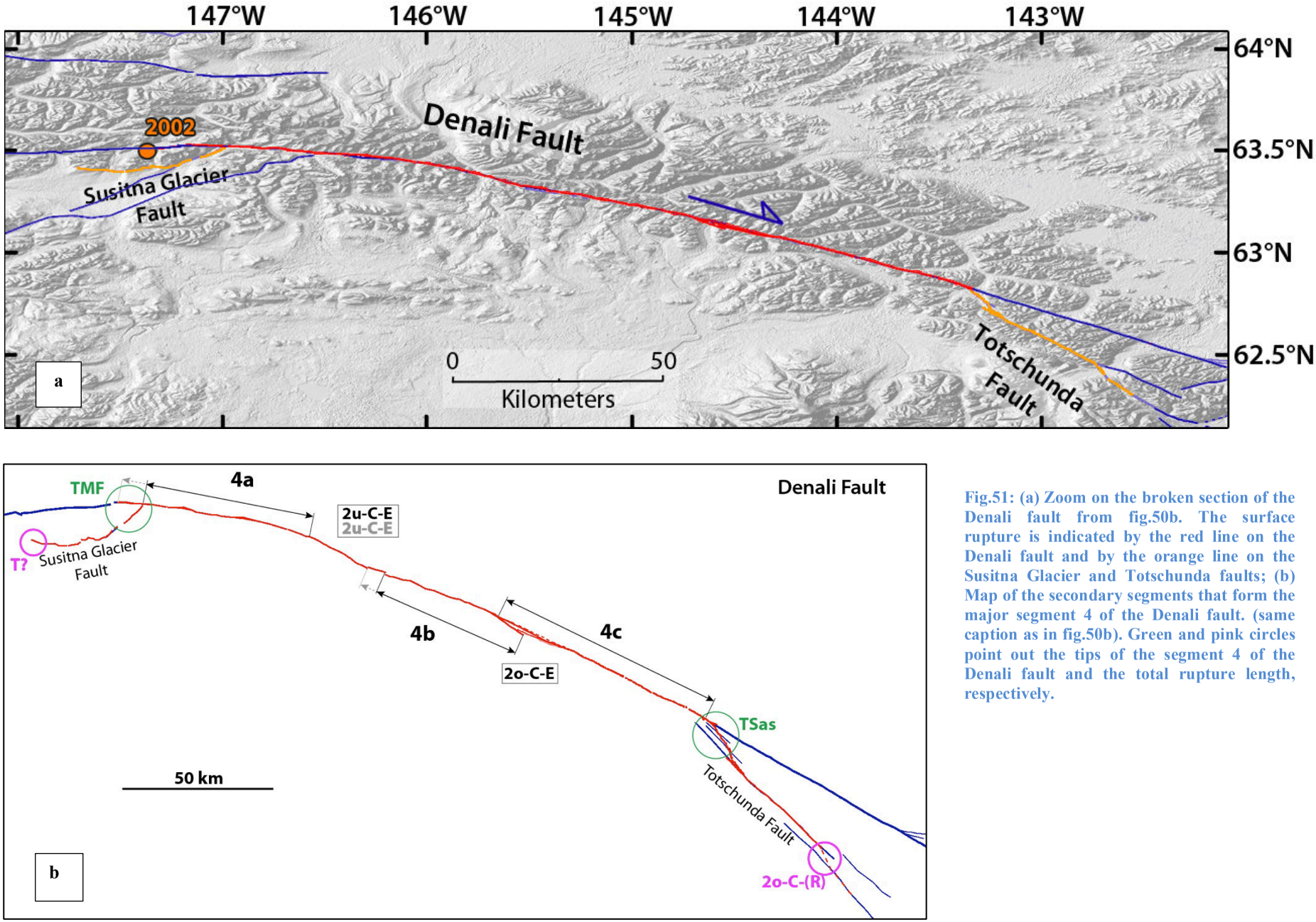


Fig.51: (a) Zoom on the broken section of the Denali fault from fig.50b. The surface rupture is indicated by the red line on the Denali fault and by the orange line on the Susitna Glacier and Totschunda faults; (b) Map of the secondary segments that form the major segment 4 of the Denali fault. (same caption as in fig.50b). Green and pink circles point out the tips of the segment 4 of the Denali fault and the total rupture length, respectively.

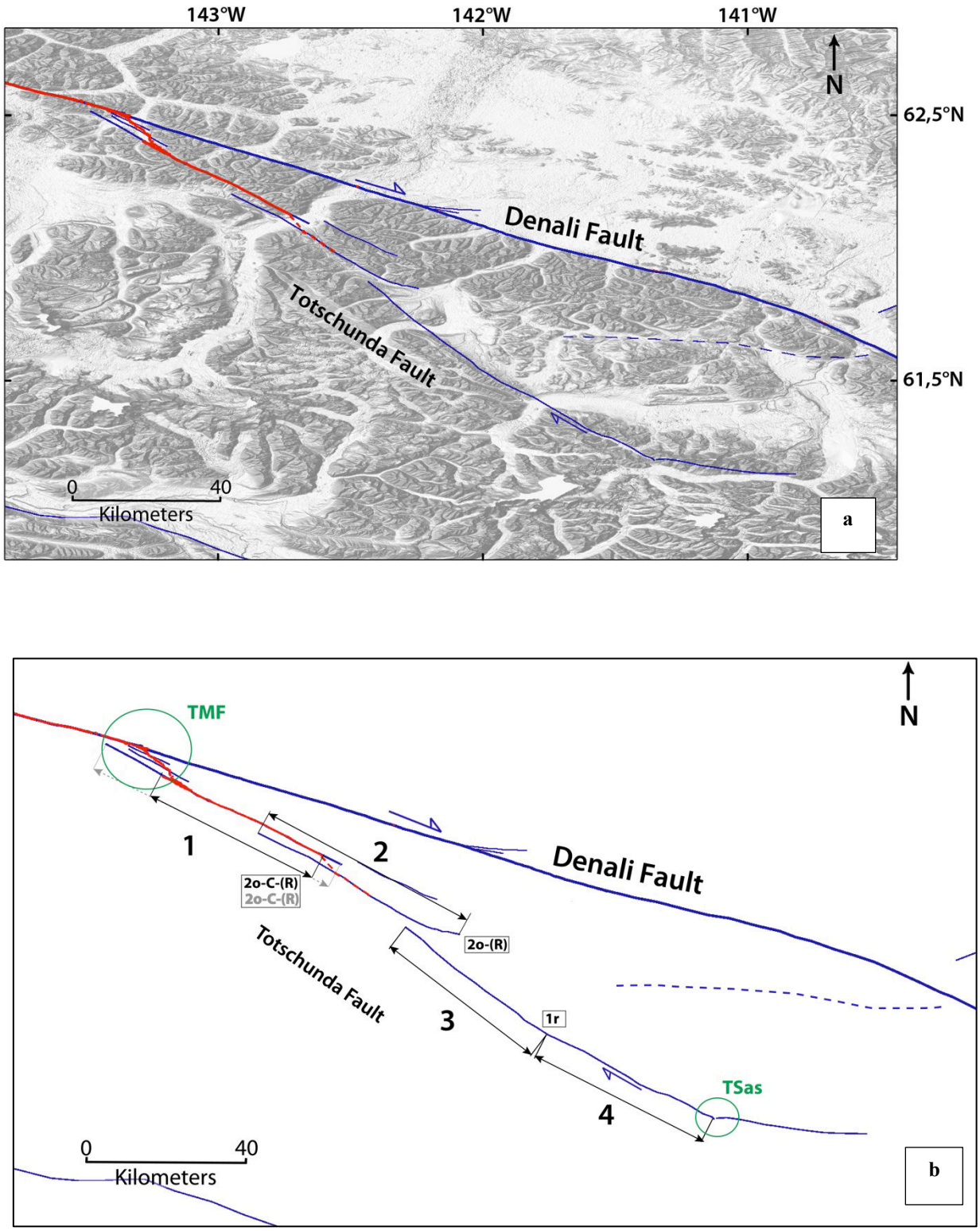


Fig.52: (a) Zoom on the Totschunda Fault and the eastern end of the surface rupture of the 2002 earthquake (in red) ; (b) Map of the segments that form the Totschunda Fault. (same caption as in Fig.50b).

2002 Coseismic rupture

Surface trace and location on long-term Denali Fault :

- The eastern half of the 2002 surface rupture is clear on Google Earth images and available LiDAR data (opentopograhy.org). The western half of the rupture is obscured with glaciers and snow, that disturb also InSAR data (Lu et al., 2003; Wright et al., 2004). From numerous field measurements and remote sensing analysis, the surface trace of the earthquake was precisely mapped, and the displacements measured (See below) (Eberhart-Philipps et al., 2003; Crone et al., 2004; Haeussler et al, 2004; Taylor et al., 2008; Haeussler, 2009; Schwartz et al., 2012).
- Total surface rupture of ~300 km long.
- The earthquake initiated at a depth of about 4 km (Ratchkovski et al., 2003) in or near the major inter-segment zone 3-4 of the Denali Fault. It first produced thrust faulting on the previously unknown Susitna Glacier Fault.
- The EQ broke three distinct faults: it initiated on the small reverse Susitna Glacier Fault, oblique to the master Denali Fault; then it propagated unilaterally toward the east along the Denali Fault; it eventually broke part of the oblique Totschunda splay Fault, along which it stopped (Fig.51).
- The EQ thus broke only one major segment of the Denali Fault, the segment 4. It broke it on its entire length.
- On Denali, the rupture thus started in the inter-segment zone between major segments 3 and 4, and stopped in the inter-segment zone between major segments 4 and 5 (Fig.50b and 51). The two faults that broke just before and just after the Denali section are among the fairly large oblique splay faults that developed in the segment connection zones, as described before.
- According to its geometry, segment 4 is divided into three secondary segments, 4a, 4b, and 4c, of similar length, 60-70 km (Fig.51). The EQ thus broke the three secondary segments of major segment 4.
- The fault trace is linear along each secondary segment. The mean strike of the fault rotates clockwise when one goes from one secondary segment to the next in the east direction, with strike changes ranging between ~5 and 9°. Secondary segments 4a and 4b are connected to each other through a pronounced bend in the fault trace, and an across-fault distance of ~3,5 km (inter-segment of type $2_{U\text{-}C\text{-}E}$; Fig.18). Secondary segments 4b and 4c are connected to each other through a small pull-apart basin, with an across-fault width of ~1 km (type $2_{O\text{-}C\text{-}E}$).

→ The 2002 Denali EQ broke three distinct faults, not a single one.

→ The 2002 Denali EQ broke only 1 major segment of the Denali Fault, which is the most mature, central segment of the fault; this segment broke entirely, along the 3 secondary segments that form it.

→ The 2002 EQ initiated near the intersection of the Denali Fault with an ancient (but still active) splay fault (Susitna), and the Denali rupture stopped at a similar intersection with another splay fault (Totschunda).

Coseismic displacements measured at surface :

- *From Field measurements*: Maximum lateral slip of 8.8 ± 0.5 m (Eberhart-Philipps et al., 2003; Haeussler et al., 2004), measured on secondary segment 4c.
- *From GPS measurements*: permanent network and campaign measurements have recorded ~3.1 m of maximum horizontal slip 5 km south of the fault at the latitude of segment 4c (Heinsdottir et al., 2003, 2006).
- *From InSAR data and modeling*: the glacier and snow cover, along with the very few data available (only western half part of the rupture), prevent analyzing the rupture over its entire length and in continuity. Wright et al. (2004) modeled however a lateral slip at surface reaching ~12.5 m (Fig.53). As this modeled slip is much greater than the field measurements, it is likely overestimated.
- The complete slip profile could be measured on the field, and be inferred from GPS and seismological data modeling (Fig.53 & 54). The measured slip profile is more precise. The slip distribution is asymmetric, with the maximum displacement at the eastern termination of the major segment 4 of the Denali Fault. If we consider only the slip distribution on the Denali Fault, the envelope shape of the profile is roughly triangular. The rupture of the three secondary segments 4a, 4b and 4c on the Denali Fault is well seen in the form of three slip bumps in the overall slip profile, separated by high slip gradients (Fig.53).

→ Maximum slip well constrained at surface, of ~8.8 m. The coseismic slip increased eastwards as the rupture was propagating. Although the Denali EQ broke 3 distinct faults, its global coseismic slip profile has an overall envelop shape being fairly triangular. The slip profile on the Denali rupture is triangular and asymmetric. The maximum slip occurred on the secondary segment 4c of the Denali Fault. Maximum slip on the Totschunda Fault was ~ 3.5 m.

Source inversion models and slip distribution at depth :

We compare five source inversion models that have been published on the 2002 Denali earthquake (Fig.53 & 54). The grid data are available for two of them (Table 2).

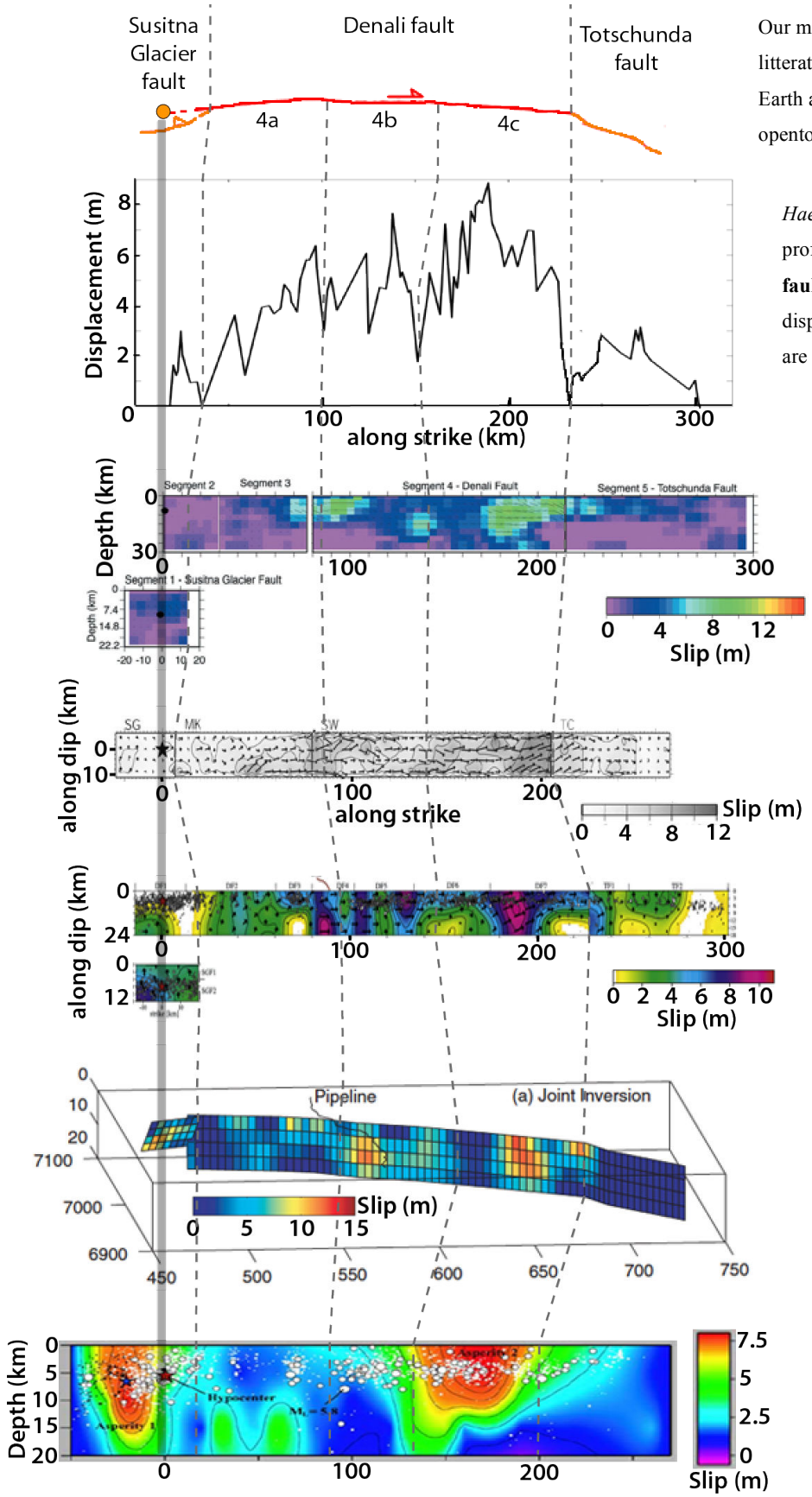
The models differ principally from the data they used:

- Ozacar et al. (2003): Teleseismic data only. The model considers the Denali earthquake, and also includes the Nenana Mountain foreshock in the west, what obscures the Denali earthquake slip. The model collapses the 3 faults implied in the rupture onto only one plane (not segmented).
- Wright et al. (2004): Insar and GPS data only, but Insar data are incomplete and noisy. The model considers the Susitna, Denali, and Totschunda sections and divides those three faults into 1, 6 and 2 segments, respectively. However the noisy dataset used in the inversion didn't allow estimating any slip on the Totschunda Fault.
- Hreinsdottir et al. (2006): Near-field GPS data only. The model considers the three Susitna, Denali, and Totschunda faults and divides them overall into 11 segments (2 for Susitna; 7 for Denali; 2 for Totschunda).
- Oglesby et al. (2004): Near-field seismic and geodetic data, and integration of surface slip. The model considers the three faults and divides them overall into 5 segments (1 for Susitna; 3 for Denali; 1 for Totschunda) in agreement with our counting of the broken segments. By contrast, the inter-segment zones defined by Oglesby et al. are not at the same location than those we mapped.
- Asano et al. (2005): Near-field seismic and geodetic data. The model considers the three faults and divides them overall into 4 segments (1 for Susitna; 2 for Denali; 1 for Totschunda).

→ We consider that the models from Oglesby et al. (2004) and Asano et al. (2005) are the most robust for they use more different and complementary data. They also segment the faults in a way that roughly coincides with our tectonic observations.

→ These two models find a fairly similar slip distribution that resembles that observed at the ground surface (triangular asymmetric profile on Denali rupture). The two profiles show 3 main slip patches that fairly well coincide with the secondary broken segments that we mapped, and find a similar maximum slip of about 10 m, localized on the secondary segment 4c where slip is also maximum at the ground surface. The two models differ in rupture width, but we note that in all models most of the slip is distributed between 0 and 15 km depth: we will use this value as the average rupture width at depth.

→ **The best source models suggest: $L_{rupture}$ ~293-310 km, D_{max} at depth ~10.5 m, 3 segments broken on the Denali Fault.**



Our mapping of the surface rupture based on litterature (e.g. Haeussler, 2009), Google Earth and Lidar imagery (available on opentopography.org).

Haeussler et al., 2004 : Co-seismic slip profile measured at surface on **Denali fault and Totschunda fault** (vertical displacement of the Susitna Glacier fault are not presented here)

Oglesby et al. 2004 :
Data : GPS, Strong motion and Surface
L = 346 km ; W = 30 km
Dmax= 10,2 m

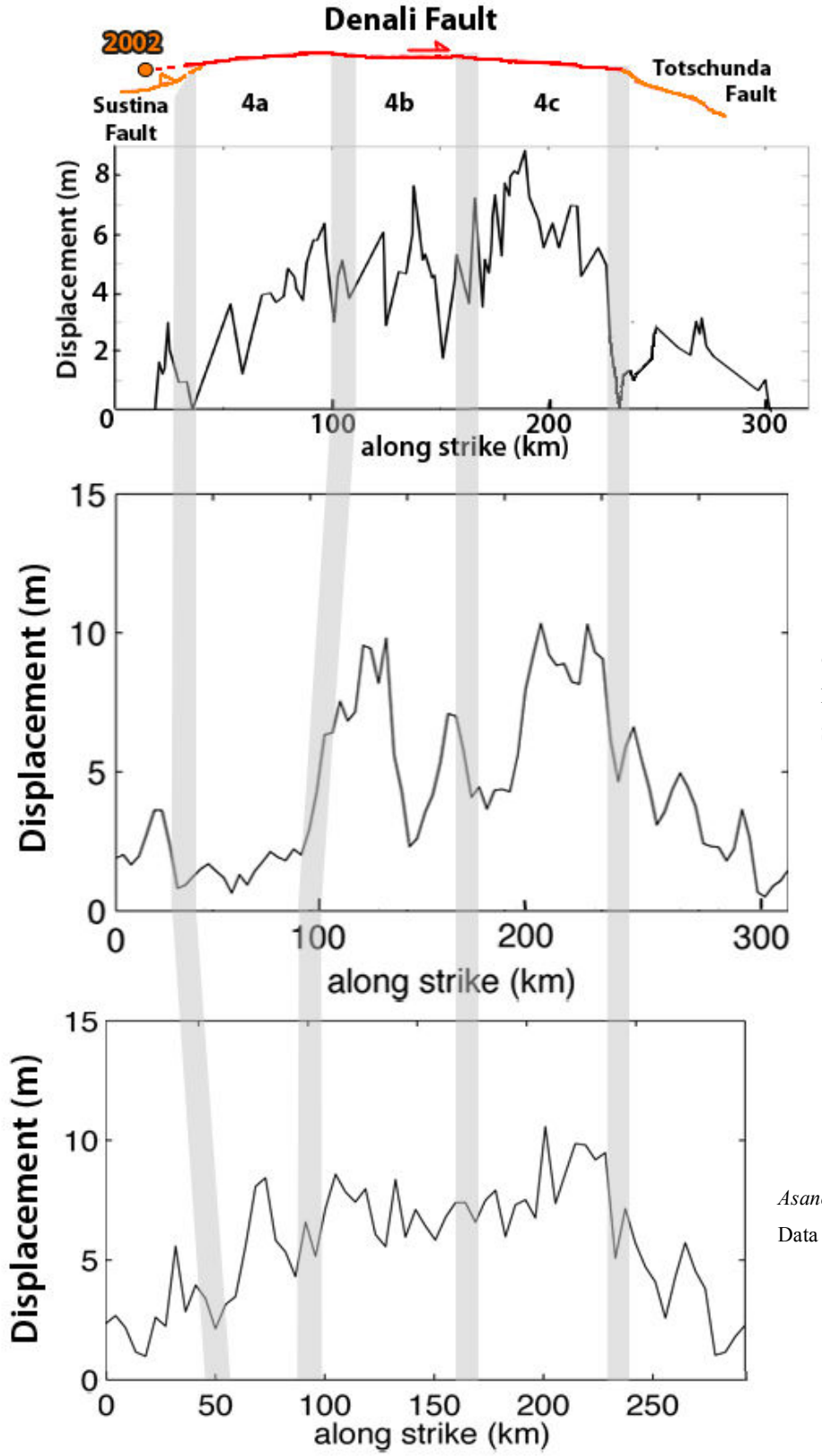
Asano et al. 2005 :
Data : GPS and strong motion
L = 293km ; W=18km ;
Dmax=10,5m

Hreinsdottir et al. 2006 :
Data : GPS and Surface
L ≈ 310km ; W=20km ; Dmax ≈ 9,2 m (12m in the model using only GPS data)

Wright et al. 2004 :
Data : GPS and InSAR
L ≈ 312km ; W=16km ;
Dmax=12,5m

Ozacar et al., 2003 :
Data : Teleseismic
L= 320km ; W=15km ; Dmax ≈ 8 m ≤ Dmax measured at surface

Fig.53: Comparison between different inversion models published on the 2002 Denali earthquake. Grey vertical line to the left represents the hypocenter location for each model. Models are at the same scale. Dashed lines are the intersegment zones highlighted by our mapping.



Our mapping of the surface rupture based on litterature (e.g. Haeussler, 2009), Google Earth and Lidar imagery (available on opentopography.org).

Haeussler et al., 2004 : Co-seismic slip profile measured at surface on **Denali fault and Totschunda fault** (vertical displacement of the Susitna Glacier fault are not presented here)

Oglesby et al. 2004 :
Data : GPS, Strong motion and Surface

Asano et al. 2005 :
Data : GPS and strong motion

Fig.54: Comparison between profiles of maximum slip measured at surface and derived from two inversion models published on the 2002 Denali earthquake. Grey areas represent the intersegment zones.

Other source parameters:

SCARDEC
Mainshock: 2002/11/03 at 22h12m41s GMT
Lat = 63.520° Lon = -147.440° (NEIC)
Mw 7.9; M0 = 8.75^{e}20 Nm; 0 <Z < 30 km;
Duration: ~ 96 s (Fig.55)
Strike, dip, rake: (20°, 69°,-17°)/ (117°,74°,-158°)

Global CMT
Mainshock: 2002/11/03 at 22h13min28s GMT
Lat = 63.23° Lon= -144.89°
Mw 7.8; M0 = 7,48e20 Nm; Z = 15 km;
Half-duration: 23.5 s
Strike, dip, slip : (296°,71°,171°)/ (29°,82°,19°)

- Ratchkowski et al. (2003) used local seismic data to define more precisely the hypocenter depth (Z ~ 4.2 km)
- The rupture duration much differs between the SCARDEC and Global CMT methods. However the SCARDEC method is more precise to determine the earthquake duration. Other studies are in agreement with its estimation (e.g. Frankel 2004)
- Moment magnitude and seismic moment range between 7.8-7.9 and 7.48-8.75e20 Nm, respectively.
- Frankel (2004) divides the Denali earthquake in three subevents, highlighted by the moment release along the Denali and the Totschunda faults (Fig.55): right after the EQ nucleation, the moment release is rather small until about 90 km east of the hypocenter. Then a high peak of moment is released from ~90 to 160 km and is associated to 2nd sub-event. It corresponds to secondary segment 4b in our mapping. Finally the 3rd sub-event corresponds to the zone of highest moment release identified as the rupture of secondary segment 4c in our mapping.
- The source time function calculated from SCARDEC method (Vallée et al., 2011) shows the same principal features: a first moderate peak followed by low values of moment rate (0-20s) would be associated with the rupture of the Susitna Glacier Fault and that of the secondary segment 4a of the Denali Fault; then a second moderate start of moment release at ~20s would correspond to the rupture of the secondary segment 4b; and then suddenly, at ~48 s, a marked increase in the energy release would mark the rupture of the secondary segment 4c. The energy release then goes on, yet markedly decreasing down to vanishing.
- The partition of the energy release along the broken Denali section is thus in keeping with the rupture of three distinct segments along that section. We note that the acceleration of the energy release has occurred as the rupture was propagating on major segment 4, which is the most mature segment of the Denali Fault and the only one to be free of adjacent faulting. It also has a linear trace, but this property is shared with most other major segments.

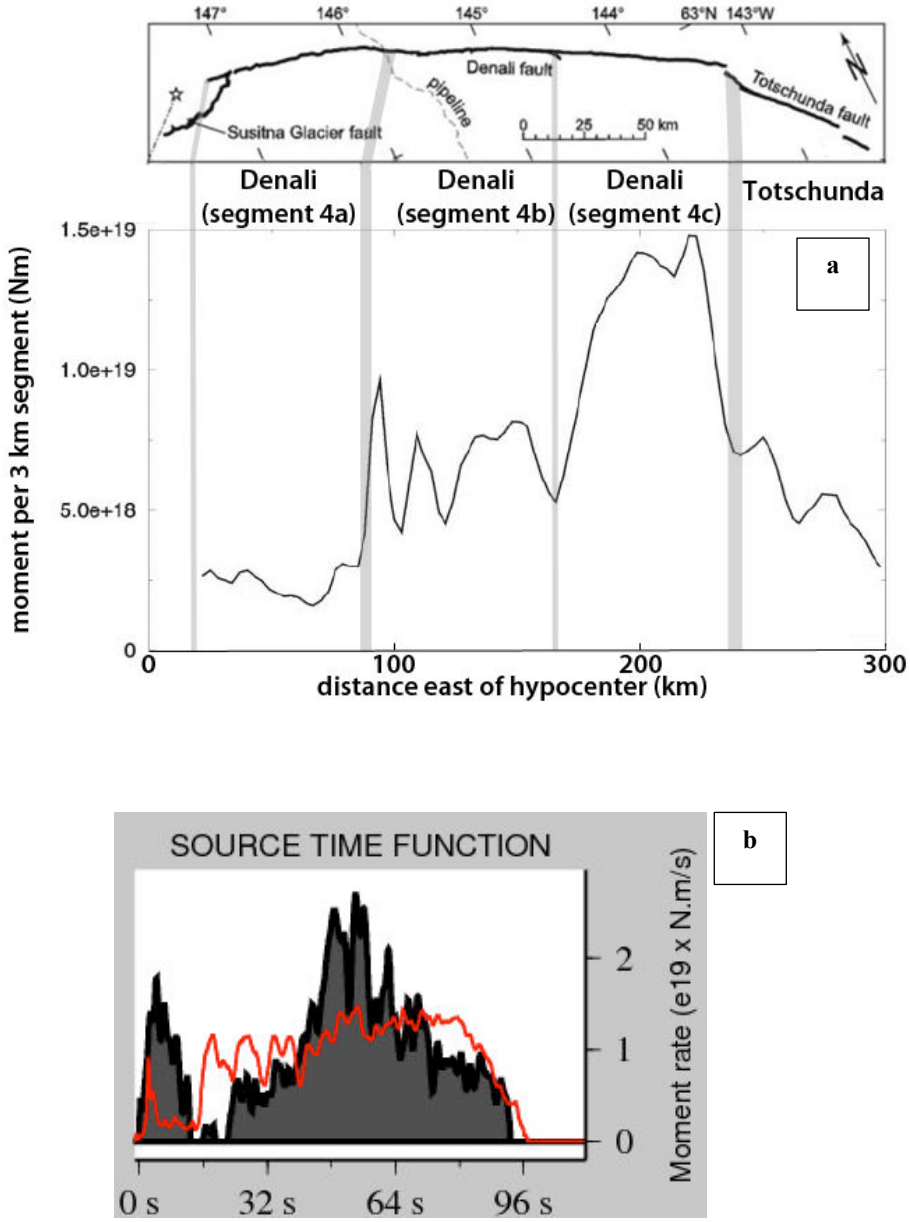


Fig.55: (a) Strike slip moment release per 3-km-long fault segment along the Denali and Totschunda faults as a function of distance along faults east of the hypocenter, derived from the inversion of displacement waveforms (modified from Frankel 2004). Grey bars show the inter-segment zones; (b) Source Time Function calculated with the SCARDEC method (Vallée et al., 2011). In grey : best STF that we use; in red : mean curve of all STFs.

Other information:

2002 EQ:

- The rupture had a super-shear velocity, mainly along secondary segment 4a (Dunham and Archuleta 2004).
- Aftershocks are mainly localized between 0 and 11 km depth and are in agreement with the extent of the surface rupture (Ratchkovski et al., 2003, 2004). The largest aftershock (M_L 5.8) occurred 20 min after the mainshock, 95 km eastward.
- 10 days before the EQ, the Nenana Mountain earthquake (Mw 6.7) broke the Denali Fault over ~30 km, due west of the 2002 main rupture. GPS and Insar data suggest that the slip produced by the foreshock was in the range 0.9-3 m (Wright et al., 2003; Hreinsdottir et al., 2006).

Past EQ activity:

- The most recent large EQ known on the Denali Fault occurred in 1912 (Mw=7.2-7.4). It is taken to have initiated in the inter-segment zone connecting the secondary segments 4a and 4b, then to have propagated unilaterally along the entire length of segment 4a. The slip produced was 1.4-2.1 m (Carver et al., 2004).
- No instrumental earthquake with a magnitude greater than Mw 5.5 has been recorded in the period 1912-2002. Yet the seismological network was sparse. The few instrumental earthquakes mainly occurred off- the Denali Fault, with reverse and strike-slip mechanisms (Doser, 2004).
- Over the 30 years before the 2002 EQ, the instrumental seismicity was very low. By contrast, the seismicity accelerated 8 months before the main shock (Ratchkovski et al., 2004).

Parameters retained to describe the 2002 Denali EQ (Tables 1 - 4):

Mw 7.8-7.9; M0 ~ 7.5-8.8e20 Nm; L_{total} ~ 310 km; Lm (Length broken on long-term Denali Fault, hence main length) ~ 200 km; W ~ 15 km; Dmax surface = 8.8 ± 0.5 m; Dmax depth ~ 10.5 m; *Hypocenter*: Z ~ 5 km.

Number of segments broken on the Denali Fault: 1 major segment, entirely, so 3 secondary segments.

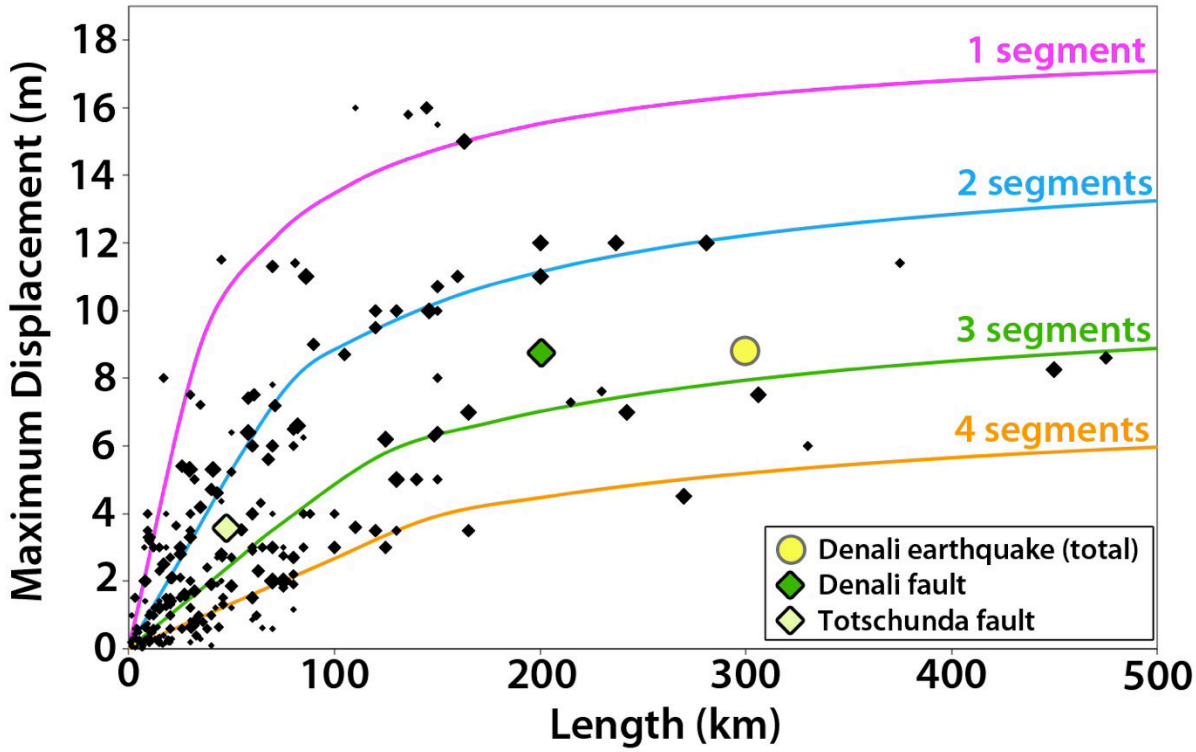


Fig.56: Earthquake displacement-length data measured at surface for 260 historical large continental earthquakes (Mw≥6). The 4 curves indicate the number of major long-term fault segments to have been broken by the earthquakes (modified from Manighetti et al., 2007 and Chapter IV).

The Denali earthquake surface and depth slip-length data fall on the third function (green curve; Fig.56 and 57, respectively) what seems to corroborate the rupture of three (secondary) segments of the long-term fault (See discussion in chapters III and VII for secondary versus major segments). However, the EQ involved the rupture of three distinct faults and it is not clear that the scaling functions presented in Fig.56 & 57 can be used to describe a multi-fault rupture. We thus also indicate the slip-length data describing the rupture of the Denali and of the Totschunda faults alone. These data, especially those at depth, are still compatible with the rupture of 3 segments on the Denali Fault, and of 2 segments on the Totschunda Fault, as observed.

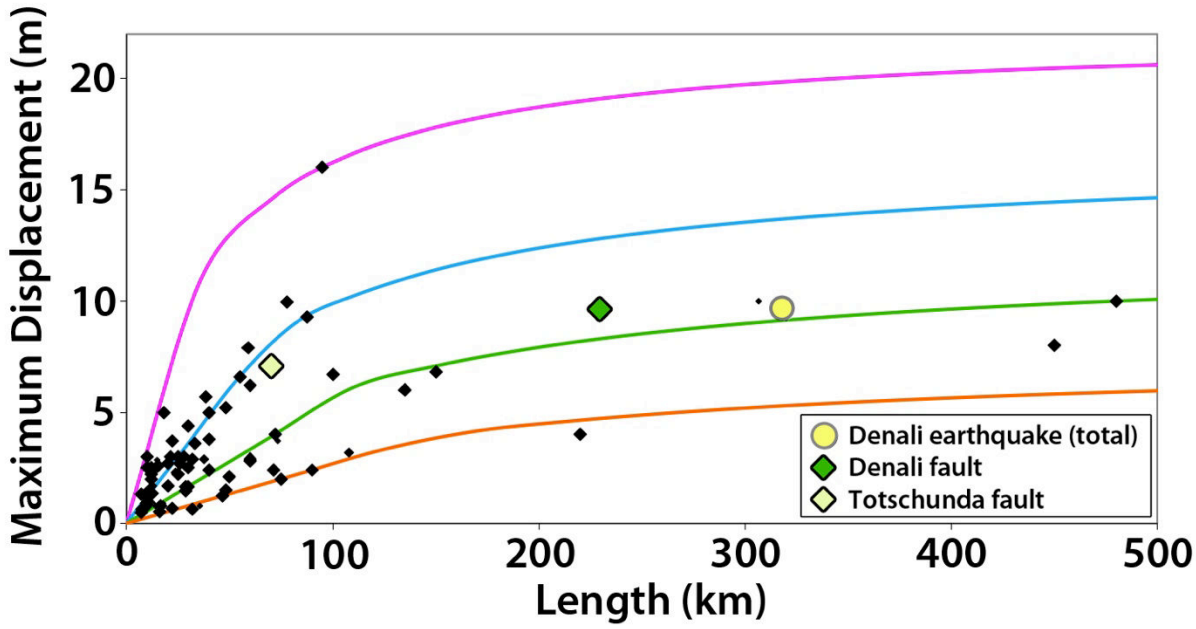


Fig.57: Earthquake displacement-length data deduced from inversion model at depth for 90 historical large continental earthquakes (Mw≥6). The 4 curves indicate the number of major long-term fault segments to have been broken by the earthquakes (modified from Manighetti et al., 2007 and Chapter IV).

References

Asano, K., Iwata, T. & Irikura, K. 2005. Estimation of Source Rupture Process and Strong Ground Motion Simulation of the 2002 Denali, Alaska, Earthquake. *Bulletin of the Seismological Society of America*, **95**, 5, 1701–1715, doi: 10.1785/0120040154

Biggs, J., Wright, T., Lu, Z. & Parsons, B. 2007. Multi-interferogram method for measuring interseismic deformation—Denali Fault, Alaska. *Geophysical Journal International*, **170**, 1,165–1,179.

Carver, G., G. Plafker, M. Metz, L. Cluff, B. Slemmons, E. Johnson, J. Roddick, & S. Sorensen. 2004. Surface rupture on the Denali Fault interpreted from tree damage during the 1912 Delta River Mw 7.2–7.4 earthquake: Implications for the 2002 Denali Fault earthquake slip distribution. *Bull. Seismol. Soc. Am*., **94**(6B), S58–S71, doi:10.1785/0120040625.

Crone, A. J., S. F. Personious, P. A. Craw, P. J. Haeussler, & L. A. Staft. 2004. The Susitna Glacier thrust fault—characteristics of surface ruptures on the fault that initiated the 2002 Denali Fault earthquake, *Bull. Seism. Soc. Am*. **94**, no. 6B, S5–S22.

Doser, D. 2004. Seismicity of the Denali-Totschunda Fault Zone in Central Alaska (1912–1988) and Its Relation to the 2002 Denali Fault Earthquake Sequence. *Bulletin of the Seismological Society of America*, **94**, No. 6B, pp. S132–S144,

Dunham, E. M. & Archuleta, R. J. 2004. Evidence for a Supershear Transient during the 2002 Denali Fault Earthquake. *Bulletin of the Seismological Society of America*, **94**, No. 6B, pp. S256–S268,

Eberhart-Phillips, Donna, Haeussler, P.J., Freymueller, J.T., Frankel, A.D., Rubin, C.M., Craw, P.A., Ratchkovski, N.A., Anderson, Greg, Carver, G.A., Crone, A.J., Dawson, T.E., Fletcher, Hilary, Hansen, Roger, Harp, E.L., Harris, R.A., Hill, D.P., Hreinsdottir, Sigrun, Jibson, R.W., Jones, L.M., Kayen, R.E., Keefer, D.K.,

Larsen, C.F., Moran, S.C., Personius, S.F., Plafker, George, Sherrod, B.L., Sieh, Kerry, Sitar, Nicholas, & Wallace, W.K. 2003. The 2002 Denali fault earthquake, Alaska—A large magnitude, slip-partitioned event. *Science*, **300**, 1,113–1,118.

Fletcher, H.J., 2002, Crustal deformation in Alaska measured using the Global Positioning System. Fairbanks, Alaska, University of Alaska Fairbanks, Ph.D. Thesis, 135 p.

Frankel, A. (2004). Rupture Process of the M 7.9 Denali Fault, Alaska, Earthquake: Subevents, Directivity, and Scaling of High-Frequency Ground Motions. *Bulletin of the Seismological Society of America*, **94**, 6B, S234–S255,

Haeussler, P.J., Schwartz, D.P., Dawson, T.E., Stenner, H.D., Lienkaemper, J.J., Sherrod, Brian, Cinti, F.R., Montone, Paola, Craw, P.A., Crone, A.J., & Personius, S.F. 2004. Surface rupture and slip distribution of the Denali and Totschunda faults in the 3 November 2002 M7.9 earthquake, Alaska. *Bulletin of the Seismological Society of America*, **94**, 6B, S23–S52.

Haeussler, P.J. 2009. Surface Rupture Map of the 2002 M7.9 Denali Fault Earthquake, Alaska; Digital Data. U.S. Geological Survey Data Series 422 [http://pubs.usgs.gov/ds/422/].

Hreinsdóttir, S., J. Freymueller, H. Fletcher, C. Larsen, and R. Bürgmann. 2003. Coseismic slip distribution of the 2002 Mw 7.9 Denali fault earthquake, Alaska, determined from GPS measurements, *Geophys. Res. Lett*. **30**, 1670, doi 10.1029/2003GL017,447

Hreinsdóttir, S., J. T. Freymueller, R. Bürgmann, & J. Mitchell. 2006. Coseismic deformation of the 2002 Denali Fault earthquake: Insights from GPS measurements, *J. Geophys. Res*., **111**, B03308, doi:10.1029/2005JB003676.

Lowey, G.W. 1998. A new estimate of the amount of displacement on the Denali fault system based on the occurrence of carbonate megaboulders in the Dezadeash Formation (Jura–Cretaceous), Yukon, and the Nutzotin Mountains Sequence (Jura–Cretaceous), Alaska. *Bulletin of Canadian Petroleum Geology*, **94**, 4,333–4,359.

Lu, Z., T. J. Wright, & C. Wicks (2003). Deformation of the 2002 Denali fault earthquakes, Alaska, mapped by Radarsat-1 interferometry, *EOS* **84**, 425, 430–431.

Manighetti, I., M. Campillo, S. Bouley, and F. Cotton (2007), Earthquake scaling, fault segmentation, and structural maturity, *Earth Planet. Sci. Lett*., **253**, 429-438, doi:10.1016/j.epsl.2006.11.004

Matmon, A., Schwartz, D.P., Haeussler, P.J., Finkel, R., Lienkaemper, J.J., Stenner, H.D., & Dawson, T.E. 2006. Denali fault slip rates and Holocene–late Pleistocene kinematics of central Alaska. *Geology*, **34**, 645–648.

Mériaux, A.-S., K. Sieh, R. C. Finkel, C. M. Rubin, M. H. Taylor, A. J. Meltzner, & F. J. Ryerson 2009. Kinematic behavior of southern Alaska constrained by westward decreasing postglacial slip rates on the Denali Fault, Alaska, *J. Geophys. Res*., **114**, B03404, doi:10.1029/2007JB005053

Nokleberg, W.J., Jones, D.L., & Silberling, N.J. 1985. Origin and tectonic evolution of the Maclaren and Wrangellia terranes, eastern Alaska Range, Alaska. *Geological Society of America Bulletin*, **96**, 1,251–1,270.

Oglesby, D. D., D. S. Dreger, R. A. Harris, N. Ratchkovski, & R. Hansen. 2004. Inverse kinematic and forward dynamic models of the 2002 Denali, Alaska earthquake, *Bull. Seismol. Soc. Am*., **94**(6B), 214–233.

Ozacar, A. A., S. L. Beck, & D. H. Christensen. 2003. Source process of the 3 November 2002 Denali Fault earthquake (central Alaska) from teleseismic observations*, Geophys. Res. Lett.*, **30**(12), 1638, doi:10.1029/2003GL017272.

Plafker, G. & Berg, H. C. (1994), The Geology of Alaska. *Geological Society of America*, 1068 p.

Ratchkovski, N. A., R. A. Hansen, J. C. Stanching, T. Cox, O. Fox, L. Rio, E. Clark, M. Lafevers, S. Estes, J. B. MacCormack, & T. Williams (2003). Aftershock sequence of theMw 7.9 Denali fault, Alaska, earthquake of 3 November 2002 from regional seismic network data, *Seism. Res. Lett*. **74**, 743–752.

Ratchkovski, N. A., S. Weimer, & R. A. Hansen. 2004. Seismotectonics of the central Denali fault, Alaska, and the 2002 Denali fault earthquake sequence, *Bull. Seismol. Soc. Am*., **94**, S156–S174, doi:10.1785/0120040621.

Richter, D. H. & Matson, JR. N. A. (1971). Quaternary Faulting in the Eastern Alaska Range. *Geological Society of America Bulletin*, **82**, 1529-1540

Schwartz, D. P., P. J. Haeussler, G. G. Seitz, & T. E. Dawson. 2012. Why the 2002 Denali fault rupture propagated onto the Totschunda fault: Implications for fault branching and seismic hazards, *J. Geophys. Res*., **117**, B11304, doi:10.1029/2011JB008918

Taylor, M.H., Leprince, S., Avouac, J.P., & Sieh, K. 2008. Detecting co-seismic displacements in glaciated regions—An example from the great November 2002 Denali earthquake using SPOT horizontal offsets. *Earth and Planetary Science Letters*, **270**, 209–220

Vallée, M., J. Charléty, A.M.G. Ferreira, B. Delouis, and J. Vergoz, (2011). SCARDEC : a new technique for the rapid determination of seismic moment magnitude, focal mechanism and source time functions for large earthquakes using body wave deconvolution, *Geophys. J. Int*., **184**, 338-358.

Wright, T. J., Z. Lu, & C. Wicks 2003. Source model for the Mw 6.7, 23 October 2002, Nenana Mountain earthquake (Alaska) from InSAR, *Geophys. Res. Lett*., **30**(18), 1974, doi:10.1029/2003GL018014.

Wright, T. J., Z. Lu, & C. Wicks. 2004. Constraining the slip distribution and fault geometry of the Mw7.9, 3 November 2002, Denali Fault earthquake with InSAR and GPS, *Bull. Seismol. Soc. Am.*, **94**(6B), 175–189.

2.6. Dixie Valley & Fairview Peak 1954

16/dec/1954, Nevada, USA

Ms 7.2 & Ms 6.8

Epicenters : 39.60°N-118.00°W/39.20°N-118.00°W

Normal fault (+ right-lateral component on Fairview)



Broken long-term faults

The Fairview Peak and Dixie Valley EQs broke two distinct nearby faults in the Basin and Range province, Nevada (Fig.58), from south to north, the Fairview Peak and the Dixie Valley faults, respectively. The two EQs occurred within an interval of a few minutes and the two broken faults are very close to each other; **we thus describe the two events and faults in the same present section.**

General characteristics of the broken faults from literature:

- The Fairview Peak and Dixie Valley faults are part of the Basin and Range Fault network, which is made of numerous NNW to NNE-trending, sub-parallel, closely-spaced normal faults bounding grabens (large-scale horst and graben systems; Fig.58a)
- The Basin & Range faulting is taken to have initiated ~ 15 Ma ago (based on dated faulted volcanic rocks and sedimentary deposits in central Nevada, e.g. Stewart 1971; Thompson and Burke 1973; Parsons 1995 and references therein), about when the Yellowstone Plume head was due north of the western part of the Basin and Range fault zone (e.g. Scott et al., 1985 and references therein; See Borah Peak section). The Basin and Range faults and the Yellowstone hot spot might thus be partly genetically related (e.g. Zoback and Thompson 1972). As a matter of fact, the Basin and Range faults abruptly end in the north along a 600-700 km long, NE-trending "line" or "corridor" which coincides with the NE path of the Yellowstone hot spot over the last ~16 Ma (e.g. Scott et al., 1985 and references therein;

Fig.58). No Basin and Range Fault continues north of this corridor except in the westernmost part of the Basin and Range region where the hot spot presence was not evidenced. This suggests that the Basin and Range faults have either been truncated by the hot spot path (in which case they formed before the hot spot impingement), or have been arrested in their northward lateral propagation by the hot spot path (in which case they formed after the hot spot impingement). The absence of the Basin and Range faults north of the hot spot corridor suggests that the later hypothesis is most likely.

- The Basin and Range Fault network actually has a peculiar overall shape in map view, resembling a triangle whose northern edge is the NE-trending hot spot corridor, the eastern edge are the ~N-S reliefs that extend from Salt Lake City to Saint-Georges (in the middle of Utah, Fig.58), and the southern edge is a WNW-trending "line". That line includes the so-called "Walker Lane" right-lateral shear zone (e.g. Stewart 1980) but also another marked "lineament" running from about Reno to Saint-Georges, that I call the Reno-Saint-Georges shear zone (Fig.58). Most Basin and Range faults end against the Reno-Saint-Georges shear zone. More precisely, the highest fault escarpments all stand north of the Reno-Saint-Georges shear zone, whereas south of this line there exist only small fault scarps, striking at some angle with the largest escarpments further north. The small fault scarps end in the south against the Walker Lane. It is not clear what the NW-trending "lines" are, but they resemble shear zones that have truncated and/or arrested the Basin and Range faults in the south. Another markedly imprinted NW-trending line exists in the middle of the Basin and Range (which we call "Indian Peak-Mahogany Peak shear zone") that resembles a shear zone truncating the faults. All the shear zones I mapped on Fig.58 have in common to show a clear trace in the topography, and to be boundaries across which the Basin and Range Fault' strikes and/or cumulative throws are changing. Therefore, we suspect that they are deep, likely right-lateral shear zones, possibly currently active (as suggested by the seismicity that underlines the two major Indian Peak-Mahogany Peak and Reno-Saint-Georges shear zones (Fig.58b), and in any case exerting some control on the development of most Basin and Range faults. Among those controls, horizontal rotations induced by the shear imposed in a sub-perpendicular direction to the B&R faults, might be expected (See Manighetti et al., 2001; Walpersdorf et al., 2014.

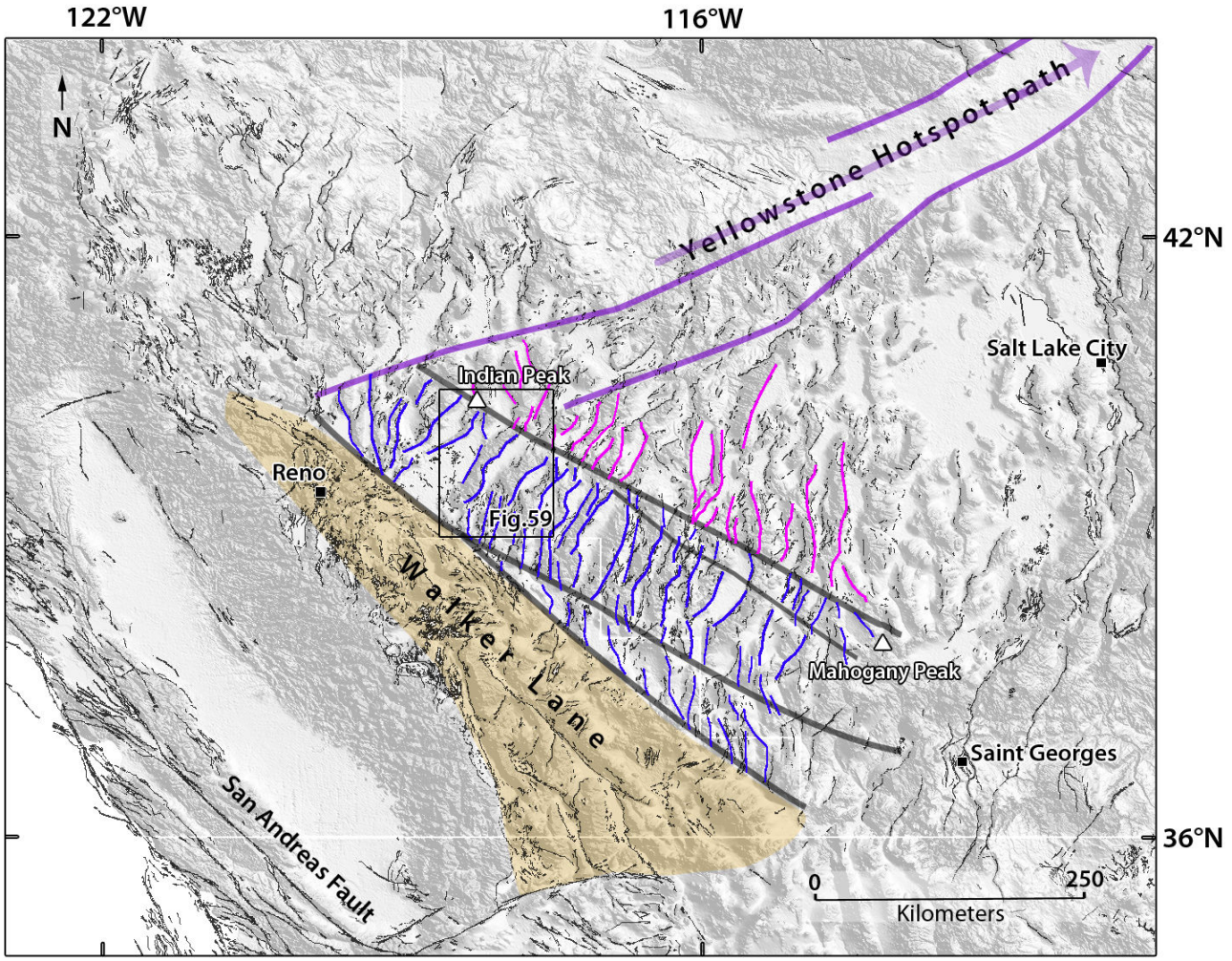


Fig.58: (a) General map of the Basin and Range province. Black Quaternary faults are from the U.S. Geological Survey and California Geological Survey, 2006. Blue and pink traces show the main faults in the domains separated by the oblique shear zones (See text for details). The southermost shear zone is bounded by the so-called « Walker Lane Belt »(orange area). Purple lineaments are linked to the activity of the Yellowstone Hospot, which propagated as indicated with the purple arrow.

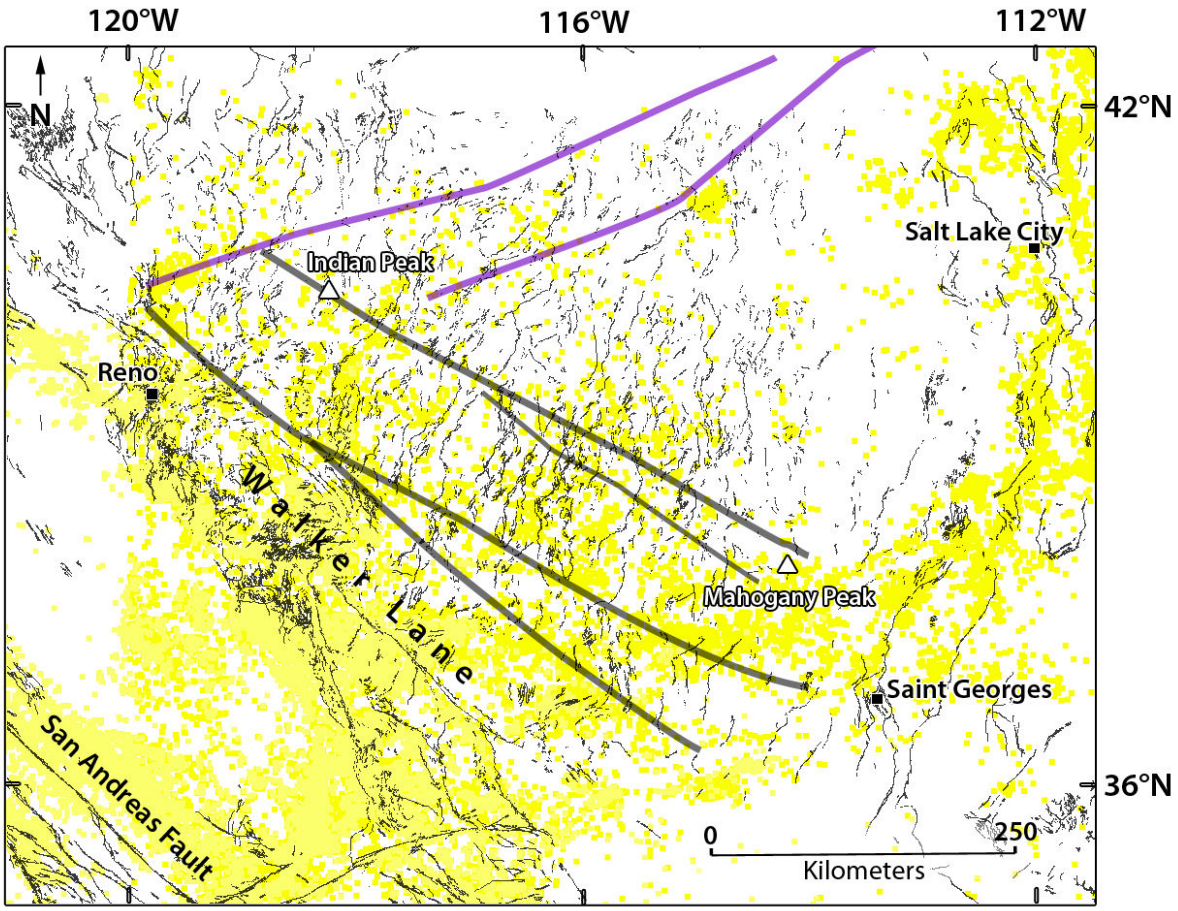


Fig.58: (b) Same fault map as in Fig.58a (same caption). The yellow dots are the instrumental earthquakes (Mw>2) from the ANSS catalog from the Northern California Data Center (1935-2014).

- The Fairview Peak and Dixie Valley faults are, as the other Basin and Range faults, normal faults striking NNE overall. They are located in between the Reno-Saint-Georges shear zone in the south and the Indian Peak-Mahogany Peak zone in the north (Fig.59). The Fairview Peak and Dixie Valley faults both dip eastwards.
- The apparent (i.e., topographic) cumulative vertical throw on the northern Dixie Valley faults is ~1.5 km, but its actual maximum vertical cumulative slip is estimated of 4-5 km from refraction imaging, gravity and magnetic measurements (Thompson et al., 1967; Smith et al., 1968; Thompson and Burke 1973).
- The apparent cumulative vertical throw on the southern Fairview Peak Fault is much lower, about 0.7 km. I found no data on its actual maximum vertical cumulative slip.
- The decrease in the cumulative vertical slip from north to south suggests that the Fairview Peak-Dixie Valley Fault system might have been propagating southward over geological time (e.g., Manighetti et al., 2001 for discussion on slip decrease versus lateral propagation).

On the Dixie Valley Fault, a long-term (over last ~ 12 ka) vertical slip rate of 0.5-1 mm/yr has been estimated based on paleoseismological trenches in the central part of the fault (intersegment 2-3, see below; Bell and Katzer 1990; Bell et al., 2004) and on measurements of offset shorelines and terraces in the northern part of the fault (Thompson and Burke 1973). On the Fairview Peak Fault, an average net slip rate of 0.1-0.2 mm/yr was estimated based on the measurement of a ~8 m cumulative vertical slip whose age is estimated in the range 35-100 ka (on segment 1, see below; Bell et al., 2004).

- A current horizontal extension rate of ~1 mm/yr is estimated from only two GPS sites either side of the northern Fairview Peak Fault (Thatcher et al., 1999; Bennett et al., 2003). If the fault dips by 50-60° (Caskey et al., 1996), this extension rate would convert into a vertical on-fault slip of 1.5-2 mm/yr. This slip rate is not well constrained however and is different from the long-term slip rate, and hence should be considered with caution.
- The vertical slip rate on the Fairview-Dixie Fault system might thus be in the range 1-1.5 mm/yr. Had this slip rate kept constant over time, it would imply that the Fairview-Dixie Fault system initiated 3-5 Ma ago, and hence fairly recently.

→ The 1954 Fairview Peak and Dixie Valley earthquakes broke two distinct nearby normal faults, the Fairview Peak and the Dixie Valley faults, which both are fairly immature (L < 100 km, I-Age 3-5 Ma, MR < 2 mm/yr, D_{total} 4-5 km). The overall Dixie Valley-Fairview Peak Fault system might have propagated southward over geological time.

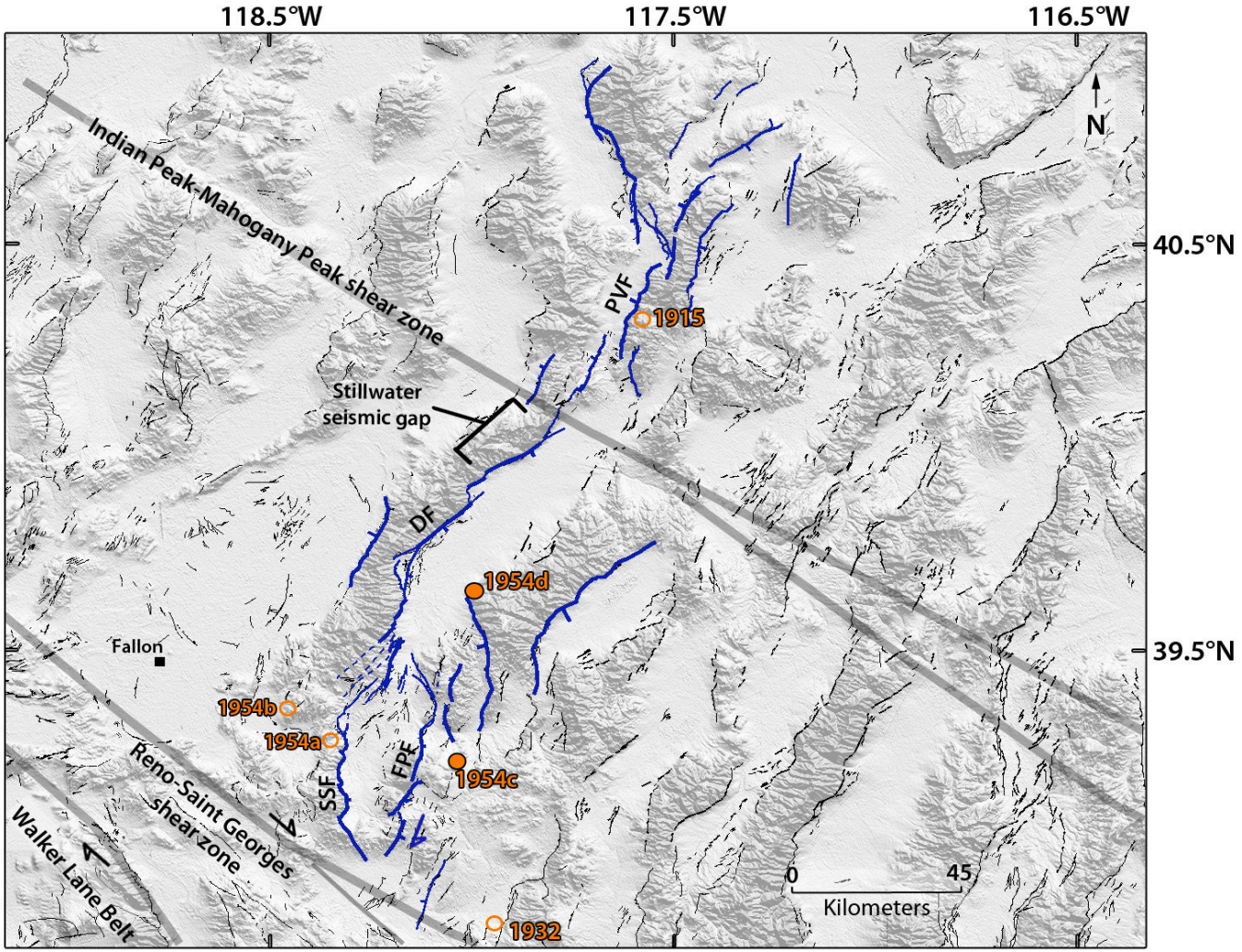


Fig.59: Zoom on the main long-term faults (in blue) involved during the 1954 earthquakes in the Basin and Range province, from Fig.58 (same caption). DF : Dixie Valley Fault ; FPF : Fairview Peak Fault ; SSF : Sand Springs Fault ; PVF : Pleasant Valley Fault. Orange full circles show the 1954c Fairview Peak and 1954d Dixie Valley earthquakes epicenters. Epicenters of the 1915 Pleasant Valley, 1932 Cedar Mountain, 1954a and 1954b Rainbow Mountain are also indicated (orange empty circles).

Architecture and lateral major segmentation of the broken faults, from our mapping :

- Mapping done from Google Earth, Landsat and Aster GDEM v.2 data combined with literature information.

Fairview Peak Fault

- The Fairview Peak Fault has a fairly linear trace and is ~50 km long. It is divided into three major collinear segments of similar length (10-15 km), arranged in a left-stepping echelon along the mean NNE strike of the fault (See Fig.60 where they are numbered). The en echelon arrangement suggests a right-lateral component of slip on the Fairview Peak Fault in addition to its dominant normal one, as recognized in other studies (Slemmons 1957; Caskey et al., 1996). The 3 major segments are thus separated with fairly narrow (1-2 km) step-over relay zones of types 2_O. They are hardly connected to each other at the ground surface.
- The fault trace curves counterclockwise to the north (when one goes from south to north) in a clear attempt to connect with the nearby Dixie Valley Fault, located 8-10 km further to the west. This suggests that the Fairview Peak Fault is currently propagating northward and in the process of connecting with the Dixie Valley Fault.
- To the south, the Fairview Peak Fault terminates by splaying into several small branches that all basically stop at the Reno-Saint Georges shear zone. This geometry of the southern fault termination thus suggests, on the one hand that the Fairview Peak Fault might also have propagated laterally southward over geological time –what would make its long-term propagation being bilateral, and on the other hand that the Fairview Peak Fault is currently arrested in its southward lateral propagation by the Reno-Saint Georges shear zone.

→ The Fairview Peak Fault might have propagated bilaterally over geological time. It is in the process of connecting with the Dixie Valley Fault further north. It is arrested to the south by the Reno-Saint Georges shear zone (part of the Walker Lane Belt). It is made of three major collinear segments; the central one (n° 2, see below) might thus be the most mature along the fault.

Dixie Valley Fault:

- Long-term fault trace well expressed in surface morphology and topography.
- The Dixie Valley Fault has a slightly curved overall trace, of ~85 km long.
- To the north, the Dixie Valley Fault terminates by splaying into several small oblique branches, some of them might interact with the antithetic Pleasant Valley Fault further north. The northern end of the Dixie Valley Fault coincides with the Indian Peak-Mahogany Peak shear zone.
- To the south, the Dixie Valley Fault trace also splays into several small oblique branches; some connect with the synthetic Sand Springs Fault further southwest (separation distance of 6-7 km), whereas others connect with the synthetic Fairview Peak Fault further southeast (separation distance of 8-10 km).
- This overall geometry suggests that the Dixie Valley Fault has been propagating southward over geological time, likely from the pre-existing Indian Peak-Mahogany Peak shear zone. The Dixie Valley Fault is in the current process of connecting with both the Sand Springs and the Fairview Peak faults to form a single larger-scale fault.
- The Dixie Valley Fault is divided into four major segments of similar length, 15-25 km (See Fig.60 where they are numbered). The strike of the segments rotates clockwise as one goes from south to north, with a total azimuth change of ~37°. Despite of those azimuth changes, the four major segments are well connected to each other at the ground surface. As a matter of fact, major segments 1 and 2 are separated by a relay zone of type 2 and are connected by a small sub-perpendicular fault. Major segments 2 and 3 are separated by a large relay zone of type 1-2, made of multiple distributed small faults and cracks, but this relay zone is presently crosscut by the master fault so that major segments 2 and 3 are now directly and simply connected to each other (See also Bell and Katzer 1990). Finally major segments 3 and 4 are separated with a relay zone of type 2, made of multiple distributed small faults and cracks.

→ The Dixie Valley Fault seems to have propagated southward over geological time, from the Indian Peak-Mahogany Peak shear zone in the north. It is in the process of connecting with both the Sand Springs and the Fairview Peak faults further south. It is made of four major collinear segments, the northern ones (n° 1-2) are the most mature along the fault.

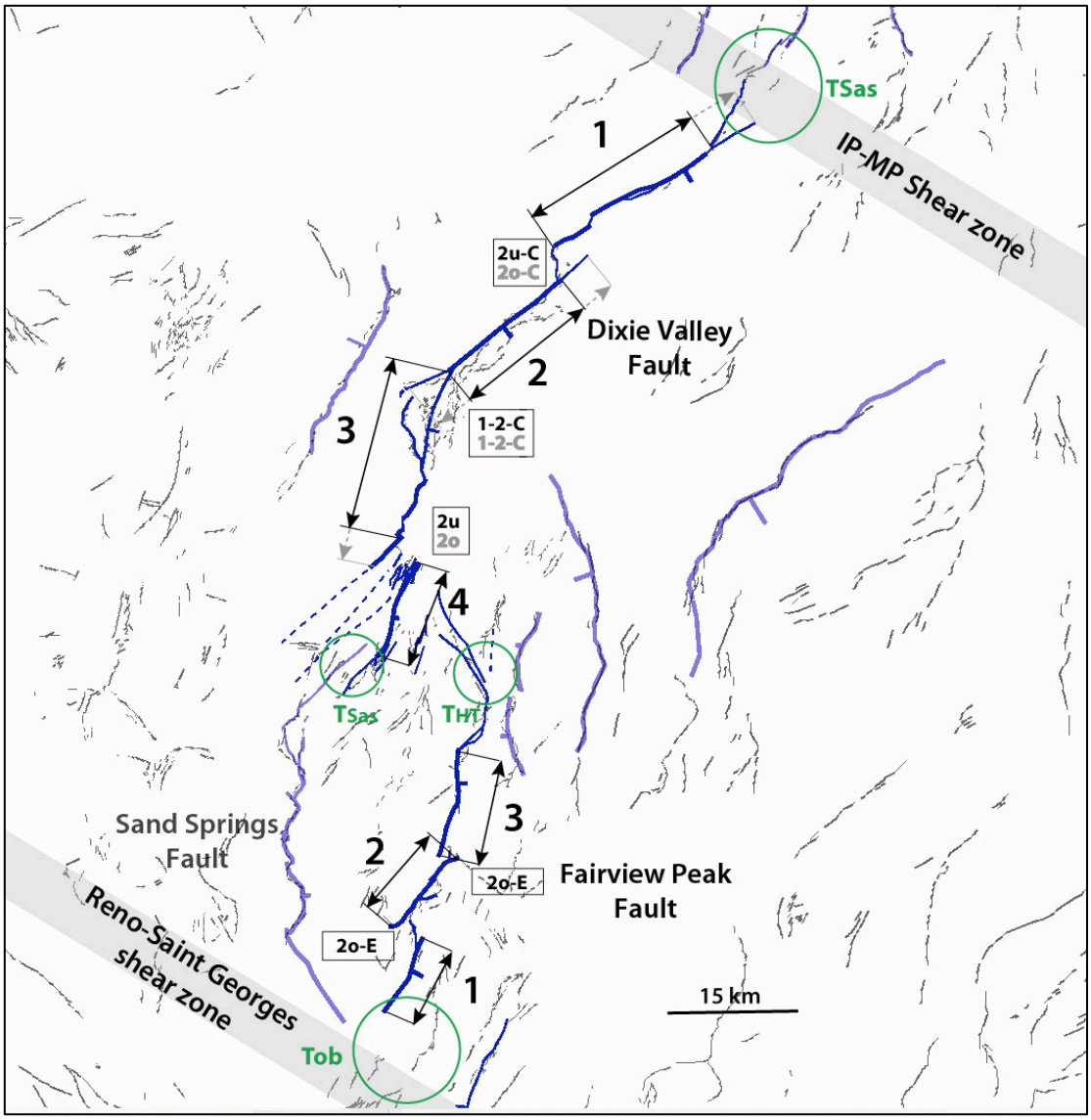


Fig.60: Focus on the major segments that form the Fairview Peak and Dixie Valley faults. The segments are indicated by black arrows parallel to their mean strike. The grey prolongation of the arrows indicates the uncertainties on the segment lengths. The nature of the inter-segment zones is indicated in letters within boxes explained in Table 6. The nature of the fault tips is indicated in green (Table 6). Grey areas show the oblique Reno-Saint Georges shear zone and the Indian Peak-Mahogany Peak (IP-MP) shear zone.

1954 Coseismic ruptures

Surface trace and location on the long-term Dixie Valley and Fairview Peak Faults :

- The 1954 Fairview Peak and Dixie Valley EQs occurred at a 4 min interval (Fairview Peak EQ first in the south, followed by Dixie Valley EQ in the north). This short time between the two events obscured the discrimination of the surface traces. While it was clear that the

rupture traces observed on the main Fairview Peak and Dixie Valley faults could be attributed to the Fairview Peak and the Dixie Valley EQs, respectively, the additional traces that were observed on small nearby faults could not be attributed with certainty to one event or the other. The interpretation of the secondary ruptures is thus fairly arbitrary and hence must be taken with caution (Fig.61).

- The 1954 surface ruptures are still fairly clear on Google Earth images. The surface traces of the two earthquakes were precisely mapped on the field and from aerial image analysis, and the displacements were measured on the field (See below) (e.g. Slemmons 1957; dePolo et al., 1991; Caskey et al., 1996; Zhang et al., 1999)
- **The Fairview Peak EQ** broke the two central major segments (n° 2-3) of the long-term Fairview Peak Fault. It also broke a part of the small branch (Louderback) that forms the curved northern horsetail termination of the Fairview Peak Fault. Other traces were observed on small faults in the vicinity of the Fairview Peak master fault (so-called West Gate, Gold King and Phillips Wash faults), and were attributed, yet without certainty, to the Fairview Peak EQ. Among those small adjacent ruptures, it has to be noted that the rupture trace on the Phillips Wash Fault was not observed in the immediate field investigations conducted by Slemmons (1957).
- We thus retain that the Fairview Peak EQ mainly broke two major segments of the Fairview Peak Fault, along with a part of its splaying tip branch, altogether producing a rupture length of ~40 km (similar to the "primary length" defined by Zhang et al., 1999). The two broken segments are the most mature along the fault.
- The Fairview Peak earthquake is taken to have initiated in the center of the Fairview Peak Fault, i.e., nearby the connection zone between major segments 2 and 3, and to have propagated bilaterally (Doser 1986). The rupture stopped to the south at the connection zone between major segments 1 and 2, whereas it vanished to the north as the long-term fault does.
- The Fairview rupture got a small lateral component of slip in addition to its dominant normal one. The existence and sense of lateral slip are in keeping with the left-stepping arrangement of the major segments along the fault.
- Four minutes later, **the Dixie Valley EQ** nucleated further north, on the Dixie Valley Fault, nearby the connection zone between the major segments 2 and 3 of the Dixie Valley Fault. The rupture then propagated bilaterally towards both the north and the south (Doser 1986). The EQ mainly broke the 2 central major segments (n° 2-3) of the Dixie Valley Fault, over a

length of ~40 km. The broken major segment 2 is one of the most mature along the fault. To the south, the rupture stopped in the large step-over that separates major segments 3 and 4. To the north, the rupture stopped in the large left-stepping relay zone that separates major segments 1 and 2.

- The Dixie Valley rupture had no lateral component of slip.

→ Each of the Fairview Peak and the Dixie Valley EQs broke 2 major long-term segments of the Fairview Peak and Dixie Valley faults, respectively. The broken segments are among the most mature segments of the two faults.

Coseismic displacements measured at surface (Fig.61) :

Fairview Peak EQ:

- *From Field measurements*: Both vertical and lateral components were measured, fairly continuously along the fault. A maximum vertical slip of 3.8 m was found locally (Fig.61); however, most measurements rather suggest a maximum vertical slip of ~2.5 m. Dextral slip was also measured, with a maximum value of 2.9 m (Slemmons 1957; Caskey et al., 1996). Since both slip components characterize the fault motion, assuming that the Fairview Peak Fault dips by 50-70° (Caskey et al., 1996), we infer a maximum combined on-fault displacement of ~5.3 m (single, hence likely outlier value), and more likely of ~4 m (Fig.61).
- *From Triangulations and leveling data*: Maximum vertical and lateral slip of 1.5 m and 3 m, respectively (U.S. Coast and Geodetic Survey in Slemmons, 1957), in agreement with field measurements.
- The complete slip profile was measured. If we consider the slip distribution on the main Fairview Peak Fault only (including the Louderback horsetail fault), the overall shape of the Fairview Peak EQ slip profile is fairly triangular and asymmetric, with maximum slip deported at the southern tip of the rupture, and slip decreasing fairly regularly from its maximum value to zero at the northern end of the rupture. The maximum slip thus occurred on major segment 2, which is the most mature along the fault.

→ The Fairview Peak EQ produced a maximum on-fault composite slip (vertical and lateral) of ~4 m at the surface, on the most mature segment 2 of the Fairview Peak Fault.

Dixie Valley EQ:

- *From Field measurements*: The vertical slip was measured fairly continuously along the fault. No lateral slip was described. A maximum vertical slip value of ~2.8 m was found locally; however, most measurements rather suggest a maximum vertical slip of ~2.5 m (Fig.61). Assuming that the Dixie Valley fault dips by 50° (Caskey et al., 1996), we infer a maximum on-fault dip slip of ~3.3 m (Fig.62).
- *From Triangulations and leveling data*: Maximum vertical slip of 2.1 m (U.S. Coast and Geodetic Survey in Slemmons, 1957), in agreement with field measurements.
- The complete slip profile was measured. If we ignore the outlier single value at 3.7 m, the slip profile has a fairly triangular overall shape, rather symmetric. The maximum slip is rather located on major segment 2, which is the more mature of the two broken segments. The maximum slip might be slightly underestimated because it occurred nearby a zone of distributed faulting, where part of the slip might have been difficult to measure. The slip profile shows two distinct peaks of large slip, which well coincide with the rupture of the two major segments. A small slip patch is also observed in the south that coincides with very little slip on a small section of major segment 4.

→ The Dixie Valley EQ produced a maximum on-fault dip slip of ~3.3 m at the surface, on the most mature segment 2 of the Dixie Valley Fault.

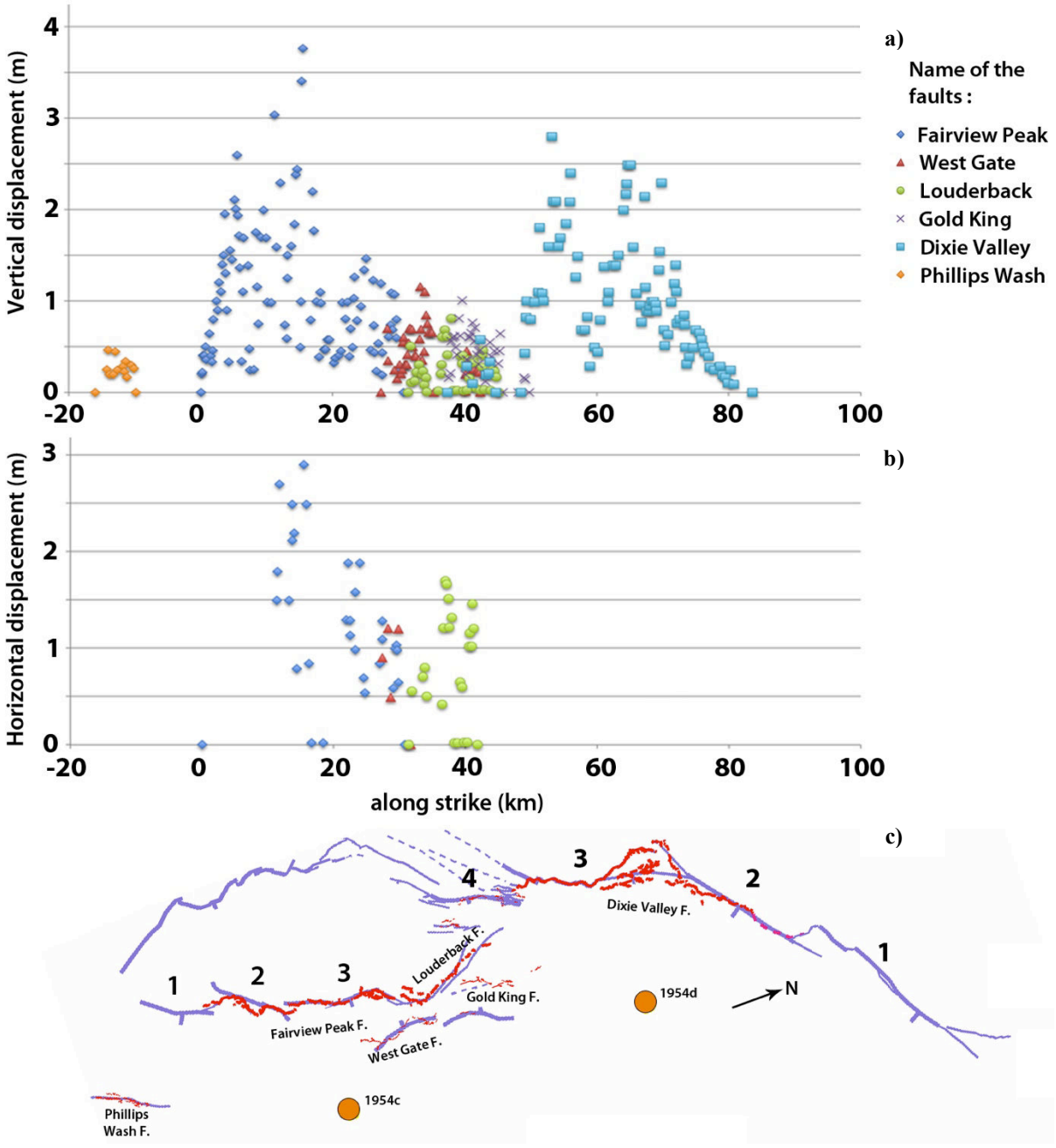


Fig.61: (a) Vertical displacements and (b) horizontal displacements measured at the surface after the Fairview Peak and Dixie Valley earthquakes (modified from Caskey et al., 1996). (c) surface ruptures of the 1954 earthquakes (in red) and long term faults (in blue). Major segments are numbered. Orange circles are epicenters.

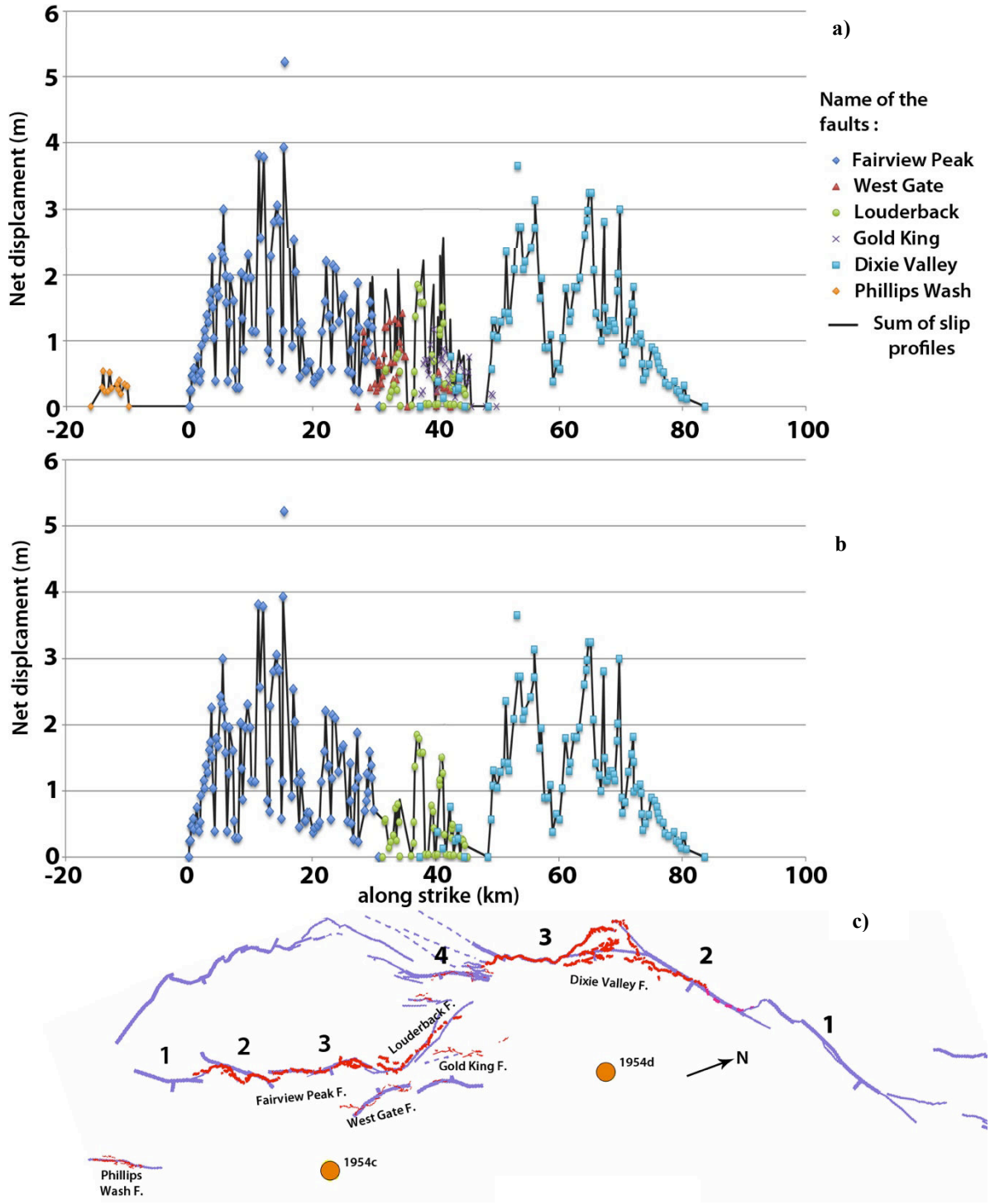


Fig.61: Net displacements calculated along the 1954 surface ruptures. Mean dip used for each fault section are from Caskey et al. (1996) : 70° (Louderback F.), 60° (Fairview Peak F., West Gate F., Gold King F., Phillips Wash F.) and 50° (Dixie Valley F.). Offset measurements of all rupture sections are considered(a). Only offsets measured on the main faults are considered (b). Black curve represents the sum of the displacements of both earthquakes. surface ruptures of the 1954 earthquakes (in red) and long term faults (in blue) (c). Major segments are numbered. Orange circles are epicenters.

Source parameters:

Doser (1986) from teleseismic body wave modelling

Faiview Peak: 1954/12/16 at 11h07min GMT
Duration 12-22s
M 7.2; M0=5.3^{e}19 N.m; Z=15 km
Strike, dip, rake (°): 350,50,-160

Dixie Valley: 1954/12/16 at 11h11min GMT
Duration 10s
M 6.7; M0=9.9^{e}18 N.m ; Z=12 km
Strike, dip, rake (°) : 350, 50, -90

Doser (1986) divides the Fairview Peak earthquake in two and possibly three sub-events (6s each) and the Dixie Valley EQ in two sub-events (5s each).

→ The source time function data suggest the rupture of two distinct elements on each of the Fairview Peak and Dixie Valley faults. Though the surface length of the Dixie Valley EQ is similar to that of the Fairview Peak EQ (~40 km in both cases), the Dixie Valley EQ produced a slightly lower slip (~3.3 m versus ~4 m), was shorter in duration (10 s versus 12-22 s), and had a smaller magnitude (Mw 6.7 versus 7.2).

Other information :

1954 EQs:

- In 1954, the Fairview Peak and Dixie Valley EQs were preceded by two large events that broke neighboring sub-parallel faults, possibly including the Sand Springs Fault due west of the Fairview Peak Fault (Fig.59): the Rainbow Mountain EQ in July 6, (1954a, Mw 6.2) and the August 24, EQ (1954b, Mw 6.5) (e.g. Doser et al., 1986; Hodgkinson et al., 1996).
- No precise record of aftershocks exists for the two major 1954 EQs.

Past EQ activity:

- In 50 years, 4 large historical earthquakes (Mw > 6.5) occurred in the region (Fig.59): the 1915 Pleasant Valley EQ (Mw 7.5-7.7; see section Pleasant Valley), the 1932 Cedar Mountain EQ (Mw 7.2), the 1954 Fairview Peak (Mw 7.2) and the Dixie Valley 1954 EQs (Mw 6.8) (e.g. Doser et al., 1986, 1988).
- The so-called « Stillwater seismic gap » is located to the NE of the Dixie Valley Fault, close to the Indian Peak-Mahogany Peak shear zone (Fig.59): no historical rupture younger than 300 years is known in this area, while instrumental seismicity is few (Wallace 1977; Wallace and Whitney 1984).

Parameters retained to describe the Fairview Peak 1954 EQ (Tables 1 & 3)

Mw 7.2; M0 ≈ 5.3e19 Nm; L ~40 km; Dmax surface ~4 m.

Hypocenter: Z ~ 15 km.

Number of major segments broken on the Fairview Peak Fault: 2

Parameters retained to describe the Dixie Valley 1954 EQ (Tables 1 & 3)

Mw 6.8; M0 ≈ 9.9e18 Nm; L ~ 35-40 km; Dmax surface ~ 3.3 m (lower bound).

Hypocenter: Z = 12 km.

Number of major segments broken on the Dixie Valley Fault: 2

The Fairview Peak and Dixie Valley earthquake surface slip-length data fall fairly well on the second function (blue curve; Fig.63). This is in keeping with these two earthquakes having each broken 2 major segments of the fault on which they occurred.

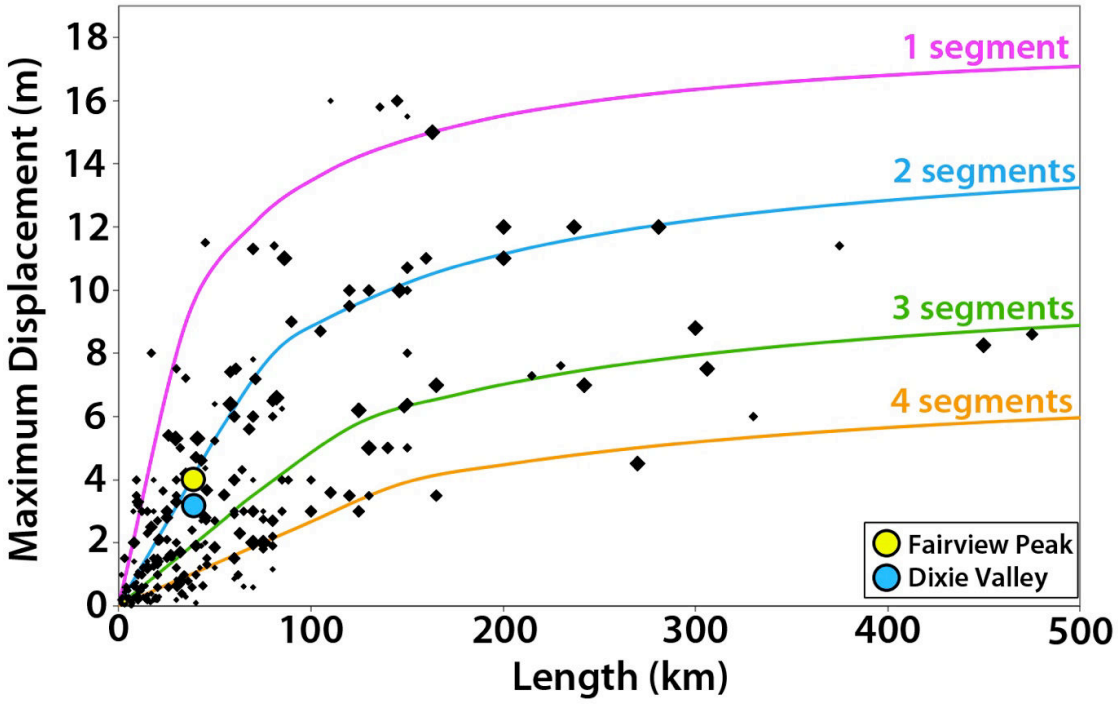


Fig.63: Earthquake displacement-length data measured at surface for 260 historical large continental earthquakes (Mw≥6). The 4 curves indicate the number of major long-term fault segments to have been broken by the earthquakes (See Chapter IV).

References

Bell, J. & T. Katzer (1990). Timing of late Quaternary faulting in the 1954 Dixie Valley earthquake area, central Nevada, *Geology* **18**, 622-625.

Bell, J. W., Caskey, S. J., Ramelli, A. R., & Guerrieri, L. (2004). Pattern and rates of faulting in the central Nevada seismic belt, and paleoseismic evidence for prior beltlike behavior. *Bulletin of the Seismological Society of America*, **94**(4), 1229-1254.

Bennett, R. A., B. P. Wernicke, N. A. Niemi, A. M. Friedrich, & J. L. Davis (2003). Contemporary strain rates in the northern Basin and Range province from GPS data, *Tectonics*, **22**(2), 1008, doi:10.1029/2001TC001355.

Caskey, S.J., Wesnousky, S.G., Zhang, P., Slemmons, D.B. (1996). Surface faulting of the 1954 Fairview Peak (Ms 7.2) and Dixie Valley (Ms 6.9) earthquakes, Central Nevada. *Bull Seismol. Soc. Am*. **86**, 761–787.

dePolo, C.M., Clark, D.G., Slemmons, D.B. & Ramallie, A. (1991). Historical Basin and Range Province surface faulting and fault segmentation. *J. Struct. Geol*. **13**, 123–136.

Doser, D. I. (1986). Earthquake processes in the Rainbow Mountain-Fairview Peak-Dixie Valley, Nevada, Region 1954-1959. *Jour. Geophys. Res., **91**, 12,572-12,586*

Doser, D. I. (1988). Source Parameters of Earthquakes in the Nevada Seismic Zone , 1915-1943. *Jour. Geophys. Res.,* **93**, 15,001-15,015.

Hodgkinson, K. M., Stein, R. S. & King, G. C. P. (1996). The 1954 Rainbow Mountain-Fairview Peak-Dixie Valley earthquakes : A triggered normal faulting sequence. *J. Geoph. Res.,* **101,** 25,459-25,471.

Manighetti, I., Tapponnier, P., Courtillot, V., Gallet, Y., Jacques, E., & Gillot, P. Y. (2001). Strain transfer between disconnected, propagating rifts in Afar. *Journal of Geophysical Research,* **106**(B7), 13613-13665.

Manighetti, I., M. Campillo, S. Bouley, and F. Cotton (2007), Earthquake scaling, fault segmentation, and structural maturity, Earth Planet. Sci. Lett., 253, 429-438, doi:10.1016/j.epsl.2006.11.004

Parsons, T. (1995). The Basin and Range Province. *Continental Rifts: Evolution, Structure, Tectonics*, **25**, 277-324.

Scott, W.E., Pierce, K. L. & Hait, M. H. Jr. (1985) Quaternary tectonic setting of the 1983 Borah Peak earthquake, Central Idaho, *Bull. Seism. Soc. Am*., **75**, 1053-1066.

Slemmons, D. B. (1957). Geological effects of the Dixie Valley-Fairview Peak, Nevada, earthquakes of December 16, 1954. *Bull. seism. Soc. Am*. **47**, 353-375.

Smith, T. E. (1968). Aeromagnetic measurements in Dixie Valley, Nevada; implications on basin-range structure. *Jour. Geophys. Res.*, **73**, 1321-1331.

Stewart, J. H. (1971) Basin and Range Structure: A System of Horsts and Grabens Produced by Deep-Seated Extension. *Geological Society of America Bulletin*, **82**, 1019-1044

Thatcher, W., G. R. Foulger, B. R. Julian, J. Svarc, E. Quilty, & G. W. Bawden (1999). Present-day deformation across the Basin and Range province, western United States, *Science*, **283**, 1714 – 1718.

Thompson, G. A., Meister, L. J., Herring, A. T., Smith, T. E., Burke, D. B., Kovach, R. L., Burford, R. O., Salehi, A., & Wood, M. D. (1967). Geophysics, study of basin-range structure, Dixie Valley region, Nevada. *U.S. Air Force Cambridge Research Labs. Spec. Rept*. 66-848.

Thompson, G. A. & Burke, D. B. (1973). Rate and Direction of Spreading in Dixie Valley, Basin and Range Province, Nevada. *Geological Society of America Bulletin*, **84**, 627-632

Wallace, R. E. (1977). Profiles and ages of young fault scarps, north-central Nevada. *Bull. Geol. Soc. Am*. **88**, 1267-1281.

Wallace, R.E. & Whitney, R.A. (1984). Late Quaternary history of the Stillwater seismic gap. *Bull. Seismol. Soc. Am*., **74**, 301–314.

Walpersdorf, A., Manighetti, I., Mousavi, Z., Tavakoli, F., Vergnolle, M., Jadidi, A. Jadidi, D. Hatzfeld, A. Aghamohammadi, A. Bigot, Y. Djamour, H. Nankali & Sedighi, M. (2014). Present-day kinematics and fault slip rates in eastern Iran, derived from 11 years of GPS data, *J. Geophys. Res. Solid Earth*, **119**, 1359–1383, doi:10.1002/2013JB010620

Zhang, P., Mao, F. & Slemmons, D. B. (1999). Rupture terminations and size of segment boundaries from historical earthquake ruptures in the Basin and Range Province. *Tectonophysics,* **308**, 37–52.

Zoback, M. L., & Thompson, G. A. (1978). Basin and Range rifting in northern Nevada: Clues from a mid-Miocene rift and its subsequent offsets. *Geology*, **6**(2), 111-116.

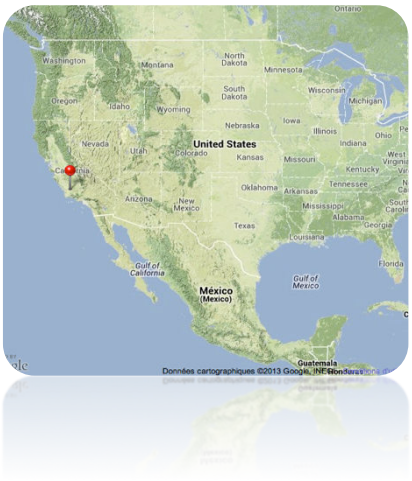
2.7. Fort Tejon 1857

09/Jan/1857, California, USA

Mw 7.9

Epicenter : 35.7°N-120.3°W

Right-lateral strike-slip



Broken long-term fault

The EQ broke the southern part of the San Andreas Fault, California, USA.

General characteristics of the San Andreas Fault from literature (Fig.64) :

- The San Andreas Fault Zone (SA) is a transform plate boundary between a transform-transform-trench triple junction off Cape Mendocino in the north and a system of seafloor spreading axes (and transform faults) in the Gulf of California in the south (e.g. Powell and Weldon 1992). It has a total length of more than 1300 km.
- Right-lateral strike-slip fault, generally divided into three main parts (Fig.64): the northern part from Mendocino to San Juan Bautista –basically locked and slipping in earthquakes; the central part which corresponds to the creeping zone (e.g. Scholz et al., 1969) (from San Juan Bautista to Parkfield section; in pink, Fig.64); and the southern part from the Parkfield section to the Gulf of California –basically locked and slipping in earthquakes (See details below).
- The transform fault zone is taken to have initiated 20-40 Ma ago (e.g. Atwater 1970; Sims 1993), based on magnetic anomalies and offsets of volcanic rocks. Shear might have started west of the actual trace of the SA Fault (e.g., Powell and Weldon 1992), before migrating eastwards up to the actual San Andreas Fault trace. The northern part of the SA Fault (north of the creeping zone) would have initiated 30-40 Ma ago, while the southern part of the SA Fault (south of the creeping zone) would have initiated later, ~12 Ma ago (e.g., http://www.sci.sdsu.edu/salton/San%20AndreasFaultSyst.html; Powell and Weldon 1992

and references therein; Sims 1993). The Gulf of California would have started to open between 10 and 5 Ma ago. As the southern part of the SA Fault offsets and/or contributes to the Gulf opening, it must be younger than 5 Ma (See below). The southward decrease in the initiation age of the SA Fault suggests that it has been propagating southward over geological time.

- Maximum cumulative dextral slip of ~ 300 km estimated from offset measurements of volcanic and sedimentary terranes along the fault from Parkfield to Tejon Pass (Fig.64) (Hill and Dibblee 1953; Wallace 1970; Clark and Nilsen 1973; Sims 1993) and seismic imaging of the basement rocks (Revenaugh and Reasoner 1997). South of Tejon Pass, the cumulative horizontal slip is lower, ~200 km (e.g. Darin and Dorsey 2013)
- Current lateral slip rate estimated from dense GPS, InSAR and leveling measurements:
    - In the creeping section, 25-35 mm/yr (Segal and Harris, 1986; Meade and Hager 2005; Titus et al., 2011; Tong et al., 2013);
    - In the Northern section ~ 10 mm/yr (e.g. Tong et al., 2013);
    - In the Southern section ~ 5 mm/yr (Meade and Hager 2005; Tong et al., 2013) on northern part (major segments 1, 2 and 3, see below) to 18-25 mm/yr on southern part (segment 4 and 5; Meade and Hager 2005; Lindsey and Fialko 2013).
- Long-term lateral slip rate of 20-35 mm/yr over the Holocene (Sieh and Jahns 1984; Weldon and Sieh 1985; Perkins et al., 1989; Sims 1993; van der Woerd et al., 2006; Titus et al., 2011) measured along the creeping and southern section of the San Andreas Fault. The slip rate seems to decrease southward along the SA Fault (Van der Woerd et al., 2006 and references therein), as the number of sub-parallel fault branches increases (Fig.66 & 67).

→ The San Andreas Fault is a mature fault (L > 1000 km; I-Age > 10 Ma; MR = few cm/yr; D_{total} > 100 km). It has propagated southward overall over the long-term. It is however divided into two distinct sections either side of a long (~130 km), central, creeping section.

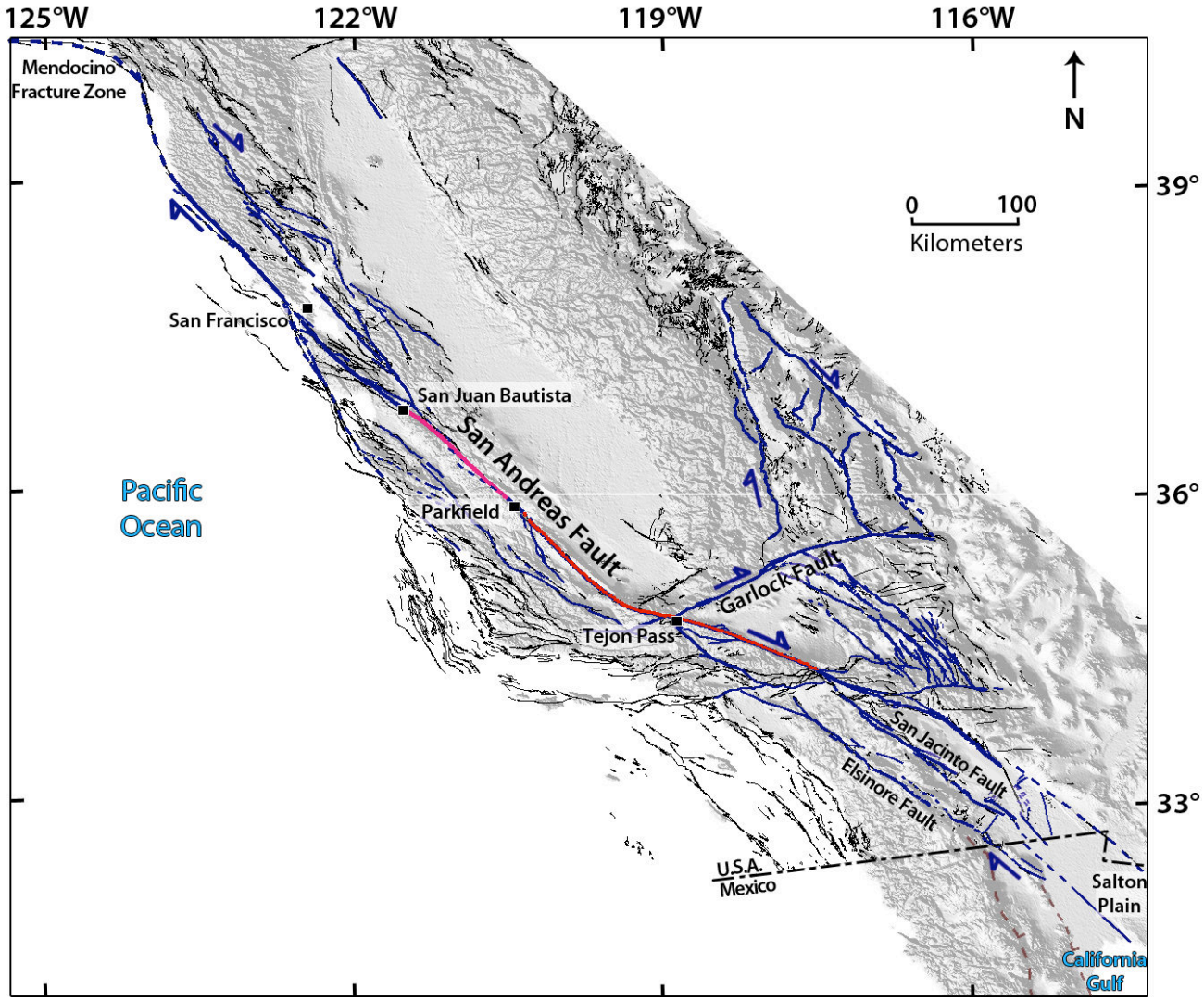


Fig.64: General map of long term faults in California. In blue are the major active faults that we mapped. In black are the other Quaternary faults mapped by the U.S. Geological Survey and California Geological Survey, 2006. Dotted brown lines are ancient faults related to the Gulf of California (See detail mapping in Fig.4). The creeping section of the San Andreas Fault is indicated by the pink line. The red line shows the surface rupture of the 1857 Fort Tejon earthquake.

Architecture and lateral major segmentation, from our and USGS mappings (Fig.65) :

- Mapping done from Google Earth, Landsat and ASTER GDEM data combined with USGS detailed mapping (U.S. Geological Survey and California Geological Survey, 2006).
- The SA Fault is not isolated, but surrounded by numerous faults and fault systems of different slip modes and sizes. The area of "adjacent" faulting is 70-180 km large on either side of the main SA Fault trace, and is enlarging southwards. Some of the adjacent faults and systems are genetically linked with the SA Fault, whereas others are not, although they might be reactivated in the regional stress field that governs the SA Fault activity (See below for more details on some of the adjacent faults).

- The SA Fault is ~1300 km long at total. However it is divided into two sections –the northern SA Fault and the southern SA Fault, likely acting as two faults, separated by the ~130 km-long, central creeping section. The northern SA Fault is ~450 km long (along strike); the southern SA Fault is at least ~600 km long (until Imperial Valley) and most likely ~800 km (until the Gulf of California; See below).

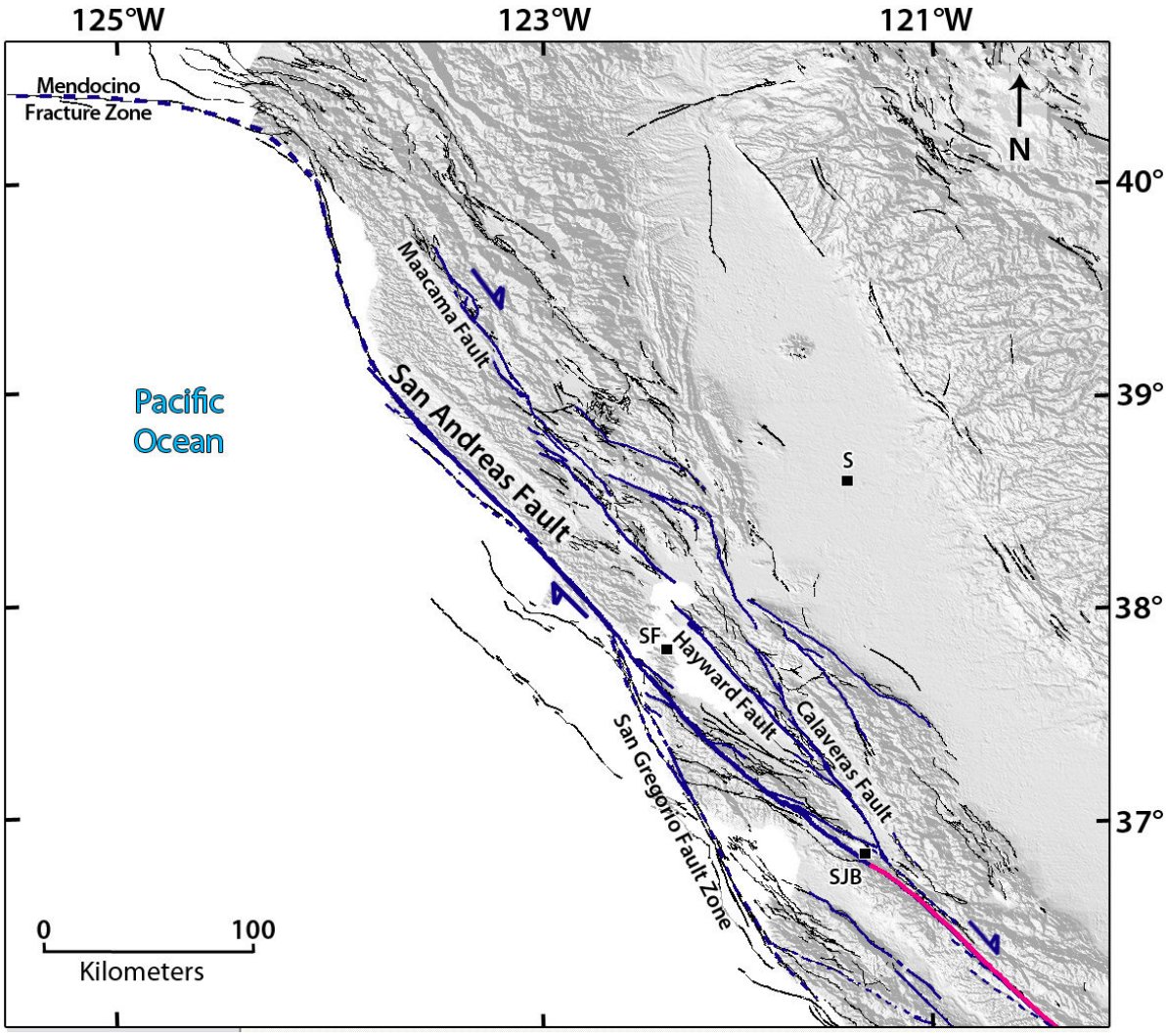


Fig.65: (a)Map of long-term faults in northern California (same caption as in Fig.64). SF : San Francisco ; SJB : San Juan Bautista ; S : Sacramento.

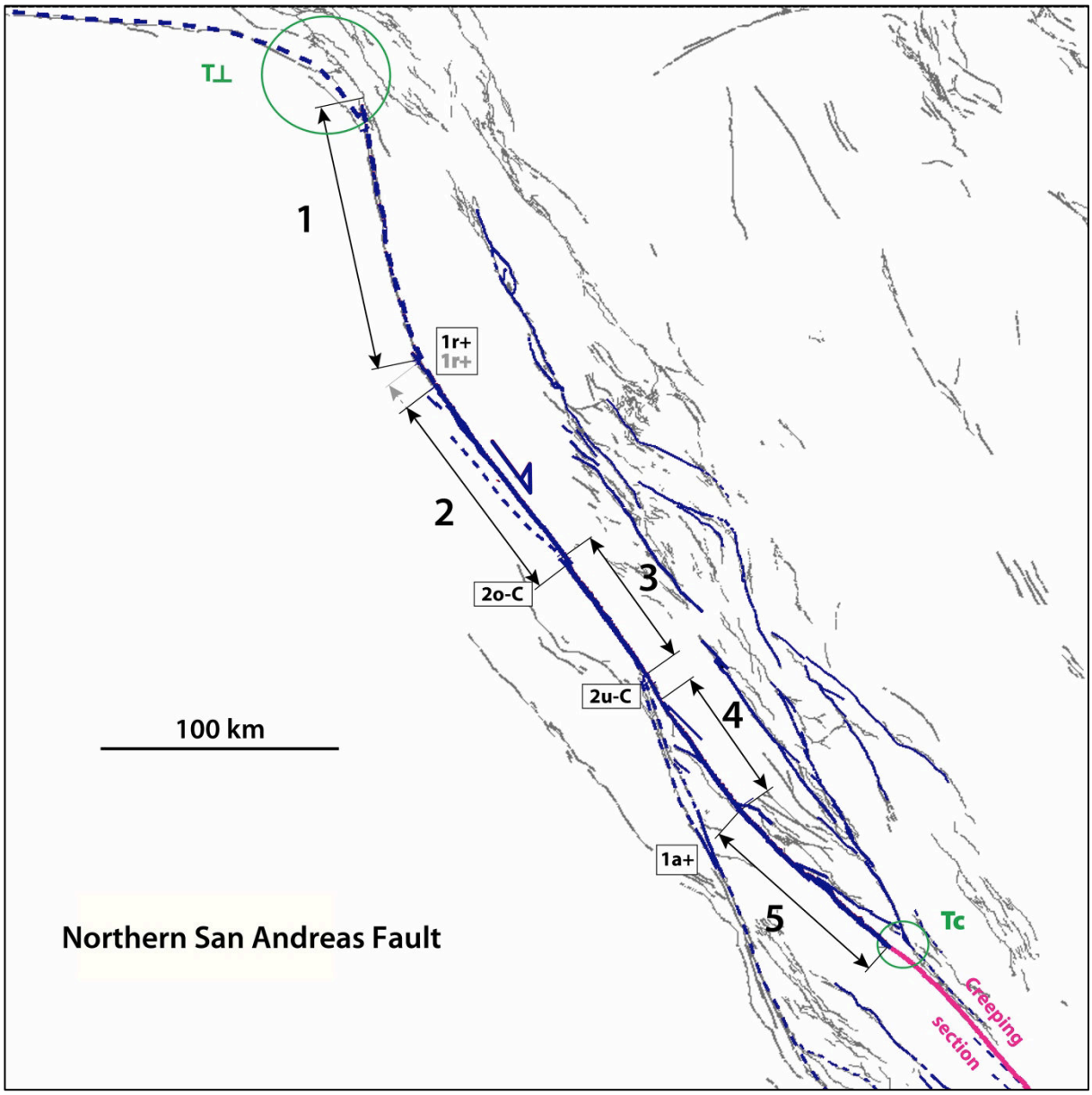


Fig.65: (b) Same active fault map as in 65(a), but with focus on the major segments of the northern San Andreas Fault. The segments are numbered from NW to SE and indicated by black arrows parallel to their mean strike. The grey prolongation of the arrows indicates the uncertainties on the segment lengths. The nature of the inter-segment zones is indicated in letters within boxes explained in Table 6. The nature of the fault tips is indicated in green (Table 6).

Northern San Andreas Fault (Fig.65)

- To the north, the northern SA Fault terminates by connecting to the almost perpendicular Mendocino fracture zone. The termination is thus of the type T⊥ (FIG.24). To the south, the northern SA Fault terminates at the junction with the creeping section. The northern SA Fault is thus about 430 km long (L along-strike 450 km).
- Except in its southernmost part, and provided that faults off-shore are well known, the northern SA Fault is pretty isolated, i.e., associated with very few nearby sub-parallel faults (the closest is the Hayward-Calaveras fault zone, 30-40 km away in across-strike direction).

- The northern SA Fault is divided into 5 major, fairly collinear segments (See Fig 2b where they are numbered). The lengths and types of the segments and inter-segments are described in details in Table 6.
- The 5 major segments have a length of similar order, in the range 60-120 km (length measured along the linear trace of each segment; Fig.65b).
- The fault trace is extremely linear along the 4 northernmost major segments (segts 1-4), and more sinuous along segment 5 in the south.
- Major segment 1 in the north is offshore and ~120 km long. Its trace is mapped as being linear. Major segment 2 has a very linear trace, mainly onshore, of ~90 km long. Segments 1 and 2 strike differently, with an angle difference of ~24 °. Segments 1 and 2 are connected through a rounded bend in the fault trace, of type 1r+. Segment 3 is almost parallel to segment 2, has a very linear trace ~70 km long, and is connected to segment 2 through a narrow (W 1 km) across-strike step of type $2_{O\text{-}C}$. An oblique NW-striking fault (of type "not splay") intersects the SA trace in the connection zone between segments 2 and 3. Segment 4 also has a linear trace on-land, of ~60 km. It is almost parallel to segment 3 and connects it through a $2_{U\text{-}C}$ type step and fault trace bending. A network of oblique, NNW-trending offshore faults (San Gregorio fault zone) connects the SA trace in the relay zone between segments 3 and 4. The overall pattern suggests that the San Gregorio Fault zone might be a splay of the northern SA Fault, and hence might mark the southern termination of the main northern SA Fault when the later was made of major segments 1, 2 and 3 only. The splay would thus suggest that the northern SA Fault has been propagating southward over geological time, in keeping with general observations (See before). Segment 5 looks different from the other 4 segments. While its ~85 km long trace is fairly linear, its overall imprint in the morphology and topography is more subtle than that of the other segments, and in particular, it does not imprint a linear corridor in the topography. The trace of segment 5 is also more discontinuous and more clearly punctuated with smaller-scale intersegments zones than along the other major segments. Also, multiple secondary oblique faults exist adjacent to the southern part of the southern SA (segments 4 and 5). Altogether these suggest that segment 5 might be younger than the other 4 segments, in keeping with the southward propagation of the fault. Segments 4 and 5 are connected through a 1r+ bend type. More details on the inter-segments can be found in Table 6.

→ The Northern San Andreas Fault is divided into 5 long-term major segments, all are well-connected to each other. The Northern SA Fault seems to have propagated

southwards over time; its northernmost section (at least coinciding with major segments 1 & 2) is thus likely the oldest and most mature.

Southern San Andreas Fault (Fig.66)

- To the north, the Southern SA Fault terminates by the ~30 km long Parkfield section, due south of the central creeping section. It is likely that, because it breaks very often due to the large stresses that accumulate at the southern tip of the creeping section, the Parkfield section is a "stress gap" and hence an efficient barrier to EQ slip that would emerge from the Southern SA Fault. The actual northern termination of the Southern SA Fault thus likely locates at the large (15*3 km) pull-part that connects the southern SA and the Parkfield section (zone circled in green in Fig.66b). To the south, the southern SA Fault terminates through a large-scale splay involving different generations of slightly oblique faults, including San Gabriel-Elsinore, San Jacinto, and San Bernardino Faults (Fig.66; Scholz et al., 2010, see also below, section "Interaction between the Northern and Southern SA Faults and the adjacent faults"). Note that the San Gabriel-Elsinore and the San Jacinto Faults are discussed in more details in the sections describing the Baja California 2010 and the Borrego Mountain 1968 EQs, respectively. The large-scale splay suggests that the Southern SA Fault has been propagating southward over geological time, in agreement with the southward decrease in both cumulative slip and slip rate (See *general characteristics* section above; and Fig.68). It seems to have continued propagating southward over recent times, forming the more subtle fault traces in the Mexicali-Yuma area (See sections Baja California and Borrego Mountain). The southern SA Fault is thus at least 600 km long and likely more, up to 800 km.
- In the south, the SA and its main branches intersect and interact with some of the NNW normal Faults that bound the Gulf of California to the west. Those faults are represented in dotted brown lines in Fig.67, whereas the interaction zone between the two fault types is represented in brown in the Fig.67. Clearly, the SA Fault and branches offset the NNW Gulf faults, and hence are younger in this area. However, both faults are kinematically consistent and hence their slips are likely coeval (at the time scale of several EQ cycles); dextral slip on the SA branches might in particular reactivate slip on the NNW faults. In the Salton Sea plain, numerous NE-trending small lineaments are observed, that we suspect to be ancient small faults developed at the northern tip of the major, normal NNW Gulf Faults. We discuss those faults in more details in the sections describing the Borrego Mountain, Imperial Valley and Superstition Hills EQs.

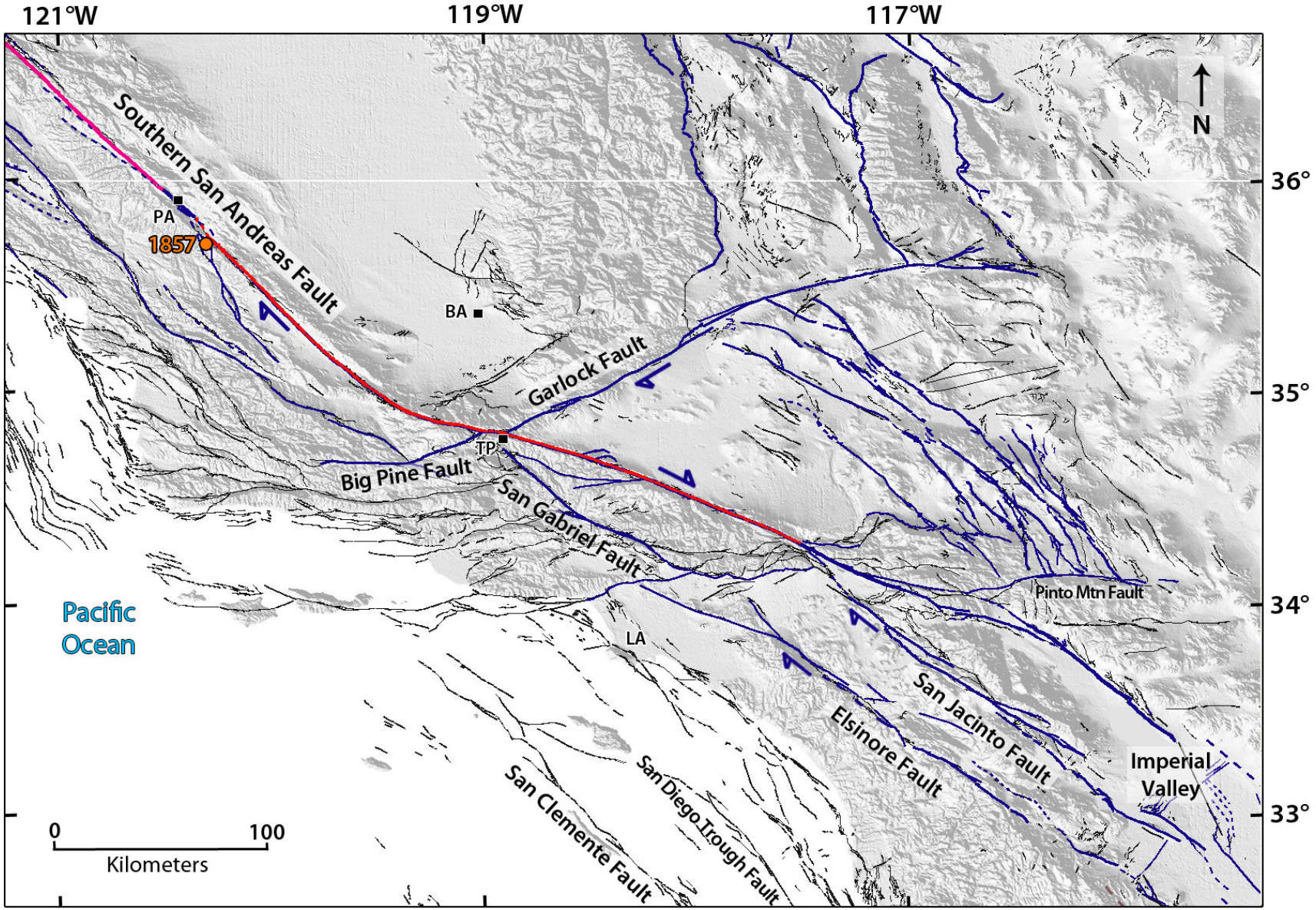


Fig. 66:(a) Map of long-term faluts in southern California (same caption as in Fig.64). The surface rupture of the 1857 Fort Tejon earthquake is indicated by the red line. The orange circle shows the 1857 epicenter. LA: Los Angeles ; PA: Parkfield; TP : Tejon Pass ; BA : Bakersfield

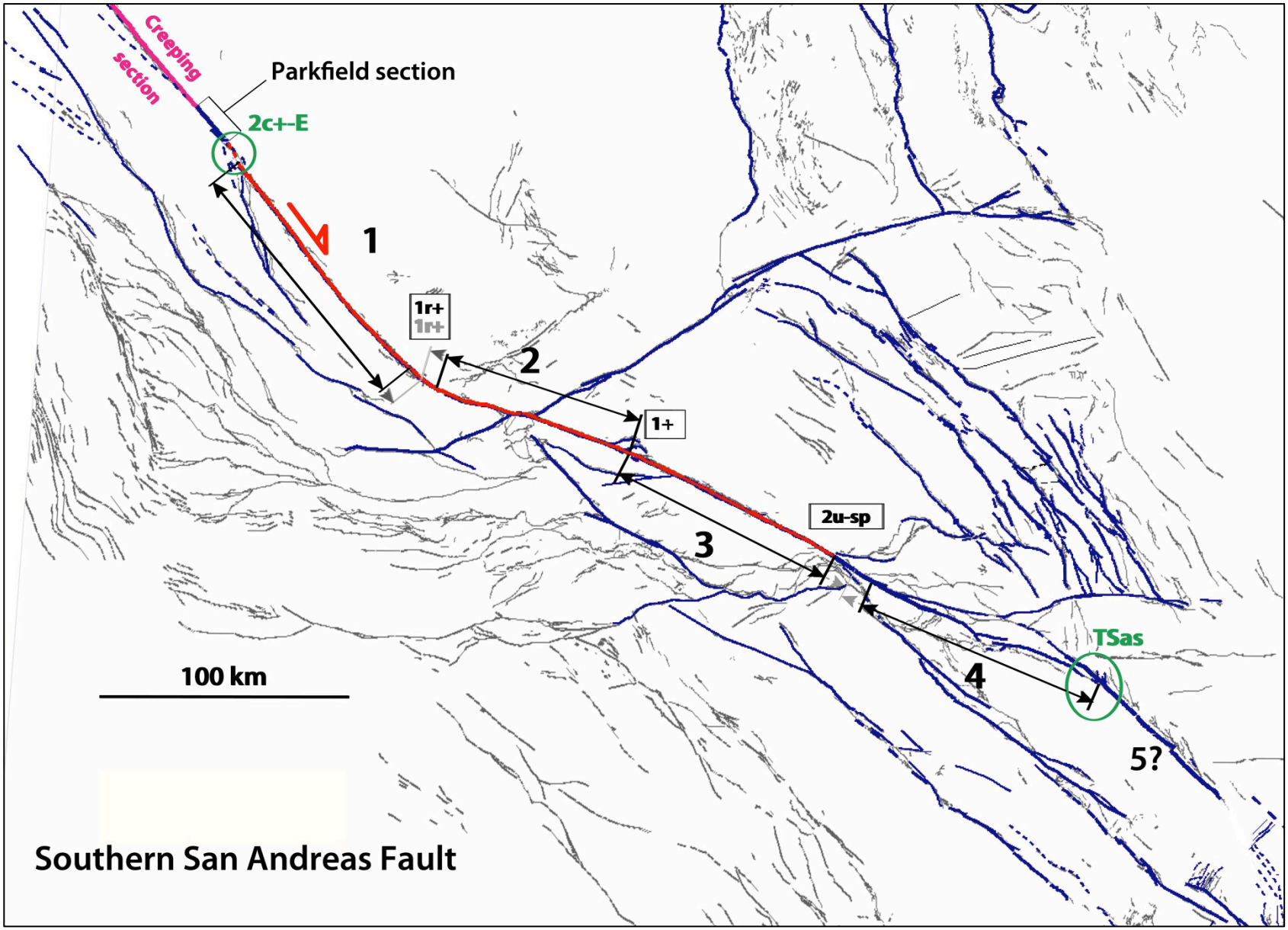


Fig.66:(b) Same active fault map as in 66a, but with focus on the major segments of the southern San Andreas fault. The segments are numbered from NW to SE and indicated by black arrows parallel to their mean strike. The grey prolongation of the arrows indicates the uncertainties on the segment lengths. The nature of the inter-segment zones is indicated in letters within boxes explained in Table 6. The nature of the fault tips is indicated in green (Table 6).

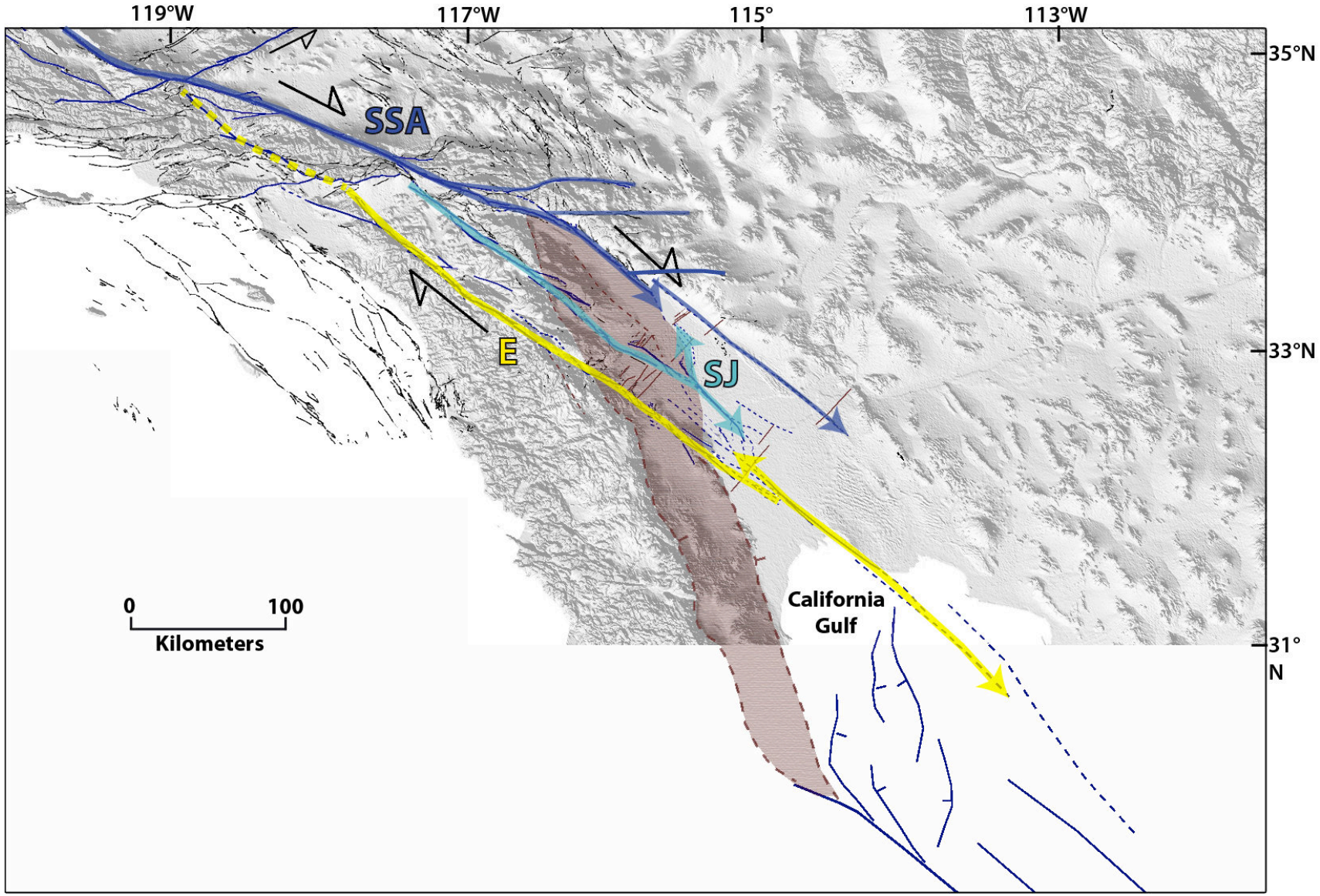


Fig. 67: General map showing the interaction zone between the southern San Andreas fault system and the Gulf of California (brown area). SSA : Southern San Andreas fault (Dark blue); SJ: San Jacinto fault (pale blue); E : Elsinore fault (yellow). In dotted brown lines are ancient faults related to the Gulf of California. Faults situated off shore in the Gulf of California are modified from Dorsey (2010).

- The southern termination of the Southern SA Fault zone is thus basically where it intersects the Gulf of California Faults.
- Except in its northernmost part, the southern SA Fault is not isolated, but rather surrounded by many nearby faults, most are strongly oblique to the SA trace.
- The southern SA Fault is divided into 4 major, fairly collinear segments (See Fig.66b where they are numbered). A fifth major segment might be defined in the south, although it is not collinear with its neighboring segments (Fig.66b). The lengths and types of the segments and inter-segments are described in details in Table 6.
- The 5 major segments have a length of similar order, in the range 85-120 km (length measured along the linear trace of each segment; Fig.66b).
- The fault trace is very linear along the 3 northernmost major segments (segments 1-3), and more sinuous and subtle along segment 4 (and also 5) in the south.
- Major segment 1 in the north is ~120 km long and has a very linear trace. Major segment 2 is ~90 km long, and has a trace fairly linear, yet with a small bend in its center. From that bend (that likely indicates a smaller-scale inter-segment), the San Gabriel oblique fault starts and continues further south where it gives pace to the Elsinore Fault. Segments 1 and 2 strike differently, with an angle difference of ~ 33°. Segments 1 and 2 are connected through a rounded bend in the fault trace, of type 1r+. The bend and connection resemble those for segments 1 and 2 along the northern SA Fault. The bend is deported with respect to the intersection between the Southern SA and the Garlock (and Big Pine southern counterpart) Faults. Segment 3 is almost parallel to segment 2 (as in the north), has a very linear trace ~95 km long, and is connected to segment 2 through a compressive bend of type 1+. Segment 4 looks different from the other 3 segments. While its ~100 km long trace is fairly linear overall, its imprint in the morphology and topography is more subtle and more discontinuous (more clearly punctuated with smaller-scale intersegments zones) than that of the other segments. Segments 3 and 4 are connected through a $2_{U\text{-}Sp}$ type relay. Several large oblique faults (including San Jacinto) diverge from the segments 3-4 inter-segment zones, forming a splay at the segment 3 southern termination. Several large oblique faults of splay type are also connected to segment 4, especially at its southern tip where they form a large-scale splay. Segment 5 is likely the main splay that emerges from the southern tip of segment 4. Together these suggest that the Southern SA Fault has been and is still propagating southward, and that segment 4 (and 5) is younger than the other 3 major segments.

- It seems that the Southern SA Fault is currently propagating southward at the northern boundary of the Salton Plain (Fig.64) in Mexico where it imprints a subtle trace.

→ The Southern San Andreas Fault is divided into 4 long-term, major, well-connected collinear segments. The Southern SA Fault seems to have propagated southwards over time; its northernmost section (at least coinciding with major segments 1 & 2) is thus likely the oldest and most mature. The San Jacinto and San Gabriel-Elsinore Faults are the major splays developed at the propagating Southern San Andreas Fault tip.

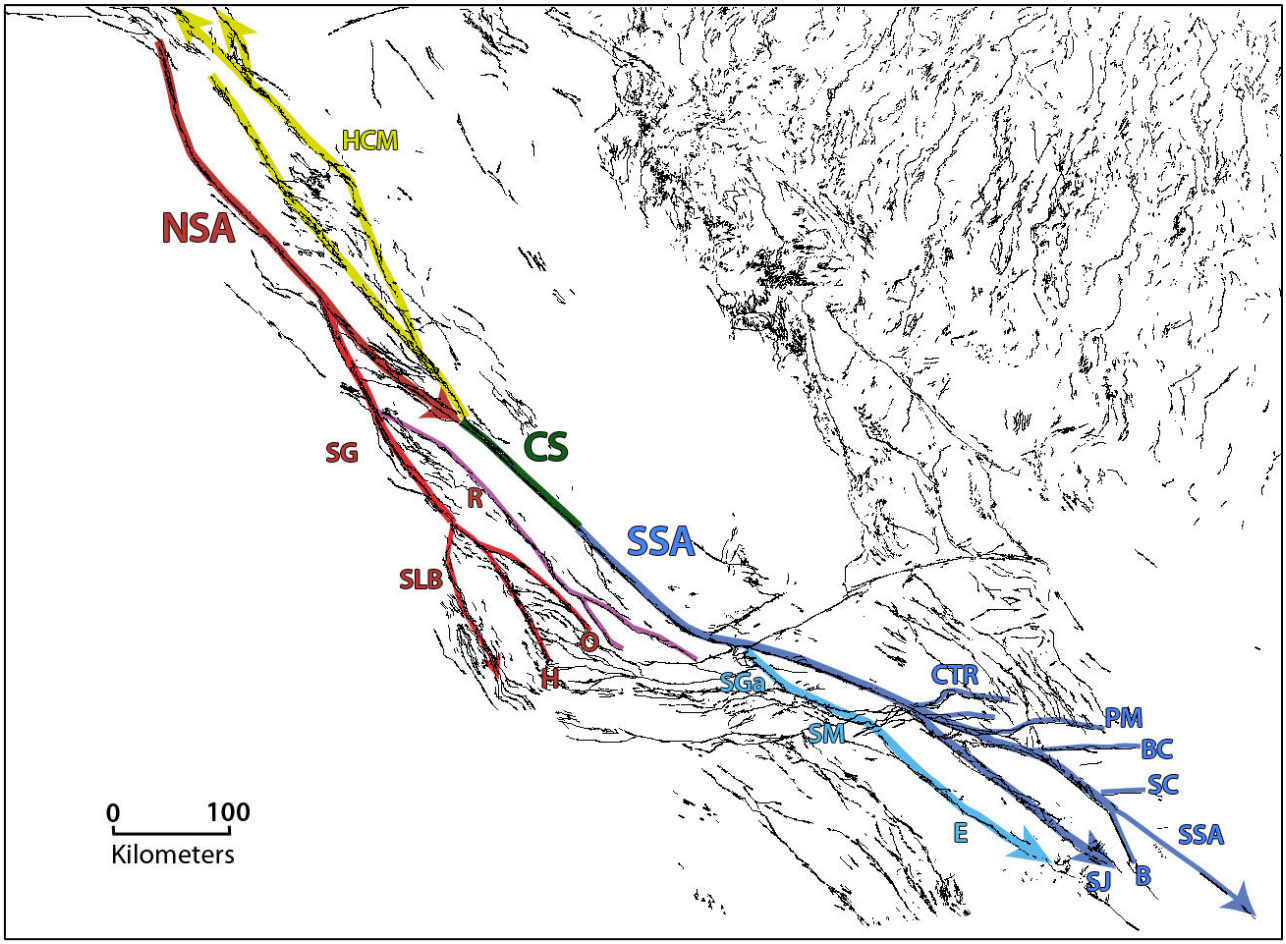


Fig.68: Sketch showing the major faults systems and their direction of propagation. NSA: North San Andreas; CS: Creeping Section of the San Andreas Fault; SSA; South San Andreas; HCM: Hayward-Calaveras-Maacama; SG: San Gregorio; SLB: Santa Lucia Bank; H: Hosgri; O: Oceanic; R: Reliz; SGa: San Gabriel; SM: Sierra Madre; E: Elsinore; CTR: Cleghorn-Tunnel Ridge; PM: Pinto Mountain; BC; Blue Cut ; SC: Salt Creek; B: Brawley; SJ: San Jacinto.

Interaction between the Northern and Southern SA faults and the adjacent faults (Fig.68) :

- We interpret the San Gregorio Fault as a major splay of the Northern SA Fault, formed (or reactivated?) as a result of its southward propagation. The San Gregorio splay likely formed when the Northern SA was made of major segments 1-2-3 only.
- We interpret the Reliz Fault (and associated southern faults) as a major splay of the San Gregorio Fault, formed as a result of its own southward propagation
- We interpret the faults named "Oceanic", "Hosgri" and "Santa Lucia Bank" on the USGS maps, as recent splays of the southward propagating San Gregorio Fault.
- We suggest that the Garlock and Big Pine (and a few other associated parallel ENE left-lateral and reverse faults) formed at a time when the Southern SA Fault tip was located at their latitude (tip of major segment 1 or 2) and somehow stalled in its overall process of southward propagation.
- We interpret the San Gabriel-Elsinore Fault zone as a major splay of the Southern SA Fault, formed as a result of the southward propagation of the Southern SA Fault, when the later was made only of major segments 1 and 2.
- We interpret the Cleghorn-Tunnel Ridge and the San Jacinto Faults as splay faults of the Southern SA Fault, which formed as a result of the southward propagation of the Southern SA Fault, when the later was made of major segments 1, 2 and 3. The WNW Sierra Madre Fault zone might have formed at that time (when tip of major segment 3 was somehow stalled in its overall process of southward propagation). This would explain why the Sierra Madre Fault zone offsets the San Gabriel-Elsinore Fault zone.
- We interpret the Pinto Mountains, Blue Cut, Salton Creek and possibly the Brawley Faults as recent splays of the southward propagating Southern SA Fault (more details in sections Borrego Mountain, Imperial Valley and Superstition Hills EQs).
- The 1940 and 1979 Imperial Valley, 1968 Borrego Mountain, 1987 Superstition Hills and 2010 Baja CA large EQs attest that the San Jacinto and the Elsinore splay faults are currently active and likely propagating southward.
- The origin of the San Diego-San Clemente Faults (Fig.65) to the west and of the Helendale-Jonhson Valley-Camprock-Calico (etc) to the east (See Fig.82 in Hector Mine section) is less clear, yet might be searched in distributed off-fault deformation associated with the southward propagation of the Northern and Southern SA faults (when the later was stalled at the tips of major segments 1 or 2).

- We interpret the Hayward-Calaveras fault zone as a northward propagating system that would have formed fairly recently from the northern tip of the central creeping zone (where stresses are high), to accommodate the part of the strain that the Northern SA Fault cannot accommodate in the north (reduced slip rate on the northern SA Fault). Because the central creeping zone arrests the southward propagation of the Northern SA Fault, and hence limits its length, the slip accumulation on the Northern SA Fault cannot overcome a certain threshold (See curve of worldwide cumulative Dmax-L Fig.11 in chapter I), what may explain that part of the slip must be distributed onto other adjacent faults.

→ The most ancient and most mature 'core' of the SA Fault is that free of splay, i.e., the central creeping section, the northernmost major segments 1-2-3 of the northern San Andreas Fault (if no fault is missing off-shore), and the northernmost major segments 1 and 2, then 3 (in time) of the southern San Andreas Fault. Those most mature sections (but the creeping section) coincide with the parts of the SA Fault showing the less dense seismicity, both on- and off- the fault (Fig.69).

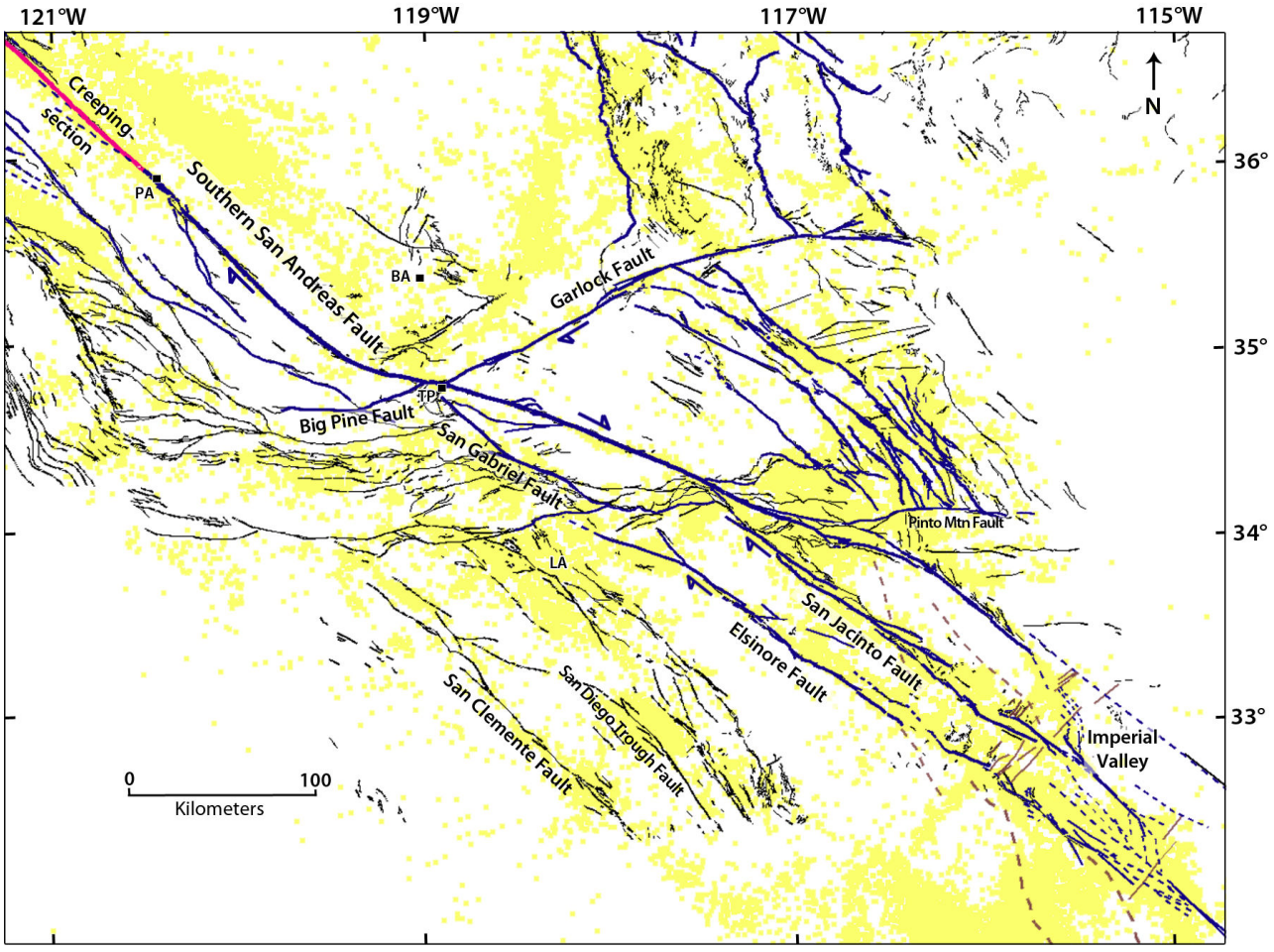


Fig.69: Same active fault map as in Fig.66 (a). The yellow dots are the instrumental earthquakes (Mw>2) recorded between 1981 and 2011 (Hauksson et al., 2012).

1857 Fort Tejon Coseismic rupture

Surface trace and location on long-term San Andreas Fault :

- The 1857 surface rupture is clear on Google Earth images. The surface trace of the earthquake has been precisely mapped, and the displacements measured (See below), both on the field and from Lidar imagery (e.g. Sieh 1978a; Grant Ludwig et al., 2010; Zielke et al., 2010; 2012).
- Surface rupture of 330 km long (Sieh 1978a).
- The EQ broke three major segments of the southern San Andreas Fault: the northernmost major segments 1, 2 and 3 (Fig.66).
- It initiated close to the intersegment zone between the Parkfield section and the major segment 1 and propagated unilaterally toward the south.
- The rupture terminated at the southwestern tip of major segment 3, where the southern San Andreas Fault splays into multiple secondary faults (mainly, San Jacinto and Cleghorn-Tunnel Ridge Faults).

→ The Fort Tejon EQ broke 3 major segments of the Southern San Andreas Fault. The broken segments are the most mature of the Southern San Andreas Fault. The rupture nucleated on the most mature part of the fault.

Coseismic displacements measured at surface :

- *From Field measurements*: Maximum lateral slip ~ 9 m (Sieh 1978a) measured on northernmost major segment 1.
- *From LiDAR data*: Recently some authors updated the maximum lateral coseismic slip and found it lower, ~ 6 m (Grant Ludwig et al., 2010; Zielke et al., 2010, 2012; Fig.70). This suggests that the 9 m offset found by Sieh (1978a) might result from more than one event.
- The complete slip profile was measured both by Sieh (1978) and subsequent authors (Grant Ludwig et al., 2010; Zielke et al., 2010, 2012; Fig.70). The slip profile estimated by Sieh is clearly triangular and asymmetric, with maximum slip deported to the north of the rupture. The slip profile estimated by Zielke et al. (2012) has a more rounded shape, yet still fairly asymmetric with maximum slip in the northern part of the rupture. The slip profile of Sieh shows 3 pronounced slip bumps that well coincide with the 3 major broken segments. It is more difficult to distinguish slip gradients in the slip profile of Zielke et al. (2012) because

the method that is used to measure the slip smoothes out the slip distribution (1 slip measurement every 10 km).

→ Although the available data differ on the maximum coseismic slip, they converge to show that maximum slip occurred in the northern part of the rupture, i.e., on the most mature segment (n°1) of the broken fault. They also converge to show that the slip profile was basically asymmetric, tapering toward the south. The maximum coseismic slip at surface ranges between 6 and 9 m.

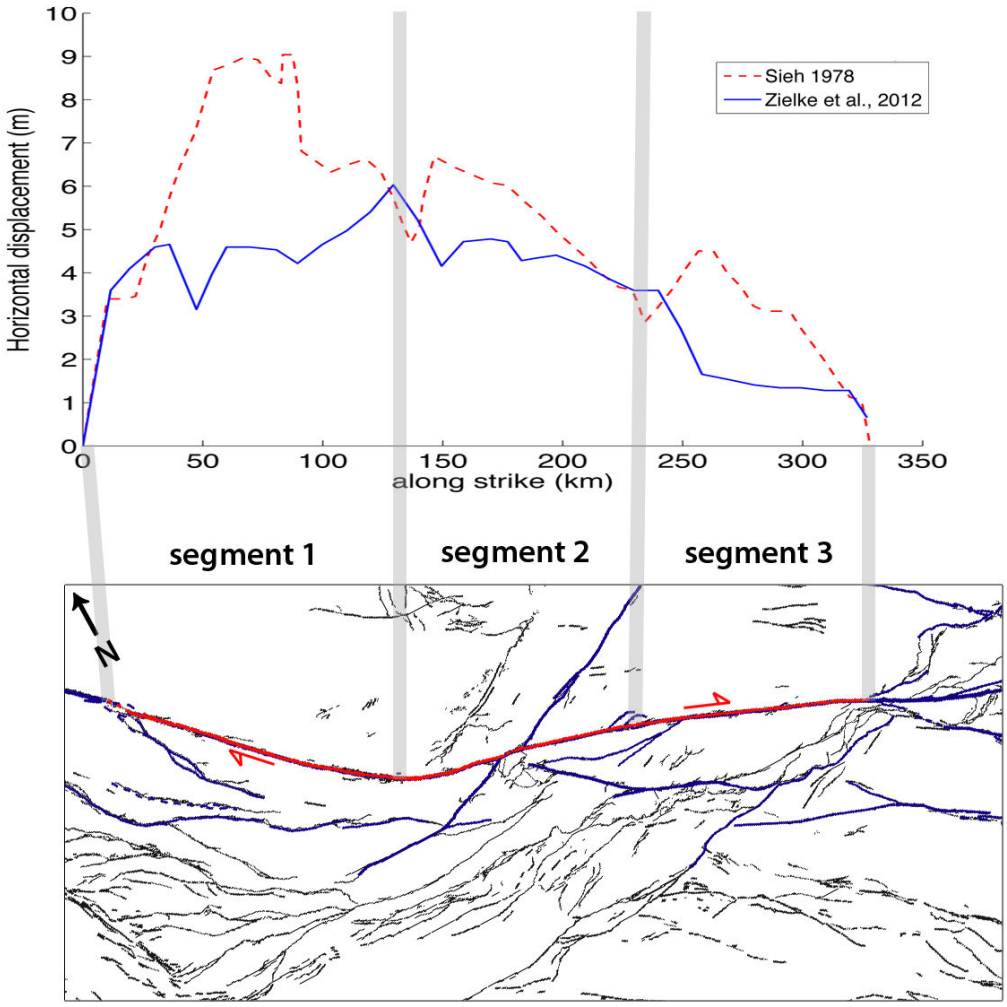


Fig.70: Coseismic displacements measured at surface (Sieh 1978a ; Zielke et al., 2012) along the 1857 surface rupture. Grey areas correspond to the major intersegments highlighted by our mapping.

Other source parameters :

Available source parameters of the 1857 EQ are not really constrained. The seismic moment was inferred from field observations of rupture length and mean coseismic offset (using M0 = μDS). Large uncertainties affect the mean slip value and the rupture width. This explains why the seismic moment ranges between 4e20 N.m and 9e20 N.m (Mw 7.7 to 7.9) among the

various studies (Hanks et al., 1975; Sieh 1978a; Hanks and Kanamori 1979; Zielke et al., 2012).

Other information:

1857 EQ:

- Three foreshocks (~5<M<~6) occurred one, two and four hours before the mainshock in a large area at the northwestern tip of the rupture (Parkfield section; Sieh 1978b). The location of the foreshocks was the strongest evidence used to infer the hypocenter position at the northwestern tip of the rupture. It was considered that strain accumulation through time due to the creeping motion north of the broken zone, as well as the repeating moderate earthquakes in the Parkfield area, have contributed to increase the stress at the northern termination of the Southern San Andreas Fault and so doing, have contributed to trigger the 1857 earthquake (Meltzner and Wald 1999).
- The largest aftershocks of Mw 6.25 and 6.7 occurred the 09th and 16th January 1857 respectively and were located close to Los Angeles (south of major segment 3) (Meltzner and Wald 1999).

Past EQ activity:

- The 1857 Fort Tejon and the 1906 San Francisco EQs are the largest historical events that broke the southern and northern San Andreas Fault, respectively.
- The analysis of cumulative fault offsets along the major segments 1, 2 and 3 of the southern San Andreas Fault suggests that three to four pre-historical large earthquakes broke the fault prior to 1857 and produced lateral slips of amplitude similar to that of the 1857 slip, in the range 9.5-12.3 m (Sieh and Jahns 1984). However, more recent paleoseismological investigations suggest that coseismic slip amounts rather varied from one large EQ to the other (Akciz et al., 2010; Grant Ludwig et al., 2010; Zielke et al., 2012). Therefore it is not clear whether the 9.5-12.3 m slips represent one or several events.

Parameters retained to describe the 1857 Fort Tejon event (Tables 1 & 3) :

Mw 7.7-7.9; M0 ~ 4-9e20 N.m ; L ~ 330 km ; Dmax surface **6**-9 m ;

W and depth of hypocenter are unknown. However the seismogenic crust in Southern California is ~ 15 km thick (Nazareth and Hauksson 2004).

Number of segments broken on the Southern San Andreas Fault: 3 major segments.

Despite of the uncertainty on the maximum coseismic slip value, the Fort Tejon earthquake surface slip-length data fall fairly well on the third function (green curve; Fig.71), in keeping with the EQ having broken 3 major segments of the Southern San Andreas Fault.

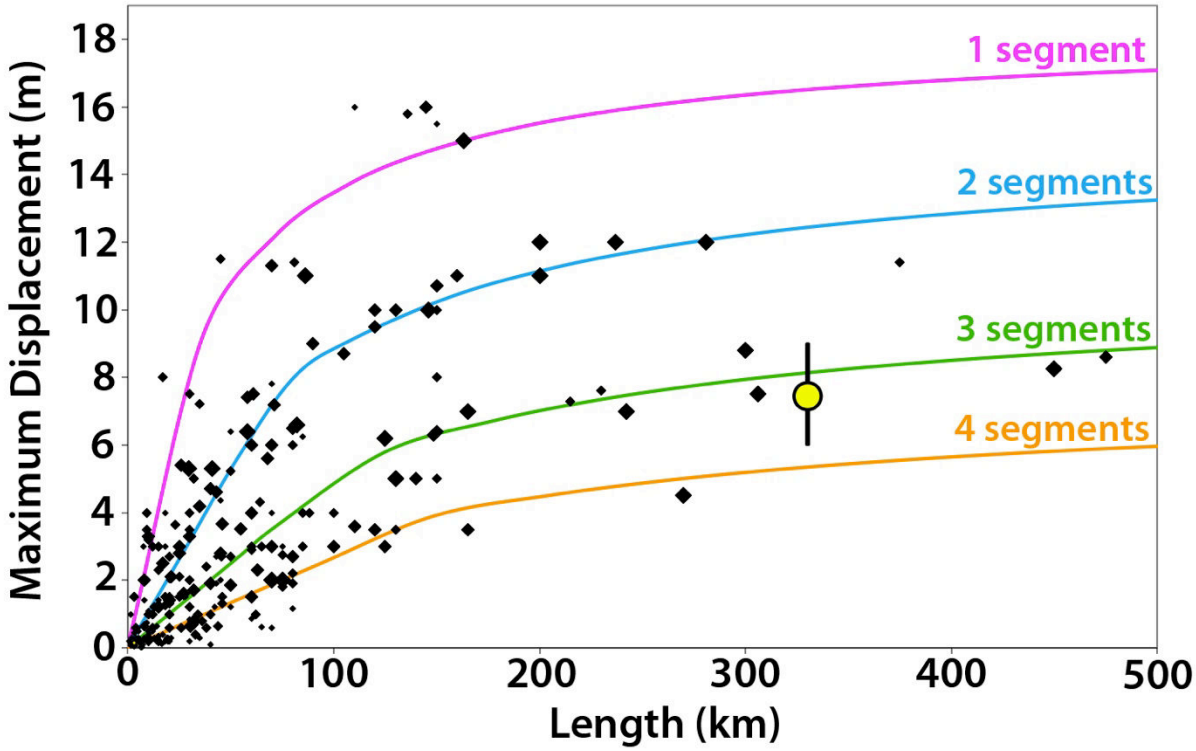


Fig.71: Earthquake displacement-length data measured at surface for 260 historical large continental earthquakes (Mw≥6). The 4 curves indicate the number of major long-term fault segments to have been broken by the earthquakes (modified from Manighetti et al., 2007 and Chapter IV). Yellow dot show the 1857 Fort Tejon earthquake surface slip-length data.

References

Akciz, S. O., L. Grant Ludwig, J R. Arrowsmith, & O. Zielke (2010). Century-long average time intervals between earthquake ruptures of the San Andreas fault in the Carrizo Plain, California, *Geology,* **38**, 9, 787–790, doi 10.1130/G30995.1.

Atwater, T. (1970) Implications of Plate Tectonics for the Cenozoic Tectonic Evolution of Western North America *Geological Society of America Bulletin,* **81**, 3513-3536, doi:10.1130/0016-7606(1970)81[3513:IOPTFT]2.0.CO;2

Clarke, S. E. Jr. & Nilsen, T. H. (1973). Displacement of Eocene strata and Implications for the History of Offset Along the San Andreas Fault, Central and Northern California, *in* Kovach, R. L. ed, Proceedings of the Conference on Tectonic Problems of the San Andreas Fault System. *Stanford University Press,* 494 p.

Darin, M. H. & R. J. Dorsey (2013) Reconciling disparate estimates of total offset on the southern San Andreas fault *Geology*, G34276.1, first published online July 22, 2013, doi:10.1130/G34276.1

Dorsey, R. J. (2010). Sedimentation and crustal recycling along an active oblique-rift margin: Salton Trough and northern Gulf of California. *Geology*, **38**(5), 443-446.

Grant Ludwig, L., S. O. Akciz, G. N. Noriega, O. Zielke, & J. R. Arrowsmith (2010). Climate modulated channel incision and rupture history of the San Andreas fault in the Carrizo Plain, *Science,* **327**, 5969, 1117–1119, doi 10.1126/science.1182837.

Hanks, T. C., Hileman, J. A. & Thatcher, W. (1975). Seismic Moments of the Larger Earthquakes of the Southern California Region. *Geological Society of America Bulletin*, **86**, 1131-1139, doi:10.1130/0016-7606(1975)86<1131:SMOTLE>2.0.CO;2

Hanks, T. C., & H. Kanamori (1979). A moment magnitude scale, *J. Geophys. Res*., **84**(B5), 2348–2350, doi:10.1029/JB084iB05p02348.

Hauksson, E., W. Yang, & P.M. Shearer (2012). Waveform Relocated Earthquake Catalog for Southern California (1981 to June 2011*); Bull. Seismol. Soc. Am.,* **102**, doi:10.1785/0120120010.

Hill, M. L. & T. W. Dibblee, E. Jr. (1953). San Andreas, Garlock and Big Pine faults, California, a study of the character, history and tectonic significance of their displacements. *Geol. Soc. Am. Bull.* **64**, 4, 443-458, doi:10.1130/00167606(1953)64[443:SAGABP]2.0.CO;2

Manighetti, I., M. Campillo, S. Bouley, and F. Cotton (2007), Earthquake scaling, fault segmentation, and structural maturity, *Earth Planet. Sci. Lett*., **253**, 429-438, doi:10.1016/j.epsl.2006.11.004

Meade, B. J., & B. H. Hager (2005), Block models of crustal motion in southern California constrained by GPS measurements, J. Geophys. Res., 110, B03403, doi:10.1029/2004JB003209.

Meltzner, A. J. & Wald, D. J. (1999). Foreshocks and Aftershocks of the Great 1857 California Earthquake. *Bull. Seismol. Soc. Am.*, **89**, 4, 1109-1120

Nazareth, J. J., & Hauksson, E. (2004). The seismogenic thickness of the southern California crust. *Bulletin of the Seismological Society of America*, **94**(3), 940-960.

Perkins, J. A., Sims, J. D. & Sturgess, S. S. (1989). Late Holocene Movement Along the San Andreas Fault at Melendy Ranch : Implications for the Distribution of Fault Slip in Central California. *J. of Geoph. Res.,* **94,** 10,217-10,230.

Powell, R.E., & Weldon, R.J., II (1992), Evolution of the San Andreas fault: *Annual Review of Earth and Planetary Sciences*, **20**, 431–468, doi:10.1146/annurev.ea.20.050192.002243.

Revenaugh, J., & C. Reasoner (1997) Cumulative offset of the San Andreas fault in central California: A seismic approach, *Geology*, **25**, 123-126.

Scholz, C. H., M. Wyss, and S. W. Smith (1969), Seismic and aseismic slip on the San Andreas Fault, *J. Geophys. Res.,* **74**(8), 2049–2069, doi:10.1029/JB074i008p02049.

Segall, P. & Harris, R. (1986). Slip Deficit on the San Andreas Fault at Parkfield, California, as Revealed by Inversion of Geodetic Data. *Science,* New Series, **233,** 4771, 1409-1413.

Sieh, K. E. (1978a). Slip along the San Andreas fault associated with the great 1857 earthquake, *Bull. Seismol. Soc. Am*. **68**, 5, 1421–1448.

Sieh, K. E. (1978b). Central California foreshocks of the great 1857 earthquake, *Bull. Seismol. Soc. Am*. **68**, no. 5, 1731-1749.

Sieh, K. E., and R. H. Jahns (1984). Holocene activity of the San Andreas fault at Wallace Creek, California, *Geol. Soc. Am. Bull*. **95**, 883–896.

Sims, J. (1993). Chronology of displacement on the San Andreas fault in central California : Evidence from reversed positions of exotic rock bodies near Parkfield, California, *in* Powell, R. E., Weldon, R. J., Matti, J. C.

eds, The San Andreas Fault System : Displacement, Palinspastic Reconstruction and Geologic Evolution : Boulder, Colorado, *Geological Society of America Memoir* **178.**

van der Woerd, J., Y. Klinger, K. Sieh, P. Tapponnier, F. J. Ryerson, & A.-S. Mériaux (2006), Long-term slip rate of the southern San Andreas Fault from ^{10}Be-^{26}Al surface exposure dating of an offset alluvial fan, *J. Geophys. Res*., **111** B04407, doi:10.1029/2004JB003559

Wallace, R. E. (1970). Earthquake Reccurrence Intervals on the San Andreas Fault. *Geological Society of America Bulletin*, **81,** 2875-2890.

Weldon, R. J., & K. E. Sieh (1985), Holocene rate of slip and tentative recurrence interval for large earthquakes on the San Andreas fault, Cajon Pass, southern California, *Geol. Soc. Am. Bull.,* **96**, 793–812.

Titus, S. J., M. Dyson, C. DeMets, B. Tikoff, F. Rolandone, & R. Bürgmann (2011). Geologic versus geodetic deformation adjacent to the San Andreas fault, central California. *GSA Bulletin*, **123**, no. 5/6, 794–820; doi: 10.1130/B30150.1;

Tong, X., D. T. Sandwell, & B. Smith-Konter (2013). High-resolution interseismic velocity data along the San Andreas Fault from GPS and InSAR, *J. Geophys. Res. Solid Earth*, **118**, doi:10.1029/2012JB009442.

Zielke, O., J R. Arrowsmith, L. Grant Ludwig, & S. O. Akciz (2010). Slip in the 1857 and earlier large earthquakes along the Carrizo Plain, San Andreas fault, *Science* **327**, 1119–1122, doi 10.1126/science.1182781.

Zielke, O., J R. Arrowsmith, L. Grant Ludwig, & S. O. Akciz (2012). High-Resolution Topography-Derived Offsets along the 1857 Fort Tejon Earthquake Rupture Trace, San Andreas Fault, *Bulletin of the Seismological Society of America,* **102**, 3, 1135–1154, doi: 10.1785/0120110230

2.8. Fuyun 1931

19/08/1931, China

Mw 8.0

Epicentre : 46,8°N-89,9°E

Right-lateral strike-slip



Broken long-term fault:

The EQ broke the Fuyun Fault, within the Mongolian Altay Range.

General characteristics from literature:

- Fairly linear, NNW-trending right-lateral strike-slip fault, about 430 km long.
- Transpressive deformation occurring in the Gobi-Altai region between 8 and 2 Ma (e.g. Vassalo et al., 2007) as a result of India-Eurasia convergence (e.g. Tapponnier and Molnar 1977) which started in Paleocene-Eocene on Himalaya front (Molnar and Tapponnier 1975; Tapponnier and Molnar 1979). The actual initiation age of the fault is unknown but it thus might be at most a few Ma.
- Maximum cumulative lateral slip of ~ 20 km, estimated from lateral offset of Devonian formations and of the Irtysh thrust fault (Etchebes, 2011).
- Current lateral slip rate is unknown. Calais et al. (2003; GPS data) estimate mean lateral slip rate of ~5 mm/yr across the whole Altay domain (with respect to Eurasia), what suggests that the lateral slip rate of the Fuyun Fault is low, less than a few mm/yr.
- Long-term lateral slip rate is unknown.

→ The Fuyun Fault is likely a fairly immature fault (L ~430 km, I-Age < few Ma, MR < few mm/yr, D_{Total} ~20 km)

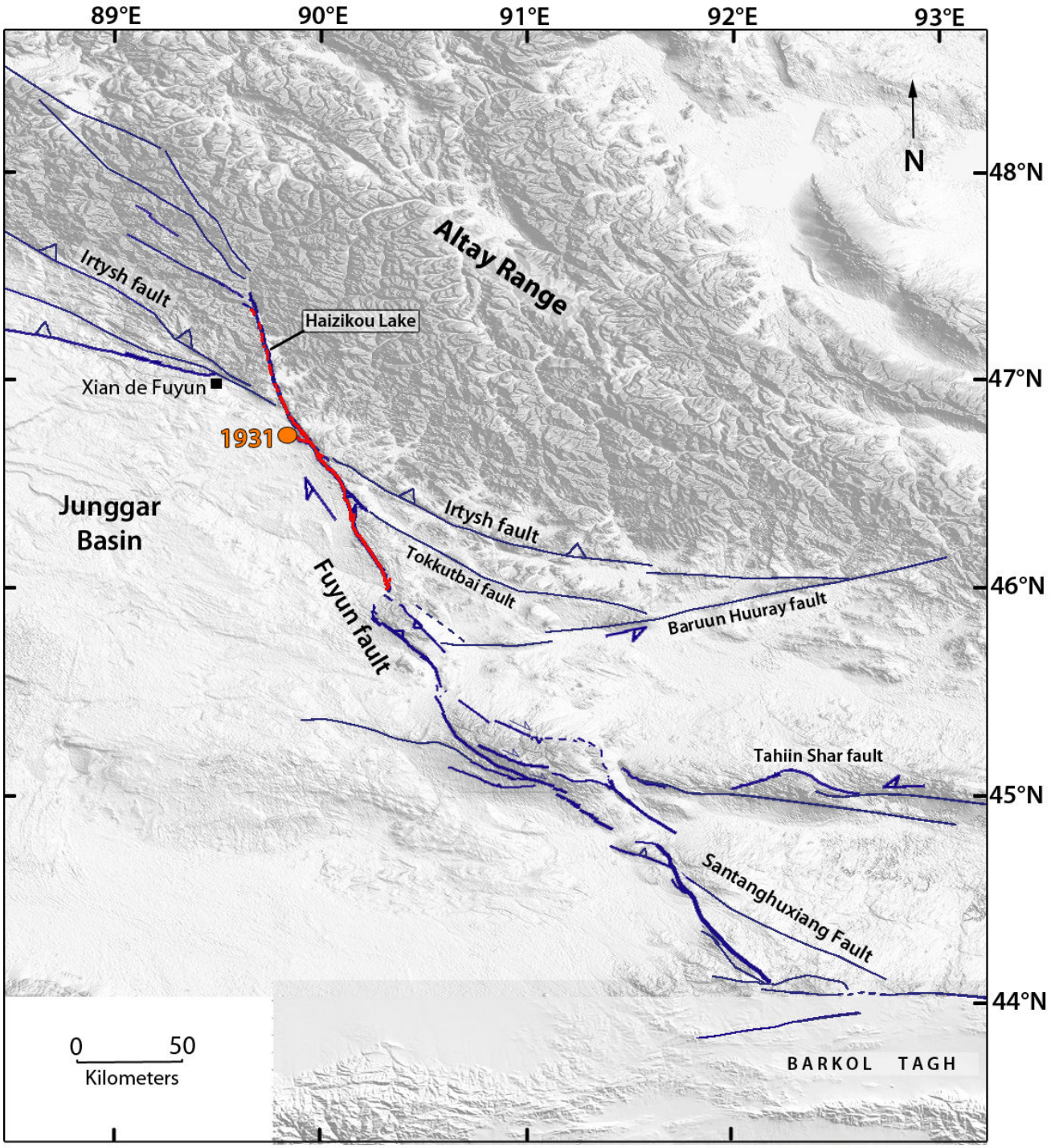


Fig.72: Long term faults that I mapped of the south Altay Range (blue) and surface rupture of the 1931 Fuyun earthquake. The orange circle shows the epicenter of the 1931 earthquake.

Architecture and major lateral segmentation, from our mapping (Fig.72 & 73)

- Mapping done from Google Earth, Landsat and SRTM data combined with literature information (Jianbang et al., 1984; Lin and Lin 1998; Etchebes 2011)

- Northern half of long-term fault trace well expressed in surface morphology and topography; southern half more subtle.
- The Fuyun Fault is fairly isolated in terms of sub-parallel NNW-trending faults in the region.
- By contrast, it cuts and/or connects with a dense network of E-W to WNW-trending secondary faults, almost perpendicular to the Fuyun Fault, being mainly reverse with an additional component of left-lateral slip on some of them (Fig.72). To the north, the Fuyun Fault trace ends in a large-scale splay of secondary faults, which, however, have tenuous traces (Type T_{Sas}). Such subtle traces might suggest that the splay faults are recent. In the south, the Fuyun Fault trace abuts and ends against a ~E-W trending large fault (Barkol Tagh Thrust in eastern TienShan; Type T_{ob}). The Santanghuxiang Fault near the SE tip of the Fuyun Fault might be a splay of the Fuyun master fault. The overall geometry of the Fuyun Fault network therefore suggests that the Fuyun Fault might have propagated bilaterally over geological time. Presently, its lateral southward propagation seems to be arrested by the Barkol Tagh range. By contrast, the tenuous traces of the splays in the north suggest that the northward lateral propagation might be recent. If this is correct, we infer that the Fuyun Fault has been mainly propagating southward over geological time, but has changed recently (due to its arrest in the south) to propagate most towards the north.
- Oblique, secondary, reverse faults also exist on either sides of the central part of the Fuyun Fault (e.g. Irtysh Fault, Tokkutbai Fault); the trace of the Irtysh Fault seems to be dextrally offset by ~20 km by the Fuyun Fault (e.g. Etchebes 2011).
- The Fuyun Fault is divided into 3 roughly collinear major segments (mean strikes are considered here) that are separated by large across-strike distances in the range 10-20 km (See Fig.73 where they are numbered). Segment 2 is slightly more westerly striking than the other two segments, and hence accommodates an additional reverse component of slip. The mean strike of segment 2 is not well defined however, and has an uncertainty of about 10 ° (Fig.73a).
- The 3 major segments have a similar length of 125-165 km.
- The fault trace is approximately linear overall along each major segment; yet, in detail, it shows some winding. Segment 1 has a fairly continuous and linear trace, whereas segments 2 and 3 have more sinuous and segmented traces. In particular, although the trace of segment 2 is unique and fairly linear in its northern and southern thirds, it is made of several parallel branches in its central part. Those branches are mainly strike-slip, yet associated with reverse secondary sub-parallel faults (Fig72 & 73). In the south, the trace of segment 2

is made of smaller segments, en echelon disposed. Segment 3 is made of disconnected en echelon branches.

- Segment 1 is supposed to have a normal component of slip, but we found it expressed only in its very northern part, north of the Haizikou Lake (Fig.72).
- The 3 major segments are separated by large and pronounced deformation zones, of compressive style (large scale compressive jogs or push-ups, Type $2_{U\text{-}R}$ /$2_{O\text{-}R}$), which thus form pronounced reliefs. The segments and inter-segments styles and sizes are reported in Table 6.

→ **The Fuyun Fault is divided into 3 major fairly collinear segments, separated by large, compressive inter-segment zones. The fault might have mainly propagated southward over geological time, but be in the present process of propagating mainly northward. The wavy trace of the major segments and the large unconnected zones that separate them confirm that the Fuyun Fault is fairly immature (hardly connected segments). The more linear and continuous trace of major segment 1 with respect to the traces of the other major segments suggests that major segment 1 is more mature than the other major segments, in keeping with the Fuyun Fault having propagated southward over geological time.**

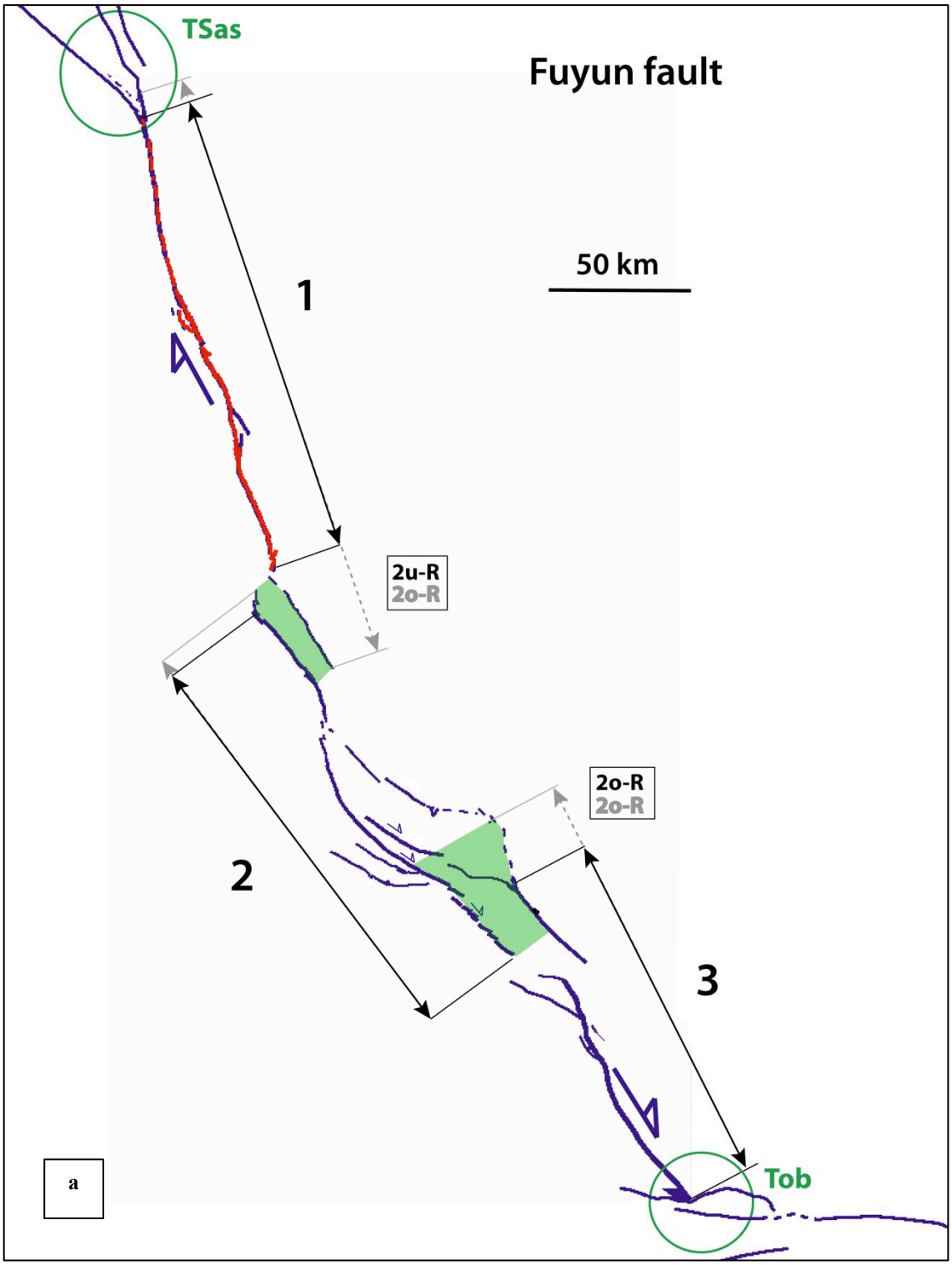


Fig.73: (a) Focus on the major segments of the Fuyun Fault. Same caption as in Fig.72. The segments are numbered from NW to SE and indicated by black arrows parallel to their mean strike. The grey prolongation of the arrows indicates the uncertainties on the segment lengths. The light green zones are the major inter-segment zones (« push-up »). The nature of the inter-segment zones is indicated in letters within boxes explained in Table 6 The nature of the fault tips is indicated in green (Table 6).

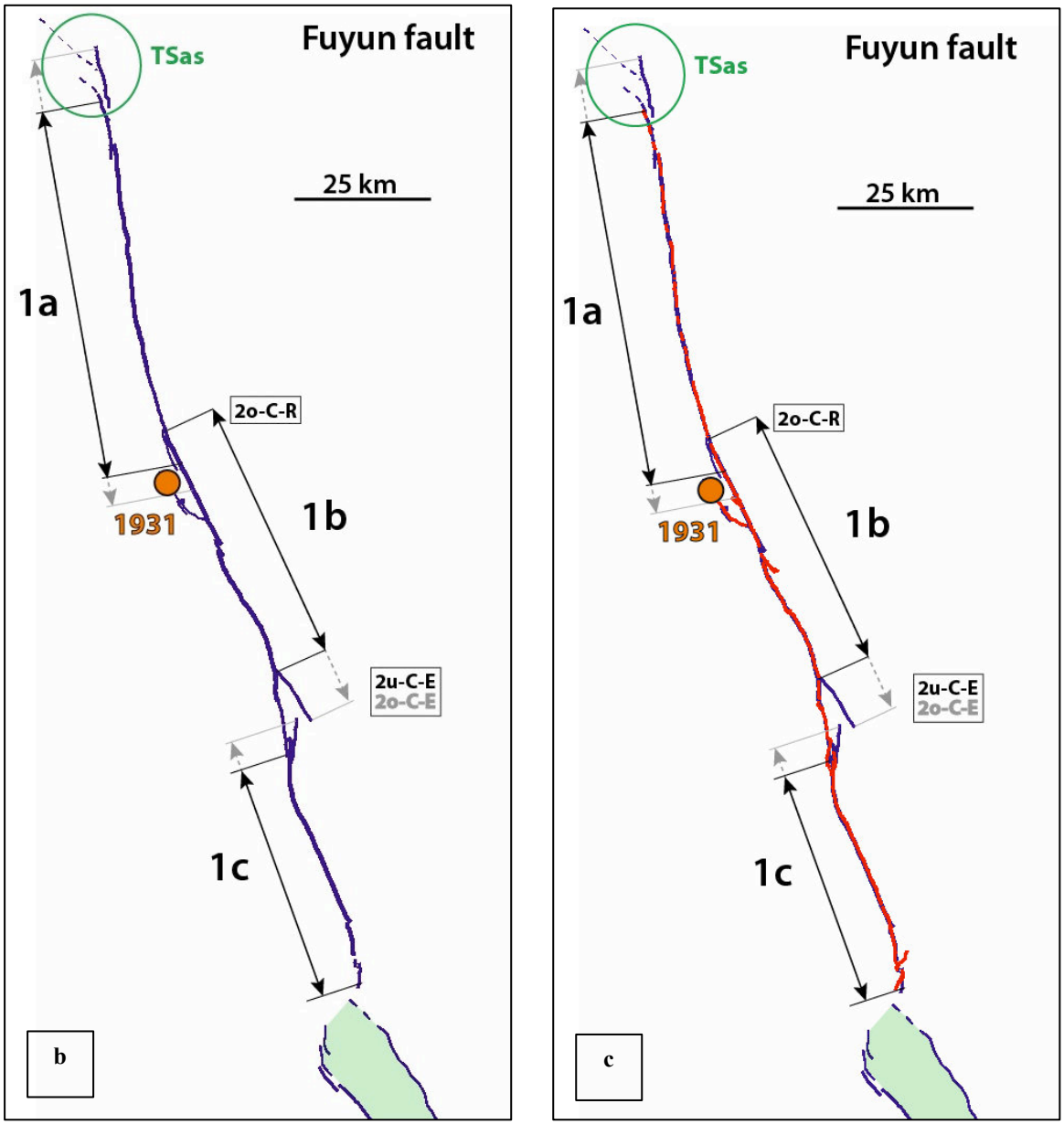


Fig.73: (b) Zoom on the broken section of the Fuyun Fault and map of the secondary segments that form the major segment 1 (same caption as in 73a); (c) surface rupture of the 1931 earthquake is indicated in red.

1931 Coseismic rupture

Surface trace and location on long-term Fuyun Fault :

- The 1931 surface rupture is still clear in the morphology, and visible on Google Earth images (with the exception of a few local places in the north, yet that do not obscure that the rupture is continuous). The surface trace of the earthquake has been precisely mapped and the displacements measured on the field (e.g. Jianbang et al., 1984; Lin and Lin 1998), and

on high resolution Quickbird satellite images (Etchebes 2011; Klinger et al., 2011) (See below).

- Surface rupture of ~165 km long.
- The EQ broke only the Fuyun Fault, over a partial section of its length.
- The EQ broke one major segment only of the Fuyun Fault, the major segment 1. It broke it on its entire length.
- According to its geometry, major segment 1 is divided into three secondary segments, of similar length, 40-70 km. The EQ thus broke the three secondary segments of major segment 1.
- The fault trace is roughly linear along each secondary segment. The mean strike of the fault slightly varies among the secondary segments, as the apparent dip at the surface. Secondary segment 1a has an apparent eastward dip in its northern and central sections, and a westward dip in its southern section. Secondary segments 1b and 1c dip westward. However, on all three secondary segments, the dips oscillate about the vertical, as it is typical on strike-slip faults having a sub-vertical mean dip. A small component of normal slip might be suggested on the northern part of secondary segment 1a.
- Secondary segments 1a and 1b overlap by ~12 km and are directly connected to each other. Their transition is also marked by a pronounced kink in the fault trace, that rotates counterclockwise by ~15° (from segments 1a to 1b) (Type $2'_{O\text{-}C\text{-}R}$). Secondary segments 1b and 1c underlap by ~15 km, but are connected through a pronounced bend in the fault trace (up to 20°) and are separated by an across-fault distance of ~5 km. A small component of normal slip might be expected in the relay zone between secondary segments 1b and 1c.
- The rupture is supposed to have started in a zone that coincides with the connection zone between secondary segments 1a and 1b (Fig.72 & 73). That zone is where the large WNW-trending and hence oblique Irtysh Fault is offset by the Fuyun Fault. The rupture then likely propagated bilaterally towards the north and the south. To the north, it stopped at the end of the fault where the later splays into multiple branches, whereas, to the south, it stopped at the large restraining inter-segment zone that separates the major segments 1 and 2 of the fault.

→ The Fuyun EQ broke only 1 major segment of the Fuyun Fault, major segment 1, which is likely the most mature along the fault. The major segment 1 broke entirely along the 3 secondary segments that form it. These secondary segments are well

connected to each other, in keeping with major segment 1 being fairly mature along the fault.

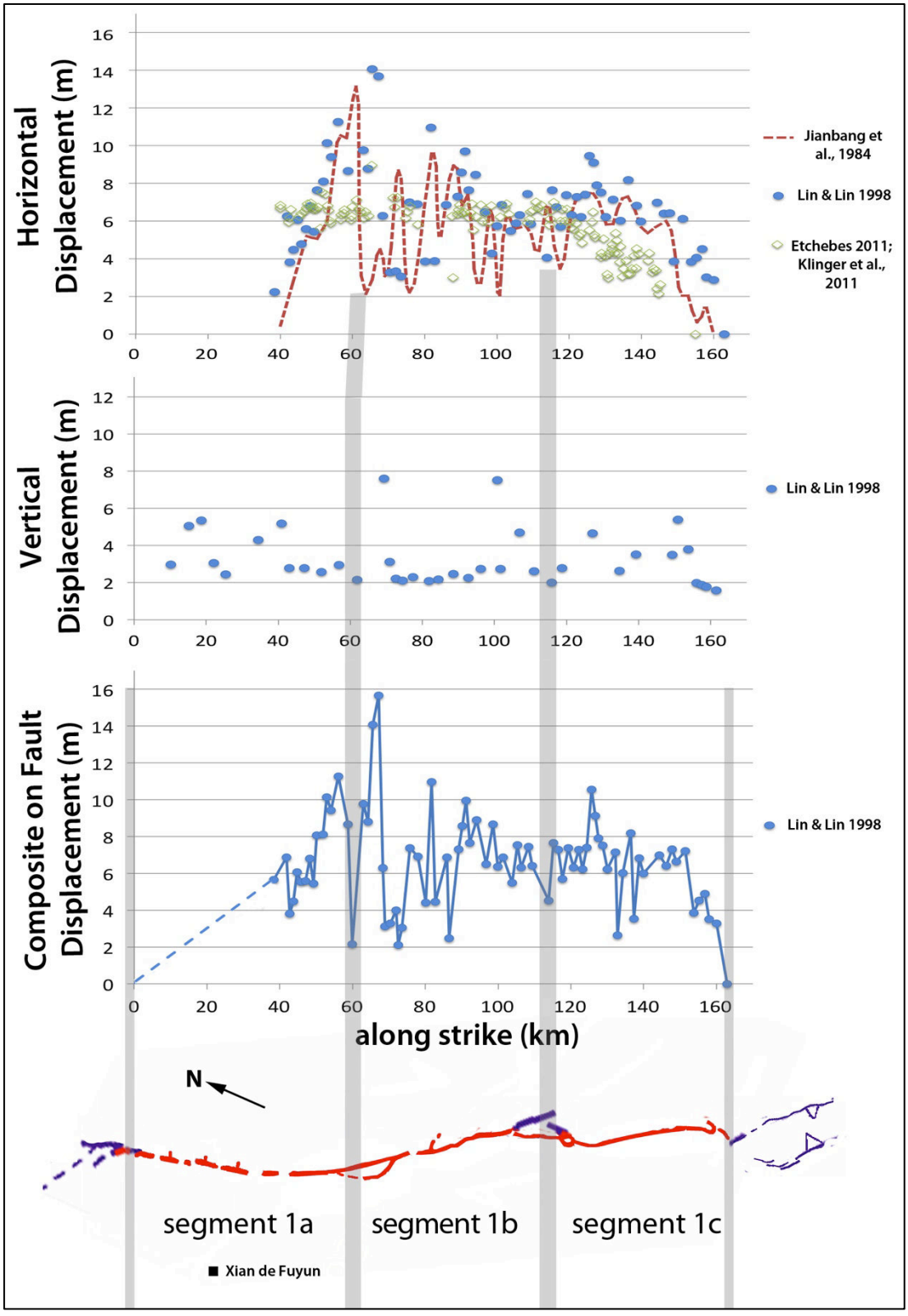


Fig.74: Compilation of coseismic surface measurements of the 1931 earthquake (modified from Klinger et al., 2011). Secondary segments are numbered and intersegment zones are shown by light grey bars.

Coseismic displacements measured at surface :

- *From Field measurements*: The rupture had a dominant component of lateral slip associated with a smaller component of vertical slip. Both slips have been measured on the field, with denser measurements for the lateral slip. Both components are reported on Fig.74. The maximum lateral slip is in the range 13-14 m (Jianbang et al., 1984; Lin and Lin 1998 and references therein), measured nearby the epicenter. It is not clear whether the maximum slip occurred on secondary segment 1a (Jianbang et al., 1984, Fig.74) or 1b (Lin and Lin 1998, Fig.74). About 3 m of vertical slip was measured on segment 1a, with a maximum of ~5 m, and stated as being normal (Lin and Lin 1998). It was postulated that segment 1a is purely normal. In our careful examination of the rupture trace on Google Earth images, we found many evidence of dextral offsets along segment 1a, at least up to the Haizikou Lake. We thus infer that segment 1a is dominantly right-lateral, as the other segments of the fault, but has an additional component of normal slip on its section ~30 km long that extends north of the Haizikou Lake. About 3 m of vertical slip is also measured on segments 1b and 1c, with a maximum of ~7 m, but it is not clear whether that dip-slip component is normal or reverse (Lin and Lin 1998). Because most sections of the fault have a reverse component, we suggest that the vertical component is mainly reverse.
- *The entire slip profiles were measured,* except in the northernmost 40 km of the rupture. The two profiles measured on the field are similar, showing an overall triangular and asymmetric shape, with maximum slip deported toward the north of the rupture, and slip decreasing fairly regularly towards the south. However, the slip end in the south is fairly abrupt in both profiles. Both slip profiles suggest three main slip zones that fairly well coincide with the rupture of secondary segments 1a, 1b and 2-1c (Fig.74).
- *From satellite imagery data*: panchromatic Quickbird satellite images (resolution**:** 60 cm) were used by Etchebes 2011 and Klinger et al. (2011). Only the lateral slip could be measured along the fault except along its 40 km northern section (segment 1a), which was obscured by clouds. A maximum lateral slip of ~9 m was found on segment 1b, about where the field measurements report ~14 m of slip (Fig.74). Overall, the rupture length and the slips measured on satellite imagery are similar to those measured on the field, although the slips are slightly lower in the epicenter region and in the south. The reasons for these differences are unclear.
- Because the rupture was both right lateral and dip-slip, we need to estimate the total composite on-fault slip by combining the two components. We use here the vertical component, and hence consider that the fault dip is vertical. Fig.74 shows the estimated total

on-fault slip (combination was done only where both data exist [dots in Fig.74]). In the ~40 northernmost km of the rupture, the lateral slip was not measured, although our examination of the rupture trace shows that it exists. The slip distribution in this northernmost part of the rupture is thus unknown. **Where it is constrained, the maximum total composite on-fault slip reaches ~15 ± 1 m, on segment 1b (or 1a?). The maximum slip thus occurred on the most mature section of the broken major segment 1.**

Other source parameters :

Calculated from long-period Rayleigh and Love wave spectral densities (Chen and Molnar 1977).

Lat = 46,89° Lon= 90,06°

M0 = 8,5e20 Nm; Focal depth not constrained.

Strike, dip, slip: (-20°, 90°, 0°)

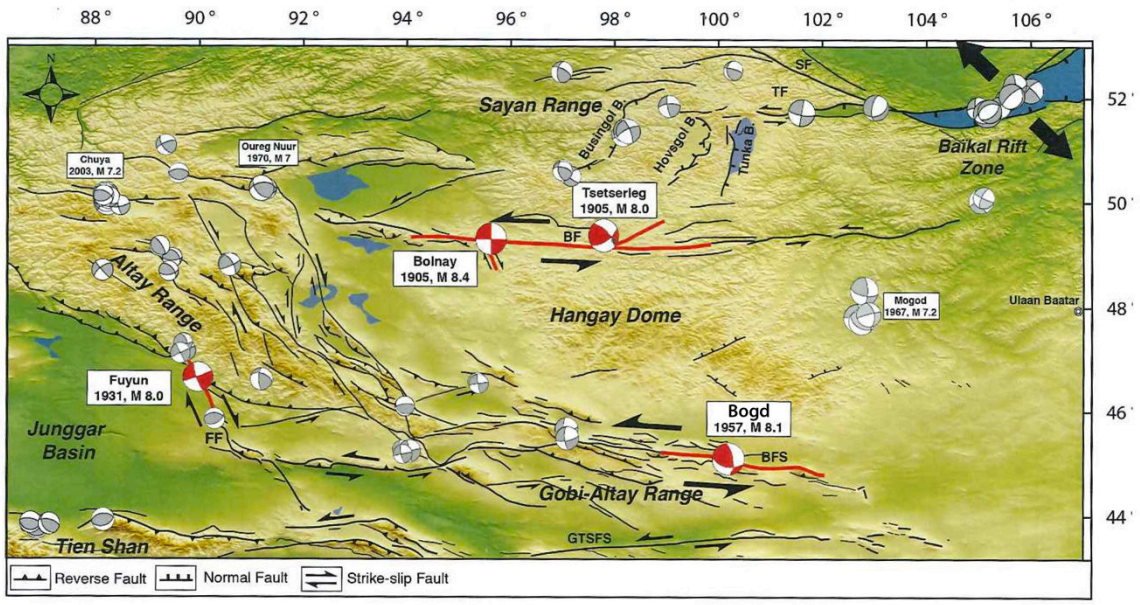


Fig.75: Topographic map showing active fault systems and major earthquakes of western Mongolia and the neighboring regions (from Etchebes, 2011). Focal mechanisms, 6<M<8 in grey, M>B in red (Bayasgalan et al. 2005). Red lines are the surface ruptures associated with the large ones. GTSFS : Gobi-Tian Shan Fault system; BFS : Bogd Fault system; FF : Fuyun Fault ; BF : Bolnay Fault; TF : Tunka Fault; SF : Sayan Fault; B. : Basin

Other information :

Past EQ activity:

- The 1931 EQ belongs to a series of large events that broke in cluster the Mongolian fault system in a very short period of time (Fig.75), between 1905 and 1957: Tsetserleg 1905 (Mw 7.9), Bolnay 1905 (Mw 8.4), Fuyun 1931 (Mw 8.0) et Bogd 1957 (Mw 8.1). This

clustering is described as stress triggering processes between faults resulting from postseismic relaxation (Chery et al., 2001; Pollitz et al., 2003 ; Vergnolle et al., 2003).

- The analysis of cumulative fault offsets on high-resolution satellite imagery suggests that the five most recent pre-historical large earthquakes on the Fuyun Fault produced lateral slips of similar amplitude, on average (i.e., mean slip) 6,3 ± 1,2 m (Etchebes 2011 ; Klinger et al., 2011).

Parameters retained to describe the 1931 Fuyun earthquake (Table 1 & 3) :

Mw ~8.0; M0 ~ 8,5e20 Nm; L ~ 160 km; Dmax surface ~ 15 ± 1 m (total composite slip).

W and depth of the hypocenter are unknown.

Number of segments broken on the Fuyun Fault: 1 major segment entirely, representing the rupture of 3 secondary segments.

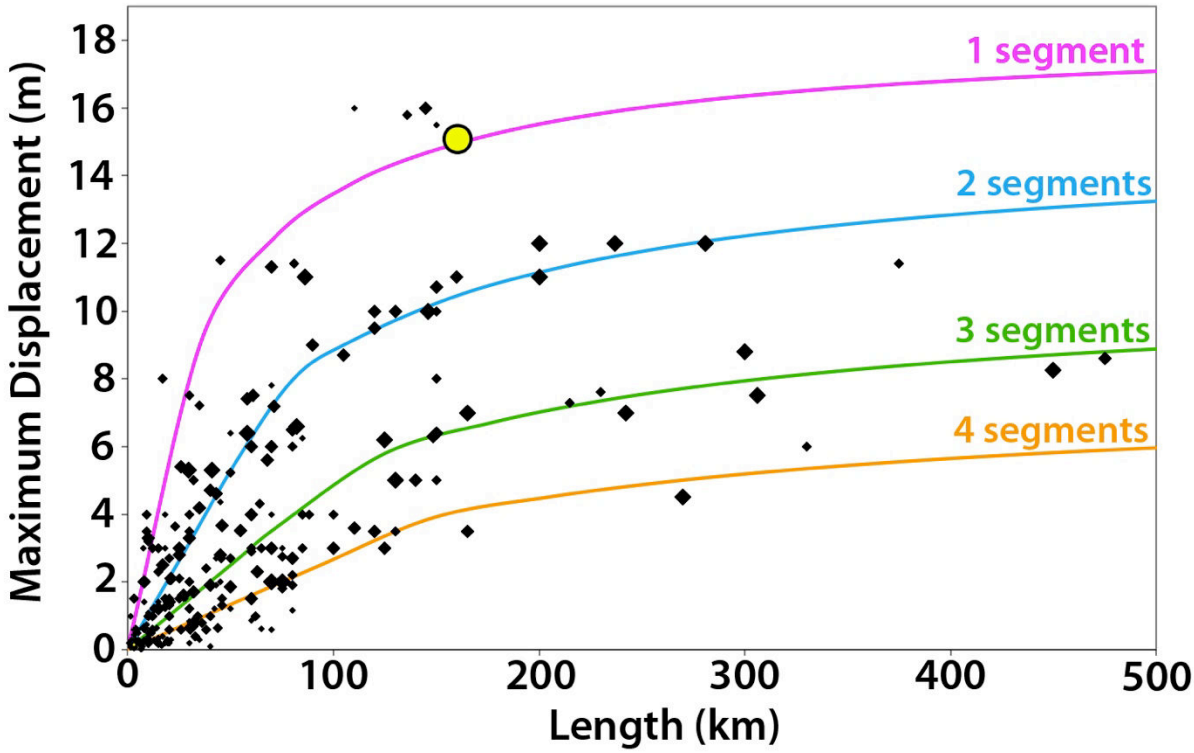


Fig.76: Earthquake displacement-length data measured at surface for 260 historical large continental earthquakes (Mw≥6). The 4 curves indicate the number of major long-term fault segments to have been broken by the earthquakes (modified from Manighetti et al., 2007 and Chapter IV). Yellow dot shows the 1931 Fuyun earthquake surface slip-length data.

The Fuyun earthquake surface slip-length data fall on the first function (pink curve; Fig.76), in keeping with the EQ having broken one major segment of the long-term fault.

References

Bayasgalan, A., Jackson, J. & McKenzie, D. (2005), Lithosphere rheology and active tectonics in Mongolia: relations between earthquake source parameters, gravity and GPS measurements. *Geophysical Journal International*, **163**: 1151–1179. doi: 10.1111/j.1365-246X.2005.02764.x

Calais, E., M. Vergnolle, V. Sankov, A. Lukhnev, A. Miroshnitchenko, S. Amarjargal, & J. Déverchère (2003). GPS measurements of crustal deformation in the Baikal-Mongolia area (1994 – 2002): Implications for current kinematics of Asia, J. Geophys. Res., 108 (B10), 2501, doi:10.1029/2002JB002373.

Chen, W. P., & P. Molnar (1977). Seismic moments of major earthquakes and the average rate of slip in Central Asia, *J. Geophys. Res*., **82**, (20), 2945-2969.

Chéry, J., S. Carretier, & J. F. Ritz (2001). Postseismic stress transfer explains time clustering of large earthquakes in Mongolia, Earth Planet. Sci. Lett., 94, 277–286.

Etchebes, M. (2011). Paléosismologie spatiale : segmentation et scénarios de ruptures sismiques, Applications à deux failles actives décrochantes asiatiques : La faille de Fuyun et la faille de Kunlun, Chine. Thèse. *Université Paris Diderot*, Paris, 387 pp.

Jianbang, S., F. Xianyue, & G. Shumo, Y. Zhang, B. Meixiang, H. Jun et al. (1984). The Fuyun earthquake fault zone in Xinjiang, China, presented at International symposium on continental seismicity and earthquake prediction (ISCSEP), *Seismological Press, Beijing*, 325-346

Klinger, Y., M. Etchebes, P. Tapponnier & C. Narteau (2011), Characteristic slip for five great earthquakes along the Fuyun fault in China Nature Geoscience 4, 389–392, doi:10.1038/ngeo1158

Lin, A., & S. Lin (1998). Tree damage and surface displacement: The 1931 M 8.0 Fuyun earthquake, *Journal of Geol*ogy, **106**, 751-757.

Manighetti, I., M. Campillo, S. Bouley, and F. Cotton (2007), Earthquake scaling, fault segmentation, and structural maturity, *Earth Planet. Sci. Lett*., **253**, 429-438, doi:10.1016/j.epsl.2006.11.004

Molnar, P. & Tapponnier, P. (1975). Cenozoic Tectonics of Asia : Effects of a Continental Collision. *Science,* **189**, 419–426.

Pollitz, F., M. Vergnolle, & E. Calais (2003). Fault interaction and stress triggering of twentieth century earthquakes in Mongolia, *J. Geophys. Res.,* **108**(B10), 2503, doi:10.1029/2002JB002375.

Vergnolle, M., F. Pollitz, & E. Calais (2003). Constraints on the viscosity of the continental crust and mantle from GPS measurements and postseismic deformation models in western Mongolia. *J. Geophys. Res*., **108**(B10), 2502, doi:10.1029/2002JB002374.

Tapponnier, P. & P. Molnar (1977). Active faulting and tectonics in China. *J. Geophys. Res*. **82**, 2905–2930.

Tapponnier, P. & P. Molnar (1979). Active faulting and Cenozoic tectonics of the Tien Shan, Mongolia and Baikal regions, *J. Geophys. Res*., **84**, 3425–3459.

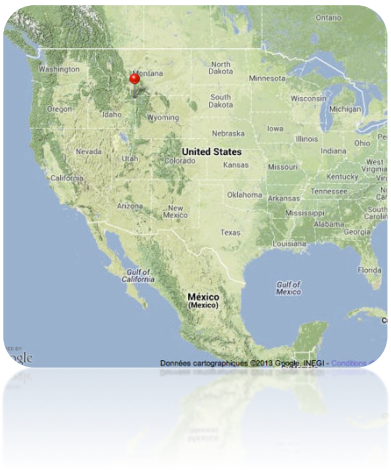
2.9. Hebgen Lake 1959

17/08/1959, Montana, USA

Mw 7.5

Epicenter : 44,80°N-111,20°W

Normal fault



Broken long-term fault

The EQ broke the Hebgen-Red Canyon Fault system, in northeastern part of the Basin and Range.

General characteristics from literature :

- In the literature, the Hebgen-Red Canyon Fault system is taken to be a ~N120°E-trending, ~ 40 km long system made of two distinct normal faults, the Hebgen Fault and the Red Canyon Fault. Our mapping reveals more details, as discussed below.
- The Hebgen-Red Canyon Fault system extends due north of the present Yellowstone caldera, and might be genetically linked to the magmatic activity in this area (Fig.77).
- The fault system would have initiated 0,6-2 Ma ago, deduced from structural correlation between faults and the age of the present Yellowstone Caldera (e.g. Scott et al., 1985; Christiansen 1986).
- Total cumulative slip is not known.
- Fault dip measured on exhumed scarps ranges from 60 to 85°, towards the south (Witkind 1964).
- Long-term slip rate: 0.5 mm/yr of horizontal extension. Assuming that the fault dips by 60-85°, the on-fault long-term vertical slip rate would be 1-6 mm/yr.
- The estimation of the current slip rate is complicated by different factors (Puskas et al., 2007): the proximity of the Yellowstone Caldera induces huge amounts of 'periodical' uplift and subsidence (until 20 mm/yr of amplitude); viscoelastic relaxation following the 1959 earthquake induced more than 30 mm of uplift between 1987 and 2003. Average horizontal

extension rates were calculated from baselines crossing the fault (trilateration and GPS) and range from 3 to 5 mm/yr (Savage et al., 1993; Puskas et al., 2007). Assuming that the fault dips by 60-85°, the on-fault current vertical slip rate would be 6-60 mm/yr. This vertical rate is clearly overestimated and this large range might be due together to non-tectonic –likely volcanic, contributions, to the fault having a shallower dip than supposed, and to the GPS and trilateration measurements having large uncertainties.

→ The Hebgen-Red Canyon Fault system is likely immature (L 40 km, I-Age < 2 Ma, MR < 6 mm/yr).

Architecture and lateral major segmentation, from our mapping (Fig.78) :

- Mapping done from Google Earth, Landsat and ASTER GDEM data combined with literature information.
- Long-term fault trace fairly well expressed in surface morphology and topography. The rupture trace is actually clear, whereas the long-term trace of the fault away from the rupture is more difficult to identify at some places, mainly due to volcanic overlay and to alluvial incision.
- Our mapping defines the fault differently than commonly done in literature (Fig.78). The so-called Hebgen and Red Canyon Faults are actually two segments of the same Hebgen-Red Canyon Fault, whose trace continues further east across and beyond volcanic fields. The EQ thus occurred on a single fault (which we still call "Hebgen-Red Canyon Fault"), trending ~EW overall and being ~75 km long. The curved scarp north of the Hebgen segment does not have the typical geometry of a tectonic fault, but rather is a landslide scarp, as suggested by some authors (Hart et al., 2012).
- To the northwest, the Hebgen-Red Canyon Fault terminates where it intersects a NE-trending lineament similar (Fig.78) to the other lineaments described north of the Snake River Plain (See section Borah Peak) and interpreted as ancient magmatic conduits related to the Yellowstone Hotspot northeastward migration. North of its intersection with the NE lineament, the Hebgen-Red Canyon Fault gives pace to a ~NS-trending, West-dipping normal fault.

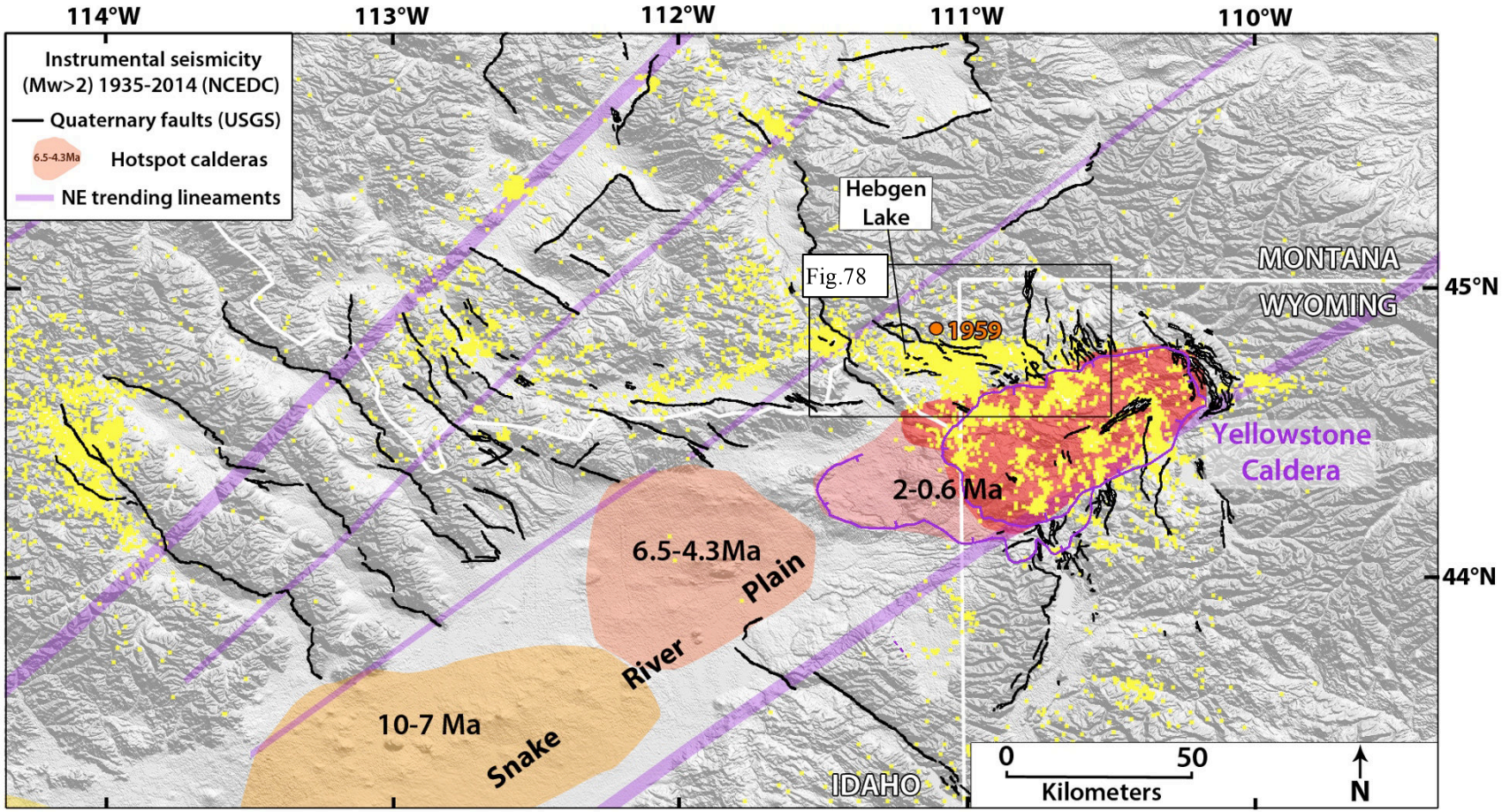


Fig.77: Track of the Yellowstone hotspot (from Smith and Siegel, 2000). Purple lines are related to the hotspot activity (See text for details). Black quaternary faults are from the U.S. Geological Survey and California Geological Survey, 2006. Yellow dots: instrumental earthquake epicenters of Mw>2 from the ANSS catalog from the Northern California Earthquake Data Center. The orange circle shows the 1959 Hebgen Lake epicenter.

- To the southeast, the Hebgen-Red Canyon Fault seems to splay in multiple oblique branches, which all converge towards the present Yellowstone Caldera. This overall geometry suggests that the Hebgen-Red Canyon Fault has been propagating towards the east over geological time. That the eastern fault tip is now meeting the active caldera suggests that the fault is not able to propagate laterally further to the east (active magmatic material acts as a soft barrier to lateral fault propagation, e.g., Manighetti et al., 2001, 2004)
- The Hebgen-Red Canyon Fault is divided into 3 to 5 major, fairly collinear segments (See Fig.78b where they are numbered). The easternmost segments 4 and 5 are difficult to trace for they are partly covered with recent volcanic lavas, and hence are more ambiguous.
- Those 5 major segments have a similar length of 12-18 km.
- The fault trace is fairly linear along each major segment. The clearest major segments 1-3 to the west are separated by left stepping intersegment zones. Major segment 1 also terminates to the east by strongly curving (angle change of 50°; Table 6) and connecting to a secondary NNW Fault. The length of segments and inter-segments are described in Table 6.
- The westernmost segment 1 is flanked to the north by a large landslide whose sliding scarp shows a typical curved shape.

→ The Hebgen-Red Canyon Fault is divided into 5 long-term major collinear segments. It seems to have propagated eastward over geological time, so that its westernmost segments are its most mature sections.

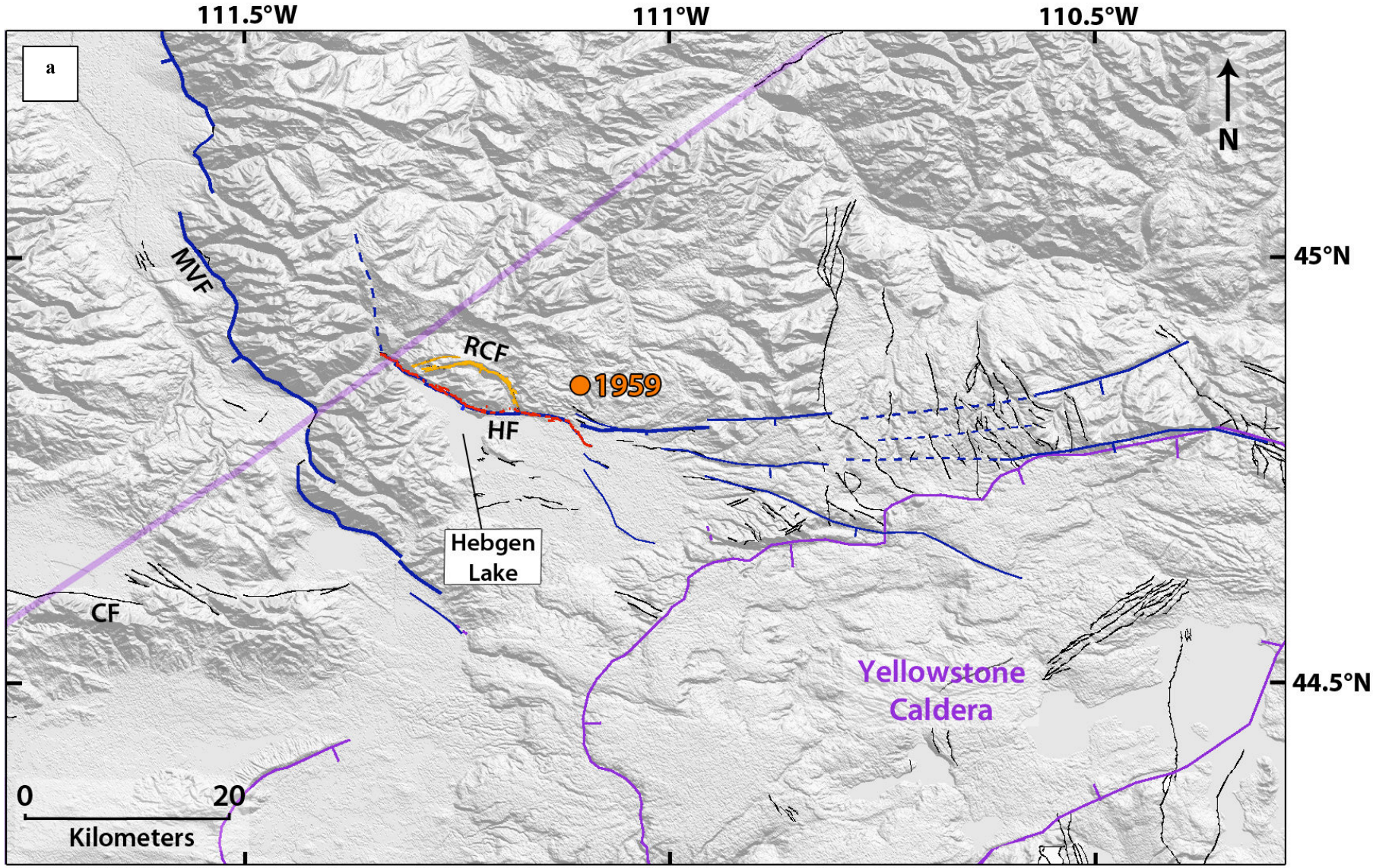


Fig.78:(a) General map of the main long term faults in the Western part of the Yellowsone Caldera. In blue are the major active faults that we mapped. In black are the other Quaternary faults mapped by the U.S. Geological Survey and California Geological Survey, 2006.). Actual limit of the Yellowstone Caldera is shown in purple line. Associated shaded purple lines show the NE trending regional lineaments described in the text. Surface rupture of the 1959 Hebgen Lake earthquake is in red for the main fault, in orange for the suspected landslide scarp. The orange circle shows the 1959 Hebgen Lake epicenter. HF : Hebgen Fault ; RCF Red Canyon Fault ; MVF : Madison Valley Fault ; CF : Centennial Fault.

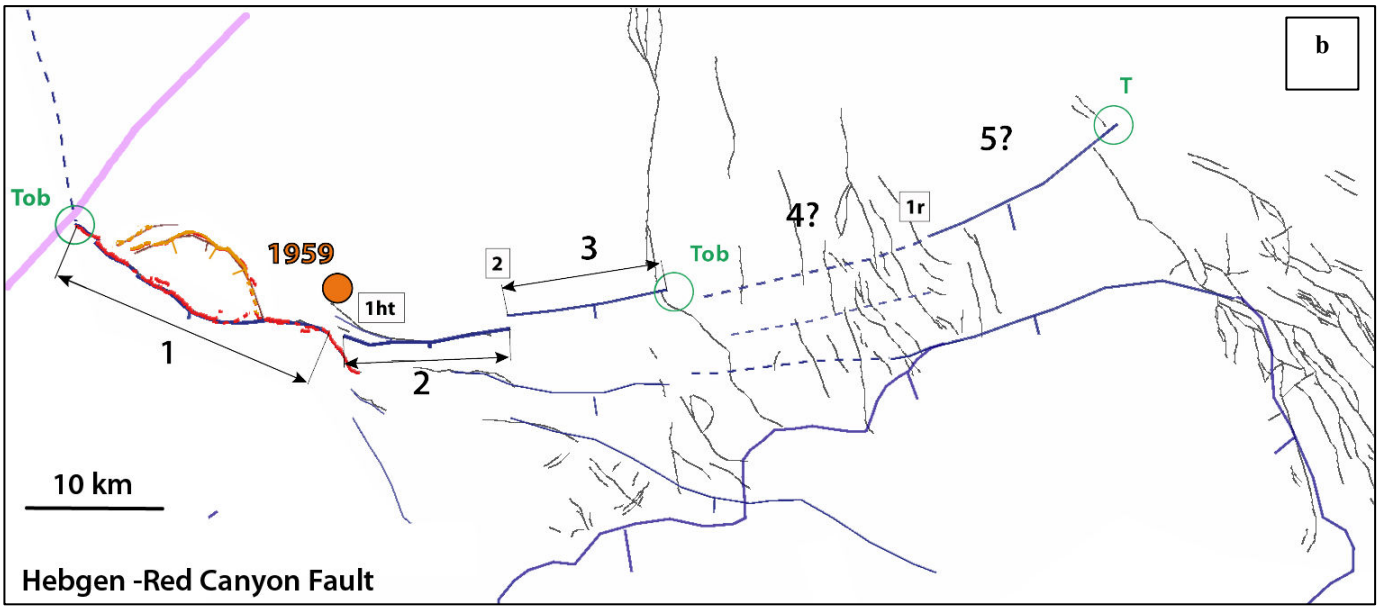


Fig.78: (b) Focus on the major segments of the Hebgen Lake Fault. The segments are numbered from W to E and indicated by black arrows parallel to their mean strike. The nature of the inter-segment zones is indicated in letters within boxes explained in Table 6. The nature of the fault tips is indicated in green (Table 6).

1959 Coseismic rupture

Surface trace and location on long-term fault :

- The 1959 surface rupture is clear on Google Earth images, despite of degradation of the scarps through time (Wallace 1980). From numerous field investigations, the surface trace of the earthquake was precisely mapped, and the displacements measured (See below) (Witkind et al., 1962; Myers and Hamilton 1964; Witkind 1964; Zhang et al., 1999).
- The rupture trace at surface is 25-35 km long (Witkind 1964; Zhang et al., 1999).
- The EQ broke only the westernmost major segment 1 of the Hebgen-Red Canyon Fault. It also induced vertical slip on the curved scarp north of the segment. This slip has been interpreted as tectonic. As other authors before (Hart et al., 2012), we argue that the northern slip is not tectonic but rather is a gravity-induced slippage along the curved landslide scarp, triggered by the EQ shaking and slip.
- Our interpretation thus differs from previous suggestions, which considered the landslide scarp as a distinct fault segment (e.g. De Polo et al., 1991).
- The hypocenter position is not well defined and changes among various analyses (Ryall 1962). In all analyses however, the hypocenter locates nearby the intersegment zone that

separates major segments 1 and 2. The rupture thus likely propagated unilaterally towards the northwest (Doser et al., 1985).

→ The Hebgen Lake EQ broke only 1 major segment of the long-term Hebgen-Red Canyon Fault. It actually broke the westernmost and most mature segment of the fault.

Coseismic displacements measured at surface (Fig.79):

- *From Field measurements*: Maximum vertical displacement of ~5,5 m measured on major segment 1, at its western end (Witkind et al., 1962; Myers and Hamilton 1964; Witkind 1964; Zhang et al., 1999).
- Because of the confusion with the landslide, several meters of slip were inferred in the central part of the rupture. Part of this slip is misleading for it results from gravity-induced collapse of the landslide along its scarp (in orange Fig.79). The central part of the slip profile is thus basically unknown.
- Despite of those limitations, the slip profile appears asymmetric and possibly triangular, with the maximum slip deported at the western end of the rupture.
- *No GPS or Insar measurement* available at the time of the Hebgen Lake EQ.

→ Maximum slip of 5.5 m well measured at surface, on the most mature segment of the fault.

Other source parameters :

- Hypocenter location is not well constrained. However, Murphy and Brazee (1964) and Doser (1985) both suggest a depth of ~12 km.
- Doser (1985) found that two subevents occurred during the mainshock: one of M0=3e18 Nm during 4s and another one of M0=7e20 Nm occurring 5s later and over 10s. Both had a similar focal mechanism (strike 102°/dip 60°) attesting of normal faulting. The two sub-events likely coincide with the rupture of the two secondary segments that form major segment 1 (1a and 1b, Fig.79).

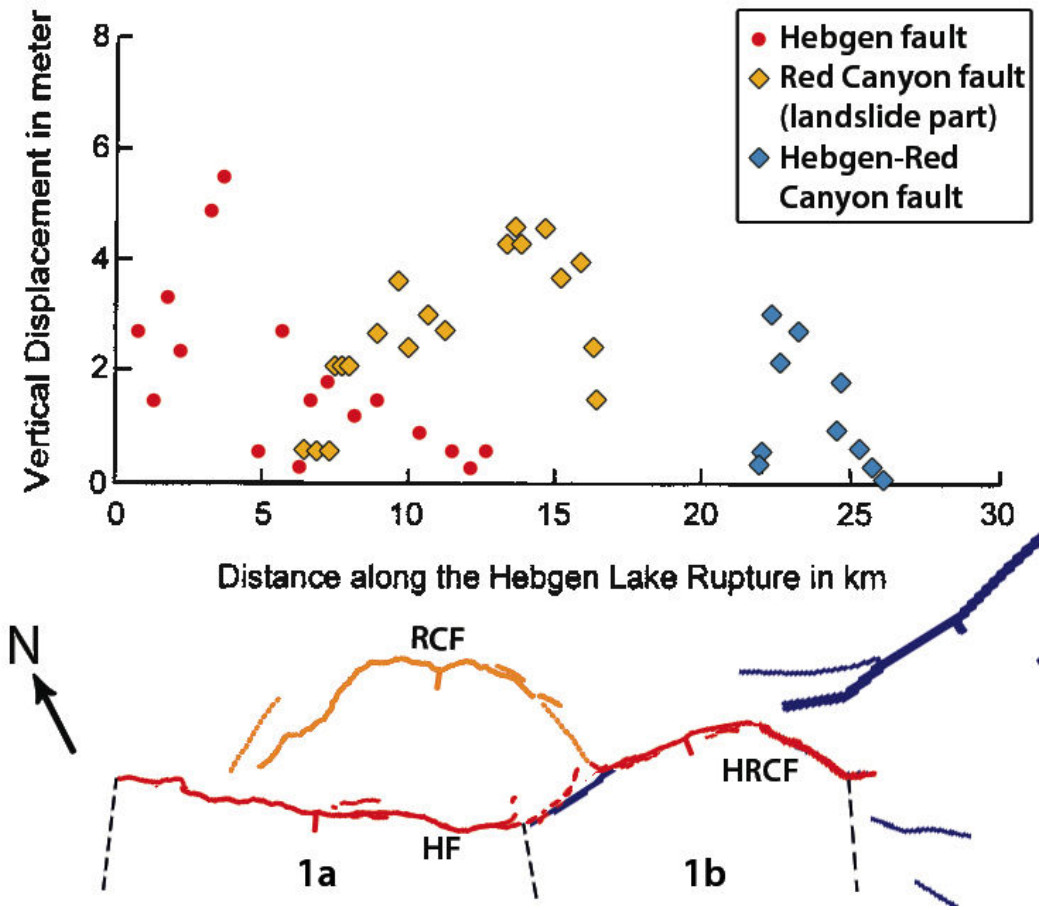


Fig.79: Co-seismic slip profile measured at surface for each fault sections (from Myers and Hamilton 1964). RCF : Red Canyon Fault ; HF : Hebgen Fault ; HRCF : Hebgen-Red Canyon Fault.

Other information :

1959 EQ:

- Two large aftershocks of Mw ~6.5 occurred 1h20 min and 8h50 min after the mainshock (they were recorded at Berkeley/Pasadena and reported in many studies; e.g. Murphy and Brazee 1964; Tocher 1962; Steinbrugge and Cloud 1962). However uncertainties exist on their magnitude. As a matter of fact, the magnitude of the mainshock was estimated at 7.1 in 1960 (Pasadena) while it is now estimated at 7.3-7.5 (USGS-UUSS).
- Geodetic data (high-precision leveling surveys) evidenced a pronounced doming (over 15 cm) over at least the 25 years that preceded the Hebgen Lake earthquake (Reilinger et al., 1977; Reilinger 1986). The inflation was likely due to magma intrusion in the area. It is not clear how those magmatic movements interacted with the tectonic fault and slip. Because of such a magmatic context, the postseismic deformations (over 30 cm of elevation change across the fault) were interpreted as resulting mainly from viscoelastic relaxation (Reilinger 1986).

Past EQ activity:

- Zreta and Noller (1998) used cosmogenic 36Cl techniques to date the exhumation phases of the central scarp of major segment 1. They found evidence for 6 large prehistorical earthquakes, having occurred in clusters at three periods of time, ~37 ka, 24-20 ka, and 7-0 ka. Those periods of intense seismic activity were separated by more quiescent times.

Parameters retained to describe the 1959 Hebgen Lake event (Table 3):

Mw ~7.5; M0 ~ 7e20 Nm; L ~ 25 km; Dmax surface ~5.5 m; Duration ~ 19 s; *Hypocenter* : Z ≈ 12 km.

Number of major segments broken on the long-term fault: 1 major segment.

The Hebgen Lake earthquake surface slip-length data fall fairly well on the first function (pink curve; Fig.80). This is in keeping with the EQ having broken one major segment only of the immature Hebgen-Red Canyon Fault.

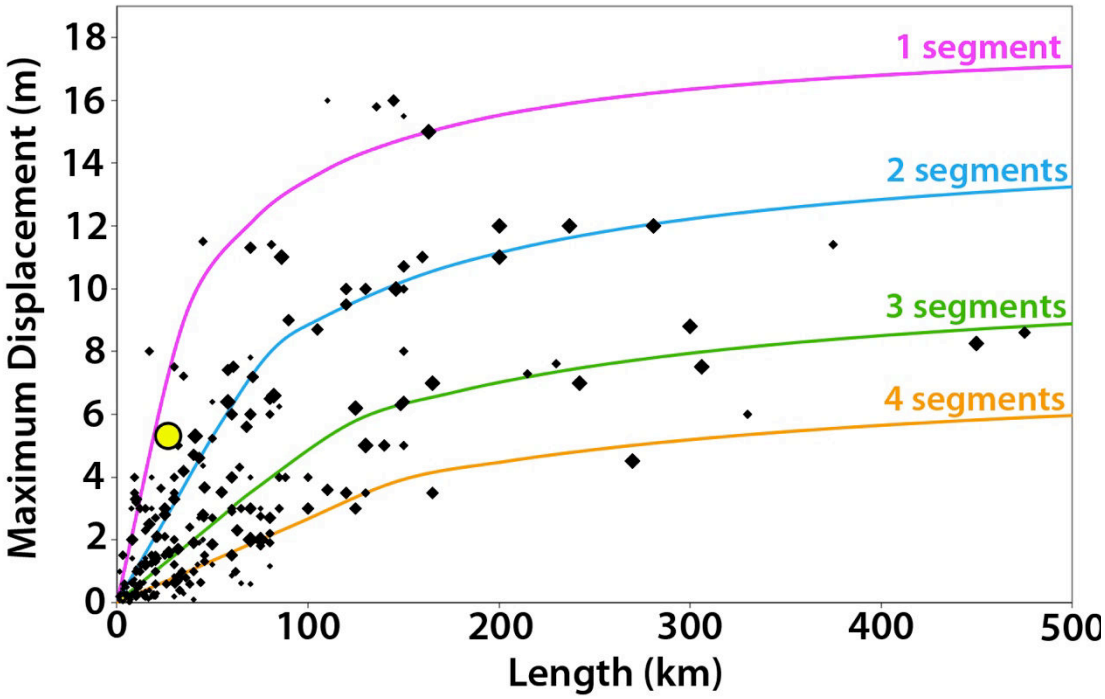


Fig.80: Earthquake displacement-length data measured at surface for 260 historical large continental earthquakes (Mw≥6). The 4 curves indicate the number of major long-term fault segments to have been broken by the earthquakes (modified from Manighetti et al., 2007 and Chapter IV). Yellow dot shows the 1959 Hebgen Lake earthquake surface slip-length data.

References

Christiansen, R. L. (1986) The Quaternary and Pliocene Yellowstone Plateau Volcanic Field of Wyoming, Idaho,and Montana. *U.S. Geol. Surv. Professional Paper* **729**-G, 145 pp.

dePolo, C. M., Clark, D. G., Slemmons, D. B. & Ramelli, A. R. (1991). Historical surface faulting in the Basin and Range Province, western North America: implications for fault segmentation. *J. Struct. Geol*. **13**, 123-136.

Doser, D. I. (1985) Source Parameters and faulting processes of the Hebgen Lake, Montana, earthquake sequence. *J. Geoph. Res.,* **90,** B6, 4537-4555

Manighetti, I., M. Campillo, S. Bouley, and F. Cotton (2007), Earthquake scaling, fault segmentation, and structural maturity, *Earth Planet. Sci. Lett*., **253**, 429-438, doi:10.1016/j.epsl.2006.11.004

Murphy, L. M. & Brazee, R. J. (1964). Seismological investigations of the Hebgen Lake earthquake. *U.S. Geol. Surv. Professional Paper* **435**-I, 13–17.

Myers, W.B. & Hamilton, W. (1964). Deformation accompanying the Hebgen Lake earthquake of August 17, 1959. *U.S. Geol. Surv. Professional Paper* **435**-I, 55–98.

Puskas, C. M., R. B. Smith, C. M. Meertens, & W. L. Chang (2007), Crustal deformation of the Yellowstone–Snake River Plain volcano-tectonic system: Campaign and continuous GPS observations, 1987–2004, *J. Geophys. Res.*, **112**, B03401, doi:10.1029/2006JB004325.

Reilinger, R. E., G. P. Citron, & L. D. Brown, Recent vertical crustal movements from precise leveling data in southwestern Montana, western Yellowstone National Park, and the Snake River plain, *J. Geophys. Res*., **82**, 5349-5359

Reilinger, R. E. (1986). Evidence for Postseismic Viscoelastic Relaxation Following the 1959 M=7.5 Hebgen Lake, Montana, Earthquake. *J. Geophys. Res*., **91**, 9488-9494

Ryall, A. (1962) The Hebgen lake, Montana, earthquake of august 18, 1959 : P Waves. *Bull. Seism. Soc. Am*., **52**, 2, 235-271.

Savage, J. C., M. Lisowski, W. H. Prescott, & A. M. Pitt (1993), Deformation from 1973 to 1987 in the epicentral area of the 1959 Hebgen Lake, Montana, earthquake (Ms = 7.5), *J. Geophys. Res*., **98**, 2145–2153.

Scott, W.E., Pierce, K. L. & Hait, M. H. Jr. (1985) Quaternary tectonic setting of the 1983 Borah Peak earthquake, Central Idaho, *Bull. Seism. Soc. Am*., **75**, 1053-1066.

Steinbrugge, K. V. & Cloud, W. K. (1962). Epicentral intensities and damage in the Hebgen lake, Montana, earthquake of august 17, 1959. *Bull. Seism. Soc. Am*., **52**, 2, 181-234

Tocher, D. (1962). The Hebgen lake, Montana, earthquake of august 17, 1959, MST. *Bull. Seism. Soc. Am*., **52**, 2, 153-162.

Wallace, F. E. (1980). Degradation of the Hebgen Lake Fault scarps of 1959, *Geology,* **8**, 225-229

Witkind, I. J. (1964) Reactivated faults north of Hebgen Lake. *U.S. Geol. Surv. Professional Paper* **435**-I, 37–50.

Witkind, I. J., Myers, W.B., Hadley, J. B., Hamilton, W. & Fraser, G. D. (1962). Geologic features of the earthquake at Hebgen Lake, Montana, August 17, 1959. *Bull. Seism. Soc. Am*., **52**, 2, 163-180

Zhang, P., Mao, F. & Slemmons, D. B. (1999). Rupture terminations and size of segment boundaries from historical earthquake ruptures in the Basin and Range Province. *Tectonophysics,* **308**, 37–52.

Zreta, M. & Noller, J. S. (1998). Ages of Prehistoric Earthquakes Revealed by Cosmogenic Chlorine-36 in a Bedrock Fault Scarp at Hebgen Lake. *Science,* **282,** 1097-1099.

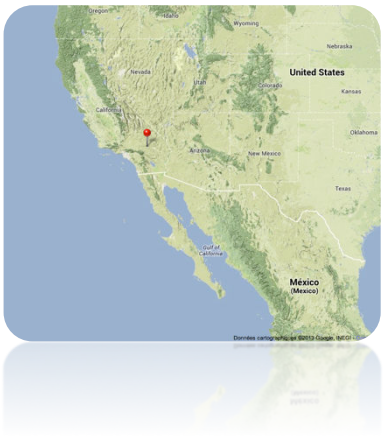
2.10. Hector Mine 1999

16/Oct/1999, California, USA

Mw 7.1

Epicenter (USGS) : 34.59°N-116.27°W

Right-lateral strike-slip



Broken long-term fault

According to our mapping, the Hector Mine EQ basically broke one single long-term fault of the East California Shear Zone (ECSZ) in the Mojave Desert, California (Fig.81): the Lavic Lake- Bullion-Mesquite Lake Fault zone (LBM Fault, best shown in Fig.83).

General characteristics of the ECSZ from literature:

- Mapping done from Google Earth, Landsat and ASTER GDEM data combined with dense literature information (e.g., U.S. Geological Survey and California Geological Survey, 2006).
- The ECSZ is a network of closely spaced (5-20 km spacing), right-lateral, sub-parallel, NW-trending faults (Dibblee 1961).
- The ECSZ faults are bounded and interrupted to the north and south by ENE-trending large right-lateral faults (some with a small reverse component) (Garlock in the north; Pinto and Blue Cut in the south; Fig.82). Smaller ENE faults also exist within the ECSZ (See below).
- The ECSZ faults are likely involved in bookshelf faulting horizontal rotations (Fig.82). Since the faults are right lateral, the rotations must be counterclockwise (e.g. Tapponnier et al., 1990; Manighetti et al., 2001). Our mapping shows that most of the faults have their trace interrupting or abruptly rotating in the ~ middle of the ECSZ zone; consequently, the northern fault traces appear more rotated counterclockwise than their southern counterparts. This pattern suggests that the rotating blocks and bounding faults have broken in their ~central part to accommodate a differential rotation, greater in the north than in the south.

The central breaking zone is thus likely a tear zone (that we call the Barstow tear zone), as commonly observed in bookshelf faulting systems (e.g., Manighetti et al., 2001; Walpersdorf et al., 2014).

- In the southern half of the ECSZ, most of the rotating faults have their strike markedly changing or interrupting along a "line" coinciding with the eastward prolongation of the so-called "northern frontal thrust system". This systematic change in fault strike might suggest that the rotating faults and blocks have also broken along another, smaller tear zone, that we call the "Southern Mojave tear zone" (Fig.82).
- Most of the rotating major faults have developed splay faults at their tips, and most of these splays extend from and south of the Southern Mojave tear zone. The other splays are at the northern tips of the faults. These multiple oblique branches might result from differential rotations, and/or indicate the sense of lateral propagation of the principal faults (Fig.82). In this later case, we infer that some of the rotating faults have been propagating northward over geological time, whereas others have propagated southwards (See Fig.82 where sense of propagation is indicated by arrows).
- The ECSZ is taken to have initiated at most ~ 10 Ma ago (Dibblee 1961; Garfunkel 1974; Dokka 1983; Dokka and Travis 1990a). The crosscutting relationships between the ENE and the NW faults suggest that the two systems have been active over the same period of time, i.e. were coeval.
- The total cumulative lateral displacement accommodated across the ECSZ fault zone is estimated from geological measurements to be ~12 km in the northern half of the zone (Dokka and Travis 1990a and references therein) and 27-38 km in the southern half of the zone (Dokka 1983; Dokka and Travis 1990a and references therein). The northern measurements seem underestimated however. Block rotation models rather suggest total lateral slip of 65-105 km (e.g. Garfunkel 1974; Dokka and Travis 1990a; 65 km is the most admitted value in the literature). If we consider that about 6 major rotating faults (See Fig.82) accommodate this total cumulative lateral slip, each might have produced a total cumulative lateral slip of about 5-10 km.
- Total, long-term lateral slip rate across the southern part of the ECSZ zone is 6-12 mm/yr (Dokka and Travis 1990b). Again, if we consider that about 6 major rotating faults (See Fig.82) accommodate this total lateral slip, each might have slipped at 1-2 mm/yr over geological time.

- Current, total lateral slip rate across the southern part of the zone is ~ 12 mm/yr (GPS; Sauber et al., 1994; McClusky et al., 2001). Similarly, each major rotating fault might thus be currently slipping at ~2 mm/yr.

General characteristics of the broken faults from literature (Fig.83) :

- Right lateral faults oriented NW-SE, about 90 km long.
- Cumulative lateral displacement of 6-14 km on the Pisgah Fault (Dokka 1983), estimated from offset measurements of volcanic and sedimentary rocks.
- Long-term lateral slip rate (late Cenozoic) of ~ 0.8 mm/yr on the Pisgah Fault, estimated from offset measurements of late Cenozoic basalt flows (Oskin et al., 2007 and references therein).

→ The ECSZ faults, including the LBM Fault, which broke in the Hector Mine event, are immature faults (L ~100 km, I-Age < 10 Ma, D_{total} < 10 km, and MR ~ 1-2 mm/yr).

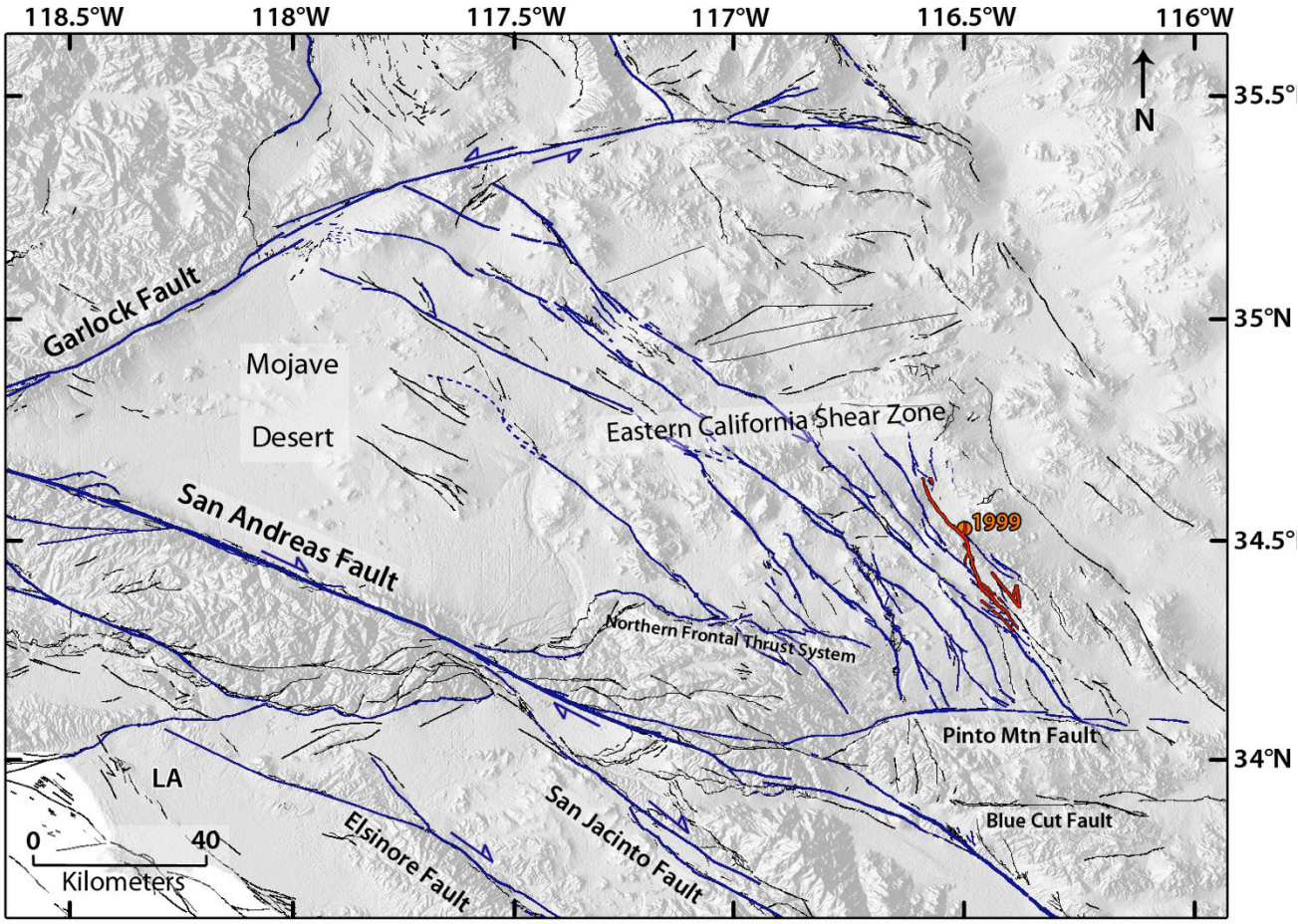


Fig.81: General map of long term faults in the East California Shear Zone. In blue are the major active faults that we mapped. In black are the other Quaternary faults mapped by the U.S. Geological Survey and California Geological Survey, 2006. In red is the surface rupture of the 1999 Hector Mines earthquake (from Treiman et al., 2002). The orange circle shows the 1999 Hector Mine epicenter.

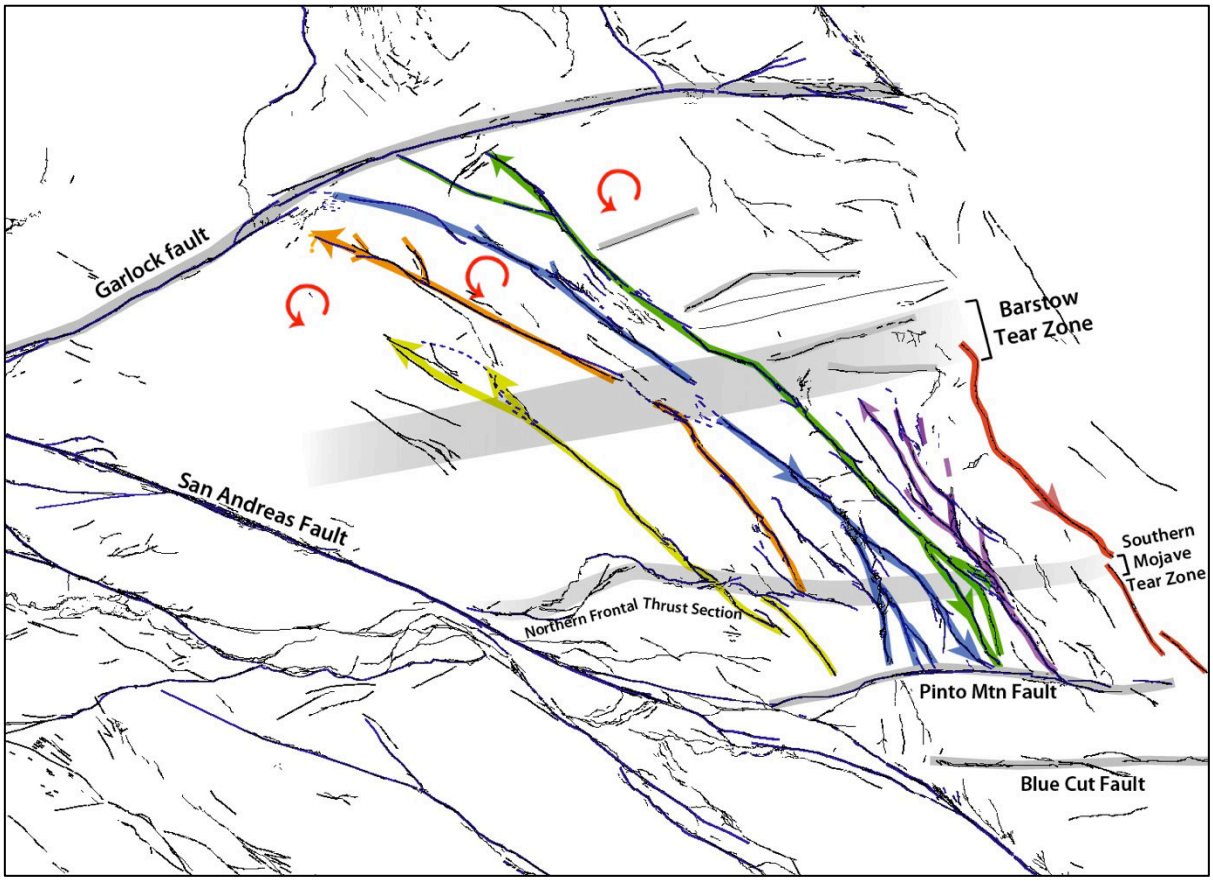


Fig.82: Same active fault map as in Fig.81, with focus on the major fault systems in the East California Shear Zone (ECSZ) and their direction of long-term propagation. Yellow: Helendale Fault; Orange : Lockhart-Lenwood faults; Blue : Harper-Camp Rock-Emerson-Homstead Valley-Johnson Valley fault system; Green : Blackwater-Calico faults; Pink: Pisgah-Bullion-Mesquite Lake faults; Red: Ludlow Fault. Red arrows indicate the block rotations. Shaded areas show the E-W trending "tear zones" through the ECSZ.

Architecture and lateral major segmentation of the broken fault, from our mapping (Fig.83):

- The LBM Fault strikes NNW and is ~ 90 km long. To the south, it stops at the ~perpendicular intersection with the Pinto Fault (Tperp. termination type). To the north, the fault trace vanishes due south of the perpendicular Barstow tear zone.
- The fault is associated with many splaying faults striking NNW to NW in the west compartment and almost N-S in the east compartment. The splaying network is developed all along the fault except in its southernmost third. This overall pattern suggests that the LBM Fault has been propagating northward over geological time.
- The LBM Fault is divided into 5 major collinear segments, of similar length, 15-22 km, most are hardly connected to each other at the surface. The fault trace is fairly linear along major segments 1, 4 and 5 but it is more sinuous or discontinuous along central segments 2

and 3. The trace of segment 3 indeed shows a bend in its center, whereas segment 2 is made of several branches forming a right-stepping compressive echelon in a mean NNW direction. The bend in the segment 3' trace coincides with its connection with a splaying fault (Pigash-Bullion Fault zone, USGS) that seems to be older than the LBM Fault but reactivated by it, as a splaying feature.

- Segments 1 and 2 are fairly well connected by a step-over (relay of type $2_{O\text{-}C}$ and across strike distance < 1 km), in keeping with their likely older age along the fault. Segments 2 and 3 are separated with a large extensive step-over (type $2_{O\text{-}C\text{-}E}$ of 3 km width). Also, a number of splaying oblique faults depart from the segment 2-3 connection zone. Furthermore, this complex zone is where the "southern Mojave tear zone" is supposed to extend, in that case possibly hampering the connection between the segments 2 and 3 (Fig.82). Segments 3 and 4 are connected to each other through a pronounced bend and hence a relay zone of type 1r-sp. East of the bend, an older fault exists –the Bullion Mountains Fault zone (Fig.83) that might have been offset by the most recent LBM Fault. Segment 5 is more disputable because the fault trace is not clearly expressed at the ground surface. Segments 4 and 5 are hardly connected to each other at the surface, being separated by a large (≅2 km) and obviously recent pull-apart (note that due east of the pull-apart, a volcanic field has developed). This is in keeping with the likely young age of segments 4 and 5. East of segment 4, a few splaying, subtle and hence likely recent faults have developed.

→ The Hector Mine EQ broke a section of a ~100 km long, NNW-striking, right-lateral fault, the LBM Fault. That fault is made of 5 major collinear segments, and has propagated northward over time. Its northernmost third seems very recent. Young and subtle splaying, ~ N-S faults flank to the east the recent northern part of the LBM Fault.

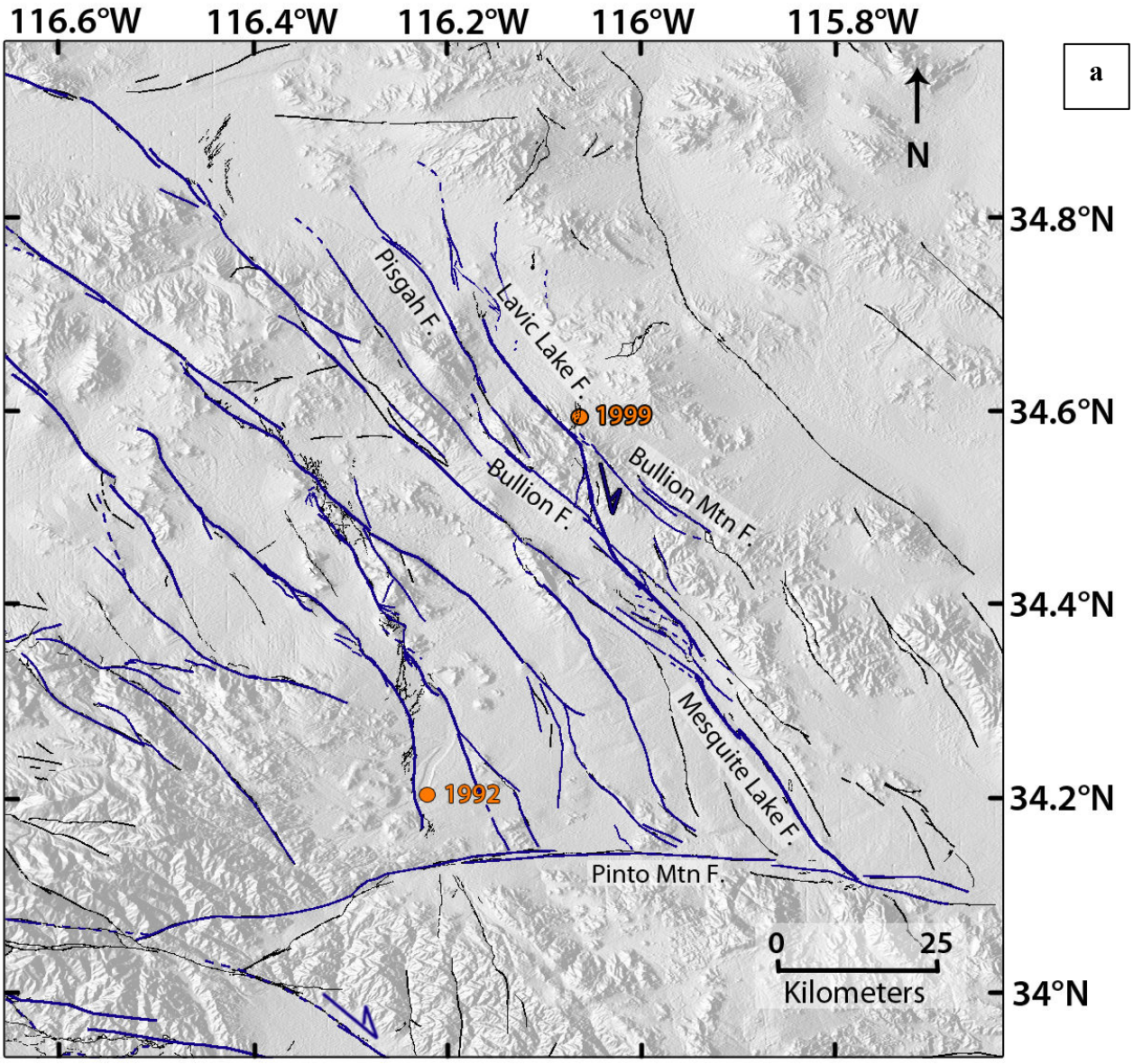


Fig.83: (a) Zoom on the broken 'LBPM' fault (same caption as in Fig.81). The epicenter location of the 1992 Landers earthquake is also indicated by the orange circle.

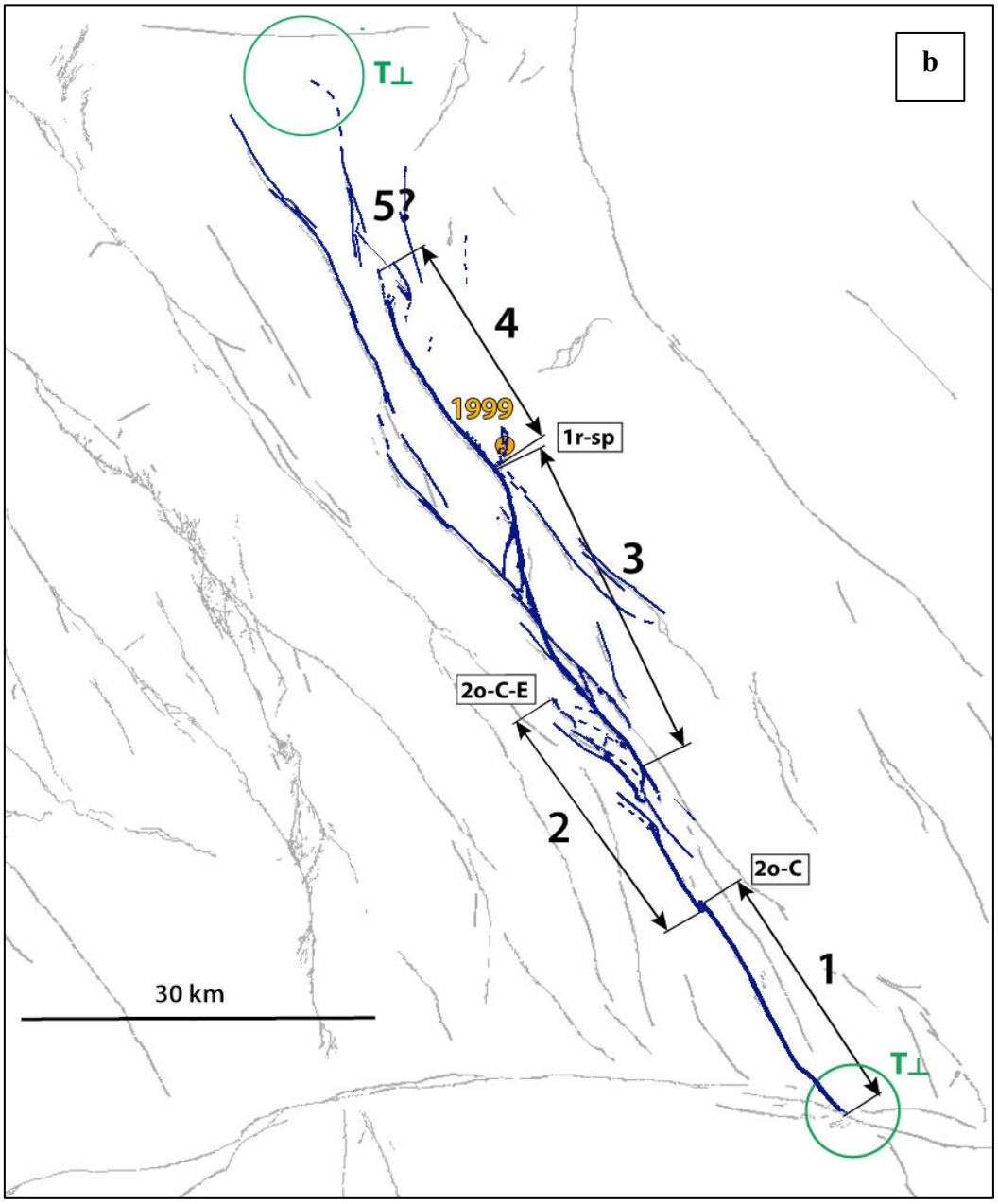


Fig.83: (b) Map of the major segments that form the LBPM Fault (in blue). The orange circle show the 1999 Hector Mine epicenter. The segments are numbered from SE to NW and indicated by black arrows parallel to their mean strike. The nature of the inter-segment zones is indicated in letters within boxes explained in Table 6. The nature of the fault tips is indicated in green (Table 6)

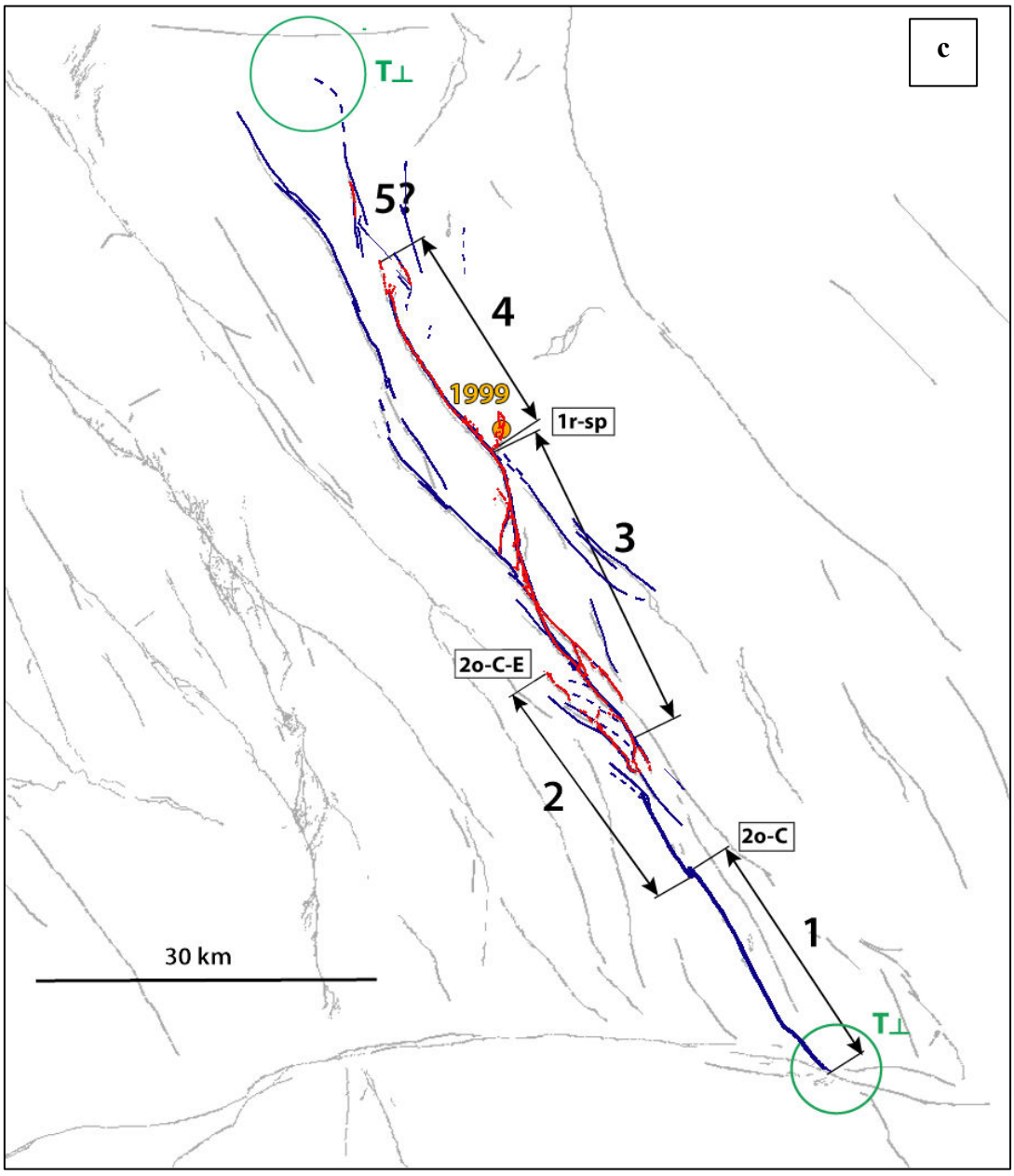


Fig.83: (c) Same caption as in Fig.83b. In red is the surface rupture of the Hector Mine 1999 earthquake (from Treiman et al., 2002).

1999 Coseismic rupture

Surface trace and location on the long-term fault:

- The 1999 surface rupture is still clear on satellite images (Google Earth). The surface trace of the earthquake has been precisely mapped, and the displacements measured (See below), both on the field (e.g. USGS et al., 2000; Treiman et al., 2002) and from radar imagery (Sandwell 2000, 2002; Peltzer et al., 2001; Jónsson et al., 2002; Simons et al., 2002; see Fig.84a).

- Total surface rupture of ~50 km (Fig.83; Treiman et al., 2002). InSAR data well agree with surface mapping and give additional insights on slip at the tips of the rupture (Ltotal ~ 55 km; Sandwell 2000, 2002; Peltzer et al., 2001; Jónsson et al., 2002; Simons et al., 2002).
- The EQ mainly broke 2 major segments of the LBM Fault: segments 3 and 4. Little slip also occurred on a few small faults connecting or associated with the two segments, on a very small part of segment 5, and on a few small faults connecting segments 3 and 2.
- The principal rupture length on segments 3 and 4 is thus ~40 km.
- The EQ initiated nearby the connection between segments 3 and 4. It thus propagated bilaterally from that initiation site, to rupture segments 3 and 4. It stopped to the north before passing the large pull-apart that separates major segments 4 and 5. It mainly stopped to the south within the large, densely faulted step-over between major segments 2 and 3.
- The aftershock distribution (Fig.84b) suggests that at least two secondary splaying faults have also broken during the EQ, east of the northern termination of the rupture. However, no slip was observed along those features at the ground surface. Taken together, the rupture traces form a Y-shape pattern.

→ The Hector Mine EQ broke two central, major segments of the LBM Fault. It also produced minor slip on a few small faults in between the segments. The rupture initiated at the intersegment zone between the two segments and propagated bilaterally. Splays were also activated during or right after the event in the northeastern side off the rupture.

Coseismic displacements measured at surface:

- *From Field measurements*: Measured maximum lateral slip of 5.3 m (USGS et al., 2000; Treiman et al 2002), near the hypocenter location, on major segment 3 (Fig.85).
- *From InSAR data and modeling*: Maximum lateral slip estimated of 6-6.5 m (Peltzer et al., 2001; Jónsson et al., 2002; Sandwell 2002; Simons et al., 2002). The decorrelation of the InSAR images close to the fault hampered however a robust slip estimation (Fig.84a).
- The on field measured and the Insar-inferred surface slip profiles are fairly similar. The slip distribution has an overall triangular and symmetric envelope shape. In more details, three major slip bumps are revealed that well coincide with the broken segments that we identified. The first bump is ~15 km long and has a maximum slip of ~ 3 m; it well coincides with the rupture of major segment 4. The second bump is ~20 km long and has a maximum slip of 5-6 m; it well coincides with the rupture of major segment 3. The third

bump is much more minor; it is ~10 km long and has a maximum slip of ~ 1 m; it coincides with the slip of the few secondary small faults between segments 2 and 3.

- We note that the individual slip profiles along major segments 3 and 4 have an overall triangular shape, tapering in opposite direction, with each taper pointing in the direction of the rupture propagation.

→ **The Hector Mine EQ produced a well-constrained, maximum slip at surface of 5.3 m. That maximum slip occurred on major segment 3, which is the most mature of the two broken segments.**

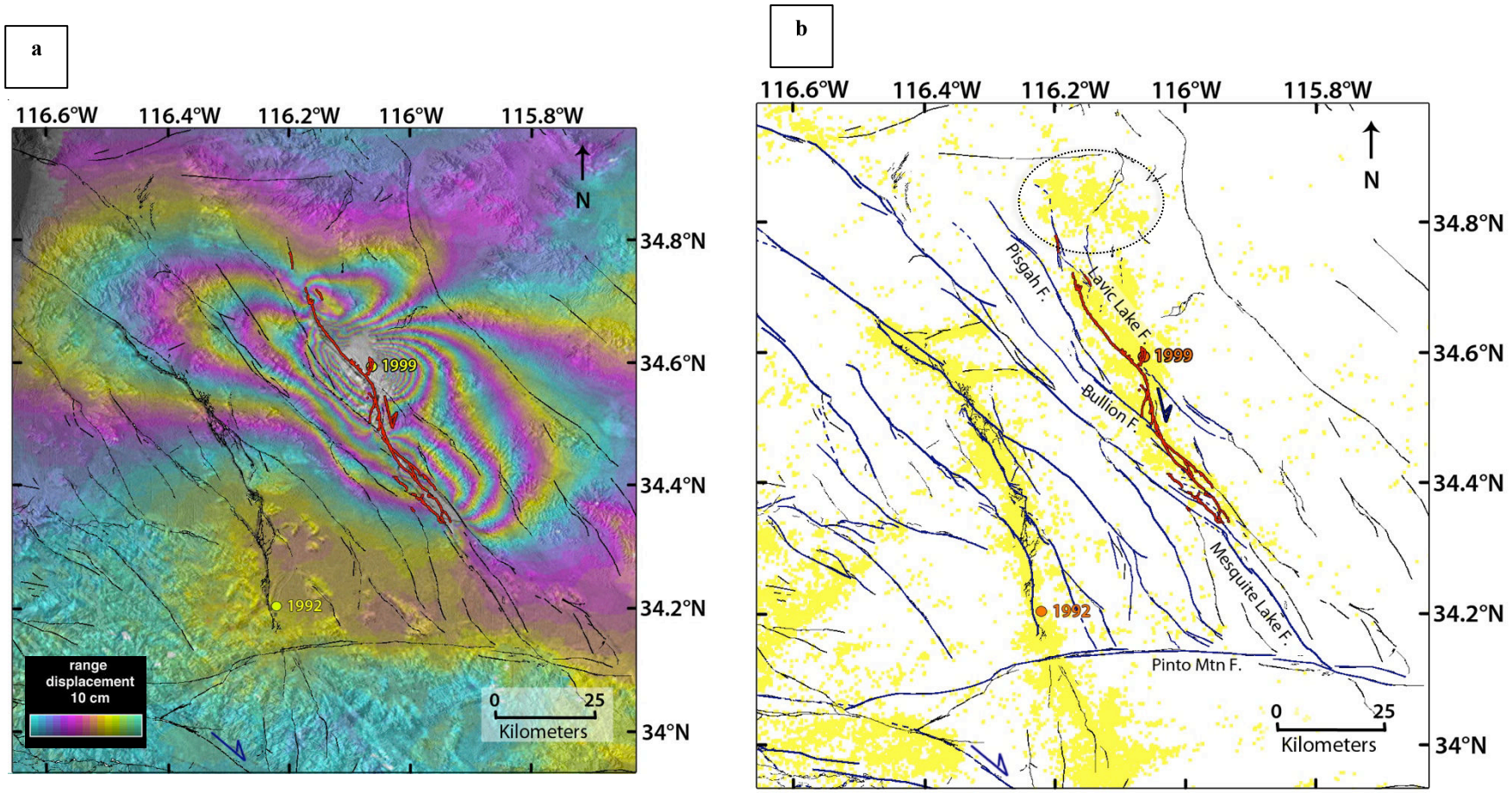


Fig.84: (a) Radar imagery (InSAR) of the ground deformation of the 1999 Hector Mine earthquake from Peltzer et al. (2001) ('Document, Courtesy of the Jet Propulsion Laboratory'; http://www-radar.jpl.nasa.gov/sect323/InSar4crust/HME/); (b) Instrumental seismicity of Mw >2 (1981-2011) including the aftershock sequence of the 1999 Hector Mine earthquake (earthquake catalog from Hauksson et al., 2012). Dotted circle shows a diffuse cluster of aftershocks north of the rupture. Faults are indicated as in Fig.81 & 83. The epicenter of the 1992 Landers earthquake is also shown.

Source inversion models and slip distribution at depth (Fig.85 & 86):

We compare four source inversion models that have been published on the 1999 Hector mine earthquake (Fig.85). The grid data are available for all of them (Table 2).

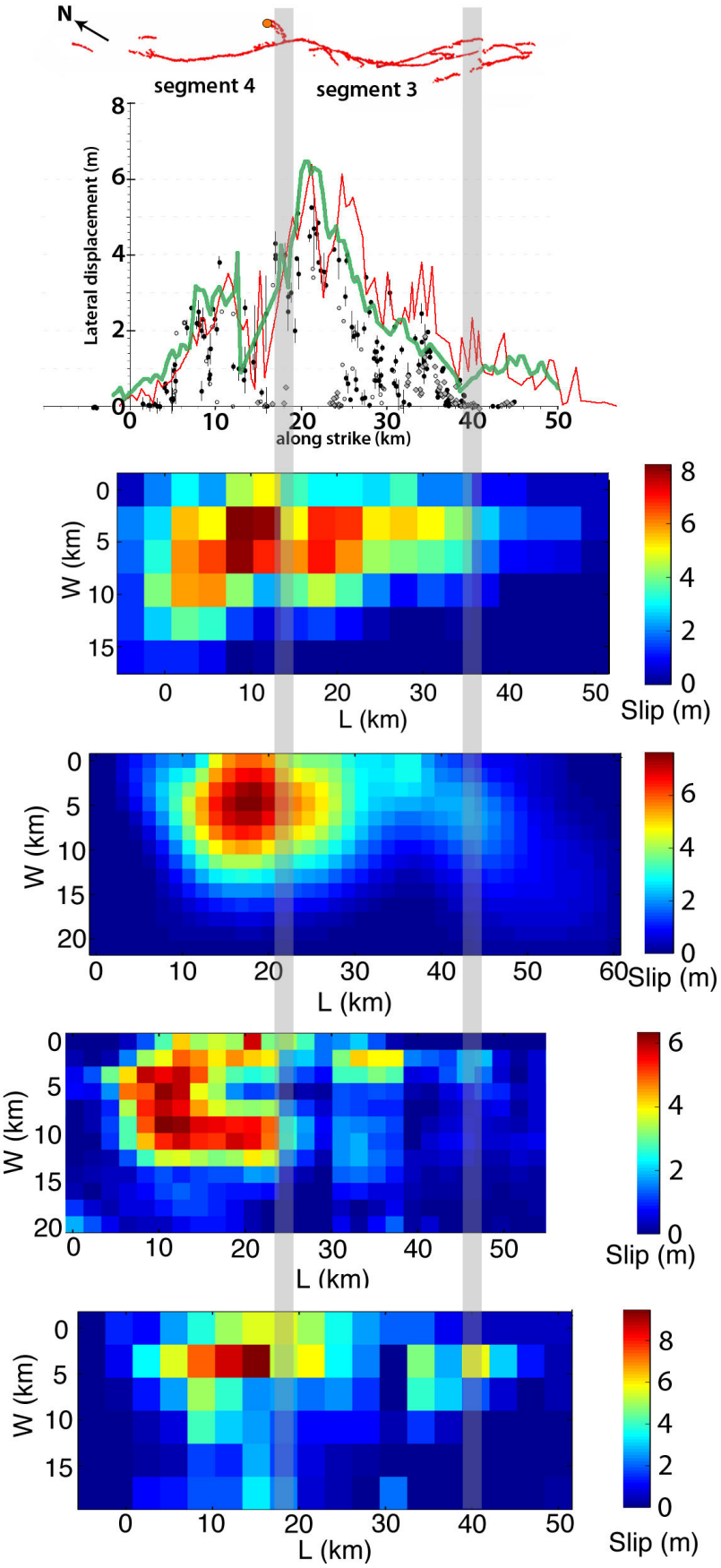
The models differ principally from the data they used:

- Ji et al. (2002): Teleseismic, strong motions, GPS and surface offset data. The model is divided in 3 sections (1 for Lavic Lake; 1 for Bending zone + northern blind splay fault suggested by aftershocks; 1 for Bullion fault):
    - Jónsson et al. (2002): InSAR and GPS data. The model is divided into 9 sections (3 for Lavic Lake; 3 for Bending zone + northern blind splay fault suggested by aftershocks; 3 for Bullion fault).
    - Kaverina et al. (2002): InSAR, GPS, local and regional seismicity and surface offset data. The model is divided into 3 sections (1 for Lavic Lake; 1 for Bending zone + northern blind splay fault suggested by aftershocks; 1 for Bullion fault).
    - Salichon et al. (2004): InSAR, GPS, teleseismic and surface offset data. The model is divided into 4 sections (2 for Lavic Lake; 1 for Bend + northern blind splay fault suggested by aftershocks; 1 for Bullion fault).
- The four models use a large amount of various data and hence are likely fairly robust. The model of Kaverina et al. (2002) is the one using more data, both local and regional.
- All four models represent the broken fault as two fault zones: whatever the segmentation of the southern part of the rupture (detailed above), the northern rupture is represented with two oblique planes, one coinciding basically with segment 4 and one coinciding with a N-S fault splaying from the northern tip of the rupture, below the clearest alignment of aftershocks (Y-shaped rupture pattern, see Fig.84b). To better compare the slip distributions, we represent the total, summed slip projected on a single plane (Fig.85 data available from the SRCMOD website).
- The main observation from Fig.85 is that all four models find a maximum slip at depth in the range 6-9 m which is deported towards the north and hence at a different location than that of the maximum displacement observed at surface (Fig.85 and 86). This suggests, either that the models are not fully correct, or that a significant fraction of the coseismic slip at depth did not propagate up to the surface. Part of this “blind” slip might have occurred on the splay fault underlined by aftershocks. As the four different models find the same result, we consider that the position of maximum slip at depth is robust. However, part of that slip

likely occurred off the main fault, so that the slip distribution at surface is well representative of the on-fault slip distribution.

- On segment 3, the maximum slip inferred at depth is at most 6-7 m, with a value of ~4 m in the model of Kaverina et al. Those values are either lower or fairly similar to the maximum slip produced at surface, and hence might be underestimated.
- All models produce a similar slip profile, with slip decreasing fairly regularly from a maximum value in the north down to the southern termination of the rupture.
- Most of slip is distributed in the depth range 0-15 km.

→ **The inversion source models suggest: L 54 km, W 15 km, Dmax at depth 6,3-9,5 m. They all consider that an adjacent oblique fault broke together with the main fault and produced a significant slip at depth only, of a few meters.**



Surface rupture mapped on the field (USGS et al., 2000 ; Treiman et al., 2002)

Co-seismic slip profile measured at surface on the field (dots ; *Treiman et al. 2002)* and inferred from InSAR (Peltzer et al., 2001 in green ; Jónsson et al., 2002 in red)

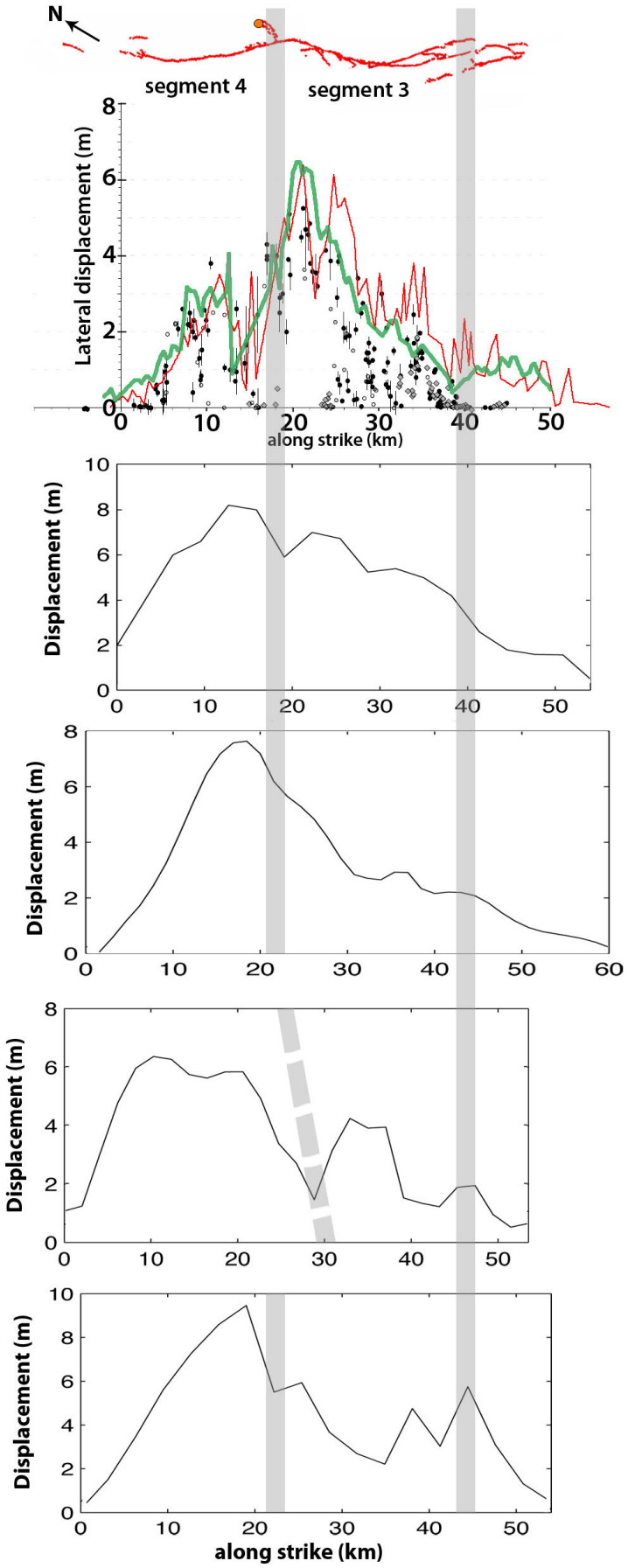
Ji et al., 2002 :
Data : Teleseismic + Strong motions + GPS + Surface
L= 54km ; W=16km ; Dmax=8,2m

Jónsson et al., 2002 :
Data : InSAR + GPS
L= 58km ; W=21km ; Dmax=7,6m

Kaverina et al. 2002 :
Data : InSAR + GPS + Local & Regional seismicity + Surface
L= 54km ; W=20km ; Dmax=6,3 m

Salichon et al. 2004 :
Data: InSAR + GPS + Teleseismic + Surface
L= 54km ; W=18km ; Dmax= 9,5 m

Fig.85: Comparison between different inversion models published on the 1999 Hector Mine earthquake. Gray line represents hypocenter location, which is used as reference for each model. Models are at the same scale along strike. Grey areas represent the intersegment zones.



Surface rupture mapped on the field (USGS et al., 2000 ; Treiman et al., 2002)

Co-seismic slip profile measured at surface on the field (dots ; *Treiman et al. 2002)* and inferred from InSAR (Peltzer et al., 2001 in green ; Jónsson et al., 2002 in red)

Ji et al., 2002 :
Data : Teleseismic + Strong motions + GPS + Surface

Jónsson et al., 2002 :
Data : InSAR + GPS

Kaverina et al. 2002 :
Data : InSAR + GPS + Local & Regional seismicity + Surface

Salichon et al. 2004 :
Data used : InSAR + GPS + Teleseismic + Surface

Fig.86: Comparison between profiles of maximum slip measured at surface and inferred at depth from source models published on the 1999 Hector Mine earthquake. Grey bars represent the intersegment zones.

Other source parameters :

SCARDEC (Vallée et al. 2011)
Mainshock: 1999/10/16 at 9h46min44s GMT;
Lat = 34.59° Lon= -116.27°
Mw 7.1; M0 = 6,40e19 Nm; Z = 13 km;
Duration: 18.2s
Strike, dip, rake: (336°, 80°, 174°)/ (67°, 84°, 10°)

Global CMT
Mainshock: 1999/10/16 at 9h46min59s GMT;
Lat = 34.71° Lon= -116.27°
Mw 7.1; M0 = 5,98e19 Nm; Z = 15 km;
Half-duration: 10.1s
Strike, dip, slip : (336°, 80°, 174°)/ (67°, 85° ,10°)

- Source parameters calculated from the GCMT and SCARDEC methods are in fair agreement.
- The rupture duration ranges between 14-18 s (Fig.87).
- The source time functions determined by Salichon et al. 2004 and SCARDEC are fairly similar (Fig.87). A first period of energy release occurs in the first ~5 s. It is followed by another peak of energy release in the following ~5 s. Then the energy release drops down more gently down to the end of the rupture. Because the rupture is bilateral, it is speculative to interpret the source time functions. However we have noted earlier that major segment 3 is more mature than major segment 4. We might thus suggest that it broke first, producing larger slip but moderate energy release (first "peak"; see more discussion in chapter VII). The second peak would thus coincide with the rupture of major segment 4, more energetic although lower slip was produced (additional slip might have however occurred on the 'blind' aftershock-marked fault line). The third phase would mark the energy drop along multiple tiny faults.

→ The source time function data suggest that two and possibly three fault sections broke during the 1999 Hector Mine EQ.

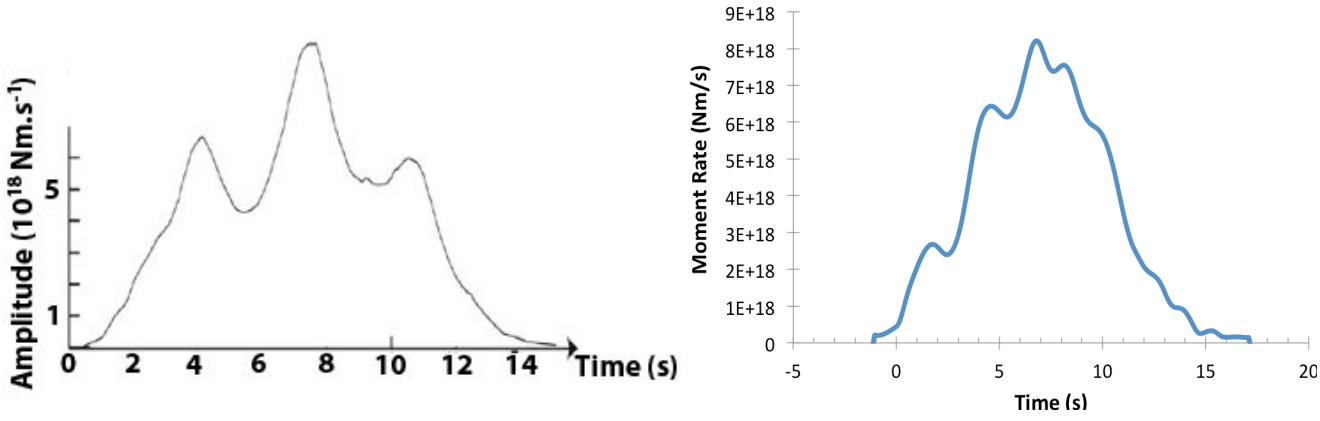


Fig.87: Source Time Function calculated from Salichon et al. (2004) (left) and using the SCARDEC method from Vallée et al. (2011) (right).

Other information:

1999 EQ:

- A foreshock activity was recorded 20h before the mainshock (18 events of 1.5<M<3.8) within a few kilometers distance of the mainshock hypocenter (Hauksson et al., 2002).
- The largest aftershock (Mw5.8) occurred 13 min after the mainshock (Hauksson et al., 2002).
- Hauksson et al. (2002) observed a diffuse cluster of events, spatially separated from the rest of the aftershocks and located 10 km north of the main rupture (Fig.84b).
- The maximum rates of postseismic deformation from both continuous and survey-mode GPS decay from ~10 cm/yr over the first 30 days to ~5 cm/yr over the following 130 days. Right-lateral afterslip was concentrated in the center of the rupture zone (bending section of segment 3) and at depth between 15 km and 30 km (Owen et al., 2002). Using ERS Interferometry, Jacobs et al. (2002) furthermore showed that additional afterslip occurred at shallow depth (0-4 km) on the segment 4, the eastern blind splay fault and at the southern tip of major segment 3.

Past EQ activity:

- In 1992, the Landers Mw 7.3 earthquake (e.g. Sieh et al., 1993) broke nearby faults of the ECSZ, ~ 20 km to the West of the Hector Mine rupture.
- Most of the large earthquakes within the ECSZ occurred in clusters, between periods of relative quiescence lasting several thousands of years (Rockwell et al., 2000). The 1992 and 1999 earthquakes might be the most recent events of a current cluster.

Parameters retained to describe the Hector Mine EQ (TableS 1 – 4):

Mw 7.1; M0 ≈ 6e19 Nm; L 47-55 km (but L surface ~40 km on the main fault); W = 15 km; Dmax at surface = 5.3-6.5 m; Dmax depth = 6,3-9,5 m.

Hypocenter : Z =13-15 km

Number of broken major segments: 2

The Hector Mine earthquake surface and depth slip-length data fall on the second function (blue curve; Fig.88 & 89, respectively): this is in agreement with the rupture of two major segments of the long term LBM Fault.

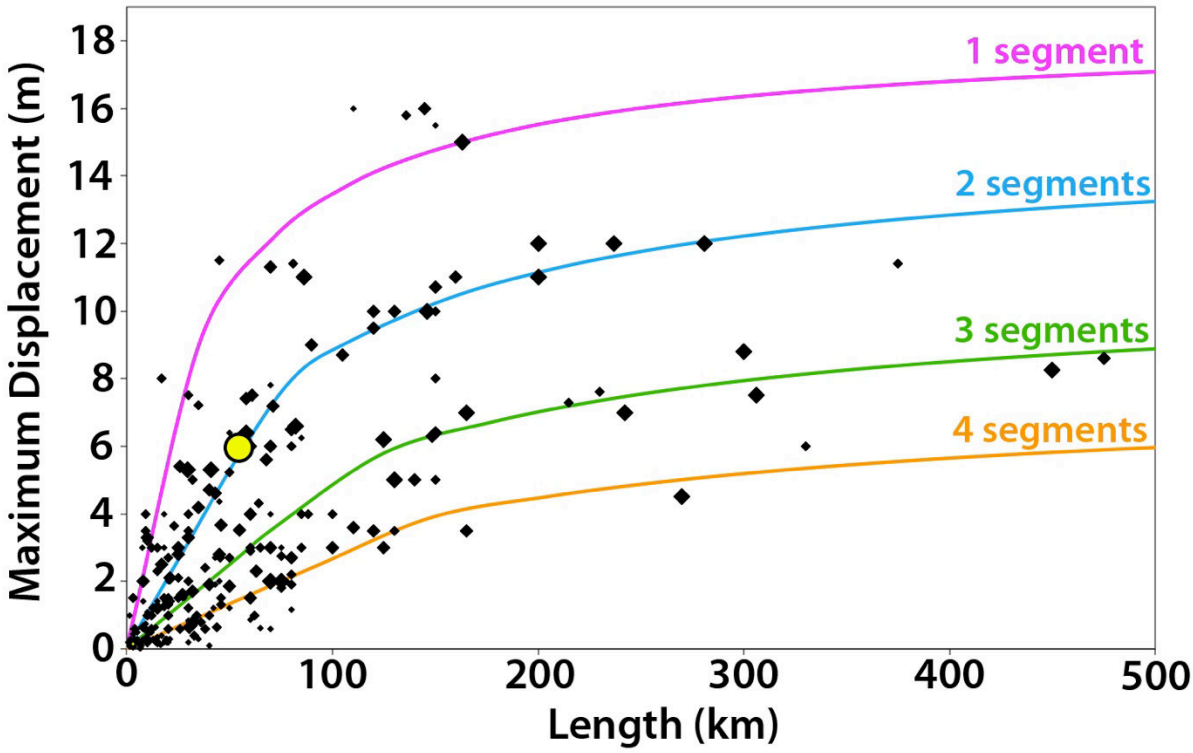


Fig.88: Earthquake displacement-length data measured at surface for 260 historical large continental earthquakes (Mw≥6). The 4 curves indicate the number of major long-term fault segments to have been broken by the earthquakes (modified from Manighetti et al., 2007 and Chapter IV). Yellow dot shows the Hector Mine earthquake surface slip length data.

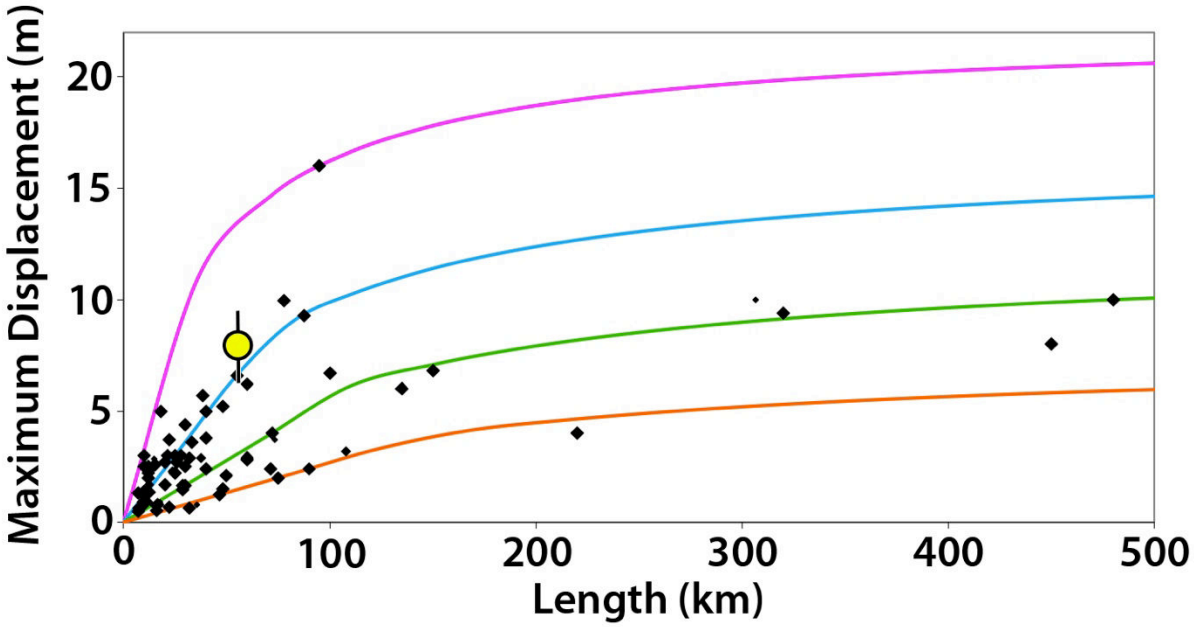


Fig.89: Earthquake displacement-length data inferred at depth for 90 historical large continental earthquakes (Mw≥6). The 4 curves indicate the number of major long-term fault segments to have been broken by the earthquakes (modified from Manighetti et al., 2007 and Chapter IV). Yellow dot shows the Hector Mine earthquake.

References

Dibblee, T. W., Jr. (1961). Evidence of strike-slip movement on northwest-trending faults in the western Mojave Desert, California: *U.S. Geological Survey Professional Paper*, **424-B**, p. B197-B199.

Dokka, R. K. (1983). Displacements on late Cenozoic strike-slip faults of the central Mojave Desert, California. *Geology,* **11,** 305-308.

Dokka, R. K., & C. J. Travis (1990a). Late Cenozoic strike-slip faulting in the Mojave Desert, California, *Tectonics*, **9**, 311 –340.

Dokka, R. K., & C. J. Travis (1990b). Role of the Eastern California Shear Zone in accommodating Pacific-North American plate motion, *Geophys. Res. Lett.,* **17**, 1323–1326.

Garfunkel, Z. (1974). Model for the late Cenozoic tectonic history of the Mojave Desert, California and for its relation to adjacent areas: *Geological Society of America Bulletin*, **85**, 1931-1944.

Hauksson, E., L. M. Jones, & K. Hutton (2002). The 1999 Mw 7.1 Hector Mine, California, earthquake sequence: complex conjugate strike-slip faulting, *Bull. Seism. Soc. Am*. **92**, 1154–1170

Hauksson, E., W. Yang, & P.M. Shearer (2012). Waveform Relocated Earthquake Catalog for Southern California (1981 to June 2011); *Bull. Seismol. Soc. Am*., **102**, doi:10.1785/0120120010.

Jacobs, A., D. Sandwell, Y. Fialko & L. Sichoix (2002). The 1999 (Mw 7.1) Hector Mine, California, Earthquake: Near-Field Postseismic Deformation from ERS Interferometry. *Bulletin of the Seismological Society of America,* **92**, 1433-1442; doi:10.1785/0120000908

Ji, C., J. D. Wald, & D. V. Helmberger (2002). Source description of the 1999 Hector Mine, California earthquake. II. Complexity of slip history, *Bull. Seism. Soc. Am*., **92**, no. 4, 1208–1226.

Jónsson, S., H. Zebker, P. Segall, & F. Amelung (2002). Fault slip distribution of the 1999 Mw 7.1 Hector Mine, California, earthquake, estimated from satellite radar and GPS measurements, *Bull. Seismol. Soc. Am*., **92**, 1377–1389, doi:10.1785/0120000922

Kaverina, A., D. Dreger, & E. Price (2002). The combined inversion of seismic and geodetic data for the source process of the 16, October, 1999, Mw7.1, Hector Mine, California earthquake, *Bull. Seism. Soc. Am.*, **92**, no. 4, 1266–1280.

Mandl, G. (1987). Tectonic deformation by rotating parallel faults: the "bookshelf" mechanism. *Tectonophysics*, **141**(4), 277-316.

Manighetti, I., Tapponnier, P., Courtillot, V., Gallet, Y., Jacques, E., & Gillot, P. Y. (2001). Strain transfer between disconnected, propagating rifts in Afar. *Journal of Geophysical Research,* **106**(B7), 13613-13665.

Manighetti, I., M. Campillo, S. Bouley, and F. Cotton (2007), Earthquake scaling, fault segmentation, and structural maturity, Earth Planet. Sci. Lett., 253, 429-438, doi:10.1016/j.epsl.2006.11.004

McClusky, S. C., S. C. Bjornstad, B. H. Hager, R. W. King, B. J. Meade, M. M. Miller, F. C. Monastero, & B. J. Souter (2001). Present day kinematics of the Eastern California Shear Zone from a geodetically constrained block model, *Geophys. Res. Lett.,* **28**, 3369–3372.

Oskin, M., L. Perg, D. Blumentritt, S. Mukhopadhyay, & A. Iriondo (2007). Slip rate of the Calico fault: Implications for geologic versus geodetic rate discrepancy in the Eastern California Shear Zone*, J. Geophys. Res*., **112**, B03402, doi:10.1029/2006JB004451.

Owen, S., G. Anderson, D. C. Agnew, H. Johnson, K. Hurst, R. Reilinger, Z.-K. Shen, J. Svarc & T. Baker (2002). Early Postseismic Deformation from the 16 October 1999 Mw 7.1 Hector Mine, California, Earthquake as Measured by Survey-Mode GPS *Bulletin of the Seismological Society of America,* **92**, 1423-1432; doi:10.1785/0120000930

Peltzer, G., Crampé, F., & Rosen, P. (2001). The Mw 7.1 Hector Mine, California earthquake, surface rupture, surface displacement field and fault slip solution from ERS SAR data. *Academie des Sciences, Paris, Comptes Rendus*, **333**, 545–555

Rockwell, T. K., S. Lindvall, M. Herzberg, D. Murbach, T. Dawson, & G. Berger (2000). Paleoseismology of the Johnson Valley, Kickapoo, and Homestead Valley faults: Clustering of earthquakes in the Eastern California Shear Zone, *Bull. Seismol. Soc. Am*., **90**, 1200–1236.

Salichon, J., P. Lundgren, B. Delouis, & D. Giardini (2004). Slip History of the 16 October 1999 Mw 7.1 Hector Mine Earthquake (California) from the Inversion of InSAR, GPS, and Teleseismic Data. *Bull. Seis. Soc. Am.,* **94**, 2015-2027.

Sandwell, D. T., L. Sichoix, D. Agnew, Y. Bock, & J-B. Minster (2000). Near-real-time radar interferometry of the Mw 7.1 Hector Mine Earthquake, *Geophys. Res. Lett.* **27**, 3101–3104.

Sandwell, D. T., L. Sichoix & B. Smith (2002). The 1999 Hector Mine Earthquake, Southern California: Vector Near-Field Displacements from ERS InSAR *Bulletin of the Seismological Society of America,* **92**, 1341-1354, doi:10.1785/0120000901

Sauber, J., W. Thatcher, S. C. Solomon, & M. Lisowski (1994). Geodetic slip rate for the eastern California shear zone and the recurrence time of Mojave desert earthquakes, *Nature*, **367**, 264– 266.

Sieh, K., L. M. Jones, E. Hauksson, K. Hudnut, D. Eberhart-Phillips, T. Heaton, S. Hough, K. Hutton, H. Kanamori, A. Lilje, S. Lindvall, S. McGill, J. Mori, C. Rubin, J. Spotila, J. Stock, H. Thio, J. Treiman, B. Wernicke, & J. Zachariasen (1993). Near-field investigations of the Landers earthquake sequence, *Science* **260**, 171–176.

Simons, M., Y. Fialko, & L. Rivera (2002). Coseismic deformation from the 1999, Mw7.1, Hector Mine earthquake as inferred from InSAR and GPS observations, *Bull. Seism. Soc. Am.*, **92**, no. 4, 1390–1402.

Tapponnier, P., Armijo, R., Manighetti, I., & Courtillot, V. (1990). Bookshelf faulting and horizontal block rotations between overlapping rifts in southern Afar. *Geophysical Research Letters*, **17**(1), 1-4.

Treiman, J. A., K. J. Kendrick, W. A. Bryant, T. K. Rockwell, & S. F. McGill (2002). Primary surface rupture associated with the Mw 7.1 16 October 1999 Hector Mine earthquake, San Bernardino County, California, *Bull. Seismol. Soc. Am*., **92**, 1171–1191.

U.S. Geological Survey, the Southern California Earthquake Center, and the California Division of Mines and Geology (2000). Preliminary report on the 16 October 1999 M7.1 Hector Mine, California, earthquake, *Seism. Res. Lett*. **71**, 11–23.

Vallée, M., J. Charléty, A.M.G. Ferreira, B. Delouis, and J. Vergoz, (2011). SCARDEC : a new technique for the rapid determination of seismic moment magnitude, focal mechanism and source time functions for large earthquakes using body wave deconvolution, *Geophys. J. Int*., **184**, 338-358.

Walpersdorf, A., Manighetti, I., Mousavi, Z., Tavakoli, F., Vergnolle, M., Jadidi, A. Jadidi, D. Hatzfeld, A. Aghamohammadi, A. Bigot, Y. Djamour, H. Nankali & Sedighi, M. (2014). Present-day kinematics and fault slip rates in eastern Iran, derived from 11 years of GPS data, *J. Geophys. Res. Solid Earth*, **119**, 1359–1383, doi:10.1002/2013JB010620.

2.11. Imperial Valley 1940 & 1979

18/May/1940 & 15/oct/1979, USA-Mexico border
Mw 7.0 & Mw 6.5
Epicenters : 32.73°N-115.63°W & 32.66°N-115.36°W
Right-lateral strike-slip



Broken long-term fault

The two EQs broke a part of the San Jacinto Fault, a southern branch of the San Andreas Fault. **Note that the San Andreas Fault is described in the sections "Fort Tejon 1857" (Southern San Andreas) and "San Francisco 1906" (Northern San Andreas). The relations of the San Andreas Fault with the San Jacinto and the Elsinore Faults are discussed in section "Fort Tejon 1857".** The San Jacinto Fault is one of the major splays of the Southern San Andreas Fault.

General characteristics of the San Jacinto Fault from literature (Fig.90):

This part is described in the section "Borrego Mountain 1968".

Architecture and lateral major segmentation, from our and USGS mappings (Fig.91):

This part is described in the section "Borrego Mountain 1968". Only the figures are shown again here.

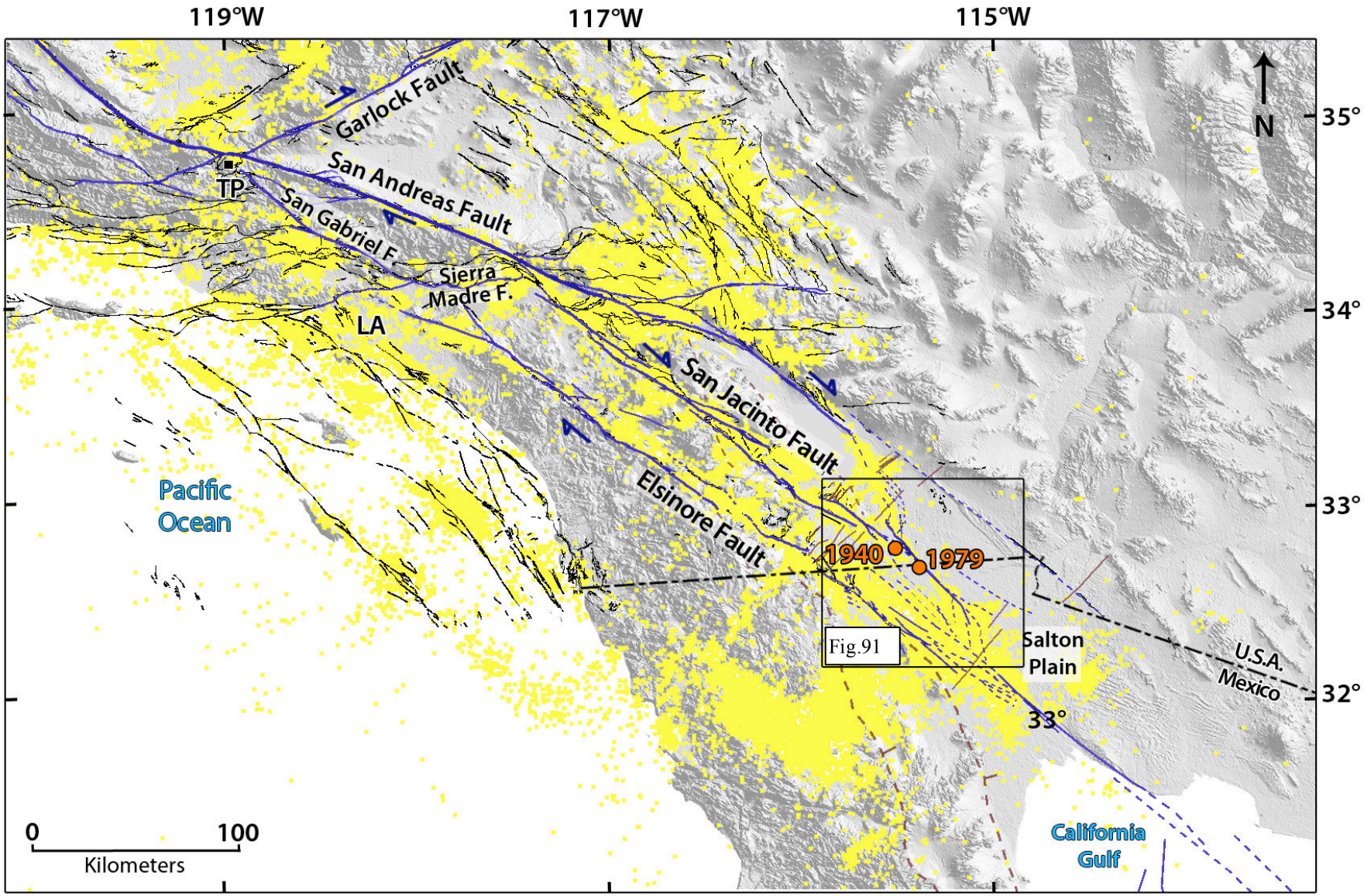


Fig.90: (a) General map of long term faults in Southern California. In blue are the major active faults that we mapped. In black are the other Quaternary faults mapped by the U.S. Geological Survey and California Geological Survey, 2006. In dotted brown are ancient faults related to the Gulf of California. In solid brown are preexisting lineaments likely related to the Gulf of California (see text). The orange circles show the 1940 and 1979 EQ epicenters. The yellow dots are the instrumental earthquakes (Mw>2) recorded between 1981 and 2011 (Hauksson et al., 2012). LA : Los Angeles ; TP : Tejon Pass.

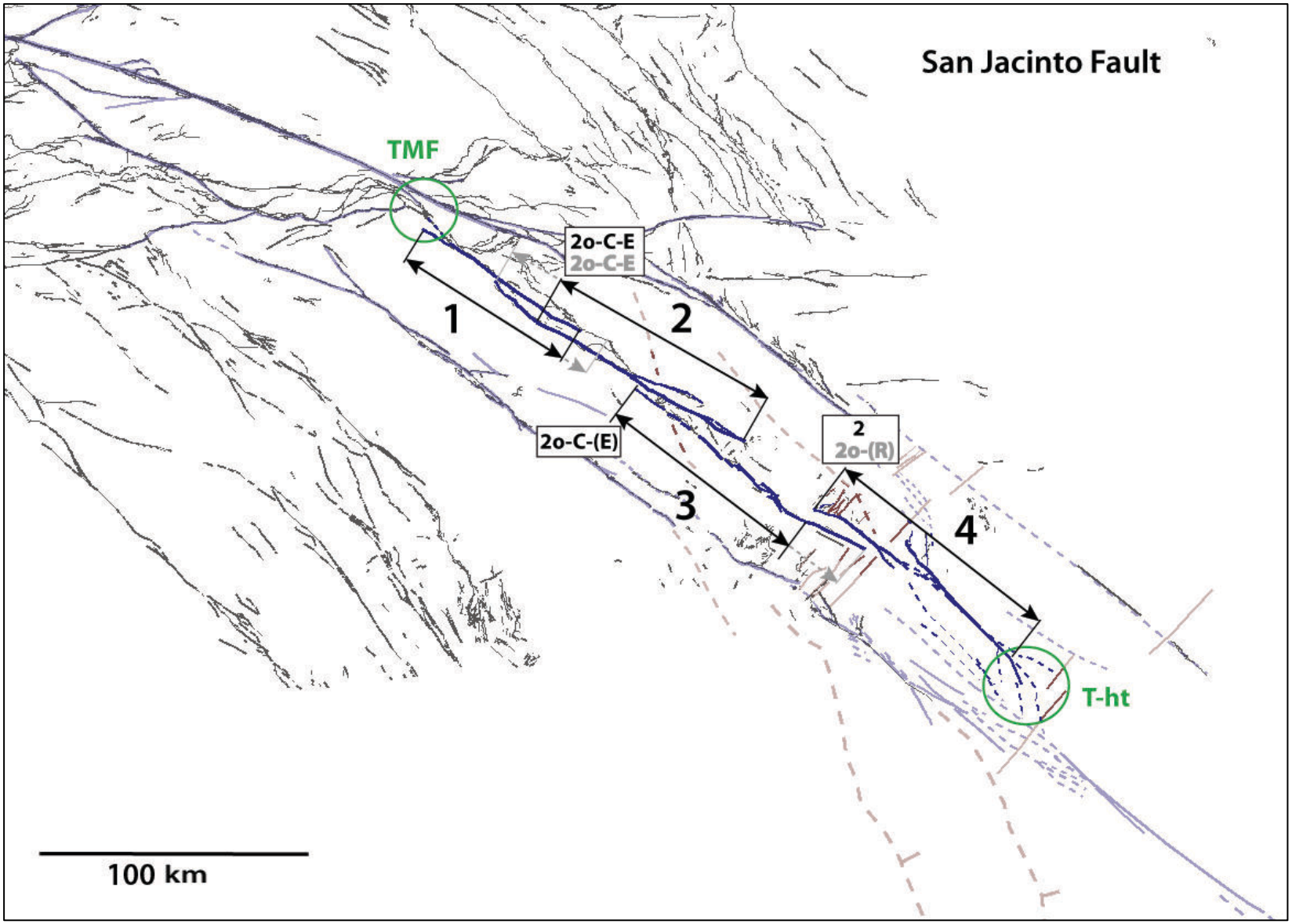


Fig.90: (b) Same active fault map as in Fig.90 (a), but with focus on the major segments of the San Jacinto fault. The segments are numbered from NW to SE and indicated by black arrows parallel to their mean strike. The grey prolongation of the arrows indicates the uncertainties on the segment lengths. The nature of the inter-segment zones is indicated in letters within boxes explained IN Table 6. The nature of the fault tips is indicated in green (Table 6).

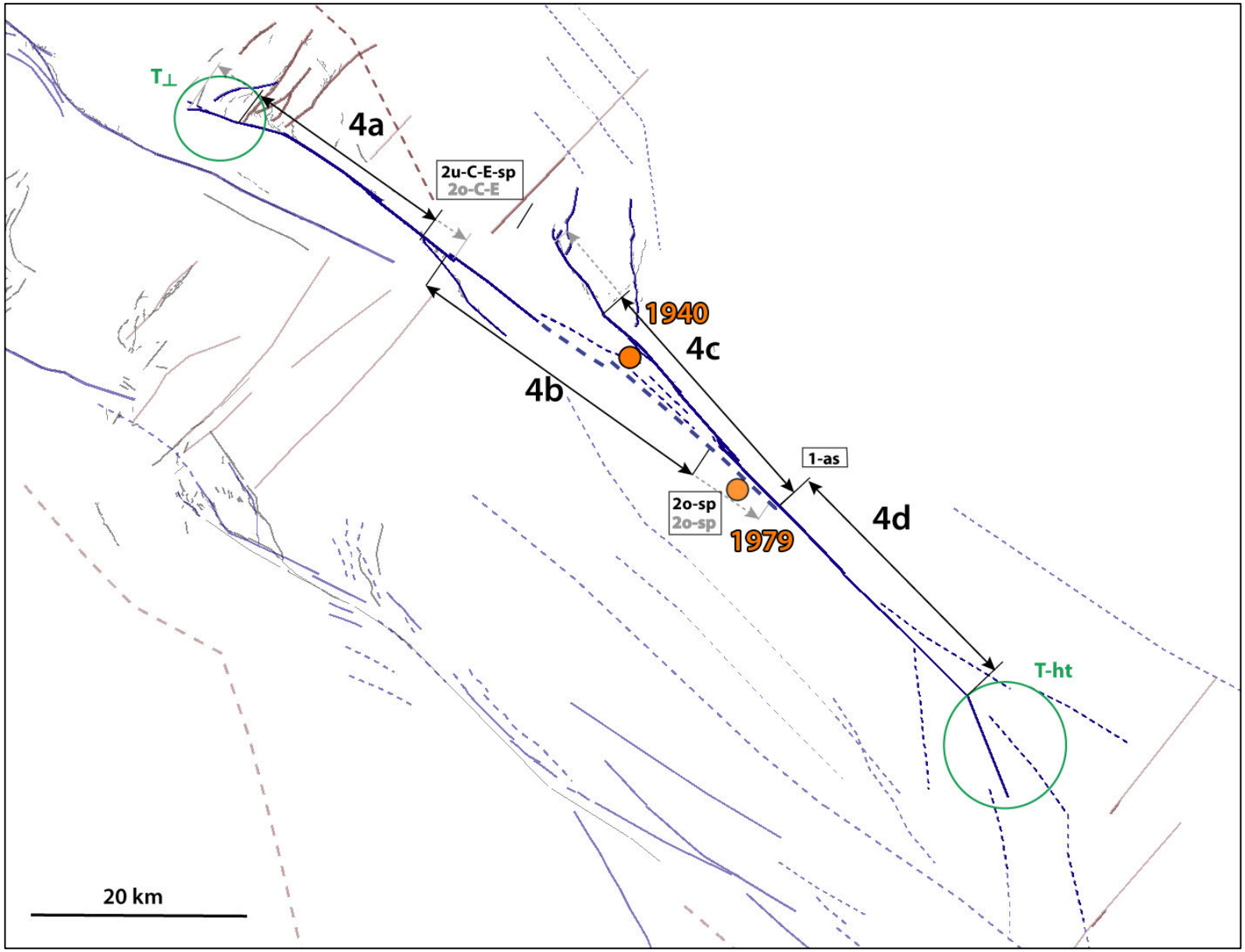


Fig.91: (a) Map of the secondary segments that form the major segment 4 of the San Jacinto fault. Same caption as in fig.90. The orange circles indicate the 1940 and 1979 EQ epicenters.

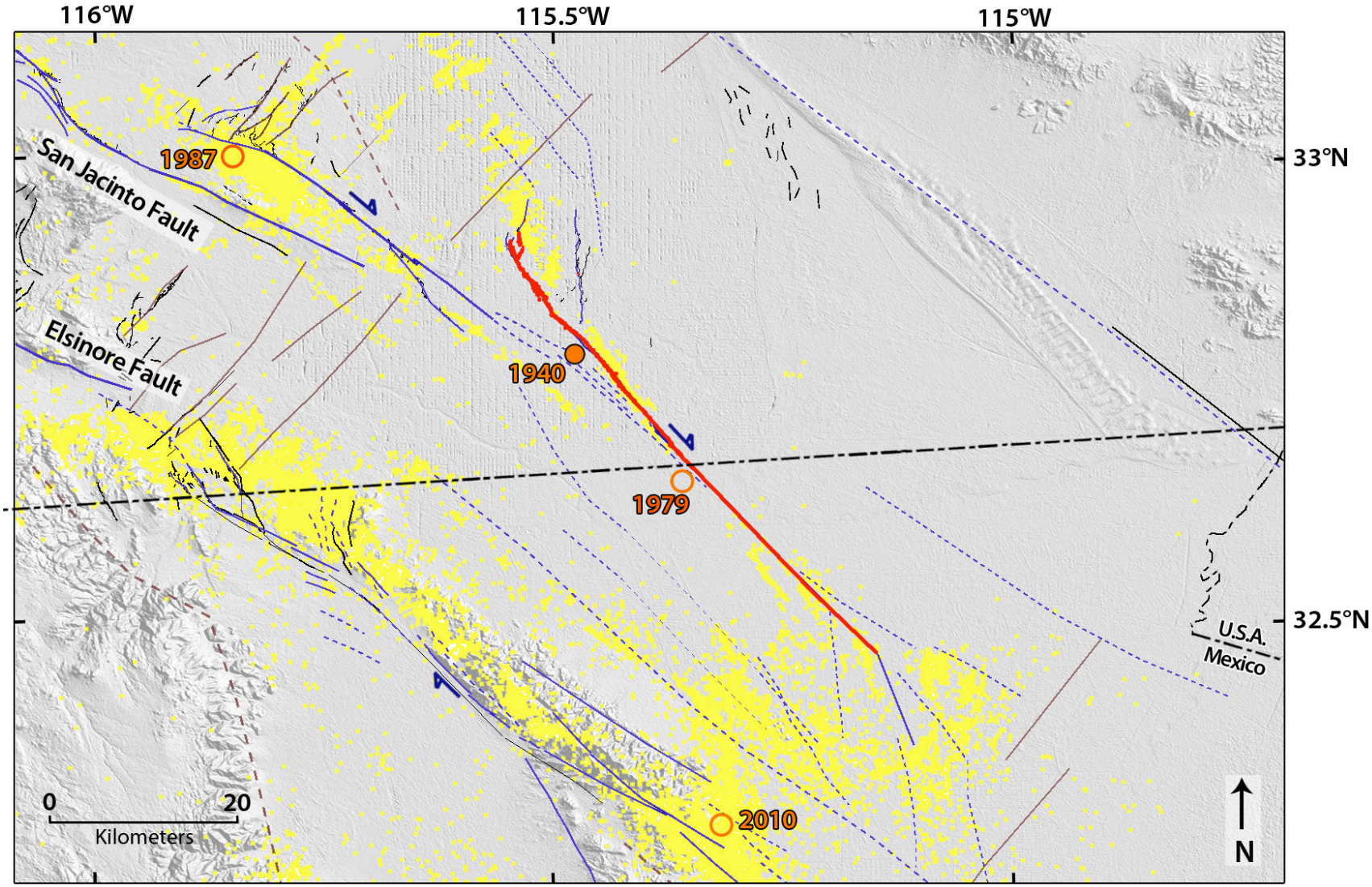


Fig.91: (b) Zoom on the broken section of the San Jacinto fault, from Fig.90 (same caption). The surface rupture of the 1940 EQ is indicated with the red line (from King & Thatcher 1998). The 1979 Imperial Valley (Mw 6.5), the 1987 Superstition Hills (Mw 6.6) and the 2010 Baja California (Mw 7.2) earthquake epicentersare also indicated.

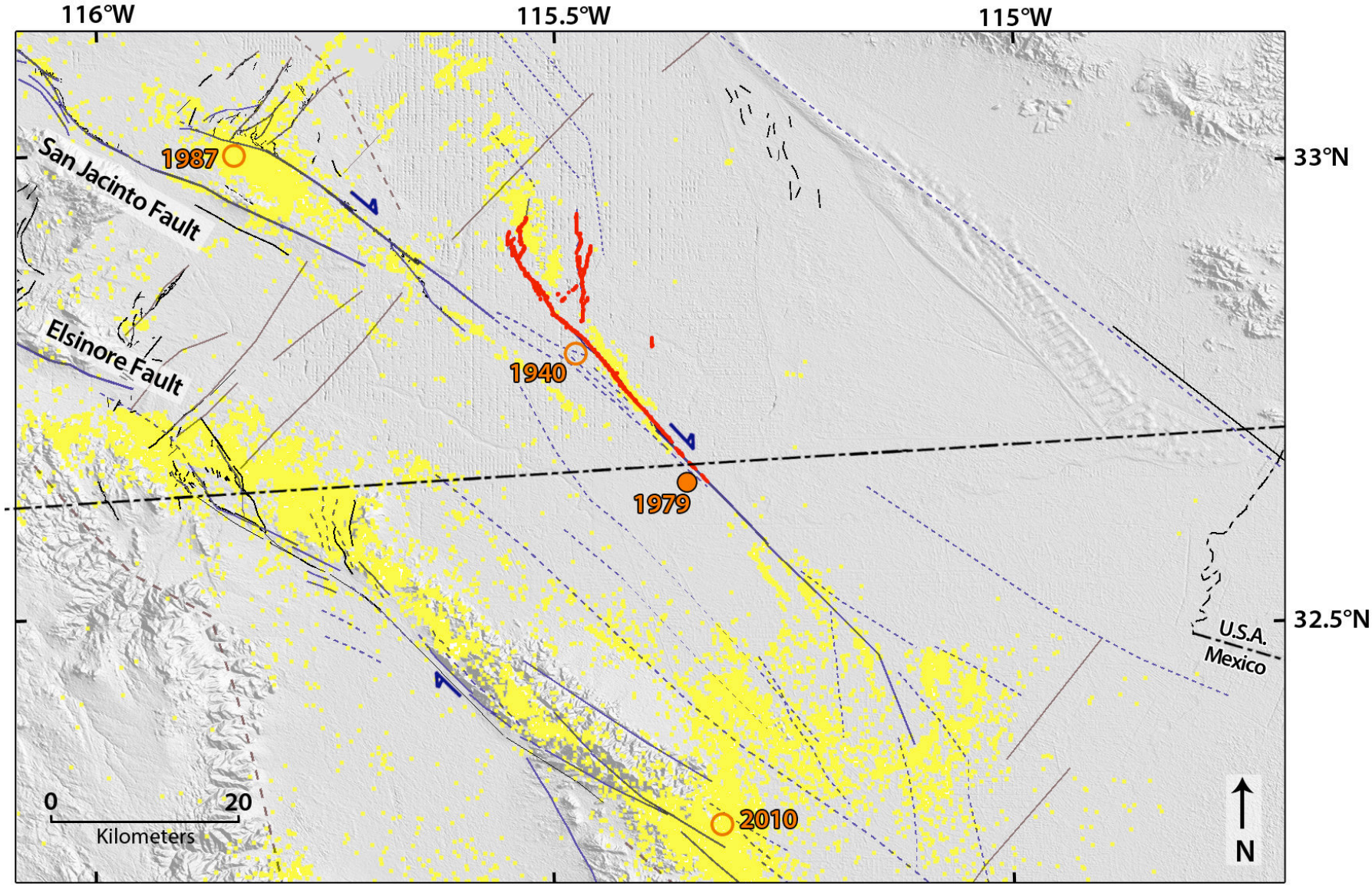


Fig.91: (c) Zoom on the broken section of the San Jacinto fault, from Fig.90 (same caption). The surface rupture of the 1979 EQ is indicated with the red line (Sharp et al., 1982). The 1940 Imperial Valley (Mw 7.0), the 1987 Superstition Hills (Mw 6.6) and the 2010 Baja California (Mw 7.2) earthquake epicenters are also indicated.

1940 Coseismic rupture

Surface trace and location on long-term San Jacinto Fault (Fig.91):

- The 1940 surface rupture cannot be discriminated, on Google Earth and Landsat images, from the cumulative fault trace, which is subtle, yet visible. The surface trace of the 1940 earthquake has been mapped on the field (e.g. Sharp 1982), whereas the displacements were measured both on the field (e.g. Sharp 1982) and from aerial imagery (Rockwell and Klinger, 2013).
- The EQ broke a part of the major segment 4 of the San Jacinto Fault.
- Major segment 4 is made of two clear parts –northern and southern, striking slightly differently (angle difference of ~12°) either side of the middle of the segment. Each part has a very linear trace. The 1940 EQ broke the southern part of major segment 4.
- Each part is itself divided into two distinct secondary segments so that, overall, major segment 4 includes 4 secondary segments –from NW to SE, 4a, 4b, 4c and 4d– of similar length, 25-30 km.
- Segment 4a is ~25 km long. Its trace is very linear. To the north, segment 4a terminates by connecting to multiple NE-trending small fractures and faults, forming a sub-perpendicular angle to the segment 4a trace. Segment 4b is also fairly linear. Its trace is fairly subtle to identify within the fields of the Salton Plain. Segments 4a and 4b are connected through a narrow step-over (< 1km wide) where a small splay fault has developed (type 2o-sp). To the south, segment 4b splays in multiple tenuous branches. Segments 4c and 4d have a very linear trace. Segment 4c differs from segment 4d in that it is associated with several secondary oblique faults while segment 4d is more isolated. Segments 4b and 4c are hardly connected at the ground surface, and are rather separated by a relay zone of type (1-) 2o-sp where multiple small faults have developed. Across the segments 4b-4c relay zone, the mean strike of the segments changes by ~15°. Although it is not completely clear, we locate the relay zone between segments 4c and 4d at the site where most small oblique faults that splay from the southern tip of segment 4b intersect the trace of segments 4c-d. Segments 4c and 4d are thus well connected to each other through a small releasing step-over (<1 km wide) of type $2_{O\text{-}C\text{-}E}$. To the north, segment 4c terminates through distributed horsetail faulting, striking at high angle (~40°) to the main fault trace. To the south, segment 4d terminates by splaying in multiple small branches; most establish a connection with the Elsinore Fault further south.

- The 1940 EQ broke the two southernmost secondary segments 4c and 4d of the major segment 4 of the San Jacinto Fault. The main rupture thus has a length of ~60 km (e.g., Rockwell and Klinger, 2013).
- The EQ nucleated in the northern part of segment 4c where the fault both splays in multiple horsetail small faults and connects to the north with oblique small faults en echelon disposed (these en echelon faults form the Brawley seismic zone defined in Trifunac and Brune 1970). The rupture has thus propagated unilaterally to the south and stopped at the southern end of major segment 4.
- Since the San Jacinto Fault has been propagating southward over geological time, segment 4c where the EQ initiated is likely more mature than segment 4d.

→ The 1940 Imperial Valley EQ broke half of the major southernmost segment 4 of the San Jacinto Fault. The EQ thus occurred on the most immature part of the San Jacinto Fault. Within the major segment, the EQ broke two secondary segments of similar length.

Coseismic displacements measured at surface (Fig.92):

- *From Field measurements*: Maximum lateral slip ~6 m (Sharp 1982) measured at the southern end of secondary segment 4c.
- *From aerial images*: Maximum lateral slip ~7 m (Rockwell and Klinger 2013) measured at the southern end of secondary segment 4c.
- The complete slip profile was measured by Sharp (1982) and also partly by Rockwell and Klinger (2013) (Fig.92). Maximum slip is well located due north of the US-Mexico border, hence in the southern part of segment 4c. From the maximum slip, the lateral displacement decreases on either side in a fairly linear fashion. About 23 km north of the border, the lateral slip on segment 4c is mixed up with measurements of off-fault slip distributed on the multiple secondary horsetail features. The slip profile characterizing segment 4c should thus be considered no further than ~23 km north of the border. South of the zone of maximum slip, the lateral displacement decreases down to zero in a fairly regular manner. The overall slip profile of the 1940 rupture is thus roughly triangular and only slightly asymmetric.
- In more details, the 1940 slip profile suggests 5 slips bumps (indicated on Fig.92) separated by more or less pronounced slip troughs, that coincide with small bends and intersegments along the fault.

- *From Geodetic measurements*: GPS stations nearby the fault recorded a maximum of 4.8 ± 0.2 m of right-lateral displacement (King and Thatcher 1998). The network of leveling stations covers only half of the rupture (north of the border), so that the inferred displacement is not well constrained.

→ Maximum slip of ~6-7 m at surface on the southern tip of secondary segment 4c, i.e., on the most mature part of the broken fault section.

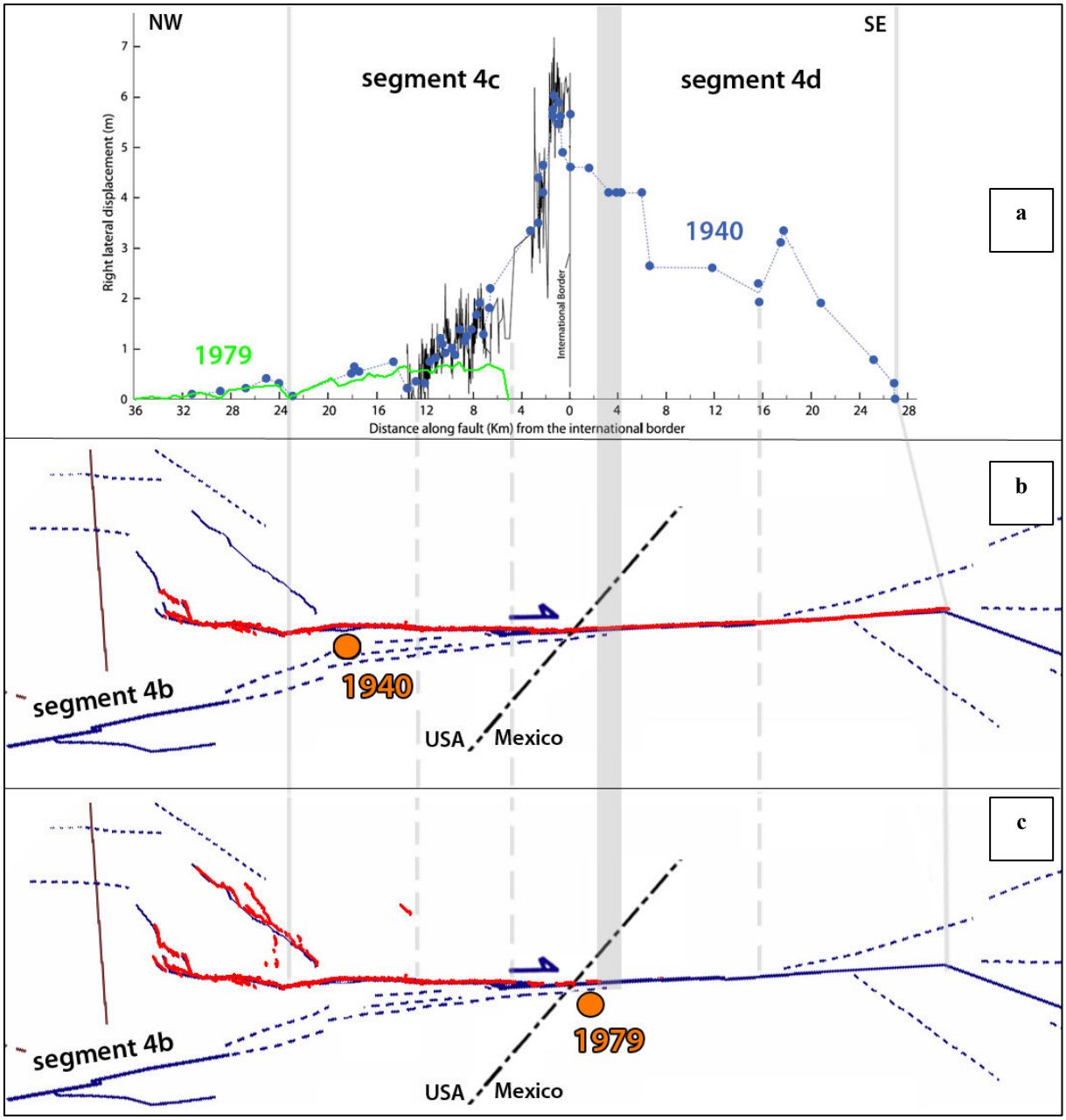


Fig.92: (a) Coseismic displacements measured at surface along the 1940 (blue dots [from J.P. Buwalda in Sharp 1982] and black line [from Rockwell and Klinger 2013]) and the 1979 Imperial Valley ruptures (green line, from Sharp et al., 1982): (b) Surface trace of the 1940 rupture; (c) Surface trace of the 1979 rupture. The grey bar indicates the major intersegment 4c-4d revealed in our mapping. The other vertical lines indicate lower scale intersegments (dotted lines) and segment tips (solid lines), all marked by both troughs in the slip distribution and small fluctuations in the fault trace.

1979 Coseismic rupture

Surface trace and location on long-term San Jacinto Fault (Fig.91 a & c):

- The 1979 surface rupture cannot be discriminated, on Google Earth and Landsat images, from the cumulative fault trace, which is subtle, yet visible. The surface trace of the 1979 earthquake has been mapped on the field (Sharp et al., 1982).
- Total surface rupture of ~30 km long.
- The EQ broke a part of the major segment 4 of the San Jacinto Fault, previously broken by the 1940 EQ.
- Major segment 4 is described above.
- The 1979 EQ broke only one secondary segment of major segment 4: the segment 4c. This segment had already broken in 1940. The main 1979 rupture thus had a length of ~30 km.
- The EQ nucleated near the inter-segment zone between segments 4c and 4d (Chavez et al., 1982) and propagated unilaterally to the north, therefore in opposite direction to the 1940 rupture.

→ **The 1979 Imperial Valley EQ re-broke one secondary segment (4c) of the major segment 4 of the San Jacinto Fault, which had already ruptured in 1940. The EQ initiated in the intersegment zone between secondary segments 4c and 4d, that is where a high coseismic slip gradient, and hence a high stress concentration, had been created by the prior 1940 rupture .**

Coseismic displacements measured at surface:

- *From Field measurements*: Maximum lateral slip ~0.6 m (Sharp et al., 1982) measured at the southern end of secondary segment 4c.
- The slip profile was obtained from fairly dense field measurements (Fig.92). However the lack of observation near the epicenter leaves an uncertainty of the slip amount over the last few southernmost kilometers of the rupture. It is actually unlikely that no surface slip was produced between the epicenter and the maximum slip observed ~5 km further north (Fig.92c). From that maximum slip, the lateral displacement decreases fairly linearly towards the north, down to zero ~30 km away. As in 1940, over the last northernmost ~8 km, the coseismic slip was diffused onto the horsetail small faults, so that it is ignored how much slip actually occurred on the main fault. Despite of the uncertainties both north and south of the rupture, the overall slip profile of the 1979 EQ is triangular and asymmetric.

→ Maximum slip of ~0.6 m at surface occurred at the southern end of secondary segment 4c, which had already broken in 1940. The 1979 maximum slip located nearby the zone of the 1940 maximum slip, on the most mature part of the broken fault section.

Source inversion models and slip distribution at depth (Fig.93 & 94):

- We compare three source inversion models that have been published on the 1979 Imperial Valley earthquake. The grid data are available for all of them (Fig.93; Table 2).
- The models differ principally from the data they used:
- Hartzell and Heaton (1983): Strong motions and teleseismic data. The model considers the broken fault as a single plane
- Olson and Apsel (1982): Strong motions data only. The model considers the broken fault as a single main plane combined with a small plane representing one of the horsetail faults at the northern tip of the rupture.
- Archuleta (1984): Strong motions data only. The model considers the broken fault as a single plane.

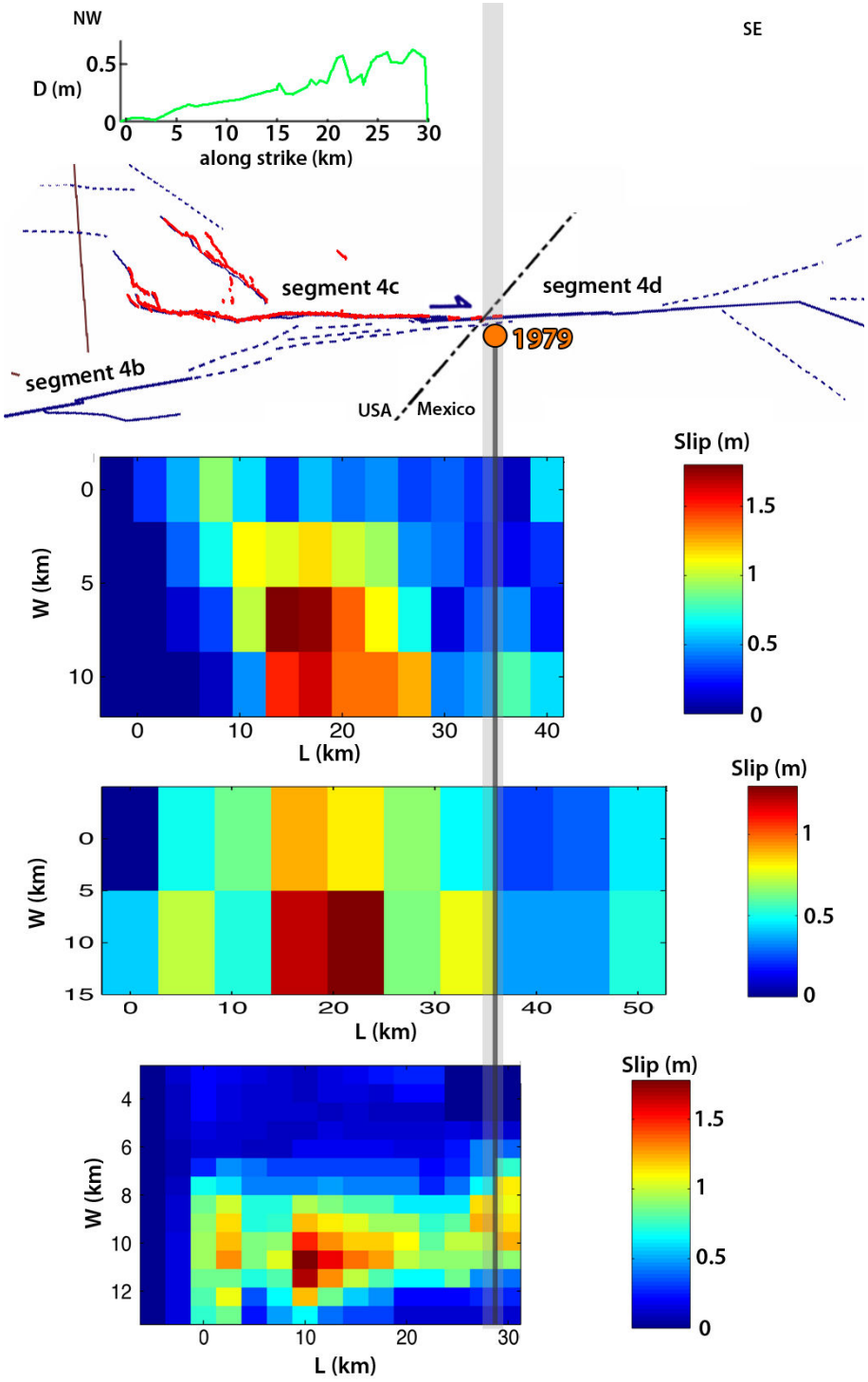
→ We consider that the model from Hartzell and Heaton (1983) is the most robust for they use more different data, and focus on the main fault plane.

→ The three models provide a similar slip distribution, with basically one clear patch of maximum displacement (1.3-1.8 m) situated at a depth of 8-12 km in the center of segment 4c (Fig.93 & 94). Olson and Apsel (1982) extend the rupture further to the south but their grid is not accurate enough to observe another patch of slip.

→ All models suggest that the slip might extend down to 10-12 km depth along the fault dip.

→ The slip distributions at surface and depth differ, mainly in the location of the maximum slip. A said earlier, it is likely however that a fraction of slip was not measured at surface in the southern part of the rupture. The slip profile might thus be less asymmetric than suggested at surface.

→ The source models suggest: L 30-35 km, W 10-12 km, Dmax at depth 1.3-1.8 m, 1 segment broken.



1979 co-seismic slip profile measured at surface (Sharp et al., 1982)

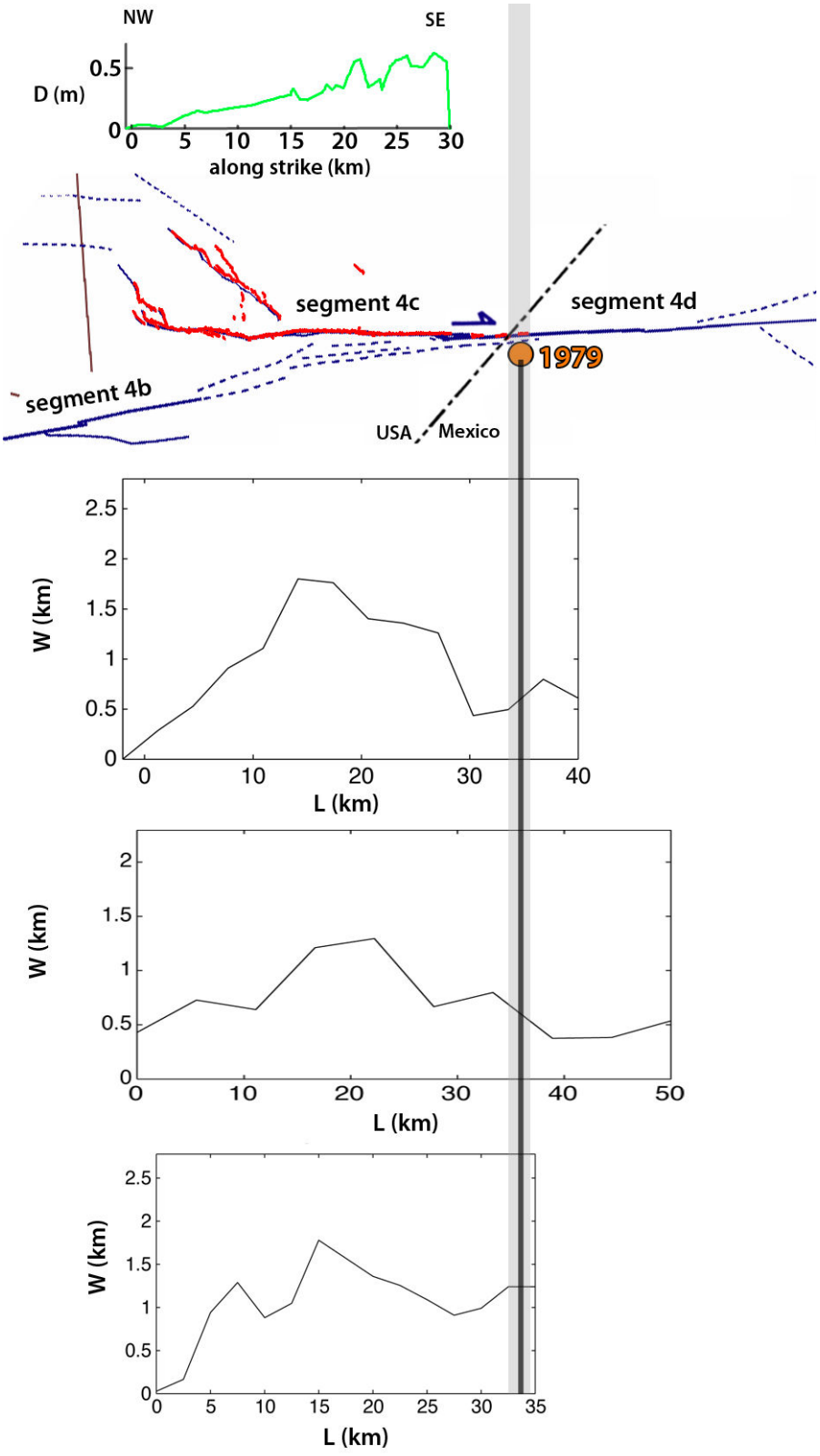
1979 surface rupture mapped on the field (in red from Sharp et al., 1982) and long term faults (in blue)

Hartzell & Heaton 1983 :
Data : Strong motions + Teleseismic
L= 44 km ; W=10 km ;
Dmax=1.8 m
Z= 9.5 km

Olson & Apsel 1982 :
Data : Strong motions
L= 50 km ; W= 10 km ;
Dmax= 1.3 m
Z = 10 km

Archuleta 1984
Data : Strong motions
L= 35 km ; W= 13 km ;
Dmax= 1.8 m
Z= 8 km

Fig.93: Comparison between different inversion models published on the 1979 Imperial Valley earthquake. Black line represents hypocenter location, which is used as a reference for each model. Grey bar represents the intersegment zone. Models are at the same scale along strike.



1979 co-seismic slip profile measured at surface (Sharp et al., 1982)

1979 surface rupture mapped on the field (in red from Sharp et al., 1982) and long term faults (in blue)

Hartzell & Heaton 1983 :
Data : Strong motions + Teleseismic

0lson & Apsel 1982:
Data : Strong motions

Archuleta, 1984
Data : Strong motions

Fig.94: Comparison between slip profiles measured at surface and inferred at depth from inversion models. Black vertical line represents the hypocenter location, which is used as a reference to co-locate each profile. Grey vertical bar represents the 4c-4d intersegment zone.

Other source parameters:

1979 EQ :

Global CMT

Mainshock: 1979/10/15 at 23h17min01s GMT ; Lat = 32.62° Lon= -115.57°

Mw 6.5 ; M0 = 7.23e18 Nm ; Z = 12 km ; Half-duration : 6s

Strike,dip,slip : (136°,39°,-180°)/(46°,90°,-51°)

Chavez et al. (1982) from U.S and Mexican local strong motion data.

Mainshock: 1979/10/15 at 23h16min54s GMT ; Lat = 32.64° Lon= -115.31°; Mw 6.6.

Other information:

Past EQ activity:

- Similar moderate earthquakes occurred on the San Jacinto Fault during the last decades: the 1968 Borrego Mountain (Mw 6.5) broke a part of the major segment 3; the 1987 Superstition Hills earthquake broke the secondary segment 4a.

1979 EQ:

- The aftershocks mainly concentrated at the northern tip of segment 4c during the first 8h after the earthquake, and hence where coseismic slip was lower (Johnson and Hutton 1982).
- Olson and Apsel (1982) and Archuleta (1984) suggested that the rupture was super-shear over ~8 km in the central part of the rupture. This is where the fault trace is very linear.

Parameters retained to describe the 1940 Imperial Valley EQ (Table 1 & 3):

Mw 7.0; L 60 km; Dmax surface = 6-7 m.

Number of segments broken on the San Jacinto Fault: 1 major segment, partly; representing the rupture of 2 secondary segments

Parameters retained to describe the 1979 Imperial Valley EQ (Table 1 – 4):

Mw 6.5; M0 = 7.23e18 Nm; L ~30-35 km; W ~10-12 km; Dmax surface ~at least 0.6 m and possibly more; Dmax depth ~1.3-1.8 m.

Number of segments broken on the San Jacinto Fault: 1 major segment, partly; representing the rupture of 1 secondary segment.

- The surface slip-length data of the 1940 Imperial Valley earthquake fall on the second function (blue curve; Fig.95) in keeping with the EQ having ruptured two distinct segments on the long term San Jacinto Fault. However the broken segments are not major but secondary segments of the San Jacinto Fault. We will discuss this point in chapter IV.

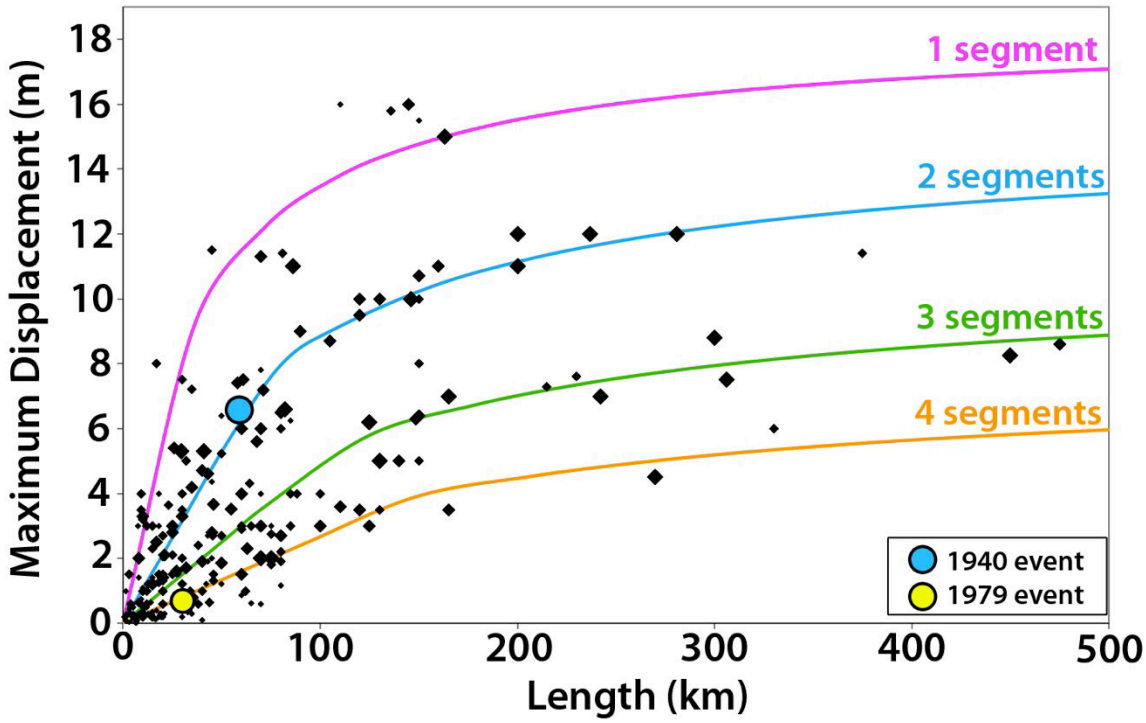


Fig.95: Earthquake displacement-length data measured at surface for 260 historical large continental earthquakes (Mw≥6). The 4 curves indicate the number of major long-term fault segments to have been broken by the earthquakes (modified from Manighetti et al., 2007 and Chapter IV). The blue and yellow dots show the 1940 and 1979 Imperial Valley earthquakes surface slip length data, respectively.

- The surface and depth slip-length data of the 1979 Imperial Valley earthquake fall approximately on the fourth function (orange curve; Fig.95 & 96), and hence not on the first function as it might be expected for the rupture of a single fault segment. One explanation might be that the prior 1940 rupture has decreased the friction on the fault, allowing an easier, faster (super-shear) and less energetic (lower stress drop and hence Dmax/L) re-breaking. We come back to this point in the discussion section. The "re-breaking" occurred in the fault zone that had slipped less in 1940, and was possibly initiated by the large stress concentration formed by the 1940 rupture in the intersegment zone between the most mature secondary segment 4c and the more immature secondary segment 4d.

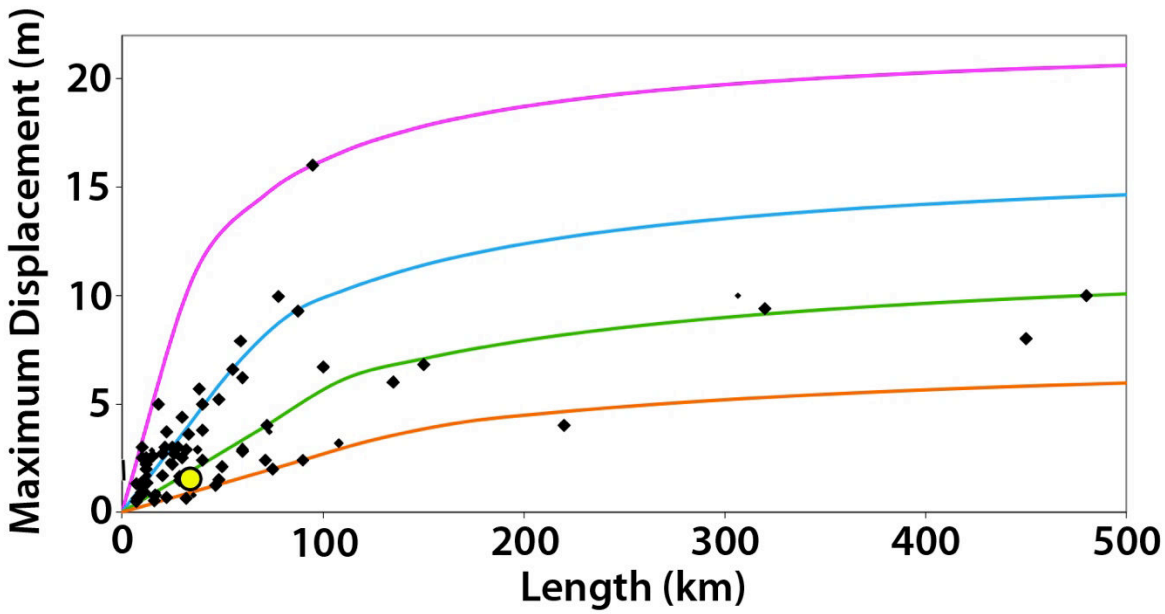


Fig.96: Earthquake displacement-length data inferred at depth for 90 historical large continental earthquakes (Mw≥6). The 4 curves indicate the number of major long-term fault segments to have been broken by the earthquakes (modified from Manighetti et al., 2007 and Chapter IV). The yellow dot shows the 1979 Imperial Valley earthquake depth slip-length data.

References

Archuleta, R. J. (1984). A faulting model for the 1979 Imperial Valley earthquake. *Journal of Geophysical Research: Solid Earth (1978–2012)*, **89**(B6), 4559-4585.

Blisniuk, K., T. Rockwell, L. A. Owen, M. Oskin, C. Lippincott, M. W. Caffee, & J. Dortch. 2010. Late Quaternary slip rate gradient defined using high-resolution topography and 10 Be dating of offset landforms on the southern San Jacinto Fault zone, California. *J. Geophys. Res.,* **115**, B08401, doi:10.1029/2009JB006346.

Chavez, D., Gonzales, J., Reyes, A., Medina, M., Duarte, C., Brune, J. N., & Johnson, C. E. (1982). Main-shock location and magnitude determination using combined US and Mexican data. *US Geol. Surv. Prof. Pap*, **1254**, 51-54.

Fialko, Y. 2006. Interseismic strain accumulation and the earthquake potential on the southern San Andreas fault system, *Nature*, **441**, 968–971, doi:10.1038/nature04797

Gurrola, L. D., & T. K. Rockwell. 1996. Timing and slip for prehistoric earthquakes on the Superstition Mountain fault, Imperial Valley, southern California*, J. Geophys. Res.,* **101**, 5977–5985, doi:10.1029/95JB03061.

Hartzell, S. H., & Heaton, T. H. (1983). Inversion of strong ground motion and teleseismic waveform data for the fault rupture history of the 1979 Imperial Valley, California, earthquake. *Bulletin of the Seismological Society of America*, **73**(6A), 1553-1583.

Hauksson, E., W. Yang, & P.M. Shearer (2012). Waveform Relocated Earthquake Catalog for Southern California (1981 to June 2011*); Bull. Seismol. Soc. Am.,* **102**, doi:10.1785/0120120010.

Hudnut, K. W., & K. Sieh. 1989. Behavior of the Superstition Hills fault during the past 330 years, *Bull. Seismol. Soc. Am*., **79**, 304–329.

Janecke, S.U., Dorsey, R.J., Forand, D., Steely, A.N., Kirby, S.M., Lutz, A.T., Housen, B.A., Belgarde, B., Langenheim, V.E., & Rittenour, T.M. (2010), High Geologic Slip Rates since Early Pleistocene Initiation of the San Jacinto and San Felipe Fault Zones in the San Andreas Fault System: Southern California, USA: *Geological Society of America Special Paper* **475**, 48 p., doi: 10.1130/2010.2475.Â isbn 9780813724751

Johnson, CE, & Hutton, LK, 1982, Aftershocks and pre-earthquake seismicity: *US Geological Survey Professional Paper* **1254**, p. 59-76

Kendrick, K. J., D. M. Morton, S. G. Wells, & R. W. Simpson. 2002. Spatial and temporal deformation along the northern San Jacinto fault, southern California: Implications for slip rates, *Bull. Seismol. Soc. Am*., **92**, 2782–2802, doi:10.1785-/0120000615.

King, N.E., & W. Thatcher (1998). The co-seismic slip distributions of the 1940 and 1979 Imperial Valley, California, earthquakes and their implications, *J. Geophys. Res*. **103**, no. B8, 18,069–18,086.

Kirby, S. M., Janecke, S. U., Dorsey, R. J., Housen, B. A., Langenheim, V. E., McDougall, K. A., & Steely, A. N. (2007). Pleistocene Brawley and Ocotillo formations: Evidence for initial strike□slip deformation along the San Felipe and San Jacinto fault zones, southern California. *The Journal of geology*, **115**(1), 43-62.

Lindsey, E. O., & Y. Fialko 2013. Geodetic slip rates in the southern San Andreas Fault system: Effects of elastic heterogeneity and fault geometry, *J. Geophys. Res. Solid Earth*, **118**, 689–697, doi:10.1029/2012JB009358.

Lundgren, P., E. A. Hetland, Z. Liu, and E. J. Fielding. 2009. Southern San Andreas-San Jacinto fault system slip rates estimated from earthquake cycle models constrained by GPS and interferometric synthetic aperture radar observations, *J. Geophys. Res*., **114**, B02403, doi:10.1029/2008JB005996

Lutz, A. T., R. J. Dorsey, B. A. Housen, & S. U. Janecke. 2006. Stratigraphic record of Pleistocene faulting and basin evolution in the Borrego Badlands, San Jacinto fault, southern California, *Geol. Soc. Am. Bull*., **118**, 1377–1397, doi:10.1130/B25946.1

Olson, A. H., & Apsel, R. J. (1982). Finite faults and inverse theory with applications to the 1979 Imperial Valley earthquake. *Bulletin of the Seismological Society of America*, **72**(6A), 1969-2001.

Rockwell, T. K., C. Loughman, & P. Merifield. 1990. Late Quaternary rate of slip along the San Jacinto fault zone near Anza, southern California, *J. Geophys. Res*., **95**, 8593–8605, doi:10.1029/JB095iB06p08593.

Rockwell, T. K., & Klinger, Y. (2013). Surface rupture and slip distribution of the 1940 Imperial Valley earthquake, Imperial Fault, Southern California: Implications for rupture segmentation and dynamics. *Bulletin of the Seismological Society of America*, **103**(2A), 629-640.

Sharp, R. V. 1967. San Jacinto fault zone in the Peninsular Ranges of southern California*, Geol. Soc. Am. Bul*l., **78**, 705–730, doi:10.1130/ 0016-7606(1967)78[705:SJFZIT]2.0.CO;2.

Sharp, R. V., Lienkaemper, J. J., Bonilla, M. G., Burke, D. B., Fox, B. F., Herd, D. G., ... & Sieh, K. E. (1982). Surface faulting in the central Imperial Valley. *The Imperial Valley, California, Earthquake of October*, *15*(1979), 119-143.

Sharp, R. V. (1982). Comparison of 1979 surface faulting with earlier displacements in the Imperial Valley. *US Geol. Surv. Prof. Pap*, **1254**, 213-221.

Trifunac, M. D., & J. N. Brune (1970). Complexity of energy release during the Imperial Valley, California, earthquake of 1940, *Bull. Seismol. Soc. Am*. **60**, 137–160.

2.12. Kunlun 2001

14/11/2001, China

Mw 7.8

Epicenter (USGS) : 35.95°N-90.54°E

Left-lateral strike-slip



Broken long-term fault

The EQ broke a part of the **Kunlun Fault**, China.

General characteristics from literature:

- Fairly linear, left-lateral strike-slip fault, about 1600 km long (e.g. Van der Woerd et al., 2002).
- Would have initiated 23-34 My ago (Oligo-Miocene to end of Eocene) (Tapponnier et al., 2001 and references therein), based on volcanism occurrence in extensional basins in the western end of the Kunlun Fault (Jolivet et al., 2003).
- Maximum cumulative lateral slip of more than 100 km, yet poorly constrained
- Current lateral slip rate: 7-11 mm/yr (e.g. Zhang et al., 2004; Meade 2007) measured locally on the central part of the Kunlun Fault and also deduced from block models.
- Long-term lateral slip rate: 10-12 mm/yr (over the Quaternary) in central and western parts of the fault (major segments 2, 3 and 4, see below; Van der Woerd et al., 1998, 2000, 2002; Li et al., 2005), decreasing down to 1-6 mm/yr in eastern part (major segment 1, see below; Kirby et al., 2007).

→ **The Kunlun Fault is a mature fault (L > 1000 km; I-Age > 10 Ma; MR > 1 cm/yr; DTotal > 100 km)**

Architecture and lateral major segmentation, from our mapping (Fig.97):

- Mapping done from Google Earth, Landsat and ASTER GDEM data combined with dense literature information.
- Long-term fault trace well expressed in surface morphology and topography.
- The Kunlun Fault is pretty isolated, i.e., quite far away from any other large sub-parallel fault. It is however connected to the Manyi Fault that forms the westward prolongation of the Kunlun Fault (See Manyi section).
- To the west, the Kunlun Fault terminates in a large-scale splay (T_{Ss}-type termination, Fig.24), i.e., a dense network of splaying secondary faults, oblique to the master fault, most being both strike-slip and reverse (Fig.97). Some of those splay faults connect with the Manyi Fault further west and south. To the east, the Kunlun Fault abuts and ends against the NE-trending Longmen Shan thrust belt (T_{ob}-type termination, Fig.24). The western splay suggests that the Kunlun Fault has been propagating westward over geological time (See below).
- The Kunlun Fault is divided into 4 (and possibly 5?) major, fairly collinear segments (See Fig.97b, where they are numbered).
- Those 4 major segments have a similar length of 225-330 km (length measured along the linear trace of each segment; Fig.97b and Table 6).
- The fault trace is linear along each major segment. The four segments are sub-parallel. The three westernmost major segments are well connected to each other through a pronounced double bend in the fault trace (bends by 10-27°), while segments 1 and 2 in the east are not clearly connected at the surface and rather overlap. Whether they are connected or not at the surface, the segment traces are well separated across the fault, with across-fault separation distances in the range 15-50 km (Table 6). The easternmost segment 1 has a discontinuous trace, contrary to the other 3 segments. Together these suggest that segment 1 is younger and more immature than the other 3 major segments. This would suggest that the Kunlun Fault has also propagated eastward over time; major segments 2, 3 and 4 might thus well constitute the most mature core of the Kunlun Fault that might have propagated bilaterally. While the eastern tip of the fault seems presently arrested by the oblique Longmen Shan fault zone, the western tip of the Kunlun Fault is still likely currently propagating.
- A fifth major segment might be suggested west of segment 4, but its trace is discontinuous and fairly short and hence the segment is not clear (for it is in the process of forming?).
- The sub-parallel Manyi Fault could be thought as another major segment of the Kunlun Fault. Yet its across-strike distance from the Kunlun Fault trace is ~75 km, likely too large

to consider the Manyi Fault as a segment of the Kunlun fault. The question is however disputable, especially because the Kunlun fault seems to be in the process of connecting with the Manyi Fault, through a large-scale pull-apart (Fig.97).

- Our identification of major segments is fairly similar to those in previous studies (e.g., Van der Woerd e al., 2002) except that we do not define as individual segments the bent fault sections that connect the major segments.

→ **The Kunlun Fault is divided into 4 to 5 long-term major collinear segments. The Kunlun Fault might have propagated bilaterally over geological time, so that its three most central, well-connected major segments 2-3-4 are likely the most mature along the fault.**

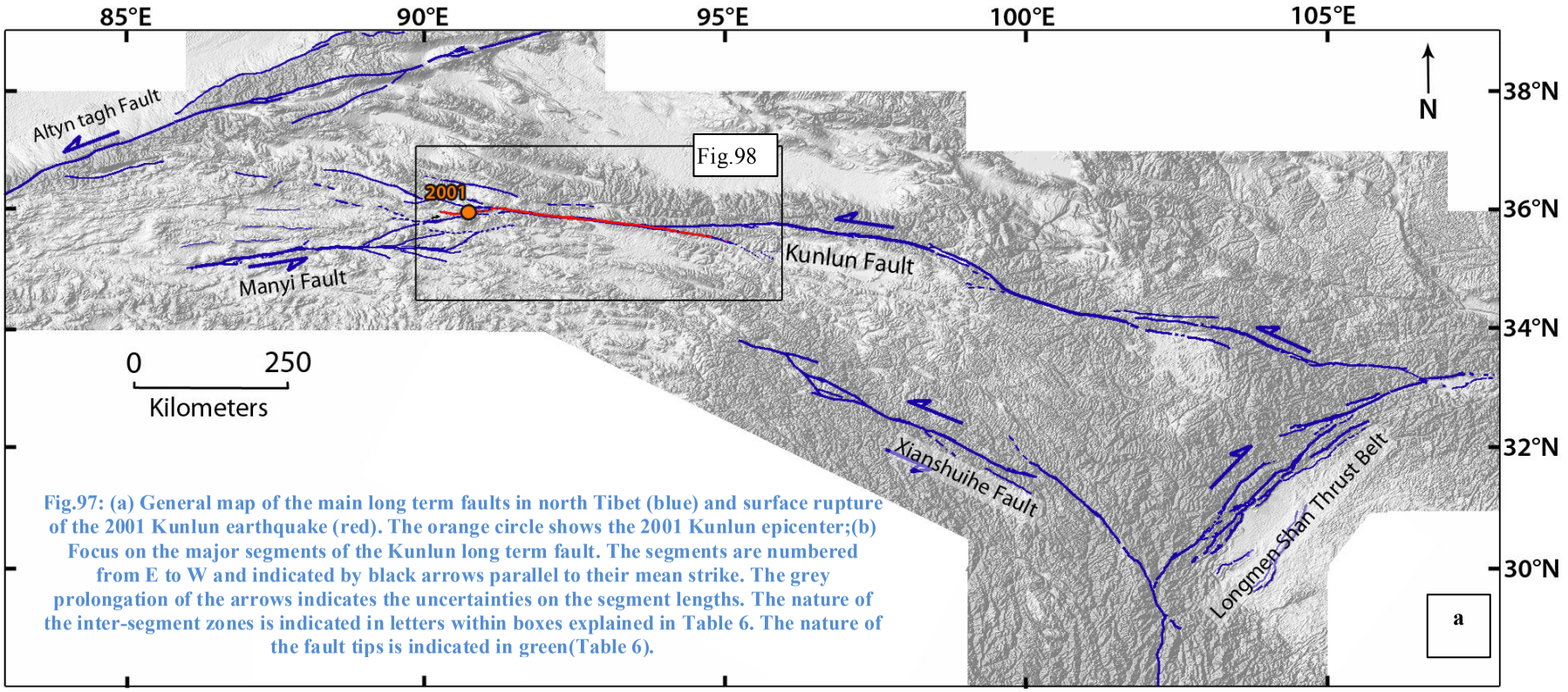
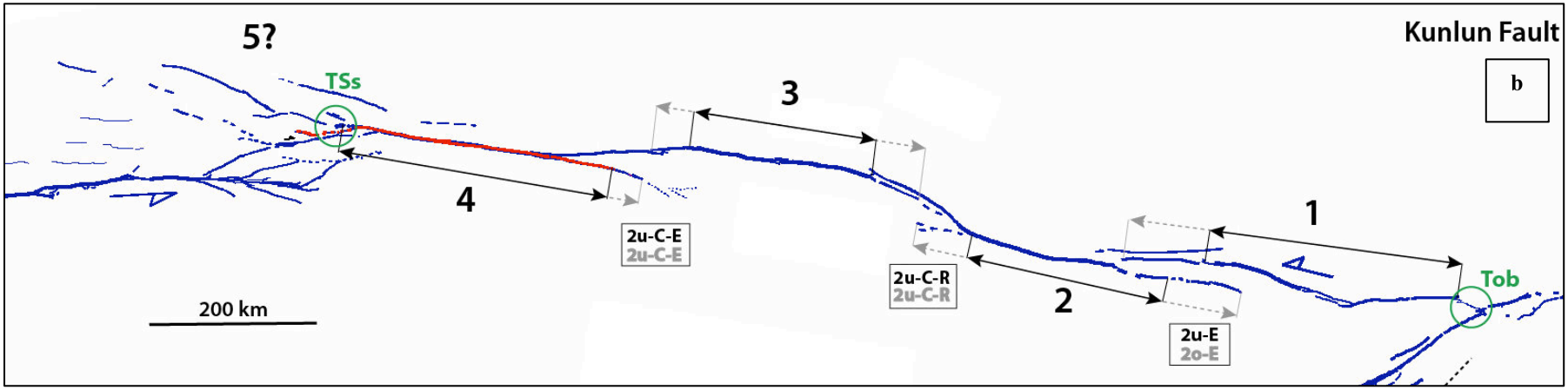


Fig.97: (a) General map of the main long term faults in north Tibet (blue) and surface rupture of the 2001 Kunlun earthquake (red). The orange circle shows the 2001 Kunlun epicenter;(b) Focus on the major segments of the Kunlun long term fault. The segments are numbered from E to W and indicated by black arrows parallel to their mean strike. The grey prolongation of the arrows indicates the uncertainties on the segment lengths. The nature of the inter-segment zones is indicated in letters within boxes explained in Table 6. The nature of the fault tips is indicated in green(Table 6).



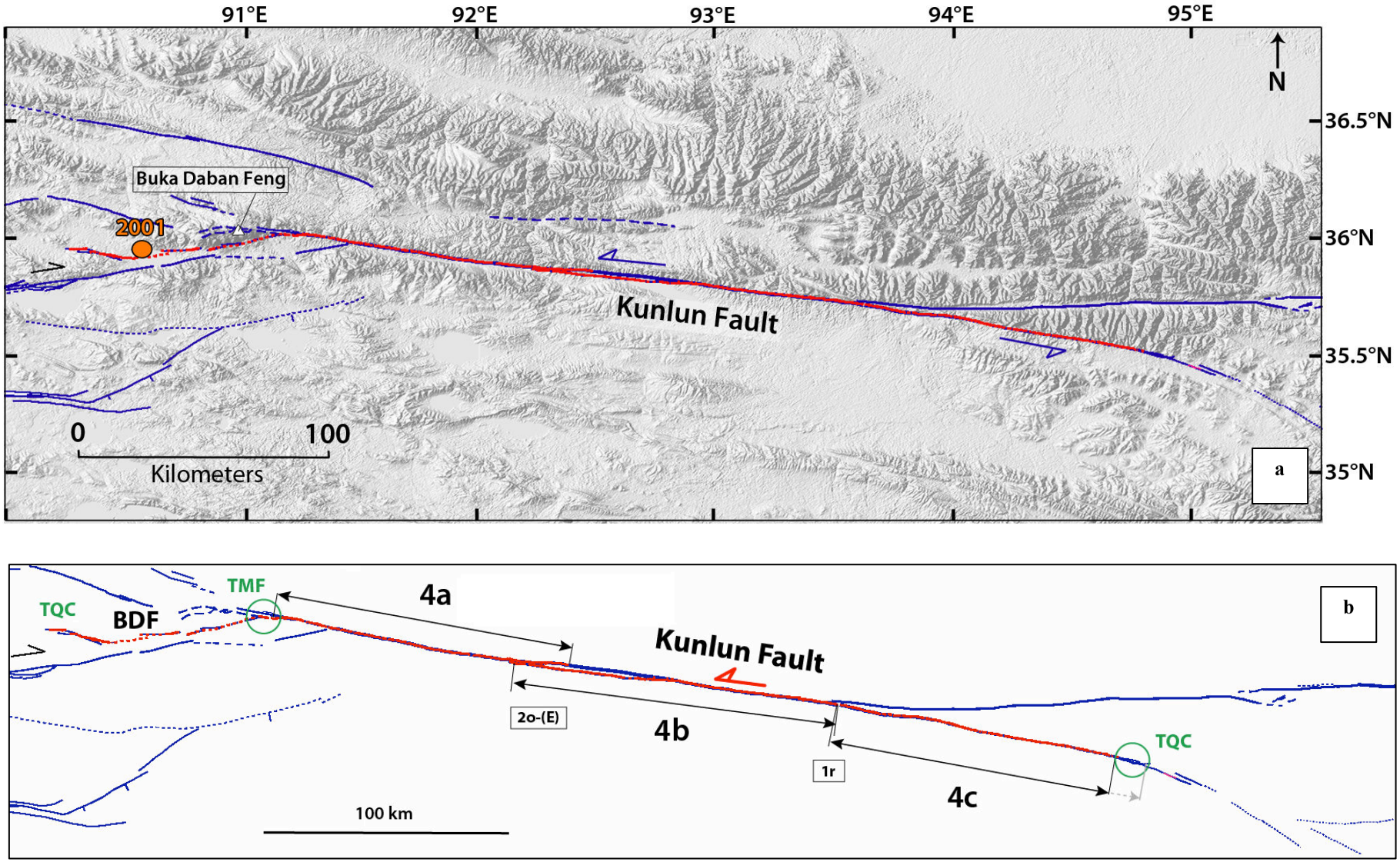


Fig.98: (a) Zoom on the broken section of the Kunlun fault, from Fig.97(a) (same caption); b) Map of the secondary segments that form the major segment 4 of the Kunlun fault.

2001 Coseismic rupture

Surface trace and location on long-term Kunlun Fault:

- The 2001 surface rupture is clear on Google Earth, Landsat 7 and Aster GDEM v2 images. The surface trace of the earthquake has been precisely mapped, and the displacements measured (See below), both on the field and from satellite imagery (e.g. Lin et al., 2002, 2003; Fu and Lin 2003; Fu et al., 2005; Klinger et al., 2005; Xu et al., 2006).
- Surface rupture of ~450 km long.
- The EQ broke two distinct faults: it initiated on a small, oblique, strike-slip and normal fault, located at the southern piedmont of the 'Buka Daban Feng' Range (Fig.98) and developed at the western tip of major segment 4. That 'Buka Daban Feng' Fault (BDF) belongs to the splay developed at the western Kunlun Fault termination (T_{MF} type connection). Then the rupture propagated unilaterally toward the east along the Kunlun Fault (Fig.98).
- The EQ broke one major segment only of the Kunlun Fault, the major segment 4. It broke it on its entire length that is ~350 km.
- On the Kunlun Fault, the rupture thus started at the western tip of major segment 4 and stopped at its eastern tip.
- According to its geometry, segment 4 is divided into three secondary collinear segments, of similar length, 100-135 km (Fig.98). The 2001 EQ thus broke the three secondary segments that form major segment 4.
- The fault trace is fairly linear along each secondary segment. Secondary segments 4a and 4b are overlapping each other on about 20 km, and this overlap marks the inter-segment zone. The across-strike distance between the two secondary segments is short, ~2 km. Secondary segments 4b and 4c are "simply" connected to each other (type 1_r, Fig.18) but they have a slightly different strike (differing by an angle of ~4°) while their zone of connection is where a ENE-trending fault has developed to connect major segment 4 with major segment 3. The angle between segment 4b and this connecting fault is ~12 °.
- The rupture terminates at the eastern tip of major segment 4, and hence at the eastern tip of secondary segment 4c (i.e., where the trace of segment 4c stops being continuous and splays into multiple tiny faults, in a horsetail fashion).

→ The Kunlun EQ broke 1 major segment only of the Kunlun Fault, major segment 4; this segment broke entirely along the 3 secondary segments that form it. The broken major segment is among the most mature segments of the fault. The rupture initiated at the splay tip of the segment (and of the fault).

Coseismic displacements measured at surface:

- *From Field measurements*: The complete slip profile has been densely measured. The maximum lateral slip is ~8 m (Fu et al., 2005; Klinger et al., 2005, 2006; Xu et al., 2006; Fig.99), measured on secondary segment 4b. Note that Lin et al. (2002) measured a local lateral slip of 16.3 m. As such a slip has not been found in any other study, it is likely misleading.
- *From InSAR data and modeling*: Fairly complete slip profile and maximum slip of ~8 m (Lasserre et al., 2005), despite of the de-correlation of the Insar images in the vicinity of the fault.
- The three available slip profiles look similar, showing an overall triangular and asymmetric shape, with maximum slip deported toward the eastern tip of the rupture (at eastern end of secondary segment 4b), and slip decreasing fairly regularly toward the west. Besides, the three slip profiles reveal 4 main slip patches that well coincide with the rupture of the BDF fault, and of the secondary segments 4a, 4b and 4c. The patches are separated by high slip gradients that coincide with the inter-segment zones. The profiles reveal additional slip gradients, which we interpret as revealing smaller-scale intersegments (See also Klinger et al., 2006).

→ The three available surface slip profiles are in fair agreement. Maximum slip of ~8 m on secondary segment 4b. Overall triangular slip profile, with major slip bumps in keeping with rupture of 3 segments on the Kunlun Fault (Fig.99b). It must noted that slip increased along the rupture length as the rupture was propagated eastward.

Source inversion models and slip distribution at depth:

- We compare two source inversion models that have been published on the 2001 Kunlun earthquake (no grid available).

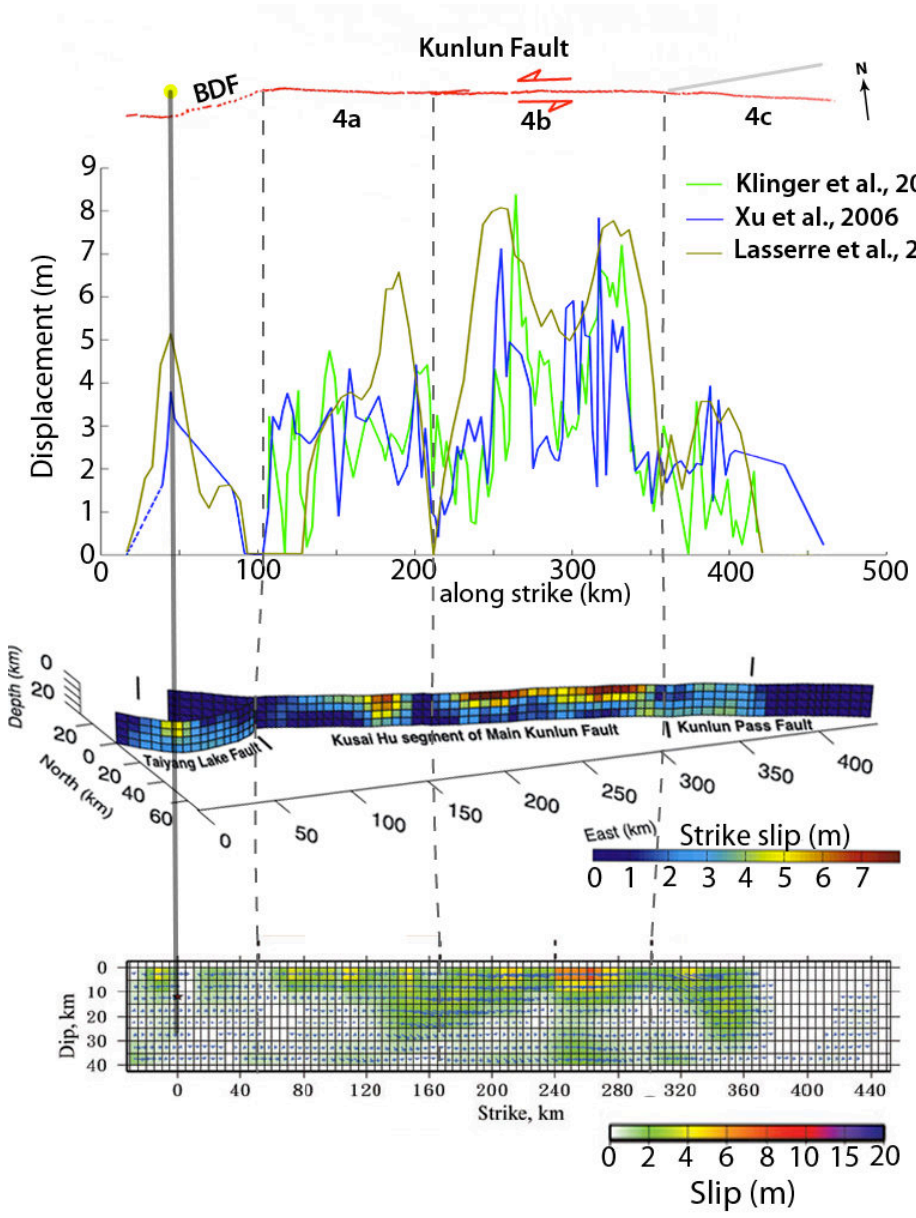
The models differ principally from the data they used:

- Wen et al. (2009): Teleseismic data only, plus inclusion of surface slip. The model divides the broken faults into 5 sections (1 for Buka Daban Feng; 4 for Kunlun) based on geological field observations from Xu et al. (2006).
- Lasserre et al. (2005): Insar data only, but Insar decorrelates in the vicinity of the fault. The model considers the Buka Daban Feng and the Kunlun sections

and divides those two faults into 2 and 4 segments, respectively, based on surface morphological analyses (high resolution satellite images).

→ None of the two models is really robustly constrained since near-field GPS and seismological data are lacking. Yet, both yield fairly similar results, with a maximum slip at depth of ~8 m on segment 4b, and 3-4 main slip patches overall. The slip inferred at depth is thus similar to that measured at surface. Both models also show that most of the slip occurred in an area of ~10 km width. We will use this value for the rupture width.

→ **The source models suggest: L ~410 km, Dmax at depth ~8 m, 4 segments supposedly broken on the Kunlun Fault**.



Mapping of the surface rupture based on Google Earth, Landsat 7 and Aster GDEM data and literature (e.g. Klinger et al., 2005)

Compilation of surface lateral displacements measured on the field (Xu et al., 2006), from correlation of SPOT images (Klinger et al., 2006) and inferred from InSAR (Lasserre et al., 2005)

Lasserre et al. 2005 :
Data : InSAR
L= 410 km minimum ;
W=20 km ; Dmax = 8 m

Wen et al. 2009 :
Data : Teleseismic and surface data from Xu et al. (2006)
L ≈ 410 km ; W=30 km ;
Dmax= 7,8 m

Fig.99: Comparison between different inversion models published on the 2001 Kunlun earthquake. Dark vertical line represents the hypocenter location for each model. Models are at the same scale. The dashed lines show the intersegment zones from our mapping. BDF : Buka Daban Feng Fault.

Other source parameters:

SCARDEC
Mainshock: 2001/11/14 at 9h26min10s GMT;
Lat = 35.95° Lon = 90.54°
Mw 7.9; M0 = 1.3e21 Nm; Z = 15 km;
Duration: 144.9 s
Strike, dip, rake: (8°, 88°, 153°)/(99°, 63°,2°)

Global CMT
Mainshock: 2001/11/14 at 9h27min16s GMT;
Lat = 35.80° Lon= 92.91° (Centroid)
Mw 7.8; M0 = 5.9e20 Nm; Z = 15 km;
Half-duration: 25.8s
Strike, dip, slip : (94°, 61°, -12°)/ (190°, 80°, -150°)

- The EQ duration much differs between the SCARDEC and Global CMT methods. However the SCARDEC method is more precise to determine earthquake duration. Other studies are in agreement with its estimation (e.g. Antolik et al., 2004).

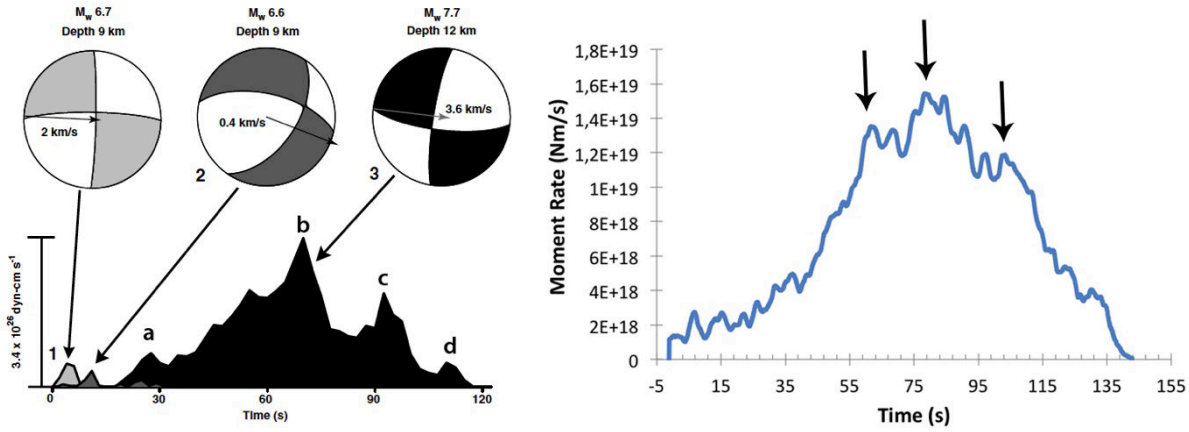


Fig.100: Two examples of Source Time Functions from Antolik et al. (2004) (left) and SCARDEC method (Vallée et al., 2011) (right). See text for details.

- Antolik et al. (2004) distinguished three sub-events (Fig.100):

1) strike slip rupture of the SW extremity of the small oblique Buka Daban Fault on which the earthquake nucleated (pale grey);
2) rupture with a normal component of the major part of the Buka Daban Fault (dark grey);
3) rupture of the main Kunlun Fault (black; our major segment
4). The source time function describing the rupture on the Kunlun Fault shows 3 to 4 distinct peaks of moment release (a, b, c and d on Fig.100, left), which suggest that the rupture broke at least 3 sections of the fault (the last small peak might be linked to the rupture stop). The total rupture duration is ~120 sec.

- The Source Time Function obtained by the SCARDEC method (Fig.100, right; Vallée et al., 2011) shows similar features: first, the moment is progressively released (0-40 s), then the moment release markedly increases up to a maximum around 65 s, followed by two other

peaks around 80 and 100 s. The 3 peaks of large moment release suggest the rupture of 3 distinct fault sections that we interpret as being secondary segments 4a, 4b and 4c.

- Both STF show a fairly gentle moment increase that culminates around 70-80 sec, followed by a faster moment decrease.
- Moment magnitude and seismic moment range between 7.8-7.9 and 0.59-1.3e21 Nm, respectively. This large range of value can be explained by the complexities of large events, which include several broken faults that are difficult to take into account by methods using global seismic networks (same observation for the Denali earthquake which broke several faults with various slip components).

→ The Kunlun source data suggest that three segments broke on the Kunlun Fault. The EQ energy first grew gently, likely on the small oblique DBF Fault, before accelerating on the Kunlun Fault.

Other information:

2001 EQ:

- The rupture had a super-shear velocity, mainly along secondary segment 4b (e.g. Bouchon and Vallée 2003, Antolik et al., 2004; Robinson et al., 2006; Vallée et al., 2008), which is the section of the fault with maximum slip.
- Aftershocks over one year after the EQ mainly localized on the small Buka Daban Fault first broken, in the inter-segment zone between secondary segments 4b and 4c, and in the inter-segment zone between major segments 4 and 3 (e.g. Robinson et al., 2006; Vallée et al., 2008). The largest aftershock had Mw 5.6.

Past EQ activity:

- The Kunlun Fault previously broke in 1937 (M~7.5) and 1963 (Ms ~7.1). Those EQs apparently broke the major segment 3 of the fault, almost entirely (e.g. Kirby et al., 2007).

Parameters retained to describe the 2001 Kunlun EQ (Tables 1 – 4):

Mw 7.8-7.9; M0 ~ 0,59-1,3 e21 Nm; L ~ 450 km ; W ~ 10 km; Dmax surface ~ 8 m; Dmax depth ~ 8 m; *Hypocenter* : Z ~ 9 km.

Number of segments broken on the Kunlun Fault: 1 major segment, entirely, representing the rupture of 3 secondary segments.

The global Kunlun earthquake surface and depth slip-length data fall on the third function (green curve; Fig.101 & 102, respectively), what seems to corroborate that the event broke three segments on the Kunlun Fault. However the EQ broke two distinct faults, not a single one, and it is not clear whether multi-fault ruptures satisfy the scaling laws described in Fig.101 & 102 (See discussion in chapter IV). When we plot the DBF and the Kunlun rupture data separately, the Kunlun slip-length data are still in keeping with the rupture of three segments on the Kunlun Fault. Besides, the DBF slip-length data suggest that three segments might also have broken on the DBF Fault. These 3 DBF broken segments might be the small peaks labeled 1, 2 and a in the STF of Antolik et al. (2004; Fig.100), whereas their existence might explain the long duration of the EQ energy acceleration (first ~0-40 s in Fig.100 right).

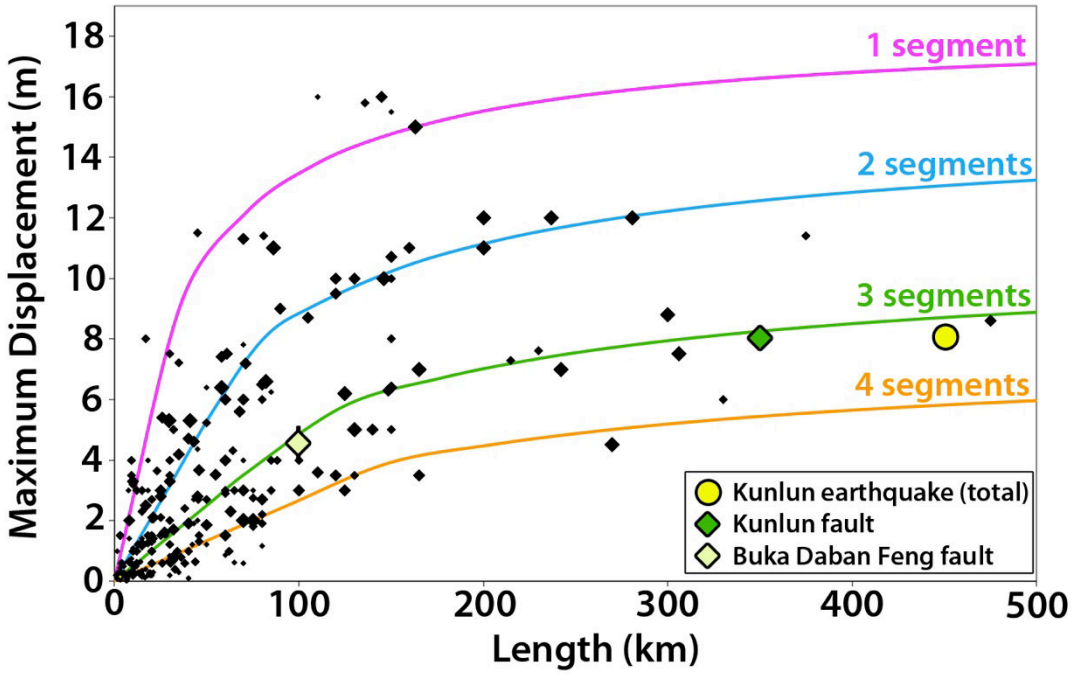


Fig.101: Earthquake displacement-length data measured at surface for 260 historical large continental earthquakes (Mw≥6). The 4 curves indicate the number of major long-term fault segments to have been broken by the earthquakes (modified from Manighetti et al., 2007 and Chapter IV).

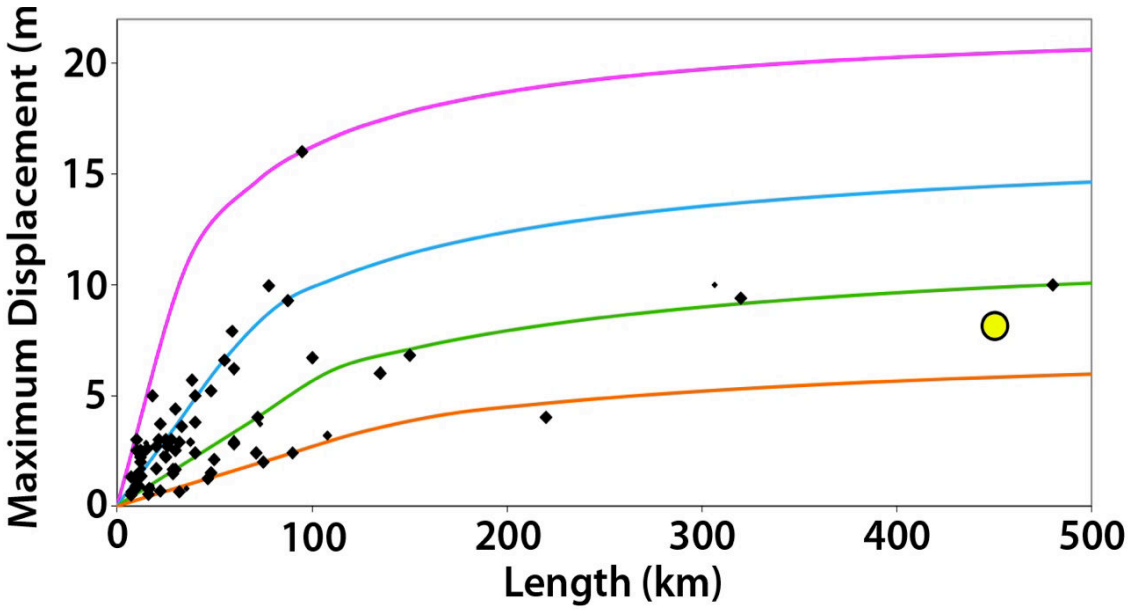


Fig.102: Earthquake displacement-length data inferred at depth for 90 historical large continental earthquakes (Mw≥6). The 4 curves indicate the number of major long-term fault segments to have been broken by the earthquakes (expanded and modified from Manighetti et al., 2007 and Chapter IV). Yellow dot shows the Kunlun earthquake depth slip length data.

References

Antolik, M., R. E. Abercrombie, & G. Ekström 2004. The 14 November, 2001 Kokoxili (Kunlunshan), Tibet earthquake: rupture transfer through a large extensional step-over, *Bull. Seism. Soc. Am*. **94**, 1173–1194.

Bouchon, M. & Vallée, M., 2003. Observation of long supershear rupture during the magnitude 8.1 Kunlunshan earthquake, *Science*, **301**, 824–826.

Fu, B. & Lin, A. 2003. Spatial distribution of the surface rupture zone associated with the 2001 Ms 8.1 Central Kunlun earthquake, northern Tibet, revealed by satellite remote sensing data. *International Journal of Remote Sensing* **24**, 2191– 2198.

Fu, B., Awata, Y., Du, J., Ninomiya, Y. & He, W. 2005. Complex geometry and segmentation of the surface rupture associated with the 14 November 2001 great Kunlun earthquake, northern Tibet, China. *Tectonophysics* **407**, 43–63.

Jolivet, M., M. Brunel, D. Seward, Z. Xu, J. Yang, J. Malavieille, F. Roger, A. Leyreloup, N. Arnaud, and C. Wu 2003. Neogene extension and volcanism in the Kunlun Fault Zone, northern Tibet: New constraints on the age of the Kunlun Fault, *Tectonics*, **22**(5), 1052, doi:10.1029/2002TC001428.

Kirby, E., Harkins, N., Wang, E., Shi, X., Fan, C. & Burbank, D. 2007. Slip rate gradients along the eastern Kunlun fault, *Tectonics*, **26**, TC2010, doi:10.1029/2006TC002033.

Klinger, Y., Xu, X., Tapponnier, P., Van Der Woerd, J., Lasserre, C. & King, G. 2005. High-resolution satellite imagery mapping of the surface rupture and slip distribution of theMw□7.8, November 14, 2001Kokoxili earthquake (Kunlun Fault, Northern Tibet, China). *Bull. seism. Soc. Am.*, **95**, 1970–1987, doi:10.1785/0120040233.

Klinger, Y., Michel, R. & King, G.C.P., 2006. Evidence for an earthquake barrier model from Mw7.8 Kokoxili (Tibet) earthquake slip-distribution, *Earth planet. Sci. Lett*., **242**, 354–364.

Manighetti, I., M. Campillo, S. Bouley, and F. Cotton (2007), Earthquake scaling, fault segmentation, and structural maturity, *Earth Planet. Sci. Lett*., **253**, 429-438, doi:10.1016/j.epsl.2006.11.004

Meade, B. (2007). Present-day kinematics at the India-Asia collision zone. *Geology,* **35**, 81—84, doi: 10.1130/G22924A.1

Lasserre C., Peltzer, G., Klinger, Y., Van Der Woerd, J. & Tapponnier, P. 2005. Coseismic deformation of the 2001 Mw = 7.8 Kokoxili earthquake in Tibet, measured by synthetic aperture radar interferometry, *J. geophys. Res*., **110**, B12408, doi:10.1029/2004JB003500.

Li Haibing, Van der Woerd, J., Tapponnier, P., Klinger, Y., Qi Xuexiang, Yang Jingsui & Zhu Yintang. 2005. Slip rate on the Kunlun Fault at Hongshui Gou, and recurrence time of great events comparable to the 14/11/2001, Mw 7.9 Kokoxili earthquake, *Earth Planet. Sci. Lett*., **237**, 285 – 299.

Robinson, D. P., C. Brough, & S. Das 2006. The Mw 7.8, 2001 Kunlunshan earthquake: Extreme rupture speed variability and effect of fault geometry, *J. Geophys. Res*., **111**, B08303, doi:10.1029/2005JB004137

Vallée, M., Landès, M., Shapiro, N. M. & Klinger, Y. 2008. The 14 November 2001 Kokoxili (Tibet) earthquake: high-frequency seismic radiation originating from the transitions between sub-Rayleigh and supershear rupture velocity regimes, *J. geophys. Res*., **113**, B07305, doi:10.1029/2007JB005520.

Vallée, M., J. Charléty, A.M.G. Ferreira, B. Delouis, and J. Vergoz, (2011). SCARDEC : a new technique for the rapid determination of seismic moment magnitude, focal mechanism and source time functions for large earthquakes using body wave deconvolution, *Geophys. J. Int*., **184**, 338-358.

Van Der Woerd, J., Ryerson, F.J., Tapponnier, P., Gaudemer, Y., Finkel, R., Meriaux, A.S., Caffee, M., Guoguang, Z. & Qunlu, H. 1998. Holocene left slip-rate determined by cosmogenic surface dating on the Xidatan segment of the Kunlun Fault (Qinghai, China), *Geology*, **26,** 695–698.

Van der Woerd, J., Ryerson, F.J., Tapponnier, P., Meriaux, A.S., Gaudemer, Y., Meyer, B., Finkel, R., Caffee, M.W., Guoguang, Z. & Zhiqin, X. 2000. Uniform slip-rate along the Kunlun Fault: Implications for seismic behavior and large-scale tectonics, *Geophys. Res. Lett.*, **27**, 2353 – 2356.

Van Der Woerd, J., Tapponnier, P., Ryerson, F.J., Meriaux, A.S., Meyer, B., Gaudemer, Y., Finkel, R., Caffee, M.W., Guoguang, Z. & Zhiqin, X. 2002. Uniform postglacial slip-rate along the central 600 km of the Kunlun Fault (Tibet), from 26Al, 10Be, and 14C dating of riser offsets, and climatic origin of the regional morphology, *Geophys. J. Int*., **148**, 356-388.

Tapponnier, P., Xu, Z., Roger, F., Meyer, B., Arnaud, N., Wittlinger, G. & Yang, J. 2001. Oblique stepwise rise and growth of the Tibet plateau, *Science*, **294**, 1671–1677.

Xu, X., Yu, G., Klinger, Y., Tapponnier, P. & Van Der Woerd, J. 2006. Re-evaluation of surface rupture parameters and faulting segmentation of the 2001 Kunlunshan earthquake (Mw 7.8), northern Tibetan Plateau, China, *J. geophys. Res*., **111**, B05316, doi:10.1029/2004JB003488.

Wen, Y. Y., Ma, K. F., Song, T. R. A. & Mooney, W. D. 2009. Validation of the rupture properties of the 2001 Kunlun, China (Ms = 8.1), earthquake from seismological and geological observations. *Geophys. J. Int*., **177**, 555–570

Zhang, P.-Z., et al. 2004. Continuous deformation of the Tibetan Plateau from global positioning system data, *Geology*, **32**, 809 – 812

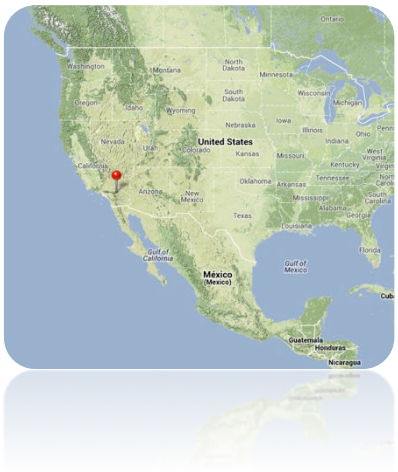
2.13. Landers 1992

28/Jun/1992, California, USA

Mw 7.3

Epicenter : 34.2°N-116.4°W

Right-lateral strike-slip



Broken long-term fault

The Landers EQ broke three faults of the East California Shear Zone (ECSZ) in the Mojave Desert, California (Fig.103), from south to north: Johnson Valley, Homestead Valley and Camp Rock-Emerson Fault. Each of the three faults was only partially ruptured.

General characteristics of the ECSZ from literature and from our mapping:

This part is presented in Hector Mine section.

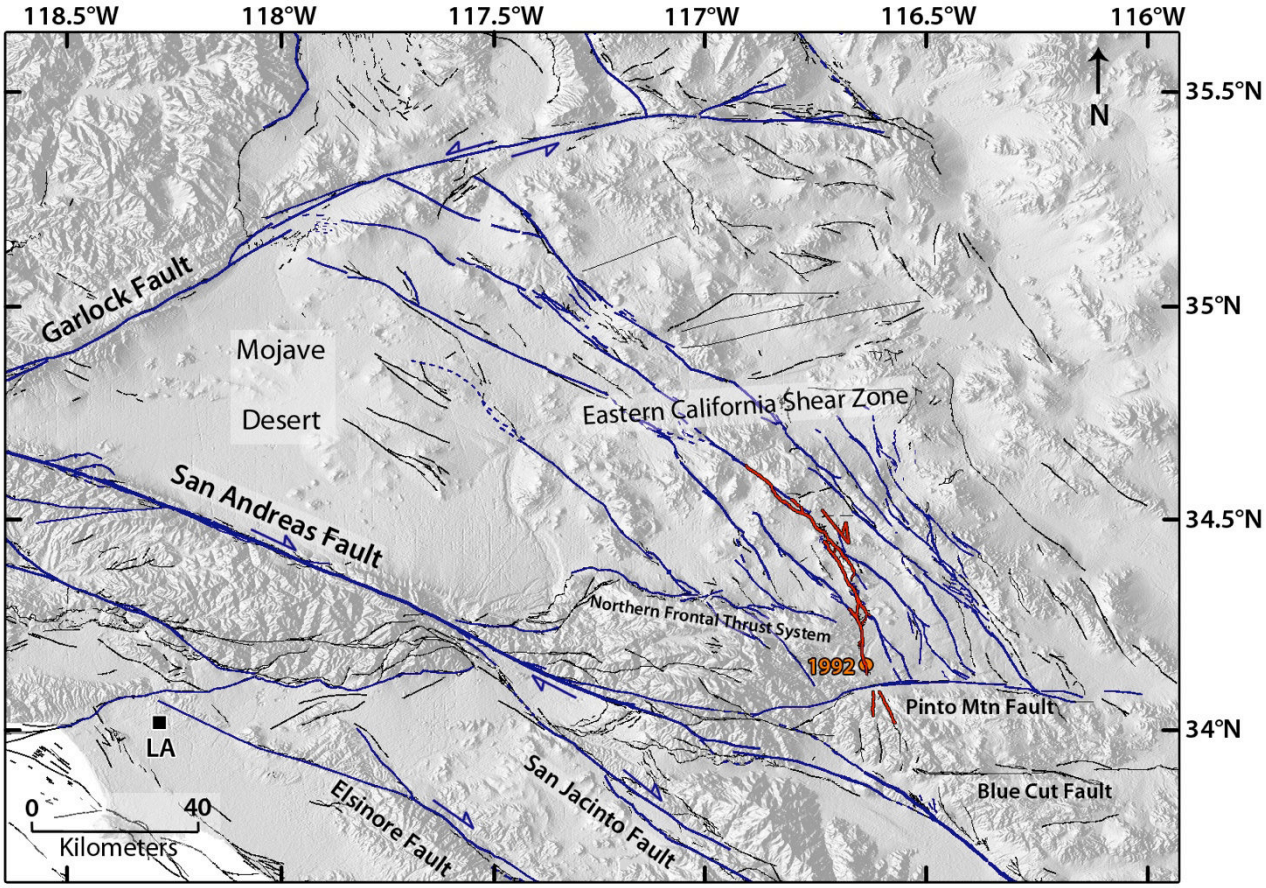


Fig.103: General map of long term faults in the East California Shear Zone. In blue are the major active faults that we mapped. In black are the other Quaternary faults mapped by the U.S. Geological Survey and California Geological Survey, 2006. In red is the surface rupture of the 1992 Landers earthquake (from Sieh et al., 1993). The orange circle shows the 1992 Landers epicenter.

General characteristics of the broken faults from literature (Fig.104 & 105):

- Right lateral faults oriented NW-SE to ~N-S (arcuate shape) about 100 km long.
- Cumulative lateral displacement of 2-4 km (Dokka 1983) to 10 km (Garfunkel 1974) based on offset measurements of volcanic and sedimentary rocks across the Camp Rock Fault.
- Long-term lateral slip rate (late Cenozoic) of 0.2-0.7 mm/yr (e.g. Rubin and Sieh 1997; Rockwell et al., 2000) based on paleoseismological trenches across the Emerson, Homestead Valley and Johnson faults.
- The EQ occurred in the southern half of the rotating ECSZ zone, where rotations are lower, suggesting that the faults are younger than further north.

→ The Camp Rock-Emerson, Homestead Valley and Johnson Valley faults which broke in the Landers event, are immature faults (L ~100 km, I-Age < 10 Ma, D_{total} < 10 km, and MR < 1 mm/yr).

Architecture and lateral major segmentation of the broken faults, from our mapping:

Camp Rock-Emerson Fault (Fig.105):

- The longest fault involved in the Landers EQ is the so-called Camp Rock-Emerson Fault (Fig.105). That fault is made of three major segments (See below). In the north, its trace vanishes into the Barstow tear zone (See Fig.82 in section Hector Mine), beyond which the trace resumes up to the Garlock Fault. In the south, the fault splays into a number of secondary, oblique branches, among which are the Homestead and Johnson Valley faults (See below for more details). The Camp Rock-Emerson Fault has thus likely been propagating southward over geological time.
- Because of the Barstow tear zone, the two sections of the Camp Rock-Emerson Fault on either sides of the tear zone are likely to presently behave as two distinct faults. Only the southern part of the fault, which we still call Camp Rock-Emerson, was involved in the Landers EQ. That fault is thus ~100 km long.
- The Camp Rock-Emerson Fault is made of three major, collinear segments, of similar length, 25-35 km. The fault trace is roughly linear along each major segment. Major segments 1 and 2 are connected with a broadly overlapping extensive relay zone (releasing step-over). The southern tip of segment 2 is mainly marked by the departure of multiple splay branches. The southern tip of segment 3 is where the segment also splays into multiple branches (See Fig.105 & Table 6).
- The Homestead Valley and Johnson Valley Faults are the largest splay branches that depart from the southern tip of the Camp Rock-Emerson segment 2.

→ The principal fault involved in the Landers EQ is the Camp Rock-Emerson Fault. That fault is made of three major segments, and has likely propagated southward over geological time, forming splay branches, which include the Homestead Valley and the Johnson Valley Faults.

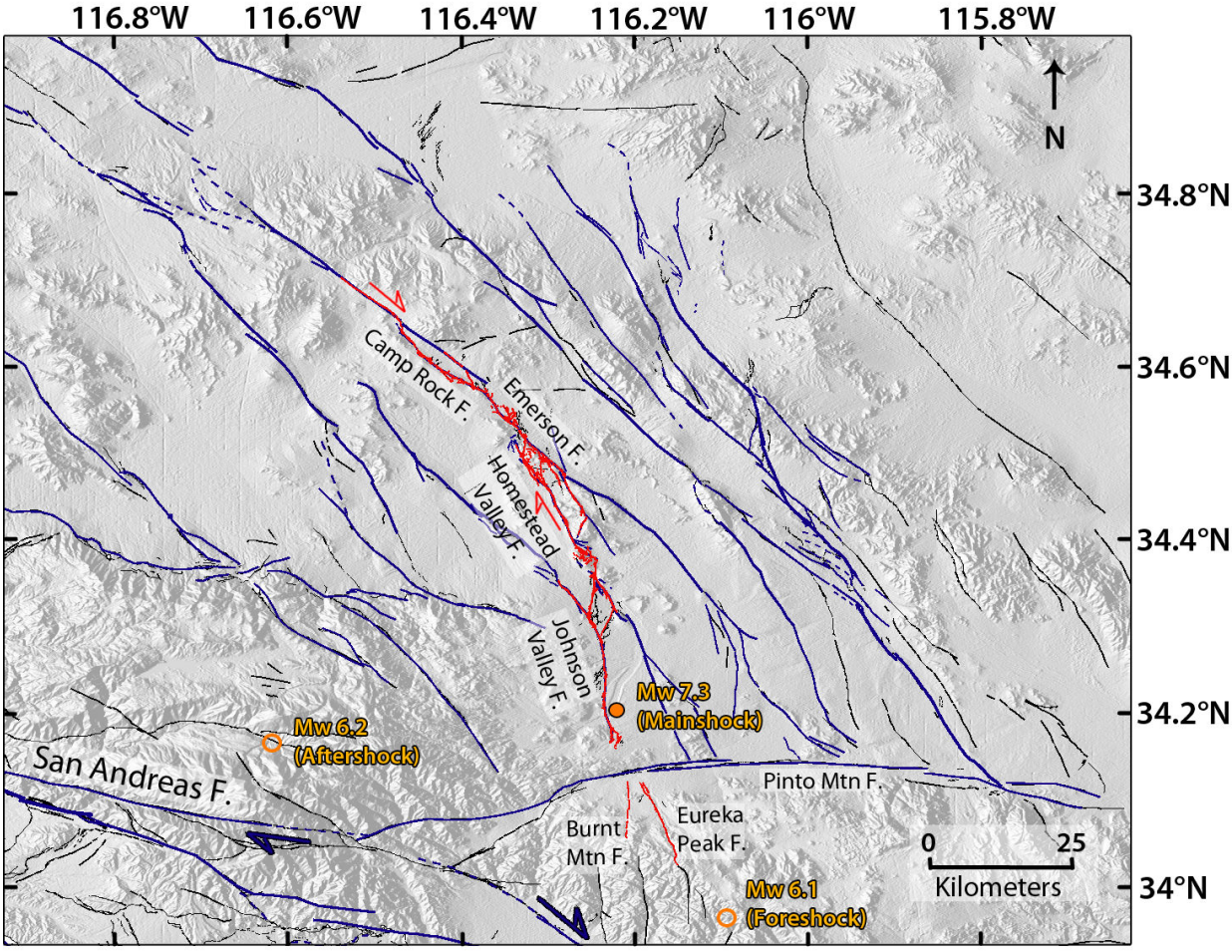


Fig.104: Zoom on the broken faults of Camp Rock-Emerson, Homestead Valley, Johnson Valley and Eureka Peak, from Fig.103 (same caption). The orange full circle shows the 1992 Landers epicenter. Orange empty circles indicate the epicenters of the Mw6.1 Joshua Tree foreshock (23 April 1992) and Mw 6.2 Big Bear aftershock (3h after the mainshock).

Homestead Valley Fault (Fig.105):

- The Homestead Valley Fault is the largest splay fault of the Camp Rock-Emerson Fault. It departs from the southern tip of the Camp Rock-Emerson segment 2. While the Homestead Valley Fault runs over ~45 km up to the Pinto Fault in the south, it connects with the nearby Johnson Valley Fault further west, through a large pull-apart.
- The Homestead Valley Fault is made of three, hardly connected major, collinear segments, of similar length, 9-15 km. Although the overall trace of each major segment is fairly linear, it appears more sinuous when observed in more details. The segments are hardly connected to each other, and are instead separated by step-overs of 1-1.5 km wide (See Table 6). Together these support that the Homestead Valley Fault is fairly immature.
- The fault ends to the south by splaying into two main branches, and this suggests that the Homestead Valley Fault has been propagating southward over recent time, in same direction as its master Camp Rock-Emerson Fault (Fig.105).

→ The Homestead Valley Fault is made of three major, hardly connected segments, among which the southernmost might be the most recent

Johnson Valley Fault (Fig.105):

- The Johnson Valley Fault is the nearest (~ 10 km) parallel, synthetic fault west of the Camp Rock-Emerson Fault. Its total length is ~55 km. The entire length of the Johnson Valley Fault is overlaid by the Camp Rock-Emerson Fault. The Johnson Valley Fault is also the nearest (~ 3 to 8 km) parallel, synthetic fault west of the Homestead Valley Fault. The entire length of the Homestead Valley Fault is overlaid by the Johnson Valley Fault.
- The Johnson Valley Fault is made of five, fairly well connected major, collinear segments, of similar length, 8-13 km. The overall trace of each major segment is fairly linear. The segments appear well connected to each other at the surface, through small step-overs (< 1km wide) and pronounced bends (15-25°) (See Table 6). Together these might suggest that the Johnson Valley Fault is more mature than the Homestead Valley neighboring fault.
- Although no long-term trace appears clearly in the morphology, the Landers EQ demonstrated that the Johnson Valley Fault is connected to the Homestead Valley Fault through a large pull-apart. The direction of the Johnson Valley Fault markedly changes from NW to N-S where it connects to the Homestead Valley Fault, so that it parallels the later. The zone of strike change coincides with the southern Mojave tear zone suspected on Fig.82 in section Hector Mine. Together these suggest that the southernmost part of the Johnson Valley Fault might have, over time, become a part of the splaying fault network that forms the southern termination of the main Camp Rock-Emerson Fault, possibly because it was, once, cross-cut by the southern Mojave tear zone.

→ The Johnson Valley Fault is made of five major, fairly well connected segments, among which the southernmost might now be part of the splaying termination of the principal Camp Rock-Emerson Fault.

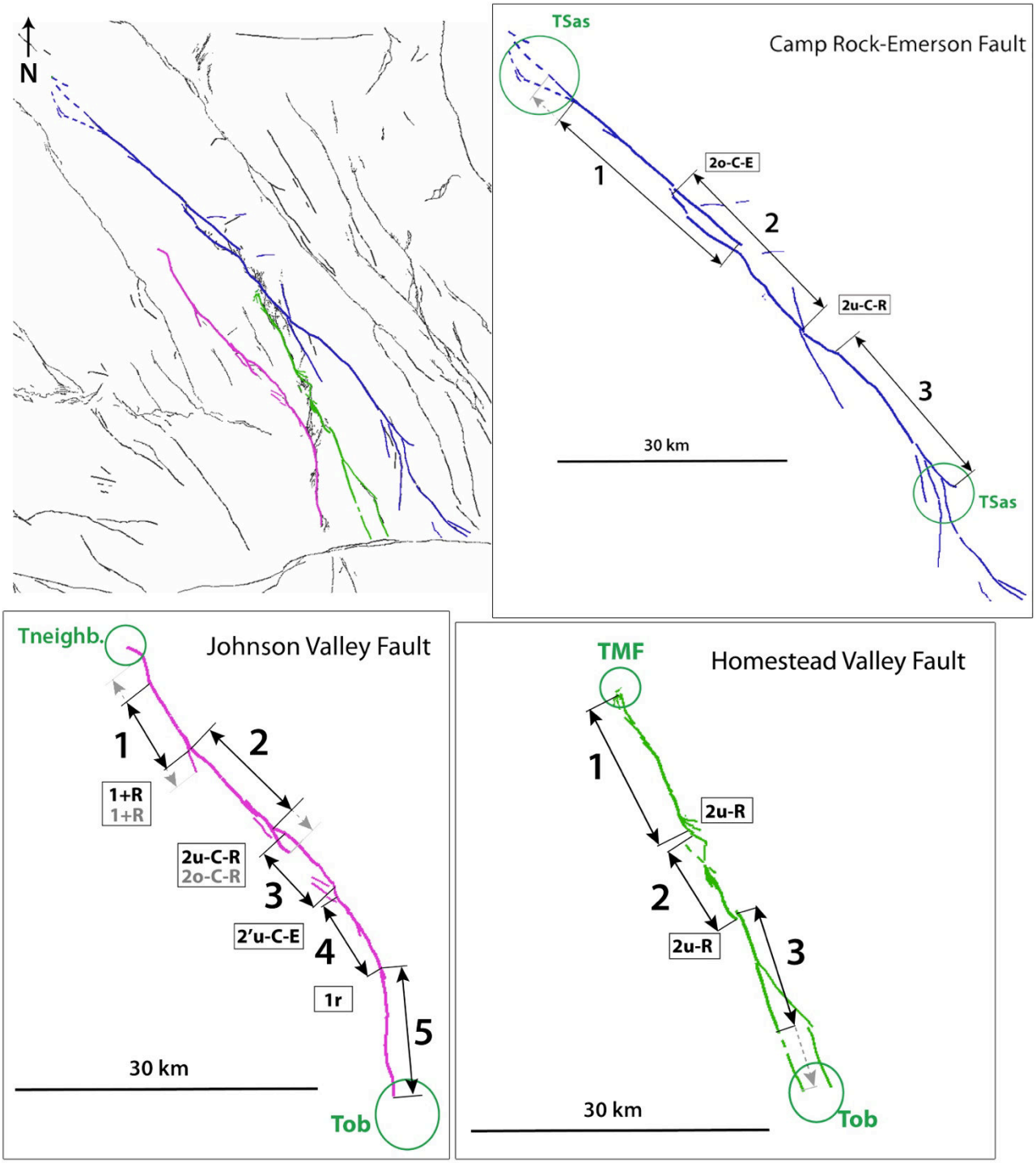


Fig.105: Map of the three major faults broken during the 1992 Landers earthquake. In blue : Camp Rock-Emerson fault, ; in green : Homestead Valley fault ; in pink : Johnson Valley fault. Major segments of each faults are numbered from NW to SE and indicated by black arrows parallel to their mean strike. The grey prolongation of the arrows indicates the uncertainties on the segment lengths. The nature of the inter-segment zones is indicated in letters within boxes explained in Table 6. The nature of the fault tips is indicated in green (Table 6).

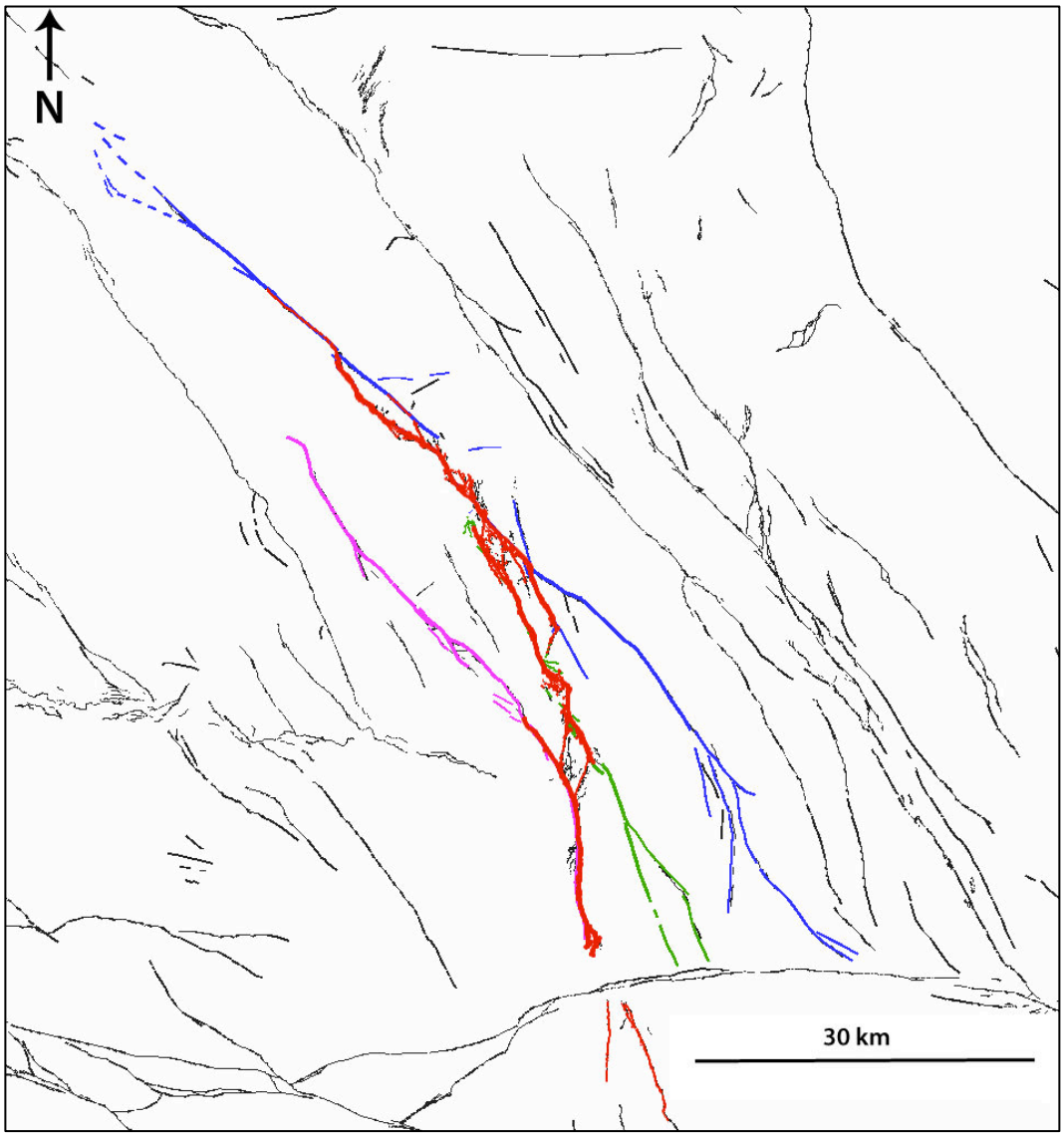


Fig.106: Same caption as Fig105. In red is the surface rupture of the 1992 Landers earthquake mapped on the field (Sieh et al., 1993).

1992 Coseismic rupture

Surface trace and location on the broken long-term faults:

- The 1992 surface rupture is still clear on satellite images (Google Earth). The surface trace of the earthquake has been precisely mapped, and the displacements measured (See next section), both on the field (e.g. Sieh et al., 1993) and from radar imagery (Massonet et al., 1993; Massonet et al., 1994; Zebker et al., 1994; Peltzer et al., 1994; See Fig.107a).
- Total surface rupture of ~85 km (Fig.104 & 106; Sieh et al., 1993) with an arcuate shape (N-S in the southern half of the rupture and NW-SE in its northern half).
- The EQ broke three distinct faults: a principal fault, Camp Rock-Emerson, and two of its splaying branches, Homestead Valley and Johnson Valley.

- The EQ initiated on and first broke the Johnson Valley southern splay of the Camp Rock-Emerson Fault. It then propagated unilaterally towards the north (Kanamori et al., 1992) and jumped to the Homestead splay across the pull-apart that connects the two branches. The rupture then jumped to the main Camp Rock-Emerson Fault, along which it broke only one major segment, the segment 2. The rupture also broke eventually a small section of the major segment 1, of ~6 km long (over the 21-26 km length of the whole segment 1). During its propagation, the rupture went through pronounced azimuth changes (~20°) between each broken faults.
- **The Landers EQ thus broke only one major segment of the principal Camp Rock-Emerson Fault, major segment 2, which is one of the most mature along the fault.** The rupture of major segment 2 followed that of two of the largest southern splay branches of the fault. The rupture thus passed through a T_{MF} type connection (Fig.24) In the south, it initiated at a T_{ob} connection (intersection with Pinto Mountain Fault). In the north, it vanished along major segment 1 and stopped at a place with no much particularity, only marked by the existence of a small step and a subtle oblique fault (Fig.105). Along this short vanishing termination, it seems that the EQ did not break much the fault at depth since no aftershock were observed north of the northern tip of major segment 2 (Fig.107b; Hauksson et al., 1993).
- Therefore, the actual northern termination of the rupture rather is at the northern tip of major segment 2, where the later connects with segment 1. There and nearby, two ENE-trending subtle fault traces exist, that intersect the Camp Rock-Emerson Fault. Those oblique features were the sites of dense aftershocks (Fig.107), suggesting that they were activated during the EQ or right after. The EQ might have thus stopped in the north in a zone being both an inter-segment of type 2_{O-C} and a T_{ob} zone.
- **The Landers EQ also broke a part of the Homestead Valley Fault, namely 2 out of the 3 major segments that form the Homestead Valley Fault, segments 1 and 2. These 2 segments are the most mature along the Homestead Valley Fault.**
- **The Landers EQ also broke a part of the Johnson Valley Fault, namely 2 out of the 5 major segments that form the fault, segments 4 and 5.**
- Another particularity of the Landers EQ is that it propagated across large step overs, most characterized by overlapping lengths of 5-6 km and across-fault separations of 2-3,5 km (Zachariasen and Sieh 1995; Spotila and Sieh 1995).
- The surface ruptures mapped south of the Pinto Fault (Eureka Peak and Burnt Mountain Faults, Fig.104) did not occur during the mainshock. There is actually no continuity between

the Johnson Valley rupture and that of the Eureka Peak, because the Pinto Fault separates the two traces. The Eureka Fault sustained some creep obviously triggered by the Landers EQ, and was site of a number of aftershocks (including a Mw 5.6 aftershock which occurred 3 min after the main shock, Haukkson et al., 1993; Hough et al., 1993; Sieh et al., 1993; Hough 1994). Additional movement on the Eureka Peak Fault probably occurred in the form of afterslip (See 'Other information' section below).

→ The Landers EQ broke 3 distinct faults. It initiated on the principal splay fault system that terminates the large Camp Rock-Emerson Fault. It propagated from the splay faults up to the main Camp Rock-Emerson Fault, from which it broke only one major segment, over ~25 km. The broken major segment is one of the most mature sections of the fault. On each of the Homestead Valley and Johnson Valley Faults, the EQ broke 2 major segments.

Coseismic displacements measured at surface:

- *From Field measurements*: Maximum lateral slip of 6-6.6 m (Wallace 1992; Sieh et al., 1993) well measured on the Camp-Rock-Emerson Fault (major segment 2).
- *From GPS data and modeling*: Maximum lateral slip of ~6.4 m (Hudnut et al., 1994).
- *From InSAR data and modeling*: Maximum lateral slip of ~6 m (Massonet et al., 1993).
- The complete slip profile could be measured on the field, and be inferred from GPS and seismological data modeling (Fig.109). The measured slip profile is more precise. The slip distribution is asymmetric, with the maximum displacement at the northern termination of the rupture. The envelope shape of the profile is roughly triangular. Three distinct slip zones are visible, separated by high slip gradients which coincide with some of the segments' tips that we described before: a first zone of large slip (up to 6.6 m) is defined between about 10 and 31 km; it coincides with the rupture of the Camp Rock-Emerson major segment 2. It is preceded by a small slip bump over the northernmost ~6 km, which coincide with the small slip that occurred on a small section of major segment 1. Another slip patch, yet lower (3-4 m), is seen from ~31 and 52 km; it mainly reveals the rupture of the Homestead Valley Fault (note the two bumps that reveal the two broken segments), with some slip added from both the Camp Rock-Emerson and the Johnson Valley ruptures where they overlap. A third zone of even lower slip (2.5-3 m) is seen between ~55 and 70 km. It reveals the rupture of the Johnson Valley Fault. Here also two smaller bumps are seen that likely show the rupture of the two distinct segments on the Johnson Valley Fault. The small slip bump plotted between

~75 and 85 km corresponds to the subsequent, post-seismic slip on the Eureka Peak Fault, and hence should not be considered together with the rest of the profile.

→ Maximum slip well constrained at surface, of 6-6.6 m, on mature segment 2 of the Camp Rock-Emerson Fault. Maximum slip on the Homestead Valley Fault is ~3-3.5 m, whereas maximum slip on the Johnson Valley Fault is ~ 3 m. Although the Landers EQ broke 3 distinct faults, its coseismic slip profile has a roughly triangular shape.

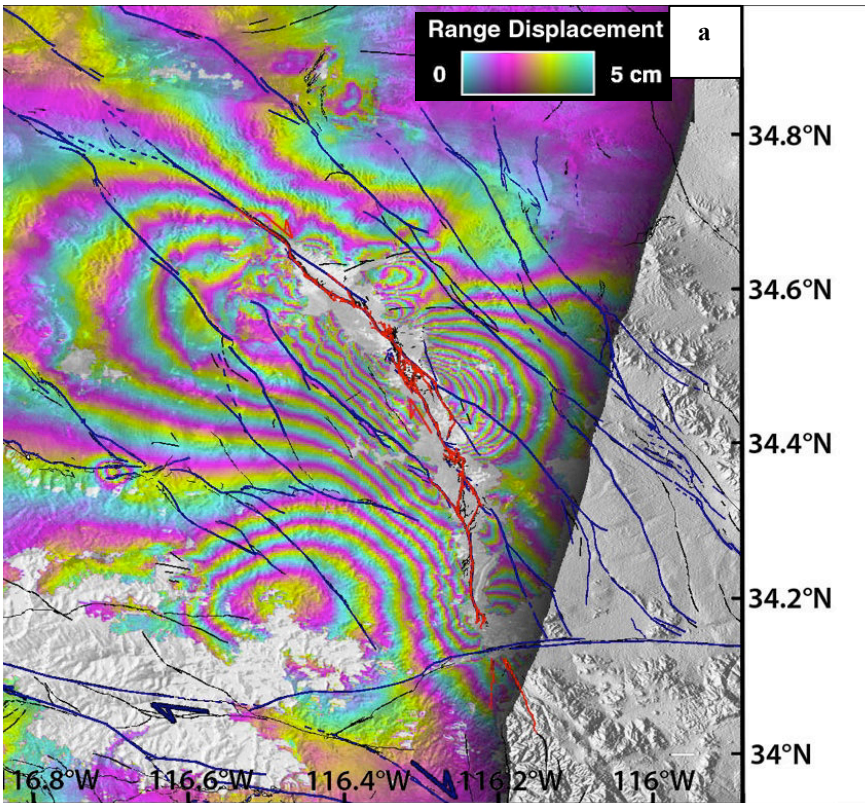


Fig.107: (a) Radar imagery (InSAR) of the ground deformation of the 1992 Landers earthquake between the 24 April 1992 and the 18 june 1993 (from Peltzer et al., 1994; 'Document, Courtesy of the Jet Propulsion Laboratory'; http://www-radar.jpl.nasa.gov/sect323/InSar4crust/ LandersCo.html). In red : 1992 surface rupture ; In blue : long term faults ;

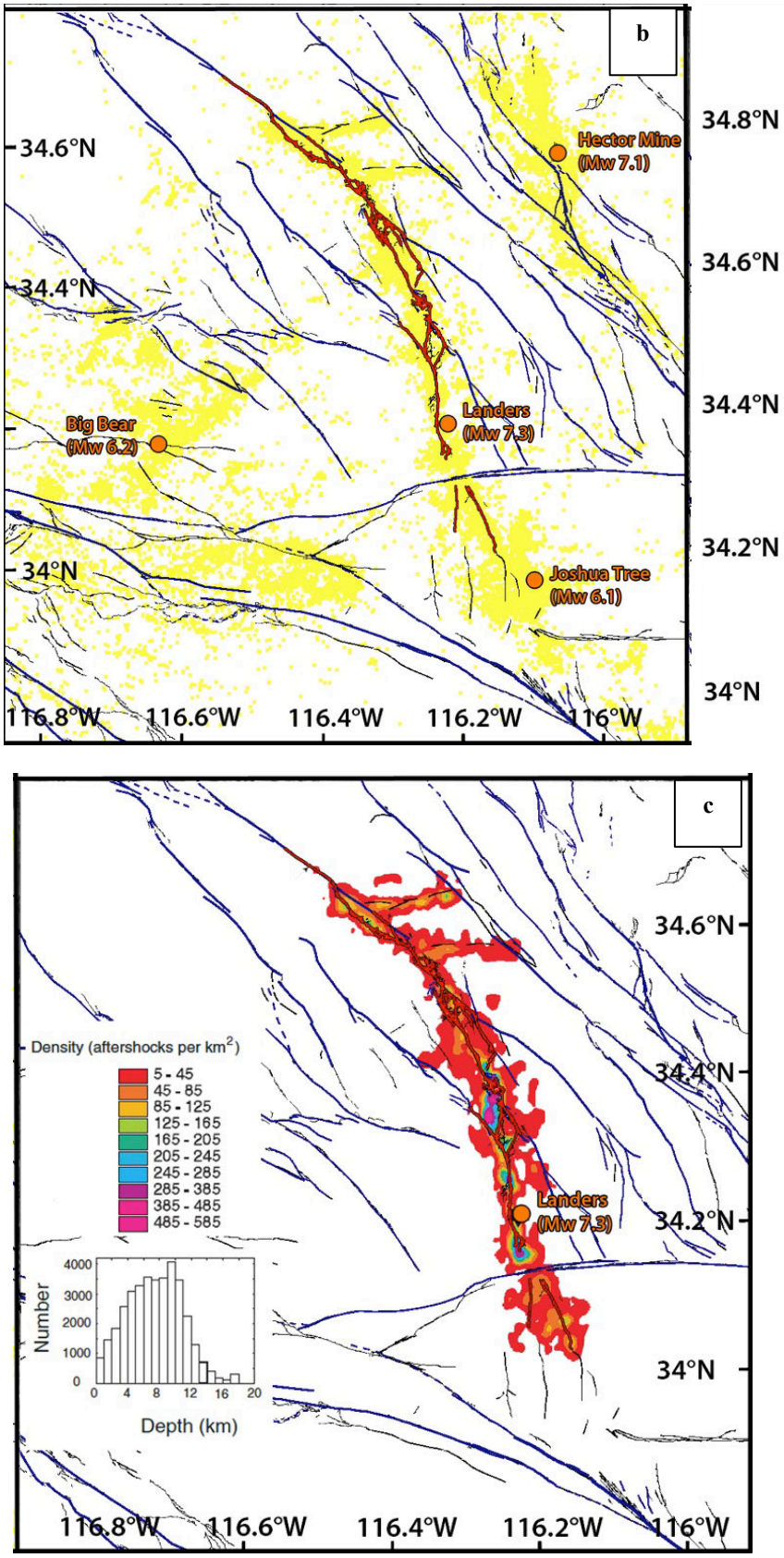


Fig.107: (b) Landers region showing the earthquake locations (Mw>2) recorded between 1981 and 2011 (Hauksson et al., 2012). Yellow dots show the epicenters of the 1992 Joshua Tree earthquake (foreshock), the 1992 Landers earthquake (Mainshock), the 1992 Big Bear earthquake (aftershock). and the 1999 Hector Mine earthquake. (c) Aftershock density distribution of the 1992 Landers earthquake. (Liu et al., 2003).

Source inversion models and slip distribution at depth (Fig.108 and 109)

- We compare four source inversion models that have been published on the 1992 Landers earthquake. The grid data are available for all of them (Fig.108; Table 2).
- All models consider three fault planes. The models differ principally from the data they used:
    - Wald and Heaton (1994): GPS, teleseismic, strong motions and surface slip data.
    - Cohee and Beroza (1994): Strong motions and surface slip data.
    - Cotton and Campillo (1995): Strong motions data only
    - Hernandez et al. (1999): GPS and InSAR data. They also use strong motions data to constrain time history of the slip.

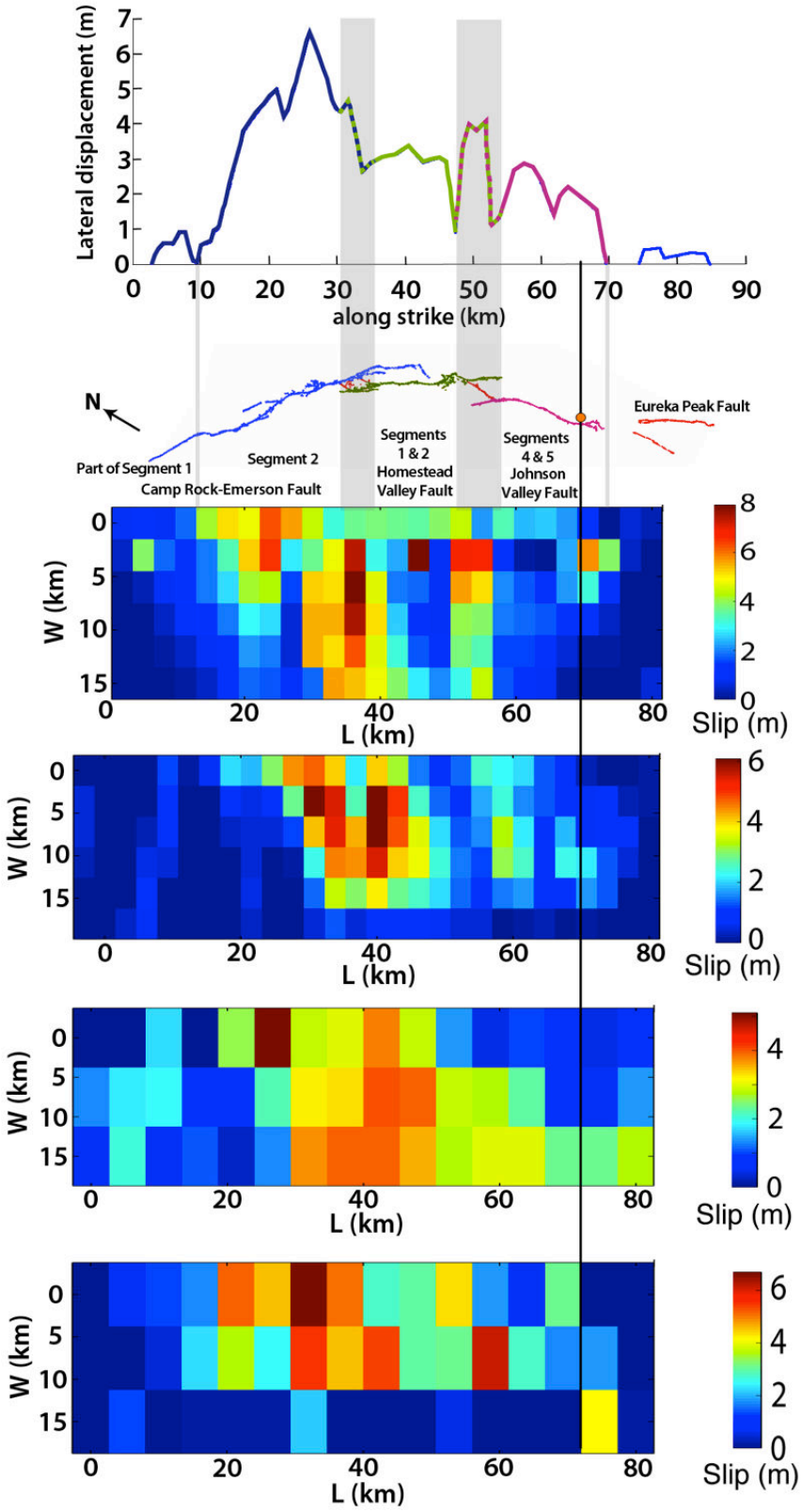
→ We consider that the model from Wald and Heaton (1994) is the most robust for they use more different and complementary data.

The other three models find a maximum slip lower or similar to the slip measured at surface, what suggests that the models are not fully correct.

→ All models find a fairly similar slip distribution, with 2-3 main slip patches coinciding fairly well with the faults that we mapped. In all models, the larger slip patch (6.7-7.9 m) locates on the Camp Rock-Emerson Fault, well coinciding with its major segment 2. Most of the slip is concentrated between 0 and 10 km depth. Another patch of lower slip (4-6 m) is located on the Homestead Valley Fault, while a lower slip of 2-3 m is found on the Johnson Valley faults. In all models, most of the slip occurs overall between 0 and 15 km depth, and this range thus well constrains the rupture width.

→ Most models reveal smaller bumps in the slip distribution, that well coincide with the segments broken on each fault (See interpretation in Fig.109).

→ The source models suggest: L 70-75 km, W 15 km, Dmax at depth 6.7-7.9 m, 3 faults broken.



Co-seismic slip profile measured at surface (Sieh et al., 1993)

Surface rupture mapped on the field (Sieh et al. 1993)

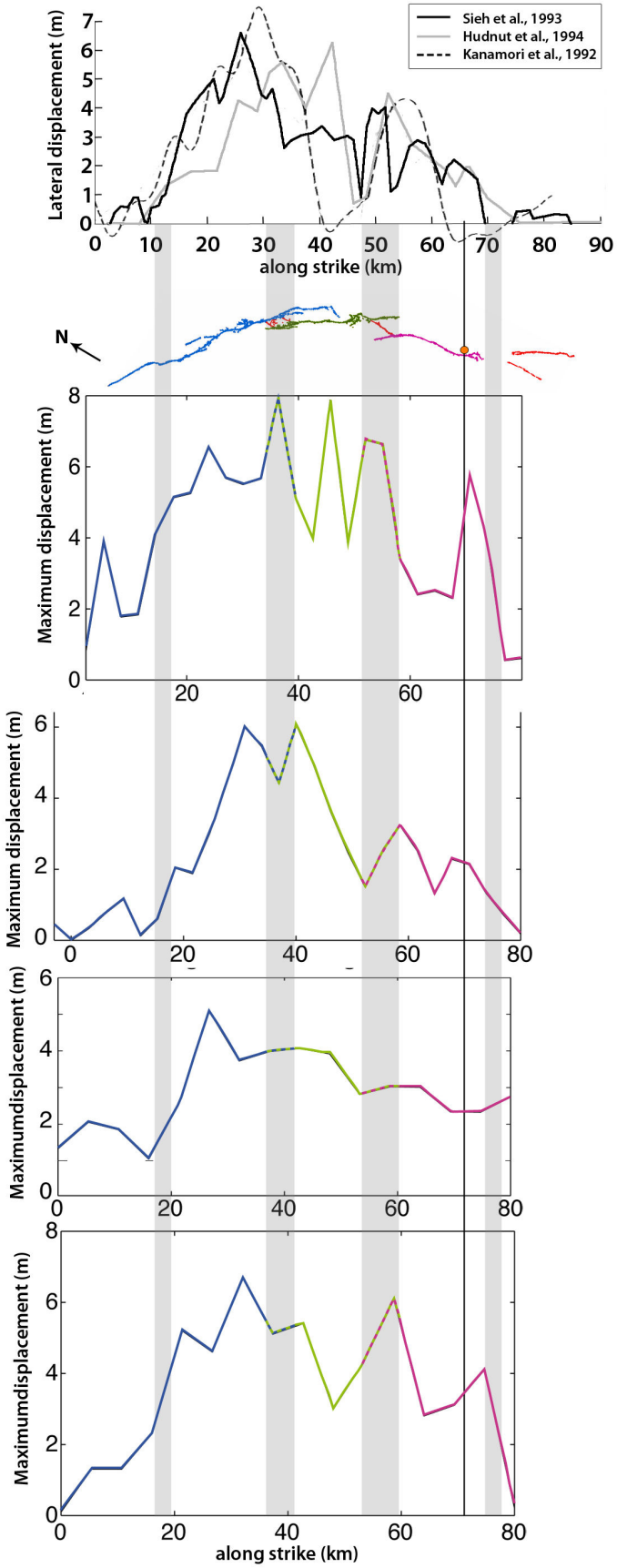
Wald and Heaton 1994 :
Data : GPS + Teleseismic + Strong motions + Surface offsets
L= 78 km ; W=15km ;
Dmax=7,9 m
Z= 7 km

Cohee and Beroza 1994 :
Data : Strong motions + Surface offsets
L= 83 km ; W= 18 km ;
Dmax= 6 m ≤ D surface
Z= 5 km

Hernandez et al. 1999 :
Data : GPS + InSAR (+ Strong motions)
L= 80 km ; W= 15 km ;
Dmax= 6,7
Z= 6 km

Cotton and Campillo 1995 :
Data : Strong motions
L= 80 km ; W= 15 km ;
Dmax= 5,1 m < D surface.
Z= 6 km

Fig.108: Comparison between different inversion models published on the 1992 Landers earthquake. Black line represents hypocenter location which is used as a reference for each model. Grey bars represent the fault jump zones. Models are at the same scale along strike.



Co-seismic slip profile measured at surface (Sieh et al., 1993) and modeled at surface from GPS data (Hudnut et al., 1994) and seismological data (Kanamori et al., 1992)

Surface rupture mapped on the field (Sieh et al. 1993)

Wald and Heaton 1994 :
Data : GPS + Teleseismic + Strong motions + Surface offsets

Cotton and Campillo 1995 :
Data : Strong motions

Hernandez et al. 1999 :
Data : GPS + InSAR (+ Strong motions)

Cohee and Beroza 1994 :
Data : Strong motions + Surface offsets

Fig.109: Comparison between profiles of maximum slip measured at surface and derived from inversion models published on the 1992 Landers earthquake. Black line represents hypocenter location which is used as reference for each model. Grey areas represent the intersegment zones.

Other source parameters :

SCARDEC (Vallée et al. 2011)
Mainshock: 1992/06/28 at 11h57min34s GMT
Lat = 34.2° Lon= -116.44°
Mw 7.4; M0 = 1.56e20 Nm; Z = 20 km;
Duration: 68 s
Strike, dip, rake: (337°, 71°, 162°)/ (73°, 73°, 20°)

Global CMT
Mainshock: 1992/06/28 at 11h57min53s GMT
Lat = 34.65° Lon= -116.65°
Mw 7.3; M0 = 1.06e20 Nm; Z = 15 km;
Half-duration: 19.2s
Strike, dip, slip : (341°, 70°, -172°)/ (248°, 82°, -20°)

- Hauksson et al. (1993) used local seismic networks to define hypocenter depth Z= 3 to 6 km.
- The rupture duration much differs between the Scardec (Fig.110) and Global CMT methods. Kanamori et al (1992) inverted teleseismic P and S waves and found two distinct sub-events about 10 sec apart, of 6 and 8 s duration. Other studies (e.g., Wald and Heaton 1994; Cohee and Beroza 1994) inferred from their models a slip duration of 22-24 s. So the rupture duration estimated with SCARDEC seems overestimated; therefore, the energy release between 25-30 and 68 s (Fig.110) might not be related with the mainshock but might more likely result from triggered subsequent ruptures and slips, such as those on the Eureka Peak Fault (Hough 1994).
- The 0-25/30 first seconds of the source time function show two large peaks of moment release proceeded by a smoother release and possibly followed with another smoother release (Fig.110). We interpret the first three zones or peaks to represent the successive rupture of the Johnson Valley, Homestead Valley and Camp Rock-Emerson faults. It remains to understand why, contrary to most EQs, the rupture gained some energy as it was propagating northwards. It abruptly stopped at the northern tip of the Camp Rock-Emerson segment 2, just living little energy to break 6 km of segment 1.
- Moment magnitude and seismic moment range between 7.3-7.4 and 1.06e20-1.56e20 Nm, respectively.

→ **The source time function data suggest that the ruptures of the Homestead Valley and the Camp Rock-Emerson faults were more energetic than that of the Johnson Valley Fault.**

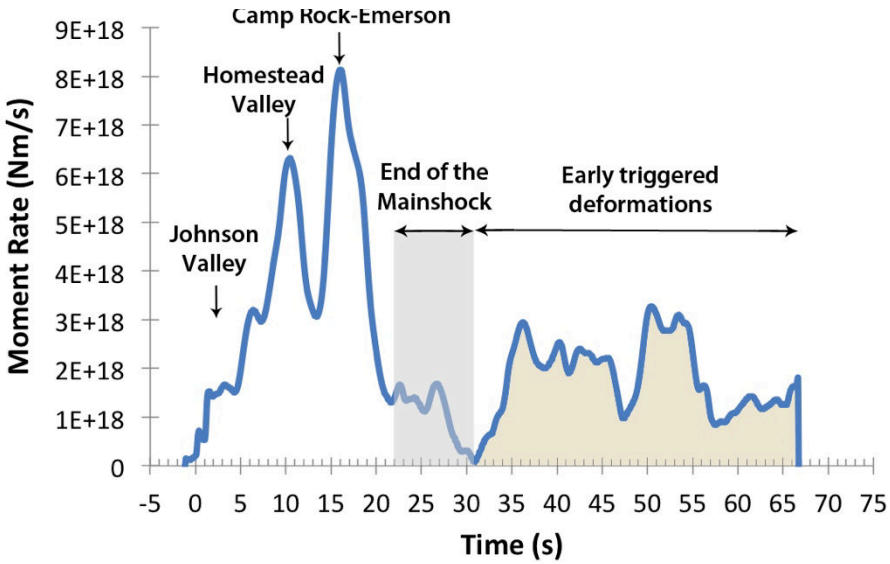


Fig.110: Mean Source Time Function calculated with the SCARDEC method (Vallée et al., 2011).

Other information:

1992 EQ:

- Two months before the Landers earthquake, the Mw 6.1 Joshua Tree foreshock occurred a few kilometers south of the Eureka Peak Fault. Right lateral rupture propagated unilaterally towards the North over a distance of 10-14 km (Hauksson et al., 1993). The foreshock did not break the ground surface. Its aftershock sequence is juxtaposed with the Landers aftershock sequence.
- Small coseismic displacements along neighboring faults (Lenwood, Calico, Pinto faults) were detected using InSAR imagery (e.g. Massonet et al., 1994; Fialko 2004a).
- The aftershocks of the Landers event well underline the surface rupture and also extend along the Eureka Peak Fault and 20 km further south where the Joshua Tree foreshock occurred (the aftershock sequences of the two events are mixed; L=100 km). The aftershocks highlight also two oblique more or less blind structures (trending ENE) at the north of the rupture, which seem to stop in the east at the intersection with the Calico Fault. (Fig.107b & c ; Hauksson et al., 1993). At depth, the aftershocks became shallower to the north, with no aftershock along the last 5 km of the surface rupture (Fig.107b).
- The largest aftershock (Mw 6.2 Big Bear earthquake) occurred 3h after the mainshock. It was located 40 km West of the Landers epicenter. Left lateral motion, no surface rupture (Hauksson et al., 1993).
- Another isolated cluster of aftershocks occurred 30-40 km north of the rupture (intersection between the Calico and Blackwater faults) 6 to 8 hours after the Landers EQ. No surface rupture (Hauksson et al., 1993).

- Most of the postseismic deformation of the Landers earthquake is localized in the inter-segment zones and in the southern half of the rupture where coseismic slip is lower. The postseismic deformation is also well correlated with the zones of higher aftershock density (Fig.107c; Liu et al., 2003).
- Postseismic deformation took place along the Eureka Peak Fault during several years after the Landers earthquake (~25 cm measured using creepmeters one year after the earthquake: Behr et al., 1994; and InSAR between 1992 and 1996: Peltzer et al., 1998)
- In 1999, the Hector Mine Mw 7.1 earthquake (USGS et al., 2000; Treiman et al 2002) broke faults of the ECSZ ~ 30 km East of the Landers rupture.

Past EQ activity:

- Most of the large earthquakes within the ECSZ occurred in clusters, separated by periods of relative quiescence lasting several thousands of years (Rockwell et al., 2000). The 1992 and 1999 earthquakes are the most recent EQs of a possible current cluster.

Parameters retained to describe the Landers EQ (Tables 1 – 4):

Globally: Mw 7.3; M0 ~ 1.06e20 Nm; L ~ 70-80 km; W ~ 15 km; Dmax surface ≈ 6-6.6 m; Dmax depth = 7.9 m; *Hypocenter*: Z ~ 3-6 km.

Yet, 3 distinct faults broke. Hence we might need to consider those faults individually.

- Camp Rock-Emerson Fault: mainly, 1 major segment broken; L ~ 25 km, Dmax ~ 6-6.6 m.
- Homestead Valley Fault: 2 major segments broken; L ~ 23 km, Dmax ~ 3.5 m.
- Johnson Valley Fault: 2 major segments broken; L ~ 21 km, Dmax ~ 3 m.

The "global" Landers earthquake surface and depth slip-length data fall on the second function (blue curve; Fig.111 & 112) but we saw that the event broke 3 distinct faults so that it is not certain that these composite slip-length data can be analyzed in the framework of the earthquake scaling law that we use. We will come back to this point in chapter IV. If we consider each broken fault independently, we see that the Camp Rock-Emerson surface slip-length data fall on the first function (pink curve) whereas the Homestead Valley and Johnson Valley slip-length data both fall on the second function (blue curve): these findings are in agreement with the rupture of one major segment on the Camp Rock-Emerson Fault and of two major segments on both the Homestead Valley and the Johnson Valley faults.

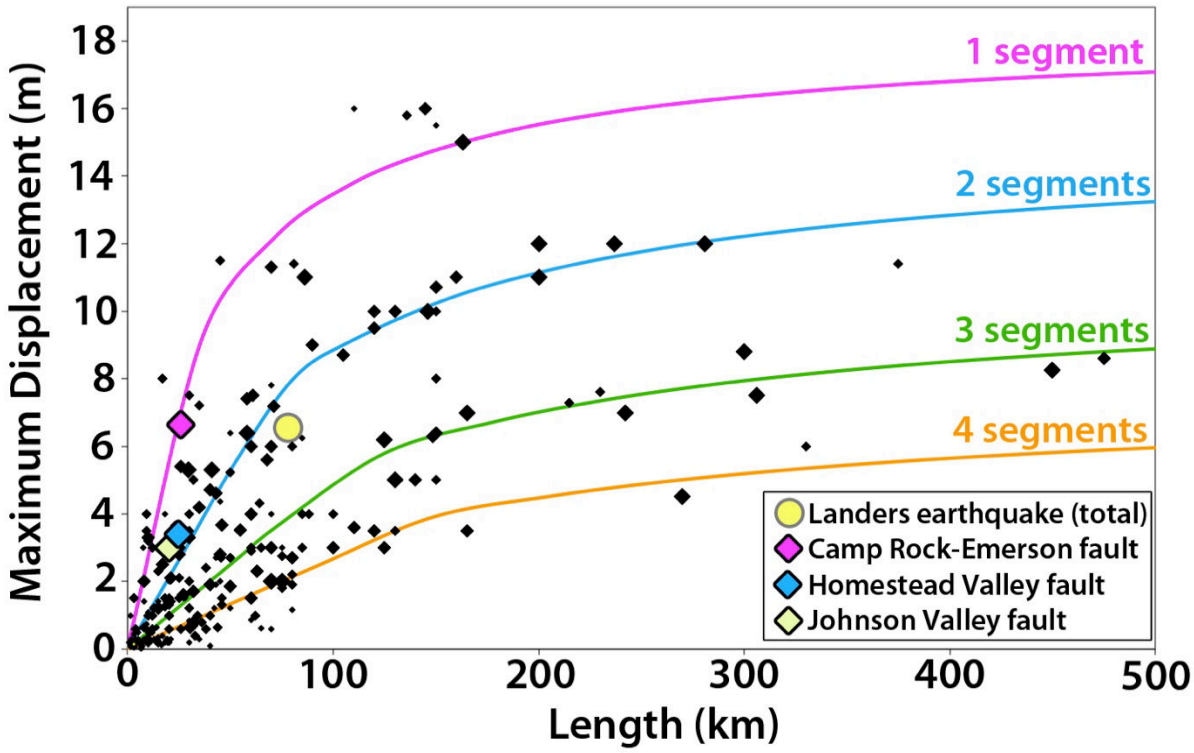


Fig.111: Earthquake displacement-length data measured at surface for 260 historical large continental earthquakes (Mw≥6). The 4 curves indicate the number of major long-term fault segments to have been broken by the earthquakes (modified from Manighetti et al., 2007). Yellow dot shows the Landers earthquake data considering all the rupture length. Pink, blue and pale green diamonds show the slip length data of the surface three disctincts faults that broke during the 1992 Landers earthquake and chapter IV.

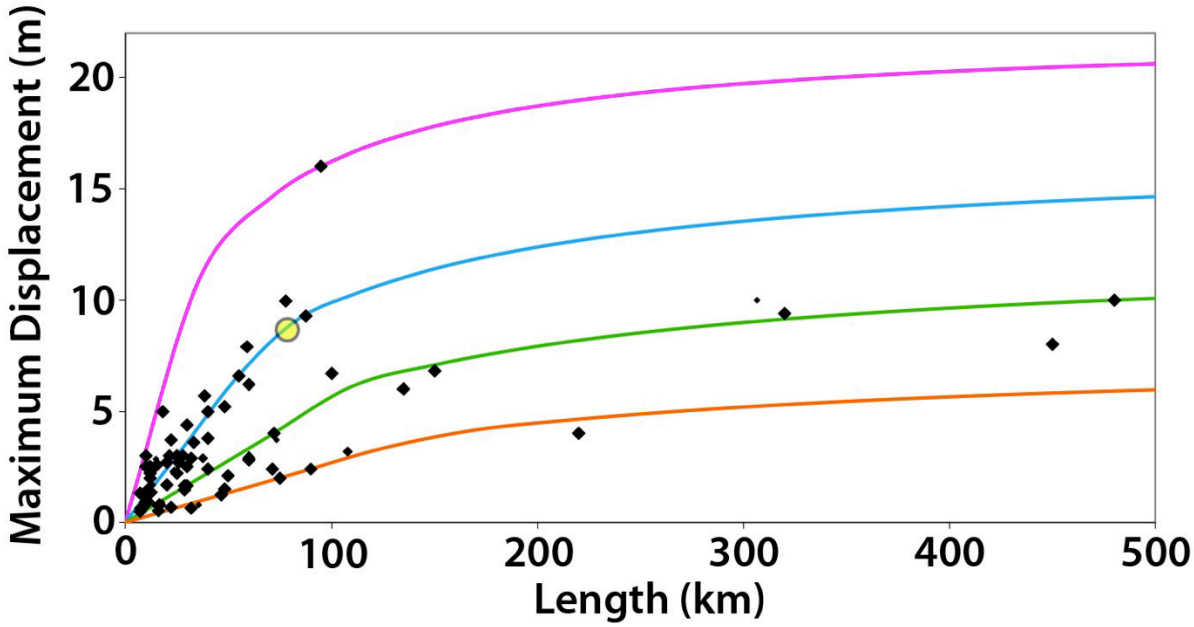


Fig.112: Earthquake displacement-length data inferred at depth for 90 historical large continental earthquakes (Mw≥6). The 4 curves indicate the number of major long-term fault segments to have been broken by the earthquakes (modified from Manighetti et al., 2007 and Chapter IV). Yellow pale dot show the 1992 Landers earthquake depth slip-length data (overall rupture).

References

Behr, J., R. Bilham, P. Bodin, and S. Gross (1994). Eureka Peak fault afterslip following the 28 June 1992 Landers earthquake, *Bull. Seismol. Soc. Am.,* **84**, 826-834

Dibblee, T. W., Jr. (1961). Evidence of strike-slip movement on northwest-trending faults in the western Mojave Desert, California: *U.S. Geological Survey Professional Paper*, **424-B**, p. B197-B199.

Dokka, R. K. (1983). Displacements on late Cenozoic strike-slip faults of the central Mojave Desert, California. *Geology,* **11,** 305-308.

Dokka, R. K., & C. J. Travis (1990a). Late Cenozoic strike-slip faulting in the Mojave Desert, California, *Tectonics*, **9**, 311 –340.

Dokka, R. K., & C. J. Travis (1990b). Role of the Eastern California Shear Zone in accommodating Pacific-North American plate motion, *Geophys. Res. Lett.,* **17**, 1323–1326.

Cohee, B. P., & G. C. Beroza (1994). Slip distribution of the 1992 Landers earthquake and its implications for earthquake source mechanics. *Bull. Seis. Soc. Am*., **84**, 692-712.

Cotton, F., & M. Campillo (1995). Frequency-Domain Inversion of Strong Motions - Application to the 1992 Landers Earthquake. *J. Geophys. Res.,***100**, 3961-3975.

Fialko, Y. (2004a), Probing the mechanical properties of seismically active crust with space geodesy: Study of the coseismic deformation due to the 1992 Mw7.3 Landers (southern California) earthquake, *J. Geophys. Res*., **109**, B03307, doi:10.1029/2003JB002756.

Fialko, Y. (2004b). Evidence of fluid-filled upper crust from observations of postseismic deformation due to the 1992 Mw7.3 Landers earthquake, *J. Geophys. Res.,* **109**, B08401, doi:10.1029/2004JB002985

Garfunkel, Z. (1974). Model for the late Cenozoic tectonic history of the Mojave Desert, California and for its relation to adjacent areas: *Geological Society of America Bulletin*, **85**, 1931-1944.

Hernandez, B., F. Cotton, & M. Campillo (1999). Contribution of radar interferometry to a two-step inversion of the kinematic process of the 1992 Landers earthquake. *J. Geophys. Res.,***104**, 13,083-13,099.

Hauksson, E., L. M. Jones, K. Hutton, & D. Eberphart-Phillips (1993). The 1992 Landers earthquake sequence: seismological observations. *J. Geophys. Res.* **98**, 835–19,858.

Hauksson, E., W. Yang, & P.M. Shearer (2012). Waveform Relocated Earthquake Catalog for Southern California (1981 to June 2011); *Bull. Seismol. Soc. Am*., **102**, doi:10.1785/0120120010.

Hough, S. E. (1994). Southern surface rupture associated with the M 7.3 1992 Landers, California, earthquake, *Bulletin of the Seismological Society of America,* **84**:817-825

Hough, S. E., Mori, J., Sembera, E., Glassmoyer, G., Mueller, C. & Lydeen, S. (1993). Southern surface rupture associated with the 1992 M7.4 Landers Earthquake: Did it all happen during the mainshock? *Geophysical Research Letters*, **20**, 2615–2618, DOI: 10.1029/93GL00666.

Hudnut, K. W., Y. Bock, M. Cline, P. Fang, Y. Feng, J. Freymueller, X. Ge, W. K. Gross, D. Jackson, M. Kim, N. E. King, J. Langbein, S. C. Larsen, M. Lisowski, Z.-K. Shen, J. Svarc, and J. Zhang (1994). Co-seismic displacements of the 1992 landers earthquake sequence. *Bulletin of the Seismological Society of America,* **84**, 625-645

Kanamori, H., Thio, H.-K., Dreger, D., Hauksson, E., & Heaton, T. (1992). Initial Investigation of the Landers, California, Earthquake of 28 June 1992 using TERRAscope, *Geophys. Res. Lett*., **19**, 2267-2270.

Liu, J., K. Sieh & E. Hauksson (2003). A Structural Interpretation of the Aftershock "Cloud" of the 1992 Mw 7.3 Landers Earthquake. *Bulletin of the Seismological Society of America*, **93**, 1333-1344, doi:10.1785/0120020060

Mandl, G. (1987). Tectonic deformation by rotating parallel faults: the "bookshelf" mechanism. *Tectonophysics*, **141**(4), 277-316.

Manighetti, I., Tapponnier, P., Courtillot, V., Gallet, Y., Jacques, E., & Gillot, P. Y. (2001). Strain transfer between disconnected, propagating rifts in Afar. *Journal of Geophysical Research,* **106**(B7), 13613-13665.

Manighetti, I., M. Campillo, S. Bouley, and F. Cotton (2007), Earthquake scaling, fault segmentation, and structural maturity, Earth Planet. Sci. Lett., 253, 429-438, doi:10.1016/j.epsl.2006.11.004

McClusky, S. C., S. C. Bjornstad, B. H. Hager, R. W. King, B. J. Meade, M. M. Miller, F. C. Monastero, & B. J. Souter (2001). Present day kinematics of the Eastern California Shear Zone from a geodetically constrained block model, *Geophys. Res. Lett.,* **28**, 3369–3372.

Massonnet, D., M. Rossi, C. Carmona, F. Adragna, G. Peltzer, K. Feigl, & T. Rabaute. (1993). The displacement field of the Landers earthquake mapped by radar interferometry. *Nature*, **364,** 138-142, doi:10.1038/364138a0

Massonnet, D., K. Feigl, M. Rossi & F. Adragna (1994). Radar interferometric mapping of the deformation in the year after the Landers earthquake. *Nature*, **369,** 227-230

Peltzer, G., K. W. Hudnut & K. Feigl (1994). Analysis of coseismic surface displacement gradients using radar interferometry: New insights into the Landers earthquake*, J. Geophys. Res*., **99**, 21,971-21,981.

Peltzer, G., P. Rosen, F. Rogez, & K. Hudnut (1996). Postseismic rebound in fault step-overs caused by pore fluid flow, *Science*, **273**, 1202– 1204, doi:10.1126/science.273.5279.1202

Peltzer, G., P. Rosen, F. Rogez, & K. Hudnut (1998). Poroelastic rebound along the Landers 1992 earthquake surface rupture, *J. Geophys. Res.,* **103**, 30,131– 30,145.

Perfettini, H., & J.-P. Avouac (2007). Modeling afterslip and aftershocks following the 1992 Landers earthquake*, J. Geophys. Res*., **112**, B07409, doi:10.1029/2006JB004399

Pollitz, F. F., G. Peltzer, & R. Bürgmann (2000). Mobility of continental mantle: Evidence from postseismic geodetic observations following the 1992 Landers earthquake, *J. Geophys. Res.,* **105**, 8035 – 8054, doi:10.1029/1999JB900380.

Rockwell, T. K., S. Lindvall, M. Herzberg, D. Murbach, T. Dawson, & G. Berger (2000). Paleoseismology of the Johnson Valley, Kickapoo, and Homestead Valley faults: Clustering of earthquakes in the Eastern California Shear Zone, *Bull. Seismol. Soc. Am*., **90**, 1200–1236.

Rubin, C. M., & K. Sieh (1997). Long dormancy, low slip rate, and similar slip-per-event for the Emerson fault, eastern California shear zone, *J. Geophys. Res.,* **102**, 15,319– 15,333.

Sauber, J., W. Thatcher, S. C. Solomon, & M. Lisowski (1994). Geodetic slip rate for the eastern California shear zone and the recurrence time of Mojave desert earthquakes, *Nature*, **367**, 264– 266.

Shen, Z.-K., D. D. Jackson, Y. Feng, M. Cline, M. Kim, P. Fang, & Y. Bock (1994). Postseismic deformation following the Landers earthquake, California, *Bull. Seismol. Soc. Am*., **84**, 780– 791.

Sieh, K., L. M. Jones, E. Hauksson, K. Hudnut, D. Eberhart-Phillips, T. Heaton, S. Hough, K. Hutton, H. Kanamori, A. Lilje, S. Lindvall, S. McGill, J. Mori, C. Rubin, J. Spotila, J. Stock, H. Thio, J. Treiman, B. Wernicke, & J. Zachariasen (1993). Near-field investigations of the Landers earthquake sequence, *Science* **260**, 171–176.

Spotila, J. A., & K. Sieh (1995). Geologic investigations of a “slip gap” in the surficial ruptures of the 1992 Landers earthquake, southern California, *J. Geophys. Res.,* **100**, 543–559, doi:10.1029/94JB02471.

Tapponnier, P., Armijo, R., Manighetti, I., & Courtillot, V. (1990). Bookshelf faulting and horizontal block rotations between overlapping rifts in southern Afar. *Geophysical Research Letters*, **17**(1), 1-4.

Treiman, J. A., K. J. Kendrick, W. A. Bryant, T. K. Rockwell, & S. F. McGill (2002). Primary surface rupture associated with the Mw 7.1 16 October 1999 Hector Mine earthquake, San Bernardino County, California, *Bull. Seismol. Soc. Am*., **92**, 1171–1191.

U.S. Geological Survey, the Southern California Earthquake Center, and the California Division of Mines and Geology (2000). Preliminary report on the 16 October 1999 M7.1 Hector Mine, California, earthquake, *Seism. Res. Lett*. **71**, 11–23.

Vallée, M., J. Charléty, A.M.G. Ferreira, B. Delouis, and J. Vergoz, (2011). SCARDEC : a new technique for the rapid determination of seismic moment magnitude, focal mechanism and source time functions for large earthquakes using body wave deconvolution, *Geophys. J. Int*., **184**, 338-358.

Wald, D. J., & T. H. Heaton (1994). Spatial and Temporal Distribution of Slip for the 1992 Landers, California, Earthquake. *Bull. Seis. Soc. Am*. **84**, 668-691.

Wallace, T. C. (1992). The 1992 Landers Earthquake Sequence. *Arizona Geology,* **22**, 3, 1-4.

Walpersdorf, A., Manighetti, I., Mousavi, Z., Tavakoli, F., Vergnolle, M., Jadidi, A. Jadidi, D. Hatzfeld, A. Aghamohammadi, A. Bigot, Y. Djamour, H. Nankali & Sedighi, M. (2014). Present-day kinematics and fault slip rates in eastern Iran, derived from 11 years of GPS data, *J. Geophys. Res. Solid Earth*, **119**, 1359–1383, doi:10.1002/2013JB010620

Zachariasen, J., & K. Sieh (1995). The transfer of slip between two en echelon strike-slip faults: A case study from the 1992 Landers earthquake, southern California, *J. Geophys. Res.,* **100**, 15281–15301, doi:10.1029/95JB00918.

Zebker, H. A., P. Rosen, R.M. Goldstein, A. Gabriel, & C.L. Werner (1994) On the derivation of coseismic displacement fields using differentiai radar interferometry: the Landers earthquake, *J. Geophys. Res*., **19**,617-19,634.

2.14. Manyi 1997

08/November/1997, China

Mw 7.6

Epicenter : 35.07°N-87.33°E

Left-lateral strike-slip



Broken long-term fault

The EQ broke the Manyi Fault, which, overall, belongs to the Kunlun fault system, China.

General characteristics from literature:

- Fairly linear, ~N76°E-trending left-lateral strike-slip fault (e.g. Peltzer et al., 1999), about 350 km long.
- The Manyi Fault forms the westward prolongation of the Kunlun Fault (See below).
- No field investigation and very few information from literature. It might be considered that the Manyi Fault has the same age than the Kunlun Fault (23-34 Ma, Tapponnier et al., 2001), but it is uncertain.
- Dip is not known precisely, but likely sub-vertical
- Total cumulative slip and long-term slip rate are not known.
- Current lateral slip rate: 2,5 ± 2,5 mm/yr, yet not measured but inferred from a large-scale modeled velocity field (Holt et al. 2007)

→ **The Manyi Fault might be of intermediate maturity, since it belongs to the most recent part of the mature Kunlun Fault system (See below).** Because it belongs to the Kunlun Fault system, it might be closer from mature than from immature, but this is not certain.

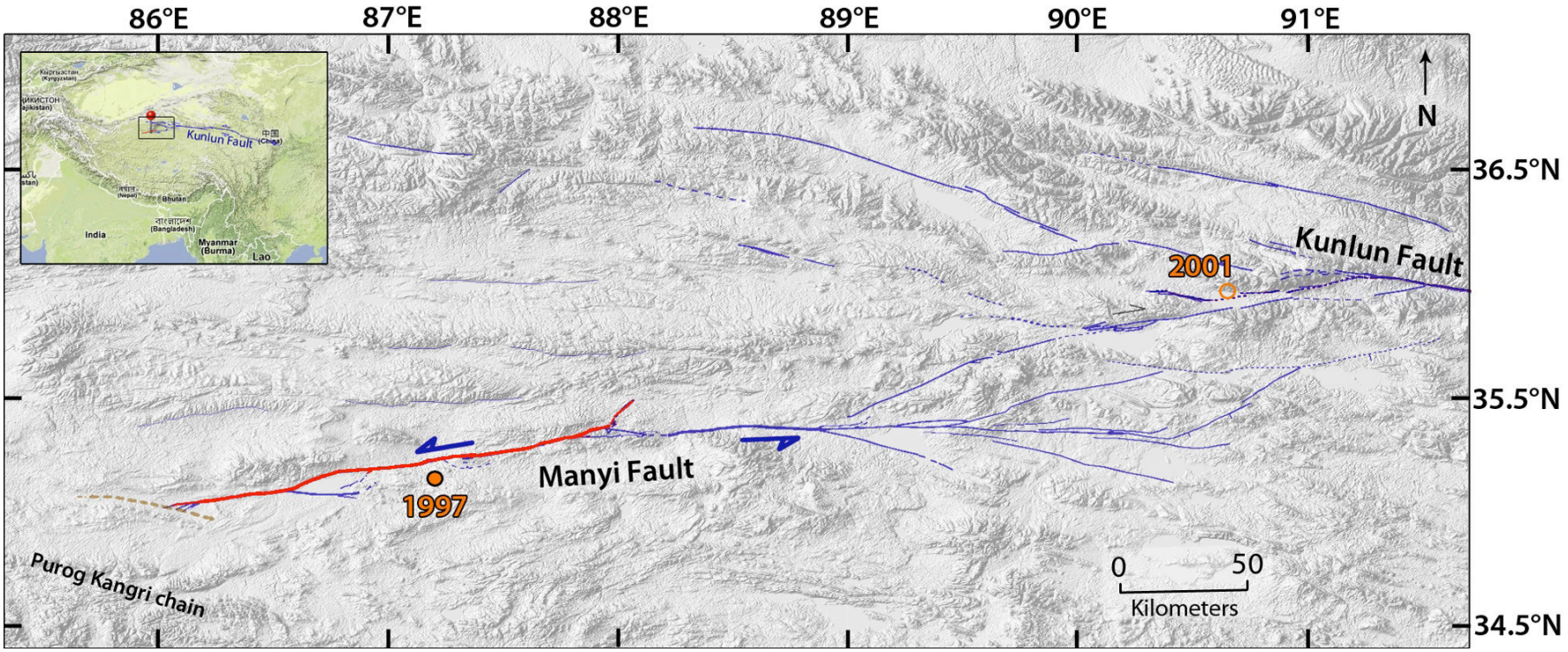


Fig.113: General map of the main long term faults in Western Kunlun (blue) and surface rupture of the 1997 Manyi earthquake (red). Dashed brown line show a fold axis at the northern edge of the Purog Kangri chain. The orange circles are the epicenters of the 1997 Manyi earthquake and the 2001 Kunlun earthquake.

Architecture and major lateral segmentation, from our mapping (Fig.113 & 114):

- Mapping done from Google Earth, Landsat and ASTER GDEM data combined with literature information
- Long-term fault trace well expressed in surface morphology and topography
- To the west, the lateral prolongation of the Manyi Fault is stopped by a high and large WNW-trending fold zone (Purog Kangri chain, only partially represented on Fig.113 & 114), forming a 25-35° angle with the Manyi Fault trace (termination of type T_{OB}, Fig.24). The Manyi Fault also splays in a small horsetail network, with the horsetail faults forming a maximum angle of ~30° to the Manyi Fault trace. To the east, the Manyi Fault terminates by a large-scale splay, rather symmetric (termination of T_{Ss} type, Fig.24). The eastern splay suggests that the Manyi Fault has been mainly propagating eastward over geological time.
- The Manyi Fault is connected to the Kunlun Fault through a large extensive relay fault system of the form of a pull-apart. The relay system is thus principally made of NE-trending faults, the longest are 150-220 km long and are both right-lateral and normal. The relay fault system is actually made of the splay faults that form both the western termination of the Kunlun Fault in the north and the eastern termination of the Manyi Fault in the south. This suggests that the Kunlun and Manyi faults have been propagating toward each other over geological time and are now in the process of connecting to each other, through the large-scale relay zone. The Manyi Fault might thus be considered as one additional major segment of the Kunlun Fault, however being not fully connected yet to the Kunlun Fault. The across-strike distance between the two fault traces is large, 80-90 km.
- The Manyi Fault is flanked by several, sub-parallel secondary faults, especially north of its trace.
- The Manyi Fault is divided into 4 major, fairly collinear segments (See Fig.114 where they are numbered).
- Those 4 major segments have a similar length of 45-60 km.
- The fault trace is fairly linear along each major segment, although showing locally some sinuosity. The 4 segments are sub-parallel. The major segments 1 and 2 are connected to each other by a ~30 x 10 km pull-apart (or 20 x 6 km when the mean direction of the segments is considered). The releasing step-over seems to be an ancient structure however, which the fault trace now cross-cuts so that the major segments 1 and 2 are fully connected; the fault trace simply bends from segment 1 to segment 2. The fault section that includes the segments 2 and 3 shows 3 fairly pronounced bends, indicated by small squares and by the

intersegment zone 2-3 on figure 114. The two outermost bends result from small (~1 km wide) pull-aparts, whereas the central bend is a compressive jog whose total width is ~6 km and where a high fold zone has developed. Because the later jog is larger and of compressive type compared to the other jogs (i.e., needing more strain to form than extensive jogs), we interpret it as a most important inter-segment along the fault, and hence we consider it as being the connection zone between major segments 2 and 3. The segments 2 and 3 are fully connected across this inter-segment, as attested by the fault trace which cross-cuts the inter-segment (See Fig.114). Finally, the major segments 3 and 4 are separated by a large (~35 x 5 km) compressional relay zone where a pronounced topographic relief attests of ongoing uplift. The relay zone is the site of multiple faults, most oblique to both segments. Major segments 3 and 4 are thus not directly connected (yet) at the surface. Segment 4 terminates to the east at the "splaying junction". Into the splay fault zone, ~E-W trending fault sections exist that might be considered as one or two additional major segments of the Manyi Fault, however not yet fully connected to the main fault and likely in the process of being formed.

→ The Manyi Fault is divided into 4 major, long-term collinear segments, among which the most mature and most connected are the three 3 westernmost (1-2-3). The Manyi Fault seems to be currently propagating eastward.

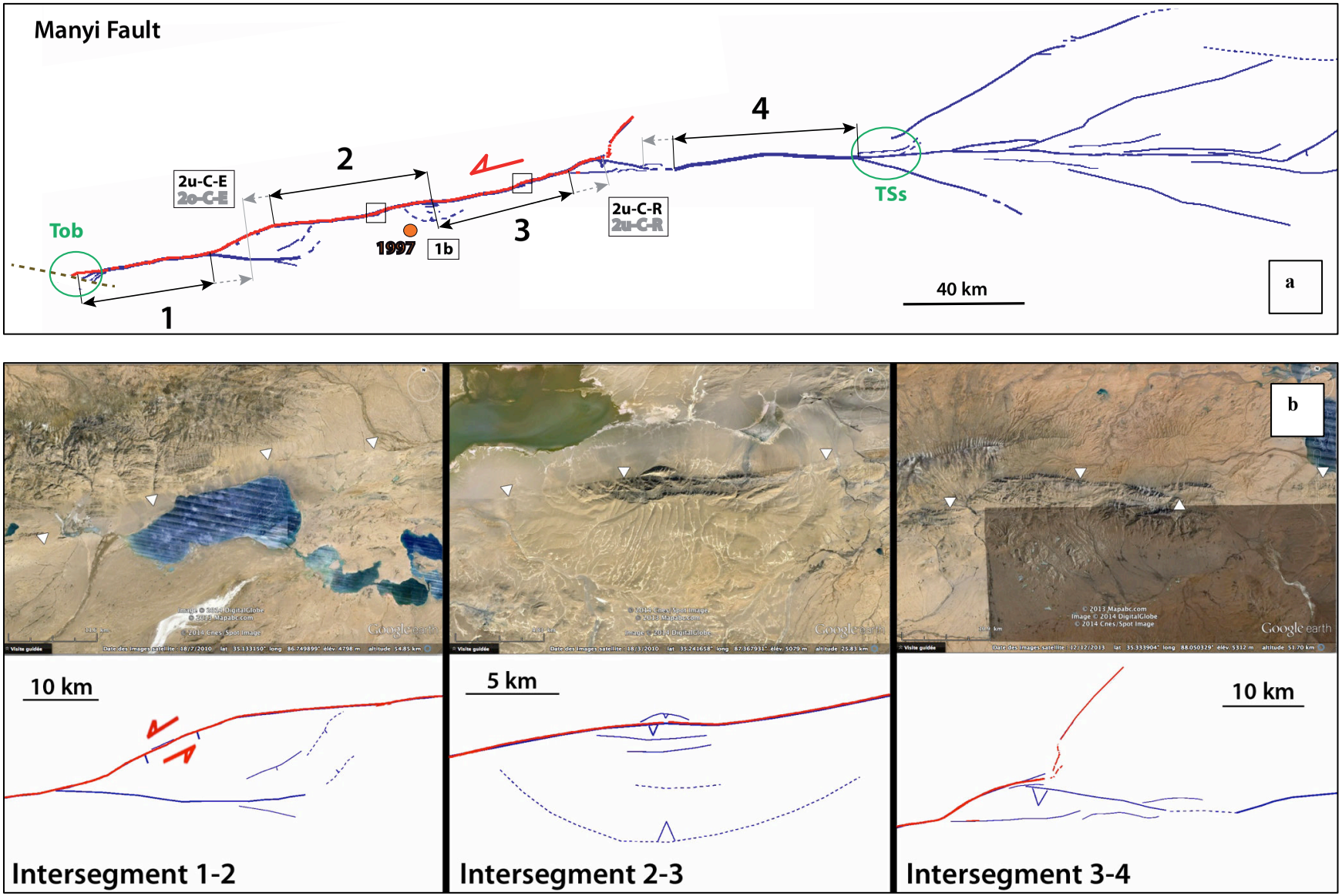


Fig.114: (a) Same active fault map as in fig.113, but with focus on the major segments of the Manyi fault. The segments are numbered from W to E and indicated by black arrows parallel to their mean strike. The grey prolongation of the arrows indicates the uncertainties on the segment lengths. The nature of the inter-segment zones is indicated in letters within boxes explained in Table 6. The nature of the fault tips is indicated in green (Table 6). Squares on surface rupture highlight small pull apart basins (see text for details) ; (b) closer view of each major intersegment zone : (1-2) Pull apart basin now cross-cut by the fault trace; (2-3) Major fold now cross-cut by the fault trace;; (3-4) Push-up structure. White triangles point out the main fault trace observed on Google Earth images.

1997 Coseismic rupture

Surface trace and location on long-term Manyi Fault:

- The 1997 surface rupture is fairly clear on Google Earth and Landsat 7 images. The surface trace of the earthquake has been mapped, and the displacements measured (See below), mainly on Insar images (e.g. Peltzer et al., 1999).
- Surface rupture of ~165 km long.
- The EQ broke no other fault than the Manyi Fault (but a tiny one at the eastern tip of the Manyi rupture, see below).
- The EQ broke the three westernmost and most mature major segments of the Manyi Fault (segments 1, 2 and 3). The EQ initiated near the inter-segment 2-3, and propagated bilaterally toward both the east and the west along the major segments 2 & 1 and 3, respectively (Fig.113 & 114).
- At many places along the fault, the rupture surface trace appears as right-stepping en echelon cracks and small faults.
- The rupture of major segments 1 and 2 is confirmed on InSAR data (Fig.115), which show two distinct concentric fringe series separated at the inter-segment 1-2. By contrast, Insar hardly discriminates segments 2 and 3. Small patches of concentric fringes are seen close to the fault line, at the small pull apart basins and at the 2-3 intersegment zone, however.
- The rupture terminates at the eastern tip of major segment 3. A small additional rupture is however suggested to the east in the NE prolongation of segment 3, over 15 km long.

→ The Manyi EQ initiated at a major inter-segment (inter-segment 2-3) and broke bilaterally the 3 westernmost and most mature major segments of the Manyi Fault.

Coseismic displacements measured at surface:

- *From Field measurements*: No field measurement has been reported for the Manyi EQ.
- *From GPS measurements*: No GPS measurement available at the time of the Manyi EQ.
- *From InSAR data and modeling*: 6-7 m (Peltzer et al., 1999; Funning et al., 2007; Wen and Ma 2010). The displacements are not fully constrained however because only descending tracks were used, offering a 1D vision of the rupture only. Therefore, to infer the coseismic slip, some assumptions had to be made, on the fault dip and on the possible existence of a vertical slip component. Slip might thus be over-estimated.

- The complete slip profile was inferred from Insar data. The slip profile shows an overall triangular and asymmetric shape, with maximum slip deported at the east of the rupture, at the junction between major segments 2 and 3, and slip decreasing fairly regularly from that maximum value towards the west. Three major slip bumps are seen, that fairly well coincide with the rupture of major segments 1, 2 and 3 (Fig.116).

→ Maximum slip estimated at surface at 6-7 m, yet not fully constrained and possibly slightly over-estimated. Maximum slip occurred in the connection zone between major segments 2 and 3. Triangular slip profile revealing rupture of 3 segments.

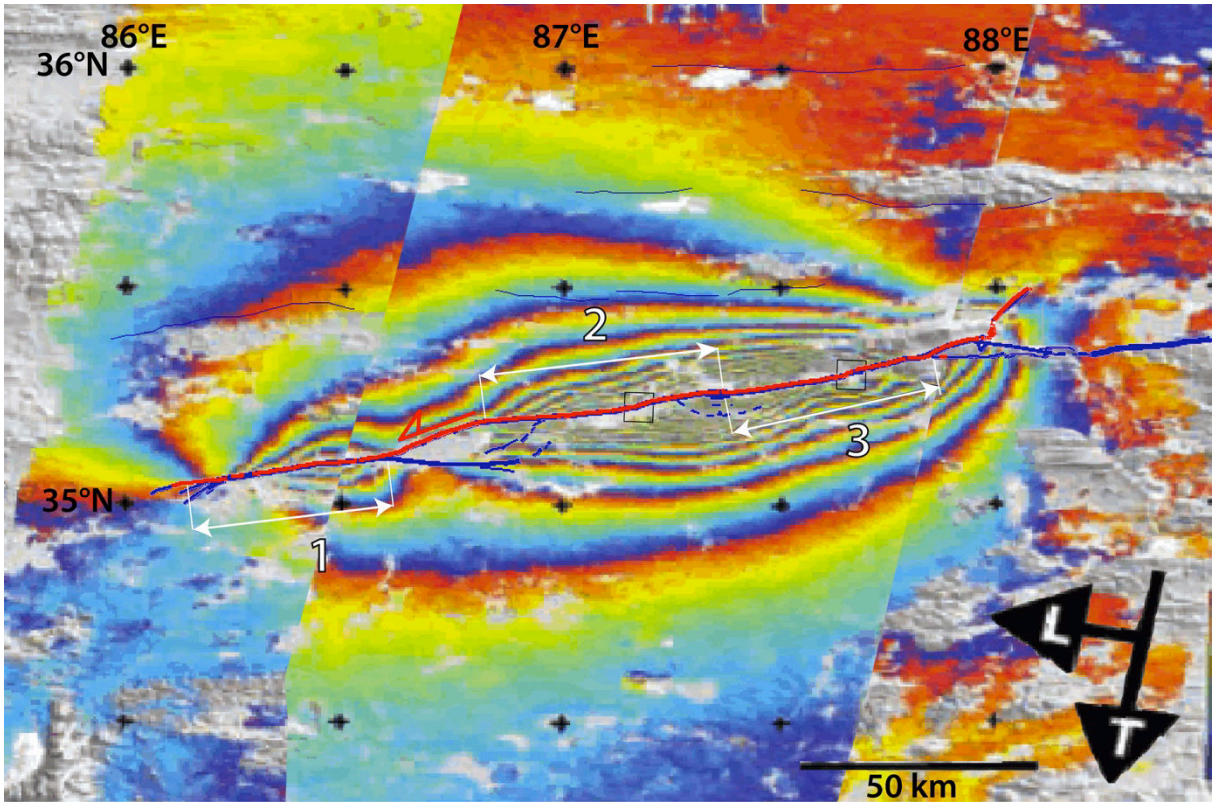


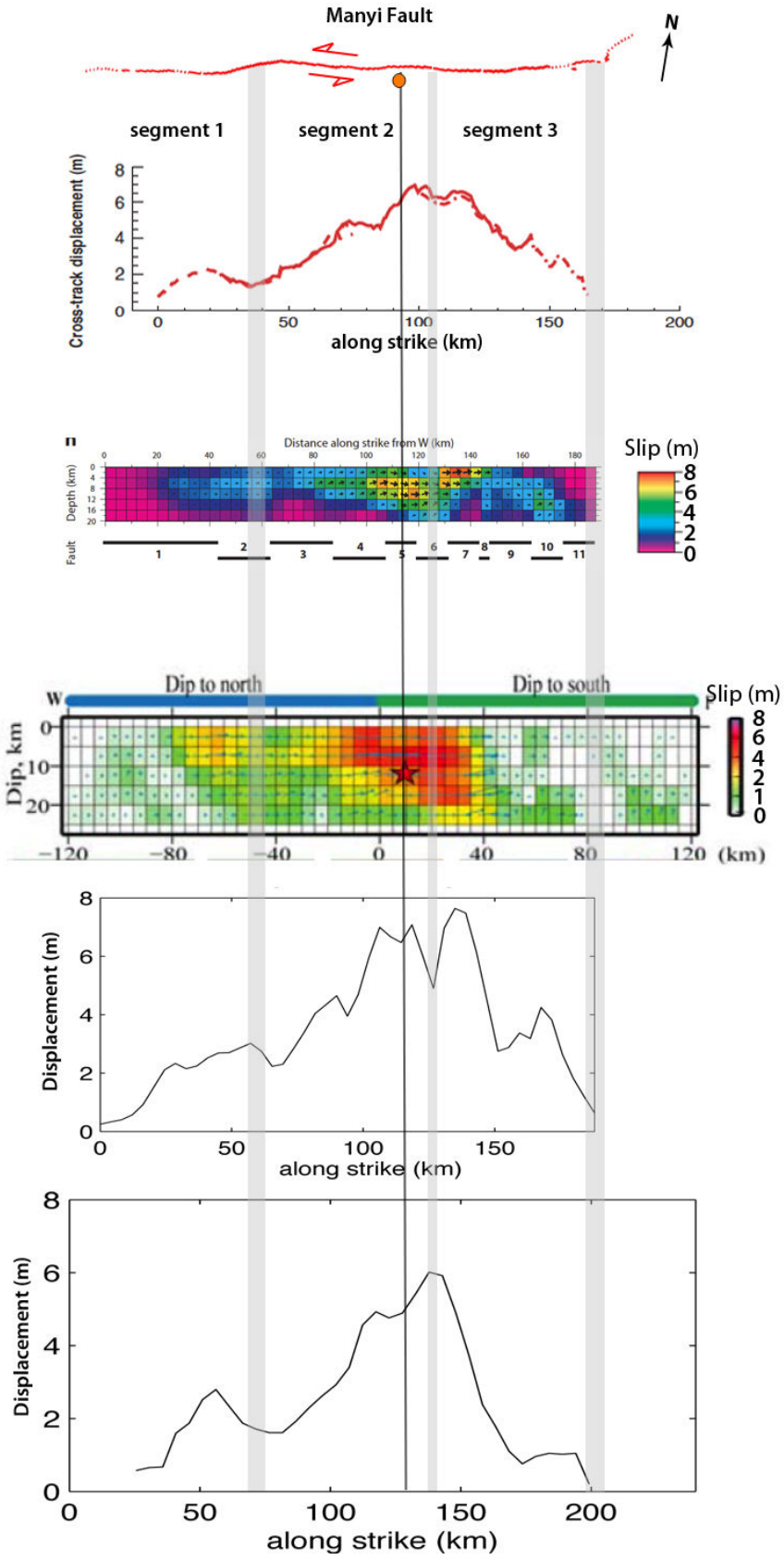
Fig.115: Radar imagery (InSAR) of the ground deformation of the 1997 Manyi earthquake (from Funning et al. 2007). In red is the 1997 surface rupture ; In blue is the long term faults from our mapping. Segments are numbered as in Fig.114a and squares show small pull-apart basins.

Source inversion models and slip distribution at depth:

- We compare two source inversion models that have been published on the 1997 Manyi earthquake, and whose grid data are available (Fig.116 and Table 2)
- The models differ principally from the data they used:
    - Funning et al. (2007): InSAR data only. The model divides the broken fault into 11 segments: the western sections (1 to 4) dip to the south; the eastern sections (5 to 11) dip to the north.

- Wen and Ma (2010): Teleseismic data only, and they use InSAR data to determine the fault geometry of their model. The model divides the fault into 2 segments: the western segment dips to the north, the eastern segment dips to the south.

→ We consider that the model from Funning et al. (2007) is the most robust for they use InSAR data covering all the rupture length and imaging deformation close to the fault.
→ Both models find a similar slip distribution, resembling that observed at surface, and showing an overall triangular shape with maximum slip in the east of the rupture. Maximum slip is 6-7 m. The profile from Funning et al. (2007) shows 3 main slip patches well coinciding with slip on major segments 1, 2 and 3. In the two models, most of the slip is distributed between 0 and 20 km.
→ **Source models suggest: L ~170-190 km, Dmax at depth ~8 m, 3 broken segments forming distinct slip patches.**



This study : Mapping of the surface rupture based on Google Earth imagery

Peltzer et al. 1999
Co-seismic slip profile modeled at surface from InSAR measurements.

Funning et al. 2007 :
Data : InSAR
L= 190 km ; W = 20 km ; Dmax = 7,6 m

Wen & Ma 2010 :
Data : Teleseismic
L = 170 km ; W= 25 km ; Dmax = 6,1 m < Dmax surface

Profile of maximum slip inferred at depth from the source model of Funning et al. (2007)

Profile of maximum slip inferred at depth from the source model of Wen & Ma (2010)

Fig.116: Comparison between different inversion models published on the 1997 Manyi earthquake and coseismic slip profiles measured at surface and inferred at depth. Dark line represents the hypocenter location for each model. Models are at the same scale. Grey areas represent the intersegment zones.

Other source parameters:

SCARDEC
Mainshock: 1997/11/08 at 10h02min52s GMT;
Lat = 35.07° Lon= 87.32°
Mw 7.5; M0 = 2,48e20 Nm; Z = 16.2 km
Duration: 41,5 s
Strike, dip, rake: (258°, 82°, 0°)/ (348°, 90°, -172°)

Global CMT
Mainshock: 1997/11/08 at 10h03min3s GMT;
Lat = 35.33° Lon= 86.96°
Mw 7.5; M0 = 2,23e20 Nm; Z = 16.4 km;
Half-duration: 14,7s
Strike, dip, slip: (79°, 69°, 2°)/ (348°, 88°, 159°)

- The range of duration values is broad between the two methods. However other studies are in agreement with estimation from the SCARDEC method (e.g. Velasco et al., 2000; Duration= 50s)
- Moment magnitude and seismic moment are in fair agreement.

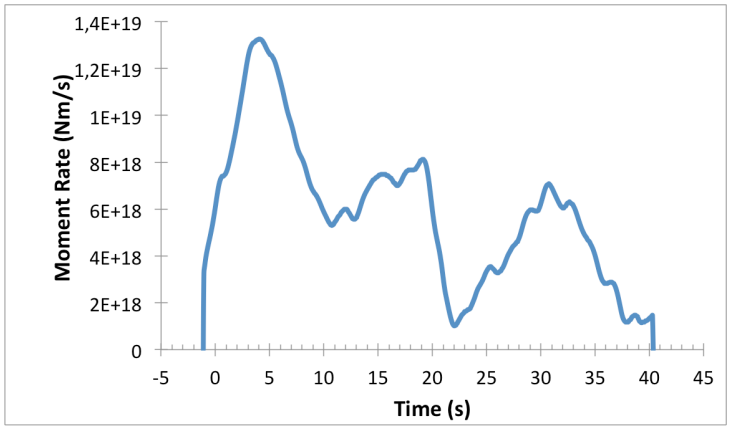


Fig.117: Mean Source Time Function calculated with the SCARDEC method (Vallée et al., 2011).

The source time function shows that the EQ started with a strong energy release that lasted about 10 s. Three peaks of moment release are distinguished –between 0-10, 10-22, and 22-37s, suggesting the rupture of three distinct sections of the fault. We interpret the first 10 s as the rupture of major segment 2 (most mature segment nearby the hypocenter; see discussion in Chapter VII), while the last 30 s likely show the coeval rupture of major segments 1 and 3.

→ The Source time function data suggest the rupture of 3 distinct sections of the Manyi Fault

Other information:

1997 EQ:

- The Manyi area is very difficult to access, explaining the lack of field measurements, except those of Xu 2000. But this study has been written in chinese and does not show any picture or figure.
- The aftershocks were poorly recorded. The largest recorded aftershock was Mw 5.1 (Velasco et al., 2000).
- The postseismic deformation was studied with InSAR data over a period of 3 years after the earthquake: Ryder et al. (2007) show that most of the postseismic deformation occurred on major segment 2, at a depth of 20-30km.

Parameters retained to describe the 1997 Manyi EQ (Table 1 – 4):

Mw 7.5; M0 ~ 2.4e20 Nm; L ~ 170 km ; W ~ 20 km ; Dmax surface 6-7 m, possibly over-estimated; Dmax depth ~ 7,6 m ; Duration ~ 46 s ; *Hypocenter* : Z ~ 16 km

Number of segments broken on the Manyi Fault: 3 major segments.

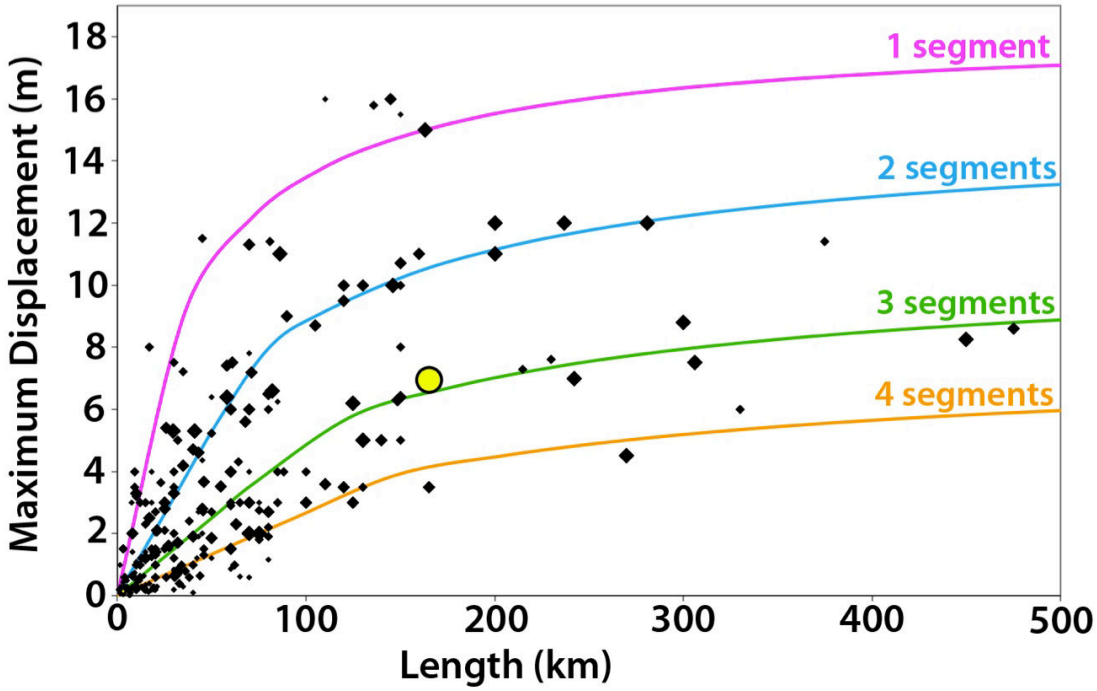


Fig.118: Earthquake displacement-length data measured at surface for 260 historical large continental earthquakes (Mw≥6). The 4 curves indicate the number of major long-term fault segments to have been broken by the earthquakes (modified from Manighetti et al., 2007 and Chapter IV). Yellow dot shows the Manyi earthquake surface slip-length data.

The Manyi earthquake surface and depth slip-length data fall on the third function (green curve; Fig.118 and 119, respectively), in keeping with the EQ having broken three major segments of the long-term fault on which it occurred.

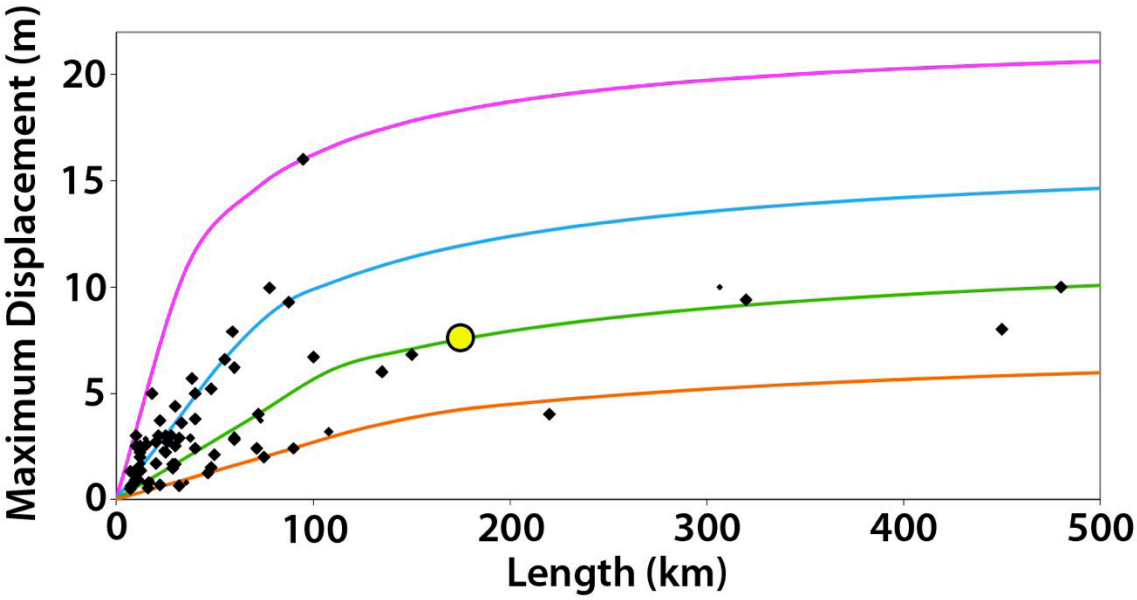


Fig.119: Earthquake displacement-length data inferred at depth for 90 historical large continental earthquakes (Mw≥6). The 4 curves indicate the number of major long-term fault segments to have been broken by the earthquakes (modified from Manighetti et al., 2007 and Chapter IV). Yellow dot shows the Manyi earthquake depth slip-length data.

References

Funning, G. J., B. Parsons, and T. J. Wright (2007). Fault slip in the 1997 Manyi, Tibet earthquake from linear elastic modelling of InSAR displacements, *Geophys. J. Int*., 169, 988–1008, doi:10.1111/j.1365-246X.2006.03318.x.

Holt, W. E., Chamot-Rooke N., Le Pichon, X., Haines, A. J., Shen-Tu, B. & Ren, J. (2000). Velocity field in Asia inferred from Quaternary fault slip rates and Global Positioning System observations. *Journal of Geoph. Research*, **105**, 19,185-19,209.

Manighetti, I., M. Campillo, S. Bouley, and F. Cotton (2007), Earthquake scaling, fault segmentation, and structural maturity, *Earth Planet. Sci. Lett*., **253**, 429-438, doi:10.1016/j.epsl.2006.11.004

Molnar, P. and Chen, W.-P. (1983). Focal depths and fault plane solutions of earthquakes under the tibetan plateau. *Journal of Geoph. Research*, **88**, 1180-1196.

Peltzer, G., F. Crampé, and G. King (1999). Evidence of nonlinear elasticity of the crust from Mw7.6 Manyi (Tibet) earthquake, *Science*, 286, 272–276, doi:10.1126/science.286.5438.272.

Ryder, I., Parsons, B., Wright, T.J. & Funning, G.J., 2007. Post-seismic motion following the 1997 Manyi (Tibet) earthquake: InSAR observations and modelling, *Geophys. J. Int*., doi:10.1111/j.1365-246X.2006.03312.x.

Vallée, M., J. Charléty, A.M.G. Ferreira, B. Delouis, and J. Vergoz, (2011). SCARDEC : a new technique for the rapid determination of seismic moment magnitude, focal mechanism and source time functions for large earthquakes using body wave deconvolution, *Geophys. J. Int*., **184**, 338-358.

Velasco, A.A.,Ammon,C.J.&Beck, S.L., 2000. Broadband source modeling of the November 8, 1997, Tibet (Mw = 7.5) earthquake and its tectonic implications, *J. geophys. Res*., 105, 28 065–28 080.

Wang, H., C. Xu, and L. Ge (2007). Coseismic deformation and slip distribution of the 1997 Mw7.5 Manyi, Tibet, earthquake from InSAR measurements, *J. Geodyn*., 44, 200–212, doi:10.1016/j.jog.2007.03.003.

Wen, Y.-Y. & Ma, K.-F. (2010). Fault geometry and distribution of asperities of the 1997 Manyi, China (Mw = 7.5), earthquake: Integrated analysis from seismological and InSAR data. *Geophys. Res. Lett.*, 37, L05303, doi:10.1029/2009GL041976

Xu, X. W. (2000), Scientific investigation of Mani earthquake in North Tibet, in *Yearbook of China Earthquake Research*, pp. 327–329, China.

2.15. Pleasant Valley 1915

03/oct/1915, Nevada, USA

Mw 7.0

Epicenter : 40.50°N-117.50°W

Normal fault



Broken long-term fault

The EQ broke a part of the Pleasant Valley fault in the Basin and Range province.

General characteristics from literature:

The Basin and Range faulting is presented in section Dixie Valley and Fairview Peak (See repeated Fig.120).

- The Pleasant Valley Fault is, as the other Basin and Range faults, a normal fault striking NNE overall, over a length of ~70 km. It extends due north of the NW-trending Indian Peak-Mahogany Peak shear zone (See section Dixie Valley and Fairview Peak), in the northward prolongation of the Fairview Peak-Dixie Valley Fault system (Fig.121). However, whereas the Fairview Peak-Dixie Valley Fault system dip eastwards, the Pleasant Valley Fault dips westwards. Therefore, the Pleasant Valley Fault is clearly distinct from the Fairview Peak-Dixie Valley fault system.
- The apparent (i.e., topographic) cumulative vertical throw on the Pleasant Valley Fault is ~1.6 km, but its actual maximum vertical cumulative slip is not known
- A long-term vertical slip rate < 0,2 mm/yr has been estimated from a 8-14 m scarp height considered formed over the last 7-15 ka (Bell et al., 2004 and references therein).
- Current vertical slip rate on the Pleasant Valley Fault is not known.

→ The 1915 Pleasant Valley earthquake broke a part of the Pleasant Valley long-term fault, which seems to be fairly immature (L 70 km, MR < 0.2 mm/yr, D_{Total} ~2 km).

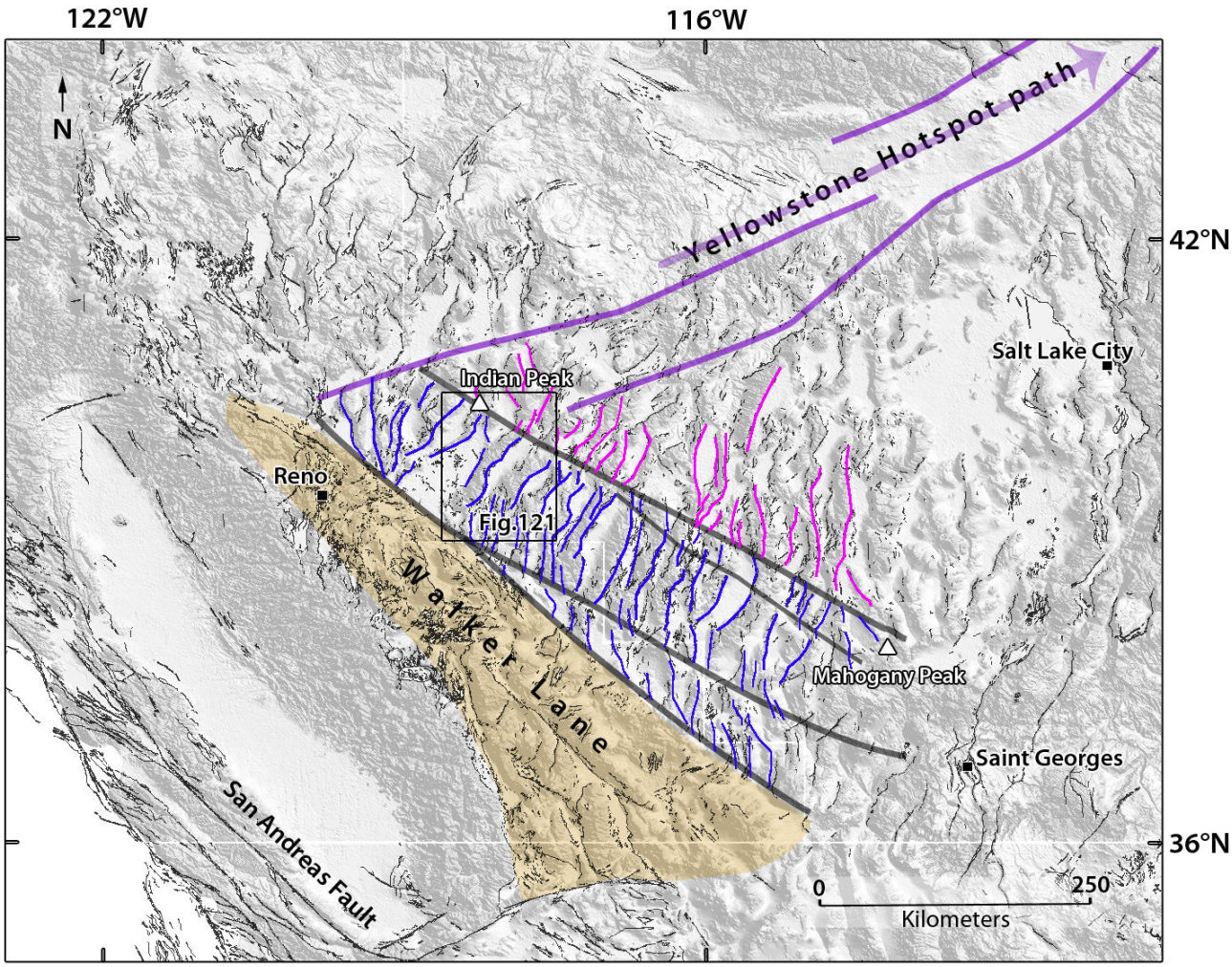


Fig.120: General map of the Basin and Range province. Black Quaternary faults are from the U.S. Geological Survey and California Geological Survey, 2006. Blue and pink traces show the main faults' domains separated by oblique shear zones (shaded dark areas ; see text for details). The southern shear zone bounds the so-called « Walker Lane Belt »(orange area). Purple lineaments are linked to the activity of the Yellowstone Hospot, whose propagation is indicated with the purple arrow.

Architecture and lateral major segmentation, from our mapping (Fig.122):

- Mapping done from Google Earth, Landsat and Aster GDEM v.2 data combined with literature information
- Long-term fault trace well expressed in surface morphology and topography
- The Pleasant Valley Fault has a fairly linear trace and is ~70 km long. It is divided into three major collinear segments of similar length (20-27 km), arranged in a right-stepping echelon along the mean NNE strike of the fault (See Fig.122, where the segments are numbered). The en echelon arrangement might suggest a small left-lateral component of slip on the Pleasant Valley Fault in addition to its dominant normal one.
- The 3 major segments are separated with fairly large (4-5 km) releasing step-overs of types $2_{O\text{-}E}$. They are hardly connected to each other at the ground surface.

- To the north, the fault trace splays in several small oblique branches, one departs from the connection zone between major segments 1 and 2 and seems to connect with the adjacent synthetic Grass Valley Fault, whereas the other branches splay from the Pleasant Valley northern fault tip.
- To the south, the Pleasant Valley Fault trace also splays into several smaller oblique branches, and stops near the Indian Peak-Mahogany Peak NW-trending shear zone.
- The overall geometry of the Pleasant Valley Fault thus suggests that it might have propagated bilaterally over geological time, from about its center. The Pleasant Valley Fault might be currently arrested in its southward propagation by the Indian Peak-Mahogany Peak shear zone.

→ The Pleasant Valley Fault might have propagated bilaterally over geological time. It is in the process of connecting with the Grass Valley Fault further northwest. It is made of three major collinear segments, the central one (n° 2) might be the most mature along the fault.

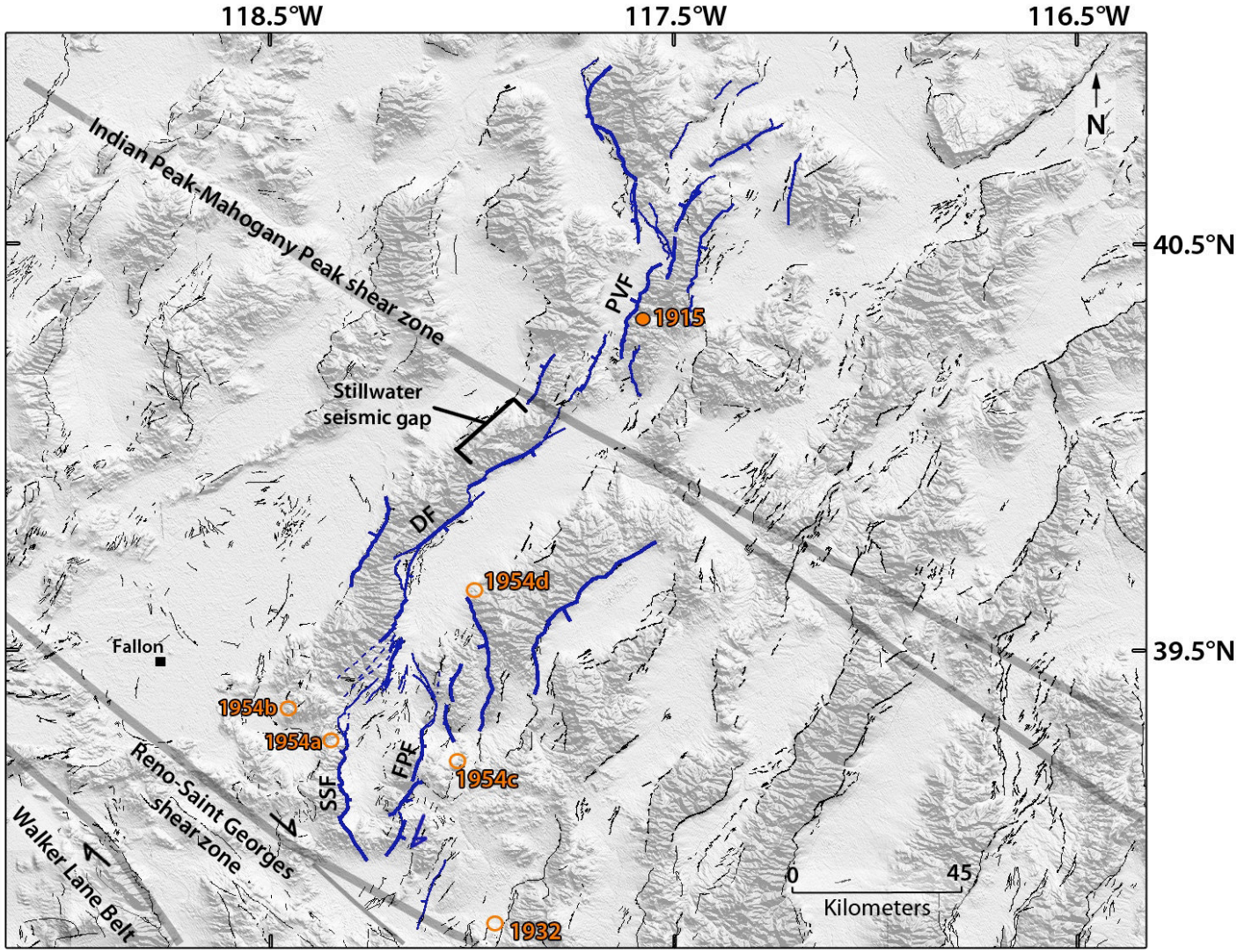


Fig.121: Zoom on the main long-term faults (in blue) involved during the 1915 Pleasant Valley earthquake in the Basin and Range province, from Fig.120 (same caption). DF : Dixie Valley Fault ; FPF : Fairview Peak Fault ; SSF : Sand Springs Fault ; PVF : Pleasant Valley Fault. Orange full circle shows the 1915 Pleasant earthquake. Epicenters of 1932 Cedar Mountain, 1954a and 1954b Rainbow Mountain, Valley 1954c Fairview Peak and 1954d Dixie Valley earthquakes are also indicated (orange empty circles).

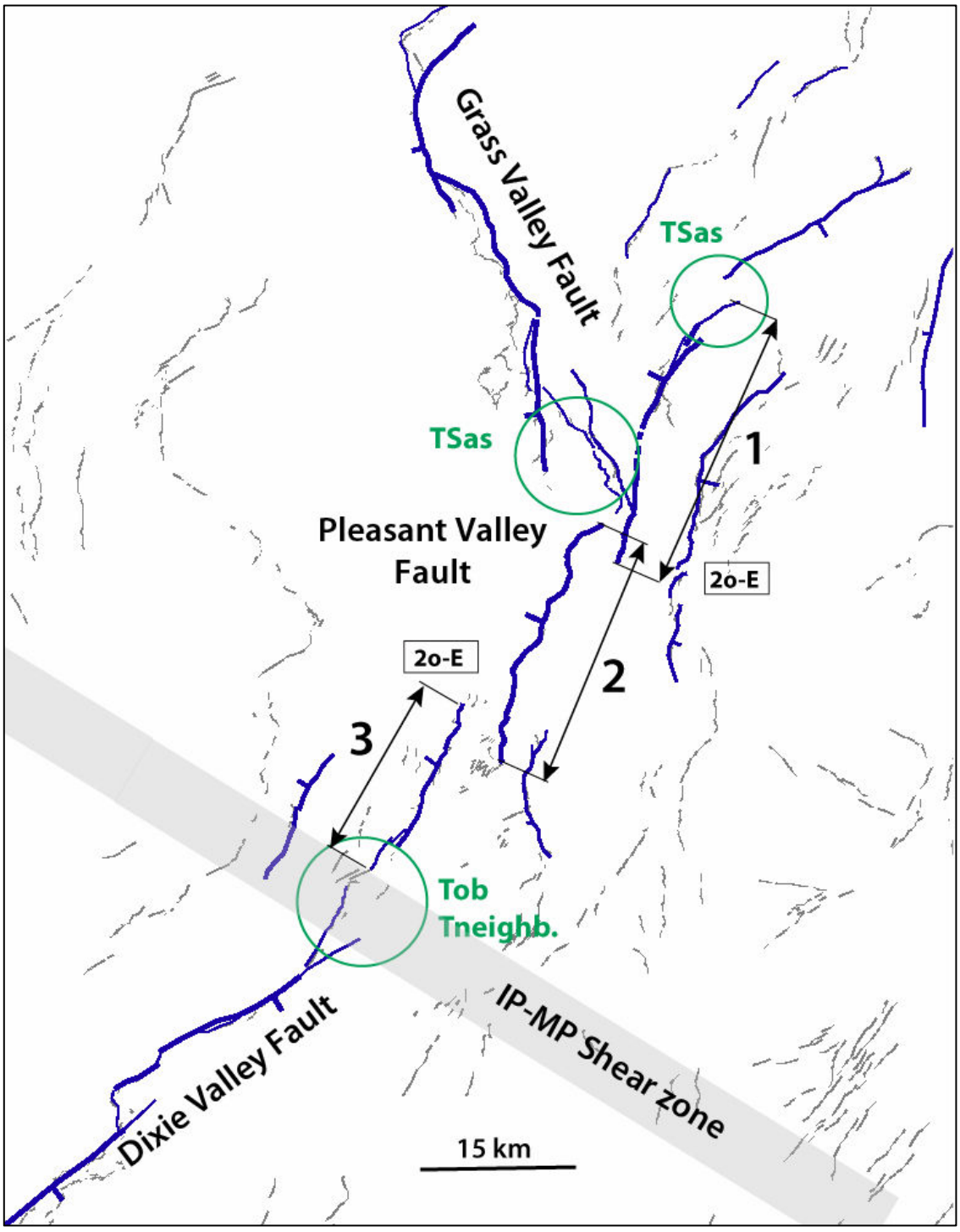


Fig.122: Focus on the major segments that form the Pleasant Valley Fault. The segments are numbered from N to S and indicated by black arrows parallel to their mean strike. The nature of the inter-segment zones is indicated in letters within boxes explained in Table 6. The nature of the fault tips is indicated in green (Table 6)

1915 Coseismic rupture

Surface trace and location on long-term Pleasant Valley Fault :

- The 1915 surface rupture is still fairly clear on Google Earth images. The surface trace of the earthquake was precisely mapped on the field, and the displacements measured (See below) (Jones 1915; Wallace 1984; dePolo et al., 1991; Zhang et al., 1999)
- Surface rupture of ~40-45 km long (Jones 1915; Wallace 1984; dePolo et al., 1991 ; Zhang et al., 1999)
- The EQ broke 2 major segments of the Pleasant Valley Fault, segments 2 and 3. To the south, the rupture stopped at the southern tip of major segment 3, whereas, to the north, the rupture stopped in the connection zone that separates major segments 1 and 2. In that zone, the EQ apparently broke a little part of the secondary oblique fault that splays towards the Grass Valley Fault, and the very southern tip of major segment 1 (so-called "Tobin scarp"). However, it is not certain that those ruptures were produced during the mainshock; they might have been produced either during the foreshocks that occurred a few hours before the mainshock, or during the large aftershocks that followed (Jones 1915; Wallace 1984; Doser 1988).
- Small rupture traces were also suggested further north on a small part of major segment 1 (called « China Mountain ruptures », Fig.123), but those were not observed during the immediate field investigations (e.g. Jones 1915); they were lately inferred from the witness of inhabitants (Wallace 1984). The China Mountain ruptures are not clearly expressed on the Google Earth images, contrary to the rest of the rupture. It is therefore likely that the China Mountain slip was not produced by the Pleasant Valley EQ.
- The hypocenter location is not well constrained. It would be situated at the northern tip of the rupture (e.g. Doser 1988), nearby the connection zone between major segments 1 and 2. If this position is correct, the rupture would have propagated unilaterally towards the south.

→ **The 1915 Pleasant Valley EQ broke two major segments of the Pleasant Valley Fault.**

Coseismic displacements measured at surface :

- *From Field measurements*: Maximum vertical slip estimated between ~ 4.6 m (Jones, 1915) and 6 m (Wallace 1984; dePolo et al., 1991; Zhang et al., 1999). The maximum slip occurred on major segment 2, which is the most mature segment of the Pleasant Valley Fault.

- The complete slip profile was measured. As said earlier, it is unlikely that the disconnected China Mountain slip was produced by the 1915 Pleasant Valley EQ. It is also unclear whether or not the Tobin slip was produced during the mainshock, or before or after. Whether we consider it or not, the overall shape of the 1915 surface slip distribution is fairly triangular and asymmetric, with maximum slip deported towards the northern tip of the rupture, and slip decreasing fairly regularly from its maximum value to zero at the southern rupture tip. The maximum slip occurred on the most mature segment of the Pleasant Valley Fault.

→ Maximum slip of 5-6 m well measured at surface, on the central most mature major segment 2 of the broken fault.

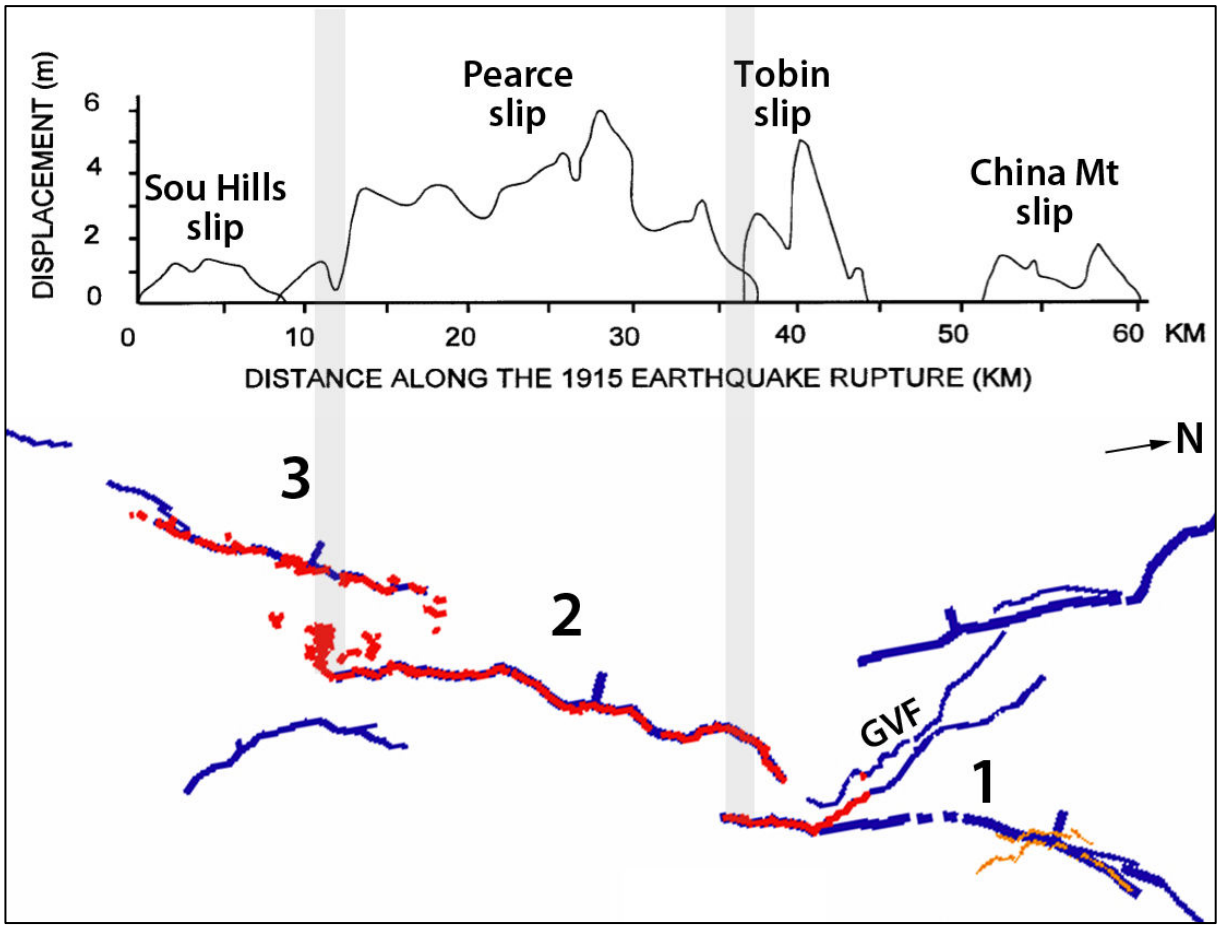


Fig.123: Coseismic slip profile of the 1915 Pleasant Valley earthquake measured along the surface rupture (in red). Orange trace shows the China Mountain scarp that we don't associate to the 1915 mainshock. Long-term faults are indicated in blue. GVF : Grass Valley Fault.. Grey bars are the intersegment zones.

Source parameters:

Doser (1988) (Fig.124)
Mainshock: 1915/10/03 at 06h53 GMT;
Lat: 40. 50°; Lon: -117.50°
Mw 6.9-7.0; M0=2.7^{e}19 N.m; Z= 9 km;
Duration = 14s
Strike, dip, rake (°): 194, 44, -61

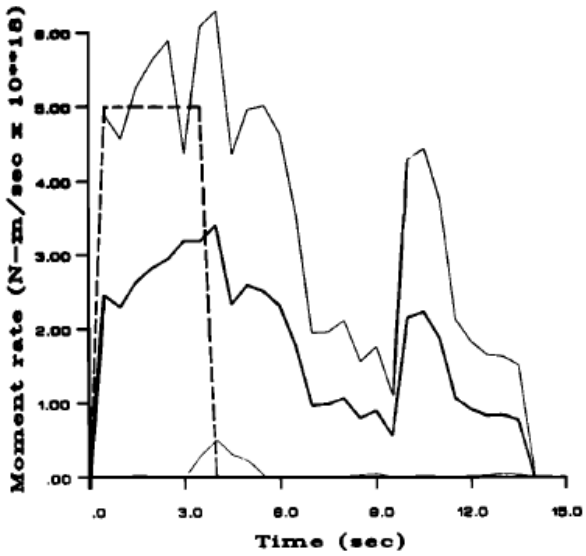


Fig.124: Range of Source Time Functions (solid lines) calculated from Doser 1988.

Doser (1988) divides the Pleasant Valley earthquake in two sub-events, attested by two peaks in the moment release function (Fig.124): the strongest peak of moment release might coincide with the rupture of major segment 2, whereas the second, smaller peak of moment release might coincide with the rupture of major segment 3.

→ **The source time function data suggest the rupture of two distinct elements of the Pleasant Valley Fault.**

Other information:

- The 1915 Pleasant Valley and the 1954 Dixie Valley rupture zones are separated by the so-called « Stillwater seismic gap » (Fig.121), where no historical rupture younger than 300 years has been reported, and where the instrumental seismicity is few (Wallace 1977; Wallace and Whitney 1984).

Parameters retained to describe the 1915 Pleasant Valley EQ (Tables 1 & 2):

Mw 6.9; M0 ~ 2,7e 19 Nm; L ~ 45 km ; Dmax surface = 5-6 m

Hypocenter: Z ~ 9 km.

Number of major segments broken on the Pleasant Valley Fault: 2

It is noteworthy that these characteristics are similar to those of the nearby, similar magnitude- 1954 Fairview Peak and Dixie Valley EQs (See section Dixie Valley and Fairview Peak EQs).

The 1915 Pleasant Valley earthquake surface slip-length data fall fairly well on the second function (blue curve; Fig.125). This is in keeping with the earthquake having broken 2 major segments of the fault on which it occurred.

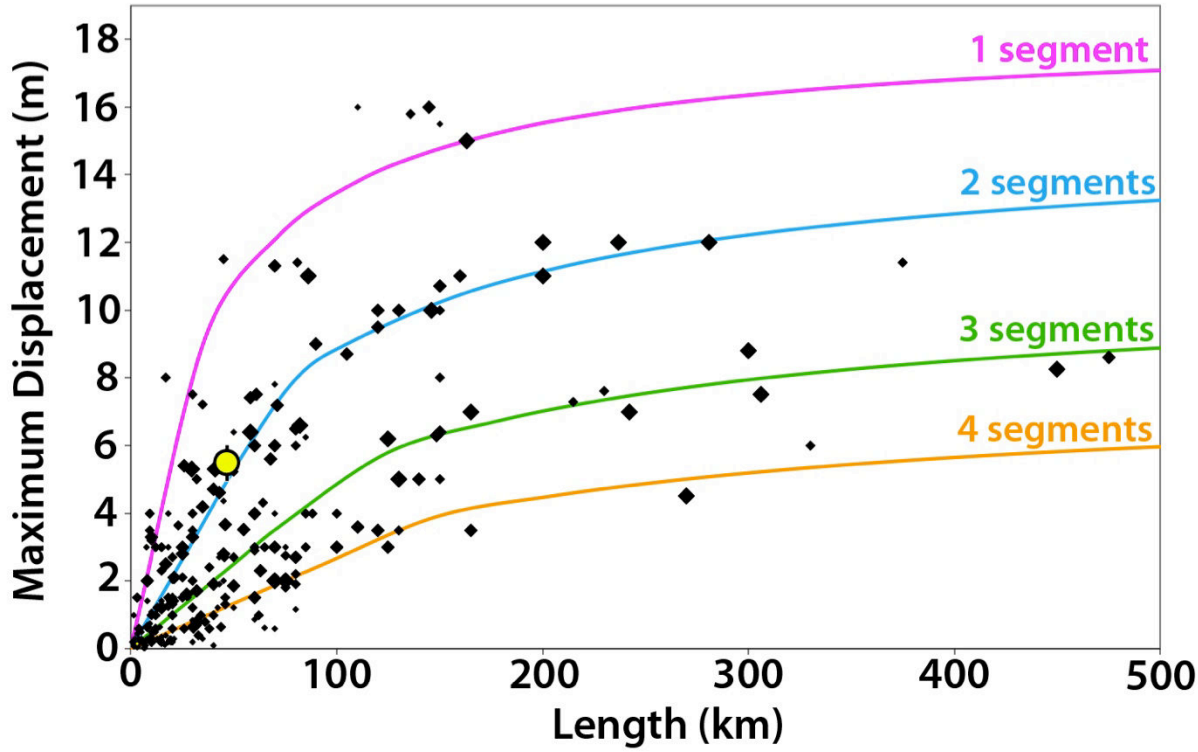


Fig.125: Earthquake displacement-length data measured at surface for 260 historical large continental earthquakes (Mw≥6). The 4 curves indicate the number of major long-term fault segments to have been broken by the earthquakes (modified from Manighetti et al., 2007 and Chapter IV). Yellow dot shows the 1915 Pleasant Valley EQ surface slip-length data.

References

Bell, J. W., Caskey, S. J., Ramelli, A. R., & Guerrieri, L. (2004). Pattern and rates of faulting in the central Nevada seismic belt, and paleoseismic evidence for prior beltlike behavior. *Bulletin of the Seismological Society of America*, *94*(4), 1229-1254.

dePolo, C.M., Clark, D.G., Slemmons, D.B., Ramallie, A. (1991). Historical Basin and Range Province surface faulting and fault segmentation. *J. Struct. Geol*. **13**, 123–136.

Doser, D. I. (1988). Source Parameters of Earthquakes in the Nevada Seismic Zone , 1915-1943. *Jour. Geophys. Res.,* **93**, 15,001-15,015.

Jones, J. C. (1915). The Pleasant Valley, Nevada, earthquake of October 2,1915. *Bull. Seismol. Soc. Am*., **5**, no. 4, p. 190-205.

Manighetti, I., Tapponnier, P., Courtillot, V., Gallet, Y., Jacques, E., & Gillot, P. Y. (2001). Strain transfer between disconnected, propagating rifts in Afar. *Journal of Geophysical Research,* **106**(B7), 13613-13665.

Manighetti, I., M. Campillo, S. Bouley, and F. Cotton (2007), Earthquake scaling, fault segmentation, and structural maturity, Earth Planet. Sci. Lett., 253, 429-438, doi:10.1016/j.epsl.2006.11.004

Parsons, T. (1995). The Basin and Range Province. *Continental Rifts: Evolution, Structure, Tectonics*, **25**, 277-324.

Scott, W.E., Pierce, K. L. & Hait, M. H. Jr. (1985) Quaternary tectonic setting of the 1983 Borah Peak earthquake, Central Idaho, *Bull. Seism. Soc. Am*., **75**, 1053-1066.

Slemmons, D. B., A. E. Jones & J. I. Gimlett (1965). Catalog of Nevada earthquakes, 1852-1960, *Bulletin of the Seismological Society of America*, **55**, 519-565

Stewart, J. H. (1971) Basin and Range Structure: A System of Horsts and Grabens Produced by Deep-Seated Extension. *Geological Society of America Bulletin*, **82**, 1019-1044

Thompson, G. A. & Burke, D. B. (1973). Rate and Direction of Spreading in Dixie Valley, Basin and Range Province, Nevada. *Geological Society of America Bulletin*, **84**, 627-632

Wallace, R. E. (1977). Profiles and ages of young fault scarps, north-central Nevada. *Bull. Geol. Soc. Am*. **88**, 1267-1281.

Wallace, R.E. (1984). Fault scarps formed during the earthquake of October 2, 1915, Pleasant Valley, Nevada and some tectonic implications. *U.S. Geol. Surv. Prof. Pap*. **1274-**A, 1–33.

Wallace, R.E. & Whitney, R.A. (1984). Late Quaternary history of the Stillwater seismic gap. *Bull. Seismol. Soc. Am*., **74**, 301–314.

Walpersdorf, A., Manighetti, I., Mousavi, Z., Tavakoli, F., Vergnolle, M., Jadidi, A. Jadidi, D. Hatzfeld, A. Aghamohammadi, A. Bigot, Y. Djamour, H. Nankali & Sedighi, M. (2014). Present-day kinematics and fault slip rates in eastern Iran, derived from 11 years of GPS data, *J. Geophys. Res. Solid Earth*, **119**, 1359–1383, doi:10.1002/2013JB010620

Zhang, P., Mao, F. & Slemmons, D. B. (1999). Rupture terminations and size of segment boundaries from historical earthquake ruptures in the Basin and Range Province. *Tectonophysics,* **308**, 37–52.

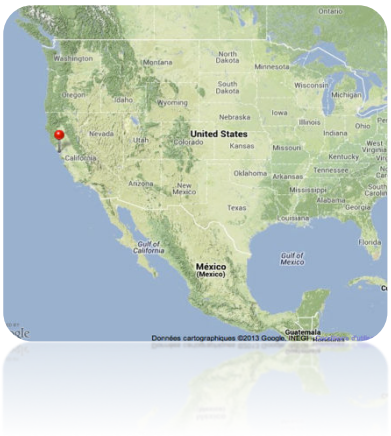
2.16. San Francisco 1906

18/Apr/1906, California, USA

Mw 7.7

Epicenter : 37.67°N-122.43°W

Right-lateral strike-slip



Broken long-term fault

The EQ broke the northern part of the San Andreas Fault, California, USA.

General characteristics of the San Andreas Fault from literature (Fig.126):

This part is presented in the Fort Tejon 1857 section. We thus only show again the figures.

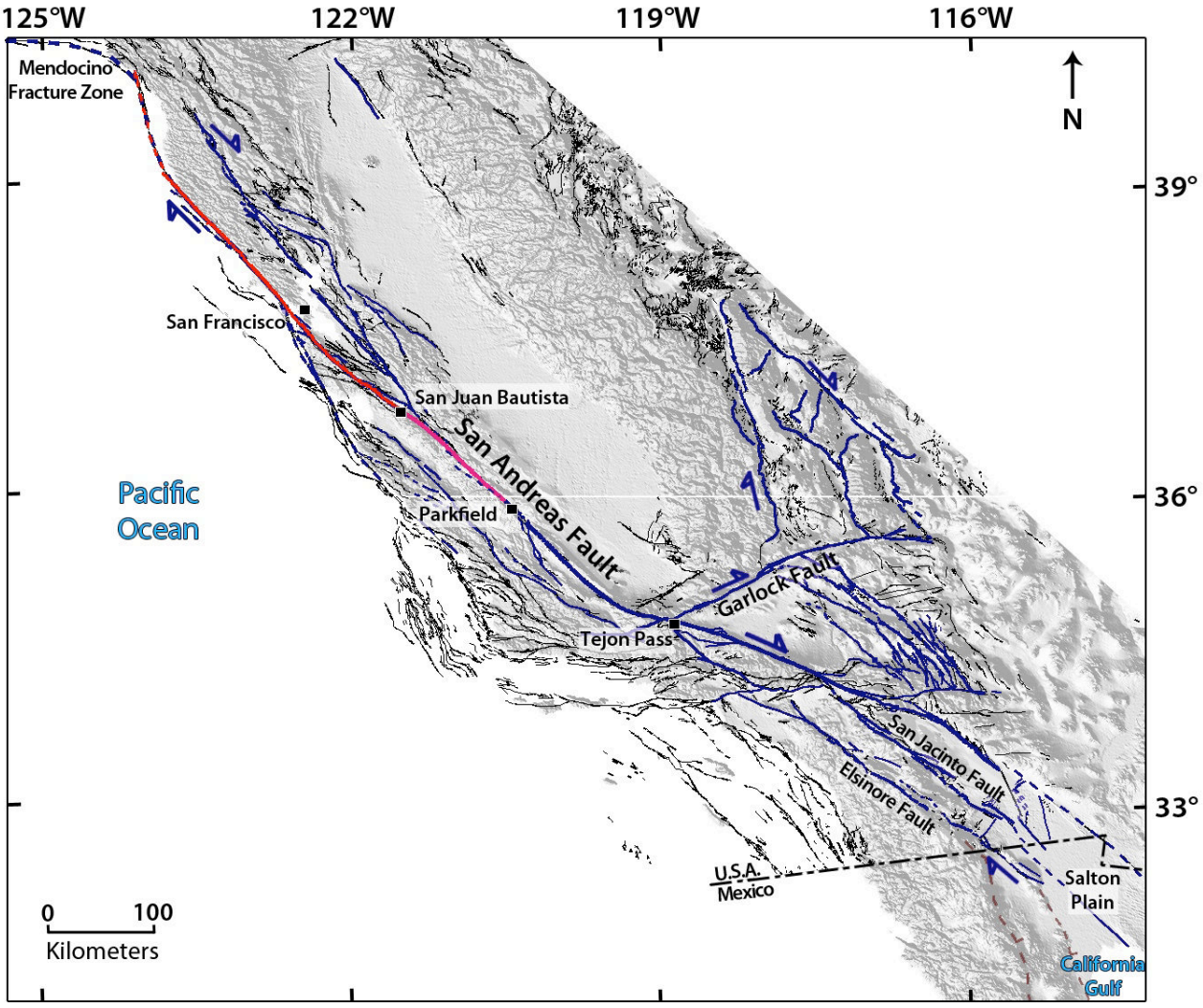


Fig.126: General map of long term faults in California. In blue are the major active faults that we mapped. In black are the other Quaternary faults mapped by the U.S. Geological Survey and California Geological Survey, 2006. Dotted brown lines are ancient faults related to the Gulf of California (See detail mapping in Fig.129). The creeping section of the San Andreas Fault is indicated by the pink trace. The red line shows the surface rupture of the 1906 San Francisco earthquake

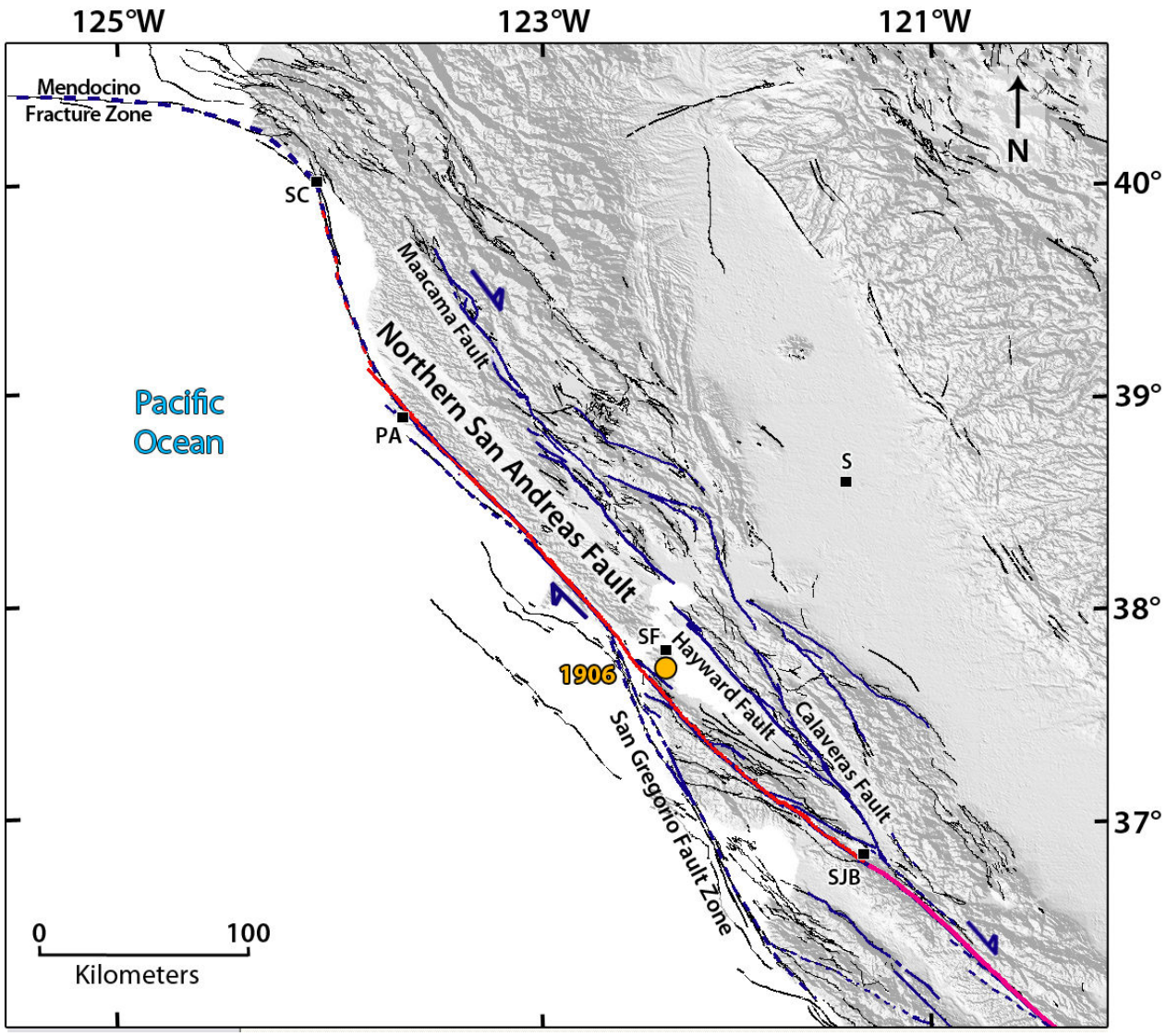


Fig.127: (a) Map of long-term faults in northern California (same caption as in Fig.126). The orange circle shows the 1906 San Francisco epicenter. SC : Shelter Cove ; PA : Point Arena ; SF : San Francisco ; SJB : San Juan Bautista ; S : Sacramento.

Architecture and lateral major segmentation, from our and USGS mappings (Fig.127):

This part has already been presented in the 1857 Fort Tejon section. However, we repeat here the information on the Northern San Andreas Fault, for it is necessary to analyze the 1906 San Francisco EQ.

- Mapping done from Google Earth, Landsat and ASTER GDEM data combined with USGS detailed mapping (U.S. Geological Survey and California Geological Survey, 2006)
- The SA Fault is not isolated, but surrounded by numerous faults and fault systems of different slip modes and sizes. The area of "adjacent" faulting is 70-180 km large on either side of the main SA Fault trace, and is enlarging southwards. Some of the adjacent faults

and systems are genetically linked with the SA Fault, whereas others are not, although they might be reactivated in the regional stress field that governs the SA Fault activity. (See below for more details on some of the adjacent faults)

- The SA Fault is ~1300 km long at total. However it is divided into two sections –the northern SA Fault and the southern SA Fault, likely acting as two faults, separated by the ~130 km-long, central creeping section. The northern SA Fault is ~450 km long (along strike); the southern SA Fault is at least ~600 km long (until Imperial valley) and most likely ~800 km (until the Gulf of California; see below).

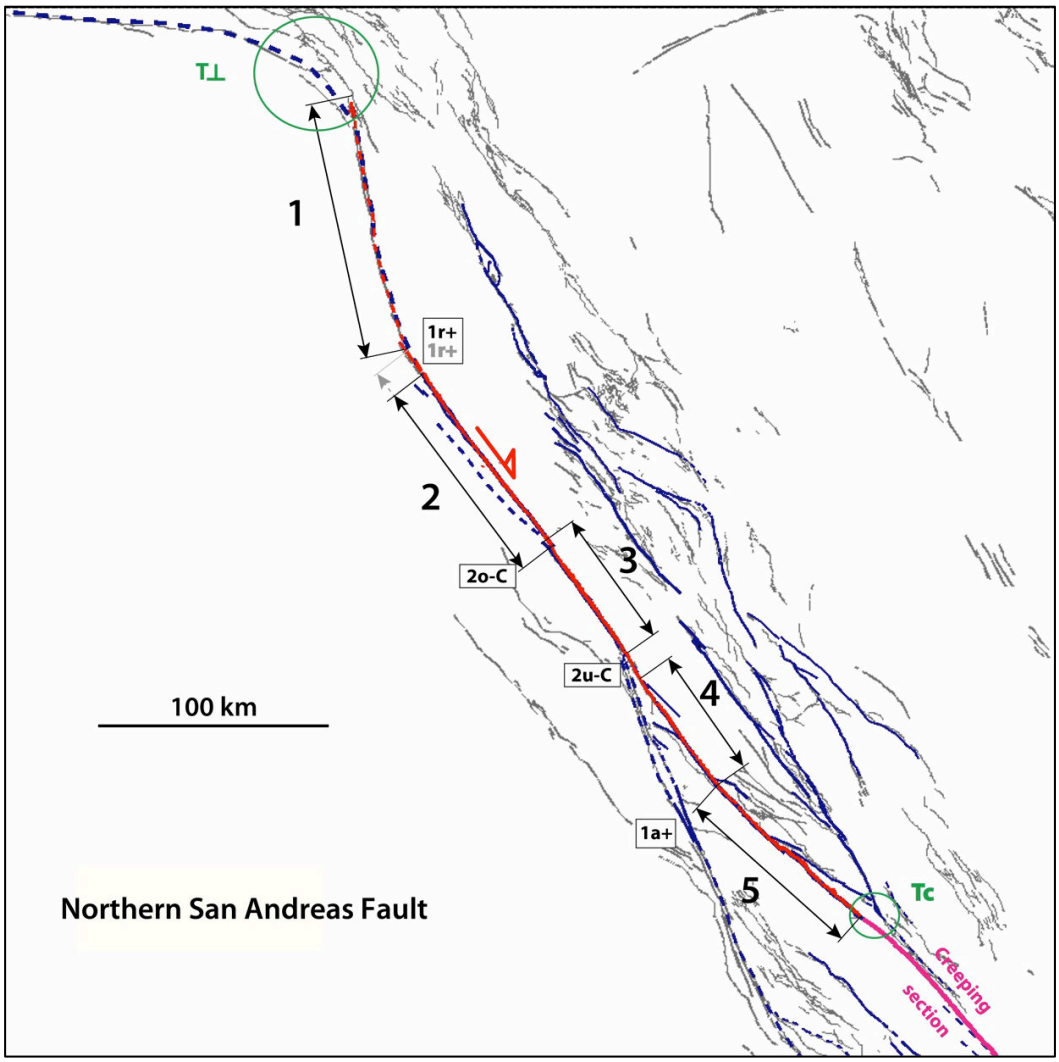


Fig.127: (b)Same active fault map as in 127a, but with focus on the major segments of the northern San Andreas Fault. The segments are numbered from NW to SE and indicated by black arrows parallel to their mean strike. The grey prolongation of the arrows indicates the uncertainties on the segment lengths. The nature of the inter-segment zones is indicated in letters within boxes explained in Table 6. The nature of the fault tips is indicated in green (Table 6).

Northern San Andreas Fault (Fig.127)

- To the north, the northern SA Fault terminates by connecting to the almost perpendicular Mendocino fracture zone. The termination is thus of the type T⊥ (Fig.24) To the south, the northern SA Fault terminates at the junction with the creeping section. The northern SA Fault is thus about 430 km long (L along-strike 450 km).
- Except in its southernmost part, and provided that faults off-shore are well known, the northern SA Fault is pretty isolated, i.e., associated with very few nearby sub-parallel faults (the closest is the Hayward-Calaveras fault zone, 30-40 km away in across-strike direction).
- The northern SA Fault is divided into 5 major, fairly collinear segments (See Fig.127b, where they are numbered). The lengths and types of the segments and inter-segments are described in details in Table 6.
- The 5 major segments have a length of similar order, in the range 60-120 km (length measured along the linear trace of each segment; Fig.127b).
- The fault trace is extremely linear along the 4 northernmost major segments (segts 1-4), and more sinuous along segment 5 in the south.

  - Major segment 1 in the north is offshore and ~120 km long. Its trace is mapped as being linear. Major segment 2 has a very linear trace, mainly onshore, of ~90 km long. Segments 1 and 2 strike differently, with an angle difference of ~24 °. Segments 1 and 2 are connected through a rounded bend in the fault trace, of type 1r+. Segment 3 is almost parallel to segment 2, has a very linear trace ~70 km long, and is connected to segment 2 through a narrow (W 1 km) across-strike step of type $2_{O\text{-}C}$. An oblique NW-striking fault (of type "not splay") intersects the SA trace in the connection zone between segments 2 and 3. Segment 4 also has a linear trace on-land, of ~60 km. It is almost parallel to segment 3 and connects it through a $2_{U\text{-}C}$ type step and fault trace bending. A network of oblique, NNW-trending offshore faults (San Gregorio fault zone) connects the SA trace in the relay zone between segments 3 and 4. The overall pattern suggests that the San Gregorio fault zone might be a splay of the northern SA Fault, and hence might mark the southern termination of the main northern SA Fault when the later was made of major segments 1, 2 and 3 only. The splay would thus suggest that the northern SA Fault has been propagating southward over geological time, in keeping with general observations (See before). Segment 5 looks different from the other 4 segments. While its ~85 km long trace is fairly linear, its overall imprint in the morphology and topography is more subtle than that of the other segments, and in particular, it does not imprint a linear corridor in the topography. The trace of segment 5 is also more discontinuous and more clearly punctuated with smaller-scale

intersegments zones than along the other major segments. Also, multiple secondary oblique faults exist adjacent to the southern part of the southern SA (segments 4 and 5). Altogether these suggest that segment 5 might be younger than the other 4 segments, in keeping with the southward propagation of the fault. Segments 4 and 5 are connected through a 1r+ bend type. More details on the inter-segments can be found in Table 6.

- The southernmost major segments 3, 4 and 5 are shorter than the northernmost major segments 1 and 2, and this observation is in keeping with the Northern San Andreas Fault having lengthened toward the south over geological time (segments more connected and hence longer in the most mature northern part of the fault).

→ The Northern San Andreas Fault is divided into 5 long-term major segments, all are well-connected to each other. The Northern SA Fault seems to have propagated southwards over time; its northernmost section (at least coinciding with major segments 1 & 2) is thus likely the oldest and most mature.

Information on the Southern San Andreas Fault and on the relations between the San Andreas Fault and adjacent faults can be found in Section Fort Tejon.

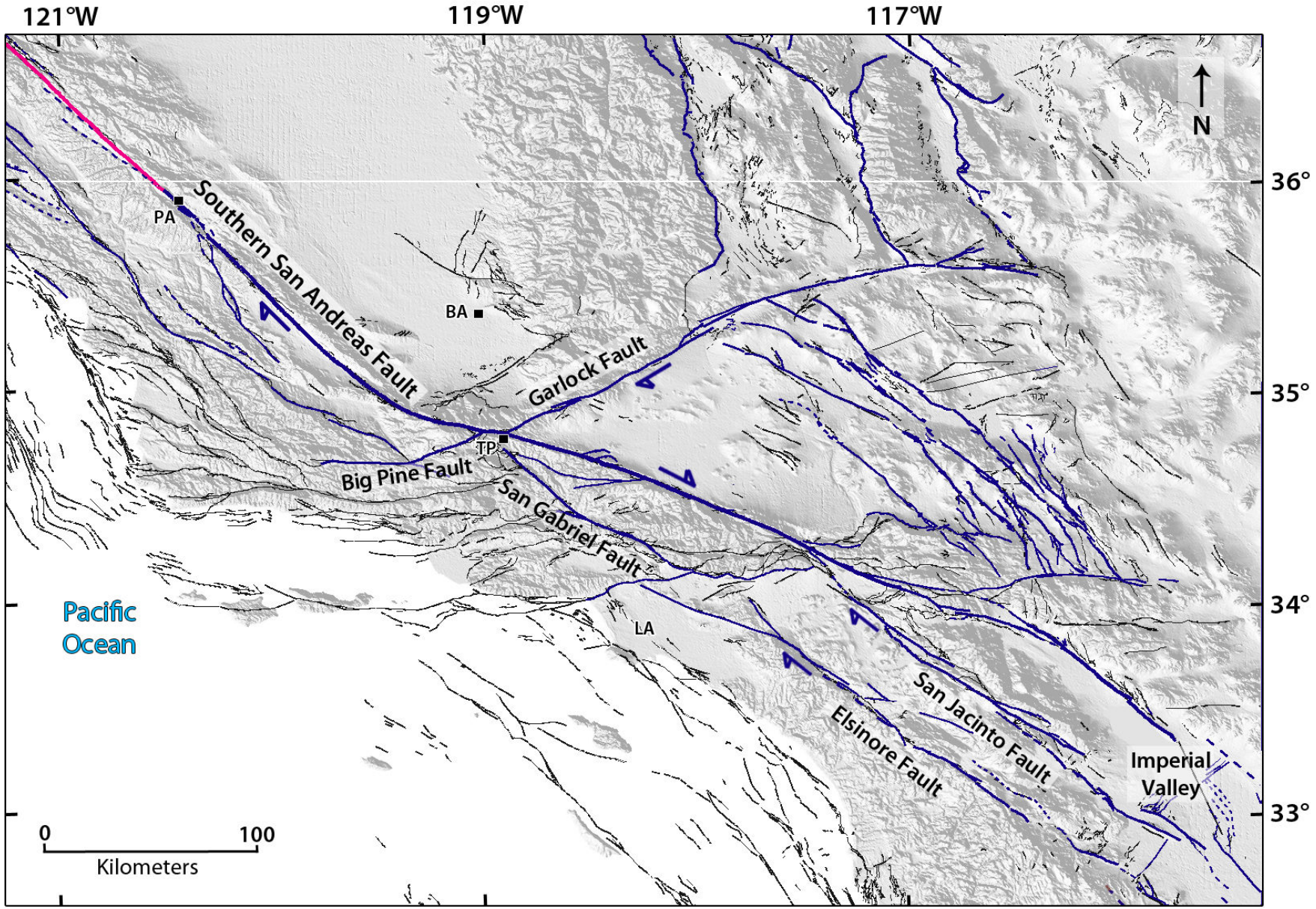


Fig. 128: (a)Map of long-term faluts in southern California (same caption as in Fig. 126. LA: Los Angeles ; PA: Parkfield; TP : Tejon Pass ; BA : Bakersfield.

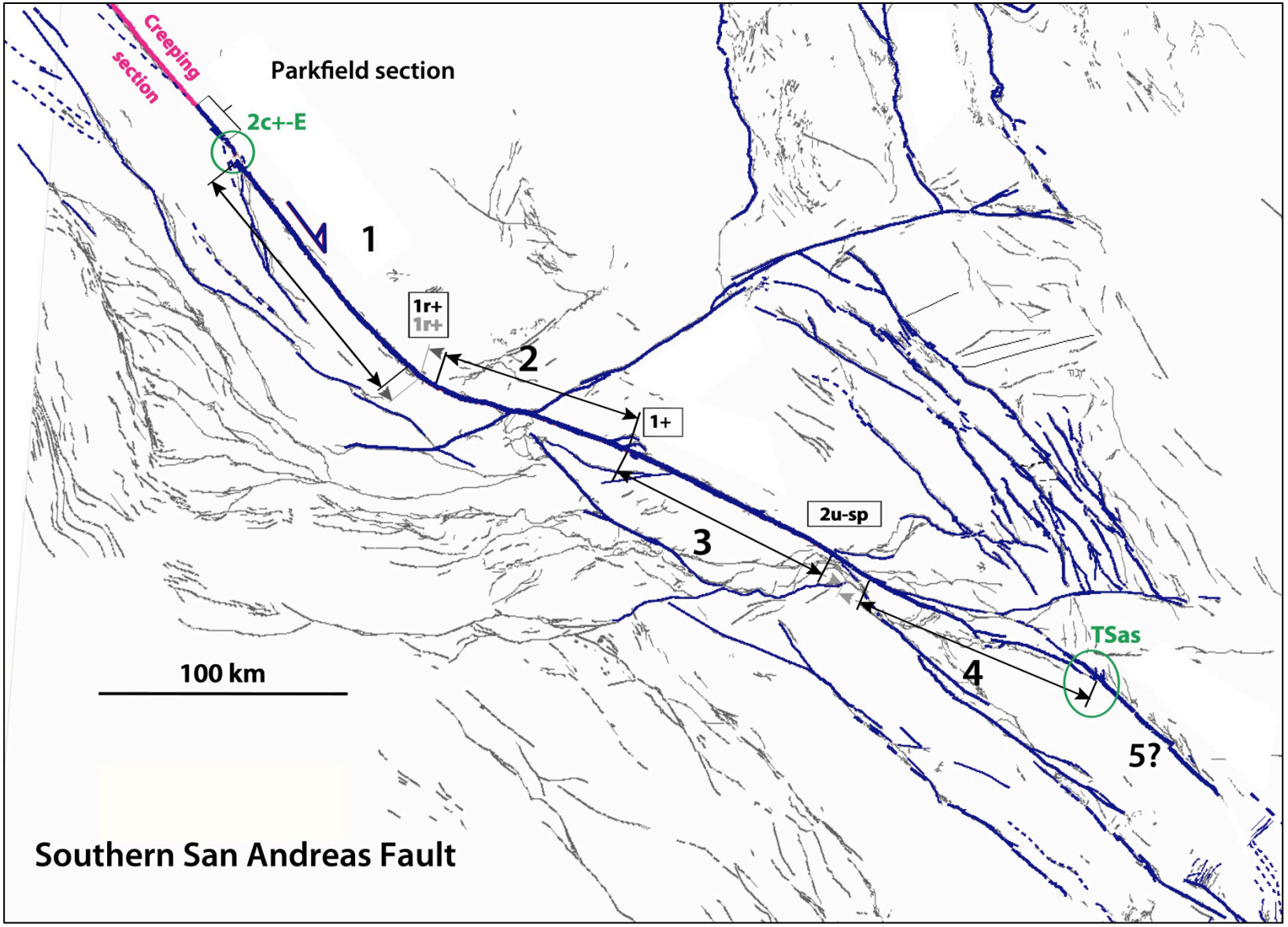


Fig.128:(b) Same active fault map as in Fig.128 (a), but with focus on the major segments of the southern San Andreas fault. The segments are numbered from NW to SE and indicated by black arrows parallel to their mean strike. The grey prolongation of the arrows indicates the uncertainties on the segment lengths. The nature of the inter-segment zones is indicated in letters within boxes explained in Table 6. The nature of the fault tips is indicated in green (Table 6)

1906 Coseismic rupture

Surface trace and location on long-term San Andreas Fault :

- The 1906 surface rupture is fairly clear on Google Earth images. The surface trace of the earthquake has been precisely mapped, and the displacements measured (See below), both on the field and from triangulation (Lawson 1908; Thatcher et al., 1997).
- Surface rupture of 450-470 km long.
- The EQ broke entirely the Northern San Andreas Fault (major segments 1, 2, 3, 4, 5; See Fig.127a & b).
- It initiated close to the intersegment zone between major segments 3 and 4 (Bolt, 1968) and propagated bilaterally.
- In the south, the rupture terminated at the intersection with both the Hayward-Calaveras Fault zone and the creeping section of the SA Fault. In the north, rupture traces were observed at Shelter Cove (Fig.127a, Lawson 1908), located at the northern tip of major segment 1, what shows that the rupture terminated at the northern tip of major segment 1.

→ The 1906 San Francisco EQ broke entirely the Northern San Andreas Fault, and hence broke its 5 major segments.

Coseismic displacements measured at surface (Fig.129) :

- *From Field measurements*: Maximum lateral slip of ~ 6 m observed near San Francisco, and hence on major segment 3 (Lawson, 1908). However, coseismic slip could not be observed in the northern part of the rupture, mainly offshore, so that it is ignored whether slip was greater in the north.
- Using triangulation networks, Thatcher et al. (1997) inferred that the maximum lateral slip actually occurred at the northern end of major segment 1 (close to Shelter Cove) and was at most ~8,6 m. The amount of slip is not well constrained however.
- The combination of measured offsets and inferred slip suggests that the coseismic slip-length profile is fairly triangular and asymmetric, with maximum slip deported in the north and slip decreasing fairly linearly toward the south of the rupture. Slip gradients are suggested, that more or less coincide with the major inter-segments along the Northern San Andreas Fault.

→ The San Francisco EQ produced a maximum lateral slip of 6-8 m likely at the northern end of the northernmost major segment 1 (off-shore), which is the most mature segment of the Northern San Andreas Fault.

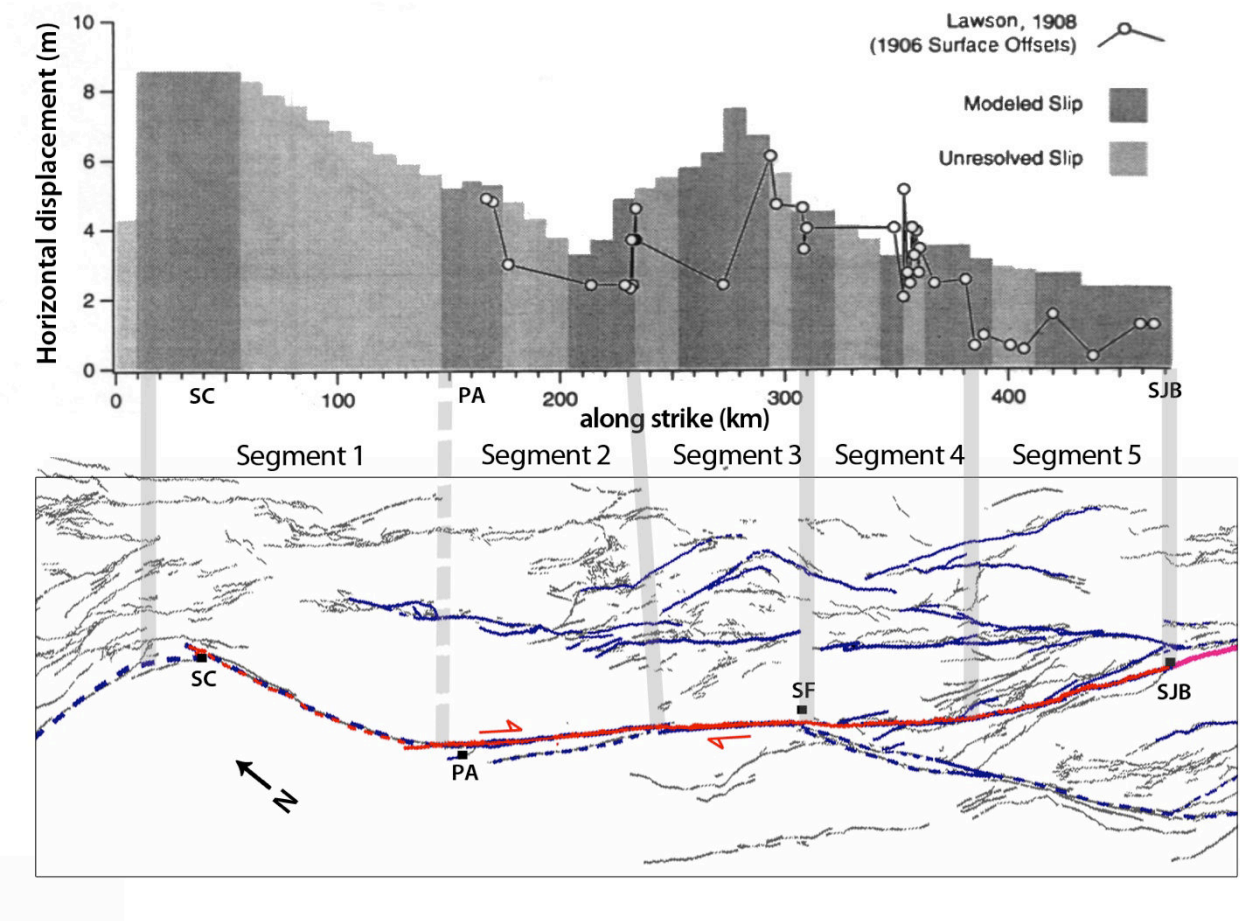


Fig.129: Coseismic displacements measured (Lawson, 1908) and modeled at surface (from Thatcher et al., 1997) along the 1906 surface rupture (in red). Grey bars correspond to the major intersegments highlighted in our mapping.. SC : Shelter Cove ; PA : Point Arena ; SJB : San Juan Bautista.

Other source parameters

Mainshock: 1906/04/18; Lat : 37.67°; Lon : -122.43° (Bolt 1968)

Seismic moment of ~4e20 Nm (Thatcher 1975), estimated from long period seismic surface waves (seismograms published in Lawson, 1908).

Other information:

- The 1857 Fort Tejon and the 1906 San Francisco earthquakes are the two largest known events on the San Andreas Fault, and both combined to break the fault almost entirely (rupture of the southern and of the northern sections of the San Andreas Fault, respectively).

- Post seismic deformation was observed over 30 years after the San Francisco earthquake at Point Arena (inter-segment zone between major segments 1 and 2; Fig.129) and on major segment 2 (Thatcher 1975; Kenner and Segall 2000).
- In 1989, the Mw 6.9 Loma Prieta earthquake broke the major segment 5 of the Northern San Andreas Fault. Major segment 5 is the major segment, which slipped less in the 1906 event.

Parameters retained to describe the 1906 San Francisco event (Table 3):

Mw ~7.7; M0 ~ 4e20 Nm; L ~ 470 km; Dmax surface: 6-8 m ;

W and the depth of the hypocenter are unknown. However, the seismogenic crust in Southern California is ~ 15 km thick (Nazareth and Hauksson 2004).

Number of major segments broken on the Northern San Andreas Fault: 5.

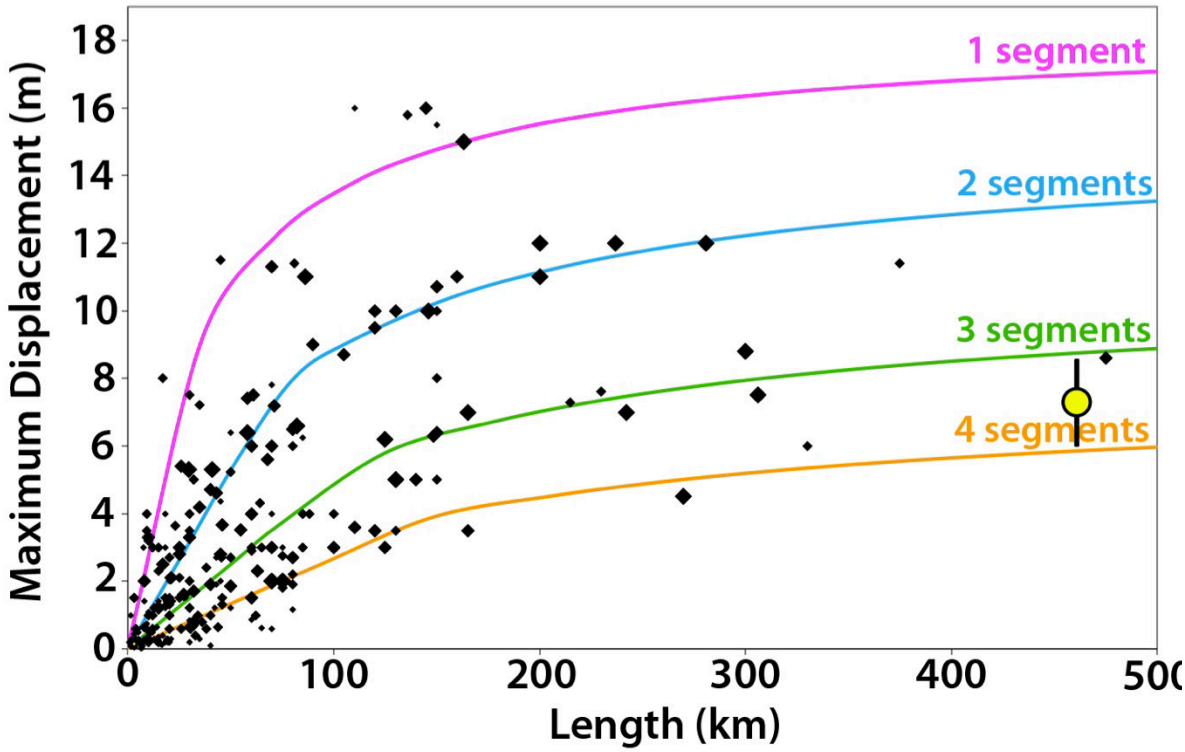


Fig.130: Earthquake displacement-length data measured at surface for 260 historical large continental earthquakes (Mw≥6). The 4 curves indicate the number of major long-term fault segments to have been broken by the earthquakes (modified from Manighetti et al., 2007 and Chapter IV). Yellow dot shows the 1906 San Francisco earthquake surface slip length data.

The surface slip-length data of the San Francisco earthquake fall between the third and the fourth functions (green and orange curves, respectively; Fig.130) of the Dmax-L scaling plot. The slip is not well constrained however. Therefore, we can only say that the slip-length data are compatible with the rupture of all major segments of the long-term Northern San Andreas Fault.

References

Atwater, T. (1970) Implications of Plate Tectonics for the Cenozoic Tectonic Evolution of Western North America *Geological Society of America Bulletin,* **81**, 3513-3536, doi:10.1130/0016-7606(1970)81[3513:IOPTFT]2.0.CO;2

Bolt, B. A. (1968). The focus of the 1906 California earthquake, *Bull. Seism. Soc. Am*. **58**, 457-471.

Clarke, S. E. Jr. & Nilsen, T. H. (1973). Displacement of Eocene strata and Implications for the History of Offset Along the San Andreas Fault, Central and Northern California, *in* Kovach, R. L. ed, Proceedings of the Conference on Tectonic Problems of the San Andreas Fault System. *Stanford University Press,* 494 p.

Hill, M. L. & T. W. Dibblee, E. Jr. (1953). San Andreas, Garlock and Big Pine faults, California, a study of the character, history and tectonic significance of their displacements. *Geol. Soc. Am. Bull.* **64**, 4, 443-458, doi:10.1130/00167606(1953)64[443:SAGABP]2.0.CO;2

Kenner, S. J., & P. Segall (2000), Postseismic deformation following the 1906 San Francisco earthquake, *J. Geophys. Res*., **105**(B6), 13195–13209, doi:10.1029/2000JB900076.

Lawson, A. C. -Chairman- (1908) The California Earthquake of April 18, 1906, Report of the State Earthquake Investigation Commission vol. I & II, *Carnegie Inst. of Washington*, Washington, D.C.

Manighetti, I., M. Campillo, S. Bouley, and F. Cotton (2007), Earthquake scaling, fault segmentation, and structural maturity, *Earth Planet. Sci. Lett*., **253**, 429-438, doi:10.1016/j.epsl.2006.11.004

Meade, B. J., & B. H. Hager (2005), Block models of crustal motion in southern California constrained by GPS measurements, J. Geophys. Res., 110, B03403, doi:10.1029/2004JB003209.

Nazareth, J. J., & Hauksson, E. (2004). The seismogenic thickness of the southern California crust. *Bulletin of the Seismological Society of America*, **94**(3), 940-960.

Perkins, J. A., Sims, J. D. & Sturgess, S. S. (1989). Late Holocene Movement Along the San Andreas Fault at Melendy Ranch : Implications for the Distribution of Fault Slip in Central California. *J. of Geoph. Res.,* **94,** 10,217-10,230.

Powell, R.E., & Weldon, R.J., II (1992), Evolution of the San Andreas Fault: *Annual Review of Earth and Planetary Sciences*, **20**, 431–468, doi:10.1146/annurev.ea.20.050192.002243.

Scholz, C. H., M. Wyss, and S. W. Smith (1969), Seismic and aseismic slip on the San Andreas Fault, *J. Geophys. Res*., **74**(8), 2049–2069, doi:10.1029/JB074i008p02049.

Segall, P. & Harris, R. (1986). Slip Deficit on the San Andreas Fault at Parkfield, California, as Revealed by Inversion of Geodetic Data. *Science,* New Series, **233,** 4771, 1409-1413.

Sims, J. (1993). Chronology of displacement on the San Andreas Fault in central California : Evidence from reversed positions of exotic rock bodies near Parkfield, California, *in* Powell, R. E., Weldon, R. J., Matti, J. C. eds, The San Andreas Fault System : Displacement, Palinspastic Reconstruction and Geologic Evolution : Boulder, Colorado, *Geological Society of America Memoir* **178.**

van der Woerd, J., Y. Klinger, K. Sieh, P. Tapponnier, F. J. Ryerson, & A.-S. Mériaux (2006), Long-term slip rate of the southern San Andreas Fault from ^{10}Be-^{26}Al surface exposure dating of an offset alluvial fan, *J. Geophys. Res*., **111** B04407, doi:10.1029/2004JB003559

Wallace, R. E. (1970). Earthquake Reccurrence Intervals on the San Andreas Fault. *Geological Society of America Bulletin*, **81,** 2875-2890.

Weldon, R. J., & K. E. Sieh (1985), Holocene rate of slip and tentative recurrence interval for large earthquakes on the San Andreas Fault, Cajon Pass, southern California, *Geol. Soc. Am. Bull.,* **96**, 793–812.

Thatcher, W. (1975), Strain accumulation and release mechanism of the 1906 San Francisco Earthquake, *J. Geophys. Res*., **80**(35), 4862–4872, doi:10.1029/JB080i035p04862.

Thatcher, W., G. Marshall, & M. Lisowski (1997), Resolution of fault slip along the 470-km-long rupture of the great 1906 San Francisco earthquake and its implications*, J. Geophys. Res*., **102**(B3), 5353–5367, doi:10.1029/96JB03486.

Titus, S. J., M. Dyson, C. DeMets, B. Tikoff, F. Rolandone, & R. Bürgmann (2011). Geologic versus geodetic deformation adjacent to the San Andreas Fault, central California. *GSA Bulletin*, **123**, no. 5/6, 794–820; doi: 10.1130/B30150.1;

Tong, X., D. T. Sandwell, & B. Smith-Konter (2013). High-resolution interseismic velocity data along the San Andreas Fault from GPS and InSAR, *J. Geophys. Res*, **118**, doi:10.1029/2012JB009442.

2.17. Sichuan 2008

12/May/2008, China

Mw 7.9

Epicenter (USGS) : 30.99°N-103.36°E

Reverse fault and right-lateral strike-slip



Broken long-term fault

The EQ broke a part of the **Longmen Shan fault system,** which bounds to the east the high (elevation over 4500 m) Tibetan Plateau. Within that system, the EQ broke the Beichuan Fault and the Pengguan faults.

General characteristics from literature:

- Fairly linear, N50°E-trending fault system, about 400 km long between the Xianshuihe Fault in the southwest and the Qingchuan Fault in the northeast. Some authors include the western part of the Qingchuan Fault in the Longmen Shan system (i.e., the part south of the intersection with the Kunlun Fault), what gives it a length of ~600 km (Densmore et al., 2007).
- The Longmen Shan Fault system is primarily a thrust belt, that includes several sub-parallel, NE-trending trusts and folds, among which the Beichuan Fault and the Pengguan faults are major features. The Beichuan Fault has a composite motion, both right-lateral and reverse, whereas the Pengguan Fault is known as a pure thrust fault.
- The geometry at depth of the Longmen Shan fault system is not clearly known. The Beichuan Fault is taken to have a steep dip, on the order of 60-80° NW, whereas the Pengguan Fault would be shallower, with a mean dip of 25-40° NW (Liu-Zeng et al., 2009; Jia et al., 2010).
- The Longmen Shan Fault system would be inherited from the Triassic Indosinian orogeny and would have been reactivated ~ 12-5 Ma ago during the India-Asia collision (e.g. Burchfiel et al., 1995, Kirby et al., 2002).

- The Longmen Shan fault system would have accommodated 10-20 km of horizontal shortening since the Cenozoic (Burchfiel et al., 2008). If the fault system has accommodated entirely the shortening on planes dipping 45°NW on average, the total reverse vertical on-fault cumulative slip would be 14-28 km.
- Current horizontal compression rate across the Longmen Shan fault system: < 3 mm/yr (King et al., 1997; Chen et al., 2000, Shen et al., 2005, Gan et al., 2007; Burchfiel et al., 2008, Zhang et al., 2008). The current vertical slip rate on the fault system was estimated very low (< 1 mm/yr) before the Sichuan EQ occurred.
- Long-term slip rate: If the inferred cumulative on-fault slip has accrued in 5-12 Myr, the long-term vertical uplift might be 0.7-1.2 mm/yr considering a topographic relief of 4 km across the Longmen Shan and the 5-8 km of denudation above the Pengguan and Baoshan massifs (Kirby et al., 2002; Burchfiel et al., 2008). The vertical slip rate on each sub-parallel fault would thus be fairly low. Cenozoic slip rate < 1.1 mm/yr (thrusting) and <1.5 mm/yr (strike-slip) were estimated by Rongjun et al. (2007) based on deformed geomorphic markers across three main faults in the southern part of the Longmen Shan fault system (including Wenchuan, Beichuan and Pengguan faults).

→ The Longmen Shan fault system is a slow-moving fault system with an intermediate maturity (300<L<1000 km; I-Age > 10 Ma; MR ~1 mm/yr?; D_{Total} of a few 10 km).

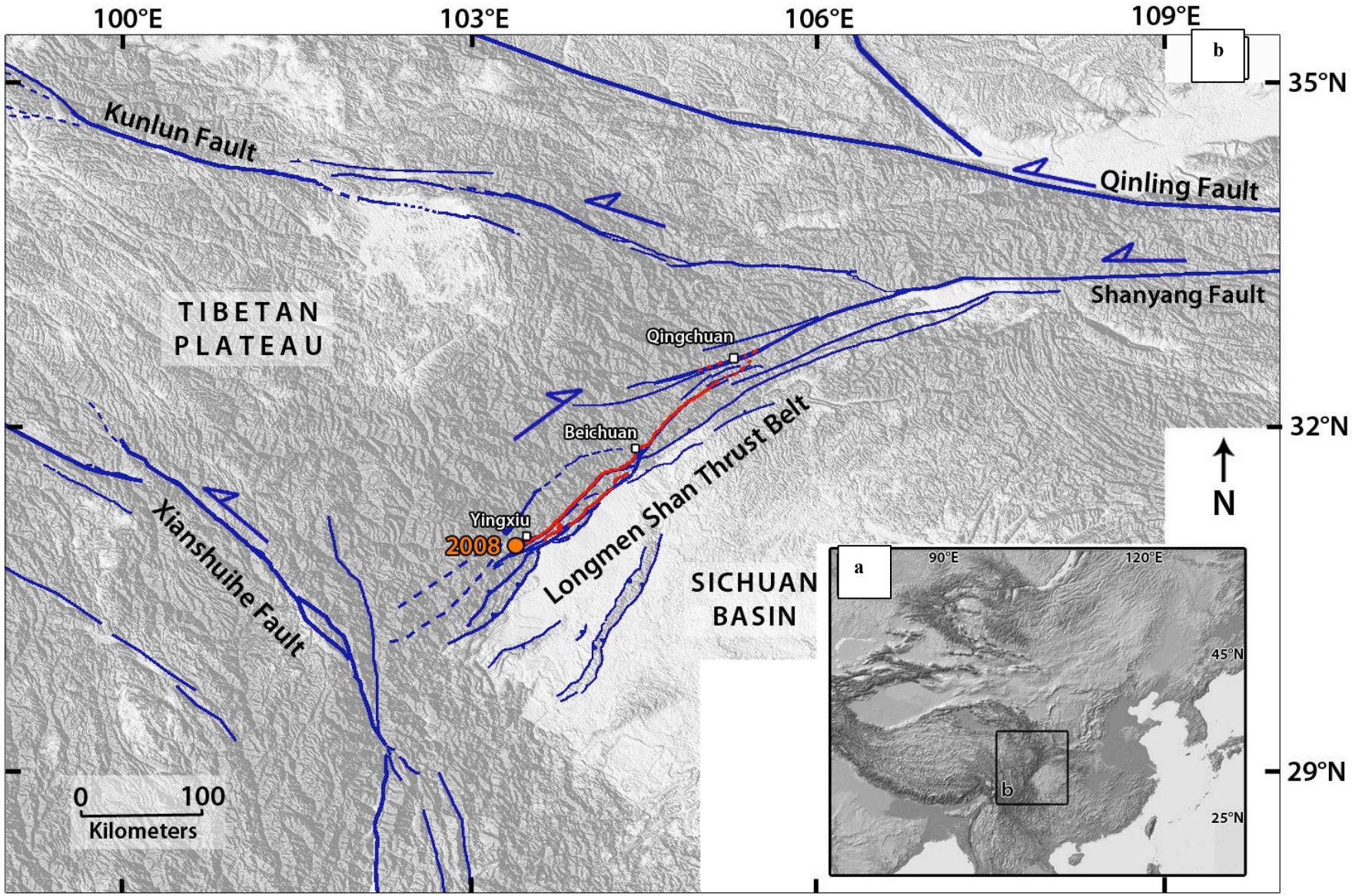


Fig.130: (a) General topographic map of the east Asia ; (b) Our map of the major active faults in eastern Tibet (in blue). In red is the surface rupture of the 2008 Sichuan earthquake (in red, from Liu-Zeng et al., 2009 ; Xu et al., 2009 ; Lin et al., 2009, 2010, 2012). The orange circle shows the 2008 Sichuan epicenter

Architecture and major lateral segmentation, from our mapping (Fig.131):

- Mapping done from Google Earth, Landsat and SRTM data combined with dense literature information.
- Long-term fault traces fairly well expressed in surface morphology and topography.
- The Longmen Shan Fault system is surrounded –and likely genetically related, with some of the largest strike-slip faults of Asia: to the SW, the Longmen Shan fault system is limited by the giant Xianshuihe left-lateral fault. The two faults are strongly oblique, differing in strike by ~85°. To the NE, the Longmen Shan Fault system is limited by the Qingchuan right lateral fault and the Shanyang left-lateral fault, which gives pace further west to the 1600 km long left-lateral Kunlun Fault. The Longmen Shan and Shanyang are oblique to each other, differing in strike by ~40°. Further north, runs the large left-lateral Qin Ling Fault, parallel to the Shanyang Fault (Fig.131). All these left-lateral giant faults have been propagating westwards over geological time, as attested by the their overall geometry, in particular the architecture of the splaying fault networks at their western tips. The antithetic Longmen Shan Fault system has developed in between the three westward propagating Xianshuihe, Qingchuan and Shanyang faults, and hence in a limited space of ~400 km length in the NE direction.
- The Longmen Shan Fault system includes multiple faults (Fig.131c). The longest and hence principal fault is the Beichuan Fault, which forms the central feature of the system. The Beichuan Fault has a ~260 km long linear and narrow trace, that reveals its dominant lateral motion. The Beichuan Fault is flanked to the north by a sub-parallel, ~230 km long fault – the Wenchuan Fault, that might also be dominantly lateral, but its trace is much less clear in the morphology, suggesting that the Wenchuan Fault has been less active recently than the Beichuan Fault. Apart these two strike-slip faults, the recent deformation in the area is distributed on numerous active reverse faults and folds, most are developed south and north of the Beichuan Fault. The Pengguan Fault is one of those reverse faults, which has developed ~10 km south of the Beichuan Fault surface trace, over ~100 km paralleling the southern half of the Beichuan Fault. The narrow spacing of the Beichuan and Pengguan faults suggests they are connected at depth.
- To the SW, the Beichuan Fault terminates into a complex zone of folding. To the NE, the Beichuan Fault ends by splaying into several small oblique branches, which form a relay with the oblique (~20° difference) Qingchuan Fault further north. The splay geometry of the Beichuan Fault northern termination suggests that the Beichuan Fault is in the process of

propagating northeastward, in a likely attempt to connect with the westward propagating Qingchuan Fault.

- The Beichuan Fault is divided into 2 major fairly collinear segments (See Fig.131c where they are numbered). The types and sizes of the major segments and inter-segments are described in Table 6.
- These 2 major segments have a similar length of 120-150 km (length measured along the linear trace of each segment; Fig.131c).
- Segment 1 has a fairly linear trace and is hardly segmented at smaller scales. Segment 2 has a more rounded trace, yet is also hardly segmented at lower scales. Segment 1 terminates in the south where it intersects both the Pengguan and the Wenchuan faults. As said earlier, segment 2 ends in the north by splaying into several oblique branches that form a relay with the Qingchuan Fault. Segments 1 and 2 are separated by a curved step-over of type 2_O and of size 19 km. The step-over is also a zone where several thrusts and folds (in the east) intersect the trace of major segment 2.
- The Pengguan Fault has a fairly linear trace over ~100 km. It connects at both tips to the Beichuan Fault, with its surface trace bending toward the trace of the Beichuan Fault.

→ **The principal Beichuan Fault is divided laterally into 2 major fairly collinear segments. It is also connected to the closely-spaced, sub-parallel Pengguan Fault. The Beichuan Fault is propagating northeastward, and thus, its major segments likely become younger towards the NE. The Beichuan Fault is in the process of connecting with the Qingchuan Fault further north.**

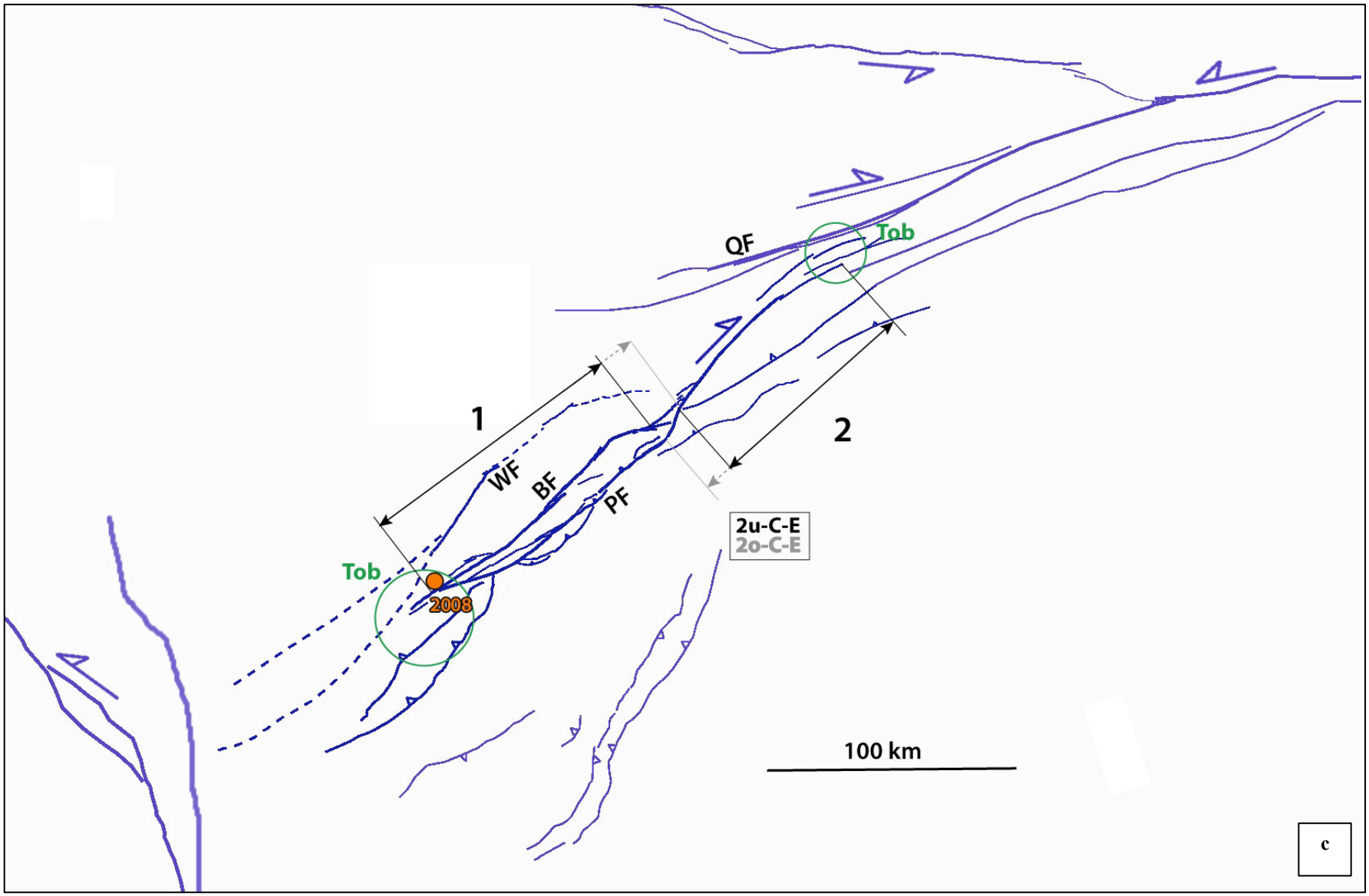


Fig.131: (c) Focus on the major segments of the Beichuan fault. The segments are numbered from SW to NE and indicated by black arrows parallel to their mean strike. The grey prolongation of the arrows indicates the uncertainties on the segment lengths.. The nature of the inter-segment zones is indicated in letters within boxes explained in Table 6. The nature of the fault tips is indicated in green (Table 6). BF : Beichuan Fault ; PF : Pengguan Fault ; WF : Wenchuan Fault ; QF : Qingchuan Fault.

2008 Coseismic rupture

Surface trace and location on long-term Beichuan and Pengguan Faults :

- The 2008 surface rupture is not clear on Google Earth images. Fortunately, the surface trace of the earthquake has been precisely mapped on the field (Liu Zeng et al., 2009; Xu et al., 2009; Zhang et al., 2010; Lin et al., 2009, 2010, 2012) and from radar imagery (Hashimoto et al., 2009; Kobayashi et al., 2009; Shen et al., 2009; Chini et al., 2010; Feng et al., 2010; deMichele et al., 2010a, 2010b; Tong et al., 2010; Wang et al., 2011; Zhang et al., 2011; Fielding et al., 2013).
- Surface rupture estimated between 240 (Liu-Zeng et al., 2009; Xu et al., 2009; Zhang et al., 2010) and 285 km long (Lin et al., 2009, 2010, 2012). The difference arises from a single author (Lin et al., 2009, 2010, 2012) having reported surface traces in the eastern splaying zone and on a small section of the Qingchuan Fault (dotted red line Fig.131b). But the existence of these traces is debated since no other author reported them. Radar imagery (e.g. Kobayashi et al., 2009) suggests that the surface rupture propagated to the NE until the intersection between the Beichuan and the Qingchuan Fault.
- The earthquake initiated at a depth of ~13 km (Global CMT) at the western tip of the major segment 1 of the Beichuan Fault.
- The rupture then propagated northeastward and broke the two major segments of the Beichuan Fault, along with the sub-parallel Pengguan Fault. The rupture ended at the northeast termination of major segment 2.

→ The 2008 EQ broke the two major segments of the Beichuan Fault. It also broke the sub-parallel Pengguan Fault on its entire length. Since the Beichuan Fault has likely been propagating northeastward over geological time, the westernmost segment 1 where the EQ nucleated is likely the most mature part of the broken fault.

Coseismic displacements measured at surface (Fig.132) :

- *From Field measurements*: The complete slip profile could be measured on the field. The two slip components, vertical and lateral, were measured. A vertical slip component was measured along the entire length of the rupture, both on the Beichuan Fault where it reaches a maximum of 6-6.5 m, and on the Pengguan Fault where it reaches a maximum of ~3.5 m (e.g. Xu et al., 2009; Lin et al., 2009, 2012). Liu Zeng et al. (2009) and Zhang et al. (2010) reported a vertical slip of 8-11 m at Beichuan. This measurement is local and departing from

the other slip measures, and hence might well represent a gravity sliding and not a tectonic slip on the main fault (Aiming Lin, personnal communication, 2013). Moreover this large offset is not observed on geodetic data (e.g. deMichele et al., 2010a).

- A lateral dextral slip was also measured, yet only on the Beichuan Fault where it reaches a maximum of ~ 4 m. Note that a sinistral slip of ~4 m was also measured locally on a small part of the rupture curving at right angle to the main fault trace. This local slip does not represent the fault displacement and hence is ignored.
- The Pengguan Fault only slipped vertically, and its slip function has an overall triangular and asymmetric shape, with maximum slip deported toward the NE tip of the rupture.
- To Beichuan Fault had a composite slip, both reverse and dextral, and hence the actual slip is a combination of both components (Fig.132 & 133)
- As said earlier, the fault dips are not known with precision. Yet, the Beichuan Fault plane is supposed to be steep, dipping by 60-80°, whereas the Pengguan has a shallower plane, dipping by 25-40°. Taking these dip ranges into account, we estimate in Fig.132 the vertical on-fault slips. As the Beichuan and the Pengguan Fault faults slipped vertically together, the total vertical slip actually produced is the sum of the contributions from the two faults. Finally, the total on-fault coseismic slip is the combination of vertical and lateral slips (Fig.133e). We infer that the 2008 Sichuan EQ produced a composite slip at surface whose maximum amplitude was in the range 10-14 m. The slip function is triangular and asymmetric overall, with maximum slip deported toward the SE end of the rupture. According to this overall shape (Fig.133e), the maximum slip at surface is more likely in the range 10-12 m and occurred ~25 km away from the EQ epicenter, on major segment 1.
- *Form GPS measurements:* Maximum lateral slip of ~2.4 m (Zhang, 2008; Feng et al., 2010) measured at the station close to Beichuan
- *From InSAR data and modeling*: Maximum vertical displacement estimated of ~5 m near Yingxiu and Beichuan (de Michele et al., 2010a). Note that a proper estimation of the surface slip close to the fault was difficult for the 2008 Sichuan earthquake: the high gradient of vertical slip observed along the entire rupture disturbs the pixel correlation between the interferogramms.

→ Maximum composite slip at surface in the range 10-12 m. The vertical component dominates the maximum slip. The maximum slip occurred at the southwestern tip of the major segment 1 of the Beichuan Fault, that is on the most mature section of the broken fault. The slip profile was triangular and asymmetric overall.

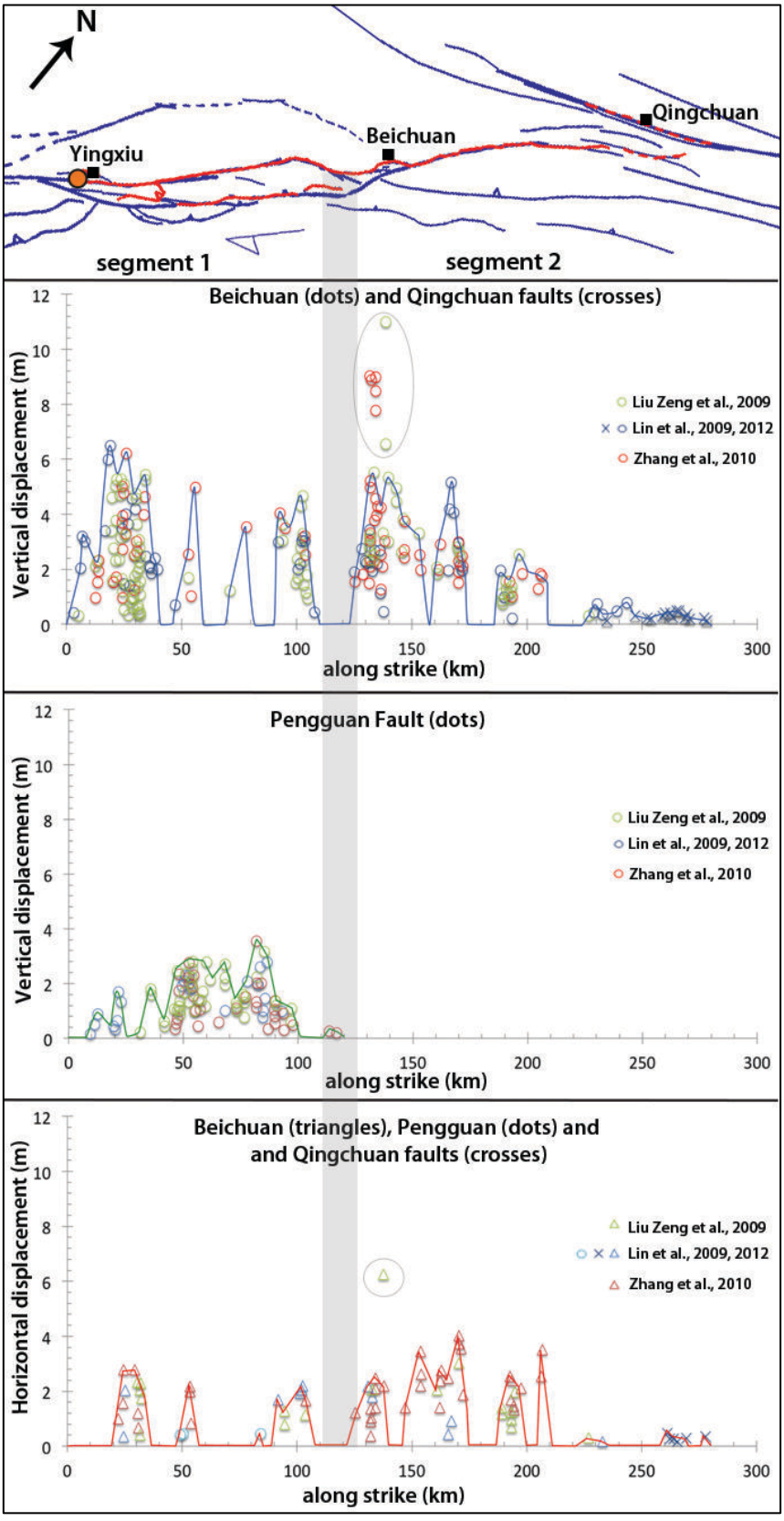


Fig.132: Surface displacements measured on the field after the 2008 Sichuan earthquake. Blue and red curves show respectively the vertical and lateral maximum slip profile on the Beichuan Fault. The green curve is the vertical maximum slip profiles along the Pengguan Fault. Grey circles highlight surface measurements that are not considered (see text for details). Grey bar shows the intersegment zone of the Beichuan Fault.

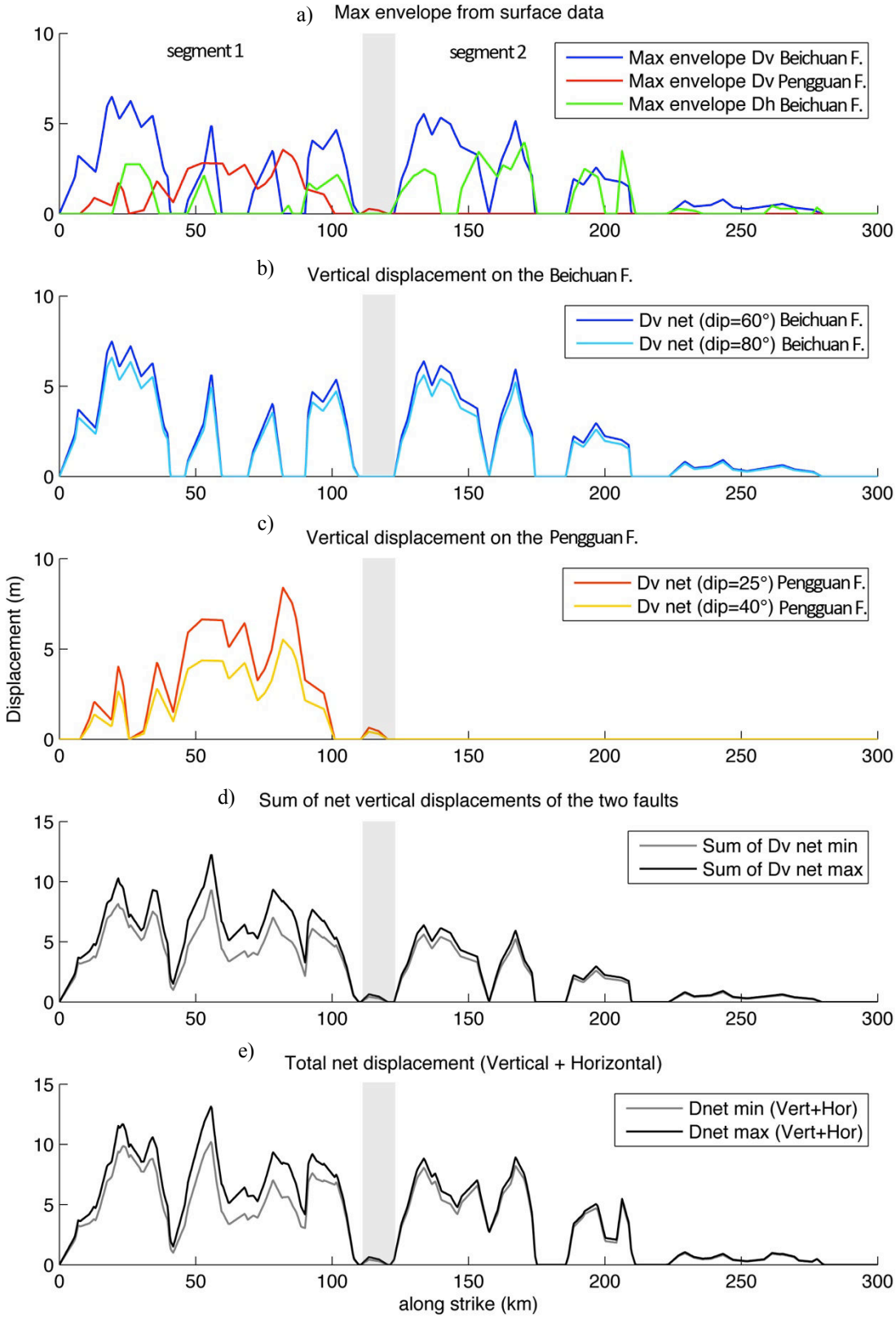


Fig.133: Maximum slip profile measured at surface (from Fig.132) and calculations of the range of total net slip on faults using various dips inferred from literature (Liu-Zeng et al., 2009 ; Jia et al., 2010). Dv : Vertical displacement ; Dh : Horizontal displacement ; Dnet : Net combined displacement on fault. Grey bar shows the intersegment zone of the Beichuan Fault.

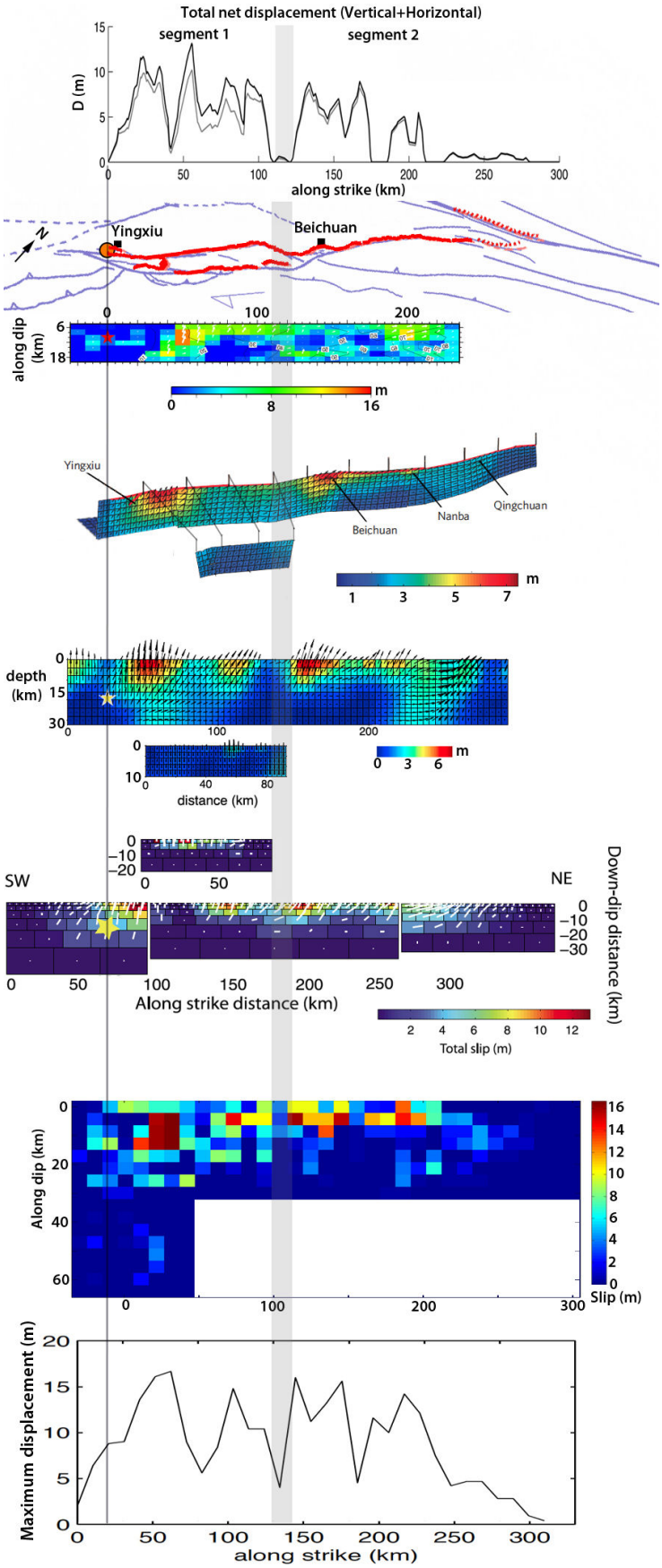
Source inversion models and slip distribution at depth :

- We compare five source inversion models that have been published on the 2008 Sichuan earthquake (Fig.134); the grid data are available for two of them (Table 2)
- The models differ principally from the data they used and from the fault plane geometry:
    - Fielding et al. (2013): GPS, InSAR and teleseismic data. The model considers 3 fault planes for the main fault (1 for segment 1 of the Beichuan Fault; 1 for segment 2 of the Beichuan Fault; 1 for Beichuan-Qingchuan junction) + 2 fault planes for the Pengguan Fault and the deep part of segment 1 (dip=0° between 30 and 64 km).
    - Tong et al. (2010): GPS and InSAR data. The model considers 3 fault planes for the main fault (2 for segment 1 of the Beichuan Fault; 1 for segment 2 of the Beichuan Fault) + 1 fault plane for the Pengguan Fault
    - Feng et al. (2010): GPS and InSAR data. The model considers 3 fault planes for the main fault (1 for segment 1 of the Beichuan Fault; 1 for segment 2 of the Beichuan Fault; 1 for Beichuan-Qingchuan junction) + 2 fault planes for the Pengguan Fault and the deep part of segment 1.
    - Shen et al. (2009): GPS and InSAR data. The model considers 11 fault planes for the main fault (5 for segment 1 of the Beichuan Fault; 6 for segment 2 of the Beichuan; 1 for Beichuan-Qingchuan junction) + 3 fault planes for the Pengguan Fault
    - Preliminary model of Caltech: Teleseismic data. The model considers 1 single fault plane.

→ Most source models (including others using geodetic data, as Zhang et al., 2011 ; Wang et al., 2011) evidence 4-5 slip patches on a ~300 km long and 25-30 km wide fault plane, among which two patches are largest in the vicinity of the Yingxiu and Beichuan towns. The sites of largest slip thus fairly well coincide with the zones of maximum slip at surface. The models of Shen et al. (2009) and Feng et al. (2010) produce a maximum slip at depth, which is markedly lower than the slip measured at the ground surface. Therefore these models do not appropriately describe the 2008 EQ. We suggest that the source model of Fielding et al. (2013) might be the most robust for it combines the larger amount of complementary data (GPS fom Wang et al., 2011), InSAR and teleseismic) while it produces a slip distribution and amplitude which well agree with the surface observations. The model of Fielding et al. (2013) show two main slip zones that well coincide with the rupture of major segments 1 and 2. Each

of these slip zones is divided into two smaller slip patches, suggesting a smaller scale segmentation (that we did not study).

→ The source inversion models suggest: L 290-300 km, Dmax at depth 13-16 m, 2 largest slip patches.



Net coseismic displacement calculated at surface (See Fig.133)

Surface rupture mapped in the field (in red, from *Liu-Zeng et al., 2009 ; Xu et al., 2009 ; Lin et al., 2009, 2012)*

Preliminary model (*Caltech website)*
Data : Teleseismic
L 260 km ; W 37 km ; Dmax 14 m

Shen et al., 2009
Data : GPS + InSAR
L 290 km ; W 28 km (56 km with horizontal deep part) ; Dmax = 5.8 m

Feng et al., 2010
Data : GPS + InSAR
L 300 km ; W 32 km ; Dmax = 6.7 m

Tong et al., 2010
Data : GPS + InSAR (+ Surface data)
L 304 km ; W 25 km ; Dmax = 13 m

Fielding et al., 2013
Data : GPS + InSAR + Teleseismic
L ≈ 300 km ; W = 28 km (64 km with horizontal deep part) ; Dmax = 16 m

Maximum slip profile inferred at depth from the source model of Fielding et al. (2013).

Fig.134: Comparison between different inversion models published on the 2008 Sichuan earthquake. Dark grey line represents hypocenter location which is used as reference for each model. Models are at the same scale along strike. Grey area shows the intersegment zone

Other source parameters :

SCARDEC
Mainshock: 2008/05/12 at 06h28min00s GMT
Lat = 31.084° Lon = 103.267° (NEIC)
Mw 8.1; M0 = 1.54e21 Nm;
Z = 0-15 km; Duration: ~102s (Fig.135)
Strike, dip, rake: (227°, 21°, 142°)/ (354°, 77°, 73°)

Global CMT
Mainshock: 2012/05/12 at6h28min40s GMT;
Lat = 31.44° Lon= 04.10°
Mw 7.9; M0 = 8.97e20 Nm; Z = 12.8 km;
Half-duration: 21.8s
Strike, dip, slip :(231°, 35°, 138°)/ (357°, 68°, 63°)

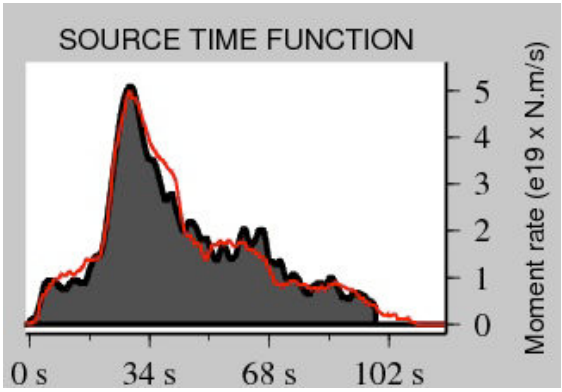


Fig.135: Source Time Function calculated with the SCARDEC method (Vallée et al., 2011). In grey : best STF ; in red : mean STF

The EQ duration much differs between the two methods. However the rupture duration calculated from source models (e.g. Fielding et al. (2013); ~110s) is in better agreement with the SCARDEC method.

- Moment magnitude and seismic moment range 7.9-8.1 and ~9e20-1.5e21 Nm, respectively.
- Two peaks are distinguished in the mean Source Time Function (Fig.135), suggesting the rupture of two sections of the fault: The EQ increased rapidly in energy, releasing a large peak at ~30 s. Then the energy decreased gently until the end of the earthquake, yet with a lower peak of moment released between 50-60s.

→ The source time function data suggest that two fault sections broke during the 2008 Sichuan earthquake.

Other information:

- The 2008 Sichuan earthquake is one of the large earthquakes that occurred in North Tibet in the last 20 years (e.g. Manyi 1997, Kunlun 2001, Yushu 2010, Lushan 2013).
- Aftershocks extend over 300 km and are localized at a depth between 10 and 20 km, which coincides with the location of the main detachment supposed to be rooted in the middle crust (Jia et al., 2010)

- The Lushan earthquake (Mw 6.6) occurred the 20th April 2013 south of the 2008 epicenter. It seems to have broken one secondary reverse fault south of major segment 1 of the Beichuan Fault.

Parameters retained to describe the 2008 Sichuan earthquake (Tables 1 – 4):

Mw 7.9-8.1; M0 ~ 9e20-1.5e21 Nm; Lsurface 240-280 km ; L depth 290 km; W ~ 28 km ; Dmax surface 10-12 m ; Dmax depth 13-16 m; Duration ~ 100 s ; Hypocenter : Z ~ 13-15 km
Number of major segments broken on the Beichuan Fault: 2.

Both the surface and depth slip-length data of the 2008 Sichuan earthquake fall fairly well on the second curve of the scaling graph, in keeping with the rupture of 2 major segments on the Beichuan Fault (Fig.136 & 137).

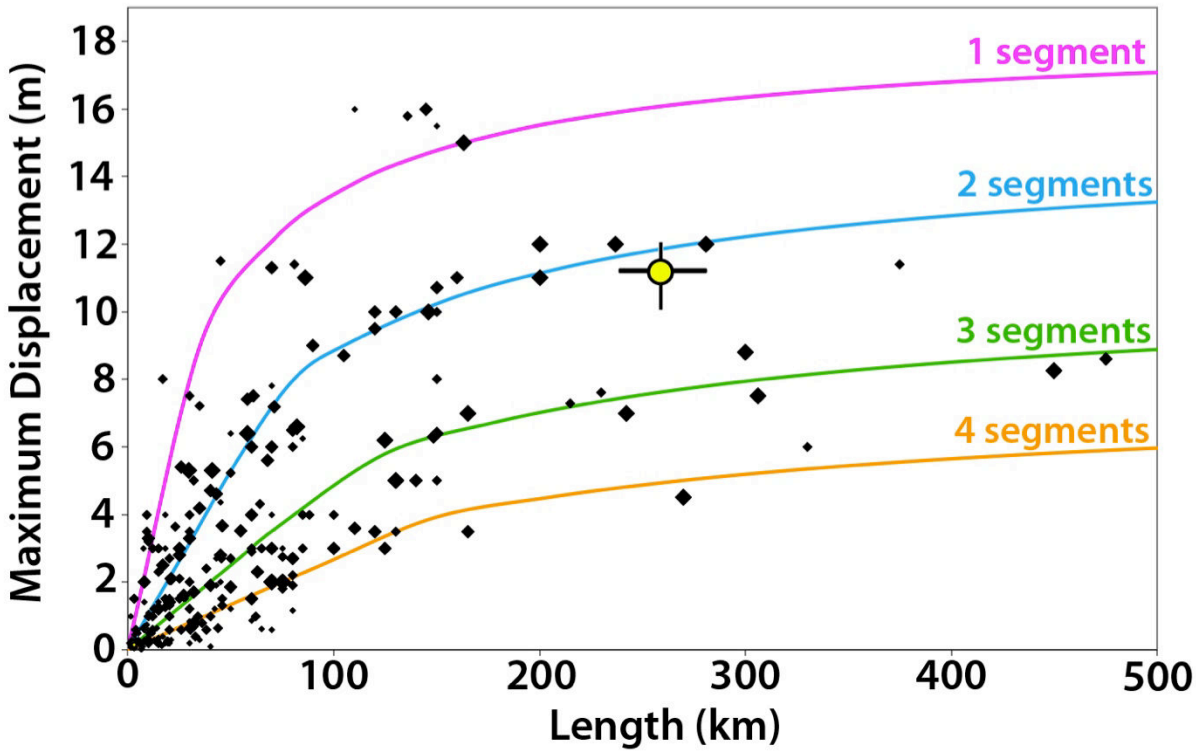


Fig.136: Earthquake displacement-length data measured at surface for 260 historical large continental earthquakes (Mw≥6). The 4 curves indicate the number of major long-term fault segments to have been broken by the earthquakes (modified from Manighetti et al., 2007 and Chapter IV). Yellow dot shows the 2008 Sichuan earthquake surface slip-length data

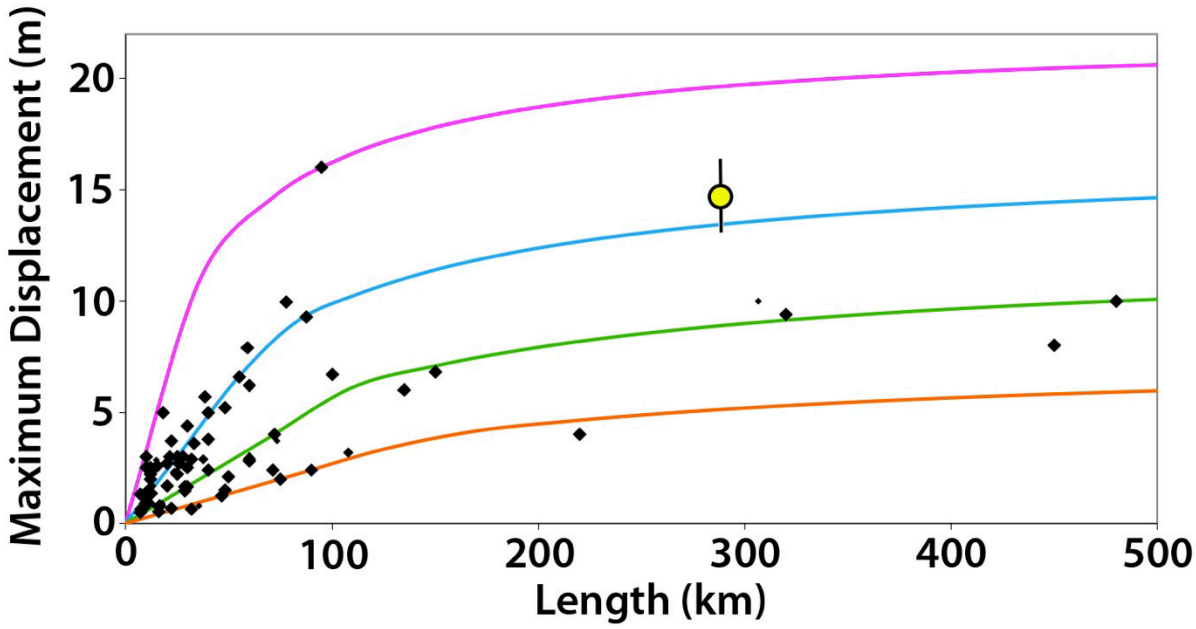


Fig.137: Earthquake displacement-length data inferred at depth for 90 historical large continental earthquakes (Mw≥6). The 4 curves indicate the number of major long-term fault segments to have been broken by the earthquakes (modified from Manighetti et al., 2007 and Chapter IV). Yellow dot show the Sichuan earthquake depth slip –length data.

References

Burchfiel, B.C., Chen, Z., Liu, Y. & Royden, L.H. (1995). Tectonics of the Longmen Shan and Adjacent regions, central China. *Int. Geol. Rev.* 37, 661–735.

Burchfiel, B.C., Royden, L.H., van der Hilst, R., Hager, B.H., Chen, Z., King, R.W., Li, C., Lü, J., Yao, H. & Kirby, E. (2008). A geological and geophysical context for the Wenchuan earthquake of 12 May 2008, Sichuan, People's Republic of China, *GSA Today*, 18, 4-11.

Chen, Z., Burchfiel, B.C., Liu, Y., King, R.W., Royden, L.H., Tang, W., Wang, E., Zhao, J. & Zhang, X. (2000). Global Positioning System measurements from eastern Tibet and their implications for India/Eurasia intercontinental deformation, J. *Geophys. Res.*, 105, 16215-16227.

Chini, M., Atzori, S., Trasatti, E., Bignami, C., Kyriakopoulos, C., Tolomei, C., & Stramondo, S. (2010). The May 12, 2008,(Mw 7.9) Sichuan earthquake (China): multiframe ALOS-PALSAR DInSAR analysis of coseismic deformation. *Geoscience and Remote Sensing Letters, IEEE*, **7**(2), 266-270.

De Michele, M., Raucoules, D., De Sigoyer, J., Pubellier, M. & Chamot-Rooke, N. (2010a). Three-dimensional surface displacement of the 2008 May 12 Sichuan earthquake (China) derived from Synthetic Aperture Radar: evidence for rupture on a blind thrust, *Geophys. J. Int.,* 183, 1097-1103.

De Michele, M., Raucoules, D., Lasserre, C., Pathier, E., Klinger, Y., Van Der Woerd, J., ... & Xu, X. (2010b). The Mw 7.9, 12 May 2008 Sichuan earthquake rupture measured by sub-pixel correlation of ALOS PALSAR amplitude images. *Earth Planets and Space*, **62**(11), 875.

Densmore, A.L., Ellis, M.A., Li, Y., Zhou, R., Hancock, G.S. & Richardson, N. (2007). Active tectonics of the Beichuan and Pengguan Faults at the eastern margin of the Tibetan Plateau, *Tectonics*, 26, TC4005, doi:4010.1029/2006TC001987.

Feng, G., E. A. Hetland, X. Ding, Z. Li, and L. Zhang (2010). Coseismic fault slip of the 2008 Mw 7.9 Wenchuan earthquake estimated from InSAR and GPS measurements, *Geophys. Res. Lett*., 37, L01302, doi:10.1029/2009GL041213

Fielding, E. J., Sladen, A., Li, Z., Avouac, J. P., Bürgmann, R., & Ryder, I. (2013). Kinematic fault slip evolution source models of the 2008 M7. 9 Wenchuan earthquake in China from SAR interferometry, GPS and teleseismic analysis and implications for Longmen Shan tectonics. *Geophysical Journal International*, **194**(2), 1138-1166.

Gan, W., P. Zhang, Z.-K. Shen, Z. Niu, M. Wang, Y. Wan, D. Zhou, & J. Cheng (2007), Present-day crustal motion within the Tibetan Plateau inferred from GPS measurements, *J. Geophys. Res.,* **112**, B08416, doi:10.1029/2005JB004120

Hashimoto, M., Enomoto, M., & Fukushima, Y. (2010). Coseismic deformation from the 2008 Wenchuan, China, earthquake derived from ALOS/PALSAR images. *Tectonophysics*, **491**(1), 59-71.

Jia, D., Li, Y., Lin, A., Wang, M., Chen, W., Wu, X., Ren, Z., Zhao, Y., Luo, L. (2010). Structural model of 2008 Mw 7.9 Wenchuan earthquake in the rejuvenated Longmen Shan thrust belt, China, *Tectonophysics*, 491, 174-184, 10.1016/j.tecto.2009.08.040.

King, R. W., Shen, F., Burchfiel, B. C., Royden, L. H., Wang, E., Chen, Z., ... & Li, Y. (1997). Geodetic measurement of crustal motion in southwest China. *Geology*, **25**(2), 179-182.

Kirby, E., Reiners, P.W., Krol, M.A., Whipple, K.X., Hodges, K.V., Farley, K.A., Tang, W., Chen, Z. (2002). Late Cenozoic evolution of the eastern margin of the Tibetan Plateau: inferences from 40Ar/39Ar and (U–Th)/He thermochronology. *Tectonics* 21, 1001. doi:10.1029/2000TC001246.

Kobayashi, T., Takada, Y., Furuya, M. & Murakami, M. (2009). Locations and types of ruptures involved in the 2008 Sichuan earthquake inferred from SAR image matching, *Geophysical Research Letters*, 36, L07302, doi:07310.01029/02008GL036907.

Lin, A.M., Ren, Z.K., Jia, D. & Wu, X.J. (2009). Co-seismic thrusting rupture and slip distribution produced by the 2008 M-w 7.9 Wenchuan earthquake, China, *Tectonophysics*, 471, 203-215.

Lin, A.M., Ren, Z.K., Jia, D. (2010). Co-seismic ground-shortening structures produced by the 2008 Mw 7.9 Wenchuan earthquake, China. *Tectonophysics* 491, 21–34

Lin, A., Rao, G., and Yan, B. (2012). Field evidence of rupture of the Qingchuan Fault during the 2008 Mw7.9 Wenchuan earthquake, northeastern segment of the Longmen Shan Thrust Belt, China, *Tectonophysics*, 522–523, 5, 243-252, ISSN 0040-1951, 10.1016/j.tecto.2011.12.012.

Liu-Zeng, J., Zhang, Z., Wen, L., Tapponnier, P., Sun, J., Xing, X., Hu, G., Xu, Q., Zeng, L., Ding, L., Ji, C., Hudnut, K.W. & van der Woerd, J., 2009. Co-seismic ruptures of the 12 May, 2008, Ms 8.0 Wenchuan earthquake, Sichuan: East-west crustal shortening on oblique, parallel thrusts along the eastern edge of Tibet, *Earth and Planetary Science Letters*, 286, 355-370.

Rongjun, Z., Yong, L., Densmore, A. L., Ellis, M. A., Yulin, H., Yongzhao, L., & Xiaogang, L. I. (2007). Active tectonics of the Longmen Shan region on the eastern margin of the Tibetan plateau. *Acta Geologica Sinica□ English Edition*, **81**(4), 593-604.

Shen, Z.K., Lü, J., Wang, M. & Bürgmann, R. (2005). Contemporary crustal deformation around the southeast borderland of the Tibetan Plateau, *J. Geophys. Res*, 110, B11409, doi:11410.11029/12004JB003421.

Shen, Z.K., Sun, J.B., Zhang, P.Z., Wan, Y.G., Wang, M., Burgmann, R., Zeng, Y.H., Gan, W.J., Liao, H. & Wang, Q.L. (2009). Slip maxima at fault junctions and rupturing of barriers during the 2008 Wenchuan earthquake, *Nature Geoscience*, 2, 718-724.

Vallée, M., J. Charléty, A.M.G. Ferreira, B. Delouis, and J. Vergoz, (2011). SCARDEC : a new technique for the rapid determination of seismic moment magnitude, focal mechanism and source time functions for large earthquakes using body wave deconvolution, *Geophys. J. Int*., 184, 338-358.

Tong, X., Sandwell, D.T. & Fialko, Y. (2010). Coseismic slip model of the 2008 Wenchuan earthquake derived from joint inversion of interferometric synthetic aperture radar, GPS, and field data*, J. Geophys. Res*., 115, B04314.

Wang, Q., Qiao, X., Lan, Q., Freymueller, J., Yang, S., Xu, C., Yang, Y., You, X., Tan, K. & Chen, G., (2011). Rupture of deep faults in the 2008 Wenchuan earthquake and uplift of the Longmen Shan, *Nature Geosci,* **4**, 634-640.

Xu, X.W., Wen, X.Z., Yu, G.H., Chen, G.H., Klinger, Y., Hubbard, J. & Shaw, J., (2009). Coseismic reverse- and oblique-slip surface faulting generated by the 2008 Mw 7.9 Wenchuan earthquake, China, *Geology*, 37, 515-518.

Zhang, G., Qu, C., Shan, X., Song, X., Zhang, G., Wang, C., Hu, J.-C. and Wang, R. (2011). Slip distribution of the 2008 Wenchuan Ms 7.9 earthquake by joint inversion from GPS and InSAR measurements: a resolution test study. *Geophysical Journal International*, 186: 207–220. doi: 10.1111/j.1365-246X.2011.05039.x

Zhang, P.-Z., Wen, X.-z., Shen, Z.-K. & Chen, J.-h. (2010). Oblique, High-Angle, Listric-Reverse Faulting and Associated Development of Strain: The Wenchuan Earthquake of May 12, 2008, Sichuan, China, *Ann. Rev. Earth Planet. Sci*., 38, 353-382.

Zhang, P.Z., Xu, X.W., Wen, X.Z. & Ran, Y.K. (2008). Slip rates and recurrence intervals of the Longmen Shan active fault zone, and tectonic implications for the mechanism of the May 12 Wenchuan earthquake, 2008, Sichuan, China, *Chinese J Geophys-Ch*, 51, 1066-1073.

Zhang, P. Z. (2008), The co-seismic surface displacement of the great Wenchuan earthquake of May 12, 2008, Sichuan, China, from GPS measurements (in Chinese), Chin. Sci., 38(10), 1195–1206.

2.18. Superstition Hills 1987

24/Nov/1987, California, USA

Mw 6.6

Epicenter : 33.01°N-115.85°W

Right-lateral strike-slip



Broken long-term fault

The EQ broke a part of the San Jacinto Fault, a southern branch of the San Andreas Fault. As the Elmore Ranch earthquake occurred in the same fault area a few hours before the Superstition Hills EQ, we describe the two EQs together.

Note that the San Andreas Fault is described in the sections "Fort Tejon 1857" (Southern San Andreas) and "San Francisco 1906" (Northern San Andreas). The relations of the San Andreas Fault with the San Jacinto and the Elsinore faults are discussed in section "Fort Tejon 1857". The San Jacinto Fault is one of the major splays of the Southern San Andreas Fault.

General characteristics of the San Jacinto Fault from literature (Fig.138) :

This part is described in the section "Borrego Mountain 1968".

Architecture and lateral major segmentation, from our and USGS mappings (Fig.139):

This part is described in the section "Borrego Mountain 1968". Only the figures are shown again here.

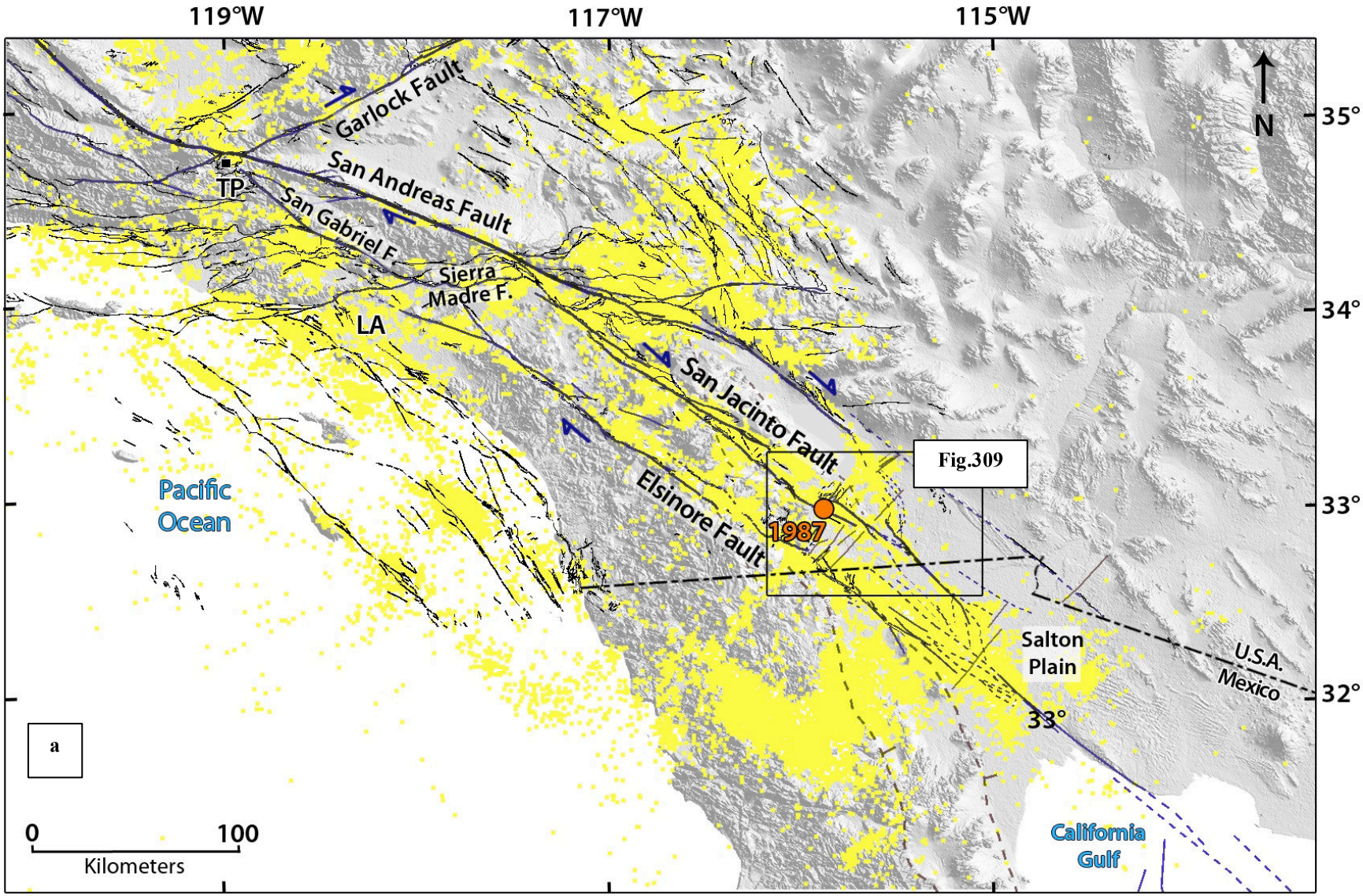


Fig.138: (a) General map of long term faults in Southern California. In blue are the major active faults that we mapped. In black are the other Quaternary faults mapped by the U.S. Geological Survey and California Geological Survey, 2006. In dotted brown are ancient faults related to the Gulf of California. In solid brown are preexisting lineaments likely related to the Gulf of California (see text). The orange circle shows the 1987 Superstition Hills EQ epicenter. The yellow dots are the instrumental earthquakes (Mw>2) recorded between 1981 and 2011 (Hauksson et al., 2012). LA : Los Angeles ; TP : Tejon Pass;

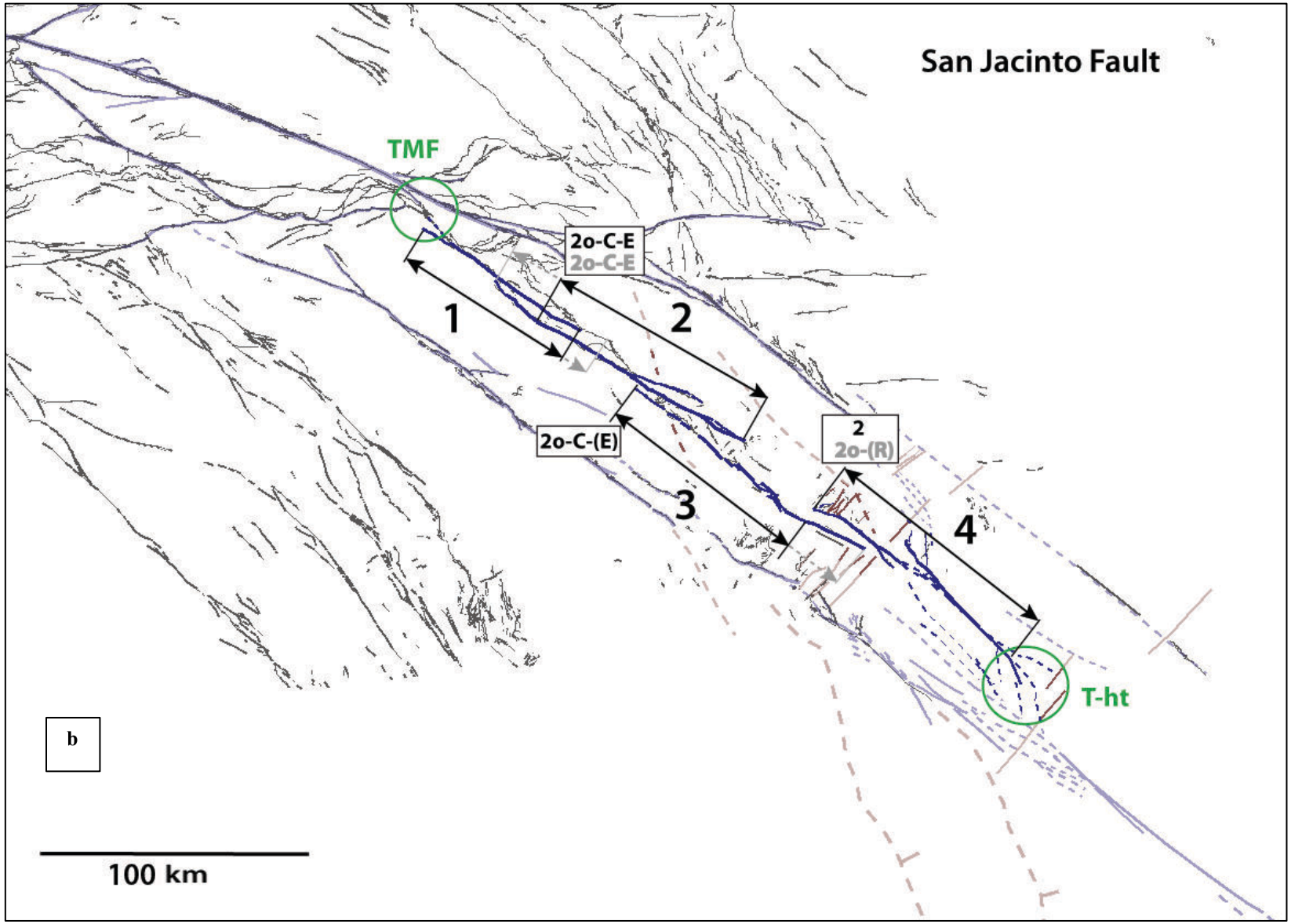


Fig.138: b) Same active fault map as in 1b, but with focus on the major segments of the San Jacinto fault. The segments are numbered from NW to SE and indicated by black arrows parallel to their mean strike. The grey prolongation of the arrows indicates the uncertainties on the segment lengths. The nature of the inter-segment zones and of the fault tips are indicated in boxes and in green, respectively, and reported I Table 6.

1987 Coseismic rupture

The Elmore Ranch foreshock

- 12 hours before the Superstition Hills EQ, the Mw 6.2 Elmore Ranch earthquake broke a network of small faults, sub-perpendicular to the San Jacinto Fault (ERF, see Fig.139a). These small faults are among the numerous similar lineaments that are observed in the Salton Plain, and which we interpret as pre-existing structures formed as a result of the California Gulf opening (See section Borrego Mountain 1968).
- The NE-trending small faults are described to be both normal and left-lateral (Hudnut et al., 1989b). Their activation is thus kinematically compatible with dextral slip on the master San Jacinto Fault.
- The 1987 surface ruptures cannot be discriminated, on Google Earth and Landsat images, from the cumulative fault traces, which are very subtle in the Plain. The surface traces of the 1987 earthquake were however mapped on the field (Hudnut et al., 1989a)
- The rupture occurred over ~10 km at surface.
- The summed slip measured on the six principal parallel faults reaches ~0.2 m (Fig.140; Hudnut et al., 1989a).

The Superstition Hills mainshock

Surface trace and location on long-term San Jacinto Fault:

- The 1987 surface rupture is clear on Google Earth images. The surface trace of the earthquake has been precisely mapped, and the displacements measured (See below), on the field (e.g. Sharp et al., 1989; Williams and Magistrale 1989).
- Surface rupture of ~27 km long.
- The EQ broke a part of one major segment of the San Jacinto Fault, major segment 4.
- Major segment 4 is made of two clear parts –northern and southern, striking slightly differently (angle difference of ~12°) either side of the middle of the segment. Each part has a very linear trace. The 1987 EQ broke the northern part of major segment 4. Before, the 1940 and 1979 EQs had broken the southern part of major segment 4.
- Each northern and southern part is itself divided into two distinct segments so that, overall, major segment 4 includes 4 secondary segments, of similar length, 25-30 km: 4a to 4d. (Fig.139b). These secondary segments are described in section “Imperial Valley 1940 & 1979”.

- The 1987 EQ broke entirely the secondary segment 4a. According to the southward long-term propagation of the San Jacinto Fault, the secondary segment 4a is the most mature section of the major segment 4.
- Segment 4a is ~25 km long. Its trace is very linear. To the north, segment 4a terminates by connecting to multiple NE-trending and hence sub-perpendicular small fractures and faults, which broke a few hours before in the Elmore Ranch EQ. Segment 4b is also fairly linear. Its trace is fairly subtle to identify within the fields of the Salton Plain, especially in the south. Segments 4a and 4b are connected through a narrow step (< 0.5 km wide) nearby where a small splay, oblique fault has developed (hence relay of type 2o-sp). To the south, segment 4b splays in multiple tenuous branches, which contribute to its connection with the southernmost segments 4c and 4d (described in section "Imperial Valley 1940 & 1979").
- The 1987 earthquake initiated at the NW tip of segment 4a, probably triggered by the previous Elmore Ranch rupture (Hudnut et al., 1989b). Then the rupture propagated unilaterally along the secondary segments 4a and stopped at the intersegment zone between secondary segments 4a and 4b.
- The rupture also broke the small splay fault that departs nearby the 4a-4b inter-segment zone.
- The segment 4a is itself formed by two smaller-scale segments (named 4a-1 and 4a-2, Fig.139 & 140), each 10-15 km long, separated by a small (W < 0.3 km) releasing step-over.

→ The 1987 Superstition Hills EQ occurred on one major segment of the San Jacinto Fault (major segment 4), which it broke partially. The rupture indeed broke 1 over the 4 secondary segments that form the major segment 4. The broken secondary segment (4a) is the most mature section of major segment 4. The EQ initiated at the northern tip of segment 4, likely triggered by the Elmore Ranch foreshock which occurred a few hours before on sub-perpendicular small faults and cracks.

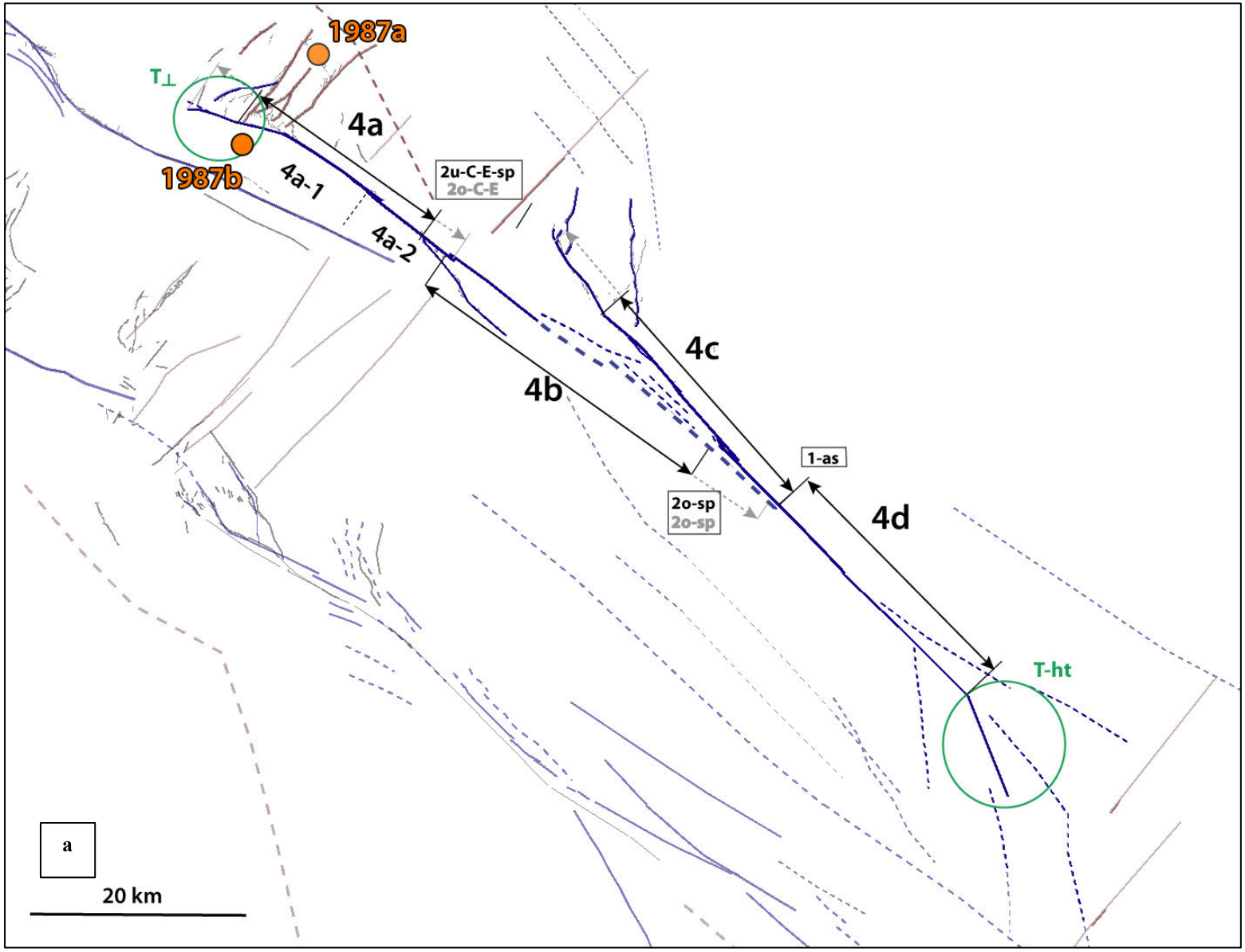


Fig.139: a) Map of the secondary segments that form the major segment 4 of the San jacinto fault. Same caption as in Fig.138. The orange circles indicate the 1987a Elmore Ranch earthquake epicenter and the 1987b Superstition Hills earthquake epicenter.

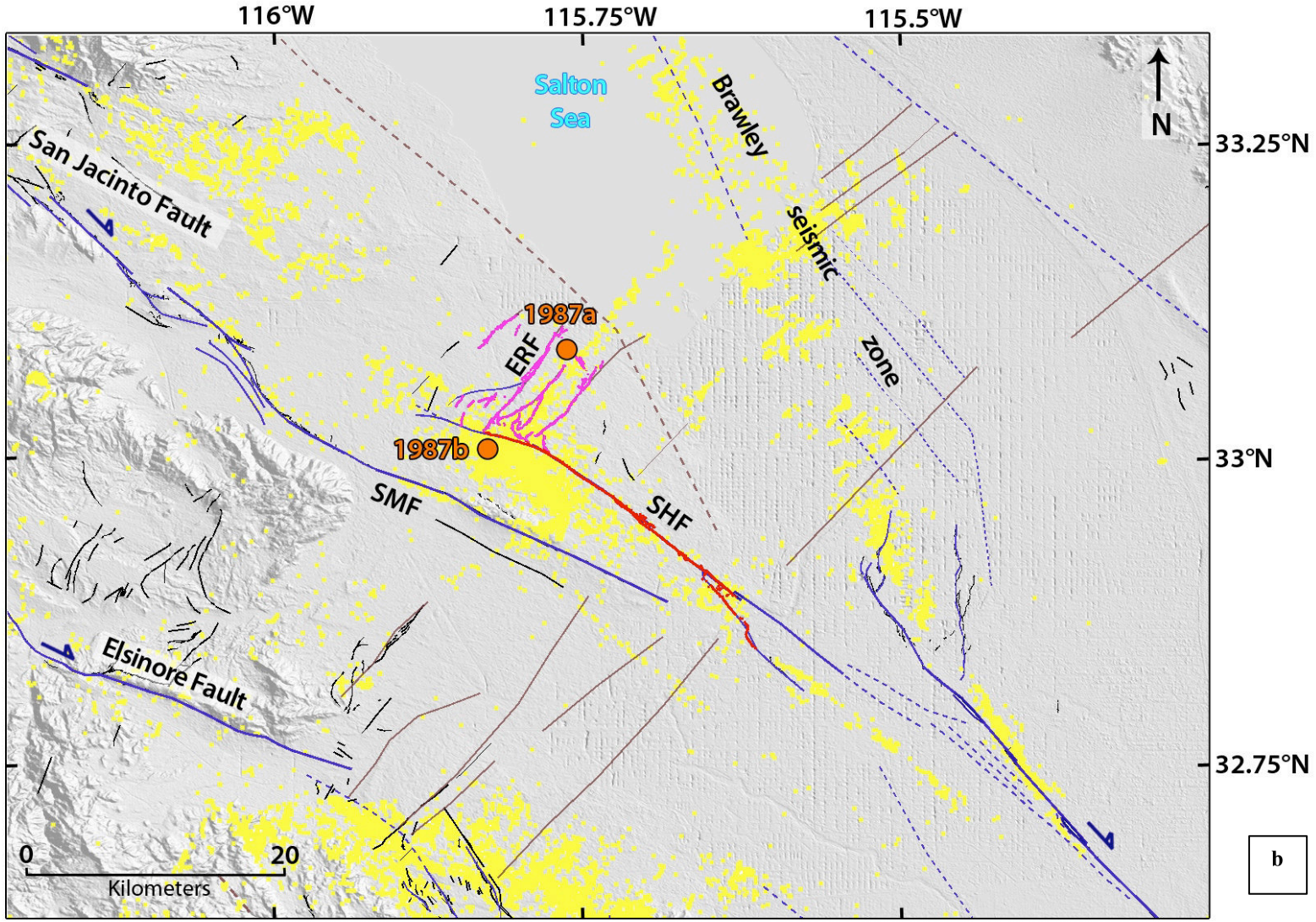


Fig.139: b) Zoom on the broken section of the San Jacinto fault, from Fig.138 (same caption). The surface rupture of the 1987 EQ is indicated with the red line (Sharp et al., 1989). Orange circles show the epicenters of the 1987a Elmore Ranch (Mw 6.1; rupture trace indicated in pink) and 1987b Superstition Hills (Mw 6.6) earthquakes. ERF : Elmore Ranch Faults ; SHF : "Superstition Hills Fault "; SMF: "Superstition Mountains Fault" (names from U.S. Geological Survey and California Geological Survey, 2006)

Coseismic displacements measured at surface:

- *From Field measurements*: maximum lateral slip of 0.5 m measured in the central part of segment 4a one day after the earthquake (Sharp et al., 1989; Williams and Magistrale 1989). The maximum slip locates due north of the small step-over that connects the two small-scale segments 4a-1 and 4a-2 of secondary segment 4a.
- Significant postseismic deformation was observed after the earthquake (See « other information section »).
- The complete coseismic slip profile was measured (Fig.140). Its overall shape is fairly triangular and symmetric, with maximum slip concentrated in the central part of the rupture.
- Three patches of slip can be distinguished however (Fig.140): a small one to the north showing the fault slip in the zone where segment 4a interacts with the sub-perpendicular faults and cracks; then a large patch coinciding with slip on small-scale segment 4a-1; then a lower slip patch coinciding with slip on small-scale segment 4a-2. Little additional slip is observed at the southern rupture tip, which coincides with slip on the small splay fault.
- *From GPS measurements*: GPS stations located close to the fault recorded 0.5 ± 0.15m of horizontal displacement between 1986 and 1990 (Larsen et al., 1992).

→ Maximum lateral slip of ~0.5 m measured at surface, on segment 4a, that is on the most mature part of the broken fault section; fairly symmetric triangular slip profile.

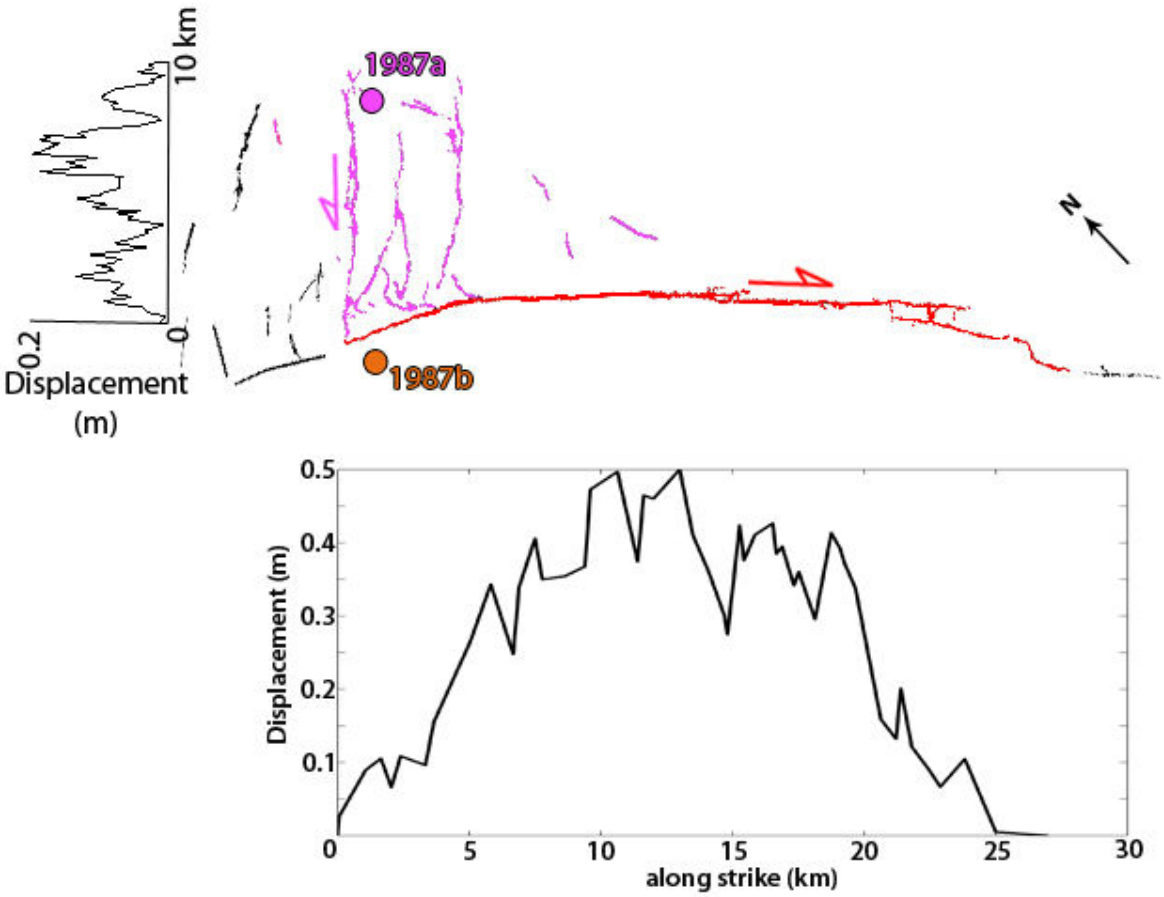


Fig.140: Top: Elmore Ranch (pink) and Superstition Hills (red) surface ruptures (Sharp et al., 1989). To the left is slip profile measured on Elmore Ranch rupture (Hudnut et al., 1989a). Bottom: Coseismic displacements measured at surface along the 1987b Superstition Hills surface rupture.

Other source parameters :

Global CMT

Mainshock: 1987/11/24 at 13h16min12s GMT; Lat = 33.02° Lon= -116.00°
Mw 6.5; M0 = 7.18e18 Nm; Z = 15 km; Half-duration: 7.2s
Strike, dip, slip : (133°, 78°, 178°)/ (224°, 88°, 12°)

Source inversion models and slip distribution at depth (Fig.141) :

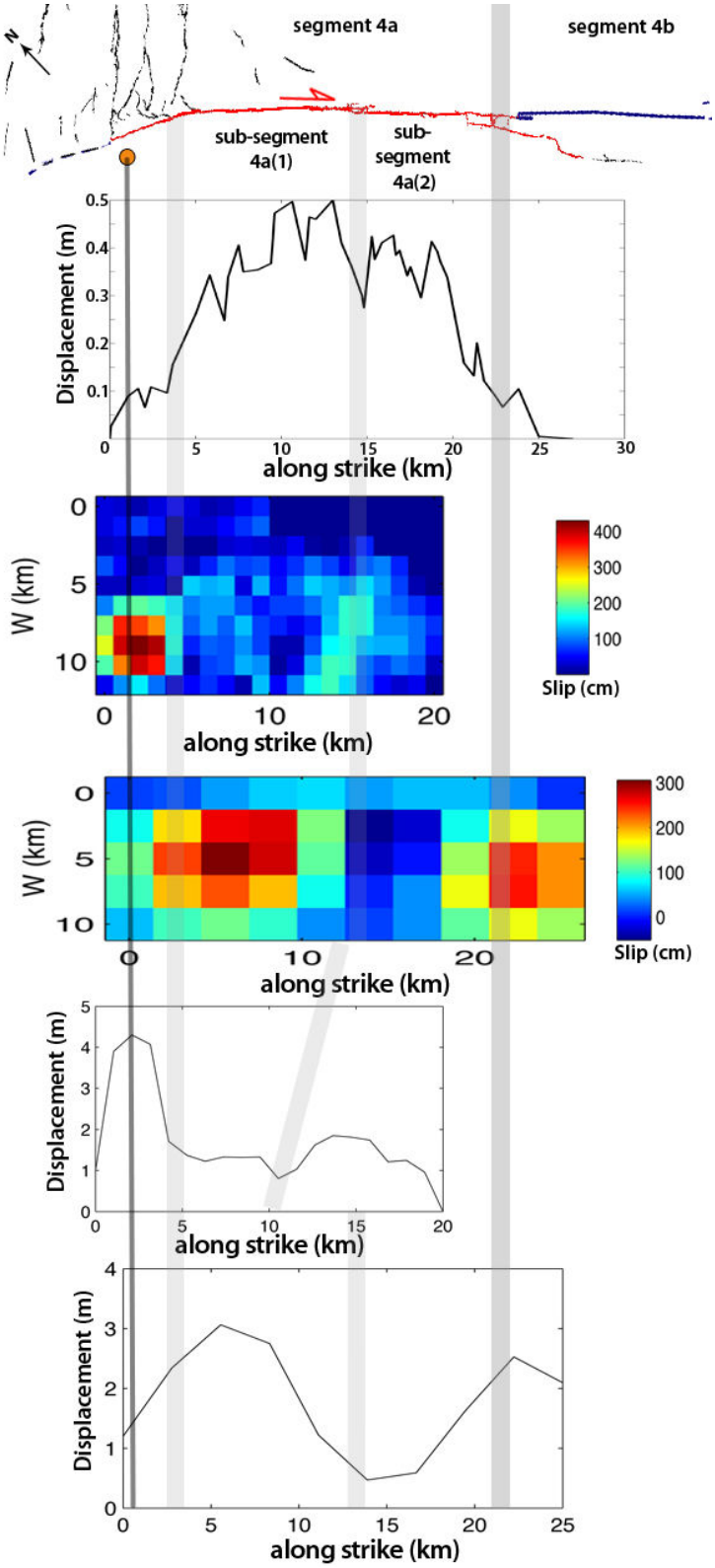
- We compare two source inversion models that have been published on the 1987 Superstition Hills earthquake; the grid data are available for the two of them (Table 2).

The models differ principally from the data they used:

- Wald et al. (1990): Strong motions data. The model considers the broken fault as a single plane (20*12 km).
- Larsen et al. (1992): GPS data + surface data. The model considers the broken fault as a single plane (25*10 km).

- The two models are not fully constrained: the model from Wald et al. (1990) is based only on a few strong motion data and uses a rupture length of 20 km (based on aftershocks distribution) which is lower than the observed surface rupture. The GPS data used in the model of Larsen et al. (1992) are sparse near the rupture and contain a significant amount of pre and postseismic slip (1986-1990). The model is also constrained with surface data that include some afterslip (Dmax=70 cm).
- Despite of their limitations, the two models provide a similar slip distribution, with basically two main patches of slip, in agreement with the observed rupture of two sub-segments within segment 4a. The maximum slip (3-4 m) is located at a depth of 5-10 km, in the northern part of the rupture. Both models suggest that the slip might extend down to 10-12 km depth along the fault dip.
- The comparison between surface and depth slip profiles (Fig.140) suggests that the coseismic slip was maximum at the northern tip of the rupture, yet did not entirely propagate up to the surface (almost no slip in the first few km below the ground surface). This is in keeping with the very low slip measured at surface all along the rupture. The slip patches inferred from the source models do not seem well-located along-strike. Taken together, the data suggest the slip was maximum in the north, i.e., on the most mature section of the broken fault zone. The slip profile might be more asymmetric than revealed at the ground surface. The slip at surface seems to be only a very small fraction of the actual slip at depth; this can be due both to part of the slip not having propagated up to the surface, and to part of slip having diffused in the soft sediments of the Salton Plain. Therefore, the slip distribution at surface might not be meaningful.

→ The source models suggest: L 20-25 km, W 10-12 km, Dmax at depth 3-4 m, 2 dominant slip patches.



(a)

(b)

(c) *Wald et al. 1990*

(d) *Larsen et al. 1992*

(e)

(f)

Fig.141: (a) Surface rupture trace, from Fig.139b; (b) Lateral slip-length profile measured at surface after the 1987 Superstition Hills earthquake (Sharp et al., 1989); (c) Inversion model from Wald et al. (1990) using strong motions data; d) Inversion model from Larsen et al. (1992) using GPS data; e) and f) profile of maximum slip inferred at depth from the models of Wald et al. (1990) and Larsen et al. (1992), respectively. Grey bars represent the intersegment zones, darker where major.

Other information:

Past EQ activity:

- Similar moderate earthquakes occurred on the San Jacinto Fault during the last decades: the 1968 Borrego Mountain (Mw 6.5) broke a part of the major segment 3; the 1940 and 1979 Imperial Valley earthquakes (Mw 7.0 & 6.5, respectively) broke the secondary segment 4c and 4d;

1987 EQs:

- The aftershocks of the Elmore Ranch foreshock extend further to the NE under the Salton Sea until they connect the Brawley seismic zone (Fig.139; Magistrale et al., 1989)
- No significant afterslip was observed along the Elmore Ranch broken faults (Hudnut et al., 1989a)
- Significant afterslip was measured a few months after the Superstion Hills mainshock: maximum lateral slip of ~1 m (Lindvall et al., 1989; Sharp et al., 1989; Williams and Magistrale 1989). The postseismic slip follows a power law that conducted some authors to calculate the coseismic slip « 1min after the earthquake » (Dmax ~ 0 .2 m; Williams and Magistrale 1989).
- Aftershocks were mainly concentrated in the NW part of the broken segment 4a, at the intersection with the perpendicular Elmore Ranch faults.
- Lindvall et al. (1989) measured geomorphic offsets along the segment 4a and found four to five prehistoric earthquakes having occurred before the 1987 Superstition Hills events. These paleoEQs would have got a surface slip distribution similar to that of the 1987 event, suggesting the possibility of characteristic events.

Parameters retained to describe the 1987 Superstition Hills EQ (Tables 2 – 4):

Mw 6.5-6.6; M0 ~ 7.18e18 Nm; L 25-27 km; W 10-12 km; Dmax surface ~ 0.5 m yet not representative of the actual EQ rupture; Dmax depth = 3-4 m.

Number of segments broken on the San Jacinto Fault: 1 major segment, partly; representing the rupture of 1 secondary segment (4a), along which 2 smaller-scale segments broke (4a-1 and 4a-2).

The slip-length surface data of the Superstition Hills earthquake fall on the fourth function (orange curve; Fig.142). Yet, as discussed earlier, they are not meaningful. The slip-length EQ data inferred at depth fall on the second function (blue curve; Fig.143), in keeping with

the rupture of two small segments along the fault. These segments are of small scale however. We come back to this point in the discussion section.

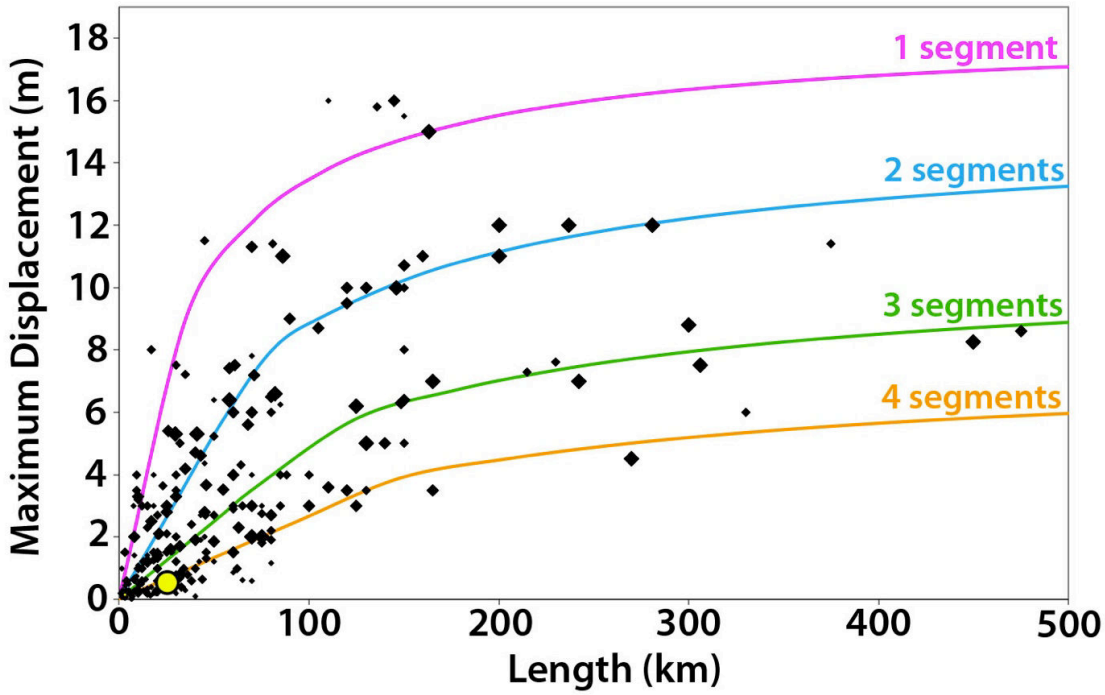


Fig.142: Earthquake displacement-length data measured at surface for 260 historical large continental earthquakes (Mw≥6). The 4 curves indicate the number of major long-term fault segments to have been broken by the earthquakes (modified from Manighetti et al., 2007 and Chapter IV). Yellow dot shows the 1987 Superstition Hills earthquake surface slip-length data

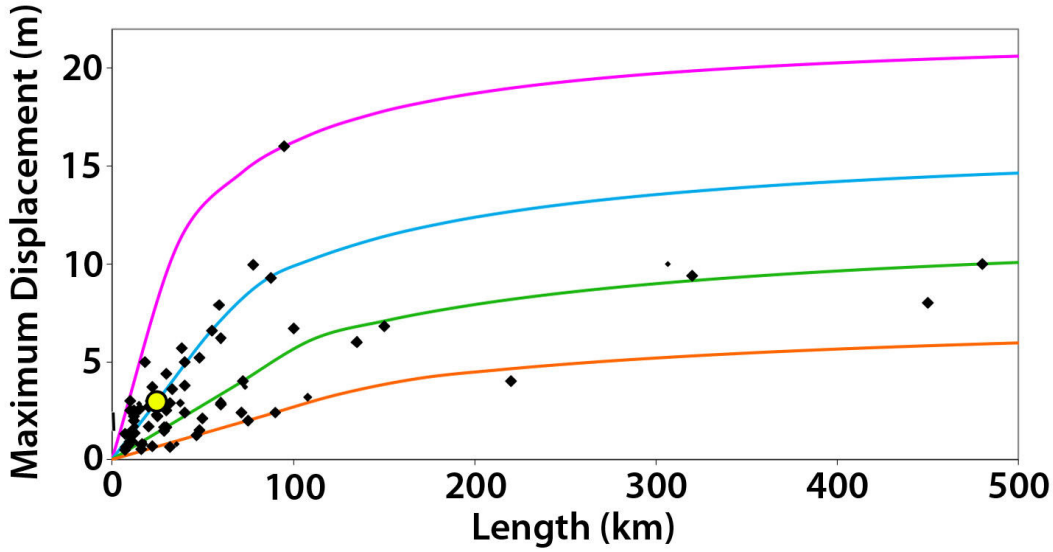


Fig.143: Earthquake displacement-length data inferred at depth for 90 historical large continental earthquakes (Mw≥6). The 4 curves indicate the number of major long-term fault segments to have been broken by the earthquakes (modified from Manighetti et al., 2007 and Chapter IV). Yellow dot shows the 1987 Superstition Hills earthquake depth slip-length data.

References.

Blisniuk, K., T. Rockwell, L. A. Owen, M. Oskin, C. Lippincott, M. W. Caffee, & J. Dortch. 2010. Late Quaternary slip rate gradient defined using high-resolution topography and 10 Be dating of offset landforms on the southern San Jacinto Fault zone, California. *J. Geophys. Res.,* **115**, B08401, doi:10.1029/2009JB006346.

Fialko, Y. 2006. Interseismic strain accumulation and the earthquake potential on the southern San Andreas Fault system, *Nature*, **441**, 968–971, doi:10.1038/nature04797

Gurrola, L. D., & T. K. Rockwell. 1996. Timing and slip for prehistoric earthquakes on the Superstition Mountain fault, Imperial Valley, southern California*, J. Geophys. Res.,* **101**, 5977–5985, doi:10.1029/95JB03061.

Hudnut, K. W., & K. Sieh. 1989. Behavior of the Superstition Hills Fault during the past 330 years, *Bull. Seismol. Soc. Am*., **79**, 304–329.

Hauksson, E., W. Yang, & P.M. Shearer (2012). Waveform Relocated Earthquake Catalog for Southern California (1981 to June 2011); *Bull. Seismol. Soc. Am*., **102**, doi:10.1785/0120120010.

Hudnut, K.W., L. Seeber, T. Rockwell, J. Goddmacher, R. Klinger, S. Lindvail, & R. McElwain. 1989a. Surface ruptures on cross-faults in the 24 November 1987 Superstition Hills, California, earthquake sequence*, Bull. Seismol. Soc. Am.,* **79**, 282-296

Hudnut, K. W., Seeber, L. & Pacheco, J. 1989b. Cross-fault triggering in the November 1987 Superstition Hills earthquake sequence, Southern California, *Geophys. Res. Lett*. **16**, 199- 202.

Janecke, S.U., Dorsey, R.J., Forand, D., Steely, A.N., Kirby, S.M., Lutz, A.T., Housen, B.A., Belgarde, B., Langenheim, V.E., & Rittenour, T.M. (2010), High Geologic Slip Rates since Early Pleistocene Initiation of the San Jacinto and San Felipe Fault Zones in the San Andreas Fault System: Southern California, USA: *Geological Society of America Special Paper* **475**, 48 p., doi: 10.1130/2010.2475.Â isbn 9780813724751

Kendrick, K. J., D. M. Morton, S. G. Wells, & R. W. Simpson. 2002. Spatial and temporal deformation along the northern San Jacinto Fault, southern California: Implications for slip rates, *Bull. Seismol. Soc. Am*., **92**, 2782–2802, doi:10.1785-/0120000615.

Kirby, S. M., Janecke, S. U., Dorsey, R. J., Housen, B. A., Langenheim, V. E., McDougall, K. A., & Steely, A. N. (2007). Pleistocene Brawley and Ocotillo formations: Evidence for initial strike□slip deformation along the San Felipe and San Jacinto Fault zones, southern California. *The Journal of geology*, **115**(1), 43-62.

Larsen, S., Reilinger, R., Neugebauer, H., & Strange, W. 1992. Global Positioning System Measurements of Deformations Associated With the 1987 Superstition Hills Earthquake : Evidence for Conjugate Faulting. *Journal of Geophysical Research*, **97**, B4, 4885-4902,

Lindvall, S. C., T. K. Rockwell, & K. W. Hudnut. 1989. Evidence for prehistoric earthquakes on the Superstition Hills Fault from offset geomorphic features, *Bull. Seismol. Soc. Am*. **79**, no. 2, 342–361.

Lindsey, E. O., & Y. Fialko 2013. Geodetic slip rates in the southern San Andreas Fault system: Effects of elastic heterogeneity and fault geometry, *J. Geophys. Res. Solid Earth*, **118**, 689–697, doi:10.1029/2012JB009358.

Lundgren, P., E. A. Hetland, Z. Liu, and E. J. Fielding. 2009. Southern San Andreas-San Jacinto Fault system slip rates estimated from earthquake cycle models constrained by GPS and interferometric synthetic aperture radar observations, *J. Geophys. Res*., **114**, B02403, doi:10.1029/2008JB005996

Lutz, A. T., R. J. Dorsey, B. A. Housen, & S. U. Janecke. 2006. Stratigraphic record of Pleistocene faulting and basin evolution in the Borrego Badlands, San Jacinto Fault, southern California, *Geol. Soc. Am. Bull*., **118**, 1377–1397, doi:10.1130/B25946.1

Manighetti, I., M. Campillo, S. Bouley, and F. Cotton (2007), Earthquake scaling, fault segmentation, and structural maturity*, Earth Planet. Sci. Lett*., **253**, 429-438, doi:10.1016/j.epsl.2006.11.004

Magistrale, H., L. Jones, & H. Kanamori. 1989. The Superstition Hills, California, earthquakes of 24 November 1987, *Bull. Seism. Soc. Am*. **79**, 239-251.

Rockwell, T. K., C. Loughman, & P. Merifield. 1990. Late Quaternary rate of slip along the San Jacinto Fault zone near Anza, southern California, *J. Geophys. Res*., **95**, 8593–8605, doi:10.1029/JB095iB06p08593.

Sharp, R. V. 1967. San Jacinto Fault zone in the Peninsular Ranges of southern California*, Geol. Soc. Am. Bul*l., **78**, 705–730, doi:10.1130/ 0016-7606(1967)78[705:SJFZIT]2.0.CO;2.

Sharp, R. V., Budding, K. E., Boatwright, J., Ader, M. J., Bonilla, M. G., Clark, M. M., Fumal, T. E., Harms, K. K., Lienkaemper, J. J., Morton, D. M., O'Neill, B. J., Ostergren, C. L., Ponti, D. J., Rymer, M. J., Saxton, J. L. & Sims, J. D. 1989. Surface faulting along the Superstition Hills Fault zone and nearby faults associated with the earthquakes of 24 November 1987, *Bull. Seism. Soc. Am*. **79**, 252- 281.

U.S. Geological Survey and California Geological Survey, 2006, Quaternary fault and fold database for the United States, accessed 2011, from USGS web site: http//earthquakes.usgs.gov/regional/qfaults/

Wald, D.J., D.V. Helmberger, & S.H. Hartzell. 1990. Rupture process of the 1987 Superstition Hills earthquake from the inversion of strong motion data. *Bull, Seismol. Soc. Am*., **80**, 1079-1098

Williams, P.L., & H.W. Magistrale. 1989. Slip along the Superstition Hills Fault associated with the 24 November 1987 Superstition Hills, California, earthquake. *Bull. Seismol.. Soc. Am.,* **79**, 390- 410

2.19. Yushu 2010

13/April/2010, China

Mw 6.9-7.1

Epicenter (USGS) : 33.22°N-96.67°E

Left-lateral strike-slip



Broken long-term fault

The EQ broke a part of the **Garze-Yushu Fault,** which forms the western continuation of the Xianshuihe fault system, China (Fig.144).

General characteristics from literature:

- Failry linear, N120°E-trending left-lateral strike-slip fault, about 380 km long
- Would have initiated ~ 13 Ma ago (e.g. Tapponnier et al., 2001) based on K/Ar and apatite fission-track ages on offset geological features (Wang et al., 2009).
- Maximum cumulative lateral slip of at least ~ 80 km, based on the lateral offset of a granitic pluton (Wang and Burchfiel 2000; Wang et al., 2009).
- Current lateral slip rate: ~20 mm/yr (e.g. Meade 2007) inferred from a large-scale block model of the India-Asia collision zone (Geodetic data).
- Long-term lateral slip rate: 9-12 mm/yr (over the Quaternary) measured on the Garze-Yushu Fault (Wen et al., 2003; Zhou et al. 2013), and 15 ± 5mm/yr for the Xianshuihe Fault (Allen et al., 1991).

→ The Garze-Yushu Fault has an intermediate structural maturity (300<L<1000 km, I-Age ~10 Ma, MR ~1 cm/yr, D_{Total} of a few 10 km) yet closer from mature than from immature (Class Interm → Mature; Table 5).

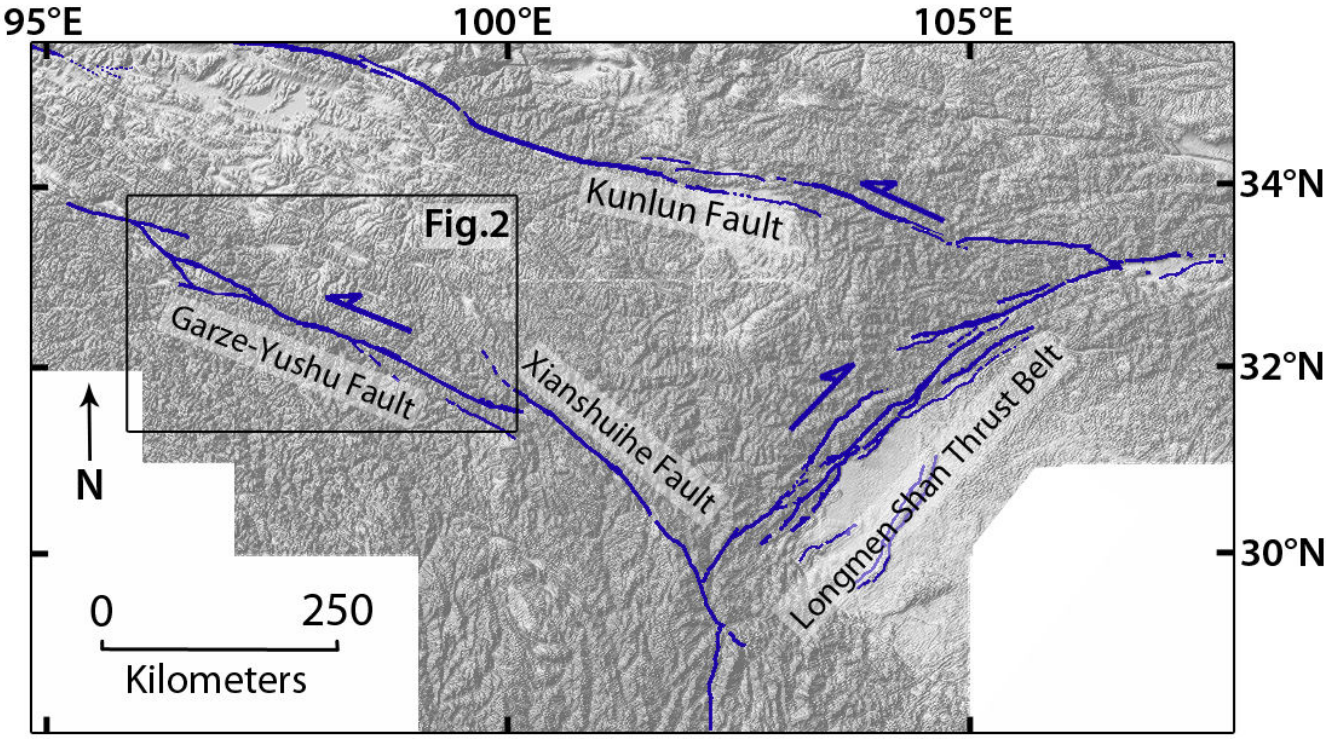


Fig.144: General map of the main long-term faults in eastern Tibet (blue).

Architecture and major lateral segmentation, from our mapping (Fig.145 & 146):

- Mapping done from Google Earth, local SPOT images, Landsat and SRTM data combined with dense literature information.
- Long-term fault trace well expressed in surface morphology and topography.
- To the southeast, the Garze-Yushu Fault gives pace to the longest Xianshuihe Fault. The Garze-Yushu Fault seems actually to be a large-scale splay of the Xianshuihe Fault. This suggests that the Xianshuihe Fault has been propagating northward over geological time, with this lateral propagation eventually forming the Garze-Yushu Fault. The two faults are overlapping on 40-70 km long, while they are separated with an across-strike distance of 15-35 km.
- To the northwest, the Garze-Yushu Fault stops at its intersection with an oblique NW-trending fault that is a part of a large-scale splay developed at the eastern tip of the WNW-striking Dangjiang Fault (splay not entirely shown on the Fig.145). The splay suggests that the Dangjiang Fault has been propagating eastward. The Garze-Yushu and Dangjiang Fault splays interact, forming a fault network that connects both faults across the step-over that separates them (across-fault separation of 25-50 km).

- The Garze-Yushu Fault is divided into 4 major, fairly collinear segments (See Fig.145b where they are numbered). The types and sizes of the major segments and inter-segments are described in Table 6.
- Those 4 major segments have a similar length of 70-100 km (length measured along the linear trace of each segment; Fig.145).
- The fault trace is linear along each major segment. The 4 segments are sub-parallel. Segments 1 and 2 are separated by a narrow step-over. The oblique Zainongda Fault splays from the northern tip of major segment 2. This geometry suggests that the Garze-Yushu is propagating westward, in keeping with the sense of propagation of its master Xianshuihe Fault and with its connection with the Dangjiang Fault. Major segments 2 and 3 are separated by a large-scale pull-apart. The eastern tip of major segment 3 is marked by the development of a small horsetail network made of multiple oblique secondary normal faults. The eastern termination of segment 4 is marked by the gap that separates the master Xianshuihe Fault from its splaying Garze-Yushu Fault.

→ The Garze-Yushu Fault is divided into 4 long-term major collinear segments. The Garze-Yushu Fault is genetically related to the Xianshuihe Fault, being its propagating splay. The Garze-Yushu Fault is propagating northwestward, and thus, its major segments likely become younger towards the NW. The Garze-Yushu Fault is in the process of connecting with the Dangjiang Fault.

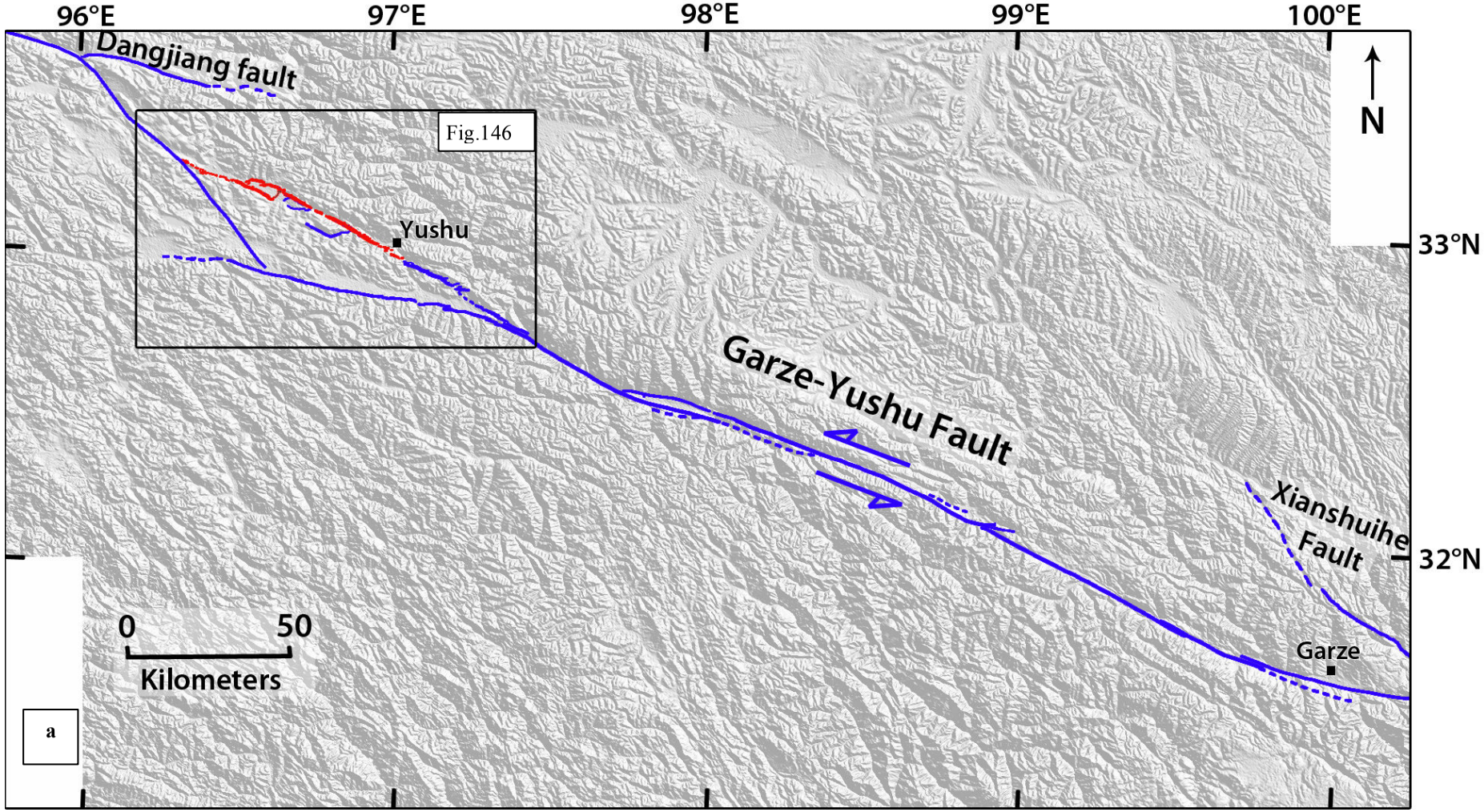


Fig.145: a) Our map of the Garze-Yushu long term fault (blue) and surface rupture of the 2010 Yushu earthquake (red).

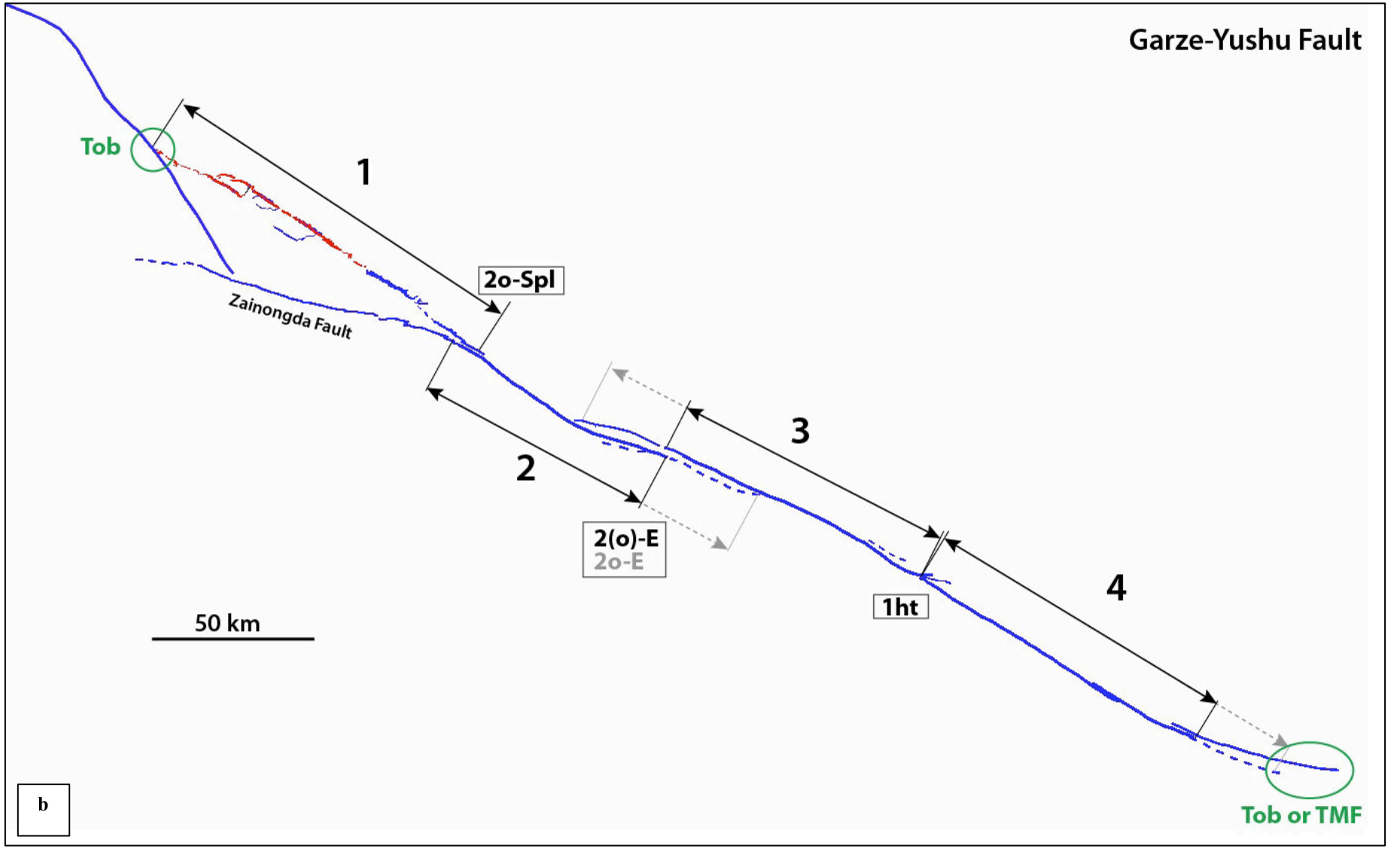


Fig.145: b) Same active fault map as in 145a, but with focus on the major segments of the Garze-Yushu fault. The segments are numbered from NW to SE and indicated by black arrows parallel to their mean strike. The grey prolongation of the arrows indicates the uncertainties on the segment lengths. The nature of the inter-segment zones is indicated in letters within boxes explained in Table 6. The nature of the fault tips is indicated in green (Table 6).

2010 Coseismic rupture

Surface trace and location on long-term Garze-Yushu Fault:

- The 2010 surface rupture is quite clear on Google Earth and SPOT5 images, especially in the half southeastern part (Fig.146). The surface trace of the earthquake has been precisely mapped on the field and from satellite imagery (Chen et al., 2010; Lin et al., 2011; Li et al., 2012).
- Surface rupture of ~75 km long. The length of the rupture is controversial however in the literature. Our mapping reveals to be in good agreement with the InSAR data (See one example in Fig.148) (Zhang et al., 2010; Li et al., 2011; Tobita et al., 2011; Qu et al., 2012 ; Zhang et al., 2013) and with several field studies (e.g., Li et al., 2012).
- The earthquake initiated at a depth of ~13 km (Wang et al., 2013) below the pull apart basin that separates the secondary segments 1a and 1b of the Garze-Yushu Fault (See below). It propagated bilaterally toward the NW and SE.
- The EQ broke no other fault than the Garze-Yushu Fault.
- The EQ broke a part of one major segment of the Garze-Yushu Fault, major segment 1.
- According to its geometry, major segment 1 is divided into 4 to 5 secondary collinear secondary segments, of similar length, 20-24 km (Fig.146). The 2010 EQ broke the secondary segments 1a, 1b and 1c of major segment 1.
- The fault trace is fairly linear along each secondary segment. Secondary segments 1a and 1b are separated by a 10 x 3 km pull apart basin. Secondary segments 1b and 1c are directly connected to each other but they dip in opposite direction. Segments 1c and 1d are separated by an extensional horsetail fault network that developed at the eastern tip of segment 1c (See Fig.147). Segment 1d also terminates to the east by a horsetail. The secondary segment 1e is more disputable because its trace is subtle.
- The rupture terminated at the eastern tip of secondary segment 1c, in the horsetail area where the trace of segment 1c stops being continuous and splays into multiple tiny oblique faults.

→ The EQ occurred on one major segment of the Garze-Yushu Fault (major segment 1), which it broke partially. The rupture indeed broke 3 over the 4-5 secondary segments that form the major segment 1. Since the Garze-Yushu Fault has likely been propagating northward over geological time, segment 1 might be the most immature part of the fault.

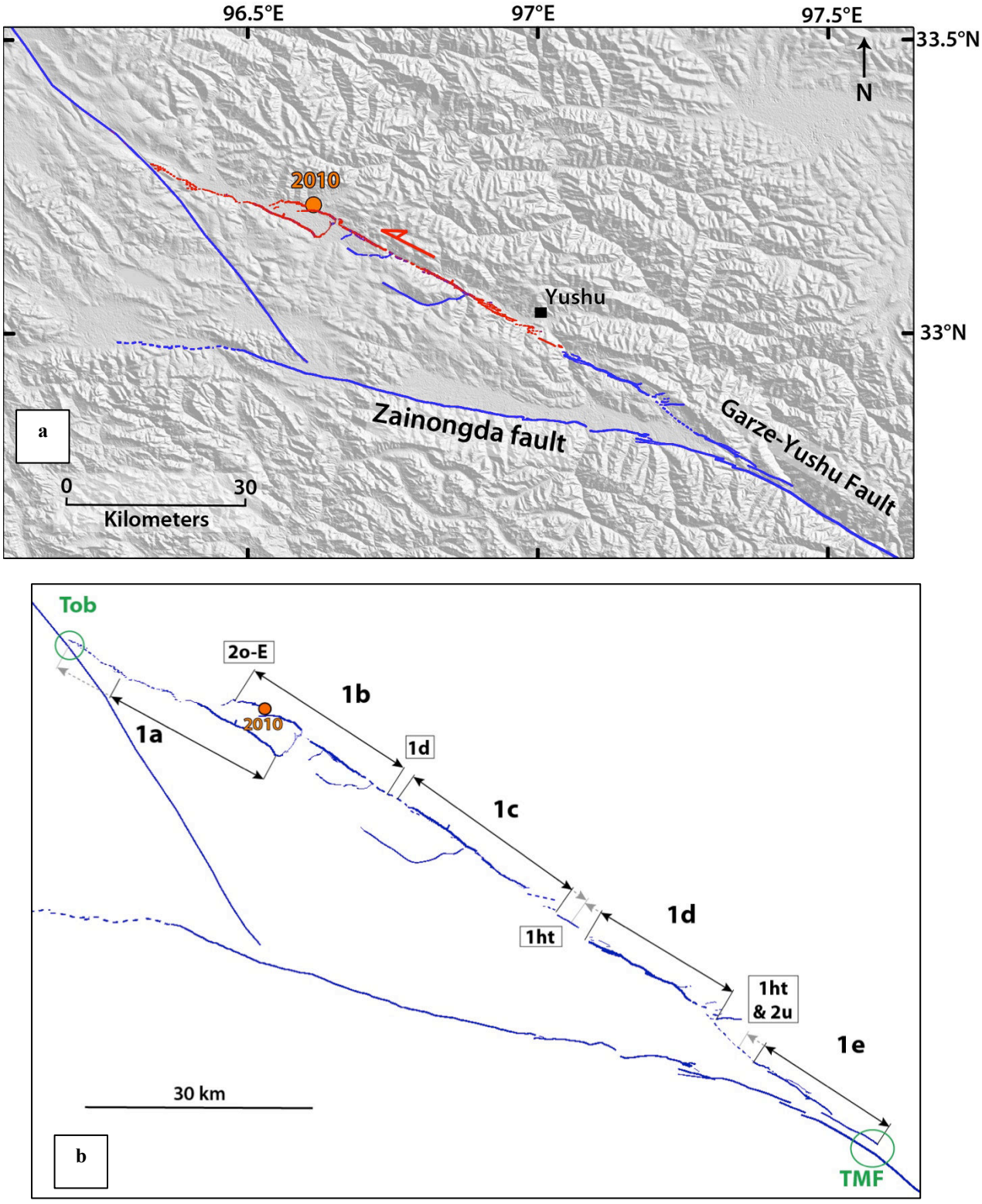


Fig.146: a) Zoom on the broken section of the Garze-Yushu Fault, from Fig.145 (same caption) The orange circle shows the 2010 Yushu epicenter. b) Map of the secondary segments that form the major segment 1 of the Garze-Yushu long term fault (blue) (same caption as in Fig.145b).



Fig.147: Satellite image of the southeastern tip of the segment 1c. White full and empty arrows show the main fault trace and associated horsetails structures, respectively.

Coseismic displacements measured at surface :

- *From Field measurements*: The measured slip profile is not complete along the rupture. The maximum lateral slip was measured on secondary segment 1c, and found between 1,8 m (Chen et al., 2010; Zhang et al., 2010; Li et al., 2012) and 3,2 m (Lin et al., 2011).
- *From InSAR data and modeling*: Maximum lateral slip estimates vary between 1,3 m (Liu et al., 2011, noisy correlation to north west), 1,5 m (Li et al., 2011), 1,9 m (Tobita et al., 2011), and 2,2 m (Zhang et al., 2013).

→ Maximum lateral slip at surface in the range 1.5-3 m, that occurred on secondary segment 1c, the most mature segment of the broken fault section

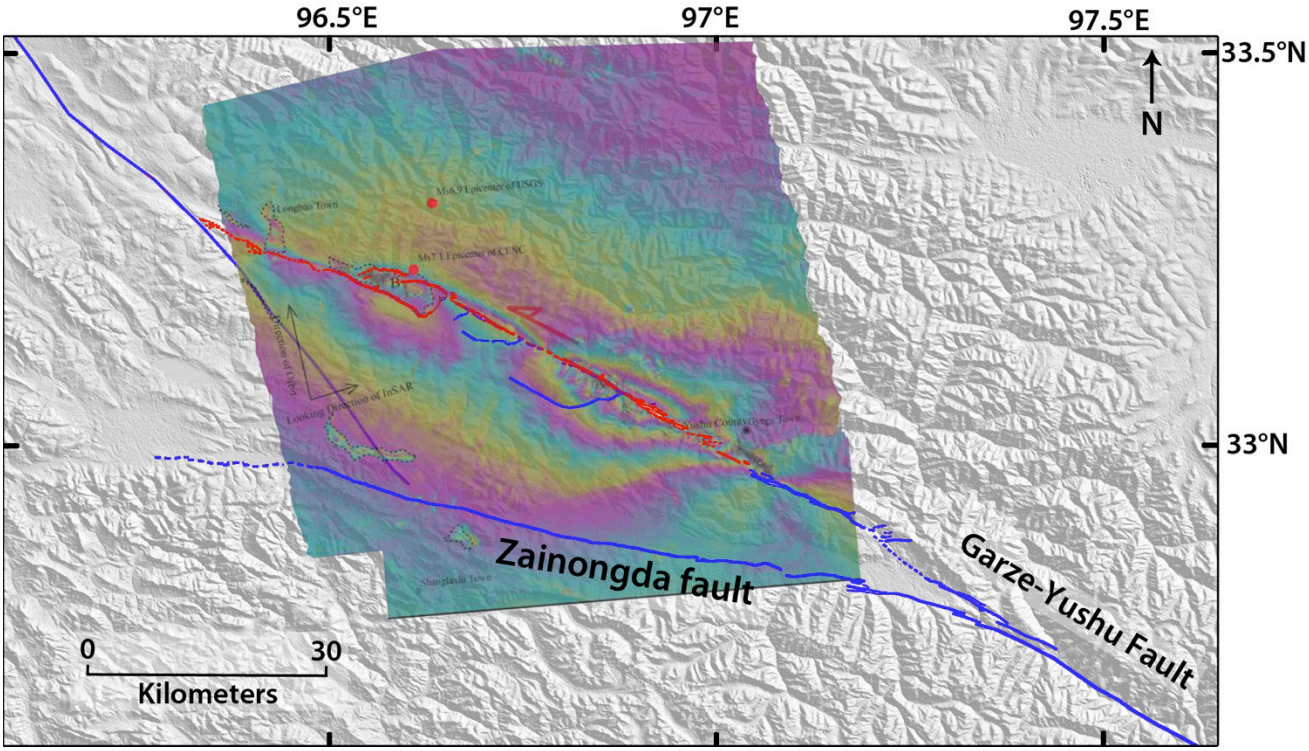


Fig.148: Radar imagery (InSAR, from Zhang et al., 2010) compared to our mapping of the surface rupture (in red).

Other source parameters:

Global CMT
Mainshock: 2010/04/13 at 23h49min46s GMT;
Lat = 33.05° Lon= 96.79°
Mw 6.9; M0 = 2.53e19 Nm; Z = 15.7 km;
Half-duration: 6.6 s
Strike, dip, slip: (210°, 67°, 178°)/ (300°, 88°, 23°)

Large Aftershock: 2010/04/14
at 01h25min18s GMT ;
Lat = 33.18° Lon= 96.53°
Mw 6.1; M0 = 1.58e18 Nm; Z = 17.9 km;
Half-duration: 2.6s
Strike, dip, slip: (296°, 65°, 2°)/ (205°, 89°, 155°)

SCARDEC
Mainshock: 2010/04/13 at 23h49m38s GMT
Lat = 33.165° Lon = 96.548° (NEIC)
Mw 6.9; M0 = 2.46e19 Nm; Z = 18 km; Duration: ~ 20s (Fig.149)
Strike, dip, rake: (120°, 79°, -4°)/ (210°, 86°, -169°)

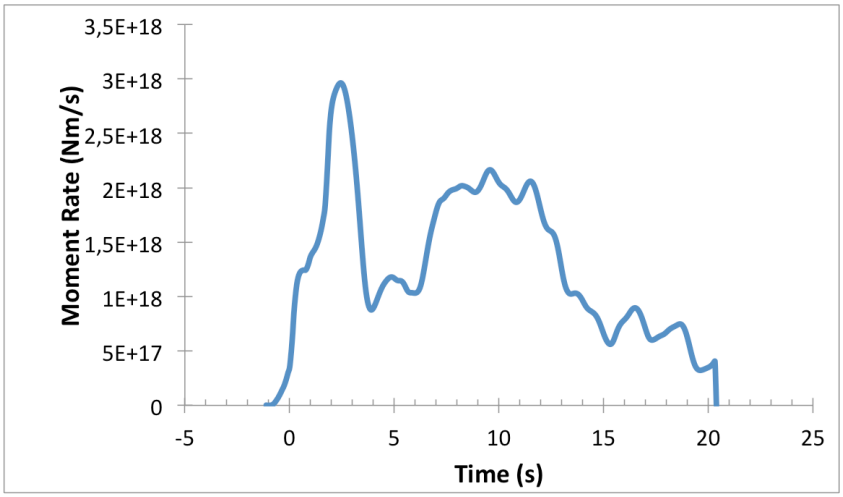


Fig.149: Mean Source Time Function calculated with the SCARDEC method from Vallée et al. (2011). See text for details.

- The EQ duration estimated with the SCARDEC method is in keeping with other estimations (e.g. Zhang et al., 2013).
- Moment magnitude and seismic moment are in fair agreement among global CMT and SCARDEC.

Three peaks are distinguished in the Source Time Function (Fig.149), suggesting the rupture of three sections of the fault. The EQ started with a strong energy release that lasted about 5 s. This might coincide with the rupture of segment 1b. Then a more moderate moment was released over the next 10 s. A last distinct phase of moment release occurred over the last 5 s. One interpretation is that the two last moment peaks coincide with the separate rupture of segments 1a and 1c. In that case, although they are of similar length, the segments would have required different times to rupture. Another interpretation is that the bilateral rupturing of segments 1a and 1c together would have produced the 10 s-long moment release peak, while the very last peak would have resulted from the abrupt rupture stop.

→ Source data suggest the rupture of a minimum of 3 distinct elements of the Garze-Yushu Fault

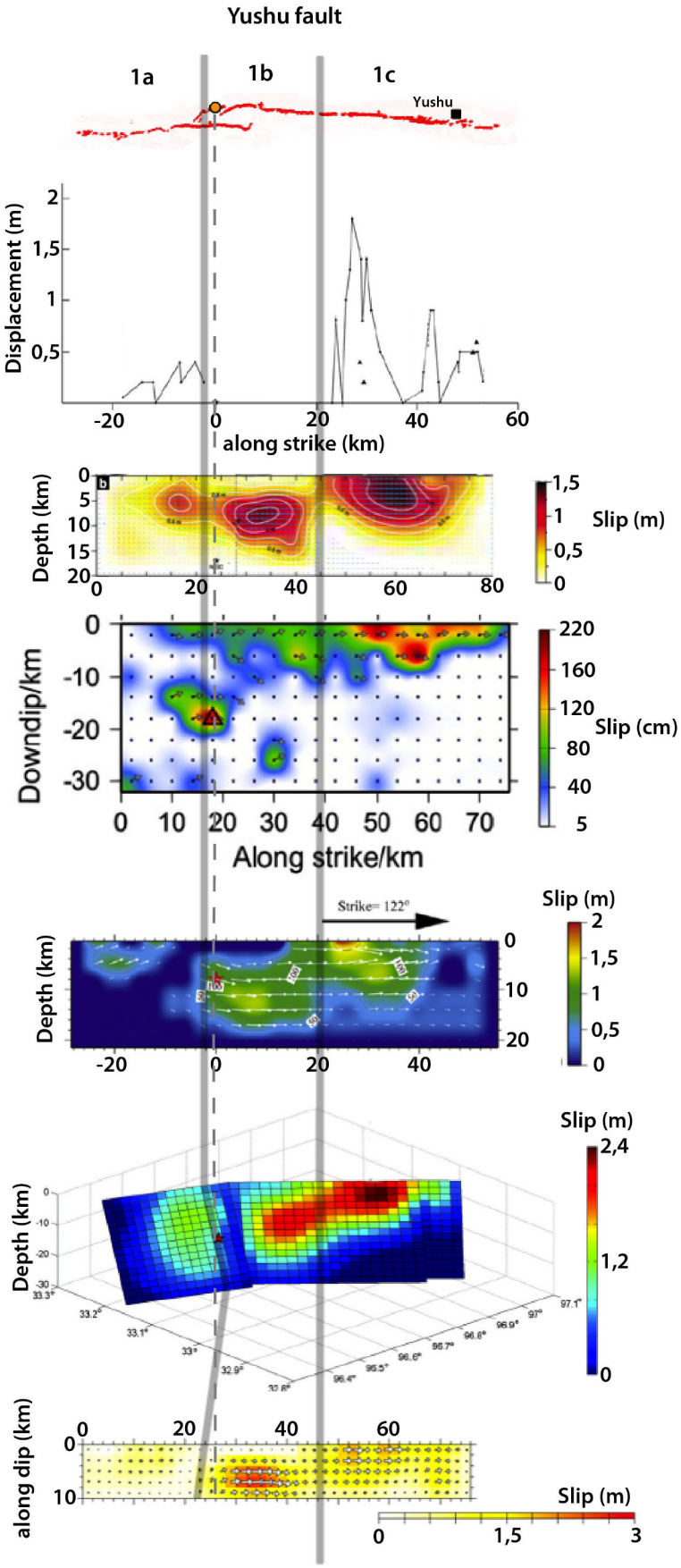
Source inversion models and slip distribution at depth (Fig.150 & 151)

- We compare five source inversion models that have been published on the 2010 Yushu earthquake (Fig.150); the grid data are available for one of them (Table 2)
- The models differ principally from the data they used and from the fault plane geometry:
    - Tobita et al. (2011): InSAR data only (PALSAR). The model divides the broken fault into 8 sections: 3 for secondary segment 1a, 2 for secondary segment 1b, 3 for secondary segment 1c.
    - Shan et al. (2011): InSAR data only (PALSAR). The model considers a single plane.
    - Li et al. (2011): InSAR data (ASAR & PALSAR). Teleseismic data and SPOT 5 image data (used to constrain the slip distribution and the fault segmentation at surface). The model divides the broken fault into 3 secondary segments in fair agreement with our mapping.
    - Qu et al. (2012): InSAR data only (ASAR & PALSAR). The model divides the broken fault into 3 sections that are different from those we mapped.
    - Zhang et al. (2013): InSAR (PALSAR), teleseismic and surface offset data. The model divides the broken fault into 5 sections: 1 for secondary segment 1a, 1 for secondary segment 1b, 3 for secondary segment 1c.

→ We consider that the models from Li et al. (2011) and Zhang et al. (2013) are the most robust for they use more different and complementary data. However both models have weak points. Li et al. (2011) take into account the fault segmentation observed at surface. However the maximum displacement that they infer at depth is lower than the maximum lateral displacement measured at surface (Fig.151). This suggests that the model is not fully appropriate. Zhang et al. (2013) produce a more realistic maximum lateral slip, but the fault segmentation that they impose in the model is not coincident with that observed at surface.

→ All models produce a similar slip distribution (mainly because InSAR data are used in all the inversions), with 2 main slip patches coinciding with slip on secondary segments 1b and 1c: one patch near the surface (~ first 5 km) in Yushu area (segment 1c), the other one at a greater depth (up to 10-15 km) near the hypocenter. Another patch of lower slip (0.5-1 m) is found coinciding with segment 1a. In all the models, the majority of the slip is distributed between 0 and 15 km depth.

→ The source inversion models suggest: L 75-80 km, Dmax at depth 2.4 m, 3 segments broken.



This study : Mapping of the surface rupture from Google earth, SPOT 5 images and litterature.
3 segments, L ≈ 75-80 km

Li et al. 2012 : Co-seismic slip profile measured at surface

Li et al. 2011 :
Data : InSAR (SAR et PALSAR), teleseismic and SPOT 5 images
L= 80 km ; W=20 km ; Dmax=1,5m < D surface.

Zhang et al. 2013 :
Data : InSAR + Teleseismic + Surface offsets
L= 76 km ; W≈22 km (model=32 km) ; Dmax=2,2 m

Shan et al. 2011 :
Data : InSAR (PALSAR)
L= 84 km ; W=21 km ; Dmax= 1,6 m < D surface

Qu et al. 2011 :
Data : InSAR (C and L bands, ENVISAT/ASAR ; ALOS/PALSAR)
L= 72 km ; W=30 km ; Dmax=2,4 m

Tobita et al. 2011 :
Data : InSAR (PALSAR)
L= 73km ; W=10 km ; Dmax=2,6 m near the hypocenter and 1,9 m near the surface (NW of Yushu)

Fig.150: Comparison between different inversion models published on the 2010 Yushu earthquake. Grey vertical lines represent the intersegment zones hilighted in our mapping. The dotted line shows the hypocenter location for each model. Models are at the same scale.

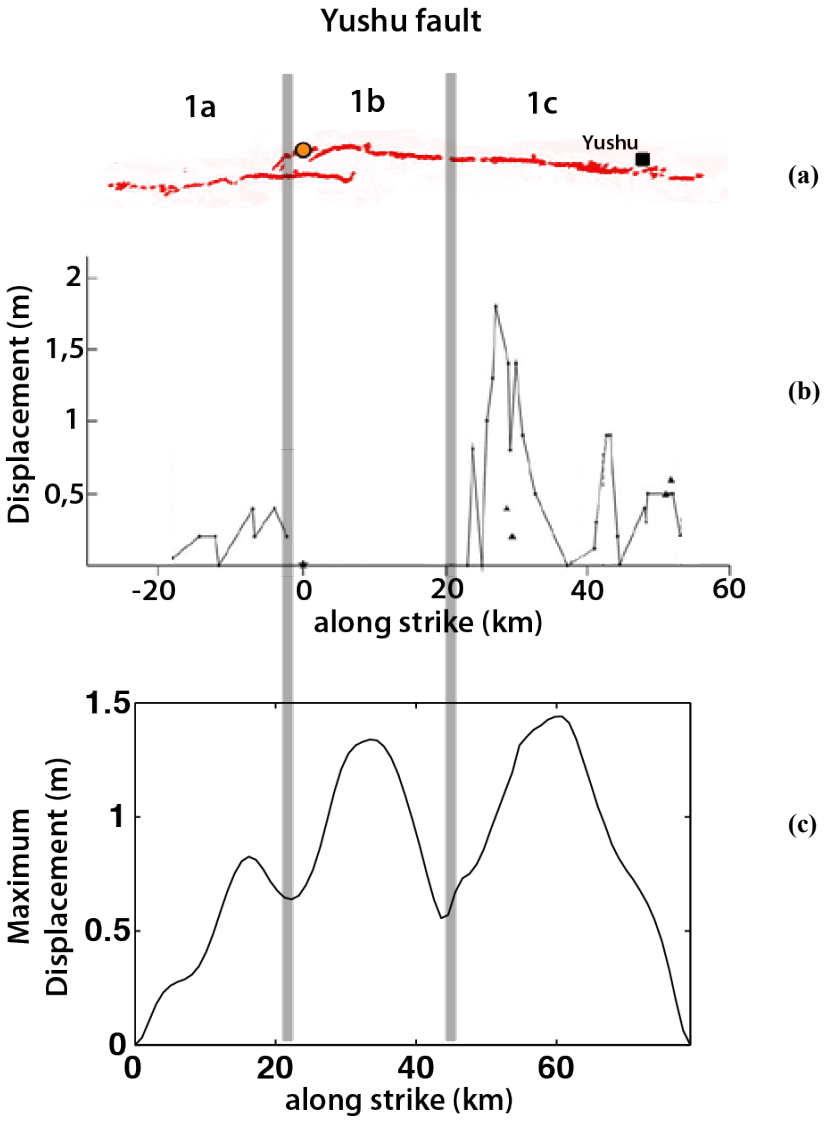


Fig.151: (a) Surface rupture trace, from Fig.145 and 146 ; (b) lateral slip-length profile measured at surface (Li et al., 2012) ; (c) profile of maximum slip inferred at depth from the source model of Li et al. (2011) (See Fig.150) . Grey vertical bars represent the intersegment zones.

Other information:

2010 EQ:

- A large aftershock (Mw 6.1) occurred 2 h after the mainshock and 10 km to the NW. It is difficult to distinguish the two events from direct observational data (field, InSAR) and to quantify the contribution of the aftershock in the rupture of the secondary segment 1a.
- Aftershocks are localized in the range 0-20 km depth and are mainly concentrated at the NW tip of secondary segment 1a and in the intersegment zone between segments 1a and 1b (Wang et al., 2013).

- Tobita et al. (2011) show that postseismic deformation was mainly observed NW of the pull apart basin (between secondary segments 1a and 1b) where the surface rupture is less clearly expressed.

Past EQ activity :

- The 2010 Yushu earthquake is one of the large earthquakes that occurred in North Tibet in the last 20 years (Manyi 1997, Kunlun 2001, Sichuan 2008, Lushan 2013).
- The Garze-Yushu Fault seems to have broken entirely during the last 300 years: the Mw 7.5 earthquake in 1738 seems to have broken the major segment 1 (the EQ would have occurred at ~the same location as the 2010 event), the Mw 7.3 earthquake in 1854 apparently broke the major segments 3 & 4, the Mw 7.7 earthquake in 1866 apparently broke the small "gap" between the Garze Yushu and Xianshuihe Faults, the Mw 7.3 earthquake in 1896 apparently broke the major segment 2. The 2010 Mw 6.9 earthquake re-broke part of the major segment 1 (e.g. Wen et al., 2003; Chen et al., 2010). However the location of the ruptures is not well constrained (this might explain the 'paradox' in the Mw versus supposed length of broken section)
- Paleoseismological trenches on major segment 2 reveal five paleoseismic events in the past 5000 BP, having occurred with a recurrence interval of ~ 400 yr (Zhou et al., 2013)

Parameters retained to describe the 2010 Yushu earthquake (Tables 2 – 4):

Mw ~6.9; M0 ~ 2,5^{e}19 Nm; L 75-80 km; W ~ 20 km; Dmax surface 1.5-3 m; Dmax depth 2.4 m (seems to be underestimated compared to surface measurements); Duration ~ 20 s; Hypocentre: Z ~ 13 km

Number of segments broken on the Garze-Yushu Fault: 1 major segment, partly; representing the rupture of 3 secondary segments.

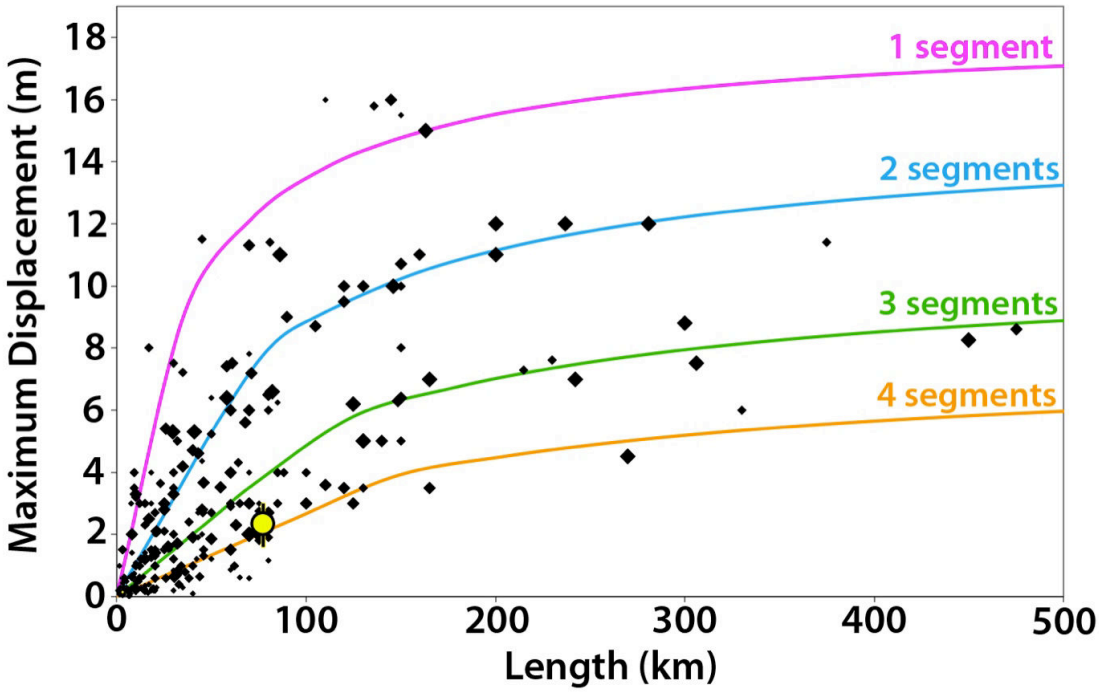


Fig.152: Earthquake displacement-length data measured at surface for 260 historical large continental earthquakes (Mw≥6). The 4 curves indicate the number of major long-term fault segments to have been broken by the earthquakes (modified from Manighetti et al., 2007 and chapter IV). Yellow dot shows the Yushu earthquake surface slip length data..

The surface and depth slip-length data of the Yushu earthquake fall on either the third or the fourth curve of the scaling graph (Fig.152 & 153), in keeping with the rupture of 3 segments of the fault. Yet the broken segments are here of secondary scale, not major segments.

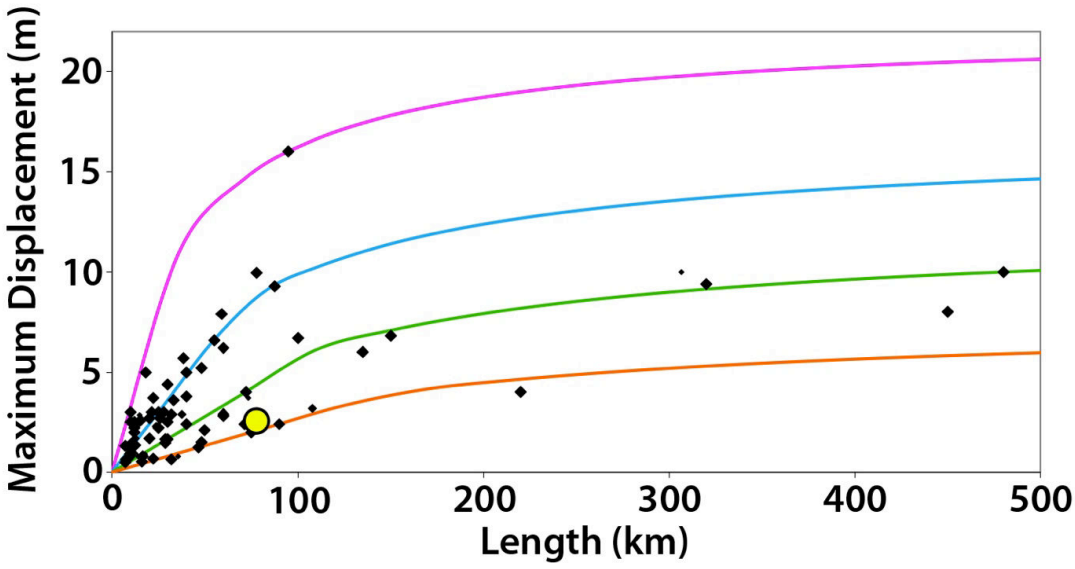


Fig.153: Earthquake displacement-length data deduced from inversion model at depth for 90 historical large continental earthquakes (Mw≥6). The 4 curves indicate the number of major long-term fault segments to have been broken by the earthquakes (modified from Manighetti et al., 2007 and Chapter IV). Yellow dot shows the Yushu earthquake depth slip-length data.

References

Allen, C.R., Qian, H., Wen, X., Zhou, H., & Huang, W. (1991). Field study of a highly active fault zone: The Xianshuihe Fault of southwestern China. *Geological Society of America Bulletin*, **103**, 1178–1199.

Chen, L., H. Wang, Y. Ran, X. Sun, G. Su, J. Wang, X. Tan, Z. Li, and X. Zhang (2010). The MS7.1 Yushu earthquake surface rupture and large historical earthquakes on the Garzê-Yushu Fault. *Chinese Sci Bull*, **55**, 3504−3509, doi: 10.1007/s11434-010-4079-2

Manighetti, I., M. Campillo, S. Bouley, and F. Cotton (2007), Earthquake scaling, fault segmentation, and structural maturity, *Earth Planet. Sci. Lett*., **253**, 429-438, doi:10.1016/j.epsl.2006.11.004

Li, Z., J. R. Elliott, W. Feng, J. A. Jackson, B. E. Parsons, and R. J. Walters (2011). The 2010 MW 6.8 Yushu (Qinghai, China) earthquake: Constraints provided by InSAR and body wave seismology*, J. Geophys. Res*., 116, B10302, doi:10.1029/2011JB008358.

Li, C.-Y., Pang, J.-Z. and Zhang Z.-Q. (2012). Characteristics, Geometry, and Segmentation of the Surface Rupture Associated with the 14 April 2010 Yushu Earthquake, Eastern Tibet, China. *Bulletin of the Seismological Society of America*, **102**, 4, 1618–1638, doi: 10.1785/0120110261

Lin, A., G. Rao, D. Jia, X. Wu, and Z. Ren (2011). Co-seismic strike-slip surface rupture and displacement produced by the 2010 Mw 6.9 Yushu earthquake, China, and implications for Tibetan tectonics, *J. Geodyn.* **52**, 249–259.

Liu, Y. H., Shan, X. J., Qu, C. Y., and Zhang, G. F. (2011). Earthquake deformation field characteristics associated with the 2010 Yushu Ms7.1 earthquake. *Sci China Earth Sci*, **54**, 571–580, doi: 10.1007/s11430-010-4116-7

Qu, C., Zhang, G., Shan, X., Zhang, G., Song, X., Liu, Y. (2012). Coseismic deformation derived from analyses of C and L band SAR data and fault slip inversion of the Yushu Ms7.1 earthquake, China in 2010. *Tectonophysics* **584**, 119–128

Shan, B., Xiong, X., Zheng, Y., Wei, S., Wen, Y., Jin, B., Ge, C. (2011). The co-seismic Coulomb stress change and expected seismicity rate caused by 14 April 2010 Ms=7.1 Yushu, China, earthquake. *Tectonophysics* **510**, 345–353

Tapponnier, P., Z. Xu, F. Roger, B. Meyer, N. Arnaud, G. Wittlinger, and J. Yang (2001). Oblique stepwise rise and growth of the Tibetan Plateau, *Science* **294**, 1671–1677.

Tobita, M., T. Nishimura, T. Kobayashi, K. X. Hao, and Y. Shindo (2011). Estimation of coseismic deformation and a fault model of the 2010 Yushu earthquake using PALSAR interferometry data, *Earth Planet. Sci. Lett*. **307**, 430–438.

Vallée, M., J. Charléty, A.M.G. Ferreira, B. Delouis, and J. Vergoz, (2011). SCARDEC : a new technique for the rapid determination of seismic moment magnitude, focal mechanism and source time functions for large earthquakes using body wave deconvolution, *Geophys. J. Int*., **184**, 338-358.

Wang, E., & Burchfiel, B.C. (2000). Late Cenozoic to Holocene deformation in southwestern Sichuan and adjacent Yunnan, China, and its role in formation of the southeastern part of the Tibetan Plateau: *Geological Society of America Bulletin*, **112**, 413–423.

Wang, S., Fang, X., Zheng, D. and Wang, E. (2009). Initiation of slip along the Xianshuihe fault zone, eastern Tibet, constrained by K/Ar and fission-track ages. *International Geology Review*, **51**, 12, 1121-1131

Wang W L, Wu J P, Fang L H & Wang C Z (2013) Relocation of the Yushu MS7.1 earthquake and its aftershocks in 2010 from HypoDD. *Science China: Earth Sciences*, **56**, 182–191, doi: 10.1007/s11430-012-4450-z

Wen, X., Xu, X., Zheng, R., Xie, Y., & Wan, C. (2003). Average slip-rate and recent large earthquake ruptures along the Ganzi–Yushu Fault: *Science in China Series D*, **46**, 276–288.

Zhang, Y., Yao, X., Xiong, T., Ma, Y., Hu, D., Yang, N. & Guo, C. (2010). Rapid Identification and Emergency Investigtion of Surface Ruptures and Geohazards Induced by the Ms 7.1 Yushu Earthquake. *Acta Geologica Sinica* (English Edition), **84,** 6, 1315-1327

Zhang, G., Shan, X., Delouis, B., Qu, C., Balestra, J., Li, Z., Liu, Y. and Zhang, G. (2013). Rupture history of the 2010 Ms 7.1 Yushu earthquake by joint inversion of teleseismic data and InSAR measurements. *Tectonophysics* **584**, 129–137

Zhou, R., Li, Y., Liang, M., Xu, X., He, Y., Wang, S., Ma, C., and Liu, Y. (2013). Determination of mean recurrence interval of large earthquakes on the Garzê-Yushu Fault (Dengke Segment) on the eastern margin of the Qinghai–Tibetan Plateau, *Quaternary International*, Available online 12 December 2013, ISSN 1040-6182, http://dx.doi.org/10.1016/j.quaint.2013.11.010.

2.20. Historical earthquakes on the North Anatolian Fault: 1939 Erzincan, 1943 Tosya, 1944 Bolu Gerede, 1999 Izmit and 1999 Duzce earthquakes

I did not get the time to analyze in great details in the literature the large historical EQs which broke the North Anatolian Fault (later referred to as NA) in the period 1939-1999. However, I mapped the entire North Anatolian long-term fault whose trace is clear in the morphology and topography (use of Landsat, SRTM, and Google Earth images), and I reported the major earthquake ruptures, whose traces were well mapped by Barka (1996).

From this first-order work, I derive a few interesting observations:

- The NA Fault is more than 1300 km long and slips at a fast long-term and current lateral rate (~30 mm/yr; e.g. Sengor 1979; Hubert-Ferrari 2002). It is thus a mature fault.
- The NA Fault is associated with multiple secondary oblique faults, most of them are splay faults developed as the NA Fault was propagating westward. Note that the westward sense of propagation is attested from independent features than the splays (decrease in cumulative offsets and age of the fault offsets becoming younger toward the west, e.g., Armijo et al., 1999, 2005; Hubbert-Ferrari et al., 2002, 2003). The faults, which broke during the Izmit and the Duzce EQs, are secondary splays developed at the western tip of major segment 4 (See below Fig.154).
- The NA Fault started to develop and propagate westward from its connection zone with the East-Anatolian Fault, in the east.
- The NA Fault is divided into 5 major fairly collinear segments, of similar length, 200-280 km. The most mature of these segments are those in the east.

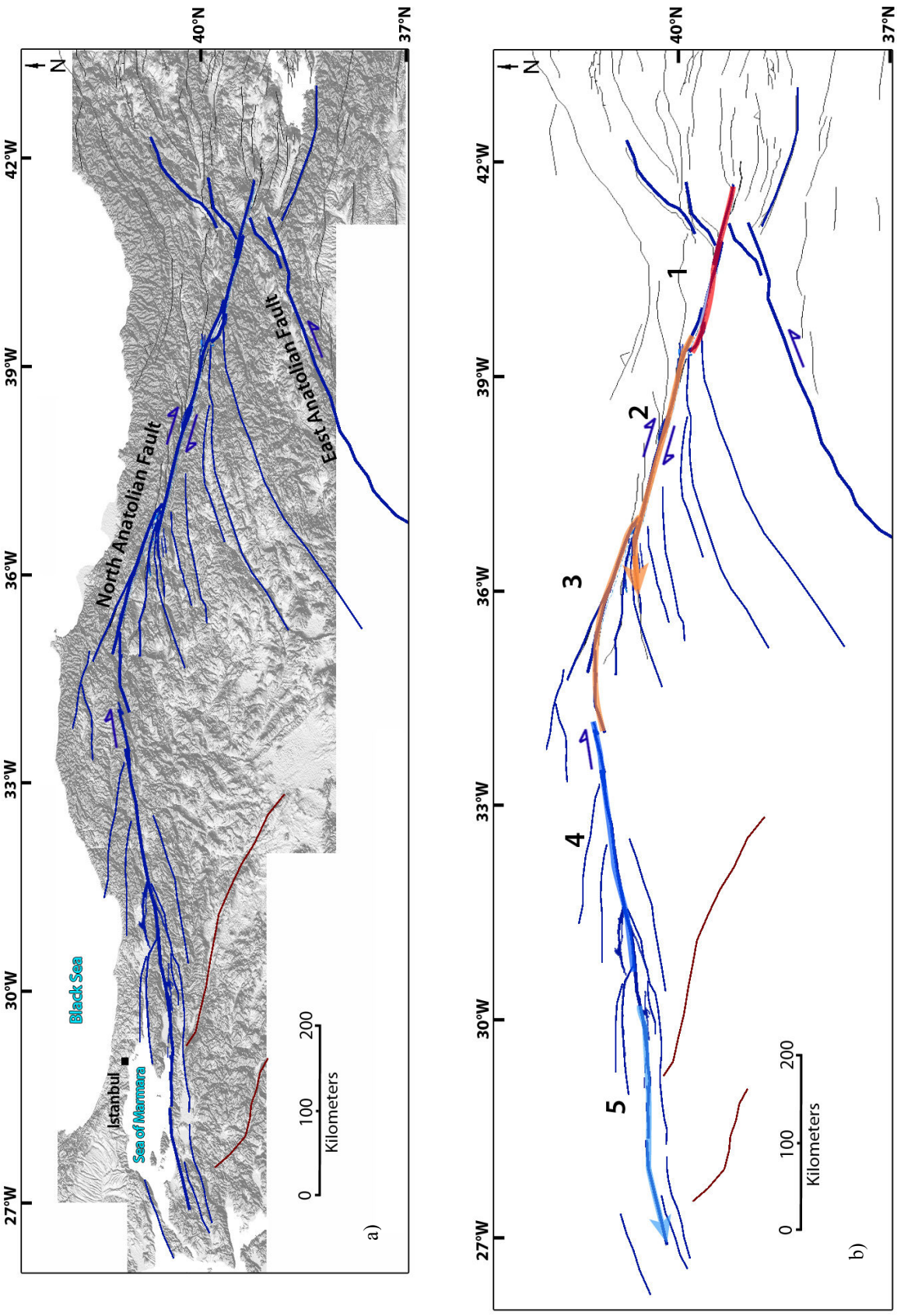


Fig.154: (a) Large scale mapping of the North Anatolian Fault and associated secondary faults (in blue). In brown are ancient faults now offset by the NA Fault. b) Identification of the major segments that form the NA Fault (numbered 1 to 5 from east to west).

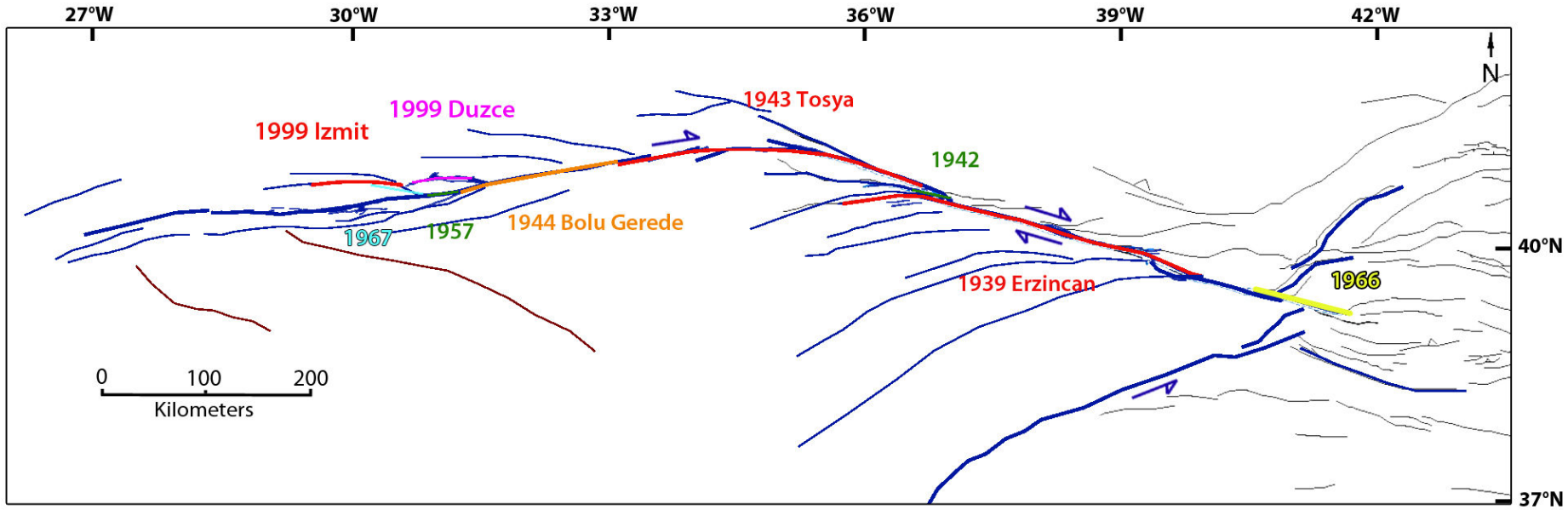


Fig.155:. Surface ruptures of the major historical large EQs on the NA fault, in the period 1939-1999, discriminated with colors. The rupture traces are taken from the literature (Barka 1996), and they well coincide with my fault mapping.

- Actually, the fault divides into two parts about a central bend in its trace. East of the central bend, the major segments 1, 2 and 3 have a linear trace and are fairly well connected to each other. West of the bend, the trace of major segment 3 becomes more discontinuous whereas major segments 3 and 4 are not fully connected at the ground surface. Major segments 4 and 5 also are separated by a fairly large step-over. Together these are in keeping with the major segments of the NA Fault becoming younger and hence more immature toward the west, and especially in the western half of the fault.
- **The 1939 Erzincan EQ** broke 1 major segment only of the NA Fault, major segment 2. It broke it entirely, in effect rupturing the 3 secondary segments 2a, 2b, and 2c that form it (Fig.156). The surface slip-length data of the Erzincan EQ (Dmax ~7.5 m; L ~305 km) are in keeping with the EQ having broken 3 segments on the NA Fault (here secondary, see discussion in Chapter V). The slip profile is triangular and asymmetric overall (Fig.156), and the maximum slip occurred at the eastern end of major segment 2, that is on the most mature section of the broken zone.

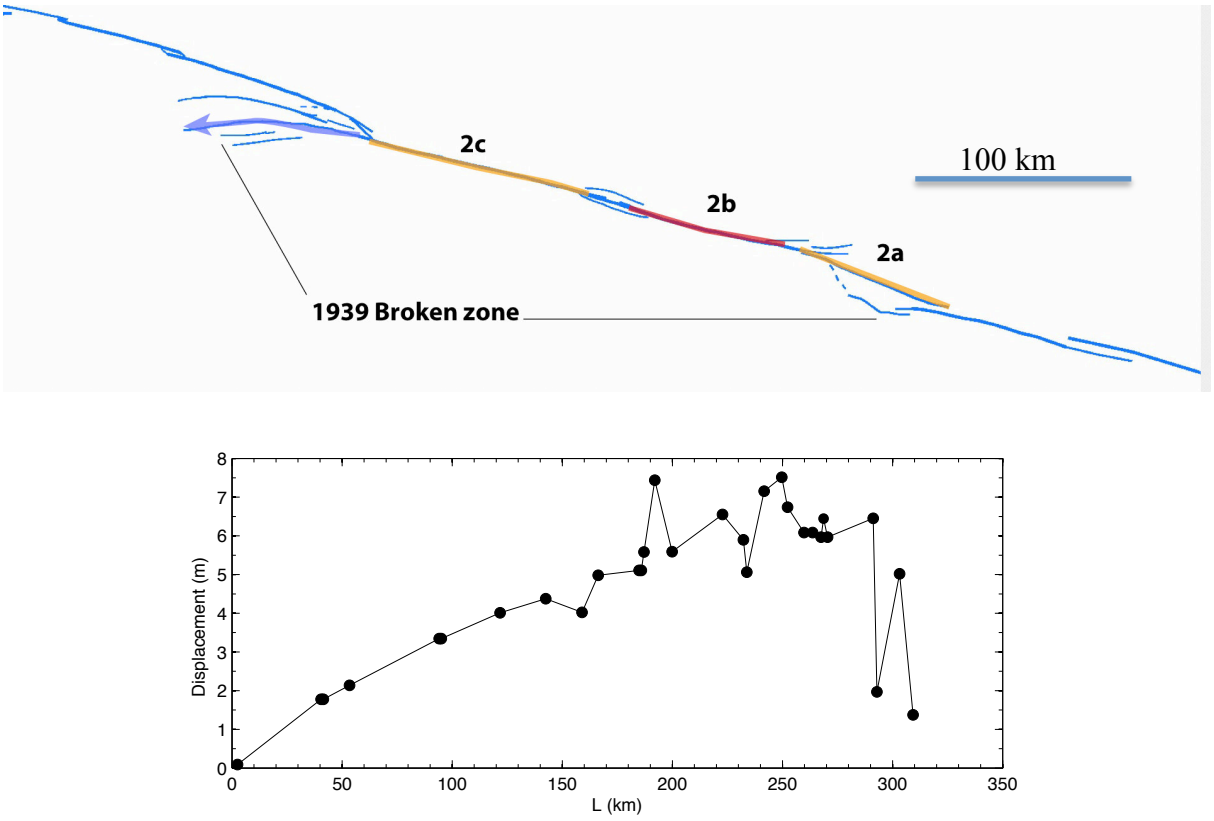


Fig.156. 1939 Erzincan earthquake : rupture trace reported on the fault segments I have mapped and surface slip profile from Barka 1996. The colors suggest the differential maturity of the segments, red for more mature. The arrow indicates the direction of long-term lateral propagation.

- **The 1943 Tosya EQ** broke 1 major segment only of the NA Fault, major segment 3. It broke it entirely, in effect rupturing the 4 secondary segments 3a, 3b, 3c and 3d that form it (Fig.157). The surface slip-length data of the Tosya EQ (Dmax ~4.5 m; L ~270 km) are in keeping with the EQ having broken 4 segments on the NA Fault (here secondary). The slip profile is fairly triangular and asymmetric overall, although not very well constrained (Fig.157). The maximum slip seems to have occurred at the western end of major segment 3, which might be the most immature section of the broken segment, unless the central major segment 3 of the NA Fault had a bilateral propagation in between the two half sections of the NA Fault.

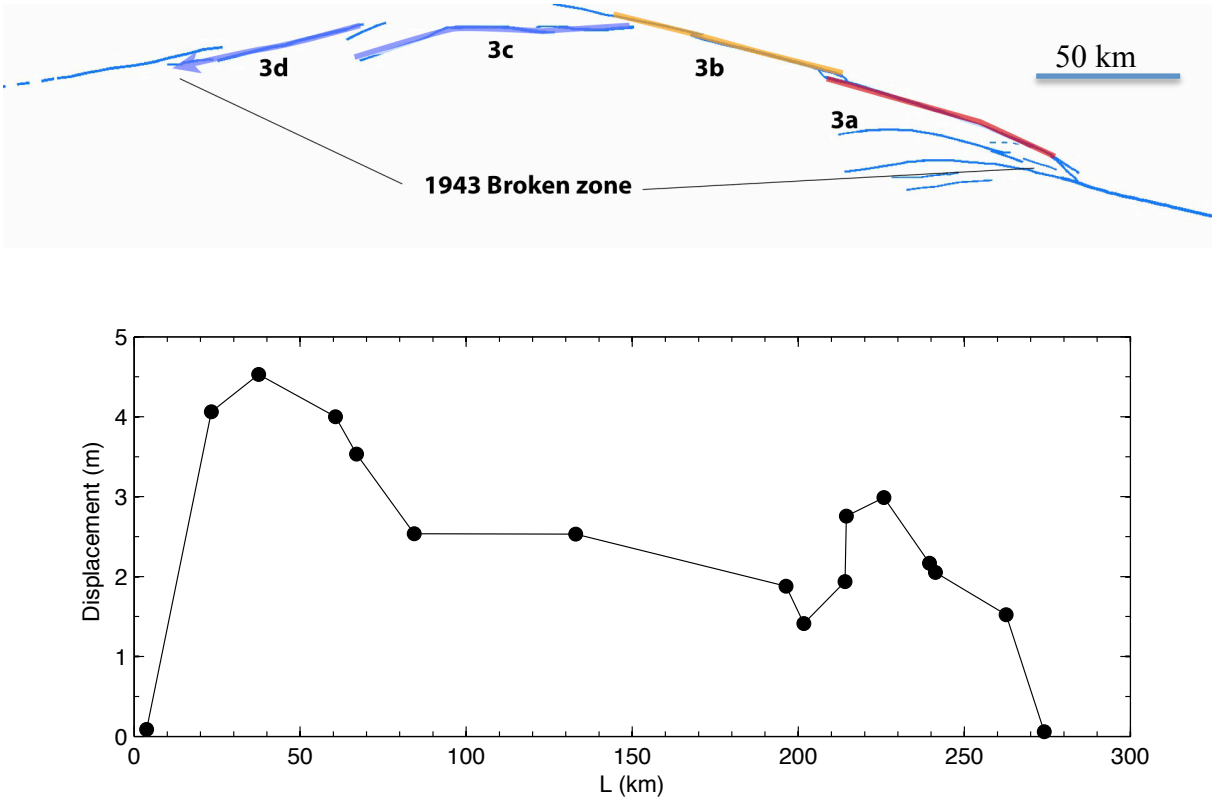


Fig.157: 1943 Tosya earthquake : rupture trace reported on the fault segments I have mapped and surface slip profile from Barka 1996. The colors suggest the differential maturity of the segments, red for more mature. The arrow indicates the direction of long-term lateral propagation

- **The 1944 Bolu Gerede EQ** broke 1 major segment only of the NA Fault, major segment 4. It broke it almost entirely, in effect rupturing 3 out of the 4 secondary segments that form it (Fig.158). The surface slip-length data of the Bolu Gerede EQ (Dmax ~4.5 m; L ~165 km) would rather suggest that the EQ broke the 4 secondary segments of the major segment 4, but the rupture mapping is not clear enough to determine whether 3 or 4 secondary segments broke. The slip profile is not well constrained either.

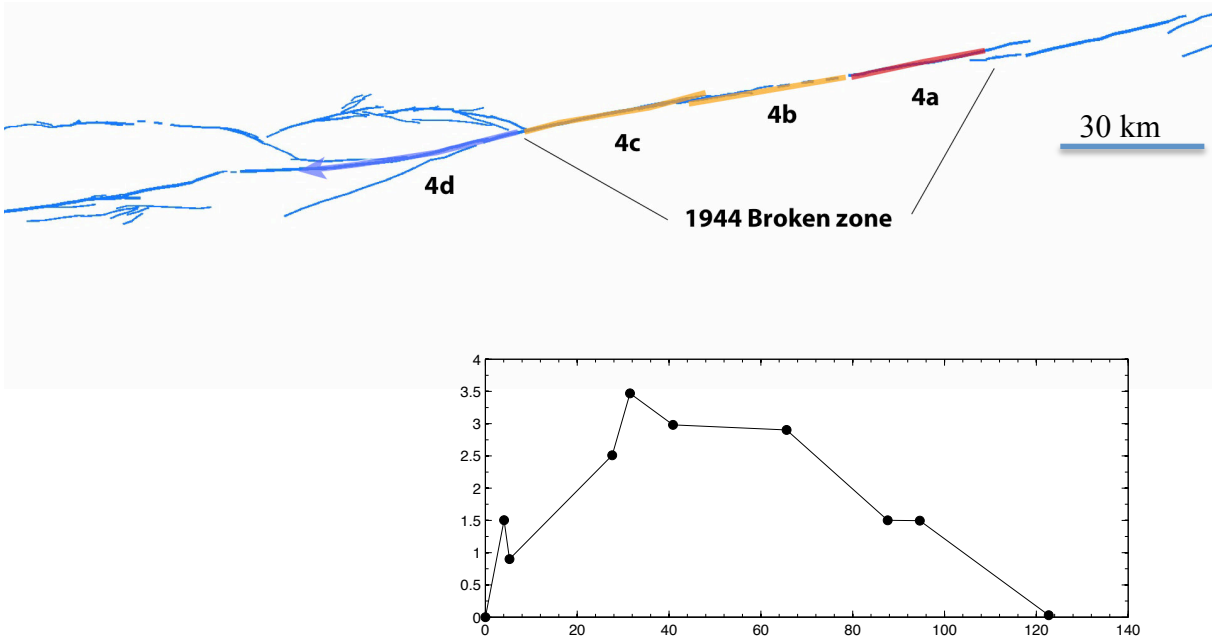


Fig.158: 1944 Bolu Gerede earthquake : rupture trace reported on the fault segments I have mapped and surface slip profile from Barka 1996. The colors suggest the differential maturity of the segments, red for more mature. The arrow indicates the direction of long-term lateral propagation

- Since **the ruptures in 1942, 1957, 1966 and 167** were much smaller, I could not confidently report their traces on my fault map

- **The 1999 Izmit EQ** broke a small secondary splay fault of the NA Fault, which I will call the "Izmit splay fault". The Izmit splay fault actually developed at the western tip of major segment 4, likely as a result of the westward propagation of the major segment 4. The Izmit splay fault is ~110 km long but it might extend a bit further west under the Marmara sea. The Izmit splay fault is divided into 4 major fairly collinear segments of similar length, ~25 km, the most mature are likely to the east since the fault has been propagating westward over the long-term (as its master NA Fault). The Izmit EQ broke the 3 easternmost and hence most mature major segments of the Izmit splay fault, major segments 1, 2 and 3. The surface slip-length data of the Izmit EQ (Dmax ~ 5 m, L ~100-120 km) are in keeping with the EQ having broken 3 segments of the Izmit splay fault. The slip profile at surface (Fig.159) is triangular and asymmetric overall, with maximum slip at the eastern end of the Izmit splay fault, that is in the most mature part of the fault. The EQ nucleated nearby the connection zone between major segments 2 and 3, where the Izmit Fault connects with oblique normal faults.

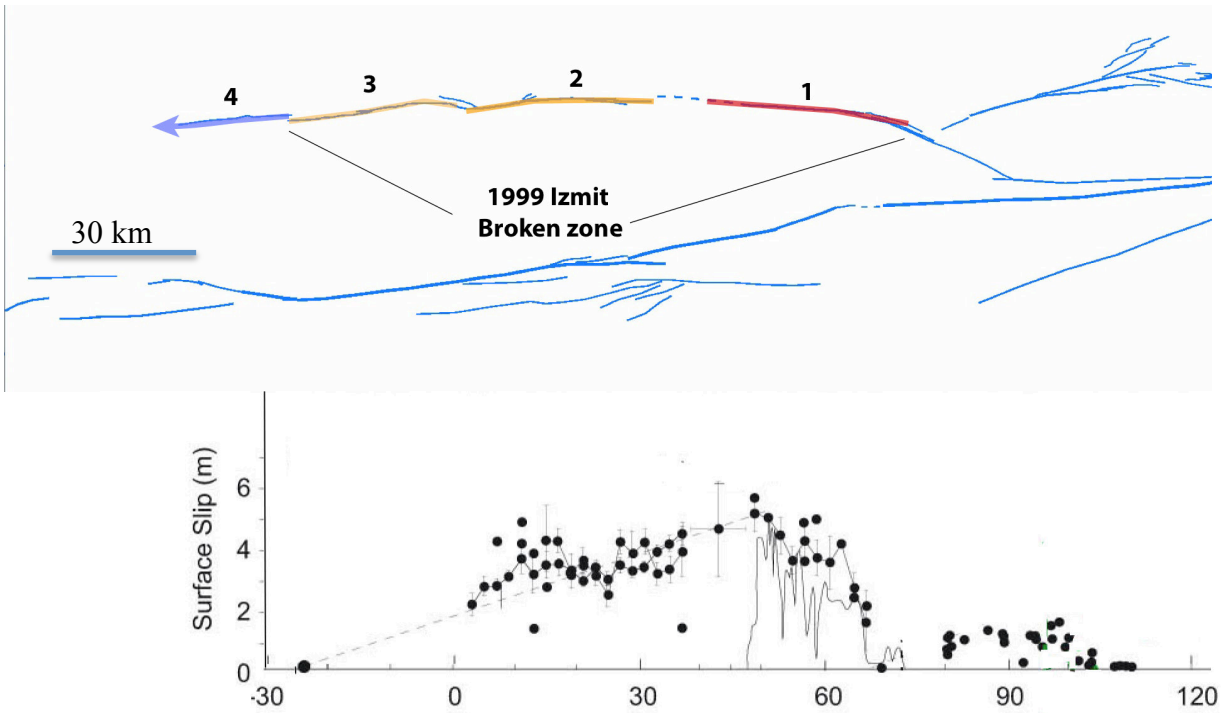


Fig.159: 1999 Izmit earthquake : rupture trace reported on the fault segments I have mapped (long-term NA Fault indicated in blue; See Fig.154) and surface slip profile from Michel and Avouac 2002 . The colors suggest the differential maturity of the segments, red for more mature. The arrow indicates the direction of long-term lateral propagation

- **The 1999 Duzce EQ** broke a small secondary fault extending between the NA Fault and the Izmit splay fault. I will call this fault the "Duzce Fault". The Duzce Fault is ~100 km long, and has a curved trace. It is flanked and associated with multiple secondary oblique faults which overall architecture suggests they might be small splay faults of the Duzce Fault, attesting from its eastward long-term propagation (Fig.160). The Duzce Fault is divided into 3 major fairly collinear segments (their mean strike is rotating clockwise however from west to east) of similar length, ~40 km, the most mature are thus likely to the west. The Duzce Fault terminates in the east in a splaying fault network. The Duzce EQ broke 1 of the major segments of the Duzce Fault, major segment 3. It broke it entirely, in effect rupturing the two secondary segments that form it. The surface slip-length data of the Duzce EQ (Dmax ~ 5,3 m, L ~40-50 km) are in keeping with the EQ having broken 2 segments of the Duzce Fault (yet those are here of small scale). The EQ nucleated nearby the connection zone between segments 3a and 3b where multiple oblique small faults are observed. The slip profile at surface is fairly triangular and symmetric (Fig.160).

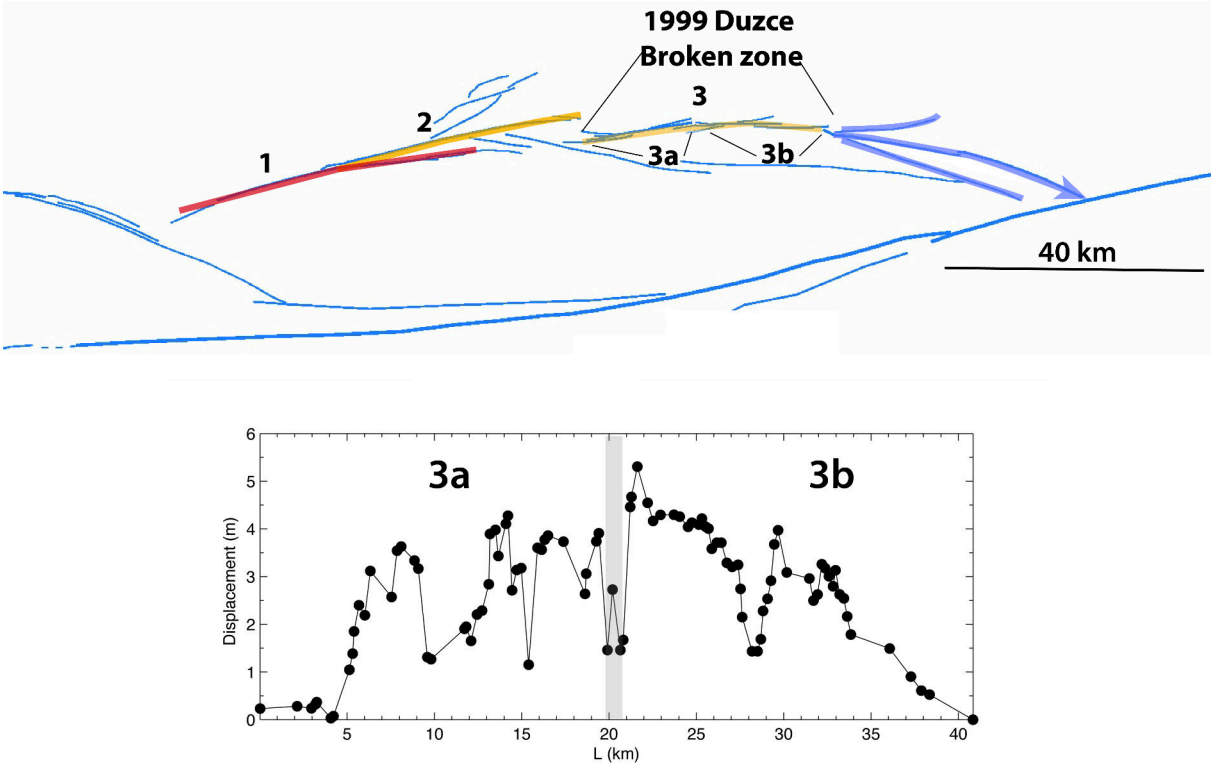


Fig.160: 1999 Duzce earthquake : rupture trace reported on the fault segments I have mapped (long-term NA fault indicated in blue; See Fig.154) and surface slip profile from Duman et al 2005. The colors suggest the differential maturity of the segments, red for more mature. The arrow indicates the direction of long-term lateral propagation

3. Other Faults and Earthquake data

In addition to the faults and EQs couples, which I have analyzed in detail, I have also compiled from the literature and analyzed data on many more EQs.

As a said earlier, I focused mainly on certain static source EQ parameters:

- Slip-length profiles along historical ruptures measured at the surface → information related to these slip length profiles are compiled in Table 1 (rupture length, maximum coseismic slip, degree of asymmetry of the slip profile, etc) ;
- Slip-length profiles along historical ruptures inferred from source inversion models (for which we use available grid data) with other static EQ source parameters (Mw, M0, W, Duration, etc) are reported in Table 2

Altogether, I gathered the types of data above for 71 EQs having occurred in the period 1857-2011, 80 % are continental EQs with Mw in range 5.5-8.1 (70 % strike-slip, 18% reverse, 12% normal), and 20 % are subduction EQs with Mw in range 6.8-9.2.

- Maximum coseismic versus rupture length data: this information is fairly dense for historical EQs, acquired at the ground surface and inferred from source inversion models. The

available Dmax-L values are reported in Tables 3 and 4, along with a quality factor to qualify the robustness of surface data. The data in Tables 3 and 4 thus combine information on the ~70 large historical EQs described above and on ~230 additional continental EQs worldwide for which only these surface slip-length data are available in the literature. These EQs have occurred in the period mainly 1500-2011, have Mw in range 4.6-8.6, and include ~70% of strike-slip, ~15% of reverse, and ~15% of normal ruptures (all data from surface measurements).

- Properties of long-term faults –those analyzed in detail but also other faults worldwide, are gathered in Table 5. More precisely, I have extracted from the literature tectonic data describing some of the major properties of ~50 of the long-term faults broken in the above EQs (including the long-term faults already described in the IDs), such as the total fault length, the maximum cumulative slip, the age of initiation of the fault, the fault slip rate. From this first-order tectonic information, I have derived a qualitative estimate of the structural maturity of the faults, as reported in the Table 5.

Note that the size and nature of the major inter-segments along the faults I have analyzed are reported in Table 6.

4. Short, preliminary synthesis

Further insights on the lateral segmentation of long-term faults

Fig.161 a & b show the number of major and secondary fault segments that I identified from my mapping of the long-term faults (See Fig.20, IDs of Chapter II and Table 5). More than 80% of the faults that I have mapped are divided in 4 ± 1 major segments, whereas more than 60% of these major segments are formed by 3-4 secondary segments. My analysis thus confirms results already suggested by Manighetti et al. (2009): independent on their size, slip mode and context, long-term faults are divided laterally into a similar number of major segments, in the range 3-5, whereas it seems that major fault segments are themselves divided into 3-4 secondary segments (Manighetti et al., 2013).

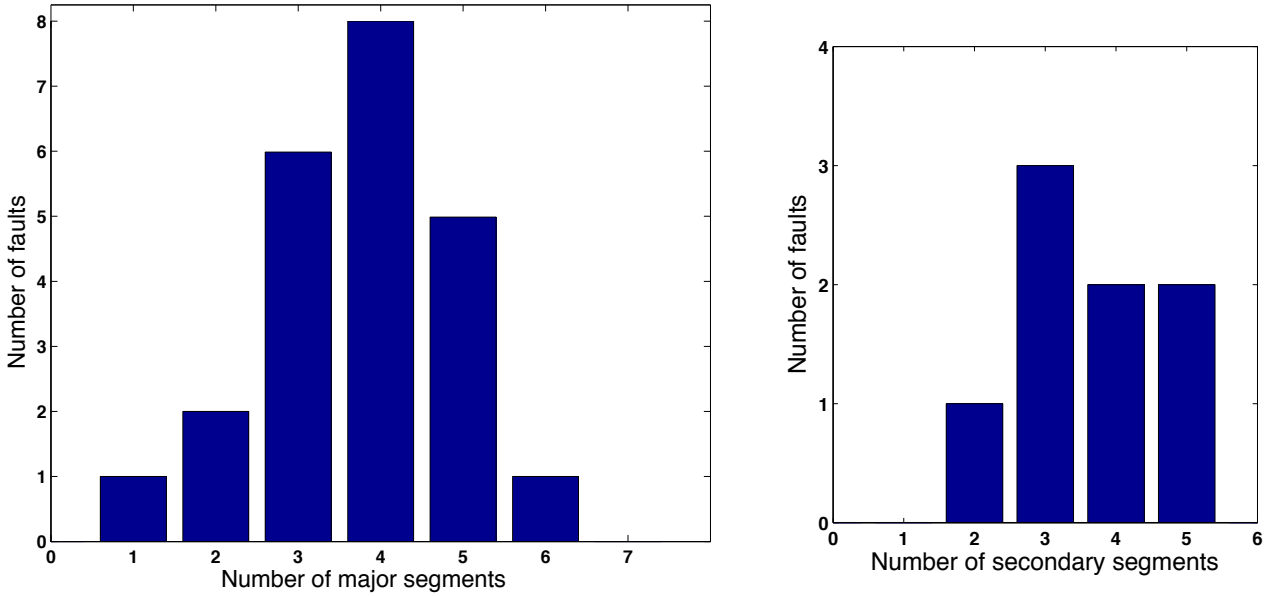


Fig.161: a) Number of major segments and b) number of secondary segments along the faults that I have mapped in the IDs of Chapter II (See also Table 5).

Further insight on long-term fault propagation

The majority of the faults that I have analyzed revealed to be associated with secondary fault networks that suggest their direction of long-term propagation. In particular, most master faults are associated with splay faults, and the geometry of these splay faults is a good indicator of the direction of propagation of the master fault over the long-term. Our work additionally shows that splay faults exist on most faults, whether those are mature or immature, and independent of their slip mode. Models of dynamic rupture have suggested so far that splay faults should develop on faults capable of supershear rupture (see references in Robinson et al., 2010). As we will discuss it later in the manuscript, we expect that those faults capable of supershear ruptures are mature faults; splays would thus preferentially develop on mature faults. Our observations suggest that it might not be the case, since splay faults are observed on most faults, independent on their degree of maturity.

Further insights on fault structural maturity

Our detailed analyses (IDs) show that the fault structural maturity exerts a significant control on the EQ ruptures. I develop this point in the following chapters.

The collected data also allow further defining what is the structural maturity. In the following, two groups of figures are shown, one group built on the basis of the best constrained fault data that I described in the previous IDs (figures labeled a), and one group built from the ID data along with other fault data extracted from the literature and compiled in Table 5 (figures labeled b). Note that the faults are considered independent on their slip mode. The fault maturity is defined in 4 classes in the IDs data, whereas it is more grossly defined in 3 classes in the collective IDs and other data. Because the maturity has been defined in both the IDs and Table 5 from one or a few of the parameters examined below (fault length, age, maximum cumulative slip, slip rate), it is expected that some relations are found between these parameters and the fault structural maturity. However, rare are the faults where the 4 parameters could be considered. Furthermore, it is important to verify that the maturity classes that we used, based on those defined by Manighetti et al. (2007), describe a real evolution of the fault parameters. The figures below allow examining this point.

Figures 162 a and b shows the relation between fault length and maximum cumulative slip on the faults: as shown in prior studies (e.g., Walsh and Watterson, 1988; Cowie and Scholz, 1992; Dawers et al., 1993; Schlische et al., 1996; Manighetti et al., 2001; Scholz, 2002), we find that there is a linear tendency between the two fault parameters. This tendency confirms that faults grow by both lengthening and accumulating more slip. Furthermore, there is obviously a maximum slip over length ratio above which a fault cannot accumulate more slip (no data point in the top-left quadrant; also discussion in Manighetti et al., 2001). This implies that faults must grow in alternative phases of lengthening (with slip accumulation?) and slip accumulation without lengthening. In any case, **the fault length and maximum cumulative slip are two related fault parameters**.

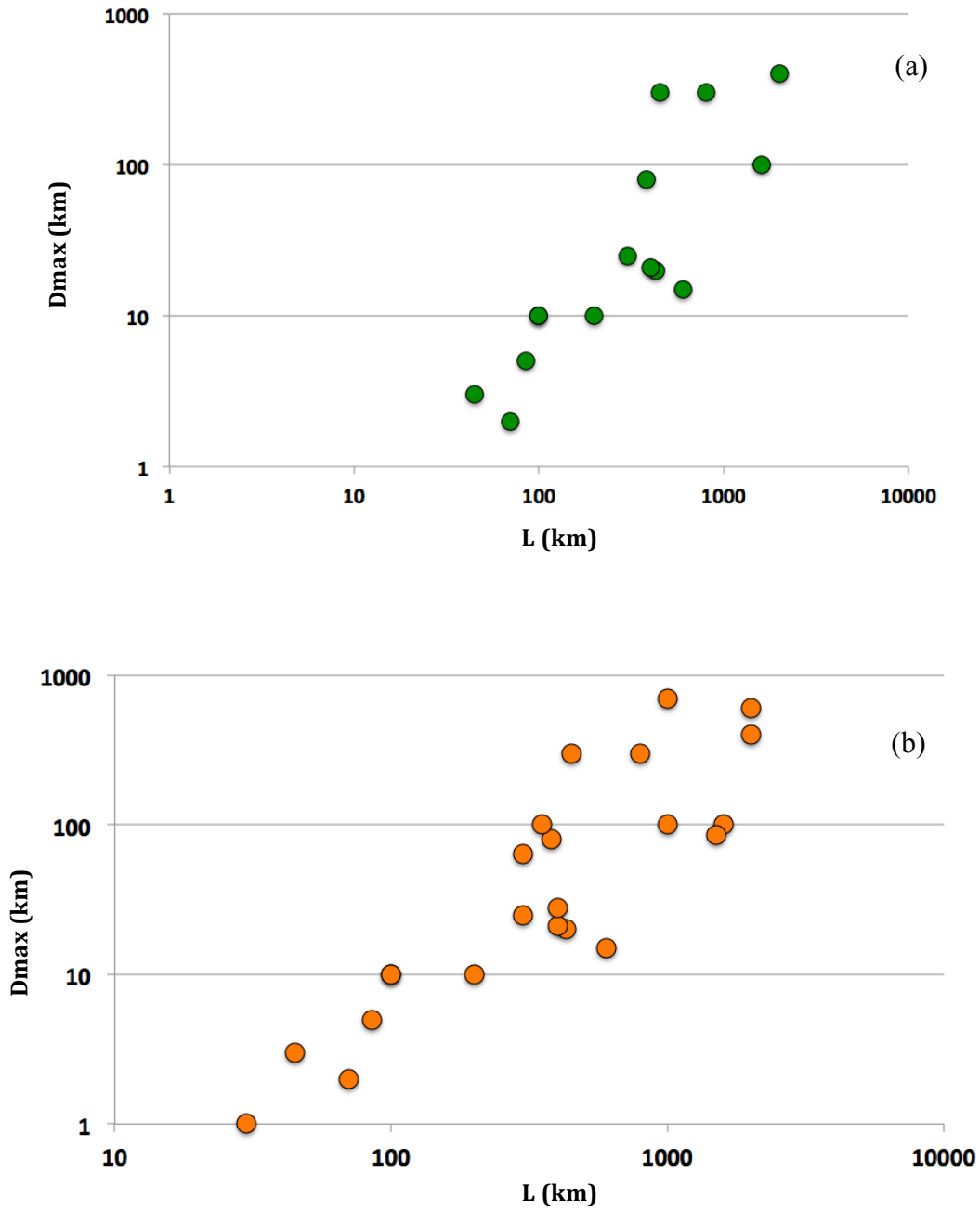


Fig.162: Relation between long-term fault length and maximum cumulative slip for the fault population analyzed in the IDs (a) and for the entire fault population (b) from Table 5.

Figures 163 a and b shows that a relation exists between fault age and fault length: overall, the older the fault, the longer it is. This confirms that faults lengthen and hence propagate laterally over time. Therefore, **the fault age and length are two related fault parameters**.

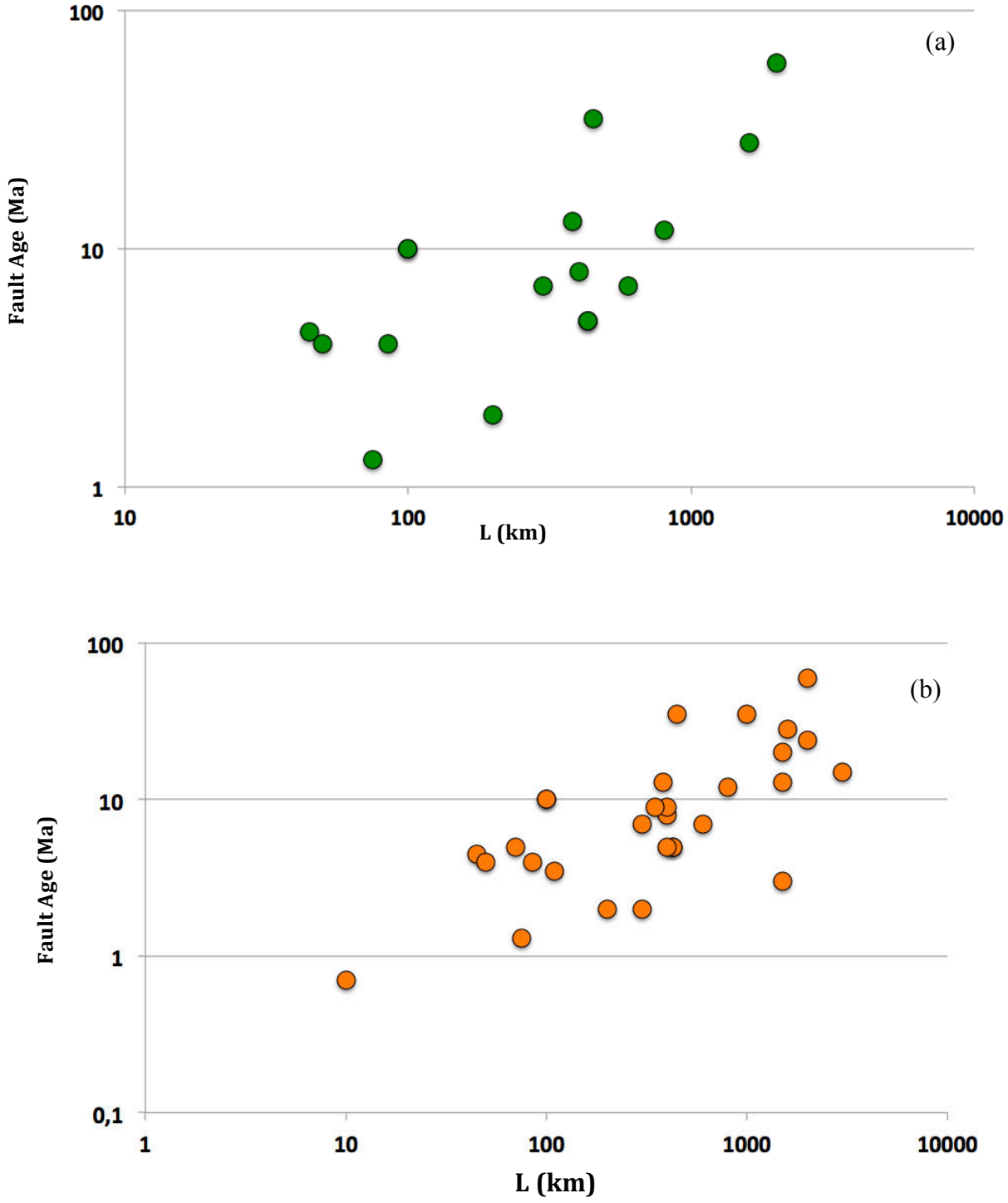


Fig.163: Relation between long-term fault length and fault age for the fault population analyzed in the IDs (a) and for the entire fault population (b) from Table 5.

Figures 164 a and b suggests that an overall relation exists between the fault length and the fault slip rate (both long-term and current): overall, the longer the fault, the faster it slips. There is some variability however. I will come back to this relation in the following. It shows that **the fault length and slip rate are two partly related fault parameters**.

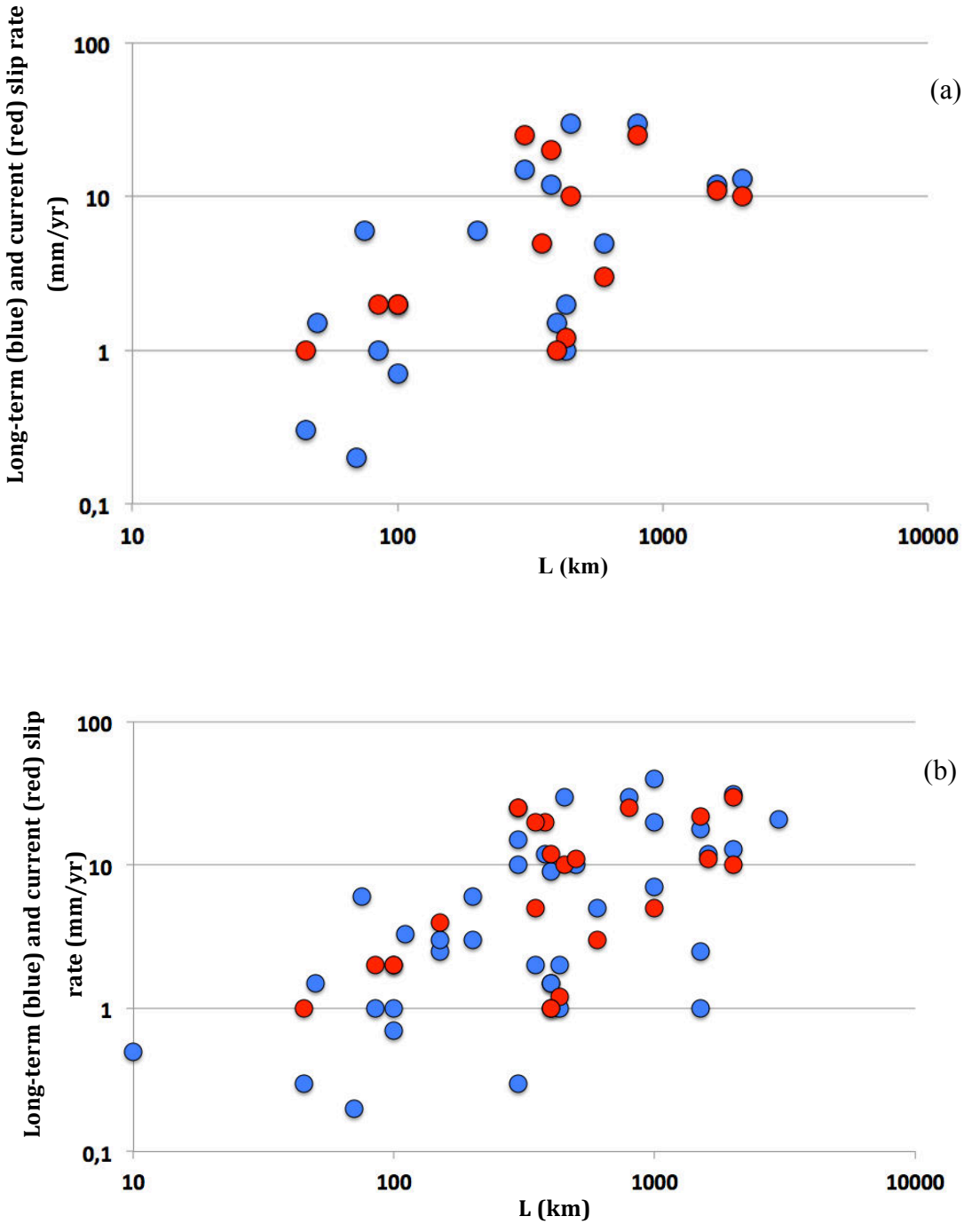


Fig.164: Relation between long-term fault length and long-term (blue) and current (red) slip rate for the fault population analyzed in the IDs (a) and for the entire fault population (b) from Table 5.

Figures 165 a and b suggest that a relation exists between the fault age and the fault slip rate (both long-term and current): overall, the older the fault, the faster it slips. I will also come back to this relation in the following. It suggests that **the fault age and the fault slip rate are two partly related fault parameters**.

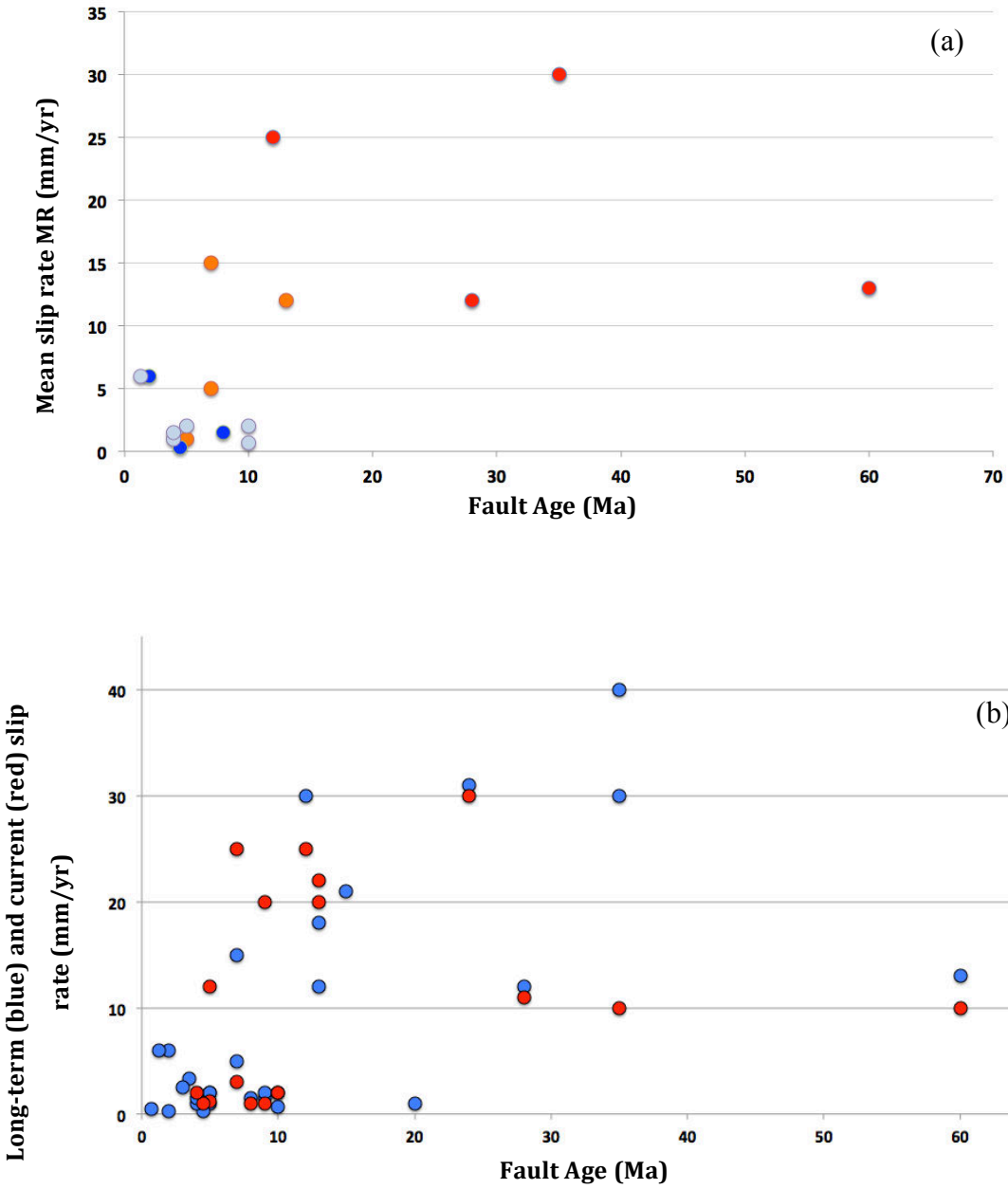


Fig.165: a) Relation between the mean slip rate and the fault age. Color is function of the maturity of the fault (from Table 5). Pale Blue: Immature ; Dark blue: Intermediate to Immature; Orange: Intermediate to Mature; Red: Mature. b) Relation between long-term (blue) and current (red) slip rate for the entire fault population from Table 5.

These above relations therefore confirm that the fault parameters length, maximum cumulative slip, age, and slip rate are more or less related. It is thus likely that they can be

used individually or collectively to define the structural maturity of the faults. Below, I examine this point in more details.

Figures 166 a and b confirms that a relation exists between the fault structural maturity and the total fault length: overall, the more mature is a fault, the longer it is. This confirms that faults lengthen as they grow and become more mature. **This additionally confirms that the total length of a fault can be used as a proxy for its structural maturity**.

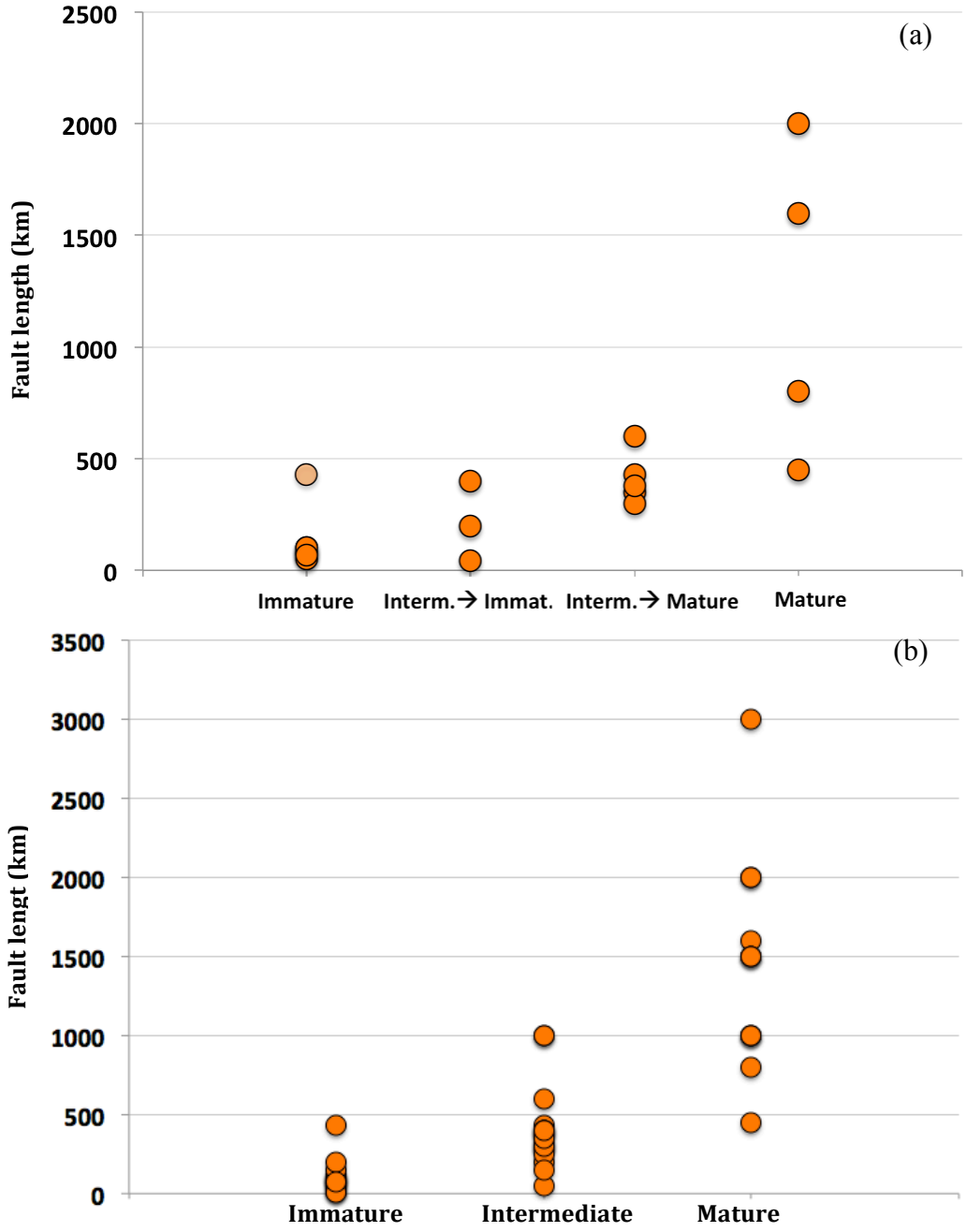


Fig.166: a) Relation between the fault length and the fault maturity declined in four classes for the fault population analyzed in IDs; Orange pale dot is the Fuyun fault, and (b) described in three classes for the entire fault population (from Table 5).

Figures 167 a and b confirms that a relation also exists between the fault structural maturity and the maximum cumulative slip on the fault: overall, the more mature is a fault, the larger is the total slip accumulated on it. This confirms that faults grow and become more mature by accumulating more slip. **This additionally confirms that the maximum cumulative slip on a fault can be used as a proxy for its structural maturity**.

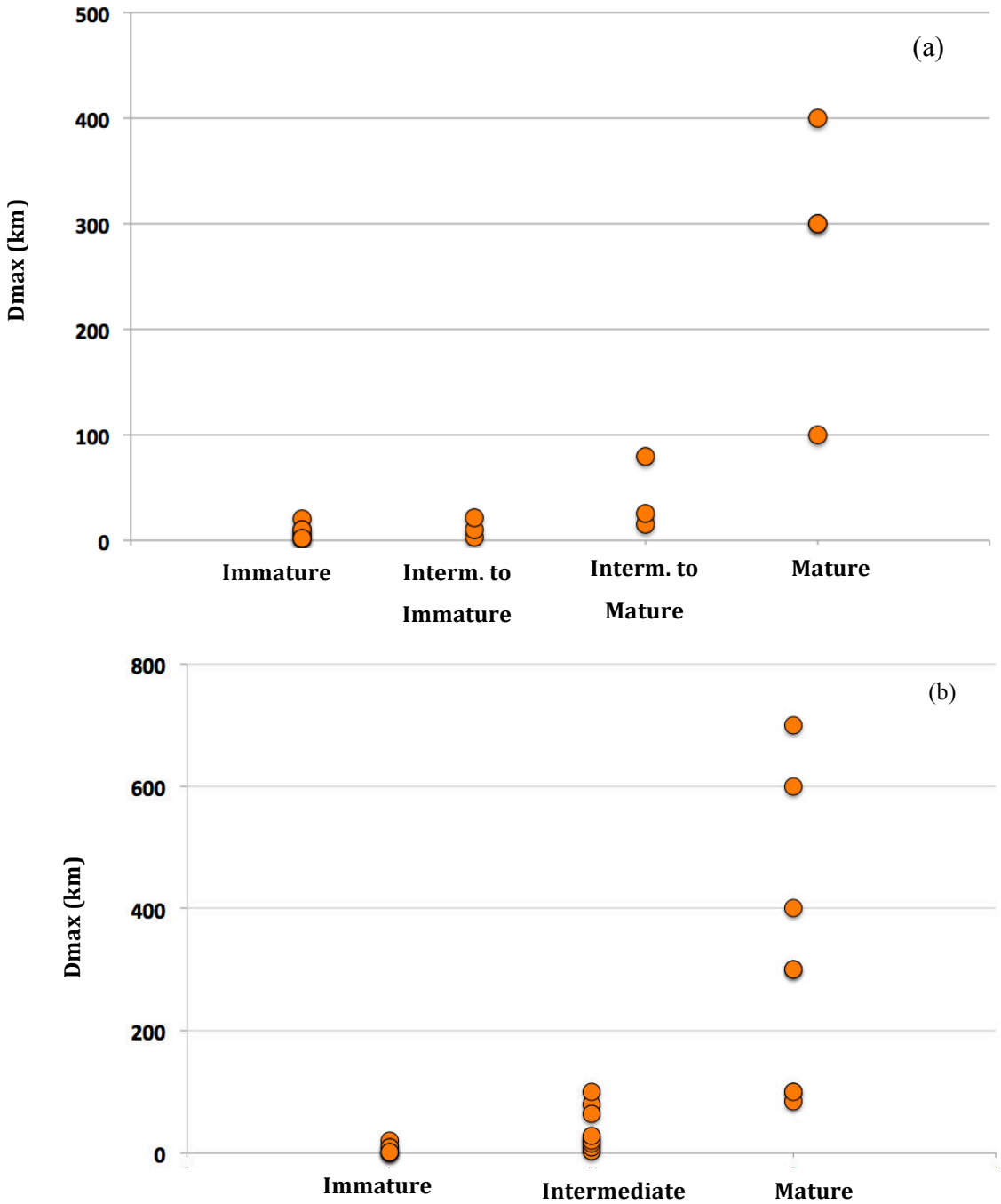


Fig.167: a) Relation between the maximum cumulative displacement and the fault maturity for the fault population analyzed in IDs ; (b) same for the entire fault population, from Table 5.

Figures 168 a and b confirms that a relation exists between the initiation age of a fault and its structural maturity: overall, the older is the fault, the more mature it is. This confirms that the fault structural maturity basically represents the fault aging over its whole history. **This additionally confirms that the age of a fault can be used as a proxy for its structural maturity**.

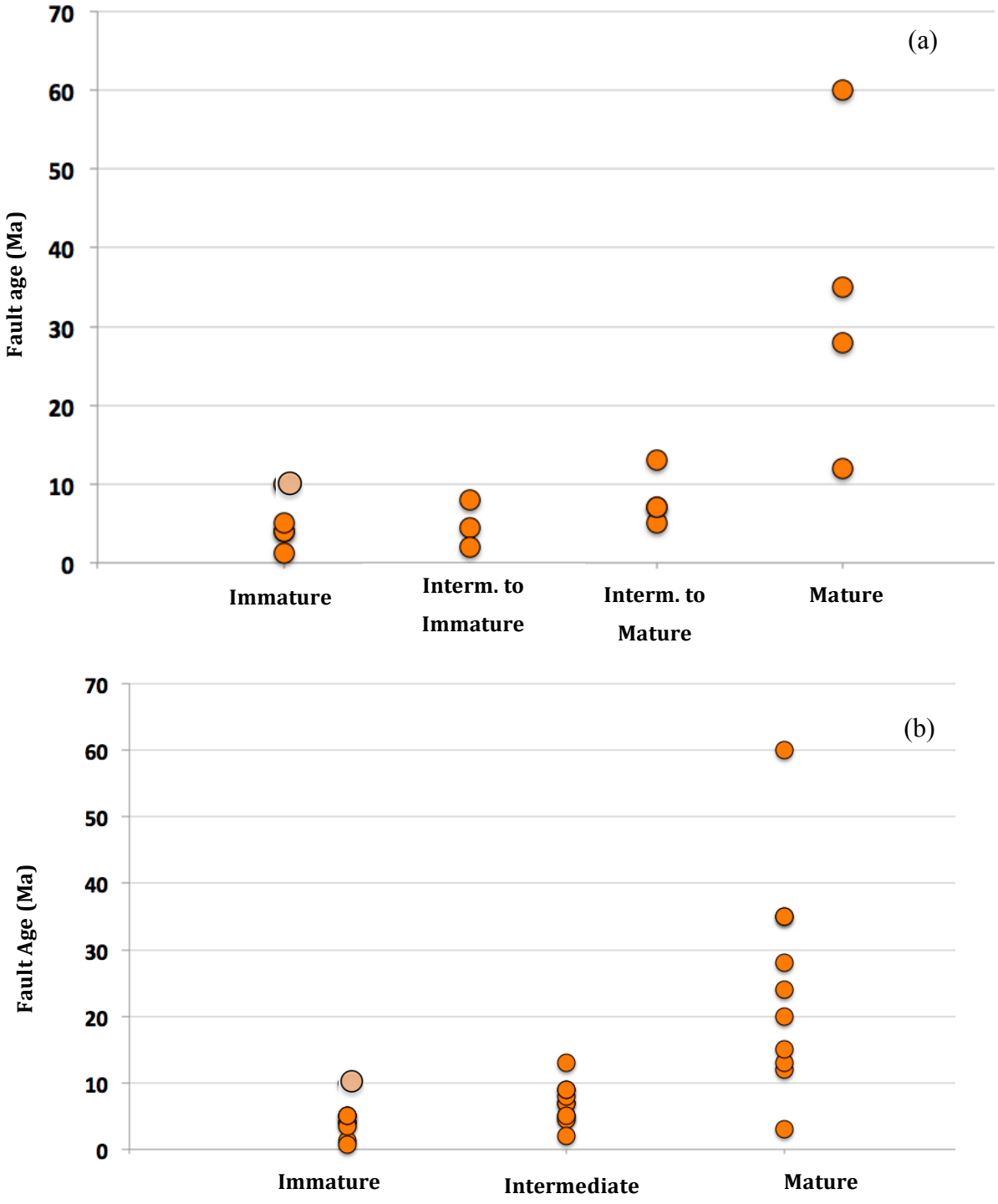


Fig.168: a) Relation between the fault age and the fault maturity for the fault population analyzed in IDs; same for the entire fault population, from Table 5. In pale orange are the faults broken during the Hector Mine and Landers earthquake (since their I-Age is < 10 Ma).

Figures 169 a and b confirms that a relation exists between the fault structural maturity and the fault slip rate (both long-term and current): overall, the more mature the fault, the faster it slips. This result suggests that the fault aging partly controls the way the fault can slip. One possible explanation might be that the fault maturation leads to reduce the friction on the fault plane (as suggested in prior works, e.g., Scholz et al., 1986; Hecker et al., 2010), what in turn allows the fault to slip at a faster rate. **This additionally confirms that the slip rate of a fault can be used as a proxy for its structural maturity**.

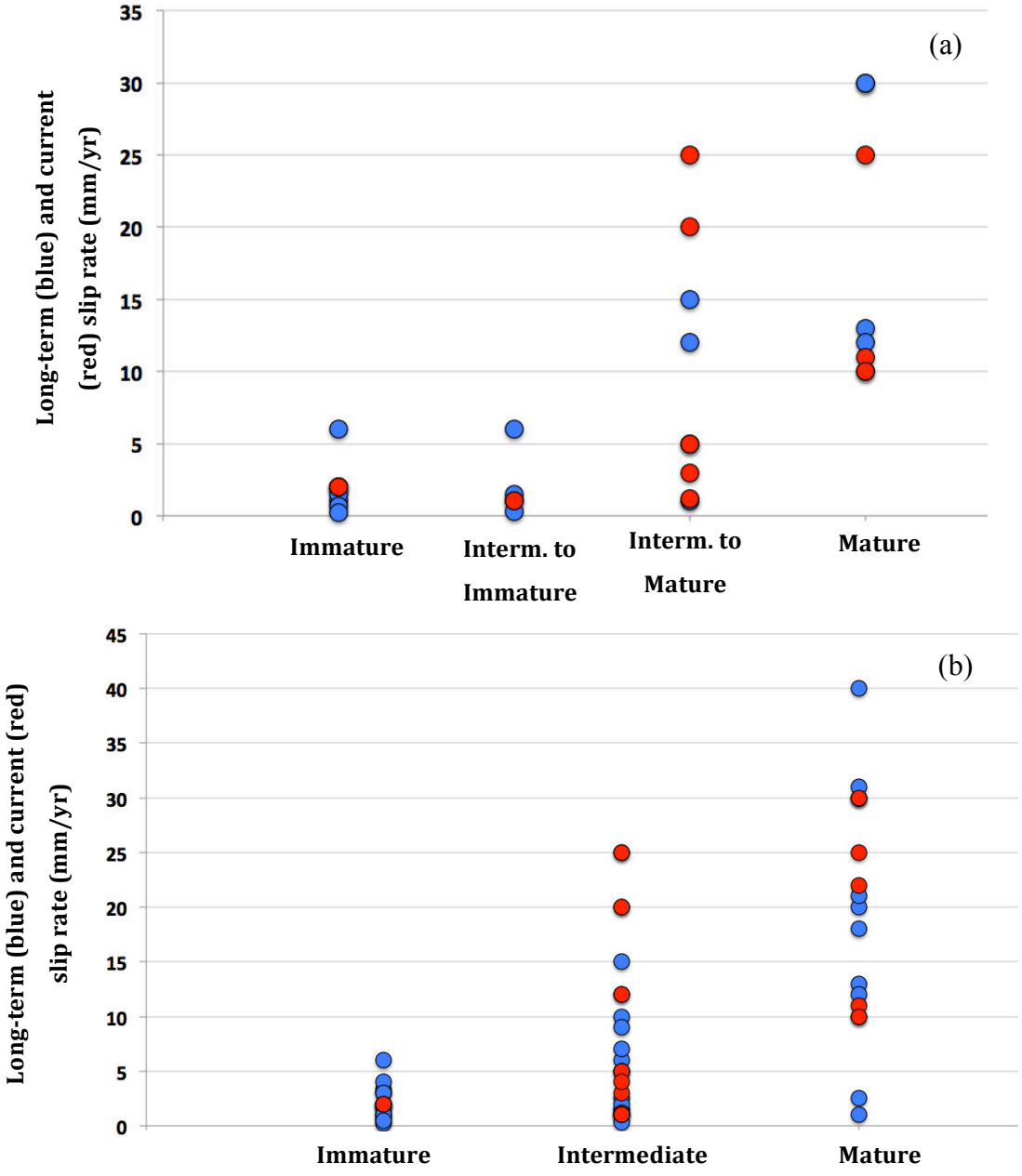


Fig.169: a) Relation between the long-term (blue) and current (red) slip rate and the fault maturity for the fault population analyzed in IDs, and (b) for the entire fault population from Table 5.

My results therefore confirm that the total fault length, the maximum cumulative slip on the fault, the fault initiation age, and the mean fault slip rate are more or less related fault parameters that can be used, individually or collectively, to assess the structural maturity of a fault. It is expected that there is a continuum in the degree of structural maturity, so that only two extreme classes –immature and mature, can be well defined, whereas, in between, there exists a broad range of faults with an "intermediate" maturity. However, the tendencies shown above allow knowing whether a fault has an intermediate maturity closer from immature or closer from mature.

CHAPTER III. ASYMETRY OF COSEISMIC SLIP PROFILES : A GENERIC PROPERTY TIGHTLY CONTROLLED BY THE EARTHQUAKE PROCESS

It has been shown that large EQs produce slip distributions that are skewed and actually triangular and asymmetric in overall shape, both along the fault strike and along the fault dip (Manighetti et al., 2005; Wesnousky, 2008). Most of the EQ slip profiles that I studied in the IDs of Chapter II confirm this observation. Together these show that the triangular envelope shape of the coseismic slip profiles is a generic property of the EQ ruptures, that is a property that is independent on the size, on the slip mode, on the location and hence on the tectonic and geological context of the EQs. Therefore, it is a property that is likely controlled by the physics of the rupture.

Furthermore, a similar triangular and generally asymmetric envelope shape is observed for cumulative slip profiles along long-term faults (Manighetti et al., 2001, 2009; Scholz, 2002; Scholz and Lowler, 2004; Shaw et al., 2002; Davis et al., 2005; Fig.17 in Chapter II). These cumulative slip profiles result from repeated EQ slips over long periods of the fault evolution. Despite of their long-term building, the cumulative slip profiles thus have a generic envelope shape that is independent on the size, on the slip mode, on the location and hence on the tectonic and geological context of the long-term faults. Therefore, the asymmetric and fairly linear slip distribution on faults is a property that is likely controlled by the physics of faulting.

Paradoxically, as I discuss it in greater details in chapter VII, the asymmetric slip distributions –either coseismic or long-term, where maximum slip is deported toward one of the rupture or fault tips, are not in keeping with the classical models of faults and EQs. These common models indeed approximate faults and EQs as cracks in a homogeneous elastic medium (e.g., Scholz, 2002; Manighetti et al., 2005; Noda et al., 2013, and more references in Chapter VI). The stress distribution on the fault and the stress drop on the EQ rupture plane are considered to be constant overall. In that framework, the slip-length distribution on either the fault or EQ rupture is expected to be elliptical in shape. However, because rocks cannot sustain infinite stresses at their tips, the theoretical elliptical shape has been modified in a ad-hoc fashion by introducing small damage features at the very tips of the faults (process zone; e.g., Cowie and Scholz, 1992a; Scholz, 2002); stresses then drop down and become finite.

In EQ physics literature, the concept of elastic crack is rarely discussed. Yet, the vast majority of the EQ source inversion models, if not all, approximate the EQ rupture as one single plane or a narrow zone of a few fairly collinear planes, embedded in a homogeneous elastic medium (e.g., discussion in Manighetti et al., 2005). The overall stress drop is taken as constant. Therefore, whether the EQ rupture is seen as an expanding crack or as a pulse, the resulting

coseismic slip distribution should be fairly elliptical in shape (Noda et al., 2013). This is not, actually, what is observed: the slip distributions produced in the source models are generally not elliptical in overall shape.

My objective here is thus to explore this paradox further, and my first step is, on the one hand to describe the actual envelope shape of the coseismic slip distributions, and on the other hand, to examine whether this shape and in particular its asymmetry are linked to other static parameters of the EQ rupture. If such links exist, they might provide keys to better understand the EQ physics.

Note that in most of the plots that follow starting from section 2, the **size** of the symbols represents the data **quality** (unless it is said differently), symbols are **empty or solid** depending on whether they represent a **single model or a best model** chosen among a denser collection, uncertainties are represented as grey lines, and **subduction EQs** are discriminated in **orange**.

1. Overall shape of earthquake slip profiles and degree of asymmetry

I have two data types in hands (Tables 1 & 2): Coseismic slip profiles measured at surface along the EQ rupture, that is 1D slip-length data; and coseismic slip distributions inferred at depth on the rupture plane from source inversion models, that is 2D slip-length and -width data. Note that I define width as the along-dip length of the rupture plane. The surface data are thus mainly derived from direct observation, whereas the depth data are derived from modeling various observations. To compare the surface and depth data, I have converted the on-fault slip distribution at depth in two 1D profiles: one showing the distribution of the maximum values of slip along the rupture length, and one showing the distribution of the maximum values of slip along the rupture width. Because the source inversion models were not produced with the same grids, to examine the slip profile shapes, I resampled the slip profiles by interpolation into a large amount of values (500) along strike and along dip in order to respect the general shape of the slip profiles. However, I have extracted the Dmax, L, W, etc values from the original model data.

Figure 170 shows a few example EQ slip-length profiles, all measured at the ground surface (see 2001 Kunlun and 1999 Hector Mine EQs IDs and Table 1). The four examples have a fairly triangular envelope shape, with different degrees of asymmetry. Using a least-square method, I have fitted the slip profiles with a triangular function for which I have fixed the displacement equal to 0 at the rupture tips. I have also fitted the slip profiles with an elliptical function also defined to have displacement equal to 0 at the rupture tips and to have a maximum amplitude equal to the maximum displacement of the best-fitting triangle. All slip-length profiles at surface and inferred at depth revealed to be best fitted by the triangular function (even in the cases, which I tested, where the best fitting elliptical function has no amplitude imposed). The slip-width profiles at depth also revealed to be best fitted by a triangular function. **This confirms that EQ slip profiles have a generic envelope shape that is basically triangular**.

This allowed me to build figure 171 where all slip profiles are plotted together so that their common shape can be better seen. In all plots, the slip profiles have been normalized to both the rupture length (or width) and the mean slip (noted Dmean); and some of them have been flipped so that maximum slip is at the right. The yellow curve is the average running curve. Figure 1b-a shows the slip profiles measured at surface (28 profiles; note that the slip profiles for the Superstition Hills, Yushu, Hebgen Lake, Baja California and Elmore Ranch are not included for reasons explained in Chapter II). Although the profiles show some slip variability, they all have a mean envelope shape clearly triangular and asymmetric. Figure 1b-b shows the slip-length profiles inferred at depth from 102 source inversion models. Again, although the profiles show some slip variability, they all have a mean envelope shape that is clearly triangular and asymmetric. Figure 1b-c is the same than figure 171b but built from the best models only (Table 2). Finally figure 171d shows the slip profiles inferred at depth along the rupture width, from the 102 source models. Although the profiles show some slip variability, the slip profiles along dip also have a mean envelope shape that is triangular and asymmetric. In the figures built from the source data, the slip of the average running curve does not go down to zero at its tips because low slips at the rupture tips are poorly constrained in the source models.

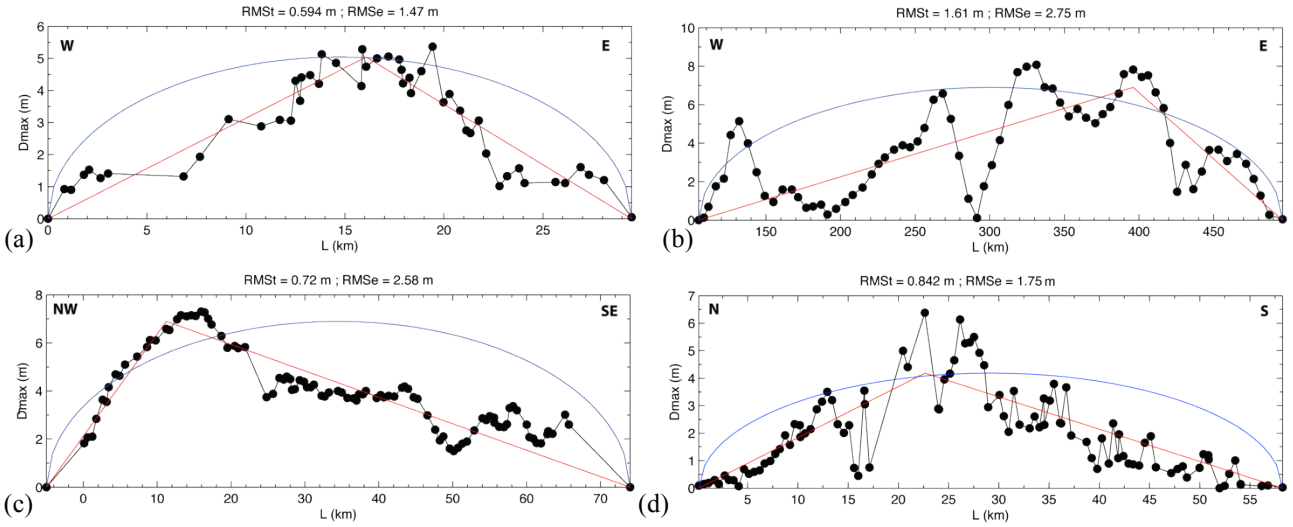


Fig. 170 : Four exemples of EQ slip-length profiles measured at surface (black dots). (a) 2010 Canterbury EQ (Quigley et al., 2011); (b) 2001 Kunlun EQ (Lasserre et al., 2005; Xu et al., 2006); (c) 2005 Muzaffarabad EQ (Avouac et al., 2006); (d) 1999 Hector Mine EQ (Jonsson et al., 2002). In red is the best fitting triangle while in blue is the best fitting elliptical function.

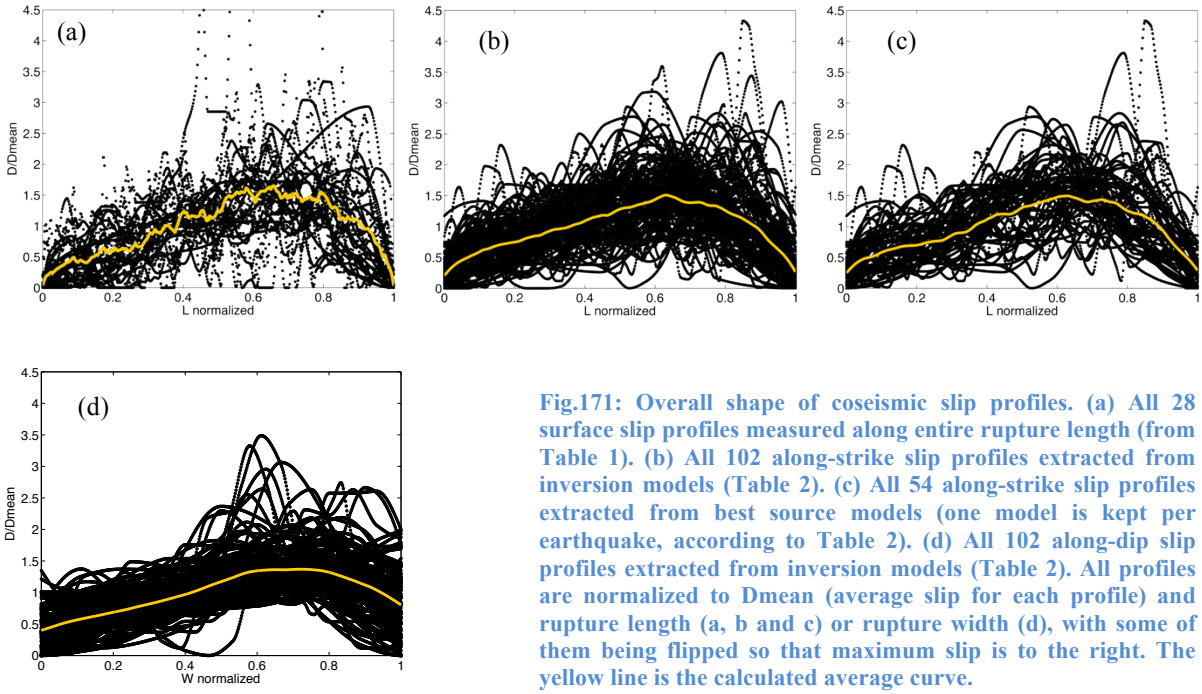


Fig.171: Overall shape of coseismic slip profiles. (a) All 28 surface slip profiles measured along entire rupture length (from Table 1). (b) All 102 along-strike slip profiles extracted from inversion models (Table 2). (c) All 54 along-strike slip profiles extracted from best source models (one model is kept per earthquake, according to Table 2). (d) All 102 along-dip slip profiles extracted from inversion models (Table 2). All profiles are normalized to Dmean (average slip for each profile) and rupture length (a, b and c) or rupture width (d), with some of them being flipped so that maximum slip is to the right. The yellow line is the calculated average curve.

In most cases, the adjustment of the slip profiles with a triangle revealed to be as reasonable in a certain range (Fig.172): a fairly similar rms was found for different adjustments and hence for different degrees of asymmetry of the fitting triangle. I thus extracted for each EQ both the best fitting triangular function with its degree of asymmetry, and the uncertainty on this degree of asymmetry which I took coinciding with the range of rms being < 5 % of the best rms value (Fig.172). In figure 173, I have represented the degrees of asymmetry together

in a histogram form (where uncertainties cannot be taken into account; in green) and as probability density functions (PDF), which allow representing the uncertainties (orange curves). I have then calculated the summed PDF curve (in blue in Fig. 173a, and in red in Fig. 173b and 173d). The peaks of the summed PDF curve show the most represented and/or the best-constrained degrees of asymmetry. Figure 173a shows the results for the surface slip profiles, figure 173b those for the slip-length profiles derived from the best source inversion models, figure 173c the comparison of the two slip-length surface and depth datasets, and figure 173d the results for the slip-width slip profiles derived from the best source inversion models. The figures show that there is a sort of a continuum in the degree of asymmetry of the EQ slip profiles: symmetric, moderately asymmetric and strongly asymmetric slip profiles all exist in the data collection, both at surface and at depth, and both along-strike and along-dip. For clarity in the figures that follow, I have however discriminated the datasets into three classes of degree of asymmetry, based on the approximate grouping suggested in Fig.173c and 173d: a significant part of the slip profiles are fairly symmetric, with a degree of asymmetry ranging between 50 and 65 % of the fault length or width; another part of the slip profiles are moderately asymmetric, with a degree of asymmetry ranging between 65 and 80 % of the fault length or width; and another part of the slip profiles are strongly asymmetric, with a degree of asymmetry greater than 80 % of the fault length or width.

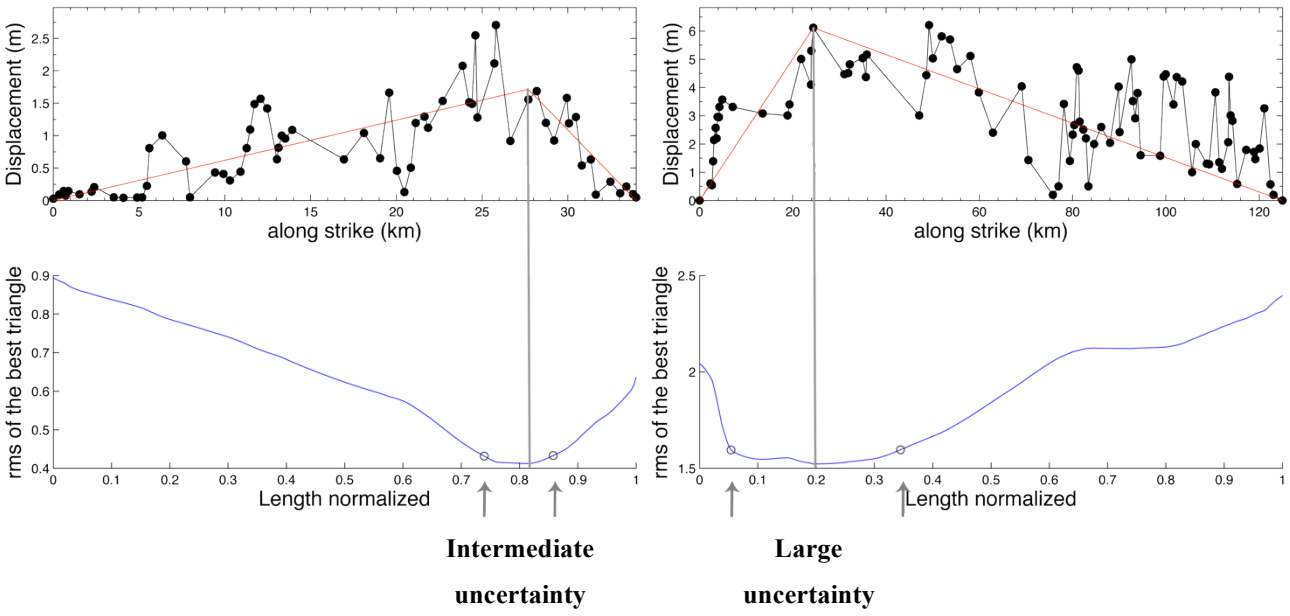


Fig.172: Two examples of determination of the uncertainty on the position of the apex of the best triangle function, and hence on the degree of asymmetry of the slip profile. (a) 1983 Borah Peak EQ (Crone and Machette 1984); (b) 1990 Luzon EQ (Punongbayan et al., 1990). Rms of the best fitting triangle functions are shown in the bottom graphs. Vertical lines show the position of the apex of the best triangle. Small circles on the rms curves show the maximum uncertainties for which rms is less than 5% of the best rms value.

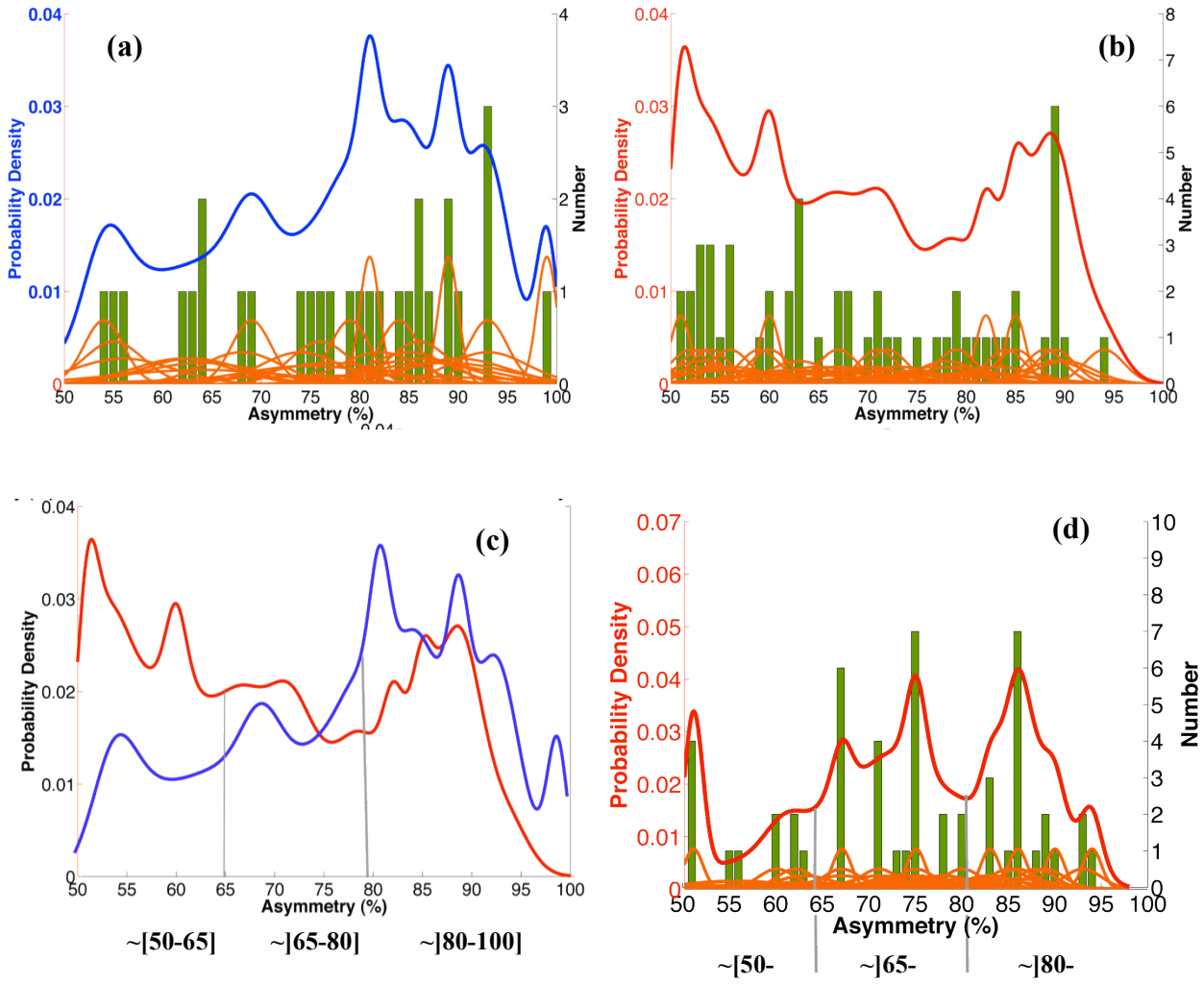


Fig.173: Variability of the degrees of asymmetry of the slip profiles, represented in both an histogram form (green) and as PDF functions (orange). The peaks in the summed PDF curves show the most represented and/or best constrained degrees of asymmetry. Figure (a) for surface slip-length profiles; figures (b) and (d) for depth slip-length and slip-width profiles, respectively, Figure (c) for comparison between surface and depth slip-length profiles

Figure 174 now shows the slip-length profiles discriminated in the three classes above. At surface (Fig.174a), about 40 % of the slip-length profiles are fairly symmetric, whereas ~20 and ~40 % are moderately or strongly asymmetric, respectively. However, we have seen in the IDs of Chapter III that several EQs actually included the rupture of several distinct faults. When only the slip profiles on the major broken fault are retained (Fig.174b), we find that only 28 % of the surface slip-length profiles are fairly symmetric, whereas 72 % are clearly asymmetric. Similar results are found for the slip-length profiles inferred from the entire model collection (Fig.174c) and from the best models only (Fig.174d). The proportion of fairly symmetric profiles is slightly larger than that observed for the surface data however. This might be due to the lower resolution of the source models. Finally, a similar distribution is found for the along-dip slip profiles (Fig.174e and 174f).

I thus conclude from this part that coseismic slip profiles are fairly triangular in envelope shape, and most of them asymmetric. The generic shape of the EQ slip distribution is found both along the fault strike and along the fault dip.

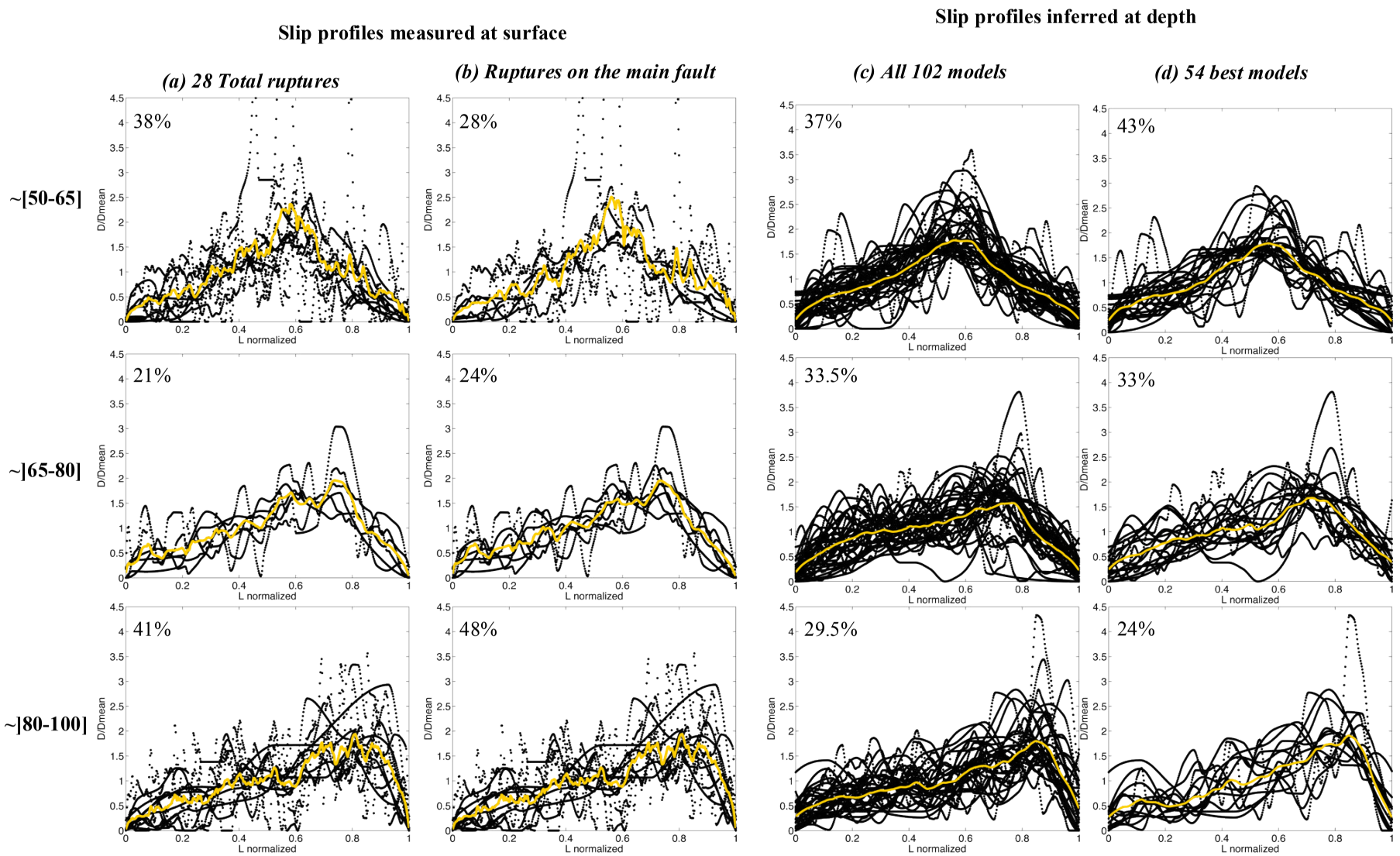


Fig.174: Slip-length profiles discriminated in the three classes of asymmetry described in the text. In yellow is the average running curve. See text for details.

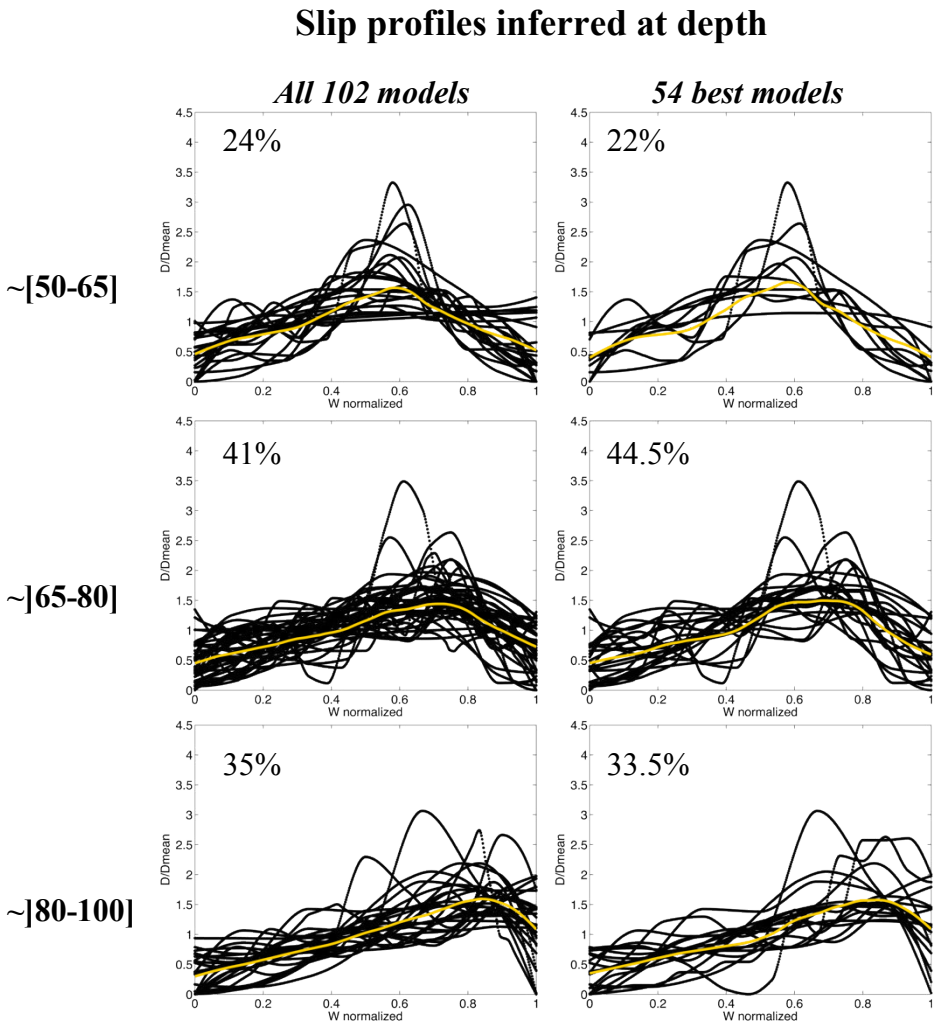


Fig.174: d) Slip-width profiles discriminated in the three classes of asymmetry described in text. In yellow is the average running curve. See text for details.

2. Relation between asymmetry of earthquake slip profiles and rupture length and width

Figure 175 examines whether a relation exists between the degree of asymmetry of the EQ slip-length profiles and the length of the ruptures. Both at surface (Fig.175a) and at depth (Fig.175b), short ruptures (L < 50-100 km) are found to have slip-length profiles showing any degree of asymmetry. By contrast, ruptures longer than 50-100 km systematically have markedly skewed slip-length profiles, whose degree of asymmetry seems to increase with the

rupture length. Only two subduction EQs depart from this overall behavior (2011 Tohoku and 2005 Sumatra EQs, in the top left quadrant of Fig.175b)

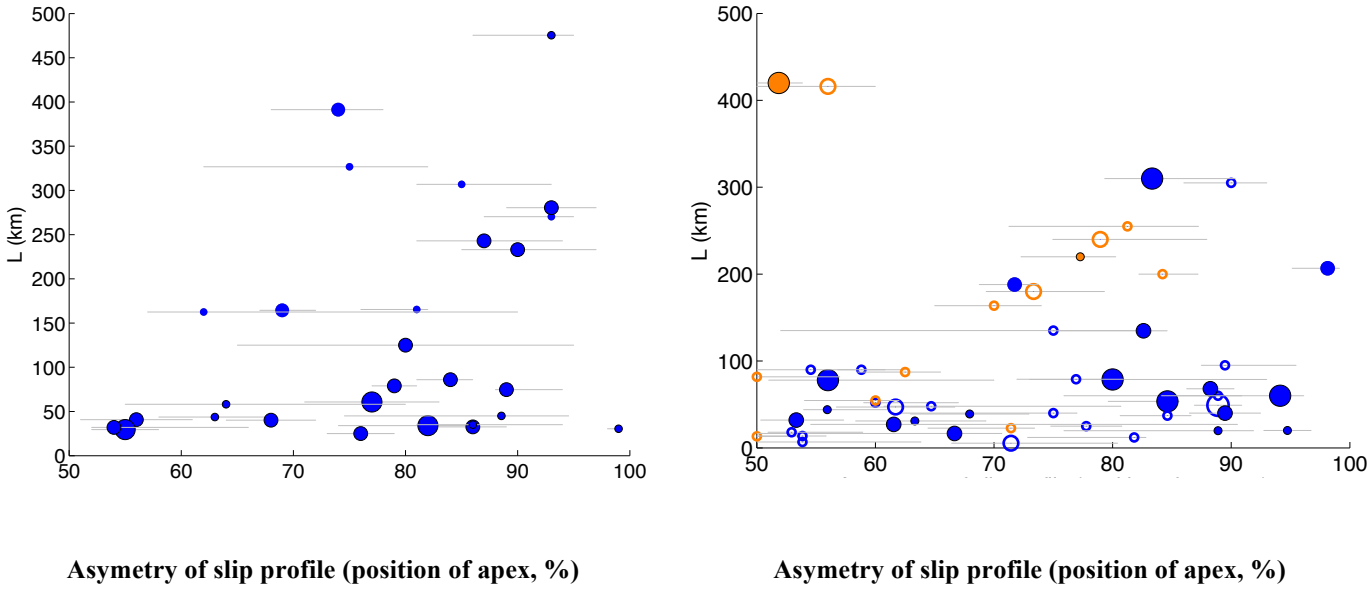


Fig.175: Degree of asymmetry of the EQ slip-length profiles as a function of rupture length. (a) surface data; (b) depth data, from best source models.

3. Relation between asymmetry of earthquake slip profiles and earthquake stress drop

The EQ stress drop can be approached by the slip to length ratio of the rupture (e.g., Shaw and Scholz, 2001).

Figure 176 examines whether a relation exists between the degree of asymmetry of the EQ slip-length profiles measured at surface and the slip to length ratio of the ruptures. In Fig.176a, the complete slip profiles are considered, whereas in Fig.176b, for the few EQ cases, which broke several faults, only the slip profile on the main broken fault is taken into account (See also Fig.176c for names of EQs). Fig.176b is thus likely more accurate than Fig. 176a. Figure 176b suggests a linear tendency between asymmetry of slip-length profiles and stress drop: the more asymmetric the coseismic slip-length profile, the smaller the stress drop on the corresponding rupture. Only a few data points depart from this overall tendency, and those are long ruptures with a length greater than 140 km (all long ruptures with $L \geq 140$ km are represented in grey). As we will show later in Chapter IV, long ruptures have their coseismic slip saturating to a similar value, so that the Dmax/L ratios that result on long

ruptures are variable and decreasing with length. Therefore it is not clear whether the Dmax/L ratios for long ruptures can be interpreted as that of all other ruptures.

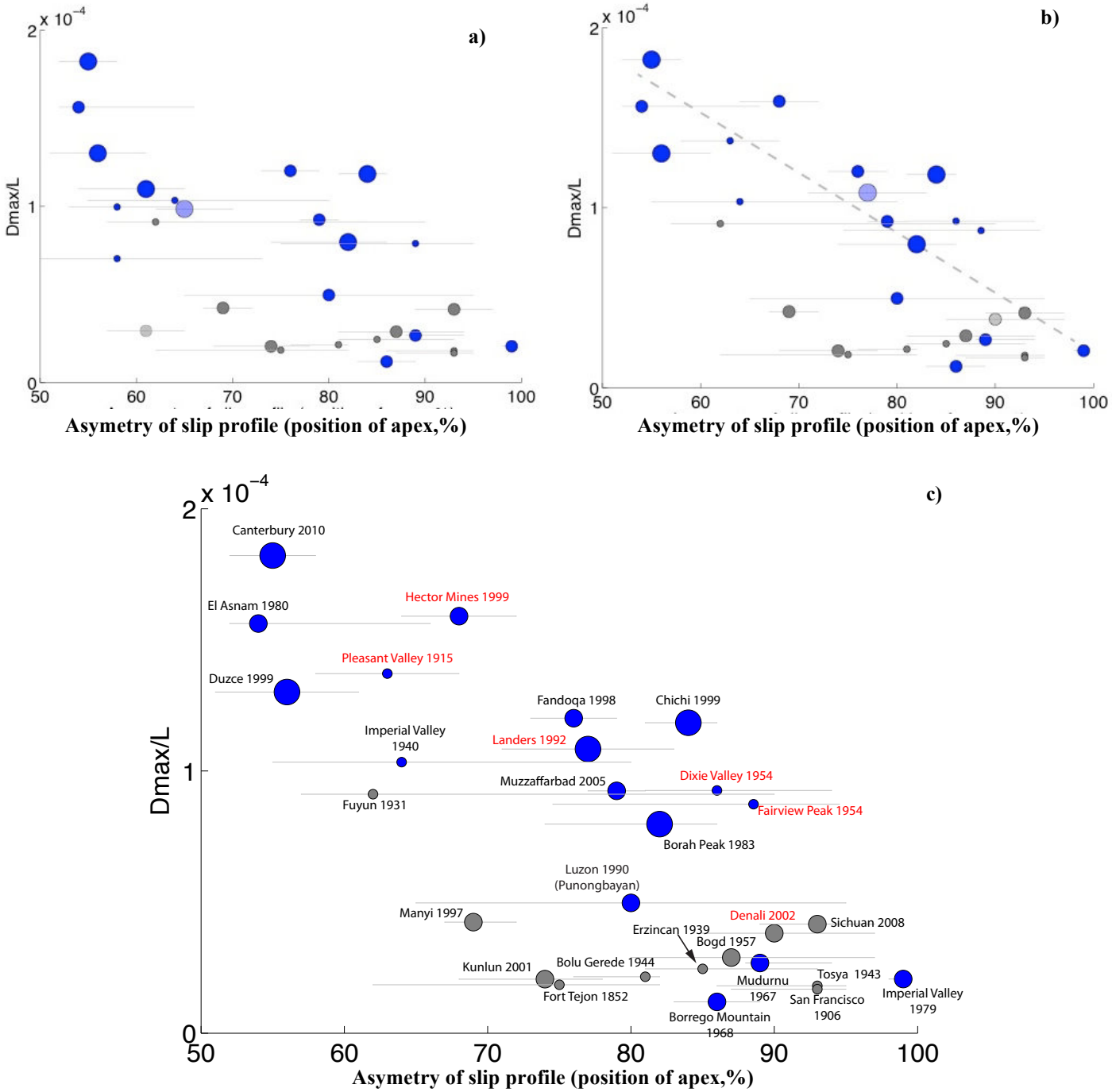


Fig.176: Degree of asymmetry of EQ surface slip-length profiles as a function of maximum slip to length ratio, which approaches the EQ stress drop. In grey are ruptures with L ≥ 140 km (a) entire ruptures are considered; those breaking several faults are indicated in pale. (b) same as (a) but for the few multi-fault ruptures, only the main rutpure is considered. (c) same as (b) with EQ names indicated.

Figure 177 additionally suggests that the Dmax/L versus asymmetry relation might better be described as discrete steps. The best-constrained data points indeed suggest sort of a grouping around four dominant [Dmax/L - Asymmetry] values. Although this result is insufficiently constrained, it suggests, on the one hand that the degree of asymmetry of the surface slip-length profiles might rather evolve in a discrete fashion, not as a continuum, and, on the other hand, that such a discrete variation in the asymmetry might be accompanied by a discrete variation in the EQ stress drop.

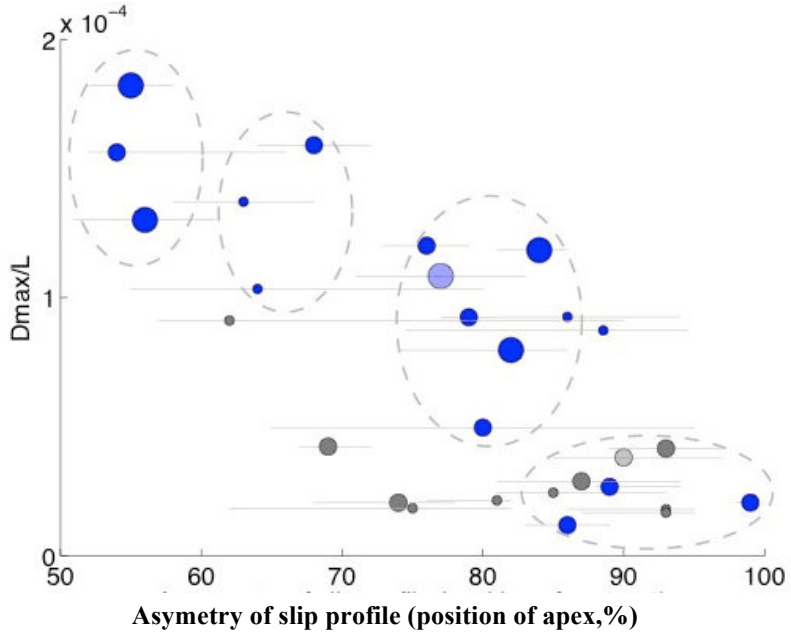


Fig.177: Same figure as Fig.176 but with suggested grouping.

Figure 178 is the same as Fig. 176 but now done with the best source model data. In Fig. 178a, only the continental EQs are shown (in grey, the EQs with L ≥ 140 km), whereas in Fig. 178b, subduction EQS are also integrated (in orange, see Fig. 178c for EQ names). The figures are no concluding. Although the data do not contradict the linear tendency observed in Fig. 176, a number of data depart from it. We note however that most of these departing data are of little quality, and hence are not well constrained. All the subduction EQs but Tohoku 2011 and Hyuga Nada 1996 have both low stress drops and slip-length profiles with variable degrees of asymmetry.

I thus conclude that the best-constrained surface observations suggest that, apart for a few long ruptures, the degree of asymmetry of the coseismic surface slip-length profiles is related to the stress drop on the ruptures. Therefore, **there exists a genetic link between the rupture process –marked by its stress drop, and the final EQ slip distribution**.

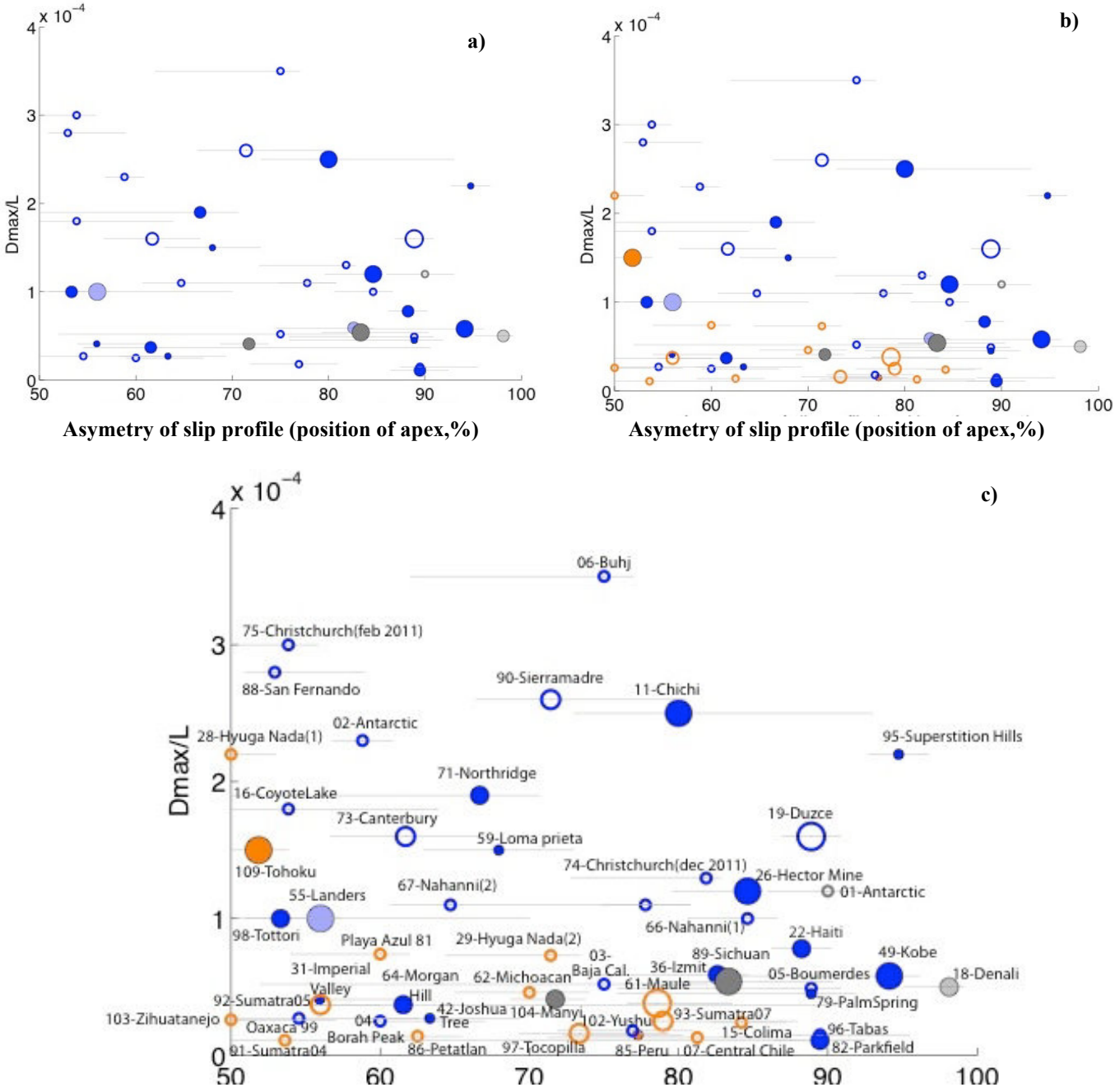


Fig.178: Degree of asymmetry of the EQ depth slip-length profiles as a function of the maximum slip to length ratio, that approaches the EQ stress drop. Only best model data are considered. In grey, EQs with L ≥ 140 km (See Chapter IV); in pale: multi-fault EQs; in orange: subduction EQs. (a) continental EQs only; (b) same as (a) but including also subduction EQs; (c) names of EQs.

4. Relation between asymmetry of earthquake slip profiles and number of broken fault segments

In Chapter II, I have determined the number of fault segments broken in each analyzed EQ. Figure 179a plots this number of broken segments as a function of the degree of asymmetry of the surface slip-length profile (See Fig. 179b for EQ names). For the few EQs having surface slip profiles but which I did not have time to analyze in detail (i.e., to analyze their long-term fault), I have reported the number of broken segments indicated in the literature. The plot suggests a linear tendency between the two types of data: overall, the larger the number of broken fault segments, the larger the degree of asymmetry of the resulting surface slip-length profile. Two EQ slightly depart from this overall tendency, namely Duzce 1999 and Sichuan 2008: for the former Duzce EQ, we can note that, while the surface slip profile is fairly symmetric, most inversion models suggest a slightly more asymmetric slip profile at depth. Thus, the symmetry of the surface slip profile might be only apparent, resulting from some surface slip lacking compared to the slip at depth. For the Sichuan EQ, we have seen in the ID in Chapter II that the maximum coseismic slip was located about 60 away from the western rupture tip. The actual degree of asymmetry of the surface slip-length profile is thus likely slightly less pronounced than represented in Fig.4a from the overall best-fitting triangular function.

Figure 180a now plots the number of broken segments derived from our mapping and from additional literature information as a function of the degree of asymmetry of the slip-length profiles inferred at depth from the best source inversion models (See Fig.180b for EQ names). The plot also suggests a linear tendency between the two types of data: overall, the larger the number of broken fault segments, the larger the degree of asymmetry of the resulting slip-length profile at depth. However the data are too scarce for the figure to be conclusive; more information on the broken segments is needed.

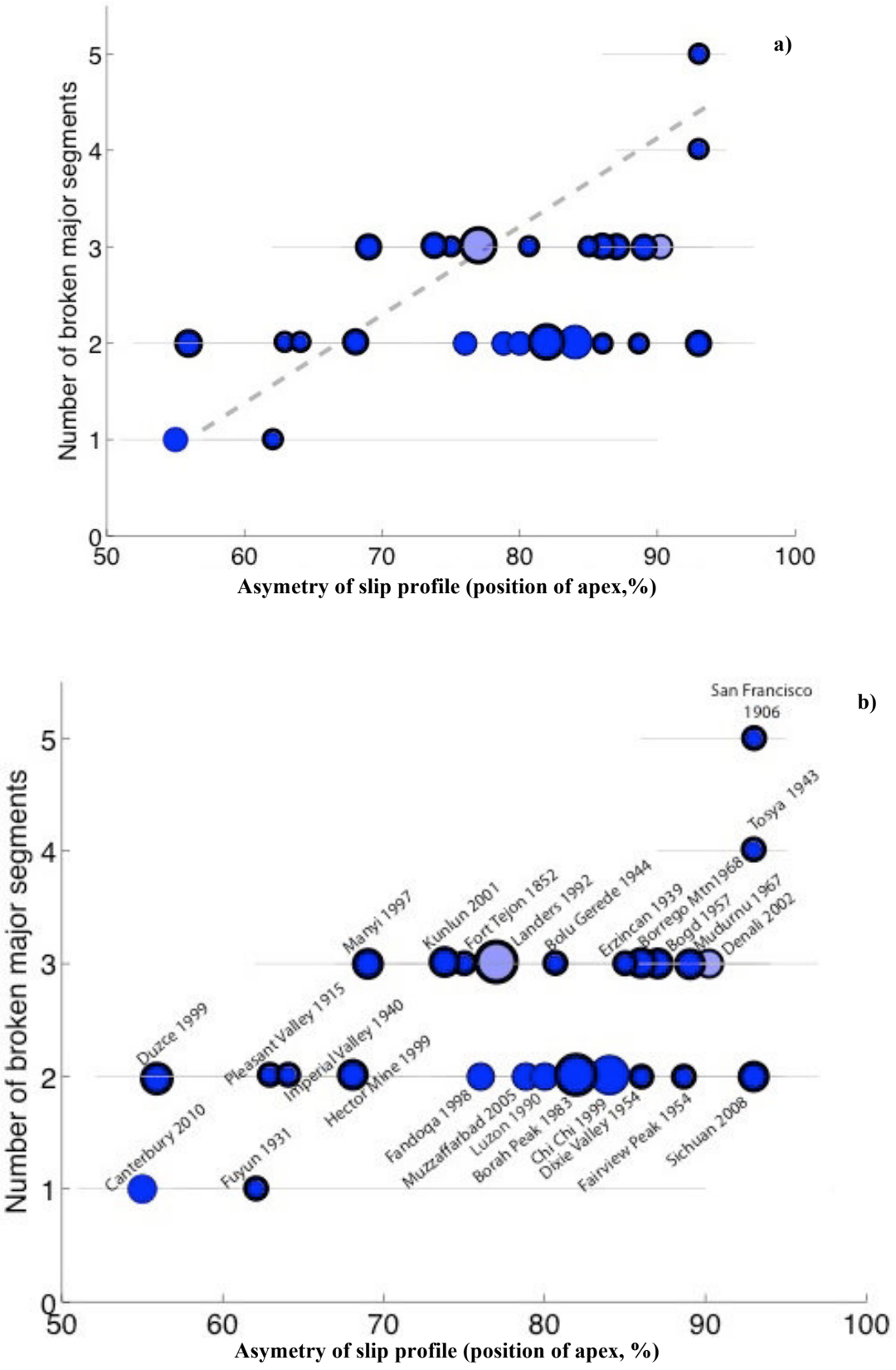


Fig.179: (a) Degree of asymmetry of the surface slip-length profiles as a function of the number of major segments broken along the faults. The number of broken segments is that defined in the IDs of Chapter II (bold-contoured symbols). For EQs with no ID, the number of broken segments is that provided in literature. Multi-fault EQs are in pale. Dotted line is an approximate overall tendency, not an actual regression. (b) same as (a) with names of EQs

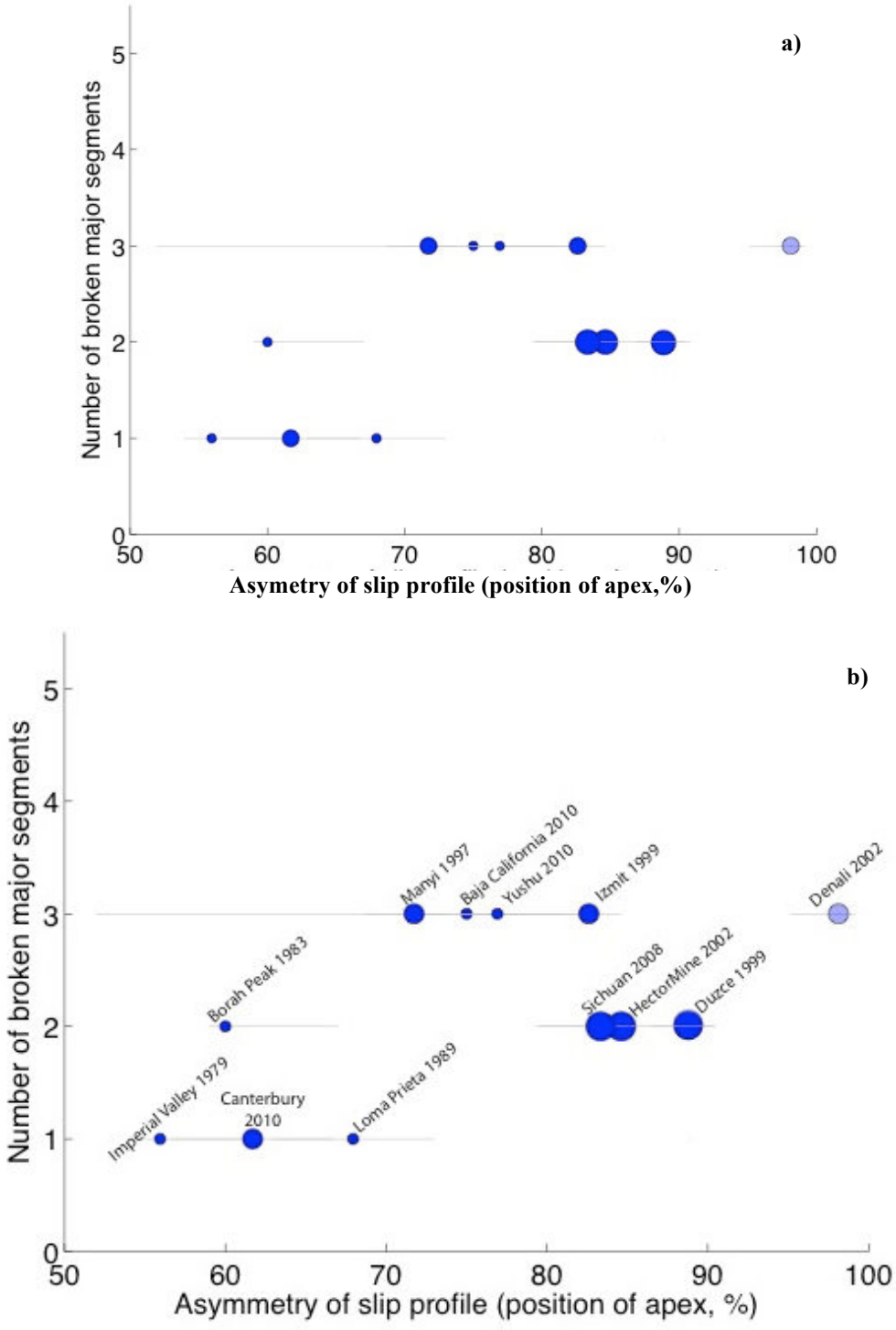


Fig.180: (a) Degree of asymmetry of the EQ slip-length profiles inferred at depth from best source models, as a function of number of broken segments along the faults. Number of broken segments comes from the IDs in Chapter II or from additional literature information. (b) same as (a) with names of EQs.

I have explored another way to determine the number of broken fault segments. It has been shown in many studies that EQ ruptures are sensitive to the lateral fault segmentation. In particular, inter-segment zones along long-term faults, which are zones of cumulative slip deficits, alter the rupture slip and propagation, and appear as zones of coseismic slip deficit (Fig. 17). Most coseismic slip-length profiles thus appear as being made of major slip bumps separated by slip troughs, and the major slip bumps are expected to coincide with the principal segments broken along the fault. Counting the number of major bumps along a rupture slip profile should thus provide the number of principal segments broken along the rupture. However, as I discussed it earlier in Chapter II, different sizes of segments can be broken along a fault, and counting the bumps cannot allow discriminating the relative size, and hence the importance, of the broken segments; some might be among the longest segments with the long-term fault, whereas others might be only small-scale features. Despite of these limitations, I have attempted to count the number of largest bumps within the coseismic slip profiles. For that, I have performed a Stockwell analysis of the slip-length profiles (Stockwell et al., 1996). The S-transform Stockwell signal processing method has been described and used by Manighetti et al. (2009) to recover the number of major segments in a dense population of long-term normal faults. I have therefore applied the same treatments as those described in Manighetti et al. (2009). The Stockwell approach allows determining the spatial frequency at which the slip energy is maximum. In effect, it divides a slip profile at all successive spatial frequencies and reveals at which frequencies the energy of the profile, i.e., the slip fluctuations, is best represented. Figure 181 shows two examples. The Muzaffarbad surface slip profile is fairly smooth yet divided into three major bumps fairly clear visually. The Stockwell energy histogram shows that the spatial frequency that best represents the slip profile is 3 (maximum amplitude of the Stockwell transform), and this means that the best representation of the slip profile is to make it including 3 major segments. The Stockwell result is thus in keeping with the visual observation. On the second example (Borah Peak EQ surface slip profile), the slip profile is more complicated, with possibly three major bumps, yet each is itself divided into multiple slip fluctuations. The Stockwell histogram indeed reveals the high frequency slip fluctuations (maximum amplitude at a spatial frequency of 15); yet it also shows that a fair representation of the slip profile can be done by dividing the profile into 6 segments, or into 3 segments.

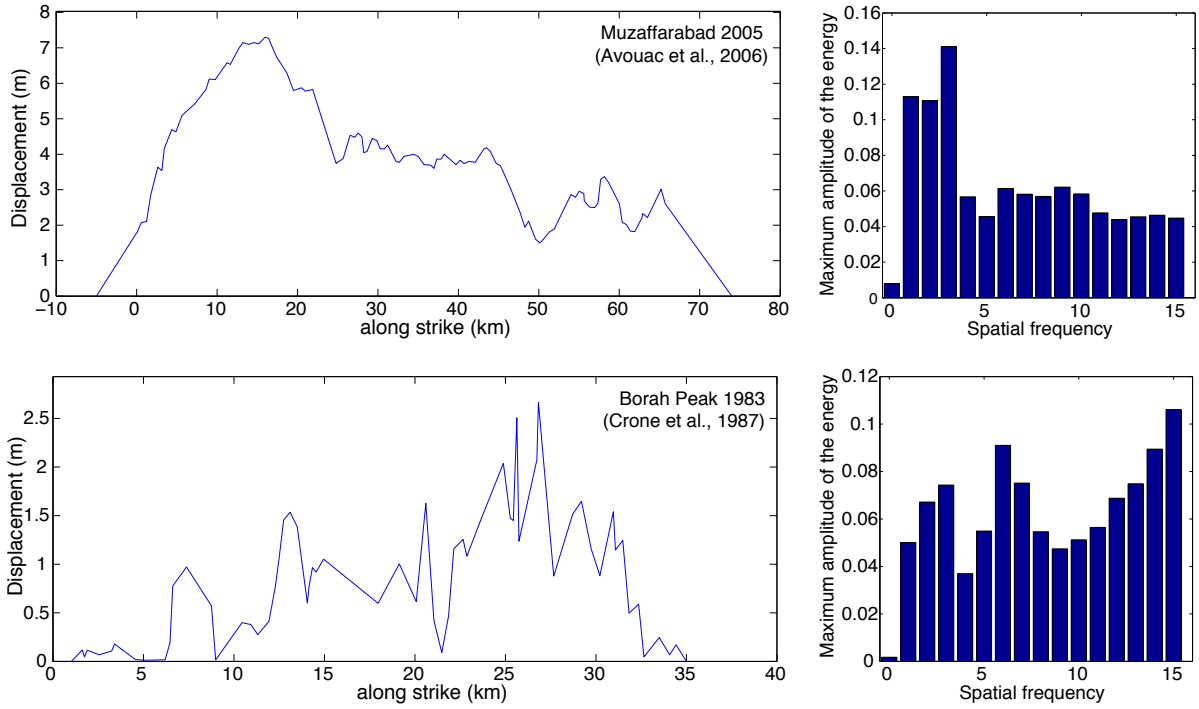


Fig. 181: Examples of S-tranform analysis of the coseismic slip profiles. To the left, two examples of surface slip-length profiles. To the right, the histograms showing the amplitude of the slip profile energy at the various spatial frequencies. See text for details.

Figure 182 shows the histogram of the "best" spatial frequencies (i.e., those coinciding with the maximum Stockwell amplitude) for the entire collection of the surface slip-length profiles (29 profiles). The majority of the slip profiles (~60 %) are best divided into 2 to 5 major slip bumps, and hence fault segments. This range is in keeping with the number of major segments found along the long-term faults (See chapter II and Manighetti et al., 2009, 2013). Based on this result, I have thus retained, for all the slip profiles, the spatial frequency in the range 1-5 that would best represent the slip profile.

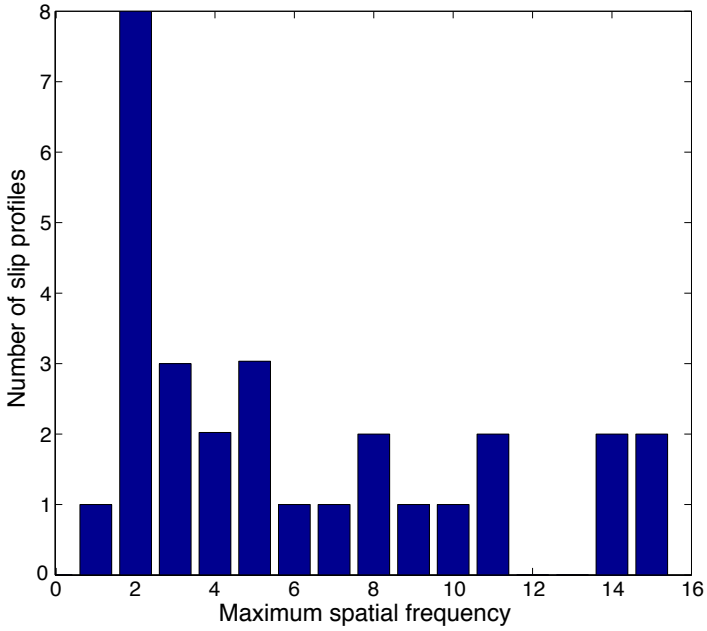


Fig.182: Histogram of the largest spatial frequencies which best represent the surface slip-length profiles.

Figure 183a shows the results, i.e., plots the number of major slip bumps determined with the Stockwell approach, as a function of the degree of asymmetry of the surface slip-length profiles (See Fig.183b for EQ names). The results are similar than those in Fig.179: an overall tendency exists that relates the number of broken segments with the degree of asymmetry of the slip profile; more precisely, the larger the number of broken segments, the more asymmetric the slip-length profile. A few data points depart from the overall tendency, but those are generally poorly constrained data (plus the Duzce case, already discussed before). The absence of "one segment' is inherent to the Stockwell method, that always divides the profile into smaller scale pieces.

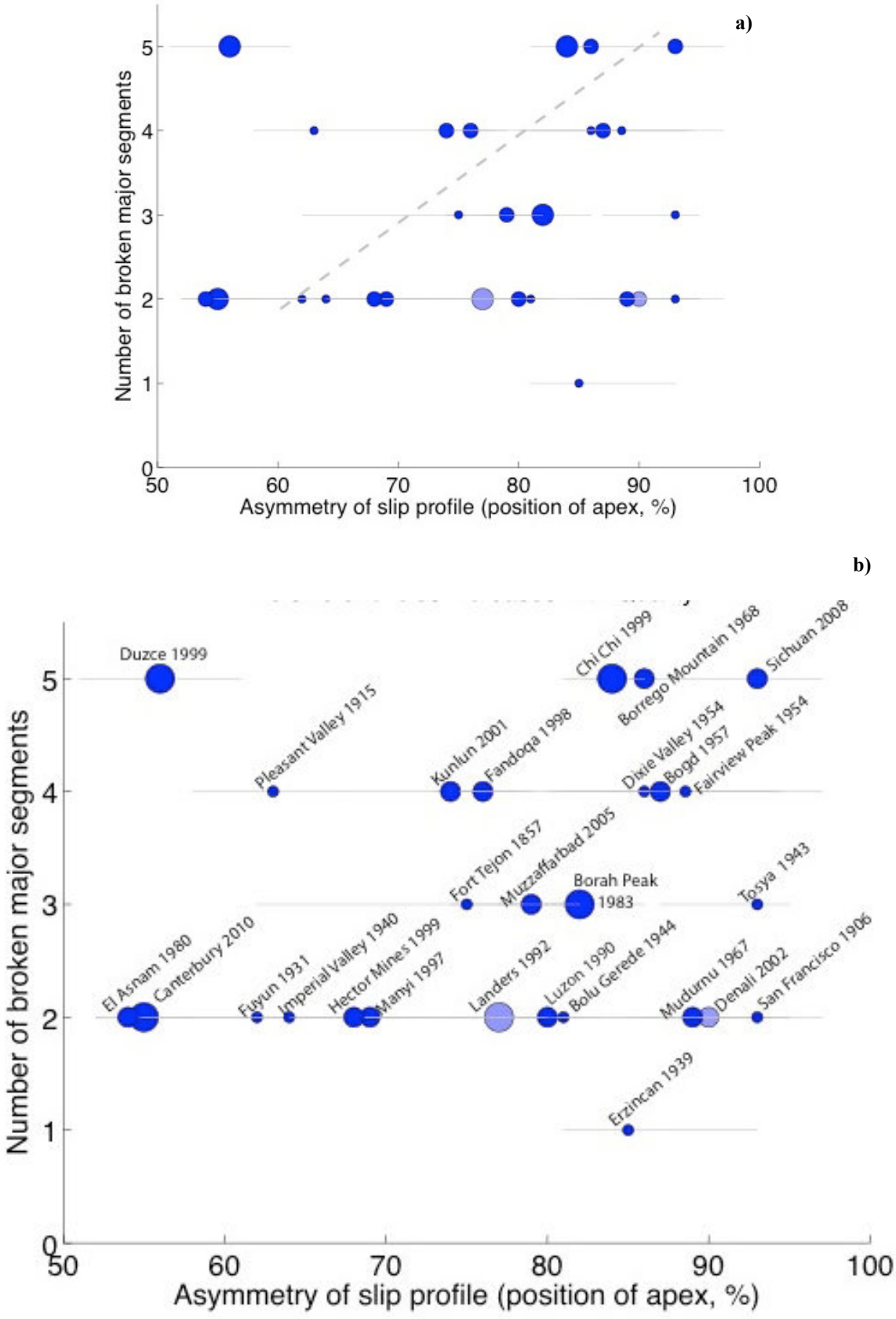
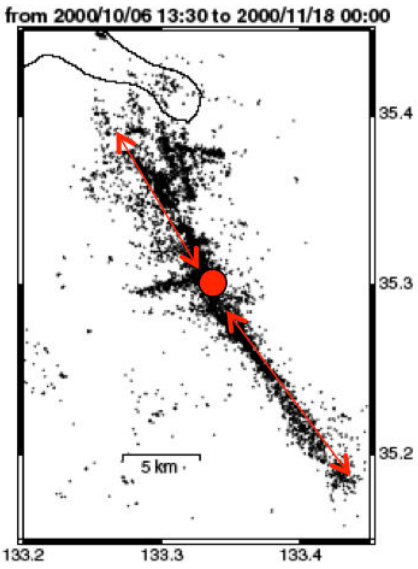


Fig.183: (a) Degree of asymmetry of the surface slip-length profiles as a function of the number of broken segments derived from the signal processing S-Transform, Stockwell method (see text for details). In pale are the mutl-fault ruptures. The dotted line indicates a tendency but is not an actual regression. (b) same as (a) with EQ names.

Figure 185a is similar to Fig. 183a but for the slip-length profiles inferred at depth from the best source inversion models (See Fig.185b for EQ names). Although it is less clear, the figure is in keeping with the results above. It must be noted that most data points that depart from the general tendency are not appropriately described. For instance, the Tottori EQ actually broke 2 segments, not 5 (See Fig.184 left); the Landers and Denali EQs are muti-fault ruptures and hence should not be included; the Parkfield EQ likely broke 4 segments (See Fig.184 right).



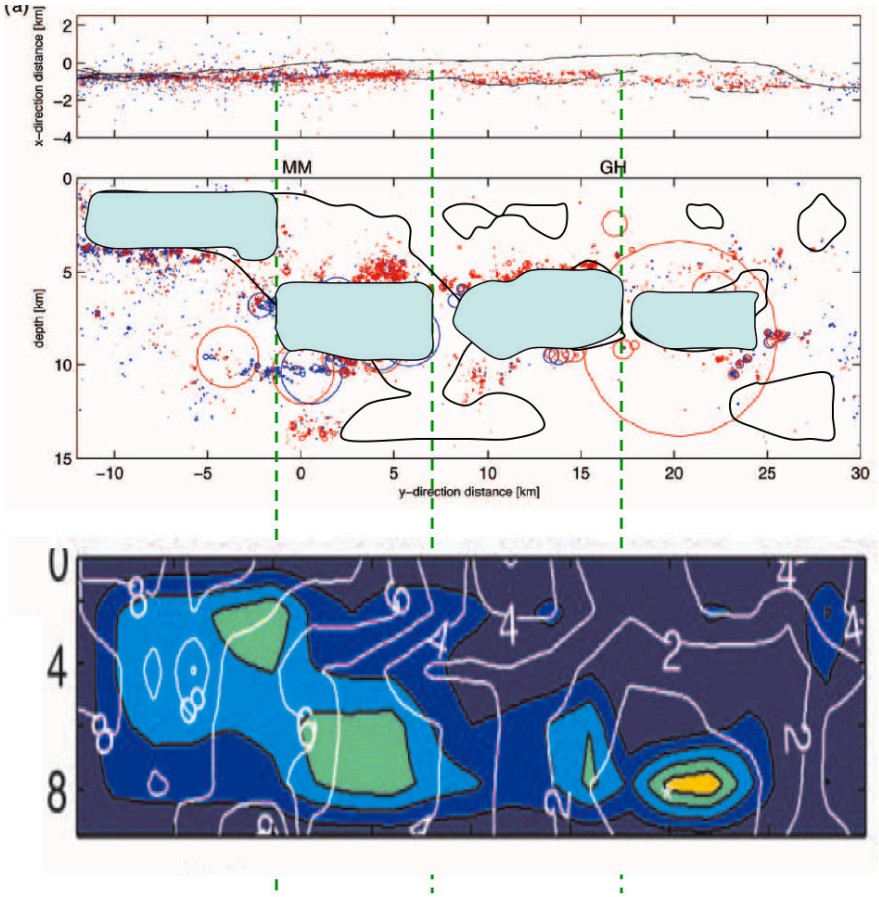


Fig.184: Left: Aftershocks of 2000 Tottori EQ (Fukuyama et al., 2003): they reveal the rupture of two major segments (indicated by arrows) either side of the hypocenter marked with the red circle. Right: The fault geometry, aftershock distribution (Thurber et al., 2006) and source modeling (Liu et al., 2006) all reveal that 4 segments broke in the 2004 Parkfield EQ (modified by me: blue zones).

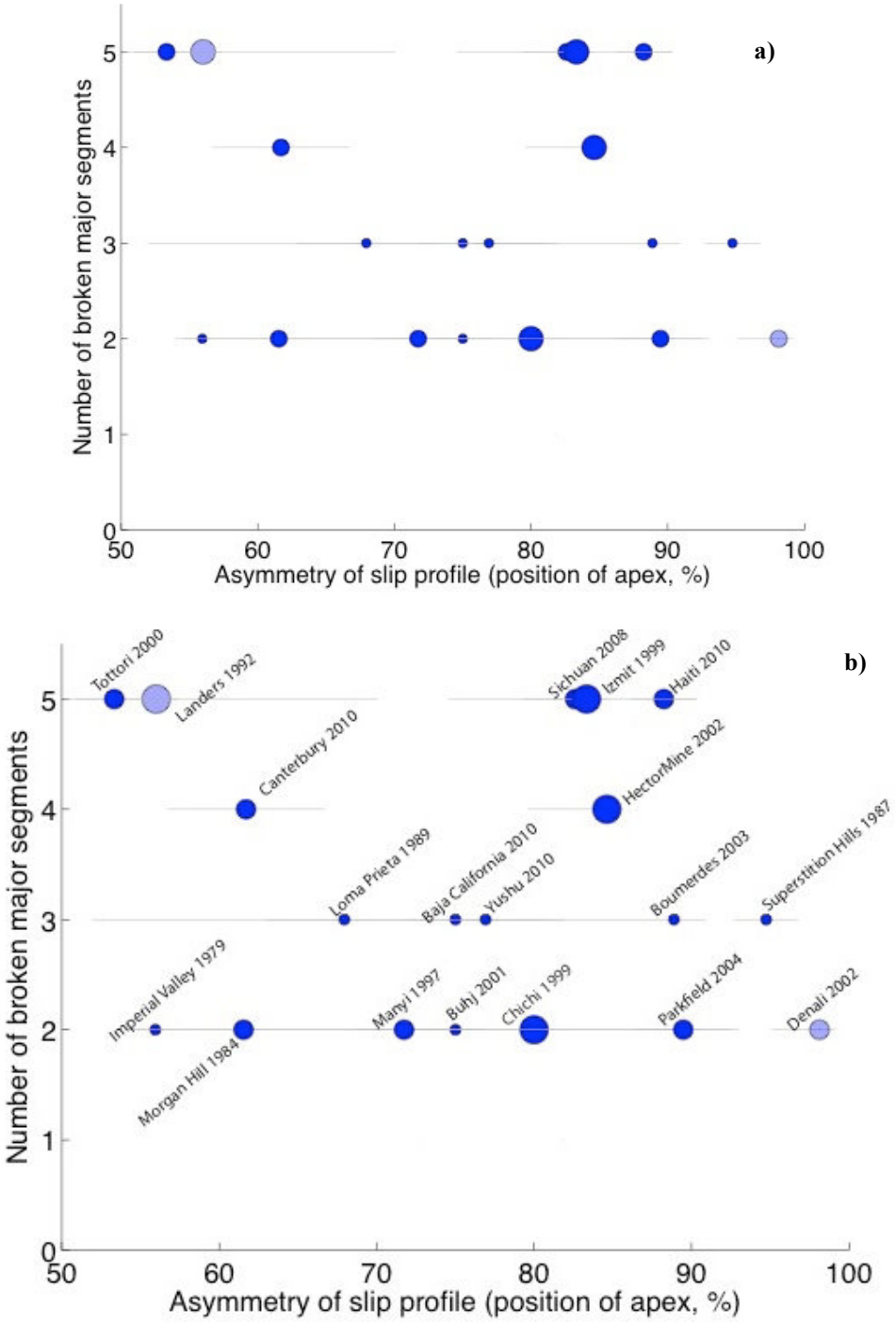


Fig.185: (a) Degree of asymmetry of the EQ slip-length profiles inferred at depth from best source models, as a function of the number of broken segments derived from the signal processing S-Transform Stockwell method (See text). In pale are multi-fault EQs. (b) Same as (a) with EQ names;

From this part of work, I thus conclude that **the degree of asymmetry of the coseismic slip-length profiles is controlled by the number of fault segments that have ruptured**.

5. Relation between asymmetry of earthquake slip profiles and rupture width

Figure 186 shows a few examples of EQ source inversion models (from Table 2). In all these examples, the coseismic slip appears distributed over an area that looks smaller overall than the total L x W surface of the modeled fault. This is not completely surprising since the source models generally overestimate the size of the broken fault to make sure that the recovered slip distribution falls in the correct broken fault dimensions. However, it is interesting to observe that the area, which concentrates the majority of the slip does not look like a smaller version of the rectangular L x W surface.

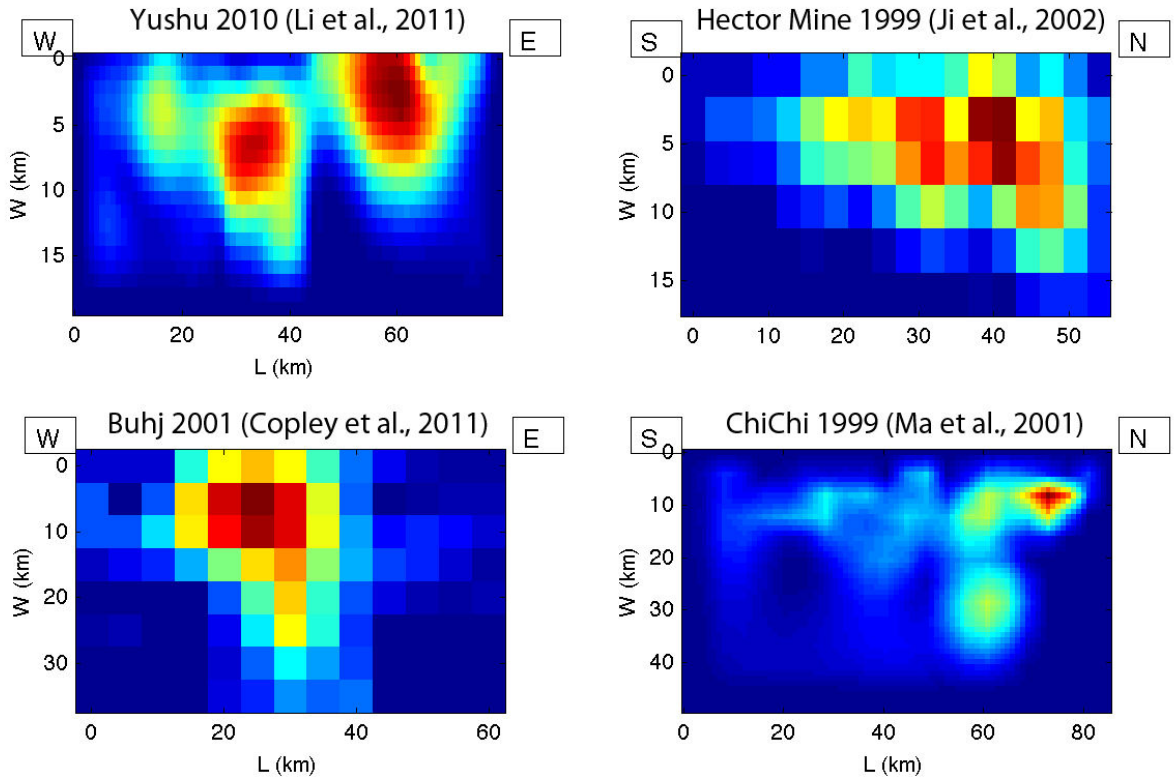


Fig.186: Four examples of EQ source inversion models (from Table 2)

Using the available EQ source models, I have thus tried to define the area where the coseismic slip is actually distributed. Because small slip amounts are generally not well resolved in the source models, and because slip artifacts are common at the model edges, I have resampled the slip values of the models to only retain those greater than 15 % of the maximum slip of the model. The 15 % value has been used in prior works to "clean" the source models (Sommerville et al., 1999). Figure 187 shows an example of the slip "cleaning". Contouring the area inside which the slip is greater than 15 % of the maximum

slip defines a zone of surface Smin where most of the slip, and actually the best-constrained slip, is distributed. In most cases, the Smin surface has a specific shape, fairly different from the rectangular L x W original fault area (model M13, Fig. 188). In a few cases however, the Smin shape remains rectangular (model M14, Fig. 188).

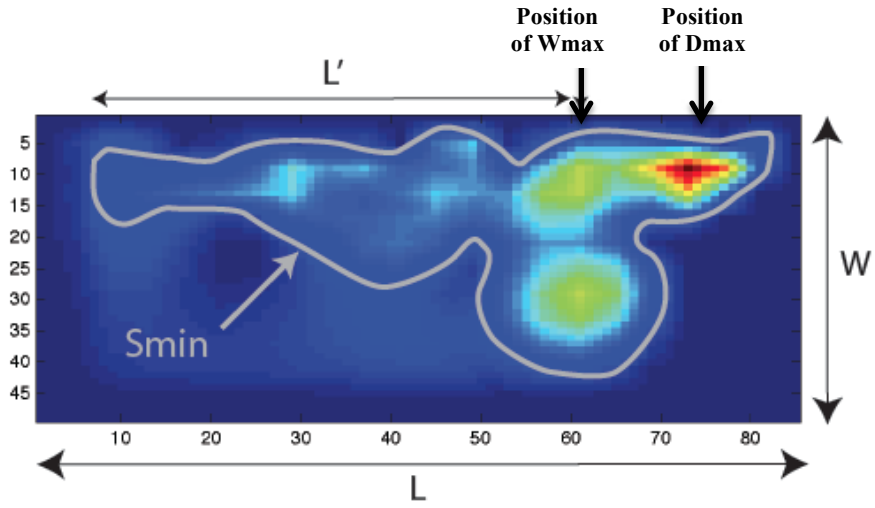


Fig.187: Definition of Smin, that I take to represent the actual broken area.

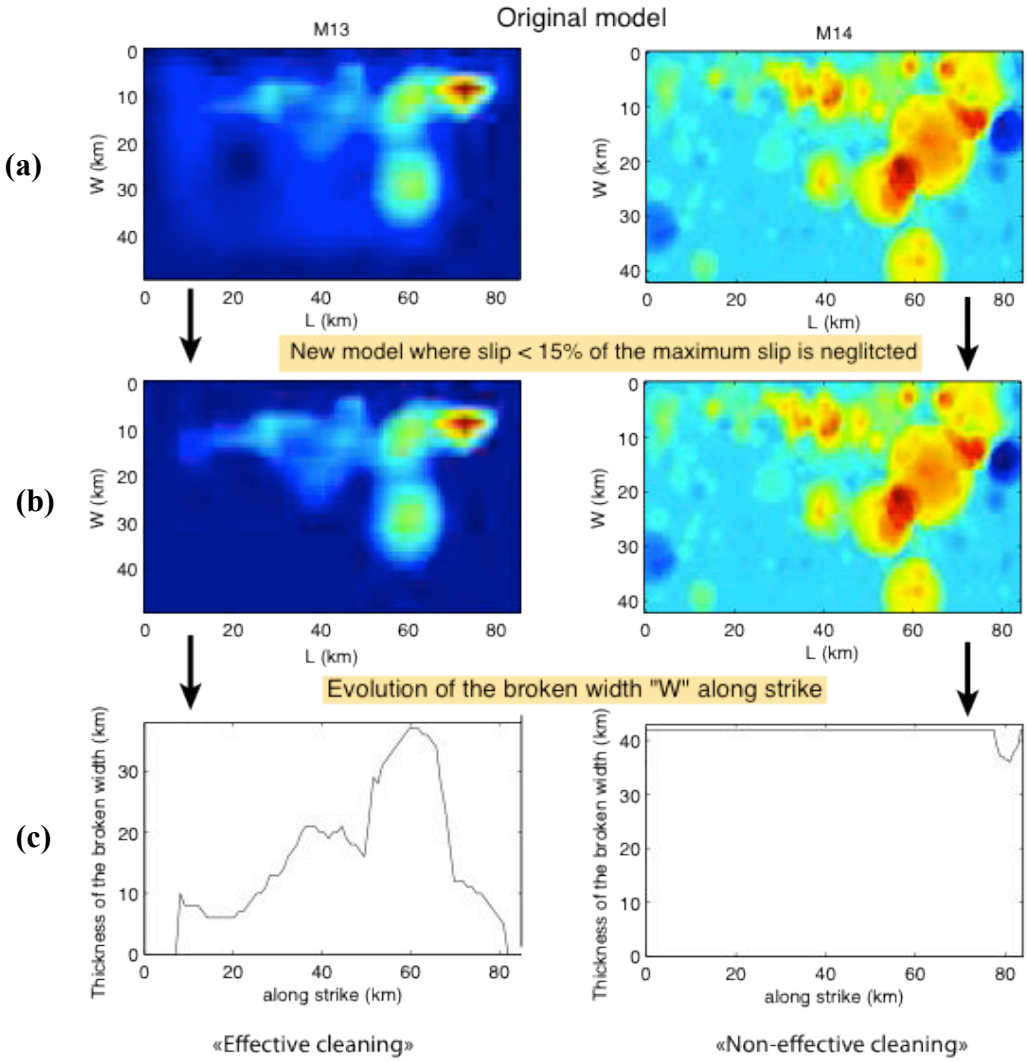


Fig.188: Examples showing how Smin is defined from original models (a) and what it looks like both on the models (b) and on profiles (c) that would represent the variation of the broken width along the rupture length.

Figure 189 plots Smin as a function of S (S equal to L x W), for the entire collection of source models in 189a, for the best models only in 189b, and for the best models with the exception of the subduction EQs in 189c. In all cases, Smin is markedly different and actually lower than the original S area. Where all types of EQs are considered, including subduction, Smin is a ~0.4 fraction of S. When subduction EQs are excluded, Smin is even lower, about a third of S.

Figures 190a-b-c are similar but now discriminate the source models depending on whether the slip-length profile derived from the model is rather symmetric (degree of asymmetry in range 0.5-0.65 % of L; in blue on the figures) or asymmetric (degree of asymmetry > 0.65 % of L; in red on the figures). In all cases, Smin is larger for the EQs whose slip-length profile is fairly symmetric, on the order of 0.4-0.5 S. For EQs with asymmetric slip-length profiles, Smin is lower, on the order of a third of the original S surface. The lowest Smin are found for

the subduction EQs. Therefore, **the actual ruptured surface is far smaller than the rectangular L x W approximation, in the range 0.3-05 of S**.

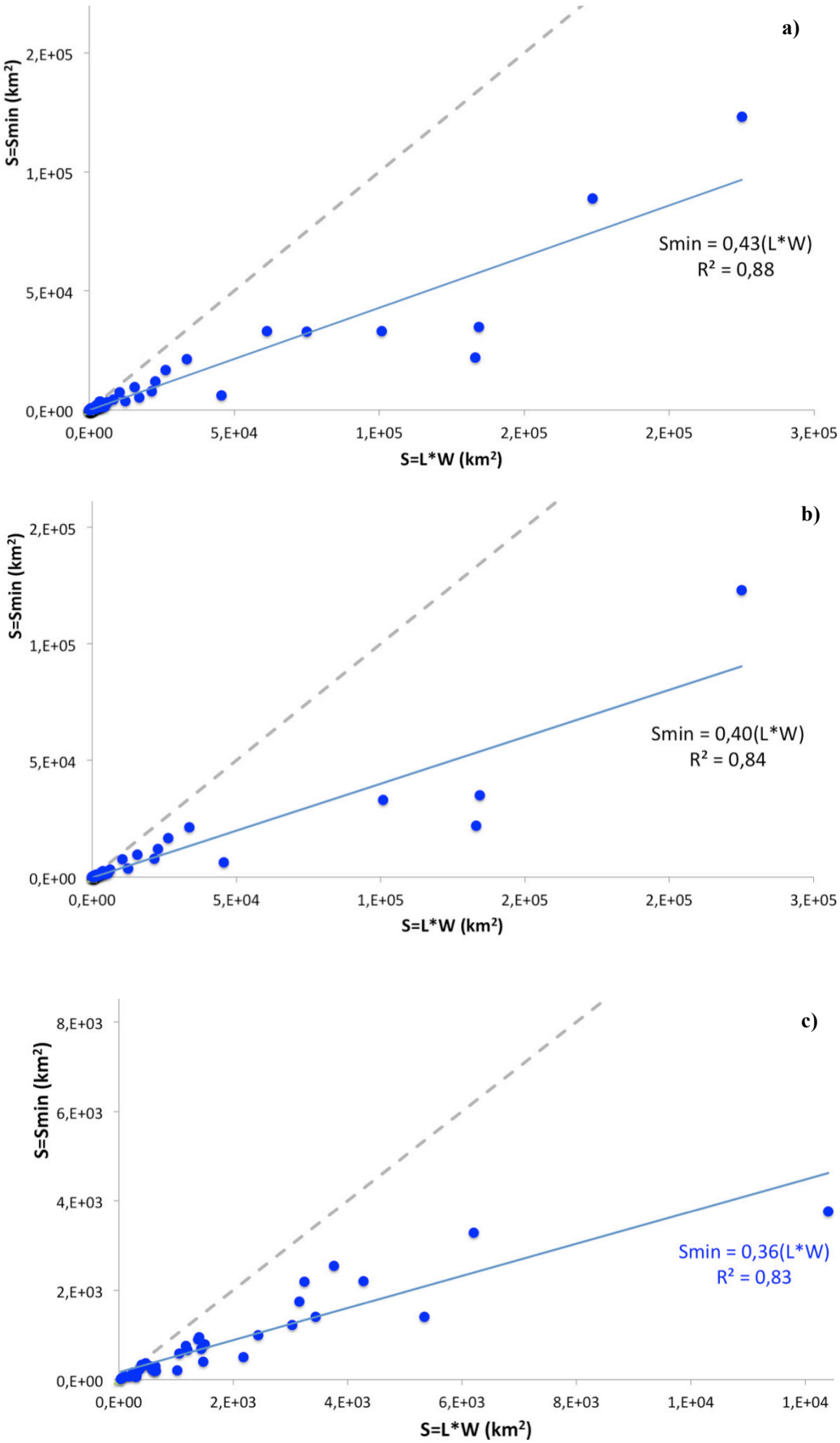


Fig.189: Smin as a function of S (S equal to L x W), for the entire collection of source models in a, for the best models only in b, and for the best models with the exception of the subduction EQs in c.

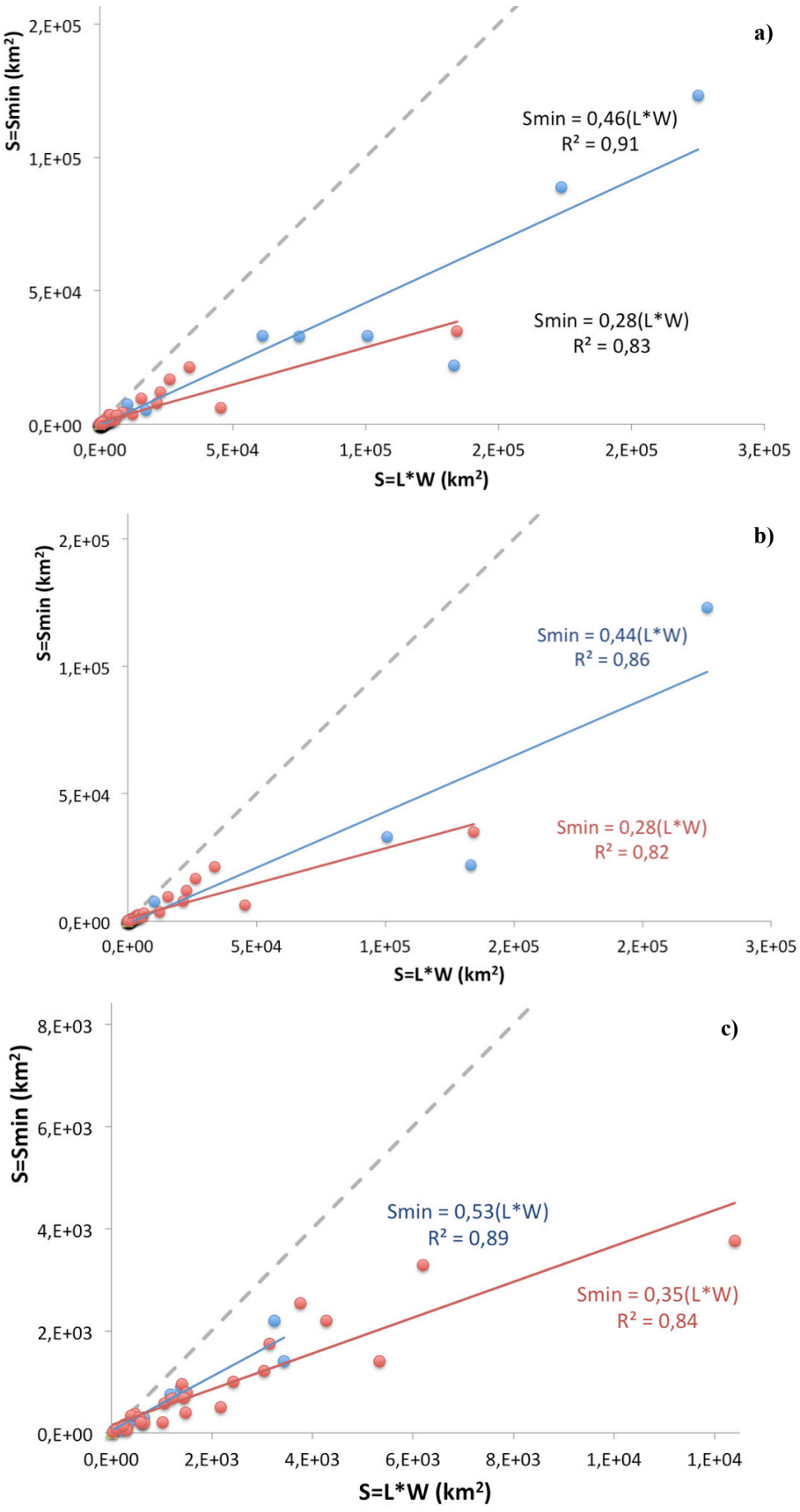


Fig.190: Sames as Fig. 189 but source models discriminated depending on whether the slip-length profile is rather symmetric (degree of asymmetry in range 50-65 % of L; in blue on the figures) or asymmetric (degree of asymmetry > 65 % of L; in red on the figures).

Figure 191a examines the distance between the zone where the broken fault width is largest and the zone where the maximum coseismic slip has developed. That distance Dmax-Wmax is normalized to the total rupture length. The histogram of the Dmax-Wmax normalized distances shows that, in most EQ cases, the ruptured fault section is largest along-dip very close to the zone of maximum slip; the distance between Wmax and Dmax is generally shorter than 10-15 % of the rupture length. Figure 5f-b provides additional details as it shows all EQs individually. The longer Dmax-Wmax distances are found on a few large subduction EQs.

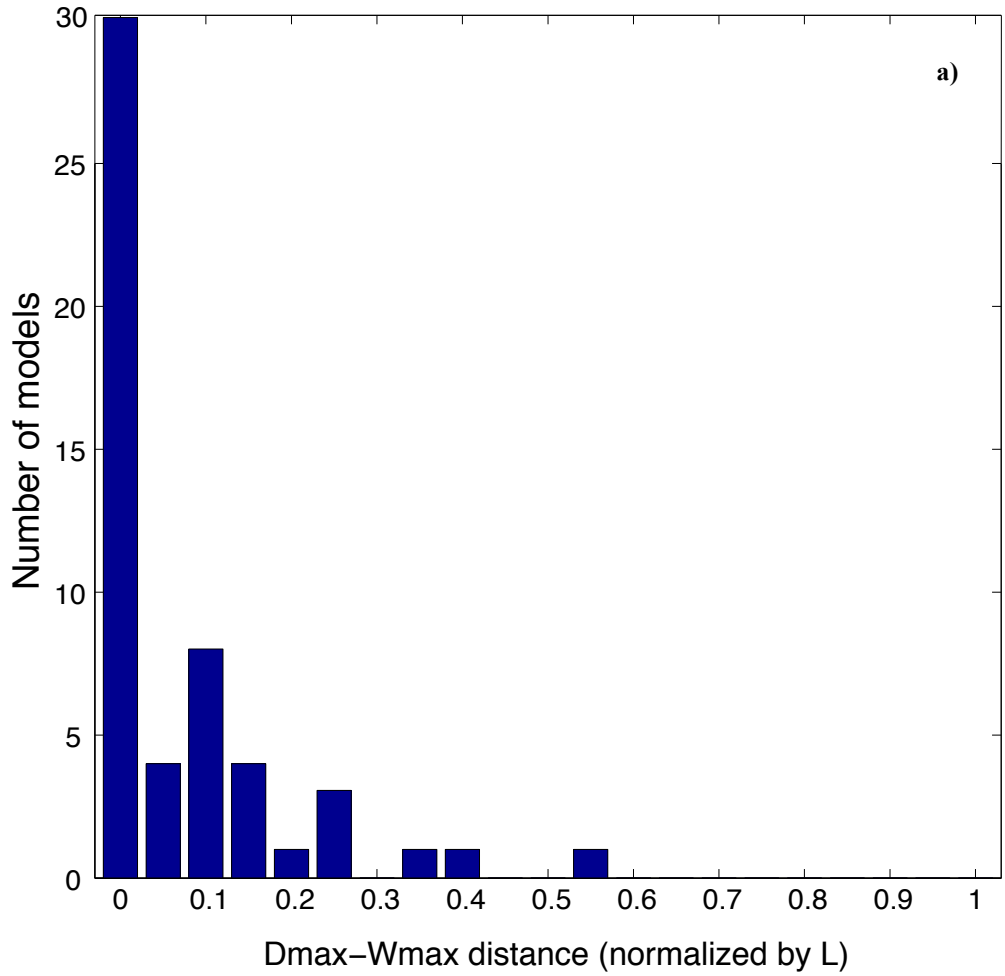


Fig.191: a) Distibution of the distances between the zone of maximum broken width and the zone of maximum coseismic slip. In most EQ cases, that distance Dmax-Wmax is very short, at most 10-15 % of the rupture length.

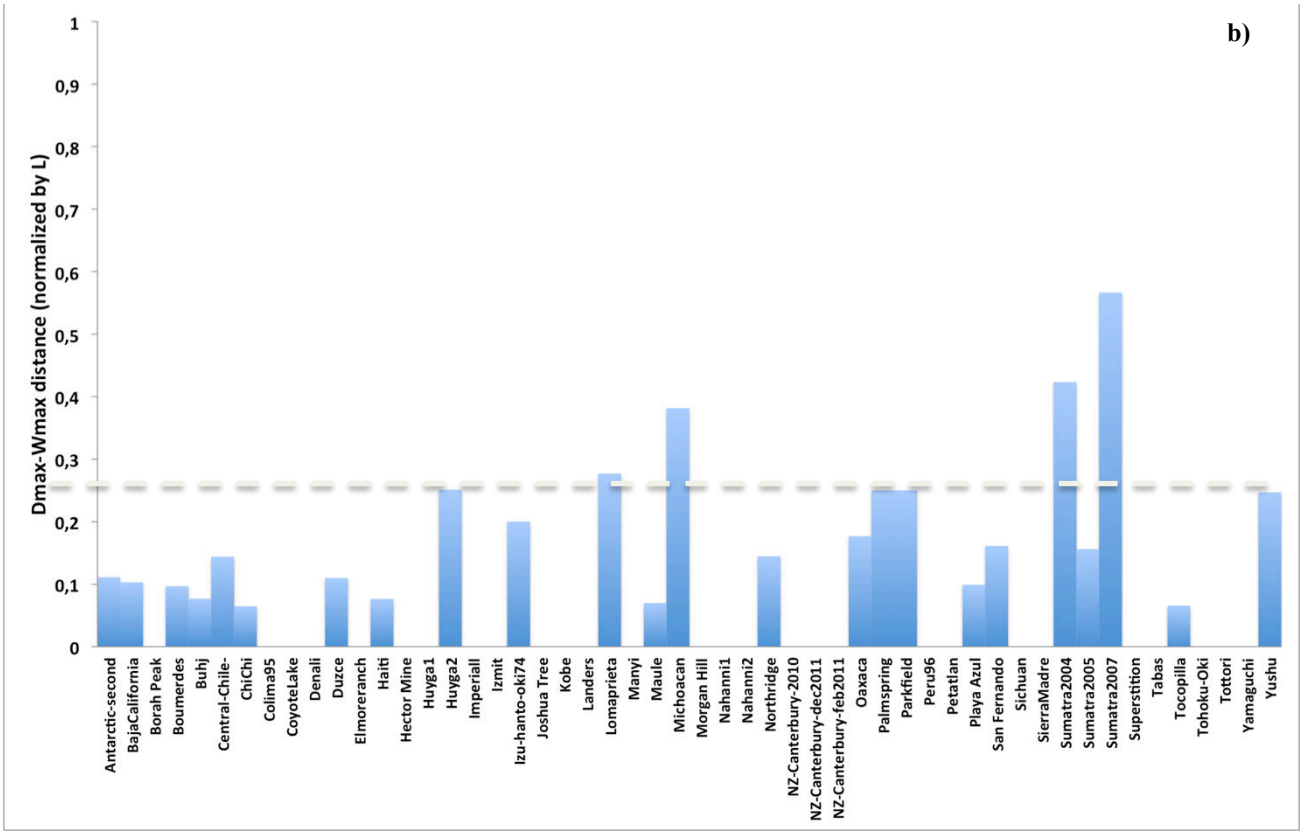


Fig.191: b) The normalized distance Dmax-Wmax is here shown for each EQ case.

Figure 192 now examines the way the rupture width varies along the rupture length. The figure only includes the EQs for which I could observe a W variation along the rupture length (~70 % of the total EQ population, best models considered, including subduction EQs). I have defined as zero along the fault length the position of the maximum width. From that zero position, I have defined a length L' which represents the longest rupture section over which W varies (See Fig.187 before). I have then measured Wi at different points along L', and plotted the ratios Wi/Wmax as a function of the normalized position along L'. Figure 192 is made for the best source models only. Figure 192a is for all best models except those for subduction EQs. It shows that W decreases fairly regularly along L', from the widest broke zone up to one of the rupture tips. Including the subduction EQS does not change the results (Fig.192b). If we now only consider the EQs whose modeled slip-length profile is asymmetric (Fig.192d), the fairly linear decrease of W as a function of L' is even clearer. A regression can be calculated that shows that **the broken fault width decreases by a ratio of ~0.7 along the rupture length, away from the largest broken part of the fault**.

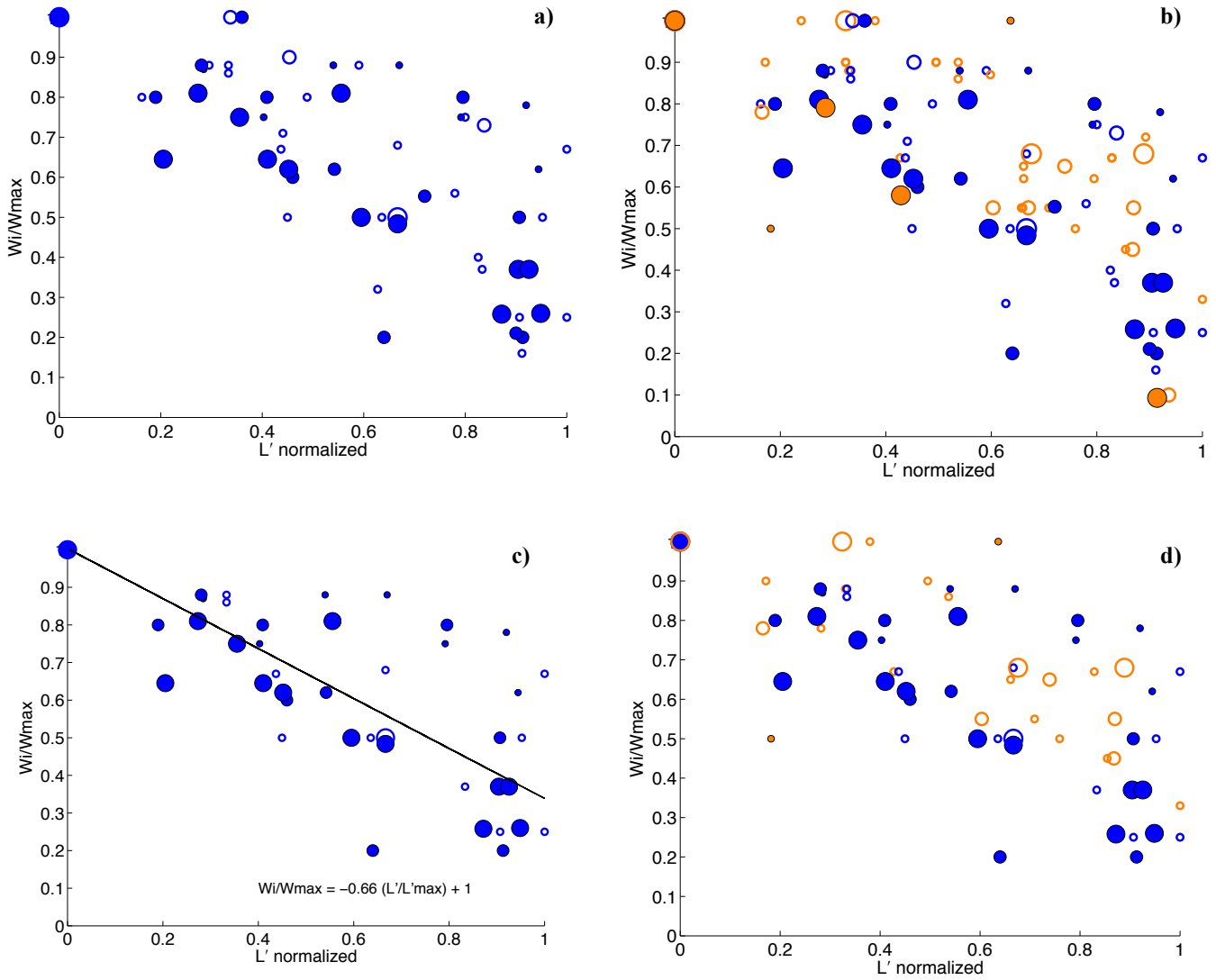


Fig.192: Variation of the broken fault width along the rupture length, considered from the site of maximum width. (a) all continental EQs from best model data; (b) All continental and subduction EQs (orange) from best model data; (c) Same as (a) but for EQs having an asymmetric slip-length profile; (d) same as (b) but for EQs having an asymmetric slip-length profile.

Figure 193 now examines whether the W variation is related to the slip distribution along the rupture. Together with the Wi measures discussed above, I have thus measured the corresponding Di slip values. I have then plotted the Wi/Wmax ratio as a function of the Di/Dmax ratio. Figure 193a is build for continental EQs (Best models; see Fig.193c for EQ names) and shows that overall, the ruptured W decreases as the coseismic slip decreases along the rupture length. In the fault section over which the coseismic slip is fairly high although slightly lower than Dmax, the rupture width remains fairly high as well although slightly lower than Wmax. But then, where Di reaches ~0.6 Dmax, both the slip and the W decrease markedly along the rupture length. Including the subduction EQs does not change the results (Fig.193b). If we now only consider the EQs whose modeled slip-length profile is asymmetric (Fig.193d-e), the concomitant decrease of W and D along the rupture length is even clearer.

Although the decrease is not strictly linear, a regression well approximates the observations and shows that **the concomitant W-D decrease follows a ~0.66 tendency**.

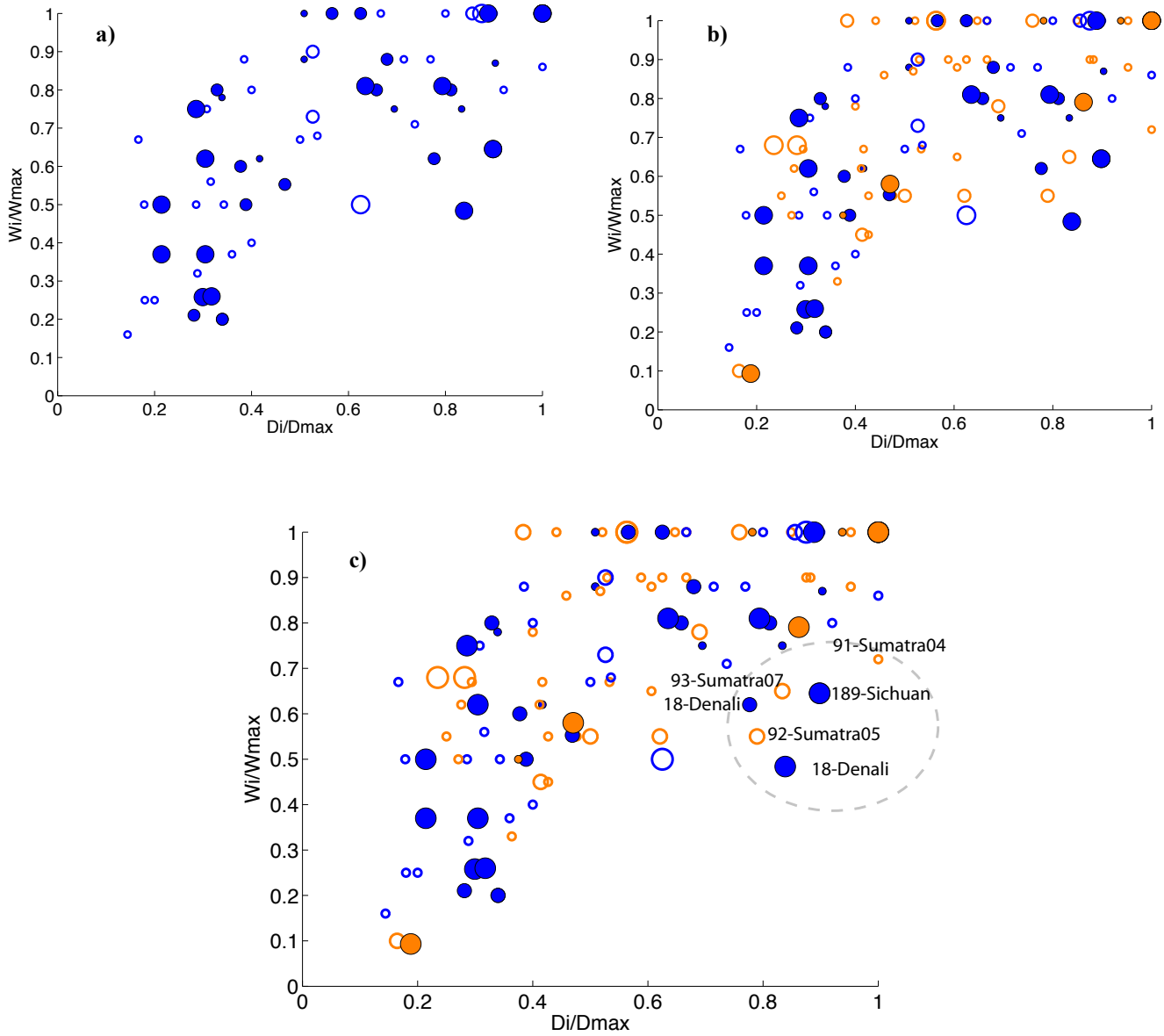


Fig.193: (a) Variation of the broken width as a function of the variation of the coseismic slip along the rupture length. For all continental EQs (best models). (b) same as (a) but with subduction EQs included (in orange). (c) same as (b) with names of EQs.

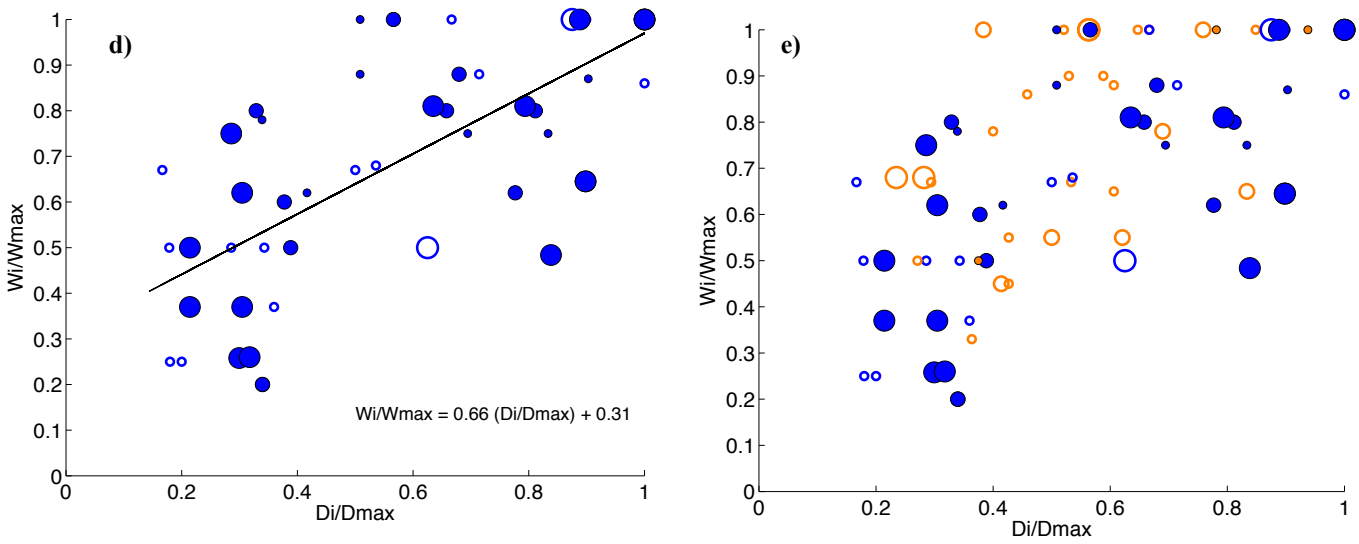


Fig. 193: (d) same as (a) but only for EQs with asymmetric slip profile. (e) same as (d) but with subduction EQs also included

In the best model collection, 26 EQs have their maximum slip located in the widest broken fault zone. When only these EQs are considered (Fig.194), the results above are even clearer. **A slope of ~2/3 controls both the decrease of W along the rupture length and the concomitant decrease of W with D**. Note that I have examined whether the W decrease along L depends on the EQ stress drop, and I found no concluding result.

Finally, Fig. 195 examines whether the ratio Wi/Wmax nearby the rupture end (along the L' section; here measured at Li = 2/3 L') –which marks the importance of the W decrease, depends on the number of broken fault segments. Unfortunately, the data are too few to conclude. With the exception of two data points, the figure suggests however that a tendency might exist between the two parameters, and hence suggest that the larger the number of broken segments, the smaller the Wi/Wmax ratio at the rupture tip and hence the more important is the W decrease. The two points outside of this tendency are the 2010 Yushu (left) and the 1997 Manyi EQs (right). We have seen in the ID of Yushu that even the best source models are not well constrained. The source model of the Manyi EQ is also poorly constrained at depth since no seismological data were used in the inversion.

This part of the work thus shows that **the width of the broken fault much varies along the rupture length, and cannot be approximated by L x W. Instead, it is overall a 0.3-0.5 fraction of L x W. The fault is most widely broken in or nearby the zone of maximum coseismic slip. The width of the broken fault then decreases along the rupture length by a factor of about 2/3, and the decrease is concomitant with the slip decrease along the**

rupture. The decrease in the width of the broken fault seems to be even more pronounced, as more segments are broken along the fault.

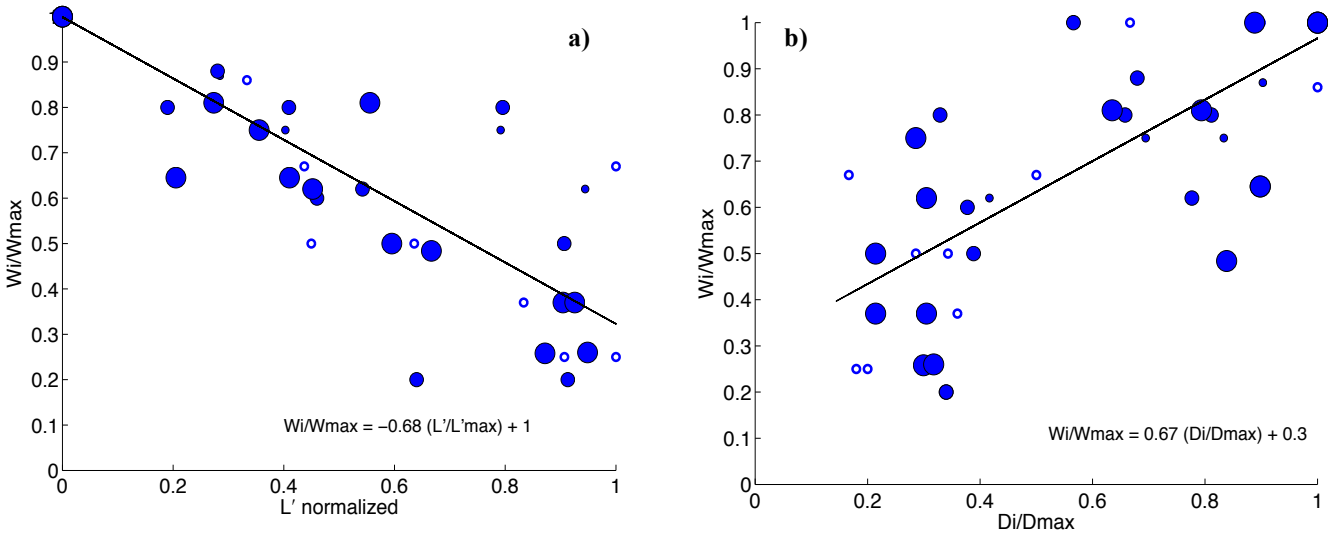


Fig. 194: (a) Variation of W along the rupture length, for EQs (best models) which have their Dmax located in the zone of Wmax. (b) Concomitant variation of W and D along the rupture length, for EQs (best models) which have their Dmax located in the zone of Wmax.

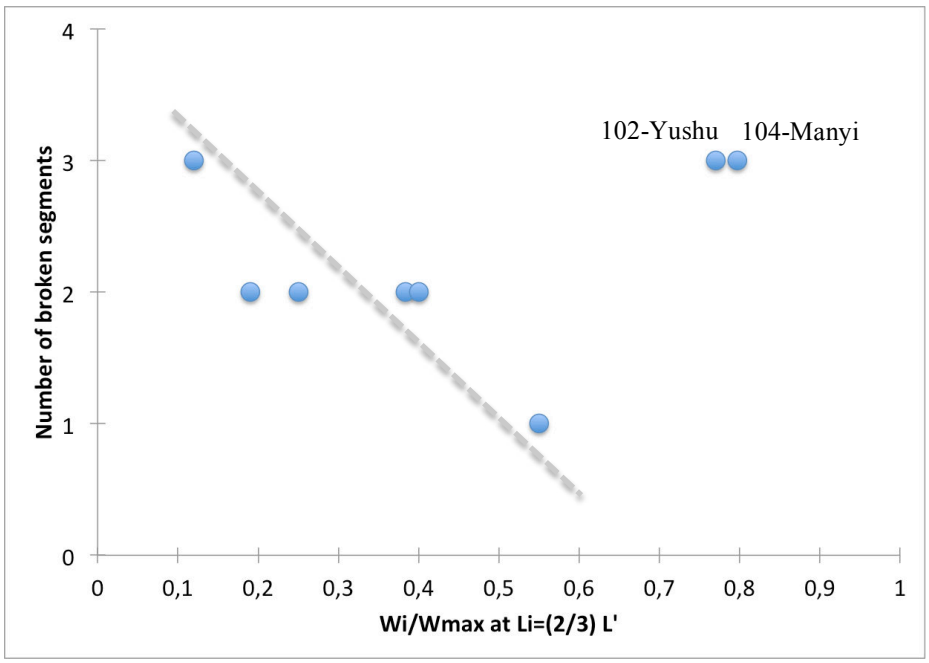


Fig. 195: Ratio Wi/Wmax nearby the rupture end (along the L' section; here measured at Li = 2/3 L') as a function of the number of broken fault segments

6. Relation between asymmetry of earthquake slip profiles and structural maturity of the broken fault

Figure 196 shows the degree of asymmetry of the slip-length profiles (196a-b: at surface; 196c-d: inferred at depth from best source models) as a function of the structural maturity of the broken faults, as defined in Table 5. The figures show that a tendency exists between the two EQ and fault parameters: **the more mature is the broken fault, the more asymmetric is the slip-length profile of the EQ that the fault has produced**. A few points depart from this general tendency in Fig. 196, but those are all poorly constrained slip-length data.

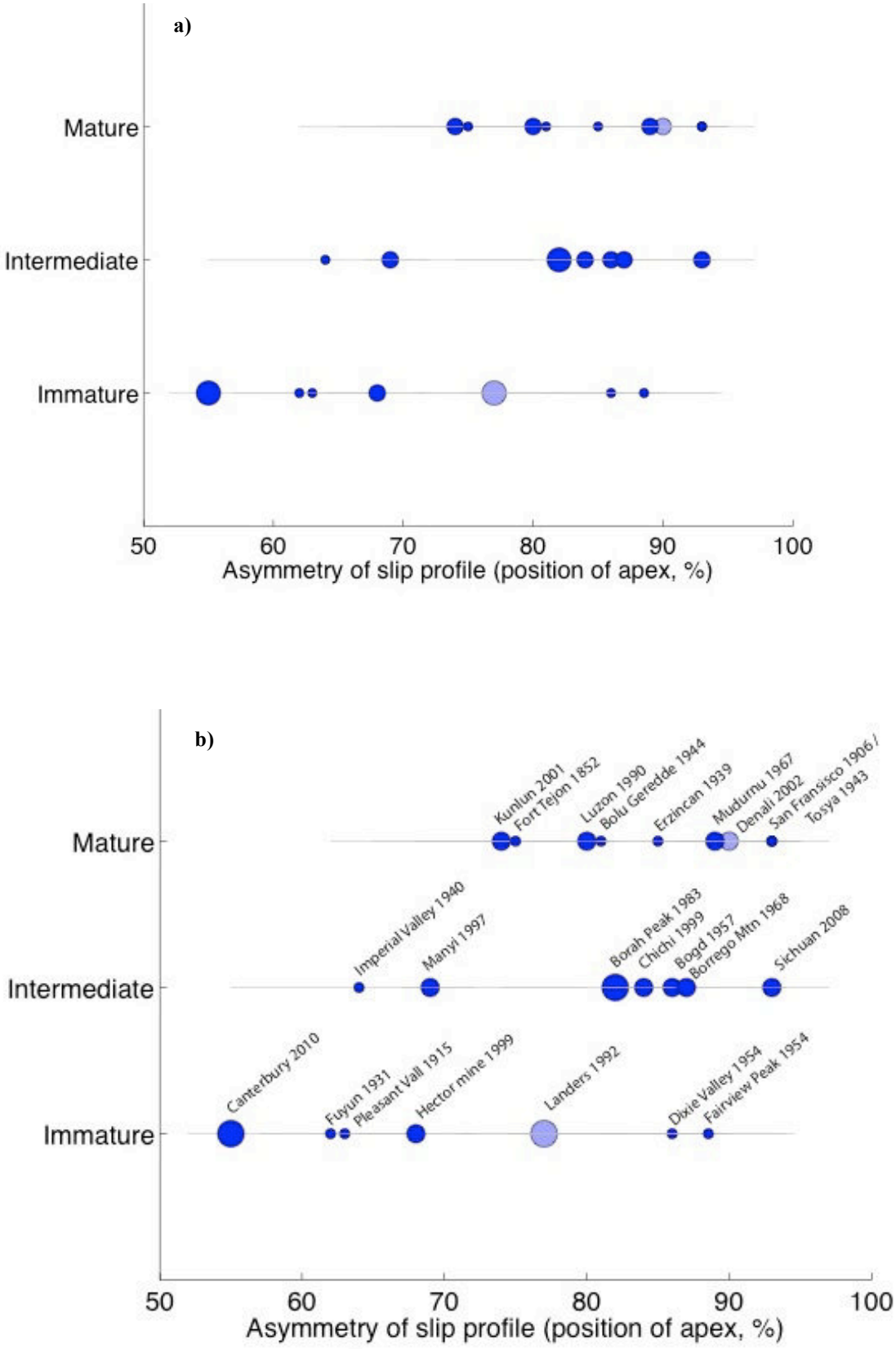


Fig.196: a) Degree of asymmetry of surface slip-length profiles as a function of the structural maturity of the broken faults (from Table 5). (b) same as (a) with names of EQs

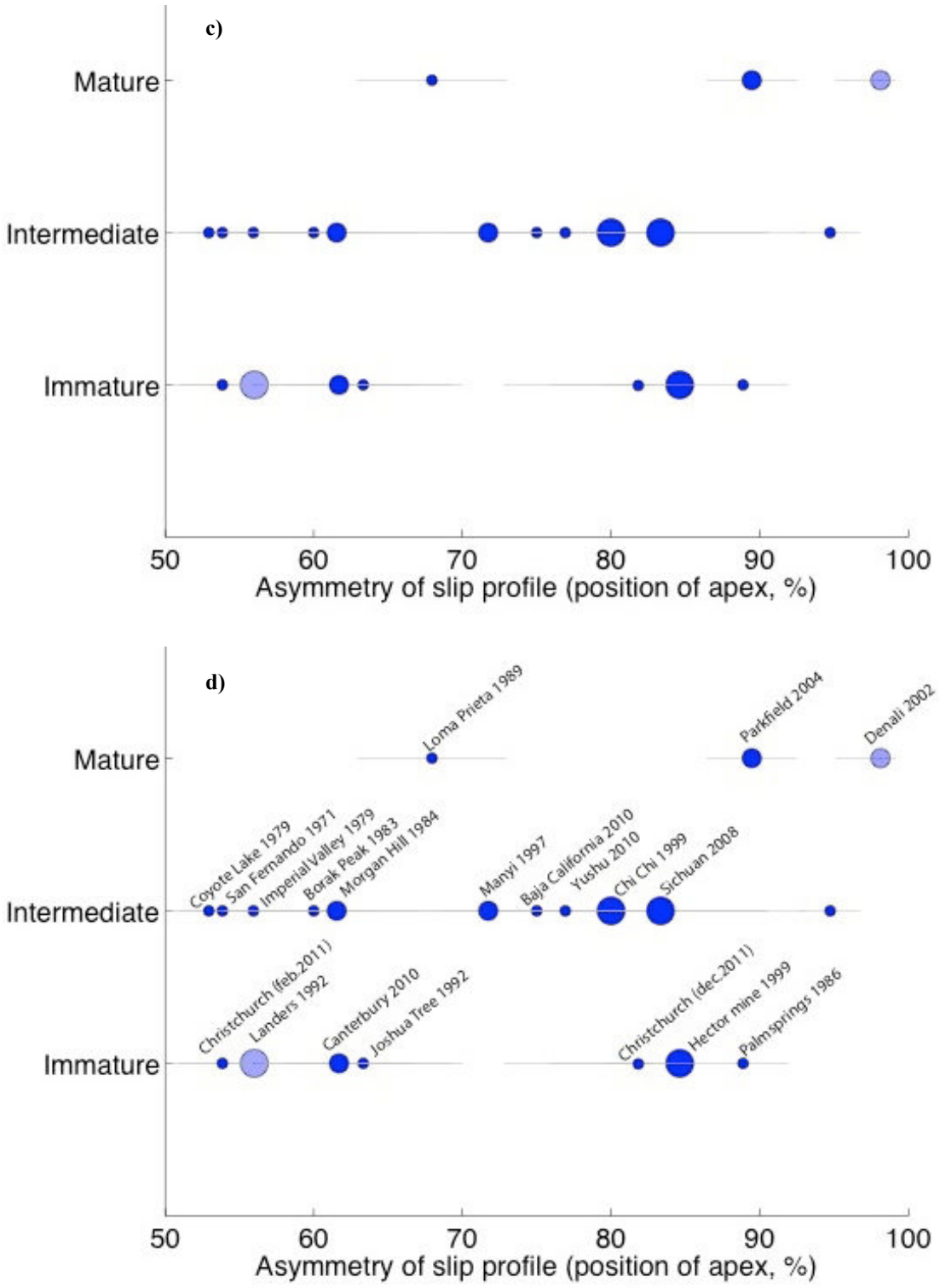


Fig.196: c) Degree of asymmetry of slip-length profiles at depth from best models) as a function of the structural maturity of the broken faults (from Table 5). (d) same as (c) with names of EQs

7. Relation between asymmetry of earthquake slip profiles and direction of long-term lateral propagation of the ruptured faults

Figure 197 focuses on the 21 EQ and fault couples that I have analyzed in the IDs of Chapter II. Complementary figures can be found for the North Anatolian EQs in the short section that describes these EQs (Chapter II). Figure 197 (and complementary figures on NA EQs) presents simplified maps of the long-term faults involved in the EQs, where I have underlined with different colors the major segments of the fault. The colors are made to qualitatively indicate the differential maturity of the successive major segments that constitute a fault, as I could derive it from the knowledge of the direction of long-term fault propagation (indicated with arrows): in the zone where the fault is supposed to have initiated, the segments are the most ancient, and I indicate them in red. Toward the present fault termination where the fault is supposed to have developed recently as a result of its lateral long-term lengthening, the segments are the youngest, and I indicate them in blue (paler blue for younger age). In between, the segments have an intermediate maturity, and I indicate them in orange. I then have reported the EQ epicenter in yellow, and the zone of maximum coseismic slip in green. Of course, this is an approximate qualitative estimate of the maturity of the different segments, and more work would need to be done (dating of fault offsets) to determine the actual age of the various segments.

Figure 197 shows that, in all EQ cases, the EQ hypocenter locates either between two major segments having a different structural maturity, or at the fault tip. Furthermore, the maximum coseismic slip develops in the most mature section of the broken fault, which is closest from the hypocenter. It seems that, once the EQ is nucleated, the rupture propagates until it meets a mature portion of the fault, where it then produces the maximum coseismic slip amplitude. Therefore, the maximum coseismic slip occurs on a mature portion of the fault, whereas the rest of the slip is lower on portions of the fault which are more immature. Together these make that a more or less asymmetric coseismic slip profile develops that tapers in the direction of long-term fault lateral propagation.

The asymmetry of the EQ slip-length profiles thus seems to be governed by the maturity properties of the broken fault segments, whereas the coseismic slip profile tapers in the direction of long-term lateral fault propagation. We thus expect the coseismic slip distribution along the rupture to have a similar envelope shape than the long-term slip

distribution on the broken fault section. It is noteworthy that the tapering of the coseismic slip profiles indicates the direction of long-term lateral propagation of the fault, but not necessarily that of the EQ rupture (See Kunlun, Yushu, Denali, Hebgen Lake, San Francisco, Landers EQs, where a long distance separates H and Dmax).

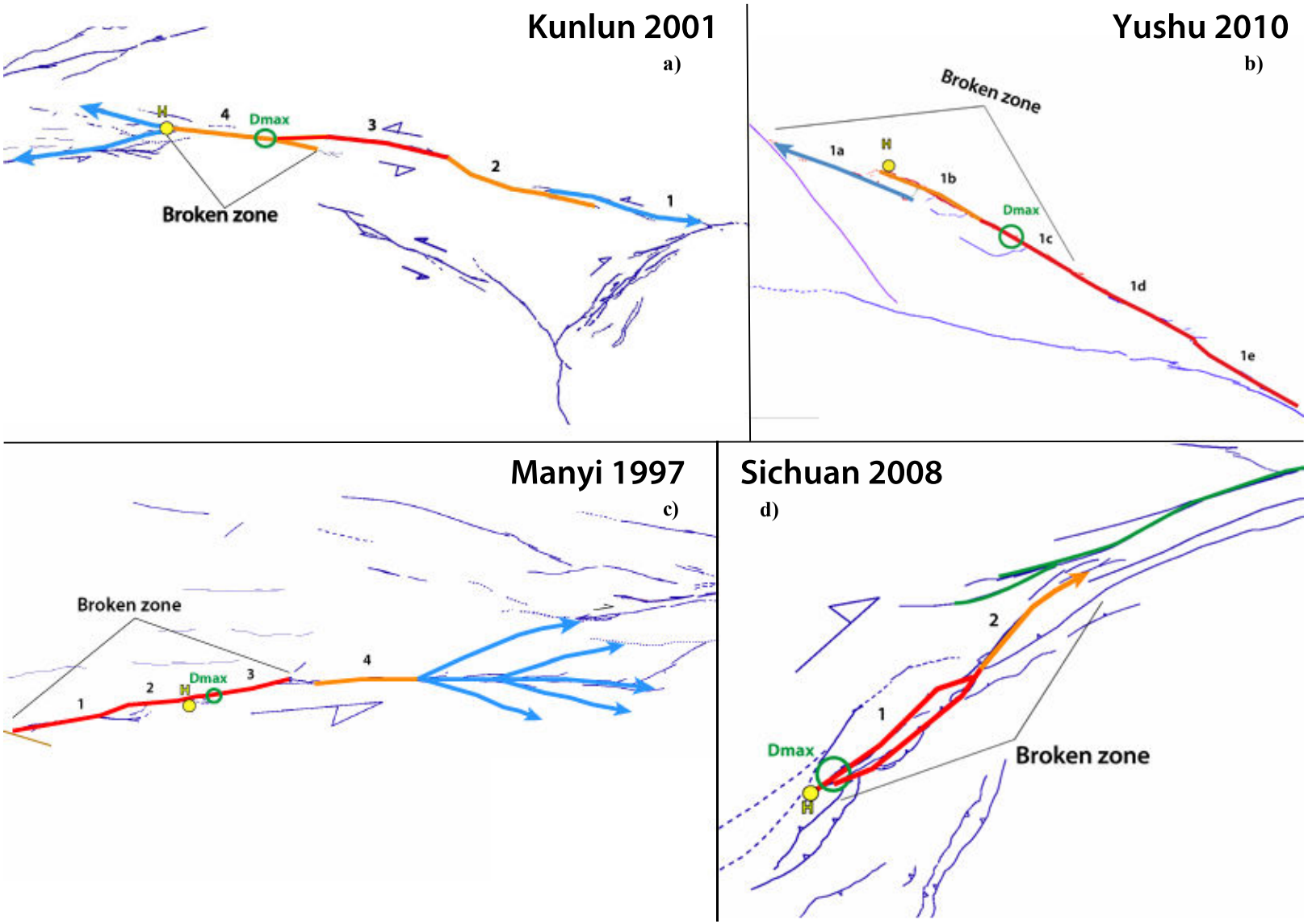


Fig.197: a) b) c) d) see caption below

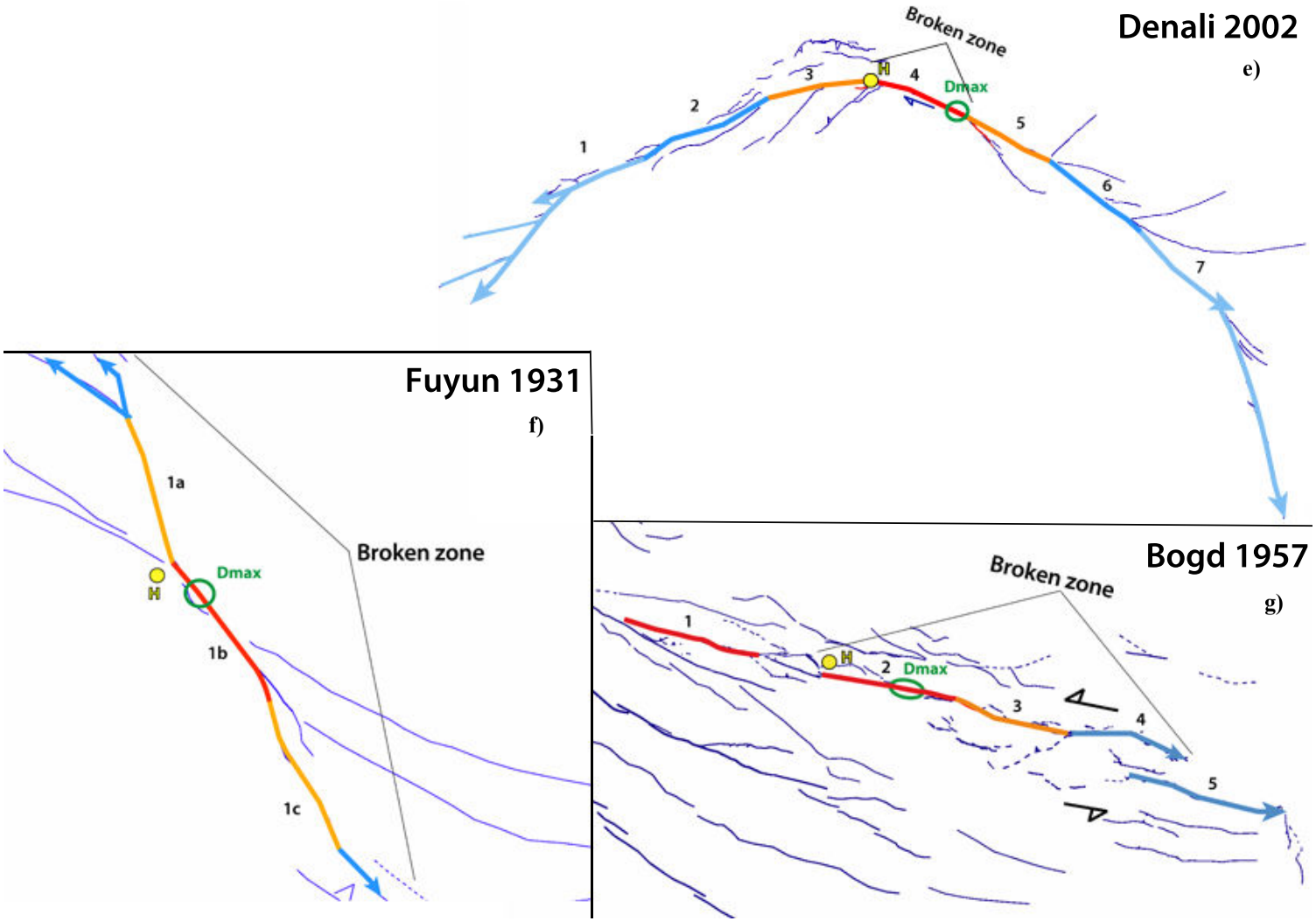


Fig. 197: e) f) g) See caption below

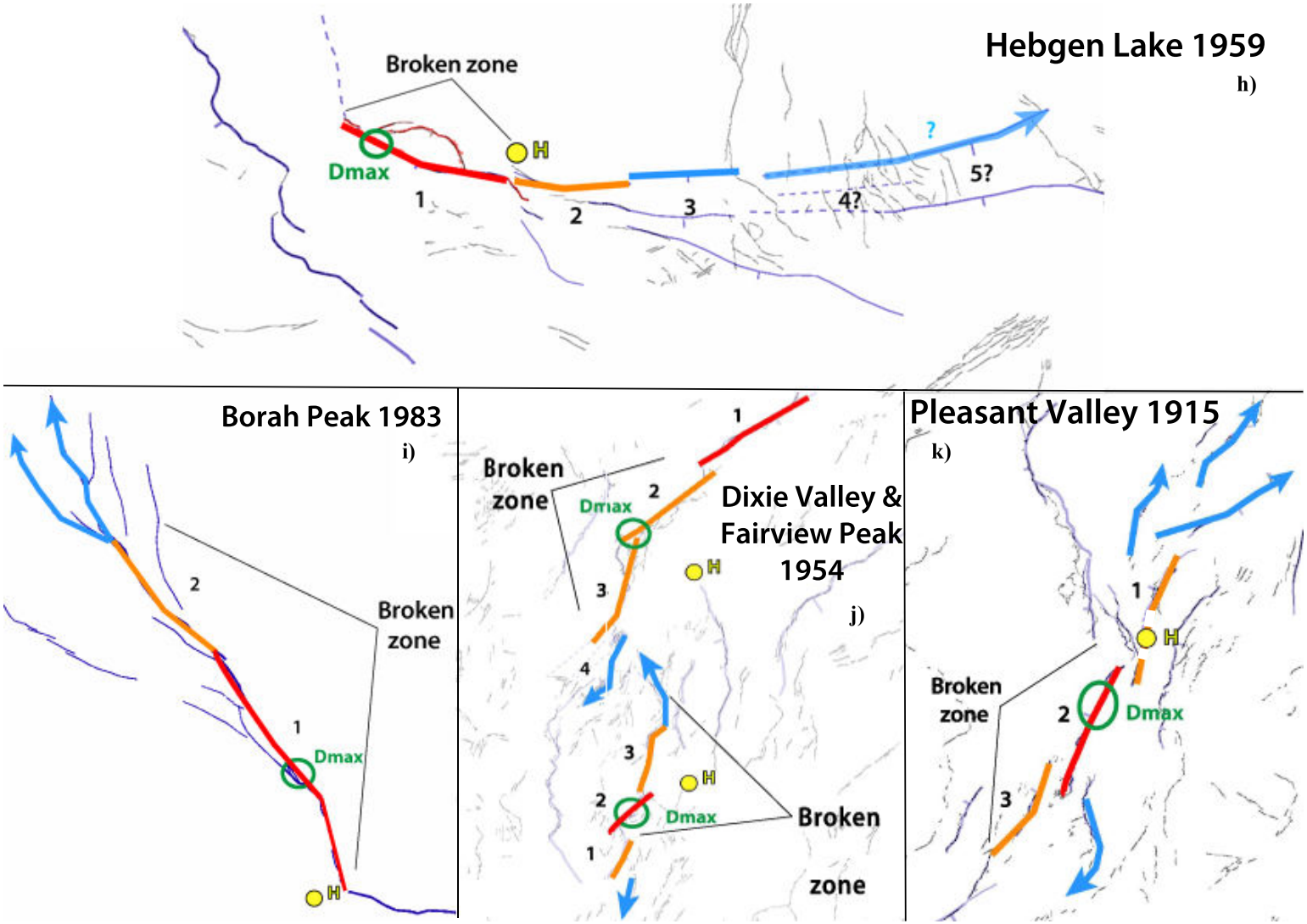


Fig. 197: h) i) j) k) See caption below.

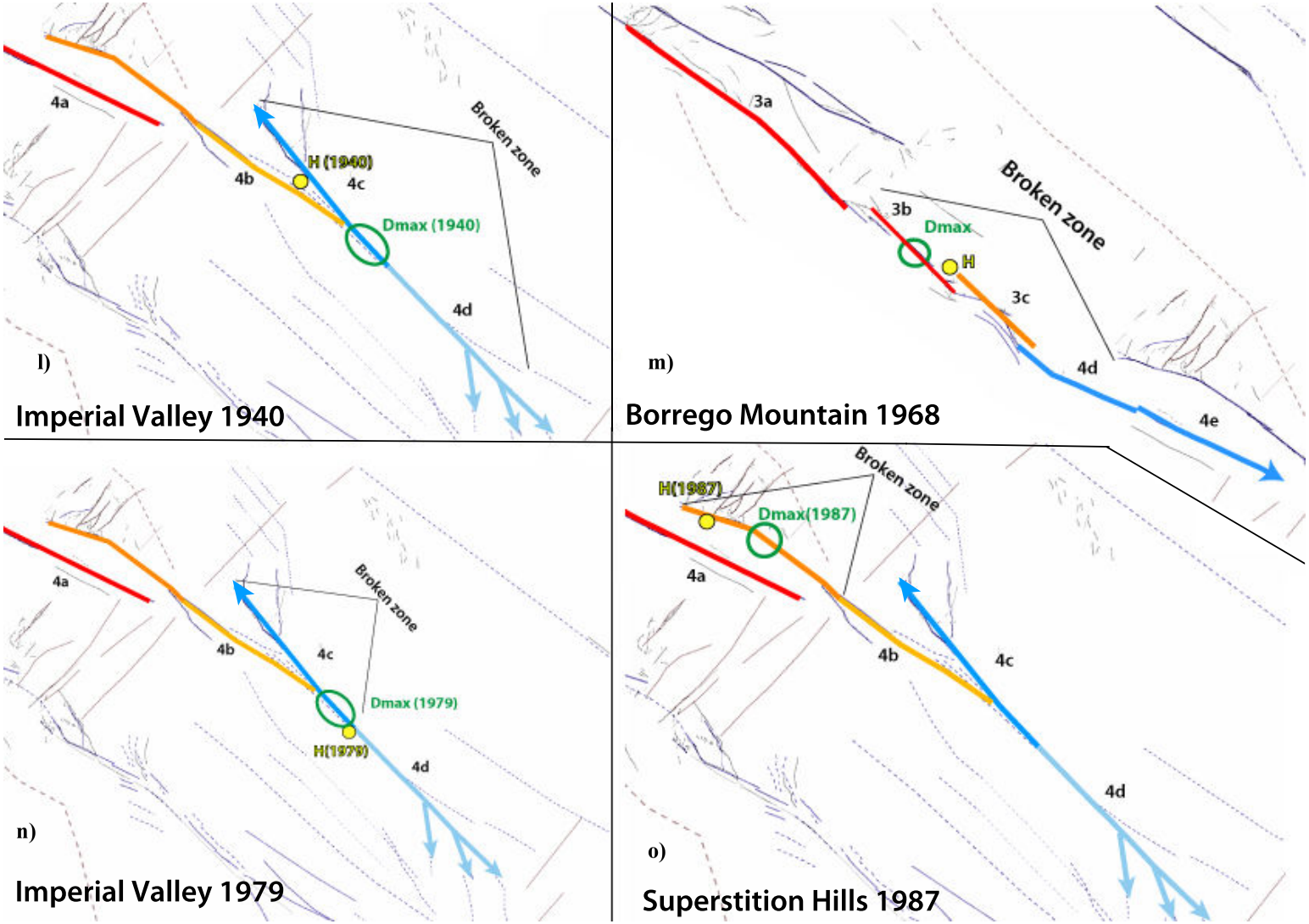
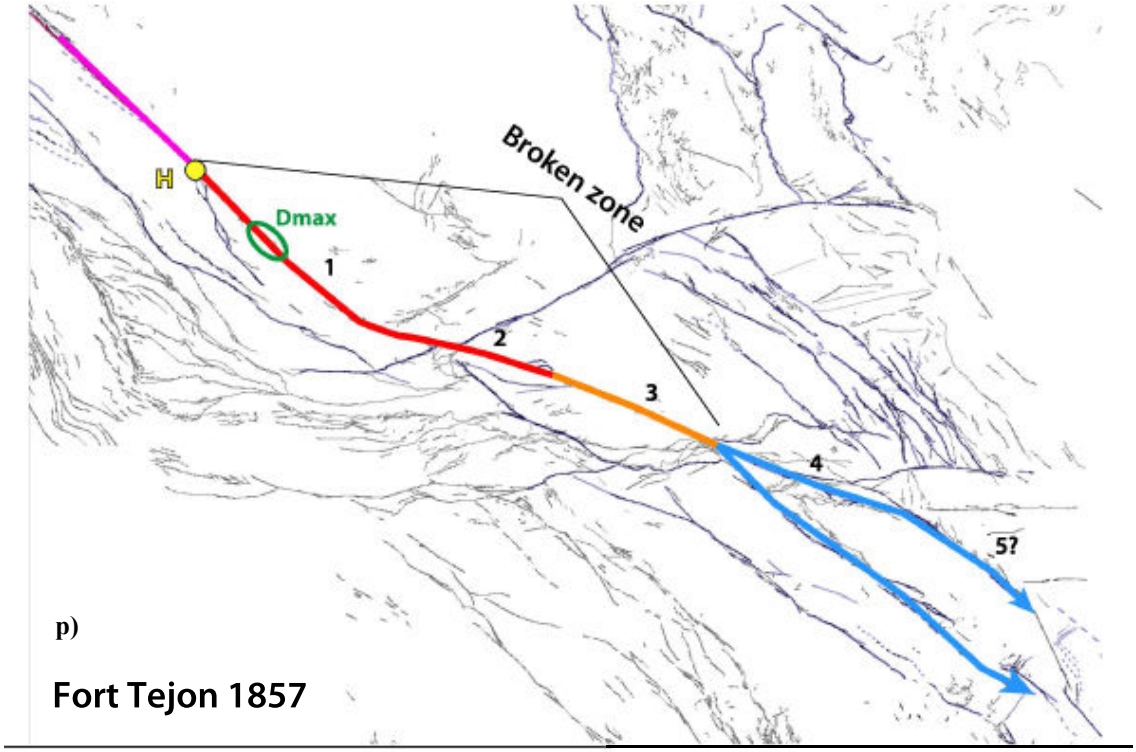


Fig. 197: l) m) n) o) See caption below.



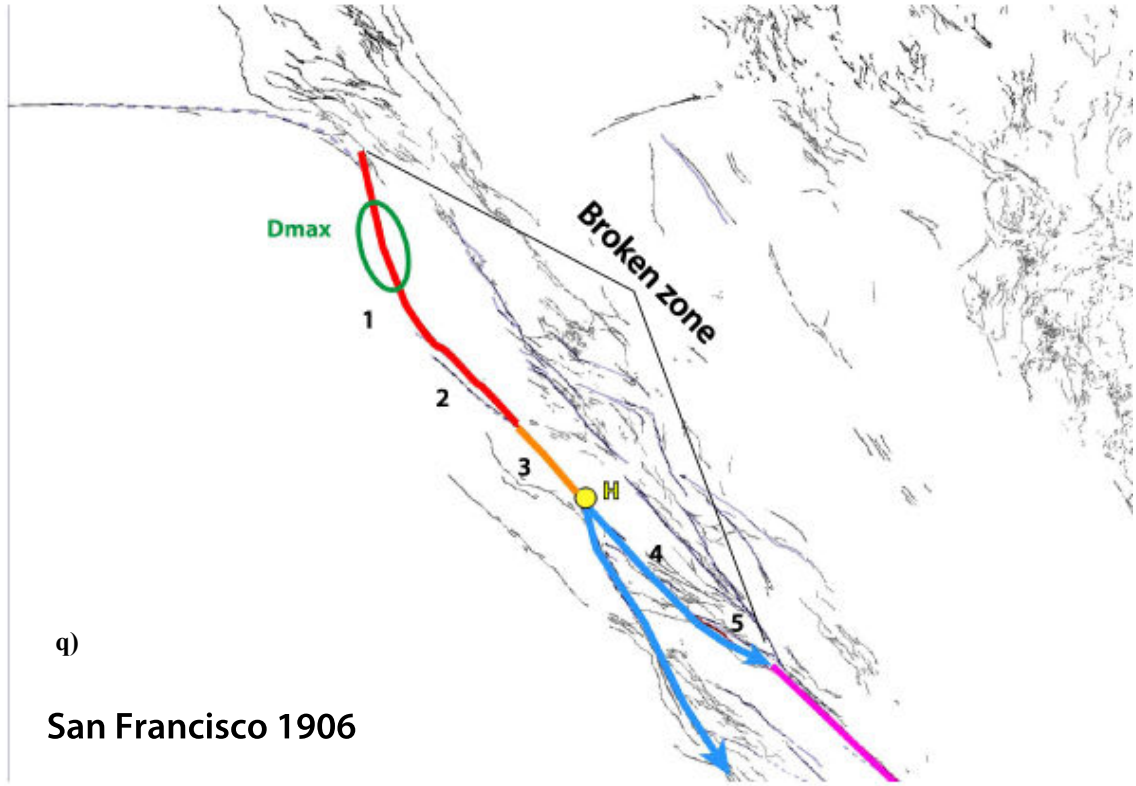


Fig. 197: p) q) See caption below

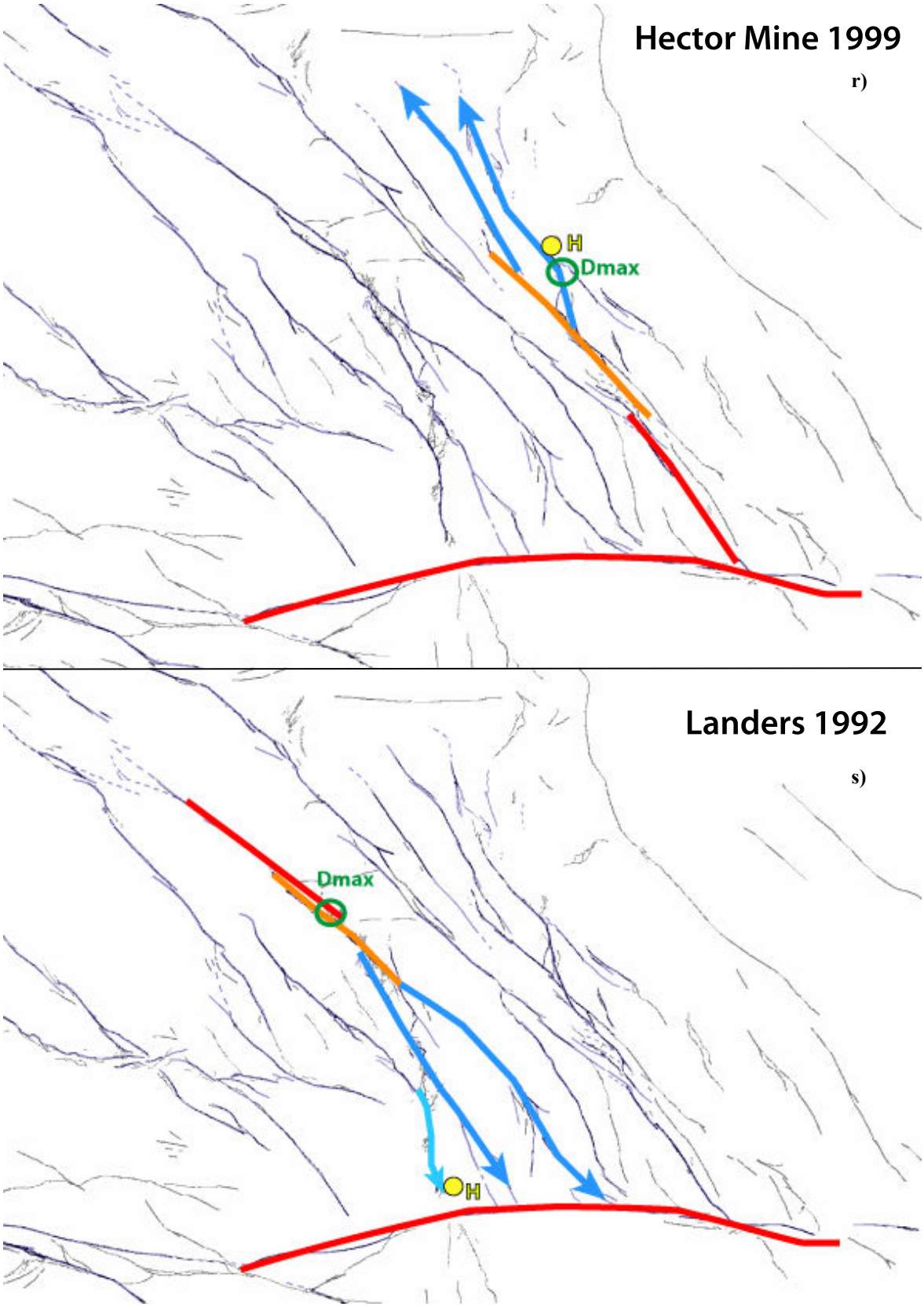


Fig. 197: r) s) See caption below

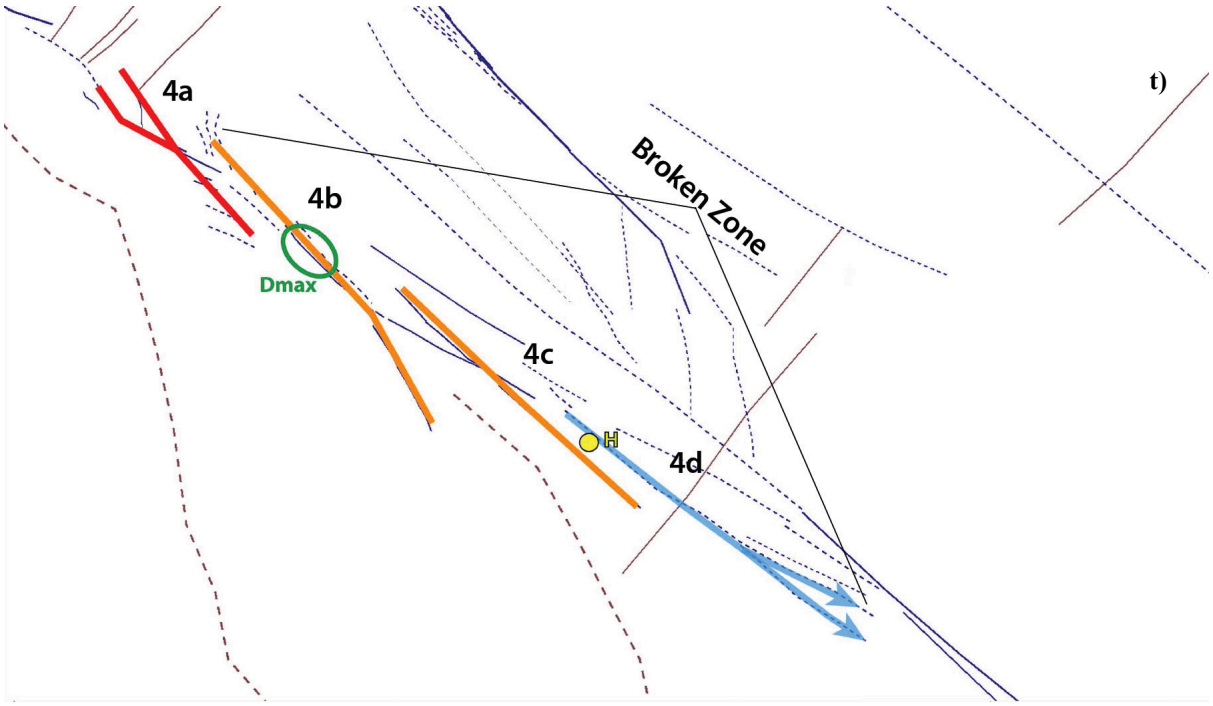


Fig. 197: t) Simplified maps of the long-term faults involved in the EQs, where I have underlined with different colors the major segments of the fault. The colors are made to qualitatively indicate the differential maturity of the successive major segments that constitute a fault, as I could derive it from the knowledge of the direction of long-term fault propagation (indicated with arrows): in the zone where the fault is supposed to have initiated, the segments are the most ancient, and I indicate them in red. Toward the present fault termination where the fault is supposed to have developed recently as a result of its lateral long-term lengthening, the segments are the youngest, and I indicate them in blue (paler blue for younger age). In between, the segments have an intermediate maturity, and I indicate them in orange. I then have reported the EQ epicenter in yellow, and the zone of maximum coseismic slip in green.

8. Relation between asymmetry of earthquake slip profiles and hypocenter position

I expand further on the question of the hypocenter position discussed above.

Figure 198 examines the position of the EQ hypocenters within the broken fault planes (198a: continental EQs; 198b: with also subduction EQs). The plot thus represents a synthetic fault plane, with the X axis the rupture length normalized to half of its maximum value, and the Y axis the rupture width normalized to its maximum value.

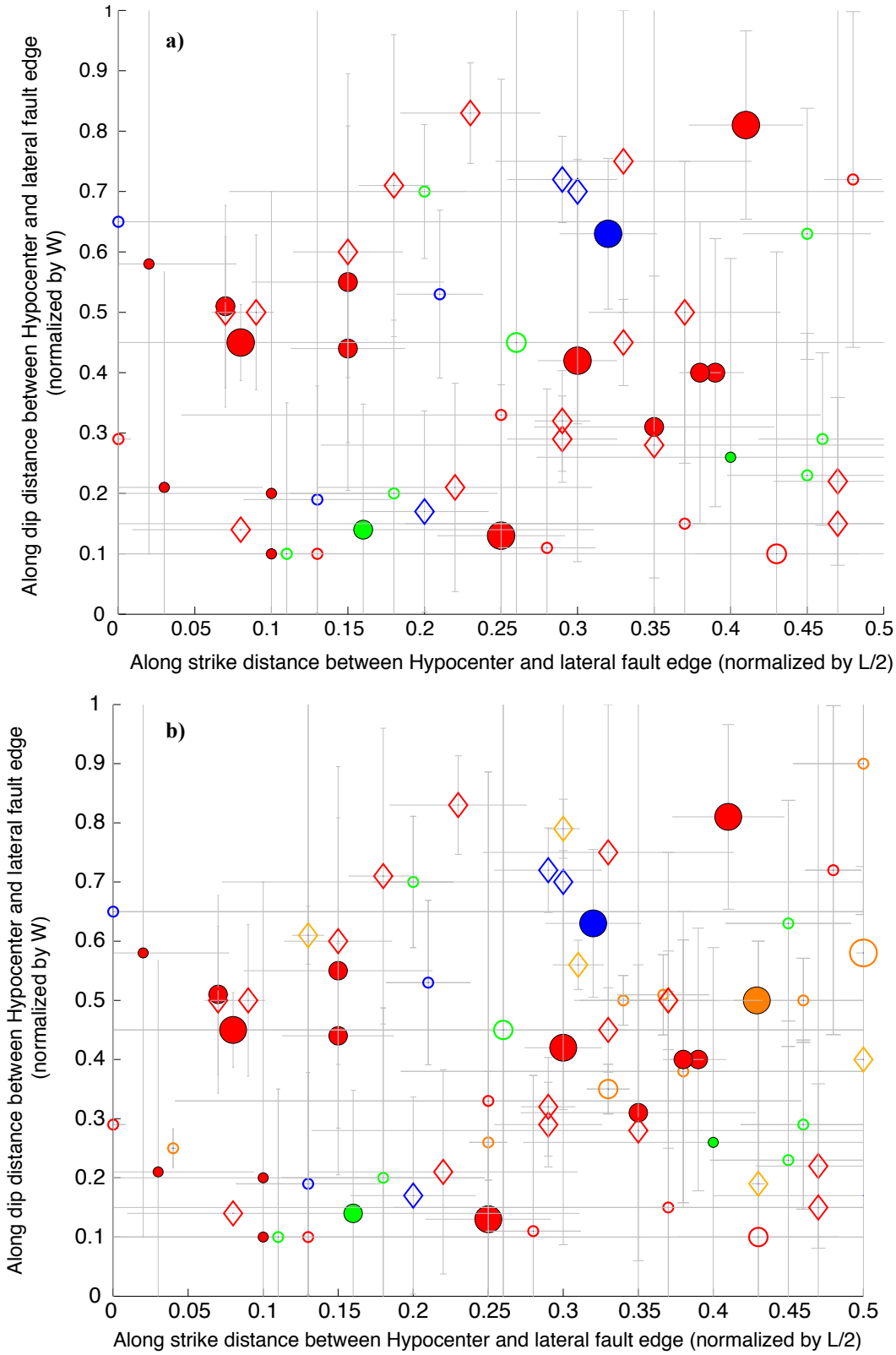


Fig.198: a) b) Position of the EQ hypocenters within the broken fault planes (a) continental EQs; (b) with also subduction EQs. The plot thus represents a synthetic fault plane, with the X axis the rupture length normalized to half of its maximum value, and the Y axis the rupture width normalized to its maximum value. . Circles: models with tabular data. Empty diamond: models with no tabular data (from Manighetti et al., 2005). Uncertainties on hypocenter positions are assigned to 5 km in both x and y.

Because we found that EQ hypocenters commonly locate at the junction between two major segments, whereas, on the other hand, 1 to 4 major segments only, furthermore of similar length, are broken during an EQ, we expect the EQ hypocenter to show a discrete distribution along the rupture length, with greater concentrations of H data around ~0, [0.25-0.33], and ~0.5 (Fig.198c). Although the data are noisy, their distribution along the rupture length is in fair agreement with this expectation. Along the rupture width, no particular distribution is seen, but we note that not all EQs nucleate near the fault base.

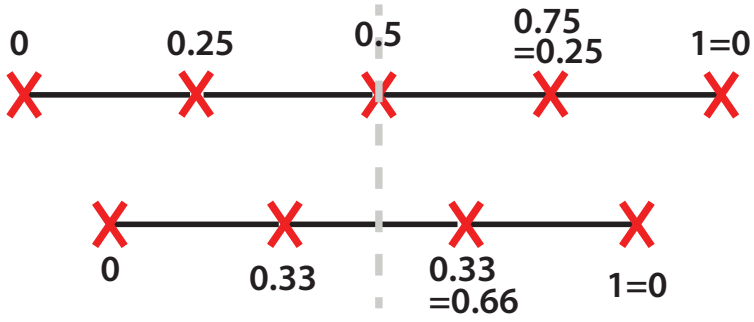


Fig. 198: c): Simplified view of the rupture trace (black) and intersegment zones (red cross). Numbers indicate the expected position of hypocenter along a normalized rupture length formed of four segments (top) and three segments (bottom). The dashed grey line represents the center of the rupture.

Figure 199 now examines the distribution of the EQ hypocenters with respect to the zone of maximum coseismic slip. The X axis is the distance H-Dmax normalized to the rupture length, whereas the Y axis is the distance H-Dmax normalized to the rupture width (Dmax localized at zero). I confirm here a result previously found by Manighetti et al. (2005): there exists two domains; one, below the dotted line, where all EQ hypocenters locate; and another one, above the dotted line where no EQ hypocenter is observed. This means that there are portions of the faults that are prone to nucleate an EQ (those below the dotted line), whereas there are portions of the faults, which are unable to nucleate an EQ (those above the dotted line). Yet, these fault portions did break since they belong to the broken zones analyzed here. This suggests that two steps occur during an EQ: 1) the EQ nucleates in a specific zone of the fault that is prone to break, and breaks a part of the fault; 2) that breaking overshoots an adjacent part of the fault that was not prone to break (i.e., that could not initiate an EQ), and makes it break. The first break coincides with that of the “major asperity” on the fault, and figure 199 allows to qualify it by the H-Dmax distance. The figure shows that the EQ nucleates (H) at a specific distance from the zone of maximum coseismic slip. Where this distance is long along the rupture length, it is shorter along the rupture width. Where this distance is long along the rupture width, it is shorter along the rupture length. When the

distance H-Dmax is expressed as a fraction of the diagonal fault length (fault represented as L x W), it appears as being generally lower than ~30 % of the diagonal fault length, and no more than 50 % (Fig. 200).

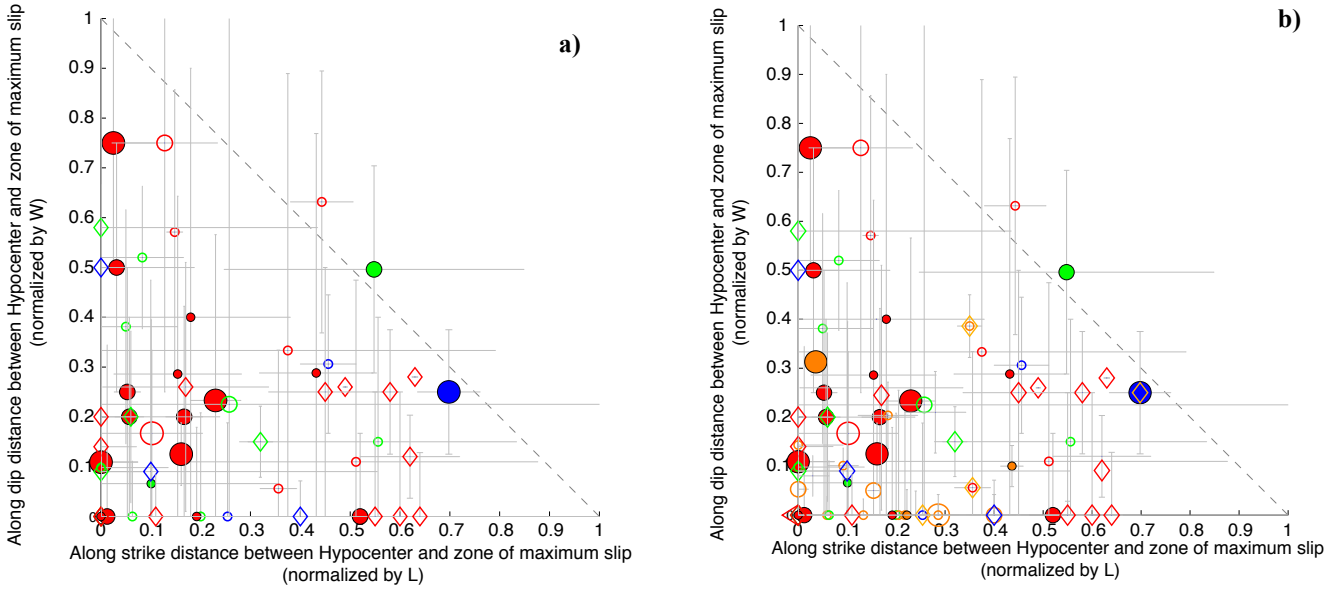


Fig.199: a) distribution of the EQ hypocenters with respect to the zone of maximum coseismic slip. The X axis is the distance H-Dmax normalized to the rupture length, whereas the Y axis is the distance H-Dmax normalized to the rupture width (Dmax localized at zero). (b) same as (a) but with subduction EQs also included. Circles: models with tabular data. Empty diamonds: models with no tabular data (from Manighetti et al., 2005). Uncertainties on hypocenter positions are assigned to 5 km in both x and y.

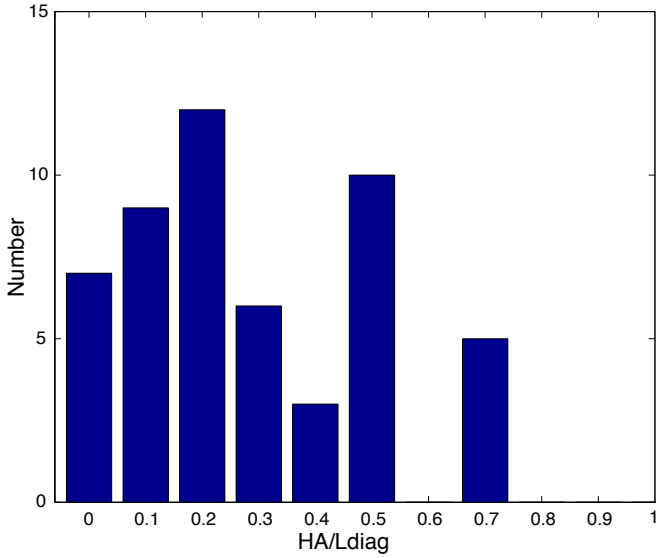


Fig.200: distance H-Dmax expressed as a fraction of the diagonal fault length (fault represented as L x W)

Note that I have examined whether the results above depend on the magnitude, stress drop and slip mode of the EQ, and the results suggest that they do not.

These results (as the others before) are discussed in the discussion section (Chapter VII).

9. Relation between asymmetry of earthquake slip profiles and off-fault strain diffusion

This part is more exploratory, and can be understood only in relation with later Chapter VI. In this later chapter, I will show that the specific triangular shape of the coseismic slip profiles can be explained provided that the main rupture plane is embedded in a pre-damaged medium (See references in chapter VI). We have observed that every long-term fault, which I analyzed is associated with networks of secondary faults, developed on one or both sides of the master fault. This has been observed also in prior works. Most of these secondary faults are genetically related to the master fault, with a large part of them attesting to its lateral lengthening. Therefore, the growth of a master fault implies the development of adjacent secondary fault networks, which damage the crustal rocks around the master fault. It results that any EQ rupture occurs on a master fault plane that is embedded in a pre-damaged crustal medium. Consequently, when an EQ occurs, while most of the coseismic strain is accommodated on the master fault, a part of it is diffused within the adjacent medium, onto the preexisting damage faults and other features (such as cracks).

The objective of this section is to try quantifying the amount of coseismic slip that can be diffused in the medium off- the main broken fault, and examine whether this amount varies with the structural maturity of the ruptured fault.

Because EQs seem to have a fairly similar stress drop independent on their magnitude, slip mode and location (See more discussion in next chapter), the framework of the elastic crack model to describe the EQ ruptures might be seen as appropriate. Would an EQ rupture behave as an elastic crack in an homogeneous elastic medium, it would produce a coseismic slip-length profile having an elliptical shape. I thus compare the actual triangular coseismic slip-length profiles with the theoretical elliptical crack function.

Figure 201 explains what I have done. I have fitted the actual slip-length profiles by an elliptical function having the actual length of the EQ rupture and the Dmax of the best fitting triangle. Then I have calculated the difference between the theoretical elliptical function and the actual slip-length profile. I call that difference the "slip deficit" because it represents the part of the "theoretically-expected" coseismic slip, which is not actually on the master fault, and hence might rather be diffused in the adjacent volume, in the form of off-fault coseismic strain (See more discussion in Manighetti et al., 2004, 2005).

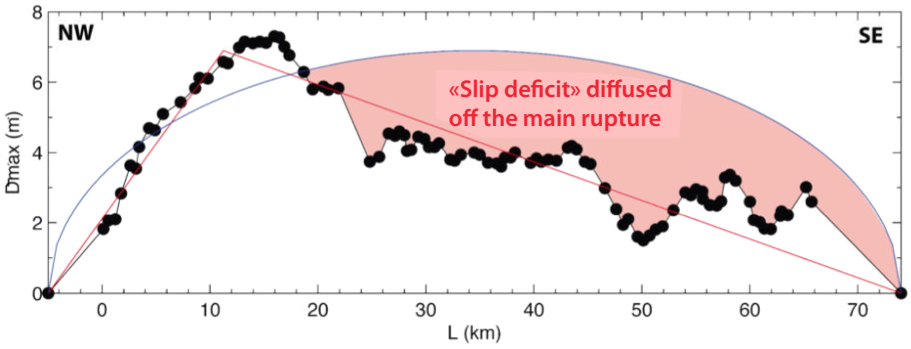


Fig.201 Explanation of how I have estimated the amount of slip possibly dissipated off-the main rupture. The so-called "slip deficit" is expressed as a fraction of the orange surface (above longer asymmetric side of the rupture)

Because the actual coseismic slip profiles are triangular, for geometrical reasons, we expect that the difference between the fitting elliptical function and the actual profile increases linearly with the degree of asymmetry of the actual triangular slip function. Figures 202a and 202b validate this expectation, and hence confirm that the EQ slip profiles are triangular.

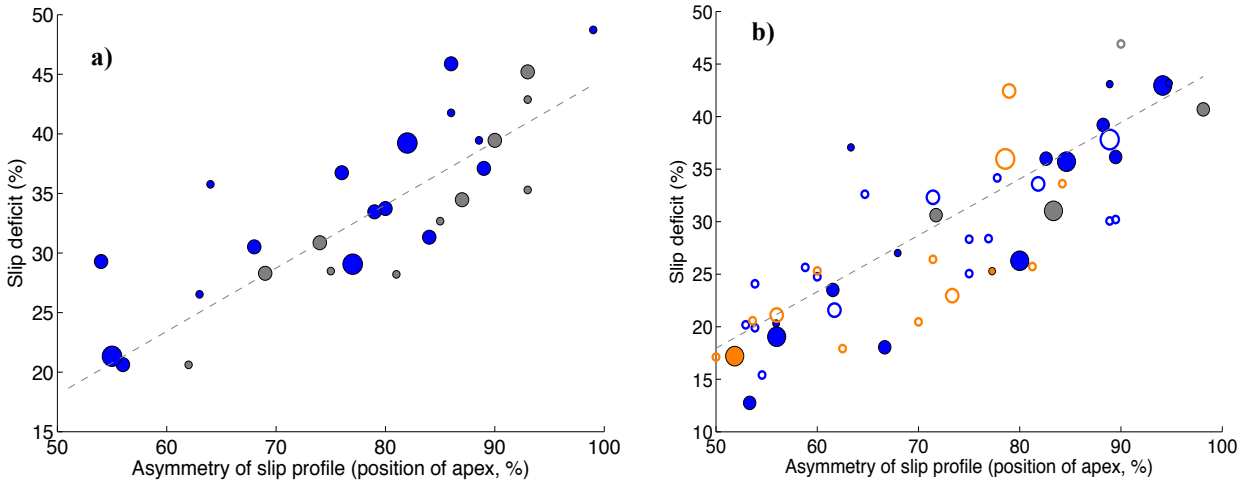


Fig.202: As expected in triangular functions, the difference between the best-fitting elliptical and triangular functions, called the "slip deficit", increases with the degree of asymmetry of the slip profile. The slip deficit is here expressed as a fraction of the total (maximum) slip "missing" between the elliptical and the triangular functions. (a) continental EQs only; (b) with subduction EQs also added.

Figures 203 now plots the calculated slip deficit as a function of the EQ stress drop, approached through the EQ Dmax/L ratio. The X axis is expressed in % of the area between the fitting ellipse and the actual profile, along the longest side of the asymmetric slip profile. The figures are done for surface data (Fig. 203a-b) and for the best model data, with and without the subduction EQs (Fig. 203c-d-e). Basically the figures show that, overall, the total coseismic slip amount to be diffused in the adjacent medium increases as the EQ stress drop decreases and hence as the structural maturity of the broken fault increases (because of the relation shown before between stress drop and maturity, Fig.15: **the more mature a fault, the larger is the slip fraction diffused off- the main rupture zone**. These results are in keeping with those found, independently, in Chapter VI. There are of course some EQ exceptions, but those are either very long ruptures on which the coseismic saturates (See Chapter IV) so that the Dmax/L values are variable, or poorly constrained data.

All the results presented in this chapter will be further discussed in the discussion section, Chapter VII.

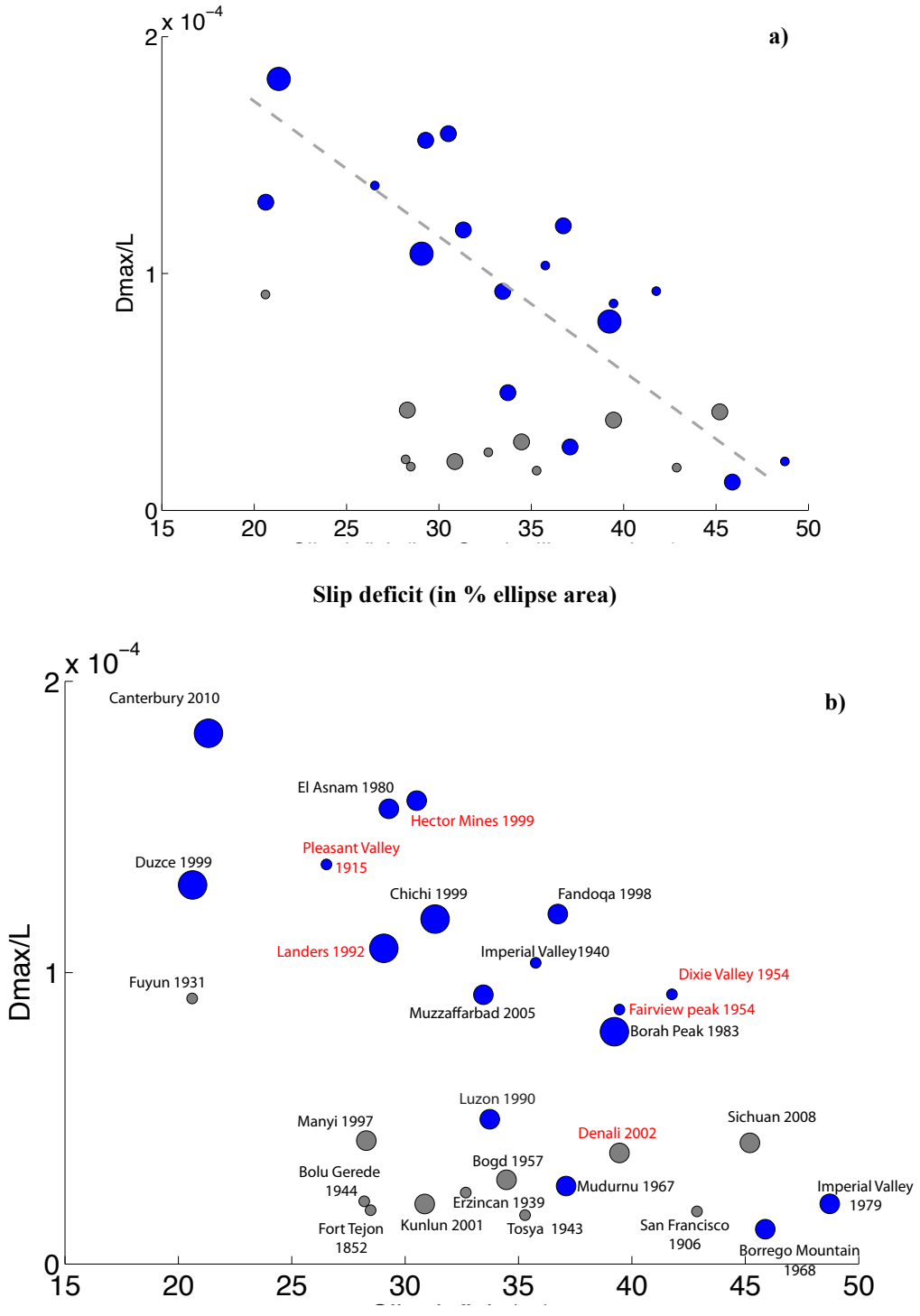
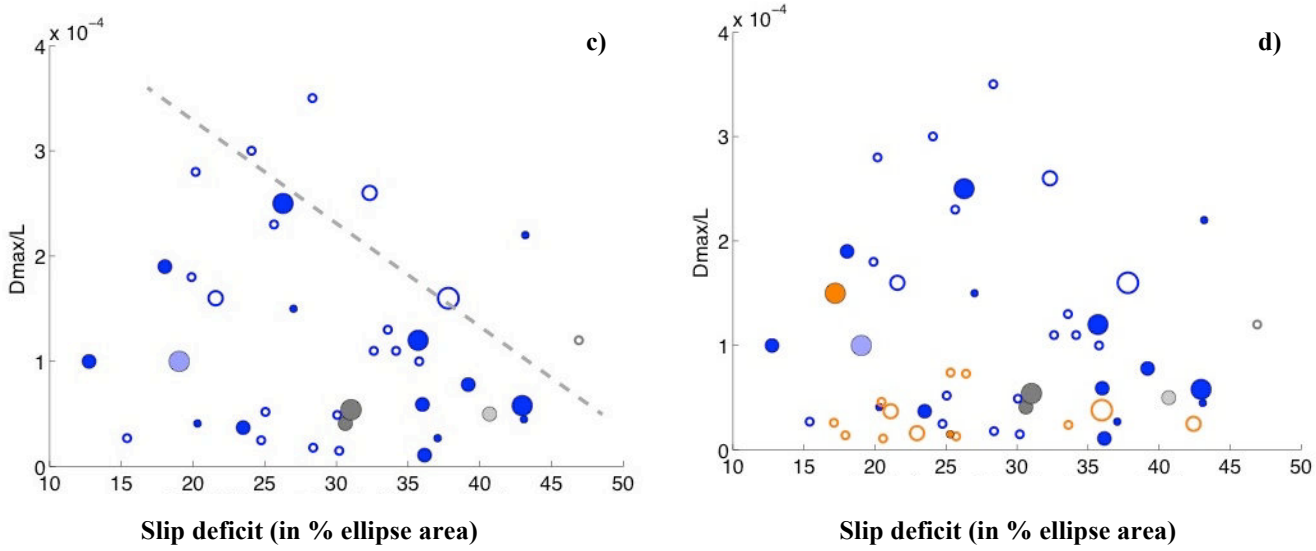


Fig.203 : Calculated slip deficit as a function of the EQ stress drop, approached through the EQ Dmax/L ratio. The X axis is here expressed in % of the area between the fitting ellipse and the actual profile (longest side). (a) continental EQ surface data. (b) same with EQ names.



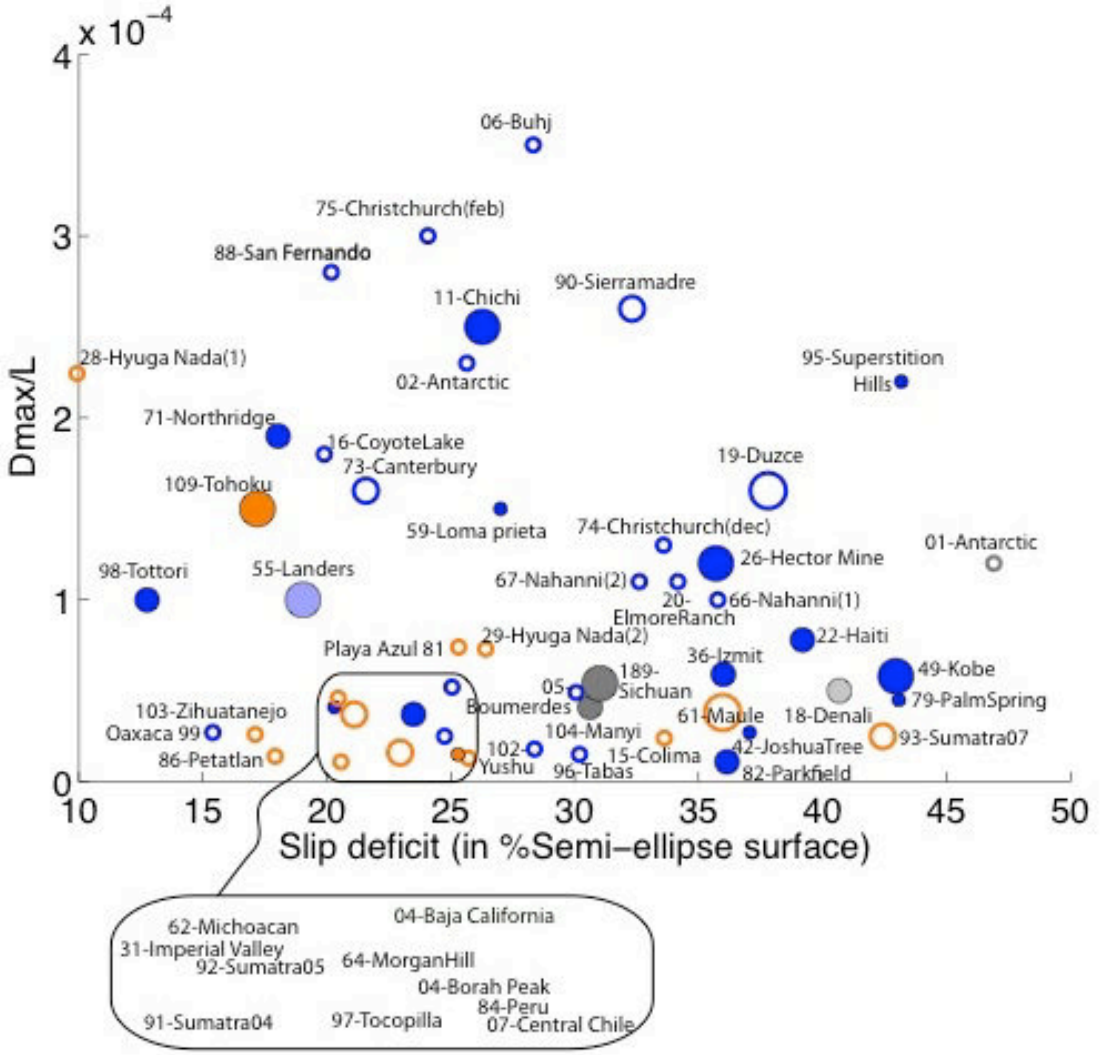


Fig.203: Calculated slip deficit as a function of the EQ stress drop, approached through the EQ Dmax/L ratio. The X axis is here expressed in % of the area between the fitting ellipse and the actual profile (longest side. (c) continental EQ depth data (best models). (d) same with subduction EQs. (e) same with EQ names.

CHAPTER IV. WHICH SCALING RELATIONS TO DESCRIBE THE EARTHQUAKE « SIZES » ?

In this chapter, my question is to try using the data that I have compiled to examine whether there exists some scaling relations between some of the EQ (and fault) parameters, which might be useful to anticipate the size, or some other properties, of the forthcoming events. There is an extremely dense seismological literature on this EQ scaling topic (See Shaw, 2010 and references therein; Hanks and Bakun, 2002 and references therein). My purpose is not to duplicate these prior studies that have already revealed a number of scaling relations. My point is to examine some of these scaling in the framework of the new insights provided by my work: I have shown that some of the intrinsic properties of the long-term geological faults, especially their structural maturity, have a strong impact on some of the properties of the EQs these faults produce. Therefore, I want to examine whether the fault maturity property somehow impacts the EQ scaling relations. I will mainly focus on simple relations between basic EQ parameters, because these basic parameters are those that can be easily acquired and used in EQ hazard assessment.

Unfortunately, this part is the less achieved part of my PhD work, for two reasons:

1) Because of the time limitation, I have only been able to analyze ~25 couples of faults and EQs (IDs in Chapter II and additional analysis of the North Anatolian EQs). This kind of coupled seismo-tectonic analysis is necessary to properly determine the fault properties and to understand what is the "significance" of the rupture within the fault. Therefore, only a small part of the EQ data which I use in this chapter have been analyzed in the appropriate manner; the remaining data are thus less well constrained, especially in terms of the fault knowledge;

2) Again because of the time limitation, I could not spend time enough to establish and examine the scaling relations. I thus only provide first order results that will definitely need to be further improved. In particular, I did not have time to discriminate the data from their quality, and thus the plots mix together data that are poorly and well constrained.

1. Earthquake slip-length scaling

As stated in the Introduction, a common hypothesis in earthquake mechanics is that earthquakes have a macroscopic behavior of cracks in an homogeneous elastic medium, with the stress drop being a material property and hence being almost constant for crustal earthquakes (e.g., Aki 1972; Kanamori and Anderson, 1975; Brune 1976; Madariaga et al., 1976; Kanamori and Brodsky, 2004). From that hypothesis, one expects maximum (Dmax) or

mean displacement (Dmean) on earthquakes to scale with rupture length (L) when $L \leq 2W_{seism}$ (W_{seism} being the thickness of the seismogenic layer), and saturates for long ruptures ($L > 2W_{seism}$). While available slip-length earthquake data have long been too few to show whether or not that behavior was real (e.g., Scholz 1982; Romanowicz 1992; Romanowicz and Rundle, 1993; Scholz, 1994a, Scholz, 1994b; Romanowicz 1994; Bodin and Brune, 1996), it is now generally admitted, from examination of denser data sets, that earthquakes more likely follow a 'W-model', and hence roughly behave as cracks (Mai and Beroza, 2000; Shaw and Scholz, 2001; Romanowicz and Ruff, 2002). Shaw and Scholz (2001) have proposed a scale-invariant physical model that includes the two D–L regimes:

- For ruptures with $L \leq 2W$; $Dmean = \alpha * (L/2)$;

- For ruptures with $L > 2W$; $Dmean = \alpha * (1/[1/L + 1/2W])$.

It is important to note that, in the formulation of that equation, Shaw and Scholz (2001) postulate that α is proportional to a constant static stress drop, while W represents the width of the seismogenic layer and thus is W_{seism}. The model roughly reproduces the first-order distribution pattern of ~55 earthquake slip-length data (See their Fig. 1), what suggests it is appropriate.

However, subsequently, Manighetti et al. (2007) examined additional slip-length EQ data and found that actual Dmax-L EQ data are much more scattered than predicted by the constant stress drop model; large earthquakes of similar size (i.e., similar length and width) are obviously producing different slips and stress drops (as it had been suggested before, e.g., Kanamori and Anderson, 1975; Romanowicz and Ruff, 2002; Scholz et al., 1986; Wells and Coppersmith, 1994; Dowrick and Rhoades, 2004; Manighetti et al., 2005). They proposed that such a variability arises from earthquakes breaking a variable number of major segments along the faults on which they occur. That number would depend on the strength of the inter-segment zones, which itself would depend on the structural maturity of the faults. Manighetti et al. (2007) thus proposed new Dmax–L parameterizations based on that idea of multiple segment-ruptures. In such parameterizations, each broken segment was found to roughly scale as a crack, while the total multi-segment rupture does not. Stress drop on individual segments was found to be roughly constant, only varying between 3.5 to 9 MPa. The slight variation that is still observed was taken to depend on the fault structural maturity, with more mature faults having lower stress drops EQs than immature ones.

My first objective has thus been to revisit these D-L EQ relations on the basis of the

additional data that I have in hands. For that, I used the data compiled in Tables 3 and 4. A large part of these data are those previously used by Manighetti et al. (2007). I have updated and completed these data with slip-length measurements on 50 additional EQs, 21 (+ 5) of them were the subject of my detailed seismo-tectonic analyses (IDs of Chapter II). I am thus using at total the surface slip-length data of 320 continental EQs worldwide, having Mw in the range 2.5-8.6, 70 % of them are strike-slip ruptures, 15 % normal ruptures and 15 % reverse ruptures. The data quality is suggested by the size of the symbols.

Note that the EQs under analysis are all intra-continental for it is mandatory to make sure that W_{seism} is fairly constant among the entire population. Subduction EQs are thus excluded from this analysis. The mean W of the entire EQ collection is ~19 km. As in Manighetti et al. (2007), I am using maximum slip instead of mean slip because the maximum EQ slip is generally better constrained than the mean slip. In any case, in triangular EQ slip functions, Dmean = Dmax/2 for geometrical reasons in triangles.

I conduct the same analysis as that in Manighetti et al. (2007), and thus I use the functional form of the Shaw and Scholz (2001) equation above. Yet, as in Manighetti et al. (2007), I give an interpretation of the parameters α and W that is different, though not contradictory, with that of Shaw and Scholz (2001): both are free parameters, and in particular, W is not the seismogenic thickness W_{seism}, but simply a length that is free to vary.

I start by analyzing the **surface slip-length data** which are more numerous.

Figure 204a shows the surface slip-length data with an attempt to fit them with either a single crack function or the Wells and Coppersmith empirical relation (1994; D_{max}= -1.38+1.02*log(L)). None of the function fits the data appropriately. Actually, the single crack function requests a W of 41 km, which does not represent anything real. Figure 204b now shows the data fitted by a single crack function in which W is imposed to be equal to the actual mean seismogenic thickness for the entire EQ collection (19 km): the fit is not appropriate either. However, the resulting stress drop is realistic, ~3 MPa. Conversely, Figure 204c shows the data fitted by a single crack function in which this is the static stress drop that is fixed to a value of 5 MPa commonly found on average on EQs. The fit is also inappropriate, whereas the W which is obtained (~11 km) does not coincide with anything real.

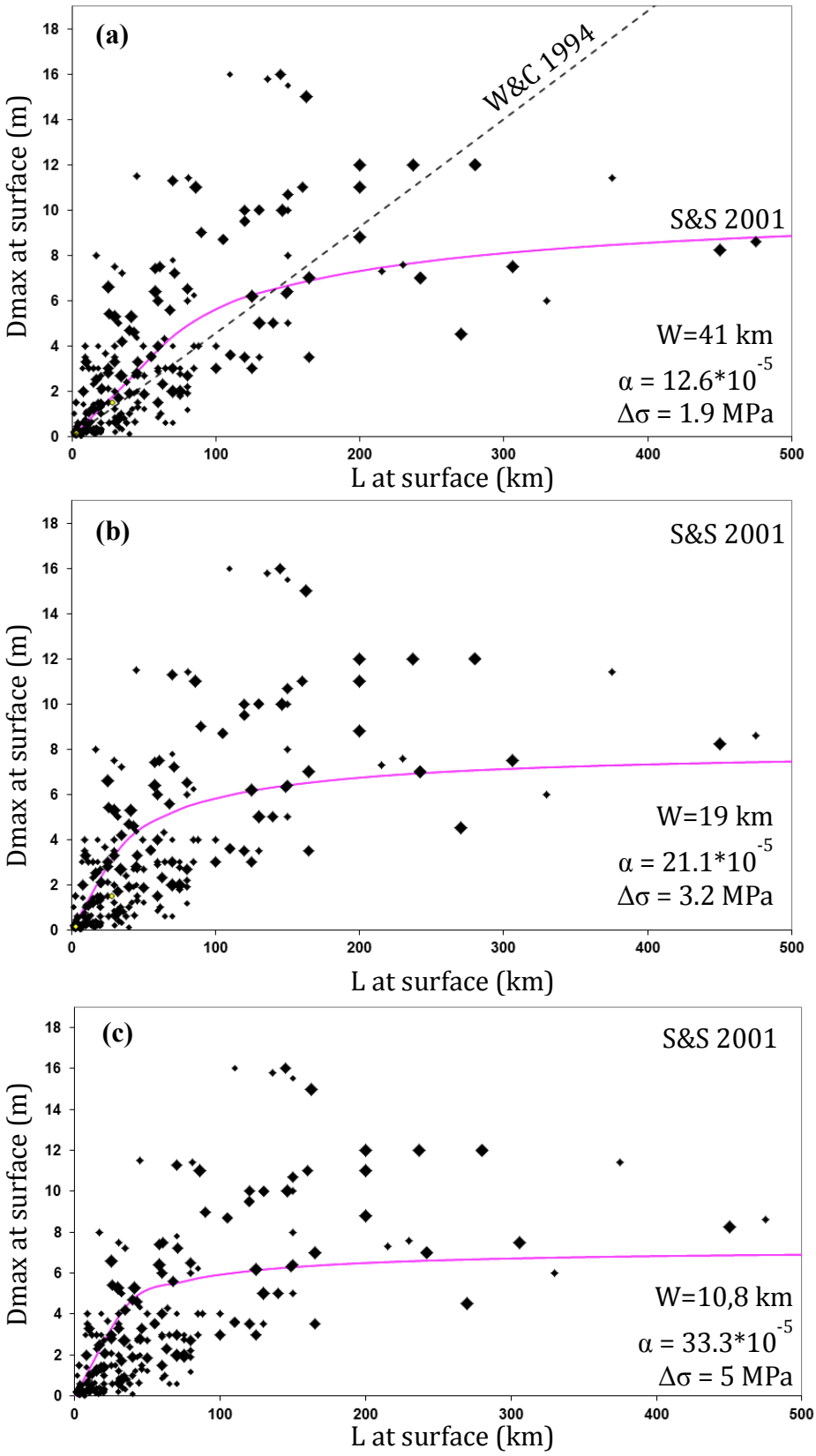


Fig. 204 : (a) Maximum displacement-length worldwide surface data (from Table 3). Symbol size is proportional to quality weight. Data are plotted together with the Wells and Coppersmith (1994) relation (W&C 1994 ; dashed line) and the Shaw and Scholz (2001) single crack function (S&S01 ; pink curve). Corresponding optimal [α,W] and static stress drop (Δσ) values are indicated. (b) Same plot as in (a) but the W parameter in the optimal S&S01 crack function is imposed to be equal to the mean width of our entire dataset (W = 19km). (c) Same plot as in (a) but the value of the static stress drop is fixed (Δσ=5MPa).

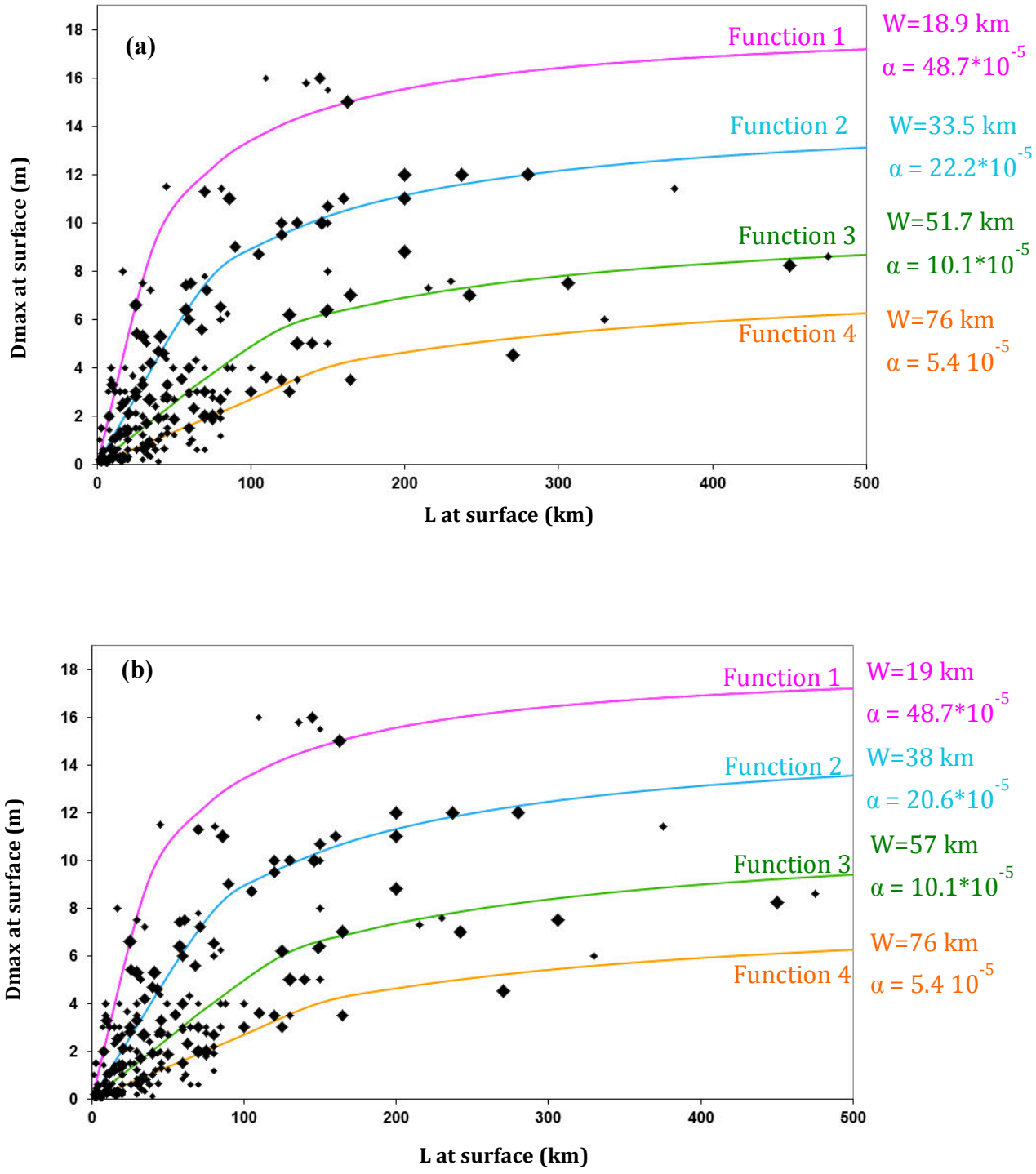


Fig. 205: (a) Maximum displacement-length surface data (from Table 3) plotted together with the four optimal S&S01 functions (modified from Manighetti et al., 2007). Corresponding optimal [α,W] values are indicated. (b) Same plot as in (a) but the W parameter of each optimal function is imposed to be exactly equal to W_{seism} multiplied by 1, 2, 3 and 4 from the top to the bottom functions.

We actually see that the data form 4 distinct subsets that each resembles the crack function (See further demonstration in Manighetti et al., 2007, that I do not repeat here). Figure 205a shows the data fitted by the 4 best fitting crack functions; that is **α** and W are free to vary among the functions, which are defined to best fit the 4 data subsets. It is found that **α** and W vary in a discrete fashion, with W being roughly W_{seism} multiplied by 1, 2, 3 and 4 from the top to the bottom functions, whereas a is roughly divided by two from one top function to the next. This poses the question of the significance of the obtained W values, which are not the actual mean seismogenic thickness of the EQ population.

Figure 205b now shows the data fitted by the 4 best-fitting theoretical functions; that is, W has been imposed to vary in a discrete fashion and to be exactly W_{seism} multiplied by 1, 2, 3 and 4 from the top to the bottom functions. These are thus the ideal functions that adjust the data. The fit is almost as good as that in Fig. 205a. Again, as W varies, the stress drop also varies in a discrete fashion, being divided by about 2 from one curve to the next.

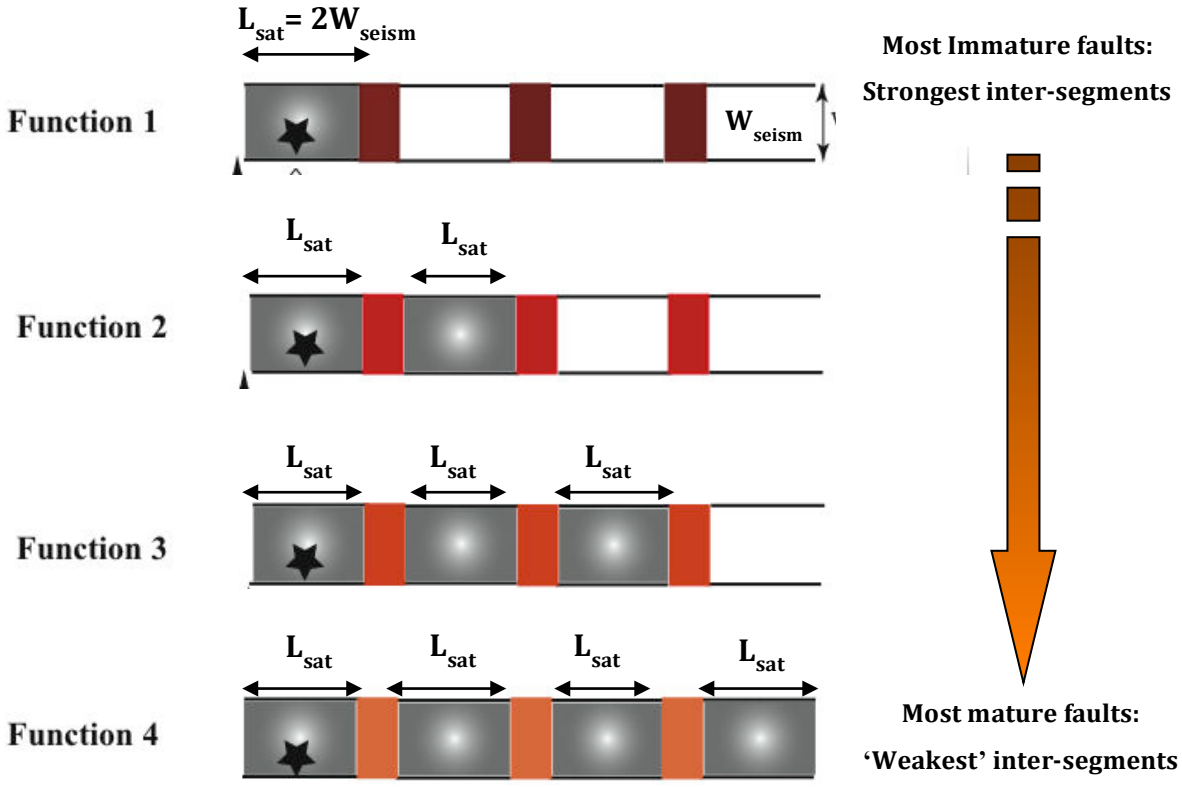


Fig.206 : Scenario proposed (modified from Manighetti et al., 2007). Earthquakes break a variable number of major segments along the faults on which they initiate. That number increases with the degree of structural maturity of the faults, for inter-segments zones have lower strength on mature faults. Coseismic slip saturates on each crack or segment at Lsat = 2Wseism, so that the rupture of different segments produces an apparent greater length of slip saturation. Converted into W values, this length produces apparent variable W values.

The revisit of the EQ surface slip-length scaling thus confirms that EQ surface slip-length data cannot be fitted by a single crack function, what in turns shows that EQs do not behave as single cracks with constant static stress drop. By contrast, four crack functions combine to well adjust the entire data set, and these functions show that W increases in a regular discrete fashion from one function to the other. Following Manighetti et al. (2007), we interpret W as the half rupture length at which slip starts saturating (L_{sat}; see Fig. 206); we actually observe that slip starts saturating at different lengths along the analyzed ruptures. Some earthquakes behave as 'single cracks', having $L_{sat} = 2W_{seism}$, while some earthquakes are more complex, with their slip starting to saturate at greater lengths observed to be 2, 3 or 4 times longer than that for a single crack ($L_{sat} = n*(2W_{seism})$ with n between 2 and 4) (Fig. 206). This behavior suggests that those earthquakes are made of several cracks juxtaposed along the rupture strike, and this recalls the lateral fault segmentation. I have indeed showed independently that most faults are divided into 1 to 4 major segments only (See Chapters II and III and references therein), of similar length. My revisit thus confirms that **most continental EQs are multi-segment ruptures, with the number of broken segments being limited, in the range 1-4 in most cases**.

Figure 207 shows an interesting observation: the maximum length of the ruptures increases gradually from the top to the bottom functions: it is ~150 km on the first function, ~300 km on the second function, ~450 km on the third function, and would be ~600 km on the fourth function if the maximum length values above are extrapolated up to that lower function. This observation suggests that the longest major segments to be broken along continental faults are ~150 km long, whereas the longest continental faults (actually, ruptures, see below), which include 4 of such segments, are ~600 km long.

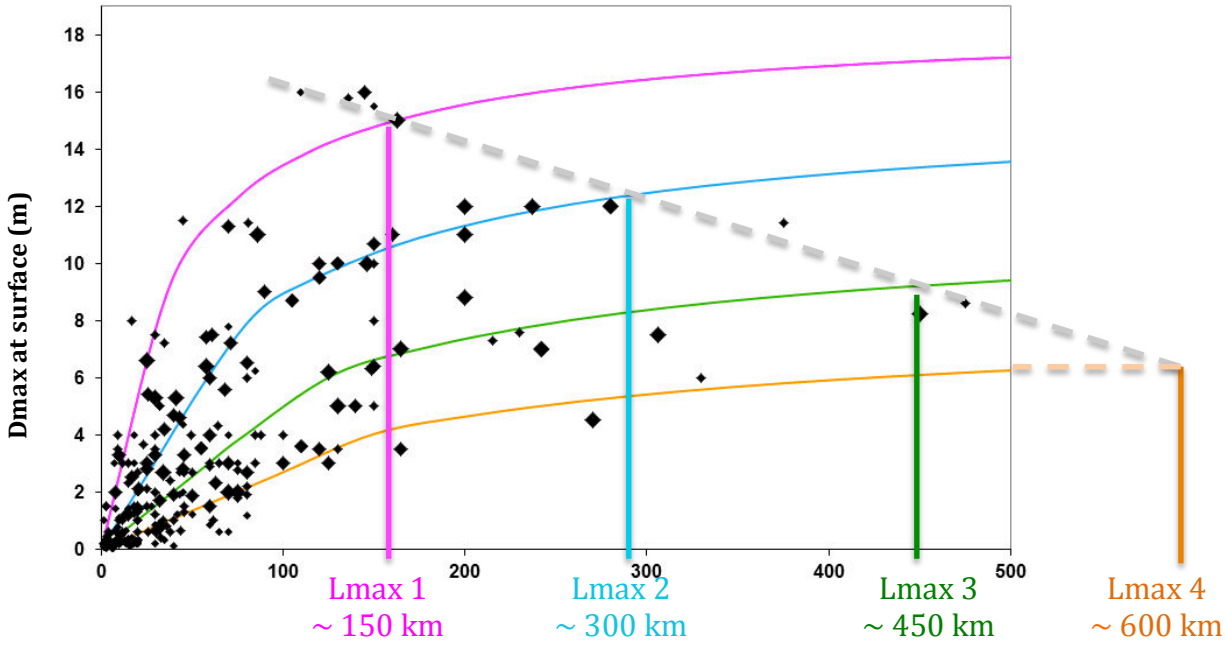


Fig.207: Maximum displacement-length surface data and optimal functions from (fig.V1-5). Grey dashed line shows the upper limit of the diplacement-length data observed at surface. Intersections between functions and the dashed grey line highlight the maximum lengths of ruptures for each function.

This calls for further discussion. Indeed, longer continental faults do exist, among which the San Andreas and the North Anatolian faults for example. However, what Fig. 207 shows are rupture lengths, not fault lengths. This suggests that there exists no historical EQ that broke a continental fault over a length greater than 600 km. This might be because, for some reasons (related to the mechanics of the continental crust and lithosphere, in particular to its capacity of absorbing the EQ waves? See chapter VII), continental EQs are unable to break more than ~600 km of fault length. If this is true, then two fault cases might exist for a large EQ:

1) The first and most common case would be a large EQ occurring on a fault shorter than ~600 km. In that case, the large EQ "sees" the fault entirely and has thus the potential to break 1, 2, 3 or 4 (on average) of the fault major segments;

2) The second case would be a large EQ occurring on a fault longer than ~600 km. In that case, the large EQ "cannot see" the entire fault. Instead, it "sees" only one or other of the fault major segments and "takes" it as the single fault on which it occurs. In that case, the large EQ has the potential to break 1, 2, 3 or 4 (on average) of the secondary segments that form the single major segment.

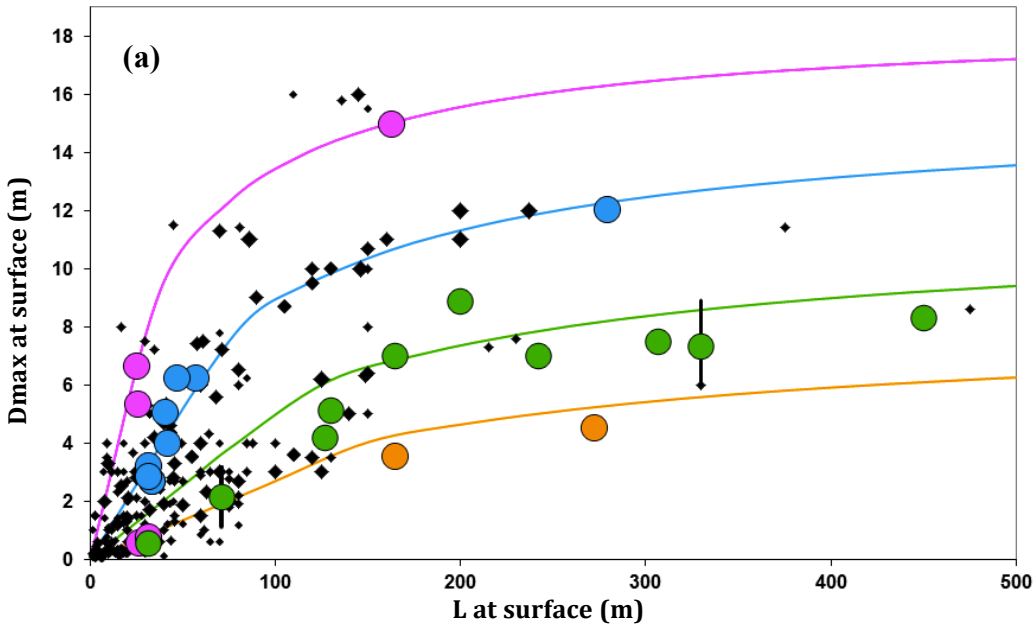


Fig.208: Maximum displacement-length surface data and optimal functions from (fig.V1-5). Dots show the number of major broken segments derived from the IDs (See chapter II). Same colors are used for the rupture of 1, 2, 3 and 4 segments and the functions 1, 2, 3 and 4, respectively.

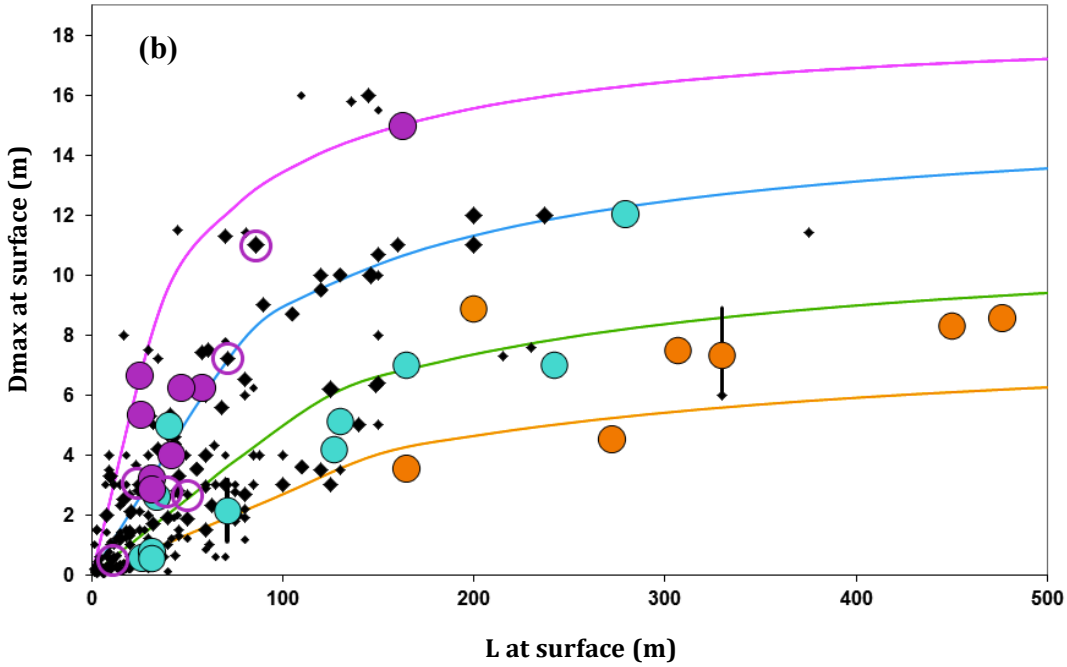


Fig 209: Dots show the maturity of the broken fault as described in the IDs (See chapter II). ; Purple : Immature ; Light blue : Intermdediate ; Orange : Mature. Empty symbols show data of EQs that I have not studied in details in dedicated IDs. The structural maturity then comes from Table 5.

The surface slip-length scaling graph of figure 207 might thus show several scales of fault segmentation, at least the two largest discussed above. When I apply the reasoning above to the EQs that I have analyzed in the IDs and indicate the number of broken segments on the graph (Fig. 208), I see a good agreement between the number of broken segments inferred from the graph interpretation and the number of large segments (major in most cases) actually broken along the faults. Figure 209 furthermore shows that the number of broken segments increases with the fault maturity, in keeping with the original model proposed by Manighetti et al. (2007), and with the relations that I have shown in Chapter III.

Of course, the above discussion suggests a lot of questions, some will be approached in the discussion section of Chapter VII; in particular: how can an EQ "know" about the length of the fault on which it initiates?

Furthermore, it is not clear how the slip-length scaling graph can be used to understand the smaller EQs, for which the scale of the broken fault segments is necessarily lower. The fairly good fit of the small EQ slip-length data suggests that the multi-segment scaling still applies at the lower scales. Yet it remains to be shown that the fault lateral segmentation is self-similar at all scales, and it remains to be understood why the smaller scale fault segments would behave (i.e., would have the same properties) as the longest segments.

It is also unclear whether the slip-length scaling graph can be used to understand the multi-fault ruptures (such as the Landers and Denali EQs). I would suggest that it cannot and hence that, for multi-fault ruptures, only the slip-length data on the main broken fault should be examined with the above scaling relations.

The following figures now show the **EQ slip-length data inferred at depth** from the source inversion models (best models).

Because the data are fewer, I only show a few of the above figures. Figure 210a shows the data fitted with 4 crack functions having free a and W values. As for the surface data, the functions suggest a discrete and fairly regular variation in both W and a. When W is imposed to be 1, 2, 3 or 4 times Wseism, the data are still well fitted, whereas the stress drops decreases in a discrete fashion from one curve to the next (Fig. 210b). The results are thus basically the same as those found from surface data. Although the data are very scarce, they are in a fair agreement with the rupture length increase observed in the surface data (Fig. 211). Finally, when we report the number of broken segments (from the IDs of Chapter II,

Fig.212) and the fault structural maturity (Fig.213) on the graph, we see a fair overall agreement.

Note that I have checked that the results above do not depend on the fault slip mode.

I will provide the estimations of stress drop by the end of this chapter.

The results presented here will be further discussed in the discussion Chapter VII. They show that, knowing the structural maturity of a fault whose length is also known, one might better anticipate the maximum slip that may be produced at surface and depth by the fortcoming event.

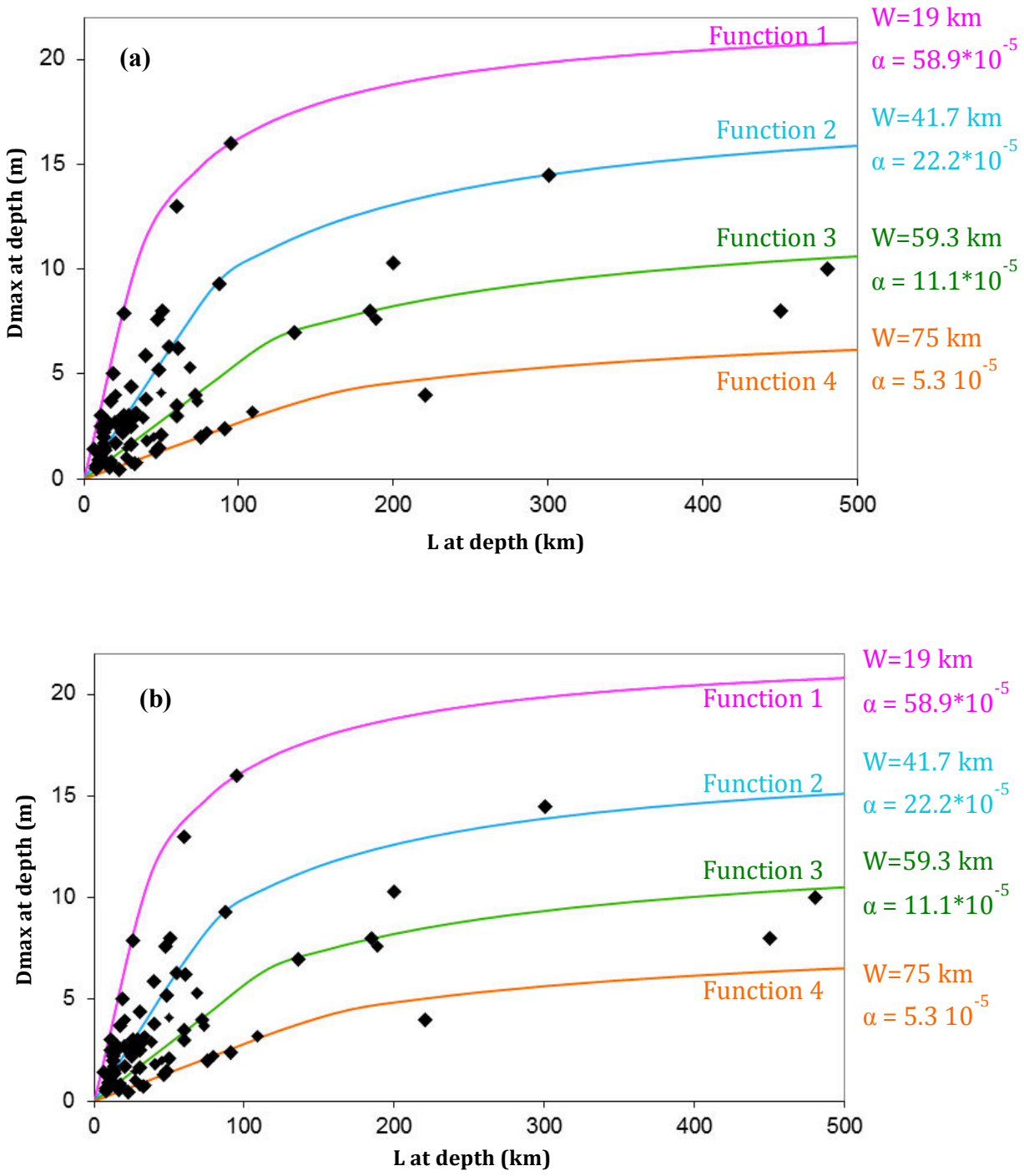


Fig.210 : (a) Maximum displacement-length depth data (from Table4) plotted together with the four optimal S&S01 functions (modified from Manighetti et al., 2007). Corresponding optimal [α,W] values are indicated. (b) Same plot as in V1-10 but the W parameter of each optimal function is imposed to be exactly equal to W_{seism} multiplied by 1, 2, 3 and 4 from the top to the bottom functions.

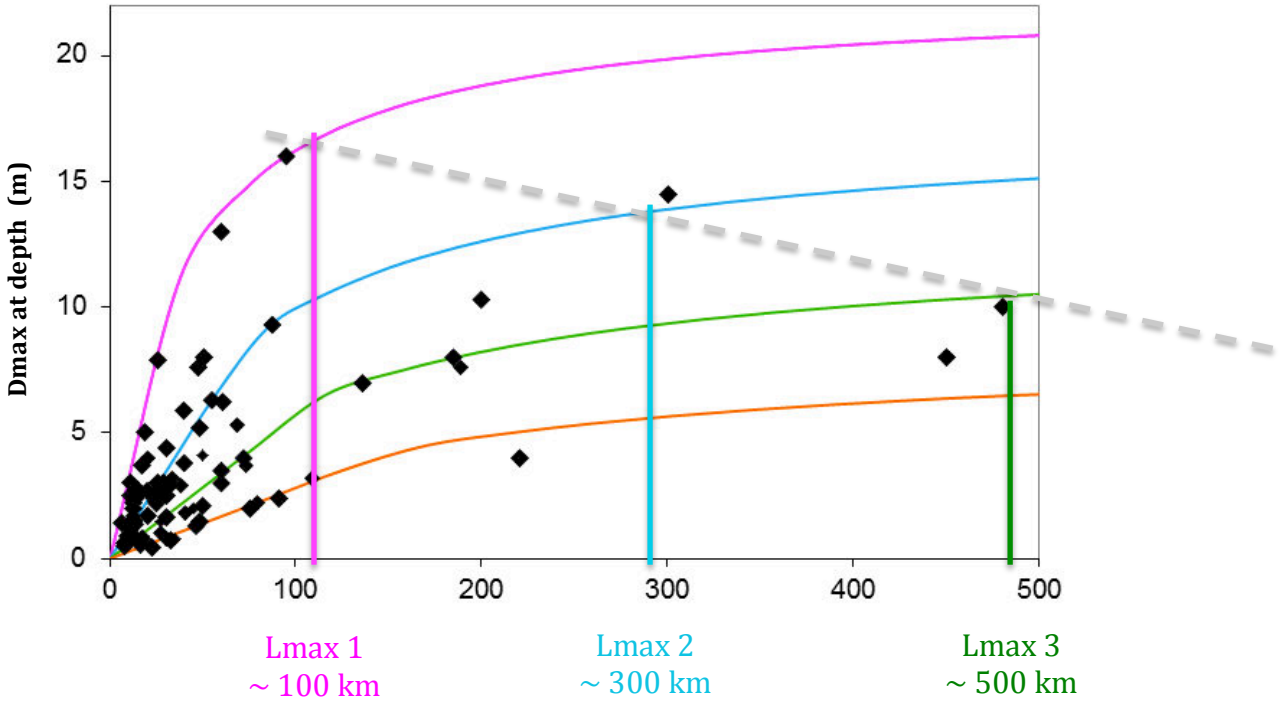


Fig.211: Maximum displacement-length depth data and optimal functions from (fig.V1-11). Grey dashed line shows the upper limit of the diplacement-length data observed at depth. Intersections between functions and the dashed grey line highlight the maximum lengths of ruptures for each function.

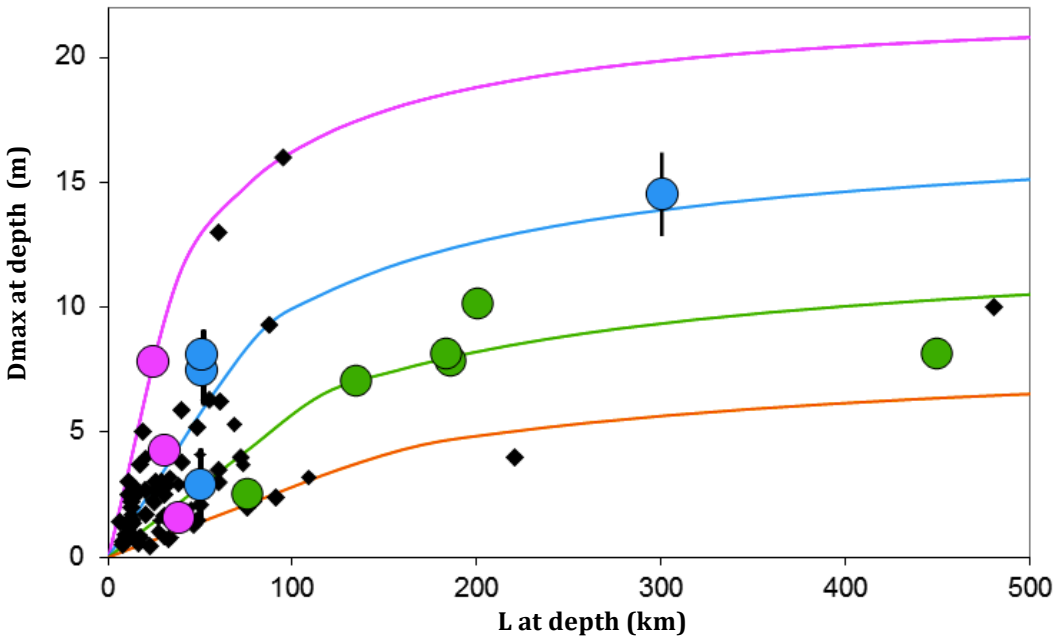


Fig. 212 : Maximum displacement-length depth data and optimal functions from fig.210. Dots show the major broken segments reported from IDs (see Chapter III). Same colors are used for the rupture of 1, 2, 3 and 4 segments and functions 1, 2, 3 and 4, respectively.

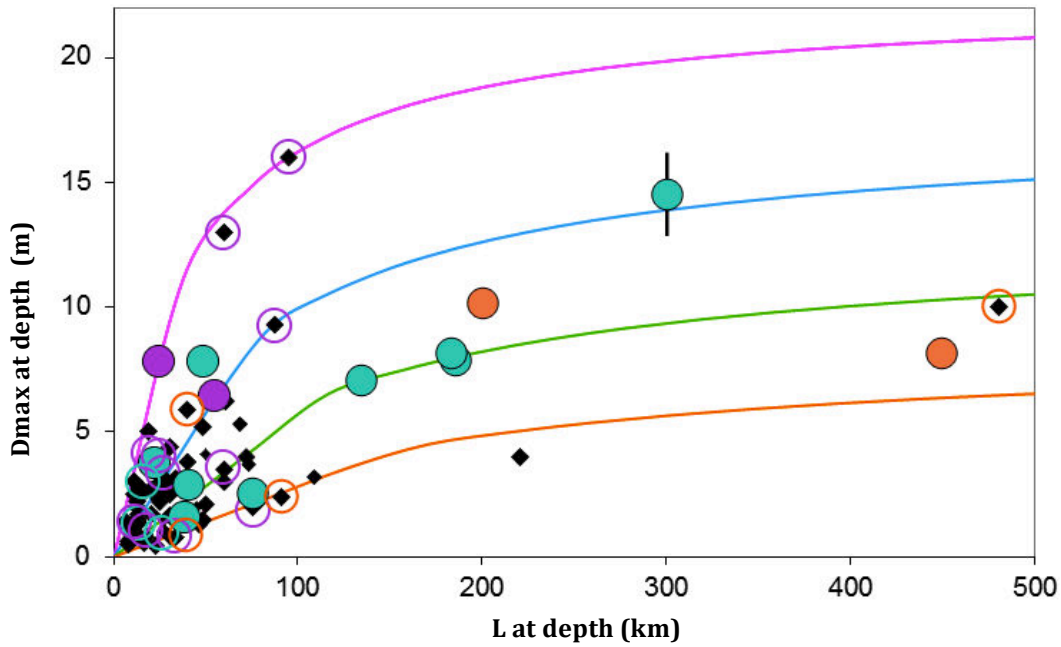


Fig. 213 Same caption as in Fig. 212 but dots show the maturity of the broken fault ; Purple : Immature ; Light blue : Intermdediate ; Orange : Mature.

2. Examining scaling relations between basic earthquake parameters

I now examine the scaling relations between some of the basic EQ parameters. Most of these relations are known for long (e.g., Hanks and Bakun, 2002; Scholz, 2002; Kanamori and Brodsky, 2004), yet I examine them by introducing the structural maturity of the broken faults, what has never been done before. Of course, many of the relations show redundant or overlapping results, or present results that were shown differently in the previous chapters. However, I feel important to show the behavior of individual basic EQ parameters, and also to provide simple relations that may be used to infer an EQ parameter from another one.

As said earlier, I did not have time to discriminate the data from their quality. By contrast, in most plots, I will distinguish the continental and the subduction EQs.

Rupture length at depth versus rupture length at surface

Figure 214 confirms an observation already done by others (e.g., Wells and Coppersmith, 1994): the rupture length measured at surface (Lsurf) is sometimes smaller than the rupture length inferred at depth (Ldepth). Figure 215 provides new information: the ratio Lsurf/Ldepth seems to vary depending on the structural maturity of the broken fault. **Overall, the more mature the fault, the larger the Lsurf/Ldepth ratio**. This might be explained by the coseismic slip propagating more easily up to the surface on mature faults because those have a lower friction (See more discussion in discussion section in Chapter VII).

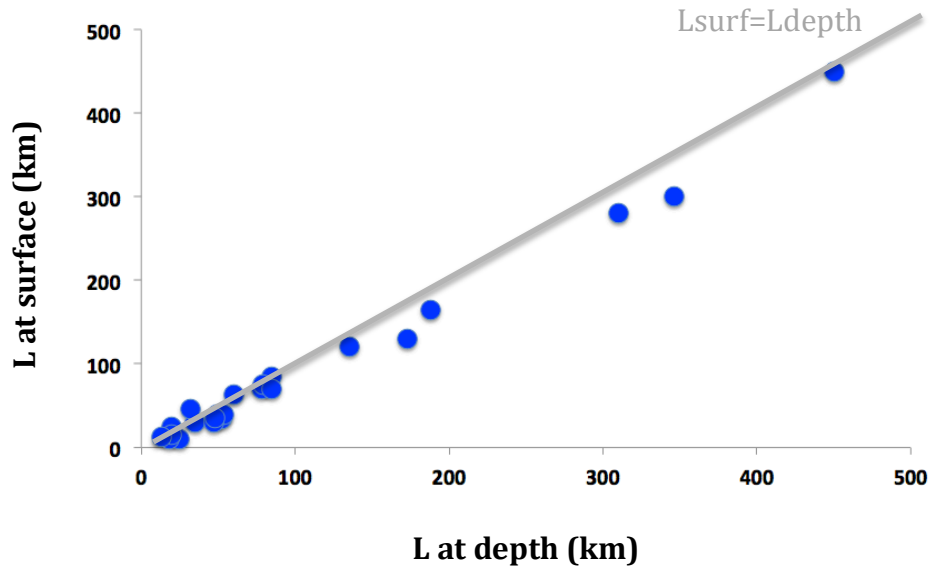


Figure 214: Relation between rupture length at depth and at surface

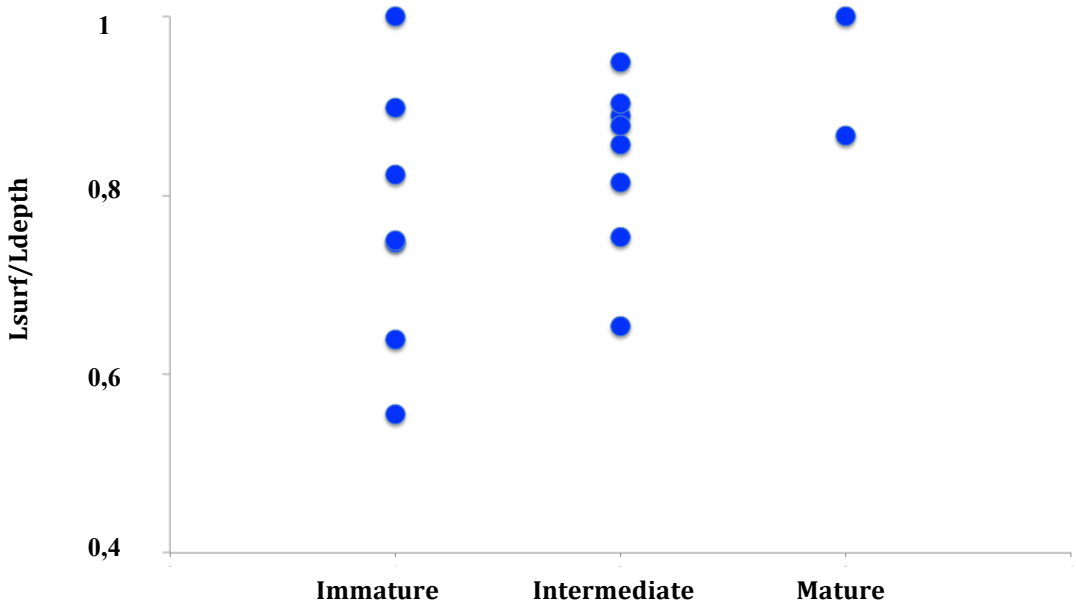


Figure 215: Ratio of rupture length at surface to rupture length at depth, as function of the structural maturity of the broken fault

Maximum slip at depth versus maximum slip at surface

Figure 216 confirms an observation already done by others (e.g., Manighetti et al., 2007; Kaneko and Fialko, 2011): the maximum coseismic slip measured at surface is generally smaller than the maximum coseismic slip inferred at depth. Figure 217 refines this

observation: the ratio D_{max_surf}/ D_{max_depth} seems to vary depending on the structural maturity of the broken fault. **Overall, the more mature the fault, the larger the D_{max_surf}/ D_{max_depth} ratio**. Again, this might be explained by the coseismic slip propagating more easily up to the surface on mature faults because those have a lower friction.

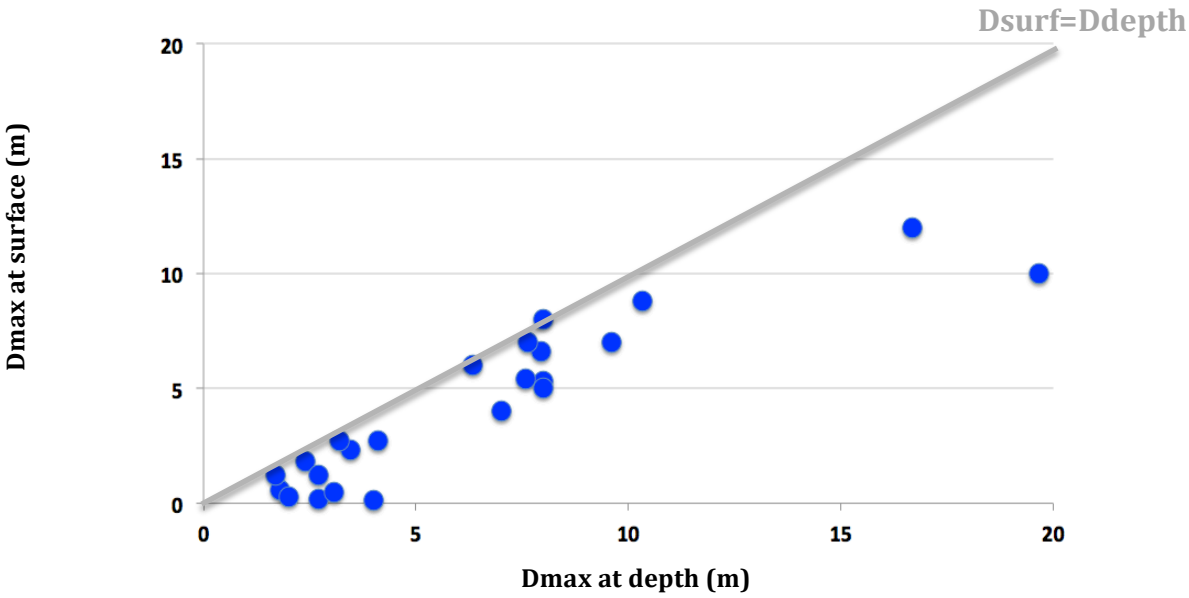


Fig.216: Relation between maximum coseismic slip at surface and maximum coseismic slip at depth

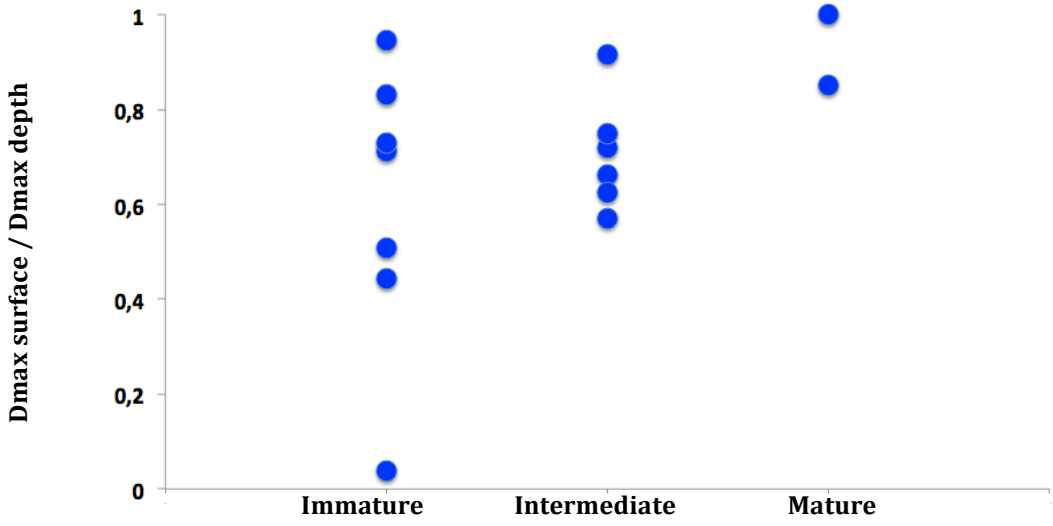


Fig.217: Ratio of maximum coseismic slip at surface to maximum slip at depth, as function of the structural maturity of the broken fault.

It might have been reasonable to expect that larger stress drop EQs would have a coseismic slip more efficiently propagating up to the surface, and hence would have a larger D_{max_surf}/ D_{max_depth} ratio. Figure 218 actually shows the opposite: **the smaller the EQ stress drop (approached through the Dmax/L ratio, here measured at depth), the larger the D_{max_surf}/ D_{max_depth} ratio**. This result confirms that the structural maturity of the broken fault plays a significant role in the efficiency of the coseismic slip propagation from depth to surface. Although an increase in maturity lowers the EQ stress drop, it also lowers the friction on the fault plane, and this likely enhances the efficiency of the slip propagation from depth to surface.

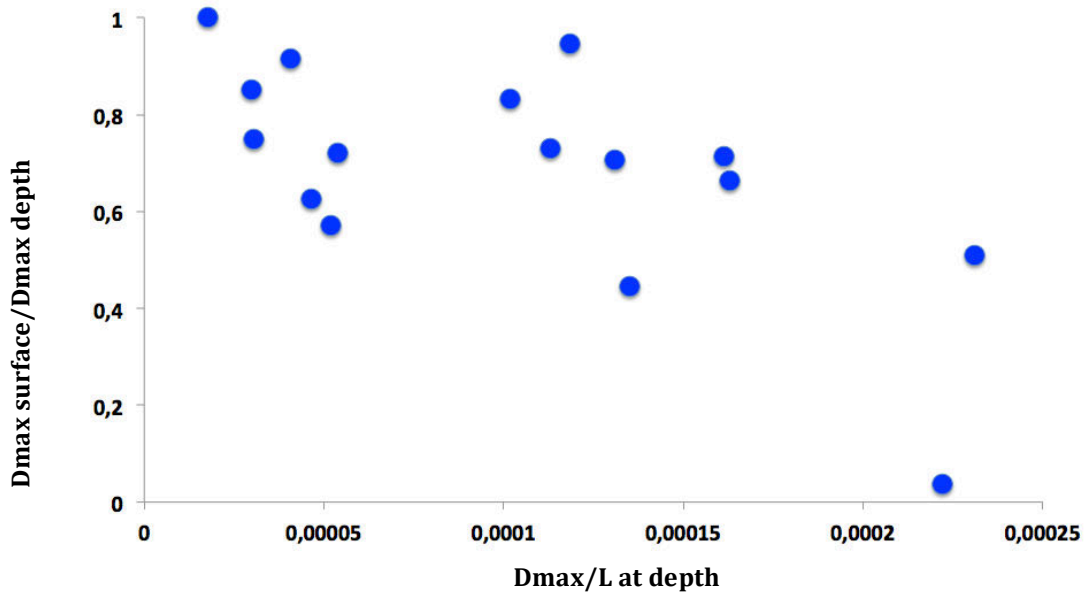


Fig.218: Relation between the EQ stress drop (approached through the Dmax/L ratio, here measured at depth) and the D_{max_surf}/ D_{max_depth} ratio.

Mw versus L (at depth)

Figure 219 examines how Mw varies as a function of the rupture length (here measured at depth). Only continental EQs are considered, and they are discriminated from the structural maturity of the broken fault. The relation between the rupture L and the Mw varies depending on the rupture size. Additionally, for a similar rupture length, the Mw of the EQs produced on mature (red) and intermediate maturity (green) faults seems to be lower than the Mw of the

EQs occurring on immature faults (blue; visible here in the range L 50-170 km). More data would however be necessary to validate this finding.

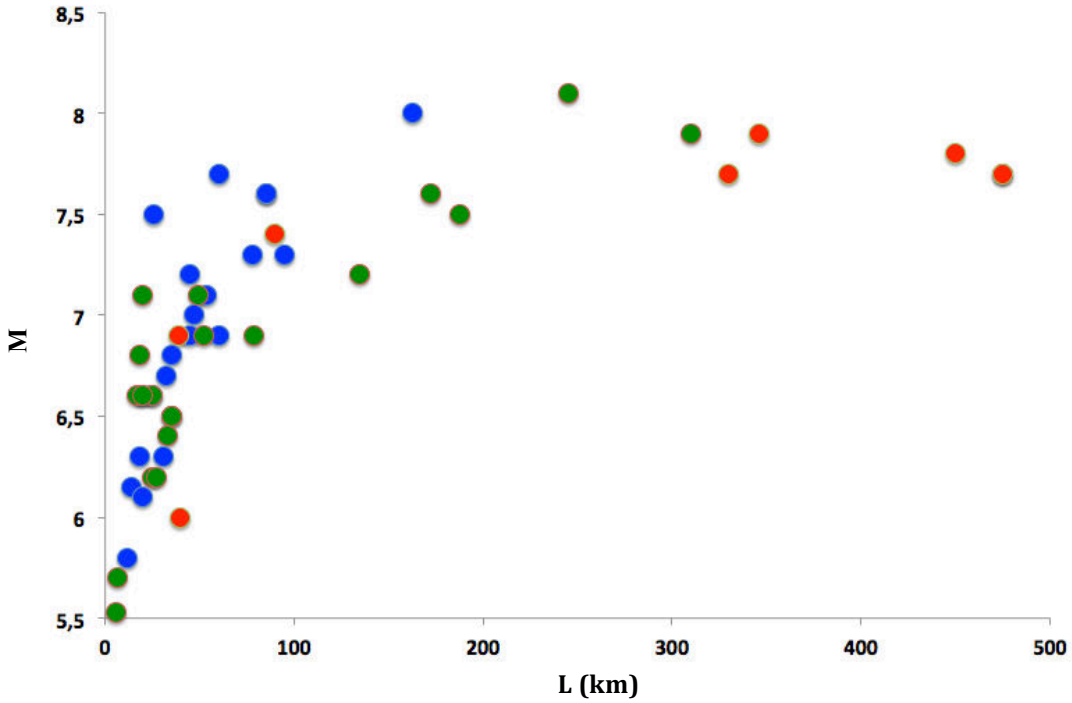


Fig.219: Relation between Mw and rupture length (here measured at depth). The colors represent the structural maturity of the broken faults, red: mature; green: intermediate; blue: immature

M0 versus L

This scaling will be shown in the following section, for it can be examined in a theoretical framework.

Mw versus maximum slip

Figures 220 a - b show the relation between Mw and Dmax at surface and depth, respectively. For a same amount of maximum slip produced by an EQ, very different magnitudes can be found. **Therefore it is not robust to estimate magnitudes from slip values, unless other information is added** (see paleoseismological studies, which commonly do that). Figure 221a furthermore suggests that, for a given magnitude, more coseismic slip (here measured at surface) is produced by EQs occurring on immature faults (blue). Figure 221b (where slip is estimated at depth) is however too noisy to validate this observation.

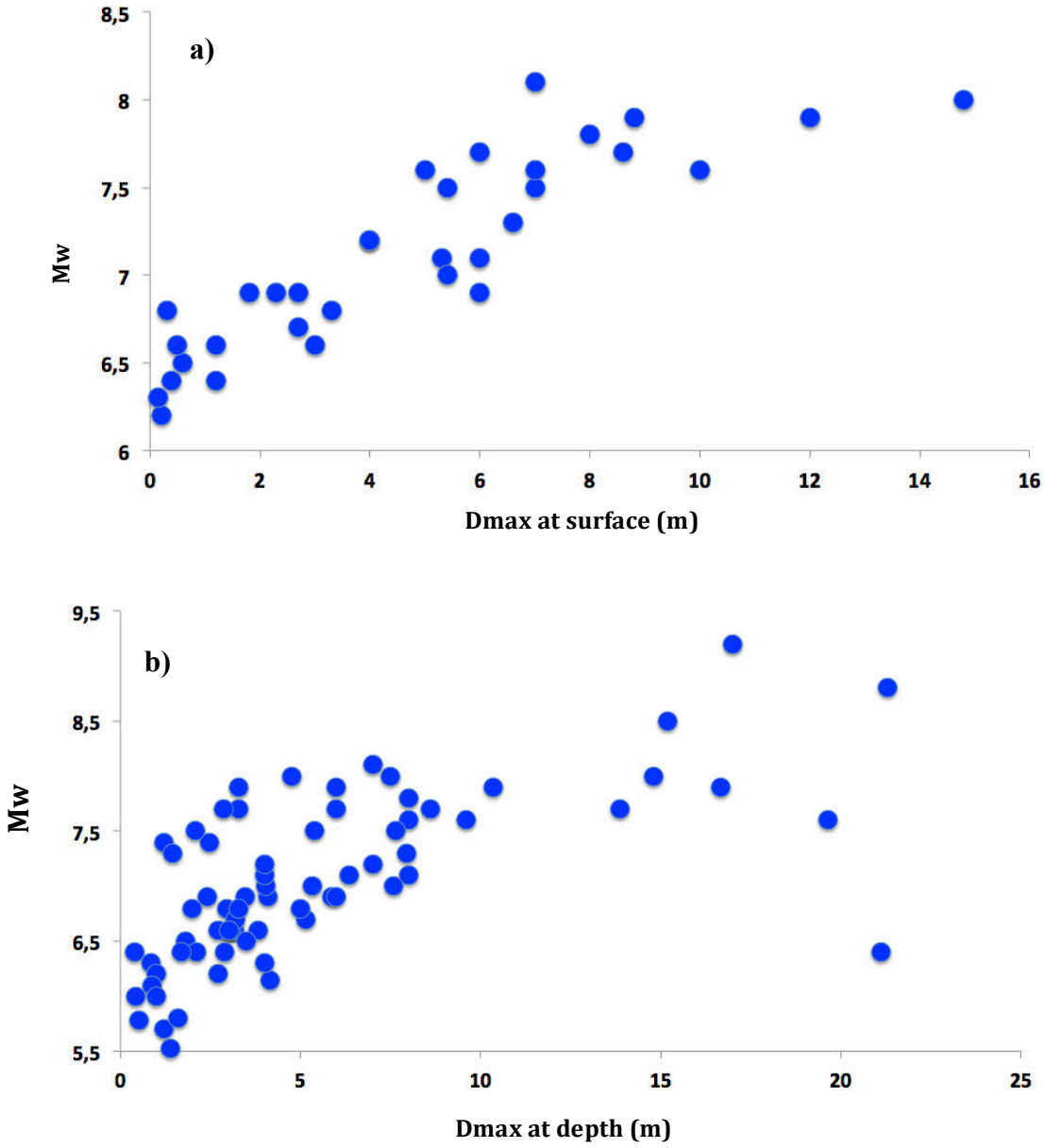


Fig.220: Relation between Mw and Dmax at surface (a) and at depth (b).

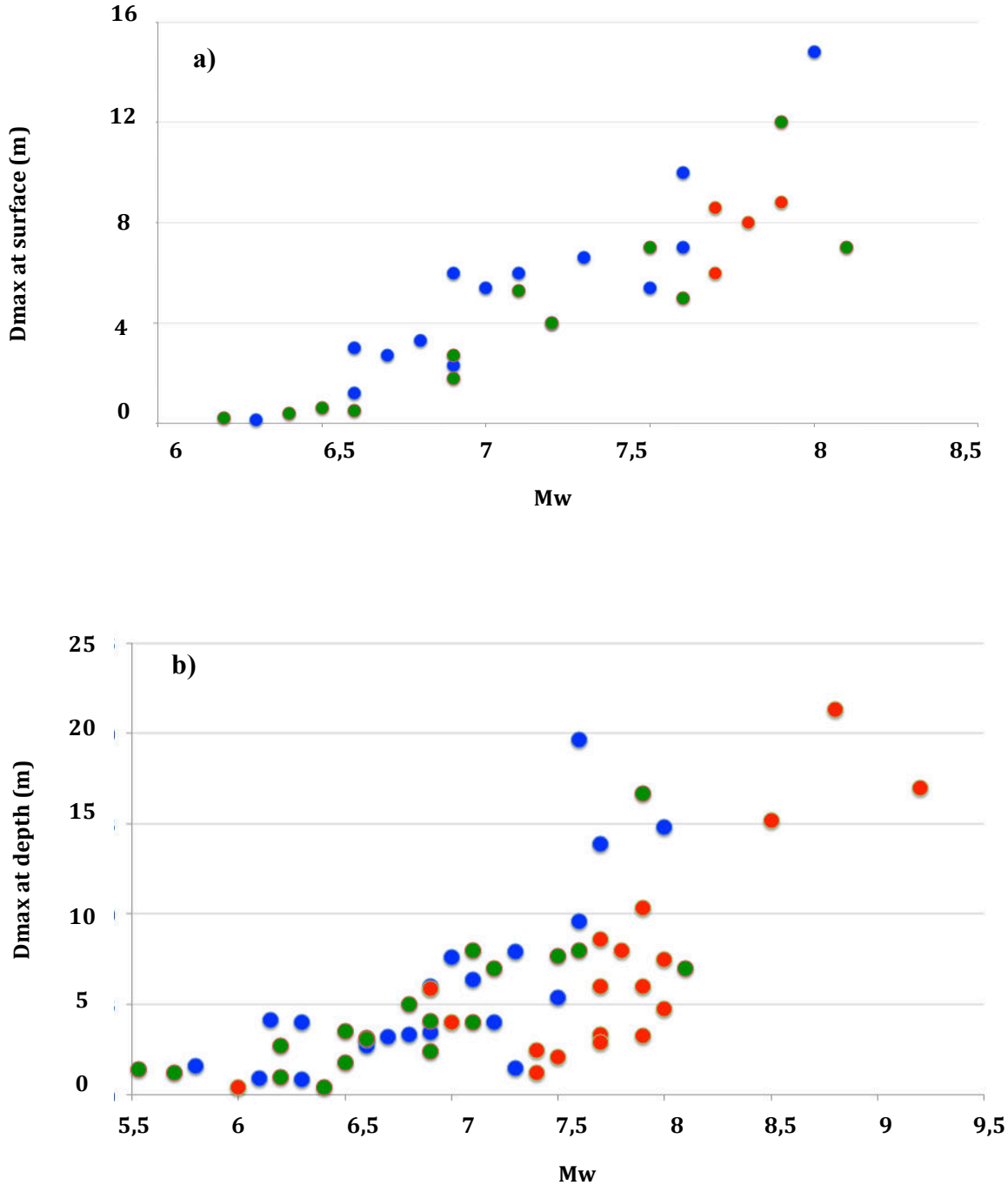


Fig.221: Relation between Mw and Dmax at surface (a) and depth (b). The colors indicate the structural maturity of the broken faults, red: mature; green: intermediate; blue: immature.

M0 versus maximum slip

Figures 222 a - b show the relation between M0 and Dmax at surface and depth, respectively. For a same amount of maximum slip produced by an EQ, very different seismic moments are produced. Overall, EQs occurring on immature faults produce lower seismic moments than EQs on mature and intermediate-maturity faults. This is likely because, although the amount of slip produced might be similar, the size of the broken fault is not; EQs on immature faults break shorter fault sections that EQs on more mature faults.

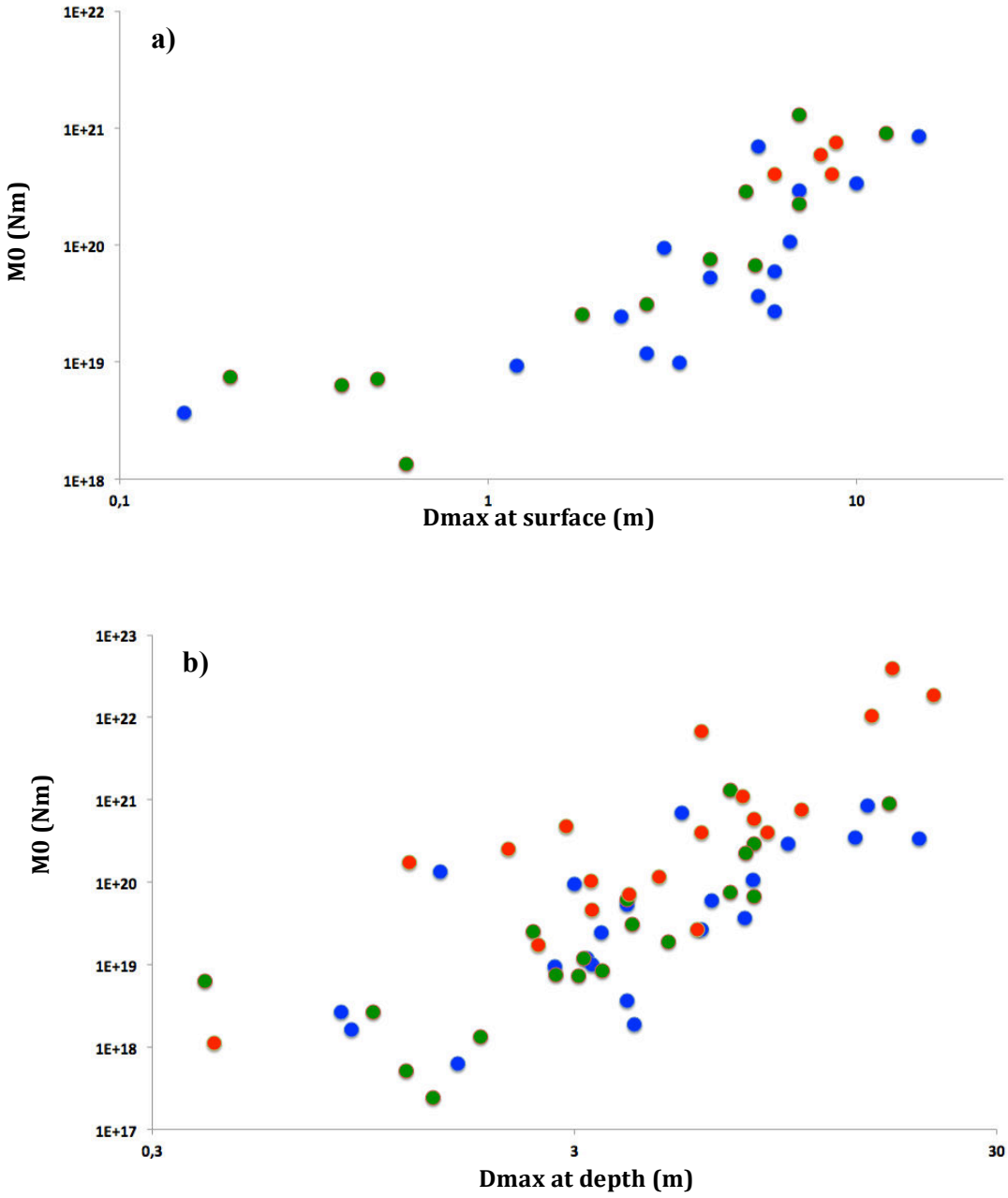


Fig.222: relation between M0 and Dmax at surface (a) and depth (b). The colors indicate the structural maturity of the broken faults, red: mature; green: intermediate; blue: immature.

Mw versus stress drop approached through Dmax/L ratio

Figures 223 a-b examine the relation between Mw and the EQ stress drop at surface and depth, respectively. In both cases, the stress drop is approached by the Dmax/L ratio of the EQ. We observe that EQs with very different stress drops can have the same magnitude. **For a given magnitude, the corresponding stress drop is higher for EQs on immature faults**. The depth data furthermore suggest that, overall, as the EQ magnitude increases, the corresponding stress drop decreases. Together these confirm that the magnitude does not appropriately measures the 'energy' of an EQ.

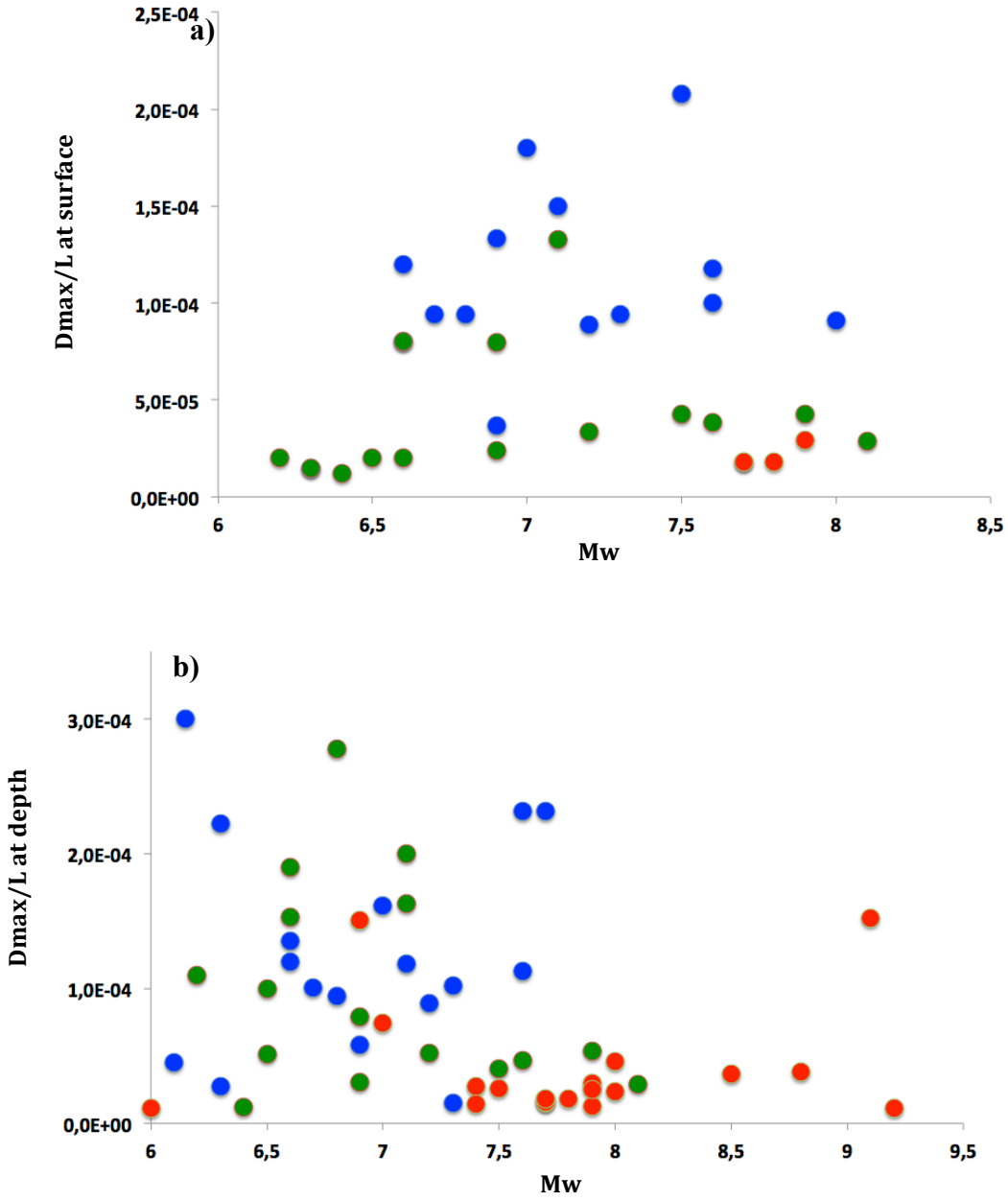


Fig.223: relation between Mw and the EQ stress drop at surface (a) and depth (b). The colors indicate the structural maturity of the broken faults, red: mature; green: intermediate; blue: immature.

Broken area versus Mw

In Chapter III, I have defined the broken area as S_{min} being the zone of coseismic slip greater than 15 % of the maximum slip at depth. Figure 224 shows the relation between S_{min} and the EQ magnitude. As expected, Mw increases overall with Smin. Yet in details, a similar rupture area can produce EQs with different magnitudes. Therefore the size of the broken zone is not the only parameter to control the EQ magnitude. Actually, we observe differences depending on the structural maturity of the broken fault: **overall, for a similar slip surface, an immature fault produces an EQ with a larger magnitude**.

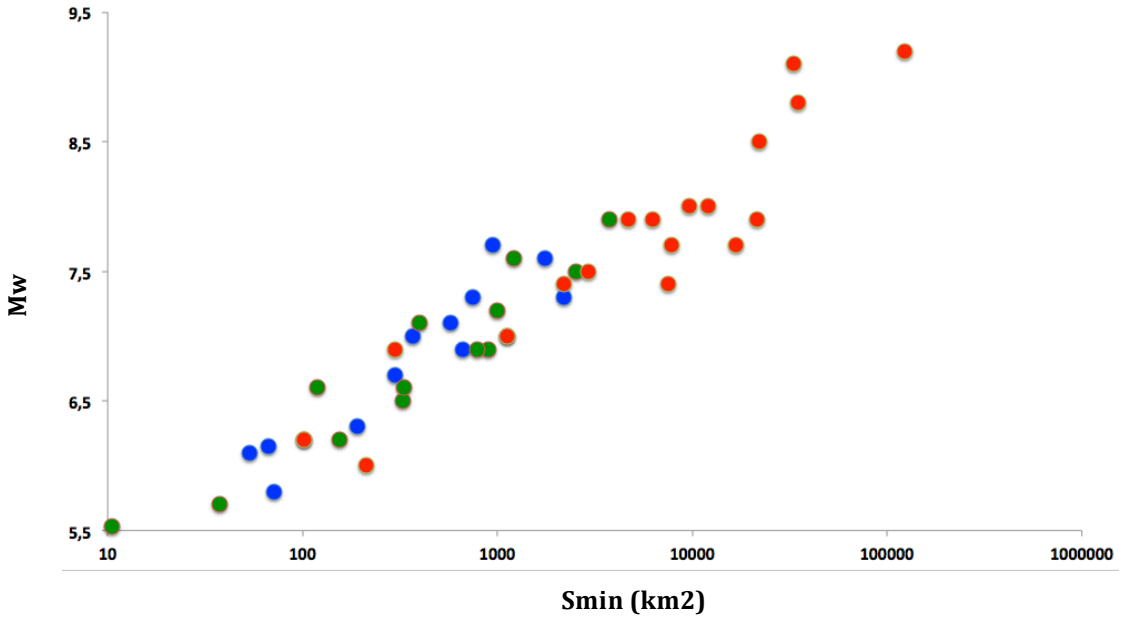


Fig.224: relation between S_{min} and EQ magnitude. The colors indicate the structural maturity of the broken faults, red: mature; green: intermediate; blue: immature.

Broken area versus stress drop approached through Dmax/L ratio

Figure 225 shows the relation between the broken area Smin and the EQ stress drop (approached by the Dmax/L ratio, here measured at depth). **Overall, the larger the broken surface, the smaller the EQ stress drop**. This is likely because, for long ruptures, the stress drop is only apparent, representing the stress drop averaged over different broken segments. I will come back to this point in section 4 below.

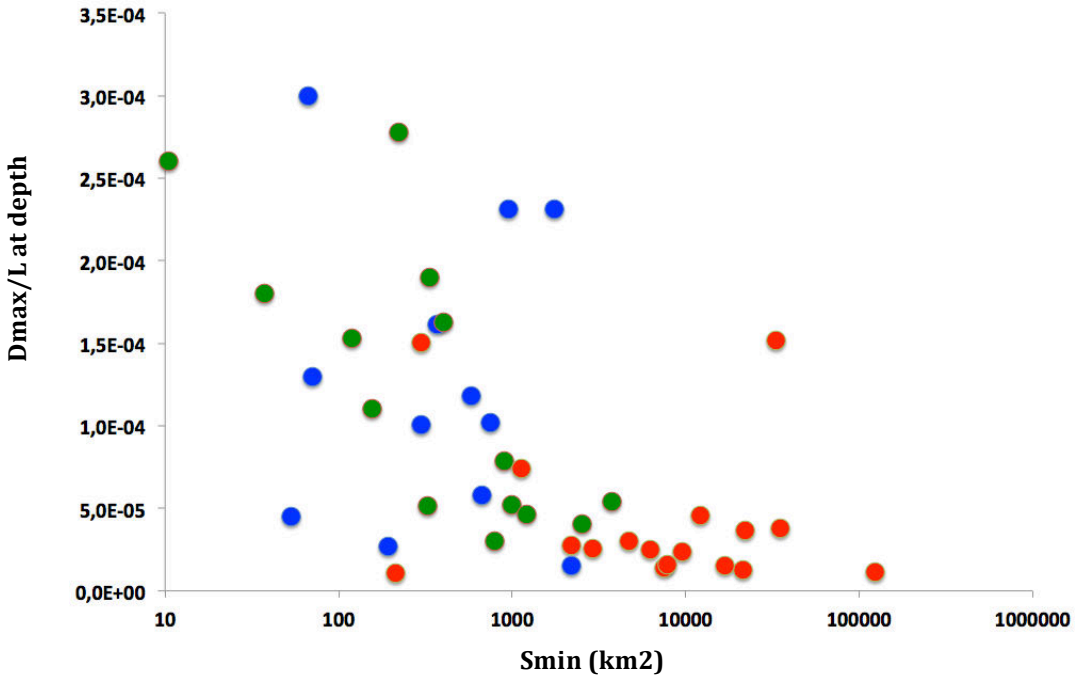


Fig.225: relation between the broken area Smin and the EQ stress drop (approached by the Dmax/L ratio, here measured at depth). The colors indicate the structural maturity of the broken faults, red: mature; green: intermediate; blue: immature.

Figure 226 now shows the ratio S_{min}/S (with S = L*W) as a function of the EQ stress drop (as before). **Overall, the S_{min}/S ratio increases with the EQ stress drop**. This is likely because the EQs with larger stress drop occur on immature faults, where they break one or two fault segments at most. The broken fault width thus does not vary much along the rupture length and so S_{min} is not that different from S. By contrast, the EQs with lower stress drop occur on more mature faults, where they break several fault segments. As we have seen in Chapter III, this multiple-segment rupture is accompanied by a decrease in the rupture width (and of the slip), and hence by a decrease in S_{min}/S. (cf Fig.193 and 195 in Chapter III).

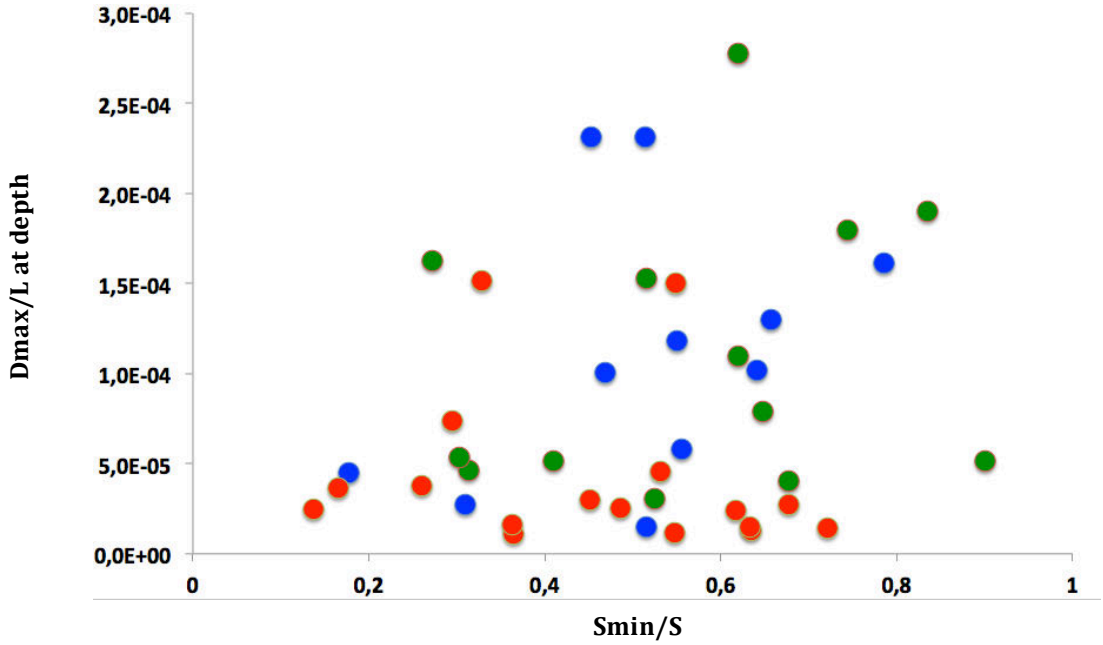


Fig.226: ratio S_{min}/S (with S = L*W) as a function of the EQ stress drop (as before). The colors indicate the structural maturity of the broken faults, red: mature; green: intermediate; blue: immature.

Broken area versus M0: described in the following section

3. Examining a few scaling relations expected from the theoretical elastic framework

M0 varying as L^2 or L^3?

In the elastic framework, $M0 = m*D_{mean}*S$, where m is the medium rigidity and is assigned a value of $3.\ 10^{10}$ ($N.m^{-2}$), D_{mean} is the mean coseismic slip (in m), and S is the broken area (in m^2).

To estimate the rupture area, different rupture models are considered, generally either circular or rectangular. I have shown in chapter III that the broken area rather has a triangular shape, which actually varies with the slip decrease, and hence depending on the number of broken fault segments and hence on the fault maturity. Thus, in general, the approximation S = L*W does not appropriately describe the broken area. On the other hand, I have shown in this section (IV-1) that the relation between Dmean (or Dmax) and the rupture length is not

unique, but actually follows four distinct functions. Each of these functions has a linear part (i.e., Dmean = k*L, with k a constant) for small ruptures with $L \leq 2W$, and a saturating, non-linear part for long ruptures.

It results that the relation between M0 and L is not trivial. On theoretical basis, it has been suggested that M0 should scale as L^3 (Kanamori and Anderson, 1975 ; Geller, 1976 ; Sato, 1979). However, for the large EQs, M0 might rather scale as L^2 (same references). Yet, Kagan (2002) argues that there is no break in the scaling, so that all EQs have their M0 scaling as L^3.

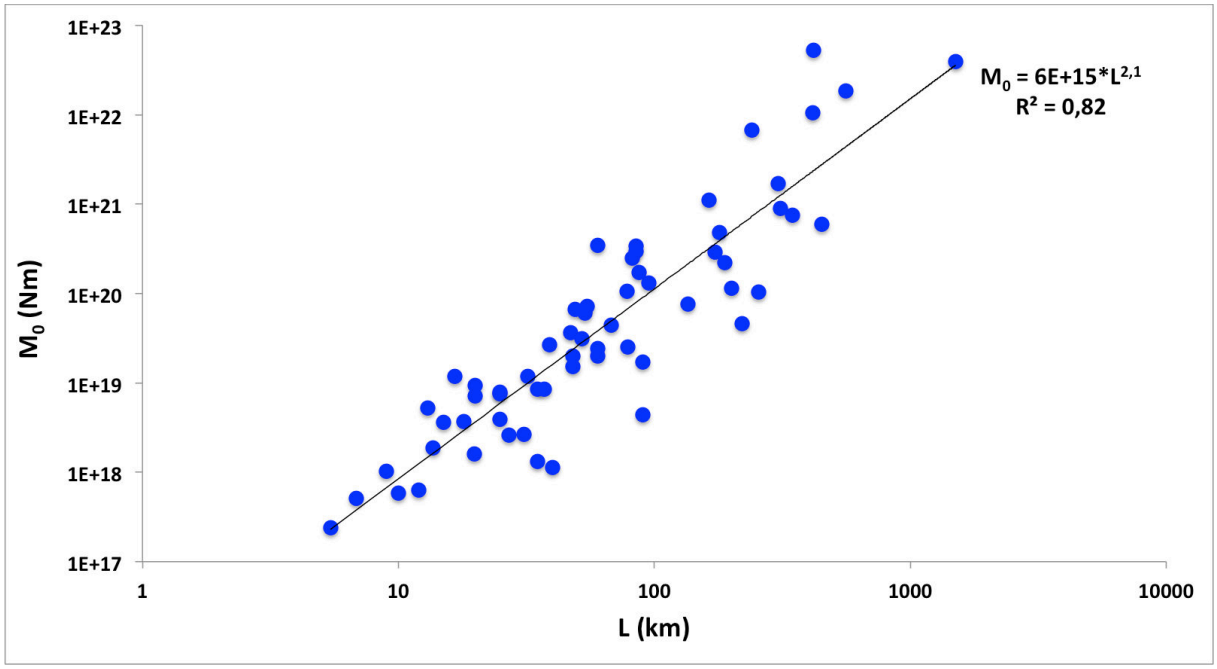


Fig.227: relation between M0 and L, for the entire set of data

Figure 227 examines this relation for the entire set of data, with no discrimination (continental and subduction EQs). A moderately constrained regression through the data suggests that M0 might vary as L^2.

Figures 228 a-b now examine the M0-L relation but for the data discriminated from the structural maturity of the broken faults. The data are also shown separately for continental EQs alone (Fig.228a), and for the EQ data including subduction EQs (Fig.228b). The discrimination in structural maturity seems to result in different M0-L scaling relations. **The EQs on immature faults seem to have their M0 varying as L^3, whereas the EQs on faults with intermediate maturity seem to have their M0 varying as L^2. The EQs on mature faults also seem to have their M0 varying as L^2** but the regression is less well constrained.

The L^3 scaling for the EQs on immature faults likely result from these EQs breaking short faults, so that, on the one hand, L ~ W, and on the other hand, Dmean ~ k*L.

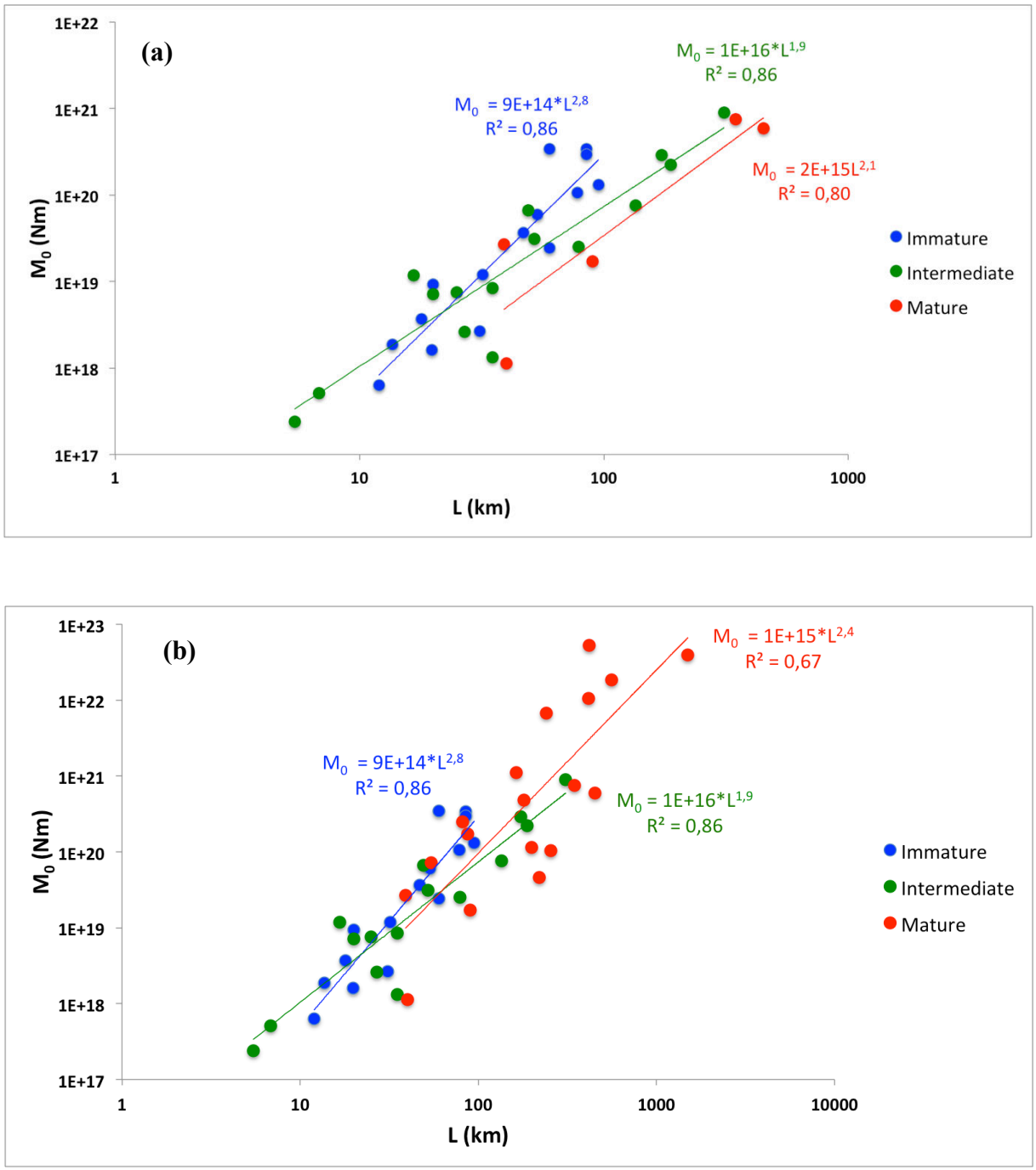


Fig.228: M0-L relation with the data discriminated from the structural maturity of the broken faults. The data are also shown separately for continental EQs alone (a), and for the EQ data including subduction EQs (b).

M0 as a function of broken area

Figures 229 and 230a-b show the relation between M0 and the broken area. In figure 229, the S and Smin possible broken areas are compared. They scale roughly similarly with M0, but it is difficult to interpret theoretically the obtained exponent. Figures 230a-b show how M0 relates to Smin, with the data being discriminated from the fault maturity, and with the continental and subduction EQs being distinguished. It is found that the exponent if higher for EQs on immature faults, but again, the variability of the exponents is difficult to interpret theoretically. The following figures are more informative.

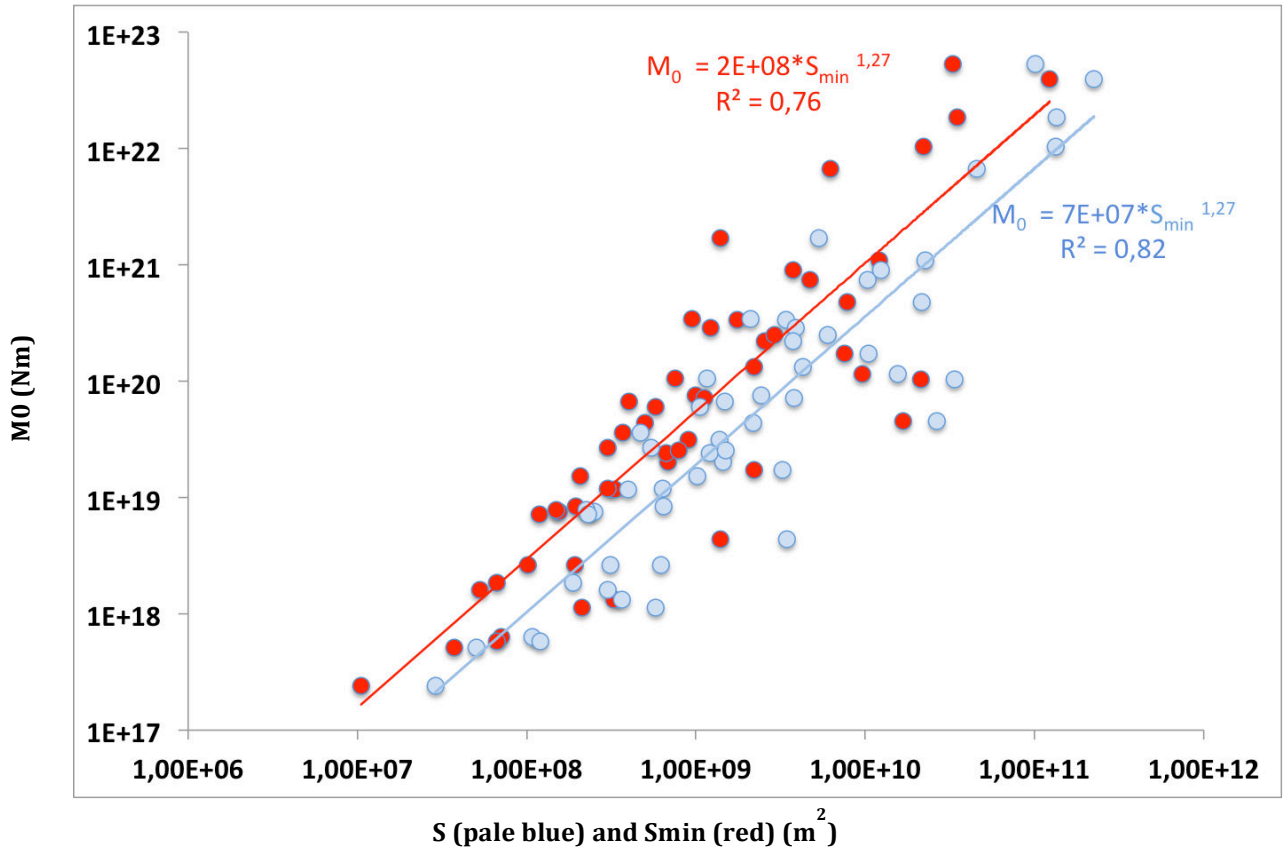
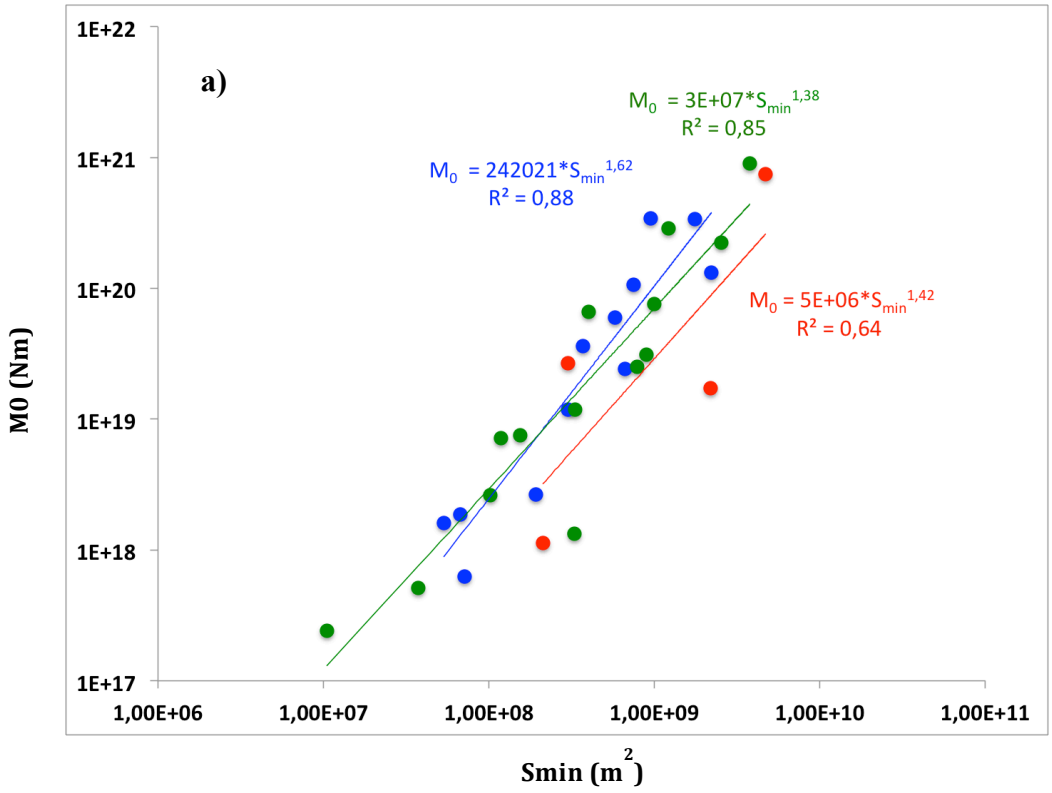


Fig. 229: relation between M0 and the broken area. The S and Smin possible broken areas are compared. They scale roughly similarly with M0.



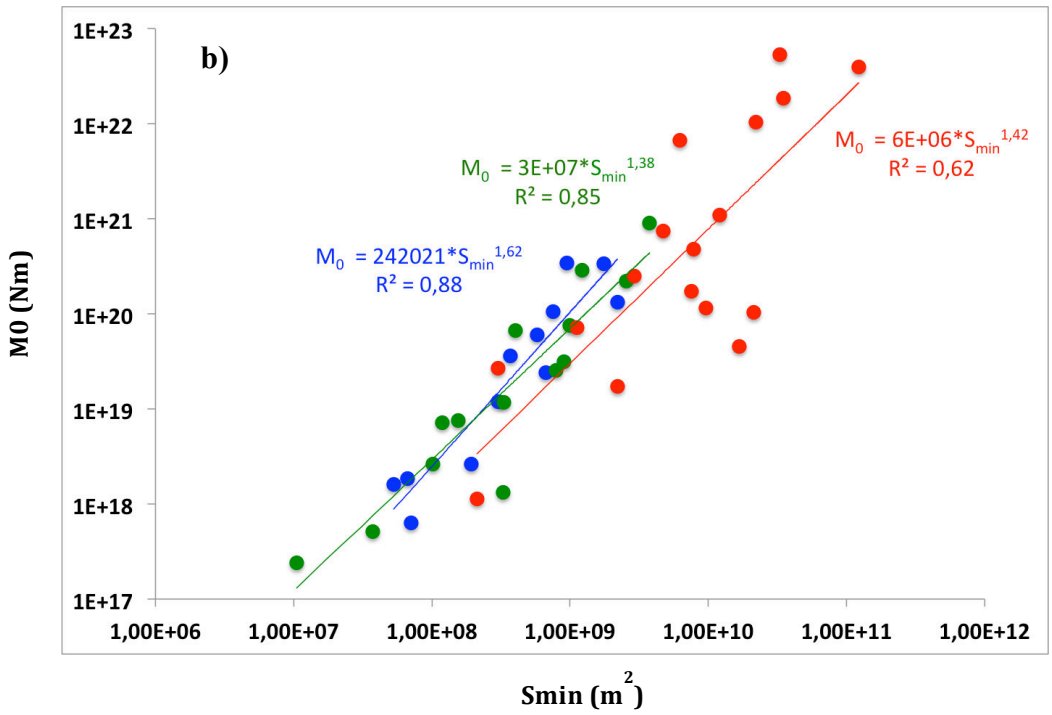


Fig. 230: relation between M0 and Smin, with the data being discriminated from the fault maturity (red: mature; green: intermediate; blue: immature), and with the continental and subduction EQs being distinguished (continental EQs only in (a), and with also subduction EQs in (b))

M0 and medium rigidity

In the theoretical equation, M0 = μ*D_{mean}*S. From our datasets, we know fairly well M0, D_{mean} (equal to Dmax/2), and the broken area which we called Smin. Therefore, plotting M0 as a function of Dmean*Smin, we should find a linear relation and derive the medium rigidity m that should be equal to 3.10^{10} $N.m^{-2}$.

Figure 231 first examines this relation when the broken area is taken as S = L*W (common approach). The data satisfy a linear relation between M0 and S*Dmean, with a m coefficient fairly similar, although slightly lower, to the expected theoretical value.

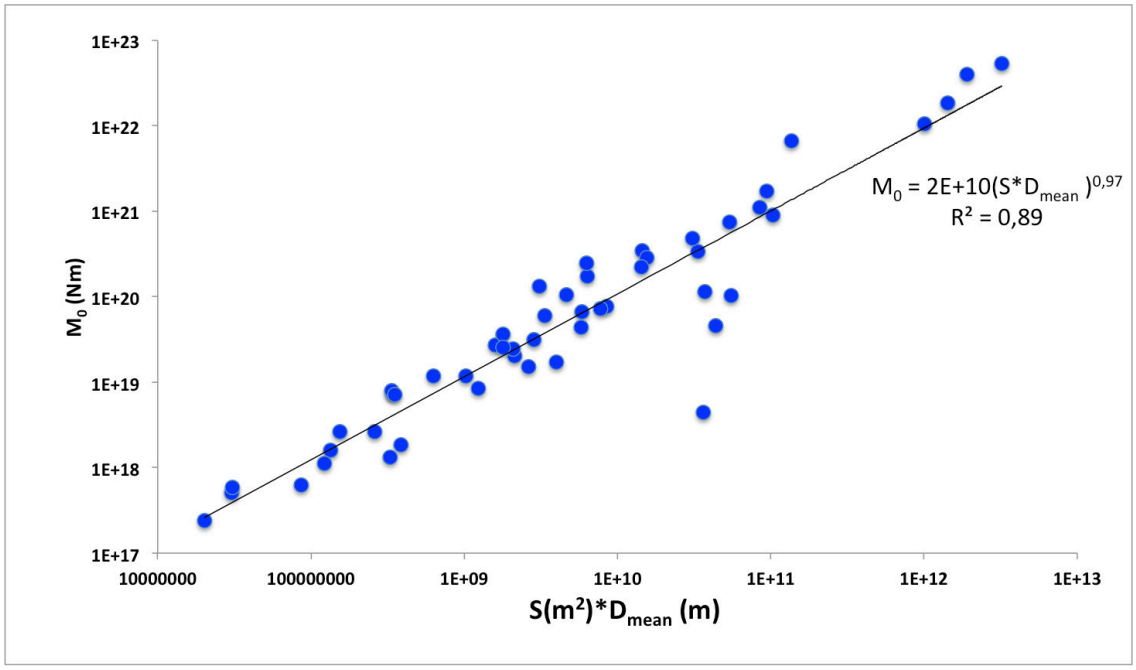


Fig. 231 : relation between M0 and S*Dmean, when the broken area is taken as S = L*W (common approach); all data are considered

However, I showed before that, in general, S= L*W does not appropriately describe the broken area. Figure 232 thus shows the same relation as before but with S= Smin. A linear relation is still found between M0 and Dmean*Smin, but m is here exactly similar to the expected theoretical value. **In the common theoretical framework, this finding suggests that Smin well describes the broken area**.

Figure 233 now shows the same relation as before but with the data discriminated from the fault maturity. The 3 scaling are linear, yet with variable μ coefficients. For EQs on immature

faults, μ is exactly the expected theoretical value. μ is twice lower for EQs on intermediate maturity-faults, whereas it is three times smaller for EQs on mature faults. Because the parameters M0, Dmean and Smin are fairly well-constrained, it is likely that the observed variations in the μ values are relevant: the medium rigidity might sometimes be lower than supposed. This is understandable since, as I will show in Chapter V, the faults and EQs slips damage the crustal rocks around them, so that it is unrealistic to believe that the rigidity of the medium can keep constant in space an time: **as they become more mature, the faults most damage the adjacent crustal medium, and therefore, it is expected that the medium rigidity decreases as faults become more mature. This is actually what we observe in the m values**.

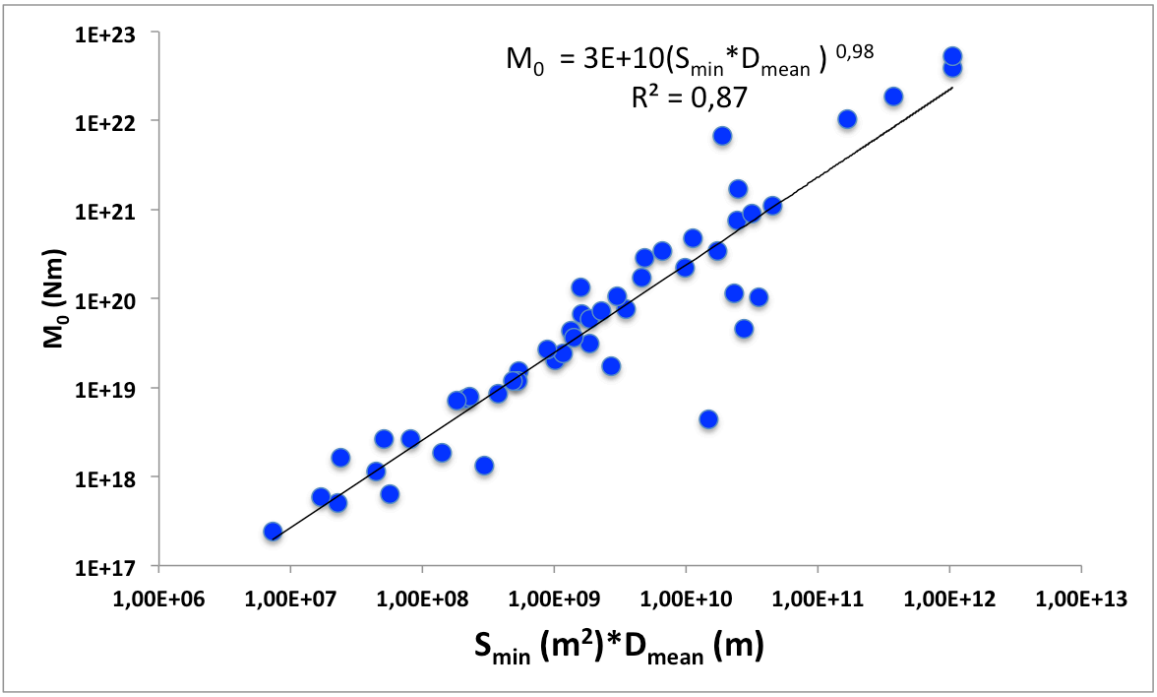


Fig.232: relation between M0 and S*Dmean, when the broken area is taken as Smin; all data are considered.

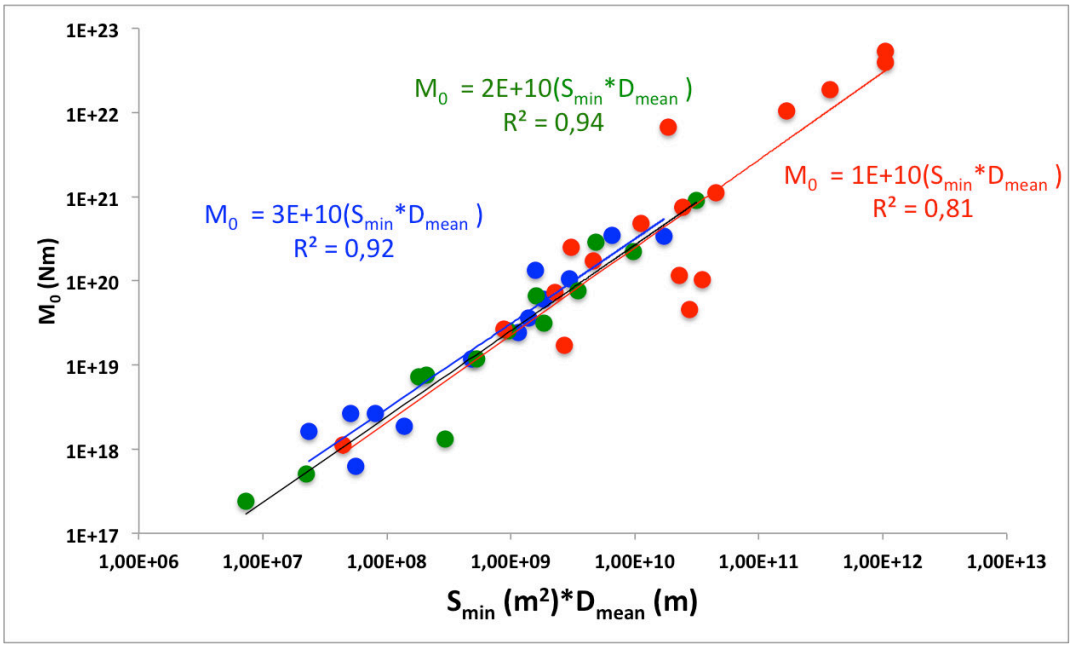
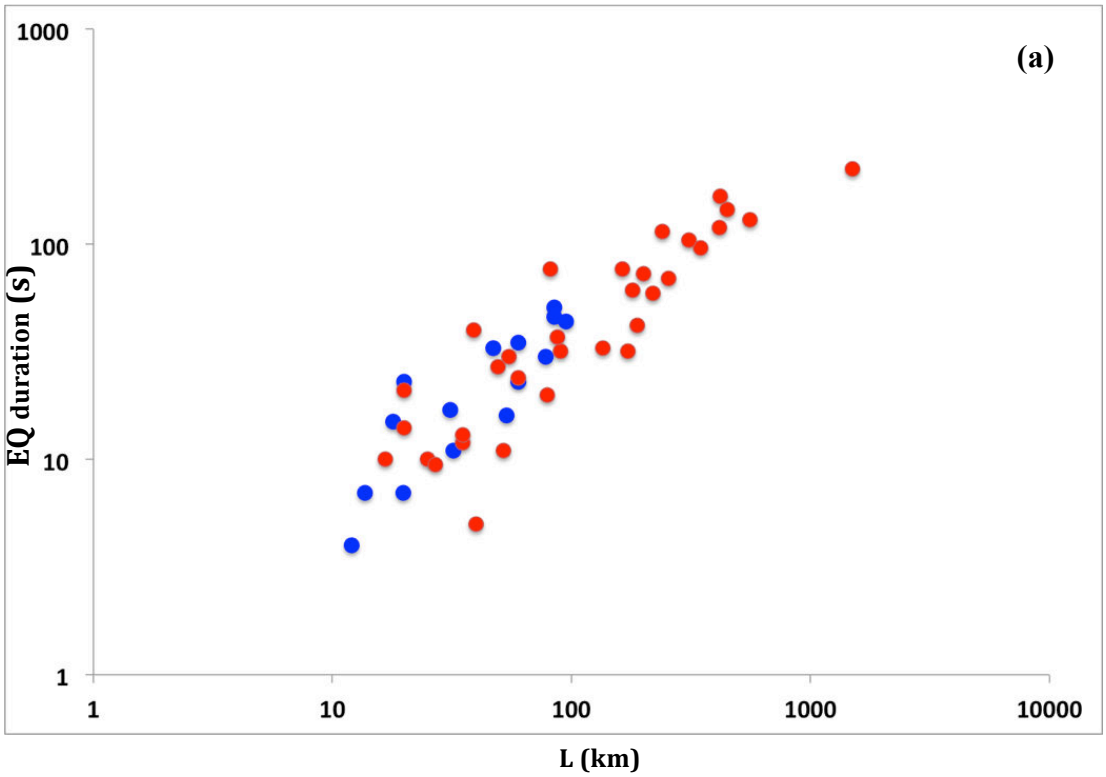


Fig.233: same as Fig. 232 but with the data discriminated from the fault maturity (red: mature, green: intremediate, blue: immature).

EQ duration as a function of structural maturity

Figure 234 shows the EQ rupture duration as a function of the rupture length. Of course, overall, as the rupture length increases, the EQ duration increases. Yet we see an additional feature: **overall, for a similar length of rupture, an EQ occurring on an immature fault lasts longer than an EQ on a more mature fault**. There are a few points contradicting this general tendency, but figure 234 shows that most of them are either poorly constrained data (fairly old EQs and hence models), or data for which the structural maturity might not be correct (ex: the fault broken in the Van EQ is likely immature as it is a secondary, fairly short fault in the area; we need to look at it in more details). The longer duration of EQs on immature faults might be due to the higher friction on these faults impeding the rupture propagation. This might be even more pronounced as most EQs on immature faults are bilateral; therefore, would these EQs be "converted" into unilateral ruptures, they would last even longer.



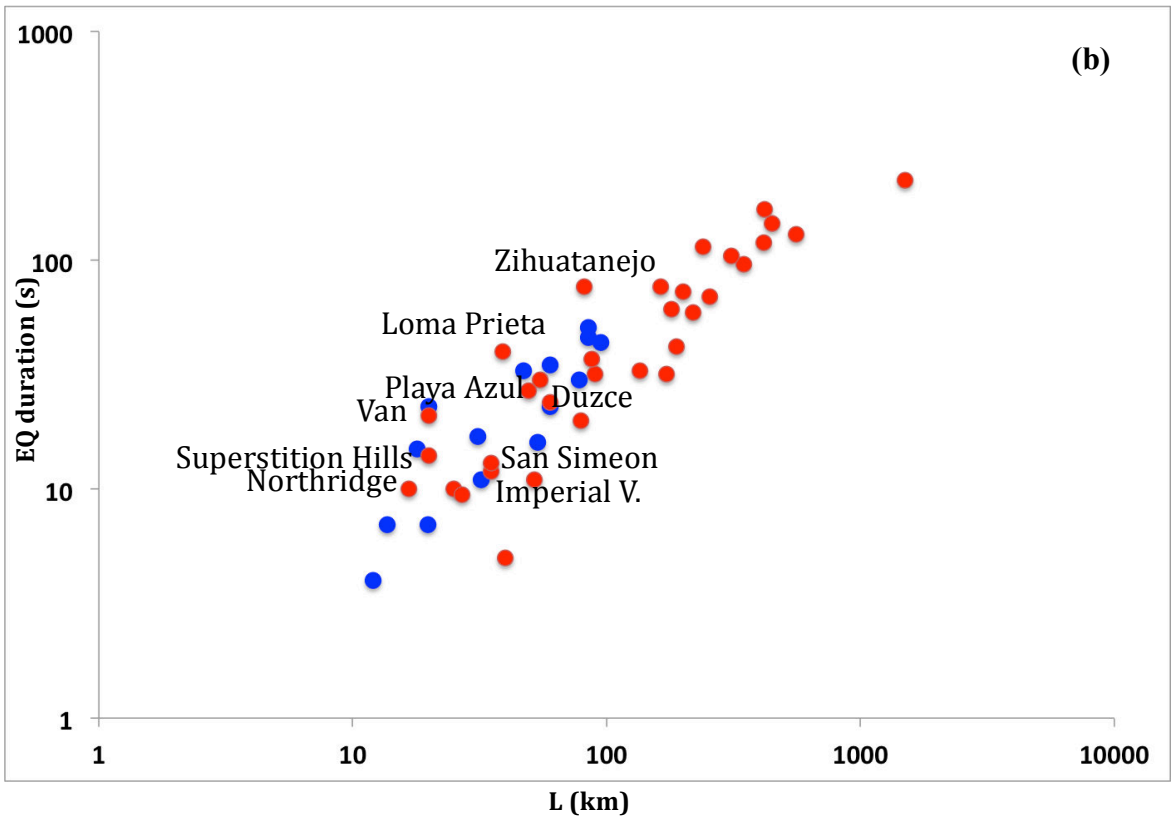
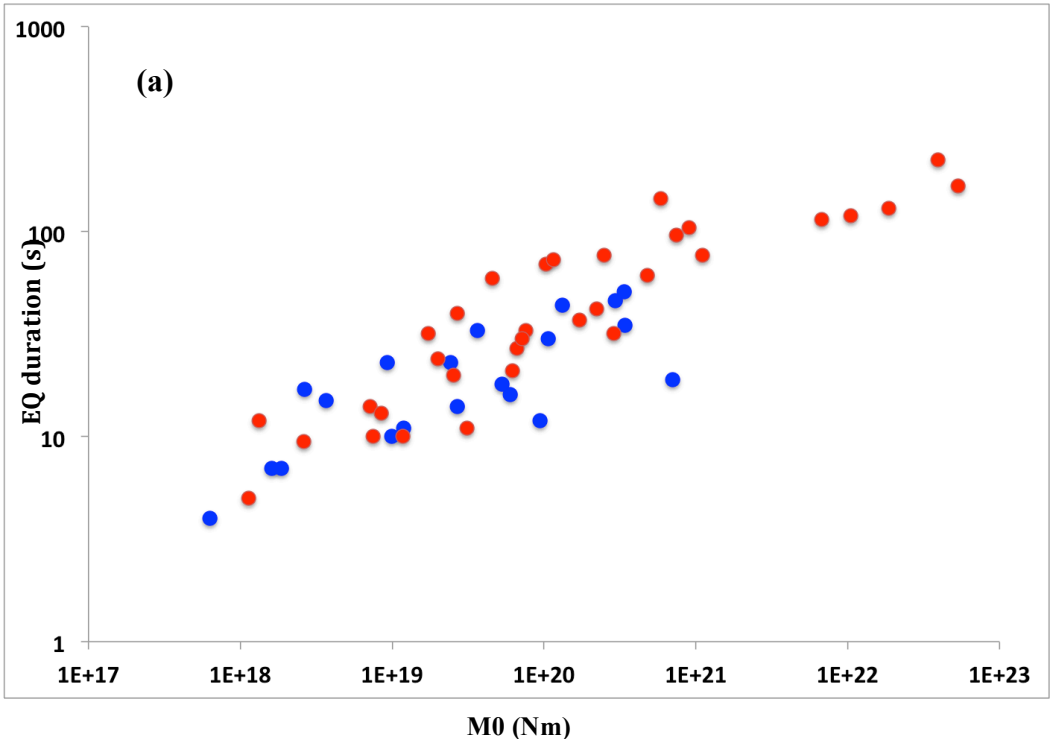


Fig. 234 : (a) EQ rupture duration as a function of the rupture length. All data are considered. Immature faults are in blue, whereas intermediate and mature faults together are in red. (b) Same as (a) with some EQs name.

Figure 235a now examines the relation between the EQ duration and the seismic moment, for all EQs only discriminated as being either immature (in blue) or mature in the broad sense (i.e., intermediate and mature taken together, in red). The figure shows that **for a given M0, ruptures on mature faults last longer than ruptures on immature faults**. This can be understood by the fact that EQs on immature faults produce fairly "compact" ruptures, for which, as we have seen before, Smin ~ S whereas Dmax/L is high. By contrast, EQs on mature faults produce long ruptures, for which Smin is much smaller than S whereas Dmax/L is low. Therefore, to reach an equivalent seismic moment than that of a rupture on an immature fault, an EQ on a mature fault must have a very long length (to compensate the lower Smin and Dmax/L). To propagate over such a long length, the duration of the rupture is longer. This explains why, for a given seismic moment, EQs on more mature faults apparently last longer than EQs on immature faults. Figure 235b shows that the scaling exponent is about 0.3 for both mature and immature ruptures, as expected from the theoretical framework, yet is smaller for EQs on immature faults (~0.26) than for EQs on more mature faults (~0.32).



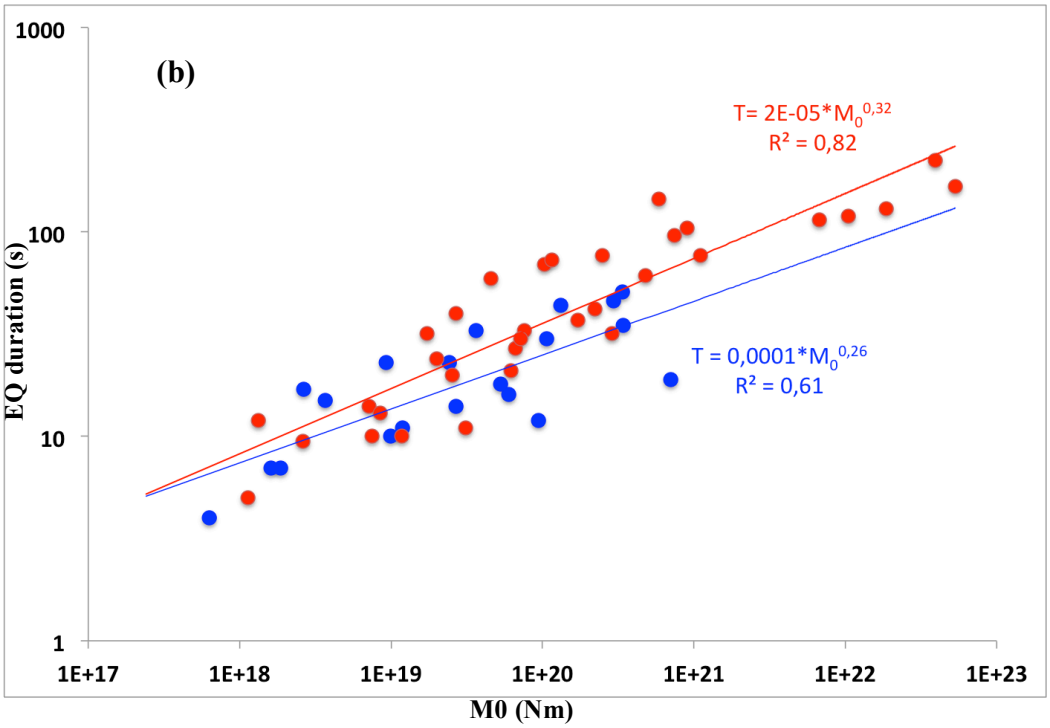


Fig. 235: (a) relation between EQ duration and seismic moment, for all EQs discriminated as being either immature (in blue) or mature in the broad sense (i.e., intermediate and mature taken together, in red). Regressions are calculated on (b).

4. Estimating the earthquake stress drop

The estimation of the EQ stress drop ($\Delta\sigma$) is generally based on theoretical considerations (e.g., Eshelby, 1957; Keilis-Borok, 1959; Knopoff, 1958; Aki, 1972; Nabelek, 2006; Noda et al., 2013), and generally restricts to the estimation of the static stress drop. However, we might try to examine these estimates.

We first need to note that estimations of the EQ stress drop are inherently inaccurate because they all rely on the hypothesis that the static stress drop is constant overall on the rupture plane. Actually, it cannot be since the coseismic slip greatly varies on the rupture plane (See our observations and also discussion in Noda et al., 2013), while the rupture width also varies. Therefore, the stress drop should be calculated locally on the rupture plane. However, a global, static measurement of the total stress drop is still informative.

Overall stress drop on total ruptures

The EQ slip-length scaling described in section IV-1 (Fig.205b and 210b) allows determining the total, overall (apparent) stress drops on the ruptures, through the use of the equations that describe it: $\Delta\sigma = \mu*(\alpha/2)$ with $\mu = 3.10^{10}$ N.m^{-2} (= 3.10^{4} MPa) and α determined by the functions. I find:

- At surface: EQs whose slip-length data fall on functions 1, 2, 3 and 4, respectively, have an average static stress drop of ~ 7.3, ~ 3.1, ~ 1.5 and ~ 0.8 MPa (average stress drop of ~3.2 MPa). These values are in agreement with the stress drop values commonly estimated on EQs worldwide. EQs on immature faults are found to have a higher stress drop than EQs on more mature faults.
- At depth: EQs whose slip-length data fall on functions 1, 2, 3 and 4, respectively, have an average static stress drop of ~ 8.8, ~ 3.4, ~1.7 and ~0.8 MPa (average stress drop of ~3.7 MPa). Again, EQs on immature faults are found to have a higher stress drop than EQs on more mature faults.

I have shown before that the μ value might differ depending on whether the fault is immature (3.10^{10} N.m^{-2}), of intermediate maturity (2.10^{10} N.m^{-2}), or mature (1.10^{10} N.m^{-2}). I have thus redone the calculations above with these different μ values. I find:

- At surface: Using m = 3.10^{10} $N.m^{-2}$ for EQs whose slip-length data fall on function 1, m = 2.10^{10} $N.m^{-2}$ for EQ data on function 2, and m = 1.10^{10} $N.m^{-2}$ for EQ data on functions 3 and 4, I find that EQs whose slip-length data fall on functions 1, 2, 3 and 4, respectively, have an average static stress drop of ~ 7.3, ~ 2.1, ~ 0.5 and ~ 0.27 MPa (average stress drop of ~2.7 MPa)
- At depth: Using m = 3.10^{10} $N.m^{-2}$ for EQs whose slip-length data fall on function 1, m = 2.10^{10} $N.m^{-2}$ for EQ data on function 2, and m = 1.10^{10} $N.m^{-2}$ for EQ data on functions 3 and 4, I find that EQs whose slip-length data fall on functions 1, 2, 3 and 4, respectively have an average static stress drop of ~ 8.8, ~ 2.3, ~0.6 and ~0.28 MPa (average stress drop of ~3 MPa).

Therefore it seems that EQs share a common average static stress drop of about 3 MPa, yet that, in detail, can range between ~0.3 and 9 MPa.

Because M0 = $m*D_{mean}*S$, Dmean = M0/($\mu*S$). On the other hand, $\Delta\sigma = c*\mu*(Dmean/L)$, with c close to 1. Therefore $\Delta\sigma \sim (M0/(L*S))$. Since the broken area is Smin, $\Delta\sigma \sim (M0/(L*Smin))$. Doing this calculation for all the EQs for which the data exist, I find **static stress drop values ranging from ~0.01 to ~6 MPa, with a mean value of ~1.4 MPa**. This value is fairly similar to that found above, though slightly lower.

Stress drop on major fault segments

The EQ slip-length scaling described in section IV-1 also allows determining the static stress drop on each broken segment, with the equation: $\Delta\sigma = n*\mu*(\alpha/2)$ with n the number of broken major segments (in the range 1-4). Doing the calculations, I find:

- From surface data: the fault segments which broke in the EQs whose slip-length data fall on functions 1, 2, 3 and 4, respectively, had an average static stress drop of ~ 7.3, ~6.2, ~4.5 and ~3.2 MPa. All individual segments therefore had a similar average stress drop of ~5 MPa.
- From depth data: the fault segments which broke in the EQs whose slip-length data fall on functions 1, 2, 3 and 4, respectively, had an average static stress drop of ~ 8.8, ~6.9, ~5 and ~3.4 MPa. All individual segments therefore had a similar average stress drop of ~6 MPa.

These results confirm the hypothesis that the broken segments behave as cracks with constant stress drop, ~6 MPa (stress drop at depth is the most relevant). The small variation that is still observed from functions 1 to 4 likely relates to fault maturity, with the static stress drop slightly decreasing as the fault maturity increases (fairly divided by two from immature to mature).

The identification of the broken fault segments in my fault maps furthermore provides precise information on the length of these segments. This information can then be complemented with the maximum slip produced on each segment (derived from surface and/or depth slip profiles) and with the mean width broken on these segments (average width). With this information in hands, I have calculated the stress drop on each major segment, and plotted it as a function of the width of the broken segment. I have also discriminated the data from the structural maturity of the broken fault. Figure 236a shows that **the static stress drop on the individual segments estimated from surface data is in the range ~0.3-5.5 MPa**, in keeping with the previous finding. The figure also shows, on the one hand that EQs on immature faults have rupturing segments with a higher stress drop than EQs on more mature faults, and on the other hand, that the segment stress drop increases overall with the segment width. Figure 236b, done similarly but with depth data, show similar results: **the static stress drop on the individual segments estimated from depth data is in the range ~0.5-7.5 MPa**, in keeping with the previous finding. **EQs on immature faults have rupturing segments with a higher stress drop than EQs on more mature faults. The segment stress drop increases overall with the segment width.** Together these results suggest that, since the width of the broken area decreases with the coseismic slip, **the static stress drop decreases along the rupture in the sense of slip tapering.**

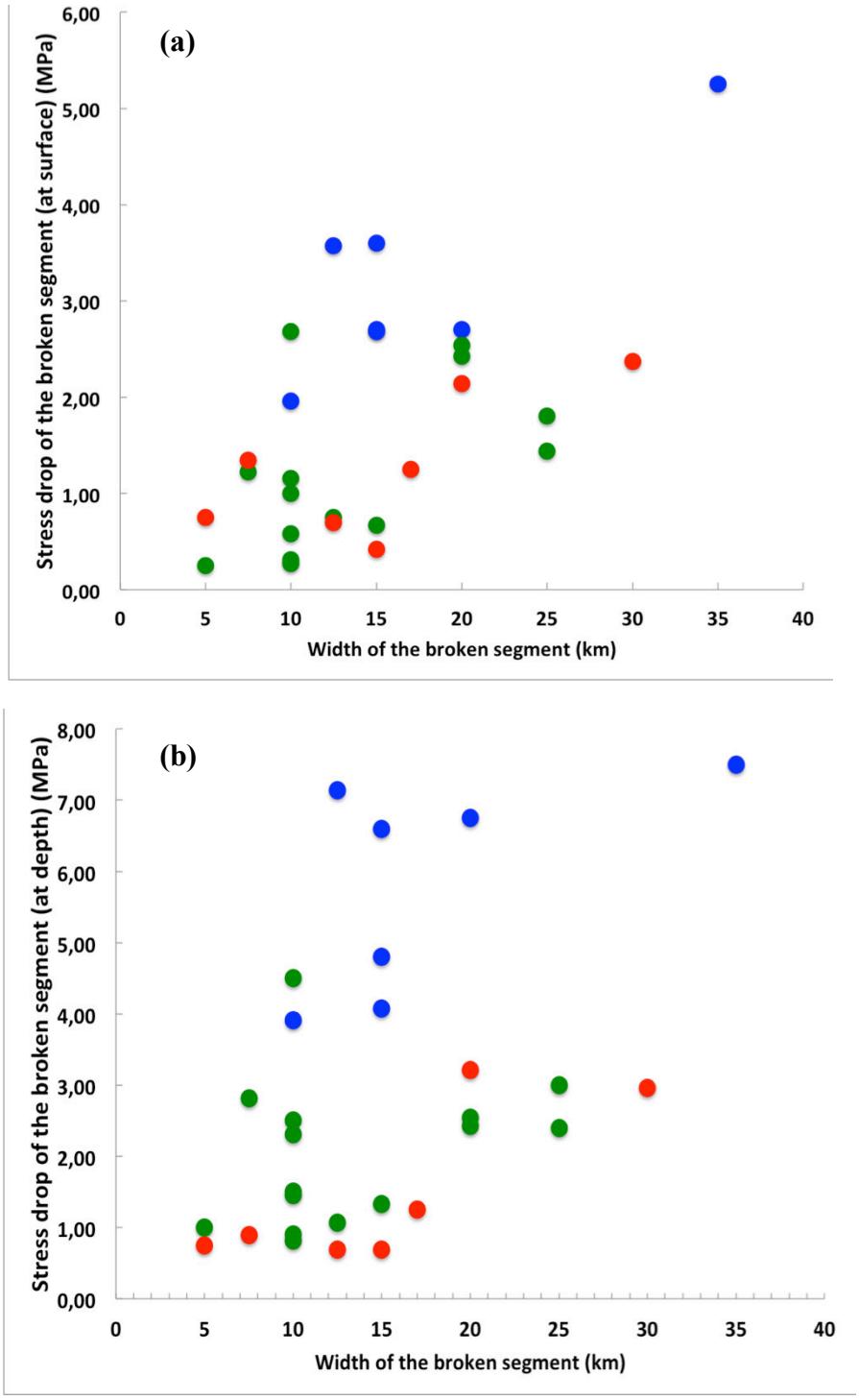


Fig. 236: Segment stress drop as a function of the segment width. The stress drop is calculated knowing the length and mean slip on each segment, derived from our fault mapping and slip profiles. The width is measured in the source models. (a) mean slip from surface data; (b) mean slip from depth data. The colors discriminate the structural maturity of the broken faults (red: mature; green: intermediate; blue: immature)

Stress drop on the most mature "asperity"

Figure 237a (surface data) and 237b (depth data) shows the same calculations as before but performed only for the "major asperity" in the rupture, that is the segment with the largest coseismic slip that we identified as being also the most mature segment in the entire broken zone. The static stress drop of these major asperities is in the range ~0.5-5.5 MPa for surface data and ~1-7.5 MPa for depth data. Although they are sparce, the data suggest that the stress drop of the major asperity decreases with the maturity of the broken fault, but does not much increase with the width of the asperity. Figures 238a (surface data) and 238b (depth data) confirm that the stress drop of the major asperity decreases with the maturity of the broken fault. **From surface data, the stress drop of the major asperity is in the range 3-5.5 MPa on immature faults, 1-3 MPa on intermediate maturity-faults, and 1-2 MPa on mature faults**. **From depth data, the stress drop of the major asperity is in the range 6-8 MPa on immature faults, 1-5 MPa on intermediate maturity-faults, and 1-3 MPa on mature faults**. More data would be needed however to better constrain these values. We note that the few EQs for which the major asperity broke lately in the rupture development (Landers, Denali, Chichi, represented in pale) obey the same general tendencies than the other EQs.

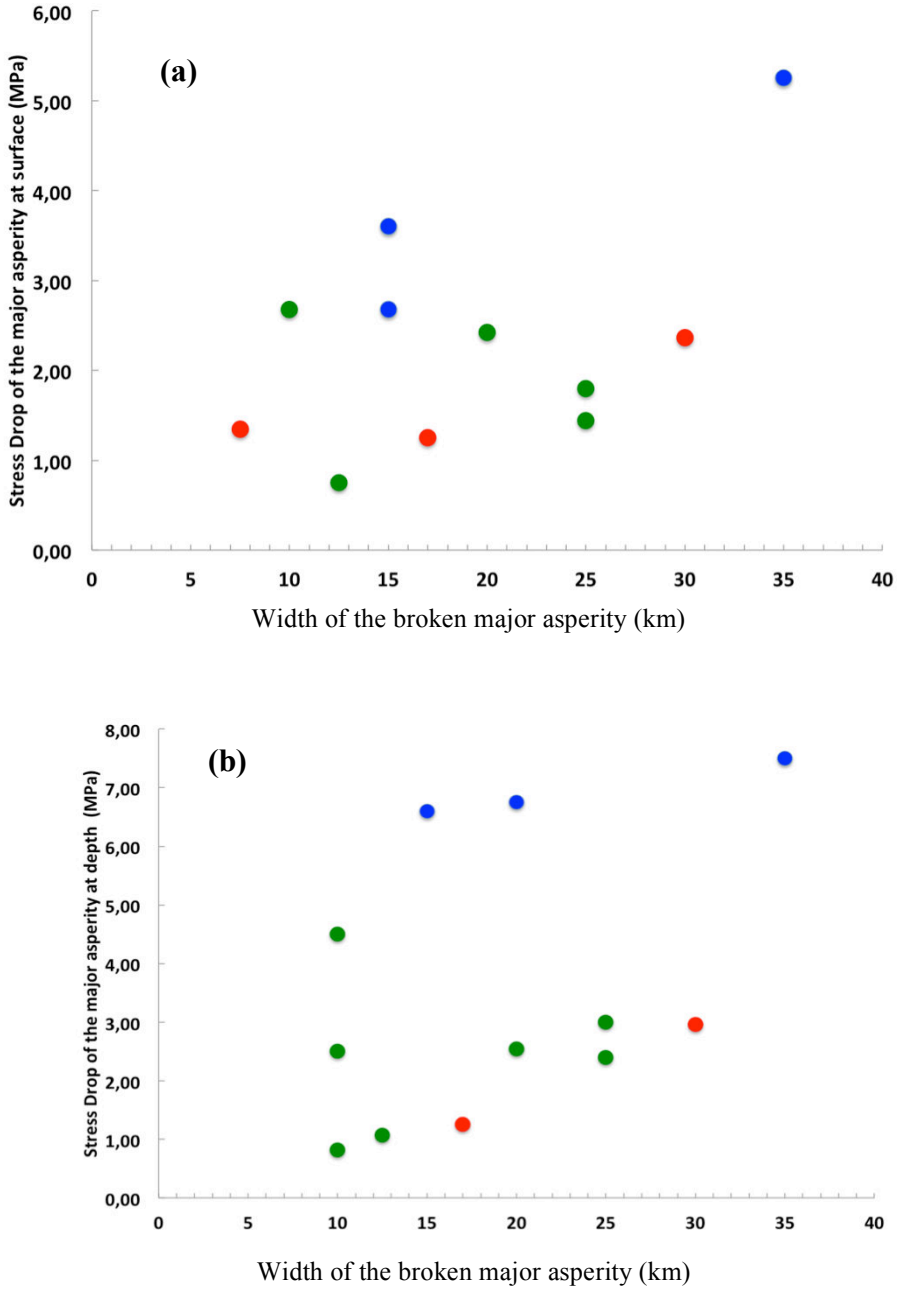


Fig.237 : Stress drop on major asperity (calculated as in previous figure) as a function of the major asperity width. (a) mean slip from surface data; (b) mean slip from depth data. The colors discriminate the structural maturity of the broken faults (red: mature; green: intermediate; blue: immature).

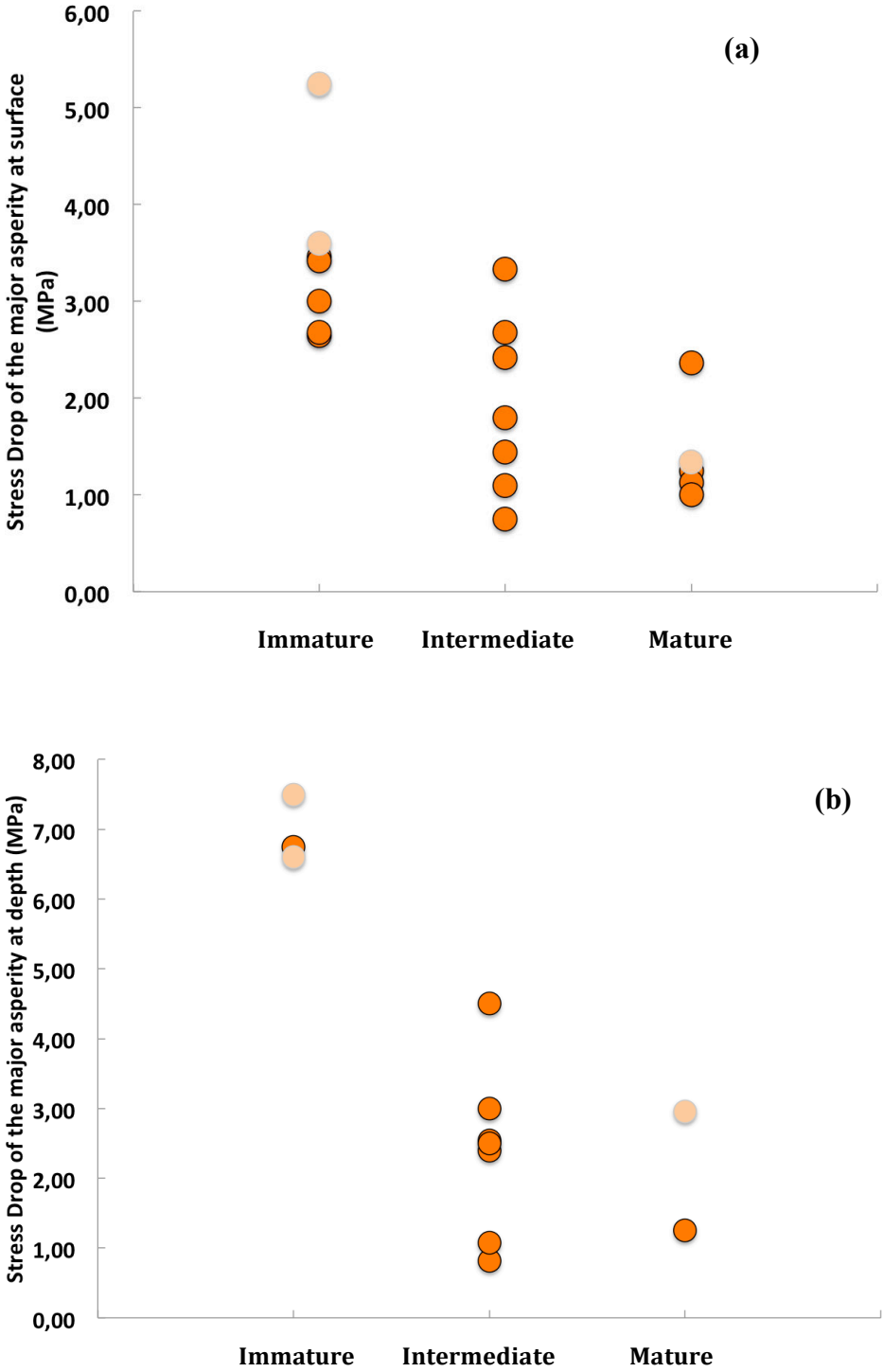


Fig.238: Stress drop on major asperity (calculated as before at surface (a) and at depth (b)) as a function of the structural maturity of the broken fault. In pale are the few EQs where the major asperity broke last in the rupture.

Finally, Figure 239 examines whether the stress drop of the major asperity exerts a control on the number of the other major segments, which are subsequently broken along the fault, as a result of the dynamic overshoot produced by the rupture of the major asperity (in the general case; exceptions are Landers, Denali, Chichi, represented in pale). The plot is made from surface data (depth data are unclear). Amazingly, a general tendency is observed which suggests that **the lower the static stress drop on the major asperity, the larger the number of segments subsequently broken along the fault**. This clearly shows that the "energy" of the major asperity is not the controlling factor for the development of a multi-segment rupture. Rather, a more or less large number of segments break in cascade along a fault depending on whether or not the inter-segment zones that separate these segments can or cannot break. **Therefore, the intrinsic properties of the long-term fault, and more specifically its structural maturity, plays a major controlling role on the development of multi-segment ruptures**.

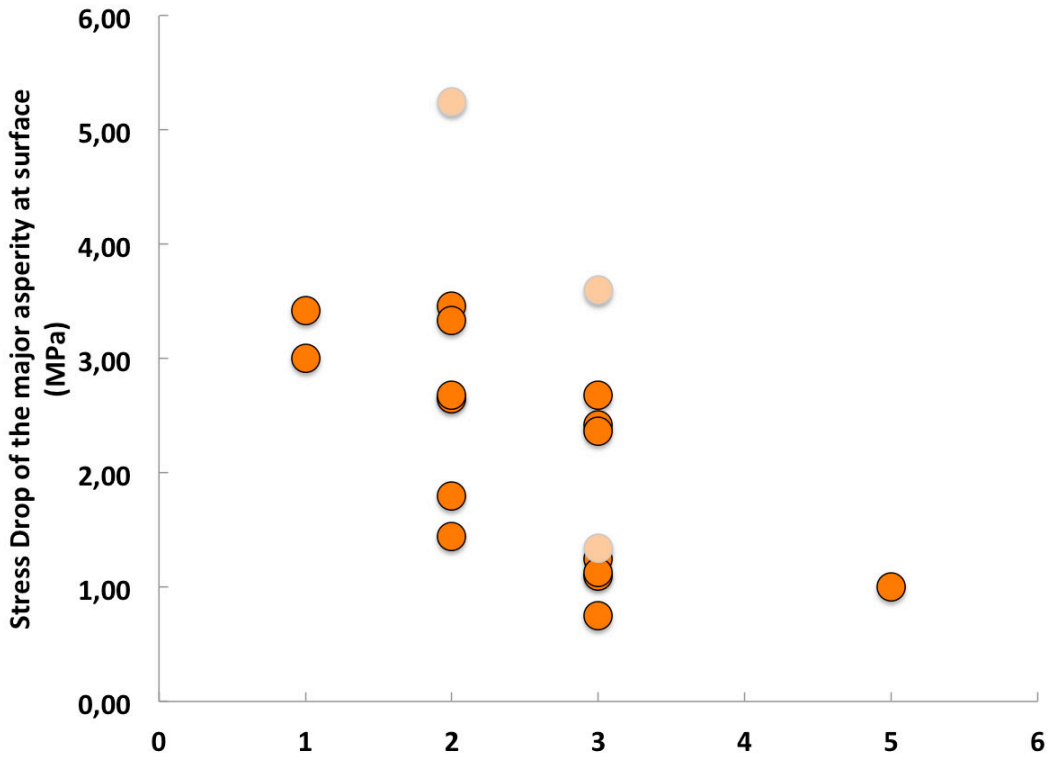


Fig.239: relation between the stress drop of the major asperity and the number of the other major segments which are subsequently broken along the fault. In pale are the few EQ cases where the major asperity broke last in the rupture.

All these results will be discussed in the discussion Chapter VII.

CHAPTER V. MODELING THE ASYMETRIC EARTHQUAKE SLIP PROFILES

Chapter V provides a paper that we have published in G3 under the reference : Cappa, F., C. Perrin, I. Manighetti, and E. Delor (2014), Off-fault long-term damage: A condition to account for generic, triangular earthquake slip profiles, *Geochem. Geophys. Geosyst.,* **15**, 1476–1493, doi:10.1002/2013GC005182.

The objective of the paper was to examine in which « fault properties conditions » the generic triangular shape of the coseismic slip profiles can be produced. The idea arises from the observation that properties of long-term faults play a major controling factor on many properties of the large EQs. We thus believe that the generic shape of the coseismic slip profiles is also, at least partly, governed by some of the fault properties. In this first work, we have focused on the properties of the long-term faults to damage the crustal rocks around them. Furthermore the damage evolves in space and time as the fault grows and lengthens over time. We show that, introducing the long-term crustal damage around faults allows reproducing the generic shape of the coseismic slip profiles. Of course, more subsequent work needs to be done to integrate other properties of the long-term faults into the rupture modeling.

The numerical modeling has been done by F. Cappa in Géoazur.

AGU PUBLICATIONS

Geochemistry, Geophysics, Geosystems

RESEARCH ARTICLE
10.1002/2013GC005182

Off-fault long-term damage: A condition to account for generic, triangular earthquake slip profiles

Frédéric Cappa[1], Clément Perrin[1], Isabelle Manighetti[1], and Elodie Delor[1]

[1]Université de Nice Sophia-Antipolis, CNRS, IRD, Observatoire de la Côte d'Azur, Geoazur UMR 7329, Valbonne, France

Key Points:
- Off-fault long-term damage controls earthquake slip
- Rupture models with along-fault variability in long-term damage properties reproduce generic shape of natural earthquake slip profiles
- Coseismic strain dissipated off the main fault is significant and occurring over large distances

Supporting Information:
- README
- Tables S1-S2

Correspondence to:
F. Cappa,
cappa@geoazur.unice.fr

Citation:
Cappa, F., C. Perrin, I. Manighetti, and E. Delor (2014), Off-fault long-term damage: A condition to account for generic, triangular earthquake slip profiles, *Geochem. Geophys. Geosyst.*, *15*, 1476–1493, doi:10.1002/2013GC005182.

Received 3 DEC 2013
Accepted 4 APR 2014
Accepted article online 8 APR 2014
Published online 29 APR 2014

Abstract Natural earthquake slip profiles have a generic triangular shape which the available rupture dynamics models fail to reproduce. Long-term faults are embedded in long-damaged crustal material, and the properties of the long-term damage vary both across and along the faults. We examine the effects of the predamaged state of the medium on the earthquake slip distributions. We simulate long-term damage by the decrease in the elastic modulus of the medium around the fault. We model the dynamic crack-like rupture of a slip-weakening planar, right-lateral strike-slip fault, and search which geometries and elastic properties of the long-term damage produce a triangular slip profile on the rupture. We find that such a profile is produced only when a laterally heterogeneous preexisting damage zone surrounds the ruptured fault. The highest on-fault slip develops in the most compliant region of the damage zone, and not necessarily above the earthquake hypocenter. The coseismic slip decreases in zones of stiffer damage. The amount of coseismic slip dissipated in the damage zone is large, at least 25–40% of maximum on-fault slip, and can occur over large distances from the fault. Our study thus emphasizes that off-fault preexisting damage should be considered for an accurate description of earthquake ruptures. It also motivates a reformulation of the available earthquake source inversion models since most of them do not include the inelastic deformations that occur in the near field of the earthquake ruptures.

Introduction

The aim of this paper is to explain slip distributions on earthquake ruptures. Based on ~100 slip distributions for natural earthquakes, Manighetti et al. (2005) showed that coseismic slip-length profiles are typically triangular and asymmetric, regardless of rupture length, earthquake magnitude ($M_w \geq \sim 6.0$), slip mode, location, and geological context (Fig. 240a). The triangular envelope shape of coseismic slip profiles is thus a generic property of earthquakes, that is, an intrinsic, common property that must result from the physics of the dynamic rupture process (Noda et al., 2013), not from site-dependent or fault-specific factors. Therefore, it is important to understand how those triangular slip distributions are formed; classical models of crack-like ruptures expanding in a self-similar manner on a planar fault

embedded in a linear elastic medium predict an elliptical characteristic slip profile (Andrews, 2005), and hence fail to reproduce the observed triangular form.

Based on prior studies of long-term faults ($\geq 10^4$-10^6 years) and related cumulative damage (Manighetti et al., 2001, 2004), and on long-standing knowledge of earthquake energy partitioning (e.g., Kostrov, 1974; Dahlen, 1977; Aki and Richards, 2002; Tinti et al., 2005; Kanamori and Rivera, 2006), Manighetti et al. (2005) suggested that the smooth linear decrease in earthquake slip might result from coseismic inelastic deformation—referred to as "coseismic damage"—affecting a large part of the medium as the rupture is developing. An increasing number of observations support this suggestion, in which significant coseismic failure and strain occurs around large earthquake ruptures (Fialko et al., 2002; Fialko, 2004; Hamiel and Fialko, 2007; Cochran et al., 2009; Fielding et al., 2009). Experimental and theoretical models have also been developed recently to examine whether off-fault coseismic damage could emerge from the dynamic rupture process (Harris and Day, 1997; Lyakhovsky et al., 1997; Yamashita, 2000; Poliakov et al., 2002; Dalguer et al., 2003; Rice et al., 2005; Andrews, 2005; Ben-Zion and Shi, 2005; Ando and Yamashita, 2007; Bhat et al., 2007; Templeton and Rice, 2008; Biegel et al., 2008; Viesca et al., 2008; Dunham and Rice, 2008; Duan and Day, 2008; Ma, 2008; Sammis et al., 2009; Dieterich and Smith, 2009; Finzi et al., 2009; Bhat et al., 2010; Biegel et al., 2010; Ma and Andrews, 2010; Shi et al., 2010; Hok et al., 2010; Savage and Cooke, 2010; Dunham et al., 2011a-b; Xu et al., 2012a-b; Ngo et al., 2012; Suzuki, 2012; Xu and Ben-Zion, 2013; Gabriel et al., 2013). Although they are based on different formalisms, all these models confirm that significant coseismic off-fault damage does develop during the earthquake rupture, with this development markedly affecting the mode and properties (i.e., speed and directivity) of the dynamic rupture and the seismic radiation. However, none of these studies have addressed the question of earthquake slip profiles; either the slip distributions that emerge from the experiment or modeling are not examined (Sammis et al., 2009; Hok et al., 2010; Suzuki, 2012; Xu and Ben-Zion, 2013; Gabriel et al., 2013), or they are examined yet found to be different from natural, generic slip profiles (Andrews, 2005; Dunham and Rice, 2008; Templeton and Rice, 2008; Dieterich and Smith, 2009; Savage and Cooke, 2010; Griffith et al., 2010; Dunham et al., 2011a-b; Xu et al., 2012a).

We suggest that the later discrepancy is due, at least in part, to the fact that most theoretical models simulate the rupture in a medium whose predamage state is not fully appropriate. As recognized for long by geologists, the growth and lateral lengthening of faults over geological time leaves behind the passage of their tips a wake of fractured, damaged rocks (e.g., Scholz et al., 1993). Even though various healing processes might occur at specific periods of the earthquake cycle and during the evolution of the fault (e.g., Brantley et al., 1990; Moore et al., 1994; Vidale and Li, 2003; Schaff and Beroza, 2004; Brenguier et al., 2008; Mitchell and Faulkner, 2009), part of the damage (i.e., cracks and faults) is persistent, so that rock damage is cumulative and permanent (e.g., Chester and Chester, 1998; Li et al., 1998; Sibson, 2003; Manighetti et al., 2004; Dor et al., 2008; Mitchell and Faulkner, 2009; Barbot et al., 2009; Cochran et al., 2009; Hearn and Fialko, 2009; Savage and Cooke, 2010; Savage and Brodsky, 2011; Griffith et al., 2012; Smith et al., 2013). Furthermore, the cumulative, long-term damage is heterogeneous, varying both across and along the fault; across the fault, the damage "intensity" (commonly taken as the crack density) decreases away from the fault (e.g., Chester and Logan, 1986; Vermilye and Scholz, 1998; Faulkner et al., 2006; Wechsler et al., 2009; Mitchell and Faulkner, 2009; Savage and Brodsky, 2011; Smith et al., 2013), whereas, along the fault, the damage zone commonly enlarges in the direction of long-term fault propagation (e.g., Manighetti et al., 2004; de Joussineau and Aydin, 2007, 2009; Schlagenhauf et al., 2008; Aydin and Berryman, 2009; Savage and Cooke, 2010; Faulkner et al., 2011) (Fig.240b). Therefore, natural earthquakes rupture faults that are embedded in a predamaged medium, with this long-term damage having properties that vary both across and along the fault. Most available theoretical models take into account the predamaged state, yet consider that predamage is uniform along the fault (Andrews, 2005; Ma, 2008; Templeton and Rice, 2008; Ma and Andrews, 2010; Kaneko and Fialko, 2011; Huang and Ampuero, 2011; Xu et al., 2012b; Gabriel et al., 2013), at best varying across the fault (Harris and Day, 1997; Ben-Zion and Huang, 2002; Ben-Zion and Shi, 2005; Rudnicki and Rice, 2006; Ampuero and Ben-Zion, 2008; Dunham and Rice, 2008). We suspect that this simplification might be one of the reasons of the discrepancy between model results and natural earthquake slip profiles.

In this paper, we explore how the predamaged state of the medium around a strike-slip fault can affect the slip distribution produced during an earthquake. In particular, we focus on the influence of the along-fault variations in the medium rigidity. Although we do not discuss the complexities or formation of fault damage, which is beyond the scope of this paper, we

simulate the preexisting long-term damage and its "intensity", by decreasing the elastic modulus of the medium around the fault. Such a decrease in elastic moduli as damage increases has been observed on natural rocks and faults, both during and immediately after earthquake ruptures (O'Connell and Budiansky, 1974; Li et al., 1998, 2006; Fialko et al., 2002; Vidale and Li, 2003; Ben-Zion et al., 2003; Fialko, 2004) and around long-term geological faults (Li et al., 1990; Gudmundsson, 2004; Faulkner et al., 2006; Aydin and Berryman, 2009; Barbot et al., 2009; Hearn and Fialko, 2009; Cochran et al., 2009). In that later case, damage is thus permanent (e.g., Cochran et al., 2009). We then model the dynamic crack-like rupture of a slip-weakening planar fault, and search which geometries and elastic properties of the long-term damage reproduce the characteristic triangular asymmetric slip profile on the earthquake rupture. We find that a generic earthquake slip profile is produced only when a laterally heterogeneous preexisting, long-term damage zone surrounds the ruptured fault. This arises from a significant part of the coseismic slip being diffused within the long-term damage zone.

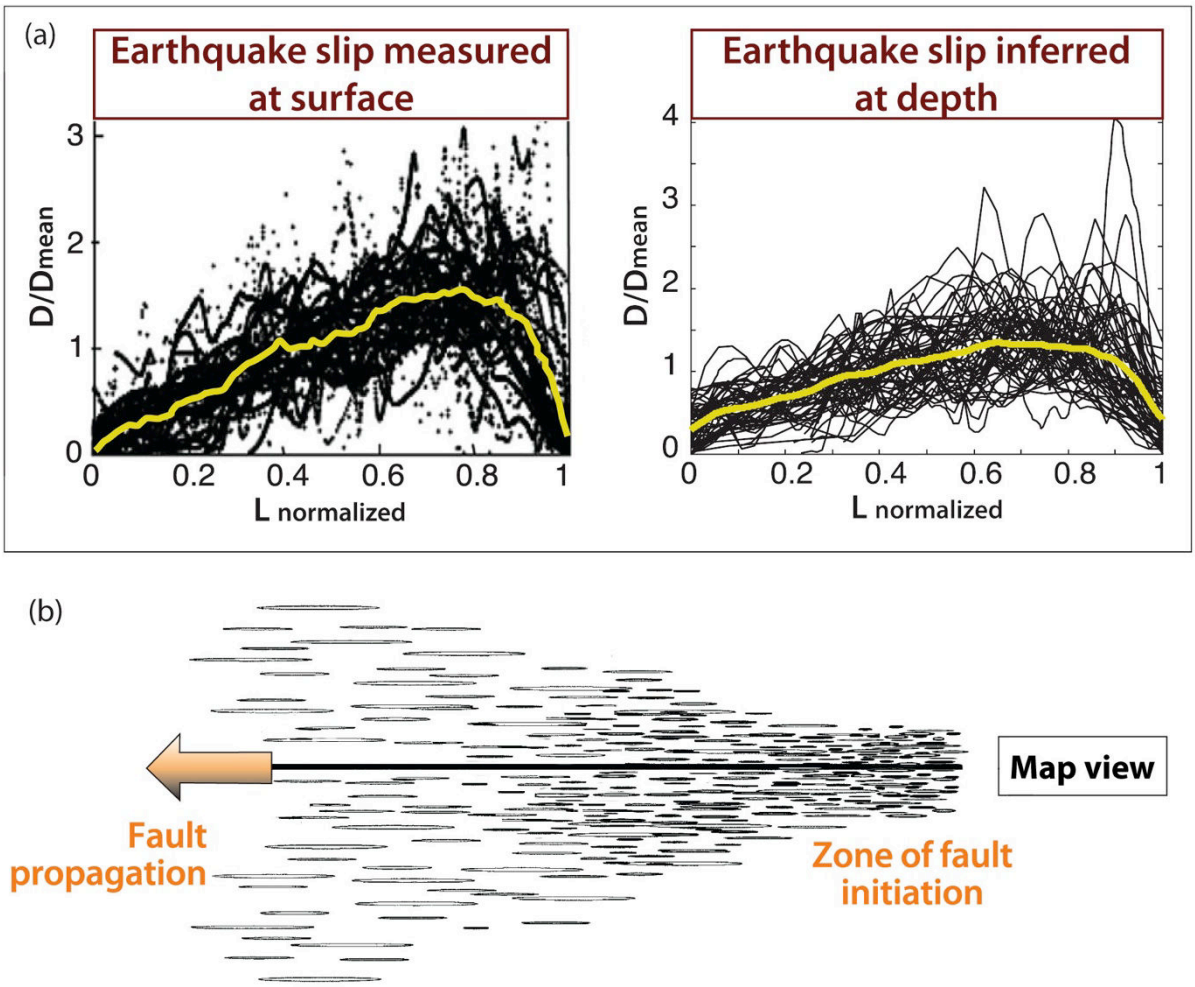


Fig.240 : (a) Earthquake slip profiles (normalized) measured at the ground surface (left) and inferred at depth from earthquake source inversion models (right) for about 50 different historical earthquakes (~100 different slip profiles among surface and depth) with different rupture lengths, magnitudes ($M_w \geq 6$), slip modes, locations worldwide (from Manighetti et al. 2005). The generic shape of the earthquake slip profiles is well represented by the average curve in yellow calculated for each dataset. (b) Schematic long-term fault architecture deduced from geological observations (from Manighetti et al., 2004). The fault plane (presented here in map view, as a solid horizontal line) is surrounded with a long-term damage zone, made of multiple small fractures and faults (here sketched as narrow, elongated ellipses either side of the fault) that formed during the fault evolution. The intensity of damage, revealed here through the density of fractures, is higher in the region where the fault originally initiated, and reduced in the direction of fault lengthening and hence of fault decreasing age. The total width of the damage zone increases in the direction of long-term fault lateral propagation. We model in Figure 7b this form of triangular damage zone.

1. Model set-up

We consider a 3-D planar, vertical strike-slip fault (30 × 15 km) embedded in an elastic medium whose properties vary spatially both across and along the fault (See below). The model is implemented in the finite difference code FLAC^{3D} (Itasca Consulting Group, 2006), which solves for elasto-dynamic wave propagation coupled to frictional sliding along the fault (Cappa and Rutqvist, 2012). The code solves the equations of motion in a 3-D elastic medium

$$\rho \ddot{u}_i = \sigma_{ij,j} + f_i \quad (1)$$

$$\sigma_{ij} = \lambda u_{k,k} \delta_{i,j} + G\left(u_{i,j} + u_{j,i}\right) \quad (2)$$

where u is the displacement, σ is the stress tensor, f is the body force, ρ is the density of the medium, λ and G are Lame's constants, and δ is the Kronecker Delta. Einstein notation and summation over repeated indices are assumed. The double dot above u implies second-order differentiation with respect to time. The fault is modeled as an internal boundary using zero-thickness joint elements where the displacement can be discontinuous. Along the fault, a friction law governs the traction, which changes with respect to the initial stress. The evolution of friction with slip along the fault is described with a linear slip-weakening formulation (Ida, 1972; Palmer and Rice, 1973); the friction coefficient (μ) depends on the amount of slip (D) and decays linearly from a peak static value (μ_s) down to a residual dynamic value (μ_d) over a critical slip distance (δ_o):

$$\mu = \begin{cases} \mu_s - (\mu_s - \mu_d)\frac{D}{\delta_o} & D < \delta_o \\ \mu_d & D > \delta_o \end{cases} \quad (3)$$

In the model, the shear strength of the fault is described as a function of the friction coefficient and the normal stress (σ_n):

$$\tau = \mu \sigma_n \quad (4)$$

The model domain has a lateral extension of 70 km and a depth of 15 km, the mean thickness of the seismogenic crust (Fig.241). This computational domain is limited laterally and at its base by absorbing conditions to avoid spurious wave reflections from boundaries. The 30 km long rupture plane where the coseismic slip occurs is represented by a zero-thickness interface (Fig.241a-c). We surround this slip plane with a damage zone having different geometries and elastic properties (See below), extending over the entire depth of the model (depth extent of natural damage zones is poorly known, but might be large, extending across much of the brittle seismogenic crust, (e.g., Fialko et al., 2002; Li et al., 2007; Barbot et al., 2009; Cochran et al., 2009; Hearn and Fialko, 2009; Griffith et al., 2012; Smith et al., 2013), and stopping at the fault tips. We refer to the "damage width" in the direction perpendicular to the fault. The damage zone is embedded in a homogeneous elastic medium, referred to as the host rock (Young's modulus E_0 of 80 GPa, Poisson's ratio of 0.25, and density of 2670 kg/m^3). The damage zone is laterally discretized into three zones in order to accommodate variations in width and elastic properties along the fault strike. We simulate the degree of damage by

different values of the Young's modulus in the damage zone (E_d), E_d decreasing as damage increases. We vary E_d in the range 10-70 GPa. The degree of rigidity contrast between the damage zone and the host rock is $\delta E/E_o = (E_0-E_d)/E_0$. Consequently, $\delta E/E_o$ ranges from ~ 12 to 90 %. This range is large enough to include realistic values; available prior works indeed estimate a rigidity reduction in damaged zones of 40-75 % relative to the ambient crust (e.g., Fialko et al., 2002; Katz et al., 2003; Gudmundsson, 2004; Hamiel and Fialko, 2007; Healy, 2008; Cochran et al., 2009; Barbot et al., 2009; Gudmundsson et al., 2011; Griffith et al., 2012). The variation in the Young's modulus encapsulates all the complex processes that might contribute to the rock damage (i.e., plastic strain, crack activation and formation, macroscopic fault slip, poroelastic effects, etc; See Lyakhovsky et al., 1997; Dalguer et al., 2003; Manighetti et al., 2004; Andrews, 2005; Ando and Yamashita, 2007; Templeton and Rice, 2008; Ma and Andrews, 2010; Xu and Ben-Zion, 2013), as well as those that might contribute to its variation over short times (such as post-seismic healing e.g., Brantley et al., 1990; Moore et al., 1994; Vidale and Li, 2003; Schaff and Beroza, 2004; Brenguier et al., 2008; Mitchell and Faulkner, 2009). In other words, the Young's modulus in the modeled damage zone represents the finite, cumulative state of the damage well within the interseismic phase of the earthquake cycle that precedes the slip event that we consider.

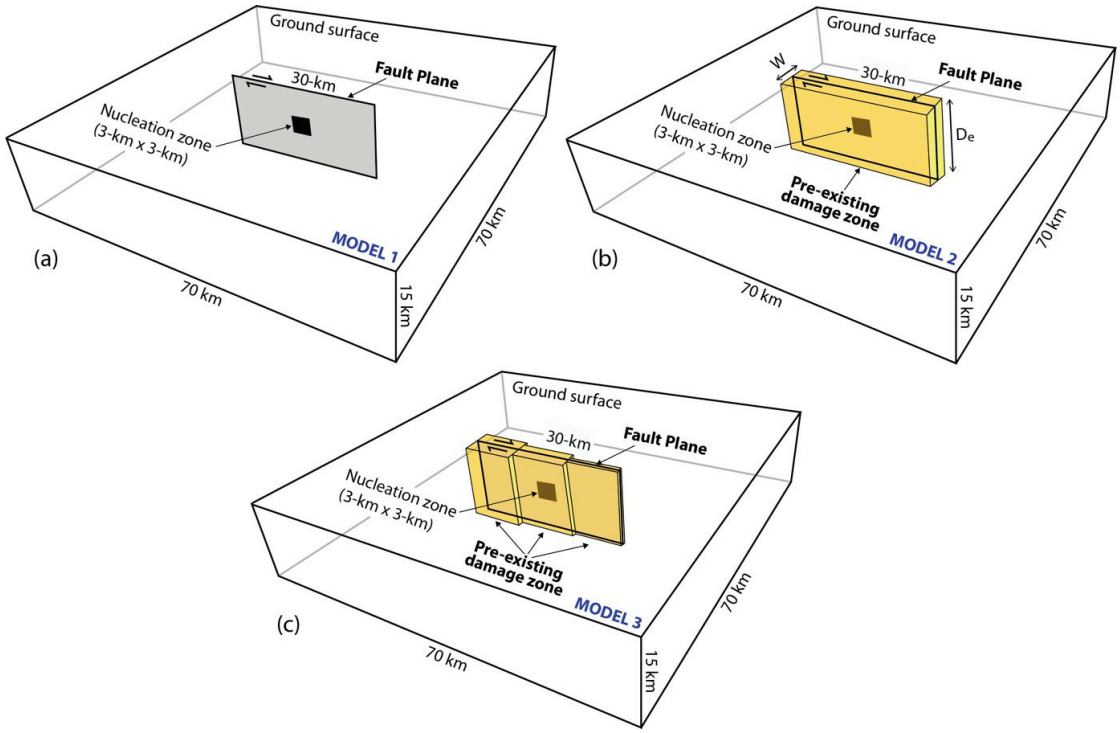


Fig.241 : Model geometry: (a) fault plane (30 × 15 km) represented as a zero-thickness slip surface in a homogeneous elastic medium (elastic crack, Model 1); (b) same fault plane surrounded by a rectangular damage zone of constant width (W) along the entire depth (De) (Model 2); (c) same fault plane surrounded by a triangular damage zone fairly similar to that in Figure 240 (b) (3 zones of 10 km length each and of variable lateral widths along the entire depth) (Model 3). In all models, the damage zone extends over the entire depth and stops at the fault tips.

The mesh size on the fault plane and in the damage zone is 50 m, while it increases gradually to 250 m towards the model boundaries. We submit the model to a homogeneous initial stress field with normal stress of 120 MPa and shear stress of 70 MPa (e.g., Noda and Lapusta, 2010; Pelties et al., 2012). The stresses are applied inside the model and at the boundaries, although the top boundary is free to move (we have also tested constant displacement boundary conditions, and the results are unchanged). Note that we are not suggesting that uniform distribution of initial stress is characteristic of active faults. However, since natural earthquake slip profiles are generic regardless of their different stress contexts, we adopt this simplifying assumption.

The rupture nucleation is initiated by a shear stress value (81.6 MPa) higher than the fault strength in a 3 km long square patch centered both along-strike and along-dip at a depth of 7.5 km, a common centroid depth for crustal earthquakes (Scholz, 2002). The fault is governed by linear slip-weakening friction (static friction, μ_s of 0.677, dynamic friction, μ_d of 0.525, and slip weakening distance δ_o of 0.4 m; commonly used parameters; e.g., Harris et al., 2009). We compute the spontaneous rupture for a total duration of 20 s. The rupture behaves as an expanding crack-like slip zone, having a constant stress drop everywhere on the fault plane.

In such a theoretical framework, the elastic properties and geometry of the damage zone are expected to exert a strong control on the on-fault slip. Assuming linear elasticity, the fault strike-slip displacement (D) is (Fialko et al., 2002; Duan et al., 2011)

$$D = w\Delta\tau\left(\frac{1}{G_d} - \frac{1}{G_o}\right) \tag{5}$$

where w is the fault zone width, $\Delta\tau$ is the shear stress change, G_d is the shear modulus of the damage zone, and G_o is the shear modulus of the ambient intact rock

$$G_d = \frac{E_d}{2(1+\nu_d)} \tag{6}$$

$$G_o = \frac{E_o}{2(1+\nu_o)} \tag{7}$$

where E_d and ν_d are the Young's modulus and Poisson ratio of the damage zone, and E_o and ν_o are those of the ambient intact rock. Assuming that variations in the Poisson ratio are small

compared with variations in the Young's modulus ($\nu \sim \nu_o \approx \nu_d$), combining Eq. 5 with Eq. 6 and Eq. 7 gives

$$D = 2(1+\nu)w\Delta\tau\left(\frac{E_o - E_d}{E_o E_d}\right) \quad (8)$$

From equations (3) and (4), the model assumes a constant shear stress change everywhere on the rupture plane. In such a context of constant $\Delta\tau$, equation (8) predicts that a fault embedded in a homogeneous (i.e., no damage) has an elliptical slip distribution, as shown in Figure 3. By contrast, the existence of a damage zone with low rigidity and/or large width around the rupture is predicted to yield an increase of the on-fault coseismic slip (Barbot et al., 2008).

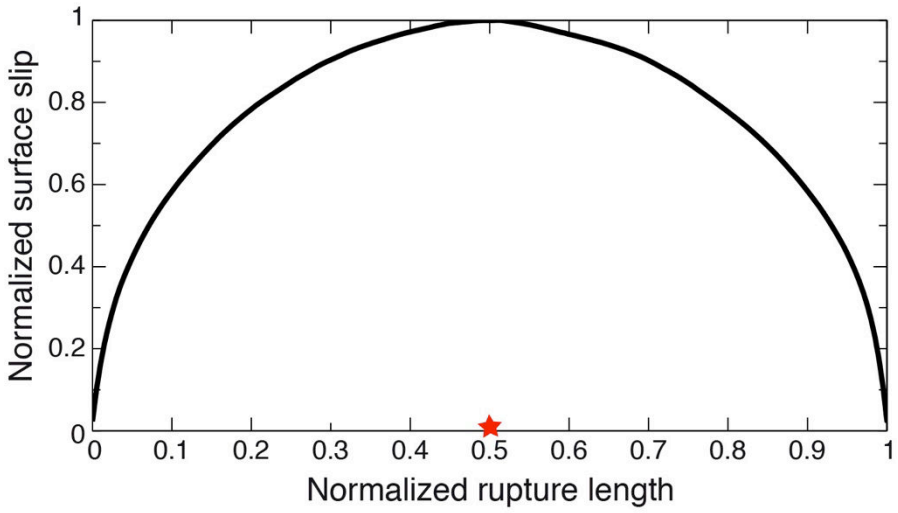


Fig.242 : Calculated earthquake slip profile at the surface as a function of the rupture length (normalized) for the elastic crack model (Model 1, Figure 241a). The red star at the center of the horizontal axis is the position of the epicenter.

We performed 82 simulations dedicated to explore those scaling relations, especially to examine the effects of the degree of damage and of the size of the damage zone on the resulting earthquake slip. Results are presented in two ways. We first show plots of the final on-fault coseismic slip (D, measured along the top boundary) normalized to the maximum slip of an elastic crack in homogeneous medium (D_0) (i.e., no damage, Fig.242), as a function of the normalized rupture length (Fig.243, 245 and 246). This dimensionless representation allows to examine the slip profile envelope shapes, and to estimate the variation in on-fault slip compared to the reference crack model. Second, all the results are synthesized in diagrams where the rigidity contrast between the damage zone and the host rock ($\delta E/E_o$), the relative size of the damage zone (width to length ratio, W/L), and the produced maximum on-fault slip (normalized to the elastic crack solution, D/D_o) are plotted together (Fig.244 and

247). This representation allows us to examine and compare for a broad range of conditions the effects of the damage zone properties on the produced on-fault slip.

2. Model results

Rectangular shape preexisting damage zone with homogeneous elastic properties

We prescribe a preexisting damage zone with a rectangular shape around the slip plane and with homogeneous elastic properties (Fig.241b). This case is that prescribed in most available theoretical models, which consider that predamage is uniform along the fault (Andrews, 2005; Ma, 2008; Templeton and Rice, 2008; Dunham and Rice, 2008; Ma and Andrews, 2010; Kaneko and Fialko, 2011; Huang and Ampuero, 2011; Xu et al., 2012b; Gabriel et al., 2013). We impose the damage zone to have different widths (W) ranging from ~ 3 to 50 % of the fault length. It is important to note that, although it has long been supposed that damage was confined only within a very narrow zone around the faults (Li et al., 1998; Ben-Zion et al., 2003; Fialko, 2004; Fielding et al., 2009; Mitchell and Faulkner, 2009), an increasing number of observations suggests that it might rather extend over large areas up to several kilometers (*Spudich and Olsen,* 2001; *Manighetti et al.,* 2004; *Oskin et al*., 2007; *Cochran et al*., 2009; *Barbot et al.*, 2009; *Shelef and Oskin*, 2010; *Griffith et al.*, 2012; *Smith et al.*, 2013). Several studies have suggested that the damage zone width might scale linearly with the fault length and/or displacement (Scholz et al., 1993; Knott et al., 1996; Vermilye and Scholz, 1998; Beach et al., 1999; Manighetti et al., 2004; Savage and Brodsky, 2011), but the actual ratios between damage zone width and fault length are still poorly known. The broad range of W/L ratios that we consider is thus made to insure that we capture realistic values. In each model, we prescribe a constant Young's modulus for the entire damage zone.

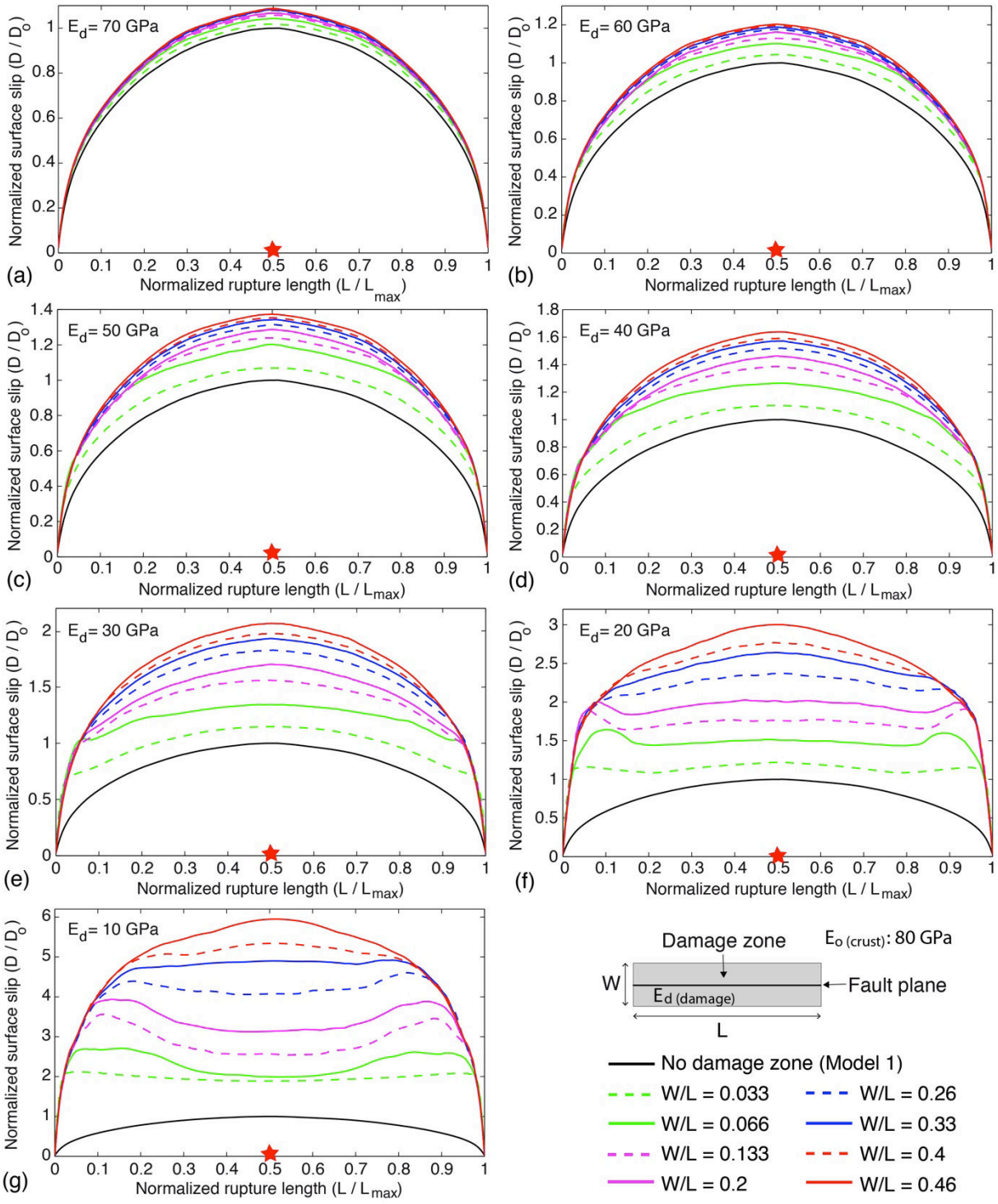


Fig.243 : Calculated earthquake slip profiles at the surface as a function of the rupture length (normalized) for a fault surrounded by a rectangular damage zone (Model 2, Figure 241b) (inset, W: damage zone width, L: fault length). In each plot, the slip profiles (D) are normalized to the maximum slip (Do) on the reference elastic crack (Fig. 242). Results are presented for constant Young's modulus Ed in the damage zone, of (a) 70 GPa, (b) 60 GPa, (c) 50 GPa, (d) 40 GPa, (e) 30 GPa, (f) 20 GPa, and (g) 10 GPa. In each plot, the colors indicate the ratio of the width of the damage zone to fault length, as listed at the bottom of the graphs. The red star at the center of the horizontal axis is the position of the epicenter. The solution for the elastic crack model with no damage (Model 1, Figure 241a) is shown in black.

Figures 243a–243g show the modeled slip profiles obtained for variable width rectangular damage zones (width varied by 2 km steps) which have a Young's modulus of 70, 60, 50, 40, 30, 20 and 10 GPa, respectively; that is, a contrast in the Young's modulus between the damage zone and the host rock ($\delta E/E_o$) of ~ 12, 25, 37, 50, 62, 75, and 87 %. In none of the tests a triangular slip profile is produced. Instead, the rupture slip profiles have an elliptical or roughly rectangular envelope shape. All the profiles are symmetric around the middle of the fault. The cases with stiffer damage actually resemble the elastic crack behavior. The amount of fault slip increases as the Young's modulus in the damage zone decreases. Meanwhile, the slip to length ratio of the profiles increases as the damage zone becomes wider (Table 7). In the cases of a narrow, very compliant damage zone (E_d = 10 and 20 GPa), more stresses accumulate near the fault tips where they induce larger on-fault slip.

Figure 244 shows the combined effect of the elastic properties and of the relative width of the rectangular damage zone on the on-fault slip. The most compliant and the widest is the damage zone, the greatest is the maximum coseismic slip on the rupture. In narrow damage zones ($W/L \leq \sim 20$ %), E_d must be lower than ~ 20 GPa for the on-fault slip to markedly increase; in large damage zones ($W/L \geq \sim 30$ %), E_d values of ~ 30 GPa are enough to significantly increase the on-fault slip.

Rectangular-shape preexisting damage zone with laterally varying elastic properties

Figure 245 presents the same simulations as before, yet with the rectangular damage zone having its Young's modulus increasing from right to left; that is, the intensity of damage decreases from right to left, while the damage zone width keeps constant along the fault. We have tested a case with a "rigid" damage zone (E_d = 70, 50, 40 GPa, Fig.245a) and another case with a more compliant damage zone (E_d = 40, 20, 10 GPa, Fig.245b). In the rigid damage zone (Fig.245a), the triangular slip profile is not produced. Instead, the rupture slip has a distorted elliptical shape whose asymmetry results from the maximum slip translating towards the less rigid part of the damage zone. In the compliant damage zone (Fig.245b), a triangular slip profile is produced, regardless of the damage zone width. The profiles are asymmetric with the maximum slip translated towards the right tip of the fault, around which damage is greatest, whereas slip linearly decreases towards the left fault tip, in the direction of damage

decrease. Therefore, a high slip gradient develops near the limit between the softer damage zone and the host rock, whereas the gradient in slip decreases as the difference in modulus between damaged and host rocks decreases. The slip to length ratio of the profiles increases as the damage zone becomes wider (Table 7). Because of the skewed shape of the profiles, the maximum slip lies away from the hypocenter.

The combined effects of the elastic properties and of the relative width of the rectangular damage zone on the on-fault slip are discussed in section 3.4.

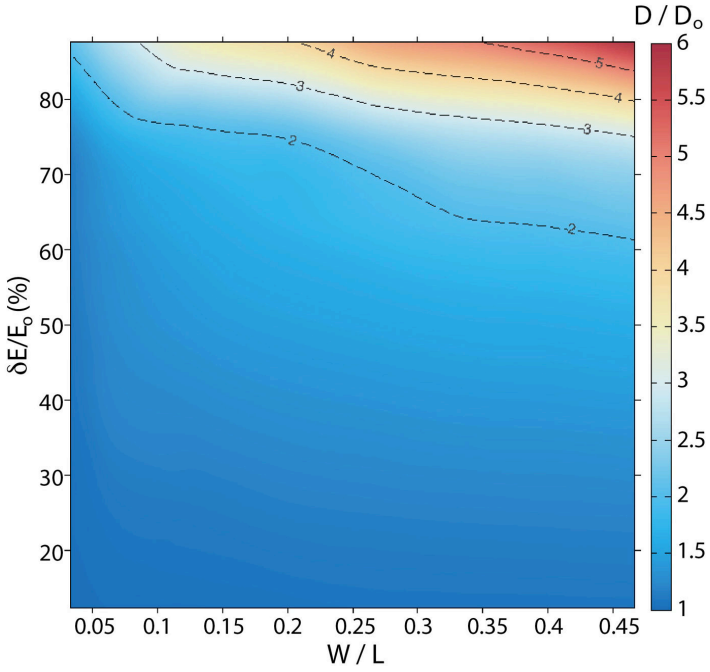


Fig.244: Diagram illustrating the combined effects of the contrast of Young's modulus between the damage zone (Ed) and the host rock (E0) (δE/Eo = (E0-Ed)/E0) and of the ratio of the damage zone width to fault length (W/L), on the maximum on-fault slip (D, normalized to the maximum slip (Do) on the reference elastic crack) for the rectangular damage zone cases, presented in Fig.243 (i.e., with both constant Young's modulus Ed and constant damage zone width).

Triangular-shape pre-existing damage zone with homogeneous elastic properties

Field observations of long-term faults and related damage (Shipton and Cowie, 2001, 2003; Kim et al., 2004; Manighetti et al., 2004; Dor et al., 2006; Faulkner et al., 2011) (Fig. 240b), as well as dynamic simulations of coseismic damage (e.g., Andrews, 2005; Templeton et al., 2008; Viesca et al., 2008; Dunham et al., 2011a-b; Xu et al., 2012a-b; Xu and Ben-Zion, 2013), suggest that damage zones around faults and ruptures commonly have an overall triangular shape in map-view, with an apex centered in the zone of fault or rupture initiation, and a damage zone widening in the direction of fault or earthquake propagation (Fig. 240b). Here we test the effect of an overall triangular-shaped preexisting damage zone of the form sketched in Fig. 240b (Fig. 241c). Figure 246a shows the simulations with a damage zone widening from right to left along the fault, having constant elastic properties. None of the

simulations produce the generic triangular shape of the earthquake slip profiles. Instead, the profiles have a quasi-elliptical shape when the difference in modulus between the damage zone and the host rock is low, and a fairly rectangular shape when the damage zone is soft (i.e., large contrast in Young's modulus). In that later case, a slight asymmetry develops in the slip distribution, as maximum slip translates towards the largest section of the compliant damage zone. Finally, the slip to length ratio of the profiles increases as the damage level increases (Table 7).

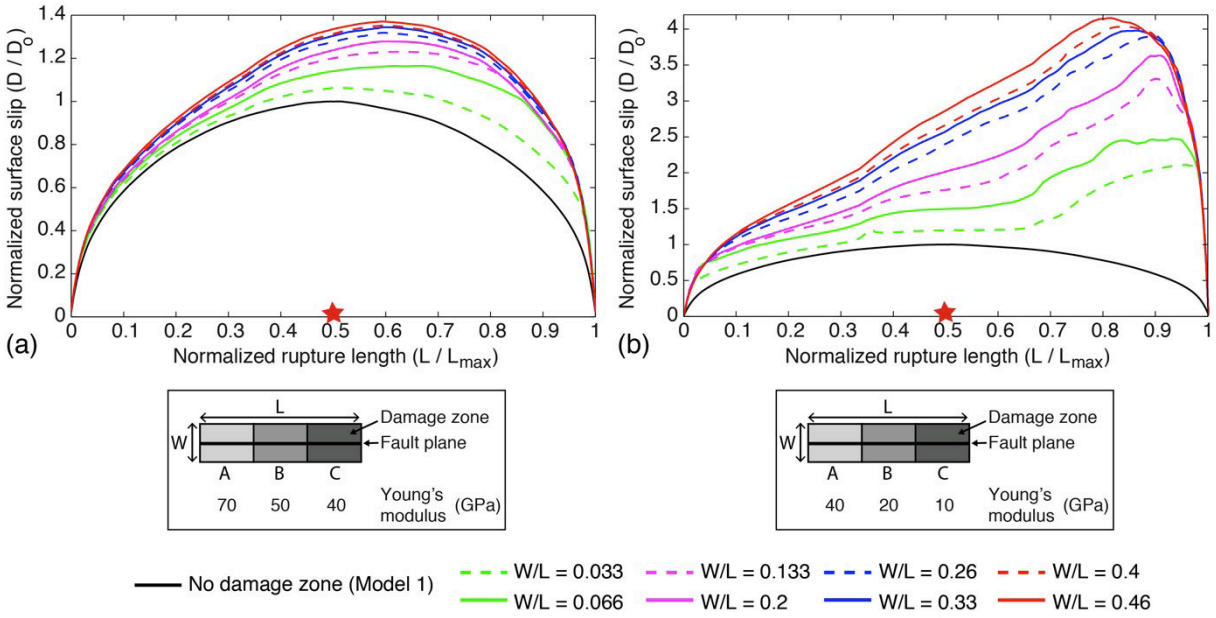


Fig.245 : Calculated earthquake slip profiles at the surface as a function of the rupture length (normalized) for a fault surrounded by a rectangular damage zone (Model 2, Fig.241b) (inset, W: damage zone width, L: fault length). In each plot, the slip profiles (D) are normalized to the maximum slip (D_o) on the reference elastic crack (Fig.242). Results are presented for Young's modulus E_d decreasing from the left tip to the right tip along 3 zones (A, B, C, respectively), 10 km long each. (a) Case with a stiff damage zone. Young's modulus E_d is 70 GPa in zone A, 50 in zone B and 40 GPa in zone C. (b) Case with a compliant damage zone. Young's modulus E_d is 40 GPa in zone A, 20 in zone B and 10 GPa in zone C. In each plot, the colors indicate the ratio of the width of the damage zone to fault length, as listed at the bottom of the graphs. The red star at the center of the horizontal axis is the position of the epicenter. For reference and comparison between results, the elastic crack model with no damage (Model 1, Fig.241a) is shown in black.

Triangular-shape preexisting damage zone with laterally varying elastic properties

Figure 246b presents the same simulations as before, yet now with the damage zone having a Young's modulus increasing from right to left (from 10 to 40 GPa); that is, the intensity of damage decreases from right to left, as the damage zone width increases along the fault. Three different width increases are tested, from 1 to 3 km (W/L up to 10 %, in green), from 2 to 6 km (W/L up to 20 %, in blue), and from 4 to 12 km (W/L up to 40 %, in magenta). All calculations produce a triangular, asymmetric earthquake slip profile, with maximum slip

translated toward the right tip of the fault, far away from the rupture hypocenter. The slip then decreases roughly linearly from its maximum value to almost zero at the other (left) tip of the fault. The slip to length ratio of the profiles increases as the damage zone becomes wider, yet in a moderate fashion since all three calculated ratios basically remain in the similar range ~4-6.5 × 10^{-4} (Table 7).

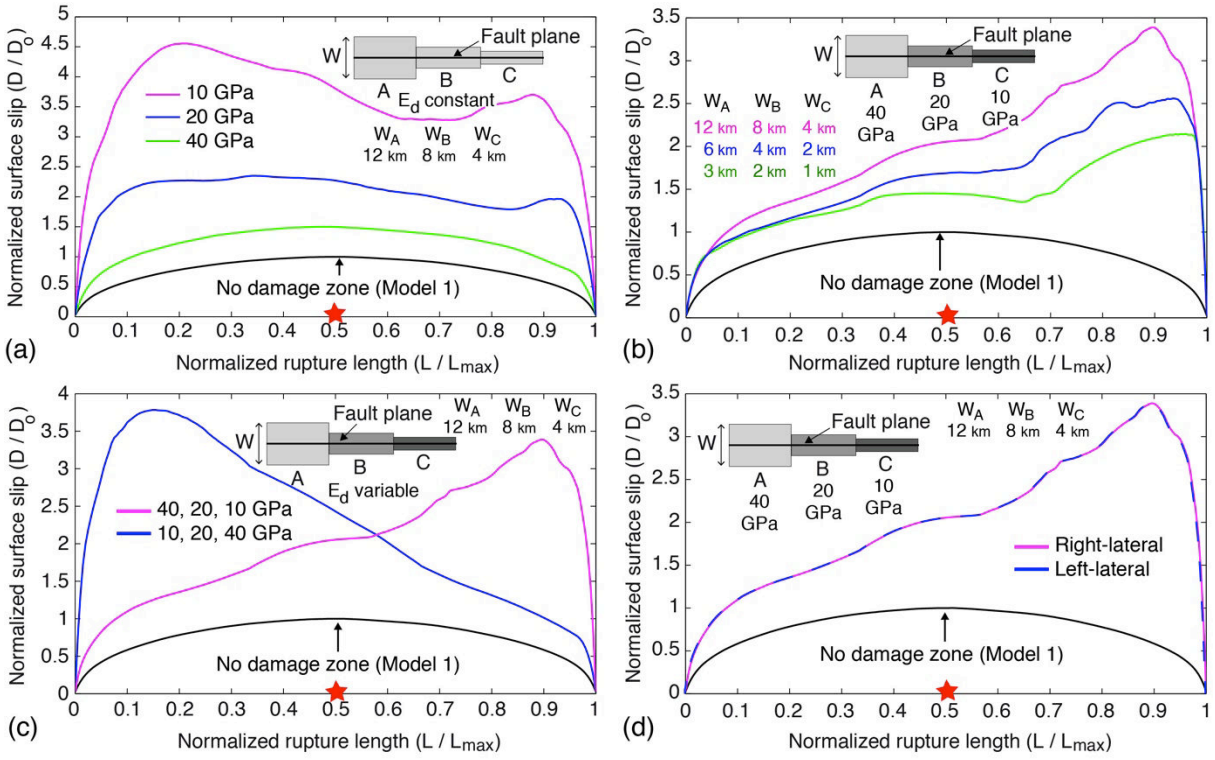


Fig. 246 : Calculated earthquake slip profiles at the surface as a function of the rupture length (normalized) for (a) a fault zone with a damage zone of variable width (regions A, B, C of similar length from left fault tip to right fault tip, and of width W_A = 12 km, W_B = 8 km, W_C = 4 km) and constant Young's modulus E_d (magenta curve: 10 GPa, blue curve: 20 GPa, green curve: 40 GPa) (Model 3, Fig.241c); (b) a fault with a damage zone of variable width (from 1 to 3 km in green, from 2 to 6 km in blue, and from 4 to 12 km in magenta) and variable Young modulus E_d (region A in light gray: 40 GPa, region B in gray: 20 GPa, and region C in dark gray: 10 GPa); (c) a Young's modulus E_d in the damage zone decreasing (blue) and increasing (magenta) in the direction of increasing damage zone width; and, (d) modeled slip profiles on right-lateral (magenta) and left-lateral (blue) ruptures. The damage zone width ranges from 4 to 12 km for results presented in (c-d). In each plot, the slip profiles (D) are normalized to the maximum slip (D_o) on the reference elastic crack (Fig.242). The red star at the center of the horizontal axis is the position of the epicenter. For reference and comparison between results, the elastic crack model with no damage (Model 1, Fig.241a) is shown in black.

Figure 246c presents the same calculations as before, yet for a damage zone whose Young's modulus now decreases from right to left (from 40 to 10 GPa) as the damage zone becomes wider. We thus prescribe here a preexisting damage that both enlarges and intensifies from right to left along the fault. The calculation is performed for a damage zone width varying from 4 to 12 km from right to left, and is compared to the result obtained previously with the same damage zone geometry and opposite Young's modulus variation (magenta profile in Fig. 246b and Fig. 246c). The resulting slip profile

is triangular and asymmetric, yet tapering in the opposite direction to that of the previous simulation (Fig. 246b). The maximum slip is thus translated towards the left tip of the fault, still away from the hypocenter. The slip to length ratio of the resulting slip profile is of the same order to the one obtained in the opposite configuration (magenta profile), yet slightly larger.

Figure 247 shows the combined effect of the elastic properties and of the relative width of the damage zone on the maximum on-fault slip, in the cases where one or both of the elastic properties and the width of the damage zone vary along fault strike. Those cases thus include the rectangular (Fig.245) and the triangular damage zones (Fig.246a-b). To account for the along-strike variation in W_d and E_d, we represent the average damage width and elastic modulus. The presence of the damage zone significantly increases the maximum on-fault coseismic slip (compared to the reference crack model) whenever the damage is compliant overall, with an average Young's modulus lower than ~ 40 GPa. There is a tradeoff, however, between the average width and the compliance of the damage zone; while narrow damage zones must be compliant to yield a significant increase in coseismic slip, wider damage zones can be stiffer (average E_d ~ 40 GPa) and still produce significant on-fault slip increase. A damage zone with an average Young's modulus between ~ 20 and 40 GPa results in the earthquake rupture accumulating increased slip, that accrues as the damage zone widens overall. When the damage zone is very compliant, with average E_d between ~ 15 and 20 GPa, the on-fault slip markedly increases, although at a slower rate than in cases of stiffer damage zones. This probably results from a significant part of the slip being accommodated within the compliant damage zone. Figure 247 suggests that an increase in on-fault slip might dramatically occur in the cases of extremely compliant damage zones (average E_d < 10-15 GPa), but those cases are probably unrealistic (i.e., the rock would be completely destroyed).

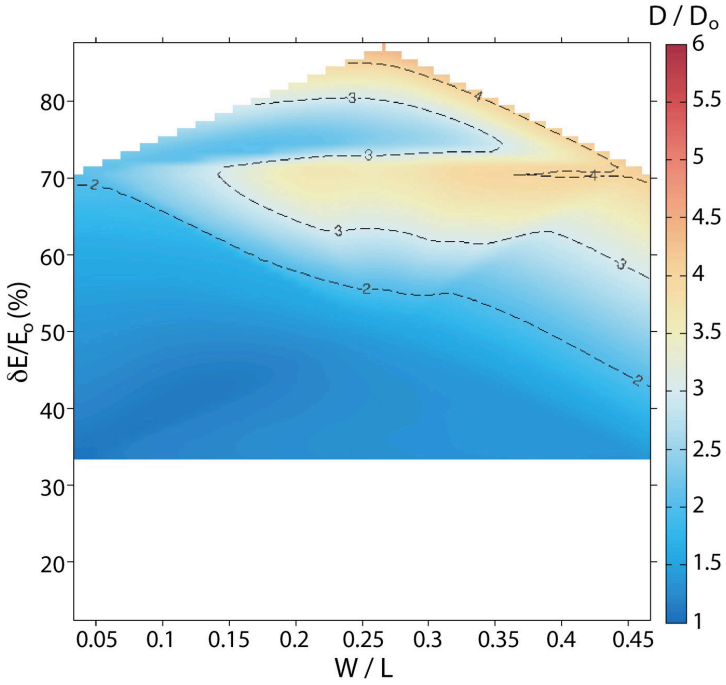


Fig. 247 : Diagram illustrating the combined effects of the contrast of Young's modulus between the damage zone (E_d) and the host rock (E_0) ($\delta E/E_o = (E_0-E_d)/E_0$) and of the ratio of the damage zone width to fault length (W/L), on the maximum on-fault slip (D, normalized to the maximum slip (D_o) on the reference elastic crack) for the heterogeneous cases i.e., with variable Young's modulus E_d and constant or variable damage zone width (rectangular and triangular damage zone cases, presented in Fig.245 and 246a-b-c). To account for the along-strike variation in W_d and E_d, we represent the average damage width and elastic modulus. See discussion in text.

Influence of the sense of lateral slip

Figure 246d shows the same calculation as in Figure 246b (right to left width increase from 4 to 12 km, magenta curve), but with a rupture that is now imposed to be left-lateral. The governing equations of the model predict invariance of slip magnitude with respect to direction of slip propagation. We verify that the model indeed produces this invariance. The resulting slip profile is exactly the same, showing that, in the chosen damage configuration (i.e., triangular-shaped, enlarging from right to left and decreasing in intensity from right to left) and under the present model assumptions, the sense of fault slip has no influence on the final shape of the coseismic slip profile.

3. Discussion

In the absence of any preexisting damage in the medium surrounding a fault, the rupture of that fault produces an elliptical slip profile, far different from the slip distributions observed on natural earthquakes. Models simulating faults and earthquakes in homogeneous, linear, elastic medium are thus inappropriate to reproduce the natural earthquakes.

Our models suggest that the map-view geometry of preexisting damage is not a major controlling factor for earthquake slip distributions; whatever the geometry of long-term damage (in the range tested here, from rectangular to triangular), the formed coseismic slip profiles are far different from being triangular if the damage elastic properties are uniform within the damage zone. Therefore, theoretical models that embed a fault within a predamaged medium with uniform properties are expected to be inappropriate in reproducing slip profiles for natural earthquakes. This finding also suggests that the width of the long-term damage zones might be variable, and not necessarily scaling with the fault length.

The factor most controlling the earthquake slip distributions seems to be the along-fault variability in the elastic properties of the pre-existing damage. Note that a similar finding has been suggested for long-term, cumulative slip profiles (Burgmann et al., 1994; Manighetti et al., 2004). We discuss further below the possible nature of long-term damage and the reasons for its lateral variability. Whatever these reasons, we find that a progressive change in the elastic properties of the preexisting damage is a sufficient condition to account for the development of a generic, triangular and asymmetric coseismic slip profile on the ruptured fault. The average elastic properties of the damage zone must be fairly compliant however (See Fig. 245a where an average E_d value of ~55 GPa does not produce a triangular profile). In those conditions, the generic slip profile forms regardless of the width (from very small [i.e., W/L ~ 3 %] to very large [W/L ~50 %]) and of the geometry (rectangular or triangular) of the pre-existing damage zone. Although other factors might contribute to shape the coseismic slip profiles, such as heterogeneous loading of the fault, lithological properties of the surrounding rocks, variable friction on the fault, local stress interactions, non-planar fault geometry, etc (e.g., Burgmann et al., 1994; Cooke, 1997; Manighetti et al., 2001; Martel and Shacat, 2006), the generic, scale and context-independent envelope shape of the natural earthquake slip distributions shows that the role of those possible additional factors is not dominant.

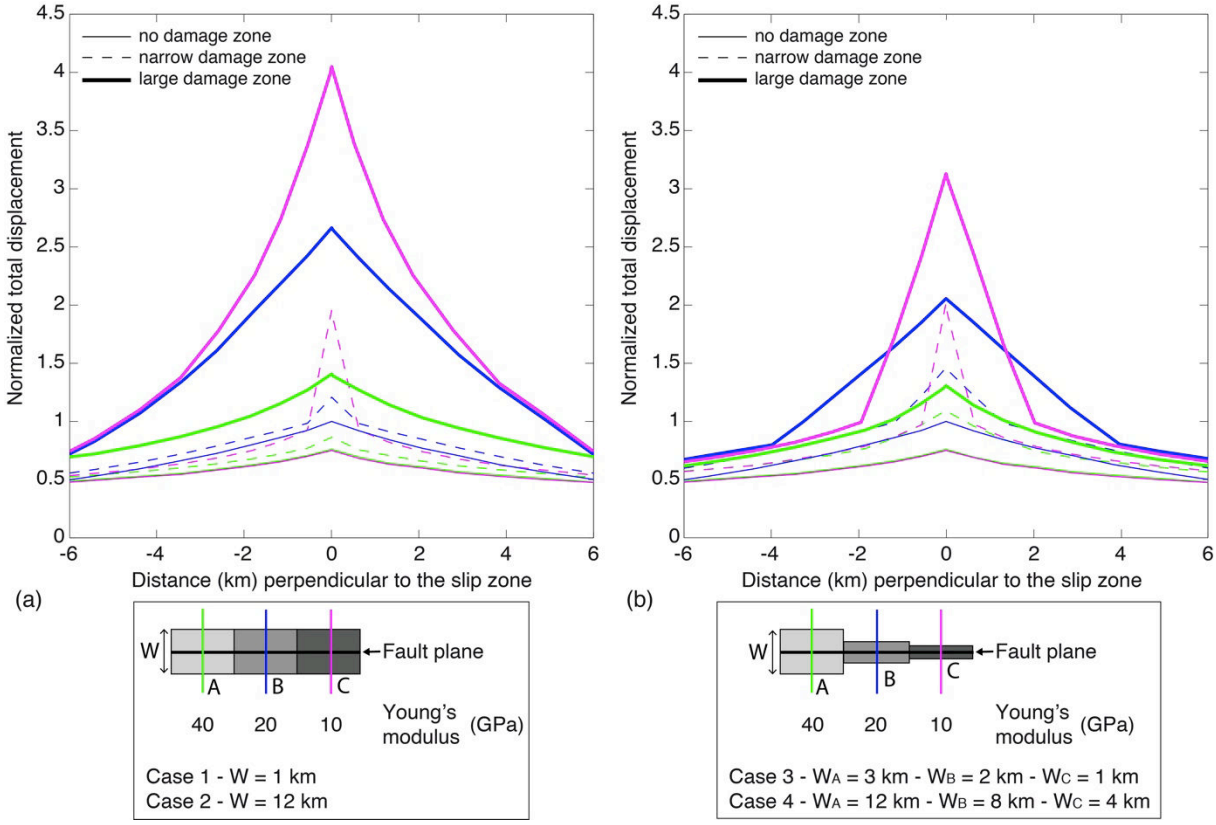


Fig. 248 : Total displacement (normalized to the maximum slip (D_0) on the reference elastic crack) measured perpendicular to the fault (located at the position "0" on the horizontal axis) along three transects in the models with (a) a rectangular (Model 2, Fig.241b) and (b) a triangular (Model 3, Fig.241c) damage zone (inset: magenta line crosses the more compliant region of the damage zone (10 GPa), blue line the intermediate region (20 GPa), and green line the stiffer damage region (40 GPa)). Solid lines correspond to the models with the largest damage zone, named cases 2 and 4: (a) W = 12 km, (b) W_A = 12 km, W_B = 8 km, W_C = 4 km, and dashed lines correspond to the models with the narrowest damage zones, named cases 1 and 3: (a) W = 1 km, (b) W_A = 3 km, W_B = 2 km, W_C = 1 km. The elastic crack solution with no damage is shown by the thin solid line. Maximum slip on the elastic crack is < 1 because the transects are at some distance from D_0. Off-slip values measured at the center of the damage zone (i.e., at mid-distance between the fault and the damage outer edge) are reported in Table 8

The existence of a preexisting heterogeneous damage zone markedly affects the slip on the ruptured fault; whatever the damage geometry, the coseismic slip is larger on the fault section surrounded by the most intense damage, whereas the coseismic slip is decreased on the fault sections surrounded by stiffer damage (Fig.245b, 246b, 247). There is a tradeoff however between the average width and the compliance of the damage zone; the stiffer the damage zone, the wider it must be to increase the on-fault coseismic slip. On the contrary, a narrow damage zone (i.e., W/L < ~ 10 %) can yield a marked increase in the on-fault coseismic slip provided that it is compliant (average E_d < 20-30 GPa). Additionally, for a similar average Young's modulus E_d in the range 20-30 GPa, a damage zone with laterally varying elastic properties can produce a larger coseismic on-fault slip (Fig.247) compared to a damage zone with constant elastic properties (Fig.247).

In addition to on-fault slip, a significant part of the coseismic slip is accommodated within the pre-existing damage zone. We estimate the off-fault slip amount in the center of the damage zone at three different sites along the fault, and for four different damage geometries (noted cases 1-4 in Fig. 248 and Table 8). In each case, the off-fault slip is in the range 23-76% of the maximum on-fault slip, implying an independence from the damage zone geometry. The amount of off-fault slip relative to the maximum on-fault slip decreases as damage becomes stiffer, in all cases by ~40-60% with respect to values in the most compliant parts of the damage zone. However, as on-fault slip decreases in the direction of damage stiffening, the proportion of off-fault to on-fault slip (on same transect) slightly increases in all cases but case 4 (from ~75 to ~90% in the narrowest damage zones (cases 1 and 3), and from ~40 to ~65% in the widest case 2 damage zone); that is, a greater proportion of the local on-fault slip is diffused in the stiffer parts of the damage zone. Within the narrowest damage zones (cases 1 and 3), 60-75% of the maximum on-fault slip is accommodated in the areas where damage is high to moderate, while this amount decreases down to ~40% in the areas of stiffer damage. Within the widest damage zones (cases 2 and 4), 40-60% of the maximum on-fault slip is accommodated in areas of high to moderate damage, while this amount decreases down to ~25% in the areas where damage is stiffer. Therefore, these results show that a large amount of slip and hence strain is dissipated within the long-term damage zone, of at least ~25-40% (relative to maximum on-fault slip) and on average ~50%. We further discuss those off-fault slip amounts below.

In the case where coseismic slip profiles are strongly dependent on the along-fault properties of preexisting damage, the generic triangular shape of slip profiles is produced regardless of the sense of slip of the rupture; if the fault is right-lateral or left-lateral, the coseismic slip is always largest on the fault section which is surrounded by the greatest pre-existing damage, and decreases where the fault is surrounded by stiffer preexisting damage.

These findings suggest that the zone of largest coseismic slip does not necessarily correlate with the location of the earthquake hypocenter, in keeping with observations of natural earthquakes (Manighetti et al., 2005). Furthermore, the direction of coseismic slip tapering does not necessarily indicate the direction of rupture propagation, as observed in several natural earthquakes (such as Landers 1992, Chi-Chi 1999, Denali 2002).
Finally, the slip-to-length ratios of the modeled slip profiles are in the range of natural earthquake slip-to-length ratios, albeit slightly larger (Table 7) (Manighetti et al., 2007). This

suggests our modeling approach is too simple to reproduce all the features of natural earthquakes.

We thus show that the predamaged state of the medium that surrounds the earthquake faults must be taken into account to reproduce the observed generic envelope shape of the coseismic slip profiles. As said earlier, this does not preclude other factors might further influence the shape of the earthquake slip functions, as suggested in both theoretical dynamic models (i.e., preearthquake stress on the fault, ambient stress, variability in fault static and dynamic friction, (e.g., Rice et al., 2005; Wolf et al., 2006; Xu and Ben-Zion, 2013; Noda et al., 2013) and fault mechanics analyses (e.g., Burgmann et al., 1994; Cooke, 1997; Martel and Shacat, 2006).

We also show that the predamaged state of the medium must be heterogeneous along the fault for an earthquake slip profile to develop a triangular and asymmetric shape. The lateral variation of cumulative damage along the faults is a well-known feature. Most faults are indeed flanked (on one or both sides) by a damaged, generally highly fractured zone. Whether those damage zones are formed only by the stress concentrations around the propagating rupture fronts (Scholz et al., 1993) or also include relicts of the long-term fault growth process through segment linkage and quasi-static fault slip (Manighetti et al., 2004) remains unresolved (Dunham et al., 2011a-b; Savage and Brodsky, 2011). Furthermore, whether the damage process dominantly includes micro-crack activation and/or formation (Lyakhovsky et al., 1997; Yamashita, 2000; Dalguer et al., 2003; Manighetti et al., 2004; Suzuki, 2012), macroscopic shear faulting (Ando and Yamashita, 2007), or plasticity (Andrews, 2005; Ben-Zion and Shi, 2005; Templeton and Rice, 2008; Viesca et al., 2008; Duan and Day, 2008; Ma and Andrews, 2010; Dunham et al., 2011a-b; Xu and Ben-Zion, 2013; Gabriel et al., 2013) also remains unresolved. Whatever the nature of the cumulative damage around the faults, the across-fault width of the long-term damage zone seems to increase as the fault lengthens laterally over time (Scholz et al., 1993; Manighetti et al., 2004; Kim et al., 2004; Faulkner et al., 2011; Savage and Brodsky, 2011). The enlargement of the damage zone with rupture lengthening is also suggested in most dynamic simulations (e.g., Andrews, 2005; Templeton and Rice, 2008; Savage and Cooke, 2010; Xu and Ben-Zion, 2013). Additionally, cumulative damage is most intense around the most ancient sections of the fault, which have slipped over longer time spans, and decreases in intensity (i.e., increase in Young's modulus) in the direction of fault lengthening, that is in the direction in which the fault becomes younger (Fig. 240b). This leads to laterally varying cumulative damage along fault with commensurate lateral variations in elastic properties.

Earthquake faults are intrinsically embedded in a predamaged, heterogeneous medium, whose properties are likely to influence the dynamics of the next events. The predamaged zones will define the zones where the dynamic stresses might be more efficiently dissipated, with this dissipation in turn controlling the velocity of the rupture propagation and the amount of coseismic slip on the earthquake fault (Harris and Day, 1997; Ben-Zion and Andrews, 1998; Ampuero and Ben-Zion, 2008; Barbot et al., 2008). Damage might also introduce some asymmetry between the two fault compartments and hence contribute to the "bi-material situation" described in several theoretical models (Andrews and Ben-Zion, 1997; Ben-Zion and Huang, 2002; Shi and Ben-Zion, 2006; Bhat et al., 2007; Biegel et al., 2008; Dunham and Rice, 2008; Ampuero and Ben-Zion, 2008.

As in other prior works (e.g., Barbot et al., 2008; Dunham et al., 2011a-b), we find that the coseismic slip is increased on the fault section that is surrounded with most intense cumulative damage. That specific fault section represents the most mature part of the fault, where the fault has accumulated greater slip. Since our calculations are performed with homogeneous friction on the fault, one possible explanation for the slip increase on the most mature fault section is that the strong reduction of elastic moduli in the damage zone leads to a significant coseismic motion amplification (Spudich and Olsen, 2001; Shi and Ben-Zion, 2006). As the damage level decreases along the fault, such a positive feedback decreases, resulting in a decrease of slip on the ruptured fault. Whatever the amount of slip on the earthquake fault, and whatever the geometry of the damage zone, a significant part of the coseismic slip – at least 25-40% of the maximum on-fault slip, is diffused in the damage zone. Since the modeled coseismic slips are greatest on the fault sections surrounded with most mature damage, we would expect earthquakes on long-lived mature faults to have larger slip to length ratios than events produced on young, immature faults. The slip to length ratios of ~250 natural earthquakes worldwide show the opposite; the most mature faults produce earthquakes with the lowest slip to length ratio (Kanamori and Anderson, 1975; Shaw and Scholz, 2001; Scholz, 2002; Manighetti et al., 2007). A possible factor contributing to this apparent paradox is that modeled slip amounts are not robustly constrained and so the models are too simple to properly reproduce the entire set of earthquake properties. In particular, we impose nucleation stresses that might be too large compared to the actual stresses required for natural earthquake slip. A second element comes from the observation that most large earthquakes, especially those on mature faults, rupture several major segments along a fault (e.g., Manighetti et al., 2007). Fault segments are connected with geometrical features such as offsets, kinks, bends, that may produce local changes of stress and strength. Earthquakes

should thus be modeled as multisegments ruptures (e.g., Kagan, 2004; Manighetti et al., 2007, 2009), not as single faults as we have done here, and as most available models do. Furthermore, as a fault accumulates more slip and hence becomes more mature, it is likely that the static and dynamic frictions on the fault plane evolve and probably decrease (e.g., Cooke, 1997). The variability of fault friction with fault maturity is therefore another parameter that should be included in earthquake slip models, and that might also explain the slip to length ratio paradox. In this study, we use a fairly high static friction of $m_s \sim 0.7$, that might be more appropriate to simulate the behavior of fairly immature faults (e.g., Cooke, 1997).

Since our modeling produces earthquake slip to length values which are slightly greater than natural data (e.g., Manighetti et al., 2007), we may expect that the actual degree of off-fault slip might be lower than the values we have inferred from our models. The amount of off-fault slip must still be significant to explain the natural earthquake slip profiles. Chester et al. (2005) and Wilson et al. (2005) found that a large part of the earthquake energy budget (possibly up to 50%) must be diffused within the damage zone to account for the fracture surface area in this zone.

Finally, our models suggest that off-fault coseismic slip and strain can occur at large distances away from the fault, up to a distance of several tens of percent of the fault length in the tested models; for the 30 km long fault modeled here, the average width of the damage zone might thus be up to several kilometers. The narrowest damage zones in our study have a W/L ratio of a few percent, which correspond to damage zone widths of 1-2 km, similar to those revealed in recent studies (e.g., Cochran et al., 2009). Our modeling suggests that the width of the damage zone can either vary or stay constant along the fault trace. Therefore, it is not clear that a scaling relation is to be expected between damage zone width and fault length or displacement (Savage and Brodsky, 2011).

4. Conclusions

Our modeling results provide new insights on the influence of preexisting long-term damage around active faults on the earthquake slip distribution. The preexisting damage encapsulates a long-term record of inelastic deformation associated with the earthquake cycles and the

possible quasi-static growth of the fault over geological time. It manifests as a relative compliance of the off-fault medium with respect to the ambient crust. Here we show that elastic heterogeneities associated with variations in damage intensity of the medium along the fault exert a significant control on the earthquake slip distribution. Our model, with along-fault variations in the elastic modulus of the long-term damage zone, successfully predicts the observed generic, triangular envelope shape of natural coseismic slip profiles. The model that best explains these earthquake slip profiles suggests that the fault experiences the highest slip across the most compliant section of the damage zone, while the coseismic slip decreases as the damage stiffness increases. However, whether damage is high or low, the off-fault coseismic slip is high in the damage zone, at least 25-40% of the maximum on-fault coseismic slip (in the center of the damage zone). Since our modeling produces earthquake slip to length values which are slightly greater than those for natural events (e.g., Manighetti et al., 2007), we may expect that actual off-fault slip amounts might be slightly lower than the inferred values. However, they still must be significant to explain the natural earthquake slip profiles. Finally, our models also suggest that off-fault coseismic slip and strain can occur at large distances away from the fault, up to a distance of several tens of percent of the fault length in the tested models, equivalent to several kilometers for a 30 km long fault.

Together with prior works, our results suggest that significant inelastic deformation occurs in the "near" field of faults and of earthquake ruptures. Paradoxically, the theory of elasticity lays the foundation for nearly every aspect of our understanding of earthquake source mechanics (e.g., Aki and Richards, 2002; Ma and Andrews, 2010). Our results, along with others before (Barbot et al., 2008, 2009; Cochran et al., 2009; Kaneko and Fialko, 2011), therefore motivate a reinterpretation and/or reformulation of the available earthquake source inversion models since most of them do not include inelastic deformation occurring in the volume around the earthquake ruptures (inversion models including damage have only been developed recently to model interseismic slip, see Barbot et al., 2013).

Our work confirms that triangular asymmetric coseismic slip profiles can emerge from natural fault behaviors and geometries. The generic triangular shape of the earthquake slip profiles has critical implications on the earthquake stress drop, as the later cannot be constant on the fault under common assumptions (See more detailed discussion in Noda et al., 2013). The coseismic slip tapering also suggests that significant strain and stress redistributions occur during an earthquake event, probably in a fairly large zone around the ruptured fault. This

might have important implications on how stress is transferred, and therefore on seismic hazard assessment.

Acknowledgements

This work was supported by the Observatoire de la Côte d'Azur through the "BQR OCA". We thank Thorsten Becker, Tom Mitchell, Sylvain Barbot and Michele Cooke for their constructive reviews and useful suggestions, which greatly helped us to improve our manuscript. We also thank James Hollingsworth for his careful reading of the paper and his thorough comments.

References

Aki, K., and P.G. Richards (2002), Quantitative seismology, 2nd Edition, *University Science Books*, pp. 339

Ando, R., and T. Yamashita (2007), Effects of mesoscopic-scale fault structure on dynamic earthquake ruptures: Dynamic formation of geometrical complexity of earthquake faults, *J. Geophys. Res.*, 112, B09303, doi:10.1029/2006JB004612.

Andrews, D.J., and Y. Ben-Zion (1997), Wrinkle-like slip pulse on a fault between different materials, *J. Geophys. Res.*, 102(B1), 553-571.

Andrews, D.J. (2005) Rupture dynamics with energy loss outside the slip zone, *J. Geophys. Res.*, 81, 5679-5687.

Ampuero, J.-P. and Y. Ben-Zion (2008), Cracks, pulses and macroscopic asymmetry of dynamic rupture on a bimaterial interface with velocity-weakening friction, *Geophys. J. Int.*, doi: 10.1111/j.1365-246X.2008.03736.x.

Aydin, A., and J.G. Berryman (2009), Analysis of the growth of strike-slip faults using effective medium theory, *J. Struct. Geol.*, doi: 10:1016/jsg.2009.11.007.

Barbot S., Y. Fialko, and D. Sandwell, (2008), Effect of a compliant fault zone on the inferred earthquake slip distribution, *J. Geophys. Res.*, 113, B06404, doi: 10.1029/2007JB005256

Barbot, S., Y. Fialko and D. Sandwell (2009), Three-dimensional models of elasto-static deformation in heterogeneous media, with application to the Eastern California Shear Zone, *Geophys. J. Int.*, 179, 500-520,doi:10.1111/j.1365-246X.2009.04194.x

Barbot, S., P. Agram, and M. De Michele (2013), Change of apparent segmentation of the San Andreas fault around Parkfield from space geodetic observations across multiple periods, *J. Geophys. Res.*, 118, 6311–6327, doi:10.1002/2013JB010442.

Beach, A., A.I. Welbon, P.J. Brockbank, and J.E. McCallum (1999), Reservoir damage around faults: Outcrop examples from the Suez rift, *Petrol. Geosci.,* 5(2), 109–116, doi:10.1144/petgeo.5.2.109

Ben-Zion, Y. and D.J. Andrews (1998), Properties and implications of dynamic rupture along a material interface, *Bull. Seismo. Soc. Am.*, 88(4), 1085-1094.

Ben-Zion, Y. and Y. Huang, (2002), Dynamic rupture on an interface between a compliant fault zone layer and a stiffer surrounding solid, *J. Geophys. Res.*, 107, 2042, doi:10.1029/2001JB000254.

Ben-Zion, Y., Z. Peng, D. Okaya, L. Seeber, L.G. Armbruster, N. Ozer, A.J. Michael, S. Baris, and M. Aktar (2003), A shallow fault zone structure illuminated by trapped waves in the Karadere□Duzce branch of the North Anatolian Fault, western Turkey, *Geophys. J. Int.*, 152, 699–717, doi: 10.1046/j.1365-246X.2003.01870.x.

Ben-Zion, Y., and Z. Shi, (2005), Dynamic rupture on a material interface with spontaneous generation of plastic strain in the bulk, *Earth Planet. Sci. Lett.*, 236, 486-496.

Bhat, H.S., R. Dmowska, G.C.P. King, Y. Klinger, and J.R. Rice (2007), Off-fault damage patterns due to supershear ruptures with application to the 2001 Mw 8.1 Kokoxili (Kunlun) Tibet earthquake, *J. Geophys. Res.*, *B06301*, doi:10.1029/2006JB004425.

Bhat, H., R.L. Biegel, A.J. Rosakis, and C.G. Sammis (2010), The effect of asymmetric damage on dynamic shear rupture propagation II: with mismatch in bulk elasticity, *Tectonophysics*, *493*(3), 263–271, doi:10.1016/j.tecto.2010.03.016.

Biegel, R.L., C.G. Sammis, and A.J. Rosakis (2008), An experimental study of the effect of off-fault damage on the velocity of a slip pulse, *J. Geophys. Res.,* 113, B04302, doi: 10.1029/2007JB005234.

Biegel, R.L., H.S. Bhat, C.G. Sammis, and A.J. Rosakis (2010), The effect of asymmetric damage on dynamic shear rupture propagation I: No mismatch in bulk elasticity, *Tectonophysics*, *493*(3), 254–262, doi:10.1016/j.tecto.2010.03.020.

Brantley, S.L., B. Evans, S.H. Hickman, and D.A. Crerar (1990), Healing of microcracks in quartz - Implications for fluid-flow, *Geology*, 18(2), 136-139.

Brenguier, F., M. Campillo, C. Hadziioannou, N.M. Shapiro, R.M. Nadeau, and E. Larose (2008), Postseismic relaxation along the San Andreas fault at Parkfield from continuous seismological observations, *Science*, 321, 1478-1481, doi: 10.1126/science.1160943.

Bürgmann, R., D.D. Pollard, and S.J. Martel (1994), Slip distributions on faults: effects of stress gradients, inelastic deformation, heterogeneous host-rock stiffness, and fault interaction, *J. Struct. Geol.,* 16(12), 1675-1690.

Cappa, F., and Rutqvist. J. (2012), Seismic rupture and ground accelerations induced by CO_2 injection in the shallow crust, *Geophys. J. Int.*, 190, 1784–1789, doi: 10.1111/j.1365-246X.2012.05606.x

Chester, J.S., F.M. Chester and A.K. Kronenberg (2005), Fracture surface energy of the Punchbowl fault, San Andreas system, *Nature*, 437, 133-136.

Chester, F.M., and J.S. Chester (1998), Ultracataclasite structure and friction processes of the Punchbowl, San Andreas system, California, *Tectonophysics*, 295, 199–221, doi: 10.1016/S0040-1951(98)00121-8.

Chester, F.M., and J.M. Logan (1986), Implications for mechanical-properties of brittle faults from observations of the Punchbowl Fault Zone, California, *Pure Appl. Geophys*., 124, 79–106

Cochran, E.S., Y.G. Li, P.M. Shearer, S. Barbot, Y. Fialko, and J.E. Vidale (2009), Seismic and geodetic evidence for extensive, long□lived fault damage zones, *Geology*, 37, 315–318, doi: 10.1130/G25306A.1.

Cooke, M.L. (1997), Fracture localization along faults with spatially varying friction, *J. Geophys. Res*., 102(B10), 22425–22434, doi:10.1029/97JB01829.

Dahlen, F.A. (1977), The balance of energy in earthquake faulting, *Geophys. J. Roy. Astron Soc.*, 48, 239-261

Dalguer, L. A., K. Irikura, and J. D. Riera (2003), Simulation of tensile crack generation by three-dimensional dynamic shear rupture propagation during an earthquake, *J. Geophys. Res.*, 108(B3), 2144, doi:10.1029/2001JB001738.

de Joussineau, G., and A. Aydin (2007), The evolution of the damage zone with fault growth in sandstone and its multiscale characteristics, *J. Geophys. Res.*, 112, B12401, doi:10.1029/2006jb004711.

de Joussineau, G., and A. Aydin (2009), Segmentation of strike-slip faults revisited, *Pure Appl. Geophys.*, 166, no.10, 1575-1594, DOI 10.1007/s00024-009-0511-4.

Dieterich, J.H. and D.E. Smith (2009), Nonplanar faults: Mechanics of slip and off-fault damage, *Pure Appl. Geophys.*, 166, 1799-1815.

Dor, O., T.K. Rockwell and Y. Ben-Zion (2006), Geological observations of damage asymmetry in the structure of the San Jacinto, San Andreas and Punchbowl faults in Southern California: A possible indicator for preferred rupture propagation direction, *Pure Appl. Geophys.*, 163(2–3), 301– 349, doi:10.1007/s00024-005-0023-9.

Dor, O., C. Yildirim, T.K. Rockwell, Y. Ben-Zion, O. Emre, M. Sisk, and T.Y. Duman (2008), Geologic and geomorphologic asymmetry across the rupture zones of the 1943 and 1944 earthquakes on the North Anatolian Fault: possible signals for preferred earthquake propagation direction, *Geophys. J. Int.*, 173, 483–504, doi:10.1111/j.1365–246X.2008.03709.x.

Duan, B., and S. M. Day (2008), Inelastic strain distribution and seismicitv radiation from rupture of a fault kink, *J. Geophys. Res.*, 113, B12311, doi:10.1029/2008JB005847.

Duan, B., J. Kang, and Y.G. Li (2011), Deformation of compliant fault zones induced by nearby earthquakes: Theoretical investigations in two dimensions, *J. Geophys. Res.*, 116, B03307, doi:10.1029/2010JB007826.

Dunham, E., and Rice, J.R. (2008), Earthquake slip between dissimilar poroelastic materials, *J. Geophys. Res*., 113, B09304, doi :10.1029/2007JB005405.

Dunham, E.M., D. Belanger, L. Cong, and J.E. Kozdon (2011a), Earthquake ruptures with strongly rate-weakening friction and off-fault plasticity, 1: Planar faults, *Bull. Seis. Soc. Am.*, 101(5), 2296-2307, doi:10.1785/0120100075.

Dunham, E.M., D. Belanger, L. Cong, and J.E. Kozdon (2011b), Earthquake ruptures with strongly rate-weakening friction and off-fault plasticity, 2: Nonplanar faults, *Bull. Seis. Soc. Am.*, 101(5), 2308-2322, doi:10.1785/0120100076.

Fialko, Y., D. Sandwell, D. Agnew, M. Simons, P. Shearer, and B. Minster (2002), Deformation on nearby faults induced by the 1999 Hector Mine earthquake, *Science*, 297, 1858–1862, doi: 10.1126/science.1074671.

Fialko, Y. (2004), Probing the mechanical properties of seismically active crust with space geodesy: Study of the co-seismic deformation due to the 1992 Mw7.3 Landers (southern California) earthquake, *J. Geophys Res.*, 109, B03307, doi:10.1029/2003JB002756.

Faulkner, D.R., Mitchell, T.M., Healy, D. and Heap, M. (2006), Slip on 'weak' faults by the rotation of regional stress in the fracture damage zone, *Nature*, 444(7121), 922-925.

Faulkner, D.R., T.M. Mitchell, E. Jensen, and J. Cembrano (2011), Scaling of fault damage zones with displacement and the implications for fault growth processes, *J. Geophys. Res.*, 116, B05403, doi: 10.1029/2010JB007788.

Fielding, E.J., Lundgren, P., Bürgmann, R., and Funning, G.J. (2009), Shallow fault-zone dilatancy recovery after the 2003 Bam earthquake in Iran, *Nature*, 458, 64-68, doi :10.1038/nature07817.

Finzi, Y., E. H. Hearn, Y. Ben-Zion, and V. Lyakhovsky (2009), Structural properties and deformation patterns of evolving strike-slip faults: Numerical simulations incorporating damage rheology, *Pure Appl. Geophys.*, 166, 1537–1573, doi:10.1007/s00024-009-0522-1.

Gabriel, A., J.P. Ampuero, L.A. Dalguer, and P.M. Mai (2013), Source properties of dynamic rupture pulses with off-fault damage, *J. Geophys. Res.*, 118(8), 4117-4126, doi: 10.1002/jgrb.50213

Griffith, W. A., S. Nielsen, G. Di Toro, and S. A. F. Smith (2010), Rough faults, distributed weakening, and off□fault deformation, *J. Geophys. Res.*, 115, B08409, doi:10.1029/2009JB006925.

Griffith, W.A., T.M. Mitchell, J. Renner, and G. Di Toro (2012), Coseismic damage and softening of fault rocks at seismogenic depths, *Earth Planet. Sci. Lett.*, 353-354, 219-230.

Gudmundsson, A. (2004), Effects of Young's modulus on fault displacement, *C. R. Geosciences*, 336, 85-92.

Gudmundsson, A., T.H. Simmenes, B. Larsen, S.L. Philipp (2011), Effects of internal structure and local stresses on fracture propagation, deflection, and arrest in fault zones, *J. Struct. Geol.*, 32, 1643-1655.

Hamiel, Y., and Y. Fialko (2007), Structure and mechanical properties of faults in the North Anatolian Fault system from InSAR observations of coseismic deformation due to the 1999 Izmit (Turkey) earthquake, *J. Geophys. Res.*, 112, B07412, doi:10.1029/2006JB004777.

Harris, R. A., and S. M. Day (1997), Effects of a low-velocity zone on a dynamic rupture, *Bull. Seis. Soc. Am.*, 87(5), 1267-1280.

Harris, R., et al. (2009), The SCEC/USGS Dynamic Earthquake Rupture Code verification exercise, *Seismol. Res. Lett.*, 80(1), 119–126, doi:10.1785/gssrl.80.1.119.

Healy, D. (2008), Damage patterns, stress rotations and pore fluid pressures in strike-slip fault zones, *J. Geophys. Res.*, 113, B12407, doi:10.1029/2008JB005655.

Hearn, E. H., and Y. Fialko (2009), Can compliant fault zones be used to measure absolute stresses in the upper crust?, *J. Geophys. Res.*, 114, B04403, doi:10.1029/2008JB005901

Huang, Y., and J.-P. Ampuero (2011), Pulse-like ruptures induced by low-velocity fault zones, *J. Geophys. Res.*, 116, B12307, doi:10.1029/2011JB008684.

Hok, S., M. Campillo, F. Cotton, P. Favreau, and I. Ionescu (2010), Off-fault plasticity favors the arrest of dynamic ruptures on strength heterogeneity: Two-dimensional cases, *Geophys. Res. Lett.*, 37, L02306, doi:10.1029/2009GL041888.

Ida, Y., (1972), Cohesive force across the tip of a longitudinal-shear crack and Griffith's specific surface energy, *J. Geophys. Res.*, 77, 3796–3805.

Itasca Consulting Group (2006), FLAC^{3D}, Fast Lagrangian Analysis of Continua in 3 Dimensions. Version 3.0. Five volumes. Minneapolis, Minnesota: Itasca Consulting Group.

Kagan, Y.Y., (2004), Short-Term Properties of Earthquake Catalogs and Models of Earthquake Source, *Bull. Seism. Soc. Am*., 94, 4, 1207-1228, doi: 10.1785/012003098

Kanamori, H., and Anderson, D.L. (1975), Theoretical basis of some empirical relations in seismology, *Bull. Seism. Soc. Am*., 65, 5, 1073-1095.

Kanamori, H., and L. Rivera (2006), Energy partitioning during an earthquake, in: Earthquakes: Radiated Energy and the Physics of Faulting, *Geophysical Monograph Series 170, AGU*, 3-13, doi: 10.1029/170GM03

Kaneko, Y. and Y. Fialko (2011), Shallow slip deficit due to large strike-slip earthquakes in dynamic rupture simulations with elasto-plastic off-fault response, *Geophys. J. Int.*, 186, 1389-1403

Katz, O., Z. Reches, and G. Baer (2003), Faults and their associated host rock deformations: Part I. Structure of small faults in a quartz-syenite body, southern Israel, *J. Struct. Geol.*, 25:1675-1689.

Knott, S.D., A. Beach, P.J. Brockbank, J.L. Brown, J.E. McCallum, and A.I. Welbon (1996), Spatial and mechanical controls on normal fault populations*, J. Struct. Geol*., 18(2–3), 359–372, doi:10.1016/S0191-8141(96)80056-3.

Kim, Y.S., D.C.P. Peacock, and S.J. Sanderson (2004), Fault damage zones, *J. Struct. Geol.*, 26, 503-517

Kostrov, B.V. (1974), Seismic moment and energy of earthquakes, and seismic flow of rock, *Izv. Earth Physics*, 1, 23-40.

Li, Y.G., P. Leary, K. Aki, and P. Malin (1990), Seismic trapped modes in the Oroville and San Andreas fault zones, *Science*, 249, 763-766.

Li, Y.G., J.E. Vidale, K. Aki, F. Xu, and T. Burdette (1998), Evidence of shallow fault zone strengthening after the 1992 M7.5 Landers, California, earthquake, *Science*, 279, 217–219, doi: 10.1126/science.279.5348.217.

Li, Y.G., P. Chen, E.S. Cochran, J.E. Vidale, and T. Burdette (2006), Seismic evidence for rock damage and healing on the San Andreas Fault associated with the 2004 M 6.0 Parkfield earthquake, *Bull. Seismo. Soc. Am.*, 96(4B), S349-S363.

Lyakhovsky, V., Y. Ben-Zion and A. Agnon (1997), Distributed damage, faulting, and friction, *J. Geophys. Res.*, 102, 27635-27649.

Ma, S. (2008), A physical model for widespread near-surface and fault zone damage induced by earthquakes, *Geochem. Geophys. Geosyst.*, 9, Q11009, doi:10.1029/2008GC002231.

Ma, S., and D.J. Andrews (2010), Inelastic off- fault response and three-dimensional dynamics of earthquake rupture on a strike-slip fault, *J. Geophys. Res.*, 115, B04,304, doi: 10.1029/2009JB006382.

Manighetti, I., G. King, Y. Gaudemer, C.H. Scholz, and C. Doubre (2001), Slip accumulation and lateral propagation of active normal faults in Afar, *J. Geophys. Res*, 106, B7, 13667-13669.

Manighetti, I., G. King, and C.G. Sammis (2004), The role of off-fault damage in the evolution of normal faults, *Earth Planet. Sci*. Lett., 217, 399-408.

Manighetti, I., M. Campillo, C.G. Sammis, P.M. Mai, and G. King (2005), Evidence for self-similar, triangular slip distributions on earthquakes: Implications for earthquake and fault mechanics, *J. Geophys. Res*., 110, B05302, doi: 10.1029/2004JB003174.

Manighetti, I., M. Campillo, S. Bouley, and F. Cotton (2007), Earthquake scaling, fault segmentation, and structural maturity, *Earth Planet. Sci. Lett.*, 253, 429-438, doi:10.1016/j.epsl.2006.11.004

Manighetti, I., D. Zigone, M. Campillo, and F. Cotton (2009), Self-similarity of the largest-scale segmentation of the faults: Implications for earthquake behavior, *Earth Planet. Sci. Lett.*, 288, 3–4, 370-381, doi: 10.1016/j.epsl.2009.09.040

Martel, S.J., and C. Shacat, (2006), Mechanics and interpretations of fault slip, *AGU Geophysical Monograph Series*, 170, 207-215.

Mitchell, T.M., and D.R. Faulkner (2009), The nature and origin of off-fault damage surrounding strike-slip fault zones with a wide range of displacements: a field study from the Atacama fault system, northern Chile, *J. Struct. Geol.*, 31, 802-816, doi: 10.1016/j.jsg.2009.05.002

Moore, D.E., D.A. Lockner, and J.D. Byerlee (1994), Reduction of permeability in granite at elevated-temperatures, *Science*, 265(5178), 1558-1561.

Ngo, D., Y. Huang, A.J. Rosakis, W.A. Griffith, and D.D. Pollard (2012), Off-fault tensile cracks: A link between geological fault observations, lab experiments and dynamic rupture models, *J. Geophys. Res.*, 117, B01307, doi:10.1029/2011JB008577.

Noda, H., and N. Lapusta (2010), Three-dimensional earthquake sequence simulations with evolving temperature and pore pressure due to shear heating: Effect of heterogeneous hydraulic diffusivity, *J. Geophys. Res.,* 115, B12314, doi:10.1029/2010JB007780.

Noda, H., N. Lapusta and H. Kanamori (2013), Comparison of average stress drop measures for ruptures with heterogeneous stress change and implications for earthquakes physics, Geophys. J. Int., *Geophys. J. Int.*, 193 (3), 1691-1712, doi:10.1093/gji/ggt074

O'Connell and Budiansky (1974), Seismic velocities in dry and saturated cracked solids, *J. Geophys. Res*., 79, 5412-5426.

Oskin, M.E., K. Le, and M.D. Strane (2007), Quantifying fault-zone activity in arid environments with high-resolution topography, *Geophys. Res. Lett.*, 34(23).

Palmer, A.C., and J.R. Rice (1973), Growth of slip surfaces in progressive failure of over□consolidated clay, *Proc. R. Soc. A.*, 332(1591), 527–548

Pelties, C., J. de la Puente, J.P. Ampuero, G.B. Brietzke, and M. Käser (2012), Three dimensional dynamic rupture simulation with a high-order discontinuous Galerkin method on unstructured tetrahedral meshes, *J. Geophys. Res.*, 117, B02309, doi: 10.1029/2011JB008857.

Poliakov, A.N.B., R. Dmowska, and J.R. Rice (2002), Dynamic shear rupture interactions with fault bends and off-axis secondary faulting, *J. Geophys. Res.*, 107(B11), 2295, doi:10.1029/2001JB000572.

Rice, J.R., C. Sammis, and R. Parsons (2005), Off-fault secondary failure induced by a dynamic slip pulse, *Bull. Seismol. Soc. Am.*, 95, 109-134.

Rudnicki, J.W., and J.R. Rice (2006), Effective normal stress alteration due to pore pressure changes induced by dynamic slip propagation on a plane between dissimilar materials, *J. Geophys. Res*., 111, B10308, doi :10.1029/2006JB004396.

Sammis, C.G., A.J. Rosakis, and H.S. Bhat (2009), Effects of off-fault damage on earthquake rupture propagation: experimental studies, *Pure Appl. Geophys.*, 166, 1629-1648, doi: 10.1007/s00024-009-052-3

Savage, H.M. and M.L. Cooke (2010), Unlocking the effects of friction on fault damage zones, *J. Struct. Geol.,* 1732-1741, doi:10.1016/j.jsg.2009.08.014.

Savage, H.M., and E.E. Brodsky (2011), Collateral damage: Evolution with displacement of fracture distribution and secondary fault strands in fault damage zones, *J. Geophys. Res.*, 116, B03405, doi: 10.1029/2010JB007665.

Schaff, D.P., and G.C. Beroza (2004), Coseismic and postseismic velocity changes measured by repeating earthquakes, *J. Geophys. Res.*, 109(B10), B10302, doi: 10.1029/2004jb003011.

Scholz, C.H., N.H. Dawers, J.Z. Yu, M.H. Anders and P.A. Cowie (1993), Fault growth and fault scaling laws: Preliminary results, *J. Geophys. Res.*, 98(B12), 21951-21961.

Scholz, C.H. (2002), The Mechanics of Earthquakes and Faulting, 2nd ed. *Cambridge University Press.* 471 pp.

Schlagenhauf, A., I. Manighetti, J. Malavieille, and S. Dominguez (2008), Incremental growth of normal faults: Insights from a laser-equipped analog experiment, *Earth Planet. Sci. Lett.*, 273, 299-311, doi:10.1016/j.epsl.2008.06.042

Shaw, B.E., and C.H. Scholz (2001), Slip-length scaling in large earthquakes: Observations and theory and implications for earthquake physics, *Geophys. Res. Lett.*, 28(15), 2995-2998.

Shelef, E., and M. Oskin (2010), Deformation processes adjacent to active faults: Examples from eastern California, *J. Geophys. Res.*, 115, B05308, doi:10.1029/2009JB006289.

Shi, Z., and Y. Ben-Zion (2006), Dynamic rupture on a bi-material interface governed by slip-weakening friction, *Geophys. J. Int.*, 165, 469-484, doi: 10.1111/j.1365-246X.2006.02853.x

Shi, Z., A. Needleman and Y. Ben-Zion (2010), Slip modes and partitioning of energy during dynamical frictional sliding between identical elastic-viscoplastic solids, *International Journal of Fracture*, 162, 51–67, doi: 10.1007/s10704-009-9388-6, 2010.

Shipton, Z., and P.A. Cowie (2001), Damage zone and slip surface evolution over μm to km scales in high-porosity Navajo sandstone, Utah, *J. Struct. Geol.*, 23, 1825-1844.

Shipton, Z., and P.A. Cowie (2003), A conceptual model for the origin of fault damage zone structures in high-porosity sandstone, *J. Struct. Geol.*, 25, 333-344.

Sibson, R.H. (2003), Thickness of the seismic slip zone, *Bull. Seis. Soc. Am.,* 93, 1169-1178.

Smith, S. A. F., A. Bistacchi, T. M. Mitchell, S. Mittempergher, and G. Di Toro (2013), The structure of an exhumed intraplate seismogenic fault in crystalline basement, *Tectonophysics*, 599(0), 29-44, doi: 10.1016/j.tecto.2013.03.031

Spudich, P., and K.B. Olsen (2001), Fault zone amplified waves as possible seismic hazard along the Calaveras fault central California, *Geophys. Res. Lett.*, 28(13), 2533-2536.

Suzuki, T. (2012), Understanding of dynamic earthquake slip behavior using damage as a tensor variable: Microcrack distribution, orientation, and mode and secondary faulting, *J. Geophys. Res.*, 117, B05309, doi:10.1029/2011JB008908.

Templeton, E.L., and J.R. Rice J.R. (2008), Off-fault plasticity and earthquake rupture dynamics : 1. Dry materials or neglect of fluid pressure changes, *J. Geophys. Res.*, 13(B9), B09306.

Tinti, E., P. Spudich, and M. Cocco (2005), Earthquake fracture energy inferred from kinematic rupture models on extended faults, *J. Geophys. Res.*, 110, B12303, doi: 12310.11029/12005JB003644.

Vermilye, J.M., and C.H. Scholz (1998), The process zone: A microstructural view of fault growth, *J. Geophys. Res.*, 103(B6), 12,223–12,237.

Vidale, J.E., and Y.G. Li (2003), Damage to the shallow Landers fault from the nearby Hector Mine earthquake. *Nature*, 421(6922), 524-526.

Viesca, R.C., E.L. Templeton, and J.R. Rice (2008), Off-fault plasticity and earthquake rupture dynamics : 2. Effects of fluid saturation, *J. Geophys. Res*., 113, B09307.

Wechsler, N., T.K. Rockwell, and Y. Ben-Zion (2009), Application of high resolution DEM data to detect rock damage from geomorphic signals along the central San Jacinto Fault, *Geomorphology*, 113, 82–96, doi:10.1016/j.geomorph.2009.06.007.

Wilson, B., T. Dewers, Z.E. Reches, and J. Brune (2005), Particle size and energetics of gouge from earthquake rupture zones. *Nature*, 434(7034), 749-752.

Wolf, S., I. Manighetti, M. Campillo and I.R. Ionescu (2006), Mechanics of normal fault networks subject to slip-weakening friction, *Geophys. J. Int.*, 165, 677-691, doi: 10.1111/j.1365-246X.2006.02910.x

Xu, S., Y. Ben-Zion, and J.-P. Ampuero (2012a), Properties of inelastic yielding zones generated by in-plane dynamic ruptures: I. Model description and basic results, *Geophys. J. Int.*, 191, 1325–1342, doi: 10.1111/j.1365-246X.2012.05679.x.

Xu, S., Y. Ben-Zion, and J.-P. Ampuero (2012b), Properties of inelastic yielding zones generated by in-plane dynamic ruptures: II. Detailed parameter-space study, *Geophys. J. Int.*, 191, 1343–1360, doi: 10.1111/j.1365-246X.2012.05685.x.

Xu, S., and Y. Ben-Zion (2013), Numerical and theoretical analyses of in-plane dynamic rupture on a frictional interface and off-fault yielding patterns at different scales, *Geophys. J. Int.*, 193, 304-320, doi: 10.1093/gij/ggs105.

Yamashita, T. (2000), Generation of microcracks by dynamic shear rupture and its effects on rupture growth and elastic wave radiation, *Geophys. J. Int.*, 143, 395– 406

The conclusions of the article presented in Chapter V can be complemented on a few points that open perspectives for additional work:

- First, we showed in the paper that left- and right-lateral slip produces identical results. This is only true if the elasticity of the damage zone is isotropic. It is clear that it cannot be; cracks and damage faults more likely have preferred orientations, due to the specific stress conditions in the damage zones. Therefore, **more work needs to be done to characterize the anisotropy of the damage features within the natural damage zones**. This might be done both from direct observation and mapping of the macroscopic damage features, and from geophysical experiments using the properties of the seismic or other types of waves to be sensitive to the preferential directions of the features that they cross.
- Second, one of the results of the paper is to suggest that the damage zones are broad around the faults, up to several km for a 30 km long fault. The width of the natural damage zones is not well constrained at present for three main reasons: 1) it has been postulated for long that the damage zones were narrow and thus limited to the immediate vicinity of the main fault. Therefore, widest damage zones have not been searched for; 2) measuring the extent of a damage zone requests identifying the damage features that form it. It is not necessarily easy for some of the damage features might not be of macroscopic scale, and hence might not be clearly identifiable. Up to now, it has been postulated that counting the fracture density nearby a main fault satisfactorily describes the evolution of the damage intensity away from the fault. Again, this is not necessarily correct as different types of features might contribute to the long-term damage (cracks and fractures, but also different sizes of faults, and zones of plastic strain); 3) the width of the long-term damage zone likely varies along the fault length, in relation with the degree of structural maturity of the different fault sections. Therefore, a 2D analysis of the damage features should be performed to recover the actual extent and map-view geometry of the damage zones.

  In any case, all the prior works which report the fracture density around major faults (See references in chapter V, but also Faulkner et al., 2006; Mitchell et al., 2011) provide a useful estimate of a likely minimum width of the long-term damage zones and hence **should be analyzed collectively to explore the possible scaling relations between fault length and damage zone width**. Furthermore, we suspect that secondary fault networks developed around the master faults are an expression of the long-term damage around these faults. Therefore, **the fault maps that I have provided in the IDs might be used to measure the maximum extent of the long-term damage zones**. This work will be done soon.

- Finally, our modeling results, along with observations on large EQs scaling relations, altogether suggest that the elastic modulus in the damage zones can be very low. Yet it remains to measure the actual elastic modulus in natural damage zones. **One way is to convert the observed crack density into elastic modulus**, and this might be done using various constitutive models (e.g., Faulkner et al., 2006; Mitchell et al., 2011). **Another way is to derive the elastic modulus from the properties of the seismic waves (or other types of waves) that propagate through natural damage zones**. So far, elastic properties derived from seismic waves have mainly been characterizing the damage zone right after a large EQ. By contrast, very few seismic studies have been conducted on long-term damage zones. This work thus remains to be done in the future.

CHAPTER VI. INITIATION AND ARREST OF EARTHQUAKE RUPTURES DESCRIBED BY EMPIRICAL RELATIONS

1. Questions posed

It is well admitted that fault are discontinuous features, which, in particular, are segmented laterally at various scales. As described in Chapter II, the longest segments of the faults can be identified, and shown to be separated by "inter-segment zones'. As recognized for long (references in Chapter II), most of these zones are step-overs between major fault sections. I have shown in Chapter II the different types and geometries of these step-overs, and I have defined their "length" and "width" in map view. The faults can also show bends in their traces, splays at their tips, and zones where they intersect other faults or specific features. Altogether these geometric characteristics –step-overs, bends, diverging splays, intersecting faults, etc, are suspected to alter an earthquake rupture propagation on the fault, and to contribute to its eventual arrest. The question posed is thus: are there any specific geometrical features along the faults which are systematically broken, or unbroken, by an earthquake occurring on the fault?

So far, the question has been approached by focusing on the step-overs and searching whether there exists specific step-over widths (across-strike distance in map view) which either break during, or arrest, an earthquake rupture (e.g., Knuepfer, 1989; Zhang et al., 1999; Lettis et al., 2002; Wesnousky, 2006; Black and Jackson 2008). Although "inter-segments" between fault sections are more complex than simple step-overs, only the width of the step-overs has been examined. It has been concluded that i) the width is more relevant than the length or area of the step-overs to examine the question of rupture arrest; ii) there exists a threshold width of 4-5 km above which, independently of the rupture size and possibly slip mode, an EQ rupture is always arrested.

Here I examine this question further, motivated by two main reasons:

1) My work is one of the rare to examine the rupture traces in the precise mapping framework of the entire long-term faults on which the EQs occurred. This is important since it is difficult to understand and measure a geometrical complexity while ignoring its relative importance on the broken fault;
2) Because our maps are precise, they provide me more accurate descriptions of the fault inter-segments and terminations (ex: whether they are marked by splays, intersection with another fault, etc), and hence allow me more precise measurements of the characteristics of the zones across which the EQ ruptures pass or are arrested, including angles along the faults.

2. Approach to perform the measurements

The description and measurements of the faults inter-segments and terminations are explained in chapter II and reported in Tables 6. However I provide more detailed descriptions below.

Although I have measured various characteristics of the inter-segment zones (such as overlapping and underlapping length, area, etc) and fault connections or terminations, I only analyze here the few main features, namely the mean width (at surface, in map view) of the step-overs (they will be represented as dots), the maximum angle between a fault and a splaying (i.e., genetically related to the fault; represented as triangles) or an intersecting (i.e., not-genetically related to the fault; represented as squares) fault, the mean angle of fault trace bends (represented as diamonds), the closest distance to the next sub-parallel, synthetic fault (represented as a dot with label "n"), the intersection of the fault with a specific feature (See below; represented as a cross).

I thus examine which of these features exist where an EQ rupture propagates or arrests. I however focus on the larger features, which are those most expected to extend at seismogenic depth. I thus ignore the very small step-overs (W< 1 km) or the small angles (< 10°), which are not very informative for they exist on almost every fault, and in any case are not the best represented values at the resolution of my data. Of course, would such of a small feature arrest a rupture, I would note it (it did not happen).

When a measurement is uncertain, I plot it as a small symbol. I have discriminated the data both as a function of the fault slip mode and as a function of the "geometrical complexity in consideration" being releasing or restraining. Yet, for simplicity, and because the results are basically the same, I only show here the data discriminated from the fault slip mode. Normal faults are represented in blue, reverse faults in green, and strike-slip faults in red. The later faults are dominant in the analyzed population.

Where the rupture passes through, the symbol is empty; where the rupture is arrested, the symbol is full (as in Wesnousky 2006). There is a few cases however where the main rupture basically stops, yet still dissipates little slip on a short distance beyond the obvious arrest zone. I indicate these arrest zones with crossed symbols.

As discussed earlier, a few EQs have actually ruptured different faults, not a single one. I indicate these few cases in paler symbols.

Where several data superimpose to each other on the plots, I sometimes slightly shift some of them on the horizontal axis, so that all can be seen.

3. Measurements

3.1. 2010 Baja California earthquake

- Stops in the NW at the NW end of secondary segment 4b in major segment 4 of the Elsinore Fault. There, the segment trace curves and ends in a horsetail fashion. The horsetail structures form a ~25° angle to the mean rupture trace. The angle is defined however with ± 10°. As some of the horsetail features also rupture, the arrest is marked with a crossed-triangle at 25°. The fault being right lateral, the horsetail is extensional (small solid blue triangle). The distance to the next segment (secondary segment 4a to the south) is difficult to precisely estimate but seems ~5 km. I suggest it by a small grey solid dot at W 5 km.
- Stops in the SE at the SE end of secondary segment 4d in major segment 4 of the Elsinore fault, and hence in the relay zone between major segments 4 and 5, which are separated by an across-strike distance of~8 km (solid grey dot at W 8 km).
- The rupture propagates across en-echelon segments, separated by across-strike distances of ~3 and ~4 km (2 empty grey dots at W 3 and W 4 km).

3.2. 1957 Bogd earthquake

- Stops in the W at the connection zone between the major segments 1 and 2 of the long-term Bogd fault. There, the rupture reaches a large ancient restraining step-over, which is now cross-cut by the main fault trace. However the main fault trace is still partly disconnected in the step-over, so that the rupture ends in a very small step-over, ~3 km-wide, within the large ancient step. Meanwhile, the rupture breaks one of the small reverse faults that bound the ancient large step-over. This suggests that the rupture arrest is partly due to the coseismic slip dissipating in the ancient large step-over. Therefore, the small 3 km-wide step-over does not contribute alone to the rupture arrest. I thus indicate it as a small red solid dot at W 3 km.
- Stops in the E in the connection zone between the major segments 4 and 5 of the long-term Bogd fault. There, the rupture reaches a ~20 km-wide restraining step-over (solid red dot at W 20 km).

- The rupture propagates across a now well-connected 4 km-wide restraining step-over (between major segments 2 and 3; empty bold-red dot at W 4 km), as through a ~2.5 km-wide releasing, hardly connected step-over (between major segments 3 and 4; empty blue dot at W 2.5 km).

3.3. 1968 Borrego Mountains earthquake

- Stops in the NW at the connection zone between secondary segments 3a and 3b of major segment 3 of the San Jacinto fault. The rupture stops in a ~3 km wide restraining step-over, where multiple en echelon small segments have developed. However, it is not clear that the step-over is entirely responsible for the arrest. Segment 3b also splays as it arrives in the step-over, with the splay forming a maximum angle of ~40° to the main fault trace. That angle might be most significant in the rupture arrest (→ small solid red dot at W 3 km, and large solid grey triangle at 40°).
- Stops in the SE at the connection zone between secondary segments 3b and 3c of major segment 3 of the San Jacinto fault. That intersegment is where major segment 3 starts overlapping the sub-parallel major segment 4, located at a distance of ~6 km (→red solid dot labeled n at W 6 km)
- The rupture propagates through two ~20-22° bends (2 grey diamonds at 20° and 22°), a ~1.5 km restraining step-over (empty red dot at W 1.5 km), and a ~2-3 km releasing, connected, step-over (empty, blue-bold, dot at W 2 km).

3.4. 1983 Borah Peak earthquake

- Stops at the NW end of the Borah Peak long-term fault, where the later splays in multiple oblique branches, forming a maximum angle to the fault trace of ~44° (solid blue triangle at 44°).
- Stops in the south at the southern end of the long-term Borah Peak fault, where the later intersects the markedly oblique Mackay fault striking at 65-70° to the mean Borah Peak trace (solid blue square at 70°). The southern rupture end is also where the Borah Peak fault intersects a sub-perpendicular lineament, likely of magmatic origin (Yellowstone hot spot path; cross at ~75°).
- The surface rupture trace interrupts over a length of ~5.5 km in the middle of the rupture line (~in connection zone between major segments 1 and 2), but it is not clear whether this interruption is only due to a smaller slip more difficult to see and measure in this zone, or

marks an actual interruption of the earthquake rupture. Because of this ambiguity, I do not indicate the rupture gap.

- The rupture propagates through two bends of ~15 and 17° (two empty blue diamonds). It also passes some intersections with splay faults developed in the western compartment. Where those splay faults connect with the Borah Peak rupture, they form a ~15° angle with the main rupture (empty blue triangle at 15°).

3.5. 2001 Denali earthquake

Since the Denali EQ broke three distinct faults, I discriminate here the rupture of the Denali fault only, and the total rupture of the three faults (in pale symbols, as Landers).

Rupture of Denali Fault only:

- Stops in the W at the western tip of major segment 4, where the fault splays into several branches, forming a maximum angle of ~45° to the main fault trace. As the splays are in the southern compartment of the dextral fault, they are in a compressive regime (solid red triangle at 45°; I use a crossed-triangle to indicate that a short rupture trace continues on the Denali fault beyond the primary arrest zone).
- Stops in the E at the eastern tip of major segment 4, where the fault splays into the Totschunda fault, that forms an angle of ~35° to the Denali fault (nearby the connection of the two faults). As the Totschunda splay fault is in the southern compartment of the dextral Denali fault, it is in an extensive regime (solid blue triangle at 35°).
- The rupture propagates across several small step-overs, the two largest ones are ~2 and 3 km-wide and releasing (2 empty blue dots at W 2 and 3 km). The rupture also propagates through small bends in the fault trace, having maximum angles of ~12° (empty grey diamond at 12°).

Total so-called 'Denali rupture' (3 faults):

- Stops in the W along sort of a splay of the Susitna fault (not very clear), that forms a ~40° angle to the main Susitna fault trace (small solid grey triangle at 40°).

- Stops in the E at a ~4-6 km-wide step-over between two segments of the Totschunda fault (solid grey dot at W 5 km).
- On the Denali fault, the rupture propagates across several small step-overs, the two largest ones are ~2-3 km-wide and releasing (2 empty blue dots at W 2 and 3 km). The rupture also propagates through small bends in the fault trace, having maximum angles of ~12° (empty grey diamond at 12°). In its path along the three faults, the rupture propagates across two splay angles of ~45° (in the west, empty grey triangle at 45°), and ~35° (in the east, empty grey triangle at 35°).

3.6. 1954 Dixie Valley earthquake

- Stops in the north at the connection zone between major segments 1 and 2 of the Dixie Valley fault. The rupture thus stops where it arrives in a 4.5-5 km-wide releasing step-over (solid blue dot at W 4.5 km). In the step-over, a ~40° oblique fault has developed (solid blue square at 40°).
- Stops in the south at the connection zone between major segments 3 and 4 of the Dixie Valley fault. The rupture thus stops where it arrives in a 3.5-4 km-wide releasing step-over (solid blue dot at W 4 km). Diffuse multiple cracking is observed in the step-over.
- The rupture has propagated through a bend of ~24° (present inter-segment 2-3; empty blue dot at 24°), apparently associated to an ancient step-over of ~3 km-wide (empty blue dot at W 3 km) (the most recent fault trace cuts across the ancient step-over).

3.7. 1954 Fairview Peak earthquake

- Stops in the north where the Fairview Peak long-term fault ends in a horsetail fashion. The rupture thus stops as it reaches the bended horsetail termination. The bend is ~40°. Although the rupture basically stops at the bend, the horsetail small faults are also ruptured. I indicate this situation by a crossed triangle (blue, at 40°). The distance to the closest sub-parallel synthetic faults (Dixie Valley fault) is ~13 km (solid blue dot at W 13 km).
- Stops in the south at the connection zone between major segments 1 and 2. The rupture thus stops at a ~3 km wide releasing step over. Furthermore, in the step-over, the main rupture trace is intersected by an oblique fault, striking at ~30° to the main fault trace (where it intersects it). Because the two features might contribute to the rupture arrest, I plot them both in small symbols (small blue solid dot at W 3 km, and small blue solid triangle at 30°).

- The rupture propagates through a ~1.5 (inter-segment 2-3) and a ~2.5 km-wide (northern end of major segment 3) releasing step-overs (two empty blue dots at W 1.5 and W 3 km), but also passes a bend of ~29° in the north (north tip of segment 3 → empty blue diamond at 29°), as a change in mean strike of ~13° (between mean strikes of segment 1 and 2 → empty blue dot at 13°; a dot is used because the strike change occurs across the step-over).

3.8. 1857 Fort Tejon earthquake

- Stops in the NW at the western end of the southern San Andreas fault, where the later basically meets the central creeping section. South of that creeping section, the small Parkfield section which frequently breaks in Mw~6 earthquakes is a stress-relaxed zone that likely represents a barrier to a rupture propagation that would emanate from the southern San Andreas break. The NW arrest of the Fort Tejon earthquake is thus likely due to this barrier. However, it coincides on the fault map to a small, ~2 km-wide releasing step-over (small solid blue dot at W 2 km). It also coincides with the intersection of the San Andreas fault with the ~16° oblique San Juan splay fault (small solid grey triangle at 16°).
- Stops in the SE at the eastern tip of major segment 3, where the southern San Andreas fault intersects and connects the markedly oblique San Gabriel fault system, that forms an angle of ~45-50° to the mean Southern San Andreas strike. As the San Gabriel-Sierra Madre Fault system is compressive, I indicate this intersection as restraining (solid red square (triangle) at 50°). The ~30° oblique San Jacinto fault also splays from the southern San Andreas in the zone of the rupture arrest (small solid grey triangle at 30°, small because I suspect that the 50° intersection most contributes to the rupture arrest).
- The rupture propagates across the major central bend of the San Andreas fault, which forms an angle of ~20-30° (depending where it is measured; empty grey diamond at mean 25°). It also passes through the connection zone between the San Andreas and the Garlock fault, and I discuss this point further below. It also propagates through the small ~1 km-wide step-over that separates major segments 2 and 3 (empty blue dot at W 1 km).

3.9. 1931 Fuyun earthquake

- Stops in the north at the northern end of the long-term Fuyun fault, where the later splays into multiple oblique branches, altogether forming a maximum angle of ~40° to the mean fault trace. As the fault is right-lateral and the splays in the western compartment, the splays are in a compressive regime (solid red triangle at 40°).

- Stops in the south at the connection zone between the major segments 1 and 2 of the Fuyun fault, and hence where the rupture reaches a ~12 km-wide restraining step-over (solid red dot at W 12 km).
- The rupture propagates through 3 bends, of ~15° between segments 1a and 1b, ~17° where segment 1b curves to connect to segment 1c, and ~19° where segment 1c curves to connect with segment 1b (3 empty grey dots at 15, 17 and 19°). The rupture also propagates through several small step-overs, the two largest ones are ~2-2.5 km-widen, one likely restraining and the other one releasing (in the north of segment 1b, and at the northern tip of segment 1c → 1 empty red dot at W 2.5 km and one blue dot at W 2 km).

3.10. 1959 Hebgen Lake earthquake

- Stops in the W at the western end of the Hebgen Lake long-term fault, where the later both connects with an oblique secondary fault striking at ~47° to its mean trace (blue triangle at 47°), and intersects the ancient Yellowstone Hot Spot shear path, which trends at high angle, ~75°, to the fault and rupture trace (black cross at 75°).
- Stops in the E at the connection zone between major segments 1 and 2. There, the fault trace markedly curves into a splay, forming an angle of ~50° to the main fault trace (blue triangle at 50°). There is also a gap in the rupture trace, of ~1 km long, that I do not indicate as it is not a step-over and is small anyway.
- The rupture propagates through very small steps that I do not indicate, and through a significant bend of ~25° (empty diamond at 25°).

3.11. 1999 Hector Mine earthquake

- Stops in the north at the likely northern end of the Hector Mine fault (the fault might continue further north however, along a fifth segment; see ID in chapter II), i.e., the northern end of its major segment 4. There, the fault splays in subtle oblique branches (well underlined by the aftershocks), forming a maximum angle of ~30° to the fault trace. As the fault is dextral and the splays in the northern compartment, the splay quadrant is releasing (solid blue triangle at 30°). The distance to the closest sub-parallel synthetic fault ("segment 5") is ~2 km (almost in continuity with the rupture trace, separated by a gap)(small solid grey dot labeled n at W 2 km).
- Stops to the south at the connection zone between major segments 2 and 3, and hence where the rupture reaches a ~3 km-wide releasing step-over. Many structures exist in the step-over,

some are markedly oblique to the main rupture trace, with a maximum angle of ~35°. As both angle and step width might combine to arrest the rupture, I indicate both with a small symbol (solid blue dot at W 3 km, and solid blue triangle at 35°).
- The rupture propagates through two bends of ~23 and ~25° (empty grey diamonds at 23 and 25°).

3.12. 1940 Imperial Valley earthquake

- Stops in the NW at the NW tip of secondary segment 4c in major segment 4 of San Jacinto fault. There, the segment 4c curves and ends in an extensional horsetail fault network, forming a maximum angle of ~40° to the mean segment trace (solid blue triangle at 40°). The distance to the closest parallel fault is ~5 km (segment 4b to the south). The step would be releasing, hence solid blue dot labeled n at W 5 km.
- Stops in the SE at the SE end of the secondary segment 4d, where the later bends and splays in multiple branches, having a maximum angle of ~35° with the mean segment strike. The splays being in the southern compartment of the dextral fault, they are in extensional quadrant (solid blue triangle at 35°). The distance to the closest sub-parallel synthetic fault (major segment 5 of Elsinore fault) is ~18 km (solid blue dot labeled n at W 18 km).
- The rupture propagates through 2 very small step-overs, < 0.5 km wide (I only indicate the largest, with an empty blue dot at W 0.4 km).

3.13. 1979 Imperial Valley earthquake

- Stops in the NW at the NW end of secondary segment 4c in major segment 4 of San Jacinto fault. There, the fault trace curves and ends in an extensional horsetail fault network, forming a maximum angle of ~40° to the mean fault trace (solid blue triangle at 40°). The distance to the closest parallel fault is ~5.5 km (to the south). The step would be releasing, hence solid blue dot at W 5.5 km.
- Stops in the SE at the connection zone between secondary segments 4c and 4d. In that zone, no major feature can be seen. The rupture stops at a small releasing step-over, < 1 km width (small solid blue dot at W 0.4 km). The arrest zone is also where a ~11° oblique fault zone intersects the main rupture trace (small solid grey square at 11°).
- The rupture propagates through a very small step-over, < 200 m wide, that I do not indicate.

3.14. 2001 Kunlun earthquake

The Kunlun EQ broke two distinct faults. I here focus only on the rupture of the principal Kunlun fault.

- Stops in the W at the western tip of the long-term Kunlun fault (for segment 5 indicated in ID is unclear), where the Kunlun fault splays into the oblique Buka Daban Feng fault, that forms a ~25-30° angle to the main Kunlun fault trace. As the splay is in the southern compartment of the left-lateral Kunlun fault, it is under extensional regime (solid blue triangle at mean 28°).
- Stops in the E at the eastern tip of major segment 4, where the segment meets an oblique fault striking at ~30° to the mean segment 4 strike (solid grey square at 30°).
- The rupture propagates across small step-overs, the largest one is ~2 km-wide between secondary segments 4a and 4b (empty blue dot at W 2 km). The rupture also passes through the connection with the oblique strand that connects major segments 4 and 3, and which forms an angle of ~14° to the mean strike of ruptured segment 4 (empty grey square at 14°).

3.15. 1992 Landers earthquake

The Landers EQ broke three distinct faults (Camp Rock-Emerson, Homestead Valley and Johnson Valley faults) and hence is peculiar. I indicate its overall behavior (total rupture), yet discriminate it in paler symbols.

- Stops in the NW at the NW end of major segment 2 of the Camp Rock-Emerson fault, and hence at a ~2 km-wide releasing step-over. The arrest zone is also where the fault intersects an ancient ~E-W trending structure (well underlined by the aftershocks), forming a ~50° angle to the main rupture trace. It is likely that this oblique structure strongly contributes to the rupture arrest → small solid blue dot at W 2 km, and large solid grey square at 50°.
- Stops in the SE at the SE end of the Johnson Valley Fault fault, where the later intersects the markedly oblique Pinto Mountain fault, forming a ~85° angle to the mean Johnson Valley fault trace (solid grey square at 85°).
- The rupture cascades among different faults, in effect propagating across a ~2.5 km-wide (jump Homestead Valley-Camp Rock) and a ~3.5 km-wide (jump Johnson Valley-Homestead Valley) releasing step-overs (2 empty blue dots at W 2.5 and W 3.5 km). The strike of the segments varies along the rupture, so that the rupture also propagated through strike changes of ~21 and 22° (2 empty blue dots at 21 and 22°).

3.16. 1997 Manyi earthquake

- Stops to the W at the western tip of the Manyi long-term fault, where the fault intersects a high and large WNW-trending mountain chain ("Purog Kangri") that overall strikes at 25-35° to the Manyi fault trace. I suspect that crossing the high topography of the chain is mechanically difficult so that this intersection might strongly contribute to the fault and hence to the rupture arrest. As it is uncertain however, I use a small symbol (small solid grey square at 30°). At its western tip, the Manyi fault also splays in a horsetail fashion, with the splays forming a maximum angle of ~30° to the fault trace. The splays being in the southern compartment of the left-lateral fault, it is under extensional regime (solid blue triangle at 30°).
- Stops in the E in a long restraining relay zone between major segments 3 and 4. The step-over is ~5 km-wide in the across-strike direction, and > 20 km-long in the fault strike direction (solid red dot at W 5 km). The Manyi fault also splays into a small secondary branch departing from the step-over, and forming a ~35° angle to the main Manyi fault trace. As the splay is in the northern compartment of the left-lateral Manyi fault, it is under extensional regime (solid blue triangle at 35°).
- The rupture propagates across an ancient large releasing step-over, which is now cross-cut by the fault which shows a continuous single trace through the step-over. The ancient step is marked in the present fault trace by the later bending by ~15 and ~18° (2 empty blue diamonds at 15 and 18°). The rupture also propagates through a small step-over, which is now fairly well-connected (ancient fold structure). These connection make the rupture propagating through a small bend of ~12° (empty grey diamond at 12°).

3.17. 1915 Pleasant Valley earthquake

- Stops in the north at the connection zone between major segments 1 and 2 of the Pleasant Valley fault. This is where the fault connects with oblique branches (bend of ~40°) that form a relay with the next synthetic fault further west (Grass Valley). The rupture passes through a ~3.5-4 km-wide releasing step-over (empty&crossed blue dot at W 4 km) and then is stopped at the bend (solid blue triangle at 38°). The distance to the closest sub-parallel synthetic fault is ~8-9 km → solid blue dot with n at W 9 km).
- Stops in the south at the southern end of the Pleasant Valley fault where the later intersects a WNW-trending ancient lineament (See Pleasant Valley ID), striking at ~90° to the mean

fault trace (cross at 90°). The distance to the closest sub-parallel synthetic fault (Buena Vista Valley fault) is ~9 km → solid blue dot with n at W 9 km).

- The rupture propagates through a ~4-4.5 km-wide releasing step-over (empty blue dot at W 4.5 km).

3.18. 1906 San Francisco earthquake

- Stops in the north at the northern termination of the northern San Andreas fault, where the later connects with the markedly oblique Mendocino fault zone, that forms an angle of ~77° with the mean northern San Andreas trace (solid grey square at 77°).
- Stops in the south at the southern end of the northern San Andreas fault, where the later meets the central creeping section. I do not indicate this specific end, for it does not coincide with any step or angle change.
- The rupture propagates through two large bends in the mean fault trace, one of ~24° between major segments 1 and 2, another one of ~12° between major segments 4 and 5 (2 empty grey diamonds at 25 and 12°). The rupture also passes by intersections with oblique faults, the major one being the San Gregorio fault that forms an angle of ~15° to the mean northern San Andreas strike (empty grey square at 15°) and the Sargent fault zone that forms an angle of ~20° to the mean strike of the segment 5 (empty grey square at 20°). The rupture also propagates across small step-overs, the largest ones are 2-2.5 km wide (~2.5 km between major segments 2 and 3; and ~2 km between major segments 3 and 4) (2 empty grey dots at 2 and 2.5 km).

3.19. 2008 Sichuan earthquake

- Stops in the NE at the Sichuan long-term fault NE end, where the fault intersects the oblique Qingchuan fault, with an angle between ~25° (between mean strikes of Sichuan fault and of western tip of Qingchuan fault) and 40° (between mean strikes of Sichuan fault and of Shanyang entire fault). I thus indicate a solid grey square at a mean angle of 33°. The distance to the closest sub-parallel synthetic Qingchuan fault is ~19 km (solid grey dot labeled n at W 19 km). The rupture also ends where the Sichuan fault splays into multiple small branches, forming a maximum angle of ~20° to the main fault trace. As it is likely that this moderate splaying contributes little to the rupture arrest compared to the step and intersection with the master Qingchuan fault, I indicate it with a small solid grey triangle at 20°.

- Stops in the SW at about the SW tip of the long-term Sichuan fault, where the later is connected to the adjacent Pengguan reverse fault. The two faults form an angle of ~15° (small solid red square at 15°). The rupture SW end is also where a number of oblique reverse faults connect with the Sichuan fault. It is thus likely that the Beichuan fault and Pengguan fault connection is not the only factor for the rupture arrest, and this is why I indicate the 15° angle with a small symbol.
- The rupture propagates through several small steps (which I do not indicate). It also propagates across the relay zone that connects major segments 1 and 2, which appear as a releasing large step-over of complex shape, whose width is thus fairly difficult to measure, yet likely on the order of 8-9 km. I thus indicate it as a small empty blue dot at W 8 km.

3.20. 1987 Superstition Hills earthquake

- Stops in the NW at the NW end of the San Jacinto major segment 4. At that end, the rupture arrives in the previously relaxed Elmore Ranch fault zone (in NE compartment of Superstition rupture), which forms a high ~85° angle with mean strike of Superstition segment. Since Superstition rupture is right lateral, the arresting intersection is extensional (→ releasing solid square at 85°). The distance to the closest sub-parallel synthetic fault is ~6 km (would be a restraining step, hence solid red dot labeld n at W 6 km).
- Stops in the SE at the connection zone between secondary segments 4a and 4b. There are 3 main features in that SE arrest zone: 1) a small, < 1 km wide step-over; 2) a fault splay striking at ~13° to the main rupture trace; and 3) a zone of sub-perpendicular lineaments (angle of ~80-85°), similar to those observed at many places in the plain (See ID) → I suspect that the intersection with the pre-existing sub-perpendicular fault zone contributes most to the rupture arrest (→ small symbols for features 1 and 2, and large, grey solid square for feature 3).
- The rupture propagates through a very small step < 1 km wide, that I do not indicate. It also propagates through a ~20° bend (empty grey diamond at 20°).

3.21. 2010 Yushu earthquake

- Stops in the W at the western end of major segment 1 of the Yushu long-term fault. There, the fault and hence the rupture abut an oblique large fault (related to the Dangjiang fault), striking at ~30° to the mean Yushu fault trace (grey solid square at 30°).

- Stops in the E at the connection zone between secondary segment 1c and 1d, which is marked by a ~10 km long gap in the main fault trace (the few rupture traces indicated in the gap are subtle and not coincident with a clear cumulative trace) (solid grey dot at W 10 km). In its eastern end, the rupture also diffuses on the multiple small horsetails oblique faults that form the eastern tip of secondary segment 1c, and are at a ~20° angle to the mean fault trace. As the fault is left-lateral, those horsetail features in the northern compartment are in extensional regime (small solid blue dot at 20°; the symbol is small because it is likely that the small horsetail features are not responsible alone of the rupture arrest).
- The rupture propagates through a ~4km-wide releasing step-over (inter-segment 1a-1b; solid blue dot at W 4 km).

4. Empirical relations and discussion

4.1. Rupture arrest: not anywhere on the broken fault

Figures 249 and 250 show the step-over widths and the angles that the ruptures –ordered by increasing length, pass through or are arrested at, respectively. Figure 249 is thus similar to Fig.2 in Wesnousky, 2006.

The first observation is that **on no fault the rupture stops at a random place**, contrary to what had been suggested before (e.g., Wesnousky, 2006). **On every fault I analyzed, the rupture arrest occurs at a specific place of the fault, commonly a step-over or a site characterized by a marked angle change** (bend, splay or intersection).

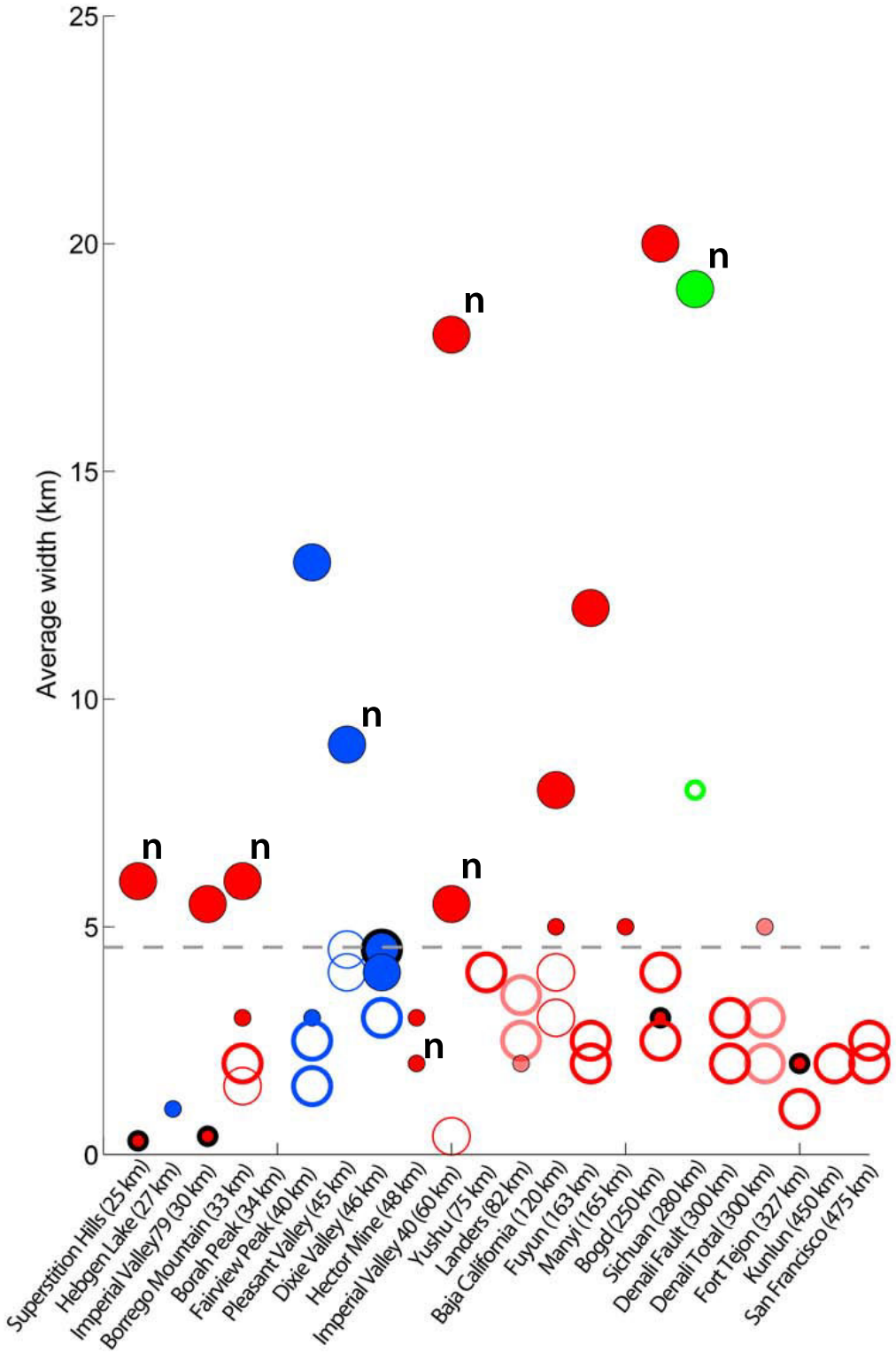
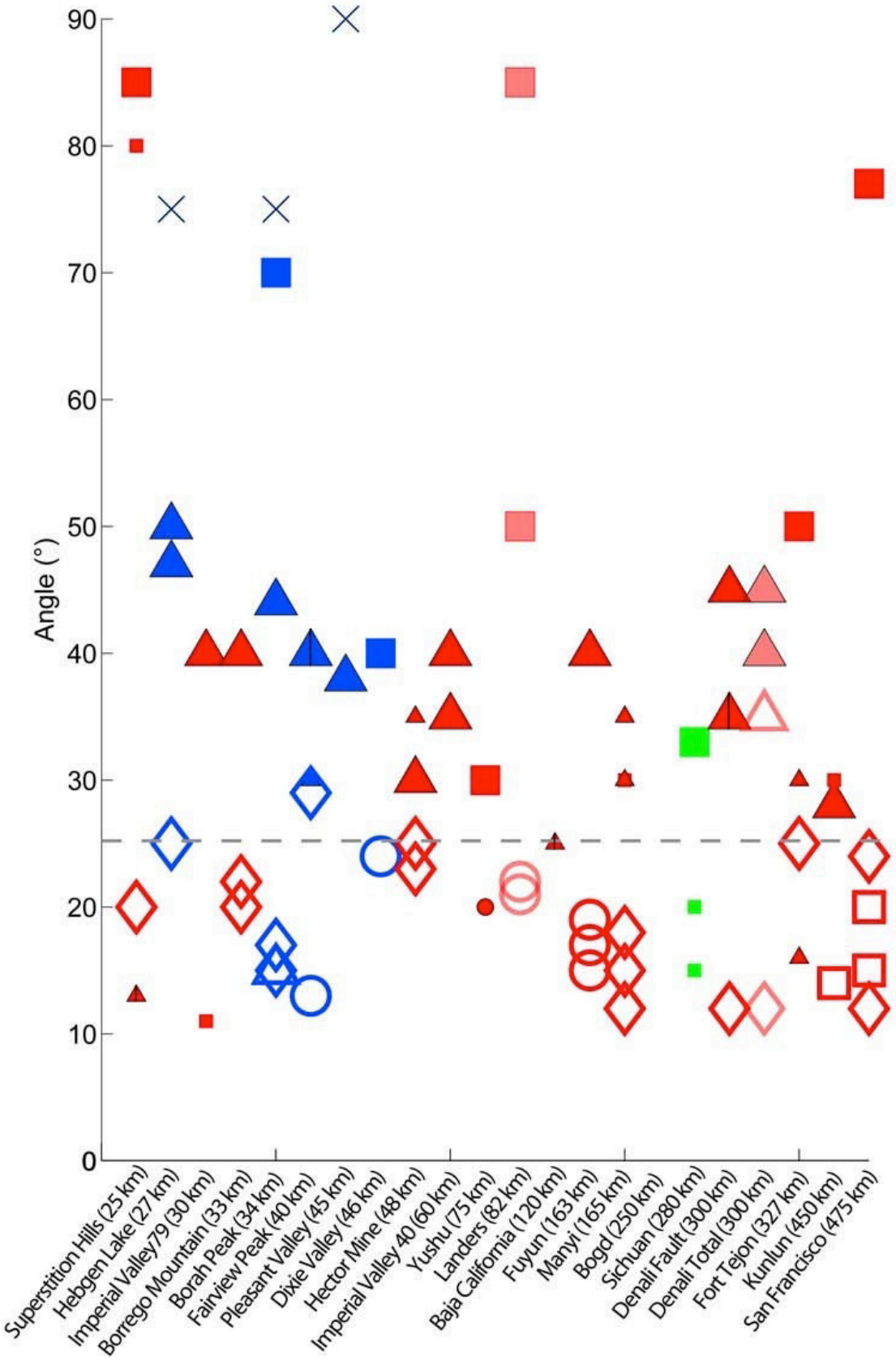


Fig.249: Average width of the step overs (across strike distance) between major segments of historical earthquake ruptures. Earthquake name and rupture length are listed on horizontal axis. The earthquake are ordered by increasing rupture length (but not scaled to distance along-axis). Discontinuities through which ruptures passed (broke through) are open symbols. Rupture arrest is shown by filled symbols. In red, blue and green are strike slip, normal and reverse ruptures. Circles have thicker contours when segments are connected. Grey dashed line indicates the apparent threshold of 4-5 km beyond which all ruptures are arrested.



Ordering by increasing length

Fig.250: same as 249 but for the angles through which the ruptures pass (empty symbols) or are arrested (solid symbols). Captions of the different symbols are in the text.

4.2. Propagation/arrest: which W and γ absolute values, and for which reasons?

Figure 249 confirms the existence of a W ~5 km threshold, as suggested in prior works: independent of the slip mode and the rupture length, **every rupture propagates across step-overs narrower than ~5 km, and is stopped at larger steps** (except the green point representing the Sichuan earthquake, and which is uncertain).

Furthermore, figure 250 shows the existence of a γ ~25° threshold: **independent of the slip mode, of the rupture length and of the type of angle change, every rupture propagates across an angle change lower than ~25-30°, and is stopped at larger angle change** (except the pale pink dot which is the Denali EQ). To our knowledge, this finding has not been described before.

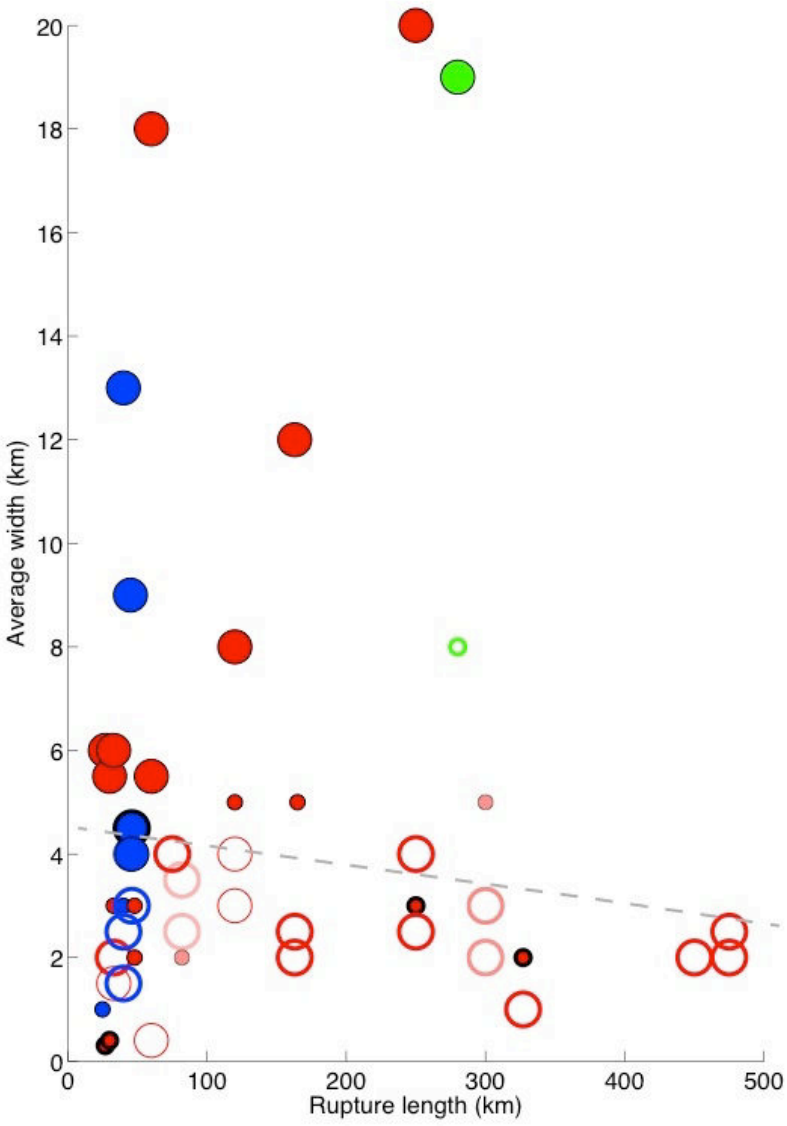


Fig.251 : step-over width as a function of the actual rupture length.

Figures 251 and 252 now show the step-over width and the angle change, respectively, as a function of the actual rupture length. Surprisingly, **the W threshold seems to decrease as the rupture length increases**. I will come back to this observation further below. On normal faults, the width of the step-overs that arrest the rupture seems to be slightly lower (~3 km) than the equivalent width on strike-slip faults (4-5 km). The results above are similar when data are discriminated by releasing/restraining character.

Figure 252 shows, on the contrary, that **the threshold angle keeps similar for all faults and ruptures, ~25° regardless of the rupture length and slip mode**. Most of the angle changes across which the ruptures pass are bends along the fault traces (diamonds). Among the angle changes that arrest the ruptures, part is genetically related to the broken fault, while another part is independent of the broken fault: most arresting angles in the range 25-50° result from splays genetically related to the fault, and generally developed at its tips (triangles). By contrast, most arresting angles in the range 70-90° result from the fault intersecting another, independent fault (squares and crosses).

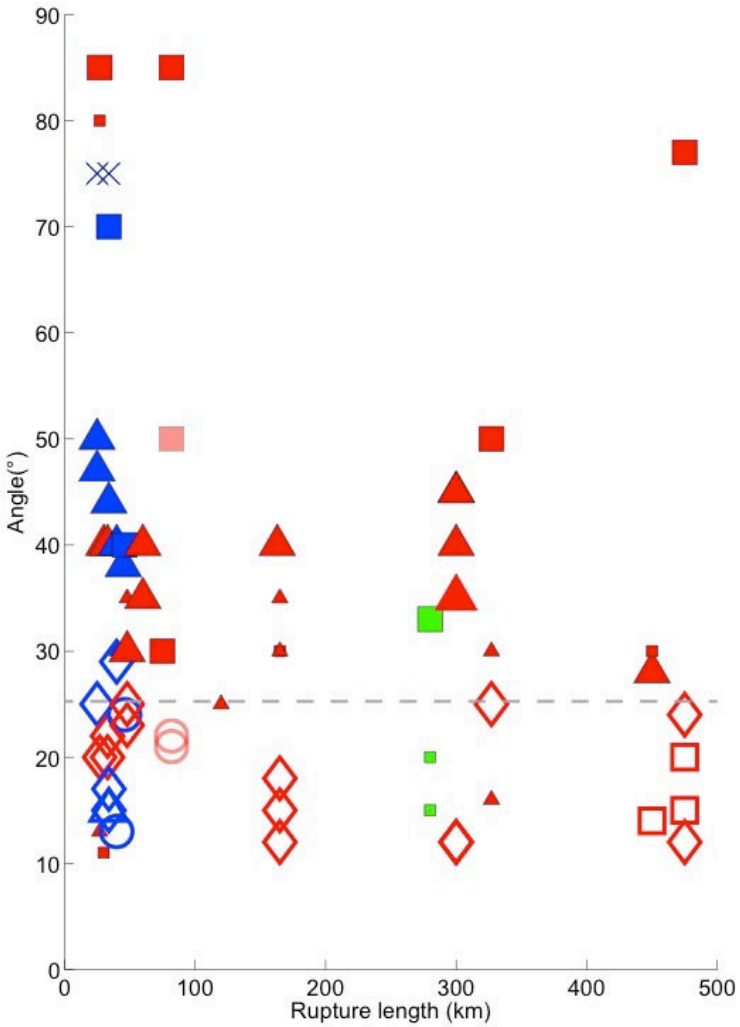


Fig.252 : angle change as a function of the actual rupture length.

Incidently, figure 252 shows another feature, i.e., the discrete distribution of the rupture lengths, all grouped at either ~20-50 km, ~160, ~300, or ~450 km. I already noted in Chapter IV (Fig.207) this discrete distribution of the rupture lengths, which I interpret as resulting from the EQs breaking a variable yet limited number of major similar-size segments along the faults on which they occur.

Figure 253 now shows the combined effect of W and g, for the ruptures where the two features –step-over and angle change, occur at the same place along the fault.

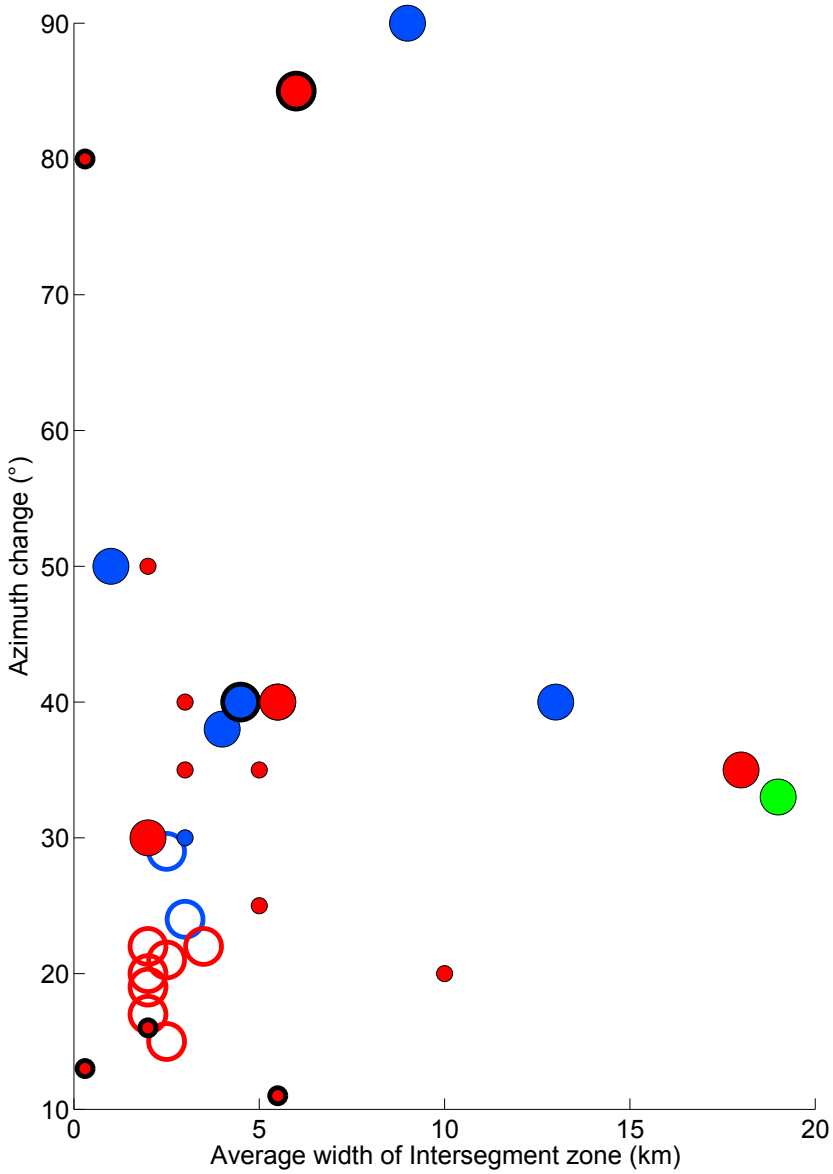


Fig. 253: combined effect of W and γ, for the ruptures where the two features –step-over and angle change, occur at the same place along the fault.

The question addressed in Figures 254 and 255 is: do the W and γ thresholds depend on the rupture directivity? I thus plot in black the W and γ values which arrest a rupture that is clearly propagating "toward them", and in grey the W and γ values beyond which the rupture simply does not extend, even though it has not (or little) propagated towards them. Figure 254 shows that the arresting step-overs which have not seen the rupture propagating towards them (or very little since lateral propagation occurs everywhere) have W widths departing from the general tendency seen in Figure 251: their W values are generally lower than expected from the general tendency.

Similarly, figure 255 shows that the arresting angles which have not seen the rupture propagating towards them (or very little) have angle values departing from the general tendency seen in Figure 252: their γ values are generally larger than expected from the general tendency, most greater than 40° (instead of greater than 25°).

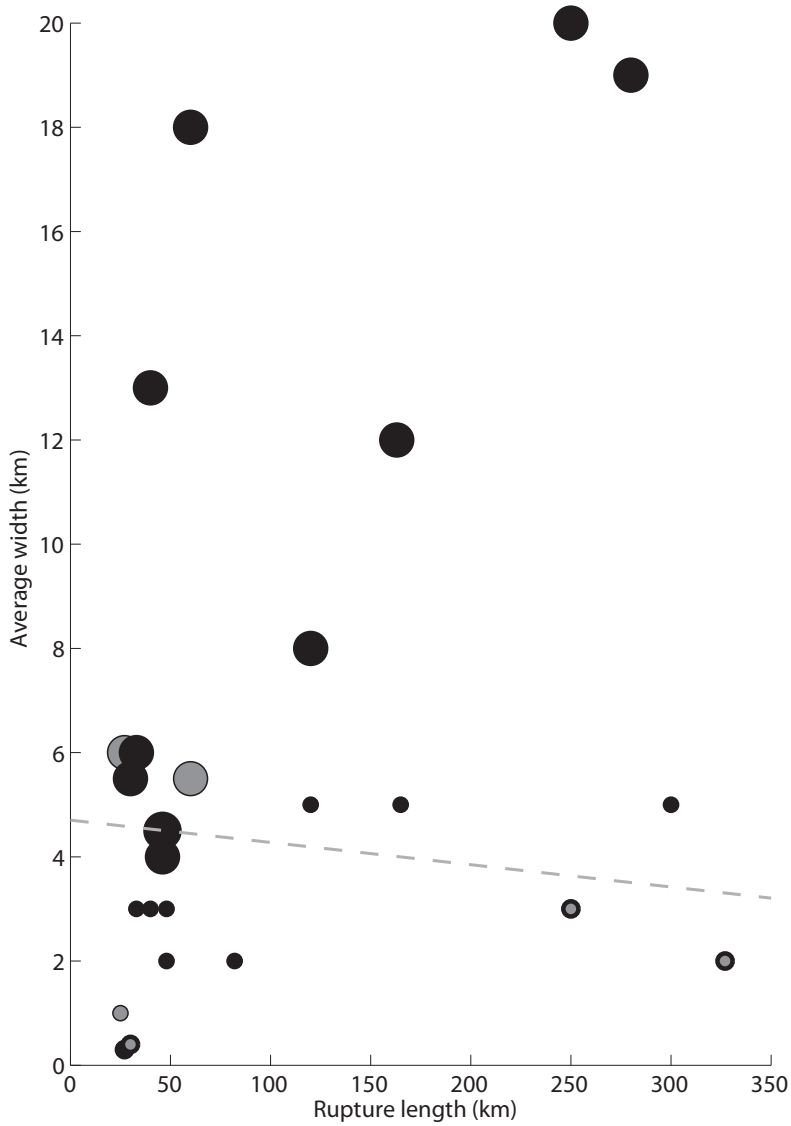


Fig.254 : in black are the W values which arrest a rupture that is clearly propagating "toward them", and in grey the W values beyond which the rupture simply does not extend, even though it has not (or little) propagated towards them.

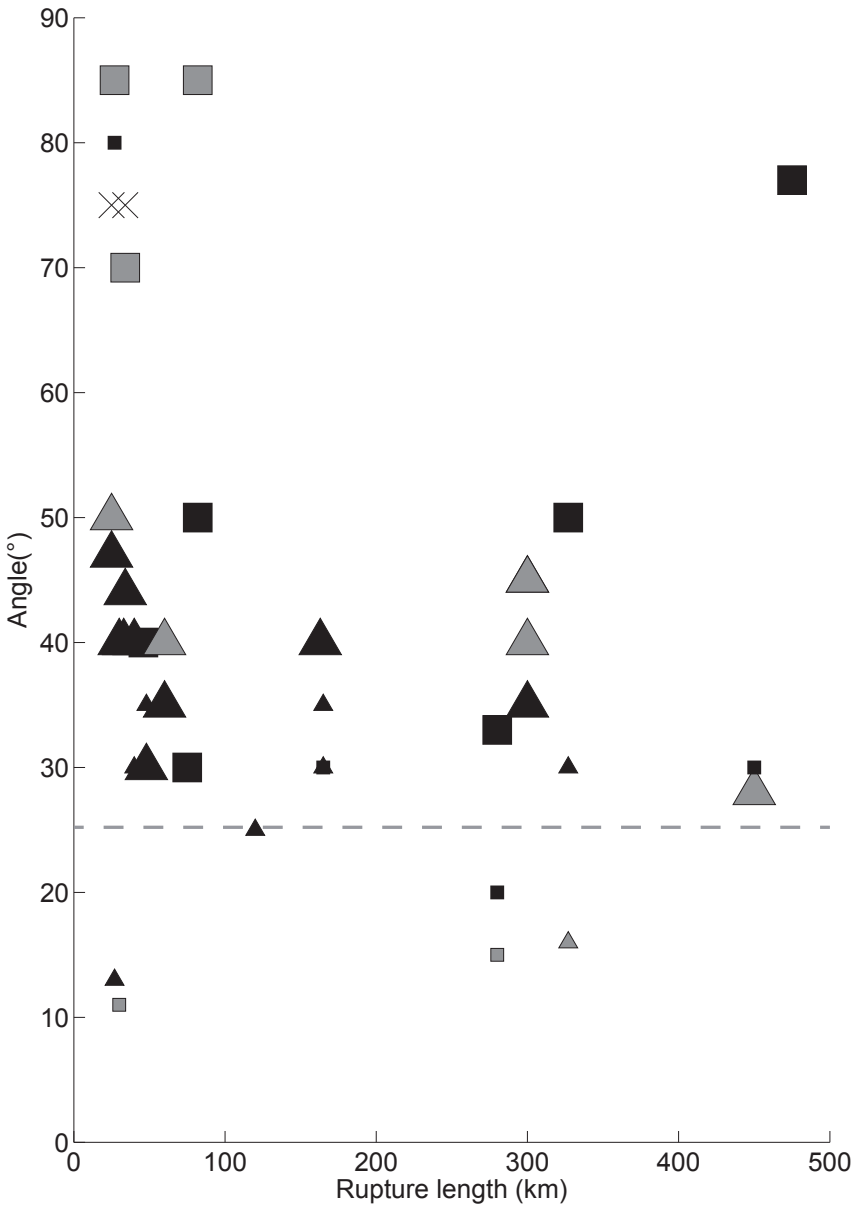


Fig.255: in black are the γ values which arrest a rupture that is clearly propagating "toward them", and in grey the γ values beyond which the rupture simply does not extend, even though it has not (or little) propagated towards them.

Figures 256 and 257 now address the question: Do the W and γ values where the ruptures propagate through depend on the cumulative length of the rupture before it reaches the zones with these values? One might expect that, as a rupture propagates and hence increases in length, it becomes more capable of passing through large step-overs or angle changes. I actually observe the opposite: as the cumulative rupture length increases, both the width of the step-overs and the angle changes across which the rupture propagates decrease. The angle evolution is not well constrained however. I suspect that the results in Figure 256 are biased by those reported in Figure 251, i.e., the threshold width decreases as the rupture length increases.

Figures 258a-b-c and 259a-b-c now address the following question: Does the threshold in W and γ values depend on the "energy" of the earthquake? One might expect that a more energetic event is more capable to propagate through a larger step-over or angle change. I approach the earthquake energy by its stress drop, itself approached by the slip to length ratio of the earthquake. Note that I consider here the surface slip-length data. Figures labeled "a" examine the effect of the overall EQ stress drop (Dmax/L ratio); figures labeled "b" the effect of the stress drop of the major asperity (i.e., the major segment hosting the largest Dmax; stress drop considered over its length); figures labeled "c" the effect of the stress drop of the major segment right before the zone where W or γ are measured (local Dmax/L). Figure 258 and 259 basically show that **the stress drop does not exert any clear control on the W and γ threshold values**. Small variations might be possible (as smaller W threshold for smaller stress drops, see Fig. 258b-c), but they are not clear. **These results suggest that the W and γ thresholds are not much related to the rupture, but are more rather controlled by the long-term fault properties**.

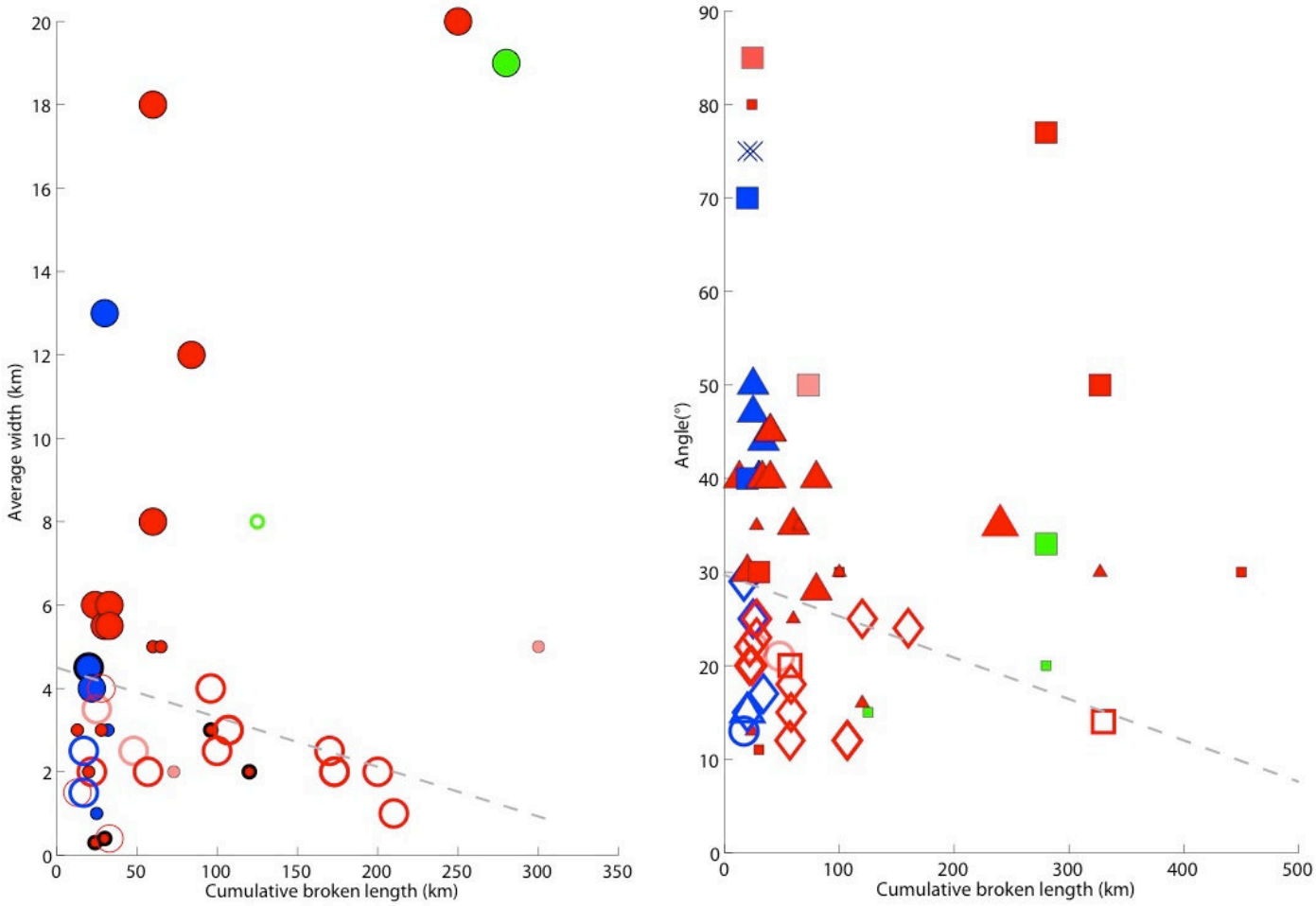
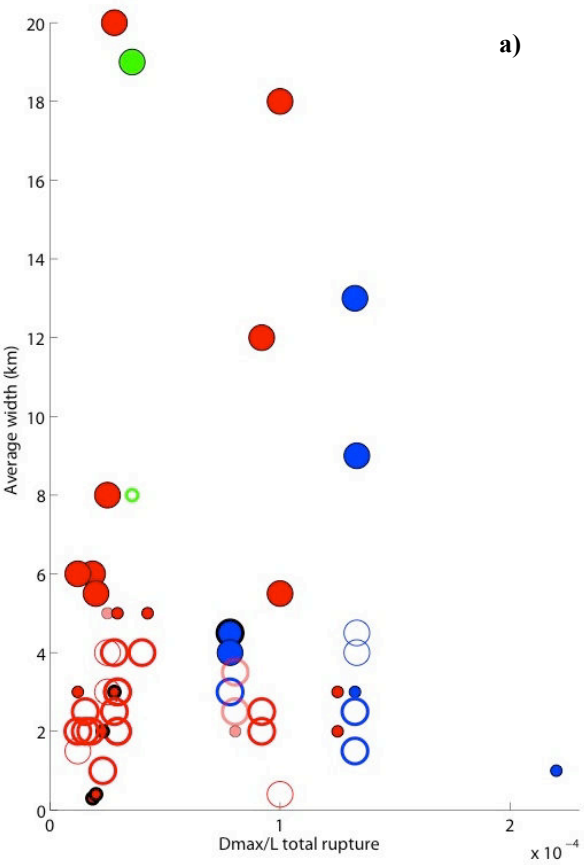
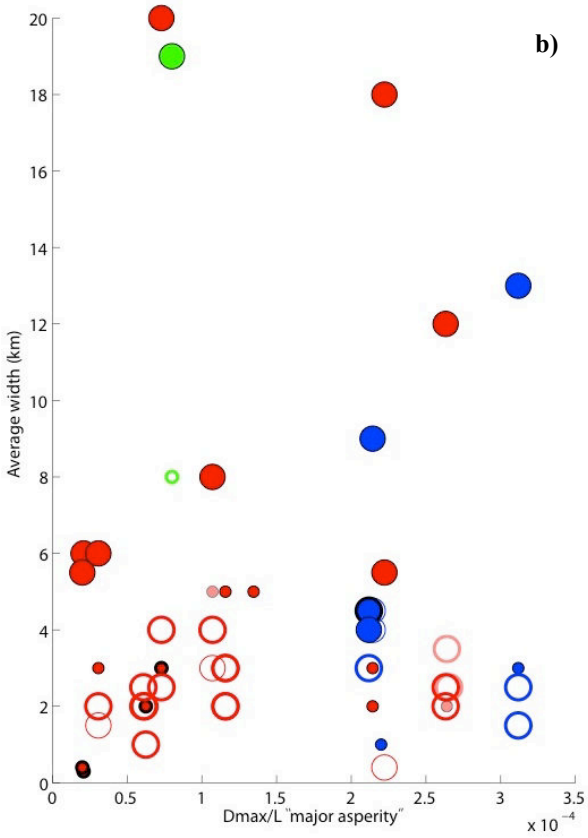


Fig. 256 (left) and 257(right) : W (256) and γ (257) values as a function of the cumulative length of the rupture before it reaches the zones with these values.





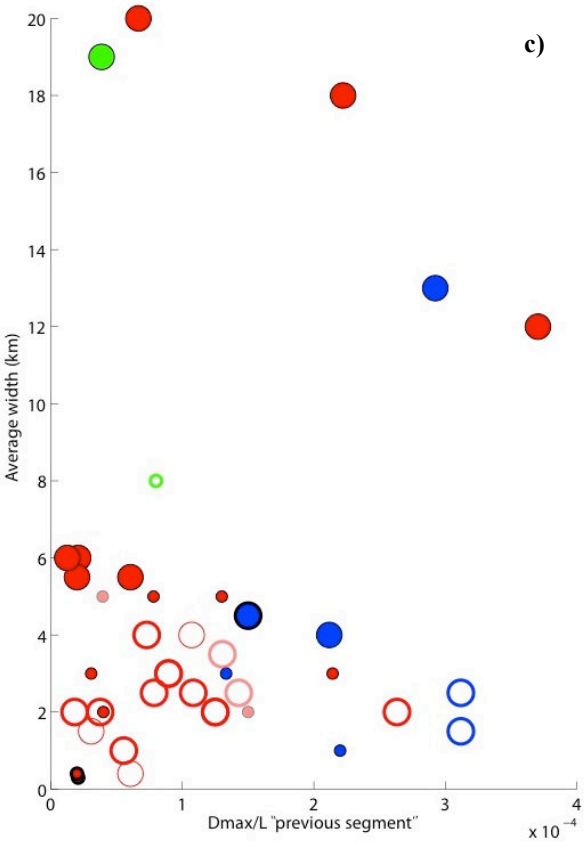


Fig.258: Impact of the EQ (a), major asperity (b) and previous segment (c) stress drop, on the W threshold.

Since we suspect that the W and γ thresholds mainly depend on the intrinsic properties of the long-term faults, figures 260a-b and 261a-b now examine their variation as a function of the structural maturity of the ruptured faults. The maturity is defined in the IDs. Figure 260b suggests that **the W threshold value beyond which a ruptured is arrested decreases with fault maturity.** By contrast, **the angle threshold keeps similar regardless of the maturity of the faults**. Figure 260a additionally suggests that ruptures on immature faults are more frequently arrested by markedly oblique independent faults (squares and crosses), whereas angular rupture arrests on mature faults more commonly occur at fault splays (triangles). Furthermore, the splay angle seems to increase on strike-slip faults as they become more mature (red triangles).

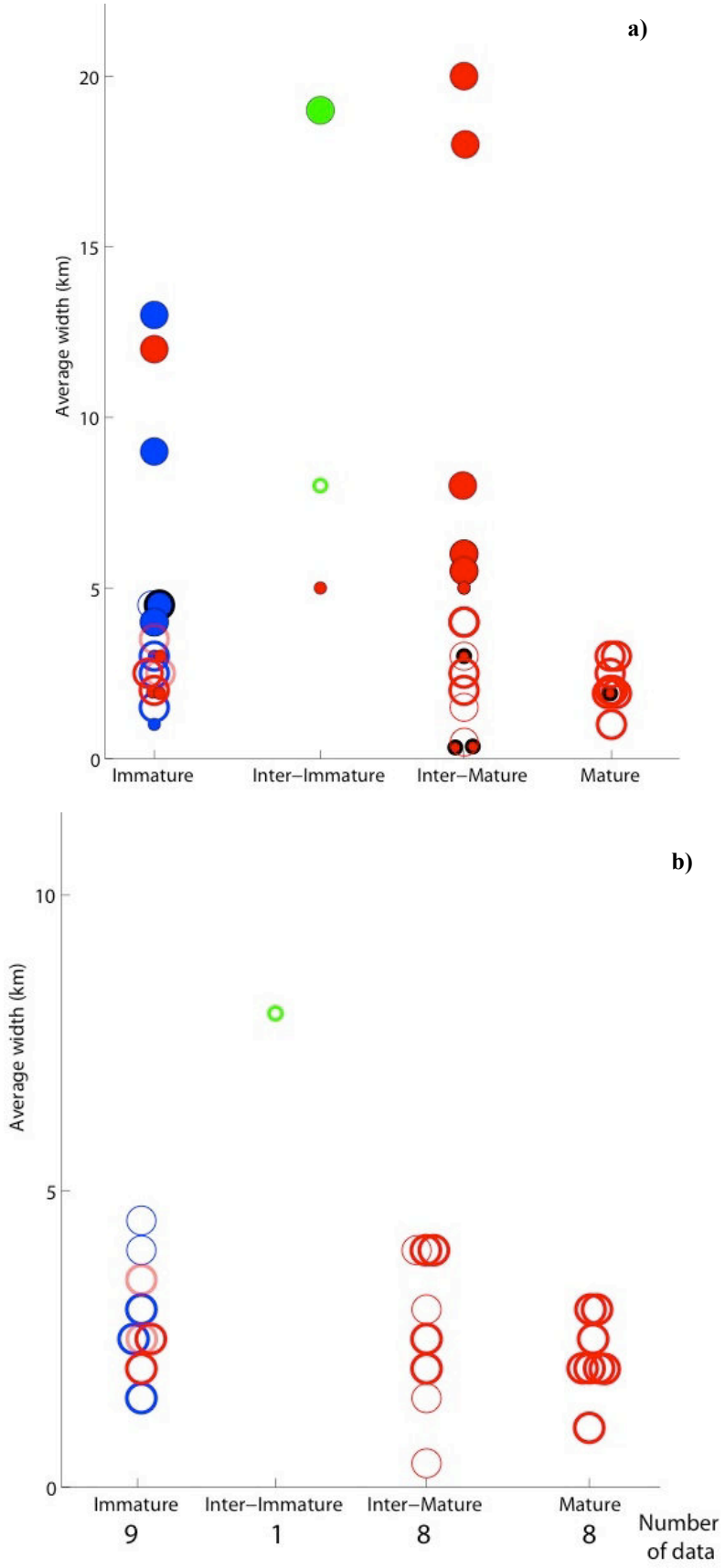


Fig.260: (a) W threshold as a function of fault maturity. (b) closer view of (a) only for discontinuities through which rupture passed (broke through)

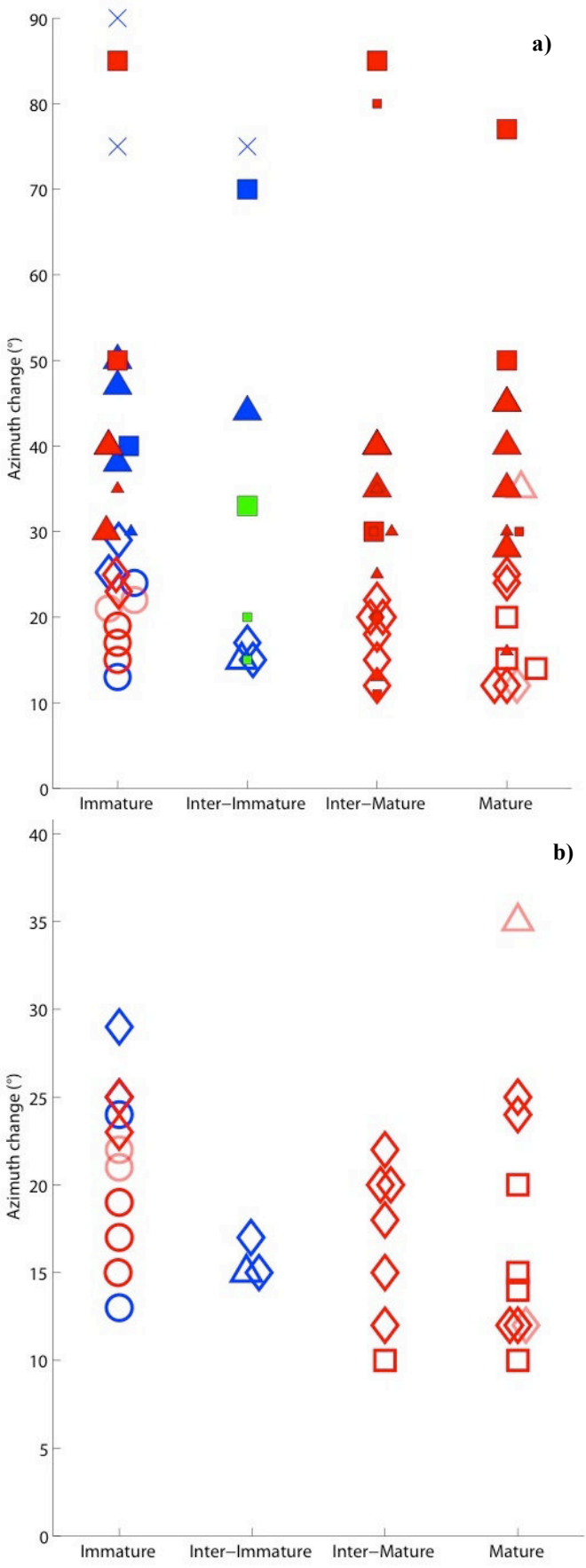


Fig.261: (a) : γ thershold as a function of the structural maturity of the broken fault. (b) closer view of (a) only for discontinuities through which rupture passed (broke through)

From this part, I conclude that **the absolute values of the W and g thresholds primarily depend on the long-term faults properties; not much on the rupture properties**.

To verify this finding, I have measured the width of all the step-overs (ignoring the very smallest with W< 0.3 km) that exist along the entire length of the faults under analysis (i.e., also outside of their rupture zone). Note that I only consider here the actual step-overs, and hence do not include the steps to the closest synthetic faults (whereas these fault-to-fault steps are considered in all the other graphs). Figure 262 shows the results, i.e., the step-over widths plotted as a function of the structural maturity of the faults. The figure confirms that the width of the step-overs decreases as the faults become more mature. Our interpretation is that, as a fault becomes more mature, its smaller step-overs are smoothed out (this has already been shown by Stirling et al., 1996). Meanwhile, its larger step-overs are replaced by the fault trace cutting through them (as the segments strongly connect to each other); bends in the fault trace therefore replace large step-over widths. Only intermediate size step-overs might subsist from place to place along the fault. This might explain why only moderate step-over widths are observed on mature faults, whereas step-overs are larger on young immature faults. By contrast, angle changes seem to keep similar regardless of the fault maturity (I haven't got the time to check this carefully however).

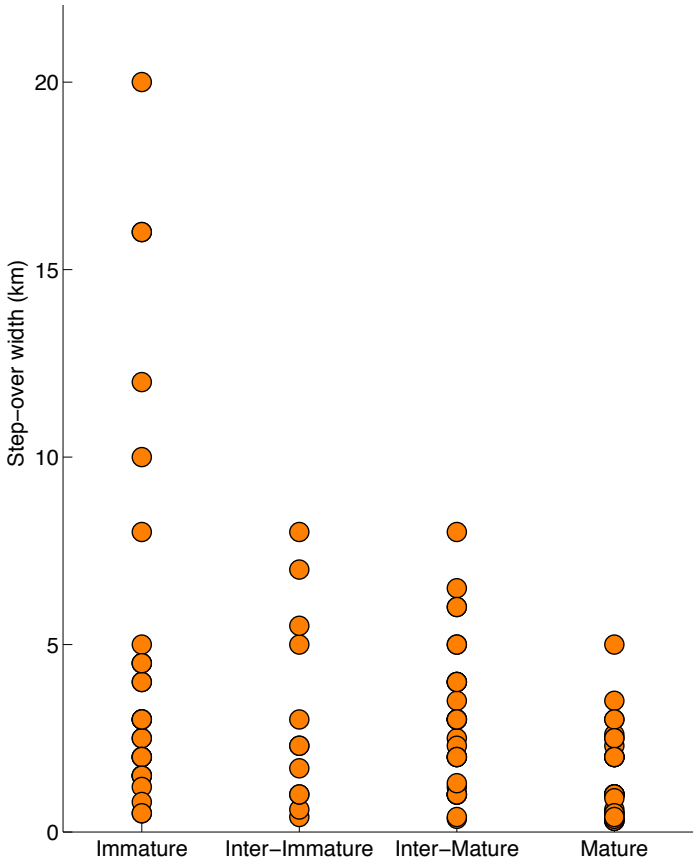


Fig.262 : step-over widths as a function of the structural maturity of the faults (step-over data all along the faults; no consideration here of the EQ ruptures).

Because it is difficult to believe that the earthquake energy does not influence the capacity of the rupture to propagate through larger or more complex discontinuities along the fault, I analyze the data below in a complementary way.

4.3. The relative importance of W on the broken fault

The question posed here is: What do the step-overs across which the rupture propagates represent on the fault? To examine this question, I normalize W to the length of the entire long-term fault.

I first examine the relative size of all the step-overs that exist along the entire length of the faults. Again, I only consider here the actual step-overs, and hence do not include the steps to

the closest synthetic faults (whereas these fault-to-fault steps are considered in all the other graphs). Figure 263 shows the step-over widths normalized to the fault length, plotted as a function of the fault maturity. As expected, **the relative 'importance' of the step-overs in terms of size decreases with fault maturity**. The relative width of the step-overs is so small on the mature faults (< 1% of L) that it is expected that the step-overs are not to play a major role in arresting a propagating earthquake rupture. In contrast, the relative size of the step-overs is very large on immature faults, up to almost 10% of L, and therefore, it is expected that step-overs are a major feature that strongly control the rupture propagation on immature faults.

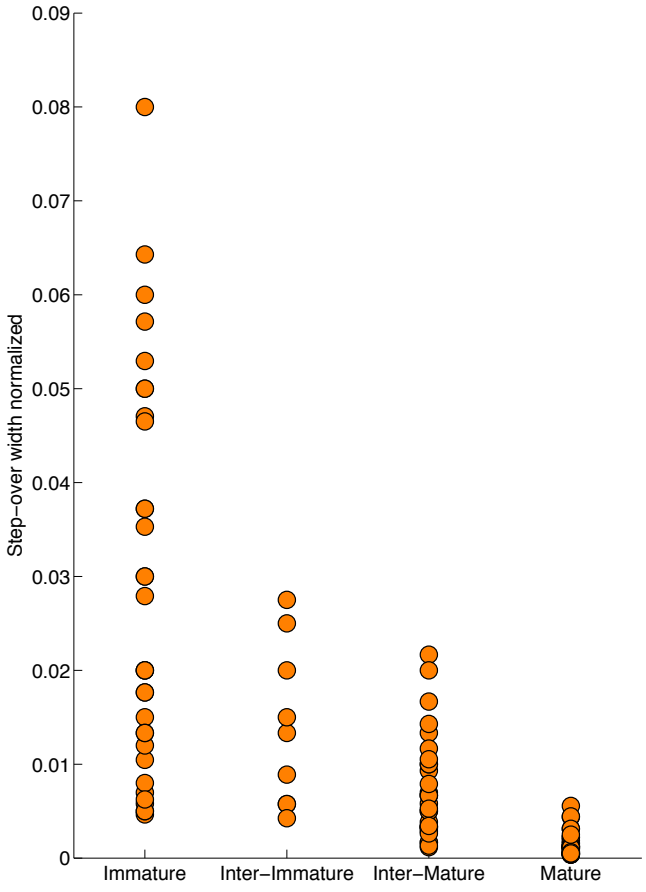


Fig.263: step-over widths normalized to the fault length, plotted as a function of the fault maturity (all step-overs along all faults, no consideration of EQ ruptures here).

Figures 264 and 265 now examine the relative size of the step-overs (and fault-to-fault steps) which arrest or not the rupture propagation. As expected, the figures show that, as the rupture length increases, the relative size of the step-overs that are broken by the rupture decreases; this is because both the absolute and the relative widths of the step-overs decrease as the faults become more mature and hence longer.

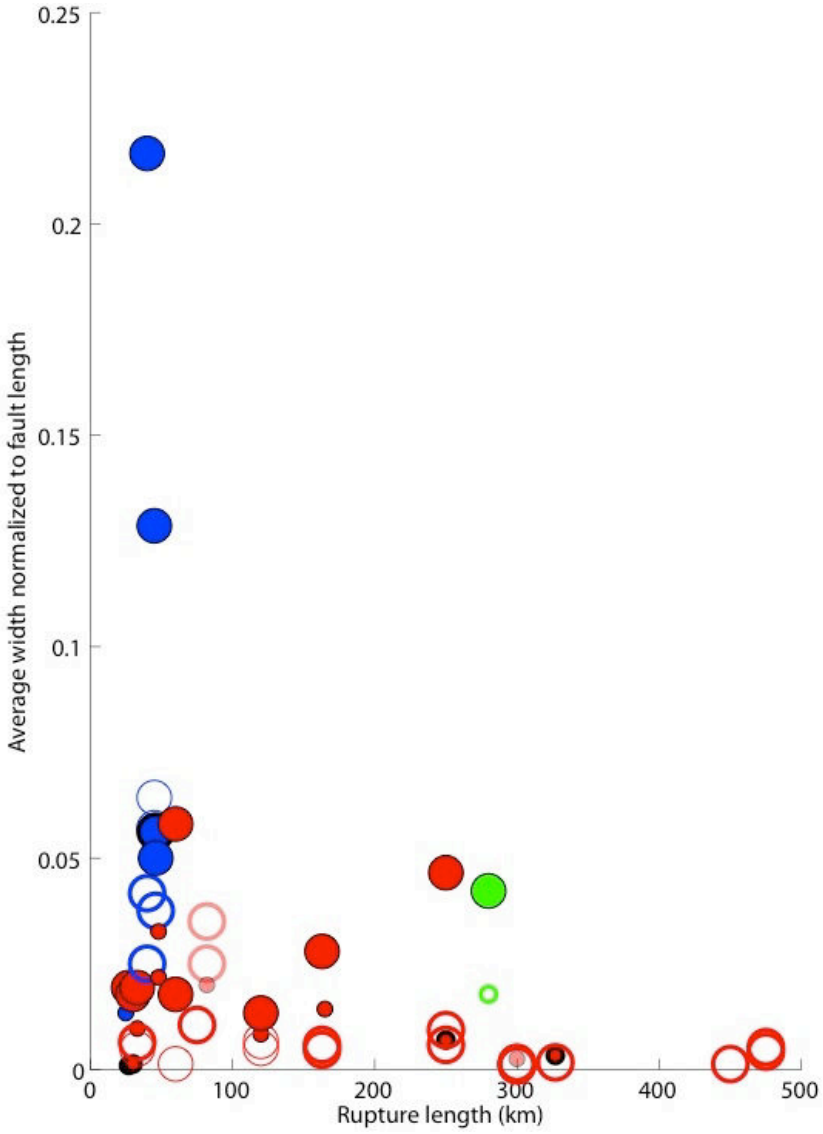


Fig.264: relative size of the step-overs (and fault-to-fault steps) which arrest or not the rupture propagation.

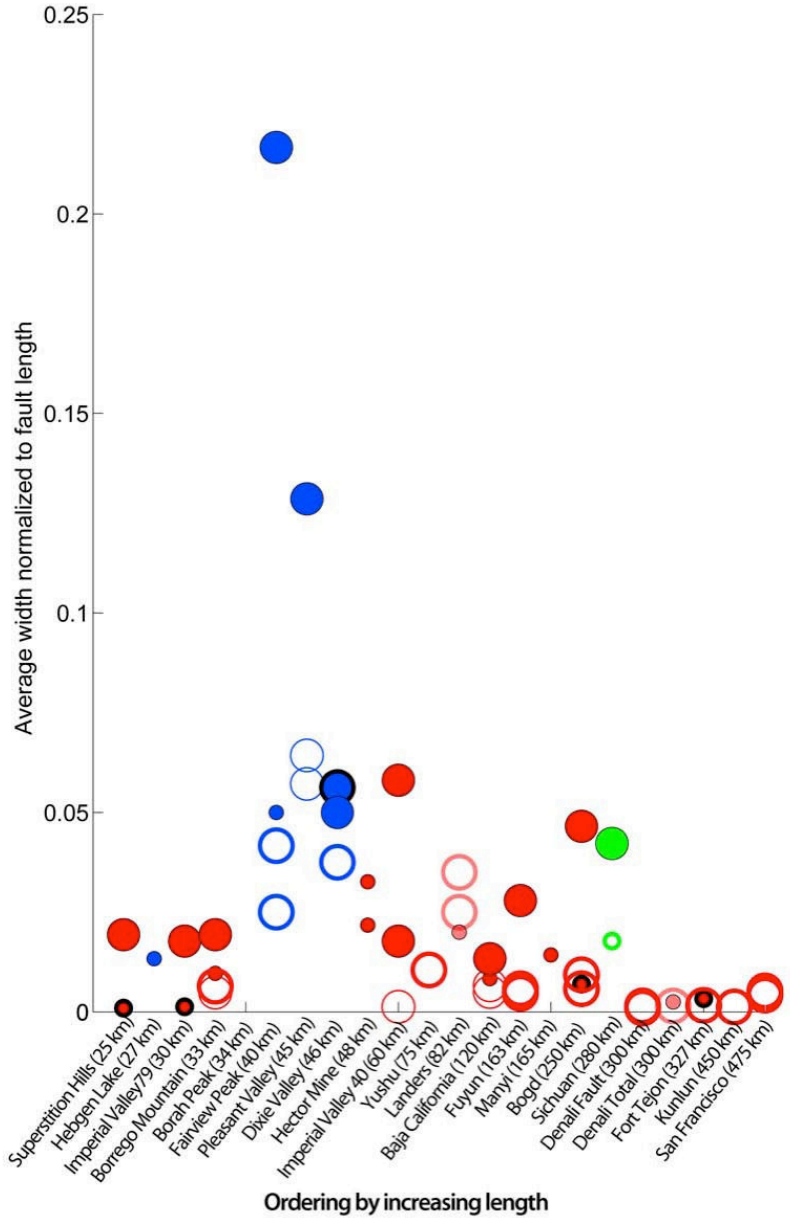
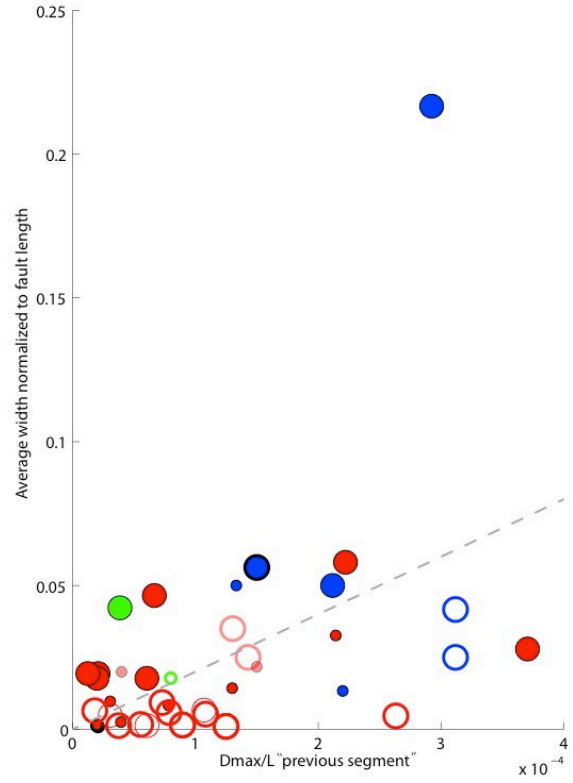
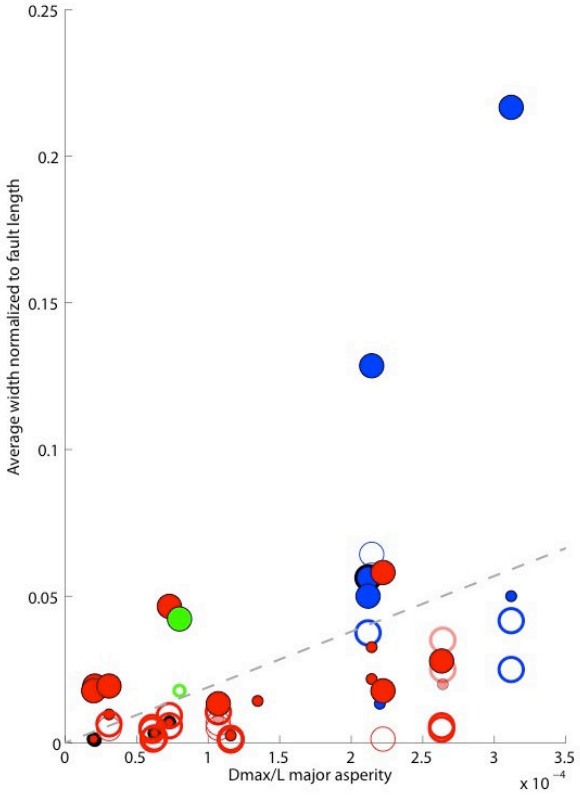


Figure.265: Same as 264 (relative size of the step-overs (and fault-to-fault steps) which arrest or not the rupture propagation) with EQs by increasing L.

Figures 266a-b-c are more informative. They show that, **as the EQ stress drop increases (either global, maximum, or local), the earthquake becomes capable of breaking through a step-over of larger relative size along the fault**. Therefore, the EQ energy does have an impact on the widths of the step-overs that can be broken: the larger step-overs on a given fault can be broken provided that the earthquake has a large stress drop.





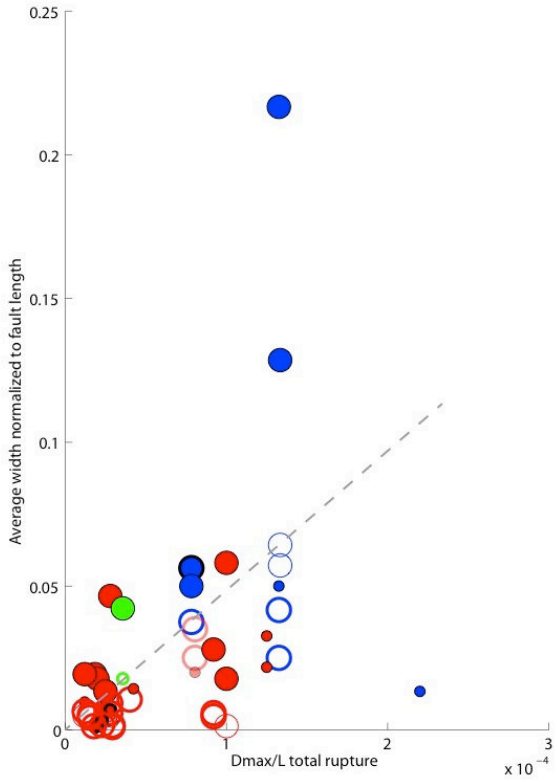


Fig.266: relative width of step-overs passed or not passed by the EQ ruptures, depending on the EQ (a), major asperity (b) or previous segment (c) stress drop.

Finally, Figures 267a-b show that **the relative size of the step-overs that can be passed through by an earthquake decreases with the degree of maturity of the broken fault**. Figure 263 showed before that immature faults have large step-overs, having widths up to ~8 % of the fault length; figure 267b now shows that all these large sizes of step-overs can be broken (at least up to W equaling ~7 % of the fault length). Mature faults have narrower step-overs (Fig. 263), and Fig. 267b shows that all these step-overs can be broken also.

It thus seems that, knowing the maturity of a fault, one can anticipate the maximum width of the step-overs across which a rupture can propagate: about 7-8 % of the fault length on immature faults, ~1-2 % of the fault length on intermediate-maturity faults, and less than 1 % of the fault length on mature faults. It is likely that, on any of these fault types, the larger the stress drop of the EQ, the wider the step that can be propagated through (in the above ranges).

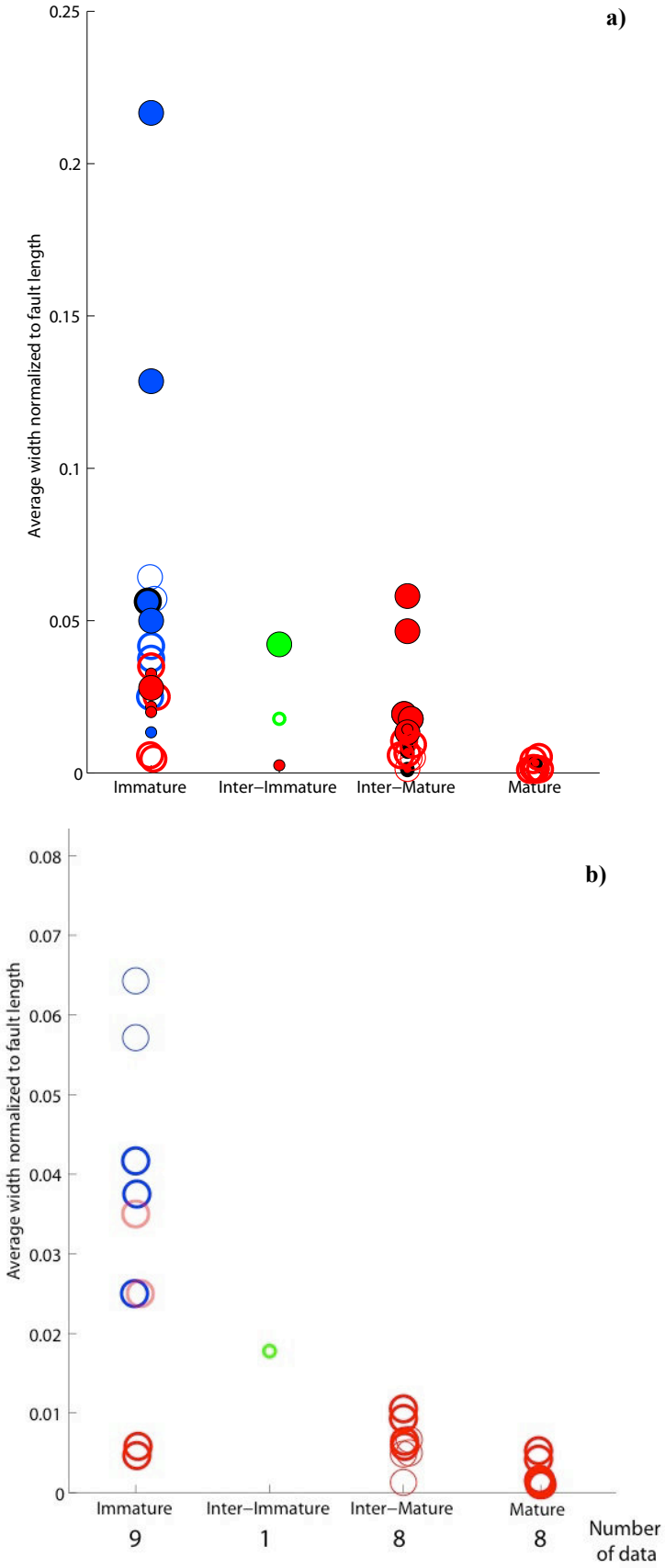


Fig.267: (a) relative width of step-overs passed or not passed by the ruptures, as a function of the structural maturity of the broken faults. (b) closer view of (a) only for discontinuities through which rupture passed (broke through).

4.4. Rupture initiation

Figure 197 in chapter III synthesizes the location of the EQ epicenters with respect to: the different fault segments; the zone of maximum coseismic slip; the direction of long-term, lateral propagation of the faults. I have shown that, in all the EQ cases that I analyzed, the EQ nucleation occurred in or nearby a connection zone between two long-term segments of the fault (major or secondary segments). Additionally, in all cases, the two segments were likely having a different degree of structural maturity; one had formed earlier than the other one, as a result of the long-term lateral propagation and hence lengthening of the fault. Figure 268 now shows detailed maps of the nucleation zones (maps from the IDs in Chapter II). In all the analyzed EQ cases, we note the existence, close to the epicenter, of a secondary fault oblique to the broken main fault. The oblique structures are dip-slip faults in more than 70% of the cases. They form a 40-50° angle to the main fault trace in 60% of the EQ cases. On the most mature faults, that angle is smaller, on average 15-30°. In more rare cases, the angle is very high, 70-85°. As these oblique faults are secondary features compared to the broken master faults, they likely are more immature than the master faults they connect with.

Therefore, **earthquakes seem to nucleate at very specific sites along the faults, characterized by:**

- **A relay between two large-scale segments (since only major and secondary segments have been observed here) having a different structural maturity;**
- **The intersection of the master fault with an oblique secondary fault forming an angle generally of 40-50° and in most cases > 40° to the main fault, and having generally a dip-slip component.**

I will come back to these findings in the discussion section in Chapter VII.

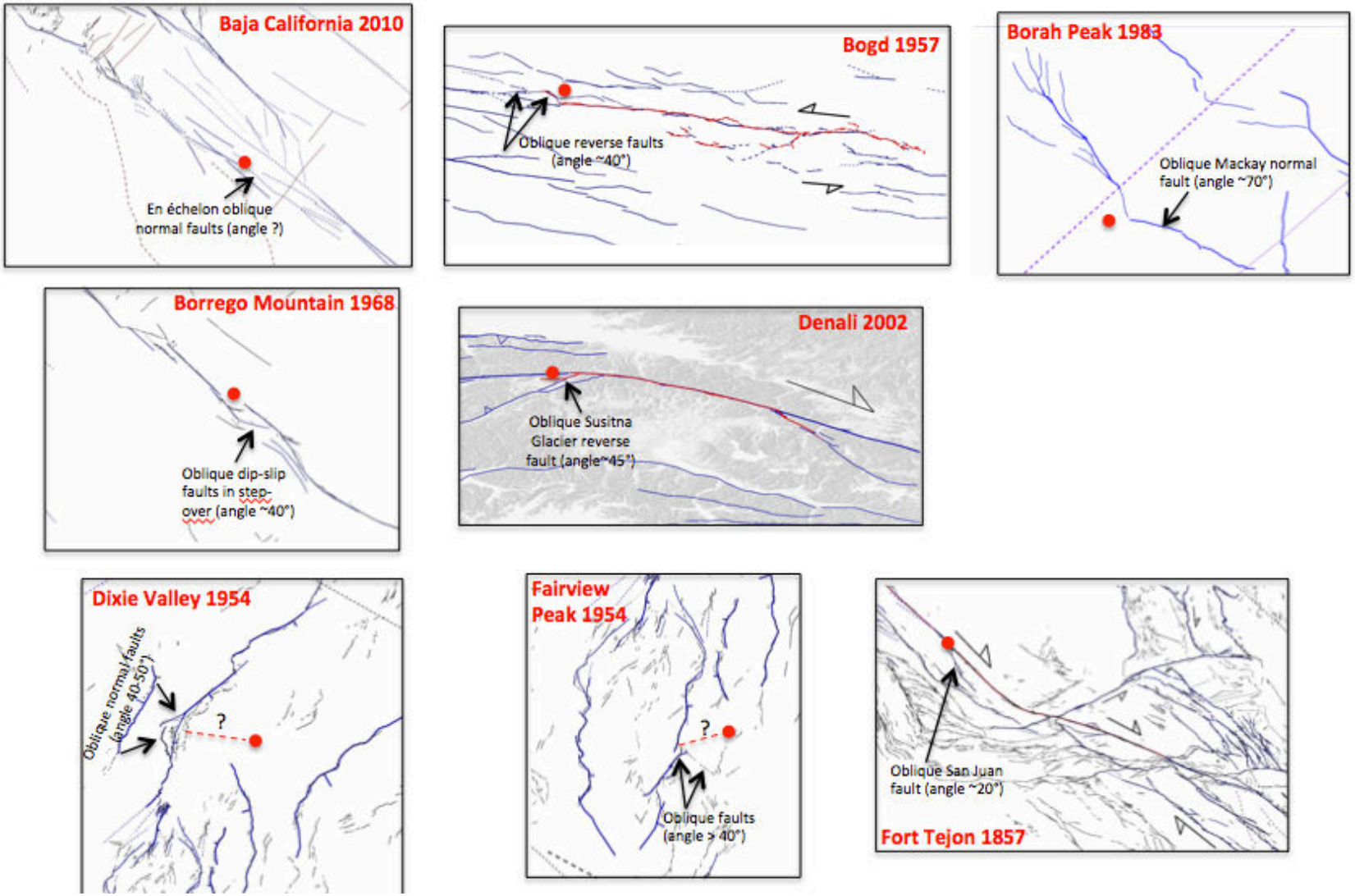


Fig.268: See caption below

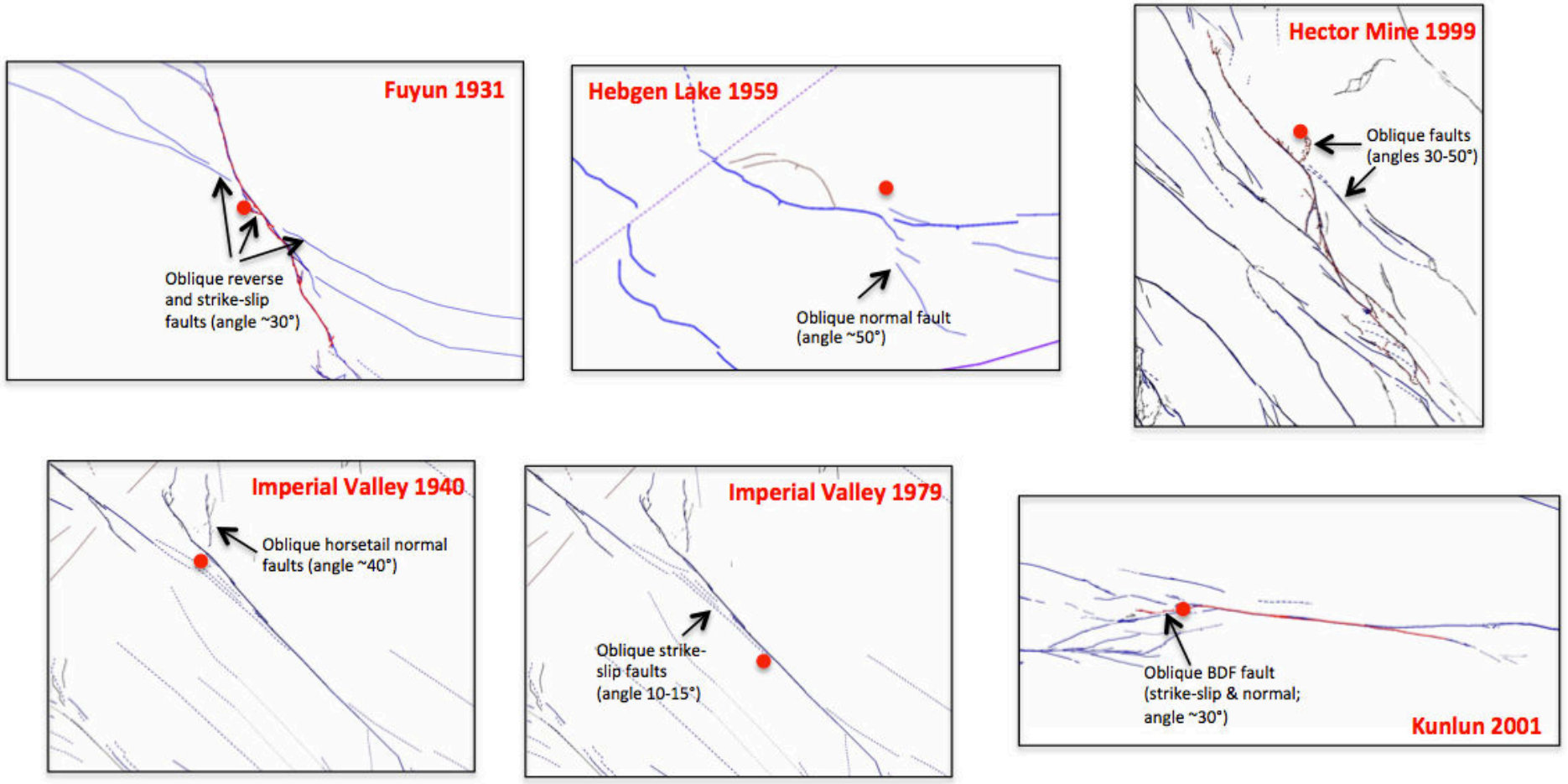


Fig.268: See caption below.

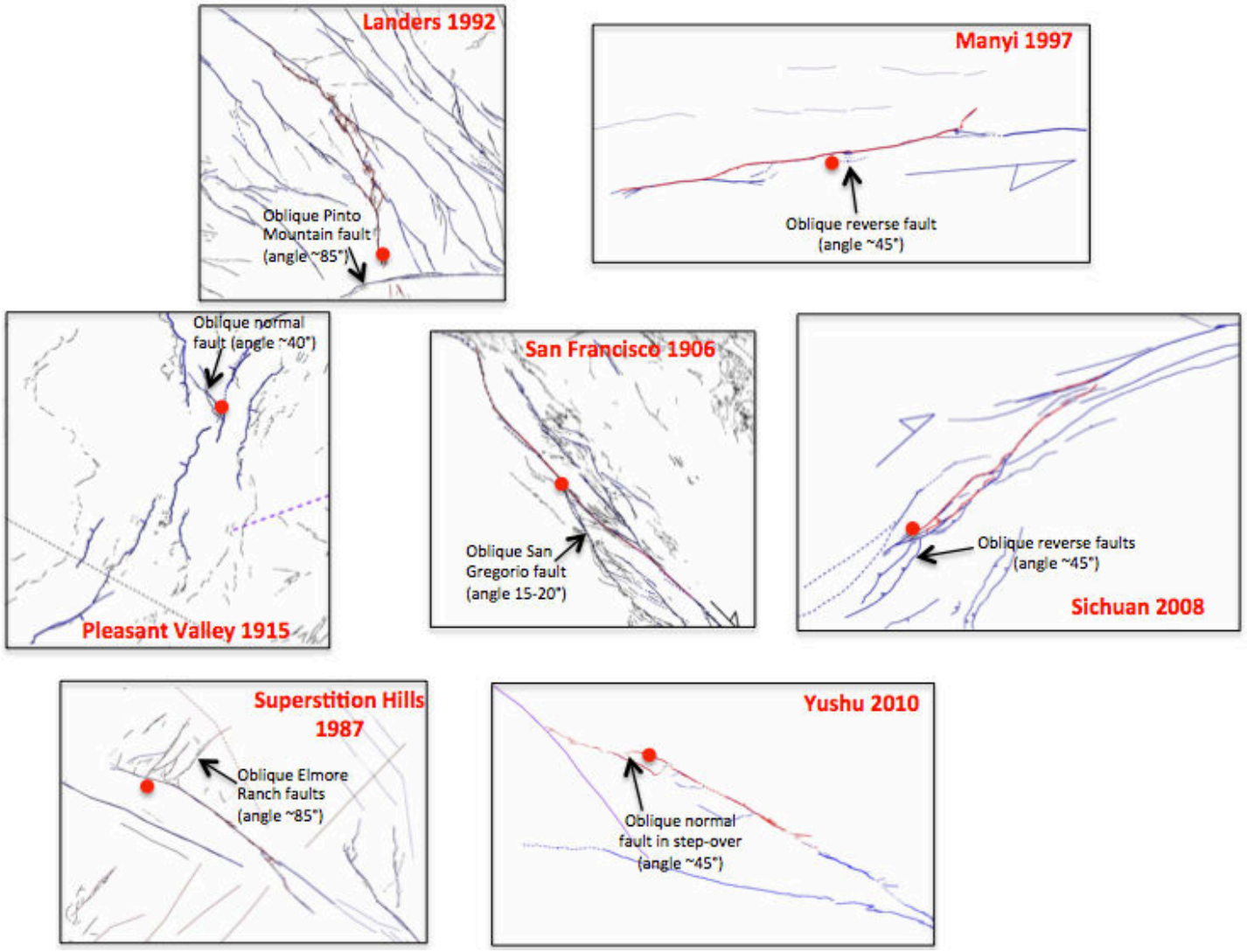


Fig.268: detailed maps of the nucleation zones of the EQs anbalyzed in the IDs in Chapter II. In all the analyzed EQ cases, we note the existence, close to the epicenter, of a secondary fault oblique to the broken main fault. . The angle of obliquity is indicated.

4.5 Synthesis of major results

This part of the work suggests a few important results:

- At the time an EQ occurs, the long-term fault which is involved has pre-established properties including a specific architecture and a proper degree of structural maturity. In particular, the number (not shown directly here, but see Stirling et al., 1996 and discussion above) and size of the step-overs that might be capable to arrest the rupture are pre-defined by the degree of structural maturity of the fault. **The size of the possible EQ jumps is thus primarily a property of the fault, not (much) of the EQ.** This result contradicts the dynamic rupture models which consider the step-over jumps as a fundamental outcome of the EQ rupture dynamics (e.g., Oglesby, 2008).

- **The step-over size which an EQ might encounter in its lateral propagation thus varies between up to ~20 km on immature faults, down to at most 4-5 km on mature faults.** This is because the larger step-overs which likely exist at the immature stage of any fault are progressively replaced, as the fault becomes more mature, by the continuous fault trace connecting the two segments (double bend in the fault trace).

- Expressed in terms of relative size, **the step-over size which an EQ might encounter in its lateral propagation varies between ~8 % of the fault length on immature faults, down to less than 1 % of the fault length on mature faults.** In the EQ collection that we analyzed, step-overs as large as ~7 % of the fault length did not arrest the rupture in some cases of immature faults, whereas the largest step-overs on mature faults did not arrest the rupture either in some cases. **This suggests that the size of the step-overs is not a unique and sufficient feature to arrest a rupture.**

- Independent of the maturity of a fault, **a larger stress drop EQ has the ability to jump larger step-overs (relative to the fault length) than would a smaller stress drop EQ.**

- EQ rupture seems to be also sensitive to the obliquity of the fault traces on which it propagates. **Angle changes of more than ~25° arrest the ruptures in the majority of cases.** This angle threshold does not seem to depend on the fault maturity. But more work needs to be done to validate this point.

- The question of the impact of the angle changes is complicated by the fact that **there exists different types of angle changes: bends in the main fault trace, splaying of the main fault into genetically-related oblique faults, intersection of the main fault with oblique**

faults not necessarily genetically-related to the main fault. We need to perform more work to explore the impact of these different types of angle changes. Similar values of angle changes seem to arrest or not to arrest the ruptures along certain faults (such as the big bend in the San Andreas trace, or the small oblique faults north at the Landers rupture).

- The arrest of an EQ rupture thus depends strongly on the more or less combined existence of a step-over and of an angle change. However, it is likely that **other features play a significant role**, such as changes in the fault dip and in the slip vector, the degree of mechanical coupling between the master fault and the adjacent secondary faults, the fault abutting specific rheological or mechanical discontinuities (such as creep zones, volcanic zones, ancient shear planes, etc), etc.
- **The EQs initiate at specific places along the faults. Those are connection zones between two large-scale segments of the fault, having a different structural maturity. The EQ nucleation also seems to require the existence, in these inter-segment zones, of a >40° oblique, preferentially dip-slip secondary fault intersecting the master fault** (this somehow meets the conclusions of the numerical models of Umeda et al., 1996).

CHAPTER VII. SYNTHESIS OF MAJOR RESULTS, DISCUSSION AND PERSPECTIVES

In this final chapter, I provide a synthesis of the major results that arise from my PhD work, I elaborate a short discussion on a few points dealing with the implications of these results on the understanding of the EQ rupture, and I open a few perspectives for future work.

1. Synthesis of major results

In the chapters before, I have shown the following major points:

- **Long-term geological continental faults do have a number of generic properties**, independent of scale, slip mode, location and context. Among these properties, they have: i) a similar architecture at the surface, made of a master fault or fault zone associated with networks of secondary, generally oblique faults which altogether show similar patterns at the various scales. The secondary networks commonly splay from the master fault, forming fairly triangular zones in map view on one or both sides of the master fault. These splaying networks likely accommodate the damage of the crust that any fault produces at it grows in both slip and length. Consequently, the architecture of the splaying networks indicates the direction of long-term lateral propagation of the faults. Splay faults thus exist associated with any slip-mode fault, strike-slip, reverse, and normal; ii) a similar lateral segmentation of the fault traces, at least at the largest scales: independent of its length and slip mode, every continental fault is divided into the same, limited number of major segments, in the range 2-5. Because the number of major segments is self-similar, their length is not. Each major segment seems itself divided into 2-5 secondary segments. Our analysis does not allow to examine whether the lateral fault segmentation keeps similar at smaller scales; iii) the nature and relative size of the inter-segment zones that separate the successive major and secondary segments are similar along the faults; the relative size slightly varies however depending on the structural maturity of the fault (See below); iv) cumulative slip profiles on long-term faults also have a similar envelope shape, although I did not show it in this work (See Fig.25 in Chapter II); independent on the fault size, slip mode, location and context, the cumulative slip-length profile is triangular and asymmetric overall, in the majority of fault cases (> 70% in Manighetti et al., 2009).

- **Geological faults evolve in space and time, and this evolution can be described as the "structural maturity" of the faults**. I have shown that the structural maturity results from a continuum in the fault growth, and can be approached through several fault parameters such as the fault initiation age, the fault length, the fault maximum cumulative slip, and the fault slip rate. Interestingly, I have shown that, the more mature is a fault, the faster it slips. This shows that **the structural maturity of the faults is an important factor that controls their overall behavior**. Furthermore, **simple fault parameters such as those listed above can be used independently or collectively to assess the structural maturity of a long-term fault**.

- **The greater maturity of a fault results in different typical features**, such as: i) a more linear and more continuous surface (and depth) trace; ii) fault segments being more strongly connected to each other and hence forming longer and more continuous fault pieces; iii) step-overs being narrower (step-overs are up to ~20 km wide on immature faults, compared to up to ~5 km on mature faults), and hence representing much smaller discontinuities along the fault (the step-over width is ~10 % of the fault length on immature faults, while it is at most 1 % of the fault length on mature faults); iv) existence of rounded double bends in the fault trace; v) development of splay faults at the master fault tip that seem to be more oblique than the splays developed on immature faults; vi) a slip rate much faster (both current and long-term).

- Because the geological faults grow in both slip and length over the long-term, most of the faults, especially the longest, have sections which formed earlier in the fault history and sections which formed more recently. Therefore, **the structural maturity of the faults also varies along their length, decreasing in the sense of long-term lateral propagation**, with implications on the properties of the fault segments and of the inter-segments.

- Every geological fault is a 3D object, made of a master fault connected with a myriad of secondary faults and likely other deformation features (fractures, small cracks, etc) which extend in a broad volume around the master fault. **The crustal rocks that embed the faults are thus markedly heterogeneous and damaged by the secondary faults** (and other types of deformation).

- **The large EQs (Mw ≥ ~6) also have a number of generic properties**, among which: i) the coseismic slip-length profiles have a similar overall shape –basically triangular and more or less asymmetric, independent of the EQ magnitudes, slip modes, locations and contexts, and whether the slip profiles are measured at surface or inferred at depth. The same observation is done for the coseismic slip-width profiles; ii) the broken width is found to decrease with the coseismic slip decrease, in same proportion for most EQs; iii) independent on the EQ magnitudes, slip modes, locations and contexts, the slip-length ratio of the EQs obeys the same four functions; iv) independent on the EQ magnitudes, slip modes, locations and contexts, the EQs break at most 1-5 major segments along a fault. Furthermore these segments have a maximum length of ~150 km. Each seems to roughly behave as an elastic crack (See below); v) independent on the EQ magnitudes, slip modes, locations and contexts, the distance between the hypocenter and the zone of maximum coseismic slip is similar, less than 30% of the diagonal rupture length in most cases; vi) independent on the EQ magnitudes, slip modes, locations and contexts, the static stress drop of the total ruptures is fairly constant, in the range 0.3-9 MPa and on average ~3 MPa, while it is even more constant on every broken major segment, in the range 3-9 MPa and on average ~6 MPa. Every major segment thus fairly behaves as an elastic crack (See discussion later); vii) there exists no historical EQ which broke a continental fault over a length greater than ~600 km.

- It has to be noted that part of these results arise from the analysis of EQ source inversion models which, as I will discuss it further below, are not fully appropriate to describe the EQ rupture. However, these results are supported with similar finding from surface direct observations. This suggests that, **although the available EQ source inversion models are not fully appropriate to describe the EQ rupture, they succeed in fairly well recovering the first-order macroscopic properties of EQs**.

- **Certain of the long-term fault properties impact some of the properties of the large EQs that are produced by the rupturing of these faults**. The fault properties that most govern the EQ ruptures are:

- ***The geometry/architecture of the fault trace (i.e., fault plane)***: indeed, the EQ ruptures are observed to initiate and to stop at specific sites along the continental faults, namely large inter-segments or fault ends. More precisely, EQs initiate in or nearby inter-segment zones where additionally a 40-50° oblique, generally dipping secondary fault commonly exists and intersects the master fault trace. EQs generally arrest also in inter-segments whose across-fault width is greater than ~5 km on average and/or angle change is greater than ~25°. However other factors control the EQ arrest (See below).
- ***The structural maturity of the fault, global and along-strike***: this is actually the fault property that most impacts the EQ properties. It controls: i) the location of the EQ hypocenter, as the later generally locates between two segments having a different structural maturity; ii) the location of the maximum coseismic slip, as the later always locates on the most mature section of the fault closest from the hypocenter; iii) the global maturity of a fault controls the size, absolute and relative, of the step-overs that exist along that fault, as the mechanical properties of these inter-segments (more breakable along mature faults). As such, the global maturity of a fault controls the number of major segments that can be broken during an EQ, and hence controls the total rupture length, the degree of asymmetry of the coseismic slip-length profile, and the overall EQ stress drop (however, the larger the EQ stress drop, the more capable is the EQ to break the major inter-segments); iv) the global maturity of a fault also controls the static friction on the fault plane (See further below), and therefore the EQ stress drop decreases with fault maturity, whereas the rupture efficiency (i.e., its capacity to propagate) and the rupture speed both increase with fault maturity; v) because the structural maturity also varies along the fault strike, it is responsible for the development of asymmetric coseismic slip profiles: the maximum coseismic slip locates on the most mature section of the rupture, whereas the rest of the coseismic slip tapers in the direction of the long-term fault lateral propagation.
- ***The 3D architecture of the faults, that is of the fault networks that they form at a larger scale***: the secondary faults associated with the master fault accommodate part of the coseismic slip, strain and stress, and hence control the coseismic slip amount "remaining" on the master fault. My estimations of the coseismic slip diffusion suggest that 25-40 % of the maximum on-fault coseismic slip may be diffused in a broad volume around the master fault rupture.

- **An EQ always is a multi-event rupture**: in the general case, a single EQ breaks several fault segments along the fault on which it nucleates, and sometimes, different faults in a larger-scale system. In the general case also, an EQ divides into two parts: a major segment first breaks and generally produces the maximum coseismic slip; this segment is the most mature in the whole zone eventually concerned by the EQ. The rupture of this first "major asperity" triggers, likely by dynamic overshoot, the rupture of other adjacent segments along the fault that were not prone to break (i.e.; not prone to nucleate a large EQ). It is important to note that it is not the stress drop of the first broken asperity which controls the number of segments eventually broken by the EQ, but rather the global structural maturity of the fault. In a few cases, the maximum coseismic slip forms lately in the EQ rupture. I discuss these cases further below. In these cases where the rupture ends abruptly while its coseismic slip is maximum, a small adjacent section of the fault is observed to break beyond the rupture arrest; this small rupturing is likely triggered by dynamic overshoot due to the high stresses at the rupture arrest.

- **Coseismic deformation is a 3D phenomenon**: a significant part of the coseismic slip is diffused in the medium off- the main rupture zone (coseismic damage); at least 25-40% of the maximum on-fault coseismic slip according to both our modeling and my slip deficit estimates. The relative part of slip diffused off-the main rupture increases in the direction of on-fault coseismic slip tapering. The most common shape of the coseismic damage zone in map view is triangular, with the apex centered in the zone of maximum coseismic slip.

2. Discussion of a few implications

Why do EQs have generic properties, and which implications on EQ physics?

The generic properties and scaling laws that I have established or suggested in this work add to the numerous scaling laws already established on EQs (See introduction). The fact that large EQs (Mw ≥ ~6) are governed by a number of relations independent of magnitude, slip mode, location and context, show that the behavior of large EQs is fairly indifferent to small scale and local complexities. This finding supports the statement made by Kanamori and

Brodsky (2004), that "**the robustness and ubiquity of [these] laws tells us that at least parts of the earthquake process are insensitive to the microscopic physics that controls the failure, the friction, and the whole rupture"**. This is even more surprising that the EQ propagation is highly inhomogeneous in space, time, and focal mechanisms (e.g., Kagan, 2004). Yet, these complexities and heterogeneities collapse at the macroscopic scale to produce a number of scale-invariant behaviors. **The scaling laws also show that the behavior of large EQs is fairly indifferent to the changes in conditions that operate in every EQ**: during each EQ, the strain drop is on the order of 10^{-4}, and thus the mechanical properties of the fault change after each EQ, so that the next event occurs in a different mechanical "environment" than the previous one (e.g., Kagan, 1994; Manighetti et al., 2001). The scaling laws show that the large EQs are fairly indifferent to these changes. Why is it so remains to be understood.

Among the scale-invariant properties, the coseismic slip profiles of the large EQs have a generic shape, always triangular, and asymmetric in ~65 % of the analyzed EQ cases. This shows that **the EQ slip and stress are not as heterogeneous as they have been supposed so far** (Kagan, 2004; Liu-Zeng et al., 2005; Lavallée et al., 2006; see also discussion in Noda et al., 2013).

The dense EQ dataset that I have analyzed shows that no historical EQ ever ruptured a continental fault over a length greater than ~600 km. Why would such a length threshold exist? We note that it differs from the subduction EQ cases, which are able to break subduction faults over much greater lengths. We also note that continental faults longer than 600 km do exist. We see two reasons that might explain the difference between continental and subduction EQs: 1) the stresses imposed within the continents are likely lower than those imposed on the subduction faults, due to the distribution of the deformation within the "softer" continental lithosphere; 2) continental faults are all segmented laterally, and their major segments are separated by large inter-segments, most of them are zones of distributed faulting and cracking very prone to absorb part of the EQ strain and stress when the EQ meets them in its lateral propagation. The inter-segments along continental faults thus are absorbing features that likely contribute to slow down and eventually arrest an EQ rupture. These features do not exist along subduction faults. Subductions faults are extremely mature, and in any case, do not propagate anymore. They are segmented laterally, yet by independent features such as ridges or fracture zones hosted in the subducting plate (e.g., Wang and Bilek,

2014 and references therein). These features are not genetically related to the subduction faults. They thus have variable properties, and they actually might be less absorbing that the genetically formed inter-segment zones along the continental faults.

Why do long-term faults have generic properties?

Long-term faults also have a number of generic properties independent of scales, slip modes, locations and contexts. Therefore the same implications are inferred: **the mechanisms for fault growth are fairly indifferent to the local and small-scale complexities and heterogeneities**. The reasons why faults develop generic properties are unclear, but have likely to be searched for in the fact that long-term faults grow through repeated EQ slip events, which themselves have generic properties. They also have to be searched for in the mechanical properties of the crust and lithosphere. We note however that, although they occur in somehow different lithospheres, continental and subduction EQ share a number of common properties.

What is the structural maturity of a fault, what does it change?

As other authors before, we think that the structural maturity is basically the aging of the fault slip zone; as the fault accumulates more slip, its slip interface(s) smoothes, likely through the wearing out of its "rugosity" whereas the wear products may form a clayish gouge (e.g., Manighetti et al., 2007; Brodsky et al., 2011). The rugosity that might be smoothed out during the fault aging includes the undulations in the fault plane, and hence the step-overs between the segments of the faults. As the fault becomes more mature, the smallest step-overs are smoothed and replaced by a small undulation in the fault plane, whereas the widest step-overs are replaced by true connection through rounded double bends in the fault trace and plane. Therefore, the inter-segments, which were initially a site of multiple fracturing and cracking altogether having a non-elastic response to the accumulated strain, progressively become, as the fault becomes more mature, a continuous and smooth fault section, which can then have a more elastic response to the imposed stresses. **The structural maturity therefore contributes both to reduce the static friction on the fault plane, and to make the fault having a more elastic response to the imposed stresses**.

The structural maturity differs globally from one fault to another. But it also varies along a given fault. Indeed, any fault lengthens over time, and hence has parts which formed at the very first stages of the fault evolution, and parts which formed much later in the most

recent stages of the fault lengthening. Therefore, the most ancient segments of the faults are more mature than the recently formed segments, developed to make the fault propagating further laterally.

The along-strike variability of the structural maturity and hence of the friction and of the ability to respond elastically, likely explains why the maximum coseismic slip always locates on the fault segment with greatest structural maturity that is closest from the EQ hypocenter.

Considered more globally, the structural maturity of the faults is expected to change many aspects of the overall fault behavior. The most mature faults are expected to slip more easily and hence more often (See below) than the immature faults. Meanwhile, they are less coupled and hence they do not relax all the imposed stresses, contrary to the immature faults. EQs occurring on mature faults thus have a lower stress drop, while they also are associated with a greater coseismic damage made to accommodate the large amounts of strain and stress than the mature fault did not accommodate on its plane. If these expectations are correct, we might expect to observe more on-fault after-slip on a mature fault just broken by a EQ (compared to an immature fault), especially on the rupture section where coseismic slip tapers. By contrast, we might expect less post-seismic relaxation on ruptures on mature faults than on ruptures on immature faults where the brutal coseismic slip is much higher.

Which conditions on a fault to initiate and develop an EQ rupture?

The data analysis has shown that a first condition to initiate a large EQ rupture on a fault is the existence of a (loaded) fairly large inter-segment (large because only the largest scales of inter-segments were concerned in the analyzed data) between two segments having likely a different structural maturity. This inter-segment must additionally be intersected by an oblique (generally 40-50°) secondary fault, generally dip-slip. This observation on the role of interaction between secondary faults and the master fault at the EQ nucleation meets the modeling results of Umeda et al. (1996).

On the other hand, a condition for the EQ development is the existence, nearby the hypocenter, of a fault segment with a fairly high structural maturity, and hence likely a fairly low static friction.

Another condition for the EQ rupture development is that the low friction segment nearby the hypocenter breaks first. This is observed in the majority of EQ cases, yet not in all cases as there exists a few EQs showing the low friction segment breaking last (ex: Denali, Landers, Chichi, Kunlun; See discussion further below). In the general case, the rupture of the low friction asperity seems to have two effects: 1) the rupture dynamically increases the stresses

on some of the adjacent fault segments, where stresses were originally too low to initiate a rupture; 2) the dynamic stresses and strain diffuse in the medium around and far beyond the broken segment, and it is likely that these off-rupture stresses contribute to lower the normal stress on the unbroken adjacent segments (e.g., Dunham and Rice, 2008), and hence contribute to de-clamp them. Altogether the two processes put the adjacent segments in the condition of rupturing, and some of them thus rupture, what makes the rupture longer.

In the few EQ cases where the lower friction asperity breaks lately in the rupture development, it seems that the rupture develops progressively: it does break first the segment with lower friction that is closest from the hypocenter. Yet when reaching the end of that first segment, the rupture meets another segment which has an even lower friction, and hence it breaks it easily. The coseismic slip then produced is larger because the friction is lower and the damage around the segment likely more pronounced (See Chapter V). Arrived at the end of that second segment, the rupture may meet again a new segment with an even lower friction. In that case, it breaks it also, with an even larger coseismic slip. To arrest the rupture, a strong feature has to operate, such as very large inter-segment (?), the rupture crossing a sub-perpendicular fault (ex: Landers and Chichi), the rupture meeting a large angle in the fault trace, for example due to its splay (ex: Denali, Kunlun). This behavior where an EQ rupture cascades from a low friction segment to an even lower friction segment might produce EQs cascading among different faults, such is the case of Landers. The jumps are not random, as supposed by some authors (e.g., Black and Jackson, 2008; Parsons et al., 2012), but instead driven by the "search" of the lowest friction segment and by the increase of the coseismic slip as lower friction segments are met. Because the existence of these low friction segments depends on the long-term fault properties, the jumps are basically governed by the long-term fault properties.

Which conditions on a fault to arrest an EQ rupture?

I have shown that most of the EQs I have analyzed have arrested in major fault intersegments, at the fault ends, or where they met a very oblique cross-cutting feature. However, the analysis suggests that the size of the inter-segments is not the only factor to control the EQ arrest since even the largest sizes of inter-segments on certain faults were broken by some of the EQs. Therefore on these faults, what did arrest the EQ?

I have shown additionally that the greater the EQ stress drop, the larger the relative size of the inter-segments that the EQ succeeds passing through.

An angle in the fault trace greater than ~25° seems a condition that generally arrests an EQ. Yet, it is not a systematic condition.

Altogether these suggest that other factors than the step-over size and angle value control the EQ arrest. We suggest that the dissipation of the EQ stresses, in both the medium through the coseismic damage, but also within the less mature inter-segments of the faults where strain and stresses are diffused, are the main controlling factors of the EQ arrest. They are absorbing conditions. This would imply, as already suggested by Kagan (2007), that **"the geometrical complexities of a fault [here the damage networks and the fault inter-segments], not friction, control the stop-and-go feature of the EQ rupture propagation"**.

How do the present results modify the common conceptual vision of EQs?

Although more data are needed to validate the scaling laws that we have developed, it appears that **integrating the structural maturity of the broken faults into the theoretical EQ scaling laws modify them**. For instance, whereas M0 overall scales as L^2 when the EQ data are taken all together with no discrimination, it appears that M0 actually scales as L^3 for EQs having occurred on immature faults. Therefore, we suggest that the structural maturity should be taken into account in the EQ scaling relations. Otherwise, the scaling factors might be sorts of averages among very distinct populations.

I have shown that **the broken area is rarely S =L*W, but instead is much smaller, on average ~0.4 of S**. When we use Smin ~0.4 S instead of S, the theoretical formula $M0 = \mu*S*D_{mean}$ is well verified (with μ equal to 3.10^{10} Nm-2).

My results pose the question of the definition of the EQ stress drop. Several findings indeed modify the classical vision of the EQ stress drop. In particular, we have shown that: i) an EQ generally is a multi-segment or even a multi-fault rupture; ii) in this multi-segment rupture, one segment generally breaks first, and this is this first breaking that makes other segments to also break; iii) the coseismic slip much varies along both the rupture length and width; iv) the broken area also varies along the rupture length, in proportion to the slip decrease; v) this results in a total broken area averaging ~0.4 S (S= L*W). Based on these findings, it is difficult to believe that the EQ stress drop can be constant (See also discussion in Scholz and Lowler, 2004). Yet, it seems to be. My estimations suggest that the overall EQ stress drop is in the range 0.3-9 MPa, whereas the different broken segments have a same stress drop, on average 6 MPa. One explanation might be that, as the coseismic slip decreases

along the rupture length, the broken area also decreases. This concomitant decrease might maintain a constant stress drop, at least when averaged over each major broken segment. I further discuss the width decrease later on.

My results also pose the question of the definition of the EQ focal mechanism. Since an EQ is generally a multi-segment or even a multi-fault rupture, the focal mechanism must vary along the rupture, depending on which segment (or fault) is considered. This 2D or even 3D evolution of the focal mechanisms has been pointed out by Kagan 2009. The question is even more posed that we have seen that EQs generally initiate on a cross-cutting oblique dip-slip fault, thus on a fault with a different mechanism than the master fault then broken.

My results also question the determination of the EQ propagation speed. Again, since an EQ is generally is a multi-segment or even a multi-fault rupture, and since the various segments and inter-segments have different properties, especially different degrees of structural maturity, we might expect that the rupture speed varies depending on the segment it propagates on, and depending on the inter-segment it meets in its propagation (inter-segments might more or less slow down, or arrest the rupture, depending on their mechanical properties, related to their structural maturity). We expect that the rupture speed is higher on the most mature sections of the broken fault.

Because the EQs and long-term faults both damage the crustal rocks around them, it is unlikely that the rigidity of the crust, m, can be constant in space and time, contrary to what is commonly assumed in the theoretical considerations. Our modeling of the coseismic slip profiles indeed showed that embedding an EQ rupture in either a homogeneous medium or a medium with across-fault variations in elastic properties, does not reproduce the observed profiles. Integrating the structural maturity in the M0-S relations also suggested that m is lower in the crustal rocks surrounding the most mature faults. Therefore, more work should be done to estimate the actual values of m, that are expected to vary depending on the structural maturity of the major faults (See Vallée, 2013 for a discussion on the variation of the medium rigidity with depth, similarly seen in EQ source scalings).

Despite of the modifications suggested above, one of our results is to confirm that the static stress drop is constant overall on the various broken segments (~6 MPa). This shows that, although the theoretical framework needs some modifications in its consideration of the entire

ruptures (a total rupture does not behave as a single elastic crack in a homogeneous medium), **it fairly well describes the behavior of the individual major segments which are broken during an EQ**: each seems to fairly behave overall as an elastic crack, yet not in a perfectly homogeneous elastic medium.

Can we propose new insights?

Three inter-related properties of the long-term faults seem to be key elements to anticipate the magnitude of a forthcoming (large) event:

1) **The fault length**: for faults shorter than 600 km, large EQs can potentially break 1 or more of the few (2-5) longest segments that form the fault; for faults longer than 600 km, it seems that large EQs cannot break more than one single major segment along the fault, and hence in effect has the potential to break 1 or more of the few (2-5) secondary segments that form the major segment.
2) **The overall structural maturity of the fault**: it dictates the number of major (or secondary) segments that can be potentially broken by a large EQ: 1 segment only on immature faults, 2 on "intermediate closer to immature" maturity-faults, 3 on "intermediate closer to mature" maturity-faults, and 4 (or 5) on mature faults.
3) **The along-strike maturity of the fault**: It is related to the lateral propagation of the fault over the long-term. It controls the potential sites where a large EQ might nucleate (in between two segments with different maturity). It also defines the parts of the fault that can slip most and "more easily" (i.e., likely more frequently).

Therefore, knowing the structural maturity of a fault and the precise fault architecture in map view, we should be able to: i) determine how the fault has been propagating laterally over the long-term; ii) identify the major segments and inter-segments along the fault; iii) determine which inter-segments are sites of oblique dip-slip faults; iv) discriminate the most mature segments, especially those closer from the inter-segments with oblique faults; v) from the different possible scenarios relating potential sites for nucleation and potential sites for larger coseismic slip, we should be able to estimate (from maturity, but also from HA generic distance; see Fig. 199 and 200) the number of adjacent segments (and to identify them) that might be broken if the identified "major asperity" breaks.

A still posed question: what really governs the EQ size?

My work of course leaves opened a very large number of questions. I cannot list them all since they are almost infinite. Yet, a major one concerns what really governs the eventual EQ

size. Said differently, the question is: “What does an EQ “know” of its final size when it initiates?” (See discussion in Umeda et al., 1996). I indeed found puzzling results: on the one hand, there is a systematic relation between the position of the EQ hypocenter –which marks the EQ initiation, and the zone of maximum coseismic slip –which marks the final state of the EQ. Therefore, the H-A relation shows that there is a link between the initial and the final states of the EQ (See also discussion in Manighetti et al., 2005). On the other hand, once an EQ has nucleated, it seems that it propagates until it reaches a fairly mature zone of the fault (i.e., with low friction), where it develops its maximum coseismic slip. Can we understand this by postulating that: if the EQ “energy” at the nucleation stage is low, the EQ is not able to reach the nearest mature section of the fault and thus the EQ rupture rapidly stops so that the EQ is eventually a small one. But if the EQ “energy” at the nucleation stage is large enough, the EQ succeeds in reaching the nearest mature section of the fault, which thus breaks. Then, the breaking of this low friction fault segment produces dynamic stresses which, depending on the maturity of the fault and hence on its “capacity to more or less resist the rupture”, are enough or not enough to break a certain number of adjacent fault segments. This chain of processes would make any small EQ capable of becoming a very large one, depending on where it nucleates, on how much stresses exist to fuel the nucleation, and on the structural maturity of the fault. Even if this vision is viable, it does not allow understanding why EQs occurring on a continental fault longer than 600 km would only “see” one of its major segments as a single fault.

A few broader implications of the results

As I said earlier, a large part of my results arise from the analysis of EQ source inversion models, which are not fully appropriate to describe the EQ rupture, since they simplify the geometry of the faults, they ignore the fundamental structural maturity property of the faults, and they consider that the crustal medium is elastic. On this later point, our modeling of the coseismic slip profiles showed an additional feature: a significant part of the coseismic strain is diffused off- the main rupture, in the medium around. This suggests that the source inversion models mainly based on far-field observations might over-estimate the coseismic slip on the main rupture for the far-field observations sum the on-fault and off-fault contributions. The EQ and segment stress drops inferred from these far-field models might thus be over-estimated. By contrast, the source inversion models mainly based on near-field observations might better recover the coseismic slip on the main rupture. However, they still

are partly incorrect since they ignore the inelastic deformation that occur off- the main fault (See also discussion in Kaneko and Fialko, 2011).

I have shown that the coseismic slip at surface is generally much lower than the coseismic slip at depth, except on mature faults. Therefore, using slip measurements made at surface to derive the EQ magnitude might be misleading. It might be even more misleading that the coseismic slip much varies along the rupture length. Therefore, local paleoseismological measurements of slip must be taken with caution.

Conversely, a coseismic slip deficit is seen from depth to surface along immature faults, and thus, such a slip deficit should be expected in the future source models of EQs occurring on immature faults.

I have shown that the coseismic slip-length profiles always taper in the direction of the long-term lateral propagation of the broken fault. Therefore, in the absence of other data, the occurrence of a single EQ with a well-constrained coseismic slip profile is enough to infer the sense in which the fault has mainly lengthened over the long-term. This is an important information in tectonics and paleoseismology. Furthermore, we expect that the coseismic (for large EQS) and long-term slip profiles resemble each other that is show coseismic slip (of large EQs) and cumulative slip tapering in the same direction.

Since the maximum coseismic slip is produced on the most mature sections of the faults, it is expected that the zones with greatest coseismic slips (produced by the largest EQs) keep the same over long periods of time. This is important for paleoseismology because it might help to target the zone of greatest paleo-EQ slips (See Schlagenhauf et al., 2011; Delor et al., AGU 2013). By contrast, the large EQs are not expected to nucleate at the same places along the faults, so that, while successive large EQs might appear somehow characteristic in terms of maximum slip position, they might not be in terms of rupture location and extent, and hence in other slip values. The coincidence of the maximum slip zones likely contributes to explain the similar triangular envelope shape found for both the coseismic and the cumulative slip profiles (compare Fig.25 and 171).

3. Perspectives

My results suggest that the available fault models should be modified to include: i) that faults are segmented laterally in a scale invariant fashion (at least for the two largest scales of segments); ii) that inter-segment zones cannot be described as having homogeneous elastic properties (as commonly done, see Harris et al., 1991; Oglesby 2008); that faults have an overall static friction that varies from one fault to another, and that also varies along the fault length (hence the static friction also varies along the fault length, as pointed out by Cooke, 1997); that the crustal medium is heterogeneous and highly damaged by the fault itself; that the faults are 3D features, made of a master fault associated, in a organized fashion, with many secondary faults.

My results also suggest that the available EQ rupture models (at least those dealing with continental EQs) should be modified to include: i) specific conditions at the EQ nucleation; ii) the large-scale fault segmentation (geometry and properties of major segments and inter-segments); iii) the structural maturity of the broken fault, overall, and along-strike; iv) that EQ almost always are multi-segment ruptures, and hence rather are earthquake sequences than single events (See also discussion in Kagan, 2004); v) the inelastic properties of the crustal medium; vi) that the EQ under study is not the only and very first event on the fault, so that the pre-EQ conditions are extremely important; vii) that new small faults and cracks and possibly other types of deformation can be created during the EQ event.

Since EQs generally are multi-segment ruptures, the successive ruptures during an EQ should be seen in the seismic waves as different pulses (See the example of the giant 2004 Sumatra EQ, e.g., Ammon et al., 2005). Sub-events should also be found in the EQ source time functions. This is actually observed. The question remains posed on how to interpret the peaks of moment release in the STFs. There is indeed a balance between two facts: on the one hand, the major asperity which generally breaks first produces the largest coseismic slip; on the other hand, it is the most mature section of the broken zone and hence it is expected to have a lower stress drop than the other broken segments. Therefore, is the major peak in a STF revealing the rupture of the major asperity (as defined here, i.e., the segment that generally breaks first and hosts the maximum coseismic slip)? Since I have shown that the broken area is wider in the zone of the maximum coseismic slip, I suggest that the combination of maximum slip and maximum width can indeed produce the largest peak in moment release.

We would thus tend to suggest that the largest peaks in the STFs indeed show the rupture of the "major asperity" as defined in this work.

The difference in structural maturity among faults should impact the deformation recovered in GPS measurements across the faults: because they have a lower friction and more easily release the strain, mature faults should have long-term and current slip rates fairly similar. A greater difference is expected on immature faults. Furthermore, because the structural maturity and hence the friction varies also along the faults, the major fault segments should have a different coupling, that should be seen in the GPS measurements.

More broadly, the faults and EQs damage the medium around them, and it is expected that the damage properties also evolve with the structural maturity of the master fault. More mature faults will inherently be surrounded with a more mature damage zone, therefore made of more mature, and hence longer fractures and secondary faults. The damage zone around mature faults is also expected to be broader. Micro-seismicity, especially aftershocks, but also post-seismic deformations, altogether attest for the response of the damage features around the master faults and ruptures. On mature faults, with respect to immature faults, we expect: more on-fault after-slip (as they slip easily to compensate any slip deficit), especially in the coseismic slip tapers; less post-seismic relaxation (as they produce a much lower coseismic slip); a broader zone of aftershocks and microseismicity; aftershocks with lower stress drops than those around immature faults; exponents in GR and Omori laws different in the two cases because the damage features do not have the same sizes. By contrast, the mature and immature fault cases share the fact that a large number of aftershocks should have a non-couple mechanism (crack opening in the damage zone) and/or an extensional mechanism (same reason).

Another perspective of the work is that it might help better defining the zone of the fault that might produce the greatest ground motions. First, Radiguet et al. (2009) showed that EQs on immature faults produce larger ground motions that EQs on mature faults. Additionally, we have seen here that every rupture includes one segment that hosts the maximum coseismic slip. Once the hypocenter of an EQ is identified, the relations HA that I have found can be used to assess immediately that the maximum slip has a great chance to be fairly close from the hypocenter (distance HA $\leq$ ~30 % of the final rupture diagonal length). This can help knowing rapidly where might be the largest ground motions. Of course, knowing the geometry and structural maturity of the fault would be of greater help since it might allow

delineating the most mature sections of the fault where the greatest slip, and hence the greatest ground motions, may be expected (although large ground motions may occur at other places, related to site effects or rupture directivity).

Every scaling law suggested in this work shows a few outlier data points. This requests further work to understand why these points are peculiar. One reason might be that the source models or the observations where they come from are not well constrained. In that case, this might help identifying the types of observations that would be needed to better constrain them. For instance, the coseismic slip measured at surface along the 1940 Imperial Valley and the 1987 Superstition Hills EQs are likely underestimated, and this might be due to the dissipation of the slip within the soft sediments of the Salton Plain. Pixel correlation of aerial pictures bracketing the events would perhaps help to better recover the coseismic slip distribution at surface.

The scaling laws suggested in this work are preliminary and need to be refined. So many scaling laws and various breaks in the scalings have been proposed so far (See discussion in Shaw, 2010) that more work is needed to fully understand how my results relate to the other results in the EQ scaling domain.

Finally, a large and important perspective is to extend the work further to the subduction EQs. Indeed, although I could examine certain aspects of the historical subduction EQS, I could not find the time to deeply analyze them. In particular, the geometry/architecture of the subduction faults and associated networks requests to be analyzed in detail but also globally so as to examine their common points. There is a sort of paradox because, on the one hand the subduction faults seem very different from the continental faults and hence it might be expected that the subduction EQs show different properties than the continental EQs, and on the other hand, I found many properties which are shared by the continental and the subduction EQs, among which: similar envelope shape of the coseismic slip-length and slip-width profiles, similar range in number of major segments being broken (2-4; See also Scholz, AGU 2013 for Cascadia), similar W decrease concomitant with the slip decrease, similar H-A relation, similar stress drop on the major segments. It might thus be possible that subduction EQs obey the same scaling laws than continental EQs. As along the continental faults, the decrease in the broken width calls for possible reasons for that decrease, and one reason could be that a vertical segmentation also exists along the fault dip. This might be the case actually for some subduction faults, as shown in the 2011 Tohoku EQ (e.g., Yomogida et al., 2011).

Conclusions

My main objective was to examine the relations between the properties of the long-term geological faults, and those of the large EQs produced by the rupture of these faults. To address this issue, I have analyzed three types of data:

1) For 26 large (Mw in range 6.4-8.1) historical continental EQs (2010 Baja California, 1957 Bogd, 1944 Bolu Gerede, 1983 Borah Peak, 1968 Borrego Mountain, 2002 Denali, 1954 Dixie Valley and Fairview Peak, 1999 Duzce, 1857 Fort Tejon, 1939 Erzincan, 1931 Fuyun, 1959 Hebgen Lake, 1999 Hector mine, 1940 and 1979 Imperial Valley, 1999 Izmit, 2001 Kunlun, 1992 Landers, 1997 Manyi, 1915 Pleasant Valley, 1906 San Francisco, 2008 Sichuan, 1987 Superstition Hills, 1943 Tosya and 2010 Yushu EQs) of various worldwide locations (mainly West USA, Asia, Turkey) and various slip modes (~75% strike-slip, 5% reverse, 20% normal), I have used satellite images and topographic data to perform a morpho-tectonic analysis of the long-term faults that were ruptured by the EQs. I mapped the entire fault traces in detail, along with the associated secondary fault networks, what allowed me to derive information on the fault slip mode, on the sense of lateral propagation of the faults over the long-term, on the lateral segmentation of the faults, on the nature of the zones that separate the different segments along the faults. For 21 of these 26 historical EQs (all EQs but those on the North Anatolian fault for which I was lacking time), I have then analyzed critically all the information available in the literature on these EQs: measurements at surface of the rupture length and extent, coseismic slips produced, other types of deformations observed; source inversion models providing the length, width, and slip distribution at depth; estimations of the EQ magnitude Mw, seismic moment and moment release function, rupture duration, etc. I have faced this seismological information to my fault maps, and in particular, I have reported the rupture traces on the long-term fault traces (note that I could often map the rupture traces since many of them are clear on the satellite images), so that to identify which parts of the long-term fault and especially which segments, were broken in the events. This coupled information, which describe in great detail both the broken fault and the EQ produced, provided me the core data of my PhD work, from which I derived many of the main results.
2) To complement the above data, I have extracted from the literature seismological data describing some of the many more historical EQs for which I hadn't got the time, or I could

not (ex: subduction EQs), analyze the ruptured long-term faults. These data are variable and include slip distributions (either at surface or at depth from source inversion models), seismic moments, rupture durations etc (I gathered this type of data for 45 additional EQs having occurred in the period 1971-2011, 70 % are continental EQs with Mw in range 5.5-8.1 [55 % strike-slip, 35% reverse, 10% normal], and 30 % are subduction EQs with Mw in range 6.7-9.2), but also couples of maximum coseismic slip and length values (I gathered this type of data for ~230 continental EQs worldwide having occurred in the period mainly 1500-2011, having Mw in range 4.6-8.6, and including ~70% of strike-slip, ~15% of reverse, and ~15% of normal ruptures; all data from surface measurements).

3) Also to complement the above data, I have extracted from the literature tectonic data describing some of the major properties of ~50 of the long-term faults broken in the above EQs, such as the total fault length, the maximum cumulative slip, the age of initiation of the fault, the fault slip rate. From this first-order tectonic information, I have derived a qualitative estimate of the structural maturity of the faults.

Although not exhaustive, the fault and EQ database that I have constructed has allowed me to analyze some of the long-term fault properties, some of the large EQ properties, and the relations between the properties of the faults and the properties of the EQs.

A first major result of this work is to show that long-term faults do have a number of generic properties that is properties independent on the fault size, slip mode, location. Among these generic fault properties, the fault networks show similar arrangements, the fault traces show a similar lateral segmentation, the cumulative slip distributions show a similar envelope shape.

A second major result is to confirm that faults evolve in space and time as they accumulate more slip and grow in length, and this evolution can be described as the fault structural maturity. Furthermore, I provide scaling relations between some of the fault parameters that help to qualify the degree of structural maturity of a fault.

A third major result is to show that large EQs also share common, generic properties, among which a similar coseismic slip-length and slip-width slip profile, a similar decrease in the rupture width along the EQ length, a similar number of broken segments, a similar stress drop on the broken segments, a similar relative distance between hypocenter and zone of maximum slip.

However the most important result is to show that some of the properties of the long-term faults govern some of the properties of the large EQs being produced. The structural maturity

of the faults is the tectonic property most impacting the behavior of the large EQs. It plays a role in the location of the EQ initiation; it dictates the place on the fault where the maximum coseismic slip eventually develops; it governs the amount of coseismic slip that can be produced; it dictates the direction of the coseismic slip decrease; it dictates the number of major fault segments that can be eventually broken by the EQ, and hence it controls the rupture length and its overall stress drop; it plays a role on the rupture propagation efficiency and speed. The structural maturity of the faults likely acts in reducing both the static friction on their plane and the geometric complexity of their trace and plane.

The existence of generic properties and scaling laws for both faults and EQs call for a better understanding on the relations between the complex micro-physics –which governs the failure, the friction and the whole rupture and faulting process, and the macro-physics which makes faults and EQs obeying more simple general laws fairly indifferent to the micro-complexities and heterogeneities.

The existence of generic properties and scaling laws for EQs also provide some keys to anticipate some of the properties of the forthcoming large events.

The emphasis of the impact of the fault structural maturity on the large EQ behavior suggests that the models of EQ source should be modified to integrate this fault property (as a first step integrated as a variable friction) along with the related fault properties such as the lateral fault segmentation, the 3D fault architecture and hence the heterogeneous state of the crustal medium around the faults.

The results provided here also suggest that EQs, at least the largest ones, should be considered as 3D multi-segment ruptures, therefore having a variable stress drop over the broken area, a variable focal mechanism along the rupture length, a variable rupture speed, A 3D strain and stress distribution.

Of course, much more work needs to be done to validate these preliminary finding. A particular focus should to be put on the subduction EQs. Although the subduction faults are much more difficult to study than continental faults, they have many aspects that can be examined globally (e.g., Heuret et al., 2011, 2012), and this global analysis might highlight

some relations between the properties of the hosting subduction faults and the properties of the subduction EQs.

I conclude by stating that, to understand the behavior and the physics of EQs, it seems inescapable to analyze jointly the tectonic properties of the broken faults and the seismological properties of the EQs. A real seismo-tectonic field of research is thus clearly opened.

References

Note that I quote here the references in the main text with the exception of the IDs section and Chapter V where references are reported at the end of each sections

Abercrombie, R. E. (1995). Earthquake source scaling relationships from− 1 to 5 ML using seismograms recorded at 2.5-km depth. *Journal of Geophysical Research: Solid Earth (1978–2012)*, *100*(B12), 24015-24036.

Aki, K. (1967). Scaling law of seismic spectrum. *Journal of Geophysical Research*, *72*(4), 1217-1231.

Aki, K. (1972). Earthquake mechanism. *Tectonophysics*, *13*(1), 423-446.

Aki, K., & Richards, P. G. (1980). Quantitative seismology: Theory and methods, 1. *I: WH Freeman and Co*.

Aki, K., & Richards, P. G. (2002). *Quantitative seismology*. University Science Books.

Ammon, C. J., Ji, C., Thio, H. K., Robinson, D., Ni, S., Hjorleifsdottir, V., ... & Wald, D. (2005). Rupture process of the 2004 Sumatra-Andaman earthquake. *Science*, *308*(5725), 1133-1139.

Anders, M. H., & Schlische, R. W. (1994). Overlapping faults, intrabasin highs, and the growth of normal faults. *The Journal of Geology*, 165-179.

Anderson, T. L. (2005). Fracture mechanics: fundamentals and applications. CRC press.

Anderson, J. G., Wesnousky, S. G., & Stirling, M. W. (1996). Earthquake size as a function of fault slip rate. *Bulletin of the Seismological Society of America*, *86*(3), 683-690.

Ando, R., Shaw, B. E., & Scholz, C. H. (2009). Quantifying natural fault geometry: statistics of splay fault angles. *Bulletin of the Seismological Society of America*, *99*(1), 389-395.

Archuleta, R. J. (1984). A faulting model for the 1979 Imperial Valley earthquake. *Journal of Geophysical Research: Solid Earth (1978–2012)*, *89*(B6), 4559-4585.

Armijo, R., Meyer, B., Hubert, A., & Barka, A. (1999). Westward propagation of the North Anatolian fault into the northern Aegean: Timing and kinematics. *Geology*, *27*(3), 267-270.

Armijo, R., Meyer, B., Navarro, S., King, G., & Barka, A. (2002). Asymmetric slip partitioning in the Sea of Marmara pull-apart: a clue to propagation processes of the North Anatolian Fault?. *Terra Nova*, *14*(2), 80-86.

Avouac, J. P., Ayoub, F., Leprince, S., Konca, O., & Helmberger, D. V. (2006). The 2005,Mw 7.6 Kashmir earthquake: Sub-pixel correlation of ASTER images and seismic waveforms analysis. *Earth and Planetary Science Letters*, *249*(3), 514-528.

Aviles, C. A., Scholz, C. H., & Boatwright, J. (1987). Fractal analysis applied to characteristic segments of the San Andreas fault. *Journal of Geophysical Research: Solid Earth (1978–2012)*, *92*(B1), 331-344.

Aydin, A., & Schultz, R. A. (1990). Effect of mechanical interaction on the development of strike-slip faults with echelon patterns. *Journal of Structural Geology*, *12*(1), 123-129.

Aydin, A., & Berryman, J. G. (2010). Analysis of the growth of strike-slip faults using effective medium theory. *Journal of Structural Geology*, *32*(11), 1629-1642.

Barka, A. (1996). Slip distribution along the North Anatolian fault associated with the large earthquakes of the period 1939 to 1967. *Bulletin of the Seismological Society of America*, *86*(5), 1238-1254.

Barka, A. A., & Kadinsky-Cade, K. (1988). Strike-slip fault geometry in Turkey and its influence on earthquake activity. *Tectonics*, *7*(3), 663-684.

Black, N. M., & Jackson, D. D. (2008). Probability of multifault rupture. *Bulletin of the Seismological Society of America*, *98*(6), 3017-3024.

Bodin, P., & Brune, J. N. (1996). On the scaling of slip with rupture length for shallow strike-slip earthquakes: Quasi-static models and dynamic rupture propagation. *Bulletin of the Seismological Society of America*, *86*(5), 1292-1299.

Bouchon, M., Bouin, M. P., Karabulut, H., Toksöz, M. N., Dietrich, M., & Rosakis, A. J. (2001). How fast is rupture during an earthquake? New insights from the 1999 Turkey earthquakes. *Geophysical Research Letters*, *28*(14), 2723-2726.

Bouchon, M., Toksöz, M. N., Karabulut, H., Bouin, M. P., Dietrich, M., Aktar, M., & Edie, M. (2002). Space and time evolution of rupture and faulting during the 1999 Izmit (Turkey) earthquake. *Bulletin of the Seismological Society of America*, *92*(1), 256-266.

Bouchon, M., & Aki, K. (1977). Discrete wave-number representation of seismic-source wave fields. *Bulletin of the Seismological Society of America*, *67*(2), 259-277.

Bouchon, M., & Vallée, M. (2003). Observation of long supershear rupture during the magnitude 8.1 Kunlunshan earthquake. *Science*, *301*(5634), 824-826.

Brodsky, E. E., Gilchrist, J. J., Sagy, A., & Collettini, C. (2011). Faults smooth gradually as a function of slip. *Earth and Planetary Science Letters*, *302*(1), 185-193.

Brune, J. N. (1970). Tectonic stress and the spectra of seismic shear waves from earthquakes. *Journal of Geophysical Research*, *75*(26), 4997-5009.

Brune, J. N. (1976). Seismic Risk and Engineering Decisions. 140p

Cao, T., & Aki, K. (1987). Effect of slip rate on stress drop. In *Friction and Faulting* (pp. 515-529). Birkhäuser Basel.

Chester, F. M., Chester, J. S., Kirschner, D. L., Schulz, S. E., & Evans, J. P. (2004). Structure of large-displacement, strike-slip fault zones in the brittle continental crust. *Rheology and Deformation in the Lithosphere at Continental Margins*, *1*, 223-260.

Clark, M.M. (1972). Surface rupture along the Coyote Creek fault, in the Borrego Mountain Earthquake of April 9, 1968, *U.S. Geol. Sur. Prof. Paper* **787**, 55-86.

Cooke, M. L. (1997). Fracture localization along faults with spatially varying friction. *Journal of Geophysical Research: Solid Earth (1978–2012)*, *102*(B10), 22425-22434.

Copley, A., Avouac, J. P., Hollingsworth, J., & Leprince, S. (2011). The 2001 Mw 7.6 Bhuj earthquake, low fault friction, and the crustal support of plate driving forces in India. *Journal of Geophysical Research: Solid Earth (1978–2012)*, *116*(B8)

Cowie, P. A., and C. H. Scholz (1992a), Physical explanation for the displacement-length relationship of faults using a post-yield fracture mechanics models, J. Struct. Geol., 14, 1133– 1148.

Cowie, P. A., and C. H. Scholz (1992b), Growth of faults by accumulation of seismic slip, J. Geophys. Res., 97, 11,085– 11,095.

Crone, A. J., & Machette, M. N. (1984). Surface faulting accompanying the Borah Peak earthquake, central Idaho. *Geology*, *12*(11), 664-667.

Das, S. (1981). Three-dimensional spontaneous rupture propagation and implications for the earthquake source mechanism. *Geophysical Journal of the Royal Astronomical Society*, *67*(2), 375-393.

Das, S. (2003). Spontaneous complex earthquake rupture propagation. In *Seismic Motion, Lithospheric Structures, Earthquake and Volcanic Sources: The Keiiti Aki Volume* (pp. 579-602). Birkhäuser Basel.

Davis, K., Burbank, D. W., Fisher, D., Wallace, S., & Nobes, D. (2005). Thrust-fault growth and segment linkage in the active Ostler fault zone, New Zealand. *Journal of Structural Geology*, *27*(8), 1528-1546.

Dawers, N. H., Anders, M. H., & Scholz, C. H. (1993). Growth of normal faults: Displacement-length scaling. *Geology*, *21*(12), 1107-1110.

de Joussineau, G. D., Mutlu, O., Aydin, A., & Pollard, D. D. (2007). Characterization of strike-slip fault–splay relationships in sandstone. *Journal of Structural Geology*, *29*(11), 1831-1842.

Delor, E., Manighetti, I., Garambois, S., Beaupretre, S., & Vitard, C. (2013, December). Repetition of large stress drop earthquakes on Wairarapa fault, New Zealand, revealed by LiDAR data. In *AGU Fall Meeting Abstracts* (Vol. 1, p. 07).

Dieterich, J. H. (1979a). Modeling of rock friction: 1. Experimental results and constitutive equations. *Journal of Geophysical Research: Solid Earth (1978–2012)*, *84*(B5), 2161-2168.

Dieterich, J. H. (1979b). Modeling of rock friction: 2. Simulation of preseismic slip. *Journal of Geophysical Research: Solid Earth (1978–2012)*, *84*(B5), 2169-2175.

Dowrick, D. J., & Rhoades, D. A. (2004). Relations between earthquake magnitude and fault rupture dimensions: how regionally variable are they?. *Bulletin of the Seismological Society of America*, *94*(3), 776-788.

Du, Y., & Aydin, A. (1995). Shear fracture patterns and connectivity at geometric complexities along strike-slip faults. *Journal of Geophysical Research: Solid Earth (1978–2012)*, *100*(B9), 18093-18102.

Duman, T. Y., Emre, O., Dogan, A., & Ozalp, S. (2005). Step-over and bend structures along the 1999 Duzce earthquake surface rupture, North Anatolian fault, Turkey. *Bulletin of the Seismological Society of America*, *95*(4), 1250-1262.

Dunham, E., and J. R. Rice (2008), Earthquake slip between dissimilar poroelastic materials, J. Geophys. Res., 113, B09304, doi:10.1029/2007JB005405.

Eshelby, J. D. (1957). The determination of the elastic field of an ellipsoidal inclusion, and related problems. *Proceedings of the Royal Society of London. Series A. Mathematical and Physical Sciences*, *241*(1226), 376-396.

Ferrill, D. A., Stamatakos, J. A., & Sims, D. (1999). Normal fault corrugation: Implications for growth and seismicity of active normal faults. *Journal of Structural Geology*, *21*(8), 1027-1038.

Fukuyama, E., Ellsworth, W. L., Waldhauser, F., & Kubo, A. (2003). Detailed fault structure of the 2000 western Tottori, Japan, earthquake sequence. *Bulletin of the Seismological Society of America*, *93*(4), 1468-1478.

Geller, R. J. (1976). Body force equivalents for stress-drop seismic sources. *Bulletin of the Seismological Society of America*, *66*(6), 1801-1804.

Gutenberg, B., & Richter, C. F. (1944). Frequency of earthquakes in California. *Bulletin of the Seismological Society of America*, *34*(4), 185-188.

Hanks, T. C., & Boore, D. M. (1984). Moment-magnitude relations in theory and practice. *Journal of Geophysical Research: Solid Earth (1978–2012)*, *89*(B7), 6229-6235.

Hanks & Schwartz, 1987;

Hanks, T. C., & Bakun, W. H. (2002). A bilinear source-scaling model for M-log A observations of continental earthquakes. *Bulletin of the Seismological Society of America*, *92*(5), 1841-1846.

Harris, R. A., & Day, S. M. (1997). Effects of a low-velocity zone on a dynamic rupture. *Bulletin of the Seismological Society of America*, *87*(5), 1267-1280.

Harris, R. A., Archuleta, R. J., & Day, S. M. (1991). Fault steps and the dynamic rupture process: 2-D numerical simulations of a spontaneously propagating shear fracture. *Geophysical Research Letters*, *18*(5), 893-896.

Haskell, N. A. (1964). Total energy and energy spectral density of elastic wave radiation from propagating faults. *Bulletin of the Seismological Society of America*, *54*(6A), 1811-1841.

Hecker, S., Dawson, T. E., & Schwartz, D. P. (2010). Normal-faulting slip maxima and stress-drop variability: A geological perspective. *Bulletin of the Seismological Society of America*, *100*(6), 3130-3147.

Heuret, A., Lallemand, S., Funiciello, F., Piromallo, C., & Faccenna, C. (2011). Physical characteristics of subduction interface type seismogenic zones revisited. *Geochemistry, Geophysics, Geosystems*, *12*(1).

Heuret, A., Conrad, C. P., Funiciello, F., Lallemand, S., & Sandri, L. (2012). Relation between subduction megathrust earthquakes, trench sediment thickness and upper plate strain. *Geophysical Research Letters*, *39*(5).

Hubert-Ferrari, A., Armijo, R., King, G., Meyer, B., & Barka, A. (2002). Morphology, displacement, and slip rates along the North Anatolian Fault, Turkey. *Journal of Geophysical Research: Solid Earth (1978–2012)*, *107*(B10), ETG-9.

Hubert-Ferrari, A., King, G., Manighetti, I., Armijo, R., Meyer, B., & Tapponnier, P. (2003). Long-term elasticity in the continental lithosphere; modelling the Aden Ridge propagation and the Anatolian extrusion process. *Geophysical Journal International*, *153*(1), 111-132.

Ide, S., M. Takeo, and Y. Yoshida. 1996. Source process of the 1995 Kobe earthquake: Determination of spatio-temporal slip distribution by Bayesian modeling. Bull. Seis. Soc. Am 86 (3):547-566.

Ide, S., & Beroza, G. C. (2001). Does apparent stress vary with earthquake size?. *Geophysical Research Letters*, *28*(17), 3349-3352.

Ishimoto, M., & Iida, K. (1939). Observations of earthquakes registered with the microseismograph constructed recently. *Bull. Earthq. Res. Inst*, *17*, 443-478.

Jónsson, S., Zebker, H., Segall, P., & Amelung, F. (2002). Fault slip distribution of the 1999 Mw 7.1 Hector Mine, California, earthquake, estimated from satellite radar and GPS measurements. *Bulletin of the Seismological Society of America*, *92*(4), 1377-1389.

Ji, C., D. J. Wald, and D. V. Helmberger. 2002. Source description of the 1999 Hector Mine, California, earthquake, part II: Complexity of slip history. Bull. Seis. Soc. Am 92 (4):1208-1226.

Kagan, Y. Y. (1994). Observational evidence for earthquakes as a nonlinear dynamic process. *Physica D: Nonlinear Phenomena*, *77*(1), 160-192.

Kagan, Y. Y. (2002). Aftershock zone scaling. *Bulletin of the Seismological Society of America*, *92*(2), 641-655.

Kagan, Y. Y. (2004). Short-term properties of earthquake catalogs and models of earthquake source. *Bulletin of the Seismological Society of America*, *94*(4), 1207-1228.

Kagan, Y. Y. (2007). Why does theoretical physics fail to explain and predict earthquake occurrence? *Lecture Notes in Physics*, 705, pp. 303–359

Kagan, Y. Y. (2009). On the geometric complexity of earthquake focal zone and fault systems: A statistical study. *Physics of the Earth and Planetary Interiors*, *173*(3), 254-268.

Kagan, Y. Y. (2013). Earthquakes: Models, Statistics, Testable Forecasts. John Wiley & Sons.

Kanamori, H. (1977). The energy release in great earthquakes. *Journal of Geophysical Research*, *82*(20), 2981-2987.

Kanamori, H., & Anderson, D. L. (1975). Theoretical basis of some empirical relations in seismology. *Bulletin of the Seismological Society of America*, *65*(5), 1073-1095.

Kanamori, H., & Brodsky, E. E. (2004). The physics of earthquakes. *Reports on Progress in Physics*, *67*(8), 1429.

Kaneko, Y., & Fialko, Y. (2011). Shallow slip deficit due to large strike-slip earthquakes in dynamic rupture simulations with elasto-plastic off-fault response. *Geophysical Journal International*, *186*(3), 1389-1403.

Keilis-Borok, V.I., (1959) On the estimation of the displacement in an earthquake source and of source dimensions, Ann. Geofis. 12, ,205- 214,

Kim, Y. S., Peacock, D. C., & Sanderson, D. J. (2004). Fault damage zones. *Journal of Structural Geology*, *26*(3), 503-517.

Klinger, Y. (2010). Relation between continental strike-slip earthquake segmentation and thickness of the crust. *Journal of Geophysical Research: Solid Earth (1978–2012)*, *115*(B7).

Knopoff, L. (1958). Energy release in earthquakes. *Geophysical Journal of the Royal Astronomical Society*, *1*(1), 44-52.

Knuepfer, P. L. K. (1989). Implications of the characteristics of end-points of historical surface fault ruptures for the nature of fault segmentation. *Fault Segmentation and Controls of Rupture Initiation and Termination*, 89-315.

Langbein, J., Murray, J. R., & Snyder, H. A. (2006). Coseismic and initial postseismic deformation from the 2004 Parkfield, California, earthquake, observed by Global Positioning System, electronic distance meter, creepmeters, and borehole strainmeters. *Bulletin of the Seismological Society of America*, *96*(4B), S304-S320.

Lasserre, C., Peltzer, G., Crampé, F., Klinger, Y., Van der Woerd, J., & Tapponnier, P. (2005). Coseismic deformation of the 2001 Mw= 7.8 Kokoxili earthquake in Tibet, measured by synthetic aperture radar interferometry. *Journal of Geophysical Research: Solid Earth (1978–2012)*, *110*(B12).

Lavallée, D., Liu, P., & Archuleta, R. J. (2006). Stochastic model of heterogeneity in earthquake slip spatial distributions. *Geophysical Journal International*, *165*(2), 622-640.

Lettis, W., Bachhuber, J., Witter, R., Brankman, C., Randolph, C. E., Barka, A., ... & Kaya, A. (2002). Influence of releasing step-overs on surface fault rupture and fault segmentation: Examples from the 17 August 1999 Izmit earthquake on the North Anatolian fault, Turkey. *Bulletin of the Seismological Society of America*, *92*(1), 19-42.

Li, Z., Elliott, J. R., Feng, W., Jackson, J. A., Parsons, B. E., & Walters, R. J. (2011). The 2010 MW 6.8 Yushu (Qinghai, China) earthquake: Constraints provided by InSAR and body wave seismology. *Journal of Geophysical Research: Solid Earth (1978–2012)*, *116*(B10).

Liu, P., Custódio, S., & Archuleta, R. J. (2006). Kinematic inversion of the 2004 M 6.0 Parkfield earthquake including an approximation to site effects. *Bulletin of the Seismological Society of America*, *96*(4B), S143-S158.

Liu-Zeng, J., Heaton, T., & DiCaprio, C. (2005). The effect of slip variability on earthquake slip-length scaling. *Geophysical Journal International*, *162*(3), 841-849.

Ma, K. F., J. Mori, S. J. Lee, and S. B. Yu. 2001. Spatial and temporal distribution of slip for the 1999 Chi-Chi, Taiwan, earthquake. Bull. Seis. Soc. Am 91 (5):1069-1087.

Madariaga, R. (1976). Dynamics of an expanding circular fault. *Bulletin of the Seismological Society of America*, *66*(3), 639-666.

Magistrale & Rockwell, 1996;

Mai, P. M., & Beroza, G. C. (2000). Source scaling properties from finite-fault-rupture models. *Bulletin of the Seismological Society of America*, *90*(3), 604-615.

Mai, P. M., & Beroza, G. C. (2002). A spatial random field model to characterize complexity in earthquake slip. *Journal of Geophysical Research: Solid Earth (1978–2012)*, *107*(B11), ESE-10.

Manighetti, I. (1993). *Dynamique des systèmes extensifs en Afar* (Doctoral dissertation).

Manighetti, I., Tapponnier, P., Courtillot, V., Gruszow, S., & Gillot, P. Y. (1997). Propagation of rifting along the Arabia-Somalia plate boundary: The gulfs of Aden and Tadjoura. *Journal of Geophysical Research: Solid Earth (1978–2012)*, *102*(B2), 2681-2710.

Manighetti, I., Tapponnier, P., Gillot, P. Y., Jacques, E., Courtillot, V., Armijo, R., ... & King, G. (1998). Propagation of rifting along the Arabia-Somalia plate boundary: Into Afar. *Journal of Geophysical Research: Solid Earth (1978–2012)*, *103*(B3), 4947-4974.

Manighetti, I., King, G. C. P., Gaudemer, Y., Scholz, C. H., & Doubre, C. (2001). Slip accumulation and lateral propagation of active normal faults in Afar. *Journal of Geophysical Research: Solid Earth (1978–2012)*, *106*(B7), 13667-13696.

Manighetti, I., Tapponnier, P., Courtillot, V., Gallet, Y., Jacques, E., & Gillot, P. Y. (2001). Strain transfer between disconnected, propagating rifts in Afar. *Journal of Geophysical Research: Solid Earth (1978–2012)*, *106*(B7), 13613-13665.

Manighetti, I., King, G., & Sammis, C. G. (2004). The role of off-fault damage in the evolution of normal faults. *Earth and Planetary Science Letters*, *217*(3), 399-408.

Manighetti, I., Campillo, M., Sammis, C., Mai, P. M., & King, G. (2005). Evidence for self-similar, triangular slip distributions on earthquakes: Implications for earthquake and fault mechanics. *Journal of Geophysical Research: Solid Earth (1978–2012)*, *110*(B5).

Manighetti, I., Campillo, M., Bouley, S., & Cotton, F. (2007). Earthquake scaling, fault segmentation, and structural maturity. *Earth and Planetary Science Letters*, *253*(3), 429-438.

Manighetti, I., Zigone, D., Campillo, M., & Cotton, F. (2009). Self-similarity of the largest-scale segmentation of the faults: Implications for earthquake behavior. *Earth and Planetary Science Letters*, *288*(3), 370-381.

Manighetti, I., De Barros, L., Caulet, C., Perrin, C., & Cappa, F. (2013, December). Deterministic, self-similar slip and stress heterogeneity on seismogenic faults. In *AGU Fall Meeting Abstracts* (Vol. 1, p. 07).

Marliyani, G. I., Rockwell, T. K., Onderdonk, N. W., & McGill, S. F. (2013). Straightening of the Northern San Jacinto Fault, California, as Seen in the Fault-Structure Evolution of the San Jacinto Valley Stepover. *Bulletin of the Seismological Society of America*, *103*(3), 2047-2061.

Marone, C. (1998). Laboratory-derived friction laws and their application to seismic faulting. *Annual Review of Earth and Planetary Sciences*, *26*(1), 643-696.

McGrath, A. G., & Davison, I. (1995). Damage zone geometry around fault tips. *Journal of Structural Geology*, *17*(7), 1011-1024.

McKenzie, D. P. (1969). The relation between fault plane solutions for earthquakes and the directions of the principal stresses. *Bulletin of the Seismological Society of America*, *59*(2), 591-601.

Michel, R., & Avouac, J. P. (2002). Deformation due to the 17 August 1999 Izmit, Turkey, earthquake measured from SPOT images. *Journal of Geophysical Research: Solid Earth (1978–2012)*, *107*(B4), ETG-2.

Murray, J., & Langbein, J. (2006). Slip on the San Andreas Fault at Parkfield, California, over two earthquake cycles, and the implications for seismic hazard. *Bulletin of the Seismological Society of America*, *96*(4B), S283-S303.

Noda, H., Lapusta, N., & Kanamori, H. (2013). Comparison of average stress drop measures for ruptures with heterogeneous stress change and implications for earthquake physics. *Geophysical Journal International*, *193*(3), 1691-1712.

Omori, F. (1894). Journal of the College of Science. *Imperial Univeristy of Tokyo*, *7*, 111-200

Oglesby, D. (2008). Rupture termination and jump on parallel offset faults. *Bulletin of the Seismological Society of America*, *98*(1), 440-447.

Oskin, M. E., K. Le, and M. D. Strane (2007), Quantifying fault-zone activity in arid environments with high-resolution topography, Geophys. Res. Lett., 34, L23S05, doi:10.1029/2007GL031295.

Parsons, T., Field, E. H., Page, M. T., & Milner, K. (2012). Possible earthquake rupture connections on mapped California faults ranked by calculated coulomb linking stresses. *Bulletin of the Seismological Society of America*, *102*(6), 2667-2676.

Peacock, D. C. P., & Sanderson, D. J. (1991). Displacements, segment linkage and relay ramps in normal fault zones. *Journal of Structural Geology*, *13*(6), 721-733.

Power, W. L., Tullis, T. E., Brown, S. R., Boitnott, G. N., & Scholz, C. H. (1987). Roughness of natural fault surfaces. *Geophysical Research Letters*, *14*(1), 29-32.

Prejean, S. G., & Ellsworth, W. L. (2001). Observations of earthquake source parameters at 2 km depth in the Long Valley caldera, eastern California. *Bulletin of the Seismological Society of America*, *91*(2), 165-177.

Punongbayan, P.S., Rimando, R.E., Daligdig, J.A., Besana, G.M., Daag, A.S., Nakata, T. & Tsutsumi, H. 1990. The July 16 Luzon Earthquake-A Technical Monograph. Philippine Institute of Volcanology and Seismology 2001 (http://www.phivolcs.dost.gov.ph)

Quigley, M., Van Dissen, R., Litchfield, N., Villamor, P., Duffy, B., Barrell, D., ... & Noble, D. (2012). Surface rupture during the 2010 Mw 7.1 Darfield (Canterbury) earthquake: Implications for fault rupture dynamics and seismic-hazard analysis. *Geology*, *40*(1), 55-58.

Radiguet, M., Cotton, F., Manighetti, I., Campillo, M., & Douglas, J. (2009). Dependency of near-field ground motions on the structural maturity of the ruptured faults. *Bulletin of the Seismological Society of America*, *99*(4), 2572-2581.

Rahe, B., Ferrill, D. A., & Morris, A. P. (1998). Physical analog modeling of pull-apart basin evolution. *Tectonophysics*, *285*(1), 21-40.

Rice, J. R. (1980). The mechanics of earthquake rupture, Physics of the Earth's Interior AM Dziewonski, E. Boschi, 555–649.

Richter, C. F. (1958). Elementary seismology.. San Francisco: W.H.Freeman

Robinson, D. P., Das, S., & Searle, M. P. (2010). Earthquake fault superhighways. *Tectonophysics*, *493*(3), 236-243.

Romanowicz, B. (1992). Strike-slip earthquakes on quasi-vertical transcurrent faults: Inferences for general scaling relations. *Geophysical Research Letters*, *19*(5), 481-484.

Romanowicz, B. (1994). Comment on "A reappraisal of large earthquake scaling" by C. Scholz. *Bulletin of the Seismological Society of America*, *84*(5), 1675-1676.

Romanowicz, B., & Ruff, L. J. (2002). On moment-length scaling of large strike slip earthquakes and the strength of faults. *Geophysical research letters*, *29*(12), 45-1.

Romanowicz, B., & Rundle, J. B. (1993). On scaling relations for large earthquakes. *Bulletin of the Seismological Society of America*, *83*(4), 1294-1297.

Ruina, A. (1983). Slip instability and state variable friction laws. *Journal of Geophysical Research: Solid Earth (1978–2012)*, *88*(B12), 10359-10370.

Salyards, S. L., Sieh, K. E., & Kirschvink, J. L. (1992). Paleomagnetic measurement of nonbrittle coseismic deformation across the San Andreas fault at Pallett Creek. *Journal of Geophysical Research: Solid Earth (1978–2012)*, *97*(B9), 12457-12470.

Savage, H. M., & Brodsky, E. E. (2011). Collateral damage: Evolution with displacement of fracture distribution and secondary fault strands in fault damage zones. *Journal of Geophysical Research: Solid Earth (1978–2012)*, *116*(B3).

Sato, R. (1979). Theoretical basis on relationships between focal parameters and earthquake magnitude. *Journal of Physics of the Earth*, *27*(5), 353-372.

Schlagenhauf, A., Manighetti, I., Malavieille, J., & Dominguez, S. (2008). Incremental growth of normal faults: Insights from a laser-equipped analog experiment. *Earth and Planetary Science Letters*, *273*(3), 299-311.

Schlagenhauf, A., Manighetti, I., Benedetti, L., Gaudemer, Y., Finkel, R., Malavieille, J., & Pou, K. (2011). Earthquake supercycles in Central Italy, inferred from 36Cl exposure dating. *Earth and Planetary Science Letters*, *307*(3), 487-500.

Schlische, R. W., Young, S. S., Ackermann, R. V., & Gupta, A. (1996). Geometry and scaling relations of a population of very small rift-related normal faults. *Geology*, *24*(8), 683-686.

Schmedes, J., Archuleta, R. J., & Lavallée, D. (2010). Correlation of earthquake source parameters inferred from dynamic rupture simulations. *Journal of Geophysical Research: Solid Earth (1978–2012)*, *115*(B3).

Scholz, C. H. (1968). The frequency-magnitude relation of microfracturing in rock and its relation to earthquakes. *Bulletin of the Seismological Society of America*, *58*(1), 399-415.

Scholz, C. H. (1982). Scaling laws for large earthquakes: consequences for physical models. *Bulletin of the Seismological Society of America*, *72*(1), 1-14.

Scholz, C. H. (1989). Mechanics of faulting. *Annual Review of Earth and Planetary Sciences*, *17*, 309-334.

Scholz, C. H. (1991), in Riste, T., Sherrington, D., 1991. (eds), *Spontaneous Formation of Space-Time and Criticality*. Dordrecht : Kluwer.

Scholz, C. H. (1994a). A reappraisal of large earthquake scaling. *Bulletin of the Seismological Society of America*, *84*(1), 215-218.

Scholz, C. H. (1994b). Reply to comments on "A reappraisal of large earthquake scaling" by C. Scholz. *Bulletin of the Seismological Society of America*, *84*(5), 1677-1678.

Scholz, C. H. (2002). *The mechanics of earthquakes and faulting*. Cambridge university press.

Scholz, C. H. (2013, December). A Holocene average seismic flux rate for the Cascadia Subduction Zone. In *AGU Fall Meeting Abstracts* (Vol. 1, p. 01).

Scholz, C. H., & Lawler, T. M. (2004). Slip tapers at the tips of faults and earthquake ruptures. *Geophysical research letters*, *31*(21).

Scholz, C. H., Aviles, C. A., & Wesnousky, S. G. (1986). Scaling differences between large interplate and intraplate earthquakes. *Bulletin of the Seismological Society of America*, *76*(1), 65-70.

Scholz, C. H., Dawers, N. H., Yu, J. Z., Anders, M. H., & Cowie, P. A. (1993). Fault growth and fault scaling laws: Preliminary results. *Journal of Geophysical Research: Solid Earth (1978–2012)*, *98*(B12), 21951-21961.

Scholz, C. H., Ando, R., & Shaw, B. E. (2010). The mechanics of first order splay faulting: The strike-slip case. *Journal of Structural Geology*, *32*(1), 118-126.

Schwartz, D. P., & Coppersmith, K. J. (1984). Fault behavior and characteristic earthquakes: Examples from the Wasatch and San Andreas fault zones. *Journal of Geophysical Research: Solid Earth (1978–2012)*, *89*(B7), 5681-5698.

Segall, P., & Pollard, D. D. (1980). Mechanics of discontinuous faults. *Journal of Geophysical Research: Solid Earth (1978–2012)*, *85*(B8), 4337-4350.

Sengör, A. M. C. (1979). The North Anatolian transform fault: its age, offset and tectonic significance. *Journal of the Geological Society*, *136*(3), 269-282.

Shaw, J. H., Plesch, A., Dolan, J. F., Pratt, T. L., & Fiore, P. (2002). Puente Hills blind-thrust system, Los Angeles, California. *Bulletin of the Seismological Society of America*, *92*(8), 2946-2960.

Shaw, B. E. (2009). Constant stress drop from small to great earthquakes in magnitude-area scaling. *Bulletin of the Seismological Society of America*, *99*(2A), 871-875.

Shaw, B. E. (2013). Earthquake Surface Slip-Length Data is Fit by Constant Stress Drop and is Useful for Seismic Hazard Analysis. *Bulletin of the Seismological Society of America*, *103*(2A), 876-893.

Shaw, B. E., & Scholz, C. H. (2001). Slip-length scaling in large earthquakes: Observations and theory and implications for earthquake physics. *Geophysical Research Letters*, *28*(15), 2995-2998.

Shimazaki, K., & Nakata, T. (1980). Time-predictable recurrence model for large earthquakes. *Geophysical Research Letters*, *7*(4), 279-282.

Sibson, R. H. (1977). Fault rocks and fault mechanisms. *Journal of the Geological Society*, *133*(3), 191-213.

Sibson, R. H. (1986). Earthquakes and rock deformation in crustal fault zones. *Annual Review of Earth and Planetary Sciences*, *14*, 149.

Sibson, R. H. (2003). Thickness of the seismic slip zone. *Bulletin of the Seismological Society of America*, *93*(3), 1169-1178.

Somerville, P., Irikura, K., Graves, R., Sawada, S., Wald, D., Abrahamson, N., ... & Kowada, A. (1999). Characterizing crustal earthquake slip models for the prediction of strong ground motion. *Seismological Research Letters*, *70*(1), 59-80.

Stirling, M. W., Wesnousky, S. G., & Shimazaki, K. (1996). Fault trace complexity, cumulative slip, and the shape of the magnitude-frequency distribution for strike-slip faults: A global survey. *Geophysical Journal International*, *124*(3), 833-868.

Stockwell, R. G., Mansinha, L., & Lowe, R. P. (1996). Localization of the complex spectrum: the S transform. *Signal Processing, IEEE Transactions on*, *44*(4), 998-1001.

Sylvester, A. G. (1988). Strike-slip faults. *Geological Society of America Bulletin*, *100*(11), 1666-1703.

Tchalenko, J. S., & Berberian, M. (1975). Dasht-e Bayaz fault, Iran: earthquake and earlier related structures in bed rock. *Geological Society of America Bulletin*, *86*(5), 703-709.

Thurber, C., Zhang, H., Waldhauser, F., Hardebeck, J., Michael, A., & Eberhart-Phillips, D. (2006). Three-dimensional compressional wavespeed model, earthquake relocations, and focal mechanisms for the Parkfield, California, region. *Bulletin of the Seismological Society of America*, *96*(4B), S38-S49.

Umeda, Y., Yamashita, T., Tada, T., & Kame, N. (1996). Possible mechanisms of dynamic nucleation and arresting of shallow earthquake faulting. *Tectonophysics*, *261*(1), 179-192.

Utsu, T. (2002). Statistical features of seismicity. *Int. Handbook of Earthquake & Engineering Seismology,* part A, ed W H K Lee et al (San Diego, CA:Academic) pp 719-724

Vallée, M., Charléty, J., Ferreira, A. M., Delouis, B., & Vergoz, J. (2011). SCARDEC: a new technique for the rapid determination of seismic moment magnitude, focal mechanism and source time functions for large earthquakes using body-wave deconvolution. *Geophysical Journal International*, *184*(1), 338-358.

Vallée, M. (2013). Source time function properties indicate a strain drop independent of earthquake depth and magnitude. *Nature communications*, *4*.

Wald, D. J. (1996). Slip history of the 1995 Kobe, Japan, earthquake determined from strong motion, teleseismic, and geodetic data. J. Phys. Earth 44 (5):489-503.

Wald, D. J., T. H. Heaton, and K. W. Hudnut. 1996. The slip history of the 1994 Northridge, California, earthquake determined from strong-motion, teleseismic, GPS, and leveling data. Bull. Seis. Soc. Am 86 (1):S49-S70.

Walsh, J. J., Watterson, J., Bailey, W. R., & Childs, C. (1999). Fault relays, bends and branch-lines. *Journal of Structural Geology*, *21*(8), 1019-1026.

Walsh, J. J., Nicol, A., & Childs, C. (2002). An alternative model for the growth of faults. *Journal of Structural Geology*, *24*(11), 1669-1675.

Walsh, J. J., & Watterson, J. (1988). Analysis of the relationship between displacements and dimensions of faults. *Journal of Structural Geology*, *10*(3), 239-247.

Wang, K., & Bilek, S. L. (2014). Invited review paper: Fault creep caused by subduction of rough seafloor relief. *Tectonophysics*, *610*, 1-24.

Wells, D. L., & Coppersmith, K. J. (1994). New empirical relationships among magnitude, rupture length, rupture width, rupture area, and surface displacement. *Bulletin of the Seismological Society of America*, *84*(4), 974-1002.

Wesnousky, S. G. (2008). Displacement and geometrical characteristics of earthquake surface ruptures: Issues and implications for seismic-hazard analysis and the process of earthquake rupture. *Bulletin of the Seismological Society of America*, *98*(4), 1609-1632.

Wesnousky, S. G. (2006). Predicting the endpoints of earthquake ruptures. *Nature*, *444*(7117), 358-360.

Xu, X., Yu, G., Klinger, Y., Tapponnier, P., & Van Der Woerd, J. (2006). Reevaluation of surface rupture parameters and faulting segmentation of the 2001 Kunlunshan earthquake (Mw7. 8), northern Tibetan Plateau, China. *Journal of Geophysical Research: Solid Earth (1978–2012)*, *111*(B5).

Yomogida, K., Yoshizawa, K., Koyama, J., & Tsuzuki, M. (2011). Along-dip segmentation of the 2011 off the Pacific coast of Tohoku Earthquake and comparison with other megathrust earthquakes. *Earth, planets and space*, *63*(7), 697-701.

Yoshida, S., K. Koketsu, B. Shibazaki, T. Sagiya, T. Kato, and Y. Yoshida. 1996. Joint inversion of near- and far-field waveforms and geodetic data for the rupture process of the 1995 Kobe earthquake. J. Phys. Earth 44 (5):437-454.

Yue, H., Lay, T., Freymueller, J. T., Ding, K., Rivera, L., Ruppert, N. A., & Koper, K. D. (2013). Supershear rupture of the 5 January 2013 Craig, Alaska (Mw 7.5) earthquake. *Journal of Geophysical Research: Solid Earth*, *118*(11), 5903-5919.

Zeng, Y., and J. Anderson. 2000. Evaluation of numerical procedures for simulating near-fault long-period ground motions using Zeng method. Report 2000/01 to the PEER Utilities Program, available at http://peer.berkeley.edu

Zhang, P., Mao, F., & Slemmons, D. B. (1999). Rupture terminations and size of segment boundaries from historical earthquake ruptures in the Basin and Range Province. *Tectonophysics*, *308*(1), 37-52.